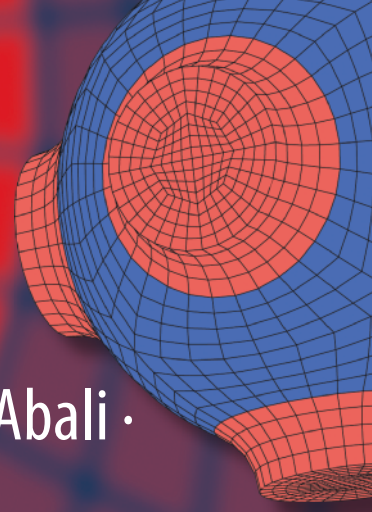


Advanced Structured Materials

Ivan Giorgio · Luca Placidi ·
Emilio Barchiesi · Bilen Emek Abali ·
Holm Altenbach *Editors*



Theoretical Analyses, Computations, and Experiments of Multiscale Materials

A Tribute to Francesco dell'Isola

 Springer


Advanced Structured Materials

Volume 175

Series Editors

Andreas Öchsner, Faculty of Mechanical Engineering, Esslingen University of Applied Sciences, Esslingen, Germany

Lucas F. M. da Silva, Department of Mechanical Engineering, Faculty of Engineering, University of Porto, Porto, Portugal

Holm Altenbach , Faculty of Mechanical Engineering, Otto von Guericke University Magdeburg, Magdeburg, Sachsen-Anhalt, Germany

Common engineering materials are reaching their limits in many applications, and new developments are required to meet the increasing demands on engineering materials. The performance of materials can be improved by combining different materials to achieve better properties than with a single constituent, or by shaping the material or constituents into a specific structure. The interaction between material and structure can occur at different length scales, such as the micro, meso, or macro scale, and offers potential applications in very different fields.

This book series addresses the fundamental relationships between materials and their structure on overall properties (e.g., mechanical, thermal, chemical, electrical, or magnetic properties, etc.). Experimental data and procedures are presented, as well as methods for modeling structures and materials using numerical and analytical approaches. In addition, the series shows how these materials engineering and design processes are implemented and how new technologies can be used to optimize materials and processes.

Advanced Structured Materials is indexed in Google Scholar and Scopus.

More information about this series at <https://link.springer.com/bookseries/8611>


Ivan Giorgio · Luca Placidi ·
Emilio Barchiesi · Bilen Emek Abali ·
Holm Altenbach
Editors


Theoretical Analyses, Computations, and Experiments of Multiscale Materials


A Tribute to Francesco dell'Isola


 Springer


Editors

Ivan Giorgio 
DICEAA
University of L'Aquila
L'Aquila, Italy

Emilio Barchiesi 
Dipartimento di Architettura
design e urbanistica
Università degli Studi di Sassari
Sassari, Italy

Holm Altenbach 
Fakultät für Maschinenbau
Otto-von-Guericke-Universität Magdeburg
Magdeburg, Germany

Luca Placidi 
Engineering Faculty
International Telematic University
UNINETTUNO
Rome, Italy

Bilen Emek Abali 
Department of Materials Science
and Engineering
Uppsala University
Uppsala, Sweden

ISSN 1869-8433

Advanced Structured Materials

ISBN 978-3-031-04547-9

<https://doi.org/10.1007/978-3-031-04548-6>

ISSN 1869-8441 (electronic)

ISBN 978-3-031-04548-6 (eBook)

© The Editor(s) (if applicable) and The Author(s), under exclusive license to Springer Nature Switzerland AG 2022, corrected publication 2022

This work is subject to copyright. All rights are solely and exclusively licensed by the Publisher, whether the whole or part of the material is concerned, specifically the rights of translation, reprinting, reuse of illustrations, recitation, broadcasting, reproduction on microfilms or in any other physical way, and transmission or information storage and retrieval, electronic adaptation, computer software, or by similar or dissimilar methodology now known or hereafter developed.

The use of general descriptive names, registered names, trademarks, service marks, etc. in this publication does not imply, even in the absence of a specific statement, that such names are exempt from the relevant protective laws and regulations and therefore free for general use.

The publisher, the authors and the editors are safe to assume that the advice and information in this book are believed to be true and accurate at the date of publication. Neither the publisher nor the authors or the editors give a warranty, expressed or implied, with respect to the material contained herein or for any errors or omissions that may have been made. The publisher remains neutral with regard to jurisdictional claims in published maps and institutional affiliations.

This Springer imprint is published by the registered company Springer Nature Switzerland AG
The registered company address is: Gewerbestrasse 11, 6330 Cham, Switzerland

*A tribute to Francesco dell'Isola, a visionary
scientist of the 21th century*

Preface

We believe ourselves to be incredibly lucky to be co-workers of Francesco dell’Isola, whom each of us met in different periods of their lives. We all have in common the fact that, soon after meeting him, we understood that he is a unique scientist, not only because of his extremely wide knowledge and erudition, but also because of his illuminating presence among his students and colleagues: Francesco dell’Isola knows that teamwork is crucially important in science. While he is always busy doing something scientifically, he puts much effort into inspiring new students as well as in helping to create ingenious connections between people.

The workshops that he organizes in Arpino, where one is allowed to interrupt the speaker to discuss any single point—the devil is in the details, after all—and where the time schedule has not to be strictly followed (like Italian trains do!), have definitely determined some of the recent research lines in theoretical and applied mechanics. Such gatherings lead to establishment of many international research collaborations. Therefore, we can confidently state that Francesco dell’Isola is a true influencer of contemporary continuum mechanics. We dedicate this book to him on the occasion of his 60th birthday, with the wish of continuing in his activities for many more years, full of energy and curiosity.

L’Aquila
Rome
Sassari
Stockholm
Magdeburg

Ivan Giorgio
Luca Placidi
Emilio Barchiesi
Bilen Emek Abali
Holm Altenbach

Fig. 1 Francesco dell'Isola with Richard Toupin, 4th Canadian Conference on Nonlinear Solid Mechanics, Montreal, July 2013



Fig. 2 Francesco dell'Isola is in action as a hobby photographer in Sora, province of Frosinone



Foreword

There are a lot of things that would be worth saying about Francesco and his scientific and academic activity. Here I prefer to spend just a few words about a quality that, although it could seem of minor interest, in my opinion, deserves to be stressed.

I dare say that (at least) in the Italian Academic Community, among appreciate scientists, there are not many that are really able to teach something to someone. And also between them there is a very limited number, quite exceptions, that can be defined (using a Latin word) *magister*, that is a scientist able not only to teach something to students but also to act as a real guide and mentor in research and life for them. They can be distinguished from the others as having not only a strong culture but also the ability to foster their students to develop autonomy, maturity, critical sense and open mindedness, being also able to really help them to grow and find a way as men/women as well as researchers.

This can be done in many ways even though a necessary condition is to encourage and help students to interact, as far as possible, with other distinguished researchers as, following Goffredo Fofi, it can be said that

(only) the bad teacher do not tolerate that their pupils could have other mentors, even though no eminent teacher ever had only one teacher in his life.

With this in mind I think that Francesco, without any doubt, can be defined a good teacher or, better, a *magister*.

Rome

Nicola Luigi Rizzi

Fig. 3 Francesco dell'Isola with Emilio Turco, Rome, January 2021



Fig. 4 Lesson on Cyclopean Wall at Arpino, 2019



Francesco dell'Isola: Scholar, Scientist, Historian, Philosopher

I am delighted to have the opportunity to present to my dear friend and valued colleague, Francesco dell'Isola, this collection of papers, authored by many of his friends and admirers, on the occasion of his 60th birthday.

Francesco is quite literally the glue that binds together a far-flung community of mechanicians, mathematical physicists, and engineers that spans the globe. Thus has emerged the dell'Isola School, concerned with real-world applications of topics such as strain-gradient elasticity, homogenization of lattice-like substructures, fabric materials, and theories of n -th grade continua, once regarded as esoterica, but now, thanks largely to Francesco's efforts, playing a central role in the understanding, modeling, and design of the advanced mechanical metamaterials so crucial to emerging technologies. Francesco dell'Isola is a person of unusually deep culture and a great aficionado of history. Thanks to his tireless efforts in translating the great works of G. Piola from 19th century Italian to modern English, the international community now has access to a profound corpus of thought on the foundations of mechanics that, remarkably, presages much of what is now viewed as the most compelling aspects of modern research.

All who have had the good fortune to interact with Francesco dell'Isola know him as a devoted mentor and protector of promising young scientists. His efforts in founding the M&MOCS center (Mathematics and Mechanics of Complex Systems), and the prestigious journal of the same name, have yielded a most auspicious milieu in which young talent can thrive and flourish.

I extend my thanks and best wishes to Francesco dell'Isola for his friendship and guidance, and for setting such a fine example of dedication and devotion to our subject.

Berkeley

David Steigmann



Fig. 5 At UC Berkeley with a view over the bay and the Golden Gate Bridge, 2018



Fig. 6 Pantographic structures get broken, too, sad but true!

It is a pleasure and honor to write this birthday message for Francesco dell'Isola—a colleague, a guide, and a friend. As he reaches a significant juncture in his life journey, Francesco has substantial accomplishments that are worthy of celebration. I am certain he will be kind enough to indulge us in this felicitation. His contributions in continuum mechanics are well known and formidable. One simply has to look at his scholarly contributions to understand the breadth and depth of his impact on contemporary continuum mechanics. The following quote from Gerard Maugin's work on developments in continuum mechanics says volumes:

“Presently, the most active and creative contributor to our field seems to be Francesco dell'Isola (born 1962). Formed in Naples with A. Romano and true mathematician in his style of approach, his interests span many particular fields . . .” (in *Continuum Mechanics through the Twentieth Century: A Concise Historical Perspective*, G.A. Maugin, Springer, Dordrecht, 2013).

His investigations cover topics ranging from his early works on non-material interfaces to recent works on metamaterials and generalized continua. It is his work on second gradient continuum theories that resulted in our fortuitous and eventful meeting at a conference in California in 2010. It was immediately clear to me that my own quest would benefit with a deeper interaction with Francesco and his research group in M&MoCS. My many interactions with him have been fruitful and have resulted in many co-authored publications.

I will not catalog here the long list of topics that Francesco has researched and published. Instead, I will highlight his commitment to the field of mechanics, its history and to its growth as a fundamental mathematical science. M&MoCS and the associated journal are efforts in this direction. So are the excellent workshops and meetings with unfettered exchange in Cisterna di Latina, in Arpino, and in Guiliano di Roma. Those who have participated in these will attest to the warm hospitality of Francesco as well as recall the lessons in ancient Roman history besides the intense scientific exchanges. The breadth of Francesco's interests are astonishing and are reflected in his publications that include works on economics as well as unclassifiable work that interweaves fiction, facts, history, and mathematics; and deals with human questions.

I have personally benefited from deep deliberations with Francesco on topic ranging from Greco-Roman history, its philosophy, mathematical and scientific achievements, and medieval Italian accomplishments, current scientific questions to cultural issues. In these interchanges, Francesco's openness and ability to accept alternative viewpoints are notable. I hope that these interchanges continue so we can live up to the ideals of the ancient mantra from Rig-veda

..आ नो भद्राः क्रतवो यन्तु विश्वत् अदब्धासो अपरीतास उद्भिदः| ... ||1.89.1||

(May we receive noble/beneficial/munificent thoughts from all directions (every side), unaltered, unconstrained, unsubdued in every possible way. . . . (1.89.1).”

On his 60th birthday, I wish him unhindered success, perfect health, and infinite energy, such that we may continue our discussions, collaborations, and explorations on wide ranging topics.

Francesco dell’Isola: a μαθητικός of Magna Graecia

Emilio Barchiesi & Emilio Turco

Biographical Sketch

Francesco dell’Isola was born in July 1962, in Naples. He graduates in Physics in 1986 at the University of Naples Federico II under the direction of Prof. Antonio Romano. Always under the direction of Prof. Romano, in 1992, he obtains the Doctorate for the research in Mathematical physics discussing a thesis entitled *Rational Thermodynamics of Nonmaterial Bidimensional Continua*. In the academic year 1991/1992 he wins a competitive selection to become Researcher in Mathematical physics at the University of Naples Federico II. Shortly after, in 1992, winner of a competitive selection for becoming Researcher in Strength of materials, he moves to the Sapienza University of Rome, where he will work with another of his Masters, Prof. Antonio Di Carlo. In 1995, he obtains the *Qualification aux fonctions de maître de conférences* in the sixtieth section (*Mécanique, génie mécanique, génie civil*) and, in 1997, becomes Associate Professor. In 2004, he takes up the role of Adjunct Associate Professor at Virginia Polytechnic Institute and State University. In 2005 he obtains the National Eligibility to the functions of Full Professor. The following year he becomes Full Professor at the Sapienza University of Rome.

In 2009 he is among the founders of the MEMOCS Research Center for Mathematics and Mechanics of Complex Systems, which since its foundation organizes every year workshops, summer schools, research weeks, prestigious conferences (Euromech Colloquia, Soriau Colloquium, ICoNSoM, ICMM, GeoMech, to name a few) and to which are affiliated more than 200 scientists from all over the world. In 2016 he moves to the University of L’Aquila, where he is also the Director of

E. Barchiesi

Dipartimento di Architettura, Design e Urbanistica, Università degli Studi di Sassari, Italia.
e-mail: barchiesiemilio@gmail.com

E. Turco

Dipartimento di Architettura, Design e Urbanistica, Università degli Studi di Sassari, Italia.
e-mail: eturco@uniss.it

the MEMOCS Center, a position he still holds. Then, in 2017, he takes the role of the Director of the Research Laboratory for the problems of strength, dynamics and service life at Lobačevskij University in Nižnij Novgorod, Russia, where he is also the Principal Investigator of a project funded under the prestigious MegaGrant program. In 2018, he becomes Russell Severance Springer Professor in the Department of Mechanical Engineering at the University of California, Berkeley.

Scientific Contributions

The scientific career of Francesco dell’Isola has been since the beginning focused on avant-garde themes. On the one hand there are the more purely theoretical studies, including early work on curved interphase interfaces, in which he began to be interested in second gradient continua, fluids in this case. The interest in second gradient theories, developed during his French period and inspired by the reading of the texts of Paul Germain, led him to write jointly with Pierre Seppecher the work *The relationship between edge contact forces, double forces and interstitial working allowed by the principle of virtual power*, published in 1995 and of considerable impact on much of the subsequent literature concerning the subject. Initially, the most applied studies concern the De Saint-Venant’s Problem (addressed starting with the contribution *Outlooks in Saint-Venant Theory I: Formal Expansions for Torsion of Bredt-like sections* published in 1994), the mechanics of large ice masses (in collaboration with Kolumban Hutter, addressed from the contribution *Continuum mechanical modelling of the dissipative processes in the sediment-water layer below glaciers* published in 1997), and then turn to passive control of beams, shells, and plates through the use of distributed piezo-electric transducers, and finally to deformable porous solids, with Olivier Coussy and Felix Darve.

Francesco dell’Isola moves with incredible agility between theoretical and applicative interests. While in 2003 he registers a patent at the US Patent Office for the development of passive control systems, the problem of the synthesis of circuits analogous to structures,¹ already addressed for the development of these control systems, stimulates the first theoretical contributions in the theory of mechanical metamaterials, led by the work written with Jean-Jacques Alibert and Pierre Seppecher in 2003, *Truss modular beams with deformation energy depending on higher displacement gradients*. In this last work some ingenious examples of micro-structures are proposed which, at the macro-scale, present higher gradient effects. It becomes increasingly clear to Francesco dell’Isola that the next challenge to face, the one in which he is still engaged, is represented by the solution of the problem of synthesis of metamaterials:

¹ It is therefore no coincidence that Francesco dell’Isola, during his lectures, is used to quote a statement taken from the twelfth of The Feynman Lectures on Physics: “The same equations have the same solutions.”

Having specified a given mechanical behavior at the macro-scale, what, if any, are the micro-structures that realize it?

In this regard, the fact that he has recently coined the terminology “ontology of metamaterials” plastically gives an idea of his intellectual spirit² (cf. *dell'Isola, F., Barchiesi, E., & Misra, A. (2020). Naive Model Theory: Its Applications to the Theory of Metamaterials Design. Discrete and Continuum Models for Complex Metamaterials, 141.*). This new branch of mechanics should deal with the question:

What are the constitutive equations, induced by the presence of a micro-structure, that can translate into observable behavior in reality?

To give a better understanding of what is meant by this terminology, he traces the origins of this new branch of mechanics to the arguments that lead to the conclusion that the Poisson's ratio for an isotropic, homogeneous solid has to take a value between -1 and 0.5.

An Eclectic Scientist

At this point, as many of his colleagues and students could testify, it will not be difficult to believe that Francesco dell'Isola's lectures and scientific presentations are characterized by the fact that, often, they include quotations from and comparisons with the thought of Francis Bacon, Sextus Empiricus, Albert Einstein, Epicurus, Galileo Galilei, Antonio Gramsci, Pierre Simon Laplace, Democritus, Giambattista Vico, Immanuel Kant, Karl Popper, Archimedes, Aristotle, Plato and many others. His propensity for interdisciplinarity is not reduced to this. We can mention, among other things, that he was also involved in analyzing, by means of game theory formalism, the short and long term consequences affecting a scientific system in which merit is evaluated only on the basis of bibliometric indicators,³ as well as the search for methods of evaluation and reward that induce virtuous behavior among researchers. We note that on this occasion he did not fail to show off his characteristic

² Probably cultivated since childhood by his dear uncle Luigi De Luca, professor of philosophy at a High School. In the book *Big-(Wo)men, Tyrants, Chiefs, Dictators, Emperors and Presidents. Towards the Mathematical Understanding of Social Groups* published by Springer publishing house, the dedication reads “This work is dedicated to the memory of my beloved uncle Luigi De Luca. He was Professor of Classical Languages— Grammar and Literature and Principal of High Schools and transmitted to many generations of students the pleasure of understanding the logic intrinsic in reality. He was capable to explain to everybody, in a precise and rigorous way, every abstract idea, even the most difficult. He has taught me nearly every concept which I later needed in my scientific career, including the basics of set theory. I will never forget his lecture about Giambattista Vico, where he let me understand Vico's dream of transforming history into the phenomenological evidence predicted by A New Science (Una Scienza Nuova). I hope that his pedagogical spirit will revive in this work.”

³ Eight years after the writing of the work in which his thoughts on the subject are reported, we can say that his theory has not yet been falsified.

irony which, at times, is also expressed in his professional and intellectual life. His considerations about the above mentioned problem are in fact collected in an article, never published by any publishing house but not for this lacking of interesting contents, *A difficult problem for artificial intelligence: how to assess originality of scientific research and the dangers of apostrophes in family names*,⁴ written in collaboration with his co-authors Francesco dell'Isola, Francesco D. Isola, and Francesco delliIsola. Among his many interests, there is the one, not unusual for a physicist, for the new technologies, believing that they are not only a useful scientific product, but also, if not especially, a means to facilitate scientific progress. To this end, he has always wanted to equip himself with cutting-edge tools, from photographic tools—he is passionate about photography and related problems in optics—to computers, passing through 3D printers, which he was among the first to use to produce prototypes of mechanical metamaterials.

As it is now clear, Francesco dell'Isola has a broad interest. What is common to the intellectual activities to which he dedicates himself, is his effort in facing them always in a rational way, even when their object does not fall among the themes typically familiar to a mathematical-physicist. In this regard, it is worth mentioning that, recently, Francesco dell'Isola has published the scientific popularization book *Big-(Women, Tyrants, Chiefs, Dictators, Emperors and Presidents. Towards the Mathematical Understanding of Social Groups*, whose intent is manifestly to try to apply the rationality typical of Lagrangian Mechanics also to the study of social behaviors of groups formed by human beings:

Modern Science, evolved from Hellenistic Science, is the tool which humans have invented to understand all natural phenomena. Scientific activity is based on the formulation of mathematical models, which “mimic” natural systems. Using mathematical model one gets the solution of some “problems” which allow for the prediction and control of natural phenomena.

In this book we try to present, in a friendly way, the mathematics which governs the dynamics of social groups: it has some aspects in common with the mathematics used to describe the behaviour of Lagrangian Mechanical systems! This similarity may attract the layman who has the curiosity to understand the intrinsic unity of natural phenomena. The reader is warned: although the scientific method has been extremely successful in the description of physical phenomena, human beings often refrain from applying it to the study of themselves as species, social groups or individuals. But human behavior is still based on specific natural laws (e.g. Darwinian selection) and the corresponding physical or psychological structures. In this work aforementioned taboo is overcome by exploiting the visionary understanding of the structure of social groups as gained by the results obtained by Le Marquis de Condorcet, Kenneth Arrow and John Nash.

In this book there is no lack of insight on animal and human psychology, as evidence of the great open-mindedness that characterizes him and, as mentioned before, does not keep him from devoting himself to areas that are not completely within the scope of his university studies. As further proof of this, Francesco dell'Isola has faced with

⁴ The article, not published, is however available online at the address: <https://hal.archives-ouvertes.fr/hal-01002678/document>

the same style of thought, even if encoding the problem in a mathematically rigorous form, the analysis of the instability of economic markets.⁵

Having made this due introduction, in the next sections, we will not dwell on particular aspects of his professional life, even if they are very representative of the man. Rather, taking advantage of our position as privileged observers, we will try to elaborate some aspects of a more general nature that, often, as the reader will not struggle to understand, are also intertwined with his professional life.

Teoria è Pratica!

These words (Theory is practice!) still echo in the mind of the first author. Year 2012. It was the beginning of his third semester at the Faculty of Engineering of the Sapienza University of Rome and he was in the middle of the so-called *biennio* (first two-year course), where the basic subjects are studied in preparation for the applied ones. Upon his arrival, on the first day of the course of Strength of Materials, Francesco dell'Isola gave to all students a sheet of paper with the *Osservazioni sulla scuola: per la ricerca del principio educativo* (Observations on the school: in search of the educational principle) taken from the Quaderno 12 (Notebook 12) of 1932, *Appunti e note sparse per un gruppo di saggi sulla storia degli intellettuali* (Memoranda and sparse notes for a group of essays on the history of intellectuals), by Antonio Gramsci. In that first lecture, he did not mention any topic related to the course, but, openly eschewing the desire to inform about the methods of examination and evaluation—a practice that he said encouraged a study lacking cultural foresight—he focused the attention of his speech on the following passage⁶:

In the old school [that organized by the Casati Law, a law entered into force in 1861 in the Kingdom of Sardinia and extended, with the unification, to the whole of Italy] the grammatical study of Latin and Greek, together with the study of their respective literatures and political histories, was an educational principle—for the humanistic ideal, symbolised by Athens and Rome, was diffused throughout society, and was an essential element of national life and culture. Even the mechanical character of the study of grammar was enlivened by this cultural perspective. Individual facts were not learnt for an immediate practical or professional end. The end seemed disinterested, because the real interest was the interior development of personality, the formation of character by means of the absorption and assimilation of the whole cultural past of modern European civilisation. Pupils did not learn Latin and Greek in order to speak them, to become waiters, interpreters or commercial letter-writers. They learnt them in order to know at first hand the civilisation of Greece and of Rome—a civilisation that was a necessary precondition of our modern civilisation: in other words, they learnt them in order to be themselves and know themselves consciously.

Francesco dell'Isola strongly believes in the importance of historical knowledge: relating current problems to their historical development, often consulting the sources

⁵ F. dell'Isola and A. del Monte, "Dynamic Flexibility, optimal organisation modes and price instability," *Studi economici*, 1995.

⁶ "On Education," in *Selections from the Prison Notebooks*. Translated and Edited by Q. Hoare and G. N. Smith. New York: International Publishers, 1979.

directly, searching for their roots, the study of the archetype, are all elements that distinguish his scientific activity, as well as his way of approaching the study of any problem. For example, in his attempt to understand the causes underlying the current situation of Southern Italy, he cultivated his natural passion for the history of Italy, turning his attention to its unification in particular. It is not unusual to hear him talk, either during presentations at conferences or during lunch breaks, about French, Russian or Turkish history. In the area of the history of Mechanics, he has successfully analyzed the works of, among others, Archimedes, Tullio Levi-Civita, Ernst Hellinger, Erwin Schrödinger, Gabrio Piola, Giuseppe Luigi Lagrangia, Leonhard Euler, Galileo Galilei, Jean-Baptiste Le Rond d'Alembert, Archita of Tarentum, the Bernoulli brothers, Richard Toupin, Leonid Ivanovich Sedov, George Green, Heinrich Hencky, James Clerk Maxwell, William Rowan Hamilton, Vladimir Igorevič Arnol'd, Claude-Louis Navier, Augustin-Louis Cauchy, Enrico Betti, Luigi Federico Menabrea, Alberto Castigliano, relating the sources to contemporary or later knowledge.

Without neglecting philological aspects either, he sometimes confronted, with the help of colleagues, the texts in the original language, of which he provided commented translations, with original historical and scientific notes. It is worth mentioning here the two volumes *The Complete Works of Gabrio Piola: Commented English Translation*, the series of exegesis of *Fundamentals of the Mechanics of Continua* by E. Hellinger, as well as the recent book *Evaluation of Scientific Sources in Mechanics. Heiberg's Prolegomena to the Works of Archimedes and Hellinger's Encyclopedia Article on Continuum Mechanics*. With his work, over the years, he has shown that it is not unusual for valid scientific ideas to be ignored—or at best lost and eventually rediscovered more or less independently in later times—because they are written in a language inaccessible to the scientific community of interest. In other words, he argues, with numerous arguments, that the establishment of a *lingua franca* for science, as English is today and Latin and French were in the past, in addition to the obvious advantages, inevitably involves significant losses of knowledge

The reasons behind the vehemence with which the lecturer in the Construction Science course taken by the first author⁷ repeated the mantra “Theory is practice!”⁸ deserve to be reported explicitly. That of the lecturer was an invitation to wake up from the drowsiness and negligence with which, often not without the bad example of the faculties, the theoretical issues underlying the results of major applicative importance that are taught in engineering courses are addressed. Perpetuating and transmitting only the “know-how,” clearly easier to do in the short time in which

⁷ Francesco dell'Isola, thanks to the reading of a book kept in the library G. Boaga of the Faculty of Civil and Industrial Engineering of La Sapienza University of Rome, was aware of the historical facts that in the Italian pre-unitary period led to the need to call professors from Vienna and Paris to re-found the School of Engineering in Milan after the promulgation of a law that allowed to become an Engineer by just doing a few years of apprenticeship in an engineering office.

⁸ This motto is also the basis of the pamphlet, which we recommend reading, “Teoria è pratica! Un saggio sul metodo scientifico con un apologo raccontato al principiante” (Theory is practice! An essay on the scientific method with an apologue told to the beginner) written by Francesco dell'Isola and published in 2008 by the Esculapio publishing house.

even degree programmes have been compressed in Italy following the introduction of the so-called “3+2 system” leads to a dangerous loss of the theoretical knowledge that generated such a “know-how.” This causes, generation after generation, a progressive cultural impoverishment. Knowing how to do something, possessing the so-called “skills,” as opposed to the theoretical knowledge at its base, does not allow one to generate new knowledge or to improve and adapt current knowledge in order to know how to do something tomorrow. The drift that such a society risks—if a mere economic question could help raise awareness on the issue—should make worry especially those countries like Italy that, poor in natural resources and lacking in low-cost labor, base their economy on the development of high technology. When the intellectual class, in our case the scientific one, dies out as it often happens—for different reasons—in rather more dramatic situations (dictatorships, wars, periods of economic crisis, etc.) society must necessarily import knowledge developed elsewhere. This appears critical especially in the strategic sectors of a country. Francesco dell'Isola is therefore strongly aware of the importance of his role as a teacher, and not only as a scientist, within society.

The Scholarly Profession

The first author recalls that, continuing the reading of the above-mentioned passage from Gramsci, the teacher placed great emphasis on the sacrifice required by *true* study:

Would a scholar at the age of forty be able to sit for sixteen hours on end at his work-table if he had not, as a child, compulsorily, through mechanical coercion, acquired the appropriate psycho-physical habits? If one wishes to produce great scholars, one still has to start at this point and apply pressure throughout the educational system in order to succeed in creating those thousands or hundreds or even only dozens of scholars of the highest quality which are necessary to every civilisation. (Of course, one can improve a great deal in this field by the provision of adequate funds for research, without going back to the educational methods of the Jesuits [known to be based primarily on discipline, coercion, and submission of the student].)

The first lecture of the Construction Science course finally concluded with the reading of the following excerpt:

The child who sweats at Barbara, Baralipon is certainly performing a tiring task, and it is important that he does only what is absolutely necessary and no more. But it is also true that it will always be an effort to learn physical self-discipline and self-control; the pupil has, in effect, to undergo, a psycho-physical training. Many people have to be persuaded that studying too is a job, and a very tiring one, with its own particular apprenticeship—involving muscles and nerves as well as intellect. It is a process of adaptation, a habit acquired with effort, tedium and even suffering. Wider participation in secondary education brings with it a tendency to ease off the discipline of studies, and to ask for “relaxations.” Many even think that the difficulties of learning are artificial, since they are accustomed to think only of manual work as sweat and toil.

The discipline and sacrifice that Francesco dell’Isola demanded from those students who really wanted to understand the reasons behind the most important results of the Science of Construction were rewarded by the fact that, in the end, they went far beyond the usual program. What a willing student received at the end of the course was a real initiation to the profession of scientist, including even knowledge of Greek philosophy, equations of mathematical physics, history of construction science, stability of dynamical systems, tensor analysis, model theory, rational mechanics, the axiomatizations of continuum mechanics, the theory of epicycles, Dedekind’s construction of real numbers, the Navier–Stokes and transport equations, chaotic systems, Pareto and Nash equilibrium.

New Generations of Scientists

The first author recalls that Francesco dell’Isola used to invite the most curious students to come to office hours, which often lasted until the evening, to talk about science in the round, including philosophy of science, epistemology and quantum mechanics, and not only strictly about the course Strength of Materials. The wide-ranging nature of his course has certainly enabled many student engineers to become “conscious” professionals, i.e. to apply practical tools with full knowledge of the underlying theoretical facts, and others to discover new cultural horizons and consciously head towards other branches of knowledge, such as philosophy, physics and mathematics. It is not a coincidence or an arbitrary choice of his that it is the Strength of Materials course that provides such a physical-mathematical vision to engineering students. In the book adopted in the course, he himself in fact writes

Probably it is the familiarity with the various models of deformable bodies—together with the necessary ability to pass from one description to another of the same physical entity and to establish relations between such different descriptions—that makes, in general, the connoisseurs of the strength of materials simultaneously so inclined to the study of applications, to mathematical abstraction and to metaphysical discussions. Another peculiar characteristic of theirs is the tendency to extreme precision in their discourses, combined with an almost maniacal care in the choice of words used. This characteristic is easily understandable when we take into account that in the use of the various models currently employed by them it is very important, under penalty of an inextricable confusion of concepts and meanings, to distinguish, giving them different names, between different entities: the physical ones, which belong to the world of phenomena that we want to describe (the deformable bodies) and the abstract ones, which serve as a mathematical model of the first (Euler’s beam, Timoshenko’s beam, Cauchy’s continuum). The necessary comparison between the performances of the various models explains, finally, both the mentioned tendencies to metaphysics and the need to choose different names to characterize the different mathematical entities used to describe the same physical entity.

The authors believe that Francesco dell’Isola has a high ethical vision of science and believes that in the academy, merit must emerge. Just as in a workshop, the proper selection of Disciples by the Master is of primary importance for the transmission of certain scientific ideas and, indeed, may determine their fate. Just from the analysis

of his co-authors, Francesco dell'Isola turns out to have been mentor to at least forty young scientists, many of which are now established professors and researchers in the most prestigious universities and research centers in the world. Francesco dell'Isola, in addition to being a Master, is in turn the heir of a noble tradition in physics and mathematics: among the scientific ancestors of Francesco dell'Isola, as reported by the database *The Mathematics Genealogy Project*,⁹ we find scientists of the caliber of Tolotti, Levi-Civita, and Betti.

From what has been said so far, it is not difficult to believe that many promising and intellectually curious young people have been, are, and will be attracted in the future by the interaction with Francesco dell'Isola and led by him towards scientific research. As proof of his vision of science, Francesco dell'Isola was early to initiate the most deserving young people into research and allow them to benefit from all the tools necessary to enhance their abilities, regardless of their economic situation. Every year the MEMOCS Research Center welcomes in its residence professors, researchers and students of bachelor, master and doctoral degrees from all over the world, for periods of varying length. In particular, a selection is made of the most deserving and needy students among those who request access to the summer schools, university-level courses and internships offered by the MEMOCS Center, supporting the most needy among the students admitted to the courses by means of financial participation in the expenses necessary for their stay at the dormitory.

Even before the founding of the MEMOCS Center and the establishment of its laboratories, Francesco dell'Isola was among the founders of the "Tullio Levi Civita" Foundation for the development of scientific culture, which, among other things, established the "Tullio Levi-Civita" School of University Excellence. The School provided scholarships for the continuation of university studies and offered the possibility of being housed in its facilities in Cisterna di Latina. In order to prepare high school students in the Province of Latina for technical-scientific university studies, the "Tullio Levi-Civita" Foundation also promoted the creation of the Preparatory School for university studies. The activities of the Preparatory School were aimed at disseminating and strengthening the scientific culture of the students of the last two classes of high school and complete the educational path related to the teachings taught in high school through supplementary courses.

In the school years 2017/2018 and 2018/2020, Francesco dell'Isola took an active role in the organization of activities for the professional updating of high school teaching staff, as part of the project "Lincei per la scuola," involving some of the top experts in physics and mathematics in Italy. In order to encourage the scientific transmission from the old to the new generations of scientists, the MEMOCS Center has established since its foundation, at the impulse of Francesco dell'Isola, the "Tullio Levi-Civita" international prize, awarded to scientists who have distinguished themselves for their highly innovative results and who have contributed to the training of young researchers.

⁹ <https://www.mathgenealogy.org/>

Amarcord¹⁰

The second author recalls meeting Francesco dell'Isola during a coffee break at the Sperlonga summer school, organized by the latter in 2013. The previous scientific experience of the second author concerned mainly, at the time, the analysis of discrete systems, both intrinsically discrete and obtained by discretization of continuous models. Francesco dell'Isola, on the contrary, up to that time had devoted himself almost exclusively to the formulation and solution of continuous models. The second author remembers that, Francesco dell'Isola, although aware of the diversity of their points of view, was willing to discuss some scientific problems related to the analysis of the nonlinear behavior of metamaterials with pantographic microstructure. It is precisely their continuous and friendly discussions, a modern reinterpretation of the discrete-continuous disputes that cyclically occur in the history of Science, see the debate between Mach and Boltzmann, which define a fruitful scientific collaboration between the two, in which the two views are adopted in a synergistic way to better understand the mechanisms underlying the exotic behavior observed in metamaterials. To date, the second author has not found a topic about which, if ready to support a constructive contradiction, one cannot speak with Francesco dell'Isola without receiving generously valuable advice.

The second author also recalls that, passing through Rome, he and Francesco dell'Isola often met at a bar in the Rione Monti. In these meetings, where the best scientific ideas discussed by the two would take shape, Francesco dell'Isola, taking up what was said to be a habit of the famous Neapolitan mathematician Renato Caccioppoli, would expound his ideas by writing on the papery placemat of the bar. Rome was also the scene of their playful photo competition, of which both are enthusiasts.

Both authors can't help but mention, when thinking about long Roman walks, the propensity that Francesco dell'Isola has for engaging in discussions while walking. Although the authors are aware of the positive effects of this habit, they cannot fail to mention how these walks are "inflicted" on them in any weather condition and in any place in Europe!

¹⁰ *Amarcord* is a 1973 Italian comedy-drama film directed by Federico Fellini. The film's title is a universion of the Romagnolo phrase "a m'arcòrd" (I remember). The title then became a neologism of the Italian language, with the meaning of "nostalgic revocation."

Happy Birthday Francesco dell'Isola!

The authors hope that this contribution will do at least partial justice to what Francesco dell'Isola has transmitted to them: they cannot but be grateful to him for being his collaborators and friends. As can be seen from the information reported so far, his lively intellectual and educational activity, which began thirty-five years ago and which the authors believe earned him the appellation of μαθητικός¹¹ of *Magna Graecia*,¹² has received due recognition from the scientific community. Nevertheless, the authors believe that his enthusiasm and curiosity are still those, genuine, of a child and that, therefore, new fruitful studies are waiting for him. On the occasion of his sixtieth birthday, the authors wish him many more years of health and scientific successes—why not, even in other fields of knowledge—as well as a good reading of the contributions that many colleagues have dedicated to him in the disciplines that have most interested him so far.

¹¹ As reported in *Henry George Liddell. Robert Scott. A Greek-English Lexicon. revised and augmented throughout by. Sir Henry Stuart Jones. with the assistance of. Roderick McKenzie. Oxford. Clarendon Press. 1940*, the Greek term μαθητικός means “fond of learning” (Pl.Ti.88c)—see also the web page <http://www.perseus.tufts.edu/hopper/text?doc=Perseus:text:1999.04.0057:entry=maqhmatico/s>

¹² In the introduction of his book *Big-(Wo)men, Tyrants, Chiefs, Dictators, Emperors and Presidents. Towards the Mathematical Understanding of Social Groups*, he writes “I did not try to hide my cultural roots, in writing this essay. I was educated in Magna Graecia, where a wonderful melting pot mixed Greek philosophy, Roman pragmatism, Longobard proud sense of freedom, Byzantine duplicity and culture, Arab initiative, inventive and tolerance, Normans loyalty and determination, French sophisticated traditions and sense of State, Spanish opportunism, Piedmontese administrative ideas.”

Contents

| | |
|---|----|
| Francesco dell’Isola: a μαθητικός of Magna Graecia | xv |
| Emilio Barchiesi & Emilio Turco | |

Part I Theoretical Analysis

| | |
|---|----|
| 1 A Different Catch for Poisson | 3 |
| A. Derya Bakiler, Ali Javili | |
| 1.1 Introduction | 3 |
| 1.1.1 Key Objectives | 6 |
| 1.1.2 Notation and Definitions | 6 |
| 1.1.3 Organization of the Manuscript | 7 |
| 1.2 Poisson’s Ratio in Classical Continuum Mechanics | 7 |
| 1.2.1 Poisson’s Ratio for Small-Strain Linear Elasticity | 8 |
| 1.2.2 Poisson’s Ratio for Large Deformations Nonlinear Elasticity | 10 |
| 1.3 Poisson’s Ratio in Peridynamics | 17 |
| 1.4 Conclusion | 22 |
| References | 22 |
| 2 Nonlinear Deformation of a Clamped-Edge Strip-Like Nano-Film | 25 |
| Anatolii Bochkarev | |
| 2.1 Introduction | 25 |
| 2.2 Problem Formulation | 26 |
| 2.3 One-Dimensional Model of Deformation of Strip-Like Nano-Film | 28 |
| 2.3.1 Nonlinear Bending under the Eigenform-Like External Loading | 28 |
| 2.3.2 Post-Critical Buckling under Compression | 30 |
| 2.3.3 Nonlinear Free Transverse Vibration | 31 |
| 2.4 Conclusion | 34 |
| References | 34 |

3 Closed-form Analytic Solutions of the Problem of a Hollow Sphere Made of Second Gradient Plastic Porous Material and Subjected to Hydrostatic Loading 37
 Roy Burson, Koffi Enakoutsa

3.1 Introduction 38

3.2 Description of the Hollow Sphere Problem 39

3.3 Solution to the Hollow Sphere Problem When the Porosity is Neglected 40

3.4 Numerical Illustrations of the Solution 45

3.5 Analytic Results in the Presence of Porosity in the Matrix 45

3.5.1 Derivation of Cauchy Stress Components 46

3.5.2 Moment Components Derivation 48

3.5.3 Discussion 51

3.6 Conclusion 52

References 66

4 Quantum Dynamics Effects on Amplitude-Frequency Response of Superharmonic Resonance of Second-Order of Electrostatically Actuated NEMS Circular Plates 69
 Dumitru I. Caruntu, Julio S. Beatriz

4.1 Introduction 70

4.2 Differential Equation of Motion 73

4.3 Superharmonic Resonance of Second-Order 76

4.4 Method of Multiple Scales: First-Order Hard Excitations Model . . 76

4.5 Stability Testing 79

4.6 Method of Multiple Scales: Second-Order Hard Excitations Model 80

4.7 Electrostatic Reduced Order Model 82

4.8 Casimir Reduced Order Model 84

4.9 Van der Waals Reduced Order Model 85

4.10 Numerical Simulations 87

4.10.1 Electrostatic Model of Microelectromechanical Systems Clamped Circular Plates 87

4.10.2 Casimir Force Effect on Nanoelectromechanical Systems Plates 93

4.10.3 Van der Waals Force Effect on Nanoelectromechanical Systems Plates 95

4.10.4 Stability 98

4.11 Discussion and Conclusions 99

References 102

5 Propagation of Chaos for a Stochastic Particle System Modelling Epidemics 105
 Alessandro Ciallella, Mario Pulvirenti, Sergio Simonella

5.1 Introduction 105

5.2 Model 106

5.3 Kinetic Limit 109

| | | |
|----------|---|------------|
| 5.4 | Particle Approximation | 111 |
| 5.5 | Concluding Remarks | 116 |
| | References | 117 |
| 6 | On the Constitutive Assumptions for a Continuum Model of Scintillating Crystals | 119 |
| | Fabrizio Daví | |
| 6.1 | Introduction | 119 |
| 6.2 | A Continuum with Microstructure Model for Scintillators | 120 |
| 6.3 | Balance Laws | 122 |
| 6.4 | Thermodynamics. Constitutive Relations | 124 |
| 6.5 | Reaction-Diffusion-Drift Equations for Scintillators: Constitutive Assumptions | 126 |
| 6.5.1 | The Gibbs Entropy | 130 |
| 6.5.2 | The Fermi–Dirac Integrals | 132 |
| | References | 134 |
| 7 | Strong Ellipticity within the Strain Gradient Elasticity: Elastic Bar Case | 137 |
| | Victor A. Eremeyev, Emanuele Reccia | |
| 7.1 | Introduction | 137 |
| 7.2 | Nonlinear Elasticity | 138 |
| 7.3 | Strain Gradient Elasticity | 140 |
| 7.4 | Conclusions | 142 |
| | References | 143 |
| 8 | Two Thermodynamic Laws in Phenomenological Mechanics of Continuum: Postulates or Definitions ? | 145 |
| | Dimitri Georgievskii | |
| 8.1 | Various Ways of Axiomatization | 145 |
| 8.2 | The General Form of Postulates in Mechanics of Continuum | 146 |
| 8.3 | Postulate IV. The Law on the Change of Internal Energy | 147 |
| 8.4 | Postulate V. The Law on the Change of Entropy | 149 |
| 8.5 | Introduction to Mathematical Model of Interactions with a New Nature | 151 |
| | References | 153 |
| 9 | On an Extended Family of Quasi-Equivalent Models of the Gradient Elasticity Theory | 155 |
| | Sergey Lurie, Petr Belov, Yury Solyaev | |
| 9.1 | Introduction | 155 |
| 9.2 | Basic Definitions | 156 |
| 9.3 | Family of Quasi-Equivalent Models | 160 |
| 9.3.1 | Kinematic Restrictions for Displacement Vector Components | 162 |
| 9.3.2 | Gradient Static Friction Model | 163 |

| | | |
|-----------|--|------------|
| 9.3.3 | Kinematic Restrictions for Components of Derivatives of Displacements | 167 |
| 9.4 | Examples of Gradient Models without Edge Conditions | 169 |
| 9.4.1 | Variational Gradient Dilation Model | 169 |
| 9.4.2 | Variant of Vector Gradient Elasticity Model | 173 |
| 9.5 | General Case of Kinematic Restrictions. Generalized Pinching . . . | 174 |
| 9.6 | The Theorem on the Self-Balance of Meniscus Forces | 178 |
| 9.7 | Conclusions | 180 |
| | References | 181 |
| 10 | Continuum Models via Granular Micromechanics | 183 |
| | Anil Misra, Luca Placidi, Emilio Barchiesi | |
| 10.1 | Introduction | 183 |
| 10.2 | Granular Micromechanics Approach | 186 |
| 10.2.1 | Piola Ansatz for Micro-Macro Kinematic Identification . . | 187 |
| 10.2.2 | Micro-Macro Kinematic Identification Using Prescribed Micromotion | 188 |
| 10.3 | Outlook | 189 |
| | References | 190 |
| 11 | Some Variational Principles in the Three-Dimensional Micropolar Theories of Solids and Thin Solids | 193 |
| | Mikhail Nikabadze, Armine Ulukhanyan | |
| 11.1 | Introduction | 194 |
| 11.2 | Some Definitions and Integral Identities | 196 |
| 11.3 | Lagrange Variational Principle (Lagrange Theorem) | 203 |
| 11.3.1 | On Compatibility Conditions in Linear Micropolar Theory | 205 |
| 11.3.2 | The Mixed Boundary Value Problems and the New Statement of the Boundary Value Problem with Respect to the Tensors of Stresses and Couple Stresses in Micropolar Solid Mechanics | 209 |
| 11.4 | Castigliano's Variational Principle (Castigliano's Theorem) | 210 |
| 11.5 | Generalized Reissner-Type Variational Principle | 217 |
| 11.6 | The Generalized Reissner-Type Variational Principle in the Micropolar Theory of Thin Bodies with One Small Size under the New Parameterization of the Body Domain | 220 |
| 11.7 | Generalized Reissner-Type Variational Principle in the Micropolar Theory of Thin Bodies with One Small Size in Moments under the New Parameterization of a Body Domain | 223 |
| 11.8 | Generalized Variational Principle of Reissner-Type in the Micropolar Theory of Multilayer Thin Bodies with One Small Size with Full Contact of the Layers | 236 |
| 11.9 | Generalized Reissner-Type Variational Principle in the Micropolar Theory of Multilayer Thin Bodies with One Small Size in the Case of Domains of Weakened Adhesion | 240 |

| | | |
|-----------|--|------------|
| 11.9.1 | Jump-Type Model. Interphase (Interlayer) Displacements and Rotation Vectors. Vectors of Generalized Interfacial Forces and Moments | 241 |
| 11.9.2 | Generalized Reissner-Type Variational Principle in the Theory of Multilayer Thin Bodies in Moments if There Are Domains of Weakened Adhesion | 246 |
| 11.10 | Conclusion | 247 |
| | References | 249 |
| 12 | Asymptotic Comparison of the Strain-Gradient and Micromorphic Models when Loading Forces Are Widely Spread | 253 |
| | Pierre Seppecher, Lukáš Jakabčín | |
| 12.1 | Introduction | 253 |
| 12.2 | Notation | 257 |
| 12.3 | Spread Loads | 259 |
| 12.4 | Fourier Expansion | 260 |
| 12.5 | Comparison of Different Models at Large Scale | 261 |
| 12.6 | Examples | 267 |
| 12.7 | Conclusion | 270 |
| | References | 271 |
| 13 | Quasiconvexity and Rank-One Convexity in Cosserat Elasticity Theory | 273 |
| | Milad Shirani, David J. Steigmann | |
| 13.1 | Introduction | 273 |
| 13.2 | Cosserat Elasticity, | 274 |
| 13.2.1 | Kinematical and Constitutive Framework | 274 |
| 13.2.2 | Virtual Power and Equilibrium | 275 |
| 13.3 | Conservative Problems and Potential Energy | 276 |
| 13.3.1 | Example: Dead-Load Problems | 277 |
| 13.4 | The Quasiconvexity Condition | 277 |
| 13.5 | Rank-One Convexity | 280 |
| 13.6 | Conclusion | 283 |
| | References | 283 |
| 14 | Models of Viscoelastic Materials: a Review on Historical Development and Formulation | 285 |
| | Marina V. Shitikova, Anastasiya I. Krusser | |
| 14.1 | Introduction | 285 |
| 14.2 | The Simplest Models of Viscoelasticity | 287 |
| 14.2.1 | Three-Element Models | 287 |
| 14.2.1.1 | Three-Element Models of the Standard Linear Solid | 288 |
| 14.2.1.2 | Three-Element Models of Standard Linear Liquid | 290 |
| 14.2.2 | Four-Element Models | 292 |

| | | | |
|-----------|----------|---|------------|
| | 14.2.2.1 | Four-Element Models of Viscoelastic Fluids . . . | 293 |
| | 14.2.2.2 | Four-Element Models of Viscoelastic Solids . . . | 294 |
| | 14.2.3 | Models with Large Numbers of Elements | 294 |
| | 14.2.3.1 | Generalization of the Maxwell Model | 295 |
| | 14.2.3.2 | Generalization of Voigt or Kelvin Models | 296 |
| 14.3 | | Viscoelastic Models with Fractional Derivatives | 300 |
| | 14.3.1 | First Applications of Fractional Calculus in Viscoelasticity | 301 |
| | 14.3.2 | The Simplest Fractional Calculus Viscoelastic Models . . . | 302 |
| | 14.3.2.1 | Maxwell Model with Fractional Derivatives . . . | 303 |
| | 14.3.2.2 | Kelvin–Voigt Model with Fractional Derivatives | 304 |
| | 14.3.2.3 | Standard Linear Solid Model with Fractional Derivatives | 305 |
| | 14.3.3 | Viscoelasticity Models with Several Different Fractional Parameters and One Relaxation (Retardation) Time | 307 |
| | 14.3.3.1 | Maxwell Models with Several Different Fractional Parameters | 307 |
| | 14.3.3.2 | Kelvin–Voigt Model with Several Different Fractional Parameters | 308 |
| | 14.3.3.3 | Standard Linear Solid Models with Several Different Fractional Parameters | 308 |
| | 14.3.3.4 | Burgers Models with Several Different Fractional Parameters | 310 |
| | 14.3.3.5 | Fractional Operator Models with Several Different Fractional Parameters | 310 |
| | 14.3.4 | Viscoelastic Models with One or More Fractional Parameters and Several Relaxation (Retardation) Times . . . | 311 |
| | 14.3.4.1 | Rabotnov Model | 311 |
| | 14.3.4.2 | Fractional Calculus Models with Several Different Fractional Parameters | 311 |
| | 14.3.5 | Models of Viscoelastic Fluids with Two or More Scott–Blair Fractional Derivative Elements | 314 |
| 14.4 | | Viscoelastic Models with Variable Viscosity | 315 |
| 14.5 | | Nonlinear Viscoelasticity Models with Fractional Derivatives | 317 |
| 14.6 | | Conclusion | 318 |
| | | References | 319 |
| 15 | | Invariance Aspects of $F = F_e F_i$ Representations in Coupled-Field Problems | 327 |
| | | Marek Werner, Kerstin Weinberg | |
| | 15.1 | Introduction | 327 |
| | 15.2 | Basic Equations and Free Energy Expressions | 330 |
| | 15.3 | Modeling Representation | 332 |
| | 15.3.1 | First Modeling Representation: $\Psi(c, \mathbf{C})$ | 332 |
| | 15.3.2 | Second Modeling Representation: $\Psi(c, \hat{\mathbf{C}}_e)$ | 334 |

15.3.3 Relation Between Both Representations 336

15.4 Discussion and Example 337

15.5 Summary and Conclusion 338

References 340

Part II Computations

16 Strain-Gradient Modeling and Computation of 3-D Printed Metamaterials for Verifying Constitutive Parameters Determined by Asymptotic Homogenization 343
 Gokhan Aydin, M. Erden Yildizdag, Bilin Emek Abali

16.1 Introduction 344

16.2 Asymptotic Homogenization 345

16.3 Computation 347

16.4 Results and Verification 348

16.4.1 Reference Solution Based on 1st-Gradient Theory 349

16.4.2 Determination of Constitutive Parameters in the Strain-Gradient Model 350

16.4.3 Simulations with 2nd-Gradient Theory and Validation 352

16.5 Conclusion 353

References 354

17 On Boundary Layers Observed in Some 1D Second-Gradient Theories 359
 Emilio Barchiesi, Alessandro Ciallella, Ivan Giorgio

17.1 Introduction 360

17.2 Euler–Bernoulli Beam 362

17.3 Pantographic Beam 367

17.3.1 Longitudinal Pantographic Beam with Nonlinear First Gradient Term 367

17.3.2 Longitudinal Pantographic Beam with Nonlinear Second Gradient Term 370

17.4 Concluding Remarks 373

References 373

18 Design and Parametric Enhancement of a Flexible Planar TEG - Numerical Study 377
 Maria Carolina Fernandes, Cristina Furtado, Daniela Campanhã, Sónia Isabel Silva Pinto

18.1 Introduction 378

18.2 Materials and Methodology 380

18.2.1 Theoretical Analysis 380

18.2.2 Numerical Analysis 382

18.2.3 Geometrical Parameters 383

18.2.4 Boundary Conditions 384

18.2.5 Material Choice 385

| | | |
|----------|------------------------------------|-----|
| 18.2.6 | Mesh Convergence Analysis | 386 |
| 18.2.7 | Sensitivity Analysis | 387 |
| 18.2.7.1 | Number of Thermocouples | 387 |
| 18.2.7.2 | Presence of Protective Coating | 388 |
| 18.2.7.3 | Substrate Material and Dimensions | 389 |
| 18.2.7.4 | Generator Thickness | 390 |
| 18.2.7.5 | Leg Dimensions | 390 |
| 18.2.7.6 | Contact Dimensions | 392 |
| 18.2.8 | Enhancement Methodology | 392 |
| 18.2.8.1 | Constraints | 392 |
| 18.2.8.2 | Numerical Parametrization | 393 |
| 18.3 | Results and Discussion | 394 |
| 18.3.1 | Parametric Theoretical Enhancement | 394 |
| 18.3.2 | Parametric Numerical Enhancement | 394 |
| 18.3.3 | Validation with the Literature | 395 |
| 18.3.4 | Final TEG design | 397 |
| 18.4 | Conclusions | 399 |
| | References | 399 |

19 Implementation and Comparison of Non-Newtonian Viscosity Models in Hemodynamic Simulations of Patient Coronary Arteries . . 403

Maria Carolina Fernandes, Luísa Costa Sousa, Catarina Ferreira de Castro,
José Manuel Laginha Mestre da Palma, Carlos Conceição António,
Sónia Isabel Silva Pinto

| | | |
|----------|--|-----|
| 19.1 | Introduction | 404 |
| 19.2 | Methodology | 405 |
| 19.2.1 | Theoretical Analysis | 405 |
| 19.2.1.1 | Hemodynamic Indices | 405 |
| 19.2.1.2 | Blood Rheology | 406 |
| 19.2.2 | Patients Data and Artery Models | 408 |
| 19.2.3 | Boundary Conditions | 408 |
| 19.2.3.1 | Pressure Boundary Condition | 408 |
| 19.2.3.2 | Velocity Boundary Condition | 410 |
| 19.2.4 | Mesh Convergence Analysis | 411 |
| 19.2.5 | Numerical Simulation Definitions | 413 |
| 19.2.6 | Validation of Numerical Method with the Literature | 414 |
| 19.3 | Results and Discussion | 414 |
| 19.3.1 | Steady-State Flow of Newtonian Blood | 415 |
| 19.3.2 | Transient Flow of Newtonian Blood | 416 |
| 19.3.3 | Steady-State Flow of Non-Newtonian Blood | 418 |
| 19.3.4 | Transient Flow of Non-Newtonian Blood | 419 |
| 19.4 | Conclusions | 424 |
| 19.5 | Appendix I. | 426 |
| | References | 427 |

20 Bending/Tension of Plate Reinforced by a System of Parallel Fiber . . . 429
 Alexander G. Kolpakov, Sergei I. Rakin

20.1 Introduction 429

20.2 Reduction of 3-D PCP (20.2) to 2-D problems 432

20.3 Numerical Computations 439

20.4 Conclusion 440

References 441

21 Semi-Automatic Method of Stent Development for Hemodynamic Simulations in Patient Coronary Arteries with Disease 443
 Luís Matias, Catarina Ferreira de Castro, Carlos Conceição António, Luísa Costa Sousa, Sónia Isabel Silva Pinto

21.1 Introduction 444

21.2 Methodology 445

21.2.1 Left Coronary Artery Geometry and Stent Design 446

21.2.1.1 Stenotic Zone Reconstruction 446

21.2.1.2 Stenotic Zone Disposal 448

21.2.1.3 Flat Stent Design 448

21.2.1.4 Bending to Cylindrical Form and Curve Adaptation 449

21.2.1.5 Combining Artery Geometry with Stent-Lumen 449

21.2.2 Mesh Generation 449

21.2.3 Blood Properties 450

21.2.4 Boundary Conditions 451

21.2.5 Numerical Method 452

21.2.6 Hemodynamic Descriptors 453

21.3 Results and Discussion 454

21.4 Conclusion 456

References 457

22 The Efficient Trabecular Bone Remodeling Numerical Tool Enabling Multiple Load Case Simulation 459
 Jan Polak, Michał Nowak

22.1 Introduction 459

22.2 The Trabecular Bone Remodeling Regulatory Model with the Lazy Zone Concept 460

22.3 Multiple Loading Conditions 461

22.4 The Simulation Approach Including the Postulates based on Shape Optimization Studies 462

22.5 The Numerical Implementation and Mesh Generation Parallelization 463

22.6 The Sample Simulation Results 467

22.7 The System Efficiency and Scalability 467

22.8 Conclusions 469

References 470

| | | |
|-----------|--|-----|
| 23 | Modeling the Magnetic Relaxation Behavior of Micropolar Ferrofluids by Means of Homogenization | 473 |
| | Wilhelm Rickert, Max Winkelmann, Wolfgang H. Müller | |
| 23.1 | Introduction | 474 |
| 23.2 | Problem Setup and Homogenization Procedure | 474 |
| 23.3 | The Governing Equations | 477 |
| 23.4 | Solution to the Microscopic Problem | 480 |
| 23.5 | Solution to the Macroscopic Problem | 481 |
| 23.6 | Homogenization and Parameter Identification | 483 |
| 23.7 | Results and Conclusion | 484 |
| | References | 486 |
| 24 | Numerical Homogenisation of Gradient Materials | 487 |
| | Felix Schmidt, Melanie Krüger, Christian Hesch | |
| 24.1 | Introduction | 487 |
| 24.2 | Basic Notation | 488 |
| 24.3 | Second Gradient Macroscopic Continuum and First Gradient Microscopic Continuum | 489 |
| 24.3.1 | Macroscopic Boundary Value Problem | 489 |
| 24.3.2 | Microscopic Boundary Value Problem (First Gradient) | 492 |
| 24.4 | Continuous Strain Energy Formulation for Fibers | 494 |
| 24.5 | Second Gradient Macroscopic Continuum and Second Gradient Microscopic Continuum | 496 |
| 24.5.1 | Microscopic Boundary Value Problem (Second Gradient) | 496 |
| 24.6 | Numerical Example: Cook Membrane | 498 |
| 24.7 | Conclusion | 499 |
| | References | 501 |
| 25 | Modeling the Slow Crack Growth of an Edge Crack within the Cohesive Zone Model Approach | 505 |
| | Mikhailo Selivanov, Lidiia Nazarenko, Holm Altenbach | |
| 25.1 | Introduction | 506 |
| 25.2 | An Edge Crack with Cohesive Zone | 508 |
| 25.3 | Solving a Problem on an Edge Crack with Cohesive Zone by the Regularization of Singular Integral Equation | 516 |
| 25.4 | Subcritical State of a Crack | 525 |
| 25.5 | Modeling the Slow Crack Growth | 528 |
| 25.6 | Conclusion | 533 |
| | References | 533 |
| 26 | An Insight into Computational Challenges in Damage Mechanics: Analysis of a Softening Hooke's Spring | 537 |
| | Salvatore Sessa, Emilio Barchiesi, Luca Placidi, Massimo Paradiso, Emilio Turco, Nahiene Hamila | |
| 26.1 | Introduction | 538 |
| 26.2 | Formulation of the Problem | 540 |

| | | |
|-----------|--|------------|
| 26.2.1 | Linearly Softening Hooke’s Spring | 542 |
| 26.3 | Analytical Solutions | 543 |
| 26.3.1 | Displacement Control Solution | 543 |
| 26.3.2 | Force Control Solution | 546 |
| 26.4 | Numerical Integration Algorithms | 548 |
| 26.4.1 | Displacement Control Integration | 549 |
| 26.4.2 | Load Control Integration | 550 |
| 26.4.2.1 | Explicit Algorithm | 550 |
| 26.4.2.2 | Newton–Raphson Algorithm | 551 |
| 26.4.2.3 | Fixed-Point Iterative Method | 552 |
| 26.4.3 | Arc-Length Control Integration | 554 |
| 26.5 | Numerical Results | 556 |
| 26.6 | Conclusions | 560 |
| | References | 561 |
| 27 | Thermodynamic Compatibility of the HystereticPoly Uniaxial Material Implemented in OpenSees | 565 |
| | Salvatore Sessa, Nicoló Vaiana, Massimo Paradiso, Luciano Rosati | |
| 27.1 | Introduction | 565 |
| 27.2 | A Review of the HystereticPoly Constitutive Model | 567 |
| 27.3 | The Thermodynamic Compatibility | 570 |
| 27.3.1 | Negative Softening | 571 |
| 27.3.2 | Hysteresis Crossing Paths | 572 |
| 27.4 | Numerical Applications | 574 |
| 27.5 | Discussion and Conclusions | 577 |
| | References | 579 |
| 28 | Studying the Higher-Order Inertia in the Second-Order Theory of Elasticity for Modeling Metamaterials | 581 |
| | Navid Shekarchizadeh, Alberto Maria Bersani | |
| 28.1 | Introduction | 582 |
| 28.2 | Model Implementation | 583 |
| 28.3 | Results and Discussion | 585 |
| 28.4 | Conclusion | 588 |
| | References | 589 |
| 29 | Structural Analysis of Doubly-Curved Shells with General Boundary Conditions | 591 |
| | Francesco Tornabene, Matteo Viscoti, Rossana Dimitri | |
| 29.1 | Introduction | 592 |
| 29.2 | Geometrical Representation of Shells in Principal Coordinates | 596 |
| 29.3 | ESL Assessment of Kinematic Quantities | 598 |
| 29.4 | Generalized Constitutive Equations | 602 |
| 29.5 | External Loads | 604 |
| 29.6 | Equation of Motion | 605 |
| 29.7 | Isogeometric Mapping of the Physical Domain | 610 |

| | | |
|-------|---|-----|
| 29.8 | Numerical Implementation via GDQ Method | 613 |
| 29.9 | Equilibrium-Based Recovery Procedure | 616 |
| 29.10 | General Boundary Conditions | 621 |
| 29.11 | Applications and Results | 624 |
| | 29.11.1 Free Vibration Analysis | 632 |
| | 29.11.2 Static Analysis | 642 |
| 29.12 | Conclusion | 649 |
| | References | 651 |

Part III Experiments

| | | |
|-----------|---|------------|
| 30 | Characterisation of Mechanical Properties of Wood: Size Effect | 659 |
| | Reza Afshar | |
| 30.1 | Introduction | 660 |
| | 30.1.1 Wood Properties and Importance | 660 |
| | 30.1.2 Size Effect | 660 |
| 30.2 | Materials and Method | 661 |
| | 30.2.1 Digital Image Correlation (DIC) Method | 663 |
| | 30.2.2 Steps for Stiffness Parameter Calculation | 664 |
| 30.3 | Results and Discussions | 664 |
| 30.4 | Conclusions and Future Work | 668 |
| | References | 668 |
| 31 | Covering a Surface with Pre-Stressed Ribbons: From Theory to Nano-Structures Fabrication | 671 |
| | Alexandre Danescu, Philippe Regreny, Pierre Cremillieu, Jean-Louis Leclercq, Ioan R. Ionescu | |
| 31.1 | Introduction | 672 |
| 31.2 | Geometric and Kinematical Settings | 673 |
| 31.3 | Weak Transversal Homogeneity and the Moment Equations | 674 |
| 31.4 | Small Strain Deformation of a Ribbon | 675 |
| 31.5 | From Theory to Fabrication of a Nano-Sphere | 678 |
| | 31.5.1 Optimal Covering with Constant Parallel Ribbons | 679 |
| | 31.5.2 Elastic Layers with Pre-Stress: Material Parameters | 680 |
| | 31.5.3 Design and Fabrication | 681 |
| 31.6 | Conclusions and Perspectives | 684 |
| | References | 686 |
| 32 | Experimental and Theoretical Investigations of Auxetic Sheet Metal . | 689 |
| | Arash Gordanshekan, Tobias Heib, Wolfgang Ripplinger, Hans-Georg Herrmann, Stefan Diebels | |
| 32.1 | Introduction | 690 |
| 32.2 | Material and Methods | 692 |
| | 32.2.1 Sample Material | 692 |
| | 32.2.2 Perforated Aluminium Sheet | 692 |
| | 32.2.3 Experimental Setup | 693 |

32.2.4 Sample Preparation 694

32.3 Results and Discussion 695

32.3.1 Mechanical Properties of Bulk AlMg3 695

32.3.2 Experiment on the Auxetic Sheet 696

32.3.3 Simulation 702

32.4 Conclusion 704

References 705

**Correction to: Theoretical Analyses, Computations, and Experiments
of Multiscale Materials..... C1**

List of Contributors

B. E. Abali

Uppsala University, Division of Applied Mechanics, Department of Materials Science and Engineering, Uppsala, Sweden
e-mail: bilenemek@abali.org

R. Afshar

Division of Applied Mechanics, Department of Materials Science and Engineering, Uppsala University, 751 03 Uppsala, Sweden
e-mail: reza.afshar@angstrom.uu.se

H. Altenbach

Otto-von-Guericke-Universität Magdeburg, Lehrstuhl für Technische Mechanik, Institut für Mechanik, Fakultät für Maschinenbau, Universitätsplatz 2, 39106 Magdeburg, Germany
e-mail: holm.altenbach@ovgu.de

C. C. António

Engineering Faculty, University of Porto, Rua Dr. Roberto Frias, s/n, 4200 – 465 Porto, Portugal
Institute of Science and Innovation in Mechanical and Industrial Engineering, LAETA-INEGI, Rua Dr. Roberto Frias, 400, 4200 – 465 Porto, Portugal
e-mail: cantonio@fe.up.pt

G. Aydin

Istanbul Technical University, Faculty of Naval Architecture and Ocean Engineering, Istanbul, Turkey
e-mail: aydingo18@itu.edu.tr

J. S. Beatriz

University of Texas Rio Grande Valley, Mechanical Engineering Department, Edinburg, Texas 78539, U.S.A.
e-mail: julio.beatriz01@outlook.com

A. D. Bakiler

Department of Mechanical Engineering, Bilkent University, 06800 Ankara, Turkey
e-mail: derya.bakiler@bilkent.edu.tr

E. Barchiesi

École Nationale d'Ingénieurs de Brest, UMR CNRS 6027, IRDL, Brest, France.
Université de Bretagne Sud, IRDL-UBS - UMR CNRS 6027, Centre de Recherche,
Rue de Saint Maudé - BP 92116 56321, Lorient, Cedex, France
International Research Center on the Mathematics and Mechanics of Complex
Systems (M&MoCS), University of L'Aquila, Italy.
Dipartimento di Architettura, design e urbanistica, Università degli Studi di Sassari,
Italy.
e-mail: emilio.barchiesi@enib.fr, barchiesiemilio@gmail.com

P. Belov

Institute of Applied Mechanics of RAS, Moscow,
e-mail: belovpa@yandex.ru

A. M. Bersani

Department of Mechanical and Aerospace Engineering, Sapienza University of
Rome, Via Eudossiana, 18, 00184 Rome, Italy
e-mail: alberto.bersani@uniroma1.it

A. Bochkarev

Faculty of Applied Mathematics and Control Processes, Saint Petersburg State
University, 7/9 Universitetskaya nab., St. Petersburg, 199804 Russia
e-mail: a.bochkarev@spbu.ru

R. Burson

Department of Mathematics, California State University, Northridge, 18111
Nordhoff Street, Northridge, CA 91330, USA
e-mail: Roy.burson.618@my.csun.edu

D. Campanhã

Centre for Nanotechnology and Smart Materials, Rua Fernando Mesquita, 2785,
4760-034 Vila Nova de Famalicão, Portugal
e-mail: dcampanha@centi.pt

D. I. Caruntu

University of Texas Rio Grande Valley, Mechanical Engineering Department,
Edinburg, Texas 78539, U.S.A.
e-mail: dimitru.caruntu@utrgv.edu, caruntud2@asme.org, dcaruntu@yahoo.com

C. F. Castro

Engineering Faculty, University of Porto, Rua Dr. Roberto Frias, s/n, 4200 – 465
Porto, Portugal
Institute of Science and Innovation in Mechanical and Industrial Engineering,
LAETA-INEGI, Rua Dr. Roberto Frias, 400, 4200 – 465 Porto, Portugal
e-mail: ccastro@fe.up.pt

A. Ciallella

Dipartimento di Ingegneria Civile, Edile – Architettura e Ambientale, Università dell'Aquila

International Research Center M&MOCS, Università dell'Aquila, via Giovanni Gronchi 18, 67100, L'Aquila, Italy

e-mail: alessandro.ciallella@univaq.it

A. Danescu, Ph. Regreny, P. Cremillieu and Jean-Louis Leclercq

Univ Lyon, Ecole Centrale de Lyon, CNRS, INSA Lyon, University Claude Bernard Lyon 1, CPE Lyon, CNRS, INL, UMR5270, 69130 Ecully, France

e-mail: alexandre.danescu@ec-lyon.fr, philippe.regreny@ec-lyon.fr,

pierre.cremillieu@ec-lyon.fr, jean-louis.leclercq@ec-lyon.fr

F. Daví

DICEA & ICRY, Università Politecnica delle Marche, Ancona, Italy

on leave at IMT-School for Advanced Studies, Lucca, Italy

e-mail: davi@univpm.it

S. Diebels

Chair of Applied Mechanics, Saarland University, Campus A4 2, 66123 Saarbrücken, Germany

e-mail: s.diebels@mx.uni-saarland.de

R. Dimitri

School of Engineering, University of Salento, Via per Monteroni, Lecce, Italy

e-mail: rossana.dimitri@unisalento.it

K. Enakoutsa

Department of Mathematics, California State University, Northridge, 18111 Nordhoff Street, Northridge, CA 91330 and Department of Mathematics, UCLA, Los Angeles, 520 Portola Plaza, Los Angeles, CA 90095, USA

e-mail: koffi.enakoutsa@csun.edu

V. A. Eremeyev

University of Cagliari, Via Marengo, 2, 09123 Cagliari, Italy

e-mail: victor.eremeev@unica.it

Gdańsk University of Technology, ul. Gabriela Narutowicza 11/12, 80-233 Gdańsk, Poland,

e-mail: vicereme@pg.edu.pl

Institute of Applied Mechanics, Russian Academy of Sciences, Leningradsky prt 7, 125040 Moscow, Russia,

e-mail: eremeyev.victor@gmail.com

M. C. Fernandes

Engineering Faculty, University of Porto, Rua Dr. Roberto Frias, s/n, 4200 – 465 Porto, Portugal

Institute of Science and Innovation in Mechanical and Industrial Engineering,

LAETA-INEGI, Rua Dr. Roberto Frias, 400, 4200 – 465 Porto, Portugal

e-mail: up201506004@fe.up.pt

C. Furtado

Centre for Nanotechnology and Smart Materials, Rua Fernando Mesquita, 2785,
4760-034 Vila Nova de Famalicão, Portugal
e-mail: cfurtado@centi.pt

D. Georgievskii

Mechanical and Mathematical Department, Moscow State University, Moscow
119991, Russia
e-mail: georgiev@mech.math.msu.su

I. Giorgio

Department of Civil, Construction-Architectural and Environmental Engineering
(DICEAA), University of L'Aquila, Italy
International Research Center on the Mathematics and Mechanics of Complex
Systems (M&MoCS), University of L'Aquila, Italy.
e-mail: ivan.giorgio@univaq.it

A. Gordanshekan

Chair of Applied Mechanics, Saarland University, Campus A4 2, 66123 Saar-
brücken, Germany
e-mail: arash.gordanshekan@uni-saarland.de

N. Hamila

École Nationale d'Ingénieurs de Brest, France
e-mail: nahiene.hamila@enib.fr

T. Heib

Chair of Lightweight Systems, Saarland University, Campus E3 1, 66123
Saarbrücken, Germany
e-mail: tobias.heib@uni-saarland.de

H.-G. Herrmann

Chair of Lightweight Systems, Saarland University, Campus E3 1, 66123
Saarbrücken, Germany
Fraunhofer IZFP Institute for Nondestructive Testing, Campus E3 1, Saarbrücken,
66123, Germany
e-mail: hans-georg.herrmann@izfp.fraunhofer.de

C. Hesch

University of Siegen, Paul-Bonatz-Straße 9-11, Siegen, Germany
e-mail: christian.hesch@uni-siegen.de

Ioan R. Ionescu

LSPM, University Sorbonne-Paris-Nord, 93430 Villetaneuse, France and IMAR,
Romanian Academy, Bucharest, Romania
e-mail: ioan.r.ionescu@gmail.com

L. Jakobčín

Laboratoire de Mécanique Gabriel Lamé, Université d'Orléans, 8 rue Léonard de Vinci, 45100 Orléans, France

e-mail: lukas.jakabcin@univ-orleans.fr

A. Javili

Department of Mechanical Engineering, Bilkent University, 06800 Ankara, Turkey

e-mail: ajavili@bilkent.edu.tr

A. G. Kolpakov

SysAn, A Nevskogo street 12-a, 34, Novosibirsk, Russia

e-mail: algk@ngs.ru

A.I. Krusser

Research Centre on Dynamics of Solids and Structures, Voronezh State Technical University, 20-Letija Oktjabrja Str. 84, 394006 Voronezh, Russia

e-mail: an.krusser@yandex.ru

M. Krüger

University of Siegen, Paul-Bonatz-Straße 9-11, Siegen, Germany

e-mail: melanie.krueger@uni-siegen.de

S. Lurie

Institute of Applied Mechanics of RAS, Moscow,

e-mail: salurie@mail.ru

L. Matias

Engineering Faculty, University of Porto, Rua Dr. Roberto Frias, s/n, 4200 – 465 Porto, Portugal

e-mail: up201502891@edu.fe.up.pt

A. Misra

Civil, Environmental and Architectural Engineering Department, University of Kansas, USA.

e-mail: amisra@ku.edu

W. H. Müller

Institute of Mechanics, Chair of Continuum Mechanics and Constitutive Theory, Technische Universität Berlin, Einsteinufer 5, 10587 Berlin, Germany

e-mail: wolfgang.h.mueller@tu-berlin.de

L. Nazarenko

Otto-von-Guericke-Universität Magdeburg, Lehrstuhl für Technische Mechanik, Institut für Mechanik, Fakultät für Maschinenbau, Universitätsplatz 2, 39106 Magdeburg, Germany

e-mail: lidiia.nazarenko@ovgu.de

M. Nikabadze

Lomonosov Moscow State University, Moscow, Russian Federation
Bauman Moscow State Technical University, Moscow, Russian Federation
Moscow Center for Fundamental and Applied Mathematics, International Research
Center on Mathematics and Mechanics of Complex Systems (M&MoCS)
e-mail: munikabadze@yandex.ru

M. Nowak

Poznan University of Technology, Department of Virtual Engineering, Poland, ul.
Jana Pawla II 24
60-965 Poznan, Poland
e-mail: Michal.Nowak@put.poznan.pl

J. M. L. M. Palma

Engineering Faculty, University of Porto, Rua Dr. Roberto Frias, s/n, 4200 – 465
Porto, Portugal
e-mail: jpalma@fe.up.pt

M. Paradiso

Department of Structures for Engineering and Architecture, University of Naples
Federico II, via Claudio, 21, 80124, Naples, Italy
e-mail: massimo.paradiso@unina.it

S. I. S. Pinto

Engineering Faculty, University of Porto, Rua Dr. Roberto Frias, s/n, 4200 – 465
Porto, Portugal
Institute of Science and Innovation in Mechanical and Industrial Engineering,
LAETA-INEGI, Rua Dr. Roberto Frias, 400, 4200 – 465 Porto, Portugal
e-mail: spinto@fe.up.pt

L. Placidi

Faculty of Engineering, International Telematic University UNINETTUNO, Italy.
e-mail: luca.placidi@uninettunouniversity.net

J. Polak

Poznan University of Technology, Department of Virtual Engineering, Poland, ul.
Jana Pawla II 24, 60-965 Poznan, Poland
e-mail: Jan.Polak@put.poznan.pl

M. Pulvirenti

Dipartimento di Matematica, Università di Roma La Sapienza, Piazzale Aldo Moro
5, 00185 Rome, Italy
International Research Center M&MOCS, Università dell'Aquila, Italy
Accademia Nazionale dei Lincei
e-mail: pulviren@mat.uniroma1.it

S. I. Rakin

Siberian Transport University, D. Koval'chuk st., 191, Novosibirsk, Russia
e-mail: rakinsi@ngs.ru

E. Reccia

University of Cagliari, Via Marengo, 2, 09123 Cagliari, Italy,
e-mail: emanuele.reccia@unica.it

W. Rickert

Institute of Mechanics, Chair of Continuum Mechanics and Constitutive Theory,
Technische Universität Berlin, Einsteinufer 5, 10587 Berlin, Germany
e-mail: rickert@tu-berlin.de

W. Ripplinger

Chair of Applied Mechanics, Saarland University, Campus A4 2, 66123
Saarbrücken, Germany
e-mail: w.ripplinger@mx.uni-saarland.de

L. Rosati

Department of Structures for Engineering and Architecture, University of Naples
Federico II, via Claudio, 21, 80124, Naples, Italy
e-mail: rosati@unina.it

F. Schmidt

University of Siegen, Paul-Bonatz-Straße 9-11, Siegen, Germany
e-mail: felix.schmidt@uni-siegen.de

M. Selivanov

S.P. Timoshenko Institute of Mechanics, National Academy of Sciences, Nesterov
St., 3, 03057, Kyiv, Ukraine
e-mail: mfs@ukr.net

P. Seppecher

Institut de Mathématiques de Toulon, Université de Toulon, BP 20132, 83957 La
Garde Cedex, France
e-mail: seppecher@imath.fr

S. Sessa

Department of Structures for Engineering and Architecture, University of Naples
Federico II, via Claudio, 21, 80124, Naples, Italy
e-mail: salvatore.sessa2@unina.it

N. Shekarchizadeh

Department of Basic and Applied Sciences for Engineering, Sapienza University of
Rome, Via Antonio Scarpa, 16, 00161 Rome, Italy
e-mail: navid.shekarchizadeh@uniroma1.it

M. Shirani

University of California, Berkeley, Department of Mechanical Engineering,
Berkeley, CA 94720, USA
e-mail: milad_shirani@berkeley.edu

M. V. Shitikova

Research Centre on Dynamics of Solids and Structures, Voronezh State Technical University, 20-Letija Oktjabrja Str. 84, 394006 Voronezh, Russia
Moscow State University of Civil Engineering, Moscow, Russia
e-mail: mvs@vgasu.vrn.ru

S. Simonella

UMPA UMR 5669 CNRS, ENS de Lyon, 46 allée d'Italie, 69364 Lyon Cedex 07, France
e-mail: sergio.simonella@ens-lyon.fr

Yu. Solyaev

Institute of Applied Mechanics of RAS and FRC CSC RAS, Moscow, Russia
e-mail: yos@iam.ras.ru

L. C. Sousa

Engineering Faculty, University of Porto, Rua Dr. Roberto Frias, s/n, 4200 – 465 Porto, Portugal
Institute of Science and Innovation in Mechanical and Industrial Engineering, LAETA-INEGI, Rua Dr. Roberto Frias, 400, 4200 – 465 Porto, Portugal
e-mail: lcsousa@fe.up.pt

D. J. Steigmann

University of California, Berkeley, Department of Mechanical Engineering, Berkeley, CA 94720, USA
e-mail: dsteigmann@berkeley.edu

F. Tornabene

School of Engineering, University of Salento, Via per Monteroni, Lecce, Italy
e-mail: francesco.tornabene@unisalento.it

E. Turco

Department of Architecture, Design and Urban planning (DADU), University of Sassari, Italy
e-mail: emilio.turco@uniss.it

A. Ulukhanyan

Moscow Center for Fundamental and Applied Mathematics, International Research Center on Mathematics and Mechanics of Complex Systems (M&MoCS)
Università degli Studi dell'Aquila, L'Aquila, Italy
e-mail: armine.ulukhanyan@gmail.com

N. Vaiana

Department of Structures for Engineering and Architecture, University of Naples Federico II, via Claudio, 21, 80124, Naples, Italy
e-mail: nicolo.vaiana@unina.it

M. Viscoti

School of Engineering, University of Salento, Via per Monteroni, Lecce, Italy
e-mail: matteo.viscoti@unisalento.it

K. Weinberg

Universität Siegen, Lehrstuhl für Festkörpermechanik, Department Maschinenbau,
Paul-Bonatz-Str. 9-11, 57076 Siegen, Germany
e-mail: kerstin.weinberg@uni-siegen.de

M. Werner

Universität Siegen, Lehrstuhl für Festkörpermechanik, Department Maschinenbau,
Paul-Bonatz-Str. 9-11, 57076 Siegen, Germany
e-mail: marek.werner@uni-siegen.de

M. Winkelmann

Multiscale Mechanics, Department of Thermal and Fluid Engineering, Faculty of
Engineering Technology, University of Twente, PO Box 217, 7500AE Enschede,
the Netherlands
e-mail: m.winkelmann@utwente.nl

M. E. Yildizdag

University of L'Aquila, International Research Center on Mathematics and
Mechanics of Complex Systems, L'Aquila, Italy
Istanbul Technical University, Faculty of Naval Architecture and Ocean Engineering,
Istanbul, Turkey
e-mail: yildizdag@itu.edu.tr

Part I
Theoretical Analysis



Chapter 1

A Different Catch for Poisson

A. Derya Bakiler, Ali Javili

Abstract Poisson's ratio, similar to other material parameters of isotropic elasticity, is determined via experiments corresponding to small strains. Yet at small-strain linear elasticity, Poisson's ratio has a dual nature; although commonly understood as a *geometrical parameter*, Poisson's ratio is also a *material parameter*. From a geometrical perspective only, the concept of Poisson's ratio has been extended to large deformations by Beatty and Stalnaker. Here, through a variational analysis, we firstly propose an alternative relationship between the Poisson ratio and stretches at finite deformations such that the nature of Poisson's ratio as a material parameter is retained. In doing so, we introduce relationships between the Poisson ratio and stretches at large deformations different than those established by Beatty and Stalnaker. We show that all the nonlinear definitions of Poisson's ratio coincide at the reference configuration and thus, material and geometrical descriptions too coincide, at small-strains linear elasticity. Secondly, we employ this variational approach to bring in the notion of nonlinear Poisson's ratio in peridynamics, for the first time. In particular, we focus on bond-based peridynamics. The nonlinear Poisson's ratio of bond-based peridynamics coincides with $1/3$ for two-dimensional and $1/4$ for three-dimensional problems, at the reference configuration.

Keywords: Non-linear Poisson's ratio · Variational elasticity · Peridynamics

1.1 Introduction

In its classical definition, that being a kinematic definition in a small deformations context, Poisson's ratio is a constant obtained from the deformation of a domain under uni-axial tension or compression in the axial and lateral directions, illustrated

A. D. Bakiler, A. Javili
Department of Mechanical Engineering, Bilkent University, 06800 Ankara, Turkey
e-mail: derya.bakiler@bilkent.edu.tr, ajavili@bilkent.edu.tr

in Fig. 1.1. More precisely, it relates to the case where an isotropic domain is subject to an axial strain ε_{ext} in a uni-axial tension test, resulting in the lateral strain ε_{lat} . For the small-strain case the Poisson's ratio definition reads

$$\nu = -\frac{\varepsilon_{\text{lat}}}{\varepsilon_{\text{ext}}}, \quad (1.1)$$

which is obviously a *purely geometrical description* in that only geometrical, and not material parameters, are present. The definition of the Poisson ratio (1.1) is the most elementary one. It stems from a purely kinematic stand point, relating the two different resultant strain values of a body, rendering a constant that essentially describes the compressibility of the material. Note that, on the one hand, Poisson's

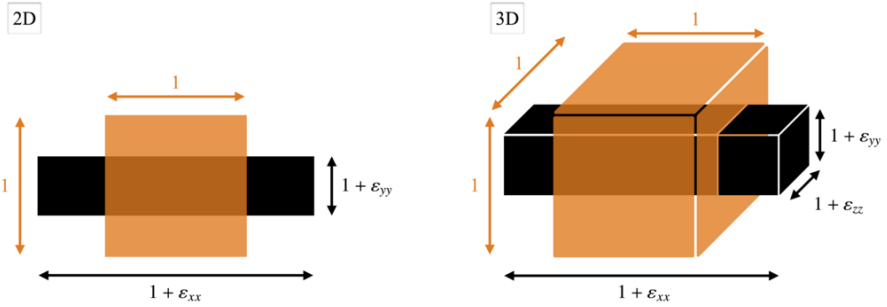


Fig. 1.1 Affine deformation of a unit domain under uni-axial tension test. Lateral deformations occur naturally to minimize the energy, while extension ε_{xx} is a prescribed value.

ratio definition is geometrical in nature and is constant for a material at small strains. On the other hand, from the linear elasticity analysis of isotropic Neo-Hookean materials, one can immediately establish a one-to-one relationship between the geometrical description of Poisson's ratio (1.1) and Lamé parameters as

$$2\text{D} \quad : \quad \nu = \frac{\Lambda}{\Lambda + 2\mu} \quad , \quad 3\text{D} \quad : \quad \nu = \frac{\Lambda}{2[\Lambda + \mu]}, \quad (1.2)$$

where Λ and μ are the first and second Lamé parameters, respectively. Table 1.1 elucidates the dual nature of Poisson's ratio associated with small-strain linear elasticity. For common (non-auxetic) materials, the Poisson ratio ranges from zero associated with a *fully compressible* material, to $\nu = 0.5$ corresponding to *incompressibility limit* in three-dimensional elasticity. The incompressibility limit for two-dimensional or plane-strain elasticity corresponds to $\nu = 1$, as it can be immediately realized from the geometrical constraints that correspond to a constant area of the domain. Henceforth, for the sake of brevity, we use the term "2D" to represent plane-strain conditions or purely two-dimensional elasticity similar to the interface elasticity theory, see (dell'Isola and Romano, 1987). Poisson's ratio can also take values less than zero, attributed to auxetic materials.

Table 1.1 Poisson’s ratio in small-strain linear elasticity and its dual nature as a material parameter (left) or a geometrical definition (right).

| | material description | geometrical description |
|----|--|---|
| 2D | $\frac{\Lambda}{\Lambda + 2\mu} = \nu$ | $= -\frac{\varepsilon_{yy}}{\varepsilon_{xx}}$ |
| 3D | $\frac{\Lambda}{2[\Lambda + \mu]} = \nu$ | $= -\frac{\varepsilon_{yy}}{\varepsilon_{xx}} = -\frac{\varepsilon_{zz}}{\varepsilon_{xx}}$ |

Table 1.2 Poisson’s ratio at large deformations nonlinear elasticity. The geometrical description of Poisson’s ratio has been extended to large deformations (top). We propose an extension of the material description of Poisson’s ratio (bottom), via a variational approach. At the reference configuration, both nonlinear variants coincide with their linear counterparts in Table 1.1.

| Beatty & Stalnaker (extension of geometrical description) | |
|---|--|
| 2D | $\nu = -\frac{E_{yy}}{E_{xx}} \quad \left\{ \begin{array}{l} \mathbf{E} = \ln \mathbf{U} \quad m = 0 \\ \mathbf{E} = \frac{1}{m} [\mathbf{U}^m - \mathbf{I}] \quad m \neq 0 \end{array} \right.$ |
| 3D | $\nu = -\frac{E_{yy}}{E_{xx}} = -\frac{E_{zz}}{E_{xx}}$ |
| current approach (extension of material description) | |
| 2D | $\mathbf{F} = \text{Diag}(\lambda, \eta) \quad \& \quad \delta\psi = 0 \quad \Rightarrow \quad \nu = \nu(\lambda, \eta)$ |
| 3D | $\mathbf{F} = \text{Diag}(\lambda, \eta, \eta) \quad \& \quad \delta\psi = 0 \quad \Rightarrow \quad \nu = \nu(\lambda, \eta)$ |

Remark on the forthcoming approach to explain the dual nature of Poisson’s ratio. Here, we have started from the elementary, geometrical definition of Poisson’s ratio since it is the more established one compared to its material description. Nonetheless, we demonstrate that for linear elasticity, the starting point is preferential because both descriptions of Poisson’s ratio render identical results. However, for the rest of the derivations we start from the material definition of Poisson’s ratio. This particular approach, as we will see shortly, is motivated by the foresight gained from the large-deformation analysis of the problem.

1.1.1 Key Objectives

This contribution aims to define Poisson's ratio from a variational perspective. The variational approach at small-strain linear elasticity does not result in new findings. At large deformations, however, it leads to an alternative description of the Poisson ratio, different from those that stem from the commonly accepted approach by Beatty and Stalnaker (1986). In summary, the objective of this contribution is two-fold.

Firstly, we show that the two descriptions of Poisson's ratio, namely the geometrical description (1.1) and the material description (1.2), coincide at small-strain elasticity. We argue that both descriptions can be extended to large deformations. The extension of the geometrical description (1.1) of Poisson's ratio to large deformation elasticity was introduced by Beatty and Stalnaker (1986). In contrast, we suggest an extension of the material description (1.2) to large deformations via a variational approach. The analysis here results in a relationship between the Poisson ratio and stretches at large deformations different than those currently established in the literature on the topic. Table 1.2 summarizes the key features of this contribution associated with Classical Continuum Mechanics (CCM).

Having established the variational formulation to capture Poisson's ratio, in the second part of the contribution, we introduce the notion of nonlinear Poisson's ratio to Peridynamics (PD). We demonstrate that the variational approach established for CMM in the first part can also be adopted to define a nonlinear Poisson's ratio in PD at large deformations. In particular, we focus on bond-based PD, for the sake of simplicity. We show that the nonlinear Poisson's ratio of bond-based PD is not constant, but it coincides with 1/3 for two-dimensional and 1/4 for three-dimensional problems, at the reference configuration.

1.1.2 Notation and Definitions

Direct notation is adopted throughout. Occasional use is made of index notation, the summation convention for repeated indices being implied. The scalar product of two vectors \mathbf{a} and \mathbf{b} is denoted $\mathbf{a} \cdot \mathbf{b} = a_i b_i$. The scalar product of two second-order tensors \mathbf{A} and \mathbf{B} is denoted $\mathbf{A} : \mathbf{B} = A_{ij} B_{ij}$. The composition of two second-order tensors \mathbf{A} and \mathbf{B} , denoted $\mathbf{A} \cdot \mathbf{B}$, is a second-order tensor with components $[\mathbf{A} \cdot \mathbf{B}]_{ij} = A_{is} B_{sj}$. The identity tensor \mathbf{i} is denoted as \mathbf{I} when it is associated with the material configuration. Trace of a second order tensor \mathbf{A} is obtained via its double-contraction with identity, i.e. $\text{Tr} \mathbf{A} = \mathbf{A} : \mathbf{I}$. The fourth-order identity tensor is denoted as \mathbb{I} . Similarly, other fourth-order constitutive tensors are also written with the same font, such as \mathbb{C} for the fourth-order constitutive tensor. The tensor product of two second-order tensors \mathbf{A} and \mathbf{B} is a fourth-order tensor $\mathbb{D} = \mathbf{A} \otimes \mathbf{B}$ with $D_{ijkl} = A_{ij} B_{kl}$. The two non-standard tensor products of two second-order tensors \mathbf{A} and \mathbf{B} are the fourth-order tensors $[\mathbf{A} \otimes \mathbf{B}]_{ijkl} = A_{ik} B_{jl}$ and $[\mathbf{A} \underline{\otimes} \mathbf{B}]_{ijkl} = A_{il} B_{jk}$.

1.1.3 Organization of the Manuscript

The remainder of this contribution is organized as follows. Section 1.2 elaborates on Poisson's ratio in the context of classical continuum mechanics (CCM), and the variational approach that underpins the discussion in this contribution is introduced. Afterwards, this variational framework is employed to formulate a uni-axial tension test for small-strain linear elasticity in Section 1.2.1, resulting in the well-known definitions of the Poisson ratio, for both two-dimensional and three-dimensional elasticity. Section 1.2.2 details on how the developed framework can be employed for large deformation elasticity, resulting in novel definitions for the nonlinear Poisson ratio that mimic the material description of the Poisson ratio rather than its geometrical one. Subsequently, Section 1.3 extends the discussion to Peridynamics (PD) and introduces the notion of a nonlinear Poisson ratio in PD, for the first time. It is shown that the variational approach can be immediately applied to bond-based PD, resulting in a varying Poisson ratio dependent on deformation. Section 1.4 concludes the work and provides further outlook.

1.2 Poisson's Ratio in Classical Continuum Mechanics

In this section, we introduce a variational approach to capture Poisson's ratio in classical continuum mechanics (CCM). To set the stage and convey the idea, we begin with the case of small-strain linear elasticity in Section 1.2.1. We then employ the same variational approach at large deformations nonlinear elasticity in Section 1.2.2. For both discussions on small strains as well as finite deformations, the underlying equation is the equilibrium of a domain under uni-axial tension. Hence, next we formulate equilibrium for the problem at hand.

Under prescribed boundary conditions, equilibrium corresponds to a relaxed state where the deformation field results in the minimum total energy functional. The total energy functional Ψ_{tot} consists of the internal and external contributions denoted Ψ_{int} and Ψ_{ext} , respectively. To minimize Ψ_{tot} , its first variation with respect to deformation, or rather motion, is set to zero as

$$\Psi_{\text{tot}} = \Psi_{\text{int}} + \Psi_{\text{ext}} \quad , \quad \delta\Psi_{\text{tot}} \doteq 0 \quad \Rightarrow \quad \delta\Psi_{\text{tot}} = \delta\Psi_{\text{int}} + \delta\Psi_{\text{ext}} \doteq 0. \quad (1.3)$$

The external energy Ψ_{ext} , in first-order classical continuum mechanics, is essentially minus work as

$$\delta\Psi_{\text{ext}} = -\delta\mathcal{W} \quad \text{with} \quad \delta\mathcal{W} = \int_{\mathcal{B}_0} \mathbf{b}_0 \cdot \delta\boldsymbol{\varphi} \, dV + \int_{\partial\mathcal{B}_0} \mathbf{t}_0 \cdot \delta\boldsymbol{\varphi} \, dA, \quad (1.4)$$

in which \mathcal{W} denotes the “working”, and \mathbf{b}_0 and \mathbf{t}_0 are the external body force density and surface force density in the material configuration, respectively. For further details and generalized boundary conditions, see (dell’Isola et al, 2012a,b; Javili et al, 2013; Auffray et al, 2015). The arbitrary variation of motion, denoted as $\delta\boldsymbol{\varphi}$,

is a vector-valued test function $\delta\varphi \in \mathcal{H}_0^1(\mathcal{B}_0)$ that is vanishing where Dirichlet-type boundary conditions are imposed. For a uni-axial tension test which is of interest here, the external body forces are zero and therefore the first integral in Eq. (1.4) vanishes identically. The second integral in Eq. (1.4) vanishes too, since (i) $\delta\varphi$ is zero where displacements are prescribed on the two ends of the domain and (ii) t_0 is zero everywhere that a homogeneous Neumann-type boundary condition is imposed. That is, *for the particular problem of a uni-axial tension test*, we seek for the solutions of $\delta\Psi_{\text{int}} = 0$. The internal energy Ψ_{int} reads

$$\Psi_{\text{int}} = \int_{\mathcal{B}_0} \psi \, dV, \quad (1.5)$$

and therefore equilibrium for the current problem reduces to

$$\delta\Psi_{\text{int}} = \int_{\mathcal{B}_0} \delta\psi \, dV \doteq 0. \quad (1.6)$$

For a uniform deformation in the domain, which holds for a uni-axial tension test, the equilibrium (1.6) then corresponds to

$$\delta\psi \doteq 0. \quad (1.7)$$

The variational constraint (1.7) is an underlying relationship that holds throughout this discussion, and also holds for finite deformations as well as small strains.

1.2.1 Poisson's Ratio for Small-Strain Linear Elasticity

Let ε be the strain tensor associated with small-strain linear elasticity. In order to establish a variational approach, one needs to begin from the scalar free energy density ψ corresponding to small-strain linear elasticity

$$\psi = \frac{1}{2} \varepsilon : \mathbb{C} : \varepsilon, \quad (1.8)$$

with \mathbb{C} being the fourth-order constitutive tensor. The fourth-order constitutive tensor in terms of the first and second Lamé parameters Λ and μ , respectively, reads

$$\mathbb{C} = \mu [\underline{\mathbf{I}} \otimes \underline{\mathbf{I}} + \underline{\mathbf{I}} \otimes \underline{\mathbf{I}}] + \Lambda \underline{\mathbf{I}} \otimes \underline{\mathbf{I}}, \quad (1.9)$$

and therefore

$$\psi = \psi(\varepsilon) = \mu \varepsilon : \varepsilon + \frac{1}{2} \Lambda \text{Tr}^2 \varepsilon. \quad (1.10)$$

Using the relationship (1.2), the free energy density (1.10) in terms of μ and Poisson's ratio ν reads

$$\begin{cases} 2\text{D} & : \quad \psi = \mu \varepsilon : \varepsilon + \frac{\mu\nu}{1-\nu} \text{Tr}^2 \varepsilon, \\ 3\text{D} & : \quad \psi = \mu \varepsilon : \varepsilon + \frac{\mu\nu}{1-2\nu} \text{Tr}^2 \varepsilon. \end{cases} \quad (1.11)$$

For a uni-axial tension test in Fig. 1.1, the strain tensor simplifies to a diagonal tensor

$$2\text{D} : \varepsilon = \text{Diag}(\varepsilon_{xx}, \varepsilon_{yy}) \quad , \quad 3\text{D} : \varepsilon = \text{Diag}(\varepsilon_{xx}, \varepsilon_{yy}, \varepsilon_{zz}), \quad (1.12)$$

wherein $\varepsilon_{yy} = \varepsilon_{zz}$ is the lateral strain in 3D. Inserting strains (1.12) into the internal energy density (1.11) furnishes

$$\begin{cases} 2\text{D} & : \quad \psi = \mu [\varepsilon_{xx}^2 + \varepsilon_{yy}^2] + \frac{\mu\nu}{1-\nu} [\varepsilon_{xx} + \varepsilon_{yy}]^2, \\ 3\text{D} & : \quad \psi = \mu [\varepsilon_{xx}^2 + 2\varepsilon_{yy}^2] + \frac{\mu\nu}{1-2\nu} [\varepsilon_{xx} + 2\varepsilon_{yy}]^2. \end{cases} \quad (1.13)$$

Next, we set $\delta\psi \doteq 0$ in order to impose equilibrium (1.7). In doing so, note that $\psi = \psi(\varepsilon_{xx}, \varepsilon_{yy})$ and therefore

$$\delta\psi = \frac{\partial\psi}{\partial\varepsilon_{xx}} \delta\varepsilon_{xx} + \frac{\partial\psi}{\partial\varepsilon_{yy}} \delta\varepsilon_{yy} \doteq 0. \quad (1.14)$$

However, for the problem at hand, the extension ε_{xx} is a prescribed quantity and therefore ε_{yy} is the only remaining variable. This immediately results in

$$\delta\psi \doteq 0 \quad \Rightarrow \quad \frac{\partial\psi}{\partial\varepsilon_{yy}} \doteq 0. \quad (1.15)$$

Finally, we insert the energy densities (1.13) into the *reduced equilibrium equation* (1.15). That is

$$\frac{\partial\psi}{\partial\varepsilon_{yy}} \doteq 0 \quad \Rightarrow \quad \begin{cases} 2\text{D} & : \quad 2\mu\varepsilon_{yy} + \frac{2\mu\nu}{1-\nu} [\varepsilon_{xx} + \varepsilon_{yy}] \doteq 0, \\ 3\text{D} & : \quad 2\mu\varepsilon_{yy} + \frac{2\mu\nu}{1-2\nu} [\varepsilon_{xx} + 2\varepsilon_{yy}] \doteq 0. \end{cases} \quad (1.16)$$

Solving each relation in Eq. (1.16), results in

$$2\text{D} : \nu = -\frac{\varepsilon_{yy}}{\varepsilon_{xx}} \quad , \quad 3\text{D} : \nu = -\frac{\varepsilon_{yy}}{\varepsilon_{xx}}, \quad (1.17)$$

which shall be compared with Eq. (1.2). That is, *starting from energy, via a variational procedure for a uni-axial tension test, one can show that the material description of Poisson's ratio indeed coincides with its geometrical definition*. This finding per se is not surprising. Nonetheless, as we will see shortly, the same procedure at finite deformations results in relationships for Poisson's ratio that are different from those previously reported in literature.

1.2.2 Poisson's Ratio for Large Deformations Nonlinear Elasticity

Consider the deformation of a continuum body, as illustrated in Fig 1.2. The continuum body occupies the material configuration $\mathcal{B}_0 \subset \mathbb{R}^3$ at time $t = 0$ that is mapped to the spatial configuration $\mathcal{B}_t \subset \mathbb{R}^3$ at any time $t > 0$ via the nonlinear deformation map φ , with \mathbf{X} and \mathbf{x} identifying points in the material and spatial configurations, respectively. The deformation gradient in the bulk, denoted \mathbf{F} , is a linear deformation map that relates an infinitesimal line element $d\mathbf{X} \in T\mathcal{B}_0$ to its spatial counterpart $d\mathbf{x} \in T\mathcal{B}_t$ via the relation $d\mathbf{x} = \mathbf{F} \cdot d\mathbf{X}$ where $\mathbf{F} := \text{Grad}\varphi$.

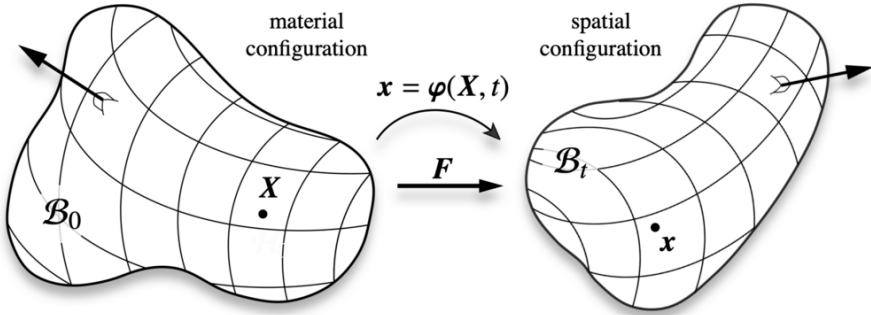


Fig. 1.2 The deformation of a continuum body which occupies the material configuration $\mathcal{B}_0 \subset \mathbb{R}^3$ at time $t = 0$ that is mapped to the spatial configuration $\mathcal{B}_t \subset \mathbb{R}^3$ at any time $t > 0$ via the nonlinear deformation map φ .

For large deformations, and from a geometrical perspective, the Poisson ratio can still be expressed as minus the ratio of lateral strain to extensional strain, similar to small-strain linear elasticity, if the strain measures themselves correspond to large deformations. That is

$$\nu = -\frac{\text{lateral strain}}{\text{extensional strain}} \quad \text{with} \quad \text{strain} \equiv \text{any finite strain measure}, \quad (1.18)$$

holds intuitively as an extension of the geometrical description of Poisson's ratio to finite strains. This case has been first explored by Beatty and Stalnaker (1986), who essentially constructed the general definition for nonlinear Poisson's ratio (1.18). In its original definition, extensional and lateral strains were the (Biot) strain measures $E_{xx} = \lambda - 1$ and $E_{yy} = \eta - 1$, respectively, with λ and η being the extensional and lateral stretches, respectively, associated with a uni-axial tension test. Nonetheless, the term "strain" can be extended to a larger Seth-Hill family of strain functions, collectively expressed as

$$\mathbf{E}(U) = \begin{cases} \ln U & \text{if } m = 0, \\ \frac{1}{m} [U^m - \mathbf{I}] & \text{if } m \neq 0, \end{cases} \quad (1.19)$$

with \mathbf{U} being the (right) stretch tensor. In particular, the most commonly used strain measures are

$$\begin{aligned}
 m = 1 & \quad \Rightarrow \quad \text{Biot} & : & \quad \mathbf{E}_B = \mathbf{U} - \mathbf{I}, \\
 m = 0 & \quad \Rightarrow \quad \text{Hencky} & : & \quad \mathbf{E}_H = \ln \mathbf{U}, \\
 m = 2 & \quad \Rightarrow \quad \text{Green} & : & \quad \mathbf{E}_G = \frac{1}{2} [\mathbf{U}^2 - \mathbf{I}], \\
 m = -2 & \quad \Rightarrow \quad \text{Almansi} & : & \quad \mathbf{E}_A = -\frac{1}{2} [\mathbf{U}^{-2} - \mathbf{I}].
 \end{aligned} \tag{1.20}$$

Obviously, the definition (1.18) is in essence the same as the previously mentioned Poisson ratio measure for linear, small deformations. What makes this case different is that for finite deformations, there is not a single measure for strain. Hence every strain measure renders a different definition of nonlinear Poisson ratio. This prohibits us from directly equating the two kinematic measures of Poisson's ratio associated with Eq. (1.1) and Eq. (1.18). For instance, for the most commonly used strain measures, the nonlinear Poisson ratio reads

$$\begin{aligned}
 \text{Biot} & : \quad \nu = \frac{1 - \eta}{\lambda - 1} & , & \quad \text{Hencky} & : \quad \nu = -\frac{\ln \eta}{\ln \lambda}, \\
 \text{Green} & : \quad \nu = \frac{1 - \eta^2}{\lambda^2 - 1} & , & \quad \text{Almansi} & : \quad \nu = \frac{1 - \eta^{-2}}{\lambda^{-2} - 1}.
 \end{aligned} \tag{1.21}$$

Note that in all the definitions (1.21), but also throughout this contribution, λ and η denote the extensional and lateral stretches, respectively, associated with the deformation gradient

$$2\text{D} : \mathbf{F} = \text{Diag}(\lambda, \eta) \quad , \quad 3\text{D} : \mathbf{F} = \text{Diag}(\lambda, \eta, \zeta), \tag{1.22}$$

wherein $\zeta = \eta$ is the lateral stretch in 3D. Notice that we now have a definition for a nonlinear Poisson's ratio where the Poisson's ratio is not simply a constant for a given material, but changes according to the stretch applied to the material.

Now moving onto the material description in a nonlinear setting, we employ the variational approach established previously. To do so, we begin from a (polyconvex) hyperelastic free energy density $\psi = \psi(\mathbf{F})$. For instance, for a compressible Neo-Hookean model ψ reads

$$\psi = \psi(\mathbf{F}) = \frac{1}{2} \mu [\mathbf{F} : \mathbf{F} - 3 - 2 \ln J] + \Lambda \left[\frac{1}{4} [J^2 - 1] - \frac{1}{2} \ln J \right], \tag{1.23}$$

where \mathbf{F} is the deformation gradient defined previously, and $J := \text{Det} \mathbf{F}$. The free energy density (1.23) shall be compared with its counterpart (1.10) for small-strain linear elasticity. Analogous to what was established in Section 1.2.1, using the relationship (1.2), the free energy density in terms of μ and Poisson's ratio ν reads

$$\begin{cases} 2\text{D} : \psi = \frac{1}{2} \mu [\mathbf{F} : \mathbf{F} - 2 - 2 \ln J] + \frac{2\mu\nu}{1-\nu} \left[\frac{1}{4} [J^2 - 1] - \frac{1}{2} \ln J \right], \\ 3\text{D} : \psi = \frac{1}{2} \mu [\mathbf{F} : \mathbf{F} - 3 - 2 \ln J] + \frac{2\mu\nu}{1-2\nu} \left[\frac{1}{4} [J^2 - 1] - \frac{1}{2} \ln J \right]. \end{cases} \quad (1.24)$$

For a uni-axial tension test, the deformation gradient \mathbf{F} simplifies to a diagonal tensor expressed in Eq. (1.22). Inserting the corresponding deformation gradient (1.22) into the internal energy density (1.24) furnishes

$$\begin{cases} 2\text{D} : \psi = \frac{1}{2} \mu [\lambda^2 + \eta^2 - 2 - 2 \ln(\lambda\eta)] \\ \quad + \frac{2\mu\nu}{1-\nu} \left[\frac{1}{4} [(\lambda\eta)^2 - 1] - \frac{1}{2} \ln(\lambda\eta) \right], \\ 3\text{D} : \psi = \frac{1}{2} \mu [\lambda^2 + 2\eta^2 - 3 - 2 \ln(\lambda\eta^2)] \\ \quad + \frac{2\mu\nu}{1-2\nu} \left[\frac{1}{4} [(\lambda\eta^2)^2 - 1] - \frac{1}{2} \ln(\lambda\eta^2) \right]. \end{cases} \quad (1.25)$$

Next, we set $\delta\psi \doteq 0$ in order to impose equilibrium (1.7). In doing so, note that $\psi = \psi(\lambda, \eta)$ and therefore

$$\delta\psi = \frac{\partial\psi}{\partial\lambda} \delta\lambda + \frac{\partial\psi}{\partial\eta} \delta\eta \doteq 0. \quad (1.26)$$

However, for the problem at hand, the extension λ is a prescribed quantity and therefore η is the only remaining variable. This immediately results in

$$\delta\psi \doteq 0 \quad \Rightarrow \quad \frac{\partial\psi}{\partial\eta} \doteq 0. \quad (1.27)$$

Finally, we use the energy densities (1.25) in the *reduced equilibrium equation* (1.27). That is

$$\frac{\partial\psi}{\partial\eta} \doteq 0 \quad \Rightarrow \quad \begin{cases} 2\text{D} : \frac{1}{2} \mu \left[2\eta - \frac{2}{\eta} \right] + \frac{2\mu\nu}{1-\nu} \left[\frac{1}{2} \lambda^2 \eta - \frac{1}{2\eta} \right] \doteq 0, \\ 3\text{D} : \frac{1}{2} \mu \left[4\eta - \frac{4}{\eta} \right] + \frac{2\mu\nu}{1-2\nu} \left[\lambda^2 \eta^3 - \frac{1}{\eta} \right] \doteq 0. \end{cases} \quad (1.28)$$

Solving each relation in Eq. (1.28), results in

$$2\text{D} : \nu = \frac{1 - \eta^{-2}}{1 - \lambda^2}, \quad 3\text{D} : \nu = \frac{1 - \eta^{-2}}{2 - \eta^{-2} - \lambda^2 \eta^2}, \quad (1.29)$$

which shall be compared with Eq. (1.21). That is, *for large deformations too, starting from energy, via a variational procedure for a uni-axial tension test, one can establish a material description of Poisson's ratio that no longer coincides with its commonly*

accepted geometrical definitions. Table 1.3 extends Table 1.2 and summarizes the aspects of Poisson’s ratio at large deformations.

Table 1.3 Poisson’s ratio at large deformations nonlinear elasticity. The geometrical description of Poisson’s ratio has been extended to large deformations (top). Via a variational approach, we propose an extension of the material description of Poisson’s ratio (bottom).

| Beatty & Stalnaker | | | |
|--|---|--|--|
| 2D | $\nu = -\frac{E_{yy}}{E_{xx}}$ | | |
| 3D | $\nu = -\frac{E_{yy}}{E_{xx}} = -\frac{E_{zz}}{E_{xx}}$ | | |
| $\left\{ \begin{array}{ll} \mathbf{E} = \ln \mathbf{U} & m = 0 \\ \mathbf{E} = \frac{1}{m} [\mathbf{U}^m - \mathbf{I}] & m \neq 0 \end{array} \right.$ | | | |
| 2D | <table border="1" style="width: 100%;"> <tr> <td style="padding: 5px;">Biot : $\nu_B = \frac{1 - \eta}{\lambda - 1}$</td> <td style="padding: 5px;">Hencky : $\nu_H = -\frac{\ln \eta}{\ln \lambda}$</td> </tr> </table> | Biot : $\nu_B = \frac{1 - \eta}{\lambda - 1}$ | Hencky : $\nu_H = -\frac{\ln \eta}{\ln \lambda}$ |
| Biot : $\nu_B = \frac{1 - \eta}{\lambda - 1}$ | Hencky : $\nu_H = -\frac{\ln \eta}{\ln \lambda}$ | | |
| 3D | <table border="1" style="width: 100%;"> <tr> <td style="padding: 5px;">Green : $\nu_G = \frac{1 - \eta^2}{\lambda^2 - 1}$</td> <td style="padding: 5px;">Almansi : $\nu_A = \frac{1 - \eta^{-2}}{\lambda^{-2} - 1}$</td> </tr> </table> | Green : $\nu_G = \frac{1 - \eta^2}{\lambda^2 - 1}$ | Almansi : $\nu_A = \frac{1 - \eta^{-2}}{\lambda^{-2} - 1}$ |
| Green : $\nu_G = \frac{1 - \eta^2}{\lambda^2 - 1}$ | Almansi : $\nu_A = \frac{1 - \eta^{-2}}{\lambda^{-2} - 1}$ | | |
| current approach | | | |
| 2D | $\mathbf{F} = \text{Diag}(\lambda, \eta) \quad \& \quad \delta\psi = 0 \quad \Rightarrow \quad \nu = \nu(\lambda, \eta)$ | | |
| 3D | $\mathbf{F} = \text{Diag}(\lambda, \eta, \eta) \quad \& \quad \delta\psi = 0 \quad \Rightarrow \quad \nu = \nu(\lambda, \eta)$ | | |
| 2D | $\nu = \frac{1 - \eta^{-2}}{1 - \lambda^2}$ | | |
| 3D | $\nu = \frac{1 - \eta^{-2}}{2 - \eta^{-2} - \lambda^2 \eta^2}$ | | |

Fig. 1.3 illustrates the different kinematic measures of Poisson’s ratio, namely that of Biot, Hencky, Green and Almansi, as gathered in Eq. (1.21), at the incompressibility limit, against the current kinetic definition (1.29). The nonlinear Poisson ratio ν , obtained for the various definitions, is plotted versus the axial stretch λ , which ranges from 0.5 to 1.5, thus covering both contraction and extension. Clearly, all of the definitions coincide at $\lambda = 1$, to the expected, incompressible value of $\nu = 1$ for 2D and $\nu = \frac{1}{2}$ for 3D. The significance of this point lies in the fact that deformations close to $\lambda = 1$ correspond to small stains. Hence as we move away from this small-strain

limit, the geometrical and material descriptions of Poisson’s ratio move away from each other, since the nonlinearity of the Poisson ratio becomes more pronounced and consequently, the different functions begin to portray different behaviors. Only the current definition and the Hencky definition at the incompressibility limit remain constant regardless of the stretch λ .

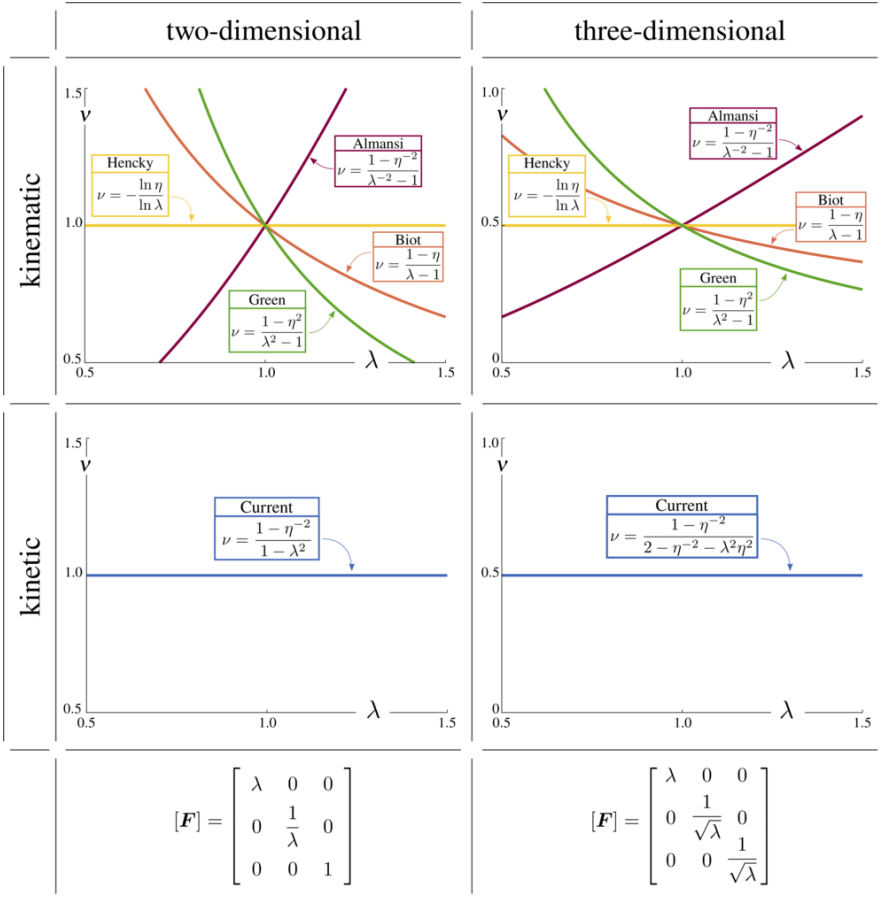


Fig. 1.3 Comparison of the current kinetic nonlinear Poisson’s ratio definition with previously established, kinematic definitions.

Equipped with the nonlinear Poisson’s ratio (1.29), another interesting aspect to investigate is the relationship between the lateral stretch η and the Jacobian J . This combination is particularly intriguing since $J = \text{Det} F$ is the ratio of the current over reference volume of the domain for 3D and the ratio of the current over reference area of the domain for 2D. Therefore J serves as an indication of compressibility of a material too. That is, for nearly incompressible materials we expect $J \rightarrow 1$.

In doing so, it proves helpful to define a dimensionless “compressibility parameter” $\alpha = \Lambda/2\mu$, with α ranging from 0 at full compressibility, to $\alpha \rightarrow \infty$ at the incompressibility limit. Using the relationships established for the nonlinear Poisson ratio (1.29), we can immediately see that α boils down to the same function in terms of η and J , for both 2D and 3D. That is

$$\alpha = \frac{\Lambda}{2\mu} \Rightarrow \left\{ \begin{array}{l} \text{2D} : \alpha = \frac{\nu}{1-\nu} \\ \text{3D} : \alpha = \frac{\nu}{1-2\nu} \end{array} \right\} \Rightarrow \alpha = \frac{1-\eta^2}{J^2-1}. \quad (1.30)$$

Therefore, it is possible to express the lateral stretch η as a function of the compressibility parameter α and the Jacobian J , where for a uni-axial tension test, $J = \lambda\eta$ in 2D and $J = \lambda\eta^2$ in 3D. That is

$$\eta = \sqrt{1 - \alpha [J^2 - 1]}. \quad (1.31)$$

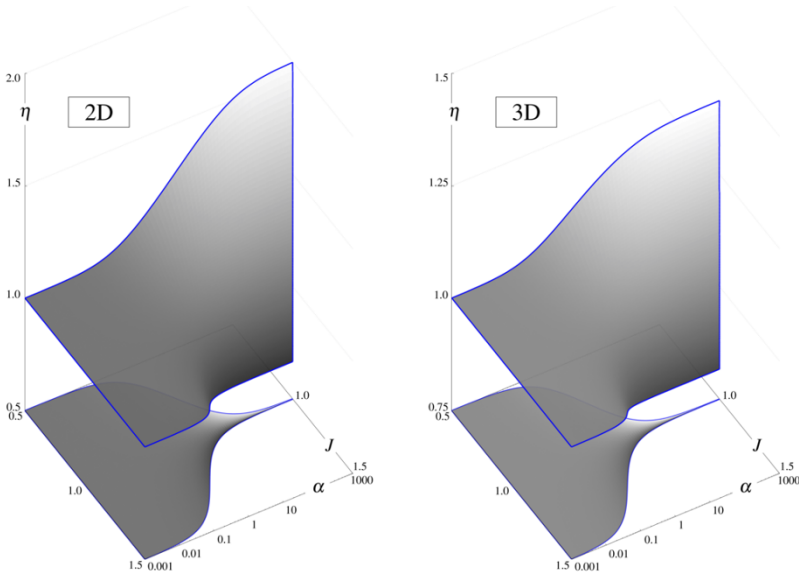


Fig. 1.4 Illustration of the lateral stretch η versus Jacobian J and compressibility parameter α for 2D (left) and 3D (right). As we move towards full incompressibility, J converges to 1, as expected.

Even though the definition (1.31) is obtained through a variational approach associated with the material description of the Poisson ratio, the geometrical interpretation of it is still visible. As the domain becomes increasingly compressible, this suggests geometrically that no matter what the axial stretch, λ is, there would be close to no contraction in the lateral direction, corresponding to $\eta \rightarrow 1$. This is clearly seen in Fig. 1.4, for both 2D (left) and 3D (right), with the curve flattening and

converging to a single value of $\eta = 1$, regardless of J hence of λ , as $\alpha \rightarrow 0$. On the other hand, as the material gets more and more incompressible with increasing α , the range of admissible values for η increases. Additionally, as we move towards full incompressibility, since at full incompressibility the volume is preserved, J converges to 1. We also see that the whole range of η becomes viable at the incompressible limit. This stems from the fact that incompressibility dictates that $J = 1$ and therefore $\eta = 1/\lambda$ in 2D, or $\eta = 1/\sqrt{\lambda}$ in 3D, which shows that for any value of axial stretch λ there exists a solution for the lateral stretch η to ensure incompressibility.

Remark on generalizing the methodology. *The variational framework here to extend the material description of Poisson's ratio to large deformations was carried out so far for the hyperelastic free energy density (1.23). This particular choice of (Ogden) free energy density was only made to simplify the derivations and highlights the key features of the procedure while avoiding technical complexities. Nonetheless, the developed framework itself is generic and can be applied to any other free energy density of an elastic material. That is, while the nonlinear Poisson ratio (1.29) is exclusively derived for the free energy density (1.23), it can be shown that any $\psi = \psi(\mathbf{F} : \mathbf{F}, J)$ furnishes a relationship between λ , η and ν akin to the nonlinear Poisson ratio (1.29). Generalizing even further, the framework can also be applied to any isotropic free energy density $\psi = \psi(I_1, I_2, I_3)$ with $I_1 := \text{Tr } \mathbf{C}$, $I_2 := \text{Tr } \text{Cof } \mathbf{C}$ and $I_3 := \text{Det } \mathbf{C}$ being the three principal invariants of the right Cauchy–Green tensor \mathbf{C} .*

Remark on the utility of the nonlinear Poisson's ratio. *One application of the nonlinear Poisson definition developed herein lies in understanding the instability behavior of soft, compressible materials under plane deformations. Instabilities that occur when a domain under compression buckles at a certain point to release energy have found several applications and are ubiquitous in nature. However, until recently, the large deformation instability analysis of a compressible domain under compression had not been thoroughly carried out. For instance, it is well-established that an incompressible half-space reaches instability at the critical stretch of $\lambda = 0.544$, referred to as Biot instability. However, with the use of a compressible material model, such as (1.23), imposing the uniform deformation related to uni-axial compression yields the nonlinear Poisson ratio (1.29). The nonlinear Poisson ratio can then be employed to solve for the critical stretch at which bifurcation occurs, showing that the critical stretch ranges from $\lambda = 0.486$ at full compressibility to $\lambda = 0.544$ at the incompressible limit. This utility is valid since, unlike the commonly accepted definitions of nonlinear Poisson's ratio, in our approach at large deformations too the Poisson's ratio is retained as a material parameter .*

1.3 Poisson's Ratio in Peridynamics

Peridynamics (PD) established by Silling (2000), following the pioneering works of Piola (dell'Isola et al, 2015, 2017), is a non-local continuum mechanics theory. In PD, the behavior of each material point is dictated by its interactions with other material points in its vicinity. Various applications and extensions of PD have been investigated in the past two decades. For a brief description of PD together with a review of its applications and related studies in different fields to date, see (Javili et al, 2019) and the references therein. Similar to the variational approach developed in Section 1.2, via minimizing the internal energy density, the Poisson ratio of bond-based peridynamics is investigated next.

Again, consider the deformation of a continuum body that is mapped from the material configuration \mathcal{B}_0 to the spatial configuration \mathcal{B}_t via the nonlinear deformation map φ , as illustrated in Fig. 1.5. Here also, \mathbf{X} and \mathbf{x} identify points in the material

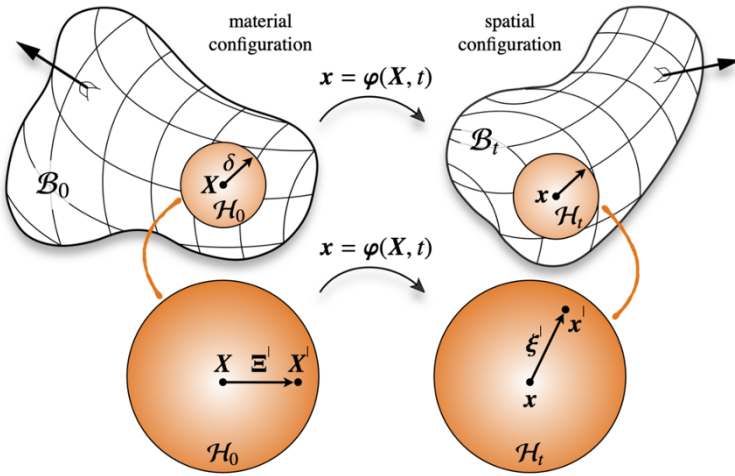


Fig. 1.5 Motion of a continuum body within the PD formulation. The neighborhood of \mathbf{X} is mapped to the neighborhood of \mathbf{x} .

and spatial configurations, respectively. The non-locality assumption of PD dictates that any point \mathbf{X} in the material configuration can interact with other points \mathbf{X}^l within its horizon $\mathcal{H}_0(\mathbf{X})$. The *measure* of the horizon in the material configuration, denoted as δ , is generally the radius of a spherical neighborhood at \mathbf{X} . The relative positions between a point and its neighbors are denoted by Ξ^l and ξ^l in the material and spatial configurations, respectively. That is

$$\Xi^l := \mathbf{X}^l - \mathbf{X} \quad , \quad \xi^l := \mathbf{x}^l - \mathbf{x} .$$

The bond stretch S^l is defined by $S^l = l^l/L^l$ with $L^l := |\mathbf{\Xi}^l|$ and $l^l := |\boldsymbol{\xi}^l|$ where L^l and l^l are the bond lengths in the material and spatial configurations respectively.

For an affine deformation, with a linear deformation map \mathbf{F} between the line elements $d\boldsymbol{\Xi}^l \in T\mathcal{B}_0$ and $d\boldsymbol{\xi}^l \in T\mathcal{B}_t$, the mapping reads

$$d\boldsymbol{\xi}^l = \mathbf{F} \cdot d\boldsymbol{\Xi}^l \quad , \quad \Rightarrow \quad \boldsymbol{\xi}^l = \mathbf{F} \cdot \boldsymbol{\Xi}^l . \quad (1.32)$$

Of particular interest for this contribution is the deformation map \mathbf{F} associated with a uni-axial tension test, illustrated in Fig. 1.6. In order to compute the Poisson ratio

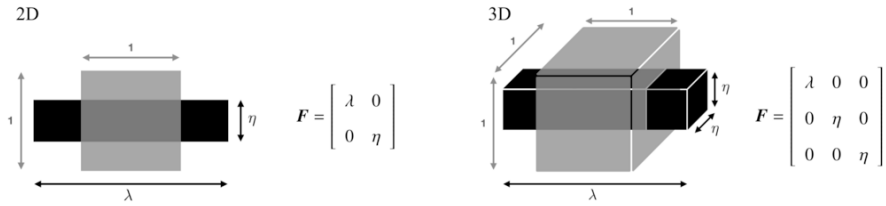


Fig. 1.6 Affine deformation of a unit domain via the linear deformation map \mathbf{F} , for 2D (left) and 3D (right). The prescribed deformation represents a uni-axial tension test. Extensional and lateral stretches are denoted as λ and η , respectively.

associated with the bond-based PD, we follow the same variational argument in Section 1.2. That is, we minimize the internal energy density via imposing $\delta\psi = 0$. In contrast to CCM, however, the free energy density ψ itself is an integral over the horizon.

For a two-dimensional domain, the internal energy density of PD per unit *area* in the material configuration is the integral of its density ψ^l over the horizon \mathcal{H}_0 . Similarly, for a three-dimensional domain, the internal energy density of PD per unit *volume* in the material configuration is the integral of its density ψ^l over the horizon \mathcal{H}_0 . Accordingly, ψ^l is the internal energy density per *area* squared for 2D and per *volume* squared for 3D in the material configuration. That is

$$\text{2D} \quad : \quad \psi = \frac{1}{2} \int_{\mathcal{H}_0} \psi^l \, dA^l \quad , \quad \text{3D} \quad : \quad \psi = \frac{1}{2} \int_{\mathcal{H}_0} \psi^l \, dV^l . \quad (1.33)$$

wherein the factor one-half before the integral is introduced to prevent double-counting since the combination of each pair of points within the horizon occurs twice when going over the global integral. This means that for each pair of points A and B , the pair-wise energy density gets counted twice, one from the sum over point A , and once from the sum over point B . The density of the internal energy density ψ^l is commonly expressed via a harmonic potential with a bond constant C . Therefore

$$\psi^l = \frac{1}{2} C L^l [S^l - 1]^2 \Rightarrow \begin{cases} 2\text{D} : \psi = \frac{1}{2} \int_{\mathcal{H}_0} \frac{1}{2} C L^l [S^l - 1]^2 dA^l, \\ 3\text{D} : \psi = \frac{1}{2} \int_{\mathcal{H}_0} \frac{1}{2} C L^l [S^l - 1]^2 dV^l. \end{cases} \quad (1.34)$$

The bond-based interaction energy density (1.34) of PD shall be compared with its counterpart (1.24) in CCM. Therefore, for the uni-axial tension test of interest here, the internal energy density ψ reads

$$\begin{cases} 2\text{D} : \psi = \frac{1}{2} \int_{\mathcal{H}_0} \frac{1}{2} C |\boldsymbol{\Xi}^l| \left[\frac{|\mathbf{F} \cdot \boldsymbol{\Xi}^l|}{|\boldsymbol{\Xi}^l|} - 1 \right]^2 dA^l, \\ 3\text{D} : \psi = \frac{1}{2} \int_{\mathcal{H}_0} \frac{1}{2} C |\boldsymbol{\Xi}^l| \left[\frac{|\mathbf{F} \cdot \boldsymbol{\Xi}^l|}{|\boldsymbol{\Xi}^l|} - 1 \right]^2 dV^l. \end{cases} \quad (1.35)$$

wherein $\mathbf{F} = \text{Diag}(\lambda, \eta)$ for 2D and $\mathbf{F} = \text{Diag}(\lambda, \eta, \eta)$ for 3D.

Next, we evaluate the internal energy densities (1.35) and identify their minimum to obtain a relationship between the lateral contraction η and the prescribed extensional stretch λ . More specifically, via setting $\delta\psi = 0$, we compute a nonlinear Poisson's ratio associated with bond-based PD. In doing so, similar to the discussion in Section 1.2.2, we recall $\psi = \psi(\lambda, \eta)$ and therefore

$$\delta\psi = \frac{\partial\psi}{\partial\lambda} \delta\lambda + \frac{\partial\psi}{\partial\eta} \delta\eta \doteq 0 \quad \Rightarrow \quad \frac{\partial\psi}{\partial\eta} \doteq 0, \quad (1.36)$$

wherein the last step follows from the fact that for the problem at hand the extension is a prescribed quantity and therefore η is the only remaining variable.

Figures 1.7 and 1.8 illustrate the energy densities (1.35) and its derivative with respect to η , for a wide range of values for λ and η .

Furthermore, these two sets of graphs demonstrate how $\partial\psi/\partial\eta$ varies with respect to the ratio $\frac{1-\eta}{\lambda-1}$ that is of particular interest since it is reminiscent of Biot nonlinear Poisson's ratio. We emphasize, the prescribed longitudinal stretch λ is not necessarily close to one and in fact, it ranges from nearly zero to four for both two-dimensional and three-dimensional cases in the numerical studies here. Clearly, large deformations can lead to Poisson's ratio other than $\frac{1}{3}$ for two-dimensional and other than $\frac{1}{4}$ for three-dimensional problems, associated with bond-based PD.

The nonlinear Poisson's ratio in these graphs follow the Biot definition. Nonetheless, a similar study can be carried out for all the other canonical definitions based on a geometrical interpretation of Poisson's ratio, as well as the material description thereof. With a little mathematical effort, and using L'Hospital's rule if necessary, it can be shown that in the vicinity of the reference configuration, the analysis leads to $\nu = \frac{1}{3}$ for all the canonical definitions of the nonlinear Poisson's ratio, as expected. That is

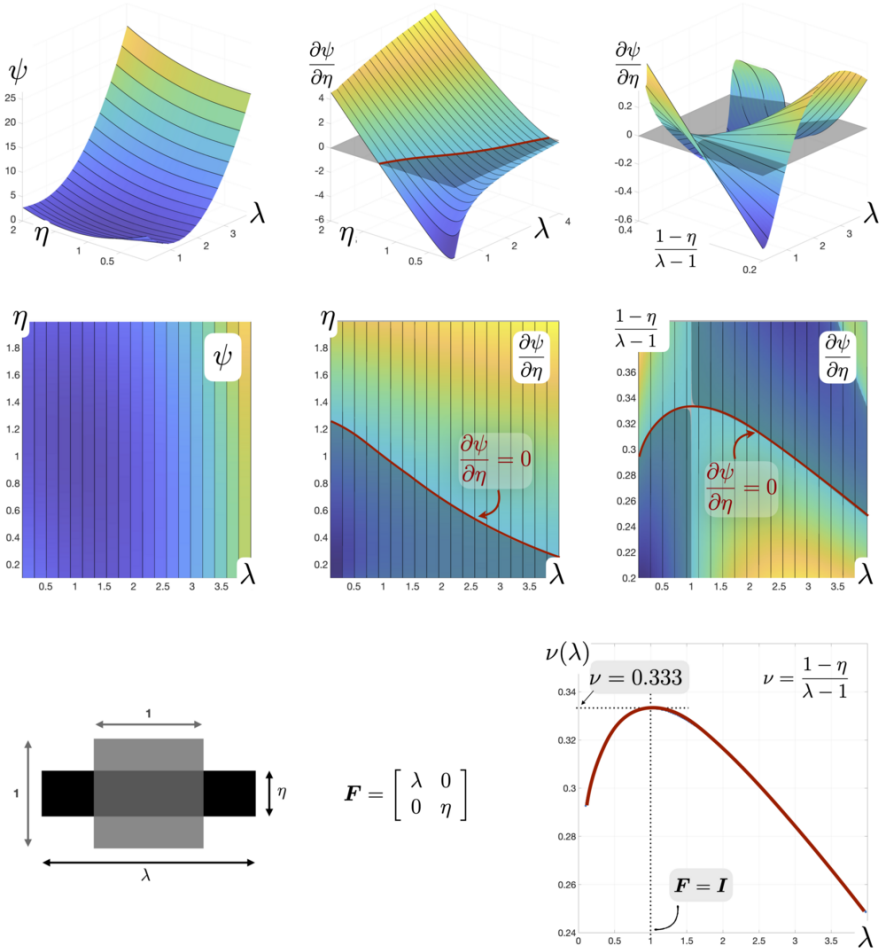


Fig. 1.7 Two-dimensional energy density ψ and its derivative with respect to the lateral stretch η and the ratio $\frac{1-\eta}{\lambda-1}$ for a wide range of values for λ and η . The ratio $\frac{1-\eta}{\lambda-1}$ depends on the stretch λ but approaches $\frac{1}{3}$ as $\lambda \rightarrow 1$, as expected. Therefore, one can identify the ratio $\frac{1-\eta}{\lambda-1}$ as a nonlinear Poisson's ratio associated with bond-based peridynamics.

$$\text{if } \frac{1-\eta}{\lambda-1} = \frac{1}{3} \Rightarrow \left\{ \begin{array}{l} \text{Biot} \quad : \quad \nu = \frac{1-\eta}{\lambda-1} \quad \Rightarrow \quad \nu = \frac{1}{3}, \\ \text{Hencky} \quad : \quad \nu = -\frac{\ln \eta}{\ln \lambda} \quad \Rightarrow \quad \nu = \frac{1}{3}, \\ \text{Green} \quad : \quad \nu = \frac{1-\eta^2}{\lambda^2-1} \quad \Rightarrow \quad \nu = \frac{1}{3}, \\ \text{Almansi} \quad : \quad \nu = \frac{1-\eta^{-2}}{\lambda^{-2}-1} \quad \Rightarrow \quad \nu = \frac{1}{3}, \\ \text{Current} \quad : \quad \nu = \frac{1-\eta^{-2}}{1-\lambda^2} \quad \Rightarrow \quad \nu = \frac{1}{3}. \end{array} \right. \quad (1.37)$$

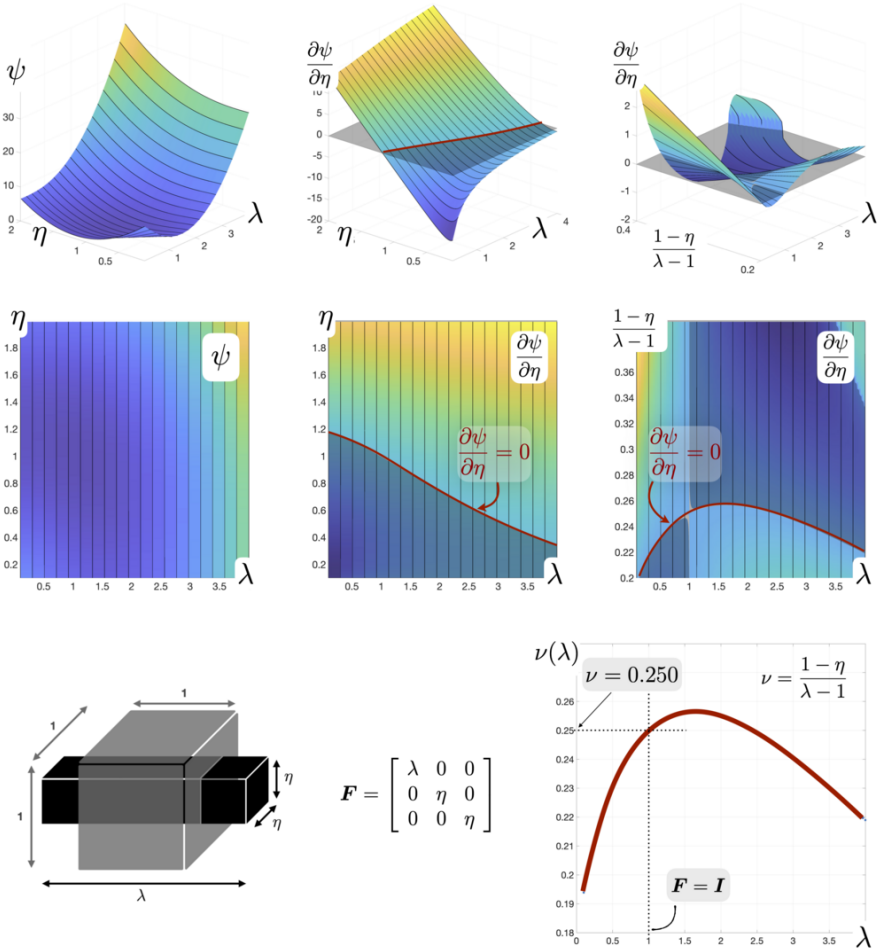


Fig. 1.8 Three-dimensional energy density ψ and its derivative with respect to the lateral stretch η and the ratio $\frac{1-\eta}{\lambda-1}$ for a wide range of values for λ and η . The ratio $\frac{1-\eta}{\lambda-1}$ depends on the stretch λ but approaches $\frac{1}{4}$ as $\lambda \rightarrow 1$, as expected. Therefore, one can identify the ratio $\frac{1-\eta}{\lambda-1}$ as a nonlinear Poisson's ratio associated with bond-based peridynamics.

The same conclusion also holds for 3D. More specifically, in the vicinity of the reference configuration, all the canonical definitions of the nonlinear Poisson's ratio coincide at $\nu = \frac{1}{4}$, as expected. That is

$$\text{if } \frac{1-\eta}{\lambda-1} = \frac{1}{4} \Rightarrow \left\{ \begin{array}{l} \text{Biot} \quad : \quad \nu = \frac{1-\eta}{\lambda-1} \quad \Rightarrow \quad \nu = \frac{1}{4}, \\ \text{Hencky} \quad : \quad \nu = -\frac{\ln \eta}{\ln \lambda} \quad \Rightarrow \quad \nu = \frac{1}{4}, \\ \text{Green} \quad : \quad \nu = \frac{1-\eta^2}{\lambda^2-1} \quad \Rightarrow \quad \nu = \frac{1}{4}, \\ \text{Almansi} \quad : \quad \nu = \frac{1-\eta^{-2}}{\lambda^{-2}-1} \quad \Rightarrow \quad \nu = \frac{1}{4}, \\ \text{Current} \quad : \quad \nu = \frac{1-\eta^{-2}}{2-\eta^{-2}-\lambda^2\eta^2} \quad \Rightarrow \quad \nu = \frac{1}{4}. \end{array} \right. \quad (1.38)$$

1.4 Conclusion

Among the material parameters of classical first-order linear elasticity, Poisson's ratio stands out in that (i) it is a dimensionless parameter and (ii) it can be interpreted both as a material or a geometrical parameter. Due to its geometrical definition in terms of strains, the Poisson ratio shall be revisited when it comes to large deformations. Beatty and Stalnaker (1986) extended the geometrical interpretation of Poisson's ratio to large deformations. In this contribution, however, we have extended the material description of Poisson's ratio via a variational approach. The variational approach at small strains leads to the trivial outcome that the material and geometrical descriptions of Poisson's ratio coincide. For an example of a hyperelastic material at finite deformations, we have proposed a novel definition for nonlinear Poisson's ratio. Inspired by the findings of the variational approach for classical elasticity, we then employed the same methodology to peridynamics, and in particular, bond-based peridynamics. It is shown that the nonlinear Poisson's ratio of bond-based peridynamics is no longer a constant, but it coincides with $1/3$ for two-dimensional and $1/4$ for three-dimensional problems, at the reference configuration, as expected. This view can be extended to other formulations of PD and lattice structures. Also, it can be utilized in the up-and-coming field of metamaterial design (Greaves et al, 2011), specifically considering auxetic materials and pantographic structures (Barchiesi et al, 2019; dell'Isola et al, 2019).

References

- Auffray N, dell'Isola F, Eremeyev V, Madeo A, Rosi G (2015) Analytical continuum mechanics à la Hamilton-Piola least action principle for second gradient continua and capillary fluids. *Mathematics and Mechanics of Solids* 20(4):375–417
- Barchiesi E, Spagnuolo M, Placidi L (2019) Bending of an infinite beam on an elastic foundation. *Mathematics and Mechanics of Solids* 24(1):212–234

- Beatty M, Stalnakar D (1986) The Poisson function of finite elasticity. *Journal of Applied Mechanics, Transactions ASME* 53(4):807–813
- dell'Isola F, Romano A (1987) On the derivation of thermomechanical balance equations for continuous systems with a nonmaterial interface. *International Journal of Engineering Science* 25(11-12):1459–1468
- dell'Isola F, Madeo A, Placidi L (2012a) Linear plane wave propagation and normal transmission and reflection at discontinuity surfaces in second gradient 3D continua. *ZAMM Zeitschrift für Angewandte Mathematik und Mechanik* 92(1):52–71
- dell'Isola F, Seppecher P, Madeo A (2012b) How contact interactions may depend on the shape of Cauchy cuts in Nth gradient continua: Approach "à la D'Alembert". *Zeitschrift für Angewandte Mathematik und Physik* 63(6):1119–1141
- dell'Isola F, Andreaus U, Placidi L (2015) At the origins and in the vanguard of peridynamics, non-local and higher-gradient continuum mechanics: An underestimated and still topical contribution of Gabrio Piola. *Mathematics and Mechanics of Solids* 20(8):887–928
- dell'Isola F, AD C, I G (2017) Higher-gradient continua: The legacy of Piola, Mindlin, Sedov and Toupin and some future research perspectives. *Mathematics and Mechanics of Solids* 22(4):852–872
- dell'Isola F, Seppecher P, Alibert J, Lekszycki T, Grygoruk R, Pawlikowski M, Steigmann D, Giorgio I, Andreaus U, Turco E, Gołaszewski M, Rizzi N, Boutin C, Eremeyev V, Misra A, Placidi L, Barchiesi E, Greco L, Cuomo M, Cazzani A, Corte A, Battista A, Scerrato D, Eremeeva I, Rahali Y, Ganghoffer J, Müller W, Ganzosch G, Spagnuolo M, Pfaff A, Barcz K, Hoschke K, Negggers J, Hild F (2019) Pantographic metamaterials: an example of mathematically driven design and of its technological challenges. *Continuum Mechanics and Thermodynamics* 31(4):851–884
- Greaves G, Greer A, Lakes R, Rouxel T (2011) Poisson's ratio and modern materials. *Nature Materials* 10(11):823–837
- Javili A, dell'Isola F, Steinmann P (2013) Geometrically nonlinear higher-gradient elasticity with energetic boundaries. *Journal of the Mechanics and Physics of Solids* 61(12):2381–2401
- Javili A, Morasata R, Oterkus E, Oterkus S (2019) Peridynamics review. *Mathematics and Mechanics of Solids* 24(11):3714–3739
- Silling S (2000) Reformulation of elasticity theory for discontinuities and long-range forces. *Journal of the Mechanics and Physics of Solids* 48(1):175–209



Chapter 2

Nonlinear Deformation of a Clamped-Edge Strip-Like Nano-Film

Anatolii Bochkarev

Abstract Nonlinear deformations of a clamped-edge nano-film are considered on the basis of an extension of von Kármán's theory of elastic plate, taken into account the Gurtin–Murdoch surface elasticity and Kirchhoff's hypothesis. Unlike most of the previous related theories, surface tension, usually omitted in the conjugation condition of Young–Laplace law in the transverse direction, is incorporated in the two-dimensional motion and constitutive relations for membrane forces together with quadratic terms equal to the von Kármán-type strains. The influence of the linear and nonlinear terms of surface tension is illustrated in the cases of nonlinear bending, post-critical compressive buckling, and free transverse vibration of a strip-like nano-film with clamped edges

Keywords: Surface elasticity · Surface tension · Young–Laplace law

2.1 Introduction

The surface elasticity or surface stresses theory proposed by (Gurtin and Murdoch, 1978) is widely used in the two-dimensional models of nano-plates and -shells. The surface stresses combine both the elastic properties of a solid and the surface tension of a liquid. The validity of this continuum approach to problems in nano-mechanics has been supported by the results of atomistic modeling (Miller and Shenoy, 2000).

Currently, many authors neglect the surface tension, taking into account only the elastic part of the surface stresses. This simplification is possibly acceptable in the plane problem of the theory of elasticity. However, in the theory of plates and shells, it is necessary to satisfy the 3D-equilibrium condition of a surface layer and bulk

A. Bochkarev

Faculty of Applied Mathematics and Control Processes, Saint Petersburg State University, 7/9 Universitetskaya nab., St. Petersburg, 199804 Russia
e-mail: a.bochkarev@spbu.ru

phase, known as Young–Laplace’s law. If the equilibrium in the tangential directions is provided mainly by the elastic part of the surface stresses, then in the transverse direction it is provided exclusively by the surface tension.

The work (Lim and He, 2004) on the nonlinear bending of nano-plates was the first one taking into account the Gurtin–Murdoch surface elasticity. In the same time, this model had an obvious flaw: the conjugation condition of Young–Laplace in the transverse direction, expressed through surface tension, was omitted. To eliminate this flaw, it was proposed by (Lu et al, 2006) in the linear theory of plates to consider that σ_{33} is nonzero in Hooke’s law. However, the results of (Huang, 2008) in the nonlinear theory showed that this refinement leads to negligible size effects, thereby confirming the basic principles of plate theory, where it is taken $\sigma_{33} \ll \sigma_{\alpha\alpha}$. Anyway, most authors (Altenbach et al, 2010; Altenbach and Eremeyev, 2011; Eremeyev, 2016; Ru, 2016; Xu, 2016; Eugster and Glocker, 2017; Shaat, 2018; Bochkarev and Grekov, 2019; Yue et al, 2019) prevailed the view that surface stresses affect bending mainly due to the difference in the values of the surface and bulk elastic moduli, and not by surface tension.

At the same time, publications appear that note the important role of gradient energy for describing nanostructures (Bochkarev, 2020b; Javanbakht et al, 2021). So in (Bochkarev, 2020b), it was shown that surface tension can significantly correct the mechanical properties of the ultra thin-walled structures if the conjugation condition of Young–Laplace in the transverse direction is correct incorporated into the bending equation. For this purpose, the model proposed by (Lim and He, 2004) was further developed in (Bochkarev, 2020b) and the nonlinearity of surface tension, equal to the von Kármán-type strain, has been taken into account also. These results were shown on the example of the nonlinear bending, transverse free vibration, and compressive buckling of a strip-like nano-film with simply supported edges. In addition in (Bochkarev, 2020a), the post-critical deformation of the compressive strip-like nano-film was shown also.

Present study develops this theme and shows the size effect with taken into account surface stresses with surface tension on the example of the nonlinear bending, transverse free vibration, and post-critical deformation of a compressive strip-like nano-film with clamped edges. This case of support is interesting because orthogonality of the linear eigenforms does not help here to simplify the nonlinear problem.

2.2 Problem Formulation

An isotropic elastic nano-plate is considered. The stresses of the bulk phase obey the constitutive relation of Hooke’s law for plates (hereinafter $\alpha, \beta, \gamma = 1, 2$)

$$\sigma_{\alpha\beta} = \frac{E}{1-\nu^2} ((1-\nu)\varepsilon_{\alpha\beta} + \delta_{\alpha\beta}\nu\varepsilon_{\gamma\gamma}) \quad (\sigma_{33} \ll \sigma_{\alpha\alpha}) \quad (2.1)$$

On the top (+) and bottom (−) faces, there are the surface stresses obeying the constitutive relations (Gurtin and Murdoch, 1978)

$$\begin{aligned}\tau_{\alpha\beta}^{\pm} &= \delta_{\alpha\beta}\tau_0 + 2(\mu_s - \tau_0)\varepsilon_{\alpha\beta}^{\pm} + \delta_{\alpha\beta}(\lambda_s + \tau_0)\varepsilon_{\gamma\gamma}^{\pm} + \tau_0(\nabla_s \mathbf{u})_{\alpha\beta}^{\pm} \\ \tau_{3\beta}^{\pm} &= \tau_0(\nabla_s \mathbf{u})_{3\beta}^{\pm}\end{aligned}\quad (2.2)$$

The bulk stresses on the faces are balanced with the surface stresses according to Young–Laplace law (Gurtin and Murdoch, 1978)

$$\nabla_s^{\pm} \cdot \boldsymbol{\tau}^{\pm} + \boldsymbol{\varphi}^{\pm} = \rho_s \ddot{\mathbf{u}}^{\pm} \pm \mathbf{n} \cdot \boldsymbol{\sigma}^{\pm} \quad (2.3)$$

Here: E , ν and ρ are Young's modulus, Poisson's ratio and density of bulk phase; the subscript s marks the surface properties – Lamé's parameters λ_s and μ_s , the density ρ_s , and also the residual surface tension τ_0 – all equal on the both faces; \mathbf{u} and $\boldsymbol{\varepsilon}$ are the displacement and the elastic strain, ∇_s is the surface nabla-operator; \mathbf{p} and $\boldsymbol{\varphi}^{\pm}$ are the external bulk and surface loads; \mathbf{n} is a normal to the middle surface.

The nonlinear Kirchhoff model of complex bending of nano-plates takes into account the surface stresses (2.2), incorporating the conjugation condition on the faces (2.3) (including in the transverse direction), and also considering nonlinearity of surface tension equal to the von Kármán-type nonlinear strain

$$\begin{aligned}\varepsilon_{\beta\alpha}^0 &= \frac{1}{2}(u_{\beta,\alpha}^0 + u_{\alpha,\beta}^0 + w_{,\alpha}w_{,\beta}) \\ \tau_0(\nabla_s u)_{\beta\alpha}^0 &= \tau_0(u_{\beta,\alpha}^0 - ww_{,\beta\alpha}), \quad \tau_0(\nabla_s u)_{3\alpha}^0 = \tau_0(w_{,\alpha} + u_{\beta}^0 w_{,\beta\alpha})\end{aligned}\quad (2.4)$$

was proposed in (Bochkarev, 2020b) and can be expressed as the von Kármán set

$$\begin{aligned}I^* \ddot{u}_{\beta}^0 &= T_{\beta\alpha,\alpha}^* - \tau_0(w_{,\alpha}^2)_{,\beta} + P_{\beta}^* \\ J^* \ddot{w}_{,\alpha\alpha} - I^* \ddot{w} &= D^* \nabla_s^2 \nabla_s^2 w - 2\tau_0 \nabla_s^2 w - T_{\beta\alpha}^* w_{,\beta\alpha} - m_{\alpha,\alpha}^* - P_3^*\end{aligned}\quad (2.5)$$

with the constitutive relation for the effective membrane forces and bending moments

$$T_{\beta\alpha}^* = 2\tau_0 \delta_{\beta\alpha} + 2\tau_0(\nabla_s u)_{\beta\alpha}^0 + C^* ((1 - \nu_t^*)\varepsilon_{\beta\alpha}^0 + \nu_t^* \delta_{\beta\alpha} \varepsilon_{\gamma\gamma}^0) \quad (2.6)$$

$$M_{\beta\alpha}^* = D^* ((1 - \nu_f^*)\kappa_{\beta\alpha} + \nu_f^* \delta_{\beta\alpha} \kappa_{\gamma\gamma}) \quad (2.7)$$

Here the all tensor quantities in the midplane (except curvature $\boldsymbol{\kappa}$ and deflection w) are marked by zero-index: in-plane strain $\boldsymbol{\varepsilon}^0$, surface tension $\tau_0(\nabla_s \mathbf{u})^0$, in-plane displacement \mathbf{u}^0 . Also, the effective elastic, inertial and load properties are used

$$\begin{aligned}\nu_t^* &= \frac{1}{C^*}(\nu C + 2(\lambda_s + \tau_0)), \quad C^* = C + 4\mu_s + 2(\lambda_s - \tau_0), \quad C = \frac{Eh}{1 - \nu^2} \\ \nu_f^* &= \frac{1}{D^*}(\nu D + \frac{h^2}{2}(\lambda_s + \tau_0)), \quad D^* = D + h^2(\mu_s + \frac{\lambda_s}{2}), \quad D = \frac{Eh^3}{1 - \nu^2}\end{aligned}\quad (2.8)$$

$$I^* = \int_{-0.5h}^{+0.5h} \rho dx_3 + 2\rho_s, \quad J^* = \int_{-0.5h}^{+0.5h} x_3^2 \rho dx_3 + \frac{h^2}{2} \rho_s \quad (2.9)$$

$$P_i^* = \int_{-0.5h}^{+0.5h} p_i dx_3 + (\varphi_i^+ - \varphi_i^-), \quad m_\alpha^* = \int_{-0.5h}^{+0.5h} p_\alpha x_3 dx_3 + \frac{h}{2}(\varphi_\alpha^+ + \varphi_\alpha^-) \quad (2.10)$$

2.3 One-Dimensional Model of Deformation of Strip-Like Nano-Film

A strip-like nano-film is considered of a finite width l along the x_1 axis and infinitely along the x_2 axis, along both edges which the nano-film is supported. External load is believed not depending on x_2 and the nano-film stays in a plane-strain deformation.

In the case, the Eq. set (2.5) is simplified

$$\begin{aligned} I^* \ddot{u}_1^0 &= (T_{11}^* - \tau_0 w'^2)' + P_1^* \\ J^* \ddot{w}'' - I^* \ddot{w} &= D^* w^{IV} - (2\tau_0 + T_{11}^*) w'' - m_{1,1}^* - P_3^* \end{aligned} \quad (2.11)$$

Considering the nonlinearity of the in-plane strains and surface tension (2.4), the constitutive relation for membrane force (2.6) gets the view

$$T_{11}^* = 2\tau_0(1 + (u_1^0)' - ww'') + C^*((u_1^0)' + w'^2/2) \quad (2.12)$$

The materials parameters for the iron free surface, taken from (Gurtin and Murdoch, 1978), were used in the computations

$$\begin{aligned} E &= 17.73 \times 10^{10} \text{ N/m}^2, \quad \nu = 0.27, \quad \rho = 7 \times 10^3 \text{ kg/m}^3 \\ \lambda_s &= -8 \text{ N/m}, \quad \mu_s = 2.5 \text{ N/m}, \quad \tau_0 = 1.7 \text{ N/m}, \quad \rho_s = 7 \times 10^{-6} \text{ kg/m}^2 \end{aligned} \quad (2.13)$$

2.3.1 Nonlinear Bending under the Eigenform-Like External Loading

The boundary problem of nonlinear bending of a clamped-edge nano-plate (2.11)-(2.12) has the view

$$\begin{cases} (T_{11}^* - \tau_0 w'^2)' = 0 \\ D^* w^{IV} = (2\tau_0 + T_{11}^*) w'' + P_3^* \\ (C^* + 2\tau_0)(u_1^0)' = T_{11}^* - 2\tau_0(1 - ww'') - (C^*/2)w'^2 \end{cases} \quad (2.14)$$

$$w(0) = w(l) = 0, \quad w'(0) = w'(l) = 0, \quad u_1^0(0) = u_1^0(l) = 0 \quad (2.15)$$

where the external load is like the deflection eigenform of the linear bending equation

$$P_3^* = P_0(1 - \cos(2\pi x_1/l)) \quad (2.16)$$

Note that the first two Eqs. (2.14) have the first integrals

$$\begin{aligned}
T_{11}^* - \tau_0 w'^2 &= N = \text{const} \\
D^* w''' &= (2\tau_0 + N)w' + (\tau_0/3)w'^3 + \int P_3^* dx_1
\end{aligned} \tag{2.17}$$

while the third equation has not and the constant N remains unknown. In the case of the simple support (the eigenform-like external load is $P_3^* = P_0 \sin(\pi x_1/l)$), the third equation (2.14) has the first integral also and the constant N has been analytically found (Lim and He, 2004; Huang, 2008) but without taking into account the transverse Young–Laplace law and the nonlinearity of the surface tension. Therefore, in the case of clamped support, the set (2.14) is reduced to the set of ordinary differential equations of 6th order in the dimensionless variables

$$\begin{cases}
y_1' = y_2 \\
y_2' = y_3 \\
y_3' = y_4 \\
y_4' = \frac{Ch^2}{D^*} \left(\frac{2\tau_0}{C} \frac{l^2}{h^2} y_3 + \frac{l^2}{h^2} y_5 y_3 + \frac{l^3}{h^3} \frac{P_3^*}{Ch} \right) \\
y_5' = \frac{h^2}{l^2} \frac{2\tau_0}{C} y_2 y_3 \\
y_6' = \frac{C}{C^* + 2\tau_0} \left(y_5 - \frac{2\tau_0}{C} + \frac{2\tau_0}{C} \frac{h^2}{l^2} y_1 y_3 - 0.5 \frac{C^*}{C} \frac{h^2}{l^2} y_2^2 \right)
\end{cases} \tag{2.18}$$

with the homogeneous boundary conditions

$$\begin{aligned}
y_1(0) = y_1(1) = 0, \quad y_2(0) = y_2(1) = 0, \quad y_6(0) = y_6(1) = 0 \\
\text{or using symmetry} \\
y_1(0) = 0, \quad y_2(0) = y_2(0.5) = 0, \quad y_4(0.5) = 0, \quad y_6(0) = y_6(0.5) = 0
\end{aligned} \tag{2.19}$$

where

$$y_1 = w/w_m, \quad y_5 = T_{11}^*/C, \quad y_6 = u_1^0/h; \quad (\dots)' = d(\dots)/d\tilde{x}_1, \quad \tilde{x}_1 = x_1/l \tag{2.20}$$

The boundary value problem (2.18)-(2.15) was solved numerically by means of the `bvp5` MATLAB[®] function. The results are shown in Fig.2.1 in comparison with results of other models: without surface effect and with surface effect but without the transverse Young–Laplace law and nonlinearity of surface tension like (Lim and He, 2004; Huang, 2008). You can see that the size effect is more pronounced in comparison with last model. An important detail when compared with a similar task for a simply supported strip (Bochkarev, 2020b): for clamped support, the size effect is opposite, that is, the surface stresses reduce the deflection amplitude.

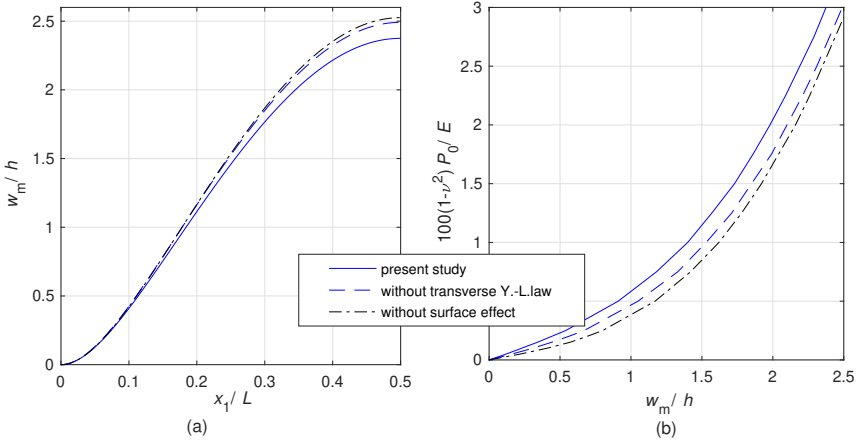


Fig. 2.1 Nonlinear bending of a clamped-edge nano-film under different models of accounting for surface effects (the thickness $h = 1$ nm): (a) deflection semi-profile for $P_0 = 0.03E/(1 - \nu^2)$, (b) transverse load-deflection ratio

2.3.2 Post-Critical Buckling under Compression

The boundary value problem of compressive buckling of a clamped-edge nano-plate (2.11)-(2.12) has the view

$$\begin{cases} (T_{11}^* - \tau_0 w'^2)' = 0 \\ D^* w^{IV} = (2\tau_0 + T_{11}^*) w'' \\ (C^* + 2\tau_0)(u_1^0)' = T_{11}^* - 2\tau_0(1 - w w'') - (C^*/2)w'^2 \end{cases} \quad (2.21)$$

$$w(0) = w(l) = 0, \quad w'(0) = w'(l) = 0, \quad T_{11}^*(0) = T_{11}^*(l) = -T \quad (2.22)$$

The first integrals (2.17) and the boundary conditions (2.22) allow to express the unknown constant $N = -T_{11}^*(0) - \tau_0 w'^2(0) = -T$, to exclude the first and third equations (2.21) and to reduce the order of the bending equation to 3

$$D^* w''' = (2\tau_0 - T)w' + (\tau_0/3)w'^3 \quad (2.23)$$

Note that the model without taking into account the nonlinearity of surface tension like (Lim and He, 2004; Huang, 2008) leads to a linear equation of bending, from which it is possible to determine only the value of the critical compressive force

$$T_{cr} = 4\pi^2 D^* / l^2 + 2\tau_0 \quad (2.24)$$

This is the specificity of the one-dimensional model of the von Kármán theory, in which, in contrast to the general two-dimensional case, there are no nonlinear equations of continuity. In the present model under consideration, such nonlinearity

is present in the equilibrium equation of internal forces, which makes it possible to simulate the buckling of the strip-like nano-film and behind the critical force.

For this purpose, we represent the compressive force with a positive increment to the value of the critical force $T = T_{cr} + \delta D^*/l^2$ and reduce the bending equation (2.23) the set of ordinary differential equations of 3rd order

$$\begin{cases} y_1' = y_2 \\ y_2' = y_3 \\ y_3' = -y_2 \left((4\pi^2 + \delta) - \frac{1}{3} \frac{\tau_0}{C} \frac{Ch^2}{D^*} y_2^2 \right) \end{cases} \quad (2.25)$$

with the homogeneous boundary conditions

$$y_1(0) = y_1(1) = 0, \quad y_2(0) = 0 \quad \text{or} \quad y_1(0) = 0, \quad y_2(0.5) = 0, \quad y_3(0) = 0 \quad (2.26)$$

As an initial approximation, we used the first eigenform of the linear bending equation

$$\begin{cases} y_1 = (w_m/h)(1 - \cos(2\pi\tilde{x}_1)) \\ y_2 = (w_m/h)2\pi \sin(2\pi\tilde{x}_1) \\ y_3 = (w_m/h)(2\pi)^2 \cos(2\pi\tilde{x}_1) \end{cases} \quad (2.27)$$

The boundary value problem (2.25)-(2.26) was also solved numerically by means of the `bvp5` MATLAB[®] function. The results are shown in Fig.2.2 in comparison with the critical Euler load. Some of them were given in (Bochkarev, 2020a). Here they are supplemented with new ones.

As expected, the clamped-edge nano-film continues to resist compression upon buckling behind the critical load. In this case, the membrane force is redistributed from a constant like a second eigenform. With an increase in the thickness of the nano-film, the size effect is weakened.

2.3.3 Nonlinear Free Transverse Vibration

In the problem of free transverse vibrations in a general nonlinear setting, like Sec. 2.3.1 and 2.3.2, the spatial and time variables are not analytically separated. Therefore, we have to resort to some simplification, taking into account, if possible, the role of the basic factors. First of all, following (Lim and He, 2004; Huang, 2008), we neglect the inertial terms in the plane of the plate, as well as the nonlinearity of the surface tension in the equation of equilibrium of membrane forces. The simplified stationary boundary value problem takes the form

$$\begin{cases} (T_{11}^*)' = 0 \\ J^* \ddot{w}'' - I^* \ddot{w} = D^* w^{IV} - (\tau_0 + T_{11}^*) w'' \\ (C^* + 2\tau_0)(u_1^0)' = T_{11}^* - 2\tau_0(1 - ww'') - (C^*/2)w'^2 \end{cases} \quad (2.28)$$

$$w(0) = w(l) = 0, \quad w'(0) = w'(l) = 0, \quad u_1^0(0) = u_1^0(l) = 0 \quad (2.29)$$

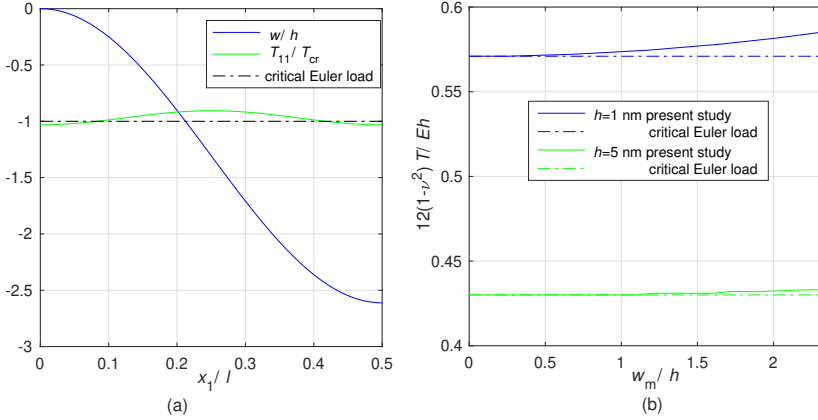


Fig. 2.2 Post-critical compressive buckling of a clamped-edge nano-film: (a) deflection and membrane semi-profile for the thickness $h = 1$ nm, (b) compressive load-deflection ratio for the thickness $h = 1$ and 5 nm

From the first equation (2.28) it follows that $T_{11}^* = N$ is a spatial constant, and we arrive at an oscillation equation of that is linear in the spatial coordinate with one unknown coefficient $N(t)$ – a function of time

$$J^* \ddot{w}'' - I^* \ddot{w} = D^* w^{IV} - (2\tau_0 + N(t)) w'' \quad (2.30)$$

Separating spatial and time variables and using the first eigenform

$$w(x_1, t) = w_m T(t) (1 - \cos(2\pi x_1/l)) \quad (2.31)$$

the third equation (2.28) can be integrated also, and the unknown $N(t)$ is expressed in terms of $T(t)$

$$N(t) = C \left(\frac{2\tau_0}{C} + \pi^2 \frac{C^*}{C} + \frac{4\tau_0}{C} (w_m/h)^2 (h/l)^2 T^2(t) \right) \quad (2.32)$$

Substitution of expressions 2.31) and 2.32) for w and $N(t)$ into the oscillation equation 2.30) leads to Duffing's equation

$$c \ddot{T}(t) + a C T(t) + b C (w_m/h)^2 T^2(t) = 0 \quad (2.33)$$

where the constants are

$$a = \frac{4\pi^2}{(l/h)^2} \left(\frac{4\pi^2}{(l/h)^2} \frac{D^*}{C h^2} + \frac{4\tau_0}{C} \right), \quad b = \frac{4\pi^4}{(l/h)^4} \frac{C^*}{C}, \quad c = I^* h^2 + J^* \frac{\pi^2}{(l/h)^2} \quad (2.34)$$

As is known, the nonlinear vibration frequency is expressed in terms of an elliptic integral of the first kind with the parameter k

$$\omega = \frac{\pi}{2} \frac{\sqrt{(a + b(w_m/h)^2)/c}}{K(k, \pi/2)}, \quad k = \frac{(w_m/h)}{\sqrt{2((w_m/h)^2 + (a/b))}} \quad (2.35)$$

In particular, disregarding surface elasticity, the constants of Duffing's equation (2.33) are expressed through the usual elastic stiffnesses and moments of inertia

$$a_0 = \frac{4\pi^4}{3(l/h)^4}, \quad b_0 = \frac{4\pi^4}{(l/h)^4}, \quad c_0 = \rho h^3 \left(1 + \frac{1}{12} \frac{\pi^2}{(l/h)^2}\right) \quad (2.36)$$

and the nonlinear vibration frequency is similar to (2.35)

$$\omega_0 = \frac{\pi}{2} \frac{\sqrt{(a_0 + b_0(w_m/h)^2)/c_0}}{K(k_0, \pi/2)}, \quad k_0 = \frac{(w_m/h)}{\sqrt{2((w_m/h)^2 + (a_0/b_0))}} \quad (2.37)$$

The frequency-amplitude ratio of free transverse vibration is shown in Fig.2.3 in comparison with results of other models: without surface effect and with surface effect but without the transverse Young-Laplace law like (Lim and He, 2004; Huang, 2008). It can be seen that taking into account the Young-Laplace law in the transverse direction can double the size effect in comparison with last model.

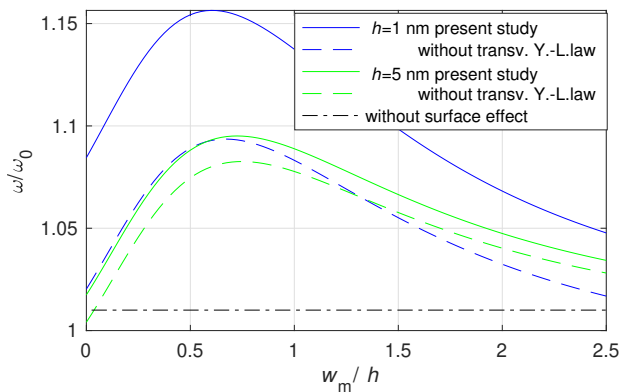


Fig. 2.3 Frequency-amplitude ratio of free transverse vibration of a clamped-edge nano-film under different models of accounting for surface effects

2.4 Conclusion

The plate theory proposed by (Lim and He, 2004) was further developed as an extension of von Kármán nonlinear theory of elastic plates incorporated the Gurtin–Murdoch surface elasticity including the linear and nonlinear terms of surface tension from the conjugation condition of the Young–Laplace law in the transverse direction. The examples of nonlinear deformation of a clamped-edge strip-like nano-film considered above confirmed the previously obtained results of solving the same problems for a simple supported nano-film. The surface tension in the transverse direction introduces an additional linear term in the bending equation, which can significantly affect the size effect. Taking into account the nonlinearity of surface tension allows one to simulate more subtle nonlinear features of deformation, in particular, post-critical deformation during compressive buckling.

References

- Altenbach H, Eremeyev V (2011) On the shell theory on the nanoscale with surface stresses. *International Journal of Engineering Science* 49(12):1294–1301
- Altenbach H, Eremeyev V, Morozov N (2010) On equations of the linear theory of shells with surface stresses taken into account. *Mechanics Solids* 45:331–342
- Bochkarev A (2020a) Comment on "on taking into account surface tension in models of nano-plate bending". *Mechanics Research Communications* 108:103,578
- Bochkarev A (2020b) On taking into account surface tension in models of nano-plate bending. *Mechanics Research Communications* 106:103,521
- Bochkarev A, Grekov M (2019) Influence of surface stresses on the nanoplate stiffness and stability in the kirsch problem. *Physical Mesomechanics* 22:209–223
- Eremeyev V (2016) On effective properties of materials at the nano- and microscales considering surface effects. *Acta Mechanica* 227:29–42
- Eugster S, Glocker C (2017) On the notion of stress in classical continuum mechanics. *Mathematics and Mechanics of Complex Systems* 5(3–4):299–338
- Gurtin M, Murdoch A (1978) Surface stress in solids. *International Journal of Solids and Structures* 14:431–440
- Huang D (2008) Size-dependent response of ultra-thin films with surface effects. *International Journal of Solids and Structures* 45:568–579
- Javanbakht M, Ghaedi MS, Barchiesi E, Ciallella A (2021) The effect of a pre-existing nanovoid on martensite formation and interface propagation: a phase field study. *Mathematics and Mechanics of Solids* 26(1):90–109
- Lim C, He L (2004) Size-dependent nonlinear response of thin elastic films with nano-scale thickness. *International Journal of Mechanical Sciences* 46:1715–1726
- Lu P, He L, Lee H, Lu C (2006) Thin plate theory including surface effects. *International Journal of Solids and Structures* 43:4631–4647
- Miller R, Shenoy V (2000) Size-dependent elastic properties of nanosized structural elements. *Nanotechnology* 11:139–147
- Ru C (2016) A strain-consistent elastic plate model with surface elasticity. *Continuum Mechanics and Thermodynamics* 28:263–273
- Shaat M (2018) Effects of surface integrity on the mechanics of ultra-thin films. *International Journal of Solids and Structures* 136–137:259–270

- Xu M (2016) Effect of surface and interface energies on the nonlinear bending behaviour of nanoscale laminated thin plates. *Mechanics of Composite Materials* 52:673–686
- Yue Y, Xu K, Tan Z, Wang W, Wang D (2019) The influence of surface stress and surface-induced internal residual stresses on the size-dependent behaviors of kirchhoff microplate. *Archive of Applied Mechanics* 89:1301–1315



Chapter 3

Closed-form Analytic Solutions of the Problem of a Hollow Sphere Made of Second Gradient Plastic Porous Material and Subjected to Hydrostatic Loading

Roy Burson, Koffi Enakoutsa

Abstract Gologanu, Leblond, Perrin, and Devaux (GLPD) developed a constitutive model for ductile fracture for porous metals based on generalized continuum mechanics assumptions. The model predicted accurately ductile fracture process in porous metallic structures under several complex loads. The GLPD model's performances over its competitors has attracted the attention of several authors who explored further capabilities of the model. The aim of this paper is to provide analytical solutions for the problem of a porous hollow sphere subjected to hydrostatic loadings, the matrix of the hollow sphere obeying the GLPD model. The exact solution for the expressions of the stress and the generalized stress the GLPD model involved are illustrated for the case where the matrix material does not contain any voids. The results show that the singularities obtained in the stress distribution with the local Gurson model are smoothed out, as expected with any generalized continuum models. The paper also presents some elements of the analytical solution for the case where the matrix is porous and obeys the full GLPD model at the initial time when the porosity is fixed. These analytical solutions can serve as benchmark solutions to assess numerical implementations of any second gradient constitutive model.

Keywords: Gradient model · Analytical solutions · Plasticity · Hollow sphere problem · Fracture

R. Burson

Department of Mathematics, California State University, Northridge, 18111 Nordhoff Street, Northridge, CA 91330, USA
e-mail: Roy.burson.618@my.csun.edu

K. Enakoutsa

Department of Mathematics, California State University, Northridge, 18111 Nordhoff Street, Northridge, CA 91330 and Department of Mathematics, UCLA, Los Angeles, 520 Portola Plaza, Los Angeles, CA 90095, USA
e-mail: koffi.enakoutsa@csun.edu

3.1 Introduction

Metal structures often fail by ductile rupture when they are subjected to external static or dynamic forces. The requirement to develop constitutive models (whether they are physics, mechanics and/or mathematics based) that can predict precisely ductile fracture processes in metals has become a key point in metal structure design community. So far, such community has widely accepted that the model proposed by Gurson (1977) and extended by Tvergaard (1981); Tvergaard and Needleman (1984) to account for cavities interactions and coalescence (these features were disregarded in Gurson (1977)'s original work) following an earlier suggestion by Rice and Tracey (1969) can adequately describes ductile fracture in metals. Several extensions have followed these pioneering works; among them, let us mention the contributions of Perrin and Leblond (1990, 2000), and recently Nahshon and Hutchinson (2008). The latter has modified Gurson model to include shear failure which often occurs, for instance, during high velocity impact failures of many steel materials.

Another modification of Gurson model including a characteristic length scale aimed at eliminating the pathological post-bifurcation mesh dependence issues proposed by Leblond et al (1994) based on a previous suggestion of Pijaudier-Cabot and Bažant (1987) in the context of concrete damage was adopted by Tvergaard and Needleman (1995, 1997). This proposal was studied in details by Enakoutsa (2007); Enakoutsa et al (2007) and adopted (thanks to its successes) in the context of high rate deformation and failure of materials by Enakoutsa et al (2012a), Enakoutsa et al (2012b), and Ahad et al (2014). However, the proposal was of less satisfaction from a theoretical and physical view points since it does not rely on any serious physical justification. This was the motivation of the development by Gologanu, Leblond, Perrin, and Devaux Gologanu et al (1997) of a second-gradient micromorphic model¹ for porous plastic materials. The GLPD model was obtained from a refinement of Gurson (1977)'s original homogenization procedure, which was based on conditions of homogeneous boundary strain rate.

In contrast, the boundary velocity in the GLPD model approach was assumed to be a quadratic, rather than linear, function of the coordinates. The physical idea behind this assumption was to account in this way for possible quick variations of the macroscopic strain rate over very short distances, for example at the scale of the elementary cell the GLPD model is based on. The output of the procedure was a model of "micromorphic" nature, involving the second gradient of the macroscopic velocity and generalized macroscopic stresses of "moment" type (homogeneous to the product of a stress and a distance.) Other type of higher-order gradient models involving third-rank stress tensor with applications in bone remodeling design and other domain of interest exist. Among them let us mention the works by Scerrato et al (2021); Giorgio et al (2017); dell'Isola et al (2017).

In practice, the GLPD model was extensively studied by Enakoutsa (2007); Enakoutsa and Leblond (2009) who have notably shown that the model has the ability to predict mesh-independent FE solutions and to reproduce satisfactorily

¹ micromorphic model will simply be denoted by GLPD model for shortness.

ductile fracture tests. Other numerical simulations involving second gradient models are available in the literature, see for instance Andreaus et al (2016); Reiher et al (2017); Placidi et al (2021). A recent modification of the GLPD model numerical implementation developed in Enakoutsa (2007); Enakoutsa and Leblond (2009) was suggested by Bergheau et al (2014) and yielded the same conclusions. The assessment of the reliability and accuracy of these two algorithms requires the development of analytical solutions that have served as critical cross references, see Enakoutsa (2007, 2014, 2015). These solutions are based on two crude approximations so as for analytical solutions to be amenable: the porosity in the matrix material of the geometry considered was assumed to vanish.

The objective of the present paper is to follow up the study of applications of the GLPD model to simple problems that might be of interest to validate the numerical implementation of this model into a finite element code. The problem considered here is a hollow sphere subjected to a hydrostatic tension and made of porous plastic material, obeying the GLPD model. We found the analytic solution of the hollow sphere problem in terms of deformation, stress and moment distributions under the conditions that the matrix obeys a reduced GLPD model for the case where the porosity vanishes. We also consider some elements of solution of the problem in the presence of porosity in the matrix material, which is a rather complex type of problem. The complexity of the latter problem (a highly non-linear type of problem) forces us to present only some elements of the analytical solution at the initial time when the porosity is held constant. The rest of the paper is structured as follows.

- The first section describes the problem model, whereas the next section presents the details of the analytical derivation of the exact solution for the case where the porosity vanishes as in Enakoutsa (2013a).
- The follow up section assesses the solution obtained for the case where the porosity vanishes. An algorithm that simulates the behavior of his model and analyzes the effects of the characteristic length scale on the distribution of stress and moments is also presented.
- Finally, we considered the solution of the problem for the case where the porosity does not vanish at the initial time. We provide implicit analytic expressions for the Cauchy stress and moment components based on a highly non linear ordinary differential equation, which involves the characteristic length scale of the GLPD model.

3.2 Description of the Hollow Sphere Problem

We consider a hollow sphere of inner radius r_i , outer radius r_e , representing an elementary cell of a porous plastic metal, see Figure 3.1. The boundary of the central void is free of traction whereas the outer boundary is subjected to some overall hydrostatic tension T . The details of the derivation of these boundary conditions can be found in Enakoutsa (2014). The matrix material of the porous hollow sphere is supposed to obey the GLPD constitutive model.

The hollow sphere model problem presented here have served to find the solutions of several ductile fracture problems the solution of which have yields micromechanics based models for ductile porous metals under various loading conditions. Some of these problems as well as their solutions can be found in the works of Perrin and Leblond (2000, 1990); Enakoutsa (2007, 2014) to mention a few of them.

3.3 Solution to the Hollow Sphere Problem When the Porosity is Neglected

We are seeking a solution of the spherical shell problem for purely ideal-plastic behavior, the yield stress in simple tension being denoted by Σ_0 and the porosity in the matrix neglected. As a result, the yield criterion Eq. (3.57) reduces

$$\Phi(\Sigma, M, \Sigma) \equiv \frac{1}{\bar{\Sigma}^2} \left(\Sigma_{eq}^2 + \frac{Q^2}{b^2} \right) - 1 = 0. \quad (3.1)$$

In this equation Σ represents the ordinary second-rank symmetric Cauchy stress tensor and M is the third-rank "moment tensor" symmetric in its first two indices only. The components of M are related through the conditions.

$$M_{ijj} = 0. \quad (3.2)$$

In the same expression:

- $\Sigma_{eq} \equiv \left(\frac{3}{2} \Sigma' : \Sigma' \right)^{1/2}$ (Σ' : deviator of Σ) is the von Mises equivalent stress.
- Σ represents a kind of average value of the yield stress in the heterogeneous metallic matrix.

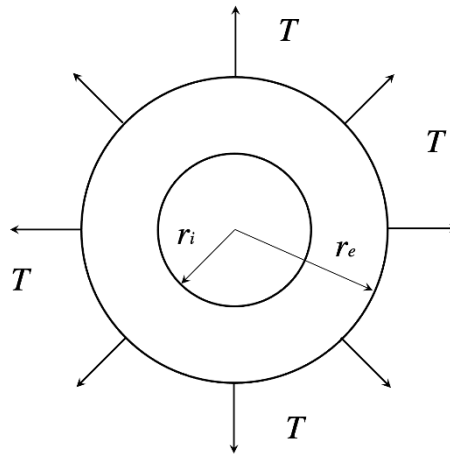


Fig. 3.1 An illustration of the hollow sphere model problem

- Q^2 is a quadratic form of the components of the moment tensor given by

$$Q^2 \equiv A_1 \mathcal{M}_1 + A_2 \mathcal{M}_2 \quad , \quad \begin{cases} A_1 = 0.194 \\ A_2 = 6.108 \end{cases} \quad (3.3)$$

where \mathcal{M}_1 and \mathcal{M}_2 are the quadratic invariants of \mathbf{M} defined by:

$$\begin{cases} \mathcal{M}_1 \equiv M_{mi} M_{mi} \\ \mathcal{M}_2 \equiv \frac{3}{2} M'_{ijk} M'_{ijk}, \end{cases} \quad (3.4)$$

$M_{mi} \equiv \frac{1}{3} M_{hhhi}$ and \mathbf{M}' denoting the mean and deviatoric parts of \mathbf{M} , taken over its first two indices.

- b represents the characteristic length scale.

The flow rule, Eq. (3.61), becomes, after development (see Enakoutsa (2007); Enakoutsa and Leblond (2009) for the details),

$$\begin{cases} \dot{D}_{ij}^p = \eta \frac{3}{\Sigma_0^2} \Sigma'_{ij} \\ \left((\nabla \dot{D})^p \right)_{ijk} = \frac{\eta}{\Sigma_0^2 b^2} \left(\frac{2}{3} A_I \delta_{ij} M_{mk} + 3 A_{II} M'_{ijk} \right) + \delta_{ik} U_j + \delta_{jk} U_i, \end{cases} \quad (3.5)$$

$M_{mk} \equiv \frac{1}{3} M_{hhkk}$ and \mathbf{M}' denoting the mean and deviatoric parts of \mathbf{M} , taken over its first two indices; η is the plastic multiplier, determined from the consistency condition and defined as

$$\eta = \begin{cases} = 0 & \text{if } \Phi(\boldsymbol{\Sigma}, \mathbf{M}, \Sigma) < 0 \\ \geq 0 & \text{if } \Phi(\boldsymbol{\Sigma}, \mathbf{M}, \Sigma) = 0. \end{cases}$$

We shall also assume that the parameter $A_I=0$ for the analytical solution to be amenable. Another, more elaborate reason for this choice is that the value of A_I in the GLPD model, 0.194, is very small with respect to that of A_{II} , 6.108; hence, the value of A_I can safely be neglected.

We are looking for a solution in which the spherical shell is entirely plastic, so that the yield function $\Phi(\boldsymbol{\Sigma}, \mathbf{M}, \Sigma_0, f)$ is zero everywhere. Since such a solution was already presented in Enakoutsa (2013a), only a summary of the procedure is given in this work.

Let us consider the velocity, strain rate and its gradient fields first. As in the case of purely elastic behavior, the matrix of spherical shell is incompressible; as a result, the velocity field is radial and given by

$$\mathcal{U} = \frac{A}{r^2}, \quad (3.6)$$

where A is a parameter which is independent of the material point position r . (In fact, the expression of the velocity field \mathcal{U} is obtained by writing the constraint that $\text{div}(\mathcal{U})$ equals zero because of the assumption of incompressibility of the matrix of

the spherical shell.) Following this definition, the non-zero components of the strain rate are found as

$$D_{rr} = -\frac{2A}{r^3}, \quad D_{\theta\theta} = D_{\phi\phi} = \frac{A}{r^3}. \quad (3.7)$$

Thanks to the spherical symmetries involved in the problem, the components of the gradient of the strain rate are defined, here also, as

$$\begin{cases} (\nabla D)_{rrr} \\ (\nabla D)_{\theta\theta r} = (\nabla D)_{\phi\phi r} \\ (\nabla D)_{r\theta\theta} = (\nabla D)_{r\phi\phi} \\ \text{other } (\nabla D)_{ijk} = 0. \end{cases} \quad (3.8)$$

The resulting strain gradient components are defined as in Enakoutsa (2013b).

The non-zero components of the stress and moment fields are found using the flow rule, Eq. (3.5), and the incompressibility of the material (which yields $\mathbf{U}=0$). These components are obtained as

$$\begin{cases} \Sigma'_{rr} = \frac{1}{\eta} \left(-\frac{2A\Sigma_0^2}{3r^2} \right) \\ \Sigma'_{\theta\theta} = \Sigma'_{\phi\phi} = \frac{1}{\eta} \left(\frac{A\Sigma_0^2}{3r^2} \right) \end{cases} \quad (3.9)$$

and

$$\begin{cases} M'_{rrr} = \frac{1}{\eta} \frac{2A\Sigma_0^2 b^2}{A_{II} r^4} \\ M'_{\theta\theta r} = M'_{\phi\phi r} = -\frac{1}{\eta} \frac{A\Sigma_0^2 b^2}{A_{II} r^4} \\ M_{r\theta\theta} = M_{r\phi\phi} = -\frac{1}{\eta} \frac{A\Sigma_0^2 b^2}{A_{II} r^4} \end{cases} \quad (3.10)$$

The conditions Eq. (3.50) and a combination of the definitions of M'_{rrr} and $M_{r\theta\theta}$ given by the relations Eq. (3.10)₁ and Eq. (3.10)₃ yield

$$\begin{cases} M_{rrr} = -2M_{r\theta\theta} \\ M_{\theta\theta r} = M'_{\theta\theta r}. \end{cases} \quad (3.11)$$

Replacing the formulas for the stress Eq. (3.9) and moment Eq. (3.10) in the reduced yield criterion, Eq. (3.1), we get the following expression for the plastic multiplier η :

$$\eta = \frac{A\Sigma_0}{r^3} \sqrt{1 + \frac{15}{A_{II}} \frac{b^2}{r^2}}. \quad (3.12)$$

The explicit relation of the plastic multiplier in Eq. (3.12) completes the definition of the non-zero components of the moment tensor. However, the full expressions of the non-zero components of the ordinary stress tensor are still unknown. After a tedious but straightforward calculation which uses

- (i) the expressions of the non-zero components of the moment tensor,
- (ii) the spherical symmetry properties of the problem, and
- (iii) the fact that $\Sigma_{rr} - \Sigma_{\theta\theta} = \Sigma'_{rr} - \Sigma'_{\theta\theta}$,

the formulas for the non-zero components of the ordinary Cauchy stress tensor are obtained as

$$\frac{d\Sigma_{rr}}{dr} = f(r) \quad (3.13)$$

with

$$\left\{ \begin{array}{l} f(r) = \frac{2A\Sigma_0^2}{\eta r^3} + \frac{2(\eta''\eta^2 - 2\eta'^2\eta)}{\eta^4} \frac{A\Sigma_0^2 b^2}{A_{II} r^4} - \frac{28\eta'}{\eta^2} \frac{A\Sigma_0^2 b^2}{A_{II} r^5} \\ - \left(\frac{72}{\eta} + \frac{2\eta'}{\eta^2} \right) \frac{A\Sigma_0^2 b^2}{A_{II} r^6} - \frac{8A\Sigma_0^2 b^2}{\eta A_{II} r^7} \end{array} \right. \quad (3.14)$$

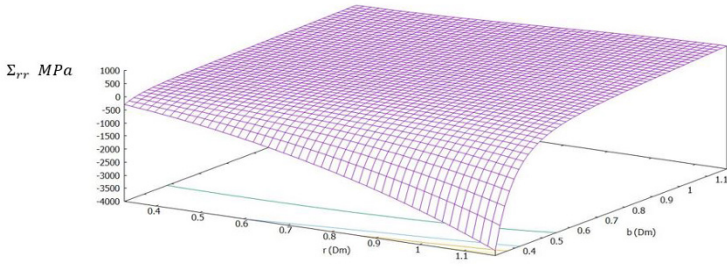
where η' and η'' denote the first and second derivatives of the plastic multiplier η with respect to r . Eq. (3.13) implicitly defines the expression of the component Σ_{rr} of the stress tensor. The non-zero components of the stress tensor are obtained as

$$\Sigma_{rr} = \int_{r_i}^r f(\tau) d\tau; \quad \Sigma_{\theta\theta} = \Sigma_{\phi\phi} = \Sigma_{rr} - \frac{1}{\eta} \left(\frac{A\Sigma_0^2}{r^2} \right). \quad (3.15)$$

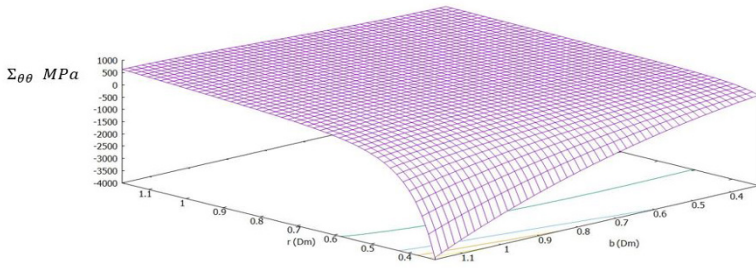
The solution of Eq. (3.15) along with the non-zero components of the moment provided above automatically satisfy the balance equations.

Table 3.1 List of constants parameters

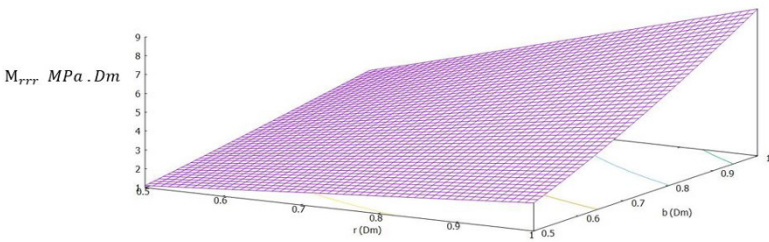
| Quantity | Symbol | Value | Unit |
|-----------------|------------|-------|------|
| internal radius | r_i | 0.05 | m |
| yield stress | Σ_0 | 100 | MPa |
| parameter 1 | A | 0.001 | m |
| parameter 2 | A_1 | 0.194 | |
| parameter 3 | A_2 | 6.108 | |



(a) Stress component Σ_{rr}



(b) Stress component $\Sigma_{\theta\theta}$



(c) Moment component M_{rrr}

Fig. 3.2 Illustration of the stress components Σ_{rr} , $\Sigma_{\theta\theta}$ and moment component M_{rrr} .

3.4 Numerical Illustrations of the Solution

The purpose of this section is to illustrate analytical solution presented in Enakoutsa (2013b). More specifically, we shall derive the explicit expressions for the stress and moment tensors left off from Enakoutsa (2013b)'s findings. We do so by evaluating the integral Eq. (3.15) using a FORTRAN routine we developed. Each integral has also been evaluated analytically so that we possess the exact solution. The explicit solution to each integral is provided in Appendix (b) on p.56. We evaluate the following integrals:

$$\begin{aligned}
 & \int_{r_i}^{r_e} \frac{2A\Sigma_0^2}{\eta r^3} dr , \\
 & \int_{r_i}^{r_e} \frac{2(\eta''\eta - \eta'^2)}{\eta^2} \left(\frac{A\Sigma_0^2 b^2}{A_2 r^4} \right) dr , \\
 & \int_{r_i}^{r_e} \frac{20\eta' + 8\eta'\eta}{\eta^2} \left(\frac{A\Sigma_0^2 b^2}{A_2 r^5} \right) dr , \\
 & \int_{r_i}^{r_e} \frac{(72 + 2\eta')}{\eta} \left(\frac{A\Sigma_0^2 b^2}{A_2 r^6} \right) dr , \\
 & \int_{r_i}^{r_e} \frac{A\Sigma_0^2 b^2}{\eta A_2 r^7} dr
 \end{aligned} \tag{3.16}$$

Table 3.1 identifies the material and model parameters that are used to obtain the results mentioned in this work. Figures 3.2a, 3.2b, and 3.2c illustrate the solutions for the stress components Σ_{rr} , $\Sigma_{\theta\theta}$, and the moment components M_{rrr} and $M_{r\theta\theta}$ respectively. Figure 3.2 illustrates the analytical expressions of the non-zero components of the Cauchy stress and the moment tensors as obtained in Enakoutsa (2013a). The figure shows that singularities are absent from the stress. Also, there is no discontinuity near the void as the first gradient Gurson model would have predicted.

3.5 Analytic Results in the Presence of Porosity in the Matrix

In this section we present the solution to the hollow sphere problem for the case where the matrix obeys the full GLPD model described in the Appendix § 3.6. Therefore, we loose the simplification that yields the prior results Enakoutsa (2013a). Most of the results, if not all of them, presented in the works Perrin and Leblond (2000, 1990); Enakoutsa (2007, 2014) assume incompressibility within the matrix of the material. This being said a complete solution of the hollow sphere problem obeying the GLPD model has not been provided yet.

3.5.1 Derivation of Cauchy Stress Components

The setup of the problem is provided by the balance equation of the problem which are provided in Enakoutsa (2013a) (and are not duplicated here), the yield criterion, and the boundary conditions which are also given in Enakoutsa (2013a):

$$\left\{ \begin{array}{l} \frac{d\Sigma_{rr}}{dr} + \frac{2}{r}(\Sigma_{rr} - \Sigma_{\theta\theta}) - \frac{d^2 M_{rrr}}{dr^2} - \frac{4}{r} \frac{dM_{rrr}}{dr} - \frac{2}{r^2} M_{rrr} \\ \quad + \frac{2}{r^2} \frac{dM_{\theta\theta r}}{dr} + \frac{4}{r} \frac{dM_{r\theta\theta}}{dr} + \frac{8}{r^2} M_{r\theta\theta} = 0 \end{array} \right. \quad (3.17.a)$$

$$\left\{ \begin{array}{l} \frac{1}{\Sigma^2} \left(\Sigma_{eq}^2 + \frac{Q^2}{b^2} \right) + 2p \cosh \left(\frac{3}{2} \frac{\Sigma_m}{\Sigma} \right) - 1 - p^2 = 0, \end{array} \right. \quad (3.17.b)$$

with M_{rrr} and $M_{r\theta\theta}$ the components of the moment tensor \mathbf{M} , Σ_{rr} and $\Sigma_{\theta\theta}$ the non-zero components of the stress tensor Σ , Σ_m the mean stress, Σ_{eq} the von Mises stress. The boundary conditions are

$$\left\{ \begin{array}{l} r^2 \Sigma_{rr} - \frac{d(r^2 M_{rrr})}{dr} + 4r M_{r\theta\theta} = 0, \\ M_{rrr} = 0, \end{array} \right.$$

for $r = r_i$ and $r = r_e$. The stress components Σ_{rr} and $\Sigma_{\theta\theta}$ in the balance equation Eq. (3.17).a can be expressed in terms of the invariants Σ_m and Σ_{eq} as followed (see Appendix (c) on p. 58)

$$\frac{d\Sigma_{rr}}{dr} + \frac{2}{r}(\Sigma_{rr} - \Sigma_{\theta\theta}) = \frac{2}{3\sqrt{3}} \frac{d}{dr} \Sigma_{eq} + \frac{2}{r\sqrt{3}} \Sigma_{eq} + \frac{d}{dr} \Sigma_m \quad (3.18)$$

Upon substituting Eq. (3.18) into Eq. (3.17).a and using the yield criterion Eq. (3.17).b we then find the differential equation

$$\begin{aligned} \frac{d}{dr} \Sigma_{eq} \left(\sqrt{\Sigma_0 - \Sigma_{eq}^2} - 2\Sigma_{eq} \right) + \frac{2\alpha}{r} \Sigma_{eq} \left(\sqrt{\Sigma_0 - \Sigma_{eq}^2} \right) - \alpha (\Sigma_0 - \Sigma_{eq}^2) \\ = \sinh(\gamma \Sigma_m) \left(\rho \frac{d}{dr} \Sigma_m - 2p \right) \end{aligned} \quad (3.19)$$

with $\alpha = 3\sqrt{3}$, $\gamma = \frac{3}{2\Sigma_0}$, and $\rho = p\Sigma_0$. Since the invariants Σ_{eq} and Σ_m are independent of one another both sides of Eq. (3.19) must be equal to some constant value, say λ , so then

$$\frac{d}{dr} \Sigma_{eq} \left(\sqrt{\Sigma_0 - \Sigma_{eq}^2} - \beta \Sigma_{eq} \right) + \frac{2\alpha}{r} \Sigma_{eq} \left(\sqrt{\Sigma_0 - \Sigma_{eq}^2} \right) - \alpha (\Sigma_0 - \Sigma_{eq}^2) = \lambda$$

and

$$\rho \sinh(\gamma \Sigma_m) \frac{d}{dr} \Sigma_m - 2p \sinh(\gamma \Sigma_m) = \lambda. \quad (3.20)$$

The value λ is to be determined later. We found that the solution for Σ_m satisfies the implicit expression

$$\rho \left(\frac{\Sigma_m}{p} - \frac{\lambda \ln \left(\frac{|2pe^{-\gamma\Sigma_m} - \sqrt{4p^2 + \lambda^2} - \lambda|}{|2pe^{-\gamma\Sigma_m} + \sqrt{4p^2 + \lambda^2} - \lambda|} \right)}{\gamma p \sqrt{4p^2 + \lambda^2}} \right) = r + C, \quad (3.21)$$

for some arbitrary constant C which is to be determined from the boundary condition (see Appendix (c) on p. 58). The formulation for Σ_{eq} is determined by the differential equation

$$\frac{d}{dr} \Sigma_{eq} = \frac{\alpha(\Sigma_0 - \Sigma_{eq}^2) - \frac{6}{r} \Sigma_{eq} \left(\sqrt{\Sigma_0 - \Sigma_{eq}^2} \right) + \lambda}{\sqrt{\Sigma_0 - \Sigma_{eq}^2} - \beta \Sigma_{eq}}. \quad (3.22)$$

The constant C is provided by the formula

$$C = \frac{\rho \left(\frac{\Sigma_m(r_i)}{p} - \frac{\lambda \ln \left(\frac{|2pe^{-\gamma\Sigma_m(r_i)} - \sqrt{4p^2 + \lambda^2} - \lambda|}{|2pe^{-\gamma\Sigma_m(r_i)} + \sqrt{4p^2 + \lambda^2} - \lambda|} \right)}{\gamma p \sqrt{4p^2 + \lambda^2}} \right)}{2} - r_i \quad (3.23)$$

The constant λ is found by solving the root to the equation

$$\begin{aligned} & \frac{\Sigma_m(r_e) - \Sigma_m(r_i)}{p} \\ & - \frac{\lambda \ln \left(\frac{|2pe^{-\gamma\Sigma_m(r_e)} - \sqrt{4p^2 + \lambda^2} - \lambda|}{|2pe^{-\gamma\Sigma_m(r_e)} + \sqrt{4p^2 + \lambda^2} - \lambda|} \right) \times \frac{|2pe^{-\gamma\Sigma_m(r_i)} - \sqrt{4p^2 + \lambda^2} - \lambda|}{|2pe^{-\gamma\Sigma_m(r_i)} + \sqrt{4p^2 + \lambda^2} - \lambda|}}{\gamma p \sqrt{4p^2 + \lambda^2}} \\ & - \frac{2(r_i - r_e)}{\rho} = 0 \end{aligned} \quad (3.24)$$

From here we completely solve for Σ_{eq} and Σ_m for which we easily deduce Σ_{rr} and $\Sigma_{\theta\theta}$ by solving the linear system

$$\begin{pmatrix} \Sigma_{eq} \\ \Sigma_m \end{pmatrix} = \begin{pmatrix} \sqrt{3} & -\sqrt{3} \\ 1 & 2 \end{pmatrix} \begin{pmatrix} \Sigma_{rr} \\ \Sigma_{\theta\theta} \end{pmatrix} \quad (3.25)$$

The solution is

$$\begin{pmatrix} \Sigma_{rr} \\ \Sigma_{\theta\theta} \end{pmatrix} = \frac{1}{3\sqrt{3}} \begin{pmatrix} 2 & \sqrt{3} \\ -1 & \sqrt{3} \end{pmatrix} \begin{pmatrix} \Sigma_{eq} \\ \Sigma_m \end{pmatrix} \quad (3.26)$$

or simply

$$\begin{pmatrix} \Sigma_{rr} = \frac{2}{3\sqrt{3}}\Sigma_{eq} + \frac{1}{3}\Sigma_m, \\ \Sigma_{\theta\theta} = \frac{1}{3}\Sigma_m - \frac{1}{3\sqrt{3}}\Sigma_{eq} \end{pmatrix} \quad (3.27)$$

where the invariants Σ_m and Σ_{eq} are provided by the formula in Eq.(3.21) and the solution to the ordinary differential equation 3.22.

3.5.2 Moment Components Derivation

In this section we solve the components of the moment tensor \mathbf{M} . Using the derivations for the invariants Σ_m and Σ_{eq} provided in Appendix (c) on p.58, we have an analytic expression for the function \mathbf{M}^* (which was defined in the last section). Recall from the constraint equations of the GLPD model Eq. (B.5) in Enakoutsa (2013a)

$$M_{ijj} = 0$$

which leads to the relation

$$M_{rrr} = -2M_{r\theta\theta}.$$

The moment components M_{ijk} are recovered by the use of the flow rule Eq. (3.61) and the velocity field, which we assume can be represented as

$$\mathcal{U} = (f(r), 0, 0)$$

for some function $f(r)$ dependent on the spherical radial coordinate r . This assumption is crude but nonetheless provided one with a mechanical insight into the solution of the problem under consideration. A more generalized velocity field will be considered in future work by the authors of this paper. With this assumption the flow rule Eq. (3.61) will reduce to

$$\nabla D_{mk} = \frac{2}{3}\eta U_k$$

where η is the plastic multiplier and U the velocity field (see Enakoutsa (2013a) for exact details.)

In accordance with (Enakoutsa, 2013a, Eq. (36)) when $A_1 = 0$ (this assumption is necessary to simplify the solution for the moment components; maintaining a nonzero value for A_1 will not bring any significant difference with respect to the analytic solution of the moment components we shall find in the subsequent results (Enakoutsa, 2013a, see for instance)), the strain rate components become

$$\left\{ \begin{array}{l} (\nabla D)_{rrr} = \frac{df}{dr} = \frac{\eta}{\Sigma_0^2 b^2} 3A_2 M'_{rrr} \\ (\nabla D)_{r\theta\theta} = 0 = \frac{\eta}{\Sigma_0^2 b^2} 3A_2 M'_{\theta\theta r} \\ (\nabla D)_{\theta\theta r} = \frac{1}{r} \frac{df}{dr} = \frac{\eta}{\Sigma_0^2 b^2} 3A_2 M'_{r\theta\theta} \\ (\nabla D)_{r\phi\phi} = \frac{1}{r} \frac{df}{dr} = \frac{\eta}{\Sigma_0^2 b^2} 3A_2 M_{r\theta\theta} \end{array} \right. \quad (3.29)$$

Let $\kappa = \frac{\Sigma_0^2 b^2}{3A_2}$ then the deviatoric parts of the moment \mathbf{M} satisfy

$$M'_{rrr} = \frac{\kappa}{\eta} \frac{df}{dr}, \quad M'_{\theta\theta r} = 0, \quad M'_{r\theta\theta} = \frac{\kappa}{\eta} \frac{1}{r} \frac{df}{dr}, \quad M_{r\theta\theta} = \frac{\kappa}{\eta} \frac{1}{r} \frac{df}{dr}.$$

The value of Q^2 then is computed as follows

$$\begin{aligned} Q^2 &= \frac{3}{2} A_2 \left(M_{rrr}^2 + 2M_{\theta\theta r}^2 + 4M_{r\theta\theta}^2 \right) \\ &= \frac{3}{2} A_2 \left(\left(\frac{\kappa}{\eta} \frac{df}{dr} \right)^2 + \left(\frac{\kappa}{\eta} \frac{1}{r} \frac{df}{dr} \right)^2 \right) \\ &= \frac{3}{2} A_2 \left(\frac{df}{dr} \frac{\kappa}{\eta} \right)^2 \left(\frac{r^2 + 1}{r^2} \right) \end{aligned} \quad (3.30)$$

Using the yield criterion

$$\frac{1}{\Sigma^2} \left(\Sigma_{eq}^2 + \frac{Q^2}{b^2} \right) + 2p \cosh \left(\frac{3}{2} \frac{\Sigma_m}{\Sigma} \right) - 1 - p^2 = 0. \quad (3.31)$$

we have

$$Q^2 = b^2 \left(\Sigma^2 \left(p^2 + 1 - 2p \cosh \left(\frac{3}{2} \frac{\Sigma_m}{\Sigma} \right) \right) - \Sigma_{eq}^2 \right). \quad (3.32)$$

Therefore the function f then satisfies the ordinary differential equation

$$\left(\frac{df}{dr} \right)^2 = \frac{2}{3A_2} \left(\frac{\eta}{\kappa} \right)^2 \left(\frac{r^2}{r^2 + 1} \right) b^2 \left(\Sigma^2 \left(p^2 + 1 - 2p \cosh \left(\frac{3}{2} \frac{\Sigma_m}{\Sigma} \right) \right) - \Sigma_{eq}^2 \right) \quad (3.33)$$

Using (Enakoutsu, 2013a, Eq. (37)), ones gets the deviatoric part of the stress

$$\Sigma'_{rr} = -\frac{\Sigma_0^2}{3} \frac{1}{\eta} f(r), \quad \Sigma'_{\theta\theta} = \frac{\Sigma_0^2}{3} \frac{1}{\eta} f(r). \quad (3.34)$$

Since

$$\Sigma_{ij} = \Sigma'_{ij} + \Sigma_m \delta_{ij} \quad (3.35)$$

were Σ'_{ij} is the deviatoric part of the stress the mean stress can then be expressed as

$$\Sigma_m = \Sigma_{rr} + \frac{\Sigma_0^2}{3} \frac{1}{\eta} f(r). \quad (3.36)$$

Hence, the plastic multiplier then satisfies

$$\eta = \frac{\Sigma_0^2}{3} \frac{f(r)}{(\Sigma_m - \Sigma_{rr})} \quad (3.37)$$

Using Eq. (3.32) gives us the expression in terms of the invariants

$$\eta = \frac{\Sigma_0^2}{2} \frac{f(r)}{\left(\Sigma_m - \frac{1}{\sqrt{3}\Sigma_{eq}} \right)} \quad (3.38)$$

were Σ_m and Σ_{eq} are provided in the previous section. Substituting Eq. (3.38) into Eq. (3.33) gives one the relation

$$\left(\frac{df}{dr} \right)^2 = f(r)^2 p(r) \quad (3.39)$$

where $p(r)$ is provided by

$$p(r) = h(r)\iota(r)j(r) \quad (3.40)$$

were

$$\iota(r) = \left(\frac{\Sigma_0^4}{6(\Sigma_m - \frac{1}{\sqrt{3}\Sigma_{eq}})^2 \kappa^2 A_2} \right), \quad j(r) = \left(\frac{r^2}{r^2 + 1} \right), \quad (3.41)$$

and

$$h(r) = \left(b^2 \left(\Sigma^2 \left(p^2 + 1 - 2p \cosh \left(\frac{3}{2} \frac{\Sigma_m}{\Sigma} \right) \right) - \Sigma_{eq}^2 \right) \right). \quad (3.42)$$

The solution for the function f reads

$$f(r) = \exp \left(\int_{r_i}^r \sqrt{p(r)} dr \right). \quad (3.43)$$

Next the non-zero components of the moment are recovered by the formulas in Eq. (3.29)

$$\left\{ \begin{array}{l} M'_{rrr} = \frac{\kappa}{\eta} \frac{df}{dr} \\ M'_{\theta\theta r} = M'_{\phi\phi r} = \frac{-\kappa}{\eta} \frac{1}{r} \frac{df}{dr} \\ M'_{r\theta\theta} = M_{r\theta\theta} = \frac{\kappa}{\eta} \frac{1}{r} \frac{df}{dr} \end{array} \right. \quad (3.45)$$

where η and κ are again given as

$$\left\{ \begin{array}{l} \eta = \frac{\Sigma_0^2}{2} \frac{f(r)}{\left(\Sigma_m - \frac{1}{\sqrt{3}\Sigma_{eq}} \right)} \\ \kappa = \frac{\Sigma_0^2 b^2}{3A_2} \end{array} \right.$$

The conditions (3.50) relate the rest of the non-zero components of the moment tensor, M_{rrr} and $M_{r\theta\theta}$ as follows:

$$M_{rrr} + 2M_{r\theta\theta} = 0 \quad (3.47)$$

Furthermore, combining Eq. (3.47) and the values of M_{rrr} and $M_{r\theta\theta}$ given by the relations in Eq. (3.46), we find

$$M_{mr} = M_{rrr} - M'_{rrr} = 2M_{r\theta\theta} - M'_{r\theta\theta}, \quad (3.48)$$

where M_{mr} denotes the deviatoric part of the tensor \mathbf{M} over its first two indices. The formula immediately yields $M_{\theta\theta r} = M'_{\theta\theta r}$. The formula Eq. (3.48) immediately gives

$$M_{r\theta\theta} = M'_{\theta\theta r} \quad (3.49)$$

3.5.3 Discussion

In this section we elaborate on some of the results found in this work. If the characteristic length scale b vanishes then all of the moment components also vanish by Eq. (3.29). This means that any second gradient effects in the GLPD model no longer exist. The yield criterion Eq. (3.63) reduces to the original Gurson model yield criterion and the stress state of the material does not contain any length scale effects (as one can expect). Unlike in the work of Enakoutsa (2013a) where a vanishing porosity is considered, this work was derived while the porosity is kept constant i.e. at the initial time where the porosity has not yet evolved. Such effect is left for future investigations by the authors. However, let us mention that the works by Perrin

and Leblond (2000, 1990) have addressed such problem (the hollow sphere problem with evolving porosity) but the model their analysis is based on does not contain any strain gradient effects.

3.6 Conclusion

In this work we develop the complete solution for the micromorphic hollow sphere model under tension obeying the GLPD constitutive model when the porosity is constant at the initial time and we illustrate the analytic solutions provided previously by Enakousta's work when the porosity is neglected, but some effects of the strain gradient were involved. We express the stress solutions in terms of the invariants of the Cauchy stress tensor. The solution of the nonzero components of the moments due to the strain gradient effects are also provided in this work. The solution produced in this work depends on the characteristic length scale and can be used as benchmark solution to assess micromorphic gradient models; the solution can also be used to test the efficiency of numerical implementation of gradient models into finite element software.

Appendix (a)

Generalities

In the GLPD model, internal forces are represented through some ordinary second-rank symmetric Cauchy stress tensor Σ plus some additional third-rank "moment tensor" \mathbf{M} symmetric in its first two indices only². The components of \mathbf{M} are related through the three conditions

$$M_{ijj} = 0. \quad (3.50)$$

(These conditions may be compared to the condition of plane stress in the theory of thin plates or shells).

The virtual power of internal forces is given by the expression

$$\mathcal{P}^{(i)} \equiv - \int_{\Omega} (\Sigma : \mathbf{D} + \mathbf{M} \dot{:} \nabla \mathbf{D}) d\Omega \quad (3.51)$$

where Ω denotes the domain considered, $\mathbf{D} \equiv \frac{1}{2} [\nabla \mathbf{V} + (\nabla \mathbf{V})^T]$ (\mathbf{V} : material velocity) the Eulerian strain rate, $\nabla \mathbf{D}$ its gradient, $\Sigma : \mathbf{D}$ the double inner product $\Sigma_{ij} D_{ij}$ and $\mathbf{M} \dot{:} \nabla \mathbf{D}$ the triple inner product $M_{ijk} D_{ij,k}$.

² The component M_{ijk} is noted $M_{k|ij}$ in Gologanu et al (1997)'s original paper. The present notation leads to more natural-looking expressions.

The virtual power of external forces is given by

$$\mathcal{P}^{(e)} \equiv \int_{d\Omega} \mathbf{T} \cdot \mathbf{V} \, dS \quad (3.52)$$

where \mathbf{T} represents some surface traction³.

The hypothesis of additivity of elastic and plastic strain rates reads

$$\begin{cases} \mathbf{D} & \equiv \mathbf{D}^e + \mathbf{D}^p \\ \nabla \mathbf{D} & \equiv (\nabla \mathbf{D})^e + (\nabla \mathbf{D})^p. \end{cases} \quad (3.53)$$

The elastic and plastic parts $(\nabla \mathbf{D})^e$, $(\nabla \mathbf{D})^p$ of the gradient of the strain rate here do *not* coincide in general with the gradients $\nabla(\mathbf{D}^e)$, $\nabla(\mathbf{D}^p)$ of the elastic and plastic parts of the strain rate.

Hypoelasticity Law

The elastic parts of the strain rate and its gradient are related to the rates of the stress and moment tensors through the following hypoelasticity law:

$$\begin{cases} \frac{d\Sigma_{ij}}{dt} & = \lambda \delta_{ij} D_{kk}^e + 2\mu D_{ij}^e \\ \frac{dM_{ijk}}{dt} & = \frac{b^2}{5} \left[\lambda \delta_{ij} (\nabla D)_{hhk}^e + 2\mu (\nabla D)_{ijk}^e \right. \\ & \quad \left. - 2\lambda \delta_{ij} U_k^e - 2\mu (\delta_{ik} U_j^e + \delta_{jk} U_i^e) \right]. \end{cases} \quad (3.54)$$

In these expressions λ and μ denote the Lamé coefficients and b the mean half-spacing between neighboring voids. (In the homogenization procedure, b is the radius of the spherical elementary cell considered). Also, $\frac{d\Sigma_{ij}}{dt}$ and $\frac{dM_{ijk}}{dt}$ are the Jaumann (objective) time-derivatives of Σ_{ij} and M_{ijk} , given by

$$\begin{cases} \frac{d\Sigma_{ij}}{dt} & \equiv \dot{\Sigma}_{ij} + \Omega_{ki} \Sigma_{kj} + \Omega_{kj} \Sigma_{ik} \\ \frac{dM_{ijk}}{dt} & \equiv \dot{M}_{ijk} + \Omega_{hi} M_{hjk} + \Omega_{hj} M_{ihk} + \Omega_{hk} M_{ijh} \end{cases} \quad (3.55)$$

where $\Omega \equiv \frac{1}{2} [\nabla \mathbf{V} - (\nabla \mathbf{V})^T]$ is the antisymmetric part of the velocity gradient. Finally \mathbf{U}^e is a vector the value of which is fixed by equations (3.50) (written in rate form, $\frac{D M_{ijj}}{Dt} = 0$):

$$U_i^e = \frac{\lambda (\nabla D)_{hhi}^e + 2\mu (\nabla D)_{ihh}^e}{2\lambda + 8\mu}. \quad (3.56)$$

³ The general equilibrium equations and boundary conditions corresponding to the expressions (3.51) and (3.52) of the virtual powers of internal and external forces need not be given since they are not necessary for the numerical implementation.

(This vector may be compared to the through-the-thickness component of the elastic strain rate in the theory of thin plates or shells, the value of which is fixed by the condition of plane stress).

Yield Criterion

The plastic behavior is governed by the following Gurson-like criterion:

$$\frac{1}{\Sigma^2} \left(\Sigma_{eq}^2 + \frac{Q^2}{b^2} \right) + 2p \cosh \left(\frac{3}{2} \frac{\Sigma_m}{\Sigma} \right) - 1 - p^2 \leq 0. \quad (3.57)$$

In this expression:

- $\Sigma_{eq} \equiv \left(\frac{3}{2} \Sigma' : \Sigma' \right)^{1/2}$ (Σ' : deviator of Σ) is the von Mises equivalent stress.
- $\Sigma_m \equiv \frac{1}{3} \text{tr } \Sigma$ is the mean stress.
- Σ represents a kind of average value of the yield stress in the heterogeneous metallic matrix, the evolution equation of which is given below.
- p is a parameter connected to the porosity (void volume fraction) f through the relation:

$$p \equiv qf^*, f^* \equiv \begin{cases} f & \text{if } f \leq f_c \\ f_c + \delta(f - f_c) & \text{if } f > f_c \end{cases} \quad (3.58)$$

where q is *Tvergaard's parameter*, f_c the *critical porosity at the onset of coalescence of voids*, and $\delta (> 1)$ a factor describing the accelerated degradation of the material during coalescence Tvergaard (1981), Tvergaard and Needleman (1984).

- Q^2 is a quadratic form of the components of the moment tensor given by

$$Q^2 \equiv A_1 \mathcal{M}_1 + A_2 \mathcal{M}_2 \quad , \quad \begin{cases} A_1 = 0.194 \\ A_2 = 6.108 \end{cases} \quad (3.59)$$

where \mathcal{M}_1 and \mathcal{M}_2 are the quadratic invariants of \mathbf{M} defined by:

$$\begin{cases} \mathcal{M}_1 \equiv M_{mi} M_{mi} \\ \mathcal{M}_2 \equiv \frac{3}{2} M'_{ijk} M'_{ijk}, \end{cases} \quad (3.60)$$

$M_{mi} \equiv \frac{1}{3} M_{hhi}$ and \mathbf{M}' denoting the mean and deviatoric parts of \mathbf{M} , taken over its first two indices.

- Again, b is the mean half-spacing between neighboring voids.

Flow Rule

The plastic parts of the strain rate and its gradient are given by the flow rule associated to the criterion (3.57) through normality:

$$\left\{ \begin{array}{l} D_{ij}^p = \eta \frac{d\Phi}{d\Sigma_{ij}}(\boldsymbol{\Sigma}, \mathbf{M}, \Sigma, f) \\ (\nabla D)_{ijk}^p = \eta \frac{d\Phi}{dM_{ijk}}(\boldsymbol{\Sigma}, \mathbf{M}, \Sigma, f) + \delta_{ik} U_j^p \\ \quad + \delta_{jk} U_i^p \end{array} \right\} \quad (3.61)$$

where

$$\eta = \begin{cases} = 0 & \text{if } \Phi(\boldsymbol{\Sigma}, \mathbf{M}, \Sigma, f) < 0 \\ \geq 0 & \text{if } \Phi(\boldsymbol{\Sigma}, \mathbf{M}, \Sigma, f) = 0 \end{cases} \quad (3.62)$$

The term $\delta_{ik} U_j^p + \delta_{jk} U_i^p$ in equation (3.61) represents a rigid-body motion of the elementary cell, which is left unspecified by the flow rule but fixed in practice by conditions (3.50). (The vector \mathbf{U}^p may be compared to the through-the-thickness component of the plastic strain rate in the theory of thin plates or shells, the value of which is fixed by the condition of plane stress).

The values of the derivatives of the yield function $\Phi(\boldsymbol{\Sigma}, \mathbf{M}, \Sigma, f)$ in equations (3.61) are easily calculated to be

$$\left\{ \begin{array}{l} \frac{d\Phi}{d\Sigma_{ij}}(\boldsymbol{\Sigma}, \mathbf{M}, \Sigma, f) = 3 \frac{\Sigma'_{ij}}{\Sigma^2} + \frac{p}{\Sigma} \delta_{ij} \sinh\left(\frac{3}{2} \frac{\Sigma_m}{\Sigma}\right) \\ \frac{d\Phi}{dM_{ijk}}(\boldsymbol{\Sigma}, \mathbf{M}, \Sigma, f) = \frac{1}{\Sigma^2 b^2} \left(\frac{2}{3} A_1 \delta_{ij} M_{mk} + 3 A_2 M'_{ijk} \right) \end{array} \right\} \quad (3.63)$$

Evolution of Internal Parameters

The evolution of the porosity is governed by the classical equation resulting from approximate incompressibility of the metallic matrix:

$$\dot{f} = (1 - f) \operatorname{tr} \mathbf{D}^p. \quad (3.64)$$

The parameter Σ is given by

$$\Sigma \equiv \Sigma(E) \quad (3.65)$$

where $\Sigma(\epsilon)$ is the function which provides the yield stress of the matrix material in terms of the local equivalent cumulated plastic strain ϵ , and E represents some average value of this equivalent strain in the heterogeneous matrix. The evolution of E is governed by the following equation:

$$(1 - f) \Sigma \dot{E} = \boldsymbol{\Sigma} : \mathbf{D}^p + \mathbf{M} \cdot (\nabla \mathbf{D})^p. \quad (3.66)$$

Appendix (b)

In this section we present the complicate analytic derivations of the integrals for the hollow sphere problem while neglecting the porosity. Although, the formulation is long and tedious we found some need to put it into a single equation. This equation reads:

$$\begin{cases} f(r) = \frac{2A\Sigma_0^2}{\eta r^3} + \frac{2(\eta''\eta^2 - 2\eta'^2\eta)}{\eta^4} \frac{A\Sigma_0^2 b^2}{A_{II} r^4} - \frac{28\eta'}{\eta^2} \frac{A\Sigma_0^2 b^2}{A_{II} r^5} \\ - \left(\frac{72}{\eta} + \frac{2\eta'}{\eta^2} \right) \frac{A\Sigma_0^2 b^2}{A_{II} r^6} - \frac{8A\Sigma_0^2 b^2}{\eta A_{II} r^7} \end{cases} \quad (3.67)$$

To obtain the result we integrated this formulation term by term. Evaluating the integral of the first term in the expression for f we found

$$\begin{aligned} \int_{r_i}^r \frac{2A\Sigma_0^2}{\eta(t)t^3} dt &= 2\Sigma_0 \int_{r_i}^r \frac{dt}{\sqrt{1 + \frac{15b^2}{A_2 t^2}}} \\ &= 2\Sigma_0 \left(\sqrt{\frac{A_2 r^2 + 15b^2}{A_2}} - \sqrt{\frac{A_2 r_i^2 + 15b^2}{A_2}} \right) \end{aligned} \quad (3.68)$$

The second term in the expression for f is broken into two smaller integrals. The result reads

$$\begin{aligned} \int_{r_i}^r \frac{2A\Sigma_0^2 b^2}{A_2} \frac{\eta(t)''\eta(t) - \eta(t)'}{\eta(t)^2 t^4} dt &= \frac{2A\Sigma_0^2 b^2}{A_2} \left[\int_{r_i}^r \frac{\eta(t)''}{\eta(t)t^4} dt - \int_{r_i}^r \frac{\eta(t)'}{\eta(t)t^4} dt \right] \\ &= \frac{2A\Sigma_0^2 b^2}{A_2^3} \left[\int_{r_i}^r \frac{12A_2^2 t^4 + 495A_2 b^2 t^2 + 4500b^4}{t^{10} \left(1 + \frac{15b^2}{A_2 t^2}\right)^2} dt + \frac{1}{A_2} \int_{r_i}^r \frac{60b^2 + 3A_2 t^2}{t^7 \left(1 + \frac{15b^2}{A_2 t^2}\right)} dt \right] \end{aligned} \quad (3.69)$$

Evaluating these two integrals we obtain

$$\begin{aligned} \int_{r_i}^r \frac{12A_2^2 t^4 + 495A_2 b^2 t^2 + 4500b^4}{t^{10} \left(1 + \frac{15b^2}{A_2 t^2}\right)^2} dt &= \left[\frac{A_2^5 r}{450A_2 b^4 r^2 + 6750b^6} \right. \\ &- \frac{11A_2^{\frac{9}{2}} \arctan\left(\frac{\sqrt{A_2} r}{\sqrt{15b}}\right)}{2 \cdot 15^{\frac{3}{2}} b^5} - \frac{2A_2^4}{75b^4 r} + \frac{7A_2^3}{45b^2 r^3} - \frac{4A_2^2}{r^5} + \frac{11a_2^{\frac{9}{2}} \arctan\left(\frac{\sqrt{A_2} r_i}{\sqrt{15b}}\right)}{2 \cdot 15^{\frac{5}{2}} b^5} \\ &\left. - \frac{A_2^5 r_i}{450A_2 b^4 r_i^2 + 6750b^6} + \frac{2A_2^4}{75b^4 r_i} - \frac{7A_2^3}{45b^2 r_i^3} + \frac{4A_2^2}{r_i^5} \right] \end{aligned} \quad (3.70)$$

and

$$\int_{r_i}^r \frac{60b^2 + 3A_2t^2}{t^7(1 + \frac{15b^2}{A_2t^2})} dt = \left[\frac{A_2^3 \ln(|A_2r_i^2 + 15b^2|) - A_2^3 \ln(|A_2r^2 + 15b^2|)}{450b^4} \right. \\ \left. + \frac{A_2^3 \ln(r) - A_2^3 \ln(r_i)}{225b^4} - \frac{A_2^2}{20b^2r_i^2} + \frac{A_2}{r_i^4} + \frac{A_2^2}{30b^2r^2} - \frac{A_2}{r^4} \right] \quad (3.71)$$

The integration of the third term for the function f is broken into two smaller integrals. The result reads

$$\int_{r_i}^r \left(\frac{A\Sigma_0^2b^2}{A_2} \right) \frac{20\eta(t)' + 8\eta(t)\eta'(t)}{\eta(t)^2t^2} dt = \frac{A\Sigma_0^2b^2}{A_2} \left[\int_{r_i}^r \frac{20\eta(t)'}{\eta(t)^2t^2} dt + \int_{r_i}^r \frac{8\eta(t)'}{\eta(t)t^2} dt \right] \\ = - \left[\frac{20\Sigma_0b^2}{A_2^2} \int_{r_i}^r \frac{60b^2 + 3A_2t^2}{t^2(1 + \frac{15b^2}{A_2t^2})^{\frac{3}{2}}} dt + \frac{8A\Sigma_0^2b^2}{A_2} \int_{r_i}^r \frac{60b^2 + 3A_2t^2}{A_2t^5 + 15bt^3} dt \right] \quad (3.72)$$

Now evaluating these two less complicated integrals, we obtain

$$\int_{r_i}^r \frac{60b^2 + 3A_2t^2}{t^2(1 + \frac{15b^2}{A_2t^2})^{\frac{3}{2}}} dt = \left[\frac{3^{\frac{3}{2}} \cdot \sqrt{5} (A_2r^2 + 10b^2) |r|}{\frac{r\sqrt{15}\sqrt{A_2r^2+16b^2}}{A_2}} \right. \\ \left. - \frac{3^{\frac{3}{2}} \cdot \sqrt{5} (A_2r_i^2 + 10b^2) |r_i|}{\frac{r_i\sqrt{15}\sqrt{A_2r_i^2+16b^2}}{A_2}} \right] \quad (3.73)$$

and

$$\int_{r_i}^r \frac{60b^2 + 3A_2t^2}{A_2t^5 + 15bt^3} dt = \left[\frac{A_2^3 \ln(|A_2r^2 + 15b^2|) - A_2^3 \ln(|A_2r_i^2 + 15b^2|)}{6750b^6} \right. \\ \left. + \frac{A_2^3 \ln(r_i) - A_2^3 \ln(r)}{3375b^6} + \frac{A_2^2}{450b^4r_i^2} - \frac{A_2}{60b^2r_i^4} + \frac{2}{3r^6} \right. \\ \left. - \frac{A_2^2}{450b^4r^4} + \frac{A_2}{60b^2r^4} - \frac{2}{3r^6} \right] \quad (3.74)$$

The integration of the fourth term for the function f is broken into two smaller integrals. The result reads

$$\int_{r_i}^r \frac{(72 + 2\eta'(t))}{\eta(t)} \left(\frac{A\Sigma_0^2b^2}{A_2t^6} \right) dt = \frac{A\Sigma_0b^2}{A_2} \left[\int_{r_i}^r \frac{72}{\eta(t)t^6} dt + \int_{r_i}^r \frac{2\eta(t)'}{\eta(t)t^6} dt \right] \\ = \frac{72b^2}{A_2} \left[\int_{r_i}^r \frac{dt}{t^3 \sqrt{1 + \frac{15b^2}{A_2t^2}}} - \frac{2A\Sigma_0b^2}{A_2^2} \int_{r_i}^r \frac{60b^2 + 3A_2t^2}{t^9(1 + \frac{15b^2}{A_2t^2})} dt \right] \quad (3.75)$$

Integrating these two integrals we obtain

$$\int_{r_i}^r \frac{dt}{t^3 \sqrt{1 + \frac{15b^2}{A_2 t^2}}} = \frac{A_2 \left[r \sqrt{\frac{A_2 r_i^2 + 15b^2}{A_2}} - \sqrt{\frac{A_2 r^2 + 15b^2}{A_2}} r_i \right]}{15b^2 r r_i} \quad (3.76)$$

and

$$\begin{aligned} \int_{r_i}^r \frac{60b^2 + 3A_2 t^2}{t^9 \left(1 + \frac{15b^2}{A_2 t^2}\right)} dt &= \left[\frac{A_2^4 \ln(|A_2 r^2 + 15b^2|)}{6750b^6} - \frac{A_2^4 \ln(|A_2 r_i^2 + 15b^2|)}{6750b^6} \right. \\ &+ \frac{A_2^4 \ln(r_i) - A_2^4 \ln(r)}{3375b^6} + \frac{A_2^3}{450b^4 r_i^2} - \frac{A_2^3}{60b^2 r_i^4} + \frac{2A_2}{3r_i^6} - \frac{A_2^3}{450b^4 r^2} + \frac{A_2^2}{60b^2 r^4} - \left. \frac{2A_2}{3r^6} \right] \end{aligned} \quad (3.77)$$

Now integrating the last term in the expression for f , we get

$$\begin{aligned} \int_{r_i}^r \frac{2A \Sigma_0^2 b^2}{\eta(t) t^2} dt &= 2\Sigma_0 b^2 \int_{r_i}^r \frac{t}{\sqrt{1 + \frac{15b^2}{A_2 t^2}}} dt \\ &= \left(\frac{2\sqrt{a_2} r_i \sqrt{a_2 r_i^2 + 15b^2}}{4A_2} - \frac{15b^2 \ln\left(\frac{|\sqrt{a_2} \sqrt{a_2 r_i^2 + 15b^2} - a_2 r_i|}{a_2 r_i}\right)}{4a^2} \right) \\ &\quad - \frac{15b^2 \ln\left(\frac{\sqrt{a_2} \sqrt{a_2 r_i^2 + 15b^2} + a_2 r_i}{a_2 r_i}\right)}{4A_2} - \frac{15b^2 \ln\left(\frac{|\sqrt{a_2} \sqrt{a_2 r^2 + 15b^2} - a_2 r|}{a_2 r}\right)}{4A_2} \\ &\quad + \frac{15b^2 \ln\left(\frac{\sqrt{a_2} \sqrt{a_2 r^2 + 15b^2} + a_2 r}{a_2 r}\right)}{4A_2} - \frac{-2\sqrt{a_2} r \sqrt{a_2 r^2 + 15b^2}}{4a_2} \end{aligned} \quad (3.78)$$

Appendix (c)

Stress Equations

In this section we present the mathematical detail that was missing from the solution to the hollow sphere problem when the porosity is present. The Von Mises stress Σ_{eq}^2 reduces

$$\begin{aligned} \Sigma_{eq}^2 &= \frac{3}{2} (\Sigma'_{ij} : \Sigma'_{ij}) \\ &= \frac{3}{2} ((\Sigma_{rr} - \Sigma_{\theta\theta})^2 + (\Sigma_{\theta\theta} - \Sigma_{\phi\phi})^2 + (\Sigma_{\phi\phi} - \Sigma_{rr})^2) \\ &= 3 (\Sigma_{rr} - \Sigma_{\theta\theta})^2 \end{aligned} \quad (3.79)$$

By the last equality in Eq. (3.79) we find

$$\Sigma_{eq} = \sqrt{3}(\Sigma_{rr} - \Sigma_{\theta\theta}) \quad (3.80)$$

Solving for Σ_{rr} in Eq. (3.80) we have $\Sigma_{rr} = \frac{1}{\sqrt{3}}\Sigma_{eq} + \Sigma_{\theta\theta}$. Taking the derivative $\frac{d}{dr}$ we see that

$$\frac{d}{dr}\Sigma_{rr} = \frac{1}{\sqrt{3}}\frac{d}{dr}\Sigma_{eq} + \frac{d}{dr}\Sigma_{\theta\theta} \quad (3.81)$$

Now since $\frac{1}{\sqrt{3}}\Sigma_{eq} = \Sigma_{rr} - \Sigma_{\theta\theta}$ by adding $3\Sigma_{\theta\theta}$ to both sides we get $\frac{1}{\sqrt{3}}\Sigma_{eq} + 3\Sigma_{\theta\theta} = \Sigma_{rr} + 2\Sigma_{\theta\theta}$. Multiplying throughout by $\frac{1}{3}$ yields $\frac{1}{3\sqrt{3}}\Sigma_{eq} + \Sigma_{\theta\theta} = \frac{1}{3}(\Sigma_{rr} + 2\Sigma_{\theta\theta})$. Since, $\Sigma_m = \frac{1}{3}(\Sigma_{rr} + 2\Sigma_{\theta\theta})$ it then follows that $\frac{1}{3\sqrt{3}}\Sigma_{eq} + \Sigma_{\theta\theta} = \Sigma_m$. Rearranging the last equality gives us $\Sigma_{\theta\theta} = \Sigma_m - \frac{1}{3\sqrt{3}}\Sigma_{eq}$. Taking the derivative of both sides we find that

$$\frac{d}{dr}\Sigma_{\theta\theta} = \frac{d}{dr}\Sigma_m - \frac{1}{3\sqrt{3}}\frac{d}{dr}\Sigma_{eq} \quad (3.82)$$

Thus we can compute the value of $\frac{d\Sigma_{rr}}{dr} + \frac{2}{r}(\Sigma_{rr} - \Sigma_{\theta\theta})$ as follows

$$\begin{aligned} \frac{d\Sigma_{rr}}{dr} + \frac{2}{r}(\Sigma_{rr} - \Sigma_{\theta\theta}) &= \frac{d\Sigma_{rr}}{dr} + \frac{2}{r\sqrt{3}}\Sigma_{eq} \\ &= \left(\frac{1}{\sqrt{3}}\frac{d}{dr}\Sigma_{eq} + \frac{d}{dr}\Sigma_{\theta\theta} \right) + \frac{2r}{\sqrt{3}}\Sigma_{eq} \\ &= \frac{2}{3\sqrt{3}}\frac{d}{dr}\Sigma_{eq} + \frac{2}{r\sqrt{3}}\Sigma_{eq} + \frac{d}{dr}\Sigma_m \end{aligned} \quad (3.83)$$

Von Mises and Mean Stress Formula

In this section we work out the mathematical detail that was left off in Section 3.5. First let \mathbf{M}^* be given by the rule

$$\mathbf{M}^* = \frac{d^2 M_{rrrr}}{dr^2} + \frac{6}{r}\frac{dM_{rrrr}}{dr} + \frac{6}{r^2}M_{rrrr}\frac{4}{r} - \frac{dM_{r\theta\theta}}{dr} - \frac{8}{r^2}M_{r\theta\theta} \quad (3.84)$$

According to Section 3.5, we may rewrite Eq. (3.84) as follows

$$\mathbf{M}^* = \frac{2}{3\sqrt{3}}\frac{d}{dr}\Sigma_{eq} + \frac{2}{r\sqrt{3}}\Sigma_{eq} + \frac{d}{dr}\Sigma_m \quad (3.85)$$

Now we calculate Σ_{eq} and $\frac{d}{dr}\Sigma_{eq}$ using the yield criteria. The result reads

$$\Sigma_{eq} = \sqrt{(p\Sigma_0)^2 + \Sigma_0 - 2p\Sigma_0^2 \cos\left(\frac{3}{2}\frac{\Sigma_m}{\Sigma_0}\right) - \left(\frac{Q}{b}\right)^2} \quad (3.86)$$

and

$$\frac{d}{dr} \Sigma_{eq} = \frac{2p\Sigma_0^2 \sinh\left(\frac{3}{2} \frac{\Sigma_m}{\Sigma_0}\right) \frac{3}{2\Sigma_0} \frac{d}{dr} \Sigma_m + \frac{1}{b^2} \frac{d}{dr} Q^2}{2\sqrt{(p\Sigma_0)^2 + \Sigma_0 - 2p\Sigma_0^2 \cosh\left(\frac{3}{2} \frac{\Sigma_m}{\Sigma_0}\right) - \left(\frac{Q}{b}\right)^2}} \quad (3.87)$$

Substituting Eq. (3.86) and Eq. (3.87) into Eq. (3.85) gives us the result

$$\begin{aligned} \mathbf{M}^* &= \frac{1}{3\sqrt{3}} \left(\frac{2p\Sigma_0^2 \sinh\left(\frac{3}{2} \frac{\Sigma_m}{\Sigma_0}\right) \frac{3}{2\Sigma_0} \frac{d}{dr} \Sigma_m + \frac{1}{b^2} \frac{d}{dr} Q^2}{\sqrt{(p\Sigma_0)^2 + \Sigma_0 - 2p\Sigma_0^2 \cosh\left(\frac{3}{2} \frac{\Sigma_m}{\Sigma_0}\right) - \left(\frac{Q}{b}\right)^2}} \right) \\ &+ \frac{2}{r} \left(\sqrt{(p\Sigma_0)^2 + \Sigma_0 - 2p\Sigma_0^2 \cosh\left(\frac{3}{2} \frac{\Sigma_m}{\Sigma_0}\right) - \left(\frac{Q}{b}\right)^2} \right) + \frac{d}{dr} \Sigma_m \end{aligned} \quad (3.88)$$

By subtracting Eq. (3.88) from Eq. (3.85) we find

$$\begin{aligned} \frac{2}{3\sqrt{3}} \frac{d}{dr} \Sigma_{eq} + \frac{2}{r\sqrt{3}} \Sigma_{eq} &= \frac{1}{3\sqrt{3}} \left(\frac{2p\Sigma_0^2 \sinh\left(\frac{3}{2} \frac{\Sigma_m}{\Sigma_0}\right) \frac{3}{2\Sigma_0} \frac{d}{dr} \Sigma_m + \frac{1}{b^2} \frac{d}{dr} Q^2}{\sqrt{(p\Sigma_0)^2 + \Sigma_0 - 2p\Sigma_0^2 \cosh\left(\frac{3}{2} \frac{\Sigma_m}{\Sigma_0}\right) - \left(\frac{Q}{b}\right)^2}} \right) \\ &+ \frac{2}{r} \left(\sqrt{(p\Sigma_0)^2 + \Sigma_0 - 2p\Sigma_0^2 \cosh\left(\frac{3}{2} \frac{\Sigma_m}{\Sigma_0}\right) - \left(\frac{Q}{b}\right)^2} \right) \end{aligned} \quad (3.89)$$

Moving over terms and then squaring both sides of Eq. (3.89) we have

$$\begin{aligned} \left(\frac{2}{3\sqrt{3}} \frac{d}{dr} \Sigma_{eq} + \frac{2}{r\sqrt{3}} \Sigma_{eq} - \frac{1}{3\sqrt{3}} \left(\frac{2p\Sigma_0^2 \sinh\left(\frac{3}{2} \frac{\Sigma_m}{\Sigma_0}\right) \frac{3}{2\Sigma_0} \frac{d}{dr} \Sigma_m + \frac{1}{b^2} \frac{d}{dr} Q^2}{\sqrt{(p\Sigma_0)^2 + \Sigma_0 - 2p\Sigma_0^2 \cosh\left(\frac{3}{2} \frac{\Sigma_m}{\Sigma_0}\right) - \left(\frac{Q}{b}\right)^2}} \right) \right)^2 \\ = \left(\Sigma_0^2 + \Sigma_0 - 2p\Sigma_0^2 \cosh\left(\frac{3}{2} \frac{\Sigma_m}{\Sigma_0}\right) - \left(\frac{Q}{b}\right)^2 \right). \end{aligned} \quad (3.90)$$

Finally dividing Eq. (3.90) throughout by Σ_0^2 and after adding the value $p^2 + \left(\frac{\Sigma_{eq}}{\Sigma_0}\right)^2$ to both sides of the equation we find

$$\begin{aligned} \frac{1}{\Sigma_0^2} \left(\frac{2}{3\sqrt{3}} \frac{d}{dr} \Sigma_{eq} + \frac{2}{r\sqrt{3}} \Sigma_{eq} - \frac{1}{3\sqrt{3}} \left(\frac{2p\Sigma_0^2 \sinh\left(\frac{3}{2} \frac{\Sigma_m}{\Sigma_0}\right) \frac{3}{2\Sigma_0} \frac{d}{dr} \Sigma_m + \frac{1}{b^2} \frac{d}{dr} Q^2}{\sqrt{(p\Sigma_0)^2 + \Sigma_0 - 2p\Sigma_0^2 \cosh\left(\frac{3}{2} \frac{\Sigma_m}{\Sigma_0}\right) - \left(\frac{Q}{b}\right)^2}} \right) \right)^2 \\ = \frac{1}{\Sigma_0} - \left(\frac{\Sigma_{eq}}{\Sigma_0} \right)^2 \end{aligned} \quad (3.91)$$

taking the square root of both sides of Eq. (3.91) and multiplying by Σ_0 gives

$$\begin{aligned} \frac{2}{3\sqrt{3}} \frac{d}{dr} \Sigma_{eq} + \frac{2}{r\sqrt{3}} \Sigma_{eq} - \frac{1}{3\sqrt{3}} \left(\frac{2p\Sigma_0^2 \sinh\left(\frac{3}{2} \frac{\Sigma_m}{\Sigma_0}\right) \frac{3}{2\Sigma_0} \frac{d}{dr} \Sigma_m + \frac{1}{b^2} \frac{d}{dr} Q^2}{\sqrt{(p\Sigma_0)^2 + \Sigma_0 - 2p\Sigma_0^2 \cosh\left(\frac{3}{2} \frac{\Sigma_m}{\Sigma_0}\right) - \left(\frac{Q}{b}\right)^2}} \right) \\ = \Sigma_0 \sqrt{\frac{1}{\Sigma_0} - \left(\frac{\Sigma_{eq}}{\Sigma_0}\right)^2} \end{aligned} \quad (3.92)$$

Now we do the same procedure to get rid of any terms involving the quadratic term Q . By moving over terms in Eq. (3.92) it follows that

$$\begin{aligned} \frac{2}{3\sqrt{3}} \frac{d}{dr} \Sigma_{eq} + \frac{2}{r\sqrt{3}} \Sigma_{eq} - \Sigma_0 \sqrt{\frac{1}{\Sigma_0} - \left(\frac{\Sigma_{eq}}{\Sigma_0}\right)^2} \\ = \frac{1}{3\sqrt{3}} \left(\frac{2p\Sigma_0^2 \sinh\left(\frac{3}{2} \frac{\Sigma_m}{\Sigma_0}\right) \frac{3}{2\Sigma_0} \frac{d}{dr} \Sigma_m + \frac{1}{b^2} \frac{d}{dr} Q^2}{\sqrt{(p\Sigma_0)^2 + \Sigma_0 - 2p\Sigma_0^2 \cosh\left(\frac{3}{2} \frac{\Sigma_m}{\Sigma_0}\right) - \left(\frac{Q}{b}\right)^2}} \right) \end{aligned} \quad (3.93)$$

Dividing both sides of Eq. (3.93) by

$$\frac{1}{3\sqrt{3}} \left(2p\Sigma_0^2 \sinh\left(\frac{3}{2} \frac{\Sigma_m}{\Sigma_0}\right) \frac{3}{2\Sigma_0} \frac{d}{dr} \Sigma_m + \frac{1}{b^2} \frac{d}{dr} Q^2 \right)$$

we obtain

$$\begin{aligned} \frac{\frac{1}{3\sqrt{3}} \frac{d}{dr} \Sigma_{eq} + \frac{2}{r\sqrt{3}} \Sigma_{eq} - \Sigma_0 \sqrt{\frac{1}{\Sigma_0} - \left(\frac{\Sigma_{eq}}{\Sigma_0}\right)^2}}{\frac{1}{3\sqrt{3}} \left(2p\Sigma_0^2 \sinh\left(\frac{3}{2} \frac{\Sigma_m}{\Sigma_0}\right) \frac{3}{2\Sigma_0} \frac{d}{dr} \Sigma_m + \frac{1}{b^2} \frac{d}{dr} Q^2 \right)} \\ = \frac{1}{\sqrt{(p\Sigma_0)^2 + \Sigma_0 - 2p\Sigma_0^2 \cosh\left(\frac{3}{2} \frac{\Sigma_m}{\Sigma_0}\right) - \left(\frac{Q}{b}\right)^2}} \end{aligned} \quad (3.94)$$

reciprocating both sides of Eq. (3.94) and then after squaring both sides gives the relation

$$\begin{aligned} \left(\frac{\frac{1}{3\sqrt{3}} \left(2p\Sigma_0^2 \sinh\left(\frac{3}{2} \frac{\Sigma_m}{\Sigma_0}\right) \frac{3}{2\Sigma_0} \frac{d}{dr} \Sigma_m + \frac{1}{b^2} \frac{d}{dr} Q^2 \right)}{\frac{1}{3\sqrt{3}} \frac{d}{dr} \Sigma_{eq} + \frac{2}{r\sqrt{3}} \Sigma_{eq} - \Sigma_0 \sqrt{\frac{1}{\Sigma_0} - \left(\frac{\Sigma_{eq}}{\Sigma_0}\right)^2}} \right)^2 \\ = (p\Sigma_0)^2 + \Sigma_0 - 2p\Sigma_0^2 \cosh\left(\frac{3}{2} \frac{\Sigma_m}{\Sigma_0}\right) - \left(\frac{Q}{b}\right)^2 \end{aligned} \quad (3.95)$$

Again dividing Eq. (3.95) throughout by Σ_0^2 and after adding the value $p^2 + \left(\frac{\Sigma_{eq}}{\Sigma_0}\right)^2$ to both sides gives us the relation

$$\frac{1}{\Sigma_0^2} \left(\frac{\frac{1}{3\sqrt{3}} \left(2p\Sigma_0^2 \sinh\left(\frac{3}{2}\frac{\Sigma_m}{\Sigma_0}\right) \frac{3}{2\Sigma_0} \frac{d}{dr}\Sigma_m + \frac{1}{b^2} \frac{d}{dr}Q^2 \right)}{\frac{1}{3\sqrt{3}} \frac{d}{dr}\Sigma_{eq} + \frac{2}{r\sqrt{3}}\Sigma_{eq} - \Sigma_0 \sqrt{\frac{1}{\Sigma_0} - \left(\frac{\Sigma_{eq}}{\Sigma_0}\right)^2}} \right)^2 = \frac{1}{\Sigma_0} - \left(\frac{\Sigma_{eq}}{\Sigma_0}\right)^2 \quad (3.96)$$

Now assume $\Sigma_{eq} \geq \sqrt{\Sigma_0}$ so that $\frac{1}{\Sigma_0} - \left(\frac{\Sigma_{eq}}{\Sigma_0}\right)^2 \geq 0$. In this case solving for $\frac{1}{b^2} \frac{d}{dr}Q^2$ in Eq. (3.96) gives us

$$\begin{aligned} \frac{1}{b^2} \frac{d}{dr}Q^2 &= \frac{3\sqrt{3}}{1} \left(\frac{1}{3\sqrt{3}} \frac{d}{dr}\Sigma_{eq} + \frac{2}{r\sqrt{3}}\Sigma_{eq} - \Sigma_0 \sqrt{\frac{1}{\Sigma_0} - \left(\frac{\Sigma_{eq}}{\Sigma_0}\right)^2} \right) \times \\ &\left(\Sigma_0 \sqrt{\frac{1}{\Sigma_0} - \left(\frac{\Sigma_{eq}}{\Sigma_0}\right)^2} \right) - \left(2p\Sigma_0^2 \sinh\left(\frac{3}{2}\frac{\Sigma_m}{\Sigma_0}\right) \frac{3}{2\Sigma_0} \frac{d}{dr}\Sigma_m \right) \end{aligned} \quad (3.97)$$

But also by the yield criteria 3.57 we know that

$$-\frac{1}{b^2} \frac{d}{dr}Q^2 = 2p \sinh\left(\frac{3}{2}\frac{\Sigma_m}{\Sigma_0}\right) \left(\frac{3}{2\Sigma_0} \frac{d}{dr}\Sigma_m \right) - 2\Sigma_{eq} \frac{d}{dr}\Sigma_{eq} \quad (3.98)$$

Finally by adding Eq. (3.98) and Eq. (3.97) we have

$$\begin{aligned} &\frac{3\sqrt{3}}{1} \left(\frac{1}{3\sqrt{3}} \frac{d}{dr}\Sigma_{eq} + \frac{2}{r\sqrt{3}}\Sigma_{eq} - \Sigma_0 \sqrt{\frac{1}{\Sigma_0} - \left(\frac{\Sigma_{eq}}{\Sigma_0}\right)^2} \right) \times \\ &\left(\Sigma_0 \sqrt{\frac{1}{\Sigma_0} - \left(\frac{\Sigma_{eq}}{\Sigma_0}\right)^2} \right) = 2\Sigma_{eq} \frac{d}{dr}\Sigma_{eq} + \left(2p\Sigma_0^2 \sinh\left(\frac{3}{2}\frac{\Sigma_m}{\Sigma_0}\right) \frac{3}{2\Sigma_0} \frac{d}{dr}\Sigma_m \right) \\ &\quad - 2p \sinh\left(\frac{3}{2}\frac{\Sigma_m}{\Sigma_0}\right) \end{aligned} \quad (3.99)$$

Since $\Sigma_0 \sqrt{\frac{1}{\Sigma_0} - \left(\frac{\Sigma_{eq}}{\Sigma_0}\right)^2} = \sqrt{\Sigma_0 - \Sigma_{eq}^2}$ Eq. (3.99) becomes

$$\begin{aligned} &\frac{3\sqrt{3}}{1} \left(\frac{1}{3\sqrt{3}} \frac{d}{dr}\Sigma_{eq} + \frac{2}{r\sqrt{3}}\Sigma_{eq} - \left(\sqrt{\Sigma_0 - \Sigma_{eq}^2}\right) \right) \left(\sqrt{\Sigma_0 - \Sigma_{eq}^2}\right) \\ &= 2\Sigma_{eq} \frac{d}{dr}\Sigma_{eq} + \left(2p\Sigma_0^2 \sinh\left(\frac{3}{2}\frac{\Sigma_m}{\Sigma_0}\right) \frac{3}{2\Sigma_0} \frac{d}{dr}\Sigma_m \right) - 2p \sinh\left(\frac{3}{2}\frac{\Sigma_m}{\Sigma_0}\right) \end{aligned} \quad (3.100)$$

Let $\alpha = 3\sqrt{3}$, $\gamma = \frac{3}{2\Sigma_0}$, and $\rho = p\Sigma_0$ then Eq. (3.100) reads

$$\begin{aligned}
& \left(\frac{d}{dr} \Sigma_{eq} + \frac{6}{r} \Sigma_{eq} - \alpha \left(\sqrt{\Sigma_0 - \Sigma_{eq}^2} \right) \right) \left(\sqrt{\Sigma_0 - \Sigma_{eq}^2} \right) \\
& = 2 \Sigma_{eq} \frac{d}{dr} \Sigma_{eq} + \left(\rho \sinh(\gamma \Sigma_m) \frac{d}{dr} \Sigma_m \right) - 2p \sinh(\gamma \Sigma_m)
\end{aligned} \tag{3.101}$$

Combining like terms in Eq. (3.101) gives us the result

$$\begin{aligned}
& \left(\frac{d}{dr} \Sigma_{eq} + \frac{6}{r} \Sigma_{eq} - \alpha \left(\sqrt{\Sigma_0 - \Sigma_{eq}^2} \right) \right) \left(\sqrt{\Sigma_0 - \Sigma_{eq}^2} \right) \\
& = 2 \Sigma_{eq} \frac{d}{dr} \Sigma_{eq} + \sinh(\gamma \Sigma_m) \left(\rho \frac{d}{dr} \Sigma_m - 2p \right)
\end{aligned} \tag{3.102}$$

Factoring the left side of Eq. (3.102) and combining terms yields

$$\begin{aligned}
& \frac{d}{dr} \Sigma_{eq} \left(\sqrt{\Sigma_0 - \Sigma_{eq}^2} - 2 \Sigma_{eq} \right) + \frac{6}{r} \Sigma_{eq} \left(\sqrt{\Sigma_0 - \Sigma_{eq}^2} \right) - \alpha \left(\Sigma_0 - \Sigma_{eq}^2 \right) \\
& = \sinh(\gamma \Sigma_m) \left(\rho \frac{d}{dr} \Sigma_m - 2p \right)
\end{aligned} \tag{3.103}$$

Since Σ_{eq} and Σ_m are independent of one another both sides of Eq. (3.103) must be equal to some constant value, say λ , then we can solve the system of ODE

$$\begin{aligned}
& \frac{d}{dr} \Sigma_{eq} \left(\sqrt{\Sigma_0 - \Sigma_{eq}^2} - \beta \Sigma_{eq} \right) + \frac{6}{r} \Sigma_{eq} \left(\sqrt{\Sigma_0 - \Sigma_{eq}^2} \right) - \alpha \left(\Sigma_0 - \Sigma_{eq}^2 \right) = \lambda \\
& \rho \sinh(\gamma \Sigma_m) \frac{d}{dr} \Sigma_m - 2p \sinh(\gamma \Sigma_m) = \lambda
\end{aligned} \tag{3.104}$$

where the value λ is to be determined later. By rearranging the above equation we get

$$\frac{\rho \sinh(\gamma \Sigma_m)}{\lambda + 2p \sinh(\gamma \Sigma_m)} d\Sigma_m = dr \tag{3.105}$$

Integrating both sides of Eq. (3.105) we have

$$\int \frac{\rho \sinh(\gamma \Sigma_m)}{\lambda + 2p \sinh(\gamma \Sigma_m)} d\Sigma_m = r + C_1 \tag{3.106}$$

for some constant C_1 . The integral on the left is complicated but nonetheless can be evaluated by analytical means. Applying linearity Eq. (3.106) writes

$$\int \frac{\rho \sinh(\gamma \Sigma_m)}{\lambda + 2p \sinh(\gamma \Sigma_m)} d\Sigma_m = \rho \int \frac{\sinh(\gamma \Sigma_m)}{\lambda + 2p \sinh(\gamma \Sigma_m)} d\Sigma_m \tag{3.107}$$

Next let $u = \gamma \Sigma_m$ then $\frac{du}{d\Sigma_m} = \gamma$ so $\frac{du}{\gamma} = d\Sigma_m$. Therefore in terms of u Eq. (3.107) writes

$$\rho \int \frac{\sinh(\gamma \Sigma_m)}{\lambda + 2p \sinh(\gamma \Sigma_m)} d\Sigma_m = \frac{\rho}{\gamma} \int \frac{\sinh(u)}{\lambda + 2p \sinh(u)} du \quad (3.108)$$

Write $\sinh(u)$ as $\sin(u) = \frac{1}{2p} (2p \sinh(u) + \lambda) - \frac{\lambda}{2p}$ then

$$\begin{aligned} \int \left(\frac{\sinh(u)}{2p \sinh(u) + \lambda} \right) du &= \int \left(\frac{\frac{1}{2p} (2p \sinh(u) + \lambda)}{2p \sinh(u) + \lambda} - \frac{\frac{\lambda}{2p}}{2p \sinh(u) + \lambda} \right) du \\ &= \frac{u}{2p} - \frac{\lambda}{2p} \int \frac{1}{2p \sinh(u) + \lambda} du \end{aligned} \quad (3.109)$$

Now we solve

$$\int \left(\frac{1}{2p \sinh(u) + \lambda} \right) du.$$

By the tangent half angle substitution, otherwise known as the Weierstrass substitution, the integral writes

$$\int \left(\frac{1}{2p \sinh(u) + \lambda} \right) du = \int \left(\frac{1}{\frac{4p \tanh\left(\frac{u}{2}\right)}{1 - \tanh^2\left(\frac{u}{2}\right)} + \lambda} \right) du \quad (3.110)$$

Substitute $\kappa = \tanh\left(\frac{u}{2}\right)$ so that $\frac{d\kappa}{du} = \frac{\text{sech}^2\left(\frac{u}{2}\right)}{2}$, $du = \frac{2}{\text{sech}^2\left(\frac{u}{2}\right)}$, and $d\kappa =$

$\frac{2}{1 - \kappa^2} du$ we obtain

$$\begin{aligned} \int \left(\frac{1}{\frac{4p \tanh\left(\frac{u}{2}\right)}{1 - \tanh^2\left(\frac{u}{2}\right)} + \lambda} \right) du &= -2 \int \frac{1}{\lambda \kappa^2 - 4p\kappa - \lambda} d\kappa \\ &= -2 \int \frac{d\kappa}{\left(\sqrt{\lambda}\kappa - \frac{2p}{\sqrt{\lambda}}\right)^2 - \frac{4p^2}{\lambda} - \lambda} \end{aligned} \quad (3.111)$$

Next, let $w = \frac{\lambda \kappa - 2p}{\sqrt{\lambda} \sqrt{-\frac{4p^2}{\lambda} - \lambda}}$ then $\frac{dw}{dv} = \frac{\sqrt{\lambda}}{-\frac{4p^2}{\lambda} - \lambda}$ so $dw \frac{-\frac{4p^2}{\lambda} - \lambda}{\sqrt{\lambda}} = dv$.

Upon substitution we get

$$\begin{aligned}
-2 \int \frac{d\kappa}{\left(\sqrt{\lambda}\kappa - \frac{2p}{\sqrt{\lambda}}\right)^2 - \frac{4p^2}{\lambda} - \lambda} &= -2 \int \frac{\sqrt{-\frac{4p^2}{\lambda} - \lambda}}{\sqrt{\lambda} \left(\left(-\frac{4p^2}{\lambda} - \lambda\right) w^2 - \frac{4p^2}{\lambda} - \lambda \right)} dw \\
&= \left(\frac{1}{\frac{1}{\sqrt{\lambda}} \sqrt{-\frac{4p^2}{\lambda} - \lambda}} \right) \int \frac{1}{w^2 + 1} dw \\
&= \left(\frac{1}{\frac{1}{\sqrt{\lambda}} \sqrt{-\frac{4p^2}{\lambda} - \lambda}} \right) \arctan(w)
\end{aligned} \tag{3.112}$$

After plugging in $w = \frac{\lambda\kappa - 2p}{\sqrt{\lambda}\sqrt{-\frac{4p^2}{\lambda} - \lambda}}$ we find

$$-2 \int \frac{d\kappa}{\left(\sqrt{\lambda}\kappa - \frac{2p}{\sqrt{\lambda}}\right)^2 - \frac{4p^2}{\lambda} - \lambda} = \frac{\arctan\left(\frac{\lambda \tanh\left(\frac{u}{2}\right) - 2p}{\sqrt{\lambda}\sqrt{-\frac{4p^2}{\lambda} - \lambda}}\right)}{\sqrt{\lambda}\sqrt{-\frac{4p^2}{\lambda} - \lambda}} \tag{3.113}$$

Upon substitution $u = \gamma\Sigma_m$ the integral is solved as

$$\int \frac{\rho \sinh(\gamma\Sigma_m)}{\lambda + 2p \sinh(\gamma\Sigma_m)} d\Sigma_m = \frac{\rho \left(\frac{\Sigma_m}{p} - \frac{\lambda \ln\left(\frac{2pe^{-\gamma\Sigma_m} - \sqrt{4p^2 + \lambda^2} - \lambda}{2pe^{-\gamma\Sigma_m} + \sqrt{4p^2 + \lambda^2} - \lambda}\right)}{\gamma p \sqrt{4p^2 + \lambda^2}} \right)}{2} \tag{3.114}$$

Therefore, by Eq. (3.106) we find Σ_m satisfies the implicit expression

$$\frac{\rho \left(\frac{\Sigma_m}{p} - \frac{\lambda \ln\left(\frac{2pe^{-\gamma\Sigma_m} - \sqrt{4p^2 + \lambda^2} - \lambda}{2pe^{-\gamma\Sigma_m} + \sqrt{4p^2 + \lambda^2} - \lambda}\right)}{\gamma p \sqrt{4p^2 + \lambda^2}} \right)}{2} = r + C_1 \tag{3.115}$$

We solve λ by solving the root of the equation

$$\frac{\Sigma_m(r_e) - \Sigma_m(r_i)}{p} - \frac{2(r_i - r_e)}{\rho} \cdot \frac{\lambda \ln \left(\frac{2pe^{-\gamma \Sigma_m(r_e)} - \sqrt{4p^2 + \lambda^2} - \lambda}{2pe^{-\gamma \Sigma_m(r_e)} + \sqrt{4p^2 + \lambda^2} - \lambda} \cdot \frac{2pe^{-\gamma \Sigma_m(r_i)} - \sqrt{4p^2 + \lambda^2} - \lambda}{2pe^{-\gamma \Sigma_m(r_i)} + \sqrt{4p^2 + \lambda^2} - \lambda} \right)}{\gamma p \sqrt{4p^2 + \lambda^2}} \quad (3.116)$$

References

- Ahad FR, Enakoutsa K, Solanki KN, Bammann DJ (2014) Nonlocal modeling in high-velocity impact failure of 6061-T6 aluminum. *International Journal of Plasticity* 55:108–132
- Andreas U, dell'Isola F, Giorgio I, Placidi L, Lekszycki T, Rizzi NL (2016) Numerical simulations of classical problems in two-dimensional (non) linear second gradient elasticity. *International Journal of Engineering Science* 108:34–50
- Bergheau JM, Leblond JB, Perrin G (2014) A new numerical implementation of a second-gradient model for plastic porous solids, with an application to the simulation of ductile rupture tests. *Computer Methods in Applied Mechanics and Engineering* 268:105–125
- dell'Isola F, Della Corte A, Giorgio I (2017) Higher-gradient continua: The legacy of Piola, Mindlin, Sedov and Toupin and some future research perspectives. *Mathematics and Mechanics of Solids* 22(4):852–872
- Enakoutsa K (2007) *Modèle non-locaux en rupture ductile des métaux*. PhD thesis, Pierre et Marie Curie, Paris VI (in French)
- Enakoutsa K (2013a) Exact results for the problem of a hollow sphere subjected to hydrostatic tension and made of micromorphic plastic porous material. *Mechanics Research Communications* 49:1–7
- Enakoutsa K (2013b) Exact results for the problem of a hollow sphere subjected to hydrostatic tension and made of micromorphic plastic porous material. *Mechanics Research Communications* 49:1–7
- Enakoutsa K (2014) Some new applications of the GLPD micromorphic model of ductile fracture. *Mathematics and Mechanics of Solids* 19(3):242–259
- Enakoutsa K (2015) An analytic benchmark solution to the problem of a generalized plane strain hollow cylinder made of micromorphic plastic porous metal and subjected to axisymmetric loading conditions. *Mathematics and Mechanics of Solids* 20(9):1013–1025
- Enakoutsa K, Leblond JB (2009) Numerical implementation and assessment of the GLPD micromorphic model of ductile rupture. *European Journal of Mechanics-A/Solids* 28(3):445–460
- Enakoutsa K, Leblond JB, Perrin G (2007) Numerical implementation and assessment of a phenomenological nonlocal model of ductile rupture. *Computer Methods in Applied Mechanics and Engineering* 196(13-16):1946–1957
- Enakoutsa K, Ahad FR, Solanki KN, Tjiptowidjojo Y, Bammann DJ (2012a) Using damage delocalization to model localization phenomena in Bammann-Chiesa-Johnson metals. *Journal of engineering materials and technology* 134(4)
- Enakoutsa K, Solanki KN, Ahad FR, Tjiptowidjojo Y, Bammann DJ (2012b) Damage smoothing effects in a delocalized rate sensitivity model for metals. *Theoretical and Applied Mechanics Letters* 2(5):051,005
- Giorgio I, Andreas U, dell'Isola F, Lekszycki T (2017) Viscous second gradient porous materials for bones reconstructed with bio-resorbable grafts. *Extreme Mechanics Letters* 13:141–147
- Gologanu JB, Mand Leblond, Perrin G, Devaux J (1997) Recent extensions of Gurson's model for porous ductile metals. In: Suquet P (ed) *Continuum micromechanics*, vol CISM Courses and Lectures 377, Springer, pp 61–130

- Gurson AL (1977) Continuum theory of ductile rupture by void nucleation and growth: Part I—Yield criteria and flow rules for porous ductile media. *Journal of Engineering Materials and Technology* 99(1):2–15
- Leblond JB, Perrin G, Devaux J (1994) Bifurcation effects in ductile metals with nonlocal damage. *Journal of Applied Mechanics* 61:236–242
- Nahshon K, Hutchinson JW (2008) Modification of the Gurson model for shear failure. *European Journal of Mechanics-A/Solids* 27(1):1–17
- Perrin G, Leblond JB (1990) Analytical study of a hollow sphere made of plastic porous material and subjected to hydrostatic tension-application to some problems in ductile fracture of metals. *International Journal of Plasticity* 6(6):677–699
- Perrin G, Leblond JB (2000) Accelerated void growth in porous ductile solids containing two populations of cavities. *International Journal of Plasticity* 16(1):91–120
- Pijaudier-Cabot G, Bazant ZP (1987) Nonlocal damage theory. *Journal of engineering mechanics* 113(10):1512–1533
- Placidi L, Barchiesi E, Misra A, Timofeev D (2021) Micromechanics-based elasto-plastic–damage energy formulation for strain gradient solids with granular microstructure. *Continuum Mechanics and Thermodynamics* 33:2213–2241
- Reiher JC, Giorgio I, Bertram A (2017) Finite-element analysis of polyhedra under point and line forces in second-strain gradient elasticity. *Journal of Engineering Mechanics* 143(2):04016,112
- Rice JR, Tracey DM (1969) On the ductile enlargement of voids in triaxial growth holes. *Journal of the Mechanics and Physics of Solids* 17(3):201–217
- Scerrato D, Bersani AM, Giorgio I (2021) Bio-inspired design of a porous resorbable scaffold for bone reconstruction: A preliminary study. *Biomimetics* 6(1):18
- Tvergaard V (1981) Influence of voids on shear band instabilities under plane strain conditions. *International Journal of fracture* 17(4):389–407
- Tvergaard V, Needleman A (1984) Analysis of the cup-cone fracture in a round tensile bar. *Acta metallurgica* 32(1):157–169
- Tvergaard V, Needleman A (1995) Effects of nonlocal damage in porous plastic solids. *International Journal of Solids and Structures* 32(8-9):1063–1077
- Tvergaard V, Needleman A (1997) Nonlocal effects on localization in a void-sheet. *International Journal of Solids and Structures* 34(18):2221–2238



Chapter 4

Quantum Dynamics Effects on Amplitude-Frequency Response of Superharmonic Resonance of Second-Order of Electrostatically Actuated NEMS Circular Plates

Dumitru I. Caruntu, Julio S. Beatriz

Abstract This work deals with the effects of Casimir and/or van der Waals forces (quantum dynamics phenomena) on the amplitude-frequency response of the superharmonic resonance of second-order of axisymmetric vibrations of electrostatically actuated nanoelectromechanical systems (NEMS) clamped circular plates. Electrostatic actuation consists of alternating current (AC) voltage of magnitude to produce hard excitations and of frequency near one fourth the natural frequency of the clamped circular plate. The intermolecular forces Casimir and van der Waals, damping force, and electrostatic force are the forces acting on the NEMS plate. Six Reduced Order Models (ROMs) with one and up to 6 modes of vibration are used. The ROM with one mode of vibration is solved using the Method of Multiple Scales (MMS) in which the hard excitations are modeled using first-order and second-order models of hard excitations electrostatic force. Also, Taylor polynomials up to 25th degree are used to approximate the electrostatic, Casimir and van der Waals forces in the ROM with one mode of vibration. MMS predicts the amplitude-frequency response (bifurcation diagram) of the resonance. The other ROMs, using from two to six modes of vibration are solved using two methods, namely continuation and bifurcation using AUTO software package to predict the amplitude-frequency response, and numerical integration using Matlab to predict time responses of the NEMS plate. The amplitude-frequency response predicts a softening effect, and the existence of three branches, two stable and one unstable. A saddle-node bifurcation point of amplitude of 0.24 of the gap, and end points of amplitudes of 0.66 and 0.75 of the gap of unstable and stable branches, respectively, are predicted. The increase of Casimir and/or van der Waals forces shifts the branches, bifurcation points, and endpoints to lower frequencies.

The original version of this chapter was revised: The authors names have been corrected in the xml file. The correction to this chapter is available at https://doi.org/10.1007/978-3-031-04548-6_33

D. I. Caruntu, J. S. Beatriz
University of Texas Rio Grande Valley, Mechanical Engineering Department, Edinburg, Texas 78539, U.S.A.
e-mail: dumitru.caruntu@utrgv.edu, caruntud2@asme.org, dcaruntu@yahoo.com, julio.beatriz01@outlook.com

© The Author(s), under exclusive license to Springer Nature Switzerland AG 2022, corrected publication 2022

I. Giorgio et al. (eds.), *Theoretical Analyses, Computations, and Experiments of Multiscale Materials*, Advanced Structured Materials 175, https://doi.org/10.1007/978-3-031-04548-6_4

Keywords: MEMS, NEMS, non-linear, amplitude-frequency response, superharmonic resonance of second-order, circular plate resonators, Casimir effect, van der Waals effect

4.1 Introduction

Micro- and Nano-electromechanical systems (M/NEMS) are known for their small size, and variety of forms. By taking advantage of their size, these devices can be used in several applications, while maintaining high efficiency and performance (Ashoori et al, 2017). Their variety of shapes such as circular plates (Sajadi et al, 2018; Caruntu and Oyervides, 2017, 2016; Liao et al, 2009), beams (Caruntu et al, 2019, 2013; Zhang et al, 2015), membranes (Dorfmeister et al, 2018), carbon nanotubes (Caruntu and Juarez, 2019; Caruntu and Luo, 2014; Khadem et al, 2012), provide options that allow one to decide which benefits a specific application the most. These applications include, but are not limited to, micropumps (Wang and Fu, 2018; Nisar et al, 2008), ultrasonic transducers (Ahmad and Pratap, 2010), energy harvesters (Zhang et al, 2015), and shock switches (Khadem et al, 2012). Furthermore, these systems are able to perform with a huge assortment of actuation methods, such as thermal actuation (Varona et al, 2007), piezoelectric (Wang and Fu, 2018; Nisar et al, 2008; Maurini et al, 2006), and electrostatic (Caruntu and Juarez, 2019; Nisar et al, 2008). Electrostatic actuation in M/NEMS plates involves the use of parallel plates, one of which is fixed and the other flexible. By applying a voltage between the plates, an electrostatic force is induced between the plates, which leads to a deformation of the flexible plate. By applying an alternating current (AC) voltage, the flexible plate vibrates. However, these devices might also have a direct current (DC) voltage component, which induces a static deflection onto the flexible plate (Liao et al, 2009).

The frequency and amplitude of the AC voltage has a direct effect on the behavior of the system. As these systems are non-linear, changing the voltage can have an effect on the stability of the system. As shown by Sajadi et al (2018), different parameters such as differential pressure can lead to unexpected behavior, i.e increased stability with increasing voltage. Other parameters such as intermolecular forces Casimir and van der Waals should be taken into consideration when designing NEMS. Intermolecular forces are significant at nano scales, reaching the point of the intermolecular forces overcoming the natural resistance of the structure (Batra et al, 2008). It should be said that Casimir and van der Waals forces cannot occur at the same time. They describe the same phenomenon at different scales. For gaps greater than 100 nm, Casimir force describes the intermolecular interaction, and for gaps less than 50 nm, van der Waals force (Caruntu and Reyes, 2020; Caruntu et al, 2016; Batra et al, 2008). If one reaches a critical voltage, or a combination of factors in the system, pull-in can occur. Pull-in is a phenomenon in which the flexible plate gets in contact with the ground plate (Caruntu and Reyes, 2020; Liao et al, 2009). This occurs when the attracting forces overcome the natural resistance of the structure.

M/NEMS circular plates are also affected by damping (Ishfaqe and Kim, 2017; Shabani et al, 2013) or surface effects (Lin et al, 2018). Damping depends on the environment in which the M/NEMS are being used. Shabani et al (2013) mentioned that if the fluid is a liquid, the model should take into consideration the damping effect, as well as added mass. This has a great effect on the behavior of the system, due to the energy loss. Designs such as perforated circular plates (Ishfaqe and Kim, 2017) were also taken into consideration in order to control the level of damping the system is influenced by. Surface effects including surface stress and elasticity affect the pull-in voltage. Surface effects are significant if the circular plates are quite thin or have a large surface to volume ratio (Lin et al, 2018). A variety of models have been reported in the literature. Such models include the Kirchoff thin plate theory (Anjomshoa and Tahani, 2016; Rahim, 2010a), or the Mindlin plate theory (Rahim, 2010a). The Mindlin plate theory takes into consideration the shear strain, while the Kirchhoff does not.

Secondary resonances that occur at fractions of the natural frequency and under hard excitations, i.e. superharmonic resonance, constitute a very important topic. Many studies have been conducted on M/NEMS under secondary resonances (Caruntu et al, 2021, 2019; Kacem et al, 2012; Najjar et al, 2010; Nayfeh and Younis, 2005). Better understanding of the behavior of the system, would help to better design and optimize it. Superharmonic resonances occur at a frequency less than that of the natural frequency, causing larger than normal amplitudes to occur due to hard excitations. As shown by Kacem et al (2012); Najjar et al (2010); Nayfeh and Younis (2005), the behavior of a system varies, and depending on the situation, softening and hardening behavior can occur. Furthermore, Najjar et al (2010) showed that even superharmonic resonances behave differently.

This paper investigates the amplitude-frequency response of superharmonic resonance of second-order of electrostatically actuated M/NEMS clamped circular plate resonators. Only AC voltage is considered in this work. This investigation has been conducted using Reduced Order Models (ROMS) with a number of modes of vibration (Caruntu et al, 2013) from one to six. These models have been solved using the Method of Multiple Scales (MMS), continuation and bifurcation using AUTO, and numerical integration using Matlab (*fsolve* and *ode15s*). The effects of various parameters, such as voltage, damping, Casimir and van der Waals effects are reported. The effect of higher degree Taylor polynomials approximating electrostatic, Casimir, and van der Waals forces in the ROM with one mode of vibration on the amplitude-frequency response is also reported. The effects of parameters voltage and damping on the amplitude-frequency response are reported as well. ROMs are also numerically integrated to predict time responses. While similar methods have been used for circular plates (Caruntu and Oyervides, 2017, 2016), this is the first time a second-order model for hard excitations is used, and an investigation regarding the effect of the degree of Taylor polynomials approximating the electrostatic, Casimir and van der Waals forces on the amplitude-frequency response are conducted. In comparison to data reported in the literature, the behavior of the clamped circular plate is similar to Kim and Lee (2015); Najjar et al (2010) who investigated other structures than circular plates. For example, (Kim and Lee, 2015) used a model in-

cluding only *AC* which causes the super harmonic resonance of order two to appear in carbon nanotubes. They reported a more linear behavior. This is different from the predictions of present work for clamped circular plates in which the branches split at higher amplitudes showing a strong nonlinear behavior. Similar behavior with (Kim and Lee, 2015) is shown for clamped circular plates. Najari et al (2010) focused on cantilevers. In their case the branches split as in present work. However their results show a hardening effect, not a softening effect as in present work.

The novelty of this paper consists of:

1. Reporting the amplitude-frequency response of superharmonic resonance of *M/NEMS* clamped circular plates,
2. in order to include quantum dynamics effects such as Casimir and van der Waals forces.
3. The amplitude-frequency response (bifurcation diagram) predicts the existence of a saddle-node bifurcation at an amplitude around 0.25 of the gap and three branches, two stable and one unstable.
4. The two branches in higher amplitudes are shown to have endpoints around 0.7 of the gap, which leads to a narrow interval for which pull-in occurs.
5. Six ROMs are used in this investigation using from one to six modes of vibration (terms).
6. The ROM using one term (1T ROM) is solved using MMS,
7. in which two models of hard excitations are proposed,
8. and an investigation regarding the degree of Taylor polynomials approximating the electrostatic, Casimir and van der Waals forces is conducted.
9. The other ROMs using from two to six terms are solved using a continuation and bifurcation software package AUTO, and are numerically integrated using Matlab.
10. It is shown that ROM with 6 modes of vibration (6T ROM) is the one with the best prediction for all amplitudes in the bifurcation diagram.
11. This work predicts that both Casimir and van der Waals forces in *NEMS* shift the steady-state amplitudes in the bifurcation diagram to lower frequencies and increase the softening effect.
12. It also predicts that hard excitations with dimensionless voltage parameter $\delta > 3$ and dimensionless damping parameter $b \leq 0.025$ lead to superharmonic resonance of second-order. Several papers used MMS or the ROM with more than one mode of vibration to simulate the behavior of these systems, whether they were cantilevers (Caruntu et al, 2021, 2019, 2013; Liu et al, 2014; Kahrobaiyan et al, 2011; Najari et al, 2010), carbon nanotubes (Caruntu and Juarez, 2019; Caruntu and Luo, 2014; Kim and Lee, 2015), or plates (Caruntu and Oyervides, 2017, 2016; Sharafkhani et al, 2012; Batra et al, 2008). Most of the literature, except for (Kim and Lee, 2015; Liu et al, 2014), model electrostatic actuation with both *DC* and *AC*. Yet, these exceptions do not consider an MMS model for hard excitation for circular plates.

4.2 Differential Equation of Motion

Figure 4.1 shows an M/NEMS circular plate, which is parallel to a ground plate at a gap distance d . The radius and thickness of the plate are R and h , respectively. Between the M/NEMS circular plate and the ground plate there is an AC voltage of amplitude V_0 of frequency $\hat{\Omega}$. The AC voltage produces an electrostatic force between the circular plate and the ground plate, which leads to the circular plate into vibrations with the dimensional deflections $\hat{u}(\hat{r}, \hat{t})$, where \hat{r} , \hat{t} are the dimensional current radius and dimensional time, respectively. This work considers only axisymmetrical vibrations. The partial differential equation of motion describing the clamped circular plate (Caruntu and Oyervides, 2017, 2016), Fig. 4.1, is based on Kirchoff plate theory (classical plate theory) valid for thin plates (Rahim, 2010b; Lee et al, 1998; Baecker et al, 2015), i.e. thickness to diameter radius ratio less than 0.05 (Zietlow et al, 2012), and it includes Casimir and van der Waals forces:

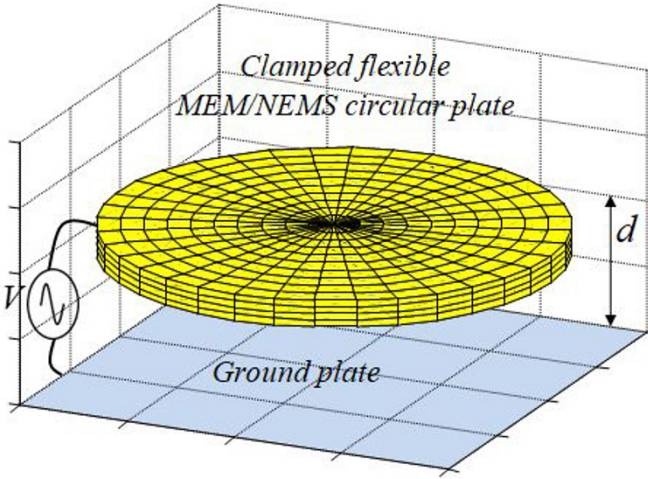


Fig. 4.1 Circular plate suspended above ground plate

$$\rho h \frac{\partial^2 \hat{u}(\hat{t}, \hat{r})}{\partial \hat{t}^2} + 2c_1 \frac{\partial \hat{u}(\hat{t}, \hat{r})}{\partial \hat{t}} + D \left[\frac{\partial^4 \hat{u}(\hat{t}, \hat{r})}{\partial \hat{r}^4} + \frac{2}{\hat{r}} \frac{\partial^3 \hat{u}(\hat{t}, \hat{r})}{\partial \hat{r}^3} - \frac{1}{\hat{r}^2} \frac{\partial^2 \hat{u}(\hat{t}, \hat{r})}{\partial \hat{r}^2} + \frac{1}{\hat{r}^3} \frac{\partial \hat{u}(\hat{t}, \hat{r})}{\partial \hat{r}} \right] = \frac{\epsilon^* V_0^2 \cos^2 \hat{\Omega} \hat{t}}{2[d - \hat{u}(\hat{t}, \hat{r})]^2} + \frac{H}{6\pi[d - \hat{u}(\hat{t}, \hat{r})]^3} + \frac{\hbar c \pi^2}{240[d - \hat{u}(\hat{t}, \hat{r})]^4}, \quad (4.1)$$

where ρ is plate density, c_1 damping coefficient, D flexural rigidity, ϵ^* electrical permittivity, V_0 magnitude of AC voltage, H Hamaker constant, \hbar reduced Plank constant, and c the speed of light in vacuum. The following dimensionless variable are introduced: dimensionless radial coordinate r , dimensionless deflection u and

dimensionless time t . They are written in terms of the dimensional variables \hat{r} , \hat{u} and \hat{t} (Caruntu and Oyervides, 2017, 2016) are as follows:

$$r = \frac{\hat{r}}{R}, \quad u = \frac{\hat{u}}{d}, \quad t = \hat{t} \sqrt{\frac{D}{\rho h R^4}}. \quad (4.2)$$

The dimensionless partial-differential equation of motion to include both intermolecular forces, Casimir and van der Waals, is given by

$$\frac{\partial^2 u(t, r)}{\partial t^2} + b \frac{\partial u(t, r)}{\partial t} + P[u] = \frac{\delta \cos^2 \Omega t}{[1 - u(t, r)]^2} + \frac{\mu}{[1 - u(t, r)]^3} + \frac{\alpha}{[1 - u(t, r)]^4}, \quad (4.3)$$

where μ and α cannot be different than zero at the same time since Casimir and van der Waals forces describe the same phenomenon but at different scales. Operator $P[u]$ is given by

$$P[u] = \frac{\partial^4 u(t, r)}{\partial r^4} + \frac{2}{r} \frac{\partial^3 u(t, r)}{\partial r^3} - \frac{1}{r^2} \frac{\partial^2 u(t, r)}{\partial r^2} + \frac{1}{r^3} \frac{\partial u(t, r)}{\partial r}. \quad (4.4)$$

The dimensionless parameters are as follows: Ω is the dimensionless AC frequency, b is dimensionless damping parameter, α is the dimensionless Casimir parameter, μ is the dimensionless van der Waals parameter, δ the dimensionless voltage parameter and ω_i are the dimensionless natural frequencies of clamped circular plates. These dimensionless parameters are as follows:

$$\Omega = \hat{\Omega} \sqrt{\frac{\rho h R^4}{D}}, \quad b = 2c_1 \sqrt{\frac{R^4}{\rho h D}}, \quad \delta = \frac{R^4 \epsilon^* V_0^2}{2Dd^3}, \quad \alpha = \frac{R^4 \hbar c \pi^2}{240Dd^5}, \quad (4.5)$$

$$\mu = \frac{R^4 H}{6\pi Dd^4}, \quad \omega_i = \hat{\omega}_i \sqrt{\frac{\rho h R^4}{D}}, \quad D = \frac{Eh^3}{12(1 - \nu^2)},$$

where E is the Young's modulus, ν is Poisson's ratio. Furthermore, $\hat{\omega}_i$ are the dimensional natural frequencies. The first six dimensionless natural frequencies of clamped circular plate are given in Table 4.1. The values of the constants of the

Table 4.1 First six natural frequencies

| | $i = 1$ | $i = 2$ | $i = 3$ | $i = 4$ | $i = 5$ | $i = 6$ |
|------------|---------|---------|---------|----------|----------|----------|
| ω_i | 10.2158 | 39.7711 | 89.1041 | 158.1842 | 247.0064 | 355.5693 |

system are given below in Table 4.2, and the dimensional system parameters are given in Tables 4.3, 4.4, and 4.5 for 3 cases, namely electrostatic, $\alpha = \mu = 0$, in Eq. (4.3), Casimir, $\mu = 0$; and van der Waals, $\alpha = 0$, respectively. The material properties are of polysilicon (Ouakad, 2017; Lee et al, 1998; Sharpe et al, 1997) and are in Table 4.2. The plate dimensions in Tables 4.3-4.5 satisfy criteria for thin

plates from the classical plate theory (Zietlow et al, 2012). Tables 4.2-4.5 result in the dimensionless system parameters shown in Table 4.6. The dimensionless mode

Table 4.2 Constants

| | | |
|----------------------------|--------------|---|
| Young's modulus | E | 169 GPa |
| Poisson's ratio | ν | 0.22 |
| Permittivity of free space | ϵ^* | $8.854 \times 10^{-12} \text{ C}^2/\text{N/m}^2$ |
| Density of material | ρ | 2330.0 kg/m ³ |
| Planck's constant / 2π | \hbar | $1.0546 \times 10^{-34} \text{ m}^2 \text{ kg/s}$ |
| Speed of light in vacuum | C | 299.972 km/s |
| Hamaker constant | H | $4.4 \times 10^{-19} \text{ J}$ |

Table 4.3 Dimensional parameters, electrostatic case MEMS

| | | |
|----------------------|-------|--------------------------|
| Initial gap distance | d | 1.014 μm |
| Plate thickness | h | 3.01 μm |
| Radius of plate | R | 250 μm |
| Damping | c_1 | 10.64 N s/m ³ |
| Voltage | V_0 | 9.865 V |

Table 4.4 Dimensional parameters, Casimir case NEMS

| | | |
|----------------------|-------|---------------------------|
| Initial gap distance | d | 0.15 μm |
| Plate thickness | h | 0.4 μm |
| Radius of plate | R | 57.675 μm |
| Damping | c_1 | 3.5307 N s/m ³ |
| Voltage | V_0 | 0.5109 V |

Table 4.5 Dimensional parameters, van der Waals case NEMS

| | | |
|----------------------|-------|---------------------------|
| Initial gap distance | d | 0.05 μm |
| Plate Thickness | h | 0.0301 μm |
| Radius of Plate | R | 2.1561 μm |
| Damping | c_1 | 14.305 N s/m ³ |
| Voltage | V_0 | 1.4522 V |

Table 4.6 Dimensionless system parameters

| | | |
|-------------------------|----------|-------|
| Voltage Parameter | δ | 4.0 |
| Damping Parameter | b^* | 0.025 |
| Casimir Parameter | α | 0.2 |
| van der Waals parameter | μ | 0.2 |

shapes ϕ_i of the clamped circular plates are given in terms of J_0 and I_0 which are Bessel functions of first kind and modified first kind, respectively, as follows:

$$\phi_i(r) = \frac{J_0(\sqrt{\omega_i} \cdot r)}{J_0(\sqrt{\omega_i})} - \frac{I_0(\sqrt{\omega_i} \cdot r)}{I_0(\sqrt{\omega_i})} \quad (4.6)$$

The dimensionless mode shapes form an orthonormal set. The relationship between the mode shapes ϕ_1 and the natural frequency (Rao, 2007) is given by

$$\phi_i^{(4)} + \frac{2}{r} \phi_i''' - \frac{1}{r^2} \phi_i'' + \frac{1}{r^3} \phi_i' = \omega_i^2 \phi_i \quad (4.7)$$

4.3 Superharmonic Resonance of Second-Order

The dimensionless frequency Ω of the AC voltage, that produces electrostatic force, is considered to be nearly one fourth of the natural frequency

$$\Omega = \frac{\omega_1}{4} + \epsilon\sigma \quad (4.8)$$

where σ is the detuning parameter, and ϵ a bookkeeping parameter used in MMS. The bookkeeping parameter ϵ is assumed to be small such that it indicates a small detuning parameter in Eq. (4.8), and indicates the small terms in the equations of motion of Sections 4.4 and 4.6. The dimensionless voltage V , Eq. (4.3), is given by

$$V = \sqrt{\delta} \cos \Omega t \quad (4.9)$$

As the electrostatic force is proportional to the square of the voltage, the frequency of the electrostatic force is twice the AC frequency. This leads to superharmonic resonance of the second-order. The square of the dimensionless voltage is as follows:

$$V^2 = \delta \cos^2 \Omega t = \delta \frac{1 + \cos 2\Omega t}{2} = \delta \left(\frac{1}{2} + \frac{e^{2i\Omega t} + e^{-2i\Omega t}}{4} \right) \quad (4.10)$$

4.4 Method of Multiple Scales: First-Order Hard Excitations Model

All forces at the right-hand side of Eq. (4.3), are approximated by Taylor polynomials. In the first-order hard excitations model, the first term of the Taylor polynomial of the electrostatic force on the right-hand side of the equation is being treated as significant so it does not have the bookkeeping parameter ϵ as coefficient. All other terms of the Taylor polynomial of the electrostatic force, the Taylor polynomials of Casimir and/or van der Waals forces, as well as the damping force, are considered small, so all these terms have the bookkeeping parameter ϵ as coefficient as follows:

$$\begin{aligned} \frac{\partial^2 u}{\partial t^2} + \epsilon b \frac{\partial u}{\partial t} + P[u] = & \delta \frac{1 + \cos 2\Omega t}{2} + \epsilon \delta (2u + 3u^2 + 4u^3) \frac{1 + \cos 2\Omega t}{2} \\ & + \epsilon \mu (1 + 3u + 6u^2 + 10u^3) + \epsilon \alpha (1 + 4u + 10u^2 + 20u^3), \end{aligned} \quad (4.11)$$

where $P[u]$ is given by Eq. (4.4). The first-order hard excitations model is also called one term no epsilon (1TnE) model in this work. The solution of Eq. (4.11) uses the first mode of vibration that is given by

$$u(t,r) = u_1(t)\phi_1(r), \quad (4.12)$$

where $u_1(t)$ is a function of time to be determined and $\phi_1(r)$ is the first modeshape of the clamped circular plate. Assume a uniform expansion (Caruntu et al, 2021) of $u_1(t)$ as follows:

$$u_1(t) = u_{10}(t) + \epsilon u_{11}(t). \quad (4.13)$$

Two time scales are considered, a fast time scale $T_0 = t$ and a slow time scale $T_1 = \epsilon \cdot t$. The partial derivatives with respect to the time scales are given by

$$D_0 = \frac{\partial}{\partial T_0}, \quad D_1 = \frac{\partial}{\partial T_1} \quad (4.14)$$

and the time derivatives become

$$\frac{\partial}{\partial t} = D_0 + \epsilon D_1, \quad \frac{\partial^2}{\partial t^2} = D_0^2 + 2\epsilon D_1 D_0. \quad (4.15)$$

Substituting Eqs. (4.12)-(4.15) into Eq. (4.11), using Galerkin method by multiplying the resulting equation by $r\phi_1$ and integrating from 0 to 1, introducing the following notations

$$g_1 = \int_0^1 r\phi_1 dr, g_2 = \int_0^1 r\phi_1^2 dr, g_3 = \int_0^1 r\phi_1^3 dr, g_4 = \int_0^1 r\phi_1^4 dr \quad (4.16)$$

and then collecting the terms having the same power of ϵ , a zero-order problem and a first-order problem result as follows:

$$\epsilon^0 : D_0^2 u_{10} + u_{10} \omega_1^2 = g_1 \delta \left(\frac{1}{2} + \frac{e^{2i\Omega T_0} + e^{-2i\Omega T_0}}{4} \right) \quad (4.17)$$

$$\begin{aligned} \epsilon^1 : D_0^2 u_{11} + u_{11} \omega_1^2 = & -2D_0 D_1 u_{10} - b D_0 u_{10} + \delta(2u_{10} + 3u_{10}^2 g_3 \\ & + 4u_{10}^3 g_4) \left(\frac{1}{2} + \frac{e^{2i\Omega T_0} + e^{-2i\Omega T_0}}{4} \right) + \mu(g_1 + 3u_{10} + 6u_{10}^2 g_3 + 10u_{10}^3 g_4) \\ & + \alpha(g_1 + 4u_{10} + 10u_{10}^2 g_3 + 20u_{10}^3 g_4) \end{aligned} \quad (4.18)$$

It should be noted that $g_2 = 1$. The zero-order problem Eq. (4.17) has the following solution

$$u_{10} = A e^{i\omega_1 T_0} + \bar{A} e^{-i\omega_1 T_0} + \Lambda e^{2i\Omega T_0} + \Lambda e^{-2i\Omega T_0} + K, \quad (4.19)$$

where Λ and K are given by

$$\Lambda = \frac{\delta}{4} \frac{g_1}{(\omega_1^2 - 4\Omega^2)}, \quad K = \frac{\delta g_1}{2\omega_1^2}. \quad (4.20)$$

After substituting Eq. (4.19) into Eq. (4.18), the secular terms are collected and their sum is set to zero. The complex amplitude A and its conjugate \bar{A} , written in terms

of the real phase β_1 and real amplitude a_1 are as follows:

$$A = \frac{1}{2}a_1 e^{i\beta_1}, \quad \bar{A} = \frac{1}{2}a_1 e^{-i\beta_1}. \quad (4.21)$$

Substituting Eq. (4.21) into the secular terms equation, dividing the resulting equation by $e^{i\beta_1}$, and separating the real and imaginary parts, the following amplitude-phase differential equations result

$$a_1' = -\frac{b}{2}a_1 + \frac{\Lambda \sin \gamma}{2\omega_1} \left\{ \delta + g_3 [3\delta(\Lambda + K) + 4\Lambda(3\mu + 5\alpha)] \right. \\ \left. + g_4 [\delta(12K\Lambda + 8\Lambda^2 + 6K^2 + \frac{3}{2}a_1^2) + 60K\Lambda(\mu + 2\alpha)] \right\}, \quad (4.22)$$

$$\gamma' = 4\sigma + \frac{1}{2\omega_1} [\delta + 3\mu + 4\alpha] + \frac{\delta}{2a_1\omega_1} \Lambda \cos \gamma \\ + \frac{1}{a_1\omega_1} \left\{ g_3 \left[\frac{3}{2}\delta(K + \Lambda)(a_1 + \Lambda \cos \gamma) + 2(3\mu + 5\alpha)(\Lambda^2 \cos \gamma + a_1 K) \right] \right. \\ \left. + g_4 \left[3\delta(K^2 a_1 + 2K\Lambda a_1 + 2\Lambda^2 a_1 + \frac{1}{4}a_1^3 + \Lambda(2K\Lambda + \frac{4}{3}\Lambda^2 + K^2 \right. \right. \\ \left. \left. + \frac{3}{4}a_1^2) \cos \gamma) + 15(\mu + 2\alpha)(2K\Lambda^2 \cos \gamma + a_1 K^2 + 2a_1 \Lambda^2 + \frac{1}{4}a_1^3) \right] \right\}, \quad (4.23)$$

where ' is the derivative with respect to the slow scale T_1 , and γ is given by

$$\gamma = 4\sigma T_1 - \beta_1. \quad (4.24)$$

In order to find the steady-state amplitudes, the derivatives of the amplitude a_1 and phase γ are set to zero ($a_1' = \gamma' = 0$). The resulting equations predicting the amplitude-frequency response are

$$\sigma = \frac{-1}{4a_1\omega_1} (A_1 a_1^3 + B_1 a_1^2 + C_1 a_1 + D_1), \quad (4.25)$$

where

$$A_1 = \frac{3}{4}g_4(\delta + 5\mu + 10\alpha) \\ B_1 = \frac{9}{4}\delta g_4 \Lambda \cos \gamma \\ C_1 = \frac{\delta}{2} + \frac{3}{2}\mu + 2\alpha + g_3 \left[\frac{3}{2}\delta(\Lambda + K) + 2K(3\mu + 5\alpha) \right] \\ + g_4 [3\delta(K^2 + 2\Lambda^2 + 2K\Lambda) + 15(\mu + 2\alpha)(K^2 + 2\Lambda^2)] \\ D_1 = \Lambda \cos \gamma \left\{ \frac{1}{2}\delta + g_3 \left[\frac{3}{2}\delta(\Lambda + K) + 2\Lambda(3\mu + 5\alpha) \right] \right. \\ \left. + g_4 [\delta(3K^2 + 4\Lambda^2 + 6K\Lambda) + 30K\Lambda(\mu + 2\alpha)] \right\} \quad (4.26)$$

and

$$a_1 = \frac{-B_2 \pm \sqrt{B_2^2 - 4A_2C_2}}{2A_2}, \quad (4.27)$$

where

$$\begin{aligned} A_2 &= \frac{3\delta g_4 \Lambda}{4\omega_1} \sin \gamma \\ B_2 &= \frac{-b}{2} \\ C_2 &= \frac{\Lambda \sin \gamma}{\omega_1} \left\{ \frac{1}{2} \delta + g_3 \left[\frac{3}{2} \delta (\Lambda + K) + 2\Lambda (3\mu + 5\alpha) \right] \right. \\ &\quad \left. + g_4 [\delta (3K^2 + 4\Lambda^2 + 6K\Lambda) + 30\Lambda K (\mu + 2\alpha)] \right\}. \end{aligned} \quad (4.28)$$

4.5 Stability Testing

In order to test the stability of the steady-state solutions of the system of equations (4.22 , 4.23) of the 1TnE electrostatic MMS model, the Jacobian

$$J = \begin{bmatrix} \frac{\partial a_1'}{\partial a_1} & \frac{\partial a_1'}{\partial \gamma} \\ \frac{\partial \gamma'}{\partial a_1} & \frac{\partial \gamma'}{\partial \gamma} \end{bmatrix} = \begin{bmatrix} V_1 & V_2 \\ V_3 & V_4 \end{bmatrix} \quad (4.29)$$

is needed. The eigenvalues of the Jacobian are given by

$$\det \begin{bmatrix} V_1 - \lambda & V_2 \\ V_3 & V_4 - \lambda \end{bmatrix} = 0, \quad (4.30)$$

where

$$\begin{aligned} V_1 &= \frac{1}{2\omega_1} \left(-b\omega_1 + 3\delta g_4 a_1 \Lambda \sin \gamma \right), \\ V_2 &= \frac{\Lambda \cos \gamma}{2g_2 \omega_1} \left[\delta g_2 + 3\delta g_3 (\Lambda + K) + \delta g_4 (12K\Lambda + 8\Lambda^2 + 6K^2 + \frac{9}{2}a_1^2) \right], \\ V_3 &= \frac{-\cos \gamma}{2a_1^2 \omega_1} \left[\delta \Lambda + 3\delta g_3 \Lambda (\Lambda + K) + g_4 (12K\Lambda^2 - \frac{3a_1^3}{\cos \gamma} + 8\Lambda^3 + 6K^2\Lambda \right. \\ &\quad \left. - \frac{9}{2}a_1^2 \Lambda) \right], \\ V_4 &= \frac{-\Lambda \sin \gamma}{2a_1^2 \omega_1} \left[\delta + 3\delta g_3 (\Lambda + K) + \delta g_4 (12K\Lambda + 8\Lambda^2 + 6K^2 + \frac{3}{2}a_1^2) \right]. \end{aligned} \quad (4.31)$$

4.6 Method of Multiple Scales: Second-Order Hard Excitations Model

In the second-order hard excitations model, the first two terms of the Taylor polynomial of the electrostatic force are considered significant, so they do not have the bookkeeping parameter ϵ as coefficient

$$\begin{aligned} \frac{\partial^2 u}{\partial t^2} + \epsilon b \frac{\partial u}{\partial t} + P[u] &= \delta \frac{1 + \cos 2\Omega t}{2} \\ + 2\delta u \frac{1 + \epsilon \cos 2\Omega t}{2} + \epsilon \delta (3u^2 + 4u^3) \frac{1 + \cos 2\Omega t}{2} \\ + \epsilon \mu (1 + 3u + 6u^2 + 10u^3) + \epsilon \alpha (1 + 4u + 10u^2 + 20u^3) \end{aligned} \quad (4.32)$$

The second-order hard excitations model is also called two-term no epsilon (2TnE) model in this work, This model allows for a better approximation of the solution. Using Eqs. (4.12-4.16) and Eq. (4.7), the resulting zero-order and the first-order problems are as follows:

$$\epsilon^0 : D_0^2 u_{10} + u_{10} \bar{\omega}_1^2 = g_1 \delta \left(\frac{1}{2} + \frac{e^{2i\Omega T_0} + e^{-2i\Omega T_0}}{4} \right), \quad (4.33)$$

$$\begin{aligned} \epsilon^1 : D_0^2 u_{11} + u_{11} \bar{\omega}_1^2 &= -2D_0 D_1 u_{10} - b D_0 u_{10} + \delta u_{10} \frac{e^{2i\Omega T_0} + e^{-2i\Omega T_0}}{2} \\ + \delta (3u_{10}^2 g_3 + 4u_{10}^3 g_4) &\left(\frac{1}{2} + \frac{e^{2i\Omega T_0} + e^{-2i\Omega T_0}}{4} \right) \\ + \mu (g_1 + 3u_{10} + 6u_{10}^2 g_3 + 10u_{10}^3 g_4) &+ \alpha (g_1 + 4u_{10} + 10u_{10}^2 g_3 + 20u_{10}^3 g_4), \end{aligned} \quad (4.34)$$

where $\bar{\omega}_1^2$ is given by

$$\bar{\omega}_1^2 = \omega_1^2 - \delta. \quad (4.35)$$

The solution of the zero-order problem is as follows:

$$u_{10} = A e^{i\bar{\omega}_1 T_0} + \bar{A} e^{-i\bar{\omega}_1 T_0} + \Lambda e^{2i\Omega T_0} + \Lambda e^{-2i\Omega T_0} + K, \quad (4.36)$$

where Λ and K are defined as

$$\Lambda = \frac{\delta}{4} \frac{g_1}{(\bar{\omega}_1^2 - 4\Omega^2)}, \quad K = \frac{\delta g_1}{2\bar{\omega}_1^2}. \quad (4.37)$$

Equation (4.36) is then substituted into the first-order problem Eq. (4.34), and the resulting equation is then expanded. This allows the secular terms for this resonance case to be gathered and their sum set equal to zero. The complex amplitudes Eq. (4.21), are substituted into the resulting equation, which is then divided by $e^{i\beta_1}$. Eq. (4.24) is used in the resulting equation and its real and imaginary parts are separated resulting into the following amplitude-phase differential equations

$$a_1' = -\frac{b}{2}a_1 + \frac{\Lambda \sin \gamma}{2\bar{\omega}_1} \left\{ \delta + g_3 [3\delta(\Lambda + K) + 4\Lambda(3\mu + 5\alpha)] \right. \\ \left. + g_4 [\delta(12K\Lambda + 8\Lambda^2 + 6K^2 + \frac{3}{2}a_1^2) + 60K\Lambda(\mu + 2\alpha)] \right\}, \quad (4.38)$$

$$\gamma' = 4\sigma + \frac{1}{2\bar{\omega}_1} [3\mu + 4\alpha] + \frac{\delta}{2a_1\bar{\omega}_1} \Lambda \cos \gamma \\ + \frac{1}{a_1\bar{\omega}_1} \left\{ g_3 \left[\frac{3}{2}\delta(K + \Lambda)(a_1 + \Lambda \cos \gamma) + 2(3\mu + 5\alpha)(\Lambda^2 \cos \gamma + a_1 K) \right] \right. \\ \left. + g_4 \left[3\delta(K^2 a_1 + 2K\Lambda a_1 + 2\Lambda^2 a_1 + \frac{1}{4}a_1^3 + \Lambda(2K\Lambda + \frac{4}{3}\Lambda^2 + K^2 \right. \right. \\ \left. \left. + \frac{3}{4}a_1^2) \cos \gamma) + 15(\mu + 2\alpha)(2K\Lambda^2 \cos \gamma + a_1 K^2 + 2a_1 \Lambda^2 + \frac{1}{4}a_1^3) \right] \right\}. \quad (4.39)$$

After setting the derivatives equal to zero, one can solve for the steady-state solutions, $a_1' = \gamma' = 0$. The equations predicting the amplitude-frequency response are

$$\sigma = \frac{-1}{4a_1\bar{\omega}_1} (A_1 a_1^3 + B_1 a_1^2 + C_1 a_1 + D_1), \quad (4.40)$$

where

$$A_1 = \frac{3}{4}g_4(\delta + 5\mu + 10\alpha), \\ B_1 = \frac{9}{4}\delta g_4 \Lambda \cos \gamma, \\ C_1 = \frac{3}{2}\mu + 2\alpha + g_3 \left[\frac{3}{2}\delta(\Lambda + K) + 2K(3\mu + 5\alpha) \right] \\ + g_4 [3\delta(K^2 + 2\Lambda^2 + 2K\Lambda) + 15(\mu + 2\alpha)(K^2 + 2\Lambda^2)], \\ D_1 = \Lambda \cos \gamma \left\{ \frac{1}{2}\delta + g_3 \left[\frac{3}{2}\delta(\Lambda + K) + 2\Lambda(3\mu + 5\alpha) \right] \right. \\ \left. + g_4 [\delta(3K^2 + 4\Lambda^2 + 6K\Lambda) + 30K\Lambda(\mu + 2\alpha)] \right\}, \quad (4.41)$$

and

$$a_1 = \frac{-B_2 \pm \sqrt{B_2^2 - 4A_2 C_2}}{2A_2}, \quad (4.42)$$

where

$$\begin{aligned}
A_2 &= \frac{3\delta g_4 \Lambda}{4\bar{\omega}_1} \sin \gamma , \\
B_2 &= \frac{-b}{2} , \\
C_2 &= \frac{\Lambda \sin \gamma}{\bar{\omega}_1} \left\{ \frac{1}{2} \delta + g_3 \left[\frac{3}{2} \delta (\Lambda + K) + 2\Lambda (3\mu + 5\alpha) \right] \right. \\
&\quad \left. + g_4 \left[\delta (3K^2 + 4\Lambda^2 + 6K\Lambda) + 30\Lambda K (\mu + 2\alpha) \right] \right\} .
\end{aligned} \tag{4.43}$$

4.7 Electrostatic Reduced Order Model

This electrostatic ROM is valid for MEMS circular plates with the gap distance greater than one micron, $d > 10^{-6}$ m. ROM, if enough number of modes of vibration included, gives accurate results for both weak and strong nonlinearities. The electrostatic ROM includes only the electrostatic force, so no Casimir or van der Waals forces are present, see Eq. (4.3). Therefore the differential equation of motion Eq. (4.3), has the Casimir and van der Waals parameters α and μ set to zero. This equation is then multiplied by $(1 - u)^2$ in order to have no denominator in the differential equation. So Eq. (4.3) becomes

$$\ddot{u}(1 - 2u + u^2) + \dot{u}b(1 - 2u + u^2) + (1 - 2u + u^2)P[u] = \delta \cos^2 \Omega t , \tag{4.44}$$

where $P[u]$ is given by Eq. (4.4). The solution u , which describes the deflection of the plate, is written in terms of the first N dimensionless modeshapes of the circular plate as follows:

$$u(r, t) = \sum_{i=1}^N u_i(t) \phi_i(r) , \tag{4.45}$$

where $\phi_i(r)$ are the dimensionless modeshapes and $u_i(t)$ are time functions to be determined. Substituting Eqs. (4.45) and (4.7) into Eq. (4.44), it results

$$\begin{aligned}
&\sum_{i=1}^N \ddot{u}_i \left[\phi_i - 2 \sum_{j=1}^N u_j \phi_i \phi_j + \sum_{j,k=1}^N u_j u_k \phi_i \phi_j \phi_k \right] \\
&+ b \sum_{i=1}^N \dot{u}_i \left[\phi_i - 2 \sum_{j=1}^N u_j \phi_i \phi_j + \sum_{j,k=1}^N u_j u_k \phi_i \phi_j \phi_k \right] \\
&+ \sum_{i=1}^N u_i \omega_i^2 \left[\phi_i - 2 \sum_{j=1}^N u_j \phi_i \phi_j + \sum_{j,k=1}^N u_j u_k \phi_i \phi_j \phi_k \right] = \delta \cos^2 \Omega t ,
\end{aligned} \tag{4.46}$$

where N is the number of modes of vibration used in the ROM. Using Galerkin procedure, Eq. (4.46) is multiplied by r and ϕ_n and then integrated from 0 to 1, i.e.

Eq. (4.46) is transformed by the following operator

$$\int_0^1 \bullet r \phi_n(r) dr . \quad (4.47)$$

One should mention that $n = 1, 2, \dots, N$, so a system of N second-order differential equation is obtained, where the h -coefficients are given by Eq. (4.48). Since this work includes three ROMs, i.e. electrostatic ROM which includes only the electrostatic force but no Casimir and van der Waals, Casimir ROM which includes the electrostatic and Casimir forces, and van der Waals ROM which includes electrostatic and van der Waals forces, h -coefficients are given by Eq. (4.48) for all three cases. The electrostatic ROM only uses the first four, h_n, h_{ni}, h_{nij} , and $h_{nij k}$, the van der Waals ROM uses $h_n, h_{ni}, h_{nij}, h_{nij k}$, and $h_{nij kl}$, and the Casimir model uses $h_n, h_{ni}, h_{nij}, h_{nij k}, h_{nij kl}$, and $h_{nij klm}$,

$$\begin{aligned} h_n &= \int_0^1 r \phi_n dr , \quad h_{ni} = \int_0^1 r \phi_n \phi_i dr , \quad h_{nij} = \int_0^1 r \phi_n \phi_i \phi_j dr , \\ h_{nij k} &= \int_0^1 r \phi_n \phi_i \phi_j \phi_k dr , \quad h_{nij kl} = \int_0^1 r \phi_n \phi_i \phi_j \phi_k \phi_l dr , \\ h_{nij klm} &= \int_0^1 r \phi_n \phi_i \phi_j \phi_k \phi_l \phi_m dr . \end{aligned} \quad (4.48)$$

New variables y_k are introduced as follows:

$$y_{2k-1} = u_k, y_{2k} = \dot{u}_k, \dot{y}_{2k} = \ddot{u}_k, k = 1, 2 \dots N \quad (4.49)$$

With these new variables the system of N second-order differential equations is transformed into a system of $2N$ first-order differential equations given by

$$\begin{cases} \dot{y}_{2n-1} = y_{2n} \\ \sum_{i=1}^N \dot{y}_{2i} A_{ni} = -b \sum_{i=1}^N y_{2i} A_{ni} - \sum_{i=1}^N \omega_i^2 \cdot y_{2i-1} A_{ni} + \delta h_n \cos^2 \Omega t \end{cases} \quad (4.50)$$

where $n = 1, 2, \dots, N$ and A_{ni} are as follows

$$A_{ni} = h_{ni} - 2 \sum_{j=1}^N h_{nij} \cdot y_{2j-1} + \sum_{j,k=1}^N h_{nij k} \cdot y_{2j-1} \cdot y_{2k-1} . \quad (4.51)$$

In order to predict the amplitude-frequency response (bifurcation diagram) of the superharmonic resonance of second-order of the MEMS circular plate, the continuation and bifurcation method (AUTO 07p software package) is used to solve Eqs. (4.50). Also, same Eqs. (4.50) are numerically integrated using Matlab in order to predict time responses of the MEMS circular plate.

4.8 Casimir Reduced Order Model

Casimir ROM is valid for NEMS circular plates with the gap distance d less than one micron and greater than 100 nanometers, $100 \times 10^{-9}\text{m} < d < 10^{-6}\text{m}$. The governing equation of the Casimir ROM is given by

$$\ddot{u}(1 - 4u + 6u^2 - 4u^3 + u^4) + \dot{u}b(1 - 4u + 6u^2 - 4u^3 + u^4) + (1 - 4u + 6u^2 - 4u^3 + u^4)P[u] = (1 - 2u + u^2)\delta \cos^2 \Omega t + \alpha, \quad (4.52)$$

where Eq. (4.3) was multiplied by $(1 - u)^4$. The van der Waals parameter was set to zero. $P[u]$ is given by Eq.(4.4). Substituting Eq. (4.45) and Eq. (4.7) into Eq.(4.52), it results

$$\begin{aligned} & \sum_{i=1}^N \ddot{u}_i \left[\phi_i - 4 \sum_{j=1}^N u_j \phi_i \phi_j + 6 \sum_{j,k=1}^N u_j u_k \phi_i \phi_j \phi_k \right. \\ & \left. - 4 \sum_{j,k,l=1}^N u_j u_k u_l \phi_i \phi_j \phi_k \phi_l + \sum_{j,k,l,m=1}^N u_j u_k u_l u_m \phi_i \phi_j \phi_k \phi_l \phi_m \right] \\ & + b \sum_{i=1}^N \dot{u}_i \left[\phi_i - 4 \sum_{j=1}^N u_j \phi_i \phi_j + 6 \sum_{j,k=1}^N u_j u_k \phi_i \phi_j \phi_k \right. \\ & \left. - 4 \sum_{j,k,l=1}^N u_j u_k u_l \phi_i \phi_j \phi_k \phi_l + \sum_{j,k,l,m=1}^N u_j u_k u_l u_m \phi_i \phi_j \phi_k \phi_l \phi_m \right] \\ & + \sum_{i=1}^N u_i \omega_i^2 \left[\phi_i - 4 \sum_{j=1}^N u_j \phi_i \phi_j + 6 \sum_{j,k=1}^N u_j u_k \phi_i \phi_j \phi_k \dots \right. \\ & \left. \dots - 4 \sum_{j,k,l=1}^N u_j u_k u_l \phi_i \phi_j \phi_k \phi_l + \sum_{j,k,l,m=1}^N u_j u_k u_l u_m \phi_i \phi_j \phi_k \phi_l \phi_m \right] \\ & = \delta \left[1 - 2 \sum_{i=1}^N u_i \phi_i + \sum_{i,j=1}^N u_i u_j \phi_i \phi_j \right] \cos^2 \Omega t + \alpha \end{aligned} \quad (4.53)$$

where N is the number of modes of vibration in the ROM. Multiplying Eq. (4.53) by Eq. (4.47) and using Eqs. (4.48) and (4.49) it results

$$\begin{cases} \dot{y}_{2n-1} = y_{2n} \\ \sum_{i=1}^N \dot{y}_{2i} B_{ni} = -b \sum_{i=1}^N y_{2i} B_{ni} - \sum_{i=1}^N \omega_i^2 \cdot y_{2i-1} B_{ni} \\ + \delta \left[h_n - 2 \sum_{i=1}^N h_{ni} \cdot y_{2i-1} + \sum_{i,j=1}^N h_{nij} \cdot y_{2i-1} \cdot y_{2j-1} \right] \cos^2 \Omega t + \alpha h_n \end{cases} \quad (4.54)$$

where $n = 1, 2, \dots, N$ and B_{ni} are as follows:

$$\begin{aligned} B_{ni} = & h_{ni} - 4 \sum_{j=1}^N h_{nij} \cdot y_{2j-1} + 6 \sum_{j,k=1}^N h_{nij k} \cdot y_{2j-1} \cdot y_{2k-1} \\ & - 4 \sum_{j,k,l=1}^N h_{nij kl} \cdot y_{2j-1} \cdot y_{2k-1} \cdot y_{2l-1} \\ & + \sum_{j,k,l,m=1}^N h_{nij klm} \cdot y_{2j-1} \cdot y_{2k-1} \cdot y_{2l-1} \cdot y_{2m-1} . \end{aligned} \quad (4.55)$$

The amplitude-frequency response of the superharmonic resonance of second-order is predicted using continuation and bifurcation (AUTO 07p software package) to solve Eqs. (4.54). Also, time responses are predicted through numerical integration of Eqs. (4.54) using Matlab.

4.9 Van der Waals Reduced Order Model

Van der Waals ROM is valid for NEMS circular plates with the gap distance d less than 50 nanometers, $d < 50 \times 10^{-9}$ m. The ROM takes into consideration the effect of van der Waals forces. Hence in Eq. (4.3) the Casimir parameter α is set to zero. Multiplying both sides by $(1 - u)^3$ as it is the largest denominator, and expanding, it results

$$\begin{aligned} & \ddot{u}(1 - 3u + 3u^2 - u^3) + \dot{u}b(1 - 3u + 3u^2 - u^3) + (1 - 3u + 3u^2 - u^3)P[u] \\ & = \delta(1 - u) \cos^2 \Omega t + \mu . \end{aligned} \quad (4.56)$$

Substituting Eq.(4.45) and Eq.(4.7) into Eq.(4.56), it results

$$\begin{aligned}
& \sum_{i=1}^N \ddot{u}_i \left[\phi_i - 3 \sum_{j=1}^N u_j \phi_i \phi_j + 3 \sum_{j,k=1}^N u_j u_k \phi_i \phi_j \phi_k - \sum_{j,k,l=1}^N u_j u_k u_l \phi_i \phi_j \phi_k \phi_l \right] \\
& + b \sum_{i=1}^N \dot{u}_i \left[\phi_i - 3 \sum_{j=1}^N u_j \phi_i \phi_j + 3 \sum_{j,k=1}^N u_j u_k \phi_i \phi_j \phi_k - \sum_{j,k,l=1}^N u_j u_k u_l \phi_i \phi_j \phi_k \phi_l \right] \\
& + \sum_{i=1}^N u_i \omega_i^2 \left[\phi_i - 3 \sum_{j=1}^N u_j \phi_i \phi_j + 3 \sum_{j,k=1}^N u_j u_k \phi_i \phi_j \phi_k - \sum_{j,k,l=1}^N u_j u_k u_l \phi_i \phi_j \phi_k \phi_l \right] \\
& = \delta \left[1 - \sum_{i=1}^N u_i \phi_i \right] \cos^2 \Omega t + \mu .
\end{aligned} \tag{4.57}$$

where N is the number of modes of vibration in the ROM. Multiplying (4.57) by Eq. (4.47), and using (4.48) and (4.49), it results

$$\begin{cases} \dot{y}_{2n-1} = y_{2n} \\ \sum_{i=1}^N \dot{y}_{2i} C_{ni} = -b \sum_{i=1}^N y_{2i} C_{ni} - \sum_{i=1}^N \omega_i^2 \cdot y_{2i-1} C_{ni} \\ + \delta \left[h_n - \sum_{i=1}^N h_{ni} \cdot y_{2i-1} \right] \cos^2 \Omega t + \mu h_n , \end{cases} \tag{4.58}$$

where $n = 1, 2, \dots, N$ and C_{ni} are given by

$$\begin{aligned}
C_{ni} &= h_{ni} - 3 \sum_{j=1}^N h_{nij} \cdot y_{2j-1} + 3 \sum_{j,k=1}^N h_{nij k} \cdot y_{2j-1} \cdot y_{2k-1} \\
&- \sum_{j,k,l=1}^N h_{nij kl} \cdot y_{2j-1} \cdot y_{2k-1} \cdot y_{2l-1} .
\end{aligned} \tag{4.59}$$

The system of $2N$ first-order differential equations is solved numerically using AUTO 07p for predicting the bifurcation diagram, and numerically integrated using Matlab's built-in solver *ode15s* for time responses.

4.10 Numerical Simulations

4.10.1 Electrostatic Model of Microelectromechanical Systems Clamped Circular Plates

Figure 4.2 shows the amplitude-frequency response in the case of MEMS, i.e. the gap distance, $d > 10^{-6}$ m. The horizontal axis represents the detuning frequency σ , where at $\sigma = 0$, the AC frequency is exactly one fourth of the first dimensionless natural frequency of the MEMS clamped circular plate. The vertical axis represents the dimensionless amplitude at the center of the plate U_{max} . The stable branches are denoted by solid lines, and the unstable branches by dashed lines. Figure 4.2 shows the predictions of three methods, 1) one term ROM of second-order model of hard excitations (2TnE), and 25th degree Taylor polynomial to approximate the electrostatic force, that was solved using MMS in order to predict the amplitude-frequency response, 2) a six term (6T) ROM numerically integrated using Matlab that predicted time responses, and 3) six term (6T) ROM solved using the continuation and bifurcation method (AUTO) that predicted the amplitude-frequency response. These methods predict the existence of saddle-node bifurcation point A . As the frequency is swept up, the 6T ROM AUTO predicts that the steady state amplitude increases along branch 1 until the system reaches point A , where it experiences a jump phenomenon, the amplitude jumping up from point A to branch 3. If the frequency continues to be swept up the steady-state amplitudes decreases along branch 3. If the frequency is swept down, the amplitude increases along branch 3 until it reaches point C . At this point the system loses stability and experiences pull-in, i.e., the dimensionless amplitude reaches the value of 1. In the case of constant frequency, and initial amplitude above branch 3, the amplitudes settle on the stable branch 3. For frequencies between σ_B and σ_C and initial amplitudes above branch 2, the MEMS circular plate experiences pull-in. For frequencies less than σ_B , regardless the value of the initial amplitude, the amplitudes settle on the stable branch 1. For any initial amplitude below branch 2, and for frequencies between σ_B and σ_A , the amplitudes settle on the stable branch 1. For any initial amplitude above branch 2, and frequencies greater than σ_C , the amplitudes settle on branch 3. One should mention that for zero initial amplitude and frequencies less than σ_A , the amplitudes settle on branch 1. Figures 4.3 and 4.4 show predicted time responses resulted from numerical integration of the 6T ROM. They are in agreement with the predictions resulted from continuation and bifurcation of 6T ROM AUTO. Figures 4.3a and 4.3c for $\sigma = -0.08$, and Figs. 4.4a and 4.4c for $\sigma = -0.12$, show time responses for initial amplitudes $U_0 = 0.4$ and $U_0 = 0.8$. One can notice that depending on the initial amplitude U_0 , the amplitude settles either on branch 3 or 1, which is in agreement with AUTO predictions. Figures 4.3b and 4.3d show time responses from zero initial amplitudes $U_0 = 0.0$ and frequencies greater than σ_A . The amplitudes settle on branch 3. Figures 4.4a and 4.4b do not contradict the existence of end points B and C . Figures 4.4b and 4.4d show time responses from high initial amplitudes $U_0 = 0.8$ and frequencies less than σ_B . For both time responses the amplitudes settle on

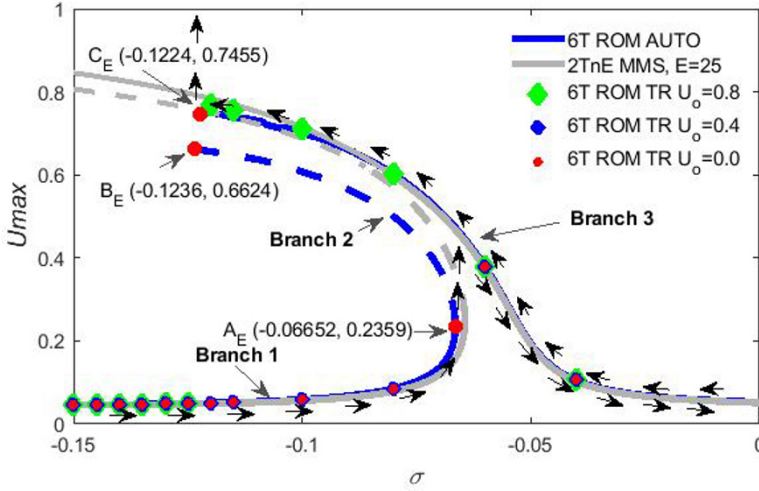


Fig. 4.2 Amplitude-frequency response using Electrostatic 6T ROM and Electrostatic 2TnE MMS $E = 25$, $\delta = 4$, $b = 0.025$, $\alpha = 0$, $\mu = 0$, where E is the degree of the electrostatic Taylor polynomial in MMS

branch 1. This is in agreement with 6T ROM AUTO predictions. Figure 4.5 shows the effect of increasing the number of modes of vibration (terms) in ROM. ROMs with two terms, three terms, four terms, five terms, and six terms are included. One can notice that there is no significant difference between ROMs with five terms, and six terms. This is the reason the 6T ROM is used in this research. Figure 4.6 illustrates the convergence of MMS predictions with respect to the degree E of the Taylor polynomial approximating the electrostatic force. The one term no epsilon model (1TnE) is also compared to the two term no epsilon model (2TnE). As the number of terms in the Taylor polynomial for the 2TnE model increases, the upper part of the branches moves to lower amplitudes, toward AUTO predictions. As mentioned before, MMS cannot predict the end points of the amplitude-frequency response. Additionally, MMS is limited to good results in lower amplitudes, amplitudes less than 0.2 of the gap. Overall, the change in lower amplitudes with increasing the degree of Taylor polynomial is not significant. A polynomial of degree 25 was deemed sufficient, as no significant changes in the predictions of 2TnE for degrees of Taylor polynomial great than $E = 25$ were observed. However, MMS is not reliable in predicting higher steady-state amplitudes.

Figure 4.7 shows the effect of voltage parameter on the amplitude-frequency response using two methods, 6T ROM AUTO and MMS 2TnE. For a smaller voltage of $\delta = 2$, both methods show only one branch with a relatively small peak amplitude and rather a linear behavior. MMS is in agreement with AUTO for amplitudes less than 0.2 of the gap, regardless of the voltage values. As the voltage increases from $\delta = 2$ to $\delta = 3$ the peak amplitude increases. As the voltage increases to $\delta = 4$ the three

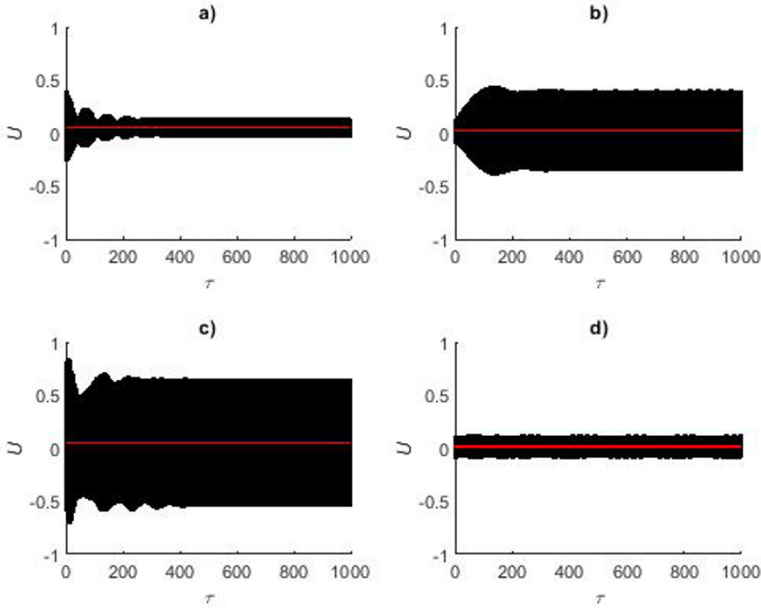


Fig. 4.3 Electrostatic 6T ROM Time Responses: $\delta = 4$, $b = 0.025$, $\alpha = 0$, $\mu = 0$: a) $U_0 = 0.4$, $\sigma = -0.08$, b) $U_0 = 0.0$, $\sigma = -0.06$, c) $U_0 = 0.8$, $\sigma = -0.08$, d) $U_0 = 0.0$, $\sigma = -0.04$

branches 1,2, and 3 are born showing a consistent nonlinear behavior. The existence of the unstable branch 2 explains the fact that for different initial amplitudes the system can settle to either a small amplitude on branch 1, or a larger amplitude on branch 3. Also in the case $\delta = 4$ branches 2 and 3 have end points predicting the existence of pull-in phenomenon for frequencies between σ_B and σ_C .

Figure 4.8 shows the effect of damping on the amplitude-frequency response. This effect is investigated at high voltage $\delta = 4$. In a similar fashion to the effect of the voltage on the amplitude-frequency response, MMS predictions are in agreement with 6T ROM AUTO for amplitudes lower than 0.2 of the gap. For damping parameter values $b = 0.035$ and $b = 0.025$, the difference between MMS and 6T ROM AUTO is quite significant in large amplitudes. Significant differences of the two methods, MMS and 6T ROM AUTO, are seen in the case of smaller damping $b = 0.025$. For higher damping $b = 0.045$, the peak amplitudes reduce, as well as the difference between MMS and 6T ROM AUTO.

Figure 4.9 shows the voltage bias using 6T ROM AUTO. This bias is directly related to Fig. 4.2. As shown in Fig. 4.9, the bias is at less than 5.5 % of the gap distance d . This suggests that the bias does not have a significant influence on the behavior of the system.

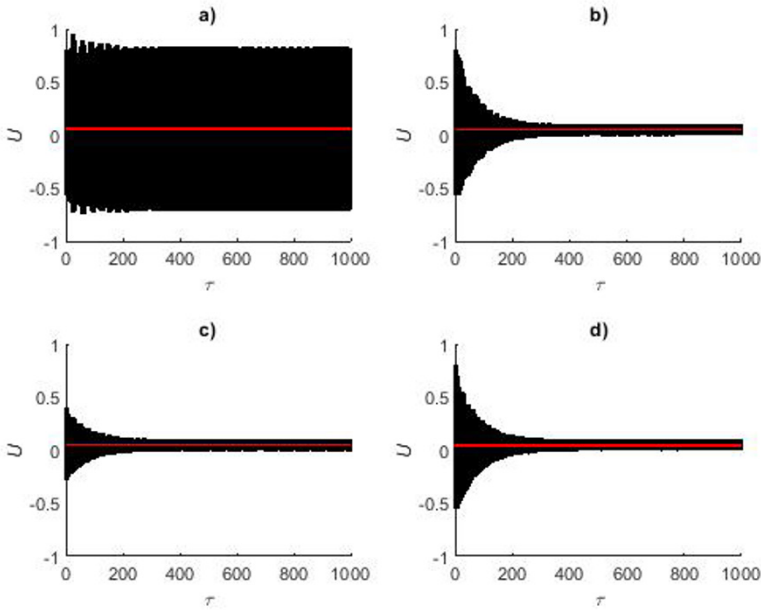


Fig. 4.4 Electrostatic 6T ROM Time Responses: $\delta = 4, b = 0.025, \alpha = 0, \mu = 0$: a) $U_0 = 0.8, \sigma = -0.12$, b) $U_0 = 0.8, \sigma = -0.125$, c) $U_0 = 0.4, \sigma = -0.12$, d) $U_0 = 0.8, \sigma = -0.15$

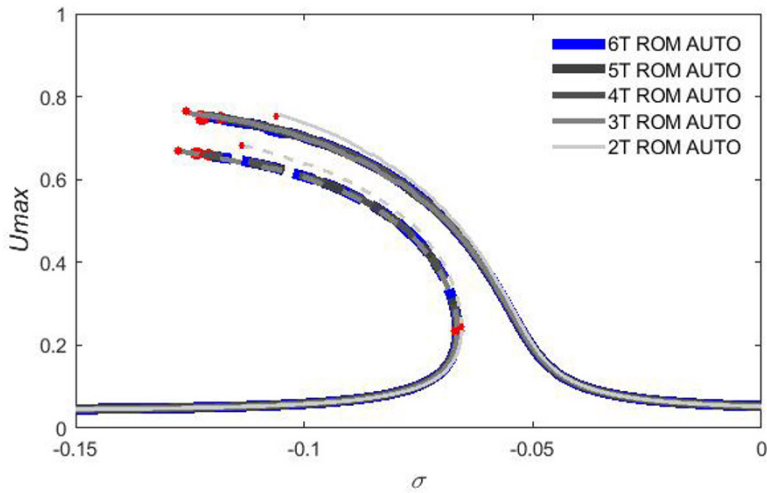


Fig. 4.5 Effect of the number of modes of vibration N in ROM on the amplitude-frequency response: $\delta = 4, b = 0.025, \alpha = 0, \mu = 0$

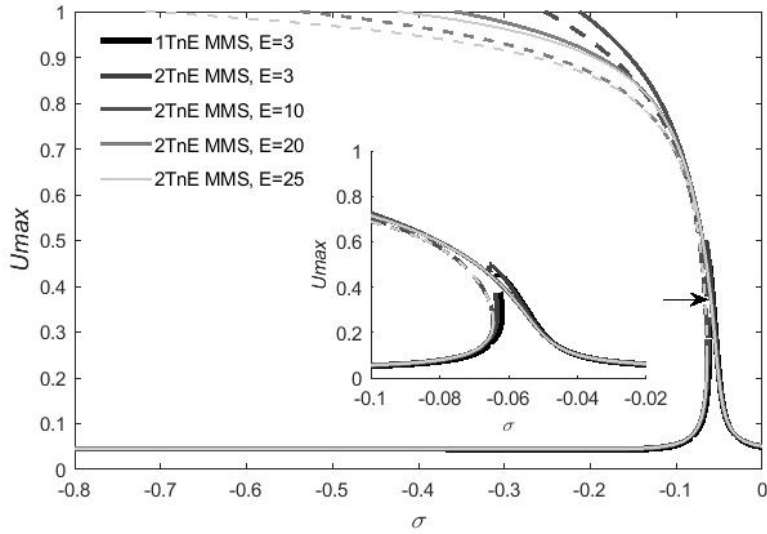


Fig. 4.6 Effect of E , the degree of the Taylor polynomial approximating the electrostatic force in MMS, on the amplitude-frequency responses $\delta = 4$, $b = 0.025$, $\alpha = 0$, $\mu = 0$

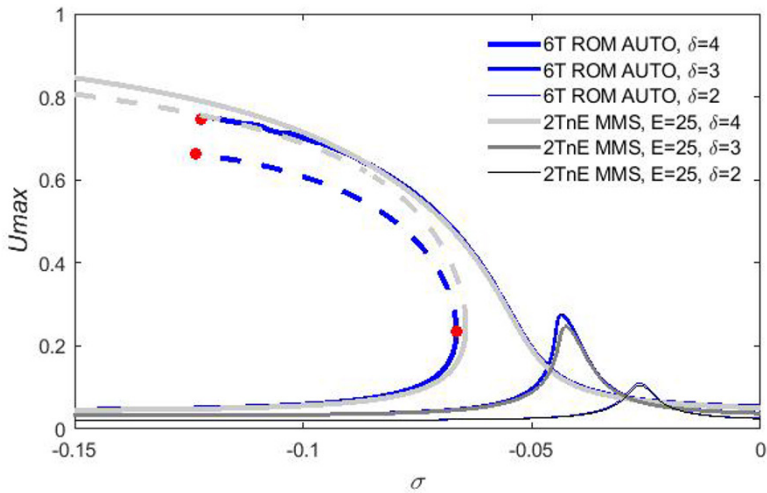


Fig. 4.7 Effect of δ , the dimensionless voltage parameter, on the amplitude-frequency response using electrostatic 6T ROM AUTO, and electrostatic 2TnE MMS polynomial of $E = 25$ degree: $b = 0.025$, $\alpha = 0$, $\mu = 0$

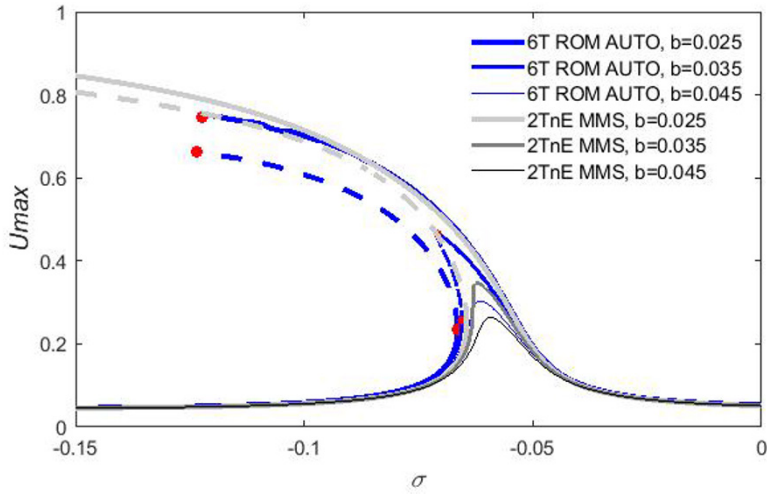


Fig. 4.8 Effect of b , the dimensionless damping parameter, on the amplitude-frequency response using Electrostatic 6T ROM AUTO and Electrostatic 2TnE MMS polynomial of $E = 25$ degree, $\delta = 4$, $\alpha = 0$, $\mu = 0$

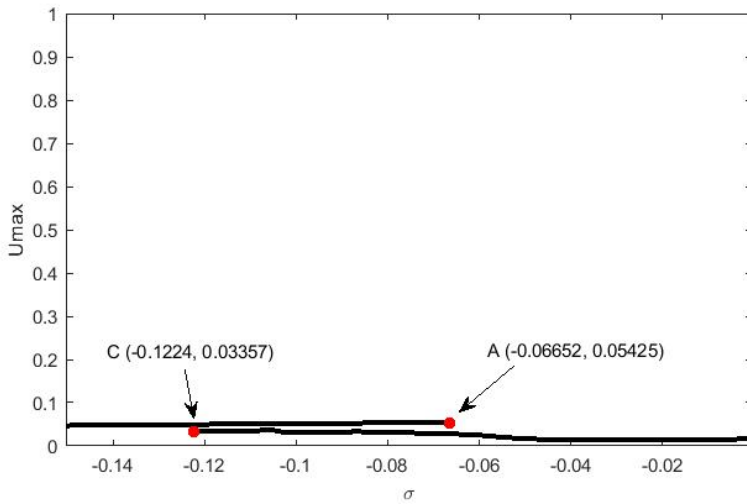


Fig. 4.9 Voltage Bias using 6T ROM AUTO, $\delta = 4$, $b = 0.025$

4.10.2 Casimir Force Effect on Nanoelectromechanical Systems Plates

Figure 4.10 shows the effect of the Casimir parameter α on the amplitude-frequency response. Increasing the Casimir parameter α leads to an increase of the softening effect, a decrease of the steady-state amplitudes for a given frequency σ in the resonance zone, and/or a shifting of the amplitude-frequency response to lower frequencies. MMS predictions are in agreement with 6T ROM AUTO for amplitudes less than 0.2 of the gap, if $\alpha = 0$, and amplitudes less than 0.1 of the gap if $\alpha = 0.2$. This is consistent with the fact that MMS is valid for weak nonlinearities and small amplitudes. The increase of the Casimir parameter shifts the bifurcation point A and the endpoints B and C to lower frequencies. The bifurcation point A is significantly shifted to lower frequencies. Figure 4.11 shows the amplitude-frequency response

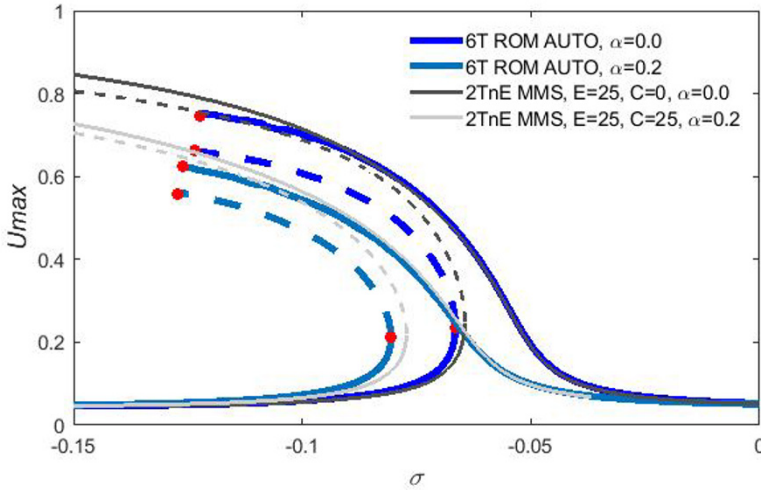


Fig. 4.10 Effect of α , the dimensionless Casimir parameter, on the amplitude-frequency response using electrostatic and Casimir 6T ROM AUTO and 2TnE MMS polynomials of 25th degree. $\delta = 4$, $b = 0.025$, $\mu = 0$, E is the degree of the electrostatic Taylor polynomial, C is the degree of the Casimir Taylor polynomial. It should be noted that if $\alpha = 0$, then the model used was the electrostatic model.

in the case of Casimir effect, $\alpha = 0.2$, using 6T ROM AUTO. Also time responses using 6T ROM are shown in Figs. 4.12 and 4.13. As one can see, the two methods are in agreement. Figure 4.12a shows a time response with an initial amplitude $U_0 = 0.2$ and detuning frequency $\sigma = -0.085$. This point is towards the left of bifurcation point A , and moves away from the unstable branch 2 towards the stable branch 1. Figure 4.12b shows a time response from $U_0 = 0.0$ and $\sigma = -0.08$ that settles on branch 3. This is not in disagreement with the existence of bifurcation point A . For

the same $\sigma = -0.085$ as Fig. 4.12a, the time response in Fig. 4.12c starts now from a $U_0 = 0.7$ and the amplitude settles on stable branch 3. Figure 4.12d shows a point in the lower amplitudes of branch 3. Figures 4.13a and 4.13c show time responses for a frequency $\sigma = -0.125$ and initial amplitudes, $U_0 = 0.7$ and $U_0 = 0.4$, respectively. The initial amplitude $U_0 = 0.4$ is below the unstable branch 2, so the amplitude settles on branch 1. In the case of $U_0 = 0.7$, which is above branch 3, the amplitude settles on branch 3. Figures 4.13b and 4.13d show time responses from initial amplitude, $U_0 = 0.7$ and frequencies $\sigma = -0.13$ and $\sigma = -0.15$, for which the amplitudes settle on branch 1. Figure 4.14 shows the effect of the degree

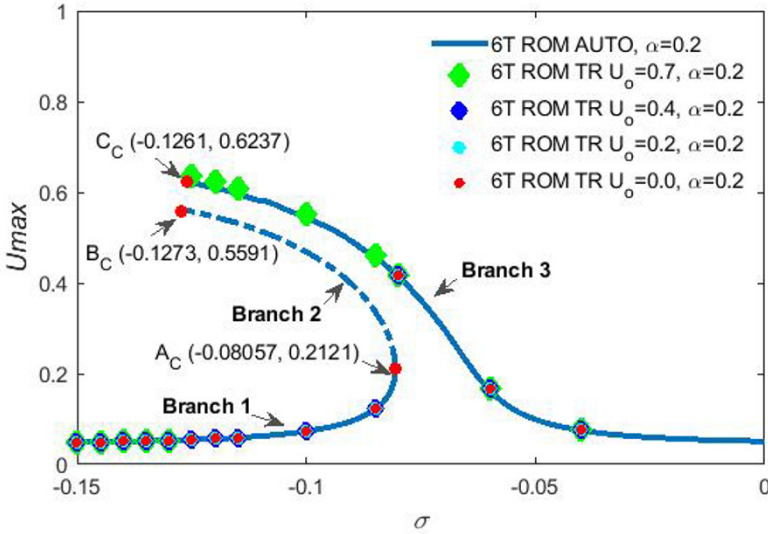


Fig. 4.11 Amplitude-frequency response using Casimir 6T ROM AUTO and Casimir 6T ROM Time Responses, $\delta = 4$, $b = 0.025$, $\alpha = 0.2$, $\mu = 0$

of Taylor polynomial approximating the Casimir force, E and C are the degrees of Taylor polynomials approximating the electrostatic and Casimir forces, respectively. The 2TnE model is also compared with the 1TnE model. The 2TnE predicts a stronger softening effect, which is more accurate. Furthermore, 1TnE MMS model does not predict the existence of the three branches in higher amplitudes. In order to see the effect of increasing the degree of the Casimir Taylor polynomial, the 2TnE model used a 25th degree electrostatic Taylor polynomial. Overall, increasing the degree of the Casimir Taylor polynomial shows a similar behavior to that of the electrostatic Taylor polynomial effect, in which the branches show a stronger softening effect. As there was no significant difference in the amplitude-frequency response between Casimir Taylor polynomials of 20th and 25th degree, the 25th degree Casimir Taylor polynomial was sufficient.

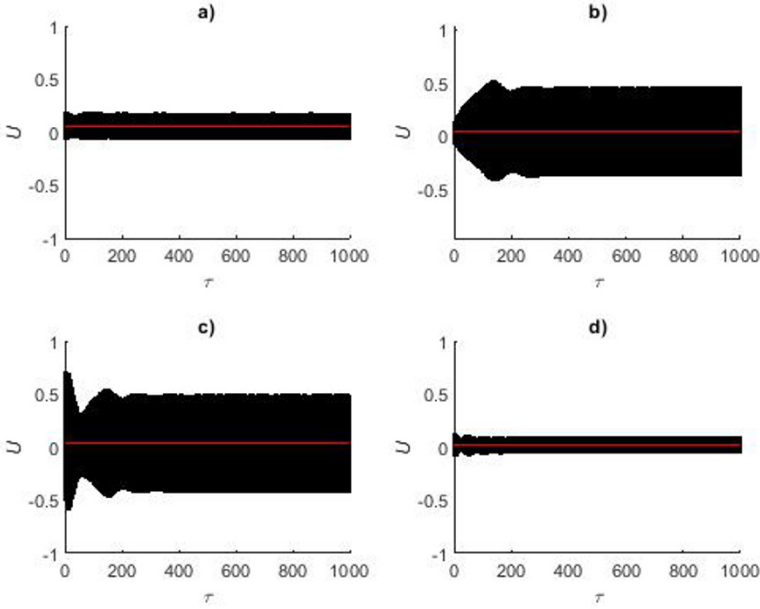


Fig. 4.12 Casimir 6T ROM Time Responses, $\delta = 4$, $b = 0.025$, $\alpha = 0.2$, $\mu = 0$: a) $U_0 = 0.2$, $\sigma = -0.085$, b) $U_0 = 0.0$, $\sigma = -0.08$, c) $U_0 = 0.7$, $\sigma = -0.085$, d) $U_0 = 0.0$, $\sigma = -0.04$

4.10.3 Van der Waals Force Effect on Nanoelectromechanical Systems Plates

Figure 4.15 shows the effect of the van der Waals parameter on the amplitude-frequency response using 6T ROM AUTO and 2TnE MMS. The van der Waals parameter effect on the amplitude-frequency response is similar to the effect of Casimir parameter, it causes a reduction of the higher amplitudes for both MMS and ROM predictions. Furthermore, it also causes a shifting of stable and unstable branches towards lower frequencies, which can also be seen in the case of saddle-node bifurcation point *A*. The lower amplitudes remain unaffected outside the resonance zone. Figure 4.16 shows the amplitude-frequency response to include van der Waals forces. Both 6T ROM AUTO and 6T ROM time responses are included. Time response with $U_0 = 0.25$ and $\sigma = -0.08$ settles to an amplitude on the stable branch 1, Fig. 4.17a. Time response with $U_0 = 0.0$ and $\sigma = -0.075$ settles to an amplitude on branch 3, Fig. 4.17b. Figure 4.17c shows a time response from higher initial amplitude $U_0 = 0.75$ and $\sigma = -0.08$, that settles to an amplitude on branch 3. Figure 4.17d shows a time response from $U_0 = 0.0$ and $\sigma = -0.04$, which settles to an amplitude on branch 3. Figures 4.18a and 4.18c show time responses at $\sigma = -0.12$ from different initial amplitudes. Figure 4.18a starts from $U_0 = 0.75$

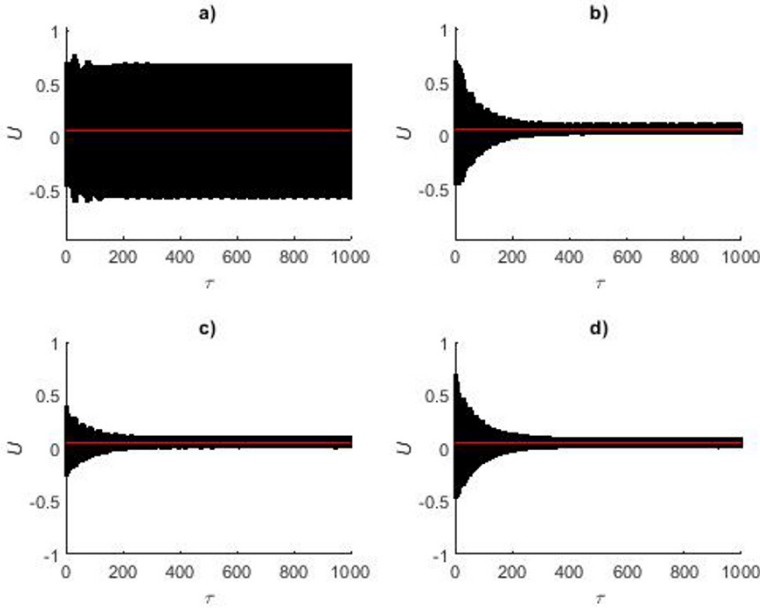


Fig. 4.13 Casimir 6T ROM Time Responses, $\delta = 4$, $b = 0.025$, $\alpha = 0.2$, $\mu = 0$: a) $U_0 = 0.7$, $\sigma = -0.125$, b) $U_0 = 0.7$, $\sigma = -0.13$, c) $U_0 = 0.4$, $\sigma = -0.125$, d) $U_0 = 0.7$, $\sigma = -0.15$

and settles on stable branch 3, while 4.18c starts at $U_0 = 0.25$ and settles on stable branch 1. Figure 4.18b shows a point from a higher initial amplitude $U_0 = 0.75$ and at a frequency $\sigma = -0.125$, which is lower than the end points B and C that settles to an amplitude on the stable branch 1. This is not in disagreement with the endpoints predicted by AUTO. Figure 4.18d shows behavior similar to that of Fig. 4.18b. Figure 4.19 shows the effect of the degree of the Taylor polynomial approximating the van der Waals force, where E and V are the degrees of the Taylor polynomials approximating the electrostatic force and the van der Waals force, respectively. As in the Casimir case and the Electrostatic case, the 2TnE model of the van der Waals case is more accurate than the 1TnE. Therefore the Taylor polynomials in the 2TnE model are used. The 1TnE MMS model also shows no splitting of the branches 2 and 3, unlike the 2TnE. As the degree of the Taylor polynomial increases, the 2TnE MMS model shows a behavior similar to that predicted by the 6T ROM AUTO. One can notice that there is no significant difference in predictions between $V = 20$ and $V = 25$. Therefore a van der Waals Taylor polynomial of 25th degree has been used.

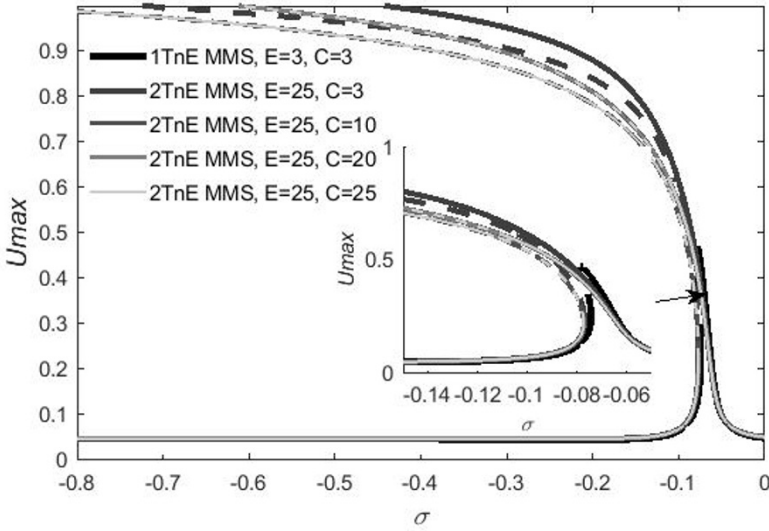


Fig. 4.14 Effect of C , the degree of the Taylor polynomial approximating the Casimir force in MMS, on the amplitude-frequency response using 1TnE MMS $E = 3$ and 2TnE MMS $E = 25$, $\delta = 4$, $b = 0.025$, $\alpha = 0.2$, $\mu = 0$, E is the degree of electrostatic Taylor polynomial, C is the degree of the Casimir Taylor polynomial

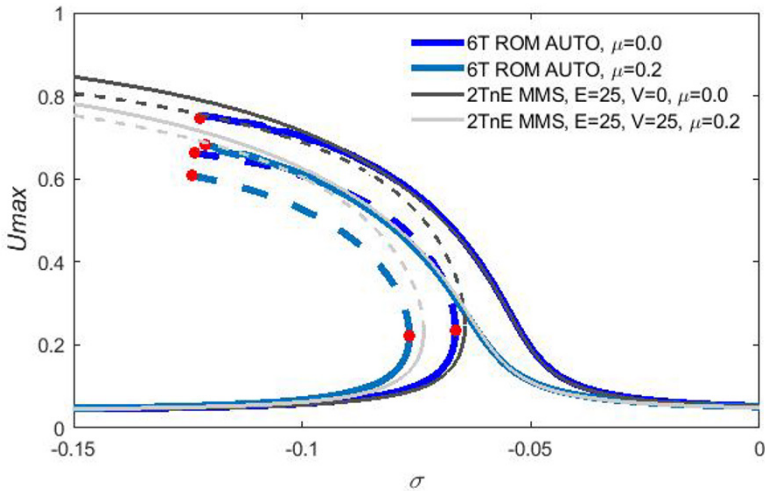


Fig. 4.15 Effect of μ , the dimensionless van der Waals parameter, on the amplitude-frequency response using electrostatic and van der Waals 6T ROM AUTO and 2TnE MMS polynomials of 25th degree, $\delta = 4$, $b = 0.025$, $\mu = 0$, E is the degree of electrostatic Taylor polynomial, V is the degree of the van der Waals Taylor polynomial. It should be noted that if $\mu = 0$, then the model used was the electrostatic model.

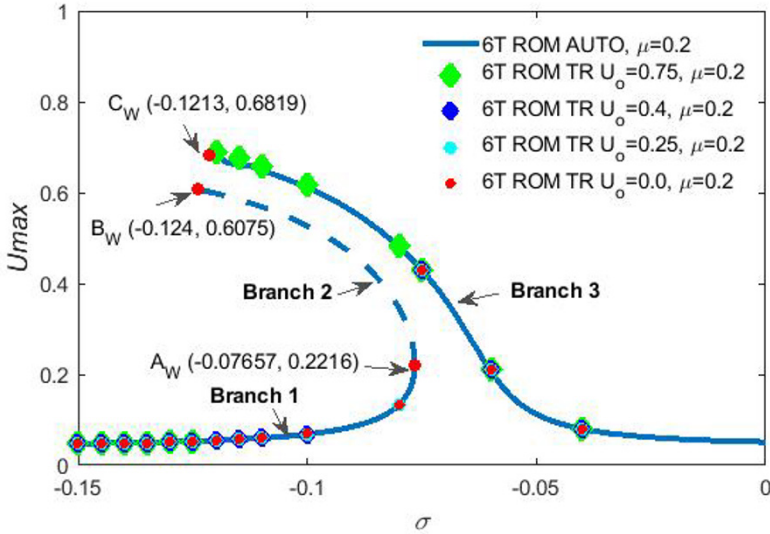


Fig. 4.16 Amplitude-frequency response using van der Waals 6T ROM AUTO and van der Waals 6T ROM Time response, $\delta = 4$, $b = 0.025$, $\alpha = 0$, $\mu = 0.2$

4.10.4 Stability

Figure 4.20 shows points of the amplitude-frequency response that have been tested for stability. The eigenvalues λ_1 and λ_2 of the Jacobian Eq. (4.30) are given in Table 4.7. One can notice that points *D*, *F* and *G* have complex eigenvalues with negative real parts which correspond to stable spiral points. Point *E* has two real eigenvalues, one positive and one negative, which corresponds to a saddle point, which is unstable. This does not contradict the stability of branches predicted by 6T ROM AUTO.

Table 4.7 Stability testing

| Point on Fig. 4.20 | a_0 | γ_0 | σ | λ_1, λ_2 |
|--------------------|---------|------------|----------|--------------------------------------|
| D | 0.00580 | 0.05 | -0.11763 | -0.01249+0.25708i, -0.01249-0.25708i |
| E | 0.08843 | 0.8 | 0.06196 | -0.07606, 0.05253 |
| F | 0.11703 | 2.0 | -0.05943 | -0.01127+0.09531i, -0.01127-0.09531i |
| G | 0.00482 | 3.1 | 0.01996 | -0.01249+0.30561i, -0.01249-0.30561i |

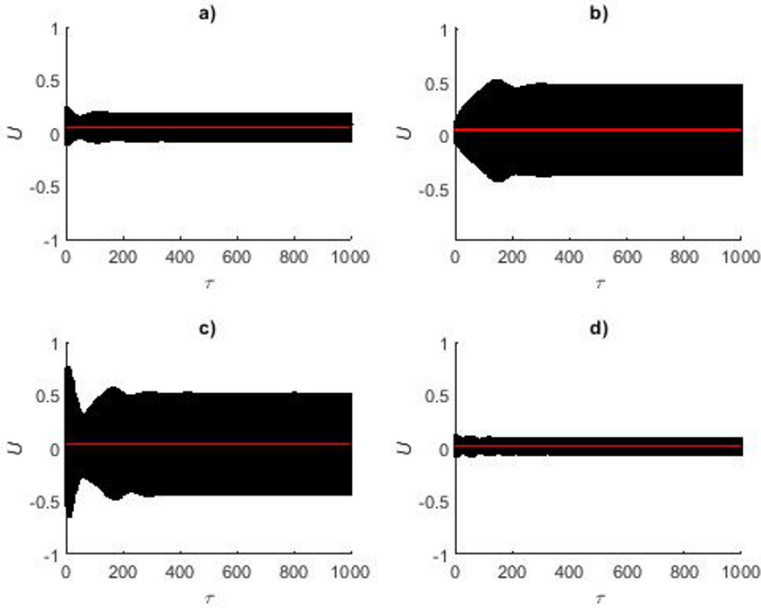


Fig. 4.17 van der Waals 6T ROM Time Responses, $\delta = 4$, $b = 0.025$, $\alpha = 0$, $\mu = 0.2$: a) $U_0 = 0.25$, $\sigma = -0.08$, b) $U_0 = 0.0$, $\sigma = -0.075$, c) $U_0 = 0.75$, $\sigma = -0.08$, d) $U_0 = 0.0$, $\sigma = -0.04$

4.11 Discussion and Conclusions

The novelty of this research consists of predicting the amplitude-frequency response of superharmonic resonance of second-order of electrostatically actuated clamped M/NEMS circular plates to include Casimir and van der Waals effects. Two MMS models of hard excitations have been proposed, and an investigation on the degree of Taylor polynomials approximating the electrostatic, Casimir, and van der Waals forces has been conducted. Several ROMs have been used in this work, and it has been concluded that the ROM using six modes of vibrations (6T) is the most viable method in all amplitudes, lower and higher. The 6T ROM has been solved using AUTO, a software package for continuation and bifurcation, and numerical integration Matlab for time responses. 6T ROM AUTO and 6T ROM time responses were in agreement.

Overall MMS is a fast and easy way to predict the frequency response of clamped circular plate resonators. MMS predicts the lower amplitudes quite well, as it matches those of the 6T ROM. Furthermore, for parameters in which MMS branches are split, the lack of endpoints B and C of branches 2 and 3 in the MMS model is a serious deficiency in predicting the occurrence of pull-in. Also MMS does not necessarily provide very accurate results in high amplitudes and definitely cannot predict B

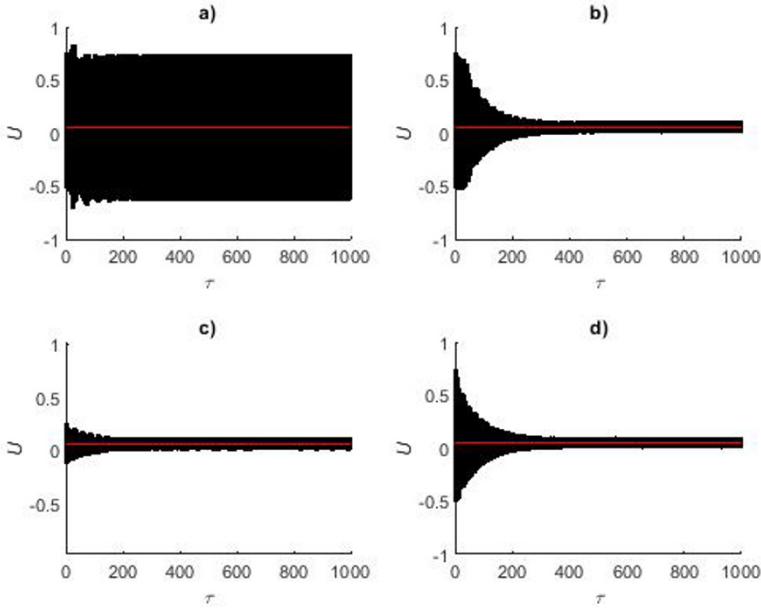


Fig. 4.18 van der Waals, 6T ROM Time Responses, $\delta = 4$, $b = 0.025$, $\alpha = 0$, $\mu = 0.2$: a) $U_0 = 0.75$, $\sigma = -0.12$, b) $U_0 = 0.75$, $\sigma = -0.125$, c) $U_0 = 0.25$, $\sigma = -0.12$, d) $U_0 = 0.75$, $\sigma = -0.15$

and C . However, MMS predicts the amplitude-frequency response quite well in the case of higher damping and/or low voltage. Secondary resonance superharmonic of second-order has been reported in the literature (Kim and Lee, 2015; Liu et al, 2014), for AC electrostatic actuation and for different structures than plates. Najar et al (2010); Kim and Lee (2015) have shown similar results, although for different structures and a hardening effect rather than softening effect as in this research.

In this paper two models for hard excitations were used for MMS, a one term no epsilon model (1TnE) and a two term no epsilon model (2TnE) for the electrostatic actuation. 2TnE was the most accurate of the two and it was used to investigate the effect of the degrees of the MMS Taylor polynomials approximating electrostatic, Casimir and van der Waals forces. This investigation showed that beyond the Taylor polynomial of 25th degree, there is no significant difference in the predictions. The ROM shows various benefits when compared to the MMS models. 6T ROM AUTO was able to predict the endpoints B and C , and the stable branches are in agreement with the predictions of time responses. Furthermore, the convergence of the ROM showed that 6T ROM was deemed sufficient for this research. These methods were used to investigate the effects influences of different parameters, such as voltage, and damping on the amplitude-frequency response. Increasing the voltage led to a stronger nonlinear behavior, such as the appearance of the unstable branch 2, when

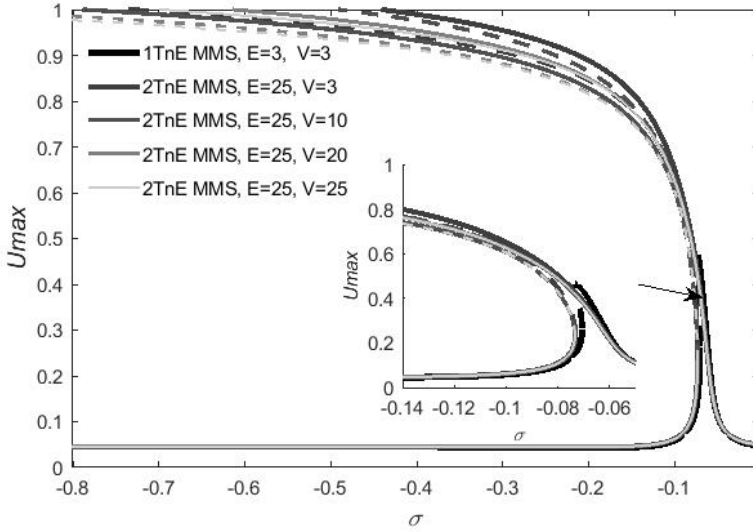


Fig. 4.19 Effect of V , the degree of the Taylor polynomial approximating the van der Waals force in MMS on the amplitude-frequency response using 1TnE MMS $E = 3$ and 2TnE MMS $E = 25$, $\delta = 4$, $b = 0.025$, $\alpha = 0$, $\mu = 0.2$, E is the degree of the electrostatic Taylor polynomial, V is the degree of the van der Waals Taylor polynomial.

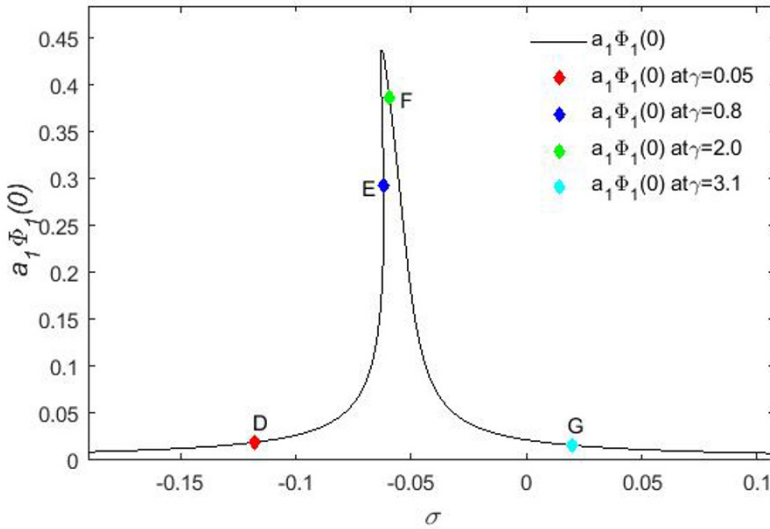


Fig. 4.20 Stability Testing, $\delta = 4$, $b = 0.025$, $\alpha = 0$, $\mu = 0.2$

the branches were split. Increasing damping led to a more linear behavior. The increase of the Casimir and the van der Waals parameters, led to an increase of the softening effect, and therefore a decrease of higher amplitudes. The lower amplitudes did not differ from the electrostatic models.

References

- Ahmad B, Pratap R (2010) Elasto-electrostatic analysis of circular microplates used in capacitive micromachined ultrasonic transducers. *IEEE Sensors Journal* 10(11):1767–1773
- Anjomshoa A, Tahani M (2016) Vibration analysis of orthotropic circular and elliptical nano-plates embedded in elastic medium based on nonlocal Mindlin plate theory and using Galerkin method. *Journal of Mechanical Science and Technology* 30(6):2463–2474
- Ashoori A, Vanini SS, Salari E (2017) Size-dependent axisymmetric vibration of functionally graded circular plates in bifurcation/limit point instability. *Applied Physics A* 123(4):1–14
- Baecker D, Kuna M, Haeusler C (2015) Eigenfunctions of crack problems in the Mindlin plate theory. *ZAMM-Journal of Applied Mathematics and Mechanics/Zeitschrift für Angewandte Mathematik und Mechanik* 95(8):765–777
- Batra R, Porfiri M, Spinello D (2008) Reduced-order models for microelectromechanical rectangular and circular plates incorporating the Casimir force. *International Journal of Solids and Structures* 45(11-12):3558–3583
- Caruntu DI, Juarez E (2019) Voltage effect on amplitude–frequency response of parametric resonance of electrostatically actuated double-walled carbon nanotube resonators. *Nonlinear Dynamics* 98(4):3095–3112
- Caruntu DI, Luo L (2014) Frequency response of primary resonance of electrostatically actuated CNT cantilevers. *Nonlinear Dynamics* 78(3):1827–1837
- Caruntu DI, Oyervides R (2016) Voltage response of primary resonance of electrostatically actuated MEMS clamped circular plate resonators. *Journal of Computational and Nonlinear Dynamics* 11(4):041,021
- Caruntu DI, Oyervides R (2017) Frequency response reduced order model of primary resonance of electrostatically actuated MEMS circular plate resonators. *Communications in Nonlinear Science and Numerical Simulation* 43:261–270
- Caruntu DI, Reyes CA (2020) Casimir Effect on Amplitude-Frequency Response of Parametric Resonance of Electrostatically Actuated NEMS Cantilever Resonators. In: *Developments and Novel Approaches in Biomechanics and Metamaterials*, Springer, pp 267–289
- Caruntu DI, Martinez I, Knecht MW (2013) ROM analysis of frequency response of AC near half natural frequency electrostatically actuated MEMS cantilevers. *Journal of Computational and Nonlinear Dynamics* 8(3):031,011
- Caruntu DI, Martinez I, Knecht MW (2016) Parametric resonance voltage response of electrostatically actuated Micro-Electro-Mechanical Systems cantilever resonators. *Journal of Sound and Vibration* 362:203–213
- Caruntu DI, Botello MA, Reyes CA, Beatriz JS (2019) Voltage–amplitude response of superharmonic resonance of second order of electrostatically actuated MEMS cantilever resonators. *Journal of Computational and Nonlinear Dynamics* 14(3):031,005
- Caruntu DI, Botello MA, Reyes CA, Beatriz JS (2021) Frequency-amplitude response of superharmonic resonance of second order of electrostatically actuated MEMS resonators. *International Journal of Non-Linear Mechanics* 133:10,371
- Dorfmeister M, Schneider M, Schmid U (2018) Static and dynamic performance of bistable MEMS membranes. *Sensors and Actuators A: Physical* 282(15):259–268
- Ishfaqe A, Kim B (2017) Analytical solution for squeeze film damping of MEMS perforated circular plates using Green’s function. *Nonlinear Dynamics* 87(3):1603–1616

- Kacem N, Baguet S, Hentz S, Dufour R (2012) Pull-in retarding in nonlinear nanoelectromechanical resonators under superharmonic excitation. *Journal of Computational and Nonlinear Dynamics* 7(2):021,011
- Kahrobaiyan MH, Asghari M, Hoore M, Ahmadian MT (2011) Nonlinear size-dependent forced vibrational behavior of microbeams based on a non-classical continuum theory. *Journal of Vibration and Control* 18(5):696–711
- Khadem S, Rasekh M, Toghraee A (2012) Design and simulation of a carbon nanotube-based adjustable nano-electromechanical shock switch. *Applied Mathematical Modelling* 36(6):2329–2339
- Kim I, Lee S (2015) Nonlinear resonances of a single-wall carbon nanotube cantilever. *Physica E: Low-dimensional Systems and Nanostructures* 67:159–167
- Lee S, Cho C, Kim J, Park S, Yi S, Kim J, Cho DiD (1998) The effects of post-deposition processes on polysilicon Young's modulus. *Journal of Micromechanics and Microengineering* 8(4):330–337
- Liao LD, Chao PC, Huang CW, Chiu CW (2009) DC dynamic and static pull-in predictions and analysis for electrostatically actuated clamped circular micro-plates based on a continuous model. *Journal of Micromechanics and Microengineering* 20(2):025,013
- Lin MX, Lee SY, et al (2018) Dynamic characteristic analysis of an electrostatically-actuated circular nanoplate subject to surface effects. *Applied Mathematical Modelling* 63:18–31
- Liu C, Yue S, Xu Y (2014) Nonlinear resonances of electrostatically actuated nano-beam. *Journal of Vibroengineering* 16(5):2484–2493
- Maurini C, Pouget J, dell'Isola F (2006) Extension of the Euler-Bernoulli model of piezoelectric laminates to include 3D effects via a mixed approach. *Computers & Structures* 84(22-23):1438–1458
- Najar F, Nayfeh A, Abdel-Rahman E, Choura S, El-Borgi S (2010) Nonlinear analysis of MEMS electrostatic microactuators: primary and secondary resonances of the first mode. *Journal of Vibration and Control* 16(9):1321–1349
- Nayfeh AH, Younis MI (2005) Dynamics of MEMS resonators under superharmonic and subharmonic excitations. *Journal of Micromechanics and Microengineering* 15(10):1840–1847
- Nisar A, Afzulpurkar N, Mahaisavariya B, Tuantranont A (2008) MEMS-based micropumps in drug delivery and biomedical applications. *Sensors and Actuators B: Chemical* 130(2):917–942
- Ouakad HM (2017) Comprehensive numerical modeling of the nonlinear structural behavior of MEMS/NEMS electrostatic actuators under the effect of the van der Waals forces. *Microsystem Technologies* 23(12):5903–5910
- Rahim FC (2010a) A numerical approach to investigate of pull-In phenomenon of circular micro plate subjected to nonlinear electrostatic pressure. *Sensors & Transducers* 117(6):41–49
- Rahim FC (2010b) Investigation Effect of Residual Stress on Pull-In Voltage of Circular Micro Plate Subjected to Nonlinear Electrostatic Force. *Sensors & Transducers* 123(12):25
- Rao SS (2007) *Vibration of Continuous Systems*: John Wiley & Sons. New Jersey
- Sajadi B, Alijani F, Goosen H, van Keulen F (2018) Effect of pressure on nonlinear dynamics and instability of electrically actuated circular micro-plates. *Nonlinear Dynamics* 91(4):2157–2170
- Shabani R, Sharafkhani N, Tariverdilo S, Rezazadeh G (2013) Dynamic analysis of an electrostatically actuated circular micro-plate interacting with compressible fluid. *Acta Mechanica* 224(9):2025–2035
- Sharafkhani N, Rezazadeh G, Shabani R (2012) Study of mechanical behavior of circular FGM micro-plates under nonlinear electrostatic and mechanical shock loadings. *Acta Mechanica* 223(3):579–591
- Sharpe WN, Yuan B, Vaidyanathan R, Edwards RL (1997) Measurements of Young's modulus, Poisson's ratio, and tensile strength of polysilicon. In: *Proceedings IEEE the Tenth Annual International Workshop on Micro Electro Mechanical Systems. An Investigation of Micro Structures, Sensors, Actuators, Machines and Robots, IEEE*, pp 424–429
- Varona J, Tecpoyotl-Torres M, Hamoui A (2007) Modeling of MEMS thermal actuation with external heat source. In: *Electronics, Robotics and Automotive Mechanics Conference (CERMA 2007), IEEE*, pp 591–596

- Wang YN, Fu LM (2018) Micropumps and biomedical applications—A review. *Microelectronic Engineering* 195:121–138
- Zhang Jh, Ma Sl, Qin Lf (2015) Analysis of frequency characteristics of MEMS piezoelectric cantilever beam based energy harvester. In: 2015 Symposium on Piezoelectricity, Acoustic Waves, and Device Applications (SPAWDA), IEEE, pp 193–197
- Zietlow DW, Griffin DC, Moore TR (2012) The limitations on applying classical thin plate theory to thin annular plates clamped on the inner boundary. *AIP Advances* 2(4):042,103



Chapter 5

Propagation of Chaos for a Stochastic Particle System Modelling Epidemics

Alessandro Ciallella, Mario Pulvirenti, Sergio Simonella

Abstract We consider a simple stochastic N -particle system, already studied by the same authors in Ciallella et al (2021b), representing different populations of agents. Each agent has a label describing his state of health. We show rigorously that, in the limit $N \rightarrow \infty$, propagation of chaos holds, leading to a set of kinetic equations which are a spatially inhomogeneous version of the classical SIR model. We improve a similar result obtained in Ciallella et al (2021b) by using here a different coupling technique, which makes the analysis simpler, more natural and transparent.

Keywords: Multi-agent stochastic systems · Epidemiological behavior · Propagation of chaos · Coupling

5.1 Introduction

We consider a stochastic particle system representing agents moving independently according to a random flight. Each agent may be susceptible, infected, or recovered

The original version of this chapter was revised: The authors names have been corrected in the xml file. The correction to this chapter is available at https://doi.org/10.1007/978-3-031-04548-6_33

A. Ciallella

Dipartimento di Ingegneria Civile, Edile – Architettura e Ambientale, Università dell’Aquila
International Research Center M&MOCS, Università dell’Aquila, via Giovanni Gronchi 18, 67100,
L’Aquila, Italy
e-mail: alessandro.ciallella@univaq.it

M. Pulvirenti

Dipartimento di Matematica, Università di Roma La Sapienza, Piazzale Aldo Moro 5, 00185 Rome,
Italy
International Research Center M&MOCS, Università dell’Aquila, Italy
Accademia Nazionale dei Lincei
e-mail: pulviren@mat.uniroma1.it

S. Simonella

UMPA UMR 5669 CNRS, ENS de Lyon, 46 allée d’Italie, 69364 Lyon Cedex 07, France
e-mail: sergio.simonella@ens-lyon.fr

© The Author(s), under exclusive license to Springer Nature Switzerland
AG 2022, corrected publication 2022

I. Giorgio et al. (eds.), *Theoretical Analyses, Computations,
and Experiments of Multiscale Materials*, Advanced Structured Materials 175,
https://doi.org/10.1007/978-3-031-04548-6_5

at the initial time. When an infected particle and a susceptible particle are sufficiently close, they may interact and become both infected. Each infected agent can recover independently of the others in a random time of fixed rate. As in the classical SIR model by Kermack and McKendrick (1927), recovered agents can no longer become susceptible or infected. However, at variance with the SIR model, we intend to allow spatially inhomogeneous distributions of the populations. A simple proposal for such a model has been given in Ciallella et al (2021b), which we reconsider in the present paper. Our purpose is not to provide realistic modelling of spatial patterns (even though this can be important in applications), but rather follow a natural approach, inspired by the kinetic theory of rarefied gases; see for instance Bellomo et al (2020); Albi et al (2021) and references therein. There is therefore no focus on identifying realistic interactions between agents. In particular, we shall neglect possible individual strategies, and assume a binary interaction. In spite of its simplicity, the kinetic model still provides a good description of the qualitative behaviour of SIR-like equations, because the essential aspects of the evolution are weakly dependent on the microscopic details (Pulvirenti and Simonella (2020); Ciallella et al (2021a,b)).

In this paper we show that, in the limit $N \rightarrow \infty$, the N -particle model introduced in Ciallella et al (2021b) reduces to kinetic equations ((5.15) below) for the one-particle marginals of the probability measure describing the statistical behaviour of the system. In particular as a crucial step, we prove *propagation of chaos*, namely the asymptotic statistical independence of the agents. We use a coupling method, which improves the result obtained in Ciallella et al (2021b) (obtained via the hierarchy method) providing a simpler and more effective proof. More precisely we introduce a second random process, accounting for the kinetic equations *formally* associated with the limit $N \rightarrow \infty$, and construct a realization of both processes on the same probability space. This coupling is then used to estimate the distance between the processes and verify that the two models are asymptotically equivalent.

The plan of the paper is the following. In Sections 5.2 and 5.3 we present the model and the limiting kinetic equation, respectively. In Section 5.4 we discuss the convergence of the particle model in the kinetic limit following the coupling argument. Finally, Section 5.5 is devoted to concluding remarks.

5.2 Model

We now define the system we are going to study. We refer also to Ciallella et al (2021b) for the description of the model and the derivation of the formal kinetic limit. Consider N particles, representing the agents of the system, moving a square in the plane \mathbb{R}^2 with periodic boundary conditions, i.e., the torus $\Lambda = [0, D] \times [0, D]$, where $D > 0$ is a fixed parameter. The particles are assumed to move with velocities of modulus 1 so that the velocities belong to the unit circle S^1 . Each particle has a label $a_i \in \{S, I, R\} =: L$, $i = 1, 2, \dots, N$, representing the class of the agent (susceptible, infected, recovered). We introduce the notations

$Z_N = (z_1, z_2, \dots, z_N)$, where $z_i = (x_i, v_i) \in \Lambda \times \mathcal{S}^1$, and $A_N = (a_1, a_2, \dots, a_N)$. At any time, the state of the system is described by the $(4N)$ -tuple of coordinates $(Z_N; A_N)$ belonging to the phase space $(\Gamma \times L)^N$, where $\Gamma := \Lambda \times \mathcal{S}^1$.

The system evolves in time according to the following generator:

$$\mathcal{L} = \mathcal{L}_0 + \mathcal{L}_1 + \mathcal{L}_d + \mathcal{L}_{int}^N, \quad (5.1)$$

where we have generators for which we omit the dependence on N since they are acting independently on single particles (\mathcal{L}_0 , \mathcal{L}_1 and \mathcal{L}_d), and a binary interaction term between particles \mathcal{L}_{int}^N .

More precisely, $\mathcal{L}_0 + \mathcal{L}_1$ is the generator of N independent copies of a random walk:

$$\mathcal{L}_0 = \sum_{i=1}^N v_i \cdot \nabla_{x_i} \quad (5.2)$$

is the generator of free motion (particles are moving of linear motion with velocities v_i , $i = 1, \dots, N$), and jumps happen as described by

$$\mathcal{L}_1 \Phi(Z_N) = \sum_{i=1}^N \frac{1}{2\pi} \int_{\mathcal{S}^1} dw [\Phi(z_1, \dots, x_i, w, \dots, z_N) - \Phi(Z_N)]. \quad (5.3)$$

In particular, when we select the test function Φ of the form of a function of a single particle state only, for instance of the first one $\Phi(Z_N) = \phi(z_1)$, we get

$$\mathcal{L}_1 \Phi(Z_N) = \frac{1}{2\pi} \int_{\mathcal{S}^1} dw [\phi(x_1, w) - \phi(x_1, v_1)]. \quad (5.4)$$

Note that labels are not involved in the random flight process, so here we have left out the dependency on them to shorten the notations.

The other contributions in the generator are instead acting on the labels of the particles only. The term \mathcal{L}_d describes the decay of infected agents I into recovered R . It takes the form

$$\mathcal{L}_d \Phi(Z_N; A_N) = \gamma \sum_{i=1}^N [\Phi(Z_N; a_1, \dots, \tilde{a}_i, \dots, a_N) - \Phi(Z_N; A_N)], \quad (5.5)$$

$\gamma > 0$ being a constant parameter representing the rate of decay, and where the transition of an a_i label into a \tilde{a}_i is defined by

$$\tilde{a}_i = R \quad \text{if } a_i = I; \quad \tilde{a}_i = a_i \quad \text{otherwise.} \quad (5.6)$$

Finally, the binary interaction term describing the infection process has generator

$$\mathcal{L}_{int}^N \Phi(Z_N; A_N) = \frac{\lambda}{N} \sum_{\substack{i,j=1 \\ j>i}}^N [\Phi(Z_N; a_1, \dots, a'_i, \dots, a'_j, \dots, a_N) - \Phi(Z_N; a_1, \dots, a_N)]. \quad (5.7)$$

Here, $\lambda > 0$ is the constant representing the rate of the process and for the involved particles the transition from (a_i, a_j) into (a'_i, a'_j) is defined by

$$\begin{cases} \text{if } \chi_{i,j} = 1 \text{ and } a_i = I, a_j = S \text{ or } a_j = I, a_i = S \text{ then } a'_i = a'_j = I; \\ \text{otherwise } a'_i = a_i, a'_j = a_j. \end{cases} \quad (5.8)$$

The characteristic function $\chi_{i,j}$ is introduced to allow two particles to interact only when they are sufficiently close: fixing $R_0 > 0$, we define

$$\chi_{i,j} := \mathbb{1}_{\{x_i, x_j \mid |x_i - x_j| < R_0\}}. \quad (5.9)$$

Thus, the evolution due to the defined generator (5.1) is describing the following behaviour. Each agent is moving in the space Λ performing a random flight, where the velocity jumps happen with rate 1. Each particle has a label describing its state: susceptible (S), infected (I), or recovered (R). According to a Poisson process with overall rate $\frac{(N-1)\lambda}{2}$, a pair of agents is selected uniformly. Whenever the chosen agents are at a distance smaller than R_0 , the infection process takes place only for pairs made by an infected and a susceptible agent, which are changed in a couple of infected agents. Finally, each infected agent becomes recovered according to a different Poisson process with rate γ .

A statistical description is in order for dealing with such a system with a large number of agents N . The initial configuration of the system at time zero is given by the probability density W_0^N , *symmetric* in the exchange of particles, such that

$$W_0^N : (\Gamma \times L)^N \rightarrow \mathbb{R}^+, \quad \sum_{A_N} \int_{\Gamma^N} dZ_N W_0^N(Z_N; A_N) = 1. \quad (5.10)$$

The time evolved measure $W_t^N(Z_N; A_N)$, $t > 0$ is given by

$$\begin{aligned} \sum_{A_N} \int dZ_N W_t^N(Z_N; A_N) \Phi(Z_N; A_N) = \\ \sum_{A_N} \int dZ_N W_0^N(Z_N; A_N) \mathbb{E}[\Phi(Z_N(t); A_N(t))], \end{aligned} \quad (5.11)$$

where Φ is a test function, $(Z_N; A_N) \rightarrow (Z_N(t); A_N(t))$ is the process and $\mathbb{E} = \mathbb{E}_{(Z_N, A_N)}$ is the expectation conditioned to the initial value $(Z_N; A_N)$. Integrating with respect to the last $N - j$ particle positions, velocities and labels, $j = 1, \dots, N - 1$, we build the j -particle marginal f_j^N , that gives the probability density of finding j particles with labels A_j in the configuration Z_j :

$$f_j^N(Z_j; A_j; t) = \sum_{\bar{A}_{N-j} \in L^{N-j}} \int d\bar{Z}_{N-j} W_t^N(Z_j, \bar{Z}_{N-j}; A_j, \bar{A}_{N-j}). \quad (5.12)$$

We consider particles distributed independently at time zero. Given the one-particle density distribution f_0 , with normalization

$$\sum_{a \in L} \int dz f_0(z; a) = 1, \quad (5.13)$$

the initial state is

$$W_0^N(Z_N; A_N) = \prod_{i=1}^N f_0(x_i, v_i; a_i) := (f_0)^{\otimes N}(Z_N; A_N). \quad (5.14)$$

It is crucial to keep in mind that, even when at time zero the particles are independent, they do not remain independent at positive times. In fact, the dynamics creates correlations between particles so that the measure is no longer factorized at positive times. However, we will prove that the so-called ‘propagation of chaos’ holds. This means that this independence is recovered asymptotically in the limit $N \rightarrow \infty$.

5.3 Kinetic Limit

We aim at proving that the system we introduced in the previous section is asymptotically equivalent to the system one formally obtains in the limit $N \rightarrow \infty$ assuming the propagation of chaos. We refer to Ciallella et al (2021b) for such formal derivation, and for a proof of the rigorous result through the hierarchy of equations satisfied by the marginals $f_j^N(Z_j; A_j; t)$. In the following section, we shall proceed in a simpler and more natural way.

According to the formal limit, the triple of single-particle densities

$$(f(z; S; t), f(z; I; t), f(z; R; t))$$

satisfies the following system of kinetic equations ($z = (x, v)$):

$$\begin{cases} (\partial_t + v \cdot \nabla_x) f(z; S) = \mathcal{L}_1 f(z; S) - \lambda f(z; S) \int f(z_1; I) \chi(|x - x_1| < R_0) dz_1 \\ (\partial_t + v \cdot \nabla_x) f(z; I) = \mathcal{L}_1 f(z; I) - \gamma f(z; I) \\ \quad + \lambda f(z; S) \int f(z_1; I) \chi(|x - x_1| < R_0) dz_1 \\ (\partial_t + v \cdot \nabla_x) f(z; R) = \mathcal{L}_1 f(z; R) + \gamma f(z; I) \end{cases} \quad (5.15)$$

Note that the sum

$$f(z, t) := \sum_{a \in L} f(z; a; t)$$

satisfies the simple random flight equation

$$(\partial_t + v \cdot \nabla_x) f(z, t) = \mathcal{L}_1 f(z, t) .$$

Moreover, the system of kinetic equations (5.15) provides a more detailed description of the classical SIR model when dealing with spatially inhomogeneous data (see Ciallella et al, 2021b).

We now introduce as second model the process associated with the kinetic equations (5.15) that we will eventually couple with the one introduced in Section 5.2. The single-particle generator is

$$\tilde{\mathcal{L}} = \tilde{\mathcal{L}}_0 + \tilde{\mathcal{L}}_1 + \tilde{\mathcal{L}}_d + \tilde{\mathcal{L}}_i \quad (5.16)$$

where $\tilde{\mathcal{L}}_0$, $\tilde{\mathcal{L}}_1$ and $\tilde{\mathcal{L}}_d$ are the operators defined in Section 5.2, namely \mathcal{L}_0 , \mathcal{L}_1 and \mathcal{L}_d respectively, in the case $N = 1$; while the infection generator is given by the non-linear (f -dependent) term

$$\tilde{\mathcal{L}}_i \phi(z; b) = \lambda \mathcal{N}_f(z) \{ \phi(z; b') - \phi(z; b) \}, \quad (5.17)$$

where \mathcal{N}_f (depending on time through f) is defined as

$$\mathcal{N}_f(z) = (f(I; t) * \chi_{R_0})(z) := \int f(z_1; I; t) \chi(|x - x_1| < R_0) dz_1, \quad (5.18)$$

$\chi(A)$ is the indicator function of A , and $(z; b) \in \Gamma \times L$. We are keeping the same notation associated with the prime sign as in Section 5.2, i.e., $b' = I$ if $b = S$, while in the other cases $b' = b$.

We now consider the N -particle process defined by N independent copies of the one-particle nonlinear process introduced above. The N -particle generator is

$$\tilde{\mathcal{L}}^N = \mathcal{L}_0 + \mathcal{L}_1 + \mathcal{L}_d + \tilde{\mathcal{L}}_i^N \quad (5.19)$$

where \mathcal{L}_0 , \mathcal{L}_1 , \mathcal{L}_d are given by (5.2)-(5.5) and, for $(Z_N; B_N) \in (\Gamma \times L)^N$,

$$\tilde{\mathcal{L}}_i^N \Phi(Z_N; B_N) = \lambda \sum_{i=1}^N \mathcal{N}_f(z_i) \{ \Phi(Z_N; B_N^i) - \Phi(Z_N; B_N) \} \quad (5.20)$$

with

$$\begin{cases} B_N^i = (b_1, \dots, b_{i-1}, I, b_{i+1}, \dots, b_N) & \text{if } B_N = (b_1, \dots, b_{i-1}, S, b_{i+1}, \dots, b_N) \\ B_N^i = B_N & \text{otherwise} \end{cases} . \quad (5.21)$$

5.4 Particle Approximation

We are now ready to prove the validity of the kinetic equations (5.15) for the model introduced in Section 5.2, in the limit $N \rightarrow \infty$. We are assuming (5.13) and (5.14) at time zero, i.e., the initial datum is factorized. On the other hand the dynamics of labels creates correlations as

$$f_2^N(z_1, z_2; a_1, a_2; t) \neq f_1^N(z_1; a_1; t) f_1^N(z_2; a_2; t).$$

To show that these correlations are vanishing as $N \rightarrow \infty$, we now introduce a coupling between the process described by the generator (5.1) and the process associated to the kinetic equations (5.15).

We start by considering a different equivalent form for the generator

$$\begin{aligned} & \mathcal{L}_{int}^N \Phi(Z_N; A_N) \\ &= \frac{\lambda}{2N} \sum_{i=1}^N \sum_{\substack{j=1 \\ j \neq i}}^N \delta_{a_j, I} \{ \Phi(Z_N; a_1, \dots, a'_i, \dots, a'_j, \dots, a_N) - \Phi(Z_N; A_N) \} \\ &= \frac{\lambda}{N} \sum_{i=1}^N \sum_{\substack{j=1 \\ j \neq i}}^N \delta_{a_j, I} \chi_{i,j} \{ \Phi(Z_N; A_N^i) - \Phi(Z_N; A_N) \} \\ &= \lambda \sum_{i=1}^N \mathcal{J}_{emp}^i \{ \Phi(Z_N; A_N^i) - \Phi(Z_N; A_N) \}, \end{aligned} \tag{5.22}$$

where we use the prime superscript with the meaning of (5.8), i.e

$$\begin{cases} a'_i = I & \text{if } a_j = I, a_i = S \text{ and } \chi_{i,j} = 1, \\ a'_i = a_i, a_j = a'_j & \text{otherwise} \end{cases},$$

and the i superscript (as in (5.21)) when we prefer to make explicit the role of both $\delta_{a_j, I}$ and $\chi_{i,j}$, i.e.

$$\begin{cases} A_N^i = (a_1, \dots, a_{i-1}, I, a_{i+1}, \dots, a_N) & \text{if } A_N = (a_1, \dots, a_{i-1}, S, a_{i+1}, \dots, a_N) \\ A_N^i = A_N & \text{otherwise} \end{cases} \tag{5.23}$$

having introduced

$$\mathcal{J}_{emp}^i = \mathcal{J}_{emp}^i(Z_N; A_N) = \frac{1}{N} \sum_{\substack{j=1 \\ j \neq i}}^N \delta_{a_j, I} \chi_{i,j}. \tag{5.24}$$

In words, we are interpreting the behaviour in the following equivalent way. The N agents are still moving in Λ via a random flight, with velocity jumps in \mathcal{S}^1 taking

place with rate 1 per agent and each infected agent becomes recovered according to a Poisson process of rate γ . In the infection process we choose with rate N an agent i uniformly and then, with a rate λ , we evaluate the interaction with an uniformly picked agent. So that, if this latter is an infected agent and the i -th is a susceptible one and if their distance is smaller than R_0 , then a_i becomes I , otherwise nothing happens.

We want to compare the behaviour of this process with that of the one-particle non-linear process associated to the kinetic equation (5.15), described by the generator (5.17). The idea is now to couple the two processes. We remark that the positions and velocities are the same, so that the difference is only in the distributions of the labels. Let us call \mathcal{E}^i the following difference

$$\mathcal{E}^i := \mathcal{N}_f(z_i) - \mathcal{J}_{emp}^i(Z_N; B_N). \quad (5.25)$$

We expect that, by the law of large numbers, \mathcal{E}^i gives a vanishing contribution as $N \rightarrow \infty$ and hence, for sufficiently large N , generates a small perturbation in the evolution of distributions of labels.

We consider as coupling the process $t \rightarrow (Z_N(t); A_N(t), B_N(t))$ with generator

$$Q^N = \mathcal{L}_0 + \mathcal{L}_1 + Q_d^N + Q_i^N, \quad (5.26)$$

where the decay term is defined as

$$Q_d^N \Phi(Z_N; A_N, B_N) = \gamma \sum_{i=1}^N [\Phi(Z_N; \tilde{A}_N^i, \tilde{B}_N^i) - \Phi(Z_N; A_N, B_N)], \quad (5.27)$$

denoting by $\tilde{A}_N^i = (a_1, \dots, \tilde{a}_i, \dots, a_N)$ the transition on the i -th agent as defined in (5.6), and analogous definition for \tilde{B}_N^i . The interaction term is

$$\begin{aligned} Q_i^N \Phi(Z_N; A_N, B_N) = & \lambda \sum_{i=1}^N \mathcal{J}^i \{ \Phi(Z_N; A_N^i, B_N^i) - \Phi(Z_N; A_N, B_N) \} \\ & + \lambda \sum_{i=1}^N \mathcal{J}_1^i \{ \Phi(Z_N; A_N^i, B_N) - \Phi(Z_N; A_N, B_N) \} \\ & + \lambda \sum_{i=1}^N \mathcal{J}_2^i \{ \Phi(Z_N; A_N, B_N^i) - \Phi(Z_N; A_N, B_N) \} \\ & + \lambda \sum_{i=1}^N \mathcal{E}^i \{ \Phi(Z_N; A_N, B_N^i) - \Phi(Z_N; A_N, B_N) \}, \end{aligned} \quad (5.28)$$

where A_N^i, B_N^i follows the transition rule (5.23), and the label jump associated to \mathcal{J}_1^i only affects the transition for A_N , while the terms corresponding to \mathcal{J}_2^i and \mathcal{E}^i only affect the transition for B_N . Instead, the jumps described by the first term in (5.28) and in (5.27) are simultaneous for particles labelled by both A_N and B_N (which is

optimal for what concerns the propagation of chaos). We set

$$\begin{aligned} \mathcal{J}^i &= \frac{1}{N} \sum_{\substack{j=1 \\ j \neq i}}^N \delta_{a_j, I} \delta_{b_j, I} \chi_{i, j}, \\ \mathcal{J}_1^i &= \frac{1}{N} \sum_{\substack{j=1 \\ j \neq i}}^N \delta_{a_j, I} (1 - \delta_{b_j, I}) \chi_{i, j}, \\ \mathcal{J}_2^i &= \frac{1}{N} \sum_{\substack{j=1 \\ j \neq i}}^N (1 - \delta_{a_j, I}) \delta_{b_j, I} \chi_{i, j} \end{aligned}$$

(being $\delta_{a_j, I}$ the Dirac delta taking value 1 if and only if $a_j = I$ and 0 otherwise, and analogously for the other deltas). Note that thanks to this choice, one has that

$$\mathcal{J}^i + \mathcal{J}_1^i = \mathcal{J}_{emp}^i(Z_N; A_N), \quad \mathcal{J}^i + \mathcal{J}_2^i + \mathcal{E}^i = \mathcal{J}_{emp}^i(Z_N; B_N) + \mathcal{E}^i = \mathcal{N}_f(z_i)$$

so that Q^N is actually generating a coupling of the two previously described processes, i.e., we recover as the two marginals the two processes we are considering, obtained by integrating over B_N and A_N , respectively.

Let $R^N(t)$ be the law at time t for the coupled process, and we consider as the initial distribution at time 0 the factorized distribution with the same distribution of labels for both a and b -labelled particles, i.e. $R^N(0) = f_0^{\otimes N}(Z_N; A_N) \delta_{A_N, B_N}$. We define $D_N(t)$ as the average fraction of particles having different labels a_i, b_i , i.e. we choose the test function $\Phi(Z_N; A_N, B_N) = \frac{1}{N} \sum_{i=1}^N d(a_i, b_i)$, where $d(a, b) = 1 - \delta_{a, b}$: thanks to the symmetry

$$D_N(t) = \int dR^N(t) \frac{1}{N} \sum_{i=1}^N d(a_i, b_i) = \int dR^N(t) d(a_1, b_1). \tag{5.29}$$

We notice that $D_N(0) = 0$ and that $D_N(t)$ is positive. Our aim is to prove that $D_N(t)$ can be estimated by an arbitrarily small quantity for finite time, provided that N is sufficiently large.

Theorem 5.1. *For any $t > 0$, the fraction of particles with different labels satisfies*

$$D_N(t) \leq \frac{t\lambda}{N} e^{2\lambda t}. \tag{5.30}$$

for sufficiently large N .

Remark. The above estimate says that, for any positive time, for the time evolved joint measure associated to the N -particle systems of the process whose generator is (5.1), and of the one whose generator is (5.17), the fraction of particles with different labels is arbitrarily small, provided that N is sufficiently large.

Proof. We evaluate

$$\frac{d}{dt} \int dR^N(t) d(a_1, b_1) = \int dR^N(t) (\mathcal{L}_0 + \mathcal{L}_1 + Q_d^N + Q_1^N) d(a_1, b_1), \quad (5.31)$$

where the contribution due to the terms \mathcal{L}_0 and \mathcal{L}_1 is vanishing since $d(a_1, b_1)$ does not depend on x and v .

The contribution due to the decay term (5.27) is

$$\gamma \int dR^N(t) (d(\tilde{a}_1, \tilde{b}_1) - d(a_1, b_1)) = -\gamma \int dR^N(t) (\delta_{\tilde{a}_1, \tilde{b}_1} - \delta_{a_1, b_1}). \quad (5.32)$$

It is easy to verify that this contribution is non-positive. Indeed, in the case where a_1 and b_1 are equal, also \tilde{a}_1 and \tilde{b}_1 remain equal, and the contribution is vanishing. In the case when a_1 and b_1 are different, after the transformation \tilde{a}_1 and \tilde{b}_1 can either remain different, or (if at the beginning there were an I and an R -labelled agent) both become R . This last case is the only one in which the contribution is not vanishing, but negative.

The same argument applies to the first term in the right hand side of the interaction (5.28). This term can be written as

$$-\lambda \int dR^N(t) \mathcal{J}^1(\delta_{a'_1, b'_1} - \delta_{a_1, b_1}), \quad (5.33)$$

and, in the same way as previously, $a_1 = b_1$ implies that after the transformation $a'_1 = b'_1$, so that the only non-zero contribution is negative, and it happens when an S and an I -labelled particle are transformed into two I -particles.

Now, let us evaluate the second term in the right hand side of the interaction (5.28). It can be written as

$$\begin{aligned} (\text{II}) &= \lambda \int dR^N(t) \mathcal{J}_1^1(Z_N; A_N, B_N) (d(a'_1, b_1) - d(a_1, b_1)) \\ &= -\lambda \int dR^N(t) \mathcal{J}_1^1(Z_N; A_N, B_N) (\delta_{a'_1, b_1} - \delta_{a_1, b_1}). \end{aligned} \quad (5.34)$$

Here, the difference of the deltas can take the values -1, 0, or 1. Then

$$\begin{aligned} |(\text{II})| &\leq \lambda \int dR^N(t) \frac{1}{N} \sum_{j=2}^N \delta_{a_j, I} (1 - \delta_{b_j, I}) \chi_{1, j} \\ &\leq \lambda \int dR^N(t) \frac{1}{N} \sum_{j=2}^N d(a_j, b_j) \leq \lambda D_N(t). \end{aligned} \quad (5.35)$$

The third term in (5.28) can be estimated in exactly the same way.

Finally,

$$\begin{aligned}
\int dR^N(t) \mathcal{E}^1 &= \int dR^N(t) \mathcal{N}_f(z_1) - \int dR^N(t) \mathcal{J}_{emp}^1(Z_N; B_N) \\
&= \sum_a \int dz dz_1 f(z; a; t) \chi(|x - x_1| < R_0) f(z_1; I; t) \\
&\quad - \int dR^N(t) \frac{1}{N} \sum_{j=2}^N \delta_{b_j, I} \chi(|x_j - x_1| < R_0).
\end{aligned} \tag{5.36}$$

The last term, thanks to the symmetry, can be written as

$$-\frac{N-1}{N} \sum_a \int dz dz_1 f(z; a; t) \chi(|x - x_1| < R_0) f(z_1; I; t), \tag{5.37}$$

so that

$$\left| \int dR^N(t) \mathcal{E}^1 \right| \leq \frac{1}{N} \sum_a \int dz dz_1 f(z; a; t) \chi(|x - x_1| < R_0) f(z_1; I; t) \leq \frac{1}{N}. \tag{5.38}$$

In conclusion, recalling that $D_N(0) = 0$, we find that

$$\frac{d}{dt} D_N(t) \leq 2\lambda D_N(t) + \frac{\lambda}{N} \tag{5.39}$$

and the Theorem is proven by Grönwall's Lemma. \square

We conclude this section with some comments. Theorem 5.1 implies the convergence of the one-particle marginal $f_1^N(z; a; t)$ to the solution $f(z; a; t)$ of the kinetic equations (5.15). To see this one can use the Wasserstein distance \bar{W} , which we recall. Given two measures μ and ν on a metric space X with the discrete metric \bar{d} ,

$$\bar{W}(\mu, \nu) := \inf_{R \in \mathcal{C}(\mu, \nu)} \int dR(z, z') \bar{d}(z, z')$$

where $\mathcal{C}(\mu, \nu)$ is the set of the joint representations of μ and ν , i.e. measures on $X \otimes X$ with marginals μ and ν respectively. This metric is equivalent to the Total Variation and hence to the L^1 -norm, whenever such measures have suitable densities (Villani, 2003).

Arguing now on the phase space $\Gamma \times L$ endowed with the discrete metric

$$\bar{d}(z_1, z_2) + d(a_1, a_2),$$

we construct a joint representation of $df_1^N(z; a; t)$ and $df(z; a; t)$, denoted by $dR^N(t)$, along the coupled process. Since the trajectories (on Γ) of the two processes are the same, the configurational contribution vanishes and

$$\bar{W}(df_1^N(t), df(t)) \leq \frac{t\lambda}{N} e^{2\lambda t}.$$

This also controls $\|f_1^N(t) - f(t)\|_{L^1}$ and, along similar lines, one can also show that

$$\|f_j^N(t) - f(t)^{\otimes j}\|_{L^1} \leq Cj \frac{t\lambda}{N} e^{2\lambda t}$$

for some geometrical positive constant C .

The obtained estimates slightly improve the quantitative results obtained via the hierarchy as sketched in Ciallella et al (2021b).

5.5 Concluding Remarks

In this paper we performed a mathematical analysis, based on a coupling method, of a toy model for epidemic spread in a system of N individual agents as proposed in Ciallella et al (2021b).

The study of epidemiological models has been obviously very fertile over recent times (see Pulvirenti and Simonella, 2020; Flandoli et al, 2020; Ciallella et al, 2021a; Bertaglia et al, 2021; Boscheri et al, 2021; Ciallella et al, 2021b; Loy and Tosin, 2021; V. Vuong et al, 2021, for a very non-exhaustive list of recent mathematical works oriented toward kinetic theory). Even in this context, the use of coupling methods is not new. We can mention classical work as Whittle (1955) on the comparison of birth-death processes with the SIR model, and several other contributions over more recent times as for instance Ball and Donnelly (1995); Häggström and Pemantle (1998). Of course coupling arguments have been a powerful tool for studying the behaviour of stochastic processes for several years now. In particular such arguments have been used to approximate kinetic equations of Boltzmann type (and justify related numerical schemes) with particle systems in the spirit of Kac; see e.g. Graham and Méléard (1997); Cortez and Fontbona (2016).

Multi-agent systems are important in a wide range of fields. As an example in the theory of epidemic spread, the most common models divide the population in several classes, going from the classical susceptible-infected-recovered quoted above, to recent generalizations with several additional species (as the SUIHTER model with susceptible uninfected individuals, undetected infected, isolated, hospitalized, threatened, extinct, and recovered, proposed in Parolini et al, 2021). The models aim at describing the evolution of average fractions for the different species, as in the predator-prey system of Lotka–Volterra type (see Diz-Pita and Otero-Espinar, 2021, for a recent review). We would like to mention here, as another example, the case of mathematical models describing the behaviour of bones, which include cellular automata models (for instance Czarnecki et al, 2014; Van Scoy et al, 2017) or empirical models based on variational formulation; see Giorgio et al (2019, 2021); Lekszycki and dell’Isola (2012) among others.

References

- Albi G, Bertaglia G, Boscheri W, Dimarco G, Pareschi L, Toscani G, Zanella M (2021) Kinetic modelling of epidemic dynamics: social contacts, control with uncertain data, and multiscale spatial dynamics. arXiv preprint arXiv:211000293
- Ball F, Donnelly P (1995) Strong approximations for epidemic models. *Stochastic processes and their applications* 55(1):1–21
- Bellomo N, Bingham R, Chaplain MA, Dosi G, Forni G, Knopoff DA, Lowengrub J, Twarock R, Virgillito ME (2020) A multiscale model of virus pandemic: Heterogeneous interactive entities in a globally connected world. *Mathematical Models and Methods in Applied Sciences* 30(08):1591–1651
- Bertaglia G, Boscheri W, Dimarco G, Pareschi L (2021) Spatial spread of covid-19 outbreak in italy using multiscale kinetic transport equations with uncertainty. *Mathematical Biosciences and Engineering* 18:7028
- Boscheri W, Dimarco G, Pareschi L (2021) Modeling and simulating the spatial spread of an epidemic through multiscale kinetic transport equations. *Mathematical Models and Methods in Applied Sciences* pp 1–39
- Ciallella A, Pulvirenti M, Simonella S (2021a) Inhomogeneities in Boltzmann-SIR models. *Mathematics and Mechanics of Complex Systems* 9(3):273–292
- Ciallella A, Pulvirenti M, Simonella S (2021b) Kinetic sir equations and particle limits. *Rendiconti Lincei-Matematica e Applicazioni* 32(2):295–315
- Cortez R, Fontbona M (2016) Quantitative propagation of chaos for generalized kac particle systems. *Ann Appl Probab* 26(2):892–916
- Czarnecki JS, Blackmore M, Jolivet S, Lafdi K, Tsonis PA (2014) Bone growth on reticulated vitreous carbon foam scaffolds and implementation of cellular automata modeling as a predictive tool. *Carbon* 79:135–148
- Diz-Pita É, Otero-Espinar M (2021) Predator–prey models: A review of some recent advances. *Mathematics* 9(15):1783
- Flandoli F, Grotto F, Papini A, Ricci C (2020) Epidemic models as scaling limits of individual dynamics. arXiv:200705855
- Giorgio I, dell’Isola F, Andreaus U, Alzahrani F, Hayat T, Lekszycki T (2019) On mechanically driven biological stimulus for bone remodeling as a diffusive phenomenon. *Biomechanics and modeling in mechanobiology* 18(6):1639–1663
- Giorgio I, Spagnuolo M, Andreaus U, Scerrato D, Bersani AM (2021) In-depth gaze at the astonishing mechanical behavior of bone: A review for designing bio-inspired hierarchical metamaterials. *Mathematics and Mechanics of Solids* 26(7):1074–1103
- Graham C, Méléard S (1997) Stochastic particle approximations for generalized boltzmann models and convergence estimates. *The Annals of probability* 25(1):115–132
- Hägström O, Pemantle R (1998) First passage percolation and a model for competing spatial growth. *Journal of Applied Probability* 35(3):683–692
- Kermack WO, McKendrick AG (1927) A contribution to the mathematical theory of epidemics. *Proceedings of the royal society of london Series A, Containing papers of a mathematical and physical character* 115(772):700–721
- Lekszycki T, dell’Isola F (2012) A mixture model with evolving mass densities for describing synthesis and resorption phenomena in bones reconstructed with bio-resorbable materials. *ZAMM-Journal of Applied Mathematics and Mechanics/Zeitschrift für Angewandte Mathematik und Mechanik* 92(6):426–444
- Loy N, Tosin A (2021) A viral load-based model for epidemic spread on spatial networks. *Mathematical Biosciences and Engineering* 18:5635
- Parolini N, Dede L, Antonietti PF, Ardenghi G, Manzoni A, Miglio E, Pugliese A, Verani M, Quarteroni A (2021) Suihter: A new mathematical model for covid-19. application to the analysis of the second epidemic outbreak in italy. *Proceeding of the Royal Society A* 477

- Pulvirenti M, Simonella S (2020) A kinetic model for epidemic spread. *Mathematics and Mechanics of Complex Systems* 8(3):249–260
- V Vuong Y, Hauray M, Pardoux E (2021) Conditional propagation of chaos in a spatial stochastic epidemic model with common noise. arXiv:211102733
- Van Scoy GK, George EL, Asantewaa FO, Kerns L, Saunders MM, Prieto-Langarica A (2017) A cellular automata model of bone formation. *Mathematical biosciences* 286:58–64
- Villani C (2003) *Topics in optimal transportation*, vol 58. American Mathematical Soc.
- Whittle P (1955) The outcome of a stochastic epidemic—a note on Bailey’s paper. *Biometrika* 42(1-2):116–122



Chapter 6

On the Constitutive Assumptions for a Continuum Model of Scintillating Crystals

Fabrizio Daví

Abstract For inorganic scintillating crystals, we show how the evolution equation for the charge carriers densities can be obtained by modeling the crystal as a continuum with structure. The resulting equation is a Reaction-Diffusion-Drift one. We deal with various hypotheses on the reaction/recombination term which are induced by two different choices for the associated entropy, namely those based either on the Gibbs-Boltzmann or Fermi–Dirac statistics.

Keywords: Evolution equations · Scintillating crystals · Gibbs entropy · Fermi–Dirac potentials

6.1 Introduction

A scintillating crystal or scintillator is a crystal that acts as a wavelength shifter, *i.e.* that converts incoming ionizing energy into photons in the frequency range of visible. In a previous paper (Daví, 2019) we modelled inorganic scintillators by the means of a continuum with structure model, to arrive at a reaction-diffusion-drift system which describes the evolution and the recombination in photons of the charged carriers. A model of this kind, first proposed for scintillators in Vasil'ev (2008), was used subsequently in many papers to get a phenomenological description of scintillation. In this and similar models the diffusion-drift part and the recombination term (which describes how the radiation-excited charge carriers recombine radiatively to generate visible photons or lose energy through non-radiatively processes) were borrowed directly either from the kinetics of chemical reactions or from similar models for semiconductors.

F. Daví
DICEA & ICRES, Università Politecnica delle Marche, Ancona, Italy
on leave at IMT-School for Advanced Studies, Lucca, Italy
e-mail: davi@univpm.it

In Daví (2019) we showed how the reaction-diffusion-drift boundary value problem for scintillators can be obtained, in a coherent and consistent manner, by the means of the mechanics of continua with microstructure (Capriz, 1989) for a non-deformable crystal. Moreover, we showed how the reaction term can be obtained, by using the formalism of chemical reaction kinetics, to deal with the recombination mechanisms. Further, we showed that the whole boundary value problem admits a gradient flow structure: for the various mathematical aspects and results *vid. e.g.* the review in Daví (2021).

The aim of the present work is two-fold: first to extend the results of Daví (2019) to deformable continua and then to investigate the effects of different constitutive assumptions for the dissipative terms (which are represented by an entropy functional) on the recombination term. In particular, we look at two possible choices for the entropy functional, namely the Gibbs (or Boltzmann–Gibbs) entropy and the one which is based on the Fermi–Dirac statistics. This last one seems more appropriate to describe recombination in scintillator, but this is obtained by losing the simpler mathematical structure induced by the Gibbs entropy and which is well studied from a mathematical point of view (Daví, 2021). Accordingly, reaction-diffusion-drift equations based on the Fermi–Dirac statistics deserve further study.

6.2 A Continuum with Microstructure Model for Scintillators

In a series of previous papers (Daví, 2019, 2021), we obtained a model for the evolution and recombination of charge carriers in inorganic scintillating crystals: here we recall the main results obtained.

Let $\Omega \subset \mathcal{E}$ be a region of the three-dimensional euclidean space \mathcal{E} which we identify with the reference configuration of a continuum body, which we assume comprised of a dielectric, non-magnetizable and deformable scintillating crystal. Let

$$y(x, t) : \Omega \rightarrow \mathcal{E} \times [0, \tau), \quad (6.1)$$

be a motion and let $\Omega_t = y(\Omega, t)$ be the current configuration of Ω .

When incoming ionizing radiations hit Ω_t at given (y, t) , the radiation energy generates a distribution of charged particles (electrons, holes, bounded electron-hole pairs called exciton, and many others) collectively referred as *excitation carriers*. These excitation carriers which evolves in the matter according to the Bethe-Bloch equation (Inokuti, 1971), (Ziegler, 1999), follow a complicated path with many kinks and bends for about 10 microns until either they lose their energy, excite other particles or recombine, generating a shower of charged particle within a region $\mathcal{P} \subset \Omega_t$ whose diameter is about 100 microns (Jaffe, 2007). We call the region \mathcal{P} about (y, t) the *Scintillation region*: it is within this region that the charged carriers recombine, some of them generating photons.

In the initial stages, the particles follow a straight path of few nanometers: in (Daví, 2019) we showed how, by the means of a suitable scaling procedure of an

approximate solution of the Bethe-Bloch equation (Ulmer, 2007), we may obtain a mesoscopic state variable N , the *excitation carrier density*. Such a variable, which represents the particle density in the initial stage, brings to the mesoscopic scale the material properties and the ray-energy which impinges the material at (y, t) . We henceforth assume N a continuous field on the scintillation region

$$N : \mathcal{P} \times [0, \tau] \rightarrow \mathbb{R}^+, \quad (y, t) \mapsto N(y, t) > 0. \quad (6.2)$$

Since the charged particles may have different charge sign and also exhibits different recombination and dissipation mechanics it is useful to differentiate them by introducing an *excitation carrier vector*, the k -dimensional array:

$$\mathbf{n} \equiv (n_1, n_2, \dots, n_k), \quad \sum_{j=1}^k n_j(x, t) = N(y, t), \quad n_j \geq 0; \quad (6.3)$$

the simplest non-trivial case is for $k = 2$ with say, n_1 representing the electrons density (which is equal to the holes density) and n_2 the exciton density, *i.e.* bounded electron-hole pairs which evolve together. However we may have cases with $k = 3$ (Williams et al, 2011; Moses et al, 2012), $k = 7$ (Gridin et al, 2015) or $m \geq 11$ as in Vasil'ev (2008). We notice that, since N is finite, this implies that \mathbf{n} is bounded in the $L^1(\mathcal{P})$ norm:

$$\int_{\mathcal{P}} N = \int_{\mathcal{P}} \sum_{j=1}^k |n_j| = \|\mathbf{n}\|_{L^1(\mathcal{P})} < \infty. \quad (6.4)$$

For e the elementary charge, the excitation carrier densities (6.3) induce a free-charge density ρ_f within the scintillation volume:

$$\rho_f = e\mathbf{q} \cdot \mathbf{n}, \quad \text{in } \mathcal{P}, \quad (6.5)$$

where $\mathbf{q} = (q_1, q_2, \dots, q_k)$, $q_j \in \mathbb{Z}$ is the charge number vector. We assume that within the scintillation region \mathcal{P} there are no bound charges and hence the excitation carrier density induces an electric potential φ (Wang, 1979):

$$\begin{aligned} -\epsilon \Delta \varphi &= \rho^*, & \text{in } \mathbb{R}^3 \\ \llbracket \text{grad} \varphi \rrbracket \cdot \mathbf{m} &= 0, & \text{on } \partial \mathcal{P}, \end{aligned} \quad (6.6)$$

where \mathbf{m} is the outward unit normal to $\partial \mathcal{P}$ and:

$$\rho^* = \begin{cases} e\mathbf{q} \cdot \mathbf{n}, & \text{in } \mathcal{P}, \\ 0, & \text{in } \mathbb{R}^3 / \mathcal{P}. \end{cases} \quad (6.7)$$

We define the Gibbs free-energy generated by the excitation carriers as the electrostatic energy associated to (6.6) plus an entropic term which depends on the

excitation carrier density

$$S(\mathcal{P}) = \int_{\mathbb{R}^3} \frac{1}{2} \epsilon \|\text{grad} \varphi\|^2 + \theta k_B \int_{\mathcal{P}} \mathfrak{F}(\mathbf{n}), \quad (6.8)$$

where k_B is the Boltzmann constant and θ is the absolute temperature.

Let $\Pi_{\text{self}}(\mathcal{P})$ be the *Scintillation self-power*, that is the power which the charge carriers in \mathcal{P} expend on \mathcal{P} itself: then, by following a constitutive assumption introduced in (DeSimone and Podio Guidugli, 1996) we set:

$$\Pi_{\text{self}}(\mathcal{P}) + \frac{d}{dt} S(\mathcal{P}) = 0; \quad (6.9)$$

by (6.6), from (6.9) and by the Reynold's theorem and a procedure proposed in (DeSimone and Podio Guidugli, 1996) we arrive at:

$$\Pi_{\text{self}}(\mathcal{P}) = - \int_{\mathcal{P}} (\mathbf{g} \cdot \dot{\mathbf{n}} + \mathbf{T}^{ms} \cdot \text{grad} \mathbf{v}), \quad (6.10)$$

where \mathbf{v} is the material velocity:

$$\mathbf{v}(y, t) = \left. \frac{\partial y}{\partial t}(x, t) \right|_{x(y, t)}. \quad (6.11)$$

In (6.10) the *Scintillation potential*, the k -dimensional array whose components represent the potential associated to each charge carrier descriptor and which expends power for the rate-of-change of the excitation carriers densities, is defined by:

$$\mathbf{g}(\mathbf{n}) = e q \varphi(\mathbf{n}) + \theta k_B \frac{\partial \mathfrak{F}}{\partial \mathbf{n}}(\mathbf{n}), \quad (6.12)$$

whereas the symmetric *Maxwell-Scintillation* stress tensor is defined as:

$$\mathbf{T}^{ms} = \epsilon (\text{grad} \varphi \otimes \text{grad} \varphi - \frac{1}{2} \|\text{grad} \varphi\|^2 \mathbf{I}) + (e q \cdot \mathbf{n} \varphi + \theta k_B \mathfrak{F}) \mathbf{I}, \quad (6.13)$$

which differs from the classical Maxwell stress for the presence of the scintillation-depending term.

6.3 Balance Laws

We assume that the scintillation region \mathcal{P} is comprised of a macroscopic continuum superposed to a continuum with microstructure which, according to (Capriz, 1989) we represent with a director $\mathbf{d} = \mathbf{d}(y, t)$ and which belongs to a manifold \mathcal{M} : at this stage, we didn't specify nor the manifold neither the physical meaning of \mathbf{d} . The *volume microforce* \mathbf{b} and the *surface microforce* \mathbf{s} represent the external actions on the microstructure in \mathcal{P} , whereas the *microstress* \mathbf{T} represents the internal action and

the *interactive microforce* \mathbf{k} accounts for the interaction between the microstructure and the macroscopic continua. As far as the macroscopic state variables we assume the *Cauchy stress* tensor \mathbf{T} and the *volume* and *surface densities* pair (\mathbf{b}, \mathbf{s}) whereas we assume that the crystal is *isothermal* with the absolute temperature fixed and uniform.

We may accordingly define the *external power* expended on \mathcal{P} by both the micro- and macroscopic volume and surface densities as:

$$\Pi_{\text{ext}}(\mathcal{P}) = \int_{\mathcal{P}} (\mathbf{b} \cdot \mathbf{v} + \mathbf{b} \cdot \dot{\mathbf{d}}) + \int_{\partial\mathcal{P}} (\mathbf{s} \cdot \mathbf{v} + \mathbf{s} \cdot \dot{\mathbf{d}}), \quad (6.14)$$

and likewise, the *internal power*

$$\Pi_{\text{int}}(\mathcal{P}) = \int_{\mathcal{P}} ((\mathbf{T} + \mathbf{T}^{ms}) \cdot \text{grad}\mathbf{v} + \mathbb{T} \cdot \text{grad}\dot{\mathbf{d}} + \mathbf{k} \cdot \dot{\mathbf{d}}); \quad (6.15)$$

since the *Total power* is given by

$$\Pi(\mathcal{P}) = \Pi_{\text{ext}}(\mathcal{P}) + \Pi_{\text{int}}(\mathcal{P}) - \Pi_{\text{self}}(\mathcal{P}). \quad (6.16)$$

In order to make (6.16) a linear functional of the set $\{\mathbf{v}, \text{grad}\mathbf{v}, \dot{\mathbf{d}}, \text{grad}\dot{\mathbf{d}}\}$ we need to identify the rate-of-change of director with the scintillation potential:

$$\mathbf{g} = \dot{\mathbf{d}}; \quad (6.17)$$

accordingly, $\mathcal{M} \equiv \mathbb{R}^k \cup \{0\}$, and the components of the director represents the *Lagrangian action*:

$$d_j(y, t) = d_j(y, 0) + \int_0^t g_j(y, \tau) d\tau, \quad j = 1, 2, \dots, k. \quad (6.18)$$

By (6.10), (6.14), (6.15), with (6.12) and by the divergence theorem we get

$$\begin{aligned} \Pi(\mathcal{P}, \mathbf{v}, \mathbf{g}) &= \int_{\mathcal{P}} (\text{div}\mathbb{T} - \mathbf{k} + \mathbf{b} - \dot{\mathbf{n}}) \cdot \mathbf{g} + \int_{\partial\mathcal{P}} (\mathbf{s} - \mathbb{T}\mathbf{m}) \cdot \mathbf{g} \\ &+ \int_{\mathcal{P}} (\text{div}(\mathbf{T} + \mathbf{T}^{ms}) + \mathbf{b}) \cdot \mathbf{v} + \int_{\partial\mathcal{P}} (\mathbf{s} - \mathbf{T}\mathbf{m}) \cdot \mathbf{v}; \end{aligned} \quad (6.19)$$

we follow Mariano (2001) and require that the total power (6.19) be invariant under the change of observer

$$\Pi(\mathcal{P}, \mathbf{v}, \mathbf{g}) = \Pi(\mathcal{P}, \mathbf{v}^*, \mathbf{g}^*), \quad \mathbf{g}^* = \mathbf{g} + \mathbf{g}_o, \quad \mathbf{v}^* = \mathbf{v} + \mathbf{v}_o + \mathbf{W}(y - o), \quad (6.20)$$

where \mathbf{g}_o and \mathbf{v}_o are constant and \mathbf{W} is a skew-symmetric tensor. We remark that the total power is invariant for scintillation potentials which differs by a constant, as it is customary, whereas for the velocity we required the usual Galileian and Leibnizian invariance: from such an invariance request we obtain both the macroscopical

$$\begin{aligned} \operatorname{div}(\mathbf{T} + \mathbf{T}^{ms}) + \mathbf{b} &= \mathbf{0}, & \text{in } \mathcal{P} \times [0, \tau), \\ (\mathbf{T} + \mathbf{T}^{ms})\mathbf{m} &= \mathbf{s}, & \text{on } \partial\mathcal{P} \times [0, \tau). \end{aligned} \quad (6.21)$$

and the microscopical balance laws:

$$\begin{aligned} \operatorname{div}\mathbf{T} - \mathbf{k} + \mathbf{b} &= \dot{\mathbf{n}}, & \text{in } \mathcal{P} \times [0, \tau), \\ \mathbf{T}\mathbf{m} &= \mathbf{s}, & \text{on } \partial\mathcal{P} \times [0, \tau). \end{aligned} \quad (6.22)$$

If we multiply both sides of (6.22)₁ by the elementary charge e , we may see that the physical meaning of the microscopical balance laws is, on a dimensional basis, that of the conservation of the k electric currents associated to each charge carrier.

The balance laws (6.21) can be reformulated in a slightly different manner, by writing the Maxwell-scintillation stress tensor as a volume and surface density pair $(\mathbf{b}^*, \mathbf{s}^*)$ defined as

$$\begin{aligned} \mathbf{b}^* &= \epsilon(\operatorname{grad}\operatorname{grad}\varphi)\operatorname{grad}\varphi - (e\mathbf{q} \cdot \mathbf{n})\operatorname{grad}\varphi + (\operatorname{grad}^T \mathbf{n})\mathbf{g}, \\ \mathbf{s}^* &= (\epsilon \frac{1}{2} \|\operatorname{grad}\varphi\|^2 - (e\mathbf{q} \cdot \mathbf{n})\varphi - \theta k_B \tilde{\mathfrak{F}})\mathbf{m}, \end{aligned} \quad (6.23)$$

to get:

$$\begin{aligned} \operatorname{div}\mathbf{T} + \mathbf{b}^* + \mathbf{b} &= \mathbf{0}, & \text{in } \mathcal{P} \times [0, \tau), \\ \mathbf{T}\mathbf{m} &= \mathbf{s}^* + \mathbf{s}, & \text{on } \partial\mathcal{P} \times [0, \tau). \end{aligned} \quad (6.24)$$

6.4 Thermodynamics. Constitutive Relations

We assume that within the scintillation region \mathcal{P} it is well-defined a *Gibbs free-energy* $\psi = \psi(y, t)$ such that the dissipation inequality holds

$$\frac{d}{dt} \int_{\mathcal{P}} \psi \leq \Pi_{\text{int}}(\mathcal{P}), \quad (6.25)$$

and whose local form leads to the *reduced dissipation inequality*:

$$\dot{\psi} - \mathbf{T} \cdot \operatorname{grad}\mathbf{v} - \mathbf{T} \cdot \operatorname{grad}\dot{\mathbf{d}} - \mathbf{k} \cdot \dot{\mathbf{d}} \leq 0. \quad (6.26)$$

The constitutive hypotheses we are going to assume for the deformable scintillating crystals are the following:

- the Gibbs free-energy depends at most on \mathbf{F} , \mathbf{d} and \mathbf{D} :

$$\psi = \hat{\psi}(\mathbf{F}, \mathbf{d}, \mathbf{D}); \quad (6.27)$$

- the microstress and the interactive microforce can be split additively into a conservative and a non-conservative (dissipative) part:

$$\mathbf{T} = \mathbf{T}^c + \mathbf{T}^d, \quad \mathbf{k} = \mathbf{k}^c + \mathbf{k}^d. \quad (6.28)$$

In force of these constitutive hypotheses then (6.26) can be rewritten, by the means of the identities (Gurtin et al, 2010)

$$\text{grad} \mathbf{v} = \dot{\mathbf{F}} \mathbf{F}^{-1}, \quad \text{gradd} = \dot{\mathbf{D}} + \mathbf{D} \text{grad} \mathbf{v}, \quad \mathbf{D} = \text{gradd}, \quad (6.29)$$

as

$$\dot{\psi} - (\mathbf{T} + \mathbf{D}^T \mathbf{T}^c) \mathbf{F}^{-T} \cdot \dot{\mathbf{F}} - \mathbf{T}^c \cdot \dot{\mathbf{D}} - \mathbf{k}^c \cdot \dot{\mathbf{d}} - \mathbf{T}^d \cdot \text{grad} \mathbf{g} - \mathbf{k}^d \cdot \mathbf{g} \leq 0, \quad (6.30)$$

which in turn leads to:

$$\begin{aligned} & \left(\frac{\partial \hat{\psi}}{\partial \mathbf{F}} - \mathbf{T} - \mathbf{D}^T \mathbf{T}^c \right) \cdot \dot{\mathbf{F}} + \left(\frac{\partial \hat{\psi}}{\partial \mathbf{D}} - \mathbf{T}^c \right) \cdot \dot{\mathbf{D}} \\ & + \left(\frac{\partial \hat{\psi}}{\partial \mathbf{d}} - \mathbf{k}^c \right) \cdot \dot{\mathbf{d}} - \mathbf{T}^d \cdot \text{grad} \mathbf{g} - \mathbf{k}^d \cdot \mathbf{g} \leq 0. \end{aligned} \quad (6.31)$$

By a customary procedure then from (6.31) we are led to the constitutive relations:

$$\begin{aligned} \mathbf{T}(\mathbf{F}, \mathbf{d}, \mathbf{D}) &= \frac{\partial \hat{\psi}}{\partial \mathbf{F}} - \mathbf{D}^T \frac{\partial \hat{\psi}}{\partial \mathbf{D}}, \\ \mathbf{T}^c(\mathbf{F}, \mathbf{d}, \mathbf{D}) &= \frac{\partial \hat{\psi}}{\partial \mathbf{D}}, \\ \mathbf{k}^c(\mathbf{F}, \mathbf{d}, \mathbf{D}) &= \frac{\partial \hat{\psi}}{\partial \mathbf{d}}, \end{aligned} \quad (6.32)$$

and, by a Lemma given in Gurtin and Voorhees (1993), to the representation of the dissipative terms by the means of two $m \times m$ positive definite matrices \mathbb{S} and \mathbb{H} :

$$\begin{aligned} \mathbf{T}^d(\mathbf{F}, \mathbf{d}, \mathbf{D}, \mathbf{g}, \text{grad} \mathbf{g}) &= \mathbb{S}(\mathbf{F}, \mathbf{d}, \mathbf{D}, \mathbf{g})[\text{grad} \mathbf{g}], \quad \mathbf{T}_{ij}^d = \mathbb{S}_{ijkl} \mathbf{g}_{h,k}, \\ \mathbf{k}^d(\mathbf{F}, \mathbf{d}, \mathbf{D}, \mathbf{g}, \text{grad} \mathbf{g}) &= \mathbb{H}(\mathbf{F}, \mathbf{d}, \mathbf{D}, \text{grad} \mathbf{g}) \mathbf{g}, \quad \mathbf{k}_i^d = \mathbb{H}_{ij} \mathbf{g}_j, \end{aligned} \quad (6.33)$$

to this regard we remark that, since by (6.12), (6.17) and (6.18) \mathbf{d} , \mathbf{D} , \mathbf{g} and $\text{grad} \mathbf{g}$ depends implicitly on \mathbf{n} , then we can formally rewrite (6.33) as in (Davi, 2019):

$$\begin{aligned} \mathbf{T}^d(\mathbf{F}, \mathbf{n}, \text{grad} \mathbf{g}) &= \mathbb{S}(\mathbf{F}, \mathbf{n})[\text{grad} \mathbf{g}], \\ \mathbf{k}^d(\mathbf{F}, \mathbf{n}, \mathbf{g}) &= \mathbb{H}(\mathbf{F}, \mathbf{n}) \mathbf{g}. \end{aligned} \quad (6.34)$$

By using (6.28), (6.32) and (6.34) into (6.22) we finally arrive at the evolution equations for the excitation carrier density:

$$\begin{aligned} \text{div} \left(\frac{\partial \hat{\psi}}{\partial \mathbf{D}} + \mathbb{S}[\text{grad} \mathbf{g}] \right) - \left(\frac{\partial \hat{\psi}}{\partial \mathbf{d}} + \mathbb{H} \mathbf{g} \right) + \mathbf{b} &= \dot{\mathbf{n}} \quad \text{in } \mathcal{P} \times [0, \tau), \\ \mathbf{g} &= \dot{\mathbf{d}}, \\ \left(\frac{\partial \hat{\psi}}{\partial \mathbf{D}} + \mathbb{S}[\text{grad} \mathbf{g}] \right) \mathbf{m} &= \mathbf{s} \quad \text{in } \partial \mathcal{P} \times [0, \tau), \end{aligned} \quad (6.35)$$

which are coupled with the Laplace equation (6.6)

$$\begin{aligned} -\epsilon \Delta \varphi &= \rho^*, & \text{in } \mathbb{R}^3 \times [0, \tau) \\ \llbracket \text{grad} \varphi \rrbracket \cdot \mathbf{m} &= 0, & \text{on } \partial \mathcal{P} \times [0, \tau), \end{aligned} \quad (6.36)$$

and with the macroscopic balance laws, in the form (6.24),

$$\begin{aligned} \text{div} \left(\frac{\partial \hat{\psi}}{\partial \mathbf{F}} \mathbf{F}^T - \mathbf{D}^T \frac{\partial \hat{\psi}}{\partial \mathbf{D}} \right) + \mathbf{b}^* + \mathbf{b} &= \mathbf{0}, & \text{in } \mathcal{P} \times [0, \tau), \\ \text{skw} \left(\frac{\partial \hat{\psi}}{\partial \mathbf{F}} \mathbf{F}^T - \mathbf{D}^T \frac{\partial \hat{\psi}}{\partial \mathbf{D}} \right) &= \mathbf{0}, & (6.37) \\ \left(\frac{\partial \hat{\psi}}{\partial \mathbf{F}} \mathbf{F}^T - \mathbf{D}^T \frac{\partial \hat{\psi}}{\partial \mathbf{D}} \right) \mathbf{m} &= \mathbf{s}^* + \mathbf{s}, & \text{in } \partial \mathcal{P} \times [0, \tau). \end{aligned}$$

In the evolution equation (6.35)₁ we have two different regimes: one which depends on the pair $(\mathbf{g}, \text{grad} \mathbf{g})$ and which is purely dissipative, the other which depends on the pair (\mathbf{d}, \mathbf{D}) : the first regime describes the generation and recombination of excitons into photons, a process whose decay in time is fast, in the order of few nanoseconds. With the second regime, we may describe phenomena that decays in longer times, like *e.g.* persistent luminescence and related phenomena, which evolves in a time scale that ranges from seconds to hours and accordingly can be assumed as conservative at the scale of scintillation. In the macroscopic balance laws, instead, the coupling between scintillation and stress is given by the pair $(\mathbf{b}^*, \mathbf{s}^*)$ and through the presence of $\mathbf{D} = \text{gradd}$.

6.5 Reaction-Diffusion-Drift Equations for Scintillators: Constitutive Assumptions

If we assume that the Gibbs free-energy simply represents the elastic energy density:

$$\psi = \tilde{\psi}(\mathbf{C}), \quad \mathbf{C} = \mathbf{F}^T \mathbf{F}, \quad (6.38)$$

and assume that the volume and surface microforces are negligible, $\mathbf{b} = \mathbf{0}$, $\mathbf{s} = \mathbf{0}$, then from (6.32)_{1,2} the conservative part of the stress and interactive microforce both vanish and $\mathbf{T} = \mathbf{T}^d$, $\mathbf{k} = \mathbf{k}^d$, with (6.34) still holding. Then, from (6.22) we obtain the evolution equations in term of the scintillation potential:

$$\begin{aligned} \text{div} \mathbb{S}[\text{grad} \mathbf{g}] - \mathbb{H} \dot{\mathbf{g}} &= \dot{\mathbf{n}}, & \text{in } \mathcal{P} \times [0, \tau), \\ \mathbb{S}[\text{grad} \mathbf{g}] \mathbf{m} &= \mathbf{0}, & \text{on } \partial \mathcal{P} \times [0, \tau), \end{aligned} \quad (6.39)$$

and which can be put in the gradient-flow form (Mielke, 2011)

$$\dot{\mathbf{n}} = -D\Psi(\text{gradg}, \mathbf{g}), \quad \Psi = \int_{\mathcal{P}} \frac{1}{2} (\mathbb{S}[\text{gradg}] \cdot \text{gradg} + \mathbb{H}[\mathbf{g}] \cdot \mathbf{g}), \quad (6.40)$$

where D denotes the Frechet derivative and Ψ is the *conjugate dissipation* functional.

As far as the macroscopic balance laws are concerned, they reduces to a simpler form where the coupling with scintillation is given only by the pair $(\mathbf{b}^*, \mathbf{s}^*)$:

$$\begin{aligned} \text{div} \left(\frac{\partial \hat{\psi}}{\partial \mathbf{F}} \mathbf{F}^T \right) + \mathbf{b}^* + \mathbf{b} &= \mathbf{0}, \quad \text{in } \mathcal{P} \times [0, \tau), \\ \text{skw} \left(\frac{\partial \hat{\psi}}{\partial \mathbf{F}} \mathbf{F}^T \right) &= \mathbf{0}, \\ \left(\frac{\partial \hat{\psi}}{\partial \mathbf{F}} \mathbf{F}^T \right) \mathbf{m} &= \mathbf{s}^* + \mathbf{s}, \quad \text{in } \partial \mathcal{P} \times [0, \tau). \end{aligned} \quad (6.41)$$

We are going now to write the evolution equation (6.39) in terms of the excitation carrier vector \mathbf{n} for a generic choice of the entropic term $\mathfrak{F}(\mathbf{n})$. Since from (6.12):

$$\text{gradg} = e\mathbf{q} \otimes \text{grad}\varphi + \theta k_B \mathbb{F} \text{gradn}, \quad \mathbb{F}(\mathbf{n}) = \frac{\partial^2 \mathfrak{F}}{\partial \mathbf{n}^2}(\mathbf{n}), \quad (6.42)$$

then by (6.33) we have

$$\mathbf{T} = \mathbb{S}(\mathbf{F}, \mathbf{n})[\text{gradg}] = e\mathbb{S}(\mathbf{F}, \mathbf{n})[\mathbf{q} \otimes \text{grad}\varphi] + \theta k_B \mathbb{S}(\mathbf{F}, \mathbf{n})\mathbb{F}(\mathbf{n})[\text{gradn}]. \quad (6.43)$$

First of all we define the $k \times k$ *Diffusivity* matrix \mathbb{D} as

$$\mathbb{D}(\mathbf{F}, \mathbf{n}) = \theta k_B \mathbb{S}(\mathbf{F}, \mathbf{n})\mathbb{F}(\mathbf{n}); \quad (6.44)$$

then the $k \times k$ *Mobility* matrix \mathbb{M} is related to the Diffusivity matrix by the means of the relation (Lindholm and Ayers, 1968; San Li and Lindholm, 1968; Nillson, 1973)

$$\mathbb{M} = -\mathbb{N}^{-1}\mathbb{G}\mathbb{D}, \quad (6.45)$$

where the $k \times k$ matrix \mathbb{G} is

$$\mathbb{G} = \frac{d\mathbf{n}}{d(\mathbf{q}\varphi)}, \quad (6.46)$$

and $\mathbb{N}(\mathbf{n})$ is the $k \times k$ matrix:

$$\mathbb{N}(\mathbf{n}) \equiv \text{diag}\{n_1, \dots, n_k\}, \quad (6.47)$$

whose formal inverse $\mathbb{N}^{-1}(\mathbf{n})$ is the $m \times m$ diagonal matrix whose entries are $1/n_k$ for $n_k \neq 0$ and 0 for $n_k = 0$.

Accordingly, from (6.45) and provided \mathbb{G} be invertible, we have the generalized Einstein–Smoluchowsky relation

$$\mathbb{D} = -\mathbb{G}^{-1}\mathbb{N}\mathbb{M}, \quad (6.48)$$

and then, by (6.44) and (6.48),

$$e\mathbb{S} = \frac{e}{\theta k_B} \mathbb{D}\mathbb{F}^{-1} = -\frac{e}{\theta k_B} \mathbb{G}^{-1} \mathbb{N}\mathbb{M}\mathbb{F}^{-1}. \quad (6.49)$$

If we denote

$$\mathbb{M}^* = -\frac{e}{\theta k_B} \mathbb{G}^{-1} \mathbb{N}\mathbb{M}, \quad (6.50)$$

then from the expression (6.43) for the microstress we recover the Nernst–Planck relation:

$$\mathbb{T} = \mathbb{D}[\text{grad}\mathbf{n}] + \mathbb{M}^* \mathbb{F}^{-1}[\mathbf{q} \otimes \text{grad}\varphi]. \quad (6.51)$$

We turn our attention to the dissipative microforce, which describes the recombination mechanisms, both radiative and non-radiative. We follow the analogous treatment given by Mielke (2011) for semiconductors and then we deal with the recombination mechanism with the language of the chemical reactions. Therefore, we assume that we may have s reversible recombination mechanisms described by the $2s$, k -dimensional arrays:

$$\mathbf{a}^h \equiv (a_1^h, a_2^h, \dots, a_k^h), \quad \mathbf{b}^h \equiv (b_1^h, b_2^h, \dots, b_k^h), \quad h = 1, \dots, s, \quad (6.52)$$

whose recombination rates $k^h = k^h(\mathbf{F})$ may depend on the deformation

$$\mathbf{a}^h \xrightleftharpoons{k^h} \mathbf{b}^h, \quad h = 1, 2, \dots, s. \quad (6.53)$$

Then we assume as a constitutive hypothesis, by following the suggestions provided in Liero et al (2017); Peletier et al (2020); Esposito et al (2021) that in the conjugate dissipation functional (6.40)₂ the term ruled by the matrix \mathbb{H} can be represented as

$$\frac{1}{2} \mathbb{H}(\mathbf{F}, \mathbf{n}) \mathbf{g} \cdot \mathbf{g} = \sum_{h=1}^s k^h(\mathbf{F}) \alpha\left(\frac{\mathbf{n}^{\mathbf{a}^h}}{w^{\mathbf{a}^h}}, \frac{\mathbf{n}^{\mathbf{b}^h}}{w^{\mathbf{b}^h}}\right) \xi((\mathbf{a}^h - \mathbf{b}^h) \cdot \mathbf{g}), \quad (6.54)$$

where

- the *dual dissipation functional* $\xi : \mathbb{R} \rightarrow \mathbb{R}^+$ is such that

$$\mathbb{R} \ni s \mapsto \xi(s) \in \mathbb{R}, \quad \xi(0) = \xi'(0) = 0, \quad \xi''(s) > 0, \forall s \in \mathbb{R}; \quad (6.55)$$

- the *interpolation function* $\alpha(u, v) : \mathbb{R}^+ \times \mathbb{R}^+ \rightarrow \mathbb{R}^+$ obeys

$$\min\{u, v\} \leq \alpha(u, v) \leq \max\{u, v\}. \quad (6.56)$$

- the symbol \mathbf{v}^u denotes the product:

$$\mathbf{v}^u = \prod_{j=1}^k v_j^{u_j} = v_1^{u_1} v_2^{u_2} \dots v_k^{u_k}; \quad (6.57)$$

- the *detailed balance* condition holds: in writing (6.54) we implicitly assumed that the recombination mechanism represents what is called in the language of chemical reactions a detailed balance, that is for any recombination mechanism there exists a steady recombination state $\mathbf{w} \equiv (w_1, \dots, w_k)$ such that

$$k_f^h \mathbf{w}^{a^h} = k_b^h \mathbf{w}^{b^h} = k^h, \quad h = 1, 2, \dots, s, \quad (6.58)$$

where $k_{f,b}^h$ represent the forward and backward recombination rates, respectively.

The recombination term follows from (6.54) by keeping in mind that the Onsager relation holds

$$\mathbb{H}(\mathbf{F}, \mathbf{n})\mathbf{g} = \mathbf{r}(\mathbf{F}, \mathbf{n}), \quad (6.59)$$

and that

$$\mathbb{H}\mathbf{g} = D \int_{\mathcal{P}} \frac{1}{2} \mathbb{H}\mathbf{g} \cdot \mathbf{g}, \quad (6.60)$$

from which we get

$$\mathbf{r}(\mathbf{F}, \mathbf{n}) = \sum_{h=1}^s k^h(\mathbf{F}) \alpha \left(\frac{n^{a^h}}{w^{a^h}}, \frac{n^{b^h}}{w^{b^h}} \right) \xi' \left((a^h - b^h) \cdot \mathbf{g} \right) (a^h - b^h). \quad (6.61)$$

The recombination mechanisms described by (6.52) involve charged excitation carriers: since for any mechanism the charge must be conserved, hence

$$\mathbf{q} \cdot \mathbf{a}^h = \mathbf{q} \cdot \mathbf{b}^h, \quad h = 1, 2, \dots, s, \quad (6.62)$$

and we have the condition of electrical neutrality of each recombination mechanism

$$\mathbf{q} \cdot (\mathbf{a}^h - \mathbf{b}^h) = 0, \quad h = 1, 2, \dots, s; \quad (6.63)$$

therefore, by (6.63) the recombination term (6.61) modifies into

$$\mathbf{r}(\mathbf{F}, \mathbf{n}) = \sum_{h=1}^s k^h(\mathbf{F}) \alpha \left(\frac{n^{a^h}}{w^{a^h}}, \frac{n^{b^h}}{w^{b^h}} \right) \xi' \left(\theta k_B (\mathbf{a}^h - \mathbf{b}^h) \cdot \frac{\partial \mathfrak{F}}{\partial \mathbf{n}} \right) (\mathbf{a}^h - \mathbf{b}^h), \quad (6.64)$$

whose explicit expression depends of the set $(\alpha, \xi, \mathfrak{F})$ which will be the object of constitutive assumptions.

We say that the set $(\alpha, \xi, \mathfrak{F})$ is *compatible* if, for $h = 1, 2, \dots, s$

$$\alpha \left(\frac{n^{a^h}}{w^{a^h}}, \frac{n^{b^h}}{w^{b^h}} \right) \xi' \left(\theta k_B (\mathbf{a}^h - \mathbf{b}^h) \cdot \frac{\partial \mathfrak{F}}{\partial \mathbf{n}}(\mathbf{n}) \right) = \frac{n^{a^h}}{w^{a^h}} - \frac{n^{b^h}}{w^{b^h}}; \quad (6.65)$$

then a compatible set leads to a polynomial expression for the recombination term, like the one which is widely used into the existing phenomenological models for scintillation like *e.g.* in Bizzarri et al (2009b,a); Moses et al (2012),

$$\mathbf{r}(\mathbf{F}, \mathbf{n}) = \sum_{h=1}^s k^h(\mathbf{F}) \left(\frac{n^{\mathbf{a}^h}}{w^{\mathbf{a}^h}} - \frac{n^{\mathbf{b}^h}}{w^{\mathbf{b}^h}} \right) (\mathbf{a}^h - \mathbf{b}^h). \quad (6.66)$$

From (6.39) and by (6.51) and (6.64), we arrive at a Reaction-Diffusion-Drift evolution equations for the charge carriers densities

$$\operatorname{div}(\mathbb{D}[\operatorname{grad} \mathbf{n}] + \mathbb{M}^* \mathbb{F}^{-1}[\mathbf{q} \otimes \nabla \varphi]) - \mathbf{r} = \dot{\mathbf{n}}, \quad \text{in } \mathcal{P} \times [0, \tau), \quad (6.67)$$

$$\mathbb{D}[\operatorname{grad} \mathbf{n}] \mathbf{m} = \mathbf{0}, \quad \text{in } \partial \mathcal{P} \times [0, \tau),$$

where we took into account the boundary condition (6.36)₂ and which is coupled with (6.41) and (6.36).

As a final remark, we may notice that we can choose the scintillation volume \mathcal{P} as the smallest volume such that on its boundary the Neumann-type boundary conditions (6.36)₂ and (6.67)₂ hold: then we can safely assume \mathcal{P} as the smallest ball where the generation and recombination take place with no electric field and current fluxes across its boundary $\partial \mathcal{P}$.

6.5.1 The Gibbs Entropy

We made, in this and the following subsections, some constitutive assumptions on the set $(\alpha, \xi, \mathfrak{F})$ which lead to different expressions for the mobility and the recombination terms in (6.67) and whose mathematical consequences are in some cases yet to be studied.

We begin by choosing for the entropy functional $\mathfrak{F}(\mathbf{n})$ the Gibbs entropy, which is associated to the Gibbs-Boltzmann statistics:

$$\mathfrak{F}(\mathbf{n}) = \sum_{k=1}^m n_k \left(\log\left(\frac{n_k}{c_k}\right) - 1 \right), \quad (6.68)$$

where the normalizing constants c_k have dimension Lengt^{-3} . The Gibbs entropy describes an ensemble entropy, defined as a weighted sum over entropies of all the microstates, expressed by an analogous to the Boltzmann entropy definition for a macrostate. Accordingly, it appears more appropriate to describe a system with low energy and non-interacting particles, a description which is not completely suitable for the charge carriers densities. However, as we shall remark later, it allows for a simpler mathematical formulation of the evolution equation (6.67).

From (6.68), by using (6.45) and then (6.49), we obtain

$$\frac{\partial \mathfrak{F}}{\partial \mathbf{n}} = \log\left(\frac{\mathbf{n}}{\mathbf{c}}\right) = \left(\log\left(\frac{n_1}{c_1}\right), \dots, \log\left(\frac{n_k}{c_k}\right) \right), \quad \mathbb{F} = \frac{\partial^2 \mathfrak{F}}{\partial \mathbf{n}^2} = \mathbb{N}^{-1}; \quad (6.69)$$

further, since by (6.69) relation (6.12) can be inverted to get

$$n = c \exp\left(\frac{\mathfrak{g} - e\mathfrak{q}\varphi}{\theta k_B}\right), \quad (6.70)$$

then we have the explicit result

$$\mathbb{G} = -\frac{e}{\theta k_B} \mathbb{N}, \quad (6.71)$$

which leads to

$$\mathbb{M}^* \mathbb{F}^{-1} = \mathbb{M} \mathbb{N}. \quad (6.72)$$

We turn our attention to the recombination term $r(\mathbf{F}, n)$ to search for the interpolation function and the dual dissipation functional which, together with the Gibbs entropy, make the set $(\alpha, \xi, \mathfrak{F})$ admissible and the recombination term polynomial. The simplest choice is a quadratic dual dissipation functional

$$\xi(s) = \frac{1}{2} s^2, \quad \xi'(s) = s, \quad (6.73)$$

which in turn implies the *logarithmic mean* as interpolation function, as in Mielke (2011),

$$\alpha(u, v) = \begin{cases} \frac{u - v}{\theta k_B (\log u - \log v)}, & u \neq v, \\ u, & u = v; \end{cases} \quad (6.74)$$

in this case, provided the identification $w = c$, the recombination term reduces to a polynomial function of n ,

$$r(\mathbf{F}, n) = \sum_{h=1}^s k^h(\mathbf{F}) \left(\frac{n^{a^h}}{c^{a^h}} - \frac{n^{b^h}}{c^{b^h}} \right) (a^h - b^h). \quad (6.75)$$

A different choice was instead proposed in Mielke et al (2014) (*see also* Liero et al, 2017; Peletier et al, 2020; Esposito et al, 2021): the dual dissipation functional, motivated by a large-deviation Markovian principle and which still leads to a gradient-flow structure, is of the hyperbolic cosine type:

$$\xi(s) = 4 \left(\cosh \frac{s}{2} - 1 \right), \quad (6.76)$$

which reduces to the quadratic functional (6.73) to within higher-order terms

$$\xi(s) = \frac{1}{2} s^2 + O(s^4). \quad (6.77)$$

In this case the interpolation function which makes the set $(\alpha, \xi, \mathfrak{F})$ admissible is the (modified) *geometric mean*:

$$\alpha(u, v) = 2 \sqrt{(uv)^{\theta k_B}} \frac{v - u}{v^{\theta k_B} - u^{\theta k_B}}, \quad (6.78)$$

and then we recover once again (6.75).

Provided (6.72) and (6.75) hold, then from the evolution equation (6.35)₁ we arrive at the same reaction-diffusion-drift equation obtained in Daví (2019),

$$\operatorname{div}(\mathbb{D}[\operatorname{grad}n] + \operatorname{MIN}[\mathbf{q} \otimes \nabla\varphi]) - \mathbf{r} = \dot{n}, \quad \text{in } \mathcal{P} \times [0, \tau), \tag{6.79}$$

$$\mathbb{D}(\theta)[\operatorname{grad}n]\mathbf{m} = \mathbf{0}, \quad \text{in } \partial\mathcal{P} \times [0, \tau);$$

equations (6.79)₁ are the same as proposed in Vasil’ev (2008) by following ideas given by Fok (1964); Antonov-Romanovskiy (1966) and which was widely used in its *Kinetic* or *Diffusive* approximation (disregarding respectively the microstress or the interactive microforce) in many experimental and theoretical papers like *e.g* Bizzarri and Dorenbos (2007); Bizzarri et al (2009b,a); Li et al (2011); Williams et al (2011); Singh (2011); Moses et al (2012); Khodyuk and Dorenbos (2012); Grim et al (2012); Khodyuk et al (2012); Singh and Koblov (2015); Williams et al (2015); Gridin et al (2015); Lu et al (2015); Vasil’ev (2017); Lu et al (2017). The same result was obtained, by starting from a very different approach, in (Albinus et al, 2002), (Mielke, 2011) for semiconductors. Such an equation has obtained a great attention in recent years (Fischer, 2017; Chen and Jüngel, 2017; Fellner and Kniely, 2018; Chen and Jüngel, 2019), with results concerning both the existence of solutions and the estimate of the scintillator decay time—for a comprehensive review of these mathematical aspects, see also Daví (2021).

6.5.2 The Fermi–Dirac Integrals

The advantages and the limits of the choice (6.68) are discussed in some detail in Mielke (2011): indeed, given the nature of the recombination process in scintillators it would be more appropriate (as in the case of semiconductors) to choose for the term $\mathfrak{F}(n)$ an expression based on the Fermi–Dirac statistics (Blatt, 1957; Dingle, 1957; Blakemore, 1982), as it was proposed in Albinus et al (2002):

$$\mathfrak{F}(n) = \sum_k^m c_k \left(z F_{\gamma-1}^{-1}(z) - F_{\gamma}(F_{\gamma-1}^{-1}(z)) \right), \quad z = \frac{n_k}{c_k}, \tag{6.80}$$

where

$$F_{\gamma}(z) = \frac{1}{\Gamma(\gamma + 1)} \int_0^{\infty} \frac{s^{\gamma}}{1 + \exp(s - z)} ds, \quad \gamma > -1, \tag{6.81}$$

is the Fermi–Dirac integral of index γ (Huang, 2010).

The Fermi–Dirac integral (6.81) has the following properties (Blakemore, 1982; Kim et al, 2019):

- its derivatives obeys

$$F'_{\gamma}(z) = F_{\gamma-1}(z); \tag{6.82}$$

- in the classical Boltzmann limit, non-degenerate case with $z \ll 0$ and small charge carriers density it reduces to

$$F_\gamma(z) \approx \exp(z), \quad (6.83)$$

and we recover the same results we obtained when we used the Gibbs entropy:

- in the Fermi–Dirac degenerate extreme case with $z \gg 0$ and very large charge carriers density it becomes:

$$F_\gamma(z) \approx \frac{1}{\Gamma(\gamma + 2)} z^{\gamma+1}. \quad (6.84)$$

The Fermi–Dirac integral relates the energy levels, here represented by the scintillation and the electric potential, with the charge carriers density and in the standard parabolic band-edges approximation the index γ takes the value $\gamma = 3/2$ (Albinus et al, 2002): therefore, we shall henceforth assume this value for which, given its importance, some explicit results are known. The scintillation potential and its gradient are given, in the case $\gamma - 1 = 1/2$, by

$$\begin{aligned} \mathbf{g} &= e\mathbf{q}\phi + \theta k_B \mathbf{f}, \\ \text{gradg} &= e\mathbf{q} \otimes \text{grad}\phi + \theta k_B \mathbb{F}(\mathbf{n})[\text{gradn}], \end{aligned} \quad (6.85)$$

where the k -dimensional array \mathbf{f} is given by

$$\mathbf{f}\left(\frac{\mathbf{n}}{\mathbf{c}}\right) = \left(F_{1/2}^{-1}\left(\frac{n_1}{c_1}\right), F_{1/2}^{-1}\left(\frac{n_2}{c_2}\right), \dots, F_{1/2}^{-1}\left(\frac{n_k}{c_k}\right)\right), \quad (6.86)$$

whereas

$$\mathbb{F} = \text{diag}\left\{\left(c_1 F_{-1/2}\left(\frac{n_1}{c_1}\right)\right)^{-1}, \dots, \left(c_k F_{-1/2}\left(\frac{n_k}{c_k}\right)\right)^{-1}\right\}. \quad (6.87)$$

As a consequence of (6.85)₁ and (6.82), then (6.70) is replaced by

$$n_i = c_i F_{\gamma-1}\left(\frac{eq_i \phi - g_i}{k_B \theta}\right), \quad i = 1, 2, \dots, k, \quad (6.88)$$

and then from (6.46) we get

$$\mathbb{N}^{-1} \mathbb{G} = -\frac{\theta k_B}{e} \text{diag}\left\{\frac{F_{-1/2}\left(\frac{n_1}{c_1}\right)}{F_{1/2}\left(\frac{n_1}{c_1}\right)}, \dots, \frac{F_{-1/2}\left(\frac{n_i}{c_i}\right)}{F_{1/2}\left(\frac{n_i}{c_i}\right)}\right\}. \quad (6.89)$$

The diffusivity matrix \mathbb{D} is still defined by the relation (6.44) with \mathbb{F} given by (6.87), whereas from the generalized Einstein–Smoluchowsky relation (6.48) we get

$$\mathbb{D} = \frac{\theta k_B}{e} \text{diag}\left\{\frac{F_{1/2}\left(\frac{n_1}{c_1}\right)}{F_{-1/2}\left(\frac{n_1}{c_1}\right)}, \dots, \frac{F_{1/2}\left(\frac{n_i}{c_i}\right)}{F_{-1/2}\left(\frac{n_i}{c_i}\right)}\right\} \mathbb{M}, \quad (6.90)$$

and

$$\mathbb{M}^* = \text{diag} \left\{ \frac{F_{1/2}(\frac{n_1}{c_1})}{F_{-1/2}(\frac{n_1}{c_1})}, \dots, \frac{F_{1/2}(\frac{n_i}{c_i})}{F_{-1/2}(\frac{n_i}{c_i})} \right\} \mathbb{M}. \quad (6.91)$$

When the Fermi–Dirac integrals are taken into account, the recombination term modifies strongly: indeed as pointed out in Mielke (2011) a linear combination of scintillation potentials can no longer be written as a product of excitation carrier densities, which is a special property of the logarithm which is associated to the Gibbs entropy. Accordingly, we generalize here the results given in Albinus et al (2002) and Mielke (2011) and write the recombination term as a function of a linear combination of the scintillation potentials

$$r(\mathbf{F}, n) = \sum_{h=1}^s k^h(\mathbf{F}) \zeta'((a^h - b^h) \cdot \mathbf{g})(a^h - b^h), \quad (6.92)$$

which by (6.63) can be rewritten as

$$r(\mathbf{F}, n) = \sum_{h=1}^s k^h(\mathbf{F}) \zeta' \left(\theta k_B (a^h - b^h) \cdot \mathbf{f} \left(\frac{n}{c} \right) \right) (a^h - b^h). \quad (6.93)$$

Finally, the evolution equation for the charge carriers is in the case of the Fermi–Dirac is formally identical to (6.67), provided \mathbb{D} , \mathbb{M}^* , \mathbb{F}^{-1} and r are respectively defined by (6.90), (6.91), the inverse of (6.87) and (6.93). These equations need a further investigation in terms of the existence and asymptotic decay of solutions, as is currently done for the boundary value problem (6.79).

Acknowledgements This research is within the scope of CERN R&D Experiment 18 “Crystal Clear Collaboration” and the PANDA Collaboration at GSI-Darmstadt. The author is on sabbatical leave at IMT-School for Advanced Studies in Lucca (I), whose hospitality is acknowledged. I also wish to thank the reviewer for their suggestions.

References

- Albinus G, Gajewski H, Hünlich R (2002) Thermodynamic design of energy models of semiconductor devices. *Nonlinearity* 15:367–383
- Antonov-Romanovskiy V (1966) *Photoluminescence Kinetics of Crystal Phosphors*. Nauka, Moscow
- Bizzarri G, Dorenbos P (2007) Charge carriers and exciton dynamics in $\text{LaBr}_3:\text{Ce}^{3+}$ scintillators: Experiment and model. *Physical Review B* 75:184,302
- Bizzarri G, Cherepy N, Chong W, Hull G, Moses W, Payne S, Singh J, Valentine J, Vasil’ev A, Williams R (2009a) Progress in studying scintillator proportionality: Phenomenological model. *IEEE Transaction on Nuclear Science* 56:2313–2316
- Bizzarri G, Moses W, Singh J, Vasil’ev A, Williams R (2009b) An analytical model of nonproportional scintillator light yield in terms of recombination rates. *J of Applied Physics* 105:044,507
- Blakemore JS (1982) Approximations for Fermi–Dirac integrals, especially the function $f_{1/2}(\eta)$ used to describe electron density in a semiconductor. *Solid State Electronics* 25(11):1067–1076

- Blatt FJ (1957) Theory of mobility of electrons in solids. *Solid State Physics* 4:199–366
- Capriz G (1989) Continua with microstructure. *Springer Tracts in Natural Philosophy*, Springer Verlag, Berlin
- Chen X, Jüngel A (2017) Global renormalized solutions to reaction-cross diffusion systems. preprint ArXiv177101463v1 pp 1–30
- Chen X, Jüngel A (2019) Weak-strong uniqueness of renormalized solutions to reaction-cross-diffusion systems. *Mathematical Models and Methods in Applied Sciences* 29(02):237–270
- Daví F (2019) A Continuum Theory of Scintillation in Inorganic Scintillating Crystals. *European Physical Journal B* 92(1):16
- Daví F (2021) A brief overview of existence results and decay time estimates for a mathematical modeling of scintillating crystals. *Math Meth Appl Sci* 44:13,833–13,854
- DeSimone A, Podio Guidugli P (1996) On the continuum theory of deformable ferromagnetic solids. *Arch Rat Mech Anal* 136:201–233
- Dingle RB (1957) The Fermi–Dirac integrals. *Appl sci Res., Section B* 6:225–239
- Esposito A, Patacchini F, Schlichting A, Slepcev D (2021) Nonlocal-interaction Equation on Graphs: Gradient Flow Structure and Continuum Limit. *Arch Rational Mech Anal* 240:699–760
- Fellner K, Kniely M (2018) On the entropy method and exponential convergence to equilibrium for a recombination-drift-diffusion system with self-consistent potential. *Applied Mathematics Letters* 79:196–204
- Fischer J (2017) Weak-strong uniqueness of solutions to entropy-dissipating reaction-diffusion equations. *Nonlinear Analysis* 159:181–207
- Fok M (1964) Introduction to Luminescence Kinetics of Crystal Phosphors. Nauka, Moscow
- Gridin S, Belsky A, Dujardin C, Getkin A, Shiran N, Vasil'ev A (2015) Kinetic Model of Energy Relaxation in CsI:A (A=TI and In) Scintillators. *The Journal of Physical Chemistry C* 119:20,578–20,590
- Grim J, Li Q, Ucer K, Burger A, Bizarri G, Moses W, Williams R (2012) The roles of thermalized and hot carrier diffusion in determining light yield and proportionality of scintillators. *Phys Status Solidi A* 209:2421–2426
- Gurtin M, Fried E, Anand L (2010) *The Mechanics and Thermodynamics of Continua*. Cambridge University Press, Cambridge (UK)
- Gurtin ME, Voorhees PW (1993) The continuum mechanics of coherent two-phase elastic solids with mass transport. *Proc R Society London A* 440:323–343
- Huang K (2010) *Introduction to Statistical Physics, Second Edition*. International series of monographs on electronics and instrumentation, CRC press, Boca Raton
- Inokuti M (1971) Inelastic Collisions of Fast Charged Particles with Atoms and Molecules - The Bethe Theory Revisited. *Reviews of Modern Phys* 43(3):297–347
- Jaffe J (2007) Energy and length scales in scintillator nonproportionality. *Nuclear Instruments and Methods in Physics Research A* 570:72–83
- Khodyuk I, Dorenbos P (2012) Trends and patterns of scintillator nonproportionality. *IEEE Transaction on Nuclear Science* 59(6):3320–3331
- Khodyuk I, Quarati F, Alekhin M, Dorenbos P (2012) Charge carrier mobility and non proportionality of LaBr₃:Ce scintillators. arXiv preprint arXiv:12095278
- Kim R, Wang X, M L (2019) Notes on the Fermi–Dirac integrals, 4th edition. <https://arxiv.org/abs/08110116>
- Li Q, Grim J, Williams R, Bizarri G, Moses W (2011) A transport-based model of material trends in nonproportionality of scintillators. *J of Applied Physics* 109:123,716
- Liero M, Mielke A, Peletier M, Renger D (2017) On microscopic origins of generalized gradient structures. *Discrete & Continuous Dynamical Systems - S* 10(1):1–35
- Lindholm FA, Ayers RW (1968) Generalized Einstein Relation for Degenerate Semiconductors. *Proceedings of IEEE May*:317–372
- Lu X, Li Q, Bizarri G, Yang K, Mayhugh M, Menge P, Williams R (2015) Coupled rate and transport equations modeling proportionality of light yield in high-energy electron tracks: CsI at 295 K and 100 K; CsI:tl at 295 K. *Physical Review B* 92:115,207

- Lu X, Gridin S, Williams R, Mayhugh M, Gektin A, Syntfeld-Kazuch A, Swiderski L, Moszynski M (2017) Energy-Dependent Scintillation Pulse Shape and Proportionality of Decay Components for CsI:Tl: Modeling with Transport and Rate Equations. *Physical Review Applied* 7:014,007
- Mariano P (2001) Multifield theories in mechanics of materials. *Adv. Appl. Mech.*, Academic Press, Orlando
- Mielke A (2011) A gradient structure for reaction-diffusion systems and for energy-drift diffusion systems. *Nonlinearity* 24:1329–1346
- Mielke A, Peletier M, Renger D (2014) On the Relation between Gradient Flows and the large-deviation principle, with Applications to Markov Chains and Diffusion. *Potential Anal* 41:1293–1327
- Moses W, Bizzarri G, Williams R, Payne S, Vasil'ev A, Singh J, Li Q, Grim J, Chong W (2012) The Origins of Scintillator Non-Proportionality. *IEEE Transaction on Nuclear Science* 59(5):2038–2044
- Nilsson NG (1973) An Accurate Approximation of the Generalized Einstein Relation for Degenerate Semiconductors. *Phys Stat Sol (a)* 19:K75–K78
- Peletier M, Rossi R, Savaré G, Tse O (2020) Jump processes as generalized gradient flows. *arXiv preprint arXiv:200610624*
- San Li S, Lindholm FA (1968) Alternative Formulation of Generalized Einstein Relation for Degenerate Semiconductors. *Proceedings of IEEE* July:1256–1257
- Singh J (2011) Study of nonproportionality in the light yield of inorganic scintillators. *J of Applied Physics* 110:024,503
- Singh J, Koblov A (2015) Influence of Excitonic Processes in the Energy Resolution of Scintillators. In: Singh J, Williams R (eds) *Excitonic and Photonic Processes in Materials*, Springer Series in Materials Science, vol 203, Springer, Heidelberg
- Ulmer W (2007) Theoretical aspects of energy-range relations, stopping power and energy straggling of protons. *Radiation Physics and Chemistry* 76:1089–1107
- Vasil'ev A (2008) From Luminescence Non-Linearity to Scintillation Non-Proportionality. *IEEE Transaction on Nuclear Science* 55(3):1054–1061
- Vasil'ev A (2017) Microtheory of Scintillation in Crystalline Materials. In: Korzhik M, Gektin A (eds) *Engineering of Scintillation Materials and Radiation Technologies*, Springer Proceedings in Physics, vol 200, Springer, Heidelberg, pp 1–32
- Wang C (1979) *Mathematical Principles of Mechanics and Electromagnetism. Part B: Electromagnetism and Gravitation*. Springer Science, New York
- Williams R, Grim J, Li Q, Ucer K, Moses W (2011) Excitation density, diffusion-drift, and proportionality in scintillators. *Phys Status Solidi B* 248:426–438
- Williams R, Grim G, Li Q, Ucer K, Bizzarri A, Burger A (2015) Scintillation Detectors of Radiation: Excitations at High Densities and Strong Gradients. In: Singh J, Williams R (eds) *Excitonic and Photonic Processes in Materials*, Springer Series in Materials Science, vol 203, Springer, Heidelberg
- Ziegler J (1999) The Stopping of Energetic Light Ions in Elemental Matter. *J Appl Phys/Rev Applied Phys* 85:1249–1272



Chapter 7

Strong Ellipticity within the Strain Gradient Elasticity: Elastic Bar Case

Victor A. Eremeyev, Emanuele Reccia

Abstract In this note we discuss the strong ellipticity condition within the nonlinear strain gradient elasticity. Considering a one-dimensional case, i.e. an elastic bar loaded by a tensile force, we analyze the correspondence of violation of the strong ellipticity condition and compare the results with classic nonlinear elasticity. The correspondence of ellipticity loss to the non-uniqueness of solutions are discussed in more detail.

Keywords: Strong ellipticity · Strain gradient elasticity · Nonlinear elasticity · Elastic bar · Non-uniqueness

7.1 Introduction

Nowadays the generalized models of continua such as the strain gradient elasticity found various fruitful applications in modelling of solids and fluids at the nanoscale, see e.g. Forest et al (2011); Cordero et al (2016); Bertram and Forest (2020), and for description of composite materials with essential difference in mechanical properties of their constituents, see Alibert et al (2003); dell’Isola and Steigmann (2015, 2020); Abdoul-Anziz and Seppecher (2018); Skrzat and Eremeyev (2020); Mawassy et al

V. A. Eremeyev

University of Cagliari, Via Marengo, 2, 09123 Cagliari, Italy

e-mail: victor.eremeev@unica.it

Gdańsk University of Technology, ul. Gabriela Narutowicza 11/12, 80-233 Gdańsk, Poland,

e-mail: vicereme@pg.edu.pl

Institute of Applied Mechanics, Russian Academy of Sciences, Leningradsky prt 7, 125040 Moscow, Russia,

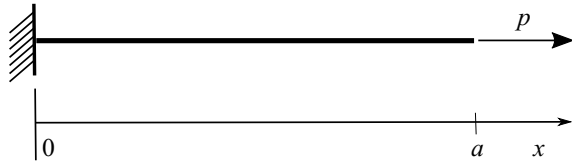
e-mail: eremeyev.victor@gmail.com

E. Reccia

University of Cagliari, Via Marengo, 2, 09123 Cagliari, Italy,

e-mail: emanuele.reccia@unica.it

Fig. 7.1 An elastic bar of length a loaded by force p .



(2021). It is also worth to note the pantographic beam-lattice metamaterials which modelling bring us a particular class of strain gradient media (Rahali et al, 2015; Giorgio et al, 2017; dell’Isola et al, 2019a,b; Giorgio, 2021). Within the strain gradient elasticity there exists a strain energy density given as a function of strains and their gradients or higher-order gradients of the displacements, see the original works by Toupin (1962, 1964); Mindlin (1964, 1965); Mindlin and Eshel (1968). As a result, we face a system of higher-order partial differential equations (PDEs).

Considering it within the theory of elliptic systems of PDEs as in Agranovich (1997); Fichera (1965); Hörmander (1983), we can characterize its properties using the ellipticity notion. Let us note that in the nonlinear elasticity the strong ellipticity condition and its weak form called Hadamard’s inequality plays an important role, see Lurie (1990); Ogden (1997); Truesdell (1966). In particular, it relates to infinitesimal instability of solids. For the strain gradient elasticity the relation between ellipticity and stability is less straightforward, see e.g. Eremeyev (2021) and the reference therein. Moreover, some models of pantographic structures relate to differential operators which are neither strongly elliptic nor elliptic but hypoelliptic ones, see Eremeyev et al (2018b).

The aim of this chapter is to discuss the strong ellipticity condition and its violation within the strain gradient elasticity. In order to underline the possible results of the ellipticity loss we consider a one-dimensional (1D) case, that is stretching of an elastic bar. We consider two cases of the 1D constitutive equations using classic nonlinear elasticity in Section 7.2 and the strain gradient elasticity in Section 7.3. In both cases we have an ordinary differential equation (ODE) as the equilibrium equation and the strong ellipticity results in a simple inequality. So the analysis of ellipticity loss and its relation to the behaviour of solutions is more simple than in the general case. We show that similar to the case of simple nonlinear elastic materials, the loss of ellipticity for strain gradient materials may result in non-existence of smooth solutions of the corresponding boundary-value problem (BVP).

7.2 Nonlinear Elasticity

For a simple nonlinearly elastic material the loss of strong ellipticity may result in some issues related to static solutions, see Lurie (1990); Ogden (1997); Truesdell (1966). In order to demonstrate such a behavior let us discuss a one-dimensional case. In what follows we consider an elastic bar of length a , which is loaded by a load p at the right end of the bar and clamped at the left end, see Fig. 7.1. Introducing

a displacement field

$$u = u(x), \quad u(0) = 0, \tag{7.1}$$

where x is an axial Lagrangian coordinate, we can setup the corresponding problem as follows. The equilibrium conditions follow from the variational equation

$$\delta \mathcal{E} = 0, \tag{7.2}$$

where \mathcal{E} is the functional of total energy given by

$$\mathcal{E} = \int_0^a W \, dx - pu(a), \tag{7.3}$$

$W = W_{ne}(\varepsilon)$ is a strain energy density, and $\varepsilon = u_x$ is a strain. Hereinafter for brevity we use the following notations for derivatives with respect to x :

$$u_x = \frac{du}{dx}, \quad u_{xx} = \frac{d^2u}{dx^2}, \quad \text{etc.} \tag{7.4}$$

Using the standard technique of the calculus of variations from (7.2) we get the equilibrium equation and the static boundary condition

$$\sigma_x = 0, \quad x \in (0, a); \quad \sigma = p, \quad x = a, \tag{7.5}$$

where σ is a stress given by

$$\sigma = \frac{\partial W}{\partial \varepsilon}. \tag{7.6}$$

For one-dimensional case the strong ellipticity condition has a simple form

$$\frac{\partial \sigma}{\partial \varepsilon} = \frac{\partial^2 W}{\partial \varepsilon^2} > 0. \tag{7.7}$$

Let us consider typical stress-strain dependencies shown in Fig. 7.2. We have the

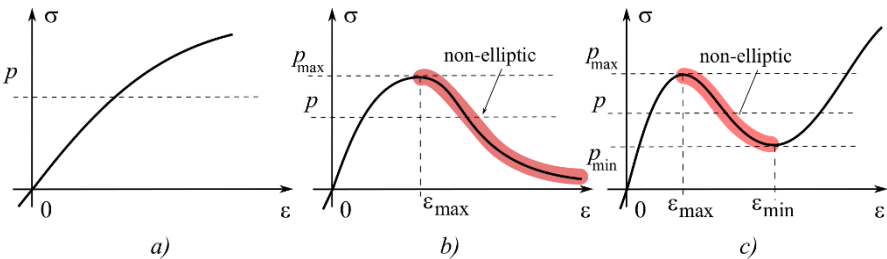


Fig. 7.2 Stress vs. strain curves: a) monotonic dependence, elliptic $\forall \varepsilon$, one solution of $\sigma = p$; b) curve with fading part, non-elliptic after $\varepsilon \geq \varepsilon_{\max}$, two solutions for $p < p_{\max}$; c) curve with fading part, non-elliptic for $\varepsilon_{\max} \leq \varepsilon \leq \varepsilon_{\min}$, three solutions for $p_{\min} < p < p_{\max}$. Non-elliptic zones are marked in red.

violation of (7.7) along declined parts of the curves given in Fig. 7.2 b) and c). Let us note that in Fig. 7.2 we can observe three types of material behavior, monotonic growth Fig. 7.2 a), softening after a certain threshold Fig. 7.2 b), and softening with further stiffening Fig. 7.2 c). In particular, the last case was studied by Ericksen (1975), see also Truskinovsky and Zanzotto (1995, 1996). Obviously, if we observe non-ellipticity, this may result in non-uniqueness or even non-existence of static solutions. Indeed, solving of (7.5) results in the equation $\sigma = p$, which has no solution for $p > p_{\max}$ (Fig. 7.2 b). For the case shown in Fig. 7.2 c) we have three static solutions for $p_{\min} < p < p_{\max}$, whereas for Fig. 7.2 b) we have two solutions if $p < p_{\max}$.

Thus, we have seen that for an elastic bar made of nonlinearly elastic material, non-ellipticity results in non-uniqueness of solutions or non-existence of solutions, see Ericksen (1975); Truskinovsky and Zanzotto (1995, 1996) for further details.

7.3 Strain Gradient Elasticity

Let us now discuss the same problem considering the strain gradient elasticity approach. We assume the following kinematic boundary condition

$$u(0) = 0, \quad u_x(0) = 0, \quad (7.8)$$

and a strain energy density in the form

$$W = W_{\text{sg}}(\varepsilon, \varepsilon_x). \quad (7.9)$$

From (7.2) and (7.9) it follows the equations of equilibrium and static boundary conditions

$$\sigma_x - \tau_{xx} = 0, \quad x \in (0, a); \quad (7.10)$$

$$\sigma - \tau_x = p, \quad \tau = 0, \quad x = a. \quad (7.11)$$

Here stress σ and hyper stress τ are given by

$$\sigma = \frac{\partial W}{\partial \varepsilon}, \quad \tau = \frac{\partial W}{\partial \varepsilon_x}. \quad (7.12)$$

For the general framework of the variational approach to the strain gradient media we refer to Abali et al (2017); Bertram and Forest (2020); dell'Isola and Steigmann (2020); Eremeyev et al (2018a) and the references therein.

In this case the strong ellipticity condition takes the form

$$\frac{\partial \tau}{\partial \varepsilon_x} = \frac{\partial^2 W}{\partial \varepsilon_x^2} > 0, \quad (7.13)$$

which is different from (7.7).

In what follows we use the simple form of (7.9) given by

$$W = W_{\text{ne}}(\varepsilon) + \frac{1}{2}\alpha\varepsilon_x^2, \quad (7.14)$$

which could be treated as a higher-order regularization of (7.3). Here we have introduced an additional elastic modulus α . For (7.14) the strong ellipticity condition results in the simple inequality

$$\alpha > 0, \quad (7.15)$$

$\sigma = \sigma(\varepsilon)$ is given by (7.5), the hyper stress takes the form $\tau = \alpha\varepsilon_x$. So Eqs. (7.10) and (7.11) transform into

$$[\sigma - \alpha\varepsilon_{xx}]_x = 0, \quad x \in (0, a); \quad (7.16)$$

$$\sigma - \alpha\varepsilon_{xx} = p, \quad \varepsilon_x = 0, \quad x = a. \quad (7.17)$$

From (7.16) and (7.17)₁ it follows the nonlinear ODE with respect to ε

$$\sigma(\varepsilon) - \alpha\varepsilon_{xx} = p, \quad x \in (0, a). \quad (7.18)$$

So we have reduced the BVP (7.16) and (7.17) to (7.18) with the following boundary conditions

$$\varepsilon(0) = 0, \quad \varepsilon_x(a) = 0. \quad (7.19)$$

Using standard technique as in Arnold (1989) Eq. (7.18) could be integrated as follows:

$$\frac{\alpha}{2}\varepsilon_x^2 = W_{\text{ne}}(\varepsilon) - p\varepsilon + C, \quad (7.20)$$

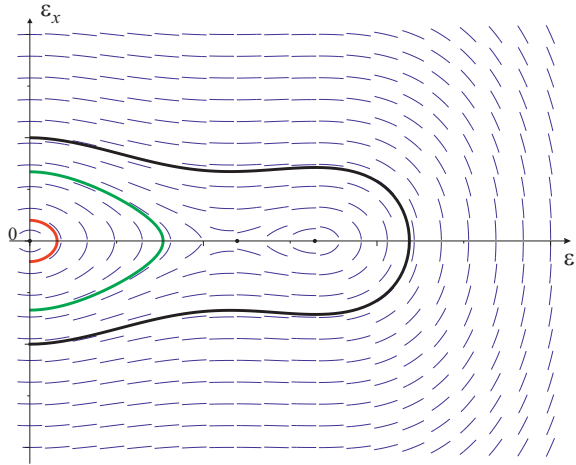
where C is an integration constant which should be found from (7.17)₂. So we transform the problem under consideration to an ordinary differential equation. Its solution is given in an implicit form as follows:

$$\int_0^\varepsilon \frac{d\varepsilon}{\sqrt{2[W(\varepsilon) - p\varepsilon + C]/\alpha}} = x. \quad (7.21)$$

For the further analysis of the problem under consideration we can use the phase portrait of (7.18). Let us consider the most interesting case shown in Fig. 7.2 c). If the strong ellipticity condition is fulfilled, i.e. if $\alpha > 0$, a typical phase portrait is given in Fig. 7.3. A solution of (7.18) satisfying boundary conditions (7.19) corresponds to an integral curve in $(\varepsilon - \varepsilon_x)$ -plane, which starts at the vertical axis $\varepsilon = 0$ and ends at the horizontal line $\varepsilon_x = 0$. As an example, in Fig. 7.3 one can see three integral curves. Obviously, for $\alpha > 0$ BVP (7.18) and (7.19) always has a unique solution. The black dots in Fig. 7.3 correspond to the extremes of $W - p\varepsilon$. They constitute two centers and one saddle point between centers.

The situation changes dramatically if $\alpha < 0$. In this case we have a phase portrait as shown in Fig. 7.4. Here one can also see three integral curves. The black dots in Fig. 7.4 correspond to the extremes of $p\varepsilon - W$. They constitute two saddle points

Fig. 7.3 Phase portrait for the strongly elliptic case, $\alpha > 0$.



and one center point between them. Obviously, since the first saddle locates at $(0, 0)$, here such an integral curve which begins at $\varepsilon = 0$ and finish at $\varepsilon_x = 0$ does not exist. In other words, BVP (7.18) with (7.19) has no solution. So for the non-elliptic case we may have no solutions. Note that we consider here smooth enough solutions only.

Similar conclusions can be done for other cases shown in Fig. 7.2.

7.4 Conclusions

Considering an elastic bar in the framework of the nonlinear strain gradient elasticity we illustrate the consequences of the strong ellipticity loss. The main conclusion consists the ellipticity violations may lead to some issues in the solvability of the corresponding boundary-value problems. So the strong ellipticity condition plays

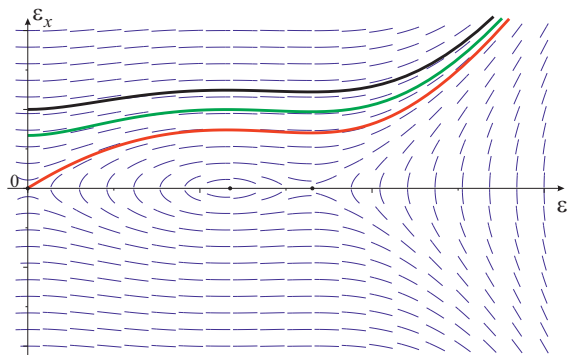


Fig. 7.4 Phase portrait for the non-elliptic case, $\alpha < 0$.

the same crucial role within higher-order models of continua as in the case of nonlinear elasticity of simple materials. In particular, we see that under strong ellipticity condition the second-order term ε_x^2 in constitutive relation may regularize the solution. Let us also note that for 3D case, i.e. considering BVPs for strain gradient media in the general framework, the situation with ellipticity could be more complex, see e.g. Eremeyev (2021).

Acknowledgements The author acknowledges the support by the Russian Science Foundation under grant 20-41-04404 issued to the Institute of Applied Mechanics of Russian Academy of Sciences.

References

- Abali BE, Müller WH, dell’Isola F (2017) Theory and computation of higher gradient elasticity theories based on action principles. *Archive of Applied Mechanics* 87(9):1495–1510
- Abdoul-Anziz H, Seppecher P (2018) Strain gradient and generalized continua obtained by homogenizing frame lattices. *Mathematics and Mechanics of Complex Systems* 6(3):213–250
- Agranovich M (1997) Elliptic boundary problems. In: Agranovich M, Egorov Y, Shubin M (eds) *Partial Differential Equations IX: Elliptic Boundary Problems*. Encyclopaedia of Mathematical Sciences, Springer, Berlin, vol 79, pp 1–144
- Alibert JJ, Seppecher P, dell’Isola F (2003) Truss modular beams with deformation energy depending on higher displacement gradients. *Mathematics and Mechanics of Solids* 8(1):51–73
- Arnold VI (1989) *Mathematical Methods of Classical Mechanics*, 2nd edn. Springer, New York
- Bertram A, Forest S (eds) (2020) *Mechanics of Strain Gradient Materials*. Springer International Publishing, Cham
- Cordero NM, Forest S, Busso EP (2016) Second strain gradient elasticity of nano-objects. *Journal of the Mechanics and Physics of Solids* 97:92–124
- dell’Isola F, Steigmann D (2015) A two-dimensional gradient-elasticity theory for woven fabrics. *Journal of Elasticity* 118(1):113–125
- dell’Isola F, Steigmann DJ (2020) *Discrete and Continuum Models for Complex Metamaterials*. Cambridge University Press, Cambridge
- dell’Isola F, Seppecher P, Alibert JJ, Lekszycki T, Grygoruk R, Pawlikowski M, Steigmann D, Giorgio I, Andraus U, Turco E, Gołaszewski M, Rizzi N, Boutin C, Eremeyev VA, Misra A, Placidi L, Barchiesi E, Greco L, Cuomo M, Cazzani A, Corte AD, Battista A, Scerrato D, Eremeeva IZ, Rahali Y, Ganghoffer JF, Müller W, Ganzosch G, Spagnuolo M, Pfaff A, Barcz K, Hoschke K, Neggers J, Hild F (2019a) Pantographic metamaterials: an example of mathematically driven design and of its technological challenges. *Continuum Mechanics and Thermodynamics* 31(4):851–884
- dell’Isola F, Seppecher P, Spagnuolo M, Barchiesi E, Hild F, Lekszycki T, Giorgio I, Placidi L, Andraus U, Cuomo M, Eugster SR, Pfaff A, Hoschke K, Langkemper R, Turco E, Sarikaya R, Misra A, De Angelo M, D’Annibale F, Bouterf A, Pinelli X, Misra A, Desmorat B, Pawlikowski M, Dupuy C, Scerrato D, Peyre P, Laudato M, Manzari L, Göransson P, Hesch C, Hesch S, Franciosi P, Dirrenberger J, Maurin F, Vangelatos Z, Grigoropoulos C, Melissinaki V, Farsari M, Muller W, Abali BE, Liebold C, Ganzosch G, Harrison P, Drobnicki R, Igumnov L, Alzahrani F, Hayat T (2019b) Advances in pantographic structures: design, manufacturing, models, experiments and image analyses. *Continuum Mechanics and Thermodynamics* 31(4):1231–1282
- Eremeyev VA (2021) Strong ellipticity conditions and infinitesimal stability within nonlinear strain gradient elasticity. *Mechanics Research Communications* 117:103,782

- Eremeyev VA, Cloud MJ, Lebedev LP (2018a) Applications of Tensor Analysis in Continuum Mechanics. World Scientific, New Jersey
- Eremeyev VA, dell'Isola F, Boutin C, Steigmann D (2018b) Linear pantographic sheets: existence and uniqueness of weak solutions. *Journal of Elasticity* 132(2):175–196
- Ericksen JL (1975) Equilibrium of bars. *Journal of Elasticity* 5(3):191–201
- Fichera G (1965) Linear elliptic differential systems and eigenvalue problems, *Lecture Notes in Mathematics*, vol 8. Springer, Berlin
- Forest S, Cordero NM, Busso EP (2011) First vs. second gradient of strain theory for capillarity effects in an elastic fluid at small length scales. *Computational Materials Science* 50(4):1299–1304
- Giorgio I (2021) Lattice shells composed of two families of curved Kirchhoff rods: an archetypal example, topology optimization of a cycloidal metamaterial. *Continuum Mechanics and Thermodynamics* 33(4):1063–1082
- Giorgio I, Rizzi NL, Turco E (2017) Continuum modelling of pantographic sheets for out-of-plane bifurcation and vibrational analysis. *Proceedings of the Royal Society A: Mathematical, Physical and Engineering Sciences* 473(2207):20170,636
- Hörmander L (1983) *The Analysis of Linear Partial Differential Operators. II. Differential Operators with Constant Coefficients*, A Series of Comprehensive Studies in Mathematics, vol 257. Springer, Berlin
- Lurie AI (1990) *Non-linear Theory of Elasticity*. North-Holland, Amsterdam
- Mawassy N, Reda H, Ganghoffer JF, Eremeyev VA, Lakiss H (2021) A variational approach of homogenization of piezoelectric composites towards piezoelectric and flexoelectric effective media. *International Journal of Engineering Science* 158:103,410
- Mindlin RD (1964) Micro-structure in linear elasticity. *Archive for Rational Mechanics and Analysis* 16(1):51–78
- Mindlin RD (1965) Second gradient of strain and surface-tension in linear elasticity. *International Journal of Solids and Structures* 1(4):417–438
- Mindlin RD, Eshel NN (1968) On first strain-gradient theories in linear elasticity. *International Journal of Solids and Structures* 4(1):109–124
- Ogden RW (1997) *Non-Linear Elastic Deformations*. Dover, Mineola
- Rahali Y, Giorgio I, Ganghoffer JF, dell'Isola F (2015) Homogenization à la Piola produces second gradient continuum models for linear pantographic lattices. *International Journal of Engineering Science* 97:148–172
- Skrzatz A, Eremeyev VA (2020) On the effective properties of foams in the framework of the couple stress theory. *Continuum Mech Thermodyn* 32:1779–1801
- Toupin RA (1962) Elastic materials with couple-stresses. *Archive for Rational Mechanics and Analysis* 11(1):385–414
- Toupin RA (1964) Theories of elasticity with couple-stress. *Archive for Rational Mechanics and Analysis* 17(2):85–112
- Truesdell C (1966) *The Elements of Continuum Mechanics*. Springer, New York
- Truskinovsky L, Zanzotto G (1995) Finite-scale microstructures and metastability in one-dimensional elasticity. *Meccanica* 30(5):577–589
- Truskinovsky L, Zanzotto G (1996) Ericksen's bar revisited: Energy wiggles. *Journal of the Mechanics and Physics of Solids* 44(8):1371–1408



Chapter 8

Two Thermodynamic Laws in Phenomenological Mechanics of Continuum: Postulates or Definitions ?

Dimitri Georgievskii

Abstract The role of the fourth and fifth postulates of continuum mechanics, also known as the first and second laws of thermodynamics, in the axiomatization of phenomenological theory is discussed. It is shown that, in contrast to the statistical and molecular approaches, the internal energy and entropy of an individual (liquid) volume can be fully determined by specifying their source, flow across the boundary, and production. Thus, two thermodynamic postulates serve as definitions. Energy conjugate pairs of quantities of different physical nature and the possibility of extending the table of postulates are discussed.

Keywords: Thermodynamics · Analysis · Axioms vs. postulates

8.1 Various Ways of Axiomatization

Hilbert's sixth problem, formulated at the Second International Congress of Mathematicians in Paris in 1900, is related to the issues of clear and internally correct axiomatization of physics. The degree of global solution of this problem by the end of the XX century is devoted to extensive discussions in the natural science literature (Corry, 1997). An important sub-problem, for the analysis of which it would already be possible to use a powerful mathematical apparatus, is the creation of a strict theory of the limiting transition from processes described at the quantum level to processes in the continuum. This can be viewed as an exclusively mathematical problem (Gorban and Karlin, 2014; Saint-Raymond, 2009; Slemrod, 2013), as well as the question of the axiomatization of continuum mechanics, in the phenomenological interpretation of which, generally speaking, there are no concepts of atoms, molecules, etc. A significant contribution in this direction was made by the creators of the classic

D. Georgievskii

Mechanical and Mathematical Department, Moscow State University, Moscow 119991, Russia
e-mail: georgiev@mech.math.msu.su

and internationally recognized courses of continuum mechanics (among others, see Germain, 1962; Gurtin et al, 2010; Ilyushin, 1990; Kondepudi and Prigozhine, 2000; Lurie, 2005; Malvern, 1969; Maugin, 2013; Noll, 1974; Novozhilov, 1961; Reddy, 2013; Sedov, 1997; Truesdell, 1977).

Perhaps, thermodynamics (Müller, 2007; Müller and Müller, 2009; Müller and Weiss, 2005) precisely, in the sense of a branch of continuum mechanics, is the most variable and difficult part of physics to axiomatize. It is not surprising that there is a joke among physicists that thermodynamics is a humanitarian science. What are definitions, what are postulates, and what are proved statements in the construction of a strict theory? Is it true that the formulation of any postulate should contain only the quantities previously defined in the chosen axiomatization? Otherwise, it turns into a definition itself. Are there universal equations of thermodynamic balance and is their form of writing unique (dell’Isola and Romano, 1987)? It is known that the theory is more perfect and “closer to mathematics” (any theory tends to be “closer to mathematics”...), the fewer axioms and postulates in it, and the more deducible propositions. The answers to the questions formulated above in each of the mentioned courses are given their own, in many ways they are original (see also Georgievskii, 2019; Pobedria and Georgievskii, 2015, 2016).

8.2 The General Form of Postulates in Mechanics of Continuum

As is known, classical mechanics of continuum is axiomatically based on five phenomenological postulates that have the unified integral form of writing as laws of change (conservation) of certain thermomechanical quantities $A_V(t)$:

$$\frac{dA_V}{dt} = B_V + C_\Sigma + D_V, \quad (8.1)$$

$$\begin{aligned} A_V(t) &= \int_V \rho a(\mathbf{x}, t) dV, & B_V(t) &= \int_V \rho b(\mathbf{x}, t) dV, \\ C_\Sigma(t) &= \int_\Sigma c(\mathbf{y}, t) \cdot \mathbf{n}(\mathbf{y}, t) d\Sigma, & D_V(t) &= \int_V d(\mathbf{x}, t) dV \end{aligned} \quad (8.2)$$

where

- $\rho(\mathbf{x}, t)$ is the scalar field of volume density at point \mathbf{x} at time t ;
- $a(\mathbf{x}, t)$ is the mass density of the value $A_V(t)$ in the volume V ;
- $b(\mathbf{x}, t)$ is the mass density of the value $B_V(t)$ being a *source* of A_V in V ;
- $c(\mathbf{y}, t) \cdot \mathbf{n}(\mathbf{y}, t)$ is the surface density of the value $C_\Sigma(t)$ being a *flow* of A_V across the boundary $\Sigma = \partial V$ at each point of which $\mathbf{y} \in \Sigma$ the unit external normal \mathbf{n} exists;
- $d(\mathbf{x}, t)$ is the volume density of the value $D_V(t)$ which is called a *production* A_V in V .

In (8.2) V is some arbitrary finite volume of the medium at any time consisting of the same Lagrangian particles. It has various names in the literature: moving volume of constant mass; individual volume; liquid volume; mobile Lagrangian volume.

The field $a(\mathbf{x}, t)$ can be scalar or vector; the tensor nature of the other quantities included in (8.1) and (8.2) depends on this: $\text{rang } a = \text{rang } b = \text{rang } c - 1 = \text{rang } d$.

In Table 8.1, for each of the five postulates I–V it is indicated what the notation introduced in (8.1) and (8.2) corresponds to. Here \mathbf{v} is the velocity of particles; $\tilde{\nu}$ is the symmetric strain rate tensor; $\tilde{\sigma}$ is the symmetric Cauchy stress tensor; \mathbf{F} are the mass forces; $\mathbf{P}^{(n)} = \tilde{\sigma} \cdot \mathbf{n}$ are the surface loadings on Σ ; q is the mass density of heat sources in V ; \mathbf{q} is the vector of heat flow; u and s are the specific internal energy and the specific entropy in V ; w^* is the volume density of energy dissipation in V ; T is absolute temperature. Taking advantage of the fact that the volume of V

Table 8.1 General balance equations with the notation introduced in (8.1) and (8.2)

| | a | b | $c \cdot \mathbf{n}$ | d |
|-----|--------------------------------|-----------------------------------|---|---|
| I | 1 | 0 | 0 | 0 |
| II | \mathbf{v} | \mathbf{F} | $\mathbf{P}^{(n)}$ | 0 |
| III | $\mathbf{x} \times \mathbf{v}$ | $\mathbf{x} \times \mathbf{F}$ | $\mathbf{y} \times \mathbf{P}^{(n)}$ | 0 |
| * | $\frac{ \mathbf{v} ^2}{2}$ | $\mathbf{F} \cdot \mathbf{v}$ | $\mathbf{P}^{(n)} \cdot \mathbf{v}$ | $-\tilde{\sigma} : \tilde{\nu}$ |
| IV | $\frac{ \mathbf{v} ^2}{2} + u$ | $\mathbf{F} \cdot \mathbf{v} + q$ | $\mathbf{P}^{(n)} \cdot \mathbf{v} - \mathbf{q} \cdot \mathbf{n}$ | 0 |
| V | s | $\frac{q}{T}$ | $-\frac{\mathbf{q} \cdot \mathbf{n}}{T}$ | $\frac{w^*}{T} - \frac{\mathbf{q} \cdot \text{grad } T}{T^2}$ |

inside the medium is arbitrary, it is not difficult to derive a differential consequence from the integral equality (8.1):

$$\rho \frac{da}{dt} = \rho b + \text{Div } c + d, \quad \mathbf{x} \in V. \tag{8.3}$$

The number of local equations (8.3) coincides with the number of integral equalities (8.1).

8.3 Postulate IV. The Law on the Change of Internal Energy

The first three postulates I–III, namely the law of mass conservation and the laws of change of both impuls and moment of impuls, use only isothermic quantities. The fourth row of the table, marked with an asterisk, corresponds to an integral statement called the kinetic energy theorem. It is usually written in terms of finite differentials:

$$dK = \delta A^{(e)} + \delta A^{(i)}, \tag{8.4}$$

$$\begin{aligned}
 K &= \frac{1}{2} \int_V \rho |\mathbf{v}|^2 dV, \\
 \delta A^{(i)} &= - \int_V \tilde{\boldsymbol{\sigma}} : d\tilde{\boldsymbol{\varepsilon}} dV, \quad \delta A^{(e)} = \int_V \rho \mathbf{F} \cdot d\mathbf{u} dV + \int_{\Sigma} \mathbf{P}^{(n)} \cdot d\mathbf{u} d\Sigma,
 \end{aligned}
 \tag{8.5}$$

where K is the kinetic energy contained inside the volume V ; $\delta A^{(e)}$ is the sum of changing the work of mass and surface forces on actual displacements $d\mathbf{u}$; $\delta A^{(i)}$ is changing the work of internal forces. If the external loads \mathbf{F} and $\mathbf{P}^{(n)}$ have scalar potentials with respect to \mathbf{u} , and also there is a scalar stress potential $\tilde{\boldsymbol{\sigma}}$ with respect to strains $\tilde{\boldsymbol{\varepsilon}}$ for a given medium, then the differential relation (8.4) admits the first integral, called the energy integral.

The kinetic energy theorem (8.4) is not an independent postulate (so it is not assigned a separate number in the table), but is a consequence of postulates I–III. But it plays an important role in the energy transition to the formulation of the non-isothermal postulate IV — the law on the change of internal energy. In such a transition, it is stated that the change in the stress-strain state of the medium can involve thermal effects determined by the mass density $q(\mathbf{x}, t)$ of heat sources inside the volume V and the heat flow $(\mathbf{q} \cdot \mathbf{n})(\mathbf{y}, t)$ across the boundary Σ . The heat flow vector is defined, generally speaking, in the entire volume of V .

Then the row IV of the table is formed by the extension of the row * as follows. Let us assume that the mass density of the total energy contained in the volume V consists of the term $|\mathbf{v}|^2/2$, which is already present in the row *, and some function $u(\mathbf{x}, t)$, to which we give the meaning of the mass density of the internal energy. We require this function that: a) its source in V is only the heat sources $q(\mathbf{x}, t)$; b) its flow through Σ is only the heat flow $-(\mathbf{q} \cdot \mathbf{n})(\mathbf{y}, t)$ inside Σ ; c) the total energy $|\mathbf{v}|^2/2 + u$ production is zero.

Taking the difference between the rows IV and *, we get the local equality (8.3) for the function u :

$$\rho \frac{du}{dt} = \rho q - \operatorname{div} \mathbf{q} + \tilde{\boldsymbol{\sigma}} : \tilde{\boldsymbol{\nu}}, \quad \mathbf{x} \in V,
 \tag{8.6}$$

which is well-known as the local energy equation. Its integral analog, written in finite differentials

$$dU = \delta Q - \delta A^{(i)},
 \tag{8.7}$$

$$U = \int_V \rho u dV, \quad \delta Q = dt \left(\int_V \rho q dV - \int_{\Sigma} \mathbf{q} \cdot \mathbf{n} d\Sigma \right),
 \tag{8.8}$$

is one of the possible statements of the first thermodynamic law.

Thus, from the point of view of the axiomatic construction, it is natural to consider the row IV as *the definition* of that new function, namely, the mass density $u(\mathbf{x}, t)$ of the internal energy that appeared in it in comparison with the row *. This function, as one of the four possible thermodynamic potentials (all of them are related to each other by Legendre transformations), plays a major role in the theory of constitutive relations of continuum thermomechanics.

One can also suggest another, “mirror”, version of the axiomatics, i.e. the extension of the row * of the table to the row IV, in which the latter will not be the definition of internal energy. To do this, one must abandon the postulation of the physical meaning of the thermal quantities $q(\mathbf{x}, t)$ and $\mathbf{q}(\mathbf{x}, t)$, and only assume that the total energy $|\mathbf{v}|^2/2 + u$, which is quite reasonable, should have zero production in any individual (liquid) volume. This can be achieved by adding to $|\mathbf{v}|^2/2$ some function $u(\mathbf{x}, t)$ with non-zero production, such that the last column of the row IV has zero. Then the source of this quantity in the volume V and its flow through the boundary Σ are interpreted as the functions $q(\mathbf{x}, t)$ and $-(\mathbf{q} \cdot \mathbf{n})(\mathbf{y}, t)$, which were discussed above. With this approach, the row IV turns into *definitions* of the power of heat sources and the heat flow vector. This way seems to be an alternative, but logically more cumbersome, since here it is necessary to establish the uniqueness of the function u choice. Indeed, the existence of adjacent internal energies with the same production is certainly not excluded, but the source and flow through the boundary of which is not due to thermal effects, but for example, electromagnetic or biological and informational factors that have been actively studied recently from the point of view of mathematical modeling in Abali and Queiruga (2019); Abali and Reich (2017); Brechet and Ansermet (2014); Ericksen (2007); Hutter (1975).

8.4 Postulate V. The Law on the Change of Entropy

Note that the physical dimensions of all the quantities in the table except for the row V are expressed in the basis $\{M, L, T\}$. This includes the phenomenological functions q and \mathbf{q} , which describe purely thermal effects but have dimension L^2T^{-3} and MT^{-3} , respectively. Let us now focus on some variants of the axiomatics of the transition from all the previous rows of the table to the row V, which requires an involvement of quantities with dimensions that do not fit in the basis $\{M, L, T\}$.

We assume that the heat flow vector for each selected medium is completely determined by setting in V the scalar field of some phenomenological function $T(\mathbf{x}, t)$, namely, it depends only on the gradient of this function over \mathbf{x} . In this case, the value $T(\mathbf{x}, t)$, called the absolute temperature, cannot be given a kinematic-force interpretation, in contrast, for example, to the vector \mathbf{q} , i.e. its dimension is not expressed by a power monomial $M^\alpha L^\beta T^\gamma$, as required by dimension theory, so it is necessary to expand the basis $\{M, L, T\}$: $[T] = K$. We emphasize that here we are talking about the phenomenological introduction of temperature. In the statistical and molecular description, where the heat propagation is a result of the collisional transfer of kinetic energy from fast-moving molecules to slow ones, the inclusion of an additional variable in the basis $\{M, L, T\}$ can be avoided. In the classical model of a continuous medium the concept of “molecule” is absent.

The simplest connection between \mathbf{q} and $\text{grad } T$ is known to be the Fourier law

$$\mathbf{q} = -\tilde{\Lambda} \cdot \text{grad } T, \quad (8.9)$$

where $\tilde{\Lambda}$ is the symmetric heat conductivity tensor of an anisotropic medium. To simulate heat waves propagating at a finite speed, very popular in recent years hyperbolic theories of heat conductivity may be used. They obtained by generalizing (8.9) within the framework of the apparatus of vector-linear functions from the vector argument:

$$\mathbf{q}(\mathbf{x}, t) = - \int_0^t \tilde{\Gamma}(t - \xi) \cdot (\text{grad } T)(\mathbf{x}, \xi) d\xi. \quad (8.10)$$

In particular, if the kernel $\tilde{\Gamma}$ is exponential: $\tilde{\Gamma}(t) = (1/\tau)\tilde{\Lambda}e^{-t/\tau}$, there is a Cattaneo law with a characteristic relaxation time τ . The generalized function $\tilde{\Gamma}(t) = \tilde{\Lambda}\delta(t)$ corresponds to the Fourier law. For a homogeneous isotropic medium ($\tilde{\Lambda} = \lambda I$, where λ is the constant coefficient of heat conductivity), the field of the vector \mathbf{q} is vortex-free.

Vector relations (8.9) or more generally (8.10) are usually interpreted as constitutive relations of a heat-conducting medium with the material functions $\tilde{\Gamma}$, $\tilde{\Lambda}$, and λ . But in such relations, as in the formulations of laws, only the physical quantities defined earlier should appear. The temperature T is the first variable in the transition from the rows I–IV to V, the dimension of which includes K. Therefore, it can not be introduced on the basis of the variables available in isothermal mechanics, and the relations (8.9) or (8.10) can be approached as a phenomenological definition of T : this is a scalar function in V , the gradient of which is connected in this way with the vector \mathbf{q} already known from line IV (in the simplest case, it is counter-directed to \mathbf{q}).

The appearance of temperature leads to the need to introduce an energetically conjugate scalar value of the same non-mechanical content — mass density of entropy $s(\mathbf{x}, t)$ — and to form, along with the tensor pair $(\tilde{\sigma}, \tilde{\varepsilon})$, another scalar pair (s, T) of thermodynamic state parameters, one of which describes the process realized in the volume V of the medium, and the other the response of the medium on this process. Neither the density $s(\mathbf{x}, t)$, nor the entropy $S = \int_V \rho s dV$ of the volume V are unobservable and immeasurable by any device in the experiment, they are of an auxiliary nature.

It is easier to define the entropy s not by the row V of the table but using the local equation (8.3)

$$\rho T ds = \rho q dt - (\text{div } \mathbf{q}) dt + w^* dt, \quad \mathbf{x} \in V, \quad (8.11)$$

in one of the parts of which must necessarily be “energetic product” $T ds$, the dimension of which can be expressed in the basis $\{M, L, T\}$, and the other part represents its transcript, namely, the division into the sum of the source, flow terms and production, which carries the meaning of the definition. The need for dimensional reasons to write a local equation for the product $T ds$, and not separately for ds , leads to the appearance of the integrating factor $1/T$. Dividing both parts of the relation (8.11) by dt and integrating by V , we come to the row V, namely, the law on the change of entropy. The factor $1/T$ when integrated in parts gives rise to the term $-(\mathbf{q} \cdot \text{grad } T)/T^2$ in the entropy production.

The principle of non-decreasing entropy in an isolated system, put forward at the end of the XIX century by R. Clausius and L. Boltzmann and constituting the physical meaning of the second law of thermodynamics, in relation to the considered individual volume V is formulated as follows. If $q|_V = 0$ and $(\mathbf{q} \cdot \mathbf{n})_\Sigma = 0$ then

$$\int_V \left(\frac{w^*}{T} - \frac{\mathbf{q} \cdot \text{grad } T}{T^2} \right) dV \geq 0. \quad (8.12)$$

By virtue of the arbitrariness of V , the inequality (8.12) is equivalent to the non-negativity of the integrand at each point $\mathbf{x} \in V$. Substituting here, for example, the Fourier law (9), we obtain the following inequality for the quadratic form:

$$\text{grad } T \cdot \tilde{\Lambda} \cdot \text{grad } T \geq -T w^*, \quad \mathbf{x} \in V. \quad (8.13)$$

In the case of $w^* \equiv 0$, the non-decreasing entropy is equivalent to the positive definiteness of the heat conductivity tensor $\tilde{\Lambda}$ (the positivity of the coefficient λ in isotropic medium).

Thus, from the point of view of the phenomenological construction of axiomatics, the two thermodynamic laws and the relation connecting the heat flow vector with the temperature gradient can be approached as definitions of internal energy, entropy, and temperature change. This does not contradict the fact that the local equations of energy (8.6), entropy (8.11), as well as the Fourier law (8.9) or its hyperbolic generalizations of the type (8.10) are present in closed systems of equations. In addition to them, these systems also include constitutive relations of the medium, which specify the dependence of the function u as a thermodynamic potential (or another potential, for example, the free energy $u - Ts$) on its independent state parameters.

An attempt to avoid treating these laws as definitions usually leads to the following formulations: “*There is a certain quantity such that ...*”. But such statements are completely descriptive of the given quantity, and not postulating the existence, i.e. they are *definitions* in its essence. This applies not only to thermodynamics. So, for example, the statement “*There are inertial reference systems in which the body, which is not subject to the action of force, is at rest or moves rectilinearly and evenly*” is essentially a *definition* of an inertial frame of reference, and not the conditions for its existence.

8.5 Introduction to Mathematical Model of Interactions with a New Nature

The theory of constitutive relations in continuum mechanics operates with energetically conjugate pairs, such as $(\tilde{\sigma}, \tilde{\varepsilon})$ and (s, T) . One of the quantities included in each pair is treated as an independent parameter of the state on which a certain thermodynamic potential depends, for example, the internal energy $u(\tilde{\varepsilon}, s)$. It is as-

sumed that this element of the pair sets the process in medium. The another element in each pair, which is a tensor of the same rank as the first one, has the meaning of the response of the medium to this process and is specified by the constitutive relations of medium. In these relations there are material functions representing the experimentally obtained functions of coordinates and time (in particular, material constants) that characterize the selected medium in the given class of constitutive relations.

The physical dimensions of quantities from different energy conjugate pairs are expressed, generally speaking, in different dimensional bases, which indicates their different nature (mechanical, thermal, etc.) and irreducibility to each other.

If the thermodynamic potential is such that the constitutive relations express some of the dependent quantities not only through the independent ones of the same pair, but also through the independent parameters of other pairs, then this model is coupled and more difficult for mathematical modeling.

The introduction of a new nature, which was not taken into account earlier, into the mathematical model of interaction assumes the following:

- addition of the source and flow columns in the row IV of the table with terms related to the change in internal energy due to a new type of interaction (while the total energy production is still zero), which means giving physical sense and mathematizing the new mass density of sources in V and the surface density of the flow in Σ ;
- the presentation of an energetically conjugate pair of new quantities that characterize this interaction, which cannot be reduced or expressed in terms of existing ones, and the expansion of the multiplicative basis of dimensions;
- the formulation of an analog of the row V which defines the source, flow, and production of one of the quantities present in the new pair;
- giving the internal energy u or some adjacent potential to a new independent variable and obtaining constitutive relations connecting the dependent parameters in each of the pairs available in the model with the independent ones;
- creating (at least virtual) establishing experiments to find the material functions present in the mentioned constitutive relations, including the material functions that characterize the coupled effects.

Such a strong system of requirements, in addition to the purely mechanical and thermal interactions discussed above, is currently satisfied only by electromagnetic ones with an energetically conjugated pair (\mathbf{E}, \mathbf{H}) , where \mathbf{E} and \mathbf{H} are the vectors of electric and magnetic field strengths. Accordingly, over the past two centuries, it is generally assumed that three disciplines have formed up — isothermal continuum mechanics, phenomenological thermodynamics, and electromagnetism, as well as their various coupled variants. Although there are still many difficulties and ways to account for the interaction of these “three whales”. The next step in this series is likely to be the accounting of chemical, biological, and information interactions, which means, first of all, the mathematization of chemical energy, bioenergy, and information energy.

References

- Abali BE, Queiruga AF (2019) Theory and computation of electromagnetic fields and thermomechanical structure interaction for systems undergoing large deformations. *Journal of Computational Physics* 394:200–231
- Abali BE, Reich FA (2017) Thermodynamically consistent derivation and computation of electrothermo-mechanical systems for solid bodies. *Computer Methods in Applied Mechanics and Engineering* 319:567–595
- Brechet SD, Ansermet JP (2014) Thermodynamics of continuous media with intrinsic rotation and magnetoelectric coupling. *Continuum Mechanics and Thermodynamics* 26:115–142
- Corry L (1997) David Hilbert and the axiomatization of physical science (1894–1905). *Archive for History of Exact Sciences* 51:83–198
- dell’Isola F, Romano A (1987) On the derivation of thermomechanical balance equations for continuous systems with a nonmaterial interface. *International Journal of Engineering Sciences* 25(11–12):1459–1468
- Ericksen JL (2007) On formulating and assessing continuum theories of electromagnetic fields in elastic materials. *Journal of Elasticity* 87:95–108
- Georgievskii DV (2019) On the role of two thermodynamic postulates in the phenomenological construction of continuum mechanics (in russ.). *Chebyshevskiy Sbornik* 20(3):135–143
- Germain P (1962) *Mécanique des Milieux Continus*. Masson, Paris
- Gorban AN, Karlin I (2014) Hilbert’s 6th problem: exact and approximate hydrodynamic manifolds for kinetic equations. *Bulletin of American Mathematical Society* 51(2):186–246
- Gurtin ME, Fried E, Anand L (2010) *The Mechanics and Thermodynamics of Continua*. Cambridge Univ. Press, Cambridge
- Hutter K (1975) On thermodynamics and thermostatics of viscous thermoelastic solids in the electromagnetic fields. A Lagrangian formulation. *Archives of Rational Mechanics and Analyses* 58:339–368
- Ilyushin AA (1990) *Mechanics of Continuous Media (in Russ.)*. Moscow State Univ. Press, Moscow
- Kondepudi D, Prigozhine I (2000) *Modern Thermodynamics. From Heat Engines to Dissipative Structures*. John Sons, Chichester
- Lurie AI (2005) *Theory of Elasticity*. Springer, Berlin – Heidelberg
- Malvern LE (1969) *Introduction to the Mechanics of a Continuous Medium*. Prentice-Hall, N.-J
- Maugin GA (2013) *Continuum Mechanics Through the Twentieth Century: a Concise Historical Perspectives, Solid Mechanics and Its Applications*, vol 196. Springer, Dordrecht
- Müller I (2007) *A History of Thermodynamics. The Doctrine of Energy and Entropy*. Springer Science & Business Media, Berlin – Heidelberg
- Müller I, Müller WH (2009) *Fundamentals of Thermodynamics and Applications. With Historical Annotations and Many Citations from Avogadro to Zermelo*. Springer Science & Business Media, Berlin – Heidelberg
- Müller I, Weiss W (2005) *Entropy and Energy. A Universal Competition*. Springer Science & Business Media, Berlin – Heidelberg
- Noll W (1974) *Foundations of Mechanics and Thermodynamics*. Springer, Berlin – Heidelberg – N.-Y.
- Novozhilov VV (1961) *Theory of Elasticity*. Pergamon Press, N.-Y.
- Pobedria BE, Georgievskii DV (2015) Uniform approach to construction of nonisothermal models in the theory of constitutive relations. *Continuous and Distributed Systems: Theory and Applications II Ser Studies in Systems, Decision and Control* 30:341–352
- Pobedria BE, Georgievskii DV (2016) Two thermodynamical laws as the fourth and the fifth integral postulates of continuum mechanics. *Advances in Dynamical Systems and Control Ser Studies in Systems, Decision and Control* 69:317–325
- Reddy JN (2013) *Introduction to Continuum Mechanics*. Cambridge Univ. Press, Cambridge
- Saint-Raymond L (2009) Hydrodynamic limits of the Boltzmann equation, *Lecture Notes in Mathematics*, vol 1971. Springer-Verlag, Berlin

- Sedov LI (1997) *Mechanics of Continuous Media* (in 2 vol.). World Sci. Publ., Singapore
- Slemrod M (2013) From Boltzmann to Euler: Hilbert's 6th problem revisited. *Computers and Mathematics with Applications* 65(10):1497–1501
- Truesdell C (1977) *A First Course in Rational Continuum Mechanics*. Acad. Press, N.-Y. – San Francisco – London



Chapter 9

On an Extended Family of Quasi-Equivalent Models of the Gradient Elasticity Theory

Sergey Lurie, Petr Belov, Yury Solyaev

Abstract There are investigated the formulations of boundary value problems in the Mindlin-Tupin gradient theory characterized by a higher differential order of equilibrium equations and a varied spectrum of boundary value problems, formulated both on a piecewise smooth surface and on the edges of this surface. We consider the possibility of simplifying boundary value problems by eliminating boundary conditions at the edges by introducing an extended spectrum of gradient applied models in the class of equivalent models having the same potential energy density. For this purpose, we investigate the variational statements of boundary value problems, which establish admissible kinematic connections on the surface in the form of linear combinations of the displacement vector and the first derivatives of displacements (both normal and tangential). Classes of gradient models obtained by introducing kinematic constraints on the surface, in which there are no boundary conditions at the edges, are indicated. These include models built by introducing kinematic constraints on the displacement vector and some special classes of models in which the kinematic constraints on the surface are set to the derivatives of displacements.

Keywords: Variational statement, Kinematic restrictions, Lagrange multipliers, Edge conditions, Static friction model

9.1 Introduction

Strain gradient elasticity theory (SGET) in its general form with five additional material constants for the isotropic material was developed by Toupin and Mindlin (Toupin, 1962; Mindlin, 1964). Since their works, the discussion on the possible simplified formulations of SGET continues and the variants of gradient theories

S. Lurie, P. Belov, Yu. Solyaev
Institute of Applied Mechanics of RAS, Moscow, Russia
e-mail: salurie@mail.ru, belovpa@yandex.ru, yos@iam.ras.ru

with reduced number of additional parameters have been proposed by many authors (Kleinert, 1989; Fleck and Hutchinson, 1997; Lam et al, 2003; Askes and Aifantis, 2011; Zhou et al, 2016; Gusev and Lurie, 2017; Eremeyev et al, 2020; Lurie et al, 2021). The main question is the basic reason for the development of simplified gradient theories. Generally, the rigorous identification of all five length scale parameters of SGET can be performed based on *ab initio* calculations (Shodja et al, 2018) or by using homogenization approaches (Hua et al, 2020). Application of the five-parametric SGET have been used, e.g. recently by Giorgio et al (2017) for the simulations of the bone's porous structure.

Relations between length scale parameters and critical length of a crack have been shown recently by several authors (Askes and Susmel, 2014; Vasiliev et al, 2019, 2021), such that at least three length scales (similarly to three crack tip stress intensity factors in fracture mechanics) can be needed in strain gradient theories used in application to fracture (Askes and Susmel, 2014; Vasiliev et al, 2019, 2021; Placidi and Barchiesi, 2018; Barchiesi et al, 2020; Misra et al, 2020). The need for two additional length scales within incomplete gradient theories have been established for the pantographic metamaterials (Placidi et al, 2020; dell'Isola et al, 2019). Attractive engineering theories would contain minimal number of additional parameters (single, in the best case) needed to capture the size effects or to provide the regular solutions and mesh independent numerical methods (Barchiesi et al, 2020; Andreus et al, 2016; Solyaev and Lurie, 2020).

Apart the simplifications, there may arise the need for the extended and refined definition of the boundary conditions and loading type within the gradient theories. For example, it was shown that additional boundary conditions of SGET for the gradients of displacements and for the double stresses can be used to defined some restricted state of the body surface and specific kind of the constraints and supports (Froio and Zervos, 2019; Lomakin et al, 2019; Vangelatos et al, 2021). In the present paper we consider an approach for the development of particular models within strain gradient elasticity theory with modified boundary conditions containing additional kinematical constraints. Such constraints may arise from the specific supports (e.g., some kind of generalized elastic foundation condition). Also, as it will be shown, the presented approach can be used for the analysis and comparison of different simplified gradient theories, which contain similar form of equilibrium equations and different form of boundary conditions due to used assumptions in constitutive equations (Lurie et al, 2021; Madeo et al, 2015).

9.2 Basic Definitions

Let us consider the variational gradient linear elasticity of Mindlin–Toupin theories (Toupin, 1962; Mindlin, 1964), where a continuous vector of displacements R_i and a continuous tensor of displacement gradients $R_{i,k}$ are the generalized kinematic variables in the volume and on the surface assuming that the considered elastic body of volume V with a piecewise smooth surface F . We investigate the variational state-

ment of the gradient model in displacements, which is determined by the expression for the Lagrange functional

$$L = A - \int_V U_V dV, \quad (9.1)$$

where U_V is the density of potential energy, and A is the work of forces given in the volume and on the surface of the body.

The potential energy density has the following general form

$$2U_V = C_{ijmnl} R_{m,n} R_{i,j} + G_{ijkmnl} R_{m,nl} R_{i,jk}, \quad (9.2)$$

where C_{ijkm} is the tensor of the moduli of elasticity of the fourth rank, G_{ijkmnl} is the tensor of the gradient moduli of elasticity of the sixth rank, and the work of external forces is written in the form

$$A = \int_V P_i^V R_i dV + \int_F P_i^F R_i dF + \int_F m_i^F R_{i,p} n_p dF + \sum \oint (f_i) \delta R_i ds, \quad (9.3)$$

where P_i^V , P_i^F are external given forces in the volume V and on the surface F of the body and m_i^F and f_i is the vector of moment forces and the vector of meniscus forces, respectively, given on the surface of the body and surface edges.

The potential energy density completely determines the physical model of the considered medium. Cauchy stress tensor σ_{ij} and the double stress tensor σ_{ijk} are determined by the using Green's formulas

$$\sigma_{ij} = \frac{\partial U}{\partial R_{i,j}} = C_{ijmnl} R_{m,n}, \quad \sigma_{ijk} = \frac{\partial U}{\partial R_{i,jk}} = G_{ijkmnl} R_{m,nl}. \quad (9.4)$$

In the general case, the considered elastic body can be anisotropic, and the tensors of generalized elastic properties satisfy the potentiality conditions:

$$C_{ijkml} = C_{kmlj}, \quad G_{ijkmnl} = G_{mnlijk}. \quad (9.5)$$

Cauchy stress tensor σ_{ij} in (9.4), (9.5) can be asymmetrical $\sigma_{ij} \neq \sigma_{ji}$, but the moment stress tensor σ_{ijk} must be symmetrical in the last pair of indices due to the requirement of continuity of distortions, $R_{i,km}$ ($R_{i,km} - R_{i,mk} = 0$) (Gusev and Lurie, 2017):

$$\sigma_{ijk} = \sigma_{ikj}. \quad (9.6)$$

The last equality entails additional symmetry conditions for the tensor of elastic moduli of the sixth rank – the symmetry with respect to the permutation of the last two indices in each of the triples of indices (9.6). In particular, for an isotropic body, the tensors of the moduli of gradient elasticity have the form

$$\begin{aligned}
C_{ijklm} &= \lambda \delta_{ij} \delta_{km} + \mu (\delta_{ik} \delta_{jm} + \delta_{im} \delta_{jk}), \\
G_{ijklmnl}^T &= C_1 (\delta_{ij} \delta_{km} \delta_{nl} + \delta_{mn} \delta_{li} \delta_{jk} + \delta_{ik} \delta_{jm} \delta_{nl} + \delta_{ml} \delta_{ni} \delta_{jk}) + \\
&\quad + C_2 (\delta_{ij} \delta_{kn} \delta_{ml} + \delta_{mn} \delta_{lj} \delta_{ik} + \delta_{ij} \delta_{kl} \delta_{mn} + \delta_{ik} \delta_{jn} \delta_{ml}) + \\
&\quad + C_3 (\delta_{in} \delta_{jl} \delta_{km} + \delta_{mj} \delta_{nk} \delta_{li} + \delta_{in} \delta_{mj} \delta_{kl} + \delta_{il} \delta_{jn} \delta_{mk}) + \\
&\quad + C_4 (\delta_{im} \delta_{jn} \delta_{kl} + \delta_{im} \delta_{jl} \delta_{nk}) + \\
&\quad + C_5 (\delta_{im} \delta_{jk} \delta_{nl}),
\end{aligned} \tag{9.7}$$

where λ, μ are the Lamé coefficients.

Note that the feature of the statement of boundary value problems of gradient elasticity for the body bounded by the piecewise smooth surface F is, in contrast to classical elasticity, the possibility of formulating boundary conditions on the edges—the lines of intersection of smooth fragments of surfaces bounding the body under consideration. This feature is often interpreted as one of the advantages of gradient elasticity theories (Reiher et al, 2017), despite the fact that the question of the existence of solutions in boundary value problems with edges in the space of continuous functions with continuous derivatives (i.e., in the class of classical solutions of equations of mathematical physics) remains open. Also the numerical implementation of the high-order models with edge-type boundary conditions is challenging (Bersani et al, 2020).

The variational formulation based on the Lagrange variational principle leads to the following variational equation (see (9.1)–(9.4)):

$$\begin{aligned}
&\int_V \{ [C_{ijmn} R_{m,n} - G_{ijklmnl} R_{m,nlk}]_{,j} + P_i^V \} \delta R_i dV + \\
&\quad + \int_F \{ P_i^F - [C_{ijmn} R_{m,n} - G_{ijklmnl} G_{abkijl} R_{m,nlk}] n_j + \\
&\quad + (G_{mnlijk} R_{m,nl}) n_k \}_{,p} \delta_{pj}^* + H (G_{mnlijk} R_{m,nl}) n_k n_j \} \delta R_i dF - \\
&\quad - \int_F (G_{mnlijk} R_{m,nl}) n_j n_k \delta (\partial_n R_i) dF - \\
&\quad - \sum_k \oint_{S_k} (G_{mnlijk} R_{m,nl}) v_j n_k \delta R_i ds = 0.
\end{aligned} \tag{9.8}$$

Here the tensor $\delta_{pj}^* = \delta_{pj}^* - n_p n_j$, $\delta_{pj}^* = (s_p s_j + v_p v_j)$, where s_j, v_j are unit vectors lying in the plane orthogonal to the surface normal to 1 the surface n_j , where s_j is the unit vector tangent to the edge contour, and v_j is the unit normal vector to the edge in the tangent plane, $R_{i,p} n_p = (\partial R_i / \partial x_p) n_p = \nabla_n R_i$, $H = \nabla_p^S (n_p)$, $\nabla_p^S (\dots) = (\dots)_{,q} \delta_{qp}^*$.

The arguments of the corresponding functional in the volume of the body and on the surface are the displacement vector R_i , the scalar $R_{i,q} n_i n_q$, and on the contour formed by the intersection of the surfaces—the scalar $\delta (R_i \nu_i)$.

Let us give the following definition: A *standard variation model* is the variant model in which the components of the displacement vector and the components of the normal derivatives of the displacement vector are independent generalized kinematic variables on the surface.

Recall that, in contrast to the classical theory of elasticity, in the variational formulation of gradient elasticity, the space of possible kinematic arguments is determined not only by the continuous field of displacements and the continuous field of the distortion tensor, i.e. the first derivatives of displacements in the volume of the body and on its surface, but also by a continuous field of second derivatives in the volume. This is taken into account when we describe the mathematical formulation of gradient elasticity.

Let us write down the complete mathematical formulation for gradient elasticity in displacements, which is determined by the variational Lagrange equation (9.8). Variational equality (9.8) gives a complete mathematical formulation for gradient elasticity. The governing equilibrium equation (Euler’s equation) has the form

$$C_{ijmn}R_{m,nj} - G_{ijkmnl}R_{m,nlkj} + P_i^V = 0. \tag{9.9}$$

Consequently, the desired displacement vector must be determined by a system of fourth-order differential equations (9.9). Equilibrium equations (9.9) allow introducing the definition of “classical” stresses (total stresses) τ_{ij} , i.e. stresses satisfying the classical equilibrium equations:

$$\tau_{ij,j} + P_i^V = 0, \tag{9.10}$$

where $\tau_{ij} = \sigma_{ij} - \sigma_{ij,k} = C_{ijmn}R_{m,n} - G_{ijkmnl}R_{m,nlk}$.

For a body surface formed by planes, the spectrum of boundary value problems is determined by six pairs of alternative boundary conditions at each non-singular point of the surface

$$\int_F \left\{ [P_i^F - \tau_{ij}n_j + (G_{ijkmnl}n_k R_{m,nl})_{,p} \delta_{pj}^*] \delta R_i - (G_{ijkmnl}n_k R_{m,nl})n_j \delta(R_{i,p}n_p) \right\} dF = 0, \tag{9.11}$$

and by a pair of alternative boundary conditions on the edges, which are the focus of the intersection points of piecewise smooth planes

$$\sum \oint (G_{ijkmnl}n_k R_{m,nl})v_j \delta R_i ds = 0. \tag{9.12}$$

Conditions (9.11) and (9.12) can be rewritten in the form of the corresponding pairs of static and kinematic conditions:

On the surface of the body $F = F_1 \cup F_2 \cup \dots \cup F_{N-1} \cup F_N$, F_i , $i = 1, N$,

$$\begin{aligned}
P_i^F - \tau_{ij}n_j + (G_{ijklmnl}n_k R_{m,nl})_{,p} \delta_{pj}^* = 0, \quad \text{or} \quad R_i = R_{i0}, \\
(G_{ijklmnl}n_k R_{m,nl})n_j = 0 \quad \text{or} \quad (R_{i,p}n_p) = R_{i,n}^0,
\end{aligned} \tag{9.13}$$

On the edges $l = l_1 \cup l_2 \cup \dots \cup l_{N-1} \cup l_N$, l_i , $i = 1, N$

$$G_{ijklmnl}n_k R_{m,nl}v_j = f_i^0 \quad \text{or} \quad R_i = r_{i0}. \tag{9.14}$$

In the future, we will show that, along with the standard gradient elasticity models with potential energy density (9.2), it can be constructed an extended family of gradient elasticity models, in which the variational models have the same structure for the potential energy density. Nevertheless, models from this class differ from the standard model, the mathematical statements of the boundary conditions for them are different than for the standard model (9.8)–(9.14).

Let's give the following definition: *The models will be called quasi-equivalent models of gradient elasticity if these models have the same set of kinematic arguments and for them the density of potential energy in the volume has the same form.*

The purpose of this work is to show that, along with the standard variational models derived on the basis of the Lagrange variational principle, there is the family of the model with the same form of the potential density energy, but differing in mathematical formulation as whole, i.e. having different boundary value problems. Note that for these different approaches the constitutive equations and governing equations are the same due to the fact that the potential energy density uniquely determines the physical model and the equilibrium equations for the deformation process under consideration.

For the gradient elasticity, such a variety of models is of significant practical interest due to the following circumstances:

- the existence of an ambiguous interpretation of static boundary conditions for moment stresses and the impossibility of physical implementation of these conditions;
- the possibility of simplifying mathematical formulations and defining new classes of applied models;
- the existence of the alternative models and alternative solutions of the boundary value problems including conditions on the edges (meniscus forces) or without them.

The existence of alternative gradient elasticity models, together with the uncertainty associated with the implementation of these conditions, often requires the formulation of the criteria for choosing the most preferred models from the presented.

9.3 Family of Quasi-Equivalent Models

Let us consider as the main model the standard model of the gradient medium, for which the Lagrangian has the form (9.1)–(9.3), and the mathematical model is

determined by the variational equality (9.7), (9.8). Let us indicate the structure of quasi-equivalent models and briefly discuss these models.

Following the definition, the set of extended models are formulated by introducing linear restrictions on the body surface for variations of standard model arguments. In the general case, the variational problem on the surface of the body is associated with the variation on the body surface of six independent variables—three components of the displacement vector and normal derivatives of the displacement vector. Thus, we can introduce and consider six independent restrictions for every considered model. We assume that, in the general case, these relations include linear combinations of the displacement vector and the first derivatives of the displacement vector. They are introduced on the surface of the body F and are set by vector equations:

For any $x_i \subset F$, $F = F_1 \cup F_2 \cup \dots \cup F_{N-1} \cup F_N$, F_i , $i = 1, N$

$$L_k^{R_i \cup R_{i,j}}(R_i, R_{i,j}) = c_{ik}^a R_i + c_{ij k}^a R_{i,j} - g_k^a = 0, \quad i, j, k = 1, 2, 3, \quad a = 1, 2. \tag{9.15}$$

Here c_{ij}^a , $c_{ij k}^a$ are the tensors of the second and third rank, g_i^a are known continuous functions of surface coordinates.

The following statement holds.

Lemma. *The space of quasi-equivalent models is completely determined by the kinematical restrictions (9.15).*

Proof. Indeed, if (9.15) takes place on a piecewise smooth surface of the body, then we can introduce the extended Lagrange functional

$$\begin{aligned} \tilde{L} = L + \int_F \Lambda_k^a (c_{ik}^a R_i + c_{ij k}^a R_{i,j} - g_k^a) dF = A - \int_V U_V(R_{i,j}, R_{i,j k}) dV + \\ + \int_F \Lambda_k^a (c_{ik}^a R_i + c_{ij k}^a R_{i,j} - g_k^a) dF, \end{aligned} \tag{9.16}$$

where Λ_k^a are two vectors—Lagrange multipliers, $U_V(R_{i,j}, R_{i,j k})$ is potential energy density defined in the body volume.

The spectrum of extended models is determined by the variational equation

$$\delta \tilde{L} = 0. \tag{9.17}$$

Obviously, for all the models defined in this way (9.16), (9.17), the potential energy density is the same, equal to the potential energy density in the standard model, since it is not modified by the relations introduced on the body surface. The lemma is proved.

9.3.1 Kinematic Restrictions for Displacement Vector Components

Let us consider the simplest class of quasi-equivalent models and try to clarify their physical meaning. Suppose that an extended range of models is constructed according to the following system of kinematic restrictions

$$L_{ij}^R(R_i) = c_{ij}R_i - g_i = 0, \quad i = 1, 2, 3, \quad (9.18)$$

where $c_{ij} = c_1 n_i n_j + c_2 \delta_{ij}^*$, c_1, c_2 are constants.

Let us consider the variational form associated with the kinematic constraint (9.18)

$$\delta \Lambda_k(c_{ik}R_i - g_k) = 0, \quad (9.19)$$

where Λ_j is the vector of Lagrange multipliers.

The set of quasi-equivalent models in this case (9.19) is determined by the extended Lagrange functional

$$\begin{aligned} \tilde{L} &= L + \int_F \Lambda_k(c_{ij}R_i - g_i^a) dF \\ &= A - \int_V U_V(R_{i,j}, R_{i,jk}) dV + \int_F \Lambda_k(c_{ik}R_i - g_k) dF, \end{aligned} \quad (9.20)$$

The mathematical formulation is determined by the variational equation

$$\begin{aligned} &\int_V \{ [C_{ijmn}R_{m,n} - G_{ijkml}R_{m,nlk}]_{,j} + P_i^V \} \delta R_i dV + \\ &+ \int_F \{ P_i^F - [C_{ijmn}R_{m,n} - G_{ijkml}R_{m,nlk}]n_j + \\ &+ (G_{mnljik}R_{m,nl})n_k \}_{,p} \delta_{pj}^* + H(G_{mnljik}R_{m,nl}n_k)n_j + \Lambda_j c_{ij} \} \delta R_i dF - \\ &- \int_F (G_{mnljik}R_{m,nl})n_j n_k \delta(\partial_n R_i) dF + \int_F \delta \Lambda_k(c_{ik}R_i - g_k) dF - \\ &- \sum_k \oint_{S_k} (G_{mnljik}R_{m,nl})v_j n_k \delta R_i ds = 0. \end{aligned} \quad (9.21)$$

The Lagrange multipliers Λ_j in Eq. (9.21) are found so that the “classical” static boundary conditions are satisfied

$$\begin{aligned} \Lambda_p &= c_{ip}^{-1} \{ P_i^F - [C_{ijmn}R_{m,n} - G_{ijkml}G_{abkijl}R_{m,nlk}]n_j + \\ &+ (G_{mnljik}R_{m,nl})n_k \}_{,p} \delta_{pj}^* + H(G_{mnljik}R_{m,nl})n_k n_j \}, \quad (9.22) \\ c_{ij}c_{ip}^{-1} &= \delta_{jp}. \end{aligned}$$

The boundary value problem for an extended spectrum of quasi-equivalent models has the form:

$$\left\{ \begin{array}{l} \tau_{ij,j} + P_i^V = 0, \quad x_i \subset V. \\ \text{a) if } \Lambda_j = 0, \quad \tau_{ij}n_j + (\sigma_{ijk}n_k)_{,p}\delta_{pj}^* + H(\sigma_{ijk}n_kn_j) = P_i^F \\ \quad \text{or } R_i = R_i^0, \quad x_i \subset F, \\ \text{b) if } \Lambda_j \neq 0, \quad c_{ki}^{R_k} - g_i = 0, \quad x_i \subset F, \\ \quad \sigma_{ijk}n_jn_k = \mu_i, \quad \text{or } \partial_n R_i = 0, \quad x_i \subset F, \\ \quad \sigma_{ijk}v_jn_k = \mu_i^S \quad \text{or } R_i = R_i^{S_j}, \quad x_k \subset S, \\ S = S_1 \cup S_2 \cup \dots \cup S_j \cup \dots \cup S_N \cup l_{N-1}, \quad j = 1, N. \end{array} \right. \quad (9.23)$$

Let's note that the set of quasi-equivalent models (9.23) was established using kinematic restrictions (9.18), i.e., using the boundary conditions formulated in displacements

$$\begin{aligned} R_j &= c_{ij}^{-1}g_i, \quad x_i \subset F, \\ c_{ij}^{-1}c_{ki} &= \delta_{jk} \end{aligned} \quad (9.24)$$

together with the boundary conditions in (9.23)

$$\sigma_{ijk}n_jn_k = \mu_i \quad \text{or} \quad \partial_n R_i = 0, \quad x_i \subset F. \quad (9.25)$$

These models with conditions (9.18)–(9.24) may be more attractive in terms of applications since during the solution in displacements based on the Lagrange variational principle, the solution is defined in the class of continuous displacements, and the boundary condition on the contours of the edges in the variational formulation must be excluded. Thus, in the gradient quasi-equivalent model obtained from the standard model by taking into account the kinematic constraints (9.18) on the piecewise-smooth surface of the body, the conditions on the edge contour can be disregarded. However, meniscus forces $(G_{mnlijk}R_{m,nl})v_jn_k$ can be found after solving the boundary value problem. The question of the existence of solution for a piecewise-smooth surface in the class of continuous functions with continuous continuation on the boundaries of domains – edges, is solved in the affirmative with the help of embedding theorems.

9.3.2 Gradient Static Friction Model

In addition to (9.18) let us consider the scalar kinematic restriction between normal and tangent projection of the displacement

$$\begin{aligned} (d_1 R_i n_i - d_2 R_i s_i^*) &= g, \quad n_i s_i^* = 0, \\ s_k^* &= \frac{R_i \delta_{ik}^*}{\sqrt{R_p R_q \delta_{pq}^*}} = \frac{R_i \delta_{ik}^*}{B}, \quad B = \sqrt{R_a R_b \delta_{ab}^*}, \end{aligned} \quad (9.26)$$

where d_1, d_2 are constants, $d_1 \neq 0$.

It is easy to show that scalar kinetic equation (9.26) could not be received from (9.18) as a particular case and is the additional set of kinetic equations (9.18).

We show that it is possible to establish the variational static friction model introducing these restrictions. Let us first consider a variational model of classical elasticity and conditionally divide the surface of the body into the one on which the forces are given and another where the displacements are given $F = F_\sigma \cup F_R$

$$\int_V (\sigma_{ij,j} + P_i^V) \delta R_i dV + \int_{F_\sigma} (P_i^F - \sigma_{ij} n_j) \delta R_i dF - \int_{F_R} \sigma_{ij} n_j \delta R_i dF = 0. \quad (9.27)$$

Let the stress tensor satisfy the equilibrium equations and static boundary conditions on a part of the surface F_σ . Then for the any solutions the variational equality (9.27) for $\forall x_i \subset F_R$ can be presented as follows

$$\int_{F_R} \sigma_{ij} n_j \delta R_i dF = 0. \quad (9.28)$$

Lemma 1. *If on the part of surface $\forall x_i \subset F_R$ the components of the stress tensor are satisfied to the relations corresponding to the model of static friction with the coefficient of friction equal to k_σ , then the variational equation (9.28) corresponds to the introduction of kinematic restriction (9.26) $R - k_\sigma r = 0$, $R_i = r_j \delta_{ij}^* + R n_i$, $d_2/d_1 = -k$ on the part of the surface under consideration.*

Proof. Let us consider the stress vector $(\sigma_{ij} n_j)$ and introduce the unit vector belonging to the tangent plane and collinear to the tangent projection of the stress vector on the surface F_R , $s_k^\sigma = \sigma_{ij} \delta_{ik}^* n_j / \sqrt{(\sigma_{pa} n_a)(\sigma_{qb} n_b) \delta_{pq}^*}$, $\delta_{pq}^* = \delta_{pq}^- n_p n_q$.

We assume that normal and shear stresses satisfy the condition of the static friction model for $\forall x_i \subset F_R$, $(\sigma_{ij} n_j) = \sigma n_i + \tau s_i^\sigma$, $\tau = (\sigma_{ij} n_j) s_i^\sigma$, $\sigma = (\sigma_{ij} n_j) n_i$:

$$(\sigma_{ij} n_j) s_i^\sigma = -k_\sigma (\sigma_{ij} n_j) n_i \quad \text{or} \quad \tau = -k_\sigma \sigma, \quad (9.29)$$

where k_σ is coefficient of friction.

To prove the Lemma, let us consider the variational form (9.28) and transform it taking into account Eq. (9.29). We get

$$\begin{aligned}
\int_{F_\sigma} \sigma_{ij} n_j \delta R_i dF &= - \int_{F_\sigma} (\sigma_{aj} n_j) \delta_{ia} \delta R_i dF \\
&= \int_{F_\sigma} (\sigma_{aj} n_j) (n_a n_i + s_a^\sigma s_i^\sigma) \delta R_i dF \\
&= \int_{F_\sigma} [(\sigma_{aj} n_j) n_a n_i + (\sigma_{aj} n_j) s_a^\sigma s_i^\sigma] \delta R_i dF \\
&= \int_{F_\sigma} [(\sigma_{aj} n_a n_j) n_i + (-k \sigma_{aj} n_a n_j) s_i] \delta R_i dF \\
&= \int_{F_\sigma} (\sigma_{aj} n_a n_j) (n_i - k_\sigma s_i^\sigma) \delta R_i dF \\
&= \int_{F_\sigma} (\sigma_{aj} n_a n_j) \delta (R_i n_i - k_\sigma R_i s_i^\sigma) dF.
\end{aligned} \tag{9.30}$$

The last term in the equation above determines the possible work of the internal forces on the kinematic restriction in which the normal $R = R_i n_i$ and transverse $r = R_i s_i^\sigma$ components are linked by an equality $R/r = k$ for $k = k_\sigma$. The Lemma 1 is proven.

Consider the opposite statement and show that the quasi-equivalent models based on the kinematic restriction (9.26) give us the set of the static friction models. Assume that the condition (9.26) is satisfied in the form

$$R_i n_i - k_{R_i} s_i^* = 0. \tag{9.31}$$

Introducing the Lagrange multiply Λ and taking into account Eq. (9.29) we can write the equation as

$$\begin{aligned}
\int_{F_\sigma} \Lambda \delta (R_i n_i - k R_i s_i^*) dF &= \int_{F_\sigma} [\Lambda (n_i - k s_i^*)] \delta R_i dF = \\
&= \int_{F_\sigma} [(\Lambda) n_i + (-k \Lambda) s_i^*] \delta R_i dF - \int_{F_\sigma} \sigma_{ij} n_j \delta R_i dF = \\
&= \int_{F_\sigma} [(\Lambda) n_i + (-k \Lambda) s_i^* - \sigma_{ij} n_j] \delta R_i dF = 0.
\end{aligned} \tag{9.32}$$

Let us find the Lagrange multiplier Λ satisfying equation (9.32). To fulfill the equality (9.32), one should take

$$\begin{cases} \Lambda = \sigma_{ij} n_i n_j, \\ -k \Lambda = \sigma_{ij} s_i^* n_j \end{cases} \Rightarrow -k \sigma_{ij} n_i n_j = \sigma_{ij} s_i^* n_j \Rightarrow -k \sigma + \tau = 0, \tag{9.33}$$

where $\tau = \sigma_{ij}s_i^*n_j$, $\sigma = \sigma_{ij}n_in_j$.

As a result we found from (9.33) that the normal σ and transverse τ components are connected by the ratio $\tau = -k_\sigma\sigma$, $k_\sigma = -k$, which determines the law of static friction with the coefficient of friction k_σ . The lemma is proven.

The proved statements for the static friction model are transferred to the general case of the gradient model. It is only necessary to redefine the stresses involved in the static boundary condition through the stress $\tau_{ij}n_j + (\sigma_{ijk}n_k)_{,p}\delta_{pj}^* + H(\sigma_{ijk}n_kn_j)$ for which the static boundary conditions are written in the gradient theory

$$\hat{\sigma}_{ij} \sim \tau_{ij}n_j + (\sigma_{ijk}n_k)_{,p}\delta_{pj}^* + H(\sigma_{ijk}n_kn_j) \quad (9.34)$$

and assume that the equilibrium equations, nonclassical boundary conditions on the surface, boundary conditions on the edges, and static boundary conditions on a part of the surface F_σ are satisfied for the gradient theory. Then, the equation defining the model of static friction has the form

for $\forall x_i \subset F_R$ $(\hat{\sigma}_{ij}n_j)s_i^\sigma = -k_\sigma(\hat{\sigma}_{ij}n_j)n_i$ or $\tau = -k_\sigma\sigma$
 where $(\hat{\sigma}_{ij}n_j) = \sigma n_i + \tau s_i^\sigma$, $\tau = (\hat{\sigma}_{ij}n_j)s_i^\sigma$, $\sigma = (\hat{\sigma}_{ij}n_j)n_i$.

Remark. Let us consider scalar kinematic restriction (9.26) and present this one as the follow

$$c_i R_i = g, \\ c_i = c_n n_i + c_s s_i + c_v v_i.$$

Note that the scalar kinematic equation $c_i R_i = g$ is not a consequence of the vector kinematic condition (9.18), which were considered as kinematic constraints on the surface to elaborate the corresponding quasi-equivalent model (9.23). Consequently, condition $c_i R_i = g$ generates a special quasi-equivalent model. The mathematical formulation of this model is determined by the variational equation

$$\begin{aligned} & \int_V \left\{ [C_{ijmn}R_{m,n} - G_{ijkmnl}R_{m,nlk}]_{,j} + P_i^V \right\} \delta R_i dV + \\ & + \int_F \left\{ P_i^F - [C_{ijmn}R_{m,n} - G_{ijkmnl}R_{m,nlk}]n_j + \right. \\ & + (G_{mnlijk}R_{m,nl})n_k)_{,p}\delta_{pj}^* + H(G_{mnlijk}R_{m,nl}n_kn_j) + \Lambda c_i \left. \right\} \delta R_i dF - \\ & - \int_F (G_{mnlijk}R_{m,nl})n_j n_k \delta(\partial_n R_i) dF + \int_F \delta \Lambda (c_i R_i - g) dF - \\ & - \sum_k \oint_{S_k} (G_{mnlijk}R_{m,nl})v_j n_k \delta R_i ds = 0. \end{aligned} \quad (9.35)$$

A feature of the mathematical formulation for the gradient model that can be elaborated on the based of scalar constraint $c_i R_i - g = 0$ is that three static boundary conditions of the standard model are replaced by a system of three

conditions among which there is one scalar kinematic condition $c_i R_i - g = 0$, and the other two conditions $P_i^F(s_i - n_i c_s / c_n) - \tau_s + \sigma(c_s / c_n) = 0$ and $P_i^F(v_i - n_i c_v / c_n) - \tau_v + \sigma(c_v / c_n) = 0$, $\tau_v = \sigma_{ij} n_i v_j$ are static conditions which define the generalized friction model. The Lagrange multiplier is found so, that the static boundary condition for the normal stress component is satisfied

$$\Lambda = -P_i^F n_i / c_n + \sigma / c_n, \quad \sigma = \sigma_{ij} n_i n_j. \quad (9.36)$$

The boundary value problem for an extended specific of quasi-equivalent model based on the restriction $c_i R_i - g = 0$ has the form:

$$\tau_{ij,j} + P_i^V = 0, \quad x_i \subset V,$$

$$\begin{aligned} \text{a) if } \Lambda = 0, \quad & \tau_{ij} n_j + (\sigma_{ijk} n_k)_{,p} \delta_{pj}^* + H(\sigma_{ijk} n_k n_j) = \sigma_i^0 \\ \text{or } R_i = R_i^0, \quad & x_i \subset F, \end{aligned}$$

$$\text{b) if } \Lambda \neq 0,$$

$$\left\{ \begin{array}{l} x_i \subset F, \\ c_k R_k - g = 0, \\ P_i^F(s_i - n_i c_s / c_n) - \tau_s + \sigma(c_s / c_n) = 0, \quad \tau_s = \sigma_{ij} n_i s_j, \\ P_i^F(v_i - n_i c_v / c_n) - \tau_v + \sigma(c_v / c_n) = 0, \quad \tau_v = \sigma_{ij} n_i v_j, \\ s_i v_j n_k e_{ijk} = 0, \end{array} \right.$$

$$x_i \subset F \quad \left\{ \begin{array}{l} \sigma_{ijk} n_j n_k = \mu_i^0, \\ \text{or } \partial_n R_i = 0, \end{array} \right.$$

$$x_k \subset S, \quad S = S_1 \cup S_2 \cup \dots \cup S_j \cup \dots \cup S_N \cup l_{N-1},$$

$$j = 1, N \quad \left\{ \begin{array}{l} \sigma_{ijk} v_j n_k = \mu_i^S, \\ \text{or } R_i = R_i^{S_j}, \end{array} \right.$$

here e_{ijk} is the permutation pseudo-tensor of the Tullio Levi-Civita.

9.3.3 Kinematic Restrictions for Components of Derivatives of Displacements

Let us consider the spectrum of quasi-equivalent models built by introduction on the body surface of three kinematic restrictions of the form:

$$a_{ijk}(R_{i,j}) - f_k = 0, \quad k = 1, 2, 3, \quad (9.37)$$

a_{ijk} is a the transverse isotropy tensor of the third rank with respect to the normal to the surface, $a_{ijk} = a^1 \delta_{ij}^* n_k + a^2 \delta_{jk}^* n_i + a^3 \delta_{ki}^* n_j + a^4 n_i n_j n_k$, a^i ($i = 1 \div 4$) are constants.

Accordingly, kinematic restrictions (9.37) are introduced on the vector of multipliers of Lagrange Λ_k and the extended Lagrange functional has the form

$$\tilde{L} = L + \int_{\delta} \bar{L} = \delta L + \delta \int_F \Lambda_k [a_{ijk}(R_{i,j}) - f_k] dF. \quad (9.38)$$

In accordance with (9.37), (9.38), the variational equation for the extended spectrum of models has the form

$$\begin{aligned} \delta \tilde{L} = & \int_V (C_{ijmn} R_{m,nj} - G_{ijklmn} R_{m,nlkj} + P_i^V) \delta R_i dV + \\ & + \int_F (a_{aij} R_{i,j} - f_a^F) \delta \Lambda_a dF + \\ & + \int_F \{ [P_i^F - (C_{ijmn} R_{m,n} - G_{lmnij} R_{l,mn}) n_j + \\ & + H(G_{lmnij} R_{l,mn} n_k n_j - \Lambda_k a_{kij} n_j) + \\ & + (G_{ijklmn} R_{l,mn} n_k - \Lambda_k a_{kij})_{,p} \delta_{pj}^*] \delta R_i - \\ & - (G_{ijklmn} R_{l,mn} n_k - \Lambda_k a_{kij}) n_j \delta (R_{i,p} n_p) \} dF - \\ & - \sum \oint (G_{ijklmn} R_{l,mn} n_k - \Lambda_k a_{kij}) v_j \delta R_i ds = 0. \end{aligned} \quad (9.39)$$

Lagrange multipliers Λ_k can be found so that nonclassical boundary conditions are satisfied in (9.39)

$$(G_{ijklmn} R_{l,mn} n_k - \Lambda_k a_{kij}) n_j = 0. \quad (9.40)$$

It is easy to verify that the vector of Lagrange multipliers, ensuring the fulfillment of (9.40), has the form

$$\Lambda_p = G_{lmnij} (n_k n_j A_{pi}^{-1}) R_{l,mn} = c_{lmnp} R_{l,mn}, \quad (9.41)$$

where according to (9.37)

$$\begin{aligned} A_{ik} = a_{ijk} n_j = a^3 \delta_{ki}^* + a^4 n_i n_k, \quad A_{pi}^{-1} A_{ik} = \delta, \quad A_{pi}^{-1} = a^{-3} \delta_{pi}^* + a^{-4} n_i n_p, \\ c_{lmnp} = G_{lmnia} \left(\frac{1}{a^3} \delta_{pi}^* n_k n_a + \frac{1}{a^4} n_i n_p n_k n_a \right). \end{aligned} \quad (9.42)$$

As a result the boundary conditions on the edges could be modified due to the parameters included in the kinematic equations (9.40)

$$\sum \oint (G_{ijklmn} R_{l,mn} n_k - \Lambda_k a_{kij}) v_j \delta R_i ds = 0 \quad (9.43)$$

and meniscus forces $\psi_i = (G_{ijklmn}R_{l,mn}n_k - \Lambda_k a_{kij})v_j$ in (9.43) also can be modified due to the vector of the Lagrange multiplier using (9.41), (9.42).

Static boundary conditions following their variational equation (9.39) also can be modified due to the parameters included in the kinematic conditions (9.40) and can be presented in the terms of displacement using (9.41), (9.42).

Note that the quasi-equivalent model defined by variational equality (9.39) leads to a change in the boundary value problem by replacing the “rigid” boundary conditions $R_{i,p}n_p = \dot{R}_i^0$ in the nonclassical boundary condition with “softer” boundary conditions (9.37) under which linear combinations of the derivatives of the displacement vector are specified. Such an alternative formulation can be useful in conditions of uncertainty in the interpretation of moment factors and the corresponding kinematic factors on the body surface. The choice between such two statements should probably be made by invoking an energy criterion. In (Lurie et al, 2021), for a specific example of hydrostatic loading of a sphere, it is shown that “soft” boundary conditions are preferable for a mechanical system if the criterion of total strain energy is used.

9.4 Examples of Gradient Models without Edge Conditions

Let us consider two variants of variational gradient models of deformation, in which the use of an extended class of semi-equivalent models makes it possible to construct applied gradient models of elasticity without boundary conditions on the edges.

9.4.1 Variational Gradient Dilation Model

Let’s consider a gradient dilation model with a potential energy density in the volume of the body $2w = C_{ijmn}R_{m,n}R_{i,j} + C_{kn}\theta_k\theta_n$, $C_{kn} = Kl^2\delta_{kn}$. K is the volumetric modulus of elasticity, l^2 is the scale parameter of the model. For simplicity, we assume that the surface of a body is formed by a system of planes. Then the standard variational model has the form

$$\begin{aligned} \delta L = & \int_V [-Kl^2\Delta R_{k,ki} + C_{ijmn}R_{m,nj} + P_i^V]\delta R_i dV + \\ & + \int_F [P_i^F - C_{ijmn}R_{m,n}n_j + Kl^2\Delta\theta_{ni} + Kl^2n_p\theta_{,p}),_q\delta_{iq}^*]\delta R_i dF - \\ & - \int_F Kl^2n_p\theta_{,p}\delta(R_{i,q}n_i n_q) dF - \sum \oint Kl^2n_p\theta_{,p}\delta(R_i\nu_i) ds = 0. \end{aligned} \tag{9.44}$$

Variational equality (9.44) can also be written in stresses

$$\begin{aligned}
\delta L = & \int_V (\sigma_{ij,j} - \delta_{ij}\sigma_{k,jk} + P_i^V) \delta R_i dV + \\
& + \int_F [P_i^F - (\sigma_{ij} - \delta_{ij}\sigma_{k,k})] n_j \delta R_i dF - \\
& - \sum \oint (\sigma_k n_k v_i) \delta R_i ds + \int_F (\sigma_k n_k)_{,p} \delta_{ip}^* \delta R_i dF - \\
& - \int_F (\sigma_k n_k) \delta (R_{i,p} n_i n_p) dF = 0,
\end{aligned} \tag{9.45}$$

where $\sigma_{ij} = C_{ijklm} R_{l,m}$, $\sigma_{ijk} = G_{ijklmn} R_{l,mn} = \sigma_k \delta_{ij}$, $\sigma_k = C_{kn} \theta_n = C_{kn} R_{l,ln} = (Kl^2 \delta_{kn}) R_{l,ln}$.

The nonclassical boundary condition in (9.44) (see also (9.45)) is scalar equation. Therefore, we assume that the class of semi-equivalent models is determined by the kinematic connection on the derivatives of displacements, represented in the form of a scalar equality:

$$a_{ij} R_{i,j} = f. \tag{9.46}$$

For an isotropic body with an isotropic surface, a second-rank tensor a_{ij} can generally have the following structure, $a_{ij} = n_i n_j + a \delta_{ij}^*$, $\delta_{ij}^* n_i = 0$, where a is a constant. Therefore, the kinematic relationship (9.46) on the surface of the body can be represented in the form

$$(R_{i,q} n_q) n_i + a (R_{i,j} \delta_{ij}^*) = (\dot{R} + a (R_{i,j} \delta_{ij}^*)) = f. \tag{9.47}$$

Taking into account (9.47), the variational equality for the class of semi-equivalent models is written in the form

$$\begin{aligned}
& \delta \left\{ L + \int_F \Lambda [f - (\dot{R} + a (R_{i,j} \delta_{ij}^*))] dF \right\} = \\
& = \int_V [-Kl^2 \Delta R_{k,ki} + C_{ijmn} R_{m,nj} + P_i^V] \delta R_i dV + \\
& + \int_F [P_i^F - C_{ijmn} R_{m,nj} + Kl^2 \Delta \theta n_i + (Kl^2 n_p \theta_{,p} + a \Lambda)_{,j} \delta_{ij}^*] \delta R_i dF - \\
& - \int_F (Kl^2 n_p \theta_{,p} + \Lambda) \delta (R_{i,q} n_i n_q) dF - \sum \oint (Kl^2 n_p \theta_{,p} + a \Lambda) \delta (R_i v_i) ds + \\
& + \int_F [f - (\dot{R} + a (R_{i,j} \delta_{ij}^*))] \delta \Lambda dF = 0.
\end{aligned} \tag{9.48}$$

here Λ is the Lagrange multiplier.

Variational equality (9.48) defines the mathematical formulation for a generalized model with an extended Lagrange functional. In accordance with the method of Lagrange multipliers in the extended functional in the volume of the body, δR_i are independent variations, on the surface independent variations are δR_i vary independently and the variations $\delta(R_{i,q}n_i n_q)$, $\delta \Lambda$. The displacement vector R_i varies independently on the contour, as well as in the traditional formulation.

The Lagrange multiplier method requires all the corresponding “static” conditions to be equal to zero when all independent variables are varied:

$$[P_i^F - C_{ijmn}R_{m,n}n_j + Kl^2\Delta\theta n_i + (Kl^2n_p\theta_{,p} + a\Lambda)_{,j}\eta_{ij}] = 0, \quad x_i \in F, \tag{9.49}$$

$$(Kl^2n_p\theta_{,p} + \Lambda) = 0, \quad x_i \in F, \tag{9.50}$$

$$(Kl^2n_p\theta_{,p} + a\Lambda) = 0, \quad x_i \in S = \cup S_k, \tag{9.51}$$

$$f - (\dot{R} + a(R_{i,j}\delta_{ij}^*)) = 0, \quad x_i \in F = \cup F_k. \tag{9.52}$$

The Lagrange multiplier Λ is determined from the condition of the fulfillment of the nonclassical boundary condition (9.50):

$$\Lambda = -Kl^2n_p\theta_{,p}. \tag{9.53}$$

As a result, as follows from (9.48) and (9.49)–(9.52), in the general case, the classical vector static boundary conditions (9.49) and the scalar contour static condition (9.51) are modified due to the known Lagrange multiplier Λ satisfying the equality (9.53).

Let us note an important class of models whose boundary value problems are solved without using conditions on the edge contour, in fact, as it is in problems of elasticity theory. Due to the fact that the condition (9.50) is scalar, then if $a = 1$, the static boundary condition in the contour integral (9.51) is identically satisfied, and the classical boundary condition (9.49) is also simplified. The variational model takes the form

$$\begin{aligned} & \int_V [-Kl^2\Delta R_{k,ki} + C_{ijmn}R_{m,nj} + P_i^V]\delta R_i dV + \\ & + \int_F [P_i^F - (C_{ijmn}R_{m,n} - Kl^2\delta_{ij}\Delta\theta)n_j]\delta R_i dF + \\ & + \int_F Kl^2[f - \theta)]\delta(\theta_{,p}n_p) dF = 0. \end{aligned} \tag{9.54}$$

A feature of this model is that the equilibrium equation and the static boundary condition in (9.54) are formulated on the internal “classical” total stresses

$$\sigma_{ij} = C_{ijmn}R_{m,n} - Kl^2\delta_{ij}\Delta\theta. \tag{9.55}$$

As a result the classical first main problem (in stresses) is highlighted, and the variational formulation does not contain conditions on the contour. Nevertheless, after solving the problem as a whole and determining the Lagrange multiplier Λ , the vector ψ_i of contour forces at the points whose coordinates correspond to the edges

$$\psi_i = -\Lambda v_i. \quad (9.56)$$

Remarks.

1. Under fully kinematic boundary conditions, the standard variational gradient dilation model (9.44) completely coincides with the non-standard variational model (9.54).

2. In the case of static boundary conditions on the body surface with zero values of moment forces on the body surface, determined by the boundary nonclassical conditions in (9.45) $\sigma_k n_k = \sigma^0 = 0$, the variational formulations of the standard model (9.45) and nonstandard model (9.54) also coincide. To show this, let us consider the variational equality for the dilatation standard model and present this one as the follow

$$\begin{aligned} \delta L &= \delta A - \int_V [\sigma_{ij} \delta R_{i,j} + \sigma_{ijk} \delta R_{i,jk}] dV = \\ &= \int_V (\sigma_{ij,j} - \delta_{ij} \sigma_{k,jk} + P_i^V) \delta R_i dV + \int_F [P_i^F - (\sigma_{ij} - \delta_{ij} \sigma_{k,k}) n_j] \delta R_i dF - \\ &\quad - \sum_{\oint} (\sigma_k n_k v_i) \delta R_i ds + \int_F (\sigma_k n_k)_{,p} \delta_{ip}^* \delta R_i dF - \\ &\quad - \int_F [(\sigma_k n_k) - \sigma^0] \delta (R_{i,p} n_i n_p) dF = 0 \end{aligned} \quad (9.57)$$

The non-classical boundary condition in the above equation for moment factors has the form

$$\int_F [\sigma_k n_k - \sigma^0] \delta (R_{i,p} n_i n_p) dF = 0. \quad (9.58)$$

This equality defines a pair of moment alternative boundary conditions: static “moment” condition: $\sigma_k n_k = \sigma^0$ and the kinematic “nonclassical” condition of rigid fixation of the normal $R_{n,n} = R_{i,k} n_i n_k = R_{n,n}^0$ (no summation by n). As a rule, it is not clear how the force moment condition can be realized, therefore, it is assumed reasonable to take on the surface $\sigma_k n_k = \sigma^0 = 0$ where such a static condition arises. Then we receive that the follow two equations hold $\int_F (\sigma_k n_k)_{,p} \delta_{ip}^* \delta R_i dF = 0$ $\int_F (\sigma_k n_k) n_i \delta (R_{i,p} n_p) dF = 0$. Then it can be argued that the boundary value problem is determined by the above variational equation gives the following variation quality $\int_V (\sigma_{ij,j} - \delta_{ij} \sigma_{k,jk} + P_i^V) \delta R_i dV = 0$ and

$\int_F [P_i^F - (\sigma_{ij} - \delta_{ij}\sigma_{k,k})n_j\delta R_i] dF = 0$ and the boundary problem completely coincides with the classical boundary value problem formulated in displacements with respect to semi-classical stresses $\tau_{ij} = \sigma_{ij} - \delta_{ij}\sigma_{k,k}$. Obviously, the boundary conditions on the edges are also fully satisfied automatically and can be omitted during statement.

9.4.2 Variant of Vector Gradient Elasticity Model

Let us consider a variational standard model of general form (9.8) and assume that an extended spectrum of semi-equivalent models is constructed using the kinematic constraints on the derivatives of displacements (9.37). Following the method of Lagrange multipliers, the vector of Lagrange multipliers is found in such a way to satisfy the nonclassical boundary condition (9.39). Let us arrange at our discretion the structure of tensors in kinematic constraints and assume that the third-rank tensor c_{aij} in the definition of kinematic constraints (9.39) has the following particular form $c_{aij} = C_{akij}n_k$, where C_{akij} is the tensor of classical moduli of elasticity. Then the nonclassical boundary condition in (9.39) can be presented as follows:

$$(G_{ijkmnl}n_k R_{m,nl} - \Lambda_a C_{akij}n_k)n_j = 0. \tag{9.59}$$

Let us show that there is a particular form of the structure of the gradient elastic moduli of the sixth rank, for which the last tensor condition can be represented in the form of a convolution of two vectors. Indeed, we put that

$$G_{ijkmnl} = \frac{C_{akij}C_{almn}l^2}{C}, \quad C = \sqrt{C_{abcd}C_{abcd}}. \tag{9.60}$$

Then equality (9.59) can be rewritten as

$$\begin{aligned} &\left(\frac{C_{akij}C_{almn}l^2}{C}n_k R_{m,nl} - \Lambda_a C_{akij}n_k \right)n_j = \\ &= C_{akij}n_k n_j \left(\frac{C_{almn}l^2 R_{m,nl}}{C} - \Lambda_a \right) = 0. \end{aligned} \tag{9.61}$$

The peculiarity of the obtained structure of the nonclassical boundary condition is that the tensor equality can be satisfied exactly by choosing the vector of Lagrange multipliers

$$\Lambda_a = \frac{C_{almn}l^2 R_{m,nl}}{C}. \tag{9.62}$$

The proposed structure of the third-rank tensor c_{aij} in kinematic constraints (9.37) and a special structure of physical gradient elastic moduli (9.60)–(9.62) make it possible to simplify significantly the variational formulation of a non-standard model:

$$\begin{aligned}
\delta \tilde{L} = & \int_V (\underline{C_{ijmn} R_{m,nj} - G_{ijk mnl} R_{m,nlkj}} + P_i^V) \delta R_i dV + \\
& + \int_F \{ [P_i^F - (\underline{C_{ijmn} R_{m,n} - G_{ijk mnl} R_{m,nlk}}) n_j] \delta R_i \} dF + \quad (9.63) \\
& + \int_F (c_{aij} R_{i,j} - r_a^F) \delta C_{al mnl} l^2 R_{m,nl} / C dF.
\end{aligned}$$

The specific feature of the formulation above (9.63) is that in the presented applied model there are no boundary conditions on the edges and the first main problem is clearly distinguished, formulated for the Cauchy stress tensor

$$\sigma_{ij} = C_{ijmn} R_{m,n} - G_{ijk mnl} R_{m,nlk}. \quad (9.64)$$

The presented non-standard one-parameter gradient elasticity model with the given specific properties is a particular case of a wider set of vector models considered earlier (Lurie et al, 2017). Vector models of gradient elasticity are of practical interest because they make it possible to simplify significantly the solutions of specific problems by explicitly separating the sequence of explicitly solvable boundary value problems of second-order equations of mathematical physics instead of the original general problem with the fourth-order operator.

9.5 General Case of Kinematic Restrictions. Generalized Pinching

Let us consider the general case of kinematic constraints from the point of view of boundary conditions at the edges. As it was noted earlier, in the case of specifying three kinematic constraints for displacements, if $\|c_{ij}\| \neq 0$ in (9.15), the variational mathematical model for the class of extended models does not include conditions on the edge contour.

For the case of kinematic conditions on the derivatives of the displacement vector, there were indicated the cases when conditions on the edges are also absent in the variational formulation. More complicated is the question of the conditions on the edges in the general case of kinematic constraints (9.15).

The theorem of the solution existence in such boundary value problems in the class of continuous solutions is established by embedding theorems if the solution is sought in the space W_2^2 . The question of the existence of smoother solutions in the class of continuous functions with continuous derivatives remains open. In this section, this issue is briefly studied for a special class of boundary value problems.

By generalized pinching we will call the conditions that reduce to the requirement that the variations of two different linear combinations of standard kinematic variables and their first derivatives have to be equal to zero (9.15). Let us write the

variational equation for this non-standard extended model, assuming for simplicity that the surfaces are formed by a system of planes:

$$\begin{aligned}
\delta L = & \int_V (C_{ijmn}R_{m,nj} - G_{ijkmnl}R_{m,nlkj} + P_i^V)\delta R_i dV + \\
& + \int_F (c_{kij}^a R_{i,j} + c_{ki}^a R_i)\delta \Lambda_k^a dF + \\
& + \int_F \left\{ [P_i^F - (C_{ijmn}R_{m,n} - G_{ijkmnl}R_{m,nlk})n_j + \right. \\
& + (G_{ijkmnl}n_k R_{m,nl} + \Lambda_k^a c_{kij}^a)_{,p} \delta_{pj}^* + \Lambda_k^a c_{ki}^a] \delta R_i - \\
& - (G_{ijkmnl}n_k R_{m,nl} + \Lambda_k^a c_{kij}^a)n_j \delta (R_{i,p}n_p) \left. \right\} dF - \\
& - \sum \oint (G_{ijkmnl}n_k R_{m,nl} + \Lambda_k^a c_{kij}^a)v_j \delta R_i ds = 0.
\end{aligned} \tag{9.65}$$

Six components of two vectors of indefinite Lagrange multipliers make it possible to satisfy the requirement that all six static factors in the surface integral are equal to zero. However, it arises the question how it is possible to satisfy the requirement of equality to zero of the sum of contour integrals over edges.

If we consider the conditions on the contour as three alternative pairs of boundary conditions on the contour of each smooth surface bounded by a contour of edges, then we can assume that the displacement vector on the surface should not be determined uniquely, but up to the certain vector field, the components of which satisfy the system of differential equations of the second order on every smooth surface. Let us prove that such a field exists in the generalized pinching problem.

The following statement holds.

Theorem. *Let the kinematic conditions be satisfied*

$$c_{ijk}^a R_{j,k} + a_{ij}^a R_j = 0 \quad \text{and} \quad \|c_{kij}^{1,2} n_j\| \neq 0,$$

then, there exists a vector field satisfying a second order partial differential equation (of the type of the generalized Helmholtz equation) on each smooth surface, for which the following variational statement of the boundary value problem is formulated

$$\begin{aligned}
\delta L = & \int_F [A_{ijr} D_{rst} \delta_{pj}^* \lambda_{s,tp} + (A_{ir} D_{rsp} - A_{ijr} D_{rs} \delta_{pj}^*) \lambda_{s,p} - A_{ir} D_{rs} \lambda_s] \delta R_i dF + \\
& + \sum \oint (p_i^* - A_{ijr} v_j D_{rst} \lambda_{s,t} + A_{ijr} v_j D_{rs} \lambda_s) \delta R_i ds = 0.
\end{aligned} \tag{9.66}$$

Proof. We assume that the displacement field is determined as a solution to the system of fourth-order differential equations:

$$C_{ijmn}R_{m,nj} - G_{ijkmnl}R_{m,nlkj} + P_i^V = 0 \tag{9.67}$$

provided that the displacement field on the surface of the body satisfies the postulated constraints (9.15), which determine the boundary value problem of “generalized pinching”. Let’s consider the nonclassical boundary condition $G_{ijkmnl}n_k R_{m,nl} + \Lambda_k^a c_{kij}^a n_j = 0$ and express the components of the vector of Lagrange multipliers in terms of the second derivatives of the displacement vector. Using the condition of the theorem, we find

$$\begin{cases} \Lambda_k^1 = \Lambda_r a_{rk}^{-1} - a_{ki}^{-1} G_{ijamnl} n_j n_a R_{m,nl} / 2, \\ \Lambda_k^2 = -\Lambda_r a_{rk}^{-2} - a_{ki}^{-2} G_{ijamnl} n_j n_a R_{m,nl} / 2, \end{cases} \quad (9.68)$$

where $a_{ki}^1 = c_{kij}^1 n_j$, $a_{ki}^2 = c_{kij}^2 n_j$, $a_{ri}^{-1} a_{ki}^1 = \delta_{rk}$, $a_{ri}^{-2} a_{ki}^2 = \delta_{rk}$.

We can formulate “plane” differential equations with respect to the components Λ_r , using the classical “static boundary conditions, given in the variational equality (9.65)

$$l_r(\Lambda_k^1, \Lambda_k^2) = P_i^F - (C_{ijmn} R_{m,n} - G_{ijkmnl} R_{m,nlk}) n_j + (G_{ijkmnl} n_k R_{m,nl} + \Lambda_k^1 c_{kij}^1 + \Lambda_k^2 c_{kij}^2)_{,p} \delta_{pj}^* + \Lambda_k^1 c_{ki}^1 + \Lambda_k^2 c_{ki}^2 = 0$$

After substituting the components Λ_r into these conditions using equalities (9.68), we find the following system of differential equations for the components Λ_r

$$[P_i^F - (C_{ijmn} R_{m,n} - G_{ijkmnl} R_{m,nlk}) n_j + (g_{ijab} G_{abcmnl} n_c R_{m,nl})_{,p} \delta_{pj}^* - g_{ia} G_{abcmnl} n_b n_c R_{m,nl} / 2] + (A_{ijr} \Lambda_r)_{,p} \delta_{pj}^* + A_{ir} \Lambda_r = 0, \quad (9.69)$$

where

$$\begin{aligned} A_{ir} &= (a_{rk}^{-1} c_{ki}^1 - a_{rk}^{-2} c_{ki}^2), & A_{ijr} &= (a_{rk}^{-1} c_{kij}^1 - a_{rk}^{-2} c_{kij}^2), \\ g_{ia} &= (a_{ka}^{-1} c_{ki}^1 + a_{ka}^{-2} c_{ki}^2), & g_{ijab} &= (\delta_{ia} \delta_{jb} - a_{ka}^{-1} c_{kij}^1 n_b / 2 - a_{ka}^{-2} c_{kij}^2 n_b / 2). \end{aligned} \quad (9.70)$$

We represent the solution of the system of partial differential equations with respect to Λ_r in the form of an expansion:

$$\Lambda_r = \Lambda_r^* + D_{rst} \lambda_{s,t} - D_{rs} \lambda_s, \quad (9.71)$$

where Λ_r^* is the particular solution of the inhomogeneous system, and λ_s is the general solution to the homogeneous system, D_{rst} , D_{rs} are arbitrary transversally isotropic tensors.

In the general case, the vector field λ_s satisfies the generalized “plane” Helmholtz equation. Indeed, the homogeneous equation (9.69) for λ_s can be presented in the form

$$(A_{ijr} \delta_{pj}^* D_{rst}) \lambda_{s,tp} + (A_{ir} D_{rsp} - A_{ijr} \delta_{pj}^* D_{rs}) \lambda_{s,p} - (A_{ir} D_{rs}) \lambda_s = 0. \quad (9.72)$$

Thus, the field of total displacements is defined as a solution to the system of the fourth-order differential equations (9.67) provided that the displacement field on the surface of the body satisfies the postulated constraints (9.15), which determine the boundary value problem of “generalized pinching”. Then the variational equation (9.65) will not contain the integral over the volume, and the surface integral, containing variations of two vectors of Lagrange multipliers, takes the form:

$$\begin{aligned} \int_F \{ & [P_i^F - (C_{ijmn}R_{m,n} - G_{ijkmnl}R_{m,nlk})n_j + \\ & + (G_{ijkmnl}n_k R_{m,nl} + \Lambda_k^a c_{kij}^a)_{,p} \delta_{pj}^* + \Lambda_k^a c_{ki}^a] \delta R_i - \\ & - (G_{ijkmnl}n_k R_{m,nl} + \Lambda_k^a c_{kij}^a) n_j \delta (R_{i,p} n_p) \} dF - \\ & - \sum \oint (G_{ijkmnl}n_k R_{m,nl} + \Lambda_k^a c_{kij}^a) v_j \delta R_i ds = 0. \end{aligned} \quad (9.73)$$

Let us take into account that, in accordance with the Lagrange multiplier procedure, the components Λ_r are found in such a way that static nonclassical conditions are satisfied (the condition of equality to zero of the static multiplier at $\delta(R_{i,p} n_p)$). As a result, the equation (9.73), taking into account equalities (9.68), can be written in terms of Λ_r

$$\begin{aligned} \delta L = \int_F [& P_i^F - (C_{ijmn}R_{m,n} - G_{ijkmnl}R_{m,nlk})n_j + \\ & + (g_{ijab}G_{abcmnl}n_c R_{m,nl})_{,p} \delta_{pj}^* - \\ & - g_{ia}G_{abcmnl}n_b n_c R_{m,nl}/2 + (A_{ijr}\Lambda_r)_{,p} \delta_{pj}^* + A_{ir}\Lambda_r] \delta R_i dF - \\ & - \sum \oint (g_{ijab}G_{abcmnl}n_c R_{m,nl} + A_{ijr}\Lambda_r) v_j \delta R_i ds = 0. \end{aligned} \quad (9.74)$$

Since the displacements satisfy the equilibrium equations (9.67) and the constraints postulated on the surface (9.15), the vector of total displacements is completely determined and in further reasoning can be considered as known. Therefore, for brevity, we define the following generalized force fields:

at every non-singular point of the surface

$$\begin{aligned} P_i = & P_i^F - (C_{ijmn}R_{m,n} - G_{ijkmnl}R_{m,nlk})n_j + (g_{ijab}G_{abcmnl}n_c R_{m,nl})_{,p} \delta_{pj}^* - \\ & - g_{ia}G_{abcmnl}n_b n_c R_{m,nl}/2 \end{aligned}$$

at each point of the contour of edges on the surface

$$p_i = -(g_{ijab}G_{abcmnl}n_c R_{m,nl})v_j.$$

As a result, the variational equation (9.74) defining the vector field Λ_r takes the form

$$\begin{aligned} \delta L = & \int_F [P_i^+ (A_{ijr} \Lambda_r)_{,p} \delta_{pj}^* + A_{ir} \Lambda_r] \delta R_i dF + \\ & + \sum \oint (p_i - A_{ijr} v_j \Lambda_r) \delta R_i ds = 0. \end{aligned} \quad (9.75)$$

On each of the planes that make up the surface of the body, we can introduce a local Cartesian coordinate system and, using the expansion (9.71), reduce the variational equation (9.75) to the “multi-contact plane problem”

$$\begin{aligned} \delta L = & \int_F [A_{ijr} D_{rst} \delta_{pj}^* \lambda_{s,tp} + (A_{ir} D_{rsp}^- A_{ijr} D_{rs} \delta_{pj}^*) \lambda_{s,p} - A_{ir} D_{rs} \lambda_s] \delta R_i dF + \\ & + \sum \oint (p_i^* - A_{ijr} v_j D_{rst} \lambda_{s,t} + A_{ijr} v_j D_{rs} \lambda_s) \delta R_i ds = 0. \end{aligned} \quad (9.76)$$

Here:

$$\begin{cases} P_i + A_{ijr} \delta_{pj}^* \Lambda_{r,p} + A_{ir} \Lambda_r^* = 0, \\ p_i = p_i^* + A_{ijr} v_j \Lambda_r^*. \end{cases} \quad (9.77)$$

Thus, it was established that the vector field on each plane satisfies the generalized Helmholtz equation (9.72) and has enough arbitrariness to satisfy the requirement of continuity of the meniscus forces when passing from one plane to the neighboring one through an edge. Relations (9.68), (9.71), (9.76), (9.77) actually indicate the possibility of obtaining a vector field and prove the theorem of the existence of solution to a boundary value problem with edges for generalized pinching determined by kinematic constraints (9.15).

This indicates the set of models for which the theorem of the existence of solutions for domains with edges holds.

9.6 The Theorem on the Self-Balance of Meniscus Forces

In this part of the article, we will consider one specific formal feature of the behavior of solutions associated with integral conditions for the edges on the body surface in gradient elasticity, which is a consequence of the variational standard formulation.

Let us consider the variational Lagrange equality in stresses, has the form

$$\begin{aligned}
\delta L &= \delta A - \int_V [\sigma_{ij} \delta R_{i,j} + \sigma_{ijk} \delta R_{i,jk}] dV = \\
&= \int_V (\sigma_{ij,j} - \delta_{ij} \sigma_{k,jk} + P_i^V) \delta R_i dV + \int_F [P_i^F - (\sigma_{ij} - \delta_{ij} \sigma_{k,k}) n_j] \delta R_i dF - \\
&\quad - \sum_{\mathcal{F}} (\sigma_k n_k v_i) \delta R_i ds + \int_F (\sigma_k n_k)_{,p} \delta_{ip}^* \delta R_i dF - \\
&\quad - \int_F (\sigma_k n_k) \delta (R_{i,p} n_i n_p) dF = 0. \tag{9.78}
\end{aligned}$$

The statement takes place: Meniscus forces determined by the expression $(\sigma_k n_k v_i)$ are self-balanced along the contours formed by the edges.

Proof. Let us consider the classical boundary condition for varying displacements in (9.78), and integrate it over the body surface. We obtain the following from the variational equation.

$$\int_F [P_i^F - (C_{ijmn} R_{m,n} - G_{ijkmnl} R_{m,nlk}) n_j + (G_{ijkmnl} n_k R_{m,nl})_{,p} \delta_{pj}^*] dF = 0. \tag{9.79}$$

Obviously, equality (9.79) can be rewritten as

$$\begin{aligned}
\int_F P_i^F dF - \int_F [(C_{ijmn} R_{m,n} - G_{ijkmnl} R_{m,nlk}) n_j] dF + \\
+ \int_F [(G_{ijkmnl} n_k R_{m,nl})_{,p} \delta_{pj}^*] dF = 0. \tag{9.80}
\end{aligned}$$

Consider the second and the third terms in (9.80) and apply the Green-Ostrogradskii theorem

$$\begin{aligned}
\int_F [(C_{ijmn} R_{m,n} - G_{ijkmnl} R_{m,nlk}) n_j] dF = \\
= \int_V (C_{ijmn} R_{m,n} - G_{ijkmnl} R_{m,nlk})_{,j} dV = - \int_V P_i^V dV. \tag{9.81}
\end{aligned}$$

The equality (9.81) is obtained taking into account that displacements in the volume of the body satisfy the equilibrium equation.

Similarly, consider the third term in (9.80) and use of Green–Ostrogradski theorem

$$\begin{aligned}
\int_F [(G_{ijklmnl}n_k R_{m,nl})_{,p} \delta_{pj}^*] dF &= \sum \oint (G_{ijklmnl}n_k R_{m,nl}) v_p \delta_{pj}^* ds = \\
&= \sum \oint (G_{ijklmnl}n_k R_{m,nl}) v_j ds. \quad (9.82)
\end{aligned}$$

We take into account the equations (9.81) and (9.82) and transform the Eq. 3.2) as follows

$$\begin{aligned}
&\int_F P_i^F dF - \int_F [(C_{ijmn} R_{m,n} - G_{ijklmnl} R_{m,nlk}) n_j] dF + \\
&\quad + \int_F [(G_{ijklmnl}n_k R_{m,nl})_{,p} \delta_{pj}^*] dF = \\
&= \left(\int_F P_i^F dF + \int_V P_i^V dV \right) + \sum \oint (G_{ijklmnl}n_k R_{m,nl}) v_j ds = \\
&= \sum \oint (G_{ijklmnl}n_k R_{m,nl}) v_j ds = 0. \quad (9.83)
\end{aligned}$$

Here it is taken into account that there is an integral condition of global equilibrium

$$\int_F P_i^F dF + \int_V P_i^V dV = 0.$$

The condition of equation (9.83) implies the equality, which indicates the property of self-balance along all edges (contours)

$$\sum \oint (G_{ijklmnl}n_k R_{m,nl}) v_j ds = 0.$$

The theorem is proved.

We believe that last statement is extremely interesting for all formulations of boundary value problems that include edges.

9.7 Conclusions

There are considered mathematical statements for the Mindlin-Tupin gradient elasticity theories in displacements with the fourth-order system of governing equations, including boundary conditions, according to which six boundary conditions (kinematic or static) are formulated at each non-singular point of the surface, as well as three boundary conditions are formulated on the edges of piecewise—smooth surface. The peculiarities of mathematical and physical formulations of boundary value problems of the gradient theory are associated with the formulation of nonclassical

boundary conditions for the moments for which physical interpretations seem to be difficult, as well as with the formulation of boundary conditions on the edges of the surface.

The need to formulate boundary conditions at the edges also requires an additional study of the problem of the existence of classical solutions in the class of continuous and differentiable functions. On the other hand, the choice between generalized static and kinematic nonclassical boundary conditions is not so obvious in applied problems.

Some of the questions above are considered in the work in the context of expanding the spectrum of gradient models and boundary value problems by introducing the kinematic constraints on the body surface using the Lagrange multiplier method. Classes of gradient models obtained by introducing the kinematic constraints on the surface, in which there are no boundary conditions at the edges, are indicated. These include models built by introducing kinematic vector relations to the displacement vector. Examples of models with the same properties obtained by introducing linear combinations of the first derivatives of displacements are given.

It is considered the case when the kinematic scalar connection on the surface of the body sets the relationship between the normal and tangential components of the displacement vector and makes it possible to construct a model of static friction.

A general theorem on the self-balance of meniscus forces defined on the edges of the body surface is established.

Acknowledgements The authors would like to acknowledge the financial support of the Russian Science Foundation under the grant 20-41-04404 issued to the Institute of Applied Mechanics of Russian Academy of Sciences.

References

- Andreas U, dell'Isola F, Giorgio I, Placidi L, Lekszycki T, Rizzi N (2016) Numerical simulations of classical problems in two-dimensional (non) linear second gradient elasticity. *Intern J Eng Sci* 108:34–50
- Askes H, Aifantis E (2011) Gradient elasticity in statics and dynamics: An overview of formulations, length scale identification procedures, finite element implementations and new results. *Internat J Solids Struct* 48:1962–1990
- Askes H, Susmel L (2014) Understanding cracked materials: is linear elastic fracture mechanics obsolete? *Fatigue Fract Eng Mater Struct* 38:154–160
- Barchiesi E, Hua Y, Tran C, Placidi L, Mueller W (2020) Computation of brittle fracture propagation in strain gradient materials by the fenics library. *Math Mech Solids* 26:325–340
- Bersani AM, dell'Isola F, Seppacher P (2020) Lagrange multipliers in infinite dimensional spaces, examples of application. *Encyclopedia of continuum mechanics* pp 1425–1432
- dell'Isola F, Seppacher P, Alibert JJ, Lekszycki T, Grygoruk R, Pawlikowski M, Steigmann D, Giorgio I, Andreas U, Turco E, Golaszewski M, Rizzi N, Boutin C, Eremeyev VA, Misra A, Placidi L, Barchiesi E, Greco L, Cuomo M, Cazzani A, Corte AD, Battista A, Scerrato D, Eremeeva IZ, Rahali Y, Ganghoffer JF, Müller W, Ganzosch G, Spagnuolo M, Pfaff A, Barcz K, Hoschke K, Negggers J, Hild F (2019) Pantographic metamaterials: an example of

- mathematically driven design and of its technological challenges. *Continuum Mechanics and Thermodynamics* 31(4):851–884
- Eremeyev V, Lurie S, Solyaev Y, dell'Isola F (2020) On the well posedness of static boundary value problem within the linear dilatational strain gradient elasticity. *Z Angew Math Phys* 71:1–16
- Fleck N, Hutchinson J (1997) Strain gradient plasticity. *Adv Appl Mech* 33:295–361
- Froio F, Zervos A (2019) Second-grade elasticity revisited. *Math Mech Solids* 24:748–777
- Giorgio I, Andreaus U, dell'Isola F, Lekszycki T (2017) Viscous second gradient porous materials for bones reconstructed with bio-resorbable grafts. *Extreme Mechanics Letters* 13:141–147
- Gusev A, Lurie S (2017) Symmetry conditions in strain gradient elasticity. *Math Mech Solids* 22:683–691
- Hua Y, Abali BE, Timofeev D, Mueller WH (2020) Determination of metamaterial parameters by means of a homogenization approach based on asymptotic analysis. *Contin Mech Thermodynam* 32:1251–1270
- Kleinert H (1989) *Gauge fields in condensed matter*, vol 2. World Sci., Singapore
- Lam D, Yang F, Chong A, Wang J, Tong P (2003) Experiments and theory in strain gradient elasticity. *J Mech Phys Solids* 51:1477–1508
- Lomakin E, Lurie S, Rabinskiy L, Solyaev Y (2019) Refined stress analysis in applied elasticity problems accounting for gradient effects. *Dokl Phys* 64:482–486
- Lurie S, Belov P, Solyaev Y, Aifantis E (2017) On one class of applied gradient models with simplified boundary problems. *Mater Phys Mech* 32:353–369
- Lurie S, Kalamkarov A, Solyaev Y, Volkov A (2021) Dilatation gradient elasticity theory. *Eur J Mech – A/Solids* 88(104258)
- Madeo A, Ghiba ID, Neff P, Munch I (2015) A new view on boundary conditions in the Grioli-Koiter-Mindlin-Toupin indeterminate couple stress model. *Eur J Mech – A/Solids* 59:294–322
- Mindlin R (1964) Micro-structure in linear elasticity. *Arch Rational Mech Anal* 16:51–78
- Misra A, Placidi L, Turco E (2020) Variational methods for continuum models of granular materials in: *Encyclopedia of Continuum Mechanics*, Springer, Berlin, Heidelberg, pp 2611–2621
- Placidi L, Barchiesi E (2018) Energy approach to brittle fracture in strain-gradient modelling. *Proc Roy Soc Ser A: Math Phys Eng Sci* 474(20170878)
- Placidi L, Barchiesi E, Misra A, Andreaus U (2020) Variational Methods in Continuum Damage and Fracture Mechanics in: *Encyclopedia of Continuum Mechanics*, Springer, Berlin, Heidelberg, pp 2634–2643
- Reiher JC, Giorgio I, Bertram A (2017) Finite-element analysis of polyhedra under point and line forces in second-strain gradient elasticity. *Journal of Engineering Mechanics* 143(2):04016,112
- Shodja H, Moosavian H, Ojaghnezhad F (2018) Toupin-Mindlin first strain gradient theory revisited for cubic crystals of hexoctahedral class: Analytical expression of the material parameters in terms of the atomic force constants and evaluation via ab initio dft. *Mech Mater* 123:19–29
- Solyaev Y, Lurie S (2020) Trefftz collocation method for two-dimensional strain gradient elasticity. *Intern J Numer Meth Eng* 122:823–839
- Toupin R (1962) Elastic materials with couple-stresses. *Arch Rational Mech Anal* 11:385–414
- Vangelatos Z, Yildizdag E, Giorgio I, dell'Isola F, Grigoropoulos C (2021) Investigating the mechanical response of microscale pantographic structures fabricated by multiphoton lithography. *Extr Mech Lett* 43(101202)
- Vasiliev V, Lurie S, Salov V (2019) Estimation of the strength of plates with cracks based on the maximum stress criterion in a scale-dependent generalized theory of elasticity. *Phys Mesomech* 22:456–462
- Vasiliev V, Lurie S, Solyaev Y (2021) New approach to failure of pre-cracked brittle materials based on regularized solutions of strain gradient elasticity. *Engineering Fracture Mechanics* 258:108,080
- Zhou S, Li A, Wang B (2016) A reformulation of constitutive relations in the strain gradient elasticity theory for isotropic materials. *Internat J Solids Struct* 80:28–37



Chapter 10

Continuum Models via Granular Micromechanics

Anil Misra, Luca Placidi, Emilio Barchiesi

Abstract The utilization of continuum modelling in describing complex material systems is historically widespread because of the computational feasibility of such an approach. Nevertheless, continuum models must be informed about the micro-structure to have a satisfactory predictive capacity. Knowledge of micro-structural features is fraught with challenges due to a litany of factors, including random structure, contact conditions, and contact constitutive laws. In this scenario, the granular micromechanics approach (GMA) is a way to conveniently provide a linkage of the grain-scale behavior to the collective behavior of grains. In this short review, we describe some salient features of GMA and discuss outlook of GMA based continuum models.

Keywords: Granular micromechanics approach · Continuum modelling · Piola ansatz

10.1 Introduction

The ideas of finite divisibility of all matter goes back to early epistemic effort regarding character of matter that can be traced to 4th-5th century BCE Greek

The original version of this chapter was revised: The authors names have been corrected in the xml file. The correction to this chapter is available at https://doi.org/10.1007/978-3-031-04548-6_33

A. Misra
Civil, Environmental and Architectural Engineering Department, University of Kansas, USA.
e-mail: amisra@ku.edu

L. Placidi
Faculty of Engineering, International Telematic University UNINETTUNO, Italy.
e-mail: luca.placidi@uninettunouniversity.net

E. Barchiesi
Dipartimento di Architettura, design e urbanistica, Università degli Studi di Sassari, Italy.
e-mail: barchiesiemilio@gmail.com

© The Author(s), under exclusive license to Springer Nature Switzerland AG 2022, corrected publication 2022

I. Giorgio et al. (eds.), *Theoretical Analyses, Computations, and Experiments of Multiscale Materials*, Advanced Structured Materials 175, https://doi.org/10.1007/978-3-031-04548-6_10

atomism of Leucippus and Democritus¹, and the ancient Indian thought systems (dating 6th century BCE and earlier) of *Vaiśeṣika* Gough (1873); Kak (2016) and *Nyaya* Gotama (1913). It is worthwhile to reproduce here a particularly evocative *sutra* taken from *Nyayasutra* of Gotama that illustrates the discrete nature of matter.² Remarkably, in the *Nyayasutra*, arguments of *regressus ad infinitum* form the basis to prove the untenability of infinite divisibility exemplified so vividly in the cited *sutra*. When considering the deformability of 3D seemingly continuous mass, the vanguards of continuum mechanics, Piola, Navier, Cauchy, and Poisson (cf. Piola dell'Isola et al (2014)dell'Isola et al (2014), Navier Navier (1827), Cauchy Cauchy (1830), Poisson Poisson (1828)), in the first half of 19th century CE, indeed conceived the matter to be composed of discrete “molecules”. The application of molecular hypothesis that formed the basis of many early investigations into the mechanics of 3D deformable media leads to anisotropic elasticity with restrictions on the number of independent constants, known as Cauchy reductions. The derivation of Navier Navier (1827), for instance, resulted in a single constant for isotropic elasticity implying a singular Poisson's ratio of 1/4. Utilizing energy arguments attributed to George Green Love (1892), generalization of the molecular hypothesis has been discussed by Kelvin Kelvin (1893) to derive elastic constants of general anisotropic elasticity without the restrictions imposed by Cauchy reductions or singular Poisson's ratio. A vivid account of the debate and alternate formulations presented for the analytical description of material elasticity in the 19th century is given by Ibbetson in “Appendix III-Hookes's Law” and by Love in the “Historical Introduction” of the treatise on mathematical theory of elasticity Love (1892); Ibbetson (1887). The account includes the discussions of elasticity of anisotropic or aelotropic materials based upon the energy arguments of Green, its earliest application to crystal elasticity by Neumann, and its application to non-crystalline aelotropic materials, such as wood and laminates, by St Venant.

At some spatial scale, all matter is recognizable as composed of discrete sub-bodies or structural elements of sizes that can range from sub-nanometer to several meters. The relative geometrical arrangements and interconnectivity of these granular elements forms the microstructure of the matter irrespective of the spatial scale. In addition, the character of the interconnections, that possess their own geometrical/mechanical attributes, forms the basis of micromechanics of the matter. The combined effects produced through interaction of the microstructure and micromechanics can be termed as micro-mechano-morphology. For many materials utilized in engineering activities, their granular nature (or micro-mechano-morphology) has a profound effect on the behavior that emerges at the so-called macro-scale which represents the combined behavior of a large number of elements (numbers such that a discrete analysis is either not fruitful or not feasible from experimental and/or com-

¹ Berryman, S. Ancient Atomism. Stanford Encyclopedia of Philosophy 2016; Available from: <https://plato.stanford.edu/entries/atomism-ancient/#AtomBefoLeuc>.

² केशसमूहे तैमिरिकोपलब्धिवत्तदुपलब्धिः ॥४॥२॥१३॥

(Matter appears as whole or continuous) like a pile of hair may appear to a person of blurred vision (4.2.13).

putational viewpoints). It is worthwhile to note here that for certain cases, structural elements that are otherwise composed of large number of some other primary (discrete) elements, may be discretized into rigid elements that interact via mechanisms as in Hencky model of beams Hencky (1921); Wang et al (2020); Turco et al (2016); Giorgio (2020). Such discrete models may be further homogenized, and the reasoning maybe extended to conceive hierarchical and nested models. At the macro-scale, typically, the preferred means for description of material behavior is via the methods of continuum mechanics. The traditional approach in continuum mechanics has been to formulate these descriptions in terms of identified kinematical variables through direct postulates of balance equations in terms of proposed quantities defined for the continuum system. As noted, early development of mathematical theories of deformable media rightly recognized the discrete/granular nature of matter in their development of continuum models of deformable media.

The granular micromechanics approach (GMA) takes inspiration from the molecular hypothesis to provide a paradigm for constructing continuum models for a range of materials appealing to their underlying granular nature/motif. In this regard it is useful to **define granular material systems** as *composed of nearly rigid elements (or grains) such that the elastic strain energy is stored and/or energy dissipated in the deformable mechanisms represented through interconnections or interfaces between the grains*. In GMA, the continuum material point consists of a set of interacting grains. This granular view is consistent with the idea of coarse graining by combining atoms and molecules into larger grains necessary for modeling polymeric or complex multi-atomic systems Greene et al (2014); Misra and Ching (2013); Solar et al (2012). The key underlying feature is that relative movements of the grain centroid/barycenter can be used to describe the deformation of such material systems regardless of the location of the actual deformation following Piola's ansatz of passage from a molecular to continuum description dell'Isola et al (2014); Eugster and dell'Isola (2017, 2018b,a). Further, the GMA considers a parameterization of the effective grain-pair deformation energies. In this way, it is possible to exploit the advantage offered by GMA of interpreting the macro-scale constitutive parameters in terms of the micro-scale mechano-morphological parameters.

For example, geomaterials, such as sands and clays, can be represented as grain packing, which have been treated using analysis similar to the molecular hypothesis to determine their macro-scale stiffness by considering grain-contact stiffness starting from central interactions, in which only normal contact stiffness are considered, and extending to non-central tangential contact interactions. A brief historical outline of efforts along these lines is given in Misra et al (2020b) tracing from work of Hara Hara (1935), through Mindlin and coworkers (for example Deresiewicz (1958); Duffy and Mindlin (1957)), to Digby Digby (1981) and Walton Walton (1987), to works that appeared in late 20th and early 21st century Cambou and Danescu (2009); Chang and Misra (1990); Jenkins (1988); Koenders (1994); Kruyt and Rothenburg (2004); Rothenburg and Selvadurai (1981); Theocharis et al (2020). Stiffness matrices of granular crystals as well as granular packing with orthotropic symmetry have also been reported following a similar methodology Chang and Misra (1990); Cambou et al (2004); Chang et al (1995); Chang and Misra (1989); Jenkins (1991); Nicot and

Darve (2005). Significantly, such estimates overlook the long-range interactions that effect the behavior of a grain-pair embedded within a system of grains. A few efforts have also been made to account for these long-range effects by estimating corrections that are derived with an aim to enforce local equilibrium conditions for grains, prominent among which are Jenkins et al (2005); Jenkins and Koenders (2004); Koenders (2020); Misra and Chang (1993) or through representation of mesoscopic structures Nicot and Darve (2011); Chang et al (1992), however, these primarily focus on isotropic random grain packing and, make a number of assumptions. Notably, these estimates retain the classical format of continuum mechanics.

It is remarkable that in granular systems, in which grains interact with nearest neighbors, it is not possible to specify the effective grain-pair deformation energies without the *a priori* knowledge of grain-scale mechano-morphology of next-nearest neighbors and their neighbors and so on. Besides the long-range effects, the effort of generating estimates of the elastic constants for grain packs or systems of cemented grains in terms of the stiffness to two grains in contact is fraught with challenges due to a litany of factors, including random structure, contact conditions, contact constitutive laws etc. Nevertheless, the analysis of these materials according to molecular hypothesis gives an advantage that can provide a linkage of the grain-scale behavior to the collective behavior of grains. In this review, we describe some salient features of GMA and discuss outlook of GMA based continuum models.

10.2 Granular Micromechanics Approach

Continuum material point represents the collective behavior of numerous grains forming an infinitesimal volume element (VE) at spatial scales in which the individual grains and their motions are considered latent (concealed or unresolvable). The energy stored/dissipated in the deformation of grain collections, determines the mapping of a continuum material point from reference to present configuration in a macro body composed of such material. To this end, Piola's ansatz dell'Isola et al (2014); Eugster and dell'Isola (2017, 2018b,a) for micro-macro identification maybe utilized to get the objective kinematic descriptor for grain-pair relative displacement linked to the placement (see for example Barchiesi et al (2021b); Nejadi Sadeghi and Misra (2020a)). Thus, the continuum description is achieved by expressing grain-scale motions in terms of continuum strain measure. The macro-scale deformation energy density is then expressed as the volume average of grain-pair deformation energy and the constitutive relations determined in the manner introduced by Green Love (1892) GMA is a heuristic homogenization scheme in which the deformation energy density of a continuum material point and the granular volume it represents are the same. In this case, the RVE is a volume of a granular system whose mechanical response (deformation energy density) remains the same as the volume is moved within a specimen. We briefly describe the seminal aspects of GMA. The discussed micro-macro kinematic identification provides the pathway for formulating equiva-

lent deformation energy postulates in terms of the continuum deformation and the grain-pair deformations measures.

10.2.1 Piola Ansatz for Micro-Macro Kinematic Identification

Consider the deformation of a discrete model of granular microstructure composed of N -sub bodies, each of which is composed of many grains, and its continuum representation, as illustrated in Fig. 10.1 and described in detail in Misra et al (2021). We may use the following Piola ansatz for identification of discrete and continuum models:

$$\chi(X_i, t) = \chi_i(t), \quad P(X_i, t) = P_i(t), \quad \forall t \in \mathbb{R}^+. \quad (10.1)$$

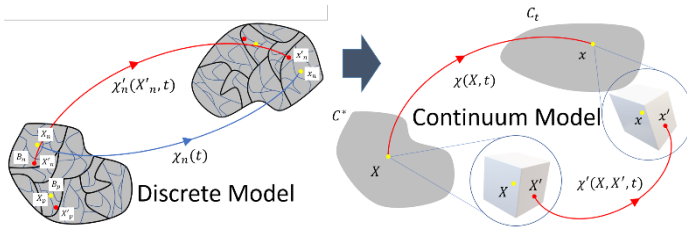


Fig. 10.1 On the left, the discrete model. Each sub-body B_n , with $n = 1, \dots, N$, in the reference configuration is represented with black boundaries and is composed by many grains. Each grain is represented with blue boundaries. For each sub-body B_n , two placements are defined. The placement of the point X_n , belonging to one of the grain of the sub-body B_n , is $\chi_n(t)$. The placement of the point X'_n , belonging eventually to another grain of the sub-body B_n , is $\chi'_n(X'_n, t)$. On the right, the continuum model. The reference configuration of the continuum body is C^* . Its generic point is $X \in C^*$ and the corresponding placement is $\chi(X, t)$. Such a point X is the representative of a micro-structure, e.g. the cube in the figure. Within the micro-structure (thus, within the cube in the figure) two placements are defined. The first, is the same placement $\chi(X, t)$ of the point X . The second placement $\chi'(X, X', t)$ defines that of any other point X' of the micro-structure.

It is clear in Eq. (10.1) that the continuum placement, $\chi(X, t)$, and microdeformation, $P(X, t)$, evaluated at X_i correspond to the placement $\chi_i(t)$ and microdeformation $P_i(t)$ of the i -th sub-body of the granular structure. Here, microdeformation is estimated using a 1st order Taylor expansion as the gradient of the grain placement within the i -th sub-body with respect to the grain at X_i . Notably, we observe, from Fig. 10.1, that microdeformation in granular systems arises as a relative movement of grains within the i -th sub-body with respect to the grain placed at X_i . Indeed, the grain motions can be quite complex depending upon the local micro-mechano-morphology (or local grain arrangements and micromechanics of grain interactions), and possibly, higher-order gradients could be significant requir-

ing the inclusion of higher-order terms. The placement and microdeformation, thus identified, are used to define the following three objective tensors that represent the material deformation traceable to the micro-scale grain-pair relative displacements

$$\begin{aligned} g^{np} &= G = \frac{1}{2} (F^T F - I) \\ m^{np} &= M + \frac{L}{2} P^T \nabla P \hat{c} = \frac{1}{2} (P^T P - I) + \frac{L}{2} P^T \nabla P \hat{c} \\ \gamma^{np} &= \Upsilon - L [\nabla P^T \hat{c}] F^{-T} = I - P^T F^{-T} - L [\nabla P^T \hat{c}] F^{-T} \end{aligned} \quad (10.2)$$

In Eq. (10.2), $F = \nabla \chi$, L is the microstructural length parameter representing separation between sub-bodies such that it can be given as a multiple of constituent grain-size, and \hat{c} is interpreted as the unit vector representing grain-pair orientations. The three tensors in Eq. (10.2) are termed as the macrostrain, microstrain and the relative strain. The effective objective relative displacement of grain-pairs oriented in the direction \hat{c} can thus be estimated decomposed into corresponding three mechanisms that can be termed as macro-displacement, micro-displacement, micro-macro relative displacement, given as follows:

$$u^{np} = 2Lg^{np}\hat{c} = 2LG\hat{c}, \quad r^{np} = 2Lm^{np}\hat{c}, \quad d^{np} = L\gamma^{np}\hat{c}. \quad (10.3)$$

In the linear approximation, it is shown Misra et al (2021) that the three tensors in Eq. (10.2) simplify to those introduced by Mindlin (1963, 1964) as macrostrain ε , microstrain Ψ and relative strain γ :

$$\varepsilon_{ij} = \frac{1}{2} (u_{i,j} + u_{j,i}), \quad \gamma_{ij} = u_{j,i} - \Psi_{ij}, \quad \kappa_{ijk} = \Psi_{jk,i}. \quad (10.4)$$

10.2.2 Micro-Macro Kinematic Identification Using Prescribed Micromotion

An alternative view in which micro-macro kinematic identification may be conceived is by tracking the motion of the grains within the sub-bodies NejadSadeghi and Misra (2020a). In particular, the continuum material point is identified with the barycenter of the sub-body and the grain motion considered with respect to this barycenter. In this case, the continuum placement, $\chi(X, t)$, introduced in Eq. (10.1) is associated to the barycenter of the sub-body. A microscale coordinate system X' attached to the barycenter of the material point is utilized to specify the placement of grains composing the sub-body given as $\chi'(X, X', t)$. Motivated by experimental observations and discrete simulations, we use a polynomial expansion to prescribe the microscale grain displacement (truncated here at order 2 for micromorphic con-

tinuum of degree 1) as follows, in which Ψ_{ij} and Ψ_{ijk} are termed microdeformation tensors NejadSadeghi and Misra (2020a)

$$u'_i = \chi'_i(X_m, X'_n) - X'_i = \Psi_{ij}(X)X'_j + \Psi_{ijk}(X)X'_jX'_k. \quad (10.5)$$

In the microscale coordinate system, the relative displacement between two neighboring grain can be expressed as

$$\delta_i^{np} = \phi_i^p - \phi_i^n = \Psi_{ij}^\phi l_j^{np} + \Psi_{ijk}^\phi J_{jk}^{np}. \quad (10.6)$$

Here $l_j^{np} = X'_j{}^p - X'_j{}^n$ is a grain-pair branch vector joining the centroids of grains n and p , the tensor product $J_{jk}^{np} \approx l_j^{np} l_k^{np} / 2$ is the gyration tensor. We now consider the linear approximation and utilize the following relative deformation tensors

$$\gamma_{ij} = u_{i,j} - \Psi_{ij}, \quad \gamma_{ijk} = \Psi_{ij,k} - \Psi_{ijk}. \quad (10.7)$$

Also we assume that the relative deformation tensor, γ_{ijk} vanishes such that the 3^{rd} rank micro-deformation tensor, $\Psi_{ij,k} = \Psi_{ijk}$. In this case, the macro-displacement, relative displacement, and micro-displacement, are given as follows

$$\delta_i^M = \varepsilon_{ij} l_j^{np}, \quad \delta_i^n = \gamma_{ij} l_j^{np}, \quad \delta_i^g = \Psi_{ij,k} J_{jk}^{np}. \quad (10.8)$$

10.3 Outlook

It is clear from the foregoing discussion, that a continuum model constructed via this identification is an approximate one. In this sense, all ‘so called’ classical continuum models are essentially approximations whose efficacy and applicability can be assessed only by careful examination of its prediction capability of all observed phenomena of significance. To this end, we cannot emphasize enough the significance of the imposed boundary conditions. Very often, the boundary conditions imposed in the laboratory and those described in theoretical models are not in consonance. For many engineering applications, it is expedient to overlook this dissonance. We further note that the assumed smallest unit in the above-described kinematic identification may be further subdivided into even smaller units (or grains) in a hierarchical manner and one may attempt to estimate the consequences of the interactions and arrangements of these smaller units in some nested manner. The necessary question that arises is how the idealization (or so-called “coarse graining”) is to be developed. In any case, the granular paradigm discussed here can be utilized to reveal the micro-scale effects on emergent macro-scale behavior as shown by the authors, for example, wave dispersion and other higher-order effects Misra and Poorsolhjoui (2016); NejadSadeghi and Misra (2020b, 2021); dependency of load-paths in damage behavior Poorsolhjoui and Misra (2017); and anisotropy evolution and emergence of chirality due to damage and plasticity Placidi et al (2021); Timofeev et al (2021). Most importantly, GMA provides a framework for developing higher-gradient Barchiesi

et al (2021b) (see also Abali et al (2021) where material coefficients of a phase-field theory of brittle damage mechanics for second gradient metamaterials are chosen using the identification in Barchiesi et al (2021b)) and higher-order NejadSadeghi and Misra (2020a); Misra et al (2021) continuum models that introduce additional kinematic measures to describe the deformation behavior with higher fidelity. Such models are necessary for elucidating many phenomena exhibited by materials whose descriptions are often times tortuous and require many *ad hoc* mathematical fixes. Furthermore, the preceding micro-macro identifications connect micro-mechanisms to emergent behavior, and therefore, can be the basis of conceiving micro-mechano morphology leading to interesting and predictable metamaterials dell'Isola et al (2020); Barchiesi et al (2021a); Misra et al (2020a); Giorgio et al (2021).

References

- Abali BE, Klunker A, Barchiesi E, Placidi L (2021) A novel phase-field approach to brittle damage mechanics of gradient metamaterials combining action formalism and history variable. *ZAMM-Journal of Applied Mathematics and Mechanics/Zeitschrift für Angewandte Mathematik und Mechanik* p e202000289
- Barchiesi E, dell'Isola F, Bersani AM, Turco E (2021a) Equilibria determination of elastic articulated duoskelion beams in 2d via a riks-type algorithm. *International Journal of Non-Linear Mechanics* 128:103,628
- Barchiesi E, Misra A, Placidi L, Turco E (2021b) Granular micromechanics-based identification of isotropic strain gradient parameters for elastic geometrically nonlinear deformations. *ZAMM-Journal of Applied Mathematics and Mechanics/Zeitschrift für Angewandte Mathematik und Mechanik* p e202100059
- Cambou B, Danescu A (2009) Multiscale techniques for granular materials. *Micromechanics of Granular Materials* pp 101–147
- Cambou B, Dubujet P, Nouguier-Lehon C (2004) Anisotropy in granular materials at different scales. *Mechanics of materials* 36(12):1185–1194
- Cauchy A (1830) Application des formules qui représentent le mouvement d'un système de molécules sollicités par des forces d'attraction ou de repulsion mutuelle a la théorie de la lumière (exercices de mathématique, cinquième année). *Oeuvres Complètes d'Augustin Cauchy* 1(12):1882–1974
- Chang CS, Misra A (1989) Theoretical and experimental study of regular packings of granules. *Journal of engineering mechanics* 115(4):704–720
- Chang CS, Misra A (1990) Packing structure and mechanical properties of granulates. *Journal of engineering mechanics* 116(5):1077–1093
- Chang CS, Misra A, Acheampong K (1992) Elastoplastic deformation for particulates with frictional contacts. *Journal of engineering mechanics* 118(8):1692–1707
- Chang CS, Chao SJ, Chang Y (1995) Estimates of elastic moduli for granular material with anisotropic random packing structure. *International journal of solids and structures* 32(14):1989–2008
- dell'Isola F, Maier G, Perego U, Andreus U, Esposito R, Forest S (2014) The complete works of Gabrio Piola. *Advanced Structured Materials* 38
- dell'Isola F, Barchiesi E, Misra A (2020) Naive model theory: Its applications to the theory of metamaterials design. *Discrete and Continuum Models for Complex Metamaterials* p 141
- Deresiewicz H (1958) Stress-strain relations for a simple model of a granular medium. *Journal of Applied Mechanics* 25(3):402–406
- Digby P (1981) The effective elastic moduli of porous granular rocks: *Journal of applied mechanics*

- Duffy J, Mindlin R (1957) Stress-strain relations and vibrations of a granular medium. *Journal of Applied Mechanics* 24(4):585–593
- Eugster SR, dell’Isola F (2017) Exegesis of the introduction and sect. i from “fundamentals of the mechanics of continua” by e. hellinger. *ZAMM-Journal of Applied Mathematics and Mechanics/Zeitschrift für Angewandte Mathematik und Mechanik* 97(4):477–506
- Eugster SR, dell’Isola F (2018a) Exegesis of sect. ii and iii. a from “fundamentals of the mechanics of continua” by e. hellinger. *ZAMM-Journal of Applied Mathematics and Mechanics/Zeitschrift für Angewandte Mathematik und Mechanik* 98(1):31–68
- Eugster SR, dell’Isola F (2018b) Exegesis of sect. iii. b from “fundamentals of the mechanics of continua” by e. hellinger. *ZAMM-Journal of Applied Mathematics and Mechanics/Zeitschrift für Angewandte Mathematik und Mechanik* 98(1):69–105
- Giorgio I (2020) A discrete formulation of kirchhoff rods in large-motion dynamics. *Mathematics and Mechanics of Solids* 25(5):1081–1100
- Giorgio I, Spagnuolo M, Andreus U, Scerrato D, Bersani AM (2021) In-depth gaze at the astonishing mechanical behavior of bone: A review for designing bio-inspired hierarchical metamaterials. *Mathematics and Mechanics of Solids* 26(7):1074–1103
- Gotama (1913) *The nyāya sutras of gotama*, translated by vidyābhūṣaṇa, mahāmahopādhyāya satīśa chandra. Allahabad: Pāṇiṇi Office
- Gough A (1873) *The Vaiśeshika Aphorisms of Kanāda: With Comments from the Upaskāra of Śāṅkara Misra and the Vivritti of Jaya-Nārāyaṇa Tarkapañchāna*. Oriental Books
- Greene MS, Li Y, Chen W, Liu WK (2014) The archetype-genome exemplar in molecular dynamics and continuum mechanics. *Computational mechanics* 53(4):687–737
- Hara G (1935) *Theorie der akustischen schwingungsausbreitung in gekörnten substanzen und experimentelle untersuchungen an kohlepulver*. *Elektr Nachr Techn* 12:191
- Hencky H (1921) *Über die angenäherte lösung von stabilitätsproblemen im raum mittels der elastischen gelenkkette*. PhD thesis, Verlag nicht ermittelbar
- Ibbetson WJ (1887) *An Elementary Treatise on the Mathematical Theory of Perfectly Elastic Solids: With a Short Account of Viscous Fluids*. Macmillan
- Jenkins J, Koenders M (2004) The incremental response of random aggregates of identical round particles. *The European Physical Journal E* 13(2):113–123
- Jenkins J, Johnson D, La Ragione L, Makse H (2005) Fluctuations and the effective moduli of an isotropic, random aggregate of identical, frictionless spheres. *Journal of the Mechanics and Physics of Solids* 53(1):197–225
- Jenkins JT (1988) Volume change in small strain axisymmetric deformations of a granular material. In: *Studies in Applied Mechanics*, vol 20, Elsevier, pp 245–252
- Jenkins JT (1991) Anisotropic elasticity for random arrays of identical. *Modern theory of anisotropic elasticity and applications* 57:368
- Kak S (2016) *Matter and Mind: The Vaisheshika Sutra of Kanada*. Ontario, Canada: Mount Meru Publishing
- Kelvin L (1893) On the elasticity of a crystal according to bosovich. *Proceedings of the Royal Society of London* 54:59–75
- Koenders M (1994) Least squares methods for the mechanics of nonhomogeneous granular assemblies. *Acta mechanica* 106(1):23–40
- Koenders MAC (2020) *The Physics of the Deformation of Densely Packed Granular Materials*. World Scientific
- Kruyt NP, Rothenburg L (2004) Kinematic and static assumptions for homogenization in micromechanics of granular materials. *Mechanics of Materials* 36(12):1157–1173
- Love AEH (1892) *A treatise on the mathematical theory of elasticity*. Cambridge University Press
- Mindlin RD (1963) *Microstructure in linear elasticity*. Tech. rep., Columbia Univ New York Dept of Civil Engineering and Engineering Mechanics
- Mindlin RD (1964) *Microstructure in linear elasticity*. *Archive for Rational Mechanics and Analysis* 16(1):51–78
- Misra A, Chang CS (1993) Effective elastic moduli of heterogeneous granular solids. *International Journal of Solids and Structures* 30(18):2547–2566

- Misra A, Ching WY (2013) Theoretical nonlinear response of complex single crystal under multi-axial tensile loading. *Scientific reports* 3(1):1–7
- Misra A, Poursolhjouy P (2016) Granular micromechanics based micromorphic model predicts frequency band gaps. *Continuum Mechanics and Thermodynamics* 28(1-2):215–234
- Misra A, NejadSadeghi N, De Angelo M, Placidi L (2020a) Chiral metamaterial predicted by granular micromechanics: verified with 1d example synthesized using additive manufacturing. *Continuum Mechanics and Thermodynamics* 32(5):1497–1513
- Misra A, Placidi L, Turco E (2020b) Variational methods for continuum models of granular materials. *Encyclopedia of continuum mechanics* pp 2611–2621
- Misra A, Placidi L, Barchiesi E, et al (2021) Identification of a geometrically nonlinear micromorphic continuum via granular micromechanics. *Zeitschrift für angewandte Mathematik und Physik* 72(4):1–21
- Navier CL (1827) Mémoire sur les lois de l'équilibre et du mouvement des corps solides élastiques. *Mémoires de l'Académie royale des sciences de l'Institut de France* 7:375–393
- NejadSadeghi N, Misra A (2020a) Extended granular micromechanics approach: a micromorphic theory of degree n . *Mathematics and Mechanics of Solids* 25(2):407–429
- NejadSadeghi N, Misra A (2020b) Role of higher-order inertia in modulating elastic wave dispersion in materials with granular microstructure. *International Journal of Mechanical Sciences* 185:105,867
- NejadSadeghi N, Misra A (2021) On the statics and dynamics of granular-microstructured rods with higher order effects. *Mathematics and Mechanics of Solids* p 10812865211009938
- Nicot F, Darve F (2005) A multi-scale approach to granular materials. *Mechanics of materials* 37(9):980–1006
- Nicot F, Darve F (2011) The h-microdirectional model: accounting for a mesoscopic scale. *Mechanics of materials* 43(12):918–929
- Placidi L, Barchiesi E, Misra A, Timofeev D (2021) Micromechanics-based elasto-plastic–damage energy formulation for strain gradient solids with granular microstructure. *Continuum Mechanics and Thermodynamics* pp 1–29
- Poisson SD (1828) Mémoire sur l'équilibre et le mouvement des corps élastiques. F. Didot
- Poursolhjouy P, Misra A (2017) Effect of intermediate principal stress and loading-path on failure of cementitious materials using granular micromechanics. *International Journal of Solids and Structures* 108:139–152
- Rothenburg L, Selvadurai A (1981) A micromechanical definition of the cauchy stress tensor for particulate media. *Mechanics of structured media* pp 469–486
- Solar M, Meyer H, Gauthier C, Fond C, Benzerara O, Schirrer R, Baschnagel J (2012) Mechanical behavior of linear amorphous polymers: Comparison between molecular dynamics and finite-element simulations. *Physical Review E* 85(2):021,808
- Theocharis A, Roux JN, Langlois V (2020) Elasticity of model weakly cemented granular materials: A numerical study. *International Journal of Solids and Structures* 193:13–27
- Timofeev D, Barchiesi E, Misra A, Placidi L (2021) Hemivariational continuum approach for granular solids with damage-induced anisotropy evolution. *Mathematics and Mechanics of Solids* 26(5):738–770
- Turco E, Dell'Isola F, Cazzani A, Rizzi NL (2016) Hencky-type discrete model for pantographic structures: numerical comparison with second gradient continuum models. *Zeitschrift für angewandte Mathematik und Physik* 67(4):1–28
- Walton K (1987) The effective elastic moduli of a random packing of spheres. *Journal of the Mechanics and Physics of Solids* 35(2):213–226
- Wang CM, Zhang H, Challamel N, Pan W (2020) Hencky Bar-Chain/Net for Structural Analysis. World Scientific



Chapter 11

Some Variational Principles in the Three-Dimensional Micropolar Theories of Solids and Thin Solids

Mikhail Nikabadze, Armine Ulukhanyan

Abstract In this work, we formulated the variational principles of Lagrange, Castigliano, the generalized Reissner-type variational principles (GRTVP), as well as the principle of virtual work and the principle of complementary virtual work of three-dimensional micropolar mechanics (MM) of solids of some rheologies in the case of potentiality, as well as nonpotentiality of stress and couple stress tensors. Proceeding from them and applying the new parametrization (NP) of the domains of single-layer and multilayer thin bodies, the variational principles corresponding to the theories of single-layer and multilayer thin bodies are formulated. In particular, the generalized Reissner-type operator of three-dimensional MM of solids is constructed, on the basis of which the generalized Reissner-type operators of three-dimensional MM of solid single-layer and multilayer thin bodies with one small size are constructed. From the latter Reissner-type operators, in turn, the GRTVP of three-dimensional MM of solid single-layer and multilayer thin bodies with one small size are derived under the NP of the domains of these bodies. It should be noted that the advantage of the NP is that it is experimentally more accessible than other parameterizations used in the scientific literature. Further, using the method of orthogonal polynomials, from the above-mentioned GRTVP, the GRTVP of MM of solid single-layer and multilayer thin bodies with one small size under the NP of the domains of these bodies in moments with respect to the system of Legendre polynomials are derived. Moreover, in the case of the theory of multilayer thin bodies, the representation of

M. Nikabadze

Lomonosov Moscow State University, Moscow, Russian Federation

Bauman Moscow State Technical University, Moscow, Russian Federation

Moscow Center for Fundamental and Applied Mathematics, International Research Center on Mathematics and Mechanics of Complex Systems (M&MoCS)

e-mail: munikabadze@yandex.ru

A. Ulukhanyan

Moscow Center for Fundamental and Applied Mathematics, International Research Center on Mathematics and Mechanics of Complex Systems (M&MoCS)

Università degli Studi dell'Aquila, L'Aquila, Italy

e-mail: armine.ulukhanyan@gmail.com

the generalized Reissner-type operator is given and the generalized Reissner-type variational principle is formulated, both in the case of complete contact of adjacent layers of a multilayer structure, and in the presence of zones of weakened adhesion. In addition, the description of obtaining of dual Reissner-type operators and the GRTVP, as well as of Lagrangian and Castiglianian and variational principles of Lagrange and Castigliano is given. The interface (interphase boundary) is described by a surface of zero thickness.

Keywords: Work generalized theorem · Legendre-type identity · Compatibility conditions · Beltrami–Michell type equations · Multilayer thin body · Jump-type model

11.1 Introduction

Variational principles and their application in many areas of natural sciences, in particular, mathematical physics, physics and mechanics, including the theory of elasticity, viscoelasticity, plasticity, economic sciences and etc., have a long history of development. However, the importance of these principles began to be realized only recently due to the development of the finite element method, which has become widespread. Variational principles are a powerful tool in the mathematical formulation of the finite element method and, conversely, the rapid development of the finite element method has stimulated the improvement of variational principles. Problems of natural science, in particular, of mathematical physics, admitting variational statements, make it possible to maximally weaken the mathematical constraints that are imposed on solutions, as well as to construct a priori stable difference schemes for their numerical implementation. The calculus of variations is at the origin of the theory of optimal control and optimal design of structures. In this regard, the popularity of variational methods in the fields of natural sciences, in particular, in the fields of mathematical physics, physics, mechanics, and engineering sciences is great. The mathematical results obtained in this direction are quickly adopted by those who deal with applied problems. This is what explains the growing demand for books on variational calculus and, in fact, there are a lot of such books in various languages. Without going into the details of the literature review, among the countless number of works we will name, for example, the books by Rektorys (1977); Washizy (1982); Berdichevsky (2009); Vanko (2010); Vekua (1970); Pobedrya (1984, 1995); Lanczos (2012); Besdo (2014); Nesbet (2002); Yourgrau (2012); Cline (2021); Mason (2013); Basdevant (2007); Ghoussoub (2008); Lovelock (2012)). Moreover, the books by Pobedrya (1984, 1995) are not books on the variational calculus. However, it is important to note that in them the original style of presentation of the basic variational principles of classical solid mechanics is given, which the authors of

this work extended to micropolar three-dimensional solid mechanics and also to single-layer and multilayer thin¹ solid bodies.

It should be noted that on the theory of elastic thin bodies, the authors of this work have published a lot of works and the interested reader is referred to, among others, Nikabadze (2014, 2001b,a); Nikabadze and Ulukhanyan (2005); Nikabadze (2006, 2007a,b,c); Nikabadze and Ulukhanyan (2016, 2019b,c,a, 2020a,b, 2021). We also note that in Vekua (1970) the variational principles of constructing the classical theory of shells using the expansion of unknown quantities in terms of the system of Legendre polynomials depending on the transverse coordinate are presented. M.U. Nikabadze spread this method on the construction of various versions of micropolar theories of elastic thin bodies, using the expansion in systems of Legendre and Chebyshev orthogonal polynomials (Nikabadze, 2014) and the Pobodria style for the presentation of the variational principles. In particular, in this work we have derived the necessary integral relations and proved the concept of living force and the generalized work theorem from which Clapeyron's theorem is derived. We have constructed Lagrangian, Castiglianian and generalized Reissner-type operators. We have given the definition of the generalized Legendre transform and obtained the Legendre-type identity. We have proved Lagrange and Castigliano's theorems concerning variational principles. We have written down the compatibility conditions with respect to tensors of strain and bending-torsion in various forms. We have presented equations of the Beltrami–Michell type for the stress and couple stress tensors with both asymmetric and symmetric differential tensor operators. We have given statements of mixed boundary value problem and initial boundary value problem with respect to vectors of displacements and rotations, as well as statements of the mixed boundary value problem and the new statement of the boundary value problem with respect to stress and couple stress tensors. We have given the definition of the generalized solution of the boundary value problem. We have proved the theorem of the minimum at the stationary point of the Lagrangian at the stationary point and the theorem of the maximum of the Castiglianian at the stationary point, as well as the theorem on the uniqueness of the generalized solution of boundary value problems.

The generalized Reissner-type operator of three-dimensional micropolar mechanics of solids is presented, on the basis of which the generalized Reissner-type operator of three-dimensional micropolar mechanics of thin solids with one small size is obtained under the new parameterization of the domains of these bodies. From the last Reissner-type operator, in turn, the generalized Reissner-type variational principle of three-dimensional micropolar mechanics of thin solids with one small size is derived under the new parametrization of the domains of these bodies. It should be noted that the advantage of the new parameterization is that it is experimentally more accessible than other parameterizations Nikabadze (2014, 2015, 2017).

Further, applying the method of orthogonal polynomials (expansion of unknown quantities in series in terms of a system of orthogonal polynomials), from the general-

¹ A three-dimensional body, one size of which is smaller than the others is called a thin body with one small size, and a solid body, two sizes of which are small compared to the third dimension is called a thin body with two small dimensions. The usual rules of tensor calculus adopted in Vekua (1970, 1978, 1982); Pobedrya (1986); Nikabadze (2015, 2017) are used.

ized Reissner-type variational principle of three-dimensional micropolar mechanics of thin solids with one small size under the new parameterization of the domains of these bodies, the Reissner variational principle of micropolar mechanics of thin solids with one small size in the moments with respect to the system of Legendre polynomials is derived. In addition, the method is described for obtaining the variational principles of Lagrange and Castigliano of micropolar mechanics of thin solid with one small size under the new parametrization of the domains of these bodies in moments with respect to systems of the first and second kind Chebyshev polynomials.

The effective parametrization of a multilayer thin domain, called a new parametrization, is considered and consists in using, in contrast to the classical approaches, several base surfaces. In addition, the new parameterization is characterized by the fact that it is experimentally more accessible than other parameterizations used in the scientific literature, since the front surfaces are used as basic ones. Also, when obtaining any relation (a system of equations, constitutive relations, boundary and initial conditions, variational principles, etc.) in the moments of the theory of multilayer thin bodies under the new parametrization of the domain of a thin body, it is sufficient in the corresponding relation of the theory of a single-layer thin body under the root letters of the quantities to supply the index α , which denotes the number of the layer α and give this index values from 1 to K , where K is the number of layers. Therefore, for the correct statement of the initial-boundary value problems to the equations of motion and the boundary and initial conditions in the moments, it is also necessary to add interlayer contact conditions, which must also be taken into account when writing the variational operators and formulating the variational principles. What has been said above can be called the rule of obtaining the desired relation in the theory of multilayer thin bodies from the corresponding relation in the theory of single-layer thin bodies. Applying this rule, below we give the representation of the generalized Reissner-type operator and formulate the generalized Reissner-type variational principle both in the case of full contact of adjacent layers of a multilayer structure and in the presence of zones of weakened adhesion. The description of obtaining of dual operators and variational principles of Reissner-type, as well as of Lagrangian and Castiglianian and variational principles of Lagrange and Castigliano is given. In the presence of domains of weakened adhesion at interphase boundaries in a multilayer thin body, one of the main problems is the problem of modeling the interface (interphase boundary). In this paper, the jump-type model (description of the interface by a surface of zero thickness) is presented in comparative detail.

11.2 Some Definitions and Integral Identities

Before formulating these variational principles, we introduce definitions and obtain certain integral identities for three-dimensional micropolar theories of solids similarly to the classical theory Pobedrya (1995).

Definition 11.1. Arbitrary continuously differentiable vector fields \mathbf{u} (displacement vector) and φ (rotation vector) are called the kinematic system, and arbitrary tensor fields $\underline{\mathbf{P}}$ (stress tensor) and $\underline{\boldsymbol{\mu}}$ (couple stress tensor) are called a static system.

Definition 11.2. A kinematically admissible system is a kinematic system that satisfies the kinematic boundary conditions

$$\mathbf{u}|_{S_1} = \mathbf{u}_0, \quad \varphi|_{S_1} = \varphi_0, \quad (11.1)$$

and in the case of a dynamic problem the kinematic system must also satisfy the initial conditions

$$\mathbf{u}|_{t=t_0} = \mathbf{f}_1, \quad \dot{\mathbf{u}}|_{t=t_0} = \mathbf{f}_2, \quad \varphi|_{t=t_0} = \mathbf{g}_1, \quad \dot{\varphi}|_{t=t_0} = \mathbf{g}_2. \quad (11.2)$$

Definition 11.3. Statically admissible system is a static system that satisfies the equilibrium equations in the case of a static or quasistatic problem

$$\nabla \cdot \underline{\mathbf{P}} + \rho \mathbf{F} = 0, \quad \nabla \cdot \underline{\boldsymbol{\mu}} + \underline{\mathbf{C}} \otimes \underline{\mathbf{P}} + \rho \mathbf{G} = 0 \quad (11.3)$$

or the motion equations in the case of a dynamic problem

$$\nabla \cdot \underline{\mathbf{P}} + \rho \mathbf{F} = \rho \frac{d\mathbf{v}}{dt}, \quad \nabla \cdot \underline{\boldsymbol{\mu}} + \underline{\mathbf{C}} \otimes \underline{\mathbf{P}} + \rho \mathbf{G} = \underline{\mathbf{J}} \cdot \frac{d\boldsymbol{\omega}}{dt}, \quad \boldsymbol{\omega} = \frac{d\varphi}{dt}, \quad (11.4)$$

and static boundary conditions

$$\mathbf{n} \cdot \underline{\mathbf{P}}|_{S_2} = \mathbf{P}_0, \quad \mathbf{n} \cdot \underline{\boldsymbol{\mu}}|_{S_2} = \boldsymbol{\mu}_0. \quad (11.5)$$

It should be noted that S_1 is one part, and S_2 is another part of the surface S of the body, \mathbf{n} is the unit outward normal vector of the surface, ∇ is Hamiltonian. In addition the following conditions are met: $S_1 \cup S_2 = S$ and $S_1 \cap S_2 = \emptyset$, where \emptyset denotes an empty set. Note also that the equations given in this paper in the form (11.3) and (11.4) can be viewed, for example, in monographies by Nowacki (1975); Kupradze et al (1976); Nikabadze (2014); Eringen (1999), in which they are presented in various forms.

Definition 11.4. The real kinematic system \mathbf{u} and φ and the real static system $\underline{\mathbf{P}}$ and $\underline{\boldsymbol{\mu}}$ are called, respectively, displacement and rotation vectors and stress and couple stress tensors, which satisfy the equilibrium equations (11.3) or movement equations (11.4) in the case of a dynamic problem, kinematic relations

$$\underline{\boldsymbol{\gamma}} = \nabla \mathbf{u} - \underline{\mathbf{C}} \cdot \varphi, \quad \underline{\boldsymbol{\varkappa}} = \nabla \varphi, \quad (11.6)$$

constitutive relations

$$\underline{\mathbf{P}} = \check{\mathbf{F}}(\underline{\boldsymbol{\gamma}}, \underline{\boldsymbol{\varkappa}}), \quad \underline{\boldsymbol{\mu}} = \check{\mathbf{G}}(\underline{\boldsymbol{\gamma}}, \underline{\boldsymbol{\varkappa}}) \quad (11.7)$$

or in the case of potential operators $\check{\mathbf{F}}$ and $\check{\mathbf{G}}$ the system satisfies the following constitutive relations

$$\underline{\mathbf{P}} = \frac{\partial \check{W}}{\partial \underline{\boldsymbol{\gamma}}}, \quad \underline{\boldsymbol{\mu}} = \frac{\partial \check{W}}{\partial \underline{\boldsymbol{\varkappa}}}, \tag{11.8}$$

kinematic (11.1) and static (11.5) boundary conditions (and initial conditions (11.2) in the case of dynamic problems).

Here $\underline{\mathbf{P}}$ is the stress tensor, $\underline{\boldsymbol{\mu}}$ is the couple stress tensor, \mathbf{u} is the displacement vector, $\boldsymbol{\varphi}$ is the rotation vector, $\underline{\boldsymbol{\gamma}} = \nabla \mathbf{u} - \underline{\mathbf{C}} \cdot \boldsymbol{\varphi}$ is the strain tensor, $\underline{\boldsymbol{\varkappa}} = \nabla \boldsymbol{\varphi}$ is the bending-torsion tensor, \mathbf{v} is the velocity vector, $\boldsymbol{\omega}$ is the vector of angular velocity, $\underline{\mathbf{C}}$ is the third order discriminant tensor (or the Levi-Civita tensor), \mathbf{F} is the vector of mass force, \mathbf{G} is the vector of mass moment, ρ is the density of the medium, $\underline{\mathbf{J}}$ is the tensor of the moment of inertia, \mathbf{n} is the unit vector of external normal to the surface to the surface of the body, $\overset{2}{\otimes}$ is the inner 2-products Vekua (1978); Nikabadze (2014, 2016); Nikabadze and Ulukhanyan (2016); Nikabadze (2017), $\check{W}(\underline{\boldsymbol{\gamma}}, \underline{\boldsymbol{\varkappa}})$ is the operator (or potential) of strain and bending-torsion tensors, and if it exists, then the constitutive relationships are defined by (11.8).

Note that in non-isothermal processes, instead of $\check{W}(\underline{\boldsymbol{\gamma}}, \underline{\boldsymbol{\varkappa}})$, the free energy $\check{E}(\underline{\boldsymbol{\gamma}}, \underline{\boldsymbol{\varkappa}}, \theta) = \check{W}(\underline{\boldsymbol{\gamma}}, \underline{\boldsymbol{\varkappa}}) - HT$ is considered, where H is the entropy, T is the temperature, and $\theta = T - T_0$ is the temperature drop.

Now let us get some integral identities. For this, we multiply the first equation (11.4) by some vector \mathbf{w} , and the second one by the vector $\boldsymbol{\psi}$. Then we integrate the obtained relations over the volume of V and apply the formula

$$\nabla \cdot (\underline{\mathbf{Q}} \cdot \mathbf{a}) = \nabla \cdot \underline{\mathbf{Q}} \cdot \mathbf{a} + \underline{\mathbf{Q}} \overset{2}{\otimes} \nabla \mathbf{a}, \quad \forall \underline{\mathbf{Q}}, \mathbf{a} \tag{11.9}$$

and the Ostrogradsky–Gauss theorem. Then, as a result, we come to the following integral identities:

$$\begin{aligned} \int_V \rho \dot{\mathbf{v}} \cdot \mathbf{w} dV &= \int_V \rho \mathbf{F} \cdot \mathbf{w} dV + \int_{\Sigma} \mathbf{n} \cdot \underline{\mathbf{P}} \cdot \mathbf{w} dV - \int_V \underline{\mathbf{P}} \overset{2}{\otimes} \nabla \mathbf{w} dV, \\ \int_V \dot{\boldsymbol{\omega}} \cdot \underline{\mathbf{J}} \cdot \boldsymbol{\psi} dV &= \int_V \rho \mathbf{G} \cdot \boldsymbol{\psi} dV + \int_{\Sigma} \mathbf{n} \cdot \underline{\boldsymbol{\mu}} \cdot \boldsymbol{\psi} dV - \int_V (\underline{\boldsymbol{\mu}} \overset{2}{\otimes} \nabla \boldsymbol{\psi} - \underline{\mathbf{P}} \overset{2}{\otimes} \underline{\mathbf{C}} \cdot \boldsymbol{\psi}) dV. \end{aligned} \tag{11.10}$$

Adding (11.10) term-by-term, we get

$$\begin{aligned} \int_V (\rho \dot{\mathbf{v}} \cdot \mathbf{w} + \dot{\boldsymbol{\omega}} \cdot \underline{\mathbf{J}} \cdot \boldsymbol{\psi}) dV &= \int_V \rho (\mathbf{F} \cdot \mathbf{w} + \mathbf{G} \cdot \boldsymbol{\psi}) dV \\ + \int_{\Sigma} (\underline{\mathbf{P}}_{(n)} \cdot \mathbf{w} + \underline{\boldsymbol{\mu}}_{(n)} \cdot \boldsymbol{\psi}) d\Sigma &- \int_V [\underline{\mathbf{P}} \overset{2}{\otimes} (\nabla \mathbf{w} - \underline{\mathbf{C}} \cdot \boldsymbol{\psi}) + \underline{\boldsymbol{\mu}} \overset{2}{\otimes} \nabla \boldsymbol{\psi}] dV. \end{aligned} \tag{11.11}$$

When writing the surface integral in the right-hand side of (11.11), we took into account the Cauchy formulas: $\mathbf{n} \cdot \underline{\mathbf{P}} = \underline{\mathbf{P}}_{(n)}$ and $\mathbf{n} \cdot \underline{\boldsymbol{\mu}} = \underline{\boldsymbol{\mu}}_{(n)}$, where $\underline{\mathbf{P}}_{(n)}$ is the stress vector, $\underline{\boldsymbol{\mu}}_{(n)}$ is the couple stress vector.

Assuming that $\mathbf{w} = \mathbf{v}$ and $\boldsymbol{\psi} = \boldsymbol{\omega}$, from (11.11) we obtain the concept of living force

$$\begin{aligned} \frac{d}{dt} \int_V \left(\rho \frac{\mathbf{v}^2}{2} + \frac{1}{2} \boldsymbol{\omega} \cdot \underline{\mathbf{J}} \cdot \boldsymbol{\omega} \right) dV &= \int_V (\rho \mathbf{F} \cdot \mathbf{v} + \rho \mathbf{G} \cdot \boldsymbol{\omega}) dV \\ &+ \int_{\Sigma} (\mathbf{P}_{(n)} \cdot \mathbf{v} + \boldsymbol{\mu}_{(n)} \cdot \boldsymbol{\omega}) d\Sigma - \int_V (\underline{\mathbf{P}} \otimes \dot{\boldsymbol{\gamma}} + \underline{\boldsymbol{\mu}} \otimes \dot{\boldsymbol{\varkappa}}) dV, \end{aligned} \quad (11.12)$$

where $\dot{\boldsymbol{\gamma}} = \nabla \mathbf{v} - \underline{\mathbf{C}} \cdot \boldsymbol{\omega}$, $\dot{\boldsymbol{\varkappa}} = \nabla \boldsymbol{\omega}$.

Introducing the notations

$$E = \int_V \left(\rho \frac{\mathbf{v}^2}{2} + \frac{1}{2} \boldsymbol{\omega} \cdot \underline{\mathbf{J}} \cdot \boldsymbol{\omega} \right) dV \quad (11.13)$$

– for kinetic energy, $\delta A^{(e)} = \delta A_1^{(e)} + \delta A_2^{(e)}$ – for changing the work of external forces and moments, where

$$\delta A_1^{(e)} = \int_V (\rho \mathbf{F} \cdot d\mathbf{u} + \rho \mathbf{G} \cdot d\boldsymbol{\varphi}) dV \quad (11.14)$$

is the change of the work of external mass forces and moments,

$$\delta A_2^{(e)} = \int_{\Sigma} (\mathbf{P}_{(n)} \cdot d\mathbf{u} + \boldsymbol{\mu}_{(n)} \cdot d\boldsymbol{\varphi}) d\Sigma \quad (11.15)$$

is the change of the work of external surface forces and moments, and also

$$\delta A^{(i)} = - \int_V (\underline{\mathbf{P}} \otimes d\boldsymbol{\gamma} + \underline{\boldsymbol{\mu}} \otimes d\boldsymbol{\varkappa}) dV, \quad (11.16)$$

– for changing the work of stress and couple stress tensors with the opposite sign, the concept of living force (11.11) can be written in a short form

$$dE = \delta A^{(e)} + \delta A^{(i)}. \quad (11.17)$$

Now let $\mathbf{w} = \mathbf{u}$, $\boldsymbol{\psi} = \boldsymbol{\varphi}$. Then, if we use the boundary conditions (11.1) and (11.5), then from (11.11) we will have

$$\begin{aligned} \int_V (\rho \dot{\mathbf{v}} \cdot \mathbf{u} + \dot{\boldsymbol{\omega}} \cdot \underline{\mathbf{J}} \cdot \boldsymbol{\varphi}) dV &= \int_V \rho (\mathbf{F} \cdot \mathbf{u} + \mathbf{G} \cdot \boldsymbol{\varphi}) dV + \int_{\Sigma_2} (\mathbf{P}_0 \cdot \mathbf{u} + \boldsymbol{\mu}_0 \cdot \boldsymbol{\varphi}) d\Sigma \\ &+ \int_{\Sigma_1} \mathbf{n} \cdot (\underline{\mathbf{P}} \cdot \mathbf{u}_0 + \underline{\boldsymbol{\mu}} \cdot \boldsymbol{\varphi}_0) d\Sigma - \int_V (\underline{\mathbf{P}} \otimes \boldsymbol{\gamma} + \underline{\boldsymbol{\mu}} \otimes \boldsymbol{\varkappa}) dV. \end{aligned} \quad (11.18)$$

Further, let us assume that the mass and surface forces and moments appearing in (11.18) have potential (or do not depend on the displacement and rotation vectors). Then the first two terms on the right side of (11.18) represent the work done by external forces and moments in displacement \mathbf{u} and rotation $\boldsymbol{\varphi}$

$$\begin{aligned}
 A^{(e)} &\equiv A_1^{(e)} + A_2^{(e)}, \quad A_1^{(e)} \equiv \int_V (\rho \mathbf{F} \cdot \mathbf{u} + \rho \mathbf{G} \cdot \boldsymbol{\varphi}) dV, \\
 A_2^{(e)} &\equiv \int_{\Sigma_2} (\mathbf{P}_0 \cdot \mathbf{u} + \boldsymbol{\mu}_0 \cdot \boldsymbol{\varphi}) d\Sigma.
 \end{aligned}
 \tag{11.19}$$

The third term on the right side of (11.18) is called the work done by surface forces and moments in the given displacement \mathbf{u}_0 and rotation $\boldsymbol{\varphi}_0$

$$A_{\Sigma_1}^{(i)} \equiv \int_{\Sigma_1} \mathbf{n} \cdot (\underline{\mathbf{P}} \cdot \mathbf{u}_0 + \underline{\boldsymbol{\mu}} \cdot \boldsymbol{\varphi}_0) d\Sigma.
 \tag{11.20}$$

The last term on the right side of (11.18) is the work of stress and couple stress tensors in the strain and the bending-torsion tensors with the opposite sign

$$A^{(i)} \equiv - \int_V (\underline{\mathbf{P}} \overset{2}{\otimes} \underline{\boldsymbol{\gamma}} + \underline{\boldsymbol{\mu}} \overset{2}{\otimes} \underline{\boldsymbol{\varkappa}}) dV.
 \tag{11.21}$$

The integral on the left side of (11.18) is the work done by D'Alembert forces (or the work of inertial forces and moments)

$$A_E \equiv \int_V (\rho \dot{\mathbf{v}} \cdot \mathbf{u} + \dot{\boldsymbol{\omega}} \cdot \underline{\mathbf{J}} \cdot \boldsymbol{\varphi}) dV.
 \tag{11.22}$$

It is easy to see that if in (11.22) the vectors \mathbf{u} and $\boldsymbol{\varphi}$ are replaced by $d\mathbf{u}$ and $d\boldsymbol{\varphi}$, respectively, then the change of work of D'Alembert forces will coincide with the change of kinetic energy (11.13)

$$dA_E = dE = \int_V (\rho \dot{\mathbf{v}} \cdot d\mathbf{u} + \dot{\boldsymbol{\omega}} \cdot \underline{\mathbf{J}} \cdot d\boldsymbol{\varphi}) dV.$$

Now let us suppose that the vectors \mathbf{w} è $\boldsymbol{\psi}$ appearing in (11.11) satisfy the conditions

$$\mathbf{w}|_{\Sigma_1} = \mathbf{u}_0, \quad \boldsymbol{\psi}|_{\Sigma_1} = \boldsymbol{\varphi}_0.
 \tag{11.23}$$

In particular, \mathbf{u}_0 and $\boldsymbol{\varphi}_0$ can be equal to zero. Then it is easy to see that the relation (11.11), taking into account (11.5) and (11.23), can be written in the form

$$\begin{aligned}
 &\int_V [\underline{\mathbf{P}}(\mathbf{u}, \boldsymbol{\varphi}) \overset{2}{\otimes} \underline{\boldsymbol{\gamma}}(\mathbf{w}, \boldsymbol{\psi}) + \underline{\boldsymbol{\mu}}(\mathbf{u}, \boldsymbol{\varphi}) \overset{2}{\otimes} \underline{\boldsymbol{\varkappa}}(\boldsymbol{\psi})] dV \\
 &= \int_V [\rho(\mathbf{F} - \ddot{\mathbf{u}}) \cdot \mathbf{w} + (\rho \mathbf{G} - \underline{\mathbf{J}} \cdot \dot{\boldsymbol{\omega}}) \cdot \boldsymbol{\psi}] dV \\
 &\quad + \int_{\Sigma_1} \mathbf{n} \cdot (\underline{\mathbf{P}} \cdot \mathbf{u}_0 + \underline{\boldsymbol{\mu}} \cdot \boldsymbol{\varphi}_0) d\Sigma + \int_{\Sigma_2} (\mathbf{P}_0 \cdot \mathbf{w} + \boldsymbol{\mu}_0 \cdot \boldsymbol{\psi}) d\Sigma.
 \end{aligned}
 \tag{11.24}$$

Hence, without inertial terms, we get

$$\begin{aligned}
 &\int_V [\underline{\mathbf{P}}(\mathbf{u}, \boldsymbol{\varphi}) \overset{2}{\otimes} \underline{\boldsymbol{\gamma}}(\mathbf{w}, \boldsymbol{\psi}) + \underline{\boldsymbol{\mu}}(\mathbf{u}, \boldsymbol{\varphi}) \overset{2}{\otimes} \underline{\boldsymbol{\varkappa}}(\boldsymbol{\psi})] dV = \int_V (\rho \mathbf{F} \cdot \mathbf{w} + \rho \mathbf{G} \cdot \boldsymbol{\psi}) dV \\
 &\quad + \int_{\Sigma_1} \mathbf{n} \cdot (\underline{\mathbf{P}} \cdot \mathbf{u}_0 + \underline{\boldsymbol{\mu}} \cdot \boldsymbol{\varphi}_0) d\Sigma + \int_{\Sigma_2} (\mathbf{P}_0 \cdot \mathbf{w} + \boldsymbol{\mu}_0 \cdot \boldsymbol{\psi}) d\Sigma.
 \end{aligned}
 \tag{11.25}$$

If in this case the kinematic boundary conditions are represented as

$$\mathbf{u}|_{\Sigma_1} = 0, \quad \boldsymbol{\varphi}|_{\Sigma_1} = 0, \quad (11.26)$$

i.e. $\mathbf{u}_0 = 0, \boldsymbol{\varphi}_0 = 0$, then from (11.25) we have

$$\begin{aligned} \int_V [\underline{\mathbf{P}}(\mathbf{u}, \boldsymbol{\varphi}) \otimes^2 \underline{\boldsymbol{\gamma}}(\mathbf{w}, \boldsymbol{\psi}) + \underline{\boldsymbol{\mu}}(\mathbf{u}, \boldsymbol{\varphi}) \otimes^2 \underline{\boldsymbol{\varkappa}}(\boldsymbol{\psi})] dV \\ = \int_V (\rho \mathbf{F} \cdot \mathbf{w} + \rho \mathbf{G} \cdot \boldsymbol{\psi}) dV + \int_{\Sigma_2} (\mathbf{P}_0 \cdot \mathbf{w} + \boldsymbol{\mu}_0 \cdot \boldsymbol{\psi}) d\Sigma. \end{aligned} \quad (11.27)$$

Note that in (11.24), (11.25) and (11.27) we have $\underline{\boldsymbol{\gamma}}(\mathbf{w}, \boldsymbol{\psi}) = \nabla \mathbf{w} - \underline{\mathbf{C}} \cdot \boldsymbol{\psi}$, $\underline{\boldsymbol{\varkappa}}(\boldsymbol{\psi}) = \nabla \boldsymbol{\psi}$.

Assume that the operators $\check{\mathbf{F}}$ and $\check{\mathbf{G}}$ are potential, i.e. there exists a deformation potential $\check{W}(\underline{\boldsymbol{\gamma}}, \underline{\boldsymbol{\varkappa}})$, by means of which the stress and couple stress tensors are defined by the formulas (11.8). Then, using the definitions of the differential of operator and the functional derivative Pobedrya (1995), it is easy to see that we will have

$$\begin{aligned} D\check{W}(\underline{\boldsymbol{\gamma}}(\mathbf{u}, \boldsymbol{\varphi}), \underline{\boldsymbol{\varkappa}}(\boldsymbol{\psi}), \underline{\boldsymbol{\gamma}}(\mathbf{w}, \boldsymbol{\psi}), \underline{\boldsymbol{\varkappa}}(\boldsymbol{\psi})) \equiv D\check{W}(\mathbf{u}, \boldsymbol{\varphi}, \mathbf{w}, \boldsymbol{\psi}) \\ = \underline{\mathbf{P}}(\mathbf{u}, \boldsymbol{\varphi}) \otimes^2 \underline{\boldsymbol{\gamma}}(\mathbf{w}, \boldsymbol{\psi}) + \underline{\boldsymbol{\mu}}(\mathbf{u}, \boldsymbol{\varphi}) \otimes^2 \underline{\boldsymbol{\varkappa}}(\boldsymbol{\psi}). \end{aligned} \quad (11.28)$$

Determining the potential energy operator of the tensors of strain and bending-torsion $\check{I}(\underline{\boldsymbol{\gamma}}, \underline{\boldsymbol{\varkappa}})$ by

$$\check{I}(\underline{\boldsymbol{\gamma}}(\mathbf{u}, \boldsymbol{\varphi}), \underline{\boldsymbol{\varkappa}}(\boldsymbol{\psi})) \equiv \int_V \check{W}(\underline{\boldsymbol{\gamma}}(\mathbf{u}, \boldsymbol{\varphi}), \underline{\boldsymbol{\varkappa}}(\boldsymbol{\psi})) dV, \quad (11.29)$$

the relation (11.27) by virtue of (11.28) and (11.29) can be presented in short form

$$D\check{I}(\mathbf{u}, \boldsymbol{\varphi}, \mathbf{w}, \boldsymbol{\psi}) - A^{(e)}(\mathbf{w}, \boldsymbol{\psi}) = 0. \quad (11.30)$$

We can see that in this case from (11.24), taking into account the inertial terms, instead of (11.30) we will have

$$D\check{I}(\mathbf{u}, \boldsymbol{\varphi}, \mathbf{w}, \boldsymbol{\psi}) - A^{(e)}(\mathbf{w}, \boldsymbol{\psi}) + A_E(\mathbf{w}, \boldsymbol{\psi}) = 0. \quad (11.31)$$

Note that in (11.30) and (11.31) we introduce next notations:

$$\begin{aligned} A^{(e)}(\mathbf{w}, \boldsymbol{\psi}) &= \int_V (\rho \mathbf{F} \cdot \mathbf{w} + \rho \mathbf{G} \cdot \boldsymbol{\psi}) dV + \int_{\Sigma_2} (\mathbf{P}_0 \cdot \mathbf{w} + \boldsymbol{\mu}_0 \cdot \boldsymbol{\psi}) d\Sigma, \\ A_E(\mathbf{w}, \boldsymbol{\psi}) &= \int_V (\rho \dot{\mathbf{v}} \cdot \mathbf{w} + \dot{\boldsymbol{\omega}} \cdot \underline{\mathbf{J}} \cdot \boldsymbol{\psi}) dV. \end{aligned} \quad (11.32)$$

Having (11.6) and (11.7), from (11.3) and (11.4) we obtain the equilibrium and motion equations represented with respect to the displacement and rotation vectors, which we symbolically write as follows:

$$\nabla \cdot \underline{\mathbf{P}}(\mathbf{u}, \boldsymbol{\varphi}) + \rho \mathbf{F} = 0, \quad \nabla \cdot \underline{\boldsymbol{\mu}}(\mathbf{u}, \boldsymbol{\varphi}) + \underline{\mathbf{C}} \otimes^2 \underline{\mathbf{P}}(\mathbf{u}, \boldsymbol{\varphi}) + \rho \mathbf{G} = 0, \quad (11.33)$$

$$\nabla \cdot \underline{\mathbf{P}}(\mathbf{u}, \varphi) + \rho \mathbf{F} = \rho \frac{d\mathbf{v}}{dt}, \quad \nabla \cdot \underline{\boldsymbol{\mu}}(\mathbf{u}, \varphi) + \underline{\mathbf{C}} \otimes \underline{\mathbf{P}}(\mathbf{u}, \varphi) + \rho \mathbf{G} = \underline{\mathbf{J}} \cdot \frac{d\boldsymbol{\omega}}{dt}. \quad (11.34)$$

It can be seen that with each problem (11.33), (11.26) and (11.5) the equality (11.27) or (11.30) is related for arbitrary differentiable vector fields \mathbf{w} and $\boldsymbol{\psi}$ satisfying the conditions

$$\mathbf{w}|_{\Sigma_1} = 0, \quad \boldsymbol{\psi}|_{\Sigma_1} = 0. \quad (11.35)$$

It should be noted that the equations (11.33) include the second derivatives with respect to the coordinates of the vectors \mathbf{u} and φ . Therefore, the solution of problem (11.33), (11.26) and (11.5) must be at least twice differentiable. Consequently, we can abandon this requirement and understand the solution of the problem (11.33), (11.26) and (11.5) in a generalized sense. In this regard, it is advisable to introduce a definition.

Definition 11.5. The vector fields \mathbf{u} and φ are called the generalized solution of the problem (11.33), (11.26) and (11.5) if for all differentiable vectors \mathbf{w} and $\boldsymbol{\psi}$ satisfying the conditions (11.35) the identity (11.27) or (11.30) is true.

Note that only the condition for the existence of integrals in the right-hand side (11.27) is required from the input data. Note also that the generalized solution will be classical if the vector fields \mathbf{u} and φ are twice continuously differentiable.

It is easy to show that if $\check{\mathbf{F}}$ and $\check{\mathbf{G}}$ are potential operators, then the change of the work of the internal forces and moments (11.16) is the total differential and the work of the internal forces and moments due to (11.29) is expressed by

$$A^{(i)} = -\check{H} = -\int_V \check{W} dV. \quad (11.36)$$

In addition, it is easy to see that if $\check{\mathbf{F}}$ and $\check{\mathbf{G}}$ are potential operators and mass and surface forces and moments are potential ($\mathbf{F} = \partial\chi_1/\partial\mathbf{u}$, $\mathbf{m} = \partial\chi_2/\partial\varphi$, $\mathbf{P}_{(n)} = \partial\chi_3/\partial\mathbf{u}$, $\boldsymbol{\mu}_{(n)} = \partial\chi_4/\partial\varphi$), the concept of living force is represented as

$$dE = dA^{(e)} + dA^{(i)},$$

whence by virtue of (11.36) it follows that

$$\check{L} = E - A^{(e)} + \check{H} = \text{const}. \quad (11.37)$$

The operator \check{L} is called the Lagrangian of a system, and the systems for which it has a constant value are conservative.

Taking into account that the $\check{\mathbf{F}}$ and $\check{\mathbf{G}}$ operators are potential, while $\check{W}(\boldsymbol{\gamma}, \boldsymbol{\varkappa})$ is a homogeneous operator of degree m , from (11.18) we come to the so-called work generalized theorem

$$A_E = A^{(e)} - m\check{H} + A_{\Sigma_1}^{(i)}. \quad (11.38)$$

If the forces and moments of inertia are absent, the kinematic boundary conditions are zero (11.26) and the operator $\check{W}(\boldsymbol{\gamma}, \boldsymbol{\varkappa})$ is quadratic, then from (11.38) the theorem of Clapeyron follows

$$A^{(e)} = 2\check{I} = 2 \int_V \check{W}(\underline{\gamma}, \underline{\varkappa}) dV.$$

Now let us consider the static (quasistatic) problem (11.3), (11.6), (11.8), (11.26) and (11.5) and let us construct the Lagrangian for this problem

$$\check{L}(\mathbf{u}, \varphi) = \check{I}(\mathbf{u}, \varphi) - A^{(e)}(\mathbf{u}, \varphi), \quad (11.39)$$

where the first term on the right side of (11.39) is determined by (11.29), and the second one is determined by the first formula (11.32) if in it we change \mathbf{w} and ψ to \mathbf{u} and φ , respectively.

11.3 Lagrange Variational Principle (Lagrange Theorem)

Theorem 11.1. *Of all kinematically admissible systems the real system is different in that for it and only for it the Lagrangian has a stationary value, i.e.*

$$D\check{L}(\mathbf{u}, \varphi, \delta\mathbf{u}, \delta\varphi) = 0, \quad (11.40)$$

or, use the definition of the differential of operator and (11.8), the equality (11.40) can be represented as

$$\int_V (\underline{\mathbf{P}} \otimes \delta\underline{\gamma} + \underline{\underline{\mu}} \otimes \delta\underline{\varkappa}) dV = \int_V (\rho\mathbf{F} \cdot \delta\mathbf{u} + \rho\mathbf{G} \cdot \delta\varphi) dV + \int_{\Sigma_2} (\mathbf{P}_0 \cdot \delta\mathbf{u} + \underline{\underline{\mu}}_0 \cdot \delta\varphi) d\Sigma, \quad (11.41)$$

where the ratios are valid

$$\delta\underline{\gamma} = \nabla \delta\mathbf{u} - \underline{\underline{\mathbf{C}}} \cdot \delta\varphi, \quad \delta\underline{\varkappa} = \nabla \delta\varphi. \quad (11.42)$$

$\delta\mathbf{u}$ and $\delta\varphi$ can be understood as the difference between two kinematically admissible systems ($\delta\mathbf{u} = \mathbf{u}_2 - \mathbf{u}_1$, $\delta\varphi = \varphi_2 - \varphi_1$).

Proof of necessity. Assuming $\rho\dot{\mathbf{v}} = 0$, $\underline{\mathbf{J}} \cdot \dot{\boldsymbol{\omega}} = 0$, $\mathbf{w} = \delta\mathbf{u}$ and $\psi = \delta\varphi$, from (11.11) immediately follows the necessity of the theorem, i.e. (11.40) or (11.41).

Proof of sufficiency. Taking into account (11.42), (11.9) and using the Ostrogradsky-Gauss theorem, by (11.26) from (11.41) we get

$$\begin{aligned} \int_V [(\nabla \cdot \underline{\mathbf{P}} + \rho\mathbf{F}) \cdot \delta\mathbf{u} + (\nabla \cdot \underline{\underline{\mu}} + \underline{\underline{\mathbf{C}}} \otimes \underline{\mathbf{P}} + \rho\mathbf{G}) \cdot \delta\varphi] dV \\ = \int_{\Sigma_2} [(\mathbf{n} \cdot \underline{\mathbf{P}} - \mathbf{P}_0) \cdot \delta\mathbf{u} + (\mathbf{n} \cdot \underline{\underline{\mu}} - \underline{\underline{\mu}}_0) \cdot \delta\varphi] d\Sigma. \end{aligned} \quad (11.43)$$

Since $\delta\mathbf{u}$ and $\delta\varphi$ are arbitrary then from (11.43) there are followed (11.3) without inertial terms and (11.5).

Thus, when formulating the Lagrange variational principle, we require the fulfillment of the kinematic relations (11.6) and the kinematic boundary conditions

(11.26), and from the stationarity condition (11.40) of the Lagrangian (11.39) the equilibrium equations (11.3) and the static boundary conditions (11.5) follow.

Now, before we formulate the Castigliano variational principle, let us introduce the notion of a generalized Legendre transform for operators and present the compatibility conditions in a micropolar theory. For this purpose, we recall that the usual Legendre transformation of a differentiable function $f(x)$, where

$$df = Xdx, \quad X = \frac{df}{dx},$$

associates with a function $F(X)$ such that

$$dF = x dX, \quad x = \frac{dF}{dX}.$$

At the same time, it is easy to show that the identity is valid

$$f(x) + F(X) - xX = \text{const.} \quad (11.44)$$

The generalization of the Legendre transformation to operators consists in replacing the usual derivative with a functional one. Let a scalar operator $\check{W}(\underline{\gamma}, \underline{\boldsymbol{\varkappa}})$ be given, where

$$D\check{W}(\underline{\gamma}, \underline{\boldsymbol{\varkappa}}, \delta\underline{\gamma}, \delta\underline{\boldsymbol{\varkappa}}) = \underline{\mathbf{P}} \otimes^2 \delta\underline{\gamma} + \underline{\boldsymbol{\mu}} \otimes^2 \delta\underline{\boldsymbol{\varkappa}}, \quad \underline{\mathbf{P}} = \frac{\partial \check{W}}{\partial \underline{\gamma}}, \quad \underline{\boldsymbol{\mu}} = \frac{\partial \check{W}}{\partial \underline{\boldsymbol{\varkappa}}}.$$

Then the generalized Legendre transformation assigns to the operator $\check{W}(\underline{\gamma}, \underline{\boldsymbol{\varkappa}})$, called the potential of strain and bending-torsion tensors, the operator $\check{w}(\underline{\mathbf{P}}, \underline{\boldsymbol{\mu}})$, called the potential of stress and couple stress tensors, such that

$$D\check{w}(\underline{\mathbf{P}}, \underline{\boldsymbol{\mu}}, \delta\underline{\mathbf{P}}, \delta\underline{\boldsymbol{\mu}}) = \underline{\boldsymbol{\gamma}} \otimes^2 \delta\underline{\mathbf{P}} + \underline{\boldsymbol{\varkappa}} \otimes^2 \delta\underline{\boldsymbol{\mu}}, \quad \underline{\boldsymbol{\gamma}} = \frac{\partial \check{w}}{\partial \underline{\mathbf{P}}}, \quad \underline{\boldsymbol{\varkappa}} = \frac{\partial \check{w}}{\partial \underline{\boldsymbol{\mu}}}. \quad (11.45)$$

Whereby similarly to (11.44) the Legendre-type identity

$$\check{W}(\underline{\boldsymbol{\gamma}}, \underline{\boldsymbol{\varkappa}}) + \check{w}(\underline{\mathbf{P}}, \underline{\boldsymbol{\mu}}) - \underline{\mathbf{P}} \otimes^2 \underline{\boldsymbol{\gamma}} - \underline{\boldsymbol{\mu}} \otimes^2 \underline{\boldsymbol{\varkappa}} = \text{const.} \quad (11.46)$$

holds true. Note that if $\check{W}(0, 0) = 0$ and $\check{w}(0, 0) = 0$, then the constant on the right side of (11.46) is zero.

Thus, the Legendre transformation assigns to the potential of strain and bending-torsion tensors the potential of stress and couple stress tensors. Obviously, similarly to the operator of the potential energy of the tensors of strain and bending-torsion (11.29), it is possible to introduce the operator of the potential energy of the tensors of stress and couple stress $\check{\pi}$. So that we will have

$$\check{\pi} = \int_V \check{w} dV, \quad D\check{\pi}(\underline{\mathbf{P}}, \underline{\boldsymbol{\mu}}, \delta\underline{\mathbf{P}}, \delta\underline{\boldsymbol{\mu}}) = \int_V (\underline{\boldsymbol{\gamma}} \otimes^2 \delta\underline{\mathbf{P}} + \underline{\boldsymbol{\varkappa}} \otimes^2 \delta\underline{\boldsymbol{\mu}}) dV. \quad (11.47)$$

It should be noted that the second and third relations (11.45) assume the solvability of the relations (11.7) in the form of

$$\underline{\gamma} = \check{\mathbf{J}}(\underline{\mathbf{P}}, \underline{\mu}), \quad \underline{\boldsymbol{\varkappa}} = \check{\mathbf{H}}(\underline{\mathbf{P}}, \underline{\mu}) \quad (11.48)$$

and, in addition, the potentiality of the operators $\check{\mathbf{J}}$ and $\check{\mathbf{H}}$, i.e.

$$\underline{\gamma} = \check{\mathbf{J}}(\underline{\mathbf{P}}, \underline{\mu}) = \frac{\partial \check{w}}{\partial \underline{\mathbf{P}}}, \quad \underline{\boldsymbol{\varkappa}} = \check{\mathbf{H}}(\underline{\mathbf{P}}, \underline{\mu}) = \frac{\partial \check{w}}{\partial \underline{\mu}}. \quad (11.49)$$

11.3.1 On Compatibility Conditions in Linear Micropolar Theory

These conditions for a simply connected domain, consisting of 18 relations and which for the first time, apparently, were obtained in Aero and Kuvshinsky (1960); Kuvshinsky and Aero (1963) (see also Sandru (1966); Nowacki (1975); Eringen (1999)), can be represented as Nikabadze (2010, 2012)

$$\begin{aligned} \nabla \times \underline{\gamma} + I_1(\underline{\boldsymbol{\varkappa}})\underline{\mathbf{E}} - \underline{\boldsymbol{\varkappa}}^T &= \underline{\mathbf{C}} \otimes \nabla \underline{\gamma} + I_1(\underline{\boldsymbol{\varkappa}})\underline{\mathbf{E}} - \underline{\boldsymbol{\varkappa}}^T = \underline{\mathbf{0}}, \\ \nabla \times \underline{\boldsymbol{\varkappa}} &= \underline{\mathbf{C}} \otimes \nabla \underline{\boldsymbol{\varkappa}} = \underline{\mathbf{0}}, \end{aligned} \quad (11.50)$$

where $\underline{\mathbf{C}}$ is the discriminant tensor.

First, applying the transposition operation, and then the rotor operator to (11.50) and taking into account the definition of the incompatibility tensor Pobedrya (1995, 1986); Nikabadze (2010, 2012)

$$\begin{aligned} \underline{\eta} \equiv \text{Ink} \underline{\mathbf{Q}} &= \nabla \times (\nabla \times \underline{\mathbf{Q}})^T \\ &= -\Delta \underline{\mathbf{Q}} - \nabla \nabla I_1(\underline{\mathbf{Q}}) + \nabla(\nabla \cdot \underline{\mathbf{Q}}) + [\nabla(\nabla \cdot \underline{\mathbf{Q}}^T)]^T + \underline{\mathbf{E}}[\Delta I_1(\underline{\mathbf{Q}}) - \nabla \nabla \otimes \underline{\mathbf{Q}}] \end{aligned}$$

and equalities

$$\nabla \times [I_1(\underline{\boldsymbol{\varkappa}})\underline{\mathbf{E}}] = -\underline{\mathbf{C}} \cdot \nabla I_1(\underline{\boldsymbol{\varkappa}}), \quad \nabla \times \underline{\boldsymbol{\varkappa}} = \underline{\mathbf{0}},$$

where $\underline{\mathbf{Q}}$ is an arbitrary second rank tensor, $I_1(\underline{\boldsymbol{\varkappa}})$ and $I_1(\underline{\mathbf{Q}})$ are the first invariants of $\underline{\boldsymbol{\varkappa}}$ and $\underline{\mathbf{Q}}$ respectively, and $\underline{\mathbf{E}}$ is the unit tensor of the second rank, we obtain the compatibility conditions in the form

$$\text{Ink} \underline{\gamma} - \underline{\mathbf{C}} \cdot \nabla I_1(\underline{\boldsymbol{\varkappa}}) = \underline{\mathbf{0}}, \quad \text{Ink} \underline{\boldsymbol{\varkappa}} = \underline{\mathbf{0}}. \quad (11.51)$$

It should be noted that the relations (11.51) are equivalent to the relations

$$\begin{aligned} \check{\mathbf{H}}(\underline{\gamma}, \underline{\varkappa}) &\equiv -\Delta \underline{\gamma} - \nabla \nabla I_1(\underline{\gamma}) + \nabla(\nabla \cdot \underline{\gamma}) + [\nabla(\nabla \cdot \underline{\gamma}^T)]^T - \underline{\mathbf{C}} \cdot \nabla I_1(\underline{\varkappa}) = \underline{\mathbf{0}}, \\ \check{\mathbf{H}}(\underline{\varkappa}) &\equiv -\Delta \underline{\varkappa} - \nabla \nabla I_1(\underline{\varkappa}) + \nabla(\nabla \cdot \underline{\varkappa}) + [\nabla(\nabla \cdot \underline{\varkappa}^T)]^T = \underline{\mathbf{0}}, \end{aligned} \tag{11.52}$$

which in the following we will call the compatibility relations in the micropolar theory.

Using (11.48) (or (11.49)), the compatibility relations (11.52) can be represented symbolically as follows:

$$\check{\mathbf{H}}(\underline{\mathbf{P}}, \underline{\boldsymbol{\mu}}) = \underline{\mathbf{0}}, \quad \check{\mathbf{H}}(\underline{\mathbf{P}}, \underline{\boldsymbol{\mu}}) = \underline{\mathbf{0}}, \tag{11.53}$$

which are called compatibility relations (equations) with respect to the tensors of stresses and couple stresses. Obviously, the number of such equations is 18.

It should be noted that we assume that the equations (11.53) are obtained for those bodies for which the constitutive relations (11.7) and (11.48) are valid simultaneously, for example, for linearly elastic bodies, and also for linearly viscoelastic bodies of arbitrary anisotropy, i.e. i.e. for those bodies for which the constitutive relations are reversible.

Next, from (11.53) we get the equations for a homogeneous isotropic linearly elastic micropolar body with a center of symmetry taking into account the equation (11.3), i.e. we want obtain equations of the Beltrami–Michell type. In the case of a homogeneous linearly elastic micropolar body with a center of symmetry, the direct and inverse constitutive relations are represented as

$$\underline{\mathbf{P}} = \underline{\mathbf{A}} \otimes \underline{\gamma}, \quad \underline{\boldsymbol{\mu}} = \underline{\mathbf{D}} \otimes \underline{\varkappa}, \quad \underline{\gamma} = \underline{\mathbf{A}}' \otimes \underline{\mathbf{P}}, \quad \underline{\varkappa} = \underline{\mathbf{D}}' \otimes \underline{\boldsymbol{\mu}}, \tag{11.54}$$

where $\underline{\mathbf{P}}$ is the stress tensor, $\underline{\boldsymbol{\mu}}$ is the couple stress tensor, \otimes is the inner 2-product Vekua (1978); Nikabadze (2014, 2016); Nikabadze and Ulukhanyan (2016); Nikabadze (2017), $\underline{\mathbf{A}}$ and $\underline{\mathbf{D}}$ are the elastic modulus tensors, and $\underline{\mathbf{A}}'$ and $\underline{\mathbf{D}}'$ are the elastic compliance tensors. For an isotropic material, they have the following expressions:

$$\begin{aligned} \underline{\mathbf{A}} &= \lambda \underline{\mathbf{C}}_{(1)} + (\mu + \alpha) \underline{\mathbf{C}}_{(2)} + (\mu - \alpha) \underline{\mathbf{C}}_{(3)}, \\ \underline{\mathbf{D}} &= \gamma \underline{\mathbf{C}}_{(1)} + (\delta + \beta) \underline{\mathbf{C}}_{(2)} + (\delta - \beta) \underline{\mathbf{C}}_{(3)}, \\ \underline{\mathbf{A}}' &= \lambda' \underline{\mathbf{C}}_{(1)} + (\mu' + \alpha') \underline{\mathbf{C}}_{(2)} + (\mu' - \alpha') \underline{\mathbf{C}}_{(3)}, \\ \underline{\mathbf{D}}' &= \gamma' \underline{\mathbf{C}}_{(1)} + (\delta' + \beta') \underline{\mathbf{C}}_{(2)} + (\delta' - \beta') \underline{\mathbf{C}}_{(3)}. \end{aligned} \tag{11.55}$$

Here $\underline{\mathbf{C}}_{(1)}$, $\underline{\mathbf{C}}_{(2)}$, $\underline{\mathbf{C}}_{(3)}$ are fourth-rank isotropic tensors, the material constants are related by the relations

$$\begin{aligned} \lambda' &= -\frac{\lambda}{6\mu K}, \quad \mu' = \frac{1}{4\mu}, \quad \alpha' = \frac{1}{4\alpha}, \quad K = \lambda + \frac{2}{3}\mu, \quad \nu = \frac{\lambda}{2(\lambda + \mu)}, \\ \gamma' &= -\frac{\gamma}{6\delta\Omega}, \quad \delta' = \frac{1}{4\delta}, \quad \beta' = \frac{1}{4\beta}, \quad \Omega = \gamma + \frac{2}{3}\delta, \quad \varepsilon = \frac{\gamma}{2(\gamma + \delta)}. \end{aligned} \tag{11.56}$$

Representing the tensors of stresses $\underline{\mathbf{P}}$ and couple stresses $\underline{\boldsymbol{\mu}}$ as the sum of the symmetric and skew-symmetric parts ($\underline{\mathbf{P}} = \underline{\mathbf{P}}^S + \underline{\mathbf{P}}^A$ and $\underline{\boldsymbol{\mu}} = \underline{\boldsymbol{\mu}}^S + \underline{\boldsymbol{\mu}}^A$) and denoting the accompanying vectors for the skew-symmetric parts $\underline{\mathbf{P}}^A$ and $\underline{\boldsymbol{\mu}}^A$ by \mathbf{q} and $\boldsymbol{\tau}$ ($\underline{\mathbf{P}}^A = -\underline{\mathbf{C}} \cdot \mathbf{q}$, $\underline{\boldsymbol{\mu}}^A = -\underline{\mathbf{C}} \cdot \boldsymbol{\tau}$), the equilibrium equations (11.3) of the micropolar theory can be written as follows:

$$\nabla \cdot \underline{\mathbf{P}}^S + \nabla \times \mathbf{q} + \rho \mathbf{F} = \mathbf{0}, \quad \nabla \cdot \underline{\boldsymbol{\mu}}^S + \nabla \times \boldsymbol{\tau} - 2\mathbf{q} + \rho \mathbf{G} = \mathbf{0}. \quad (11.57)$$

Next, finding the first invariants, for example, from (11.51), we will have

$$\nabla^2 I_1(\boldsymbol{\gamma}) = \nabla \nabla \otimes \boldsymbol{\gamma}, \quad \nabla^2 I_1(\boldsymbol{\varkappa}) = \nabla \nabla \otimes \boldsymbol{\varkappa}. \quad (11.58)$$

Based on Hooke's inverse law obtained by the corresponding relations (11.54) and (11.55), we find

$$\begin{aligned} I_1(\boldsymbol{\gamma}) &= (3\lambda' + 2\mu')I_1(\underline{\mathbf{P}}), & \nabla \nabla \otimes \boldsymbol{\gamma} &= \lambda' \nabla^2 I_1(\underline{\mathbf{P}}) + 2\mu' \nabla \nabla \otimes \underline{\mathbf{P}}, \\ I_1(\boldsymbol{\varkappa}) &= (3\gamma' + 2\delta')I_1(\underline{\boldsymbol{\mu}}), & \nabla \nabla \otimes \boldsymbol{\varkappa} &= \gamma' \nabla^2 I_1(\underline{\boldsymbol{\mu}}) + 2\delta' \nabla \nabla \otimes \underline{\boldsymbol{\mu}}, \end{aligned} \quad (11.59)$$

and by the equilibrium equations (11.57) we have

$$\begin{aligned} \nabla \nabla \otimes \underline{\mathbf{P}} &= \nabla \nabla \otimes \underline{\mathbf{P}}^S = -\rho \nabla \cdot \mathbf{F}, \\ \nabla \nabla \otimes \underline{\boldsymbol{\mu}} &= \nabla \nabla \otimes \underline{\boldsymbol{\mu}}^S = 2\nabla \cdot \mathbf{q} - \rho \nabla \cdot \mathbf{G}. \end{aligned} \quad (11.60)$$

Using (11.56), (11.59) and (11.60) from (11.58) we get

$$\begin{aligned} \nabla^2 I_1(\underline{\mathbf{P}}) + \frac{1+\nu}{1-\nu} \rho \nabla \cdot \mathbf{F} &= 0, \\ \nabla^2 I_1(\underline{\boldsymbol{\mu}}) + \frac{1+\varepsilon}{1-\varepsilon} (-2\nabla \cdot \mathbf{q} + \rho \nabla \cdot \mathbf{G}) &= 0. \end{aligned} \quad (11.61)$$

Considering (11.57) and (11.61), from (11.52) by simple transformations the desired equations can be represented in the form Nikabadze (2010, 2012)

$$\underline{\underline{\mathbf{M}}} \otimes \underline{\mathbf{P}}^S + \nabla(\nabla \times \mathbf{q}) + [\nabla(\nabla \times \mathbf{q})]^T + \rho \left(\frac{\nu}{1-\nu} \nabla \cdot \mathbf{F} \underline{\mathbf{E}} + \nabla \mathbf{F} + \nabla \mathbf{F}^T \right) = \underline{\mathbf{0}}, \quad (11.62)$$

$$\begin{aligned} \underline{\underline{\mathbf{N}}} \otimes \underline{\boldsymbol{\mu}}^S + \nabla(\nabla \times \boldsymbol{\tau}) + [\nabla(\nabla \times \boldsymbol{\tau})]^T - 2 \left(\frac{\varepsilon}{1-\varepsilon} \nabla \cdot \mathbf{q} + \nabla \mathbf{q} + \nabla \mathbf{q}^T \right) \\ + \rho \left(\frac{\varepsilon}{1-\varepsilon} \nabla \cdot \mathbf{G} \underline{\mathbf{E}} + \nabla \mathbf{G} + \nabla \mathbf{G}^T \right) = \underline{\mathbf{0}}, \end{aligned} \quad (11.63)$$

$$\nabla \nabla \cdot \mathbf{q} - 2\varepsilon' \mathbf{q} + \varepsilon'(\rho \mathbf{G} + \mathbf{C}) = \mathbf{0}, \quad \beta' \nabla \cdot \boldsymbol{\tau} = \text{const}, \quad \text{div} \mathbf{C} = 0, \quad (11.64)$$

where we have introduced the notations $\varepsilon' = \alpha(1 - 2\varepsilon)/[\delta(1 - \varepsilon)]$ and

$$\underline{\underline{\mathbf{M}}}^T \neq \underline{\underline{\mathbf{M}}} = \underline{\underline{\mathbf{E}}}\Delta + \frac{1}{1+\nu}(\underline{\underline{\mathbf{E}}}\nabla\nabla)^T, \quad \underline{\underline{\mathbf{N}}}^T \neq \underline{\underline{\mathbf{N}}} = \underline{\underline{\mathbf{E}}}\Delta + \frac{1}{1+\varepsilon}(\underline{\underline{\mathbf{E}}}\nabla\nabla)^T$$

for differential tensor-operators of equations with respect to tensors of stresses and couple stresses. It is seen that they are nonsymmetric differential tensor operators of the fourth rank and the second order.

It is easy to find the general solutions of the (11.64) equations with respect to \mathbf{q} and $\boldsymbol{\tau}$. Further, assuming that \mathbf{q} and $\boldsymbol{\tau}$ are known, we will present the general expressions for the skew-symmetric parts of the tensors of stresses and couple stresses using formulas $\underline{\underline{\mathbf{P}}}^A = -\underline{\underline{\mathbf{C}}}\cdot\mathbf{q}$, $\underline{\underline{\boldsymbol{\mu}}}^A = -\underline{\underline{\mathbf{C}}}\cdot\boldsymbol{\tau}$. After finding \mathbf{q} and $\boldsymbol{\tau}$, it is obvious that the first relation (11.57) and the equation (11.62), as well as the second relation (11.57) and the equation (11.63) make up decomposed systems of equations for finding symmetric parts $\underline{\underline{\mathbf{P}}}^S$ and $\underline{\underline{\boldsymbol{\mu}}}^S$ of tensors $\underline{\underline{\mathbf{P}}}$ and $\underline{\underline{\boldsymbol{\mu}}}$, respectively.

Applying the divergence operator to (11.62) and (11.63) and taking into account (11.61), after simple transformations we get

$$\begin{aligned} \nabla^2(\nabla\cdot\underline{\underline{\mathbf{P}}}^S + \nabla\times\mathbf{q} + \rho\mathbf{F}) &= 0, \\ \nabla^2(\nabla\cdot\underline{\underline{\boldsymbol{\mu}}}^S + \nabla\times\boldsymbol{\tau} - 2\mathbf{q} + \rho\mathbf{G}) &= 0. \end{aligned} \quad (11.65)$$

Based on (11.65) we conclude that the functions $\nabla\cdot\underline{\underline{\mathbf{P}}}^S + \nabla\times\mathbf{q} + \rho\mathbf{F}$ and $\nabla\cdot\underline{\underline{\boldsymbol{\mu}}}^S + \nabla\times\boldsymbol{\tau} - 2\mathbf{q} + \rho\mathbf{G}$ are harmonic functions in the body domain V . Therefore, if these functions on the boundary S of the domain V take zero values, then due to the properties of harmonic functions they will take zero values at all points inside the domain V . Hence, we can formulate the following theorem:

Theorem 11.2. *If the equilibrium equations (11.57) are satisfied only on the boundary S , i.e. if the relations*

$$\left.(\nabla\cdot\underline{\underline{\mathbf{P}}}^S + \nabla\times\mathbf{q} + \rho\mathbf{F})\right|_S = 0, \quad \left.(\nabla\cdot\underline{\underline{\boldsymbol{\mu}}}^S + \nabla\times\boldsymbol{\tau} - 2\mathbf{q} + \rho\mathbf{G})\right|_S = 0, \quad (11.66)$$

are true, then from (11.62) and (11.63) it follows that they hold in the whole domain V .

It should be noted that the formulated theorem is also valid for non-stationary and isothermal processes, on which we will not dwell here in order to shorten the writing.

This theorem allows us to give a new statement of the boundary value problem with respect to the tensors of stresses and couple stresses.

It is easy to see that the equations (11.62)–(11.63) can be written by using symmetric tensor operators and the equations (11.62)–(11.64) can be represented in the form

$$\begin{aligned}
\mathbb{M}^2 \otimes \mathbb{P}^S + \nabla(\nabla \times \mathbf{q}) + [\nabla(\nabla \times \mathbf{q})]^T + \rho \left(\frac{1+\nu^2}{1-\nu^2} \mathbb{E} \nabla \cdot \mathbf{F} + \nabla \mathbf{F} + \nabla \mathbf{F}^T \right) &= \mathbf{0} \\
\mathbb{N}^2 \otimes \mathbb{\mu}^S + \nabla(\nabla \times \boldsymbol{\tau}) + [\nabla(\nabla \times \boldsymbol{\tau})]^T - 2 \left(\frac{1+\varepsilon^2}{1-\varepsilon^2} \nabla \cdot \mathbf{q} + \nabla \mathbf{q} + \nabla \mathbf{q}^T \right) \\
+ \rho \left(\frac{1+\varepsilon^2}{1-\varepsilon^2} \mathbb{E} \nabla \cdot \mathbf{G} + \nabla \mathbf{G} + \nabla \mathbf{G}^T \right) &= \mathbf{0}, \\
\nabla \nabla \cdot \mathbf{q} - 2\varepsilon' \mathbf{q} + \varepsilon'(\rho \mathbf{G} + \mathbf{C}) = \mathbf{0}, \quad \beta' \nabla \cdot \boldsymbol{\tau} = \text{const}, \quad \text{div} \mathbf{C} = 0; & \quad (11.67) \\
\mathbb{M}^T = \mathbb{M} = \mathbb{E} \Delta + \frac{1}{1+\nu} [\mathbb{E} \nabla \nabla + (\mathbb{E} \nabla \nabla)^T], \\
\mathbb{N}^T = \mathbb{N} = \mathbb{E} \Delta + \frac{1}{1+\varepsilon} [\mathbb{E} \nabla \nabla + (\mathbb{E} \nabla \nabla)^T],
\end{aligned}$$

where $\mathbb{E} = 1/2(\mathbb{C}_{(2)} + \mathbb{C}_{(3)})$, $\varepsilon' = \alpha(1 - 2\varepsilon)/[\delta(1 - \varepsilon)]$, $\nu = \lambda/[2(\lambda + \mu)]$, $\varepsilon = \gamma/[2(\gamma + \delta)]$, $c_1 = \lambda$, $c_2 = \mu + \alpha$, $c_3 = \mu - \alpha$, $d_1 = \gamma$, $d_2 = \delta + \beta$, $d_3 = \delta - \beta$.

It should be noted that from the first relation (11.67), when $\mathbf{q} = \mathbf{0}$ ($\mathbb{P}^A = \mathbf{0}$), we obtain compatibility conditions with respect to the stress tensor of the classical theory of elasticity with a symmetric differential operator.

Next, we formulate the statements of mixed initial-boundary value and boundary value problems with respect to the vectors of displacements and rotations, a mixed boundary value problem with respect to the tensors of stresses and couple stresses, as well as a new statement of the boundary value problem with respect to the tensors of stresses and couple stresses.

11.3.2 The Mixed Boundary Value Problems and the New Statement of the Boundary Value Problem with Respect to the Tensors of Stresses and Couple Stresses in Micropolar Solid Mechanics

The static (or quasistatic) mixed boundary value problem consists in solving the equilibrium equations (11.3) and the compatibility equations (11.53) while satisfying the boundary conditions (11.1) and (11.5).

It should be noted that the statement of a mixed boundary value problem with respect to vectors of displacements and rotations is represented by the relations (11.3), (11.6), (11.7) (or (11.8) for potential operators), (11.1) and (11.5) (or (11.33), (11.1) and (11.5)); the statement of a mixed initial-boundary value problem with respect to the vectors of displacements and rotations is represented by the relations (11.4), (11.6), (11.7) (or (11.8) for potential operators), (11.1), (11.5) and (11.2) (or (11.34), (11.1), (11.5) and (11.2)).

The statement of the mixed boundary value problem with respect to the stress and couple stress tensors is represented by the relations (11.3), (11.53), (11.1) and (11.5).

The new statement of the static (or quasi-static) boundary value problem with respect to stress and moment stress tensors is represented by the compatibility equations (11.53) (the compatibility equations (11.62)–(11.64) with nonsymmetric differential tensor operators in the case of the homogeneous isotropic medium or the equations of compatibility (11.67) with symmetric differential tensor operators in the case of the homogeneous isotropic medium) and the boundary conditions

$$\begin{aligned} \mathbf{n} \cdot \underline{\mathbf{P}} \Big|_S &= \mathbf{P}_0, & \mathbf{n} \cdot \underline{\boldsymbol{\mu}} \Big|_S &= \boldsymbol{\mu}_0, \\ (\nabla \cdot \underline{\mathbf{P}}^S + \nabla \times \mathbf{q} + \rho \mathbf{F}) \Big|_S &= \mathbf{0}, & (\nabla \cdot \underline{\boldsymbol{\mu}}^S + \nabla \times \boldsymbol{\tau} - 2\mathbf{q} + \rho \mathbf{G}) \Big|_S &= \mathbf{0}. \end{aligned}$$

11.4 Castigliano's Variational Principle (Castigliano's Theorem)

Integrating the Legendre-type identity (11.46) over the volume of V and taking into account (11.29), the first equality (11.47), as well as the formula

$$\int_V (\underline{\mathbf{P}} \otimes \underline{\boldsymbol{\gamma}} + \underline{\boldsymbol{\mu}} \otimes \underline{\boldsymbol{\varkappa}}) dV = A^{(e)} + A_{\Sigma_1}^{(i)},$$

obtained from (11.18) with $\rho \dot{\mathbf{v}} = 0$, $\underline{\mathbf{J}} \cdot \boldsymbol{\omega} = 0$ and the notations (11.19) and (11.20), we will have

$$\check{I}(\underline{\boldsymbol{\gamma}}, \underline{\boldsymbol{\varkappa}}) - A^{(e)} = -\check{\pi}(\underline{\mathbf{P}}, \underline{\boldsymbol{\mu}}) + A_{\Sigma_1}^{(i)} + \text{const.} \quad (11.68)$$

Now for the problem (11.3) without taking into account inertial forces and moments, (11.6), (11.8), (11.1) and (11.5), we construct the so-called Castiglianian

$$\check{K} = -\check{\pi}(\underline{\mathbf{P}}, \underline{\boldsymbol{\mu}}) + A_{\Sigma_1}^{(i)}, \quad (11.69)$$

where, of course, the terms on the right-hand side are expressed by the first formula (11.47) and (11.20), respectively and formulate Castigliano's theorem.

Theorem 11.3. *Of all statically admissible systems, the real static system is distinguished by the fact that for it and only for it the Castiglianian (11.69) has a stationary value, i.e.*

$$D\check{K}(\underline{\mathbf{P}}, \underline{\boldsymbol{\mu}}, \delta\underline{\mathbf{P}}, \delta\underline{\boldsymbol{\mu}}) = 0, \quad (11.70)$$

or, using the definition of the differential of the operator and the formula (11.20) we will have

$$\int_V (\underline{\boldsymbol{\gamma}} \otimes \delta\underline{\mathbf{P}} + \underline{\boldsymbol{\varkappa}} \otimes \delta\underline{\boldsymbol{\mu}}) dV = \int_{\Sigma_1} \mathbf{n} \cdot (\delta\underline{\mathbf{P}} \cdot \mathbf{u}_0 + \delta\underline{\boldsymbol{\mu}} \cdot \boldsymbol{\varphi}_0) d\Sigma. \quad (11.71)$$

$\delta\underline{\mathbf{P}}$ and $\delta\underline{\boldsymbol{\mu}}$ can be understood as the difference of two statically admissible systems.

Proof of necessity. Assuming

$$\rho \dot{\mathbf{v}} = 0, \quad \underline{\mathbf{J}} \cdot \dot{\boldsymbol{\omega}} = 0, \quad \mathbf{w}|_{\Sigma_1} = \mathbf{u}_0, \quad \boldsymbol{\psi}|_{\Sigma_1} = \boldsymbol{\varphi}_0, \quad \underline{\mathbf{P}} = \delta\underline{\mathbf{P}}, \quad \underline{\boldsymbol{\mu}} = \delta\underline{\boldsymbol{\mu}}$$

and considering that $\delta \underline{\mathbf{P}}$ and $\delta \underline{\boldsymbol{\mu}}$ are the difference of two statically admissible systems, the necessity for the theorem follows from (11.11), i.e. (11.70) (or (11.71)).

Proof of sufficiency. In order to prove the sufficiency of the theorem, one should take into account that the Castiglianian has a conditional extremum, because in addition to (11.70) (or (11.71)), the equilibrium equation (11.3), the boundary conditions (11.5) must be met also. In this connection, we introduce the system of functions $\mathbf{a}^{(V)}(\mathbf{x})$, $\boldsymbol{\chi}^{(V)}(\mathbf{x})$, $x \in V$ and $\mathbf{a}^{(\Sigma)}(\mathbf{y})$, $\boldsymbol{\chi}^{(\Sigma)}(\mathbf{y})$, $y \in \Sigma_2$ (generalized Lagrange multipliers) and construct the operator

$$\begin{aligned} \check{I} \equiv \check{K} - \int_V [(\nabla \cdot \underline{\mathbf{P}} + \rho \mathbf{F}) \cdot \mathbf{a}^{(V)} + (\nabla \cdot \underline{\boldsymbol{\mu}} + \underline{\mathbf{C}} \otimes \underline{\mathbf{P}} + \rho \mathbf{G}) \cdot \boldsymbol{\chi}^{(V)}] dV \\ + \int_{\Sigma_2} [(\mathbf{n} \cdot \underline{\mathbf{P}} - \mathbf{P}_0) \cdot \mathbf{a}^{(\Sigma)} + (\mathbf{n} \cdot \underline{\boldsymbol{\mu}} - \boldsymbol{\mu}_0) \cdot \boldsymbol{\chi}^{(\Sigma)}] d\Sigma. \end{aligned} \quad (11.72)$$

It should be noted that using the Lagrange multiplier method, the variations $\delta \underline{\mathbf{P}}$ and $\delta \underline{\boldsymbol{\mu}}$ can be considered completely arbitrary, i.e. not subject to conditions

$$\nabla \cdot \delta \underline{\mathbf{P}} = \mathbf{0}, \quad \nabla \cdot \delta \underline{\boldsymbol{\mu}} + \underline{\mathbf{C}} \otimes \delta \underline{\mathbf{P}} = \mathbf{0}, \quad \mathbf{n} \cdot \delta \underline{\mathbf{P}}|_{\Sigma_2} = \mathbf{0}, \quad \mathbf{n} \cdot \delta \underline{\boldsymbol{\mu}}|_{\Sigma_2} = \mathbf{0}.$$

Using the definition of the differential of operator, the formula (11.9) and the Ostrogradsky-Gauss theorem, from (11.72) we get

$$\begin{aligned} D\check{I}(\underline{\mathbf{P}}, \underline{\boldsymbol{\mu}}, \delta \underline{\mathbf{P}}, \delta \underline{\boldsymbol{\mu}}) = \int_V \{ [\underline{\boldsymbol{\gamma}} - (\nabla \mathbf{a}^{(V)} - \underline{\mathbf{C}} \cdot \boldsymbol{\chi}^{(V)})] \otimes \delta \underline{\mathbf{P}} + (\underline{\boldsymbol{\kappa}} - \nabla \boldsymbol{\chi}^{(V)}) \otimes \delta \underline{\boldsymbol{\mu}} \} dV \\ - \int_{\Sigma_1} \mathbf{n} \cdot [\delta \underline{\mathbf{P}} \cdot (\mathbf{a}^{(V)} - \mathbf{u}_0) + \delta \underline{\boldsymbol{\mu}} \cdot (\boldsymbol{\chi}^{(V)} - \boldsymbol{\varphi}_0)] d\Sigma \\ - \int_{\Sigma_2} \mathbf{n} \cdot [\delta \underline{\mathbf{P}} \cdot (\mathbf{a}^{(V)} - \mathbf{a}^{(\Sigma)}) + \delta \underline{\boldsymbol{\mu}} \cdot (\boldsymbol{\chi}^{(V)} - \boldsymbol{\chi}^{(\Sigma)})] d\Sigma = 0. \end{aligned}$$

Hence, due to the arbitrariness of $\delta \underline{\mathbf{P}}$ and $\delta \underline{\boldsymbol{\mu}}$, we have

$$\begin{aligned} \underline{\boldsymbol{\gamma}} = \nabla \mathbf{a}^{(V)} - \underline{\mathbf{C}} \cdot \boldsymbol{\chi}^{(V)}, \quad \underline{\boldsymbol{\kappa}} = \nabla \boldsymbol{\chi}^{(V)}, \\ \mathbf{a}^{(V)}|_{\Sigma_1} = \mathbf{u}_0, \quad \boldsymbol{\chi}^{(V)}|_{\Sigma_1} = \boldsymbol{\varphi}_0, \quad \mathbf{a}^{(V)}|_{\Sigma_2} = \mathbf{a}^{(\Sigma)}, \quad \boldsymbol{\chi}^{(V)}|_{\Sigma_2} = \boldsymbol{\chi}^{(\Sigma)}. \end{aligned} \quad (11.73)$$

Thus, according to the last two relations (11.73) there exist only one system of functions (Lagrange multipliers) $\mathbf{a} = \mathbf{a}^{(V)}$, $\boldsymbol{\chi} = \boldsymbol{\chi}^{(V)}$ satisfying the kinematic relations (the first two relations (11.73)) and the kinematic boundary conditions (the third and fourth relations (11.73)). Knowing $\underline{\boldsymbol{\gamma}}$ and $\underline{\boldsymbol{\kappa}}$ and integrating the system of equations consisting of the first two relations (11.73), we obtain the expressions for $\mathbf{a}^{(V)}$ and $\boldsymbol{\chi}^{(V)}$. However, to integrate this system, it is necessary to fulfill the compatibility relations with respect to strain and bending-torsion tensors (11.50), which using the compatibility relations (11.49) and equilibrium equations (11.57) (see also (11.3)) can be written in the stresses and moment stresses (11.53). Therefore, the vectors $\mathbf{a}^{(V)}$ and $\boldsymbol{\chi}^{(V)}$ have the meaning of displacement and rotation vectors, respectively, and the third and fourth relations (11.73) define kinematic boundary conditions.

Consequently, in formulating the variational principle of Castigliano (11.70) (or (11.71)), it is required that the equilibrium equations (11.57) (see also (11.3)),

constitutive relations (11.49) and the static boundary conditions (11.5) are fulfilled, and the compatibility relations with respect to the stress and couple stress tensors (11.53) and the kinematic boundary conditions (11.1) follow from the stationary condition (11.70) (see also (11.71)).

It should be noted that, under certain conditions, the stationary point of the Lagrangian (Castiglianian) is the minimum (maximum) point. In order to prove these propositions, we derive identities similar to those given in Pobedrya (1995) for the case of the classical theory. In this connection, we prove the following theorem.

Theorem 11.4. *If the function*

$$\begin{aligned} f(\xi) &\equiv \check{I}\llbracket \mathbf{u}_1 + \xi(\mathbf{u}_2 - \mathbf{u}_1), \boldsymbol{\varphi}_1 + \xi(\boldsymbol{\varphi}_2 - \boldsymbol{\varphi}_1) \rrbracket \\ &\equiv \check{I}\llbracket \boldsymbol{\gamma}_1 + \xi(\boldsymbol{\gamma}_2 - \boldsymbol{\gamma}_1), \boldsymbol{\varkappa}_1 + \xi(\boldsymbol{\varkappa}_2 - \boldsymbol{\varkappa}_1) \rrbracket \end{aligned} \quad (11.74)$$

is twice continuously differentiable on the segment $0 \leq \xi \leq 1$, where $\check{I} = \iiint_V \check{W} dV$ is potential energy of deformation and bending-torsion, on this segment allows the representation

$$f(1) = f(0) + f'(0) + \frac{1}{2}f''(\eta), \quad 0 < \eta < 1, \quad (11.75)$$

then the identity holds

$$\begin{aligned} \check{I}\llbracket \mathbf{u}_2, \boldsymbol{\varphi}_2 \rrbracket &= \check{I}\llbracket \mathbf{u}_1, \boldsymbol{\varphi}_1 \rrbracket + \iiint_V \left\{ \mathbf{P}(\mathbf{u}_1, \boldsymbol{\varphi}_1) \otimes^2 [\boldsymbol{\gamma}(\mathbf{u}_2, \boldsymbol{\varphi}_2) - \boldsymbol{\gamma}(\mathbf{u}_1, \boldsymbol{\varphi}_1)] \right. \\ &\quad \left. + \boldsymbol{\mu}(\mathbf{u}_1, \boldsymbol{\varphi}_1) \otimes^2 [\boldsymbol{\varkappa}(\boldsymbol{\varphi}_2) - \boldsymbol{\varkappa}(\boldsymbol{\varphi}_1)] \right\} dV + \frac{1}{2} \iiint_V \left\{ \frac{\partial \mathbf{P}}{\partial \boldsymbol{\gamma}} [\mathbf{u}_1 + \eta(\mathbf{u}_2 - \mathbf{u}_1), \right. \\ &\quad \boldsymbol{\varphi}_1 + \eta(\boldsymbol{\varphi}_2 - \boldsymbol{\varphi}_1)] \otimes^4 [\boldsymbol{\gamma}(\mathbf{u}_2, \boldsymbol{\varphi}_2) - \boldsymbol{\gamma}(\mathbf{u}_1, \boldsymbol{\varphi}_1)] [\boldsymbol{\gamma}(\mathbf{u}_2, \boldsymbol{\varphi}_2) - \boldsymbol{\gamma}(\mathbf{u}_1, \boldsymbol{\varphi}_1)] \\ &\quad + \left[\frac{\partial \mathbf{P}}{\partial \boldsymbol{\varkappa}} [\mathbf{u}_1 + \eta(\mathbf{u}_2 - \mathbf{u}_1), \boldsymbol{\varphi}_1 + \eta(\boldsymbol{\varphi}_2 - \boldsymbol{\varphi}_1)] + \left(\frac{\partial \boldsymbol{\mu}}{\partial \boldsymbol{\gamma}} \right)^T [\mathbf{u}_1 + \eta(\mathbf{u}_2 - \mathbf{u}_1), \right. \\ &\quad \boldsymbol{\varphi}_1 + \eta(\boldsymbol{\varphi}_2 - \boldsymbol{\varphi}_1)] \left. \right] \otimes^4 [\boldsymbol{\gamma}(\mathbf{u}_2, \boldsymbol{\varphi}_2) - \boldsymbol{\gamma}(\mathbf{u}_1, \boldsymbol{\varphi}_1)] [\boldsymbol{\varkappa}(\boldsymbol{\varphi}_2) - \boldsymbol{\varkappa}(\boldsymbol{\varphi}_1)] \\ &\quad \left. + \frac{\partial \boldsymbol{\mu}}{\partial \boldsymbol{\varkappa}} \otimes^4 [\boldsymbol{\varkappa}(\boldsymbol{\varphi}_2) - \boldsymbol{\varkappa}(\boldsymbol{\varphi}_1)] [\boldsymbol{\varkappa}(\boldsymbol{\varphi}_2) - \boldsymbol{\varkappa}(\boldsymbol{\varphi}_1)] \right\} dV. \end{aligned} \quad (11.76)$$

Here expression $[\mathbf{u}_1 + \eta(\mathbf{u}_2 - \mathbf{u}_1), \boldsymbol{\varphi}_1 + \eta(\boldsymbol{\varphi}_2 - \boldsymbol{\varphi}_1)]$ is argument of that magnitude beside to which it is written, $(\partial \boldsymbol{\mu} / \partial \boldsymbol{\gamma})^T$ denotes the tensor transposed with $(\partial \boldsymbol{\mu} / \partial \boldsymbol{\gamma})$.

Proof. It is easy to check that, based on (11.74), we have

$$\begin{aligned}
f'(\xi) &= \int_V \{ \underline{\mathbf{P}} \otimes [\underline{\gamma}(\mathbf{u}_2, \varphi_2) - \underline{\gamma}(\mathbf{u}_1, \varphi_1)] + \underline{\boldsymbol{\mu}} \otimes [\underline{\boldsymbol{\varkappa}}(\varphi_2) - \underline{\boldsymbol{\varkappa}}(\varphi_1)] \} dV, \\
f''(\xi) &= \int_V \left\{ \frac{\partial \underline{\mathbf{P}}}{\partial \underline{\boldsymbol{\gamma}}} \otimes [\underline{\gamma}(\mathbf{u}_2, \varphi_2) - \underline{\gamma}(\mathbf{u}_1, \varphi_1)] [\underline{\gamma}(\mathbf{u}_2, \varphi_2) - \underline{\gamma}(\mathbf{u}_1, \varphi_1)] \right. \\
&\quad + \left[\frac{\partial \underline{\mathbf{P}}}{\partial \underline{\boldsymbol{\varkappa}}} + \left(\frac{\partial \underline{\boldsymbol{\mu}}}{\partial \underline{\boldsymbol{\gamma}}} \right)^T \right] \otimes [\underline{\gamma}(\mathbf{u}_2, \varphi_2) - \underline{\gamma}(\mathbf{u}_1, \varphi_1)] [\underline{\boldsymbol{\varkappa}}(\varphi_2) - \underline{\boldsymbol{\varkappa}}(\varphi_1)] \\
&\quad \left. + \frac{\partial \underline{\boldsymbol{\mu}}}{\partial \underline{\boldsymbol{\varkappa}}} \otimes [\underline{\boldsymbol{\varkappa}}(\varphi_2) - \underline{\boldsymbol{\varkappa}}(\varphi_1)] [\underline{\boldsymbol{\varkappa}}(\varphi_2) - \underline{\boldsymbol{\varkappa}}(\varphi_1)] \right\} dV.
\end{aligned} \tag{11.77}$$

Note that in the formulas (11.77) $\underline{\mathbf{P}}$, $\underline{\boldsymbol{\mu}}$, $\partial \underline{\mathbf{P}} / \partial \underline{\boldsymbol{\gamma}}$, $\partial \underline{\mathbf{P}} / \partial \underline{\boldsymbol{\varkappa}}$, $\partial \underline{\boldsymbol{\mu}} / \partial \underline{\boldsymbol{\gamma}}$ and $\partial \underline{\boldsymbol{\mu}} / \partial \underline{\boldsymbol{\varkappa}}$ have the argument $[\mathbf{u}_1 + \xi(\mathbf{u}_2 - \mathbf{u}_1), \varphi_1 + \xi(\varphi_2 - \varphi_1)]$, which is omitted in order to shorten the letter. Taking into account (11.74) and (11.77) for the indicated values of ξ in (11.75), we obtain (11.76), which proves the theorem.

Corollary. If \mathbf{u}_1 and φ_1 are the real kinematic system, and \mathbf{u}_2 and φ_2 are a kinematically admissible system, then from the proved theorem (11.76) we get the identity

$$\begin{aligned}
\check{H}(\mathbf{u}_2, \varphi_2) &= \check{H}(\mathbf{u}_1, \varphi_1) + A^{(e)}(\mathbf{u}_2 - \mathbf{u}_1, \varphi_2 - \varphi_1) \\
&\quad + \frac{1}{2} \iiint_V \left\{ \frac{\partial \underline{\mathbf{P}}}{\partial \underline{\boldsymbol{\gamma}}} [\mathbf{u}_1 + \eta(\mathbf{u}_2 - \mathbf{u}_1), \varphi_1 + \eta(\varphi_2 - \varphi_1)] \right. \\
&\quad \otimes [\underline{\gamma}(\mathbf{u}_2, \varphi_2) - \underline{\gamma}(\mathbf{u}_1, \varphi_1)] [\underline{\gamma}(\mathbf{u}_2, \varphi_2) - \underline{\gamma}(\mathbf{u}_1, \varphi_1)] \\
&\quad + \left[\frac{\partial \underline{\mathbf{P}}}{\partial \underline{\boldsymbol{\varkappa}}} [\mathbf{u}_1 + \eta(\mathbf{u}_2 - \mathbf{u}_1), \varphi_1 + \eta(\varphi_2 - \varphi_1)] + \left(\frac{\partial \underline{\boldsymbol{\mu}}}{\partial \underline{\boldsymbol{\gamma}}} \right)^T [\mathbf{u}_1 + \eta(\mathbf{u}_2 - \mathbf{u}_1), \right. \\
&\quad \left. \varphi_1 + \eta(\varphi_2 - \varphi_1)] \right] \otimes [\underline{\gamma}(\mathbf{u}_2, \varphi_2) - \underline{\gamma}(\mathbf{u}_1, \varphi_1)] [\underline{\boldsymbol{\varkappa}}(\varphi_2) - \underline{\boldsymbol{\varkappa}}(\varphi_1)] \\
&\quad \left. + \frac{\partial \underline{\boldsymbol{\mu}}}{\partial \underline{\boldsymbol{\varkappa}}} \otimes [\underline{\boldsymbol{\varkappa}}(\varphi_2) - \underline{\boldsymbol{\varkappa}}(\varphi_1)] [\underline{\boldsymbol{\varkappa}}(\varphi_2) - \underline{\boldsymbol{\varkappa}}(\varphi_1)] \right\} dV.
\end{aligned} \tag{11.78}$$

Theorem 11.5. If the constitutive relations (11.8) are such that for any two tensors of the second rank $\underline{\mathbf{h}}$ and $\underline{\mathbf{l}}$ the inequality

$$\begin{aligned}
\frac{\partial \underline{\mathbf{P}}}{\partial \underline{\boldsymbol{\gamma}}} \otimes (\underline{\mathbf{h}} \otimes \underline{\mathbf{h}}) + \left[\frac{\partial \underline{\mathbf{P}}}{\partial \underline{\boldsymbol{\varkappa}}} + \left(\frac{\partial \underline{\boldsymbol{\mu}}}{\partial \underline{\boldsymbol{\gamma}}} \right)^T \right] \otimes (\underline{\mathbf{h}} \otimes \underline{\mathbf{l}}) + \frac{\partial \underline{\boldsymbol{\mu}}}{\partial \underline{\boldsymbol{\varkappa}}} \otimes (\underline{\mathbf{l}} \otimes \underline{\mathbf{l}}) \\
\geq a \underline{\mathbf{h}} \otimes \underline{\mathbf{h}} + 2b \underline{\mathbf{h}} \otimes \underline{\mathbf{l}} + c \underline{\mathbf{l}} \otimes \underline{\mathbf{l}}, \quad a > 0, \quad ac - b^2 > 0,
\end{aligned} \tag{11.79}$$

is true, then the stationary point (see (11.40)) of the Lagrangian (11.39) is a minimum point and the generalized solution of the static problem (11.3), (11.6), (11.8), (11.1) and (11.5) is unique.

Introducing the tensor column $\underline{\underline{\mathbf{X}}}$, the tensor-block matrix $\underline{\underline{\mathbf{M}}}$ and the matrix G

$$\underline{\underline{\mathbf{X}}} = \begin{pmatrix} \underline{\mathbf{h}} \\ \underline{\mathbf{l}} \end{pmatrix} \quad (\underline{\underline{\mathbf{X}}}^T = (\underline{\mathbf{h}}, \underline{\mathbf{l}})), \quad \underline{\underline{\mathbf{M}}} = \begin{pmatrix} \frac{\partial \underline{\mathbf{P}}}{\partial \underline{\boldsymbol{\gamma}}} & \frac{\partial \underline{\mathbf{P}}}{\partial \underline{\boldsymbol{\varkappa}}} \\ \frac{\partial \underline{\boldsymbol{\mu}}}{\partial \underline{\boldsymbol{\gamma}}} & \frac{\partial \underline{\boldsymbol{\mu}}}{\partial \underline{\boldsymbol{\varkappa}}} \end{pmatrix}, \quad G = \begin{pmatrix} a & b \\ b & c \end{pmatrix} \tag{11.80}$$

the relation (11.79) can be written as

$$\underline{\mathbb{X}}^T \otimes \underline{\mathbb{M}} \otimes \underline{\mathbb{X}} = (\underline{\mathbb{X}}^T G) \otimes \underline{\mathbb{X}}. \quad (11.81)$$

It should be noted that the last two inequalities in (11.79) are necessary and sufficient conditions for the matrix G to be positive definiteness, and the first relation (11.79) or (11.81) is the necessary and sufficient condition for the positive definiteness of the tensor-block matrix $\underline{\mathbb{M}}$ (see (11.80)). In linear micropolar theory, the tensor-block matrix $\underline{\mathbb{M}}$ is usually a positive definite symmetric matrix and, therefore, has 18 positive eigenvalues and a complete system of eigentensor-columns consisting of 18 tensor-columns. The problem on the eigenvalues of a tensor and a tensor-block matrix of any even rank and some of their applications in mechanics are described in detail in Nikabadze (2016, 2017). We will not dwell on these questions.

Proof. Assuming in the identity (11.78) $\mathbf{u}_2 = \mathbf{w}$ and $\varphi_2 = \psi$ are any kinematically admissible system, and $\mathbf{u}_1 = \mathbf{u}$ and $\varphi_1 = \varphi$ are a solution to the problem (11.3), (11.6), (11.8), (11.1) and (11.5) (real kinematic system), by virtue of (11.79), the right-hand side of which under the indicated conditions is a positive definite quadratic form, we obtain

$$\begin{aligned} \check{L}(\mathbf{w}, \psi) &\equiv \check{I}(\mathbf{w}, \psi) - A^{(e)}(\mathbf{w}, \psi) \geq \check{I}(\mathbf{u}, \varphi) - A^{(e)}(\mathbf{u}, \varphi) \\ &+ \frac{1}{2} \int_V [a \underline{\gamma}(\mathbf{w} - \mathbf{u}, \psi - \varphi) \otimes \underline{\gamma}(\mathbf{w} - \mathbf{u}, \psi - \varphi) \\ &+ 2b \underline{\gamma}(\mathbf{w} - \mathbf{u}, \psi - \varphi) \otimes \underline{\varkappa}(\psi - \varphi) + c \underline{\varkappa}(\psi - \varphi) \otimes \underline{\varkappa}(\psi - \varphi)] dV \\ &\geq \check{I}(\mathbf{u}, \varphi) - A^{(e)}(\mathbf{u}, \varphi) \equiv \check{L}(\mathbf{u}, \varphi). \end{aligned} \quad (11.82)$$

It is proved by the inequality (11.82) that the stationary point of the Lagrangian is a minimum point. Now let us prove the uniqueness of the generalized solution. Suppose the opposite. Let there be two solutions \mathbf{u}_1, φ_1 and \mathbf{u}_2, φ_2 . Then from (11.25), it follows that these solutions satisfy the identity

$$\begin{aligned} \int_V \{ [\underline{\mathbf{P}}(\mathbf{u}_2, \varphi_2) - \underline{\mathbf{P}}(\mathbf{u}_1, \varphi_1)] \otimes \underline{\gamma}(\mathbf{w}, \psi) \\ + [\underline{\boldsymbol{\mu}}(\mathbf{u}_2, \varphi_2) - \underline{\boldsymbol{\mu}}(\mathbf{u}_1, \varphi_1)] \otimes \underline{\varkappa}(\mathbf{w}, \psi) \} dV = 0. \end{aligned} \quad (11.83)$$

Further, taking into account the equality

$$\begin{aligned} &\underline{\mathbf{P}}(\mathbf{u}_2, \varphi_2) - \underline{\mathbf{P}}(\mathbf{u}_1, \varphi_1) \\ &= \int_0^1 \frac{d}{d\xi} \{ \underline{\mathbf{P}}[\mathbf{u}_1 + \xi(\mathbf{u}_2 - \mathbf{u}_1), \varphi_1 + \xi(\varphi_2 - \varphi_1)] \} d\xi \\ &= \int_0^1 \left\{ \frac{\partial \underline{\mathbf{P}}}{\partial \underline{\gamma}} [\mathbf{u}_1 + \xi(\mathbf{u}_2 - \mathbf{u}_1), \varphi_1 + \xi(\varphi_2 - \varphi_1)] \otimes [\underline{\gamma}(\mathbf{u}_2, \varphi_2) - \underline{\gamma}(\mathbf{u}_1, \varphi_1)] \right. \\ &\quad \left. + \frac{\partial \underline{\mathbf{P}}}{\partial \underline{\varkappa}} [\mathbf{u}_1 + \xi(\mathbf{u}_2 - \mathbf{u}_1), \varphi_1 + \xi(\varphi_2 - \varphi_1)] \otimes [\underline{\varkappa}(\varphi_2) - \underline{\varkappa}(\varphi_1)] \right\} d\xi \end{aligned} \quad (11.84)$$

and the equality obtained from (11.84), if $\underline{\mathbf{P}}$ is replaced by $\underline{\boldsymbol{\mu}}$, and also, assuming that $\mathbf{w} = \mathbf{u}_2 - \mathbf{u}_1$, $\boldsymbol{\psi} = \boldsymbol{\varphi}_2 - \boldsymbol{\varphi}_1$, from (11.79) by virtue of (11.79) we shall have

$$\int_V [a|\underline{\boldsymbol{\gamma}}(\mathbf{u}_2 - \mathbf{u}_1, \boldsymbol{\varphi}_2 - \boldsymbol{\varphi}_1)|^2 + 2b\underline{\boldsymbol{\gamma}}(\mathbf{u}_2 - \mathbf{u}_1, \boldsymbol{\varphi}_2 - \boldsymbol{\varphi}_1) \otimes \underline{\boldsymbol{\kappa}}(\boldsymbol{\varphi}_2 - \boldsymbol{\varphi}_1) + c|\underline{\boldsymbol{\kappa}}(\boldsymbol{\varphi}_2 - \boldsymbol{\varphi}_1)|^2] dV \leq 0. \quad (11.85)$$

Based on (11.85), we conclude that

$$\underline{\boldsymbol{\gamma}}(\mathbf{u}_2, \boldsymbol{\varphi}_2) = \underline{\boldsymbol{\gamma}}(\mathbf{u}_1, \boldsymbol{\varphi}_1), \quad \underline{\boldsymbol{\kappa}}(\boldsymbol{\varphi}_2) = \underline{\boldsymbol{\kappa}}(\boldsymbol{\varphi}_1).$$

Hence, obviously, we obtain

$$\mathbf{u}_2 = \mathbf{u}_1 + \mathbf{u}_0 + (\mathbf{x} - \mathbf{x}_0) \cdot \underline{\mathbf{C}} \cdot \boldsymbol{\varphi}_0, \quad \boldsymbol{\varphi}_2 = \boldsymbol{\varphi}_1 + \boldsymbol{\varphi}_0, \quad (11.86)$$

where \mathbf{u}_0 and $\boldsymbol{\varphi}_0$ are two arbitrary constant vectors.

Finally, considering the kinematic boundary conditions (11.1), from (11.86) we get $\mathbf{u}_2 = \mathbf{u}_1$ and $\boldsymbol{\varphi}_2 = \boldsymbol{\varphi}_1$, i.e. the uniqueness of the generalized solution of the problem (11.3), (11.6), (11.8), (11.1) and (11.5) is proved.

It should be noted that if we have only static boundary conditions, then the solution of the problem of the micropolar solid mechanics is unique up to rigid motion

$$\mathbf{u} = \mathbf{u}_0 + (\mathbf{r} - \mathbf{r}_0) \cdot \underline{\mathbf{C}} \cdot \boldsymbol{\varphi}_0, \quad \boldsymbol{\varphi} = \boldsymbol{\varphi}_0, \quad \mathbf{u}_0 = \text{const}, \quad \boldsymbol{\varphi}_0 = \text{const}.$$

If we fix some point \mathbf{x}_0 , i.e. assume that $\mathbf{u} = 0$ and $\boldsymbol{\varphi} = 0$ for $\mathbf{x} = \mathbf{x}_0$, then rigid motion can be excluded. Note also that under static boundary conditions, we can speak about the solvability of the problem of micropolar mechanics of a rigid body only in the case when "the system is self-balanced", i.e. for the whole body, the laws of change of the momentum and the angular momentum are fulfilled, which, obviously, for the case of equilibrium can be written in the form

$$\int_V \rho \mathbf{F} dV + \int_{\Sigma} \mathbf{P}_0 d\Sigma = 0, \quad \int_V \rho (\mathbf{r} \times \mathbf{F} + \mathbf{G}) dV + \int_{\Sigma} (\mathbf{r}' \times \mathbf{P}_0 + \boldsymbol{\mu}_0) d\Sigma = 0.$$

In addition, the uniqueness of the solution of the problem implies that the Lagrangian's minimum point is unique.

It is easy to prove that, similarly to (11.76) and (11.78), the following theorem and corollary are true:

Theorem 11.6. *If the function*

$$f(\xi) = \tilde{\pi}[\underline{\mathbf{P}}_1 + \xi(\underline{\mathbf{P}}_2 - \underline{\mathbf{P}}_1), \underline{\boldsymbol{\mu}}_1 + \xi(\underline{\boldsymbol{\mu}}_2 - \underline{\boldsymbol{\mu}}_1)],$$

is twice continuously differentiable on the segment $0 \leq \xi \leq 1$, where $\tilde{\pi}$ is the potential energy of stress and couple stress tensors (11.47), which on this segment admits the representation (11.75), then the identity holds

$$\begin{aligned}
\tilde{\pi}(\underline{\mathbf{P}}_2, \underline{\boldsymbol{\mu}}_2) &= \tilde{\pi}(\underline{\mathbf{P}}_1, \underline{\boldsymbol{\mu}}_1) \\
&+ \iiint_V [\underline{\boldsymbol{\gamma}}(\underline{\mathbf{P}}_1, \underline{\boldsymbol{\mu}}_1) \otimes^2 (\underline{\mathbf{P}}_2 - \underline{\mathbf{P}}_1) + \underline{\boldsymbol{\varkappa}}(\underline{\mathbf{P}}_1, \underline{\boldsymbol{\mu}}_1) \otimes^2 (\underline{\boldsymbol{\mu}}_2 - \underline{\boldsymbol{\mu}}_1)] dV \\
&+ \frac{1}{2} \iiint_V \left\{ \frac{\partial \boldsymbol{\gamma}}{\partial \underline{\mathbf{P}}} [\underline{\mathbf{P}}_1 + \eta(\underline{\mathbf{P}}_2 - \underline{\mathbf{P}}_1), \underline{\boldsymbol{\mu}}_1 + \eta(\underline{\boldsymbol{\mu}}_2 - \underline{\boldsymbol{\mu}}_1)] \otimes^4 (\underline{\mathbf{P}}_2 - \underline{\mathbf{P}}_1) (\underline{\mathbf{P}}_2 - \underline{\mathbf{P}}_1) \right. \\
&+ \left[\frac{\partial \boldsymbol{\gamma}}{\partial \underline{\boldsymbol{\mu}}} [\underline{\mathbf{P}}_1 + \eta(\underline{\mathbf{P}}_2 - \underline{\mathbf{P}}_1), \underline{\boldsymbol{\mu}}_1 + \eta(\underline{\boldsymbol{\mu}}_2 - \underline{\boldsymbol{\mu}}_1)] \right. \\
&+ \left. \left. \left(\frac{\partial \boldsymbol{\varkappa}}{\partial \underline{\mathbf{P}}} \right)^T [\underline{\mathbf{P}}_1 + \eta(\underline{\mathbf{P}}_2 - \underline{\mathbf{P}}_1), \underline{\boldsymbol{\mu}}_1 + \eta(\underline{\boldsymbol{\mu}}_2 - \underline{\boldsymbol{\mu}}_1)] \right] \otimes^4 (\underline{\mathbf{P}}_2 - \underline{\mathbf{P}}_1) (\underline{\boldsymbol{\mu}}_2 - \underline{\boldsymbol{\mu}}_1) \right. \\
&+ \left. \left. \frac{\partial \boldsymbol{\varkappa}}{\partial \underline{\boldsymbol{\mu}}} [\underline{\mathbf{P}}_1 + \eta(\underline{\mathbf{P}}_2 - \underline{\mathbf{P}}_1), \underline{\boldsymbol{\mu}}_1 + \eta(\underline{\boldsymbol{\mu}}_2 - \underline{\boldsymbol{\mu}}_1)] \otimes^4 (\underline{\boldsymbol{\mu}}_2 - \underline{\boldsymbol{\mu}}_1) (\underline{\boldsymbol{\mu}}_2 - \underline{\boldsymbol{\mu}}_1) \right\} dV.
\end{aligned} \tag{11.87}$$

Corollary. If $\underline{\mathbf{P}}_1$ and $\underline{\boldsymbol{\mu}}_1$ are the real static system, and $\underline{\mathbf{P}}_2$ and $\underline{\boldsymbol{\mu}}_2$ are a statically admissible system, then from (11.87) we obtain the identity

$$\begin{aligned}
\tilde{\pi}(\underline{\mathbf{P}}_2, \underline{\boldsymbol{\mu}}_2) &= \tilde{\pi}(\underline{\mathbf{P}}_1, \underline{\boldsymbol{\mu}}_1) + A_{\Sigma_1}^i(\underline{\mathbf{P}}_2 - \underline{\mathbf{P}}_1, \underline{\boldsymbol{\mu}}_2 - \underline{\boldsymbol{\mu}}_1) \\
&+ \frac{1}{2} \iiint_V \left\{ \frac{\partial \boldsymbol{\gamma}}{\partial \underline{\mathbf{P}}} [\underline{\mathbf{P}}_1 + \eta(\underline{\mathbf{P}}_2 - \underline{\mathbf{P}}_1), \underline{\boldsymbol{\mu}}_1 + \eta(\underline{\boldsymbol{\mu}}_2 - \underline{\boldsymbol{\mu}}_1)] \otimes^4 (\underline{\mathbf{P}}_2 - \underline{\mathbf{P}}_1) (\underline{\mathbf{P}}_2 - \underline{\mathbf{P}}_1) \right. \\
&+ \left[\frac{\partial \boldsymbol{\gamma}}{\partial \underline{\boldsymbol{\mu}}} [\underline{\mathbf{P}}_1 + \eta(\underline{\mathbf{P}}_2 - \underline{\mathbf{P}}_1), \underline{\boldsymbol{\mu}}_1 + \eta(\underline{\boldsymbol{\mu}}_2 - \underline{\boldsymbol{\mu}}_1)] \right. \\
&+ \left. \left. \left(\frac{\partial \boldsymbol{\varkappa}}{\partial \underline{\mathbf{P}}} \right)^T [\underline{\mathbf{P}}_1 + \eta(\underline{\mathbf{P}}_2 - \underline{\mathbf{P}}_1), \underline{\boldsymbol{\mu}}_1 + \eta(\underline{\boldsymbol{\mu}}_2 - \underline{\boldsymbol{\mu}}_1)] \right] \otimes^4 (\underline{\mathbf{P}}_2 - \underline{\mathbf{P}}_1) (\underline{\boldsymbol{\mu}}_2 - \underline{\boldsymbol{\mu}}_1) \right. \\
&+ \left. \left. \frac{\partial \boldsymbol{\varkappa}}{\partial \underline{\boldsymbol{\mu}}} [\underline{\mathbf{P}}_1 + \eta(\underline{\mathbf{P}}_2 - \underline{\mathbf{P}}_1), \underline{\boldsymbol{\mu}}_1 + \eta(\underline{\boldsymbol{\mu}}_2 - \underline{\boldsymbol{\mu}}_1)] \otimes^4 (\underline{\boldsymbol{\mu}}_2 - \underline{\boldsymbol{\mu}}_1) (\underline{\boldsymbol{\mu}}_2 - \underline{\boldsymbol{\mu}}_1) \right\} dV.
\end{aligned} \tag{11.88}$$

The theorem (11.87) and the corollary (11.88) are proved exactly the same way as (11.76) and (11.78).

Theorem 11.7. If the constitutive relations (11.49) are such that for any two tensors of the second rank $\underline{\mathbf{h}}$ and $\underline{\mathbf{l}}$ the inequality

$$\begin{aligned}
\frac{\partial \boldsymbol{\gamma}}{\partial \underline{\mathbf{P}}} \otimes^4 (\underline{\mathbf{h}} \otimes \underline{\mathbf{h}}) &+ \left[\frac{\partial \boldsymbol{\gamma}}{\partial \underline{\boldsymbol{\mu}}} + \left(\frac{\partial \boldsymbol{\varkappa}}{\partial \underline{\mathbf{P}}} \right)^T \right] \otimes^4 (\underline{\mathbf{h}} \otimes \underline{\mathbf{l}}) + \frac{\partial \boldsymbol{\varkappa}}{\partial \underline{\boldsymbol{\mu}}} \otimes^4 (\underline{\mathbf{l}} \otimes \underline{\mathbf{l}}) \\
&\geq k \underline{\mathbf{h}} \otimes^2 \underline{\mathbf{h}} + 2m \underline{\mathbf{h}} \otimes^2 \underline{\mathbf{l}} + n \underline{\mathbf{l}} \otimes^2 \underline{\mathbf{l}}, \quad k > 0, \quad kn - m^2 > 0
\end{aligned} \tag{11.89}$$

is true, then the stationary point (see (11.70)) of the Castiglianian (11.69) is a maximum point.

Proof. Assuming in the identity (11.88) $\underline{\mathbf{P}}_2 = \underline{\mathbf{Q}}$ and $\underline{\boldsymbol{\mu}}_2 = \underline{\boldsymbol{\tau}}$ are any statically admissible system, and $\underline{\mathbf{P}}_1 = \underline{\mathbf{P}}$ and $\underline{\boldsymbol{\mu}}_1 = \underline{\boldsymbol{\mu}}$ are real statical system, by virtue of (11.89), the right-hand side of which under the indicated conditions is a positive definite quadratic form, we obtain

$$\begin{aligned}
\check{K}(\underline{\mathbf{Q}}, \underline{\boldsymbol{\tau}}) &\equiv -\check{\pi}(\underline{\mathbf{Q}}, \underline{\boldsymbol{\tau}}) + A_{\Sigma_1}^{(i)}(\underline{\mathbf{Q}}, \underline{\boldsymbol{\tau}}) \leq -\check{\pi}(\underline{\mathbf{P}}, \underline{\boldsymbol{\mu}}) + A_{\Sigma_1}^{(i)}(\underline{\mathbf{P}}, \underline{\boldsymbol{\mu}}) \\
&\quad - \frac{1}{2} \int_V (k \|\underline{\mathbf{Q}}\|^2 + 2m \underline{\mathbf{Q}} \otimes \underline{\boldsymbol{\tau}} + n \|\underline{\boldsymbol{\tau}}\|^2) dV \\
&\leq -\check{\pi}(\underline{\mathbf{P}}, \underline{\boldsymbol{\mu}}) + A_{\Sigma_1}^{(i)}(\underline{\mathbf{P}}, \underline{\boldsymbol{\mu}}) \equiv \check{K}(\underline{\mathbf{P}}, \underline{\boldsymbol{\mu}}),
\end{aligned} \tag{11.90}$$

what was required to prove.

It should be noted that (11.89) similarly to (11.81), can be written using the tensor-block matrix and represented in the canonical form. However, in order to shorten the letter, we will not dwell on this.

Theorem 11.8. *In the equilibrium position, characterized by the displacement \mathbf{u}^* and rotation $\boldsymbol{\varphi}^*$ vectors and stress $\underline{\mathbf{P}}^*$ and couple stress $\underline{\boldsymbol{\mu}}^*$ tensors, Lagrangian coincides with Castiglianian*

$$\check{L}(\mathbf{u}^*, \boldsymbol{\varphi}^*) = \check{K}(\underline{\mathbf{P}}^*, \underline{\boldsymbol{\mu}}^*), \tag{11.91}$$

and for arbitrary \mathbf{u} , $\boldsymbol{\varphi}$, $\underline{\mathbf{P}}$ and $\underline{\boldsymbol{\mu}}$ the inequalities

$$\check{K}(\underline{\mathbf{P}}, \underline{\boldsymbol{\mu}}) \leq \check{K}(\underline{\mathbf{P}}^*, \underline{\boldsymbol{\mu}}^*) = \check{L}(\mathbf{u}^*, \boldsymbol{\varphi}^*) \leq \check{L}(\mathbf{u}, \boldsymbol{\varphi}) \tag{11.92}$$

are true.

Proof. The equality (11.91) follows from (11.68), writing it for the equilibrium position, and from (11.91) and the previous theorems we shall obtain the inequalities (11.92).

The inequalities (11.92) are the powerful source for obtaining so-called two-sided estimates.

11.5 Generalized Reissner-Type Variational Principle

Similarly to the three-dimensional classical theory Pobedrya (1986, 1995) we consider the operator

$$\begin{aligned}
\check{R}(\mathbf{u}, \boldsymbol{\varphi}, \boldsymbol{\gamma}, \boldsymbol{\varkappa}, \underline{\mathbf{P}}, \underline{\boldsymbol{\mu}}) &= \iiint_V [\check{W}(\boldsymbol{\gamma}, \boldsymbol{\varkappa}) - \underline{\mathbf{P}} \otimes (\boldsymbol{\gamma} - \nabla \mathbf{u} + \underline{\mathbf{C}} \cdot \boldsymbol{\varphi}) \\
&\quad - \underline{\boldsymbol{\mu}} \otimes (\boldsymbol{\varkappa} - \nabla \boldsymbol{\varphi}) - \rho \mathbf{F} \cdot \mathbf{u} - \rho \mathbf{G} \cdot \boldsymbol{\varphi}] dV - \iint_{\Sigma_1} [\mathbf{n} \cdot \underline{\mathbf{P}} \cdot (\mathbf{u} - \mathbf{u}_0) \\
&\quad + \mathbf{n} \cdot \underline{\boldsymbol{\mu}} \cdot (\boldsymbol{\varphi} - \boldsymbol{\varphi}_0)] d\Sigma - \iint_{\Sigma_2} (\mathbf{P}_0 \cdot \mathbf{u} + \boldsymbol{\mu}_0 \cdot \boldsymbol{\varphi}) d\Sigma.
\end{aligned} \tag{11.93}$$

Then the generalized Reissner-type variational principle can be formulated as follows:

Of all the kinematic, static systems and systems described by the tensors $\boldsymbol{\gamma}$ and $\boldsymbol{\varkappa}$, the real system (the system of real kinematic and static systems) is distinguished by the fact that for it the operator (11.93) has a stationary value, i.e.

$$D\check{R}(\mathbf{u}, \varphi, \underline{\gamma}, \underline{\boldsymbol{\varkappa}}, \underline{\mathbf{P}}, \underline{\boldsymbol{\mu}}, \delta\mathbf{u}, \delta\varphi, \delta\underline{\boldsymbol{\gamma}}, \delta\underline{\boldsymbol{\varkappa}}, \delta\underline{\mathbf{P}}, \delta\underline{\boldsymbol{\mu}}) = 0. \quad (11.94)$$

Indeed, using the definition of the differential of the operator Pobedrya (1986, 1995) and the Ostrogradsky-Gauss theorem, by virtue of (11.6) we have

$$\begin{aligned} D\check{R} = & \iiint_V \left[\left(\frac{\partial \check{W}}{\partial \underline{\boldsymbol{\gamma}}} - \underline{\mathbf{P}} \right) \otimes \delta \underline{\boldsymbol{\gamma}} + \left(\frac{\partial \check{W}}{\partial \underline{\boldsymbol{\varkappa}}} - \underline{\boldsymbol{\mu}} \right) \otimes \delta \underline{\boldsymbol{\varkappa}} - (\underline{\boldsymbol{\gamma}} - \nabla \mathbf{u} + \underline{\mathbf{C}} \cdot \varphi) \otimes \delta \underline{\mathbf{P}} \right. \\ & - (\underline{\boldsymbol{\varkappa}} - \nabla \varphi) \otimes \delta \underline{\boldsymbol{\mu}} - (\nabla \cdot \underline{\mathbf{P}} + \rho \mathbf{F}) \cdot \delta \mathbf{u} - (\nabla \cdot \underline{\boldsymbol{\mu}} + \underline{\mathbf{C}} \otimes \underline{\mathbf{P}} + \rho \mathbf{G}) \cdot \delta \varphi \Big] dV \\ & - \iint_{\Sigma_1} \mathbf{n} \cdot [\delta \underline{\mathbf{P}} \cdot (\mathbf{u} - \mathbf{u}_0) + \delta \underline{\boldsymbol{\mu}} \cdot (\varphi - \varphi_0)] d\Sigma \\ & - \iint_{\Sigma_2} (\mathbf{n} \cdot \underline{\mathbf{P}} - \mathbf{P}_0) \cdot \delta \mathbf{u} + (\mathbf{n} \cdot \underline{\boldsymbol{\mu}} - \boldsymbol{\mu}_0) \cdot \delta \varphi d\Sigma = 0. \end{aligned} \quad (11.95)$$

From here, taken into account $\delta\mathbf{u}$, $\delta\varphi$, $\delta\underline{\boldsymbol{\gamma}}$, $\delta\underline{\boldsymbol{\varkappa}}$, $\delta\underline{\mathbf{P}}$, $\delta\underline{\boldsymbol{\mu}}$, we obtain equilibrium equations (11.3), kinematic relations (11.6), constitutive relations (11.8) and kinematic (11.1) and static (11.5) boundary conditions.

Using the Legendre-type identity (11.46), it is easy to show that, that (11.93) can be represented in the form

$$\begin{aligned} \check{R}(\mathbf{u}, \varphi, \underline{\mathbf{P}}, \underline{\boldsymbol{\mu}}) = & \iiint_V [\underline{\mathbf{P}} \otimes (\nabla \mathbf{u} - \underline{\mathbf{C}} \cdot \varphi) + \underline{\boldsymbol{\mu}} \otimes \nabla \varphi - \check{w}(\underline{\mathbf{P}}, \underline{\boldsymbol{\mu}}) \\ & - \rho \mathbf{F} \cdot \mathbf{u} - \rho \mathbf{G} \cdot \varphi] dV - \iint_{\Sigma_1} [\mathbf{n} \cdot \underline{\mathbf{P}} \cdot (\mathbf{u} - \mathbf{u}_0) + \mathbf{n} \cdot \underline{\boldsymbol{\mu}} \cdot (\varphi - \varphi_0)] d\Sigma \\ & - \iint_{\Sigma_2} (\mathbf{P}_0 \cdot \mathbf{u} + \boldsymbol{\mu}_0 \cdot \varphi) d\Sigma. \end{aligned} \quad (11.96)$$

In what follows operators (11.93) and (11.96) will be called generalized Reissner operators for a micropolar medium.

Based on the Reissner operator (11.96), the generalized Reissner-type variational principle can be formulated as follows: Of all kinematic and static systems, the real one is distinguished by the fact that for it the operator (11.96) has a stationary value, i.e.

$$D\check{R}(\mathbf{u}, \varphi, \underline{\mathbf{P}}, \underline{\boldsymbol{\mu}}, \delta\mathbf{u}, \delta\varphi, \delta\underline{\mathbf{P}}, \delta\underline{\boldsymbol{\mu}}) = 0.$$

Indeed, using the definition of the differential of the operator Pobedrya (1986, 1995) and the Ostrogradsky-Gauss theorem, from (11.96) similarly to (11.95) we obtain

$$\begin{aligned} D\check{R} = & \iiint_V \left[\left(\underline{\boldsymbol{\gamma}} - \frac{\partial \check{w}}{\partial \underline{\mathbf{P}}} \right) \otimes \delta \underline{\mathbf{P}} + \left(\underline{\boldsymbol{\varkappa}} - \frac{\partial \check{w}}{\partial \underline{\boldsymbol{\mu}}} \right) \otimes \delta \underline{\boldsymbol{\mu}} - (\nabla \cdot \underline{\mathbf{P}} + \rho \mathbf{F}) \cdot \delta \mathbf{u} \right. \\ & - (\nabla \cdot \underline{\boldsymbol{\mu}} + \underline{\mathbf{C}} \otimes \underline{\mathbf{P}} + \rho \mathbf{G}) \cdot \delta \varphi \Big] dV - \iint_{\Sigma_1} \mathbf{n} \cdot [\delta \underline{\mathbf{P}} \cdot (\mathbf{u} - \mathbf{u}_0) \\ & + \delta \underline{\boldsymbol{\mu}} \cdot (\varphi - \varphi_0)] d\Sigma - \iint_{\Sigma_2} (\mathbf{n} \cdot \underline{\mathbf{P}} - \mathbf{P}_0) \cdot \delta \mathbf{u} + (\mathbf{n} \cdot \underline{\boldsymbol{\mu}} - \boldsymbol{\mu}_0) \cdot \delta \varphi d\Sigma = 0. \end{aligned} \quad (11.97)$$

It can be seen that, taking into account the arbitrariness $\delta \mathbf{u}$, $\delta \boldsymbol{\varphi}$, $\delta \underline{\mathbf{P}}$ è $\delta \underline{\boldsymbol{\mu}}$, from (11.97), we obtain the equilibrium equations (11.3), inverse constitutive relations (11.49), kinematic (11.1) and static (11.5) boundary conditions.

It should be noted that, using the D'Alembert principle and replacing $\rho \mathbf{F}$ and $\rho \mathbf{m}$ with $\rho \mathbf{F} - \rho \partial_t^2 \mathbf{u}$ and $\rho \mathbf{m} - \underline{\mathbf{J}} \cdot \partial_t^2 \boldsymbol{\varphi}$, respectively, the variational principles of Lagrange, Castigliano, and Reissner-type can be formulated for the case when forces and moments of inertia are taken into account. In addition, it is easy to see that the Lagrangian is a special case of the operator (11.93), if we assume that the kinematic relations (11.6) and constitutive relations (11.8) are valid in advance, and the Castiglianian due to the transformation

$$\int_V (\underline{\mathbf{P}} \times \underline{\boldsymbol{\gamma}} + \underline{\boldsymbol{\mu}} \times \underline{\boldsymbol{\varkappa}}) dV = - \int_V [\nabla \cdot \underline{\mathbf{P}} \cdot \mathbf{u} + (\nabla \cdot \underline{\boldsymbol{\mu}} + \underline{\mathbf{C}} \times \underline{\mathbf{P}}) \cdot \boldsymbol{\varphi}] dV + \int_{\Sigma} \mathbf{n} \cdot (\underline{\mathbf{P}} \cdot \mathbf{u} + \underline{\boldsymbol{\mu}} \cdot \boldsymbol{\varphi}) d\Sigma$$

is a special case of the operator (11.96) if the equilibrium equations (11.3) and the static boundary conditions (11.5) are satisfied.

Note also that replacing in (11.11) \mathbf{w} and $\boldsymbol{\psi}$ by $\delta \mathbf{u}$ and $\delta \boldsymbol{\varphi}$, respectively, we obtain the principle of virtual work in the form

$$\begin{aligned} \int_V [\underline{\mathbf{P}} \otimes \delta \underline{\boldsymbol{\gamma}} + \underline{\boldsymbol{\mu}} \otimes \delta \underline{\boldsymbol{\varkappa}}] dV \\ = \int_V [\rho (\mathbf{F} - \partial_t^2 \mathbf{u}) \cdot \delta \mathbf{u} + (\rho \mathbf{G} - \underline{\mathbf{J}} \cdot \partial_t^2 \boldsymbol{\varphi}) \cdot \delta \boldsymbol{\varphi}] dV \\ + \int_{\Sigma} (\mathbf{P}_{(n)} \cdot \delta \mathbf{u} + \boldsymbol{\mu}_{(n)} \cdot \delta \boldsymbol{\varphi}) d\Sigma, \end{aligned} \quad (11.98)$$

where $\delta \underline{\boldsymbol{\gamma}} = \nabla \delta \mathbf{u} - \underline{\mathbf{C}} \cdot \delta \boldsymbol{\varphi}$, $\delta \underline{\boldsymbol{\varkappa}} = \nabla \delta \boldsymbol{\varphi}$, and $\delta \mathbf{u}$ and $\delta \boldsymbol{\varphi}$ are arbitrary virtual displacement and rotation vectors. Therefore, the left side (11.98) is the virtual work of stress and couple stress tensors on virtual tensors of strain and bending-torsion, respectively, and the right side is the virtual work of external forces and moments and inertial forces and moments.

From the above material, neglecting the characteristics of the micropolarity of the medium (the rotation vector, couple stresses tensor, volume and surface moments, etc.), it is easy to obtain the corresponding relations for classical mechanics of solids, but we did not dwell on these issues. If necessary, the interested reader can easily deal with this problem. In addition, it is easy to obtain appropriate relations for classical and micropolar media with specific rheology (for example, elastic, viscoelastic, etc.) and anisotropy (for example, isotropic, transversely isotropic, orthotropic, etc.). For this, it is sufficient to take into account the constitutive relations that correspond to the particular media.

11.6 The Generalized Reissner-Type Variational Principle in the Micropolar Theory of Thin Bodies with One Small Size under the New Parameterization of the Body Domain

Let us consider a three-dimensional thin domain V with one small size bounded by two front surfaces $S^{(-)}$ and $S^{(+)}$ and the ruled lateral surface Σ (see Fig 11.1).

The position vector of an arbitrary point of the domain of the thin body is represented in the form in Fig. 11.1.

$$\begin{aligned} \mathbf{r}(x', x^3) &= \mathbf{r}^{(-)}(x') + x^3 \mathbf{h}(x') = (1 - x^3) \mathbf{r}^{(-)}(x') + x^3 \mathbf{r}^{(+)}(x'), \\ x' &= (x^1, x^2), \quad \forall x^3 \in [0, 1], \end{aligned} \tag{11.99}$$

where the relations

$$\mathbf{r}^{(-)} = \mathbf{r}^{(-)}(x'), \quad \mathbf{r}^{(+)} = \mathbf{r}^{(+)}(x'), \quad x' = (x^1, x^2), \tag{11.100}$$

are the vector parametric equations of base surfaces $S^{(-)}$ and $S^{(+)}$, respectively, $x' = (x^1, x^2)$ is the arbitrary point on $S^{(-)}$, i.e. x^1 and x^2 are the curvilinear (Gaussian) coordinates² on the inner base surface $S^{(-)}$.

The vector-values

$$\mathbf{h}(x') = \mathbf{r}^{(+)}(x') - \mathbf{r}^{(-)}(x'), \quad x' = (x^1, x^2), \tag{11.101}$$

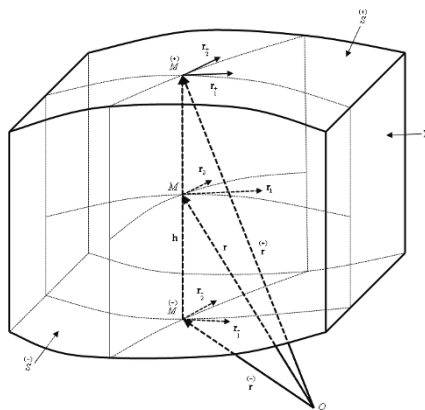


Fig. 11.1 To the new parameterization of the thin body domain

² The dependence of the quantities on x' means their dependence on the curvilinear coordinates x^1 and x^2 of the base surface. The notations and agreements adopted in previously published works (see (Nikabadze, 2001b,a; Nikabadze and Ulukhanyan, 2005; Nikabadze, 2006, 2007a,b,c, 2010, 2012, 2014, 2015, 2016; Nikabadze and Ulukhanyan, 2016; Nikabadze, 2017; Nikabadze and Ulukhanyan, 2019b,c,a, 2020a,b, 2021, and others)) are preserved.

that topologically maps the inner base surface of $\overset{(-)}{S}$ to the outer $\overset{(+)}{S}$, generally is not perpendicular to the base surfaces. The parameterization of thin domain carried out by the relation (11.99) is called the new parameterization, which can be found in detail in Nikabadze (2014, 2015, 2017).

Then the generalized Reissner-type operator (11.93) for the thin domain will be presented in the form

$$\begin{aligned}
& \check{R}(\mathbf{u}, \varphi, \underline{\gamma}, \underline{\boldsymbol{\varkappa}}, \underline{\mathbf{P}}, \underline{\boldsymbol{\mu}}, \overset{(-)}{\mathbf{u}}, \overset{(-)}{\varphi}, \overset{(-)}{\underline{\mathbf{P}}}, \overset{(-)}{\underline{\boldsymbol{\mu}}}, \overset{(+)}{\mathbf{u}}, \overset{(+)}{\varphi}, \overset{(+)}{\underline{\mathbf{P}}}, \overset{(+)}{\underline{\boldsymbol{\mu}}}) = \iiint_V [\check{W}(\underline{\gamma}, \underline{\boldsymbol{\varkappa}}) \\
& - \underline{\mathbf{P}} \otimes \overset{2}{(\underline{\gamma} - \nabla \mathbf{u} + \underline{\mathbf{C}} \cdot \varphi)} - \underline{\boldsymbol{\mu}} \otimes \overset{2}{(\underline{\boldsymbol{\varkappa}} - \nabla \varphi)} - \rho \mathbf{F} \cdot \mathbf{u} - \rho \mathbf{G} \cdot \varphi] dV \\
& - \iint_{\Sigma_1} \mathbf{m} \cdot [\underline{\mathbf{P}} \cdot (\mathbf{u} - \mathbf{u}_0) + \underline{\boldsymbol{\mu}} \cdot (\varphi - \varphi_0)] d\Sigma - \iint_{\Sigma_2} (\mathbf{P}_0 \cdot \mathbf{u} + \boldsymbol{\mu}_0 \cdot \varphi) d\Sigma \\
& - \iint_{\overset{(-)}{S_1}} \overset{(-)}{\mathbf{n}} \cdot [\overset{(-)}{\underline{\mathbf{P}}} \cdot (\overset{(-)}{\mathbf{u}} - \overset{(-)}{\mathbf{u}}_0) + \overset{(-)}{\underline{\boldsymbol{\mu}}} \cdot (\overset{(-)}{\varphi} - \overset{(-)}{\varphi}_0)] d\overset{(-)}{S} - \iint_{\overset{(-)}{S_2}} (\overset{(-)}{\mathbf{P}}_0 \cdot \overset{(-)}{\mathbf{u}} + \overset{(-)}{\boldsymbol{\mu}}_0 \cdot \overset{(-)}{\varphi}) d\overset{(-)}{S} \\
& - \iint_{\overset{(+)}{S_1}} \overset{(+)}{\mathbf{n}} \cdot [\overset{(+)}{\underline{\mathbf{P}}} \cdot (\overset{(+)}{\mathbf{u}} - \overset{(+)}{\mathbf{u}}_0) + \overset{(+)}{\underline{\boldsymbol{\mu}}} \cdot (\overset{(+)}{\varphi} - \overset{(+)}{\varphi}_0)] d\overset{(+)}{S} - \iint_{\overset{(+)}{S_2}} (\overset{(+)}{\mathbf{P}}_0 \cdot \overset{(+)}{\mathbf{u}} + \overset{(+)}{\boldsymbol{\mu}}_0 \cdot \overset{(+)}{\varphi}) d\overset{(+)}{S}; \\
& \Sigma = \Sigma_1 \cup \Sigma_2, \quad \Sigma_1 \cap \Sigma_2 = \emptyset, \quad \overset{(-)}{S} = \overset{(-)}{S_1} \cup \overset{(-)}{S_2}, \\
& \overset{(-)}{S_1} \cap \overset{(-)}{S_2} = \emptyset, \quad \overset{(+)}{S} = \overset{(+)}{S_1} \cup \overset{(+)}{S_2}, \quad \overset{(+)}{S_1} \cap \overset{(+)}{S_2} = \emptyset.
\end{aligned} \tag{11.102}$$

where \mathbf{m} is the unit outward normal vector on the lateral face Σ of the thin body.

It should be noted that the kinematic and static boundary conditions on the front surfaces are represented as

$$\begin{aligned}
& \mathbf{u}|_{\overset{(-)}{S_1}} = \overset{(-)}{\mathbf{u}}_0, \quad \varphi|_{\overset{(-)}{S_1}} = \overset{(-)}{\varphi}_0, \quad \mathbf{u}|_{\overset{(+)}{S_2}} = \overset{(+)}{\mathbf{u}}_0, \quad \varphi|_{\overset{(+)}{S_2}} = \overset{(+)}{\varphi}_0; \\
& (\mathbf{n} \cdot \underline{\mathbf{P}})|_{\overset{(-)}{S_1}} = \overset{(-)}{\mathbf{n}} \cdot \overset{(-)}{\underline{\mathbf{P}}} = \overset{(-)}{\mathbf{P}}_0, \quad (\mathbf{n} \cdot \underline{\boldsymbol{\mu}})|_{\overset{(-)}{S_1}} = \overset{(-)}{\mathbf{n}} \cdot \overset{(-)}{\underline{\boldsymbol{\mu}}} = \overset{(-)}{\boldsymbol{\mu}}_0, \\
& (\mathbf{n} \cdot \underline{\mathbf{P}})|_{\overset{(+)}{S_2}} = \overset{(+)}{\mathbf{n}} \cdot \overset{(+)}{\underline{\mathbf{P}}} = \overset{(+)}{\mathbf{P}}_0, \quad (\mathbf{n} \cdot \underline{\boldsymbol{\mu}})|_{\overset{(+)}{S_2}} = \overset{(+)}{\mathbf{n}} \cdot \overset{(+)}{\underline{\boldsymbol{\mu}}} = \overset{(+)}{\boldsymbol{\mu}}_0
\end{aligned} \tag{11.103}$$

and on the lateral face the kinematic and static boundary conditions will have the form

$$\mathbf{u}|_{\Sigma_1} = \mathbf{u}_0, \quad \varphi|_{\Sigma_1} = \varphi_0, \quad (\mathbf{m} \cdot \underline{\mathbf{P}})|_{\Sigma_2} = \mathbf{P}_0, \quad (\mathbf{m} \cdot \underline{\boldsymbol{\mu}})|_{\Sigma_2} = \boldsymbol{\mu}_0. \tag{11.104}$$

It should be noted that the following notation is used in the relations (11.103): for example, for an arbitrary value $F(x^1, x^2, x^3)$ we have

$$\begin{aligned}
& \overset{(-)}{F} = F(x^1, x^2, x^3)|_{x^3=0}, \quad \overset{(+)}{F} = F(x^1, x^2, x^3)|_{x^3=1}, \quad \text{if } 0 \leq x^3 \leq 1, \\
& \overset{(-)}{F} = F(x^1, x^2, x^3)|_{x^3=-1}, \quad \overset{(+)}{F} = F(x^1, x^2, x^3)|_{x^3=1}, \quad \text{if } -1 \leq x^3 \leq 1.
\end{aligned}$$

Using the definition of the differential of the operator Pobedrya (1986, 1995) and the Ostrogradsky-Gauss theorem, from (11.102) by virtue of kinematic relations (11.6) we obtain the desired principle in the form

$$\begin{aligned}
 D\check{R} = & \iiint_V \left[\left(\frac{\partial \check{W}}{\partial \underline{\gamma}} - \underline{\mathbf{P}} \right) \otimes \delta \underline{\gamma} + \left(\frac{\partial \check{W}}{\partial \underline{\boldsymbol{\varkappa}}} - \underline{\boldsymbol{\mu}} \right) \otimes \delta \underline{\boldsymbol{\varkappa}} - (\underline{\boldsymbol{\gamma}} - \nabla \mathbf{u} + \underline{\mathbf{C}} \cdot \underline{\boldsymbol{\varphi}}) \otimes \delta \underline{\mathbf{P}} \right. \\
 & - (\underline{\boldsymbol{\varkappa}} - \nabla \underline{\boldsymbol{\varphi}}) \otimes \delta \underline{\boldsymbol{\mu}} - (\nabla \cdot \underline{\mathbf{P}} + \rho \mathbf{F}) \cdot \delta \mathbf{u} - (\nabla \cdot \underline{\boldsymbol{\mu}} + \underline{\mathbf{C}} \otimes \underline{\mathbf{P}} + \rho \mathbf{G}) \cdot \delta \underline{\boldsymbol{\varphi}} \Big] dV \\
 & - \iint_{\Sigma_1} \mathbf{m} \cdot [\delta \underline{\mathbf{P}} \cdot (\mathbf{u} - \mathbf{u}_0) + \delta \underline{\boldsymbol{\mu}} \cdot (\underline{\boldsymbol{\varphi}} - \underline{\boldsymbol{\varphi}}_0)] d\Sigma \\
 & - \iint_{\Sigma_2} [(\mathbf{m} \cdot \underline{\mathbf{P}} - \mathbf{P}_0) \cdot \delta \mathbf{u} + (\mathbf{m} \cdot \underline{\boldsymbol{\mu}} - \boldsymbol{\mu}_0) \cdot \delta \underline{\boldsymbol{\varphi}}] d\Sigma \\
 & - \iint_{S_1^{(-)}} \underline{\mathbf{n}} \cdot [\delta \underline{\mathbf{P}} \cdot (\underline{\mathbf{u}} - \underline{\mathbf{u}}_0) + \delta \underline{\boldsymbol{\mu}} \cdot (\underline{\boldsymbol{\varphi}} - \underline{\boldsymbol{\varphi}}_0)] dS^{(-)} \\
 & - \iint_{S_2^{(-)}} [(\underline{\mathbf{n}} \cdot \underline{\mathbf{P}} - \underline{\mathbf{P}}_0) \cdot \delta \underline{\mathbf{u}} + (\underline{\mathbf{n}} \cdot \underline{\boldsymbol{\mu}} - \underline{\boldsymbol{\mu}}_0) \cdot \delta \underline{\boldsymbol{\varphi}}] dS^{(-)} \\
 & - \iint_{S_1^{(+)}} \underline{\mathbf{n}} \cdot [\delta \underline{\mathbf{P}} \cdot (\underline{\mathbf{u}} - \underline{\mathbf{u}}_0) + \delta \underline{\boldsymbol{\mu}} \cdot (\underline{\boldsymbol{\varphi}} - \underline{\boldsymbol{\varphi}}_0)] dS^{(+)} \\
 & - \iint_{S_2^{(+)}} [(\underline{\mathbf{n}} \cdot \underline{\mathbf{P}} - \underline{\mathbf{P}}_0) \cdot \delta \underline{\mathbf{u}} + (\underline{\mathbf{n}} \cdot \underline{\boldsymbol{\mu}} - \underline{\boldsymbol{\mu}}_0) \cdot \delta \underline{\boldsymbol{\varphi}}] dS^{(+)} = 0.
 \end{aligned} \tag{11.105}$$

From here, taking into account the arbitrariness of $\delta \mathbf{u}$, $\delta \underline{\boldsymbol{\varphi}}$, $\delta \underline{\boldsymbol{\gamma}}$, $\delta \underline{\boldsymbol{\varkappa}}$, $\underline{\mathbf{P}}$, $\underline{\boldsymbol{\mu}}$, $\delta \underline{\mathbf{u}}$, $\delta \underline{\boldsymbol{\varphi}}$, $\underline{\mathbf{P}}$, $\underline{\boldsymbol{\mu}}$, $\delta \underline{\mathbf{u}}$, $\delta \underline{\boldsymbol{\varphi}}$, $\underline{\mathbf{P}}$ è $\underline{\boldsymbol{\mu}}$, we obtain equilibrium equations

$$\nabla \cdot \underline{\mathbf{P}} + \rho \mathbf{F} = 0, \quad \nabla \cdot \underline{\boldsymbol{\mu}} + \underline{\mathbf{C}} \otimes \underline{\mathbf{P}} + \rho \mathbf{G} = 0,$$

kinematic and static boundary conditions (see (11.103) and (11.104)), kinematic relations (11.6), that is, a three-dimensional formulation of the problem for thin bodies with one small size. We can write down the statement of the problem taking into account the representations of the gradient and divergence under the considered parameterization. Taking into account the representations of the gradient and divergence Nikabadze (2007c, 2014); Nikabadze and Ulukhanyan (2016) in the considered parametrization (not necessarily with a new one), of course, this statement of the problem can be written at the used parametrization.

It is easy to see that at the beginning (11.105) could be written at the considered parametrization, and then the problem statement could be deduced from the obtained relation. Since the formulations of boundary value problems were given above, we will not dwell on this here.

Next, let us present the principle (11.105) under the new parametrization of the thin body domain in moments with respect to the systems of Legendre and Chebyshev polynomials.

11.7 Generalized Reissner-Type Variational Principle in the Micropolar Theory of Thin Bodies with One Small Size in Moments under the New Parameterization of a Body Domain

Before formulating the Reissner variational principle for the theory of thin bodies, let us remember some relations Nikabadze (2014) which connect the geometric characteristics included in (11.102) and (11.105). These relations have the following form:

$$dx^1 dx^2 dx^3 = \frac{dV}{\sqrt{g}} = \frac{dS dx^3}{\sqrt{g g^{33}}} = \frac{d^{(-)} S dx^3}{\sqrt{g^{(-)} g^{33}}} = \frac{d^{(+)} S dx^3}{\sqrt{g^{(+)} g^{33}}}, \tag{11.106}$$

$$\frac{d\Sigma m_I}{\sqrt{g}} = \frac{d^{(-)} \Sigma m_{-I}}{\sqrt{g^{(-)}}} = \frac{d^{(+)} \Sigma m_{+I}}{\sqrt{g^{(+)}}} = \frac{d s dx^3 m_I}{\sqrt{g g^{33}}} = \frac{d^{(-)} s dx^3 m_{-I}}{\sqrt{g^{(-)} g^{33}}} = \frac{d^{(+)} s dx^3 m_{+I}}{\sqrt{g^{(+)} g^{33}}}.$$

Now let us represent the relations (11.105) in moments with respect to the Legendre polynomial system. In this regard, we expand each factor of integrand expressions of the volume integral and integrals along the lateral face in a series of the Legendre polynomial system and transform the integrals on the right side of (11.105). It can be seen that more attention is deserved the transformation of integrals of the form

$$\iiint_V \underline{\underline{\mathbf{Q}}} \otimes \underline{\underline{\mathbf{a}}} dV, \quad \iint_{\Sigma} \mathbf{m} \cdot \underline{\underline{\mathbf{Q}}} \cdot \mathbf{b} d\Sigma, \tag{11.107}$$

and the other integrals can be easily transformed. Here $\underline{\underline{\mathbf{a}}}$ is some tensor of the second rank, and \mathbf{b} is a vector. So, we transform the first integral from (11.107). Taking into account $dV = \vartheta^{(-)} h d^{(-)} S dx^3$, coming from the first line (11.106), we get

$$\iiint_V \underline{\underline{\mathbf{Q}}} \otimes \underline{\underline{\mathbf{a}}} dV = \iint_{\Sigma} h(x') \left(\int_0^1 \vartheta^{(-)} \underline{\underline{\mathbf{Q}}} \otimes \underline{\underline{\mathbf{a}}} d^{(-)} S \right). \tag{11.108}$$

By virtue of the relations

$$\underline{\underline{\mathbf{Q}}} \otimes \vartheta^{(-)} \underline{\underline{\mathbf{a}}} = \underline{\underline{\mathbf{Q}}} \otimes \underline{\underline{\mathbf{a}}}^* = \sum_{k=0}^{\infty} \sum_{m=0}^{\infty} \underline{\underline{\mathbf{Q}}}^{(k)} \otimes \underline{\underline{\mathbf{a}}}^{(m)*} P_k(x^3) P_m(x^3), \quad \underline{\underline{\mathbf{a}}}^* = \vartheta^{(-)} \underline{\underline{\mathbf{a}}}, \quad 0 \leq x^3 \leq 1$$

and the orthogonality of the Legendre system of polynomials we have

$$\int_0^1 \underline{\underline{\mathbf{Q}}} \otimes \vartheta^{(-)} \underline{\underline{\mathbf{a}}} dx^3 = \sum_{k=0}^{\infty} \sum_{m=0}^{\infty} \underline{\underline{\mathbf{Q}}}^{(k)} \otimes \underline{\underline{\mathbf{a}}}^{(m)*} \int_0^1 P_k(x^3) P_m(x^3) dx^3$$

$$= \sum_{k=0}^{\infty} \sum_{m=0}^{\infty} \underline{\underline{\mathbf{Q}}}^{(k)} \otimes \underline{\underline{\mathbf{a}}}^{(m)*} \frac{1}{\sqrt{(2k+1)(2m+1)}} \delta_{km} = \sum_{k=0}^{\infty} \frac{1}{2k+1} \underline{\underline{\mathbf{Q}}}^{(k)} \otimes \underline{\underline{\mathbf{a}}}^{(k)*},$$

that is,

$$\int_0^1 \underline{\mathbf{Q}} \otimes \vartheta \underline{\mathbf{a}} dx^3 = \sum_{k=0}^{\infty} \frac{1}{2k+1} \underline{\mathbf{Q}}^{(k)} \otimes \underline{\mathbf{a}}^{(k)*} = \sum_{k=0}^{\infty} \frac{1}{2k+1} \underline{\mathbf{Q}}^{*(k)} \otimes \underline{\mathbf{a}}^{(k)}, \quad (11.109)$$

where $\underline{\mathbf{Q}}^{*(k)} = \vartheta^{(-)} \underline{\mathbf{Q}}^{(k)}$, $\underline{\mathbf{a}}^{(k)*} = \vartheta^{(-)} \underline{\mathbf{a}}^{(k)}$, $\hat{a} P_k(x^3)$, $0 \leq x^3 \leq 1$, is a shifted Legendre polynomial of k degree.

Considering (11.109), from (11.108) we find

$$\begin{aligned} \iint_V \underline{\mathbf{Q}} \otimes \underline{\mathbf{a}} dV &= \sum_{k=0}^{\infty} \frac{1}{2k+1} \iint_{(S)} h(x') \underline{\mathbf{Q}}^{(k)} \otimes \underline{\mathbf{a}}^{(k)*} dS \\ &= \sum_{k=0}^{\infty} \frac{1}{2k+1} \iint_{(S)} h(x') \underline{\mathbf{Q}}^{*(k)} \otimes \underline{\mathbf{a}}^{(k)} dS. \end{aligned} \quad (11.110)$$

Therefore, in (11.110) the scalar product $\underline{\mathbf{Q}} \otimes \underline{\mathbf{a}}$ can be replaced by the scalar product of tensors of any rank or by some product arbitrary tensors.

Note that the representation of the volume integral (11.110) is selected depending on the representation of the system of equations of motion (or equilibrium equations), which determines the representations of the constitutive relations and static boundary conditions under the considered parameterization of the body domain.

It is easy to see that, due to the relation in the second line of (11.106) we have the relations

$$\frac{d\Sigma \mathbf{m}}{\sqrt{g}} = \frac{d\Sigma^{(-)} \underline{\mathbf{m}}_I \mathbf{r}^I}{\sqrt{g^{(-)}}} = \frac{ds dx^3 \mathbf{m}}{\sqrt{g g^{33}}} = \frac{d^s dx^3 \underline{\mathbf{m}}_I \mathbf{r}^I}{\sqrt{g^{(-)} g^{33}}},$$

based on which the second integral (11.107) is reduced to

$$\iint_{\Sigma} \mathbf{m} \cdot \underline{\mathbf{Q}} \cdot \mathbf{b} d\Sigma = \int_{(L)} h(x') \underline{\mathbf{m}}_I^{(-)}(x') \left(\int_0^1 \vartheta \underline{\mathbf{Q}}^I \cdot \mathbf{b} dx^3 \right) d^s s. \quad (11.111)$$

Obviously, similarly to (11.109) we find

$$\begin{aligned} \int_0^1 \vartheta \underline{\mathbf{Q}}^I \cdot \mathbf{b} dx^3 &= \sum_{k=0}^{\infty} \frac{1}{2k+1} \underline{\mathbf{M}}^{(k)}(\underline{\mathbf{Q}}^I) \cdot \mathbf{b}^{(k)*} \\ &= \sum_{k=0}^{\infty} \frac{1}{2k+1} \underline{\mathbf{M}}^{(k)}(\vartheta \underline{\mathbf{Q}}^I) \cdot \mathbf{b}^{(k)}, \quad \mathbf{b}^{(k)*} = \vartheta \mathbf{b}^{(k)}. \end{aligned} \quad (11.112)$$

Considering (11.112), the integral (11.111) can be written in the form

$$\begin{aligned}
\iint_{\Sigma} \mathbf{m} \cdot \tilde{\mathbf{Q}} \cdot \mathbf{b} d\Sigma &= \sum_{k=0}^{\infty} \frac{1}{2k+1} \int_{(L)} h(x') \tilde{m}_{-I}^{(-)}(x') \tilde{\mathbf{M}}^{(k)}(\mathbf{Q}^I) \cdot \tilde{\mathbf{b}}^* d\tilde{s}^{(-)} \\
&= \sum_{k=0}^{\infty} \frac{1}{2k+1} \int_{(L)} h(x') \tilde{m}_{-I}^{(-)}(x') \tilde{\mathbf{M}}^{(k)}(\vartheta \mathbf{Q}^I) \cdot \tilde{\mathbf{b}} d\tilde{s}^{(-)}.
\end{aligned} \tag{11.113}$$

Next it is easy to see that

$$\begin{aligned}
\iint_{\Sigma} \tilde{\mathbf{P}}_0 \cdot \mathbf{u} d\Sigma &= \iint_{(\tilde{\Sigma})} (d\Sigma/d\tilde{\Sigma}) \tilde{\mathbf{P}}_0 \cdot \mathbf{u} d\tilde{\Sigma} \\
&= \int_{(L)} h(x') \left(\int_0^1 \vartheta a(x', x^3) \tilde{\mathbf{P}}_0 \cdot \mathbf{u} dx^3 \right) d\tilde{s}^{(-)},
\end{aligned} \tag{11.114}$$

where the notation $a(x', x^3) = (d\Sigma/d\tilde{\Sigma}) \vartheta^{-1}$ is introduced and, in addition, the formula $d\tilde{\Sigma} = h(x') d\tilde{s}^{(-)} dx^3$, following from the second line (11.106) is taken into account.

Due to (11.111) and (11.114) we have

$$\begin{aligned}
\iint_{\Sigma} (\mathbf{m} \cdot \tilde{\mathbf{P}} - \tilde{\mathbf{P}}_0) \cdot \mathbf{u} d\Sigma &= \int_{(L)} h(x') \left(\int_0^1 \vartheta \mathbf{T}_{(1)} \cdot \mathbf{u} dx^3 \right) d\tilde{s}^{(-)}, \\
\iint_{\Sigma} (\mathbf{m} \cdot \tilde{\boldsymbol{\mu}} - \tilde{\boldsymbol{\mu}}_0) \cdot \boldsymbol{\varphi} d\Sigma &= \int_{(L)} h(x') \left(\int_0^1 \vartheta \mathbf{T}_{(2)} \cdot \boldsymbol{\varphi} dx^3 \right) d\tilde{s}^{(-)},
\end{aligned} \tag{11.115}$$

where we introduce the notations

$$\mathbf{T}_{(1)} = \tilde{m}_{-I}^{(-)} \mathbf{P}^I - a(x', x^3) \mathbf{P}_0, \quad \mathbf{T}_{(2)} = \tilde{m}_{-I}^{(-)} \boldsymbol{\mu}^I - a(x', x^3) \boldsymbol{\mu}_0. \tag{11.116}$$

Considering (11.109), from (11.115) we get

$$\begin{aligned}
\iint_{\Sigma} (\mathbf{m} \cdot \tilde{\mathbf{P}} - \tilde{\mathbf{P}}_0) \cdot \mathbf{u} d\Sigma &= \sum_{k=0}^{\infty} \frac{1}{2k+1} \int_{(L)} h(x') \tilde{\mathbf{T}}_{(1)}^{(k)} \cdot \tilde{\mathbf{u}}^* d\tilde{s}^{(-)} \\
&= \sum_{k=0}^{\infty} \frac{1}{2k+1} \int_{(L)} h(x') \tilde{\mathbf{T}}_{(1)}^{*(k)} \cdot \tilde{\mathbf{u}} d\tilde{s}^{(-)}, \\
\iint_{\Sigma} (\mathbf{m} \cdot \tilde{\boldsymbol{\mu}} - \tilde{\boldsymbol{\mu}}_0) \cdot \boldsymbol{\varphi} d\Sigma &= \sum_{k=0}^{\infty} \frac{1}{2k+1} \int_{(L)} h(x') \tilde{\mathbf{T}}_{(2)}^{(k)} \cdot \tilde{\boldsymbol{\varphi}}^* d\tilde{s}^{(-)} \\
&= \sum_{k=0}^{\infty} \frac{1}{2k+1} \int_{(L)} h(x') \tilde{\mathbf{T}}_{(2)}^{*(k)} \cdot \tilde{\boldsymbol{\varphi}} d\tilde{s}^{(-)}, \\
\tilde{\mathbf{u}}^* &= \vartheta \mathbf{u}, \quad \tilde{\mathbf{T}}_{(1)}^* = \vartheta \mathbf{T}_{(1)}, \quad \tilde{\boldsymbol{\varphi}}^* = \vartheta \boldsymbol{\varphi}, \quad \tilde{\mathbf{T}}_{(2)}^* = \vartheta \mathbf{T}_{(2)}.
\end{aligned} \tag{11.117}$$

Further, by virtue of the formulas $f^{(-)} = \sum_{k=0}^{\infty} (-1)^k f^{(k)}$, $f^{(+)} = \sum_{k=0}^{\infty} f^{(k)}$, the surface integrals on the right-hand side of (11.105) are reduced to

$$\begin{aligned} \iint_{S_1^{(-)}} \underline{\mathbf{n}} \cdot \delta \underline{\mathbf{P}} \cdot (\underline{\mathbf{u}} - \underline{\mathbf{u}}_0) dS^{(-)} &= \sum_{k=0}^{\infty} (-1)^k \iint_{S_1^{(-)}} \underline{\mathbf{n}} \cdot \delta \underline{\mathbf{P}} \cdot (\underline{\mathbf{u}} - \underline{\mathbf{u}}_0) dS^{(-)}, \\ \iint_{S_2^{(-)}} (\underline{\mathbf{n}} \cdot \underline{\mathbf{P}} - \underline{\mathbf{P}}_0) \cdot \delta \underline{\mathbf{u}} dS^{(-)} &= \sum_{k=0}^{\infty} (-1)^k \iint_{S_2^{(-)}} (\underline{\mathbf{n}} \cdot \underline{\mathbf{P}} - \underline{\mathbf{P}}_0) \cdot \delta \underline{\mathbf{u}} dS^{(-)}, \\ \iint_{S_1^{(+)}} \underline{\mathbf{n}} \cdot \delta \underline{\mathbf{P}} \cdot (\underline{\mathbf{u}} - \underline{\mathbf{u}}_0) dS^{(+)} &= \sum_{k=0}^{\infty} \iint_{S_1^{(+)}} \underline{\mathbf{n}} \cdot \delta \underline{\mathbf{P}} \cdot (\underline{\mathbf{u}} - \underline{\mathbf{u}}_0) \underline{\eta} dS^{(+)}, \\ \iint_{S_2^{(+)}} (\underline{\mathbf{n}} \cdot \underline{\mathbf{P}} - \underline{\mathbf{P}}_0) \cdot \delta \underline{\mathbf{u}} dS^{(+)} &= \sum_{k=0}^{\infty} \iint_{S_2^{(+)}} (\underline{\mathbf{n}} \cdot \underline{\mathbf{P}} - \underline{\mathbf{P}}_0) \cdot \delta \underline{\mathbf{u}} \underline{\eta} dS^{(+)}, \\ \iint_{S_1^{(-)}} \underline{\mathbf{n}} \cdot \delta \underline{\boldsymbol{\mu}} \cdot (\underline{\boldsymbol{\varphi}} - \underline{\boldsymbol{\varphi}}_0) dS^{(-)} &= \sum_{k=0}^{\infty} (-1)^k \iint_{S_1^{(-)}} \underline{\mathbf{n}} \cdot \delta \underline{\boldsymbol{\mu}} \cdot (\underline{\boldsymbol{\varphi}} - \underline{\boldsymbol{\varphi}}_0) dS^{(-)}, \end{aligned} \quad (11.118)$$

$$\begin{aligned} \iint_{S_2^{(-)}} (\underline{\mathbf{n}} \cdot \underline{\boldsymbol{\mu}} - \underline{\boldsymbol{\mu}}_0) \cdot \delta \underline{\boldsymbol{\varphi}} dS^{(-)} &= \sum_{k=0}^{\infty} (-1)^k \iint_{S_2^{(-)}} (\underline{\mathbf{n}} \cdot \underline{\boldsymbol{\mu}} - \underline{\boldsymbol{\mu}}_0) \cdot \delta \underline{\boldsymbol{\varphi}} dS^{(-)}, \\ \iint_{S_1^{(+)}} \underline{\mathbf{n}} \cdot \delta \underline{\boldsymbol{\mu}} \cdot (\underline{\boldsymbol{\varphi}} - \underline{\boldsymbol{\varphi}}_0) dS^{(+)} &= \sum_{k=0}^{\infty} \iint_{S_1^{(+)}} \underline{\mathbf{n}} \cdot \delta \underline{\boldsymbol{\mu}} \cdot (\underline{\boldsymbol{\varphi}} - \underline{\boldsymbol{\varphi}}_0) \underline{\eta} dS^{(+)}, \\ \iint_{S_2^{(+)}} (\underline{\mathbf{n}} \cdot \underline{\boldsymbol{\mu}} - \underline{\boldsymbol{\mu}}_0) \cdot \delta \underline{\boldsymbol{\varphi}} dS^{(+)} &= \sum_{k=0}^{\infty} \iint_{S_2^{(+)}} (\underline{\mathbf{n}} \cdot \underline{\boldsymbol{\mu}} - \underline{\boldsymbol{\mu}}_0) \cdot \delta \underline{\boldsymbol{\varphi}} \underline{\eta} dS^{(+)}, \end{aligned}$$

where the formula

$$dS^{(+)} = \underline{\eta} dS^{(-)} \quad (\underline{\eta} = \sqrt{g g^{33} / (\underline{g} \underline{g}^{33})} = \underline{\vartheta} \sqrt{g^{33} / \underline{g}^{33}}, \quad \underline{\eta} = \underline{\eta}|_{x^3=1}),$$

which is obtained from the first line (11.106), is taken into account.

It should be noted that parts $S_1^{(-)}$ and $S_2^{(-)}$ of the surface $S^{(-)}$, generally, may not have common points with parts $S_1^{(+)}$ and $S_2^{(+)}$. Introducing the notations

$$\mathbf{S}_{(1)} = \nabla \cdot \underline{\mathbf{P}} + \rho \mathbf{F}, \quad \mathbf{S}_{(2)} = \nabla \cdot \underline{\boldsymbol{\mu}} + \underline{\mathbf{C}} \otimes \underline{\mathbf{P}} + \rho \mathbf{G} \quad (11.119)$$

and taking into account (11.110), (11.113) and (11.116) – (11.118), the generalized Reissner-type variational principle (11.105) in moments will present as follows

$$\begin{aligned}
D\check{R} = & \sum_{k=0}^{\infty} \frac{1}{2k+1} \left\{ \iint_{S_1^{(-)}} h(x') \left\{ [\underline{\mathbf{M}}(\vartheta \frac{\partial \check{W}}{\partial \underline{\boldsymbol{\gamma}}}) - \underline{\mathbf{P}}^*] \otimes \delta \underline{\boldsymbol{\gamma}}^{(k)} \right. \right. \\
& + [\underline{\mathbf{M}}(\vartheta \frac{\partial \check{W}}{\partial \underline{\boldsymbol{\boldsymbol{\varkappa}}})} - \underline{\boldsymbol{\mu}}^*] \otimes \delta \underline{\boldsymbol{\varkappa}}^{(k)} - [\underline{\boldsymbol{\gamma}} - \underline{\mathbf{M}}(\nabla \mathbf{u}) + \underline{\mathbf{C}} \cdot \underline{\boldsymbol{\varphi}}] \otimes \delta \underline{\mathbf{P}}^* \\
& - [\underline{\boldsymbol{\varkappa}} - \underline{\mathbf{M}}(\nabla \boldsymbol{\varphi})] \otimes \delta \underline{\boldsymbol{\mu}}^* - \mathbf{S}_{(1)}^* \cdot \delta \underline{\mathbf{u}} - \mathbf{S}_{(2)}^* \cdot \delta \underline{\boldsymbol{\varphi}} \left. \right\} dS^{(-)} \\
& - \int_{L_1} h(x') \bar{m}_I^{(-)} [\underline{\mathbf{M}}(\vartheta \delta \mathbf{P}^I) \cdot (\underline{\mathbf{u}} - \underline{\mathbf{u}}_0) + \underline{\mathbf{M}}(\vartheta \delta \underline{\boldsymbol{\mu}}^I) \cdot (\underline{\boldsymbol{\varphi}} - \underline{\boldsymbol{\varphi}}_0)] dS^{(-)} \\
& - \int_{L_2} h(x') (\mathbf{T}_{(1)}^* \cdot \delta \underline{\mathbf{u}} + \mathbf{T}_{(2)}^* \cdot \delta \underline{\boldsymbol{\varphi}}) dS^{(-)} \\
& - (-1)^k (2k+1) \left\{ \iint_{S_1^{(-)}} \delta \underline{\mathbf{P}} \cdot (\underline{\mathbf{u}} - \underline{\mathbf{u}}_0) + \delta \underline{\boldsymbol{\mu}} \cdot (\underline{\boldsymbol{\varphi}} - \underline{\boldsymbol{\varphi}}_0) \right\} dS^{(-)} \\
& - \iint_{S_2^{(-)}} [(\underline{\mathbf{n}} \cdot \underline{\mathbf{P}} - \mathbf{P}_0) \cdot \delta \underline{\mathbf{u}} + (\underline{\mathbf{n}} \cdot \underline{\boldsymbol{\mu}} - \boldsymbol{\mu}_0) \cdot \delta \underline{\boldsymbol{\varphi}}] \left. \right\} dS^{(-)} \\
& - (2k+1) \left\{ \iint_{S_1^{(+)}} \delta \underline{\mathbf{P}} \cdot (\underline{\mathbf{u}} - \underline{\mathbf{u}}_0) + \delta \underline{\boldsymbol{\mu}} \cdot (\underline{\boldsymbol{\varphi}} - \underline{\boldsymbol{\varphi}}_0) \right\} dS^{(+)} \\
& - \iint_{S_2^{(+)}} [(\underline{\mathbf{n}} \cdot \underline{\mathbf{P}} - \mathbf{P}_0) \cdot \delta \underline{\mathbf{u}} + (\underline{\mathbf{n}} \cdot \underline{\boldsymbol{\mu}} - \boldsymbol{\mu}_0) \cdot \delta \underline{\boldsymbol{\varphi}}] \left. \right\} dS^{(+)} = 0,
\end{aligned} \tag{11.120}$$

where we introduced the notations

$$\begin{aligned}
\underline{\mathbf{P}}^* &= \underline{\mathbf{M}}(\vartheta \underline{\mathbf{P}}), \quad \underline{\boldsymbol{\mu}}^* = \underline{\mathbf{M}}(\vartheta \underline{\boldsymbol{\mu}}), \\
\mathbf{S}_{(I)}^* &= \underline{\mathbf{M}}(\vartheta \mathbf{S}_{(I)}), \quad \mathbf{T}_{(I)}^* = \underline{\mathbf{M}}(\vartheta \mathbf{T}_{(I)}).
\end{aligned} \tag{11.121}$$

Note that the last two integrals in (11.120) could be replaced, for example, similarly to the last two integrals in (11.118), but this was not done. If desired, this is not difficult to do. Although, there is no need for that. And in the further presentation, we will act in a similar way.

It is easy to see that due to the arbitrariness of $\delta \underline{\boldsymbol{\gamma}}^{(k)}$, $\delta \underline{\boldsymbol{\varkappa}}^{(k)}$, $\delta \underline{\mathbf{u}}^{(k)}$, $\delta \underline{\boldsymbol{\varphi}}^{(k)}$, $\delta \underline{\mathbf{P}}^*{}^{(k)}$, $\delta \underline{\boldsymbol{\mu}}^*{}^{(k)}$ from (11.120) we obtain equilibrium equations, kinematic and static boundary conditions on the contour of the base surface and front surfaces. Obviously, the number of relations obtained from (11.120), except for the kinematic and static boundary conditions on the front surfaces, is infinite. Using the reduction methods Nikabadzé (2014), an infinite system can always be reduced to a finite.

Note that if in (11.120) the quantities $\underline{\mathbf{P}}^*{}^{(k)}$, $\underline{\boldsymbol{\mu}}^*{}^{(k)}$, $\mathbf{S}_{(I)}^*{}^{(k)}$, $\mathbf{T}_{(I)}^*{}^{(k)}$, $\underline{\mathbf{M}}(\vartheta \delta \mathbf{P}^I)$, $\underline{\mathbf{M}}(\vartheta \delta \underline{\boldsymbol{\mu}}^I)$ are replaced by $\underline{\mathbf{P}}^{(k)}$, $\underline{\boldsymbol{\mu}}^{(k)}$, $\mathbf{S}_{(I)}^{(k)}$, $\mathbf{T}_{(I)}^{(k)}$, $\underline{\mathbf{M}}(\delta \mathbf{P}^I)$, $\underline{\mathbf{M}}(\delta \underline{\boldsymbol{\mu}}^I)$ and $\underline{\boldsymbol{\gamma}}^{(k)}$, $\underline{\boldsymbol{\varkappa}}^{(k)}$, $\underline{\mathbf{u}}^{(k)}$, $\underline{\boldsymbol{\varphi}}^{(k)}$, $\underline{\mathbf{M}}(\nabla \mathbf{u})$, $\underline{\mathbf{M}}(\nabla \boldsymbol{\varphi})$ are replaced by $\underline{\boldsymbol{\gamma}}^*{}^{(k)}$, $\underline{\boldsymbol{\varkappa}}^*{}^{(k)}$, $\underline{\mathbf{u}}^*{}^{(k)}$, $\underline{\boldsymbol{\varphi}}^*{}^{(k)}$, $\underline{\mathbf{M}}(\vartheta \nabla \mathbf{u})$, $\underline{\mathbf{M}}(\vartheta \nabla \boldsymbol{\varphi})$, respec-

tively, we obtain a different form of representation of the generalized Reissner-type variational principle, but we will not dwell on it.

It should also be noted that it was possible to present the generalized Reissner-type principle (11.102) in moments, and then get (11.120). In fact, doing the same as when getting (11.120), by virtue of (11.110), (11.113) and (11.118) from (11.102) we will have

$$\begin{aligned} \check{R}(\overset{(0)}{\mathbf{u}}, \dots, \overset{(n)}{\mathbf{u}}, \dots, \overset{(0)}{\boldsymbol{\varphi}}, \dots, \overset{(n)}{\boldsymbol{\varphi}}, \dots, \overset{(0)}{\boldsymbol{\gamma}}, \dots, \overset{(n)}{\boldsymbol{\gamma}}, \dots, \overset{(0)}{\boldsymbol{\varkappa}}, \dots, \overset{(n)}{\boldsymbol{\varkappa}}, \\ \dots, \overset{(0)}{\mathbf{P}}, \dots, \overset{(n)}{\mathbf{P}}, \dots, \overset{(0)}{\boldsymbol{\mu}}, \dots, \overset{(n)}{\boldsymbol{\mu}}, \dots) = \sum_{k=0}^{\infty} \check{R}_k(\overset{(k)}{\mathbf{u}}, \overset{(k)}{\boldsymbol{\varphi}}, \overset{(k)}{\boldsymbol{\gamma}}, \overset{(k)}{\boldsymbol{\varkappa}}, \overset{(k)}{\mathbf{P}}, \overset{(k)}{\boldsymbol{\mu}}), \end{aligned} \quad (11.122)$$

where the notation

$$\begin{aligned} \check{R}_k(\overset{(k)}{\mathbf{u}}, \overset{(k)}{\boldsymbol{\varphi}}, \overset{(k)}{\boldsymbol{\gamma}}, \overset{(k)}{\boldsymbol{\varkappa}}, \overset{(k)}{\mathbf{P}}, \overset{(k)}{\boldsymbol{\mu}}) \\ = \frac{1}{2k+1} \left\{ \iint_{\overset{(-)}{S}} h(x') \{ W_k(\overset{(k)}{\boldsymbol{\gamma}}, \overset{(k)}{\boldsymbol{\varkappa}}) - \overset{(k)}{\mathbf{P}} \otimes [\overset{(k)}{\boldsymbol{\gamma}} - \overset{(k)}{\mathbf{M}}(\nabla \mathbf{u}) + \overset{(k)}{\mathbf{C}} \cdot \overset{(k)}{\boldsymbol{\varphi}}] \right. \\ \left. - \overset{(k)}{\boldsymbol{\mu}} \otimes [\overset{(k)}{\boldsymbol{\varkappa}} - \overset{(k)}{\mathbf{M}}(\nabla \boldsymbol{\varphi})] - \overset{(k)}{\mathbf{M}}(\rho \mathbf{F}) \cdot \overset{(k)}{\mathbf{u}} - \overset{(k)}{\mathbf{M}}(\rho \mathbf{G}) \cdot \overset{(k)}{\boldsymbol{\varphi}} \} dS \right. \\ \left. - \int_{\overset{(-)}{L_1}} h(x') \overset{(-)}{m}_I [\overset{(k)}{\mathbf{M}}(\overset{(-)}{\boldsymbol{\nu}} \mathbf{P}^I) \cdot (\overset{(k)}{\mathbf{u}} - \overset{(k)}{\mathbf{u}}_0) + \overset{(k)}{\mathbf{M}}(\overset{(-)}{\boldsymbol{\nu}} \boldsymbol{\mu}^I) \cdot (\overset{(k)}{\boldsymbol{\varphi}} - \overset{(k)}{\boldsymbol{\varphi}}_0)] d\overset{(-)}{s} \right. \\ \left. - \int_{\overset{(-)}{L_2}} h(x') (\overset{(k)}{\mathbf{P}}^*_{(0)} \cdot \overset{(k)}{\mathbf{u}} + \overset{(k)}{\boldsymbol{\mu}}^*_{(0)} \cdot \overset{(k)}{\boldsymbol{\varphi}}) d\overset{(-)}{s} \right. \\ \left. - (-1)^k (2k+1) \left\{ \iint_{\overset{(-)}{S_1}} \overset{(-)}{\mathbf{n}} \cdot [\overset{(k)}{\mathbf{P}} \cdot (\overset{(-)}{\mathbf{u}} - \overset{(-)}{\mathbf{u}}_0) + \overset{(k)}{\boldsymbol{\mu}} \cdot (\overset{(-)}{\boldsymbol{\varphi}} - \overset{(-)}{\boldsymbol{\varphi}}_0)] d\overset{(-)}{S} \right. \right. \\ \left. \left. - \iint_{\overset{(-)}{S_2}} (\overset{(k)}{\mathbf{P}}_0 \cdot \overset{(k)}{\mathbf{u}} + \overset{(k)}{\boldsymbol{\mu}}_0 \cdot \overset{(k)}{\boldsymbol{\varphi}}) d\overset{(-)}{S} \right\} \right. \\ \left. - (2k+1) \left\{ \iint_{\overset{(+)}{S_1}} \overset{(+)}{\mathbf{n}} \cdot [\overset{(k)}{\mathbf{P}} \cdot (\overset{(+)}{\mathbf{u}} - \overset{(+)}{\mathbf{u}}_0) + \overset{(k)}{\boldsymbol{\mu}} \cdot (\overset{(+)}{\boldsymbol{\varphi}} - \overset{(+)}{\boldsymbol{\varphi}}_0)] d\overset{(+)}{S} \right. \right. \\ \left. \left. - \iint_{\overset{(+)}{S_2}} (\overset{(k)}{\mathbf{P}}_0 \cdot \overset{(k)}{\mathbf{u}} + \overset{(k)}{\boldsymbol{\mu}}_0 \cdot \overset{(k)}{\boldsymbol{\varphi}}) d\overset{(+)}{S} \right\} \right\}, \end{aligned} \quad (11.123)$$

called the common term of a series of generalized Reissner-type operator, is introduced.

It should be noted that $W_k(\overset{(k)}{\mathbf{u}}, \overset{(k)}{\boldsymbol{\varphi}})$ is a common term of the series

$$\overset{(0)}{W}^*(\overset{(0)}{\boldsymbol{\gamma}}, \dots, \overset{(n)}{\boldsymbol{\gamma}}, \dots, \overset{(0)}{\boldsymbol{\varkappa}}, \dots, \overset{(n)}{\boldsymbol{\varkappa}}, \dots) = \int_0^1 \overset{(-)}{\boldsymbol{\nu}} \check{W}(\boldsymbol{\gamma}, \boldsymbol{\varkappa}) dx^3 = \sum_{k=0}^{\infty} \frac{1}{2k+1} W_k(\overset{(k)}{\boldsymbol{\gamma}}, \overset{(k)}{\boldsymbol{\varkappa}}). \quad (11.124)$$

We also note that in specific cases the strain and bending-torsion operator \check{W} in (11.124) can be represented in a similar to (11.109) form (for example, in the case of

the linear micropolar theory of elasticity \check{W} is the quadratic form with respect to $\underline{\gamma}$ and $\underline{\varkappa}$. We will not dwell on the consideration of special cases of the representation \check{W} .

It can be seen that the generalized Reissner operator (11.122) and (11.124) depend on infinitely many variables $\underline{\mathbf{u}}, \underline{\boldsymbol{\varphi}}, \underline{\boldsymbol{\gamma}}, \underline{\boldsymbol{\varkappa}}, \underline{\mathbf{P}}$ and $\underline{\boldsymbol{\mu}}, k = \overline{0, \infty}$, as indicated by the dots in the arguments of these operators (\check{R}_k depends only on $\underline{\boldsymbol{\gamma}}, \underline{\boldsymbol{\varkappa}}, \underline{\mathbf{P}}$ and $\underline{\boldsymbol{\mu}}$, and W_k depend on $\underline{\boldsymbol{\gamma}}$ and $\underline{\boldsymbol{\varkappa}}$, however, they themselves $\underline{\boldsymbol{\gamma}}$ and $\underline{\boldsymbol{\varkappa}}$ depend on infinitely many variables $\underline{\mathbf{u}}, \underline{\boldsymbol{\varphi}}, k = \overline{0, \infty}$, since $\underline{\mathbf{M}}(\nabla \mathbf{u})$ and $\underline{\mathbf{M}}(\nabla \boldsymbol{\varphi})$ contain infinitely many terms).

In order to get the desired principle from (11.122), we need to derive an auxiliary identity. For this purpose, integrating the identity

$$\nabla \cdot (\underline{\mathbf{Q}} \cdot \mathbf{a}) = \nabla \cdot \underline{\mathbf{Q}} \cdot \mathbf{a} + \underline{\mathbf{Q}} \otimes^2 \nabla \mathbf{a}, \quad \forall \underline{\mathbf{Q}}, \mathbf{a}$$

over the volume V and applying the Ostrogradsky–Gauss theorem, we have

$$\iiint_V \underline{\mathbf{Q}} \otimes^2 \nabla \mathbf{a} dV = \int_{\Gamma} \mathbf{n} \cdot \underline{\mathbf{Q}} \cdot \mathbf{a} dS - \iiint_V \nabla \cdot \underline{\mathbf{Q}} \cdot \mathbf{a} dV. \quad (11.125)$$

Further, applying (11.125) to the thin body with the volume V and the border $\Gamma = \overset{(-)}{S} \cup \overset{(+)}{S} \cup \Sigma$, $\overset{(-)}{S} = \overset{(-)}{S}_1 \cup \overset{(-)}{S}_2$, $\overset{(-)}{S}_1 \cap \overset{(-)}{S}_2 = \emptyset$, $\overset{(+)}{S} = \overset{(+)}{S}_1 \cup \overset{(+)}{S}_2$, $\overset{(+)}{S}_1 \cap \overset{(+)}{S}_2 = \emptyset$, $\Sigma = \Sigma_1 \cup \Sigma_2$, $\Sigma_1 \cap \Sigma_2 = \emptyset$ (see the last two lines (11.102)) and assuming, as above, that

$$\begin{aligned} \mathbf{n}|_{x^3=0} &= \overset{(-)}{\mathbf{n}}, & \mathbf{n}|_{x^3=1} &= \overset{(+)}{\mathbf{n}}, & \underline{\mathbf{Q}}|_{x^3=0} &= \overset{(-)}{\underline{\mathbf{Q}}}, \\ \underline{\mathbf{Q}}|_{x^3=1} &= \overset{(+)}{\underline{\mathbf{Q}}}, & \mathbf{a}|_{x^3=0} &= \overset{(-)}{\mathbf{a}}, & \mathbf{a}|_{x^3=1} &= \overset{(+)}{\mathbf{a}}, \end{aligned}$$

we get

$$\begin{aligned} \iiint_V \underline{\mathbf{Q}} \otimes^2 \nabla \mathbf{a} dV &= \iint_{\Sigma} \mathbf{m} \cdot \underline{\mathbf{Q}} \cdot \mathbf{a} dS + \iint_{\overset{(-)}{S}} \overset{(-)}{\mathbf{n}} \cdot \overset{(-)}{\underline{\mathbf{Q}}} \cdot \overset{(-)}{\mathbf{a}} d\overset{(-)}{S} \\ &+ \iint_{\overset{(+)}{S}} \overset{(+)}{\mathbf{n}} \cdot \overset{(+)}{\underline{\mathbf{Q}}} \cdot \overset{(+)}{\mathbf{a}} d\overset{(+)}{S} - \iiint_V \nabla \cdot \underline{\mathbf{Q}} \cdot \mathbf{a} dV. \end{aligned} \quad (11.126)$$

By virtue of (11.110), (11.113) and (11.118) from (11.126), using simple transformations, the desired identity is represented as

$$\begin{aligned}
& \frac{1}{2k+1} \iint_{\overset{(-)}{S}} h(x') \underline{\mathbf{Q}}^* \otimes \underline{\mathbf{M}}(\nabla \mathbf{a}) dS \\
&= \frac{1}{2k+1} \left(\int_{\overset{(-)}{L_1}} h(x') \underline{m}_I \underline{\mathbf{Q}}^* I \cdot \underline{\mathbf{a}} d\overset{(-)}{s} + \int_{\overset{(-)}{L_2}} h(x') \underline{m}_I \underline{\mathbf{Q}}^* I \cdot \underline{\mathbf{a}} d\overset{(-)}{s} \right) \\
&+ (-1)^k \left[\iint_{\overset{(-)}{S_1}} \underline{\mathbf{n}} \cdot \underline{\mathbf{Q}} \cdot \underline{\mathbf{a}} d\overset{(-)}{S} + \iint_{\overset{(-)}{S_2}} \underline{\mathbf{n}} \cdot \underline{\mathbf{Q}} \cdot \underline{\mathbf{a}} d\overset{(-)}{S} \right] + \iint_{\overset{(+)}{S_1}} \underline{\mathbf{n}} \cdot \underline{\mathbf{Q}} \cdot \underline{\mathbf{a}} d\overset{(+)}{S} \\
&+ \iint_{\overset{(+)}{S_2}} \underline{\mathbf{n}} \cdot \underline{\mathbf{Q}} \cdot \underline{\mathbf{a}} d\overset{(+)}{S} - \frac{1}{2k+1} \iint_{\overset{(-)}{S}} h(x') \underline{\mathbf{M}}(\vartheta \nabla \cdot \underline{\mathbf{Q}}) \cdot \underline{\mathbf{a}} d\overset{(-)}{S}, \quad k \geq 0,
\end{aligned} \tag{11.127}$$

where $\overset{(-)}{L}$ is the border (contour) of the base surface $\overset{(-)}{S}$ and $\overset{(-)}{L} = \overset{(-)}{L_1} \cup \overset{(-)}{L_2}$, $\overset{(-)}{L_1} \cap \overset{(-)}{L_2} = \emptyset$, $\underline{\mathbf{Q}}^* I = \underline{\mathbf{M}}(\vartheta \underline{\mathbf{Q}}^* I)$.

If we now in (11.127) $\underline{\mathbf{Q}}$ and $\underline{\mathbf{a}}$ first replace with $\underline{\mathbf{P}}$ and $\delta \mathbf{u}$, and then replace with $\underline{\boldsymbol{\mu}}$ and $\delta \boldsymbol{\varphi}$, respectively, and also then add the obtained identities term by term by virtue of

$$\begin{aligned}
\delta \mathbf{u}|_{\overset{(-)}{L_1}} &= 0, \quad \delta \boldsymbol{\varphi}|_{\overset{(-)}{L_1}} = 0, \quad \delta \overset{(-)}{\mathbf{u}}|_{\overset{(-)}{S_1}} = 0, \\
\delta \overset{(-)}{\boldsymbol{\varphi}}|_{\overset{(-)}{S_1}} &= 0, \quad \delta \overset{(+)}{\mathbf{u}}|_{\overset{(+)}{S_1}} = 0, \quad \delta \overset{(+)}{\boldsymbol{\varphi}}|_{\overset{(+)}{S_1}} = 0,
\end{aligned}$$

we get

$$\begin{aligned}
& \frac{1}{2k+1} \iint_{\overset{(-)}{S}} h(x') [\underline{\mathbf{P}}^* \otimes \underline{\mathbf{M}}(\nabla \delta \mathbf{u}) + \underline{\boldsymbol{\mu}}^* \otimes \underline{\mathbf{M}}(\nabla \delta \boldsymbol{\varphi})] d\overset{(-)}{S} \\
&= \frac{1}{2k+1} \int_{\overset{(-)}{L_2}} h(x') \underline{m}_I [\underline{\mathbf{M}}(\vartheta \underline{\mathbf{P}}^* I) \cdot \delta \overset{(-)}{\mathbf{u}} + \underline{\mathbf{M}}(\vartheta \underline{\boldsymbol{\mu}}^* I) \cdot \delta \overset{(-)}{\boldsymbol{\varphi}}] d\overset{(-)}{s} \\
&+ \iint_{\overset{(-)}{S_2}} \underline{\mathbf{n}} \cdot (\underline{\mathbf{P}} \cdot \delta \overset{(-)}{\mathbf{u}} + \underline{\boldsymbol{\mu}} \cdot \delta \overset{(-)}{\boldsymbol{\varphi}}) d\overset{(-)}{S} + \iint_{\overset{(+)}{S_2}} \underline{\mathbf{n}} \cdot (\underline{\mathbf{P}} \cdot \delta \overset{(+)}{\mathbf{u}} + \underline{\boldsymbol{\mu}} \cdot \delta \overset{(+)}{\boldsymbol{\varphi}}) d\overset{(+)}{S} \\
&- \frac{1}{2k+1} \iint_{\overset{(-)}{S}} h(x') [\underline{\mathbf{M}}(\vartheta \nabla \cdot \underline{\mathbf{P}}) \cdot \delta \overset{(-)}{\mathbf{u}} + \underline{\mathbf{M}}(\vartheta \nabla \cdot \underline{\boldsymbol{\mu}}) \cdot \delta \overset{(-)}{\boldsymbol{\varphi}}] d\overset{(-)}{S}, \quad k \geq 0.
\end{aligned} \tag{11.128}$$

By the definition of the differential of the operator and (11.128), as well as the formulas

$$\begin{aligned}
DW_k^*(\underline{\boldsymbol{\gamma}}, \underline{\boldsymbol{\varkappa}}, \delta \underline{\boldsymbol{\gamma}}, \delta \underline{\boldsymbol{\varkappa}}) &= \frac{\partial W_k^*}{\partial \underline{\boldsymbol{\gamma}}} \otimes \delta \underline{\boldsymbol{\gamma}} + \frac{\partial W_k^*}{\partial \underline{\boldsymbol{\varkappa}}} \otimes \delta \underline{\boldsymbol{\varkappa}}, \\
\underline{\mathbf{P}}^* &= \frac{\partial W_k^*}{\partial \underline{\boldsymbol{\gamma}}} = \underline{\mathbf{M}} \left(\vartheta \frac{\partial \check{W}}{\partial \underline{\boldsymbol{\gamma}}} \right), \quad \underline{\boldsymbol{\mu}}^* = \frac{\partial W_k^*}{\partial \underline{\boldsymbol{\varkappa}}} = \underline{\mathbf{M}} \left(\vartheta \frac{\partial \check{W}}{\partial \underline{\boldsymbol{\varkappa}}} \right)
\end{aligned}$$

from (11.122) we get (11.120).

It should be noted that it is not difficult, similarly to (11.120) to formulate the variational principles of Lagrange, Castigliano and Reissner-type or similarly to (11.122) and (11.123) introduce the Lagrangian, the Castiglianian and the generalized Reissner-type operator, and then use them to obtain the corresponding variational principles for the theory of thin bodies.

We also note that, using the D'Alembert principle and replacing the volume force $\rho\mathbf{F}$ and moment $\rho\mathbf{G}$ with $\rho\mathbf{F} - \rho\partial_t^2\mathbf{u}$ and $\rho\mathbf{G} - \mathbf{J} \cdot \partial_t^2\boldsymbol{\varphi}$ respectively, it is not difficult to formulate the variational principles presented above in the case when the force and moment of inertia are taken into account.

In conclusion, we note that the formulated variational principles (or the Lagrangian, Castiglianian, Reissner-type operators) for the thin body theories are presented in the form of series and contain infinitely many variables $\overset{(k)}{\mathbf{u}}$ and $\overset{(k)}{\boldsymbol{\varphi}}$, $k = \overline{0, \infty}$. Therefore, it is not advisable to use them in practice. In this regard, they should be reduced to finite series, which will contain a finite number of variables. There are various reduction methods Vekua (1982); Nikabadze (2014), of which we will focus only on one (simplified reduction method). This reduction method consists in the following: we fix some non-negative integer N and assume that all the moments $\overset{(k)}{\mathbf{u}} = 0$ and $\overset{(k)}{\boldsymbol{\varphi}} = 0$, if $k > N$. In this case, of course, the vectors of displacements \mathbf{u} and rotations $\boldsymbol{\varphi}$ are represented as

$$\mathbf{u}_N = \sum_{k=0}^N \overset{(k)}{\mathbf{u}}(x')P_k(x^3), \quad \boldsymbol{\varphi}_N = \sum_{k=0}^N \overset{(k)}{\boldsymbol{\varphi}}(x')P_k(x^3), \quad 0 \leq x^3 \leq 1. \quad (11.129)$$

Therefore, for the strain and bending-torsion tensors, as well as for the tensors of stresses and couple stresses, by virtue of (11.129) we will have expressions

$$\begin{aligned} \underline{\boldsymbol{\gamma}}_N &= \sum_{k=0}^N \underline{\boldsymbol{\gamma}}^{(k)}(x')P_k(x^3), & \underline{\boldsymbol{\varkappa}}_N &= \sum_{k=0}^N \underline{\boldsymbol{\varkappa}}^{(k)}(x')P_k(x^3), \\ \underline{\mathbf{P}}_N &= \sum_{k=0}^N \underline{\mathbf{P}}^{(k)}(x')P_k(x^3), & \underline{\boldsymbol{\mu}}_N &= \sum_{k=0}^N \underline{\boldsymbol{\mu}}^{(k)}(x')P_k(x^3), \quad 0 \leq x^3 \leq 1, \end{aligned}$$

that contain only moments $\overset{(k)}{\mathbf{u}}$ and $\overset{(k)}{\boldsymbol{\varphi}}$, $k = \overline{0, N}$.

Then, for example, instead of (11.122) we will have

$$\tilde{R}(\mathbf{u}_N, \boldsymbol{\varphi}_N) \equiv \tilde{R}(\overset{(0)}{\mathbf{u}}, \dots, \overset{(N)}{\mathbf{u}}, \dots, \overset{(0)}{\boldsymbol{\mu}}, \dots, \overset{(N)}{\boldsymbol{\mu}}) = \sum_{k=0}^N \tilde{R}_k(\overset{(k)}{\mathbf{u}}, \overset{(k)}{\boldsymbol{\varphi}}, \overset{(k)}{\boldsymbol{\gamma}}, \overset{(k)}{\boldsymbol{\varkappa}}, \underline{\mathbf{P}}, \underline{\boldsymbol{\mu}}), \quad (11.130)$$

called the Reissner-type operator of N order approximation.

It should be noted that based on (11.130) the Reissner-type variational principle of approximation of order N will be presented in the form

$$\begin{aligned}
 D\check{R}(\mathbf{u}_N, \boldsymbol{\varphi}_N) &\equiv D\check{R}^{(0), \dots, (N)}(\check{\mathbf{u}}, \dots, \check{\mathbf{u}}, \dots, \check{\boldsymbol{\mu}}, \dots, \check{\boldsymbol{\mu}}) \\
 &\equiv D\check{R}^{(0), \dots, (N)}(\check{\mathbf{u}}, \dots, \check{\boldsymbol{\varphi}}, \dots, \check{\boldsymbol{\varphi}}, \check{\boldsymbol{\gamma}}, \dots, \check{\boldsymbol{\gamma}}, \check{\boldsymbol{\varkappa}}, \dots, \check{\boldsymbol{\varkappa}}, \check{\mathbf{P}}, \dots, \check{\mathbf{P}}, \check{\boldsymbol{\mu}}, \dots, \check{\boldsymbol{\mu}}) \quad (11.131) \\
 &= \sum_{k=0}^N D\check{R}_k^{(k)}(\check{\mathbf{u}}, \check{\boldsymbol{\varphi}}, \check{\boldsymbol{\gamma}}, \check{\boldsymbol{\varkappa}}, \check{\mathbf{P}}, \check{\boldsymbol{\mu}}).
 \end{aligned}$$

We also note that if $f(x', x^3) = \sum_{k=0}^{\infty} f^{(k)} P_k(x^3)$, then the following uniform estimates hold Vekua (1970, 1982):

$$|f| \leq Ck^{-3/2}, \quad |R_{N+1}| \leq Ck^{-1/2}, \quad k \geq 1, \quad (11.132)$$

where C is a positive constant independent of k , and $R_{N+1}(x', x^3) = \sum_{k=N+1}^{\infty} f^{(k)} P_k(x^3)$.

Taking into account (11.132), similarly to the classical case Vekua (1970), it is easy to prove that

$$|\check{R}(\mathbf{u}, \boldsymbol{\varphi}) - \check{R}_N(\mathbf{u}_N, \boldsymbol{\varphi}_N)| = O(1/\sqrt{N}). \quad (11.133)$$

So, the Reissner operator $\check{R}(\mathbf{u}, \boldsymbol{\varphi})$ is approximated by operators of the form $\check{R}_N(\mathbf{u}_N, \boldsymbol{\varphi}_N)$. Therefore, for sufficiently large N , by virtue of (11.133), the variational principle (11.120) can be replaced by (11.131). (In case of the classical theory of elastic shells for the energy functional, the relation similar to (11.133) given in Vekua (1970) has the form $U(\mathbf{u}) - U_N(\mathbf{u}_N) = O(1/\sqrt{N})$).

It can be seen from the foregoing that in formulating the variational principles for the theory of thin bodies in moments with respect to the Legendre system of polynomials, the relations (11.110), (11.113) and (11.118) play the main role. Therefore, when applying other polynomial systems (for example, Chebyshev polynomial systems of the first and second kind), the analogous to (11.110), (11.113) and (11.118) relations will play the main role in the presentation of variational principles in moments with respect to the considered systems of polynomials. In this regard, without dwelling on a detailed presentation of the material when applying Chebyshev polynomial systems, we restrict ourselves to the derivation of similar to relations (11.110), (11.113) and (11.118) for these polynomial systems.

First of all, we note that, by virtue of the recurrence formula for the system of shifted Chebyshev polynomials of the second kind $U'_{n+1}(t) = 4(n+1)U_n(t) + U'_{n-1}(t)$ or from the definition of this system of polynomials we have

$$U_n(t) = \frac{1}{4(n+1)} [U'_{n+1}(t) - U'_{n-1}(t)] = \frac{1}{2(n+1)} T'_{n+1}.$$

From here, obviously, we get

$$\int_0^1 U_n(t) dt = \frac{1}{2(n+1)} [1 + (-1)^n], \quad \int_0^1 \hat{U}_n(t) dt = \frac{\hat{U}_0}{2(n+1)} [1 + (-1)^n], \quad (11.134)$$

where $||U_n||^{-1} = \hat{U}_0 = 2/\sqrt{\pi}$.

Further, considering the recurrence relation (see Nikabadze (2007a,b, 2014))

$$\hat{U}_{n-p}(t)\hat{U}_p(t) = \hat{U}_0(t) \sum_{s=0}^p \hat{U}_{n-2p+2s}(t),$$

based on the second relation (11.134) we find

$$A_{np} \equiv \int_0^1 \hat{U}_{n-p}(t)\hat{U}_p(t)dt = \hat{U}_0^2 \left[\sum_{s=0}^p \frac{1}{2(n-2p+2s+1)} \right] [1+(-1)^n]. \quad (11.135)$$

Quite similarly to (11.135) using the recurrence relation Nikabadze (2007a,b, 2014)

$$2^{2s}t^s \hat{U}_m(t)\hat{U}_n(t) = \hat{U}_0(t) \sum_{p=0}^m \sum_{q=0}^{2s} C_{2s}^q \hat{U}_{n-m-s+2p+q}(t)$$

and the second formula (11.134) we find

$$\begin{aligned} A_{mn}^s &= \int_0^1 2^{2s}t^s \hat{U}_m(t)\hat{U}_n(t)dt \\ &= \sum_{p=0}^m \sum_{q=0}^{2s} \frac{\hat{U}_0^2}{2(n-m-s+2p+q+1)} C_{2s}^q [1+(-1)^{n-m-s+q}]. \end{aligned} \quad (11.136)$$

In case of a system of shifted Chebyshev polynomials of the first kind, using the recurrence relation (see in Nikabadze (2007a,b, 2014))

$$4(n^2 - 1)T_n(t) = (n - 1)T'_{n+1}(t) - (n + 1)T'_{n-1}(t), \quad n \geq 1,$$

we will have

$$\int_0^1 T_n(t)dt = \begin{cases} 0, & n = 1, \\ \frac{1}{2(n^2 - 1)} [(-1)^{n+1} - 1], & n \neq 1, \quad n \geq 0. \end{cases} \quad (11.137)$$

By virtue of the recurrence relations

$$\begin{aligned} 2T_m(t)T_n(t) &= T_{n-m}(t) + T_{n+m}(t), \quad m \geq n, \\ 2^{2s}t^s T_n(t) &= \sum_{p=0}^{2s} C_{2s}^p T_{n+p-s}(t), \quad n - s \geq 0 \end{aligned} \quad (11.138)$$

it is easy to prove that the formula

$$2^{2s}t^s T_m(t)T_n(t) = \sum_{p=0}^{2s} \frac{1}{2} C_{2s}^p [T_{n-m+p-s}(t) + T_{n+m+p-s}(t)] \quad (11.139)$$

holds.

Using (11.137), from the first formula (11.138) we get

$$\begin{aligned}
 B_{mn} &= \int_0^1 T_m(t)T_n(t)dt = \frac{1}{2} \int_0^1 [T_{n-m}(t) + T_{n+m}(t)]dt \\
 &= \begin{cases} 0, & n = m + 1; \\ \frac{n^2 + m^2 - 1}{2[(n-m)^2 - 1][(n+m)^2 - 1]} [(-1)^{n+m+1} - 1], & \\ n \neq m + 1, n \geq m. \end{cases} \tag{11.140}
 \end{aligned}$$

Similarly to (11.140), by virtue of (11.137) we find

$$\begin{aligned}
 B_{mn}^{sp} &= \frac{1}{2} \int_0^1 [T_{n-m+p-s}(t) + T_{n+m+p-s}(t)]dt \\
 &= \begin{cases} 0, & n - m = 1 + s - p, \quad n - m \geq 0, \quad s \geq 0 \quad (p = \overline{0, 2s}); \\ \frac{n^2 + m^2 - 1 - (2n - s + p)(s - p)}{2[(n - m + p - s)^2 - 1][(n + m + p - s)^2 - 1]} [(-1)^{n+m+p-s+1} - 1], & \\ n - m + p - s \neq 1, \quad n \geq m, \quad s \geq 0. \end{cases} \tag{11.141}
 \end{aligned}$$

Seeing (11.141), from (11.139) we will have

$$B_{mn}^s = \int_0^1 2^{2s} t^s T_m(t)T_n(t)dt = \sum_{p=0}^{2s} C_{2s}^p B_{mn}^{sp}. \tag{11.142}$$

Let us note that $A_{mn} = A_{mn}^0, B_{mn} = B_{mn}^0 = B_{mn}^{00}$.

Having the above relations obtained by using the Chebyshev polynomial systems, it is easy to obtain similar to (11.110) and (11.113) formulas in case of using these polynomial systems. Indeed, based on (11.135), the similar equality to (11.110) in the case of applying the system of orthonormal Chebyshev polynomials of the second kind is represented in the form

$$\begin{aligned}
 \iiint_V \underline{\mathbf{Q}} \otimes \underline{\mathbf{a}} dV &= \sum_{k=0}^{\infty} \sum_{p=0}^{2k} A_{2kp} \iiint_{\underline{S}} h(x') \underline{\mathbf{Q}}^{(2k-p)} \otimes \underline{\mathbf{a}}^{(p)*} d\underline{S} \\
 &= \sum_{k=0}^{\infty} \sum_{p=0}^{2k} A_{2kp} \iiint_{\underline{S}} h(x') \underline{\mathbf{Q}}^{(2k-p)*} \otimes \underline{\mathbf{a}}^{(p)} d\underline{S}, \tag{11.143}
 \end{aligned}$$

and when applying the system of Chebyshev polynomials of the first kind, by virtue of (11.140) we will have

$$\begin{aligned}
 \iiint_V \underline{\mathbf{Q}} \otimes \underline{\mathbf{a}} dV &= \sum_{k=0}^{\infty} \sum_{p=0}^k (B_{k-pp} - B_{k-pp} \delta_{pk-p+1}) \iiint_{\underline{S}} h(x') \underline{\mathbf{Q}}^{(2k-p)} \otimes \underline{\mathbf{a}}^{(p)*} d\underline{S} \\
 &= \sum_{k=0}^{\infty} \sum_{p=0}^k (B_{k-pp} - B_{k-pp} \delta_{pk-p+1}) \iiint_{\underline{S}} h(x') \underline{\mathbf{Q}}^{(2k-p)*} \otimes \underline{\mathbf{a}}^{(p)} d\underline{S}, \tag{11.144}
 \end{aligned}$$

It is easy to show that a similar (11.113) relation when using the system of orthonormal Chebyshev polynomials of the second kind is as follows

$$\begin{aligned} \iint_{\Sigma} \mathbf{m} \cdot \mathbf{Q} \cdot \mathbf{b} d\Sigma &= \sum_{k=0}^{\infty} \sum_{p=0}^{2k} A_{2kp} \int_{(L)} h(x') \overset{(-)}{m}_I(x') \overset{(2k-p)}{\mathbf{M}}(\mathbf{Q}^I) \cdot \overset{(p)}{\mathbf{b}}^* d\overset{(-)}{s} \\ &= \sum_{k=0}^{\infty} \sum_{p=0}^{2k} A_{2kp} \int_{(L)} h(x') \overset{(-)}{m}_I(x') \overset{(2k-p)}{\mathbf{M}}(\overset{(-)}{\vartheta} \mathbf{Q}^I) \cdot \overset{(p)}{\mathbf{b}} d\overset{(-)}{s}, \end{aligned} \tag{11.145}$$

and in the case of applying the system of Chebyshev polynomials of the first kind, we obtain

$$\begin{aligned} \iint_{\Sigma} \mathbf{m} \cdot \mathbf{Q} \cdot \mathbf{b} d\Sigma &= \sum_{k=0}^{\infty} \sum_{p=0}^k (B_{k-pp} - B_{k-pp} \delta_{pk-p+1}) \int_{(L)} h(x') \overset{(-)}{m}_I(x') \overset{(k-p)}{\mathbf{Q}}^I \cdot \overset{(p)}{\mathbf{b}}^* d\overset{(-)}{s} \\ &= \sum_{k=0}^{\infty} \sum_{p=0}^k (B_{k-pp} - B_{k-pp} \delta_{pk-p+1}) \int_{(L)} h(x') \overset{(-)}{m}_I(x') \overset{(k-p)}{\mathbf{Q}}^{*I} \cdot \overset{(p)}{\mathbf{b}} d\overset{(-)}{s}, \end{aligned} \tag{11.146}$$

where $\overset{(k-p)}{\mathbf{Q}}^I = \overset{(k-p)}{\mathbf{M}}(\mathbf{Q}^I)$ and $\overset{(k-p)}{\mathbf{Q}}^{*I} = \overset{(k-p)}{\mathbf{M}}(\overset{(-)}{\vartheta} \mathbf{Q}^I)$. Note that in the more general case the formulas (11.136) and (11.142) should be used.

Further, if we take into account at the ends of the segment $[0, 1]$ the values of polynomials $\hat{U}_k(0) = (-1)^k(2/\sqrt{\pi})(k + 1)$ and $\hat{U}_k(1) = (2/\sqrt{\pi})(k + 1)$ and in the right parts (11.118) after the sign of sum, put the coefficient $(2/\sqrt{\pi})(k + 1)$ and assume that the moments are considered with respect to this system of polynomials, then we obtain relations similar to (11.118) when applying the system of orthonormal shifted Chebyshev polynomials of the second kind.

Since $T_k(0) = (-1)^k$ and $T_k(1) = 1$, when using the system of shifted Chebyshev polynomials of the first kind, the relations (11.118) will remain the same, provided that the moments should be considered with respect to the Chebyshev polynomial system.

Thus, in the form (11.143)–(11.146) and also in the form relations, on the conclusions of which were mentioned in the previous paragraph, all the promised above relations were obtained. It remains only to write out the variational principles when applying these systems of polynomials. But We will not write them out in order to shorten the letter. It should be noted that, if necessary, in the same way it is possible to obtain variational principles in moments with respect to the systems of Legendre and Chebyshev polynomials under the other parametrizations of the thin body domain that are different from the new one. We also will not dwell on these issues in order to shorten the letter.

11.8 Generalized Variational Principle of Reissner-Type in the Micropolar Theory of Multilayer Thin Bodies with One Small Size with Full Contact of the Layers

Let's consider a multilayer three-dimensional thin domain consisting of K layers, for each layer of which we use a new parameterization Nikabadze (2014, 2015, 2017). Let the layers be numbered in ascending order, i.e. if, for example, α ($1 < \alpha < K$) is the number of some layer, then the number of the previous layer will be $\alpha - 1$, and the number of the next one will be $\alpha + 1$. We assume that each layer has two front surfaces. The front surface of the layer α ($2 < \alpha < K - 1$) located on the side of the previous layer $\alpha - 1$, we call it the inner base surface and denote by $S_{\alpha}^{(-)}$, and the front surface of the layer α , located on the side of the subsequent layer $\alpha + 1$, will be called the external base surface and denoted by $S_{\alpha}^{(+)}$. Note that for $\alpha = 1$ ($\alpha = K$), the inner (outer) base surface is denoted by $S_1^{(-)}$ ($S_K^{(+)}$). Surfaces $S_1^{(-)}$ and $S_K^{(+)}$ are also called face surfaces of a multilayer thin body. We assume that the front surfaces of each layer are regular surfaces, and in the case of a bounded unclosed layer, its lateral surface is a ruled surface.

So, considering the new parameterization Nikabadze (2014, 2015, 2017) of the domain of a multilayer thin body, by virtue of what was said above and the generalized Reissner-type operator (11.102), the generalized Reissner-type operator with complete contact (perfect or ideal adhesion) of layers can be to present in the form

$$\begin{aligned}
 \tilde{R} &= \sum_{\alpha=1}^K \tilde{R}_{\alpha}(\mathbf{u}_{\alpha}, \boldsymbol{\varphi}_{\alpha}, \boldsymbol{\gamma}_{\alpha}, \boldsymbol{\varkappa}_{\alpha}, \mathbf{P}_{\alpha}, \boldsymbol{\mu}_{\alpha}, \mathbf{T}_{\alpha}, \boldsymbol{\mu}_{\alpha}^{(-)}, \boldsymbol{\varphi}_{\alpha}^{(-)}, \mathbf{P}_{\alpha}^{(-)}, \boldsymbol{\mu}_{\alpha}^{(-)}, \mathbf{u}_{\alpha}^{(+)}, \boldsymbol{\varphi}_{\alpha}^{(+)}, \mathbf{P}_{\alpha}^{(+)}, \boldsymbol{\mu}_{\alpha}^{(+)}) \\
 &= \sum_{\alpha=1}^K \iiint_V [\tilde{W}_{\alpha}(\boldsymbol{\gamma}_{\alpha}, \boldsymbol{\varkappa}_{\alpha}) - \mathbf{P}_{\alpha} \otimes (\boldsymbol{\gamma}_{\alpha} - \nabla_{\alpha} \mathbf{u}_{\alpha} + \mathbf{C}_{\alpha} \cdot \boldsymbol{\varphi}_{\alpha}) - \boldsymbol{\mu}_{\alpha} \otimes (\boldsymbol{\varkappa}_{\alpha} - \nabla_{\alpha} \boldsymbol{\varphi}_{\alpha}) \\
 &\quad - \rho_{\alpha} \mathbf{F}_{\alpha} \cdot \mathbf{u}_{\alpha} - \rho_{\alpha} \mathbf{G}_{\alpha} \cdot \boldsymbol{\varphi}_{\alpha}] dV_{\alpha} - \sum_{\alpha=1}^K \left\{ \iint_{\Sigma_{\alpha}^{(-)}} \mathbf{m}_{\alpha} \cdot [\mathbf{P}_{\alpha} \cdot (\mathbf{u}_{\alpha} - \mathbf{u}_{\alpha 0}) + \boldsymbol{\mu}_{\alpha} \cdot (\boldsymbol{\varphi}_{\alpha} - \boldsymbol{\varphi}_{\alpha 0})] d\Sigma_{\alpha}^{(-)} \right. \\
 &\quad \left. + \iint_{\Sigma_{\alpha}^{(+)}} (\mathbf{P}_{\alpha 0} \cdot \mathbf{u}_{\alpha} + \boldsymbol{\mu}_{\alpha 0} \cdot \boldsymbol{\varphi}_{\alpha}) d\Sigma_{\alpha}^{(+)} - \iint_{S_1^{(-)}} \mathbf{n}_1 \cdot [\mathbf{P}_1 \cdot (\mathbf{u}_1 - \mathbf{u}_1 0) + \boldsymbol{\mu}_1 \cdot (\boldsymbol{\varphi}_1 - \boldsymbol{\varphi}_1 0)] dS_1^{(-)} \right. \\
 &\quad \left. - \iint_{S_1^{(-)}} (\mathbf{P}_1 0 \cdot \mathbf{u}_1 + \boldsymbol{\mu}_1 0 \cdot \boldsymbol{\varphi}_1) dS_1^{(-)} - \iint_{S_K^{(+)}} \mathbf{n}_K \cdot [\mathbf{P}_K \cdot (\mathbf{u}_K - \mathbf{u}_K 0) + \boldsymbol{\mu}_K \cdot (\boldsymbol{\varphi}_K - \boldsymbol{\varphi}_K 0)] dS_K^{(+)} \right. \\
 &\quad \left. - \iint_{S_K^{(+)}} (\mathbf{P}_K 0 \cdot \mathbf{u}_K + \boldsymbol{\mu}_K 0 \cdot \boldsymbol{\varphi}_K) dS_K^{(+)} - \sum_{\alpha=1}^{K-1} \iint_{S_{\alpha}^{(+)}} \mathbf{T}_{\alpha} \cdot (\mathbf{u}_{\alpha}^{(+)} - \mathbf{u}_{\alpha+1}^{(-)}) + \boldsymbol{\mu}_{\alpha} \cdot (\boldsymbol{\varphi}_{\alpha}^{(+)} - \boldsymbol{\varphi}_{\alpha+1}^{(-)}) dS_{\alpha}^{(+)} \right\} \quad (11.147)
 \end{aligned}$$

Here, $S = S_{\alpha}^{(+)} = S_{\alpha+1}^{(-)}$ is the contact surface of the layers, $\alpha \in \overline{1, K-1}$, $\mathbf{T}_{\alpha} = \mathbf{T}_{\alpha}^{(+)} = -\mathbf{T}_{\alpha+1}^{(-)}$ is the vector of interlayer (contact) forces, and $\boldsymbol{\mu}_{\alpha} = \boldsymbol{\mu}_{\alpha}^{(+)} = -\boldsymbol{\mu}_{\alpha+1}^{(-)}$ is the vector of interlayer moments.

It should be noted that inside each volume V_{α} , $\alpha = \overline{1, K}$, it is changed the displacement and rotation vectors, the deformation and bending-torsion tensors, as well as stress and couple stress tensors, on Σ_1 , $\alpha = \overline{1, K}$, $S_1^{(-)}$ and $S_1^{(+)}$ are changed the stress and couple stress tensors, on Σ_2 , $\alpha = \overline{1, K}$, $S_2^{(-)}$ and $S_2^{(+)}$ are changed the displacement and rotation vectors, and on S_{α} are varied the vectors of contact displacements and rotations, as well as the vectors of contact forces and moments.

Further, similarly to the theory of one-layer thin bodies, we introduce the definitions:

Definition 11.6. A kinematic system is defined as arbitrary continuously differentiable vector fields \mathbf{u}_{α} (displacement vector of the α) and $\boldsymbol{\varphi}$ (rotation vector of the α layer), $\alpha = \overline{1, K}$, and a static system is defined as arbitrary tensor fields \mathbf{P}_{α} (stress tensor of the α layer) and $\boldsymbol{\mu}_{\alpha}$ (tensor of moment stresses of the α layer), $\alpha = \overline{1, K}$ (they are not necessary to satisfy the compatibility condition).

Definition 11.7. Kinematically admissible is a kinematic system that satisfies the kinematic boundary conditions

$$\mathbf{u}_{\alpha}|_{\Sigma_1} = \mathbf{u}_{\alpha 0}, \quad \boldsymbol{\varphi}_{\alpha}|_{\Sigma_1} = \boldsymbol{\varphi}_{\alpha 0}, \tag{11.148}$$

and in the case of a dynamic problem, kinematically admissible is a system that satisfies both the kinematic boundary conditions and the initial conditions

$$\mathbf{u}_{\alpha}|_{t=t_0} = \mathbf{f}_{\alpha 1}, \quad \boldsymbol{\varphi}_{\alpha}|_{t=t_0} = \mathbf{g}_{\alpha 1}, \quad \dot{\mathbf{u}}_{\alpha}|_{t=t_0} = \mathbf{f}_{\alpha 2}, \quad \dot{\boldsymbol{\varphi}}_{\alpha}|_{t=t_0} = \mathbf{g}_{\alpha 2}, \quad \alpha = \overline{1, K}. \tag{11.149}$$

Definition 11.8. Statically admissible is a static system that satisfies the equilibrium equations

$$\nabla_{\alpha} \cdot \mathbf{P}_{\alpha} + \rho_{\alpha} \mathbf{F} = 0, \quad \nabla_{\alpha} \cdot \boldsymbol{\mu}_{\alpha} + \mathbf{C}_{\alpha}^2 \otimes \mathbf{P}_{\alpha} + \rho_{\alpha} \mathbf{G} = 0, \quad \alpha = \overline{1, K} \tag{11.150}$$

or in the case of a dynamic problem it must satisfy the motion equations

$$\begin{aligned} \nabla_{\alpha} \cdot \mathbf{P}_{\alpha} + \rho_{\alpha} \mathbf{F} &= \rho_{\alpha} d\mathbf{v}/dt, \quad \mathbf{v}_{\alpha} = d\mathbf{u}_{\alpha}/dt, \\ \nabla_{\alpha} \cdot \boldsymbol{\mu}_{\alpha} + \mathbf{C}_{\alpha}^2 \otimes \mathbf{P}_{\alpha} + \rho_{\alpha} \mathbf{G} &= \mathbf{J}_{\alpha} \cdot d\boldsymbol{\omega}/dt, \quad \boldsymbol{\omega}_{\alpha} = \dot{\boldsymbol{\varphi}}_{\alpha} = d\boldsymbol{\varphi}_{\alpha}/dt, \quad \alpha = \overline{1, K} \end{aligned} \tag{11.151}$$

and static boundary conditions

$$\mathbf{n}_{\alpha} \cdot \mathbf{P}_{\alpha} = \mathbf{P}_{\alpha 0}, \quad \mathbf{n}_{\alpha} \cdot \boldsymbol{\mu}_{\alpha} = \boldsymbol{\mu}_{\alpha 0}, \quad \alpha = \overline{1, K}. \tag{11.152}$$

Definition 11.9. A real kinematic and static system in the case of a multilayer thin body is the set of displacement and rotation vectors (\mathbf{u}_α and $\boldsymbol{\varphi}_\alpha$, $\alpha = \overline{1, K}$) and stress and moment stress tensors (\mathbf{P}_α and $\boldsymbol{\mu}_\alpha$, $\alpha = \overline{1, K}$) of all layers of multilayer thin body, which satisfies the equilibrium equations (11.150) (or in the case of dynamic problem it must satisfy the motion equations (11.151)), kinematic relations

$$\boldsymbol{\gamma}_\alpha = \nabla_\alpha \mathbf{u}_\alpha - \mathbf{C}_\alpha \cdot \boldsymbol{\varphi}_\alpha, \quad \boldsymbol{\varkappa}_\alpha = \nabla_\alpha \boldsymbol{\varphi}_\alpha, \quad \alpha = \overline{1, K}, \quad (11.153)$$

constitutive relations

$$\mathbf{P}_\alpha = \check{F}_\alpha(\boldsymbol{\gamma}_\alpha, \boldsymbol{\varkappa}_\alpha), \quad \boldsymbol{\mu}_\alpha = \check{G}_\alpha(\boldsymbol{\gamma}_\alpha, \boldsymbol{\varkappa}_\alpha), \quad \alpha = \overline{1, K} \quad (11.154)$$

or at the existence of potential operators \check{F}_α and \check{G}_α , $\alpha = \overline{1, K}$, the system must satisfy the constitutive relations,

$$\mathbf{P}_\alpha = \partial \check{W}_\alpha / \partial \boldsymbol{\gamma}_\alpha, \quad \boldsymbol{\mu}_\alpha = \partial \check{W}_\alpha / \partial \boldsymbol{\varkappa}_\alpha, \quad \alpha = \overline{1, K}, \quad (11.155)$$

kinematic (11.148) and static (11.152) boundary conditions (in the case of dynamic problem it must also satisfy the initial conditions (11.149)), as well as interlayer contact conditions and boundary conditions on the front surfaces.

Here $\check{W}_\alpha(\boldsymbol{\gamma}_\alpha, \boldsymbol{\varkappa}_\alpha)$ is the operator of deformation and bending-torsion of the layer α , and if it exists, then the constitutive relations are given using the (11.155). Note that in nonisothermal processes, instead of $\check{W}_\alpha(\boldsymbol{\gamma}_\alpha, \boldsymbol{\varkappa}_\alpha)$, the free energy $\check{E}_\alpha(\boldsymbol{\gamma}_\alpha, \boldsymbol{\varkappa}_\alpha, \theta) = \check{W}_\alpha(\boldsymbol{\gamma}_\alpha, \boldsymbol{\varkappa}_\alpha) - H_\alpha T_\alpha$, is considered, where H_α is the entropy, T_α is the temperature, $\theta = T_\alpha - T_\alpha^0$ is the temperature drop of the α layer.

The generalized Reissner-type variational principle for a multilayer thin body can be formulated as: of all kinematic and static systems and systems described by the tensors $\boldsymbol{\gamma}_\alpha$ and $\boldsymbol{\varkappa}_\alpha$, $\alpha = \overline{1, K}$, only the operator for the real system (11.147) has a stationary value, i.e.

$$\begin{aligned} D\check{R} = & \\ = & \sum_{\alpha=1}^K D\check{R}_\alpha(\mathbf{u}_\alpha, \boldsymbol{\varphi}_\alpha, \boldsymbol{\gamma}_\alpha, \boldsymbol{\varkappa}_\alpha, \mathbf{P}_\alpha, \boldsymbol{\mu}_\alpha, \mathbf{T}_\alpha, \boldsymbol{\mu}_\alpha, \overset{(-)}{\mathbf{u}}_\alpha, \overset{(-)}{\boldsymbol{\varphi}}_\alpha, \overset{(-)}{\mathbf{P}}_\alpha, \overset{(-)}{\boldsymbol{\mu}}_\alpha, \overset{(+)}{\mathbf{u}}_\alpha, \overset{(+)}{\boldsymbol{\varphi}}_\alpha, \overset{(+)}{\mathbf{P}}_\alpha, \overset{(+)}{\boldsymbol{\mu}}_\alpha, \delta \mathbf{u}_\alpha, \delta \boldsymbol{\varphi}_\alpha, \\ & \delta \boldsymbol{\gamma}_\alpha, \delta \boldsymbol{\varkappa}_\alpha, \delta \mathbf{P}_\alpha, \delta \boldsymbol{\mu}_\alpha, \delta \mathbf{T}_\alpha, \delta \boldsymbol{\mu}_\alpha, \delta \overset{(-)}{\mathbf{u}}_\alpha, \delta \overset{(-)}{\boldsymbol{\varphi}}_\alpha, \delta \overset{(-)}{\mathbf{P}}_\alpha, \delta \overset{(-)}{\boldsymbol{\mu}}_\alpha, \delta \overset{(+)}{\mathbf{u}}_\alpha, \delta \overset{(+)}{\boldsymbol{\varphi}}_\alpha, \delta \overset{(+)}{\mathbf{P}}_\alpha, \delta \overset{(+)}{\boldsymbol{\mu}}_\alpha) = 0. \end{aligned} \quad (11.156)$$

Indeed, using the definition of the differential of the operator Pobedrya (1995) and the Ostrogradskii-Gauss theorem, by virtue of (11.147) and (11.153), the relation (11.156) will appear in the following form:

$$\begin{aligned}
D\tilde{R} &= \sum_{\alpha=1}^K D\tilde{R}_{\alpha} \\
&= \sum_{\alpha=1}^K \iiint_{V_{\alpha}} \left[(\partial\tilde{W}_{\alpha}/\partial\tilde{\boldsymbol{\gamma}} - \tilde{\mathbf{P}}_{\alpha}) \otimes \delta\tilde{\boldsymbol{\gamma}} + (\partial\tilde{W}_{\alpha}/\partial\tilde{\boldsymbol{\boldsymbol{\chi}}} - \tilde{\boldsymbol{\mu}}_{\alpha}) \otimes \delta\tilde{\boldsymbol{\boldsymbol{\chi}}} \right. \\
&\quad - (\nabla_{\alpha} \cdot \tilde{\mathbf{P}}_{\alpha} + \rho_{\alpha}\tilde{\mathbf{F}}) \cdot \delta\tilde{\mathbf{u}} - (\nabla_{\alpha} \cdot \tilde{\boldsymbol{\mu}}_{\alpha} + \tilde{\mathbf{C}}_{\alpha} \otimes \tilde{\mathbf{P}}_{\alpha} + \rho_{\alpha}\tilde{\mathbf{G}}) \cdot \delta\tilde{\boldsymbol{\varphi}} \\
&\quad \left. - (\tilde{\boldsymbol{\gamma}}_{\alpha} - \nabla_{\alpha}\tilde{\mathbf{u}} + \tilde{\mathbf{C}}_{\alpha} \cdot \tilde{\boldsymbol{\varphi}}) \otimes \delta\tilde{\mathbf{P}}_{\alpha} - (\tilde{\boldsymbol{\boldsymbol{\chi}}}_{\alpha} - \nabla_{\alpha}\tilde{\boldsymbol{\varphi}}) \otimes \delta\tilde{\boldsymbol{\mu}}_{\alpha} \right] dV_{\alpha} \\
&\quad - \sum_{\alpha=1}^K \left\{ \iint_{\Sigma_{\alpha}^1} \tilde{\mathbf{m}}_{\alpha} \cdot \left[\delta\tilde{\mathbf{P}}_{\alpha} \cdot (\tilde{\mathbf{u}}_{\alpha} - \tilde{\mathbf{u}}_0) + \delta\tilde{\boldsymbol{\mu}}_{\alpha} \cdot (\tilde{\boldsymbol{\varphi}}_{\alpha} - \tilde{\boldsymbol{\varphi}}_0) \right] d\Sigma_{\alpha}^1 \right. \\
&\quad \left. - \iint_{\Sigma_{\alpha}^2} \left[(\tilde{\mathbf{m}}_{\alpha} \cdot \tilde{\mathbf{P}}_{\alpha} - \tilde{\mathbf{P}}_0) \cdot \delta\tilde{\mathbf{u}} + (\tilde{\mathbf{m}}_{\alpha} \cdot \tilde{\boldsymbol{\mu}}_{\alpha} - \tilde{\boldsymbol{\mu}}_0) \cdot \delta\tilde{\boldsymbol{\varphi}} \right] d\Sigma_{\alpha}^2 \right\} \\
&\quad - \iint_{\overset{(-)}{S}_1} \left[\tilde{\mathbf{n}}_1^{(-)} \cdot \left[\delta\tilde{\mathbf{P}}_1^{(-)} \cdot (\tilde{\mathbf{u}}_1^{(-)} - \tilde{\mathbf{u}}_0) + \delta\tilde{\boldsymbol{\mu}}_1^{(-)} \cdot (\tilde{\boldsymbol{\varphi}}_1^{(-)} - \tilde{\boldsymbol{\varphi}}_0) \right] d\overset{(-)}{S}_1 \right. \\
&\quad \left. + \iint_{\overset{(-)}{S}_2} \left[(\tilde{\mathbf{n}}_1^{(-)} \cdot \tilde{\mathbf{P}}_1^{(-)} - \tilde{\mathbf{P}}_0) \cdot \delta\tilde{\mathbf{u}}_1^{(-)} + (\tilde{\mathbf{n}}_1^{(-)} \cdot \tilde{\boldsymbol{\mu}}_1^{(-)} - \tilde{\boldsymbol{\mu}}_0) \cdot \delta\tilde{\boldsymbol{\varphi}}_1^{(-)} \right] d\overset{(-)}{S}_2 \right. \\
&\quad \left. - \iint_{\overset{(+)}{K}^1} \tilde{\mathbf{n}}_K^{(+)} \cdot \left[\delta\tilde{\mathbf{P}}_K^{(+)} \cdot (\tilde{\mathbf{u}}_K^{(+)} - \tilde{\mathbf{u}}_0) + \delta\tilde{\boldsymbol{\mu}}_K^{(+)} \cdot (\tilde{\boldsymbol{\varphi}}_K^{(+)} - \tilde{\boldsymbol{\varphi}}_0) \right] d\overset{(+)}{S}_1 \right. \\
&\quad \left. + \iint_{\overset{(+)}{K}^2} \left[(\tilde{\mathbf{n}}_K^{(+)} \cdot \tilde{\mathbf{P}}_K^{(+)} - \tilde{\mathbf{P}}_0) \cdot \delta\tilde{\mathbf{u}}_K^{(+)} + (\tilde{\mathbf{n}}_K^{(+)} \cdot \tilde{\boldsymbol{\mu}}_K^{(+)} - \tilde{\boldsymbol{\mu}}_0) \cdot \delta\tilde{\boldsymbol{\varphi}}_K^{(+)} \right] d\overset{(+)}{S}_2 \right. \\
&\quad - \sum_{\alpha=1}^{K-1} \iint_{\overset{(-)}{S}_{\alpha+1}} \left[(\tilde{\mathbf{u}}_{\alpha}^{(+)} - \tilde{\mathbf{u}}_{\alpha+1}^{(-)}) \cdot \delta\tilde{\mathbf{T}}_{\alpha} + (\tilde{\boldsymbol{\varphi}}_{\alpha}^{(+)} - \tilde{\boldsymbol{\varphi}}_{\alpha+1}^{(-)}) \cdot \delta\tilde{\boldsymbol{\mu}}_{\alpha} \right] d\overset{(-)}{S}_{\alpha} \\
&\quad + \sum_{\alpha=1}^{K-1} \iint_{\overset{(+)}{S}_{\alpha}} \left[(\tilde{\mathbf{n}}_{\alpha}^{(+)} \cdot \tilde{\mathbf{P}}_{\alpha}^{(+)} - \tilde{\mathbf{T}}_{\alpha}) \cdot \delta\tilde{\mathbf{u}}_{\alpha}^{(+)} + (\tilde{\mathbf{n}}_{\alpha}^{(+)} \cdot \tilde{\boldsymbol{\mu}}_{\alpha}^{(+)} - \tilde{\boldsymbol{\mu}}_{\alpha}^{(+)}) \cdot \delta\tilde{\boldsymbol{\varphi}}_{\alpha}^{(+)} \right. \\
&\quad \left. + (\tilde{\mathbf{n}}_{\alpha+1}^{(-)} \cdot \tilde{\mathbf{P}}_{\alpha+1}^{(-)} + \tilde{\mathbf{T}}_{\alpha}) \cdot \delta\tilde{\mathbf{u}}_{\alpha+1}^{(-)} + (\tilde{\mathbf{n}}_{\alpha+1}^{(-)} \cdot \tilde{\boldsymbol{\mu}}_{\alpha+1}^{(-)} + \tilde{\boldsymbol{\mu}}_{\alpha}^{(-)}) \cdot \delta\tilde{\boldsymbol{\varphi}}_{\alpha+1}^{(-)} \right] d\overset{(-)}{S}_{\alpha} = 0.
\end{aligned} \tag{11.157}$$

It is easy to see that due to the arbitrariness of the variations $\delta\tilde{\mathbf{u}}_{\alpha}$, $\delta\tilde{\boldsymbol{\varphi}}_{\alpha}$, $\delta\tilde{\boldsymbol{\gamma}}_{\alpha}$, $\delta\tilde{\boldsymbol{\boldsymbol{\chi}}}_{\alpha}$, $\delta\tilde{\mathbf{P}}_{\alpha}$,

$\delta\tilde{\boldsymbol{\mu}}_{\alpha}$, $\delta\tilde{\mathbf{T}}_{\alpha}$, $\delta\tilde{\boldsymbol{\mu}}_{\alpha}$, $\delta\tilde{\mathbf{u}}_{\alpha}^{(-)}$, $\delta\tilde{\boldsymbol{\varphi}}_{\alpha}^{(-)}$, $\delta\tilde{\mathbf{P}}_{\alpha}^{(-)}$, $\delta\tilde{\boldsymbol{\mu}}_{\alpha}^{(-)}$, $\delta\tilde{\mathbf{u}}_{\alpha}^{(+)}$, $\delta\tilde{\boldsymbol{\varphi}}_{\alpha}^{(+)}$, $\delta\tilde{\mathbf{P}}_{\alpha}^{(+)}$ and $\delta\tilde{\boldsymbol{\mu}}_{\alpha}^{(+)}$, $\alpha = \overline{1, K}$, from (11.157)

implies the equilibrium equations (11.150), the constitutive relations (11.155), the kinematic relations (11.153), the kinematic (11.148) and static (11.152) boundary

conditions on the lateral face, as well as the kinematic and static boundary conditions

$$\begin{aligned} \overset{(-)}{\mathbf{u}}_1 &= \overset{(-)}{\mathbf{u}}_0, \quad \overset{(-)}{\boldsymbol{\varphi}}_1 = \overset{(-)}{\boldsymbol{\varphi}}_0 \quad \text{on} \quad \overset{(-)}{S}_1, \quad \overset{(-)}{\mathbf{n}}_1 \cdot \overset{(-)}{\mathbf{P}}_1 = \overset{(-)}{\mathbf{P}}_0, \quad \overset{(-)}{\mathbf{n}}_1 \cdot \overset{(-)}{\boldsymbol{\mu}}_1 = \overset{(-)}{\boldsymbol{\mu}}_0 \quad \text{on} \quad \overset{(-)}{S}_2, \\ \overset{(+)}{\mathbf{u}}_K &= \overset{(+)}{\mathbf{u}}_0, \quad \overset{(+)}{\boldsymbol{\varphi}}_K = \overset{(+)}{\boldsymbol{\varphi}}_0 \quad \text{on} \quad \overset{(+)}{S}_1, \quad \overset{(+)}{\mathbf{n}}_K \cdot \overset{(+)}{\mathbf{P}}_K = \overset{(+)}{\mathbf{P}}_0, \quad \overset{(+)}{\mathbf{n}}_K \cdot \overset{(+)}{\boldsymbol{\mu}}_K = \overset{(+)}{\boldsymbol{\mu}}_0 \quad \text{on} \quad \overset{(+)}{S}_2 \end{aligned} \quad (11.158)$$

on the front surfaces, and conditions on the interlayer boundaries (ideal contact conditions)

$$\begin{aligned} \overset{(+)}{\mathbf{u}}_\alpha &= \overset{(-)}{\mathbf{u}}_{\alpha+1}, \quad \overset{(+)}{\boldsymbol{\varphi}}_\alpha = \overset{(-)}{\boldsymbol{\varphi}}_{\alpha+1}, \quad \mathbf{T}_\alpha = \overset{(+)}{\mathbf{n}}_\alpha \cdot \overset{(+)}{\tilde{\boldsymbol{\mu}}}_\alpha = - \overset{(-)}{\mathbf{n}}_{\alpha+1} \cdot \overset{(-)}{\tilde{\boldsymbol{\mu}}}_{\alpha+1}, \\ \boldsymbol{\mu}_\alpha &= \overset{(+)}{\mathbf{n}}_\alpha \cdot \overset{(+)}{\boldsymbol{\mu}}_\alpha = - \overset{(-)}{\mathbf{n}}_{\alpha+1} \cdot \overset{(-)}{\boldsymbol{\mu}}_{\alpha+1} \quad \hat{\mathbf{n}}_\alpha \cdot \overset{(-)}{S}_\alpha, \quad \alpha = \overline{1, K-1}. \end{aligned} \quad (11.159)$$

Note that using the Legendre-type identity (11.46) one can obtain the generalized Reissner-type operator dual to the operator (11.147), and then from it one can derive the generalized Reissner-type principle dual to the principle (11.157). Based on the above, it is not difficult to consider these issues, as well as to formulate other variational principles. In this regard, we will not dwell on them.

11.9 Generalized Reissner-Type Variational Principle in the Micropolar Theory of Multilayer Thin Bodies with One Small Size in the Case of Domains of Weakened Adhesion

Before formulating this principle, let us consider some issues related to multilayer thin bodies if there are domains (or zones) of weakened adhesion. Generally, if on some parts of the interlayer boundaries during deformation of a multilayer thin body there is a violation of full (or ideal) contact, then it is said that we are dealing with a multilayer thin body with weakened adhesion (or having domains of weakened adhesion). If there are domains of weakened adhesion in interphase boundaries of the multilayer thin body, then the issue of modeling the interface (or interphase boundary) becomes to be important. There are two approaches in this direction Pelekh and Korovaichuk (1984). First, the physical approach is associated in view of certain properties of interfacial adhesion layers. Apparently, this approach was first proposed for heat conduction problems in Podstrigach (1963). Later it was generalized to problems of mechanics Podstrigach (1982). The second one is a phenomenological approach based on the representation of the interface as a surface of zero thickness which separates the volume components (such as phases, layers), and on the postulation of the existence of jumps (i.e., discontinuities) of the displacement and rotation vectors, as well as stress and couple stress vectors in zones of weakened adhesion. For these approaches, the following models are considered: a) a jump-type

model (in the case of describing the interface by a surface of zero thickness); b) a model of a smooth transition (in case of the presence of interphase layers between interacting layers); c) a model of the reduced interphase characteristics.

In the case of the first two models, the main parameters are the vectors of mutual displacements and rotations of adjacent layers (or phases). In the classical theory, of course, only vectors of mutual displacements of adjacent phases are considered. The third model is characterized by the introduction of some coefficients that reflect the effect of weakened adhesion and the named fullness coefficients of interfacial contact. Below we will consider in detail the jump-type model.

11.9.1 *Jump-Type Model. Interphase (Interlayer) Displacements and Rotation Vectors. Vectors of Generalized Interfacial Forces and Moments*

In the presence of domains of weakened adhesion it is advisable to introduce vectors of interfacial (or relative) displacements and rotations, i.e. $\mathbf{v}_\alpha(x')$ and $\boldsymbol{\psi}_\alpha(x')$ respectively, where $x' \in S_\alpha \subset S_\alpha$, S_α is the domain of weakened adhesion, $\alpha = \overline{1, K-1}$, and K is the number of layers. However, for a complete description of this model, it is necessary to consider the state parameters corresponding to the vectors of mutual displacements and rotations, namely, the vectors of interphase (generally speaking, dissipative) forces \mathbf{P}_α and moments \mathbf{Q}_α ($\alpha = \overline{1, K-1}$) in domains of weakened adhesion. Further, we omit the index under the vectors of interphase displacements, rotations, forces, moments and quantities related to this subsection, since all the relations obtained below will be valid also if the index α is preserved.

From physical reasons, the sum of the work of the interphase forces \mathbf{P} and moments \mathbf{Q} on the corresponding vectors of mutual displacements $\mathbf{v}(x')$ and rotations $\boldsymbol{\psi}(x')$ of adjacent phases must be non-negative, that is

$$\mathbf{P} \cdot \mathbf{v} + \mathbf{Q} \cdot \boldsymbol{\psi} \geq 0 \quad (11.160)$$

for any vectors \mathbf{v} and $\boldsymbol{\psi}$, provided that at least one of them is nonzero.

Note that if we are considering a non-stationary process, then instead of \mathbf{v} and $\boldsymbol{\psi}$, we should write $\dot{\mathbf{v}} = \partial_t \mathbf{v}$ and $\dot{\boldsymbol{\psi}} = \partial_t \boldsymbol{\psi}$ respectively.

From (11.160) it follows that the vectors of interphase forces \mathbf{P} and moments \mathbf{Q} must be functions of vectors of mutual displacements $\mathbf{v}(x')$ and rotations $\boldsymbol{\psi}(x')$ of adjacent phases, as well as some other parameters, namely, temperature, contact pressure, coefficient of friction and etc., i.e.

$$\mathbf{P} = \mathbf{P}(\mathbf{v}, \boldsymbol{\psi}, \dots), \quad \mathbf{Q} = \mathbf{Q}(\mathbf{v}, \boldsymbol{\psi}, \dots), \quad (11.161)$$

where three dots denotes dependence on other parameters. In the case of potential vectors \mathbf{P} and \mathbf{Q} there is a dissipative potential (or dissipative operator) $\tilde{\chi}(\mathbf{v}, \boldsymbol{\psi})$ of vectors of mutual displacement $\mathbf{v}(x')$ and rotation $\boldsymbol{\psi}(x')$ of adjacent phases, by

means of which \mathbf{P} and \mathbf{Q} are defined by the formulas

$$\mathbf{P} = \frac{\partial \tilde{\chi}}{\partial \mathbf{v}}, \quad \mathbf{Q} = \frac{\partial \tilde{\chi}}{\partial \boldsymbol{\psi}}. \quad (11.162)$$

From (11.162) it follows that the conditions in the domains of weakened adhesion are based on the construction or choice of the dissipative operator $\tilde{\chi}(\mathbf{v}, \boldsymbol{\psi})$, which expresses the interaction mechanism in these domains.

Let us consider some possible special cases of defining the operator $\tilde{\chi}(\mathbf{v}, \boldsymbol{\psi})$, corresponding to different conditions of phase interaction. In this regard, expanding $\tilde{\chi}(\mathbf{v}, \boldsymbol{\psi})$ in the Maclaurain's series in a neighborhood of the point $\mathbf{v} = 0$ and $\boldsymbol{\psi} = 0$ and neglecting the terms containing \mathbf{v} and $\boldsymbol{\psi}$ higher than the second degree, taking into account $\tilde{\chi}(0, 0) = 0$ we get

$$\begin{aligned} \tilde{\chi}(\mathbf{v}, \boldsymbol{\psi}) = & \left(\frac{\partial \tilde{\chi}}{\partial \mathbf{v}} \right)_0 \cdot \mathbf{v} + \left(\frac{\partial \tilde{\chi}}{\partial \boldsymbol{\psi}} \right)_0 \cdot \boldsymbol{\psi} \\ & + \frac{1}{2} \left\{ \left(\frac{\partial^2 \tilde{\chi}}{\partial \mathbf{v}^2} \right)_0 \otimes \mathbf{v} \mathbf{v} + \left[\left(\frac{\partial^2 \tilde{\chi}}{\partial \mathbf{v} \partial \boldsymbol{\psi}} \right)_0 + \left(\frac{\partial^2 \tilde{\chi}}{\partial \boldsymbol{\psi} \partial \mathbf{v}} \right)_0^T \right] \otimes \mathbf{v} \boldsymbol{\psi} + \left(\frac{\partial^2 \tilde{\chi}}{\partial \boldsymbol{\psi}^2} \right)_0 \otimes \boldsymbol{\psi} \boldsymbol{\psi} \right\}. \end{aligned}$$

Hence, introducing the notation

$$\begin{aligned} \mathbf{a} = & \left(\frac{\partial \tilde{\chi}}{\partial \mathbf{v}} \right)_0, \quad \mathbf{b} = \left(\frac{\partial \tilde{\chi}}{\partial \boldsymbol{\psi}} \right)_0, \quad \mathbf{f} = \left(\frac{\partial^2 \tilde{\chi}}{\partial \mathbf{v}^2} \right)_0, \\ \underline{\mathbf{g}} = & \left(\frac{\partial^2 \tilde{\chi}}{\partial \mathbf{v} \partial \boldsymbol{\psi}} \right)_0 + \left(\frac{\partial^2 \tilde{\chi}}{\partial \boldsymbol{\psi} \partial \mathbf{v}} \right)_0^T, \quad \underline{\mathbf{h}} = \left(\frac{\partial^2 \tilde{\chi}}{\partial \boldsymbol{\psi}^2} \right)_0, \end{aligned}$$

we will have

$$\tilde{\chi}(\mathbf{v}, \boldsymbol{\psi}) = \mathbf{a} \cdot \mathbf{v} + \mathbf{b} \cdot \boldsymbol{\psi} + \frac{1}{2} (\underline{\mathbf{f}} \otimes \mathbf{v} \mathbf{v} + 2 \underline{\mathbf{g}} \otimes \mathbf{v} \boldsymbol{\psi} + \underline{\mathbf{h}} \otimes \boldsymbol{\psi} \boldsymbol{\psi}). \quad (11.163)$$

1. If $\tilde{\chi}(\mathbf{v}, \boldsymbol{\psi}) = 0$, then adjacent phases do not interact, which corresponds to the complete absence of conjunction. In this case, the parameters that characterize the weakening of the interphase contact are the vectors of mutual displacements $\mathbf{v}(x')$ and rotations $\boldsymbol{\psi}(x')$ of adjacent phases.
2. If $\tilde{\chi}(\mathbf{v}, \boldsymbol{\psi})$ is a linear function with respect to $\mathbf{v}(x')$ and $\boldsymbol{\psi}(x')$, then from (11.163) we have

$$\tilde{\chi}(\mathbf{v}, \boldsymbol{\psi}) = \mathbf{a} \cdot \mathbf{v} + \mathbf{b} \cdot \boldsymbol{\psi}. \quad (11.164)$$

In this case, new parameters \mathbf{a} and \mathbf{b} of weakened adhesion appear. In the particular case, when $\mathbf{a} = a_s \mathbf{s}$ and $\mathbf{b} = b_n \mathbf{n}$, where \mathbf{s} and \mathbf{n} are the unit vectors of the tangent and normal to the interface, a_s and b_n are the coefficients that characterize the status of conjunction in areas of weakened adhesion. Note that according to (11.164), from (11.162) we find $\mathbf{P} = \mathbf{a}$ and $\mathbf{Q} = \mathbf{b}$.

3. If $\tilde{\chi}(\mathbf{v}, \boldsymbol{\psi})$ is a homogeneous quadratic form with respect to $\mathbf{v}(x')$ and $\boldsymbol{\psi}(x')$, then from (11.163) we get

$$\check{\chi}(\mathbf{v}, \boldsymbol{\psi}) = \frac{1}{2}(\underline{\mathbf{f}} \otimes \mathbf{v}\mathbf{v} + 2\underline{\mathbf{g}} \otimes \mathbf{v}\boldsymbol{\psi} + \underline{\mathbf{h}} \otimes \boldsymbol{\psi}\boldsymbol{\psi}). \quad (11.165)$$

In view of (11.165), from (11.162) we will have

$$\mathbf{P} = \underline{\mathbf{f}} \cdot \mathbf{v} + \underline{\mathbf{g}} \cdot \boldsymbol{\psi}, \quad \mathbf{Q} = \underline{\mathbf{g}} \cdot \mathbf{v} + \underline{\mathbf{h}} \cdot \boldsymbol{\psi}. \quad (11.166)$$

Here $\underline{\mathbf{f}}$, $\underline{\mathbf{g}}$, $\underline{\mathbf{h}}$ are symmetric tensors of the second rank, called tensors of friction coefficients. They can depend on the coordinates x^1, x^2 , the temperature drop, the normal component of the limiting stress vector, and other parameters. Obviously, the formulas (11.166) take into account the inhomogeneity and anisotropy of friction. Therefore, in the case of isotropic friction, $\underline{\mathbf{f}}$, $\underline{\mathbf{g}}$, $\underline{\mathbf{h}}$ are spherical tensors.

Note that we can consider other cases of the representation $\check{\chi}(\mathbf{v}, \boldsymbol{\psi})$, which we will not dwell on in order to shorten the letter. Note also that in the case of a multilayer thin body, for example, instead of (11.163) we will have

$$\check{\chi} = \sum_{\alpha=1}^K \check{\chi}_{\alpha}(\mathbf{v}_{\alpha}, \boldsymbol{\psi}_{\alpha}), \quad \check{\chi}_{\alpha}(\mathbf{v}_{\alpha}, \boldsymbol{\psi}_{\alpha}) = \mathbf{a}_{\alpha} \cdot \mathbf{v}_{\alpha} + \mathbf{b}_{\alpha} \cdot \boldsymbol{\psi}_{\alpha} + \frac{1}{2}(\underline{\mathbf{f}}_{\alpha} \otimes \mathbf{v}_{\alpha}\mathbf{v}_{\alpha} + 2\underline{\mathbf{g}}_{\alpha} \otimes \mathbf{v}_{\alpha}\boldsymbol{\psi}_{\alpha} + \underline{\mathbf{h}}_{\alpha} \otimes \boldsymbol{\psi}_{\alpha}\boldsymbol{\psi}_{\alpha}). \quad (11.167)$$

Therefore, similarly to (11.167), we can represent other relationships given above. However, we will not dwell on them in order to shorten the letter.

Let us now return to the variational principle if there are domains of weakened adhesion and formulate it. It is easy to see that in this case, similarly to (11.147), the generalized Reissner-type operator (generalized functional) will have the form

$$\begin{aligned} \check{R}^* &= \sum_{\alpha=1}^K \check{R}_{\alpha}^*(\mathbf{u}_{\alpha}, \boldsymbol{\varphi}_{\alpha}, \boldsymbol{\gamma}_{\alpha}, \boldsymbol{\varkappa}_{\alpha}, \underline{\mathbf{P}}_{\alpha}, \underline{\boldsymbol{\mu}}_{\alpha}, \mathbf{T}_{\alpha}, \underline{\boldsymbol{\mu}}_{\alpha}, \mathbf{P}_{\alpha}, \mathbf{Q}_{\alpha}, \overset{(-)}{\mathbf{u}}_{\alpha}, \overset{(-)}{\boldsymbol{\varphi}}_{\alpha}, \overset{(-)}{\underline{\mathbf{P}}}_{\alpha}, \overset{(-)}{\underline{\boldsymbol{\mu}}}_{\alpha}, \overset{(+)}{\mathbf{u}}_{\alpha}, \overset{(+)}{\boldsymbol{\varphi}}_{\alpha}, \overset{(+)}{\underline{\mathbf{P}}}_{\alpha}, \overset{(+)}{\underline{\boldsymbol{\mu}}}_{\alpha}) \\ &= \sum_{\alpha=1}^K \iiint_{V_{\alpha}} [\check{W}_{\alpha}(\boldsymbol{\gamma}_{\alpha}, \boldsymbol{\varkappa}_{\alpha}) - \underline{\mathbf{P}}_{\alpha} \otimes (\boldsymbol{\gamma}_{\alpha} - \nabla_{\alpha} \mathbf{u}_{\alpha} + \mathbf{C}_{\alpha} \cdot \boldsymbol{\varphi}_{\alpha}) - \underline{\boldsymbol{\mu}}_{\alpha} \otimes (\boldsymbol{\varkappa}_{\alpha} - \nabla_{\alpha} \boldsymbol{\varphi}_{\alpha}) - \rho_{\alpha} \mathbf{F}_{\alpha} \cdot \mathbf{u}_{\alpha} - \rho_{\alpha} \mathbf{G}_{\alpha} \cdot \boldsymbol{\varphi}_{\alpha}] dV_{\alpha} \\ &\quad - \sum_{\alpha=1}^K \left\{ \iint_{\Sigma_{\alpha}^1} \mathbf{m}_{\alpha} \cdot \left[\underline{\mathbf{P}}_{\alpha} \cdot (\mathbf{u}_{\alpha} - \mathbf{u}_{\alpha 0}) + \underline{\boldsymbol{\mu}}_{\alpha} \cdot (\boldsymbol{\varphi}_{\alpha} - \boldsymbol{\varphi}_{\alpha 0}) \right] d\Sigma_{\alpha}^1 + \iint_{\Sigma_{\alpha}^2} (\mathbf{P}_{\alpha 0} \cdot \mathbf{u}_{\alpha} + \boldsymbol{\mu}_{\alpha 0} \cdot \boldsymbol{\varphi}_{\alpha}) d\Sigma_{\alpha}^2 \right\} \\ &\quad - \iint_{\overset{(-)}{S}_1^1} \overset{(-)}{\mathbf{n}}_1 \cdot \left[\overset{(-)}{\underline{\mathbf{P}}}_1 \cdot (\overset{(-)}{\mathbf{u}}_1 - \overset{(-)}{\mathbf{u}}_{10}) + \overset{(-)}{\underline{\boldsymbol{\mu}}}_1 \cdot (\overset{(-)}{\boldsymbol{\varphi}}_1 - \overset{(-)}{\boldsymbol{\varphi}}_{10}) \right] d\overset{(-)}{S}_1^1 - \iint_{\overset{(-)}{S}_2^1} (\overset{(-)}{\mathbf{P}}_{10} \cdot \overset{(-)}{\mathbf{u}}_1 + \overset{(-)}{\boldsymbol{\mu}}_{10} \cdot \overset{(-)}{\boldsymbol{\varphi}}_1) d\overset{(-)}{S}_2^1 \\ &\quad - \iint_{\overset{(+)}{S}_K^1} \overset{(+)}{\mathbf{n}}_K \cdot \left[\overset{(+)}{\underline{\mathbf{P}}}_K \cdot (\overset{(+)}{\mathbf{u}}_K - \overset{(+)}{\mathbf{u}}_{K0}) + \overset{(+)}{\underline{\boldsymbol{\mu}}}_K \cdot (\overset{(+)}{\boldsymbol{\varphi}}_K - \overset{(+)}{\boldsymbol{\varphi}}_{K0}) \right] d\overset{(+)}{S}_K^1 - \iint_{\overset{(+)}{S}_K^2} (\overset{(+)}{\mathbf{P}}_{K0} \cdot \overset{(+)}{\mathbf{u}}_K + \overset{(+)}{\boldsymbol{\mu}}_{K0} \cdot \overset{(+)}{\boldsymbol{\varphi}}_K) d\overset{(+)}{S}_K^2 \\ &\quad - \sum_{\alpha=1}^{K-1} \iint_{\overset{(-)}{S}_{\alpha+1}^{(i)}} \left[\mathbf{T}_{\alpha} \cdot (\overset{(+)}{\mathbf{u}}_{\alpha} - \overset{(-)}{\mathbf{u}}_{\alpha+1}) + \underline{\boldsymbol{\mu}}_{\alpha} \cdot (\overset{(+)}{\boldsymbol{\varphi}}_{\alpha} - \overset{(-)}{\boldsymbol{\varphi}}_{\alpha+1}) \right] d\overset{(-)}{S}_{\alpha}^{(i)} \end{aligned}$$

$$+ \sum_{\alpha=1}^{K-1} \iint_{S_{\alpha}^0} \left[\check{\chi}_{\alpha}(\mathbf{v}_{\alpha}, \boldsymbol{\psi}) - \mathbf{P}_{\alpha} \cdot (\mathbf{v}_{\alpha} - \overset{+}{\mathbf{u}}_{\alpha} + \overset{-}{\mathbf{u}}_{\alpha+1}) - \mathbf{Q}_{\alpha} \cdot (\boldsymbol{\psi}_{\alpha} - \overset{+}{\boldsymbol{\varphi}}_{\alpha} + \overset{-}{\boldsymbol{\varphi}}_{\alpha+1}) \right] dS_{\alpha}^0, \quad (11.168)$$

where $S_{\alpha} = S_{\alpha}^0 \cup S_{\alpha}^{(i)}$, $S_{\alpha}^0 \cap S_{\alpha}^{(i)} = \emptyset$, $\alpha = \overline{1, K-1}$, S_{α}^0 is the domain of weakened adhesion, and $S_{\alpha}^{(i)}$ is the domain of ideal adhesion (perfect contact).

The stationarity condition for the operator (11.168), similarly to (11.157), can be represented as

$$\begin{aligned} D\check{R}^* = & \sum_{\alpha=1}^K \iiint_{V_{\alpha}} \left[(\partial \check{W}_{\alpha} / \partial \boldsymbol{\gamma} - \mathbf{P}_{\alpha}) \otimes \delta \boldsymbol{\gamma} + (\partial \check{W}_{\alpha} / \partial \boldsymbol{\varkappa} - \boldsymbol{\mu}_{\alpha}) \otimes \delta \boldsymbol{\varkappa} - (\nabla_{\alpha} \cdot \mathbf{P}_{\alpha} + \rho_{\alpha} \mathbf{F}) \cdot \delta \mathbf{u}_{\alpha} \right. \\ & - (\nabla_{\alpha} \cdot \boldsymbol{\mu}_{\alpha} + \mathbf{C}_{\alpha} \otimes \mathbf{P}_{\alpha} + \rho_{\alpha} \mathbf{G}) \cdot \delta \boldsymbol{\varphi}_{\alpha} - (\boldsymbol{\gamma}_{\alpha} - \nabla_{\alpha} \mathbf{u}_{\alpha} + \mathbf{C}_{\alpha} \cdot \boldsymbol{\varphi}_{\alpha}) \otimes \delta \mathbf{P}_{\alpha} - (\boldsymbol{\varkappa}_{\alpha} - \nabla_{\alpha} \boldsymbol{\varphi}_{\alpha}) \otimes \delta \boldsymbol{\mu}_{\alpha} \Big] dV_{\alpha} \\ & - \sum_{\alpha=1}^K \left\{ \iint_{\Sigma_{\alpha}^1} \mathbf{m}_{\alpha} \cdot \left[\delta \mathbf{P}_{\alpha} \cdot (\mathbf{u}_{\alpha} - \mathbf{u}_{\alpha 0}) + \delta \boldsymbol{\mu}_{\alpha} \cdot (\boldsymbol{\varphi}_{\alpha} - \boldsymbol{\varphi}_{\alpha 0}) \right] d\Sigma_{\alpha}^1 \right. \\ & - \iint_{\Sigma_{\alpha}^2} \left[(\mathbf{m}_{\alpha} \cdot \mathbf{P}_{\alpha} - \mathbf{P}_{\alpha 0}) \cdot \delta \mathbf{u}_{\alpha} + (\mathbf{m}_{\alpha} \cdot \boldsymbol{\mu}_{\alpha} - \boldsymbol{\mu}_{\alpha 0}) \cdot \delta \boldsymbol{\varphi}_{\alpha} \right] d\Sigma_{\alpha}^2 \Big\} \\ & - \iint_{\overset{(-)}{S}_1} \overset{(-)}{\mathbf{n}}_1 \cdot \left[\delta \overset{(-)}{\mathbf{P}}_1 \cdot (\overset{(-)}{\mathbf{u}}_1 - \overset{(-)}{\mathbf{u}}_{10}) + \delta \overset{(-)}{\boldsymbol{\mu}}_1 \cdot (\overset{(-)}{\boldsymbol{\varphi}}_1 - \overset{(-)}{\boldsymbol{\varphi}}_{10}) \right] d\overset{(-)}{S}_1 \\ & + \iint_{\overset{(-)}{S}_2} \left[(\overset{(-)}{\mathbf{n}}_1 \cdot \overset{(-)}{\mathbf{P}}_1 - \overset{(-)}{\mathbf{P}}_{10}) \cdot \delta \overset{(-)}{\mathbf{u}}_1 + (\overset{(-)}{\mathbf{n}}_1 \cdot \overset{(-)}{\boldsymbol{\mu}}_1 - \overset{(-)}{\boldsymbol{\mu}}_{10}) \cdot \delta \overset{(-)}{\boldsymbol{\varphi}}_1 \right] d\overset{(-)}{S}_2 \\ & - \iint_{\overset{(+)}{S}_1} \overset{(+)}{\mathbf{n}}_K \cdot \left[\delta \overset{(+)}{\mathbf{P}}_K \cdot (\overset{(+)}{\mathbf{u}}_K - \overset{(+)}{\mathbf{u}}_{K0}) + \delta \overset{(+)}{\boldsymbol{\mu}}_K \cdot (\overset{(+)}{\boldsymbol{\varphi}}_K - \overset{(+)}{\boldsymbol{\varphi}}_{K0}) \right] d\overset{(+)}{S}_1 \\ & + \iint_{\overset{(+)}{S}_2} \left[(\overset{(+)}{\mathbf{n}}_K \cdot \overset{(+)}{\mathbf{P}}_K - \overset{(+)}{\mathbf{P}}_{K0}) \cdot \delta \overset{(+)}{\mathbf{u}}_K + (\overset{(+)}{\mathbf{n}}_K \cdot \overset{(+)}{\boldsymbol{\mu}}_K - \overset{(+)}{\boldsymbol{\mu}}_{K0}) \cdot \delta \overset{(+)}{\boldsymbol{\varphi}}_K \right] d\overset{(+)}{S}_2 \\ & - \sum_{\alpha=1}^{K-1} \iint_{S_{\alpha}^{(i)}} \left[(\overset{+}{\mathbf{u}}_{\alpha} - \overset{-}{\mathbf{u}}_{\alpha+1}) \cdot \delta \mathbf{T}_{\alpha} + (\overset{+}{\boldsymbol{\varphi}}_{\alpha} - \overset{-}{\boldsymbol{\varphi}}_{\alpha+1}) \cdot \delta \boldsymbol{\mu}_{\alpha} \right] dS_{\alpha}^{(i)} \\ & + \sum_{\alpha=1}^{K-1} \iint_{S_{\alpha}^{(i)}} \left[(\overset{+}{\mathbf{n}}_{\alpha} \cdot \overset{+}{\mathbf{P}}_{\alpha} - \mathbf{T}_{\alpha}) \cdot \delta \overset{+}{\mathbf{u}}_{\alpha} + (\overset{+}{\mathbf{n}}_{\alpha} \cdot \overset{+}{\boldsymbol{\mu}}_{\alpha} - \boldsymbol{\mu}_{\alpha}) \cdot \delta \overset{+}{\boldsymbol{\varphi}}_{\alpha} \right. \\ & \left. + (\overset{-}{\mathbf{n}}_{\alpha+1} \cdot \overset{-}{\mathbf{P}}_{\alpha+1} + \mathbf{T}_{\alpha}) \cdot \delta \overset{-}{\mathbf{u}}_{\alpha+1} + (\overset{-}{\mathbf{n}}_{\alpha+1} \cdot \overset{-}{\boldsymbol{\mu}}_{\alpha+1} + \boldsymbol{\mu}_{\alpha}) \cdot \delta \overset{-}{\boldsymbol{\varphi}}_{\alpha+1} \right] dS_{\alpha}^{(i)} \end{aligned}$$

$$\begin{aligned}
& - \sum_{\alpha=1}^{K-1} \iint_{S_{\alpha}^0} \left[(\partial \tilde{\chi}_{\alpha} / \partial \mathbf{v}_{\alpha} - \mathbf{P}_{\alpha}) \cdot \delta \mathbf{v}_{\alpha} + (\partial \tilde{\chi}_{\alpha} / \partial \boldsymbol{\psi}_{\alpha} - \mathbf{Q}_{\alpha}) \cdot \delta \boldsymbol{\psi}_{\alpha} \right. \\
& \quad \left. + (\mathbf{v}_{\alpha} - \tilde{\mathbf{u}}_{\alpha}^{(+)} + \tilde{\mathbf{u}}_{\alpha+1}^{(-)}) \cdot \delta \mathbf{P}_{\alpha} + (\boldsymbol{\psi}_{\alpha} - \tilde{\boldsymbol{\varphi}}_{\alpha}^{(+)} + \tilde{\boldsymbol{\varphi}}_{\alpha+1}^{(-)}) \cdot \delta \mathbf{Q}_{\alpha} \right] dS_{\alpha}^0 \\
& \quad + \sum_{\alpha=1}^{K-1} \iint_{S_{\alpha}^0} \left[(\tilde{\mathbf{n}}_{\alpha}^{(+)} \cdot \tilde{\mathbf{P}}_{\alpha} + \mathbf{P}_{\alpha}) \cdot \delta \tilde{\mathbf{u}}_{\alpha}^{(+)} + (\tilde{\mathbf{n}}_{\alpha}^{(+)} \cdot \tilde{\boldsymbol{\mu}}_{\alpha}^{(+)} + \mathbf{Q}_{\alpha}) \cdot \delta \tilde{\boldsymbol{\varphi}}_{\alpha}^{(+)} \right. \\
& \quad \left. + (\tilde{\mathbf{n}}_{\alpha+1}^{(-)} \cdot \tilde{\mathbf{P}}_{\alpha+1} - \mathbf{P}_{\alpha}) \cdot \delta \tilde{\mathbf{u}}_{\alpha+1}^{(-)} + (\tilde{\mathbf{n}}_{\alpha+1}^{(-)} \cdot \tilde{\boldsymbol{\mu}}_{\alpha+1}^{(-)} - \mathbf{Q}_{\alpha}) \cdot \delta \tilde{\boldsymbol{\varphi}}_{\alpha+1}^{(-)} \right] dS_{\alpha}^0 = 0.
\end{aligned} \tag{11.169}$$

Note, both when obtaining (11.157), and when deriving (11.169), we used the relation

$$\begin{aligned}
& \iiint_V (\tilde{\mathbf{P}}_{\alpha} \otimes \nabla_{\alpha} \delta \mathbf{u}_{\alpha} + \tilde{\boldsymbol{\mu}}_{\alpha} \otimes \nabla_{\alpha} \delta \boldsymbol{\varphi}_{\alpha}) dV \\
& = \iint_{\Sigma_{\alpha}^2} \tilde{\mathbf{m}}_{\alpha} \cdot (\tilde{\mathbf{P}}_{\alpha} \cdot \delta \mathbf{u}_{\alpha} + \tilde{\boldsymbol{\mu}}_{\alpha} \cdot \delta \boldsymbol{\varphi}_{\alpha}) d\Sigma_{\alpha} + \iint_{\tilde{S}_{\alpha}^{(-)}} \tilde{\mathbf{n}}_{\alpha}^{(-)} \cdot (\tilde{\mathbf{P}}_{\alpha} \cdot \delta \tilde{\mathbf{u}}_{\alpha}^{(-)} + \tilde{\boldsymbol{\mu}}_{\alpha} \cdot \delta \tilde{\boldsymbol{\varphi}}_{\alpha}^{(-)}) d\tilde{S}_{\alpha}^{(-)} \\
& \quad + \iint_{\tilde{S}_{\alpha}^{(+)}} \tilde{\mathbf{n}}_{\alpha}^{(+)} \cdot (\tilde{\mathbf{P}}_{\alpha} \cdot \delta \tilde{\mathbf{u}}_{\alpha}^{(+)} + \tilde{\boldsymbol{\mu}}_{\alpha} \cdot \delta \tilde{\boldsymbol{\varphi}}_{\alpha}^{(+)}) d\tilde{S}_{\alpha}^{(+)} - \iiint_V (\nabla_{\alpha} \cdot \tilde{\mathbf{P}}_{\alpha} \cdot \mathbf{u}_{\alpha} + \nabla_{\alpha} \cdot \tilde{\boldsymbol{\mu}}_{\alpha} \cdot \boldsymbol{\varphi}_{\alpha}) dV.
\end{aligned} \tag{11.170}$$

Here we assume that $S_{\alpha} = \tilde{S}_{\alpha}^{(+)} = \tilde{S}_{\alpha+1}^{(-)} = S_{\alpha}^0 \cup S_{\alpha}^{(i)}$, $\alpha = \overline{1, K-1}$. If $S_{\alpha}^0 = \emptyset$, $\alpha = \overline{1, K-1}$, then from (11.168) we get (11.147), and from (11.169) follows (11.157).

It is easy to see that due to the arbitrariness of the variations $\delta \mathbf{u}_{\alpha}$, $\delta \boldsymbol{\varphi}_{\alpha}$, $\delta \boldsymbol{\gamma}_{\alpha}$, $\delta \boldsymbol{x}_{\alpha}$, $\delta \tilde{\mathbf{P}}_{\alpha}$, $\delta \tilde{\boldsymbol{\mu}}_{\alpha}$, $\delta \tilde{\mathbf{u}}_{\alpha}^{(-)}$, $\delta \tilde{\boldsymbol{\varphi}}_{\alpha}^{(-)}$, $\delta \tilde{\mathbf{P}}_{\alpha}^{(-)}$, $\delta \tilde{\boldsymbol{\mu}}_{\alpha}^{(-)}$, $\delta \tilde{\mathbf{u}}_{\alpha}^{(+)}$, $\delta \tilde{\boldsymbol{\varphi}}_{\alpha}^{(+)}$, $\delta \tilde{\mathbf{P}}_{\alpha}^{(+)}$, $\delta \tilde{\boldsymbol{\mu}}_{\alpha}^{(+)}$, $\alpha = \overline{1, K}$, as well as $\delta \mathbf{T}_{\alpha}$, $\delta \boldsymbol{\mu}_{\alpha}$, $\delta \mathbf{v}_{\alpha}$, $\delta \boldsymbol{\psi}_{\alpha}$, $\delta \mathbf{P}_{\alpha}$, $\delta \mathbf{Q}_{\alpha}$, $\alpha = \overline{1, K-1}$, from (11.169), we obtain the equilibrium equations (11.150), constitutive relations (11.155), kinematic relations (11.153), kinematic (11.148) and static (11.152) boundary conditions on the lateral face, kinematic and static boundary conditions on the front surfaces (11.158) (in $S_{\alpha}^{(i)}$, $\alpha = \overline{1, K-1}$), perfect contact conditions in the domains of ideal adhesion (11.159) and conditions in domains of weakened adhesion

$$\begin{aligned}
\mathbf{P}_{\alpha} &= \partial \tilde{\chi}_{\alpha} / \partial \mathbf{v}_{\alpha}, \quad \mathbf{Q}_{\alpha} = \partial \tilde{\chi}_{\alpha} / \partial \boldsymbol{\psi}_{\alpha}, \quad \mathbf{v}_{\alpha} = \tilde{\mathbf{u}}_{\alpha}^{(+)} - \tilde{\mathbf{u}}_{\alpha+1}^{(-)}, \quad \boldsymbol{\psi}_{\alpha} = \tilde{\boldsymbol{\varphi}}_{\alpha}^{(+)} - \tilde{\boldsymbol{\varphi}}_{\alpha+1}^{(-)}, \\
\mathbf{P}_{\alpha} &= -\tilde{\mathbf{n}}_{\alpha}^{(+)} \cdot \tilde{\mathbf{P}}_{\alpha} = \tilde{\mathbf{n}}_{\alpha+1}^{(-)} \cdot \tilde{\mathbf{P}}_{\alpha+1}, \quad \mathbf{Q}_{\alpha} = -\tilde{\mathbf{n}}_{\alpha}^{(+)} \cdot \tilde{\boldsymbol{\mu}}_{\alpha} = \tilde{\mathbf{n}}_{\alpha+1}^{(-)} \cdot \tilde{\boldsymbol{\mu}}_{\alpha+1}, \quad \text{in } S_{\alpha}^0, \quad \alpha = \overline{1, K-1}.
\end{aligned}$$

11.9.2 Generalized Reissner-Type Variational Principle in the Theory of Multilayer Thin Bodies in Moments if There Are Domains of Weakened Adhesion

Having the generalized Reissner-type operator (11.168) or the generalized Reissner-type variational principle (11.169), we can easily obtain the generalized Reissner-type variational principle in moments with respect to systems of orthogonal polynomials if there are domains of weakened adhesion. Indeed, taking into account the relations (11.110), (11.113) and (11.116) – (11.119), recorded for the layer α ($\alpha = \overline{1, K}$), from (11.169) we obtain the generalized Reissner-type variational principle in moments with respect to the system of Legendre polynomials in the following form:

$$\begin{aligned}
 D\check{R}^* = & \sum_{k=0}^{\infty} \left\{ \frac{1}{2k+1} \left[\sum_{\alpha=1}^K \iint_{\check{S}_{\alpha}^{(-)}} h_{\alpha}(x') \{ [\underline{\mathbf{M}}(\partial_{\check{\alpha}} \check{W} / \partial \check{\gamma}) - \underline{\mathbf{P}}_{\check{\alpha}}^*] \otimes \delta_{\check{\alpha}}^{(k)} \right. \right. \\
 & + [\underline{\mathbf{M}}(\partial_{\check{\alpha}} \check{W} / \partial \check{\boldsymbol{\varkappa}}) - \underline{\boldsymbol{\mu}}_{\check{\alpha}}^*] \otimes \delta_{\check{\alpha}}^{(k)} - \underline{\mathbf{S}}_{\check{\alpha}(1)}^* \cdot \delta_{\check{\alpha}}^{(k)} - \underline{\mathbf{S}}_{\check{\alpha}(2)}^* \cdot \delta_{\check{\alpha}}^{(k)} \\
 & - [\underline{\boldsymbol{\gamma}}_{\check{\alpha}} - \underline{\mathbf{M}}(\nabla_{\check{\alpha}} \mathbf{u}) + \underline{\mathbf{C}} \cdot \underline{\boldsymbol{\varphi}}] \otimes \delta_{\check{\alpha}}^{(k)} - [\underline{\boldsymbol{\varkappa}}_{\check{\alpha}} - \underline{\mathbf{M}}(\nabla_{\check{\alpha}} \boldsymbol{\varphi})] \otimes \delta_{\check{\alpha}}^{(k)} \} d_{\check{S}_{\alpha}^{(-)}}^{(-)} \\
 & - \sum_{\alpha=1}^K \left\{ \int_{\check{L}_{\alpha}^{(-)}} h_{\alpha}(x') \check{m}_{\alpha}^{(-)} \left[\underline{\mathbf{M}}(\vartheta_{\check{\alpha}} \delta \mathbf{P}_{\check{\alpha}}^I) \cdot (\underline{\mathbf{u}}_{\check{\alpha}} - \underline{\mathbf{u}}_{\check{\alpha}0}) + \underline{\mathbf{M}}(\vartheta_{\check{\alpha}} \delta \boldsymbol{\mu}^I) \cdot (\underline{\boldsymbol{\varphi}}_{\check{\alpha}} - \underline{\boldsymbol{\varphi}}_{\check{\alpha}0}) \right] d_{\check{S}_{\alpha}^{(-)}}^{(-)} \right. \\
 & \left. - \iint_{\check{L}_{\alpha}^{(-)}} h_{\alpha}(x') (\underline{\mathbf{T}}_{\check{\alpha}(1)}^* \cdot \delta_{\check{\alpha}}^{(k)} \underline{\mathbf{u}} - \underline{\mathbf{T}}_{\check{\alpha}(2)}^* \cdot \delta_{\check{\alpha}}^{(k)} \underline{\boldsymbol{\varphi}}) d_{\check{S}_{\alpha}^{(-)}}^{(-)} \right\} \\
 & - (-1)^k \left\{ \iint_{\check{S}_1^{(-)}} \check{\mathbf{n}} \cdot [\delta \check{\mathbf{P}} \cdot (\underline{\mathbf{u}}_1 - \underline{\mathbf{u}}_0) + \delta \check{\boldsymbol{\mu}} \cdot (\underline{\boldsymbol{\varphi}}_1 - \underline{\boldsymbol{\varphi}}_0)] d_{\check{S}_1^{(-)}}^{(-)} \right. \\
 & + \iint_{\check{S}_2^{(-)}} [(\check{\mathbf{n}} \cdot \check{\mathbf{P}} - \check{\mathbf{P}}_0) \cdot \delta_{\check{\alpha}}^{(k)} \underline{\mathbf{u}} + (\check{\mathbf{n}} \cdot \check{\boldsymbol{\mu}} - \check{\boldsymbol{\mu}}_0) \cdot \delta_{\check{\alpha}}^{(k)} \underline{\boldsymbol{\varphi}}] d_{\check{S}_2^{(-)}}^{(-)} \} \\
 & - \iint_{\check{S}_K^{(+)}} \check{\mathbf{n}} \cdot [\delta \check{\mathbf{P}} \cdot (\underline{\mathbf{u}}_K - \underline{\mathbf{u}}_0) + \delta \check{\boldsymbol{\mu}} \cdot (\underline{\boldsymbol{\varphi}}_K - \underline{\boldsymbol{\varphi}}_0)] d_{\check{S}_K^{(+)}}^{(+)} \\
 & + \iint_{\check{S}_K^{(+)}} [(\check{\mathbf{n}} \cdot \check{\mathbf{P}} - \check{\mathbf{P}}_0) \cdot \delta_{\check{\alpha}}^{(k)} \underline{\mathbf{u}} + (\check{\mathbf{n}} \cdot \check{\boldsymbol{\mu}} - \check{\boldsymbol{\mu}}_0) \cdot \delta_{\check{\alpha}}^{(k)} \underline{\boldsymbol{\varphi}}] d_{\check{S}_K^{(+)}}^{(+)} \\
 & + \sum_{\alpha=1}^{K-1} \iint_{\check{S}_{\alpha}^{(i)}} \{ (\check{\mathbf{n}} \cdot \check{\mathbf{P}} - \check{\mathbf{T}}) \cdot \delta_{\check{\alpha}}^{(k)} \underline{\mathbf{u}} + (\check{\mathbf{n}} \cdot \check{\boldsymbol{\mu}} - \check{\boldsymbol{\mu}}) \cdot \delta_{\check{\alpha}}^{(k)} \underline{\boldsymbol{\varphi}} \}
 \end{aligned}$$

$$\begin{aligned}
& +(-1)^k [(\overset{(-)}{\mathbf{n}}_{\alpha+1} \cdot \overset{(-)}{\mathbf{P}}_{\alpha+1} + \overset{(-)}{\mathbf{T}}_{\alpha}) \cdot \delta \overset{(k)}{\mathbf{u}}_{\alpha+1} + (\overset{(-)}{\mathbf{n}}_{\alpha+1} \cdot \overset{(-)}{\boldsymbol{\mu}}_{\alpha+1} + \overset{(-)}{\boldsymbol{\mu}}_{\alpha}) \cdot \delta \overset{(k)}{\boldsymbol{\varphi}}_{\alpha+1}] dS_{\alpha}^{(i)} \\
& + \sum_{\alpha=1}^{K-1} \iint_{S_{\alpha}^0} \{(\overset{(+)}{\mathbf{n}}_{\alpha} \cdot \overset{(+)}{\mathbf{P}}_{\alpha} + \overset{(+)}{\mathbf{P}}_{\alpha}) \cdot \delta \overset{(k)}{\mathbf{u}}_{\alpha} + (\overset{(+)}{\mathbf{n}}_{\alpha} \cdot \overset{(+)}{\boldsymbol{\mu}}_{\alpha} + \overset{(+)}{\boldsymbol{Q}}_{\alpha}) \cdot \delta \overset{(k)}{\boldsymbol{\varphi}}_{\alpha} \\
& +(-1)^k [(\overset{(-)}{\mathbf{n}}_{\alpha+1} \cdot \overset{(-)}{\mathbf{P}}_{\alpha+1} - \overset{(-)}{\mathbf{P}}_{\alpha}) \cdot \delta \overset{(k)}{\mathbf{u}}_{\alpha+1} + (\overset{(-)}{\mathbf{n}}_{\alpha+1} \cdot \overset{(-)}{\boldsymbol{\mu}}_{\alpha+1} - \overset{(-)}{\boldsymbol{Q}}_{\alpha}) \cdot \delta \overset{(k)}{\boldsymbol{\varphi}}_{\alpha+1}] dS_{\alpha}^0 \} \\
& - \sum_{\alpha=1}^{K-1} \iint_{S_{\alpha}^{(i)}} [(\overset{(+)}{\mathbf{u}}_{\alpha} - \overset{(-)}{\mathbf{u}}_{\alpha+1}) \cdot \delta \overset{(+)}{\mathbf{T}}_{\alpha} + (\overset{(+)}{\boldsymbol{\varphi}}_{\alpha} - \overset{(-)}{\boldsymbol{\varphi}}_{\alpha+1}) \cdot \delta \overset{(+)}{\boldsymbol{\mu}}_{\alpha}] dS_{\alpha}^{(i)} \\
& - \sum_{\alpha=1}^{K-1} \iint_{S_{\alpha}^0} [(\partial \check{\chi}_{\alpha} / \partial \mathbf{v}_{\alpha} - \overset{(-)}{\mathbf{P}}_{\alpha}) \cdot \delta \mathbf{v}_{\alpha} + (\partial \check{\chi}_{\alpha} / \partial \boldsymbol{\psi}_{\alpha} - \overset{(-)}{\boldsymbol{Q}}_{\alpha}) \cdot \delta \boldsymbol{\psi}_{\alpha} \\
& + (\mathbf{v}_{\alpha} - \overset{(+)}{\mathbf{u}}_{\alpha} + \overset{(-)}{\mathbf{u}}_{\alpha+1}) \cdot \delta \overset{(+)}{\mathbf{P}}_{\alpha} + (\boldsymbol{\psi}_{\alpha} - \overset{(+)}{\boldsymbol{\varphi}}_{\alpha} + \overset{(-)}{\boldsymbol{\varphi}}_{\alpha+1}) \cdot \delta \overset{(+)}{\boldsymbol{Q}}_{\alpha}] dS_{\alpha}^0 = 0.
\end{aligned} \tag{11.171}$$

It should be noted that according to the above, for example, the following notations were introduced

$$\begin{aligned}
\mathbf{T}_{\alpha(1)} &= \overset{(-)}{m}_{\alpha} \overset{(-)}{I}_{\alpha} \mathbf{P}_{\alpha}^I - a_{\alpha}(x', x^3) \mathbf{P}_{\alpha 0}, \quad \mathbf{T}_{\alpha(2)} = \overset{(-)}{m}_{\alpha} \overset{(-)}{I}_{\alpha} \boldsymbol{\mu}^I - a_{\alpha}(x', x^3) \boldsymbol{\mu}_{\alpha 0}, \\
\mathbf{T}_{\alpha(I)}^* &= \overset{(-)}{\vartheta}_{\alpha} \mathbf{T}_{\alpha(I)}, \quad \mathbf{S}_{\alpha(I)}^* = \overset{(-)}{\vartheta}_{\alpha} \mathbf{S}_{\alpha(I)}, \quad \mathbf{S}_{\alpha(1)} = \nabla_{\alpha} \cdot \overset{(-)}{\mathbf{P}}_{\alpha} + \rho_{\alpha} \mathbf{F}_{\alpha}, \quad \overset{(-)}{\mathbf{P}}_{\alpha}^* = \overset{(-)}{\vartheta}_{\alpha} \overset{(-)}{\mathbf{P}}_{\alpha}, \\
\mathbf{S}_{\alpha(2)} &= \nabla_{\alpha} \cdot \overset{(-)}{\boldsymbol{\mu}}_{\alpha} + \overset{(-)}{C}_{\alpha} \overset{(-)}{\otimes} \overset{(-)}{\mathbf{P}}_{\alpha} + \rho_{\alpha} \mathbf{G}_{\alpha}, \quad \overset{(-)}{\boldsymbol{\mu}}_{\alpha}^* = \overset{(-)}{\vartheta}_{\alpha} \overset{(-)}{\boldsymbol{\mu}}_{\alpha}, \quad \overset{(-)}{\mathbf{u}}_{\alpha}^* = \overset{(-)}{\vartheta}_{\alpha} \overset{(-)}{\mathbf{u}}_{\alpha}, \quad \overset{(-)}{\boldsymbol{\varphi}}_{\alpha}^* = \overset{(-)}{\vartheta}_{\alpha} \overset{(-)}{\boldsymbol{\varphi}}_{\alpha}.
\end{aligned}$$

It is easy to see that if $\mathbf{S}_0 = \emptyset$, $\alpha = \overline{1, K-1}$, then from (11.171) follows the generalized Reissner-type variational principle in moments with respect to the system of Legendre polynomials for the theory of multilayer thin bodies with perfect contact of layers and under new parametrization of the body domain.

Note also that, having (11.168) and (11.171), with the help of the Legendre-type identity (see (11.46)), it is easy to obtain from them the Reissner-type dual operator and variational principle, respectively, as well as other variational principles (Lagrange, Castigliano) under the conditions which characterize these principles. In this regard, we will not dwell on the consideration of these particular cases. However, we note that some questions concerning the variational principles considered above are presented in Nikabadze (2014).

11.10 Conclusion

Extending the narrative style of the variational principles of classical mechanics of solids, adopted in Pobedrya (1984, 1995), to three-dimensional micropolar mechan-

ics of solids of some rheologies, we formulated the variational principles of Lagrange, Castigliano, generalized Reissner-type variational principles, the principle of virtual work and the principle of additional virtual work in the case of potentiality as well as nonpotentiality of stress and couple stress tensors. In particular, we have given the definition of the generalized Legendre transform and proved the Legendre-type identity. We have constructed Lagrangian, Castiglianian and generalized Reissner-type operators and have proved Lagrange and Castigliano's theorems on variational principles. We have presented equations of the Beltrami–Michell type for the stress and couple stress tensors with both asymmetric and symmetric differential tensor-operators. The statements of mixed boundary value problem and initial boundary value problem with respect to vectors of displacements and rotations and the statements of the mixed boundary value problem and of the new statement of the boundary value problem with respect to stress and couple stress tensors are formulated. We have proved theorems on the minimum of the stationary point of the Lagrangian and the maximum of the stationary point of the Castiglianian, as well as the theorem on the uniqueness of the generalized solution of boundary value problems.

By virtue of the constructed generalized Reissner-type operator of three-dimensional micropolar mechanics of solids the generalized Reissner-type operators of three-dimensional micropolar mechanics of solid single-layer and multilayer thin bodies with one small size under the new parametrization of the domains of these bodies are obtained and from them, in turn, the generalized Reissner-type variational principles of three-dimensional micropolar mechanics of solid single-layer and multilayer thin bodies with one small size are derived. Further, using the method of orthogonal polynomials, from the above-mentioned generalized Reissner-type variational principles, the generalized Reissner-type variational principles of micropolar mechanics of solid single-layer and multilayer thin bodies with one small size under the new parameterization of the domains of these bodies in moments with respect to the system of Legendre polynomials are derived. Moreover, in the case of the theory of multilayer thin bodies, the above-mentioned generalized Reissner-type operators and the generalized Reissner-type variational principles are given, both in the case of complete contact of adjacent layers of a multilayer structure, and in the presence of zones of weakened adhesion. Besides, the description of obtaining of dual Reissner-type operators and the generalized Reissner-type variational principles, as well as of Lagrangian and Castiglianian and variational principles of Lagrange and Castigliano is given. In the presence of domains of weakened adhesion at interphase boundaries in a multilayer thin body for modeling the interface (interphase boundary) the jump-type model (description of the interface with a surface of zero thickness) is considered in comparative detail.

In the near future, the authors propose similarly to the classical theory Pobedrya (1984, 1995) to consider the new variational principle for three-dimensional micropolar mechanics of solids of various rheology, associated with a new formulation of the boundary value problem for stress and couple stress tensors. Then, based on the new variational principle and the principles set forth above, the authors assume to formulate the corresponding variational principles of micropolar mechanics of solid single-layer and multilayer thin bodies with one and two small sizes under

the different parameterizations of the domain of these bodies and different contact conditions between the layers in the case of multilayer thin bodies.

In addition, we assume to spread the Vekua method on the construction of various versions of classical and micropolar theories of solid single-layer and multilayer thin bodies with one small size of different rheology, using the expansion in systems of Legendre and Chebyshev orthogonal polynomials and the Pobedria style for the presentation of the variational principles. In particular, we suppose that these methods can be extended to the second-gradient and second-gradient type theories of solids and thin solid bodies. In this regard, it is interesting, for example, the following works: Cosserat and Cosserat (1909); Le Roux (1911, 1913); Jaramillo (1929); Mindlin (1964); Toupin (1964); Eringen (1999); dell'Isola et al (2009); Alibert et al (2003); Askes and Aifantis (2011); Aifantis (2014); dell'Isola et al (2015a,b); Abali et al (2017); Giorgio (2020); Giorgio et al (2020b); Barchiesi et al (2020); Giorgio et al (2020a); Ciallella et al (2021); Giorgio (2021); Barchiesi et al (2021).

Acknowledgements This work was supported by the financial support of the Ministry of Education and Science of the Russian Federation as part of the program of the Moscow Center for Fundamental and Applied Mathematics under the agreement No 075-15-2019-1621 and of the Shota Rustaveli National Science Foundation (project No FR-21-3926).

References

- Abali BE, Müller WH, dell'Isola F (2017) Theory and computation of higher gradient elasticity theories based on action principles. *Archive of Applied Mechanics* 87(9):1495–1510
- Aero EL, Kuvshinsky EV (1960) Basic equations of the theory of elasticity of media with rotational interaction of particles. *Fizika tverdogo tela* 2(7):1399–1409
- Aifantis EC (2014) Continuum nanomechanics for nanocrystalline and ultrafine grain materials. *IOP Conf Ser: Mater Sci Eng* 63:1–16
- Alibert JJ, Seppecher P, dell'Isola F (2003) Truss modular beams with deformation energy depending on higher displacement gradients. *Mathematics and Mechanics of Solids* 8(1):51–73
- Askes H, Aifantis EC (2011) Gradient elasticity in statics and dynamics: An overview of formulations, length scale identification procedures, finite element implementations and new results. *International Journal of Solids and Structures* 48(13):1962–1990
- Barchiesi E, Eugster SR, dell'Isola F, Hild F (2020) Large in-plane elastic deformations of bipantographic fabrics: asymptotic homogenization and experimental validation. *Mathematics and Mechanics of Solids* 25(3):739–767
- Barchiesi E, Dell'Isola F, Bersani AM, Turco E (2021) Equilibria determination of elastic articulated duoskelion beams in 2D via a Riks-type algorithm. *International Journal of Non-Linear Mechanics* 128:103,628
- Basdevant JL (2007) *Variational Principles In Physics*. Springer Science and Business Media
- Berdichevsky VL (2009) *Variational Principles of Continuum Mechanics*. Springer, Berlin, Heidelberg
- Besdo D (2014) *Examples to Extremum and Variational Principles in Mechanics*. Springer
- Ciallella A, Pasquali D, Golaszewski M, D'Annibale F, Giorgio I (2021) A rate-independent internal friction to describe the hysteretic behavior of pantographic structures under cyclic loads. *Mechanics Research Communications* 116:103,761
- Cline D (2021) *Variational Principles in Classical Mechanics*. University of Rochester
- Cosserat E, Cosserat F (1909) *Theorie des Corp Dcformables*. Herman et Fils, Paris

- dell'Isola F, Sciarra G, Vidoli S (2009) Generalized Hooke's law for isotropic second gradient materials. *Proceedings of the Royal Society A: Mathematical, Physical and Engineering Sciences* 465(2107):2177–2196
- dell'Isola F, Andreus U, Placidi L (2015a) At the origins and in the vanguard of peridynamics, non-local and higher-gradient continuum mechanics: an underestimated and still topical contribution of Gabrio Piola. *Mathematics and Mechanics of Solids* 20(8):887–928
- dell'Isola F, Seppecher P, Della Corte A (2015b) The postulations à la D'Alembert and à la Cauchy for higher gradient continuum theories are equivalent: a review of existing results. *Proceedings of the Royal Society A: Mathematical, Physical and Engineering Sciences* 471(2183):20150415
- Eringen AC (1999) *Microcontinuum Field Theories. 1. Foundation and solids*. Springer-Verlag., N.Y.
- Ghoussoub N (2008) *Self Dual Partial Differential Systems And Their Variational Principles*. Springer Science and Business Media
- Giorgio I (2020) A discrete formulation of Kirchhoff rods in large-motion dynamics. *Mathematics and Mechanics of Solids* 25(5):1081–1100
- Giorgio I (2021) Lattice shells composed of two families of curved Kirchhoff rods: an archetypal example, topology optimization of a cycloidal metamaterial. *Continuum Mechanics and Thermodynamics* 33(4):1063–1082
- Giorgio I, dell'Isola F, Misra A (2020a) Chirality in 2D Cosserat media related to stretch-micro-rotation coupling with links to granular micromechanics. *International Journal of Solids and Structures* 202:28–38
- Giorgio I, Spagnuolo M, Andreus U, Scerrato D, Bersani AM (2020b) In-depth gaze at the astonishing mechanical behavior of bone: A review for designing bio-inspired hierarchical metamaterials. *Mathematics and Mechanics of Solids* p 1081286520978516
- Jaramillo TJ (1929) A generalization of the energy function of elasticity theory. PhD thesis, Department of Mathematics. University of Chicago
- Kupradze VD, Gegelia TG, Basheleishvili MO, Burchuladze TV (1976) Three-dimensional problems of the mathematical theory of elasticity and thermoelasticity. Nauka, Moscow
- Kuvshinsky EV, Aero EL (1963) Basic equations of the theory of elasticity of media with rotational interaction of particles. *Fizika tverdogo tela* 5(9):2591–2598
- Lanczos C (2012) *The Variational Principles of Mechanics*. Courier Corporation
- Le Roux J (1911) Etude géométrique de la torsion et de la flexion, dans les déformations infinitésimales d'un milieu continu. *Annales scientifiques de l'École normale supérieure* 28(3):523–579.
- Le Roux J (1913) Recherches sur géométrie des déformations finies. *Annales scientifiques de l'École normale supérieure* 30(3):193–245
- Lovelock D (2012) *Tensors Differential Forms And Variational Principles*. Courier Corporation
- Mason J (2013) *Variational Incremental and Energy Methods in Solid Mechanics and Shell Theory*. Elsevier
- Mindlin RD (1964) Micro-structure in linear elasticity. *Arch Rat Mech and Analysis* 16(1):51–78
- Nesbet RK (2002) *Variational Principles and Methods in Theoretical Physics and Chemistry*. Cambridge University Press
- Nikabadze MU (2001a) To a version of the theory of multilayer structures. *Mechanics of Solids* 36(1):119–129
- Nikabadze MU (2001b) A variant of the theory of multilayer structures. *Izv RAN MTT* (1):143–158
- Nikabadze MU (2006) A variant of the system of equations of the theory of thin bodies. *Vestn Mosk Univ, Matem Mekhan* (1):30–35
- Nikabadze MU (2007a) Application of a system of chebyshev polynomials to the theory of thin bodies. *Vestn Mosk Univ, Matem Mekhan* (5):56–63
- Nikabadze MU (2007b) Application of Chebyshev Polynomials to the Theory of Thin Bodies. *Moscow University Mechanics Bulletin* 62(5):141–148
- Nikabadze MU (2007c) Some issues concerning a version of the theory of thin solids based on expansions in a system of chebyshev polynomials of the second kind. *Mechanics of Solids* 42(3):391–421

- Nikabadze MU (2010) To compatibility conditions in linear micropolar theory. *Vestn Mosk un-ta Ser 1 Matem Mekhan* (5):48–51
- Nikabadze MU (2012) Compatibility conditions and equations of motion in the linear micropolar theory of elasticity. *Moscow Univ Mech Bulletin* 67(1):18–22
- Nikabadze MU (2014) Development of the method of orthogonal polynomials in the classical and micropolar mechanics of elastic thin bodies. *Moscow Univ. Press, Moscow*
- Nikabadze MU (2015) On some issues of tensor calculus with applications to mechanics. *Contemporary mathematics Fundamental directions* 55:3–194
- Nikabadze MU (2016) Eigenvalue problems of a tensor and a tensor-block matrix (tmb) of any even rank with some applications in mechanics. In: Altenbach H, Forest S (eds) *Generalized continua as models for classical and advanced materials, advanced structured material*, vol 42, Springer, Cham, pp 279–317
- Nikabadze MU (2017) Topics on tensor calculus with applications to mechanics. *Journal of Mathematical Sciences* 225(1):1–194
- Nikabadze MU, Ulukhanyan AR (2005) Statements of problems for a thin deformable three-dimensional body. *Vestn Mosk Univ, Matem Mekhan* (5):43–49
- Nikabadze MU, Ulukhanyan AR (2016) Analytical solutions in the theory of thin bodies. In: Altenbach H, Forest S (eds) *Generalized Continua as Models for Classical and Advanced Materials, Advanced Structured Materials*, vol 42, Springer, Cham, pp 319–361
- Nikabadze MU, Ulukhanyan AR (2019a) Mathematical modeling of elastic thin bodies with one small size. In: Altenbach H ABE Müller W H (ed) *Higher Gradient Materials and Related Generalized Continua. Advanced Structured Materials, Advanced Structured Materials*, vol 120, Springer, Cham, pp 155–199
- Nikabadze MU, Ulukhanyan AR (2019b) Some applications of eigenvalue problems for tensor and tensor-block matrices for mathematical modeling of micropolar thin bodies. *Mathematical and Computational Applications* 24(1):1–19
- Nikabadze MU, Ulukhanyan AR (2019c) To the modeling of multilayer thin prismatic bodies. In: *IOP Conf. Ser.: Mater. Sci. Eng.*, vol 683, IOP Publishing Ltd, pp 1–7
- Nikabadze MU, Ulukhanyan AR (2020a) Modeling of multilayer thin bodies. *Continuum Mechanics and Thermodynamics* 32:8172–842
- Nikabadze MU, Ulukhanyan AR (2020b) On the decomposition of equations of micropolar elasticity and thin body theory. *Lobachevskii Journal of Mathematics* 41(10):2059–2074
- Nikabadze MU, Ulukhanyan AR (2021) On the theory of multilayer thin bodies. *Lobachevskii Journal of Mathematics* (8):1900–1911
- Nowacki W (1975) *Theory of elasticity*. Mir, Moscow
- Pelekh BL, Korovaichuk IM (1984) On the mechanics of composite media with imperfect bonds at interfaces. *Mechanics of Composite Materials* (4):606–611
- Pobedrya BE (1984) *Mechanics of Composite Materials*. Moscow University Publishing House, Moscow
- Pobedrya BE (1986) *Lectures on tensor analysis*. Moscow University Publishing House, Moscow
- Pobedrya BE (1995) *Numerical methods in the theory of elasticity and plasticity*. Moscow University Publishing House, Moscow
- Podstrigach YS (1963) Conditions of thermal contact of solids. *Reports of the Academy of Sciences of the USSR* (7):872–874
- Podstrigach YS (1982) Conditions for the jump in stresses and displacements on a thin-walled elastic inclusion in a continuous medium. *Reports of the Academy of Sciences of the USSR* (12):30–32
- Rektorys K (1977) *Variational methods in mathematics science and engineering*. Springer, Dordrecht
- Sandru N (1966) On some problems of the linear theory of the asymmetric elasticity. *International Journal of Engineering Science* 4(1):81–94
- Toupin RA (1964) Theories of elasticity with couple-stresses. *Arch Rat Mech and Analysis* 17(2):85–112

- Vanko VI (2010) Variational principles and problems of mathematical physics. Publishing house of BMSTU, Moscow
- Vekua IN (1970) Variational principles for constructing the theory of shells. Publishing house of TSU, Tbilisi
- Vekua IN (1978) Fundamentals of tensor analysis and covariant theory. Nauka, Moscow
- Vekua IN (1982) Some common methods for constructing various variants of the theory of shells. Nauka, Moscow
- Washizy K (1982) Variational Methods in Elasticity and Plasticity. Pergamon, Oxford
- Yourgrau W (2012) Variational Principles in Dynamics and Quantum Theory. Courier Corporation



Chapter 12

Asymptotic Comparison of the Strain-Gradient and Micromorphic Models when Loading Forces Are Widely Spread

Pierre Seppecher, Lukáš Jakabčín

Abstract In this paper we reconcile different homogenization results which describe the effective behavior of a heterogeneous material either by a strain-gradient model either by a micromorphic one. Indeed we prove that the solutions of both models are asymptotically very close when considering a loading with increasing wavelength. This result is obtained using the Fourier analysis on the tensor spaces and applies to a large class of micromorphic models. However, we provide an example of a micromorphic model that does not belong to this class and thus cannot be approximated by a strain-gradient model.

Keywords: Continuum mechanics · Strain-gradient · Micromorphic model

12.1 Introduction

The theory of elasticity is well founded since the work of Cauchy and generally gives satisfactory descriptions of the displacement field u of a solid submitted to an external load f . Let us recall that the deformation of the solid is, in the linear formulation, measured by the strain tensor $e(u) := (\nabla u + {}^t\nabla u)/2$. Here ∇u stands for the jacobian matrix of u and ${}^t\nabla u$ its transpose. The behavior of the solid is described by a stiffness tensor C . The elastic energy of the solid contained in a domain Ω is

P. Seppecher

Institut de Mathématiques de Toulon, Université de Toulon, BP 20132, 83957 La Garde Cedex, France

e-mail: seppecher@imath.fr

L. Jakabčín

Laboratoire de Mécanique Gabriel Lamé, Université d'Orléans, 8 rue Léonard de Vinci, 45100 Orléans, France

e-mail: lukas.jakabcin@univ-orleans.fr

$$\mathcal{E}^e(u) := \int_{\Omega} \frac{1}{2} e(u) : C : e(u) dx.$$

At equilibrium, the displacement field u^e minimizes the total energy

$$\mathcal{E}^e(u) - \int_{\Omega} f \cdot u dx.$$

The existence of a unique solution of this minimization problem is ensured if suitable boundary conditions are imposed. Here, in order to compare our results with the literature (see for instance Smyshlyaev and Cherednichenko (2000)), we assume that f and u are $[-L, L]^3$ -periodic function with vanishing mean value on any period Ω ($\int_{\Omega} u dx = 0$). Hence u^e is the unique $[-L, L]^3$ -periodic function in $L^2_{loc}(\mathbb{R}^3, \mathbb{R}^3)$ with vanishing mean value and which satisfies, in the sense of distributions on \mathbb{R}^3 , the Euler–Lagrange equation

$$\operatorname{div}(C : e(u^e)) + f = 0. \quad (12.1)$$

However Cauchy theory must sometimes be generalized. Indeed, when one focuses on small samples, scale effects are observed which cannot be explained by this theory (cf. Lam et al (2003)). Two main generalizations have been considered in order to encompass this difficulty.

- The first one, called “strain-gradient theory” consists in adding in the elastic energy a quadratic term depending on the gradient $\nabla e(u)$ of the strain tensor (see among many others: Mindlin and Tiersten, 1962; Mindlin, 1965; Germain, 2020; Casal, 1972)

$$\mathcal{E}^s(u) := \int_{\Omega} \left(\frac{1}{2} \nabla e(u) : \tilde{D} : \nabla e(u) + \frac{1}{2} e(u) : C : e(u) \right) dx.$$

This model can alternatively be called “second-gradient model” as it is well known that any quadratic form $\nabla e(u) : \tilde{D} : \nabla e(u)$ of $\nabla e(u)$ is a quadratic form $\nabla \nabla u : D : \nabla \nabla u$ of the second gradient of the displacement field and reciprocally. Hence

$$\mathcal{E}^s(u) := \int_{\Omega} \left(\frac{1}{2} \nabla \nabla u : D : \nabla \nabla u + \frac{1}{2} e(u) : C : e(u) \right) dx.$$

The equilibrium u^s is the unique $[-L, L]^3$ -periodic function in $L^2_{loc}(\mathbb{R}^3, \mathbb{R}^3)$ with zero mean value and which satisfies, in the sense of distributions on \mathbb{R}^3 , the Euler–Lagrange equation

$$\operatorname{div} \left(- \operatorname{div}(D : \nabla \nabla u^s) + C : e(u^s) \right) + f = 0. \quad (12.2)$$

- The second generalization (see Forest and Sab, 2020; Misra et al, 2021; Forest, 1999; Cosserat and Cosserat, 1896) consists in introducing a new kinematic descriptor ϕ and assuming that the elastic energy couples ϕ with ∇u and also

depends on the gradient of ϕ , reading:

$$\mathcal{E}^c(u) := \inf_{\phi} \int_{\Omega} \left(\frac{1}{2} \nabla \phi : G : \nabla \phi + \frac{1}{2} (\nabla u - \phi) : H : (\nabla u - \phi) + \frac{1}{2} e(u) : C : e(u) \right) dx.$$

The equilibrium displacement field u^c and the associated field ϕ^c are the unique $[-L, L]^3$ -periodic functions in $L^2_{loc}(\mathbb{R}^3, \mathbb{R}^3)$ and $L^2_{loc}(\mathbb{R}^3, \mathbb{R}^{3 \times 3})$ which satisfy $\int_{\Omega} u^c dx = 0$ and, in the sense of distributions on \mathbb{R}^3 ,

$$\begin{cases} \operatorname{div} (H : (\nabla u^c - \phi^c) + C : e(u^c)) + f = 0, \\ \operatorname{div} (G : \nabla \phi^c) + H : (\nabla u^c - \phi^c) = 0. \end{cases}$$

Note that the new kinematic descriptor ϕ is a tensor field of order two. In the sequel, we refer to this second generalization as the ‘‘micromorphic model.’’ A particular case of this energy is the ‘‘Cosserat model’’ in which ϕ is a skew-symmetric matrix coupled to the rotational of u (cf. Cosserat and Cosserat, 1896).

These two generalizations are strongly related (see Germain, 1973): some authors like considering \mathcal{E}^s as the limit of \mathcal{E}^c when $G = D$ and H becomes very large while others consider \mathcal{E}^c as an approximation of \mathcal{E}^s more suitable for numerical simulations.

It is convenient to remark that all the aforementioned models are particular cases of a more general one which mix non-local and strain-gradient terms with an elastic energy $\mathcal{E}^m(u)$, which is the infimum over ϕ :

$$\mathcal{E}^m(u) := \inf_{\phi} \int_{\Omega} \left(\frac{1}{2} \nabla \nabla u : D : \nabla \nabla u + \frac{1}{2} \nabla \phi : G : \nabla \phi + \frac{1}{2} (\nabla u - \phi) : H : (\nabla u - \phi) + \frac{1}{2} e(u) : C : e(u) \right) dx. \quad (12.4)$$

The corresponding equilibrium solution (u^m, ϕ^m) is the unique couple of $[-L, L]^3$ -periodic functions in $L^2_{loc}(\mathbb{R}^3, \mathbb{R}^3)$ and $L^2_{loc}(\mathbb{R}^3, \mathbb{R}^{3 \times 3})$ which satisfy $\int_{\Omega} u^m dx = 0$ and, in the sense of distributions on \mathbb{R}^3 ,

$$\begin{cases} \operatorname{div} (-\operatorname{div} (D : \nabla \nabla u^m) + H : (\nabla u^m - \phi^m) + C : e(u^m)) + f = 0, \\ \operatorname{div} (G : \nabla \phi^m) + H : (\nabla u^m - \phi^m) = 0. \end{cases} \quad (12.5)$$

Our aim is to compare these two generalizations. In this direction, the choice we have made of a periodic framework is specially suitable. It avoids discussing about the effects of boundary conditions which cannot be identical for both models and about the presence of boundary layers.

It is important to notice that all generalized models contain intrinsic lengths. Indeed any ratio of an entry of D or G to an entry of C is the square of such a length. Hence, deciding whether the supplementary terms in the energy are small perturbations of the Cauchy model is not a question about the constitutive laws of the material only but on the scale at which the effects of such supplementary terms are observed. At a very large scale all models must be close to the Cauchy model. “Large scale” means here that the characteristic size of the domain and the characteristic wavelength of the applied load are large compared to the intrinsic lengths.

On the other hand, the use of generalized models is justified in the literature by several homogenization results. It is known that, when the tensor C oscillates periodically, with a very short period, the solution of associated Cauchy elasticity problems converges to the solution of a new problem in which the displacement minimizes the so-called “effective or homogenized energy.” The study of this asymptotic problem is now well understood from the mathematical point of view when C oscillates between fixed bounds: the effective energy is still of Cauchy type and the new tensor C^{hom} can be computed through the solution of an auxiliary problem set on the rescaled periodic cell (see Allaire, 1992; Bakhvalov and Panasenko, 2012; Bensoussan et al, 1978; Sanchez-Palencia, 1980). When it oscillates between bounds whose ratio tends to infinity while the period length tends to zero, things are less clear. In this so-called “high-contrast” case, different results have been obtained (cf. Camar-Eddine and Seppecher, 2003; Abdoul-Anziz and Seppecher, 2018a,b): some still give a Cauchy model, others lead to a strain-gradient model (cf. Pideri and Seppecher, 1997; Briane and Camar-Eddine, 2007; Alibert and Della Corte, 2015; Turco et al, 2016; dell’Isola et al, 2016; Rahali et al, 2015; Alibert et al, 2003; Durand et al, 2022), still others lead to non-local models like micromorphic models (see Abdoul-Anziz and Seppecher, 2018b; Jakabčín and Seppecher, 2020). In Jakabčín and Seppecher (2020) a mixed model of type (12.5) has even been obtained. Again we must emphasize that speaking of “high-contrast” is not a purely material property: indeed the ratio between the stiffness of the stiffest part of the material to the weakest one has to be compared to the ratio of the wavelength of these variations to the size of the domain or to the wavelength of the applied load.

To sum up, in a periodic homogenization framework, there exist at least three characteristic lengths. The first one is the period ε of the oscillations of the stiffness tensor: at such a scale homogenization is irrelevant. The second one is the intrinsic length ℓ of an effective energy of strain-gradient or micromorphic type: at this scale strain-gradient or micromorphic effects are important. If such a scale is of the same order of magnitude as ε , strain-gradient or micromorphic effects are never important. The third one, L , is large compared to ℓ : at this scale the material behaves essentially like a classical Cauchy material and strain-gradient or micromorphic terms are small corrections to the Cauchy energy.

In recent studies (Smyshlyaev and Cherednichenko, 2000; Allaire et al, 2016), it has been proved that the first approximation of the solution of an elasticity problem, when the tensor C oscillates periodically with a very short period, minimizes at the leading order, the usual effective energy but that the first correction to this leading order solution corresponds to the solution of a strain-gradient model. This result

could appear in contradiction with the results of Jakabčín and Seppecher (2020); Abdoul-Anziz and Seppecher (2018a,b); Abdoul-Anziz et al (2021); Camar-Eddine and Seppecher (2003) where non-local limits are obtained. It is not, because the assumptions made by Smyshlyaev and Cherednichenko (2000) or Allaire et al (2016) prevent the appearance of a macroscopic intrinsic length ℓ in the limit energy. In other words, all the intrinsic lengths ℓ contained in the models obtained in these works are of the same order of magnitude as ε and tend to zero when ε tends to zero.

Though the results of Smyshlyaev and Cherednichenko (2000) or Allaire et al (2016) and those of Camar-Eddine and Seppecher (2003); Abdoul-Anziz and Seppecher (2018a) or Abdoul-Anziz et al (2021) seem to apply to different situations, a numerical study (Jakabčín and Seppecher, 2020) has suggested a strong correlation between them. In the present paper we show that this correlation is not fortuitous.

Our study results from the following observation: when the applied load is widely spread, then it often becomes very difficult to distinguish strain-gradient and Cosserat-type solutions (see Jakabčín and Seppecher, 2020). Considering a widely spread load is equivalent to considering the material at a large scale. As aforementioned, at such a scale, all extra energy terms become small corrections to standard elastic energy and all solutions converge toward the Cauchy solution. What we prove here is more surprising. We show that the corrections brought by strain-gradient terms or by the extra kinematic descriptor can be identical, up to a higher order correction.

The paper is organized as follows. After a short section where notation is fixed, we set the asymptotic problem when the applied load becomes wider spread in a large domain. A small parameter η characterizes this large wavelength. A change of variable brings back to a fix domain and the parameter η makes the strain-gradient and micromorphic terms small corrections of the classical Cauchy elasticity problem. We then write the equilibrium problem in the Fourier framework where it reduces to the inversion of a tensor which linearly relates the Fourier components of the applied force to the Fourier components of the solution. Our result comes from careful estimations of this inverse tensor.

These estimations need a fundamental assumption. Roughly speaking, if the micromorphic energy couples only a part of the extra kinematic variable with the gradient of the displacement field and if it also couples the gradient of this part with the gradient of the remaining part, then the micromorphic model is not asymptotically close to any strain gradient model. In Section 12.6 we provide an explicit example of this rather rare situation.

12.2 Notation

The different elastic energy densities that we have introduced contain quadratic forms. These forms are represented by tensors. We use the standard notation \otimes for the tensor product. We simply shorten some notation by writing $T^{\otimes 2}$ for $T \otimes T$.

Different conventions may be adopted for defining contraction products of tensors. Here we adopt the following ones: when Q is a fourth-order tensor and M and N are matrices, $Q : M$ and $N : Q : M$ stand for the matrix and the real defined respectively by

$$(Q : M)_{ij} = \sum_{k,l} Q_{ijkl} M_{kl} \quad \text{and} \quad N : Q : M = \sum_{i,j,k,l} N_{ij} Q_{ijkl} M_{kl}.$$

Similarly when Q is a sixth-order tensor and M and N are third-order tensors, $Q \dot{:} M$ and $N \dot{:} Q \dot{:} M$ stand for the third-order tensor and the real defined by

$$(Q \dot{:} M)_{ijk} = \sum_{l,m,n} Q_{ijklmn} M_{lmn}, \quad N \dot{:} Q \dot{:} M = \sum_{i,j,k,l,m,n} N_{ijk} Q_{ijklmn} M_{lmn}.$$

Let $\xi \in \mathbb{R}^3$. To any quadratic form Q over matrices, we can associate the symmetric matrix $\xi : Q : \xi$ defined¹ by setting, for any $u \in \mathbb{R}^3$,

$$u \cdot (\xi \cdot Q \cdot \xi) \cdot u = (u \otimes \xi) : Q : (u \otimes \xi).$$

Similarly, to any quadratic form Q over third-order tensors, we can associate the quadratic form over matrices $\xi \cdot Q \cdot \xi$ and, if N is a given matrix, the symmetric matrix $N \cdot Q \cdot N$ defined² by setting, for any matrix M or any $u \in \mathbb{R}^3$,

$$M : (\xi \cdot Q \cdot \xi) : M = (M \otimes \xi) : Q : (M \otimes \xi), \quad u \cdot (N : Q : N) \cdot u = (u \otimes N) \dot{:} Q \dot{:} (u \otimes N).$$

The tensors which represent quadratic forms are naturally symmetric: in (12.5) C and H are fourth order tensors and D and G are sixth order tensors satisfying, for any i, j, k, l, m, n in $\{1, 2, 3\}$,

$$C_{ijkl} = C_{klij}, \quad H_{ijkl} = H_{klij}, \quad D_{ijklmn} = D_{lmnijk}, \quad G_{ijklmn} = G_{lmnijk}.$$

Moreover, due to the symmetric nature of the tensor $e(u)$ on which C operates and to the natural right-symmetry of $\nabla \nabla u$ (defined by $(\nabla \nabla u)_{ijk} = \partial_j \partial_k u_i$), the tensors C and D which appear in (12.5) are assumed, without loss of generality, to satisfy the symmetries

$$C_{ijkl} = C_{ijlk} = C_{jikl}, \quad D_{ijklmn} = D_{ijklnm} = D_{ikjlmn}.$$

¹ In terms of indices $(\xi \cdot Q \cdot \xi)_{ij} = \sum_{k,l} Q_{ijkl} \xi_k \xi_l$.

² In terms of indices $(\xi \cdot Q \cdot \xi)_{ijkl} = \sum_{m,n} Q_{ijmkl n} \xi_m \xi_n$ and $(N : Q : N)_{ij} = \sum_{k,l,m,n} Q_{ikljmn} N_{kl} N_{mn}$.

In the sequel we will have to compare several quadratic forms. If Q and \tilde{Q} are quadratic forms over the same space, writing $Q \leq \tilde{Q}$ will simply mean that $\tilde{Q} - Q$ is a non-negative quadratic form or equivalently³ that, for any M , $M:Q:M \leq M:\tilde{Q}:M$.

Any fourth-order tensor Q can also be considered as a linear operator on the space of matrices. Composition of Q and \tilde{Q} corresponds to the product $Q : \tilde{Q}$ defined by

$$(Q : \tilde{Q})_{ijkl} = \sum Q_{ijmn} \tilde{Q}_{mnkl}.$$

It is also in that sense that we will use its image or kernel $Im(Q)$, $Ker(Q)$, its pseudo-inverse (Moore–Penrose inverse) Q^+ and, when invertible, its inverse Q^{-1} .

The different minimization problems that we have introduced are all well-posed because we assume that C is a positive definite quadratic form over the space \mathcal{M}^{sym} of symmetric matrices and that D, G, H are non-negative forms. Specifically, we assume that there exists $0 < \alpha < \beta$ such that, for any M in \mathcal{M}^{sym} , any matrix N and any third-order tensor T ,

$$\alpha \|M\|^2 \leq M : C : M \leq \beta \|M\|^2, \tag{12.6}$$

$$0 \leq T : D : T \leq \beta \|T\|^2, \quad 0 \leq T : G : T \leq \beta \|T\|^2, \tag{12.7}$$

$$0 \leq N : H : N \leq \beta \|N\|^2, \quad N : H^+ : N \leq \beta \|N\|^2. \tag{12.8}$$

Note that, applying assumption (12.6) to matrices $M = (u \otimes \xi + \xi \otimes u)$, gives

$$u \cdot (\xi \cdot C \cdot \xi) \cdot u = \frac{1}{4} M : C : M \geq \frac{\alpha}{4} \|M\|^2 \geq \frac{\alpha}{2} \|\xi\|^2 \|u\|^2. \tag{12.9}$$

Thus, for any $\xi \neq 0$, the matrix $\xi \cdot C \cdot \xi$ is definite positive.

Note that these assumptions ensure that the equilibrium problem (12.5) is well-posed. Indeed, any minimizing sequence (u_n) of $[-L, L]^3$ -periodic functions with zero mean value has bounded energy $\mathcal{E}^m(u) \leq \gamma$ and thus is bounded in $H^1([-L, L]^3, \mathbb{R}^3)$. As the energy functional is lower semi-continuous, the sequence converges, up to a sub-sequence, to a solution of (12.5).

12.3 Spread Loads

We consider equilibrium problems in a domain whose size is large compared with the lengths which are intrinsic to the micromorphic or second-gradient models. We also consider force fields whose characteristic wave lengths are comparable to the size of the domain. To make these assumptions precise we introduce a small parameter $\eta > 0$ and we consider the domain $Y_\eta := \frac{1}{\eta} Y$ where $Y := [-\pi, \pi]^3$. Let f be a Y -periodic vector-valued function with zero mean value. We assume that the material is submitted to the Y_η -periodic load $f_\eta(x) := f(\eta x)$.

³ The product used in this formula must be adapted to the space on which Q and \tilde{Q} apply.

We assume that the material is homogeneous: its elastic energy \mathcal{E}^m is given by (12.4) where the tensors C, D, G, H are constant. We look for a Y_η -periodic solution (u_η, ϕ_η) with $\int_{Y_\eta} u_\eta dx = 0$ of

$$\begin{cases} \operatorname{div}(-\operatorname{div}(D : \nabla \nabla u_\eta) + H : (\nabla u_\eta - \phi_\eta) + C : e(u_\eta)) + f_\eta = 0, & (12.10a) \\ \operatorname{div}(G : \nabla \phi_\eta) + H : (\nabla u_\eta - \phi_\eta) = 0. & (12.10b) \end{cases}$$

We will now study the asymptotic behavior of u_η when η tends to zero. Indeed, letting η tend to zero is considering an increasingly spread out load. To that aim we make the change of variables $v_\eta(y) = \eta^2 u_\eta(\frac{y}{\eta})$, $\psi_\eta(y) = \eta \phi_\eta(\frac{y}{\eta})$. Introducing this change of variables in the previous system of equations is straightforward. We are reduced to the search of the Y -periodic solution (v_η, ψ_η) with $\int_Y v_\eta dx = 0$ of the following system:

$$\begin{cases} \eta^2 \operatorname{div}(-\operatorname{div}(D : \nabla \nabla v_\eta) + H : (\nabla v_\eta - \psi_\eta)) + C : e(v_\eta) + f = 0, & (12.11a) \\ \eta^2 \operatorname{div}(G : \nabla \psi_\eta) + H : (\nabla v_\eta - \psi_\eta) = 0. & (12.11b) \end{cases}$$

12.4 Fourier Expansion

Owing to the periodicity framework, it is convenient to rewrite the system using periodic expansions of v_η and ψ_η . We set

$$f(x) = \Re \left(\sum_{\xi \in \mathbb{Z}^3} f^\xi e^{i \xi \cdot x} \right) \quad \text{and}$$

$$v_\eta(x) = \Re \left(\sum_{\xi \in \mathbb{Z}^3} v_\eta^\xi e^{i \xi \cdot x} \right), \quad \psi_\eta(x) = \Re \left(\sum_{\xi \in \mathbb{Z}^3} (-i) \psi_\eta^\xi e^{i \xi \cdot x} \right).$$

From $\int_Y f(x) dx = 0$ we deduce $f^0 = 0$ and, similarly, condition $\int_Y v_\eta dx = 0$ now reads $v_\eta^0 = 0$. Using the symmetry properties of C , system (12.11) is equivalent to the fact that, for any $\xi \in \mathbb{Z}^3$,

$$\begin{cases} \eta^2 (D : (v_\eta^\xi \otimes \xi \otimes \xi)) \cdot \xi \cdot \xi + (H : (v_\eta^\xi \otimes \xi - \psi_\eta^\xi)) \cdot \xi \\ \quad \quad \quad + (C : (v_\eta^\xi \otimes \xi)) \cdot \xi - f^\xi = 0, & (12.12a) \\ \eta^2 (G : \psi_\eta^\xi \otimes \xi) \cdot \xi - H : (v_\eta^\xi \otimes \xi - \psi_\eta^\xi) = 0. & (12.12b) \end{cases}$$

Equation (12.12b) can be written

$$J_\eta^\xi : \psi_\eta^\xi = H : (v_\eta^\xi \otimes \xi) \quad \text{with} \quad J_\eta^\xi = H + \eta^2 \xi \cdot G \cdot \xi. \quad (12.13)$$

As $J_\eta^\xi \geq H$, the kernels of H and J_η^ξ satisfy $Ker(J_\eta^\xi) \subset Ker(H)$ and their images satisfy $Im(H) = Ker(H)^\perp \subset Ker(J_\eta^\xi)^\perp = Im(J_\eta^\xi)$. Introducing the pseudo-inverse $(J_\eta^\xi)^+$ of J_η^ξ , the solutions of (12.13) read

$$\psi_\eta^\xi = (J_\eta^\xi)^+ : (H : (v_\eta^\xi \otimes \xi)) + \Delta$$

where Δ is any element in $Ker(J_\eta^\xi)$. We have $H : \psi_\eta^\xi = H : (J_\eta^\xi)^+ : (H : (v_\eta^\xi \otimes \xi))$ and we can eliminate ψ_η^ξ from Equation (12.12a). We get

$$K_\eta^\xi \cdot v_\eta^\xi = f^\xi \quad (12.14)$$

with

$$K_\eta^\xi = \xi \cdot (C + H - H : (J_\eta^\xi)^+ : H) \cdot \xi + \eta^2 (\xi \otimes \xi) : D : (\xi \otimes \xi). \quad (12.15)$$

The product $J_\eta^{\xi+} : J_\eta^\xi$ is the orthogonal projection onto the image $Im(J_\eta^\xi)$. We have $(J_\eta^\xi)^+ : J_\eta^\xi : (J_\eta^\xi)^+ = (J_\eta^\xi)^+$ and the fact that $Im(H) \subset Im(J_\eta^\xi)$ implies $H : J_\eta^{\xi+} : J_\eta^\xi = H$. Using these remarks, one can check that $H - H : (J_\eta^\xi)^+ : H$ is identical to

$$H \cdot (J_\eta^\xi)^+ : (J_\eta^\xi - H) : (J_\eta^\xi)^+ : H + (J_\eta^\xi - H) : (J_\eta^\xi)^+ : H : (J_\eta^\xi)^+ : (J_\eta^\xi - H).$$

Since $J_\eta^\xi - H = \eta^2 \xi \cdot G \cdot \xi$ is non-negative, we deduce that $H - H : (J_\eta^\xi)^+ : H$ is non-negative and that $K_\eta^\xi \geq \alpha \|\xi\|^2 Id$ is definite positive. The solution of (12.14) is thus given by

$$v_\eta^\xi = (K_\eta^\xi)^{-1} \cdot f^\xi. \quad (12.16)$$

12.5 Comparison of Different Models at Large Scale

Our goal is to compare the solutions of problem (12.11) for different values of the material parameters C, D, G, H when η is small. In the Fourier setting, this will be obtained by estimating the tensor $(K_\eta^\xi)^{-1}$. To that aim we first focus on the term $H : (J_\eta^\xi)^+ : H$.

Lemma 12.1. *Let $P = H^+ : H$ and $Q = Id_4 - P$ be the projectors onto the image and the kernel of H . For any $\xi \in \mathbb{R}^3$, let us consider the following generalized Schur complement:*

$$G_{//}^\xi := P : (\xi \cdot G \cdot \xi) : P - (P : (\xi \cdot G \cdot \xi) : Q) : (Q : (\xi \cdot G \cdot \xi) : Q)^+ : (Q : (\xi \cdot G \cdot \xi) : P).$$

We have

$$H : (J_\eta^\xi)^+ : H = (H^+ + \eta^2 H^+ : G_{//}^\xi : H^+)^+.$$

Proof. Let M be any matrix in $\text{Im}(H)$ and set $N := (J_\eta^\xi)^+ : H : M$. We have $H : M = J_\eta^\xi : N$ that is $H : M = (H + \eta^2 \xi \cdot G \cdot \xi) : N$. Once projected onto the image and the kernel of H this equation reads

$$H : M = (H + \eta^2 P : (\xi \cdot G \cdot \xi)) : N \quad \text{and} \quad 0 = \eta^2 Q : (\xi \cdot G \cdot \xi) : N.$$

Decomposing also $N = P : N + Q : N$, we get

$$\begin{cases} H : M = (H + \eta^2 P : (\xi \cdot G \cdot \xi) : P) : (P : N) \\ \quad \quad \quad \quad \quad + \eta^2 P : (\xi \cdot G \cdot \xi) : Q : (Q : N), \quad (12.17a) \\ 0 = \eta^2 Q : (\xi \cdot G \cdot \xi) : P : (P : N) + \eta^2 Q : (\xi \cdot G \cdot \xi) : Q : (Q : N). \quad (12.17b) \end{cases}$$

Equation (12.17b) implies

$$Q : N = -(Q : (\xi \cdot G \cdot \xi) : Q)^+ : Q : (\xi \cdot G \cdot \xi) : P : (P : N) + E$$

where E is any element of $\text{Ker}(Q : (\xi \cdot G \cdot \xi) : Q)$. We now remark that

$$(Q : (\xi \cdot G \cdot \xi) : Q) : E = 0 \implies (P : (\xi \cdot G \cdot \xi) : Q) : E = 0.$$

Indeed, for any matrix Z , the affine function of the real λ

$$\begin{aligned} Z : P : (\xi \cdot G \cdot \xi) : P : Z + 2\lambda Z : P : (\xi \cdot G \cdot \xi) : Q : E \\ = (P : Z + \lambda Q : E) : (\xi \cdot G \cdot \xi) : (P : Z + \lambda Q : E) \end{aligned}$$

is non negative and this implies that $Z : P : (\xi \cdot G \cdot \xi) : Q : E = 0$ for any matrix Z . In consequence

$$P : (\xi \cdot G \cdot \xi) : Q : (Q : N) = -P : (\xi \cdot G \cdot \xi) : Q : (Q : (\xi \cdot G \cdot \xi) : Q)^+ : Q : (\xi \cdot G \cdot \xi) : P : (P : N)$$

and Equation (12.17a) becomes $H : M = (H + \eta^2 G_{//}^\xi) : P : N$. Recalling that $P = H^+ : H$ and $N = (J_\eta^\xi)^+ : H : M$, we obtain

$$H : M = (H + \eta^2 G_{//}^\xi) : H^+ : H : (J_\eta^\xi)^+ : H : M$$

and finally

$$M = H^+ : H : M = \left(H^+ : (H + \eta^2 G_{//}^\xi) : H^+ \right) : \left(H : (J_\eta^\xi)^+ : H \right) : M.$$

As this is true for any M in the image of H and thus in the image of $H : (J_\eta^\xi)^+ : H$, we get the desired result. \square

Remark 12.1. The Schur complement corresponds to a minimization problem: for any matrix M , we have

$$\begin{aligned} & \inf_{N \in \text{Ker}(H)} \{((P : M + N) \otimes \xi) : G : ((P : M + N) \otimes \xi)\} \\ &= \inf_{N \in \text{Ker}(H)} \{(P : M + N) : (\xi \cdot G \cdot \xi) : (P : M + N)\} \\ &= \inf_{N \in \text{Ker}(H)} \{M : (P : (\xi \cdot G \cdot \xi) : P) : M + 2N : (Q : (\xi \cdot G \cdot \xi) : P) : M \\ & \quad + N : (Q : (\xi \cdot G \cdot \xi) : Q) : N\}. \end{aligned}$$

The infimum is reached when $(Q : (\xi \cdot G \cdot \xi) : P) : M + (Q : (\xi \cdot G \cdot \xi) : Q) : N = 0$ that is when $N = -(Q : (\xi \cdot G \cdot \xi) : Q)^+ : (Q : (\xi \cdot G \cdot \xi) : P) : M$. At this minimum we have

$$\begin{aligned} N : (Q : (\xi \cdot G \cdot \xi) : Q) : N &= -N : (Q : (\xi \cdot G \cdot \xi) : P) : M \\ &= M : (P : (\xi \cdot G \cdot \xi) : Q) : (Q : (\xi \cdot G \cdot \xi) : Q)^+ : (Q : (\xi \cdot G \cdot \xi) : P) : M \end{aligned}$$

and we finally get

$$\inf_{N \in \text{Ker}(H)} \{((P : M + N) \otimes \xi) : G : ((P : M + N) \otimes \xi)\} = M : G_{//}^{\xi} : M.$$

A straightforward consequence of this minimization formulation is that, for any matrix M ,

$$0 \leq M : G_{//}^{\xi} : M \leq \beta \|\xi\|^2 \|M\|^2. \quad (12.18)$$

Lemma 12.2. *We have the following estimations for K_{η}^{ξ} :*

$$K_{\eta}^{\xi} \geq \xi \cdot C \cdot \xi, \quad (12.19)$$

$$\begin{aligned} K_{\eta}^{\xi} \geq \xi \cdot C \cdot \xi + \eta^2 (\xi \cdot G_{//}^{\xi} \cdot \xi + (\xi \otimes \xi) : D : (\xi \otimes \xi)) \\ - \eta^4 \xi \cdot (G_{//}^{\xi} : H^+ : G_{//}^{\xi}) \cdot \xi, \end{aligned} \quad (12.20)$$

$$K_{\eta}^{\xi} \leq \xi \cdot C \cdot \xi + \eta^2 (\xi \cdot G_{//}^{\xi} \cdot \xi + (\xi \otimes \xi) : D : (\xi \otimes \xi)). \quad (12.21)$$

Proof. First estimation will be a consequence of

$$H : (J_{\eta}^{\xi})^+ : H \leq H \quad (12.22)$$

while the two last ones are respectively equivalent to

$$H : (J_{\eta}^{\xi})^+ : H \leq H - \eta^2 G_{//}^{\xi} + \eta^4 G_{//}^{\xi} : H^+ : G_{//}^{\xi}, \quad (12.23)$$

$$H : (J_{\eta}^{\xi})^+ : H \geq H - \eta^2 G_{//}^{\xi}. \quad (12.24)$$

As all these quadratic forms vanish outside of $Im(H)$, it is enough to check the inequalities on this space. As, on this space, $(H:(J_\eta^\xi)^+:H)^+ = H^+ + \eta^2 H^+ : G_{//}^\xi : H^+$ is invertible, we can multiply previous inequalities by this tensor on the left and on the right. In order to shorten notation, let us temporarily introduce the non-negative tensor $X^\xi = H^+ : G_{//}^\xi : H^+$. We are reduced to proving

$$\begin{aligned} H^+ + \eta^2 X^\xi &\leq (H^+ + \eta^2 X^\xi) : H : (H^+ + \eta^2 X^\xi), \\ H^+ + \eta^2 X^\xi &\leq (H^+ + \eta^2 X^\xi) : (H - \eta^2 G_{//}^\xi + \eta^4 G_{//}^\xi : H^+ : G_{//}^\xi) : (H^+ + \eta^2 X^\xi), \\ H^+ + \eta^2 X^\xi &\geq (H^+ + \eta^2 X^\xi) : (H - \eta^2 G_{//}^\xi) : (H^+ + \eta^2 X^\xi). \end{aligned}$$

This is obvious when developing the right-hand side of these three inequalities as they become respectively

$$\begin{aligned} 0 &\leq X^\xi + \eta^2 X^\xi : H : X^\xi, \\ 0 &\leq X^\xi : H : X^\xi : H : X^\xi + \eta^2 X^\xi : H : X^\xi : H : X^\xi : H : X^\xi, \\ 0 &\geq -X^\xi : H : X^\xi - \eta^2 X^\xi : H : X^\xi : H : X^\xi. \end{aligned}$$

□

Remark 12.2. From estimation (12.19), we deduce

$$\|f^\xi\| = \|K_\eta^\xi \cdot v_\eta^\xi\| \geq \alpha \|\xi\|^2 \|v_\eta^\xi\|. \tag{12.25}$$

We recover the fact that, when f belongs to L^2_{loc} , the equilibrium solution v_η belongs to H^2_{loc} :

$$\begin{aligned} \int_\Omega \|\nabla \nabla v_\eta\|^2 dx &= \pi \sum_{\xi \in \mathbb{Z}^3} \|v_\eta^\xi \otimes \xi \otimes \xi\|^2 \leq \pi \sum_{\xi \in \mathbb{Z}^3} \|v_\eta^\xi\|^2 \|\xi\|^4 \\ &\leq \pi \alpha^{-2} \sum_{\xi \in \mathbb{Z}^3} \|f^\xi\|^2 = \alpha^{-2} \int_\Omega \|f\|^2 dx. \end{aligned}$$

Theorem 12.1. *When η goes to zero, all solutions v_η converge to the solution v_0 of the classical elasticity problem. More precisely, for any $\xi \in \mathbb{Z}^3$, we have the following estimation*

$$\|v_0^\xi - v_\eta^\xi\| \leq 2\eta^2 \frac{\beta}{\alpha^2} \|f^\xi\|$$

which directly implies $\|v_\eta - v_0\|_{L^2} \leq 2\eta^2 \frac{\beta}{\alpha^2} \|f\|_{L^2}$.

Proof. When $\eta = 0$ (which is equivalent to assuming that $D = G = 0$ and $H = 0$), we have $K_0^\xi = \xi \cdot C \cdot \xi$ and equation (12.14) reduces to $(\xi \cdot C \cdot \xi) \cdot v_0^\xi = f^\xi$. From $K_\eta^\xi \cdot v_\eta^\xi = f^\xi = (\xi \cdot C \cdot \xi) \cdot v_0^\xi$, we deduce

$$K_\eta^\xi \cdot (v_0^\xi - v_\eta^\xi) = (K_\eta^\xi - \xi \cdot C \cdot \xi) \cdot v_0^\xi.$$

Using Lemma 12.2, we get

$$\alpha \|\xi\|^2 \|v_0^\xi - v_\eta^\xi\| \leq \eta^2 \|(\xi \cdot G_{//}^\xi \cdot \xi + (\xi \otimes \xi) : D : (\xi \otimes \xi)) \cdot v_0^\xi\|.$$

Definition of $G_{//}^\xi$ clearly shows that $G_{//}^\xi \leq P : (\xi \cdot G \cdot \xi) : P$ and thus that $\|(\xi \cdot G_{//}^\xi \cdot \xi) \cdot v_0^\xi\| \leq \beta \|\xi\|^4 \|v_0^\xi\|$. As we have the same estimation for the term $\|(\xi \otimes \xi) : D : (\xi \otimes \xi)\| \cdot v_0^\xi$, we get

$$\|v_0^\xi - v_\eta^\xi\| \leq 2\eta^2 \frac{\beta}{\alpha} \|\xi\|^2 \|v_0^\xi\| \leq 2\eta^2 \frac{\beta}{\alpha^2} \|f^\xi\|.$$

Therefore

$$\|v_\eta - v_0\|_{L^2}^2 = \pi \sum_{\xi \in \mathbb{Z}^3} \|v_0^\xi - v_\eta^\xi\|^2 \leq 4\eta^4 \frac{\beta^2}{\alpha^4} \|f\|_{L^2}^2.$$

□

Previous theorem states that, in any case, the minimizer of a strain-gradient or a generalized continuum energy behaves, at the main order with respect to the characteristic length of the applied force, like a classical elastic model. Clearly different models sharing the same elasticity tensor C cannot be differentiated at this order.

Let us now compare more precisely the solutions v_η and \tilde{v}_η of (12.11) associated respectively the sets of material tensors (C, D, H, G) and $(C, D+L, 0, 0)$. In Fourier setting, these equations read $K_\eta^\xi \cdot v_\eta^\xi = f^\xi$ and $\tilde{K}_\eta^\xi \cdot \tilde{v}_\eta^\xi = f^\xi$ with

$$\begin{aligned} K_\eta^\xi &= \xi \cdot (C + H - (H^+ + \eta^2 H^+ : G_{//}^\xi : H^+)^+) \cdot \xi + \eta^2 (\xi \otimes \xi) : D : (\xi \otimes \xi), \\ \tilde{K}_\eta^\xi &= \xi \cdot C \cdot \xi + \eta^2 (\xi \otimes \xi) : (D + L) : (\xi \otimes \xi). \end{aligned}$$

We have

$$\tilde{K}_\eta^\xi \cdot (v_\eta^\xi - \tilde{v}_\eta^\xi) = (\tilde{K}_\eta^\xi - K_\eta^\xi) \cdot v_\eta^\xi. \quad (12.26)$$

From Lemma 12.2 we deduce

$$\begin{cases} \tilde{K}_\eta^\xi - K_\eta^\xi \geq \eta^2 \xi \cdot (\xi \cdot L \cdot \xi - G_{//}^\xi) \cdot \xi, \\ \tilde{K}_\eta^\xi - K_\eta^\xi \leq \eta^2 \xi \cdot (\xi \cdot L \cdot \xi - G_{//}^\xi) \cdot \xi + \eta^4 \xi \cdot (G_{//}^\xi : H^+ : G_{//}^\xi) \cdot \xi. \end{cases} \quad (12.27)$$

In order to proceed further, we need an important assumption over the tensor $G_{//}^\xi$ defined in Lemma 12.1 in terms of G , P and Q , that is in terms of H and G .

Assumption 1 *The tensors H and G are such that there exists a six-order tensor $G_{//}$ satisfying, for any vector $\xi \in \mathbb{Z}^3$,*

$$\xi \cdot G_{//}^\xi \cdot \xi = (\xi \otimes \xi) : G_{//} : (\xi \otimes \xi). \quad (12.28)$$

We still call β a constant which, in addition to (12.6)-(12.7) satisfies, for any third-order tensor T ,

$$T : G_{//} : T \leq \beta \|T\|^2.$$

In many cases Assumption 1 is obtained as the consequence of stronger assumptions. Let us denote $P : G : Q$ the sixth order tensor defined by $(P : G : Q)_{ijklmn} := \sum_{p,q,u,v} P_{ijpq} G_{pqkuvn} Q_{uvlm}$. The tensor $P : G : P$ is defined in a similar way.

Assumption 2 $P : G : Q = 0$.

Indeed, in that case, Assumption 1 is satisfied with $G_{//} = P : G : P$.

Assumption 3 H is non degenerate.

Indeed, in that last case, $P = Id_4$ and $Q = 0$, Assumption 2 is obviously satisfied and we have $G_{//} = G$.

Theorem 12.2. *Assume that f is smooth and that G and H satisfy Assumption 1. Then the solution v_η of (12.11) associated with the set of material tensors (C, D, H, G) shares the same asymptotic behavior at order η^2 as the solution \tilde{v}_η of (12.11) associated with the set of material tensors $(C, D + G_{//}, 0, 0)$. More precisely, we have*

$$\|\tilde{v}_\eta^\xi - v_\eta^\xi\| \leq \eta^4 \frac{\beta^3}{\alpha^2} \|\xi\|^2 \|f^\xi\|$$

which directly implies $\|v_\eta - \tilde{v}_\eta\|_{L^2(\Omega)} \leq \eta^4 \frac{\beta^3}{\alpha^2} \|f\|_{H^2(\Omega)}$.

Reciprocally if, for any smooth force field f , v_η shares the same asymptotic behavior at order η^2 as the solution \tilde{v}_η of (12.11) associated with the set of material tensors $(C, D + L, 0, 0)$, then Assumption 1 is satisfied with $G_{//} = L$.

Proof. Indeed, replacing L by $G_{//}$ and $\xi \cdot G_{//}^\xi \cdot \xi$ by $\xi \cdot (\xi \cdot G_{//} \cdot \xi) \cdot \xi$ in (12.27), we get

$$0 \leq \tilde{K}_\eta^\xi - K_\eta^\xi \leq \eta^4 \xi \cdot (G_{//}^\xi : H^+ : G_{//}^\xi) \cdot \xi.$$

From (12.26) we get the estimation

$$\alpha \|\xi\|^2 \|\tilde{v}_\eta^\xi - v_\eta^\xi\| \leq \eta^4 \|(\xi \cdot (G_{//}^\xi : H^+ : G_{//}^\xi) \cdot \xi) \cdot v_\eta^\xi\|.$$

Using (12.25) (12.18), we obtain the desired result

$$\|\tilde{v}_\eta^\xi - v_\eta^\xi\| \leq \eta^4 \frac{\beta^3}{\alpha^2} \|\xi\|^2 \|f^\xi\|.$$

To prove the converse, let us assume that, for any smooth force field f ,

$$\frac{1}{\eta^2} \|v_\eta - \tilde{v}_\eta\|_{L^2(\Omega)} \rightarrow 0.$$

Dividing equation (12.26) by η^2 , using (12.27) and passing to the limit $\eta \rightarrow 0$, we get

$$0 = (\xi \cdot (\xi \cdot L \cdot \xi - G_{//}^\xi) \cdot \xi) \cdot v_0^\xi.$$

Let w be a C^∞ Y -periodic function satisfying $w^0 = 0$ and, for any $\xi \neq 0$, $w^\xi \neq 0$. Let $k \in \{1, 2, 3\}$. Consider the load $f := -\operatorname{div}(C : e(we^k))$. Clearly, the solution v_0 of the classical elasticity problem when this load is applied coincides with $w e^k$. For this load, previous equality reads

$$w^\xi \left((\xi \otimes \xi) : L : (\xi \otimes \xi) - \xi \cdot G_{//}^\xi \cdot \xi \right) \cdot e^k = 0.$$

As, for $\xi \neq 0$, $w^\xi \neq 0$, we have $\left((\xi \otimes \xi) : L : (\xi \otimes \xi) - \xi \cdot G_{//}^\xi \cdot \xi \right) \cdot e^k = 0$ which remains true for $\xi = 0$. This being true for any $k \in \{1, 2, 3\}$, we get for any $\xi \in \mathbb{Z}^3$,

$$(\xi \otimes \xi) : L : (\xi \otimes \xi) - \xi \cdot G_{//}^\xi \cdot \xi = 0. \quad (12.29)$$

□

12.6 Examples

We study in this section different energies which enter the general model introduced in (12.4): they correspond to the choice $D = 0$ and to different choices of the tensors H and G . Let us first provide examples for which Theorem 12.2 applies and thus which can be approximated, up to order η^4 by a strain-gradient model.

i) Micromorphic models of the type

$$\mathcal{E}(u) := \inf_{\phi} \int_{\Omega} \left(\frac{1}{2} \nabla \phi : G : \nabla \phi + \frac{1}{2} \|\nabla u - \phi\|^2 + \frac{1}{2} e(u) : C : e(u) \right) dx$$

correspond to the choice $H = Id_4$. They satisfy Assumption 3 and thus can be approximated, up to order η^4 by strain-gradient models with energy

$$\mathcal{E}(u) := \inf_{\phi} \int_{\Omega} \left(\frac{1}{2} \nabla \nabla u : G : \nabla \nabla u + \frac{1}{2} e(u) : C : e(u) \right) dx.$$

ii) Cosserat models of the type

$$\mathcal{E}(u) := \inf_w \int_{\Omega} \left(\frac{1}{2} \nabla w : B : \nabla w + \frac{1}{2} \|\nabla \times u - w\|^2 + \frac{1}{2} e(u) : C : e(u) \right) dx$$

correspond to the choice $H_{ijkl} = \sum_p \epsilon_{ijp} \epsilon_{klp}$ and $G_{ijklmn} = \sum_{p,q} \epsilon_{ijp} B_{pkqn} \epsilon_{lmq}$ where ϵ_{ijm} stands for the usual Levi-Civita symbol. The expression in terms of w instead of ϕ is simply obtained by substituting $w_i = \epsilon_{ikj} \phi_{jk}$ in the original expression. We have $P = \frac{1}{2} H$, $G : P = G$ and thus $G : Q = 0$. Assumption 2 is satisfied: Cosserat models can be approximated, up to order η^4 by strain-gradient models (actually couple-stress models) with energy

$$\mathcal{E}(u) := \inf_w \int_{\Omega} \left(\frac{1}{2} \nabla(\nabla \times u) : B : \nabla(\nabla \times u) + \frac{1}{2} e(u) : C : e(u) \right) dx.$$

iii) Consider now the following energy:

$$\int_{\Omega} \left(\frac{1}{2} \left(\left(\frac{\partial \phi_{11}}{\partial x_2} + \frac{\partial \phi_{22}}{\partial x_2} \right)^2 + \left(\frac{\partial \phi_{22}}{\partial x_2} \right)^2 \right) + \frac{1}{2} \left(\frac{\partial u_1}{\partial x_1} - \phi_{11} \right)^2 + \frac{1}{2} e(u) : C : e(u) \right) dx.$$

This energy corresponds to the choice

$$\begin{cases} D = 0, & H = (e^1 \otimes e^1)^{\otimes 2}, & (12.30a) \\ G = (e^2 \otimes e^2 \otimes e^2)^{\otimes 2} + (e^1 \otimes e^1 \otimes e^2 + e^2 \otimes e^2 \otimes e^2)^{\otimes 2}. & (12.30b) \end{cases}$$

Neither assumption 3 nor Assumption 2 are satisfied. Computation of $G_{//}^{\xi}$ needs some work. We check successively that $P = H^+ = H$ and

$$\begin{aligned} \xi \cdot G \cdot \xi &= \xi_2^2 \left((e^2 \otimes e^2)^{\otimes 2} + (e^1 \otimes e^1 + e^2 \otimes e^2)^{\otimes 2} \right), \\ P : (\xi \cdot G \cdot \xi) : P &= \xi_2^2 (e^1 \otimes e^1)^{\otimes 2}, \\ Q : (\xi \cdot G \cdot \xi) : P &= \xi_2^2 e^2 \otimes e^2 \otimes e^1 \otimes e^1, \\ P : (\xi \cdot G \cdot \xi) : Q &= \xi_2^2 e^1 \otimes e^1 \otimes e^2 \otimes e^2, \\ Q : (\xi \cdot G \cdot \xi) : Q &= 2\xi_2^2 (e^2 \otimes e^2)^{\otimes 2}, \\ (Q : (\xi \cdot G \cdot \xi) : Q)^+ &= (2\xi_2^2)^{-1} (e^2 \otimes e^2)^{\otimes 2}. \end{aligned}$$

We finally obtain

$$G_{//}^{\xi} = \frac{\xi_2^2}{2} (e^1 \otimes e^1)^{\otimes 2} = \xi \cdot \left(\frac{1}{2} (e^1 \otimes e^1 \otimes e^2)^{\otimes 2} \right) \cdot \xi.$$

Note that this computation is valid only when $\xi_2 \neq 0$ but one can easily check that the result remains true when $\xi_2 = 0$. This micromorphic model satisfies Assumption 1 with $G_{//} = \frac{1}{2} (e^1 \otimes e^1 \otimes e^2)^{\otimes 2}$ and Theorem 12.2 again applies. The model can be approximated, up to order η^4 by the strain-gradient model with energy

$$\int_{\Omega} \left(\frac{1}{4} \left(\frac{\partial^2 u_1}{\partial x_1 \partial x_2} \right)^2 + \frac{1}{2} e(u) : C : e(u) \right) dx.$$

iv) Let us now show that there exist energies for which the conclusion of Theorem 12.2 does not apply. We modify a little bit the previous example by considering the following energy:

$$\inf_{\phi} \int_{\Omega} \left(\frac{1}{2} \left(\left(\frac{\partial \phi_{11}}{\partial x_2} + \frac{\partial \phi_{22}}{\partial x_1} \right)^2 + \left(\frac{\partial \phi_{22}}{\partial x_2} \right)^2 \right) + \frac{1}{2} \left(\frac{\partial u_1}{\partial x_1} - \phi_{11} \right)^2 + \frac{1}{2} e(u) : C : e(u) \right) dx,$$

which corresponds to the choice

$$\begin{cases} D = 0, & H = (e^1 \otimes e^1)^{\otimes 2}, \\ G = (e^2 \otimes e^2 \otimes e^2)^{\otimes 2} + (e^1 \otimes e^1 \otimes e^2 + e^2 \otimes e^2 \otimes e^1)^{\otimes 2}. \end{cases} \quad (12.31a)$$

$$(12.31b)$$

Again we have $P = H^+ = H$. Computation of $G_{//}^{\xi}$ is straightforward: for any $\xi \neq 0$, we have

$$\xi \cdot G \cdot \xi = \xi_2^2 (e^2 \otimes e^2)^{\otimes 2} + (\xi_2 e^1 \otimes e^1 + \xi_1 e^2 \otimes e^2)^{\otimes 2},$$

$$P : (\xi \cdot G \cdot \xi) : P = \xi_2^2 (e^1 \otimes e^1)^{\otimes 2},$$

$$Q : (\xi \cdot G \cdot \xi) : P = \xi_1 \xi_2 e^2 \otimes e^2 \otimes e^1 \otimes e^1,$$

$$P : (\xi \cdot G \cdot \xi) : Q = \xi_1 \xi_2 e^1 \otimes e^1 \otimes e^2 \otimes e^2,$$

$$Q : (\xi \cdot G \cdot \xi) : Q = (\xi_1^2 + \xi_2^2) (e^2 \otimes e^2)^{\otimes 2},$$

$$(Q : (\xi \cdot G \cdot \xi) : Q)^+ = (\xi_1^2 + \xi_2^2)^{-1} (e^2 \otimes e^2)^{\otimes 2}.$$

$$(P : (\xi \cdot G \cdot \xi) : Q) : (Q : (\xi \cdot G \cdot \xi) : Q)^+ : (Q : (\xi \cdot G \cdot \xi) : P)$$

$$= \frac{\xi_1^2 \xi_2^2}{\xi_1^2 + \xi_2^2} (e^1 \otimes e^1)^{\otimes 2}$$

and finally

$$G_{//}^{\xi} = \frac{\xi_2^4}{\xi_1^2 + \xi_2^2} (e^1 \otimes e^1)^{\otimes 2} \quad \text{and} \quad \xi \cdot G_{//}^{\xi} \cdot \xi = \frac{\xi_2^4 \xi_1^2}{\xi_1^2 + \xi_2^2} e^1 \otimes e^1.$$

Assume, by contradiction that Assumption 1 is satisfied: for any $\xi \neq 0$ in \mathbb{Z}^3 we would have

$$\xi \cdot (\xi \cdot G_{//}^{\xi} \cdot \xi) \cdot \xi - \frac{\xi_2^4 \xi_1^2}{\xi_1^2 + \xi_2^2} e^1 \otimes e^1 = 0$$

that is, for any ξ in \mathbb{Z}^3 ,

$$(\xi_1^2 + \xi_2^2) \xi \cdot (\xi \cdot G_{//}^{\xi} \cdot \xi) \cdot \xi - \xi_2^4 \xi_1^2 e^1 \otimes e^1 = 0.$$

This polynomial identity extends to whole \mathbb{C}^3 . We get a contradiction by considering for instance $\xi = (1, i, 0)$. By converse statement of Theorem 12.2 we know that there is no strain-gradient model which can approximate the considered model more accurately than what is done at order η^2 by the standard model

$$\int_{\Omega} \frac{1}{2} e(u) : C : e(u) dx.$$

12.7 Conclusion

Our study has practical implications. Assume that you are analyzing the results of an experimental campaign, that is the equilibrium displacement fields of samples submitted to different force fields. Assume moreover that you have noticed scale effects and thus that you are suspecting your material to behave either like a strain-gradient one or a micromorphic one. Our study shows that it is rather difficult to differentiate these two possibilities. Indeed, in general, the characteristic wavelengths of the applied force fields are much larger than the intrinsic lengths of the suspected models. Let $\eta \ll 1$ be their ratio. Then both strain-gradient and micromorphic models provide a correction to the Cauchy model of order η^2 but, for well tuned material parameters, the difference between the two corrections is extremely small: of order η^4 . In other words, in order to decide whether your material is better described by a micromorphic model or by a strain-gradient one, you must be extremely precise or use force fields which vary extremely rapidly in space.

Our study gives also a new insight on recent results about periodic homogenization of elastic materials: results of Smyshlyaev and Cherednichenko (2000); Allaire et al (2016) state that the first correction which must be applied to the classical homogenized strain model is always obtained by adding in the energy a small strain-gradient term. On the other hand, results from Abdoul-Anziz and Seppecher (2018a,b); Jakabčičin and Seppecher (2020) provide micromorphic effective behaviors. These seemingly contradictory results may become coherent when spread enough forces are considered.

We must emphasize that our results apply only for micromorphic models which satisfy Assumption 1. The question of the status of models which do not satisfy this assumption remains open: previous conclusion does not apply. We suspect that such models cannot be obtained through periodic homogenization. We recall that the example that we provide in Section 12.6 corresponds to a quadratic, objective and lower-semi-continuous functional and thus, as proved in Camar-Eddine and Seppecher (2003), that it can be obtained as the limit of heterogeneous classical elastic continua. However the results of Camar-Eddine and Seppecher (2003) are obtained using non-periodic heterogeneities. This leads to a new general question: what is the subclass of all functionals which can be obtained as the limit of *periodically* heterogeneous classical elastic continua? And, in particular, is it equivalent, for a functional \mathcal{E}^m defined by (12.4), to belong to this class and to satisfy Assumption 1?

Acknowledgements The first author thanks Professor Francesco dell’Isola for countless friendly stimulating discussions about micromorphic models, strain-gradient ones and their relationships.

The authors acknowledge the support of the French *Agence Nationale de la Recherche* (ANR), under grant ANR-17-CE08-0039 (project ArchiMathOS).

References

- Abdoul-Anziz H, Seppecher P (2018a) Homogenization of periodic graph-based elastic structures. *Journal de l'Ecole polytechnique–Mathématiques* 5:259–288
- Abdoul-Anziz H, Seppecher P (2018b) Strain gradient and generalized continua obtained by homogenizing frame lattices. *Mathematics and Mechanics of Complex Systems* 6(3):213–250
- Abdoul-Anziz H, Jakabčín L, Seppecher P (2021) Homogenization of an elastic material reinforced by very strong fibres arranged along a periodic lattice. *Proceedings of the Royal Society A* 477(2246):20200,620
- Alibert JJ, Della Corte A (2015) Second-gradient continua as homogenized limit of pantographic microstructured plates: a rigorous proof. *Z Angew Math Phys* 66(5):2855–2870
- Alibert JJ, Seppecher P, dell'Isola F (2003) Truss modular beams with deformation energy depending on higher displacement gradients. *Mathematics and Mechanics of Solids* 8(1):51–73
- Allaire G (1992) Homogenization and two-scale convergence. *SIAM Journal on Mathematical Analysis* 23(6):1482–1518
- Allaire G, Briane M, Vanninathan M (2016) A comparison between two-scale asymptotic expansions and Bloch wave expansions for the homogenization of periodic structures. *SeMA Journal* 73(3):237–259
- Bakhvalov NS, Panasenko G (2012) *Homogenisation: averaging processes in periodic media: mathematical problems in the mechanics of composite materials*, vol 36. Springer Science & Business Media
- Bensoussan A, Lions JL, Papanicolau G (1978) *Asymptotic Analysis for Periodic Structures*. North-Holland, Amsterdam
- Briane M, Camar-Eddine M (2007) Homogenization of two-dimensional elasticity problems with very stiff coefficients. *Journal de mathématiques pures et appliquées* 88(6):483–505
- Camar-Eddine M, Seppecher P (2003) Determination of the closure of the set of elasticity functionals. *Archive for Rational Mechanics and Analysis* 170(3):211–245
- Casal P (1972) La théorie du second gradient et la capillarité. *Comptes Rendus Acad Sci Paris* 274:1571–1574
- Cosserat E, Cosserat F (1896) Sur la théorie de l'élasticité. premier mémoire. In: *Annales de la Faculté des sciences de Toulouse: Mathématiques*, vol 10, pp II–II16
- dell'Isola F, Giorgio I, Pawlikowski M, Rizzi N (2016) Large deformations of planar extensible beams and pantographic lattices: Heuristic homogenization, experimental and numerical examples of equilibrium. *Proceeding of the Royal Society of London, Series A: Mathematical, Physical and Engineering sciences* 472(2185)
- Durand B, Lebée A, Seppecher P, Sab K (2022) Predictive strain-gradient homogenization of a pantographic material with compliant junctions
- Forest S (1999) Homogenization methods and the mechanics of generalized continua. *Geometry, Continua and Microstructure*, ed by G Maugin, *Travaux en Cours No 60*, Hermann, Paris, France pp 35–48
- Forest S, Sab K (2020) Finite-deformation second-order micromorphic theory and its relations to strain and stress gradient models. *Mathematics and Mechanics of Solids* 25(7):1429–1449
- Germain P (1973) The method of virtual power in continuum mechanics. part 2: Microstructure. *SIAM Journal on Applied Mathematics* 25(3):556–575
- Germain P (2020) The method of virtual power in the mechanics of continuous media, i: Second-gradient theory. *Mathematics and Mechanics of Complex Systems* 8(2):153–190
- Jakabčín L, Seppecher P (2020) On periodic homogenization of highly contrasted elastic structures. *Journal of the Mechanics and Physics of Solids* 144:104,104
- Lam DC, Yang F, Chong A, Wang J, Tong P (2003) Experiments and theory in strain gradient elasticity. *Journal of the Mechanics and Physics of Solids* 51(8):1477–1508
- Mindlin RD (1965) Second gradient of strain and surface-tension in linear elasticity. *International Journal of Solids and Structures* 1(4):417–438

- Mindlin RD, Tiersten H (1962) Effects of couple-stresses in linear elasticity. *Archive for Rational Mechanics and Analysis* 11(1):415–448
- Misra A, Placidi L, dell’Isola F, Barchiesi E (2021) Identification of a geometrically nonlinear micromorphic continuum via granular micromechanics. *Zeitschrift für angewandte Mathematik und Physik* 72(4):1–21
- Pideri C, Seppecher P (1997) A second gradient material resulting from the homogenization of an heterogeneous linear elastic medium. *Continuum Mechanics and Thermodynamics* 9(5):241–257
- Rahali Y, Giorgio I, Ganghoffer JF, dell’Isola F (2015) Homogenization à la Piola produces second gradient continuum models for linear pantographic lattices. *International Journal of Engineering Science* 97:148–172
- Sanchez-Palencia E (1980) *Non-homogeneous media and vibration theory*. Springer-Verlag, Berlin
- Smyshlyaev VP, Cherednichenko KD (2000) On rigorous derivation of strain gradient effects in the overall behaviour of periodic heterogeneous media. *Journal of the Mechanics and Physics of Solids* 48:1325–1357
- Turco E, dell’Isola F, Cazzani A, Rizzi NL (2016) Hencky-type discrete model for pantographic structures: numerical comparison with second gradient continuum models. *Z Angew Math Phy* 67(4):85



Chapter 13

Quasiconvexity and Rank-One Convexity in Cosserat Elasticity Theory

Milad Shirani, David J. Steigmann

Abstract The quasiconvexity and rank-one convexity conditions of conventional nonlinear elasticity theory are extended to nonlinear Cosserat elasticity. These furnish necessary conditions for energy minimizers in conservative boundary-value problems.

Keywords: Cosserat elasticity · Quasiconvexity · Rank-one convexity

13.1 Introduction

In this work we present derivations of the quasiconvexity and rank-one convexity conditions in the framework of Cosserat elasticity theory. These are necessary conditions for strong relative minimizers of the potential energy in conservative problems, and generalize the Legendre-Hadamard necessary conditions for weak relative minimizers recently obtained in Shirani et al (2020). Background material on Cosserat elasticity may be found in Cosserat and Cosserat (1909); Truesdell and Noll (2004); Reissner (1975, 1987); Pietraszkiewicz and Eremeyev (2009); Neff (2006).

For the sake of completeness we present a brief resumé of equilibrium Cosserat elasticity theory in Section 13.2. Conservative problems are discussed in Section 13.3, and the quasiconvexity condition for energy minimizers is derived in Section

M. Shirani

University of California, Berkeley, Department of Mechanical Engineering, Berkeley, CA 94720, USA

e-mail: milad_shirani@berkeley.edu

D. J. Steigmann

University of California, Berkeley, Department of Mechanical Engineering, Berkeley, CA 94720, USA

e-mail: dsteigmann@berkeley.edu

13.4. This is used, in Section 13.5, as the basis of the derivation of the relevant rank-one convexity condition.

Concerning notation, bold face is used for vectors and tensors and a dot interposed between bold symbols is used to denote the standard Euclidean inner product. For example, if \mathbf{A} and \mathbf{B} are second-order tensors, then their inner product is $\mathbf{A} \cdot \mathbf{B} = \text{tr}(\mathbf{A}\mathbf{B}^t)$, where $\text{tr}(\cdot)$ is the trace and the superscript t is used to denote the transpose. The symbol \otimes identifies the standard tensor product of vectors. We use $\text{skw}\mathbf{A}$ to denote the skew part of \mathbf{A} . The axial vector of a skew tensor \mathbf{W} is denoted by $\text{ax}\mathbf{W}$ and defined by $\text{ax}\mathbf{W} \times \mathbf{v} = \mathbf{W}\mathbf{v}$ for any vector \mathbf{v} . The symbols ∇ and Div respectively stand for the three-dimensional referential gradient and divergence operators. For a fourth-order tensor \mathcal{A} , the notation $\mathcal{A}[\mathbf{B}]$ stands for the second-order tensor resulting from the linear action of \mathcal{A} on \mathbf{B} (Truesdell and Noll, 1965; eq. (7.10)). Its transpose \mathcal{A}^t is defined by $\mathbf{B} \cdot \mathcal{A}^t[\mathbf{A}] = \mathbf{A} \cdot \mathcal{A}[\mathbf{B}]$, and \mathcal{A} is said to possess major symmetry if $\mathcal{A}^t = \mathcal{A}$. The notation G_S stands for the second-order-tensor-valued derivative of the scalar-valued function $G(\mathbf{S})$ with respect to the second-order tensor variable \mathbf{S} . The second derivative is the fourth-order tensor G_{SS} ; this possesses major symmetry if G is twice differentiable. The second derivatives G_{ST} and G_{TS} of a twice differentiable scalar-valued function $G(\mathbf{S}, \mathbf{T})$ satisfy $\mathbf{A} \cdot G_{ST}[\mathbf{B}] = \mathbf{B} \cdot G_{TS}[\mathbf{A}]$; accordingly, $G_{TS} = (G_{ST})^t$. Finally, the Landau symbol $o(\epsilon)$ is used to identify a quantity which is such that $\epsilon^{-1}o(\epsilon) \rightarrow 0$ as $\epsilon \rightarrow 0$.

13.2 Cosserat Elasticity,

We present a brief outline of the equilibrium theory for the sake of completeness.

13.2.1 Kinematical and Constitutive Framework

The relevant kinematical variables of a Cosserat continuum are a deformation field $\chi(\mathbf{x})$ and a rotation field $\mathbf{R}(\mathbf{x})$, where \mathbf{x} is the position of a material point in a fixed reference configuration κ . Naturally these may depend on time, but this is not important for our purposes and is thus not made explicit. The deformation and rotation fields are regarded as being independent in the spirit of the conventional Cosserat theory (see § 98 Truesdell and Noll, 2004).

To model elasticity, we introduce an energy density $U(\mathbf{F}, \mathbf{R}, \nabla\mathbf{R}; \mathbf{x})$, per unit volume of κ , where $\mathbf{F} = \nabla\chi$ is the deformation gradient and $\nabla\mathbf{R}$ is the rotation gradient. In Cartesian index notation, these are

$$\mathbf{F} = F_{iA}e_i \otimes \mathbf{E}_A, \quad \mathbf{R} = R_{iA}e_i \otimes \mathbf{E}_A \quad \text{and} \quad \nabla\mathbf{R} = R_{iA,B}e_i \otimes \mathbf{E}_A \otimes \mathbf{E}_B \quad (13.1)$$

with

$$F_{iA} = \chi_{i,A}, \quad (13.2)$$

where $(\cdot)_{,A} = \partial(\cdot)/\partial x_A$. Here $\{e_i\}$ and $\{E_A\}$ are fixed orthonormal bases associated with Cartesian coordinates y_i and x_A , where $y_i = \chi_i(x_A)$.

We assume the strain energy to be Galilean-invariant and thus impose

$$U(\mathbf{F}, \mathbf{R}, \nabla \mathbf{R}; \mathbf{x}) = U(\mathbf{QF}, \mathbf{QR}, \mathbf{Q}\nabla \mathbf{R}; \mathbf{x}), \quad (13.3)$$

where \mathbf{Q} is an arbitrary spatially uniform rotation and $(\mathbf{Q}\nabla \mathbf{R})_{iAB} = (Q_{ij}R_{jA})_{,B} = Q_{ij}R_{jA,B}$. The restriction

$$U(\mathbf{F}, \mathbf{R}, \nabla \mathbf{R}; \mathbf{x}) = W(\mathbf{E}, \mathbf{\Gamma}; \mathbf{x}), \quad (13.4)$$

where (Pietraszkiewicz and Eremeyev, 2009)

$$\mathbf{E} = \mathbf{R}^t \mathbf{F} = E_{AB} \mathbf{E}_A \otimes \mathbf{E}_B; \quad E_{AB} = R_{iA} F_{iB}, \quad (13.5)$$

and

$$\mathbf{\Gamma} = \Gamma_{DC} \mathbf{E}_D \otimes \mathbf{E}_C; \quad \Gamma_{DC} = \frac{1}{2} e_{BAD} R_{iA} R_{iB,C}, \quad (13.6)$$

with W the reduced energy and e_{ABC} the permutation symbol ($e_{123} = 1$, etc.), is both necessary and sufficient for Galilean invariance. Sufficiency is obvious, whereas necessity follows by choosing $\mathbf{Q} = \mathbf{R}_{|p}^t$, where p is the material point in question, and making use of the fact that for each fixed $C \in \{1, 2, 3\}$, the matrix $R_{iA} R_{iB,C}$ is skew in the indices A, B . This follows by differentiating $R_{iA} R_{iB} = \delta_{AB}$ (the Kronecker delta). The associated axial vectors γ_C have components

$$\gamma_{D(C)} = \frac{1}{2} e_{BAD} R_{iA} R_{iB,C}, \quad (13.7)$$

yielding (Pietraszkiewicz and Eremeyev, 2009)

$$\mathbf{\Gamma} = \gamma_C \otimes \mathbf{E}_C, \quad (13.8)$$

and thus $\mathbf{\Gamma}$ - the *wryness tensor* - is isomorphic to the Cosserat strain measure $\mathbf{R}^t \nabla \mathbf{R}$. The strain measures \mathbf{E} and $\mathbf{\Gamma}$ are generally non-symmetric.

Henceforth we assume W to be a continuous function of \mathbf{x} and continuously differentiable with respect to \mathbf{E} and $\mathbf{\Gamma}$.

13.2.2 Virtual Power and Equilibrium

Equilibria are defined to be states that satisfy the virtual-power statement

$$\dot{S} = P, \quad (13.9)$$

where P is the virtual power of agencies acting on the body,

$$S = \int_{\kappa} U dv \quad (13.10)$$

is the total strain energy, and superposed dots are used to denote variational derivatives. Thus, by the chain rule,

$$\dot{U} = \dot{W} = \boldsymbol{\sigma} \cdot \dot{\mathbf{E}} + \boldsymbol{\mu} \cdot \dot{\boldsymbol{\Gamma}}, \quad (13.11)$$

where

$$\boldsymbol{\sigma} = W_{\mathbf{E}} \quad \text{and} \quad \boldsymbol{\mu} = W_{\boldsymbol{\Gamma}} \quad (13.12)$$

are evaluated at equilibrium, i.e., at states satisfying (13.9).

In (Shirani et al (2020)) it is shown that virtual powers consistent with (13.9) are of the form

$$P = \int_{\partial\kappa} (\mathbf{t} \cdot \mathbf{u} + \mathbf{c} \cdot \boldsymbol{\omega}) da + \int_{\kappa} (\mathbf{g} \cdot \mathbf{u} + \boldsymbol{\pi} \cdot \boldsymbol{\omega}) dv, \quad (13.13)$$

where $\mathbf{u} = \dot{\boldsymbol{\chi}}$ is the virtual velocity and $\boldsymbol{\omega} = ax(\dot{\mathbf{R}}\mathbf{R}^t)$ is the virtual spin; \mathbf{t} and \mathbf{c} are densities of force and couple acting on $\partial\kappa$; and \mathbf{g} and $\boldsymbol{\pi}$ are densities of force and couple acting in κ . Further, in that work it is shown that if there are no kinematical constraints; that is, if \mathbf{u} and $\boldsymbol{\omega}$ can be chosen independently and arbitrarily, then,

$$\mathbf{g} = -Div(\mathbf{R}\boldsymbol{\sigma}) \quad \text{and} \quad \boldsymbol{\pi} = -Div(\mathbf{R}\boldsymbol{\mu}) - 2ax[\mathbf{R}skw(\boldsymbol{\sigma}\mathbf{E}^t)\mathbf{R}^t] \quad \text{in } \kappa, \quad (13.14)$$

whereas

$$\mathbf{t} = (\mathbf{R}\boldsymbol{\sigma})\boldsymbol{\nu} \quad \text{on } \partial\kappa_t \quad \text{and} \quad \mathbf{c} = (\mathbf{R}\boldsymbol{\mu})\boldsymbol{\nu} \quad \text{on } \partial\kappa_c, \quad (13.15)$$

where $\boldsymbol{\nu}$ is the exterior unit normal to the (piecewise smooth) surface $\partial\kappa$; where $\partial\kappa_t$ is a part of $\partial\kappa$ where position is not assigned; and where $\partial\kappa_c$ is a part where rotation is not assigned. We assume position to be assigned on $\partial\kappa \setminus \partial\kappa_t$, so that $\mathbf{u} = \mathbf{0}$ there, and rotation to be assigned on $\partial\kappa \setminus \partial\kappa_c$, where $\boldsymbol{\omega} = \mathbf{0}$.

Equations (13.14) and (13.15) are the Euler equations for (13.9) and furnish the equilibrium conditions for an elastic Cosserat continuum.

13.3 Conservative Problems and Potential Energy

We are concerned with conservative problems for which a potential energy is available. These are such that there exists a *load potential* L , say, the variational derivative of which is equal to the virtual power. Thus,

$$\dot{L} = P, \quad (13.16)$$

and the potential energy is

$$E[\boldsymbol{\chi}, \mathbf{R}] = S - L, \quad (13.17)$$

apart from an unimportant constant. Energy minimizers are equilibria and therefore render the potential energy stationary, i.e.,

$$\dot{E} = 0, \quad (13.18)$$

for all admissible \mathbf{u} and $\boldsymbol{\omega}$. This of course is just a restatement of (13.9). Accordingly, energy minimizers, if sufficiently regular, necessarily satisfy (13.14) and (13.15).

13.3.1 Example: Dead-Load Problems

Among the simplest examples of conservative problems are the dead-load problems with vanishing volumetric densities of force \mathbf{g} and couple $\boldsymbol{\pi}$. These are characterized by load potentials of the form

$$L = \int_{\partial\kappa_t} \mathbf{t} \cdot \boldsymbol{\chi} da + \int_{\partial\kappa_c} \mathbf{M} \cdot \mathbf{R} da, \quad (13.19)$$

modulo an unimportant constant, in which \mathbf{t} and \mathbf{M} respectively, with the former assigned on $\partial\kappa_t$ and the latter on $\partial\kappa_c$, are configuration-independent vector and tensor fields. Here \mathbf{t} is as in (13.15)₁, and the couple traction in (13.15)₂ is

$$\mathbf{c} = 2ax[\text{skw}(\mathbf{M}\mathbf{R}^t)]. \quad (13.20)$$

Thus the couple traction is configuration *dependent* in the dead-load problem. Indeed, it is well known that configuration-independent couples are associated with non-conservative problems (Ziegler, 1977) for which no potential energy exists.

We seek further necessary conditions for energy minimizers. That is, we seek inequalities satisfied by those $\boldsymbol{\chi}(\mathbf{x})$ and $\mathbf{R}(\mathbf{x})$ which are such that

$$E[\boldsymbol{\chi}, \mathbf{R}] \leq E[\tilde{\boldsymbol{\chi}}, \tilde{\mathbf{R}}] \quad (13.21)$$

for all deformations $\tilde{\boldsymbol{\chi}}$ such that $\tilde{\boldsymbol{\chi}} = \boldsymbol{\chi}$ on $\partial\kappa \setminus \partial\kappa_t$, and all rotations $\tilde{\mathbf{R}}$ such that $\tilde{\mathbf{R}} = \mathbf{R}$ on $\partial\kappa \setminus \partial\kappa_c$.

13.4 The Quasiconvexity Condition

Written out explicitly for the dead-load problem, (13.21) is

$$\int_{\kappa} [U(\tilde{\mathbf{F}}, \tilde{\mathbf{R}}, \nabla \tilde{\mathbf{R}}; \mathbf{x}) - U(\mathbf{F}, \mathbf{R}, \nabla \mathbf{R}; \mathbf{x})] dv - \int_{\partial \kappa_t} \mathbf{t} \cdot (\tilde{\boldsymbol{\chi}} - \boldsymbol{\chi}) da - \int_{\partial \kappa_c} \mathbf{M} \cdot (\tilde{\mathbf{R}} - \mathbf{R}) da \geq 0, \tag{13.22}$$

for all $\tilde{\boldsymbol{\chi}}$ and $\tilde{\mathbf{R}}$ subject to the stated restrictions. Among these, we consider

$$\tilde{\boldsymbol{\chi}}(\mathbf{x}) = \boldsymbol{\chi}(\mathbf{x}) + \epsilon \phi(\mathbf{z}) \quad \text{and} \quad \tilde{\mathbf{R}}(\mathbf{x}) = \mathbf{R}(\mathbf{x}) \mathbf{Q}(\mathbf{z}; \epsilon) \quad \text{with} \quad \mathbf{z} = \epsilon^{-1}(\mathbf{x} - \mathbf{x}_0), \tag{13.23}$$

where ϵ is a positive constant and \mathbf{x}_0 is a point in the interior of κ . Here $\phi(\mathbf{z})$ is a smooth vector field and $\mathbf{Q}(\mathbf{z}; \epsilon)$ is a smooth rotation field, not to be confused with the rotation used in the discussion of Galilean invariance. Accordingly, as the composition of two rotation fields, $\tilde{\mathbf{R}}(\mathbf{x})$ is a rotation field, as required. We stipulate that $\phi(\mathbf{z})$ and $\mathbf{Q}(\mathbf{z}; \epsilon) - \mathbf{I}$, where \mathbf{I} is the identity for 3-space, be compactly supported in a region D , so that $\phi = \mathbf{0}$ and $\mathbf{Q} = \mathbf{I}$ for $\mathbf{z} \notin D$. We further suppose that D be the image of a region κ' under the inverse of the map (13.23)₃, such that κ' is a subregion of κ and $\kappa' \cap \partial \kappa$ is the empty set.

For this choice the boundary terms in (13.22) vanish, leaving the inequality

$$\int_{\kappa'} [U(\tilde{\mathbf{F}}, \tilde{\mathbf{R}}, \nabla \tilde{\mathbf{R}}; \mathbf{x}) - U(\mathbf{F}, \mathbf{R}, \nabla \mathbf{R}; \mathbf{x})] dv(\mathbf{x}) \geq 0. \tag{13.24}$$

Naturally the same restriction follows for boundary potentials that are more general than that associated with dead loading; all that is required is that these be determined by the boundary values of $\boldsymbol{\chi}$ and \mathbf{R} . Noting that the gradient of the map (13.23)₃ is $\epsilon^{-1} \mathbf{I}$, we have $dv(\mathbf{z}) = \epsilon^{-3} dv(\mathbf{x})$; and, after division by ϵ^3 , (13.24) becomes

$$\int_D U(\mathbf{F}(\mathbf{x}_0 + \epsilon \mathbf{z}) + \nabla' \phi(\mathbf{z}), \mathbf{R}(\mathbf{x}_0 + \epsilon \mathbf{z}) \mathbf{Q}(\mathbf{z}; \epsilon), \mathbf{S}(\mathbf{x}_0 + \epsilon \mathbf{z}, \mathbf{z}; \epsilon); \mathbf{x}_0 + \epsilon \mathbf{z}) dv(\mathbf{z}) \geq \int_D U(\mathbf{F}(\mathbf{x}_0 + \epsilon \mathbf{z}), \mathbf{R}(\mathbf{x}_0 + \epsilon \mathbf{z}), \nabla \mathbf{R}(\mathbf{x}_0 + \epsilon \mathbf{z}); \mathbf{x}_0 + \epsilon \mathbf{z}) dv(\mathbf{z}), \tag{13.25}$$

in which ∇' is the gradient with respect to \mathbf{z} , and $\mathbf{S}(\mathbf{x}, \mathbf{z}; \epsilon)$ is the third-order tensor field with components

$$S_{iAC} = R_{iB,C} Q_{BA} + \epsilon^{-1} R_{iB} Q'_{BA,C}, \tag{13.26}$$

where $(\cdot)'_{,C} = \partial(\cdot)/\partial z_C$.

To fulfill the stated restrictions on \mathbf{Q} , we adopt the function

$$\mathbf{Q}(\mathbf{z}; \epsilon) = \exp(\epsilon \mathbf{W}(\mathbf{z})), \tag{13.27}$$

where $\mathbf{W}(\mathbf{z})$ is a smooth skew tensor field compactly supported in D , and \exp is the tensor-valued function defined by the uniformly convergent power series

$$\exp \mathbf{A} = \sum_{n=0}^{\infty} \frac{1}{n!} \mathbf{A}^n, \quad \text{with } \mathbf{A}^0 = \mathbf{I}. \quad (13.28)$$

It is well known (Chadwick, 1976) that the right-hand side of (13.27) is a rotation at each \mathbf{z} . Moreover, as $\mathbf{W}(\mathbf{z})$ vanishes in the region exterior to D , we have $\mathbf{Q}(\mathbf{z}; \epsilon) = \mathbf{I}$ for $\mathbf{z} \notin D$ and all the conditions stipulated for \mathbf{Q} are satisfied. Then, with

$$\mathbf{Q}'_{BA,C} = \epsilon \mathbf{W}'_{BD,C} \mathbf{Q}_{DA}, \quad (13.29)$$

(13.26) reduces to

$$S_{iAC} = (R_{iD,C} + R_{iB} \mathbf{W}'_{BD,C}) \mathbf{Q}_{DA}. \quad (13.30)$$

We now divide (13.25) by ϵ , let $\epsilon \rightarrow 0$ and invoke the Dominated Convergence Theorem (Fleming, 2012). Noting that $\mathbf{Q}(\mathbf{z}; 0) = \mathbf{I}$, we thus obtain the *quasiconvexity condition*

$$\int_D [U(\mathbf{F}_0 + \nabla' \phi(\mathbf{z}), \mathbf{R}_0, \mathbf{S}(\mathbf{x}_0, \mathbf{z}; 0); \mathbf{x}_0) - U(\mathbf{F}_0, \mathbf{R}_0, (\nabla \mathbf{R})_0; \mathbf{x}_0)] dv(\mathbf{z}) \geq 0, \quad (13.31)$$

where $\mathbf{F}_0 = \mathbf{F}(\mathbf{x}_0)$, $\mathbf{R}_0 = \mathbf{R}(\mathbf{x}_0)$, $(\nabla \mathbf{R})_0 = \nabla \mathbf{R}|_{\mathbf{x}_0}$, and $\mathbf{S}(\mathbf{x}_0, \mathbf{z}; 0)$ is the tensor field with components

$$S_{iAC}^0(\mathbf{z}) = (R_{iA,C})_0 + R_{iB}^0 \mathbf{W}'_{BA,C}(\mathbf{z}), \quad (13.32)$$

in which $(R_{iA,C})_0$ are the components of $(\nabla \mathbf{R})_0$ and R_{iB}^0 , those of \mathbf{R}_0 .

If $\{\chi(\mathbf{x}), \mathbf{R}(\mathbf{x})\}$ is an energy minimizer, then inequality (13.31) must be satisfied at each $\mathbf{x}_0 \in \kappa$, and for all D , $\phi(\mathbf{z})$ and $\mathbf{W}(\mathbf{z})$ with the stated properties.

The quasiconvexity condition takes a more convenient form when expressed in terms of the reduced energy $W(\mathbf{E}, \mathbf{\Gamma}; \mathbf{x})$. To derive this form we use (13.4)-(13.6) to obtain

$$U(\mathbf{F}_0, \mathbf{R}_0, (\nabla \mathbf{R})_0; \mathbf{x}_0) = W(\mathbf{E}_0, \mathbf{\Gamma}_0; \mathbf{x}_0), \quad (13.33)$$

where $\mathbf{E}_0 = \mathbf{R}_0^t \mathbf{F}_0$ and $\mathbf{\Gamma}_0$ is the tensor with components

$$\Gamma_{DC}^0 = \frac{1}{2} \epsilon_{BAD} R_{iA}^0 (R_{iB,C})_0; \quad (13.34)$$

and,

$$U(\mathbf{F}_0 + \nabla' \phi(\mathbf{z}), \mathbf{R}_0, \mathbf{S}(\mathbf{x}_0, \mathbf{z}; 0); \mathbf{x}_0) = W(\mathbf{E}_0 + \mathbf{R}_0^t \nabla' \phi(\mathbf{z}), \mathbf{\Gamma}_0 + \mathbf{T}(\mathbf{z}); \mathbf{x}_0), \quad (13.35)$$

where $\mathbf{T}(\mathbf{z})$ is the tensor field with components

$$T_{DC}(\mathbf{z}) = \frac{1}{2} \epsilon_{BAD} \mathbf{W}'_{BA,C}(\mathbf{z}), \quad (13.36)$$

and where use has been made of $R_{iA}^0 R_{iB}^0 = \delta_{AB}$. With reference to the discussion preceding (13.7), we note that $\mathbf{\Gamma}_0 + \mathbf{T}(\mathbf{z})$ qualifies as a wryness tensor field because $W'_{BA,C} = -W'_{AB,C}$.

The quasiconvexity condition, expressed in terms of the reduced energy, is thus given by

$$\int_D [W(\mathbf{E}_0 + \mathbf{R}_0^t \nabla' \phi(\mathbf{z}), \mathbf{\Gamma}_0 + \mathbf{T}(\mathbf{z}); \mathbf{x}_0) - W(\mathbf{E}_0, \mathbf{\Gamma}_0; \mathbf{x}_0)] dv(\mathbf{z}) \geq 0. \tag{13.37}$$

13.5 Rank-One Convexity

The rank-one convexity inequality is a pointwise necessary condition for (13.37). We derive it by adapting a construction due to Graves (1939). We work in two dimensions, for the sake of illustration and to ease the presentation. Graves’s treatment is valid in n dimensions, and the rank-one convexity condition that we derive also applies in three dimensions in particular.

The origin of \mathbf{z} in (13.23)₃ is located at $\mathbf{x} = \mathbf{x}_0$. We attach an orthonormal basis $\{\mathbf{m}, \mathbf{n}\}$ to this point, and introduce Cartesian coordinates $x = \mathbf{m} \cdot \mathbf{z}$ and $y = \mathbf{n} \cdot \mathbf{z}$, so that $\mathbf{z} = x\mathbf{m} + y\mathbf{n}$. Let $R \subset D$ be the region defined by

$$R = \{(x, y) : |x| < h, \quad 0 < y < B(x)\} = R_1 \cup R_2, \tag{13.38}$$

where

$$R_1 = \{(x, y) : |x| < h, \quad 0 < y < \theta B(x)\} \quad \text{and} \quad R_2 = R \setminus R_1, \tag{13.39}$$

with $\theta \in (0, 1)$ and $B(x) = h^2 - x^2$.

Consider the continuous composite function

$$F(\mathbf{z}) = \begin{cases} (1 - \theta)y & \text{in } R_1, \\ -\theta[y - B(x)] & \text{in } R_2 \\ 0, & \text{outside } R. \end{cases} \tag{13.40}$$

For the functions $\phi(\mathbf{z})$ and $\mathbf{W}(\mathbf{z})$, we choose

$$\phi(\mathbf{z}) = F(\mathbf{z})\boldsymbol{\alpha} \quad \text{and} \quad \mathbf{W}(\mathbf{z}) = F(\mathbf{z})\boldsymbol{\Omega}, \tag{13.41}$$

where $\boldsymbol{\alpha}$ is a constant vector and $\boldsymbol{\Omega}$ is a constant skew tensor. These yield

$$\nabla' \phi(\mathbf{z}) = \boldsymbol{\alpha} \otimes \nabla' F(\mathbf{z}) \quad \text{and} \quad \nabla' \mathbf{W}(\mathbf{z}) = \boldsymbol{\Omega} \otimes \nabla' F(\mathbf{z}), \tag{13.42}$$

where

$$\nabla' F(\mathbf{z}) = F_x \mathbf{m} + F_y \mathbf{n} = \begin{cases} (1 - \theta)\mathbf{n} & \text{in } R_1 \\ -\theta\mathbf{n} - \theta(2x)\mathbf{m} & \text{in } R_2. \end{cases} \tag{13.43}$$

The gradient $\nabla' F(\mathbf{z})$ is not a continuous function, and therefore $\phi(\mathbf{z})$ and $\mathbf{W}(\mathbf{z})$ do not meet the differentiability conditions stipulated in the derivation of (13.37). This technicality, which arises frequently in the Calculus of Variations, is addressed via *mollification*, or smoothening, with no effect on the final conclusions. See the treatment of mollifiers in Section 2.3 of Giaquinta and Hildebrandt (2004), for example.

As $h \rightarrow 0$ and because $|x| < h$, we have that $F(\mathbf{z}) \rightarrow 0$ and

$$\nabla' F(\mathbf{z}) \rightarrow \left\{ \begin{array}{ll} (1 - \theta)\mathbf{n} & \text{in } R_1 \\ -\theta\mathbf{n} & \text{in } R_2 \end{array} \right\}. \quad (13.44)$$

Accordingly, $\phi(\mathbf{z})$ and $\mathbf{W}(\mathbf{z})$ vanish in the limit, whereas

$$\begin{aligned} \nabla' \phi(\mathbf{z}) &\rightarrow \left\{ \begin{array}{ll} (1 - \theta)\boldsymbol{\alpha} \otimes \mathbf{n} & \text{in } R_1 \\ -\theta\boldsymbol{\alpha} \otimes \mathbf{n} & \text{in } R_2 \end{array} \right\} \quad \text{and} \\ \nabla' \mathbf{W}(\mathbf{z}) &\rightarrow \left\{ \begin{array}{ll} (1 - \theta)\boldsymbol{\Omega} \otimes \mathbf{n} & \text{in } R_1 \\ -\theta\boldsymbol{\Omega} \otimes \mathbf{n} & \text{in } R_2 \end{array} \right\}, \end{aligned} \quad (13.45)$$

the latter implying that

$$\mathbf{T}(\mathbf{z}) \rightarrow \left\{ \begin{array}{ll} (1 - \theta)\mathbf{b} \otimes \mathbf{n} & \text{in } R_1 \\ -\theta\mathbf{b} \otimes \mathbf{n} & \text{in } R_2 \end{array} \right\}, \quad (13.46)$$

where $\mathbf{b} = ax\boldsymbol{\Omega}$, i.e., $b_D = \frac{1}{2}e_{BAD}\Omega_{AB}$.

Let V, V_1 and V_2 be the measures of R, R_1 and R_2 , respectively, i.e.,

$$V = \int_{-h}^h B(x)dx, \quad V_1 = \theta V \quad \text{and} \quad V_2 = (1 - \theta)V. \quad (13.47)$$

On dividing (13.37) by V , we obtain

$$\begin{aligned} &\frac{\theta}{V_1} \int_{R_1} W(\mathbf{E}_0 + \mathbf{R}_0^t \nabla' \phi(\mathbf{z}), \boldsymbol{\Gamma}_0 + \mathbf{T}(\mathbf{z}); \mathbf{x}_0) dv \\ &+ \frac{1 - \theta}{V_2} \int_{R_2} W(\mathbf{E}_0 + \mathbf{R}_0^t \nabla' \phi(\mathbf{z}), \boldsymbol{\Gamma}_0 + \mathbf{T}(\mathbf{z}); \mathbf{x}_0) dv - W(\mathbf{E}_0, \boldsymbol{\Gamma}_0; \mathbf{x}_0) \geq 0. \end{aligned} \quad (13.48)$$

Application of the Mean-Value Theorem to the integrals and passage to the limit $h \rightarrow 0$ then yields, after division by θ ,

$$\begin{aligned} &W(\mathbf{E}_0 + (1 - \theta)\mathbf{a} \otimes \mathbf{n}, \boldsymbol{\Gamma}_0 + (1 - \theta)\mathbf{b} \otimes \mathbf{n}; \mathbf{x}_0) \\ &+ \frac{1 - \theta}{\theta} W(\mathbf{E}_0 - \theta\mathbf{a} \otimes \mathbf{n}, \boldsymbol{\Gamma}_0 - \theta\mathbf{b} \otimes \mathbf{n}; \mathbf{x}_0) - \frac{1}{\theta} W(\mathbf{E}_0, \boldsymbol{\Gamma}_0; \mathbf{x}_0) \geq 0, \end{aligned} \quad (13.49)$$

where $\mathbf{a} = \mathbf{R}_0^t \boldsymbol{\alpha}$. For small θ we use (13.12) to obtain the estimate

$$\begin{aligned}
W(\mathbf{E}_0 - \theta \mathbf{a} \otimes \mathbf{n}, \mathbf{\Gamma}_0 - \theta \mathbf{b} \otimes \mathbf{n}; \mathbf{x}_0) = & W(\mathbf{E}_0, \mathbf{\Gamma}_0; \mathbf{x}_0) \\
& - \theta \{ \boldsymbol{\sigma}(\mathbf{E}_0, \mathbf{\Gamma}_0; \mathbf{x}_0) \cdot \mathbf{a} \otimes \mathbf{n} \} \\
& - \theta \{ \boldsymbol{\mu}(\mathbf{E}_0, \mathbf{\Gamma}_0; \mathbf{x}_0) \cdot \mathbf{b} \otimes \mathbf{n} \} + o(\theta),
\end{aligned} \tag{13.50}$$

implying, from (13.49) that

$$\begin{aligned}
W(\mathbf{E}_0 + (1 - \theta) \mathbf{a} \otimes \mathbf{n}, \mathbf{\Gamma}_0 + (1 - \theta) \mathbf{b} \otimes \mathbf{n}; \mathbf{x}_0) \geq & W(\mathbf{E}_0, \mathbf{\Gamma}_0; \mathbf{x}_0) \\
& + (1 - \theta) \{ \boldsymbol{\sigma} \cdot \mathbf{a} \otimes \mathbf{n} \\
& + \boldsymbol{\mu} \cdot \mathbf{b} \otimes \mathbf{n} \} + (1 - \theta) \frac{o(\theta)}{\theta},
\end{aligned} \tag{13.51}$$

in which $\boldsymbol{\sigma}$ and $\boldsymbol{\mu}$ are evaluated at $\{\mathbf{E}_0, \mathbf{\Gamma}_0, \mathbf{x}_0\}$. Passage to the limit $\theta \rightarrow 0$ finally delivers the *rank-one convexity* condition

$$\begin{aligned}
W(\mathbf{E}_0 + \mathbf{a} \otimes \mathbf{n}, \mathbf{\Gamma}_0 + \mathbf{b} \otimes \mathbf{n}; \mathbf{x}_0) - W(\mathbf{E}_0, \mathbf{\Gamma}_0; \mathbf{x}_0) \geq & \boldsymbol{\sigma}(\mathbf{E}_0, \mathbf{\Gamma}_0; \mathbf{x}_0) \cdot \mathbf{a} \otimes \mathbf{n} \\
& + \boldsymbol{\mu}(\mathbf{E}_0, \mathbf{\Gamma}_0; \mathbf{x}_0) \cdot \mathbf{b} \otimes \mathbf{n}.
\end{aligned} \tag{13.52}$$

This must be satisfied at all $\mathbf{x}_0 \in \kappa$ and for all vectors \mathbf{a} , \mathbf{b} and \mathbf{n} if $\{\boldsymbol{\chi}(\mathbf{x}), \mathbf{R}(\mathbf{x})\}$ is an energy minimizer.

In the derivation of this condition we have allowed for finite perturbations of $\mathbf{F}(\mathbf{x})$ and $\nabla \mathbf{R}(\mathbf{x})$. Accordingly rank-one convexity is a necessary condition for *strong relative minimizers*; *weak* relative minimizers are those configurations that minimize the energy relative to small perturbations of $\mathbf{F}(\mathbf{x})$ and $\nabla \mathbf{R}(\mathbf{x})$. The operative necessary condition in this case is obtained by estimating (13.52) for small values of $|\mathbf{a} \otimes \mathbf{n}|$ and $|\mathbf{b} \otimes \mathbf{n}|$. Taking $|\mathbf{n}| = 1$ without loss of generality, we replace \mathbf{a} and \mathbf{b} by $\theta \mathbf{a}$ and $\theta \mathbf{b}$, and, assuming W to be twice differentiable with respect to \mathbf{E} and $\mathbf{\Gamma}$, deduce from (13.52) that

$$\begin{aligned}
\theta^2 \{ \mathbf{a} \otimes \mathbf{n} \cdot W_{EE}[\mathbf{a} \otimes \mathbf{n}] + \mathbf{a} \otimes \mathbf{n} \cdot W_{E\Gamma}[\mathbf{b} \otimes \mathbf{n}] \} \\
+ \theta^2 \{ \mathbf{b} \otimes \mathbf{n} \cdot W_{\Gamma E}[\mathbf{a} \otimes \mathbf{n}] + \mathbf{b} \otimes \mathbf{n} \cdot W_{\Gamma\Gamma}[\mathbf{b} \otimes \mathbf{n}] \} + o(\theta^2) \geq 0,
\end{aligned} \tag{13.53}$$

in which the derivatives are evaluated at $\{\mathbf{E}_0, \mathbf{\Gamma}_0, \mathbf{x}_0\}$. Dividing by θ^2 and passing to the limit, we obtain the *Legendre–Hadamard* condition

$$\begin{aligned}
\mathbf{a} \otimes \mathbf{n} \cdot W_{EE}[\mathbf{a} \otimes \mathbf{n}] + \mathbf{a} \otimes \mathbf{n} \cdot W_{E\Gamma}[\mathbf{b} \otimes \mathbf{n}] + \mathbf{b} \otimes \mathbf{n} \cdot W_{\Gamma E}[\mathbf{a} \otimes \mathbf{n}] \\
+ \mathbf{b} \otimes \mathbf{n} \cdot W_{\Gamma\Gamma}[\mathbf{b} \otimes \mathbf{n}] \geq 0,
\end{aligned} \tag{13.54}$$

which was derived directly from the non-negativity of the second variation of the energy in Shirani et al (2020).

The foregoing necessary conditions apply if the deformation field $\boldsymbol{\chi}$ and rotation field \mathbf{R} are independent. This is not the case if there is any *a priori* constraint connecting these fields. An example of such a constraint is afforded by the Cosserat theory of fiber-reinforced materials (Shirani and Steigmann, 2020) in which the fibers are assumed to be convected as material curves. In this case we have obtained the operative version of the Legendre–Hadamard condition elsewhere (Shirani and

Steigmann, 2021), but the relevant quasiconvexity and rank-one convexity conditions remain open.

13.6 Conclusion

In this chapter we have derived the quasiconvexity and rank-one convexity conditions for Cosserat elasticity theory. These are necessary conditions that the deformation and rotations fields must satisfy if they are to furnish minima of the potential energy in conservative boundary-value problems. While these conditions alone do not ensure the existence of minimizers, it is to be expected, on the basis of experience with conventional nonlinear elasticity theory, that they would play a central role in any existence proof based on the direct method of the calculus of variations.

Acknowledgements This work was supported by the US National Science Foundation through grant CMMI-1931064. The work of MS was further supported by the P.M. Naghdi and B. Steidel Fellowships, administered by the Department of Mechanical Engineering at UC Berkeley.

References

- Chadwick P (1976) Continuum mechanics. concise theory and problems, 187 pp
- Cosserat E, Cosserat F (1909) Theory of deformable bodies, scientific library, a. Hermann and Sons, Paris
- Fleming W (2012) Functions of several variables. Springer Science & Business Media
- Giaquinta M, Hildebrandt S (2004) Calculus of variations I. Springer, Berlin
- Graves LM (1939) The weierstrass condition for multiple integral variation problems. *Duke Mathematical Journal* 5(3):656–660
- Neff P (2006) Existence of minimizers for a finite-strain micromorphic elastic solid. *Proceedings of the Royal Society of Edinburgh Section A: Mathematics* 136(5):997–1012
- Pietraszkiewicz W, Eremeyev V (2009) On natural strain measures of the non-linear micropolar continuum. *International Journal of Solids and Structures* 46(3-4):774–787
- Reissner E (1975) Note on the equations of finite-strain force and moment stress elasticity. *Studies in Applied Mathematics* 54(1):1–8
- Reissner E (1987) A further note on finite-strain force and moment stress elasticity. *Zeitschrift für angewandte Mathematik und Physik ZAMP* 38(5):665–673
- Shirani M, Steigmann D (2021) Necessary conditions for energy minimizers in a cosserat model of fiber-reinforced elastic solids. In: *Recent Approaches in the Theory of Plates and Plate-like Structures*. Advanced Structured Materials, Springer Switzerland, pp 235–248
- Shirani M, Steigmann DJ (2020) A cosserat model of elastic solids reinforced by a family of curved and twisted fibers. *Symmetry* 12(7):1133
- Shirani M, Steigmann DJ, Neff P (2020) The Legendre–Hadamard condition in Cosserat elasticity theory. *The Quarterly Journal of Mechanics and Applied Mathematics* 73(4):293–303
- Truesdell C, Noll W (2004) The non-linear field theories of mechanics. In: *The non-linear field theories of mechanics*, Springer, pp 1–579
- Ziegler H (1977) Principles of structural stability. Springer, Basel



Chapter 14

Models of Viscoelastic Materials: a Review on Historical Development and Formulation

Marina V. Shitikova, Anastasiya I. Krusser

Abstract A classification of different mathematical models of viscoelastic materials is presented. The review covers the classical models of viscoelasticity with integer order derivatives, as well as models with fractional derivatives and fractional operators. This paper provides a detailed historical background of the basic viscoelastic models with their mechanical schemes and mathematical formulations. A comparative analysis of contribution of Western and Russian scientists to the development of linear viscoelasticity is carried out. The paper fully tracks the recent theories on the topic of linear and nonlinear viscoelasticity.

Keywords: Viscoelasticity · Mathematical models · Fractional calculus

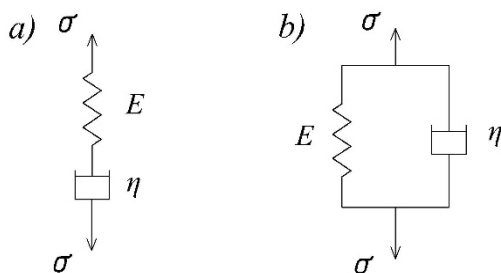
14.1 Introduction

Under the influence of different loads, the body can move or its various particles could experience relative movement, i.e. could deform. The deformation resulting from a given load will depend on the mechanical properties. It could be reversible (elastic deformation) or irreversible (viscous, plastic or permanent deformation, or flow), or it could contain both a recoverable and a residual part. Equations describing the properties of a material in a way that does not depend on the size or shape (that is, geometry) of the body and depends only on its nature are called the rheological equations (Tschoegl, 1989). The first constitutive equation for solids was formulated by Hooke in 1676 in his famous statement (Hooke, 1676) “Ut tensio sic vis” (as the extension, so the force), first published as an anagram (CEIINOSSSTTUU). Hooke

M. V. Shitikova, A. I. Krusser

Research Centre on Dynamics of Solids and Structures, Voronezh State Technical University, 20-Letija Oktjabrja Str. 84, 394006 Voronezh, Russia
Moscow State University of Civil Engineering, Moscow, Russia
e-mail: mvs@vgasu.vrn.ru, an.krusser@yandex.ru

Fig. 14.1 a) the Maxwell element (M-element), and b) the Kelvin–Voigt element (KV-element).



denoted any pure elastic solid as a spring (H-element), the relative deformation of which is directly proportional to the stress:

$$\sigma = E\varepsilon, \quad (14.1)$$

where σ is the stress, ε is the strain of the spring, and E is a constant called the modulus of elasticity. The spring has the ability to accumulate mechanical energy.

Instead of deformation of a solid, a laminar shear flow of a pure viscous fluid could be considered. The governing equation for an ideal viscous fluid, according to which the strain rate is directly proportional to the stress, was first presented by Newton in Newton (1687):

$$\sigma = \eta D\varepsilon, \quad (14.2)$$

where η is a constant known as the viscosity coefficient of the damper, and D denotes differentiation in time. By analogy with the Newtonian fluid, a pure viscous element in the theory of viscoelasticity corresponds to a dashpot (N-element) that exhibits the ability to dissipate mechanical energy.

Recently, polymeric materials with viscoelastic properties have become widespread. The behaviour of viscoelastic bodies cannot be described only from the standpoint of the classical theory of elasticity, as pure elastic solids, or the hydrodynamic theory, as a pure viscous fluid. Bodies stresses in which are determined by strains and strain rates (or higher order time derivatives of the strain) characterize the deformation process in both an ideal elastic and an ideal viscous body; therefore, they are called viscoelastic bodies. If there is a linear relationship between the components of stress, strain and strain rates, then the body exhibits linear viscoelastic behaviour (Bland, 1960).

The behaviour of a material is called viscoelastic if the material accumulates part of the deformation energy elastically, as potential energy, and dissipates the rest simultaneously through viscous forces (Tschoegl, 1989). In order to visualize the work of various viscoelastic materials, it is appropriate to consider similar mechanical models. They consist of a combination of pure elastic and pure viscous elements connected in series or in parallel (Bland, 1960; Christensen, 1971).

In 1867, Maxwell described the equation for the series connection of elastic and viscous elements, which is the simplest scheme in Fig. 14.1a, called *the Maxwell element* (M-element) (Maxwell, 1867). The connection of elastic (H-element) and

viscous (N-element) elements in series could be denoted by letters in the form of a structural formula $M=H-N$, as it was suggested in (Reyner, 1960). In this case, the stress σ is the same for the spring and the dashpot, and the total deformation ε is equal to the sum of their deformations

$$\sigma + \tau_\varepsilon D\sigma = E\tau_\varepsilon D\varepsilon, \quad (14.3)$$

where τ_ε is the relaxation time.

In 1865, Lord Kelvin in his experiments (Thomson, 1865) observed the phenomenon of a change in the rate of energy dissipation depending on the vibration frequency in various materials, which he later explained by the existence of the “elastic aftereffect” (Thomson, 1875). Kelvin also discovered that “in an elastic solid there is molecular friction, which with good reason can be called the viscosity of a solid,” and also proposed a model of a material in the form of an elastic porous solid, in which the pores and gaps between them are filled with a viscous fluid obeying Stokes’s law (which is a generalization of Newton’s law) (Reyner, 1960). Shortly thereafter, in 1892 Voigt wrote down the differential equation of the mathematical model (Voigt, 1889, 1892) describing the same behaviour of anisotropic materials that Kelvin observed in his experiments studying of the properties of various metals. This model, which is schematically represented in the form of a parallel connection of elastic and viscous elements in Fig. 14.1b, was called *the Kelvin–Voigt element* (KV-element). Parallel connection of elastic (H-element) and viscous (N-element) elements can be denoted as $KV=H|N$. In this case, the deformations ε are the same, and the stress σ is equal to the sum of the stresses in the stretched spring and dashpot

$$\sigma = E\varepsilon + E\tau_\sigma D\varepsilon, \quad (14.4)$$

where τ_σ is the retardation (creep) time, or the delayed time (Rabotnov, 1969).

In his detailed review of viscoelastic models, Thompson (1933) mentioned that Meyer in 1873 also proposed relations linearly connecting stress components in a solid with strain and strain rate components, with the help of which the author tried to describe the phenomenon of elastic aftereffect (Meyer, 1874).

14.2 The Simplest Models of Viscoelasticity

14.2.1 Three-Element Models

Three-element models consist of a combination of two springs and one dashpot or one spring and two dashpots. In the literature, there is a wide variety of names for these models and there is no unified structure for their classification (Krusser and Shitikova, 2020; Shitikova, 2022).

14.2.1.1 Three-Element Models of the Standard Linear Solid

Three-element elastic models (Bland, 1960), also called standard linear solid models (Kružík and Roubíček, 2019; Mainardi and Spada, 2011; Nonnenmacher and Glockle, 1991; Roylance, 2001; Tschoegl, 1989; Ward and Sweeney, 1983; Emri and Gergesova, 2010; Zhou et al, 2016), are obtained by connecting the spring in series with the Kelvin–Voigt element (Fig. 14.2a) or in parallel to the Maxwell element (Fig. 14.2b). In this regard, these models are also called the standard three-parameter Voigt and Maxwell models (Tschoegl, 1989), or Kelvin and Maxwell standard linear solid models (Steinmann and Runesson, 2021), respectively.

The first appearance of the model shown in Fig. 14.2a is often associated in the literature (Tschoegl, 1989; Bogomolov et al, 2016; Kružík and Roubíček, 2019; Liang and Huang, 2019) with the names of Poynting and Thomson (1902). However, when recurring to the book (Poynting and Thomson, 1902), it could be seen that the authors, considering the process of energy dissipation in metals and referring to the phenomenon of elastic aftereffect, offered only a graphical scheme of the model presented in Fig. 14.3a, which was the first attempt to “represent a linear solid in the form of a suitable mechanical model” (Zener, 1948). As it turned out, Russian

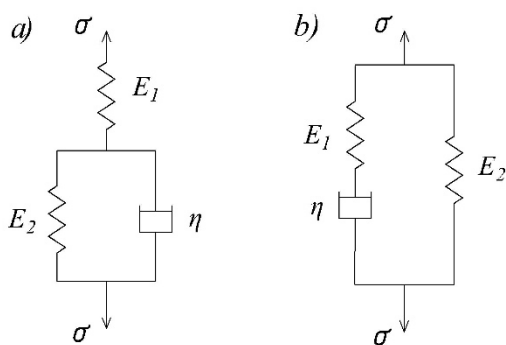


Fig. 14.2 Three-element standard linear solid models: a) H-KV-element, and b) M|H-element.

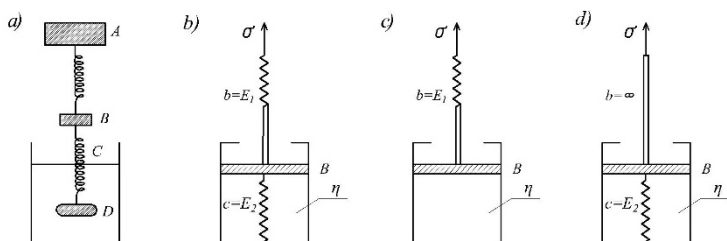


Fig. 14.3 Mechanical model of a standard linear solid: a) Poynting–Thomson model; b) Ishlinsky model; c) and d) particular cases of the Ishlinsky model.

mechanician Ishlinsky in his studies (Ishlinskiy, 1940a,b) also presented the diagram of a mechanical model that obeys this law of deformation (Fig. 14.3b), and pioneered in writing down the differential equation of the proposed model:

$$\sigma + \tau_\varepsilon D\sigma = E_0(\varepsilon + \tau_\sigma D\varepsilon), \quad (14.5)$$

where E_0 is the relaxed (prolonged or the rubbery) elastic modulus of the model and $\tau_\sigma = \eta/E_2$, $\tau_\varepsilon = \eta/(E_1 + E_2)$, $E_0 = E_1E_2/(E_1 + E_2)$ for the model in Fig. 14.2a; and $\tau_\varepsilon = \eta/E_1$, $\tau_\sigma = (E_1 + E_2)\eta/E_1E_2$, $E_0 = E_2$ for the model in Fig. 14.2b.

In his research, Ishlinsky applied the obtained equation to solve the problem of longitudinal vibrations of a homogeneous rod of length l of constant cross-section. Later, Rabotnov (1948) called this model as the Islinsky elastically relaxed body. In this regard, this model should be called the Poynting–Thomson–Ishlinsky model, which could be represented in the form of a structural formula $PTI=H-H|N=H-KV$. Figure 14.3 shows that the Poynting–Thomson–Ishlinsky standard linear solid model is a series connection of a spring and the Kelvin–Voigt element. Ishlinskiy (1945) also noted the possibility of illustrating particular cases of the presented mechanical model with a corresponding simplification of its scheme. For example, when removing the internal spring (Fig. 14.3c), then Maxwell model without aftereffect is obtained, and if, leaving the internal spring, the external spring is replaced with a rigid rod ($b = \infty$), then the model is reduced to the Kelvin–Voigt model (Fig. 14.3d).

It should be noted that Poynting, Thomson, and Ishlinsky presented a standard linear solid in the form of a mechanical model (Fig. 14.3), but its schematic representation in terms of springs and dashpot was first presented in Zener (1948) in the form as it is shown in Fig. 14.2b, while Rzhantsyn (1949) discussed both schemes according to Fig. 14.2a and Fig. 14.2b. In this regard, the three-element generalized Maxwell model (Fig. 14.2b) will henceforth be called the Zener–Rzhantsyn model, which has the formula $ZR=H|(H-N)=H|M$. Zener (1948) also drew attention to the importance of the relationship

$$\frac{\tau_\varepsilon}{\tau_\sigma} = \frac{E_0}{E_\infty} \quad (14.6)$$

where (E_∞ is the non-relaxed (instantaneous) or glassy modulus of elasticity), with which one could determine an unknown value with the given three parameters of the model. Rzhantsyn (1949) showed that both models presented in Fig. 14.2 are described by one and the same differential Eq. (14.5) within the accuracy to coefficients. He also defined the value of the relaxed (prolonged) modulus of elasticity as the value obtained “by simply throwing out all viscous elements”, and described the non-relaxed (instantaneous) modulus of elasticity as “a value determined under the assumption that viscous elements are absolutely rigid”, while that the instantaneous modulus of elasticity is always greater than the prolonged one.

Further Fedá (1992) also showed that both rheological models in Fig. 14.2 could reveal the same mechanical behaviour, although their structure is different. According to the “principle of conversion” one model can be replaced by another, and they are described by the same equation. The equivalence of the three-parameter Kelvin

(Fig. 14.2a) and Maxwell (Fig. 14.2b) models of the standard linear solid was also discussed in (Steinmann and Runesson, 2021), wherein the relations connecting the coefficients for both models and the values of the instantaneous and prolonged elastic moduli were given.

Sobotka (1981) quite rightly called the H|M model (Fig. 14.2b) as the Zener model, and the H-KV model (Fig. 14.2a) as the Poynting–Thomson model, but the author also believed that although these models are similar to each other, they were not identical.

Some authors (Chen and Ai, 2020; Huang et al, 2020, 2021) improperly refer to the model in Fig. 14.2b as the Poynting–Thomson model. Thus, Duque-Daza and Alexiadis (2021) also mistakenly refer to the model in Fig. 14.2a as the Kelvin–Voigt model, but call the real Kelvin–Voigt model as the Kelvin model.

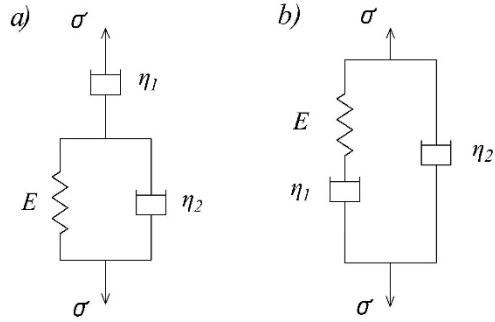
In some references (Rabotnov, 1969; Malinin, 1975; Fung, 1981; Georgiyevskii et al, 2004), researchers refer to the standard linear solid as the Kelvin body. As it was already mentioned, Rabotnov in 1948 called this model as the Ishlinsky elastically relaxing body (Rabotnov, 1948), but already in 1966 he considered the behaviour of a similar viscoelastic body, which he called the Kelvin body, although mentioned that there exist other names for this model in the literature (Rabotnov, 1969). Fung (1965), when describing the properties of linear viscoelastic materials with memory effect, considered such viscoelastic models as the Maxwell, Voigt and standard linear solid models, but in 1981 he also called the latter model as the Kelvin body (Fung, 1981). However, it should be emphasized that Lord Kelvin himself only suggested the existence of a more complex law, which obeys the behaviour of the materials under investigation, but did not provide a differential equation of this dependence or the scheme of such a model (Thompson, 1933).

It is known that authors often obtain similar results using the same mathematical models to describe phenomena and processes in various fields of science, such as mechanics, geomechanics, electrical engineering or biomechanics, while remaining ignorant of the recent achievements in related fields. For example, Christie (1964) showed that the equation of the standard linear solid model is the same as that presented in 1939 by Merchant (1939) in geomechanics, who investigated uniaxial solidification of clay rocks. Fung (1981) considering some problems in biomechanics called the model of a standard linear solid as the Kelvin model, explaining this by the fact that Lord Kelvin had shown the inconsistency of equations of the Maxwell and Voigt models when measuring the change in the rate of energy dissipation depend on the vibration frequency in various materials .

14.2.1.2 Three-Element Models of Standard Linear Liquid

Three-element viscous models (Bland, 1960) are often referred to in the literature as Jeffreys models (Jeffreys, 1929; Kružík and Roubíček, 2019; Mainardi and Spada, 2011; Reynér, 1960) or standard linear liquid models (Kružík and Roubíček, 2019; Mainardi and Spada, 2011). They could be obtained by connecting the dashpot in series with the Kelvin–Voigt element, i.e. N-KV-element in Fig. 14.4a, or in parallel

Fig. 14.4 Three-element standard linear liquid Jeffreys models with: a) N-KV-element, and b) M|N-element.



to the Maxwell element, i.e. N|M-element in Fig. 14.4b. In this regard, Tschoegl (1989) called these models as non-standard three-parameter Voigt and Maxwell models, respectively.

We could not agree with such a name for a scheme in Fig. 14.4a, which describes the behaviour of a viscoelastic fluid. In the theory of viscoelasticity all models are divided in two types: Voigt-type models describing the behaviour of viscoelastic solids and Maxwell-type models describing behaviour of viscoelastic fluids (Rzhantitsyn, 1949; Rabotnov, 1969).

Mainardi and Spada (2011) mistakenly referred to standard linear liquid models as anti-Zener models, without knowing that the equation for this model was written by Jeffreys (1917) in the following form:

$$n \left(S + t_2 \frac{dS}{dt} \right) = F + \frac{I}{t_1} \int F dt, \tag{14.7}$$

where S is the strain, F is the stress, and n, t_1, t_2 are constants.

Jeffreys (1915, 1917) also considered the possibility for describing the behaviour of impure elastic bodies using the elastic-viscous relations of Maxwell’s hypothesis or Voigt’s hypothesis, which are special cases of Eq. (14.7) for $t_2 = 0$ and $t_1 = \infty$, respectively. Later Jeffreys (1929) presented his calculations in more detail showing that Eq. (14.7) could be rewritten as:

$$\sigma + \tau_\varepsilon D\sigma = \eta_0 (D\varepsilon + \tau_\sigma D^2\varepsilon), \tag{14.8}$$

where $\tau_\varepsilon = (\eta_1 + \eta_2)/E, \tau_\sigma = \eta_2/E, \eta_0 = \eta_1$ for the model in Fig. 14.4a, and $\tau_\varepsilon = \eta_1/E, \tau_\sigma = \eta_1\eta_2/E(\eta_1 + \eta_2), \eta_0 = \eta_1 + \eta_2$ for the model in Fig. 14.4b; η_0 is the relaxed viscosity of the model, while η_∞ is the non-relaxed viscosity of the model.

By analogy with the models of a standard linear solid, for the models of a standard linear liquid the following relation is fulfilled:

$$\frac{\tau_\varepsilon}{\tau_\sigma} = \frac{\eta_0}{\eta_\infty}. \tag{14.9}$$

Note that Rzhanitsyn (1949) presented both schemes of the model of a standard linear liquid, and also showed that both models are described by one and the same second-order differential equation with a difference only in the coefficients.

14.2.2 Four-Element Models

Further increase in the number of elements, i.e. springs and dashpots, in schemes results in more intricate laws of deformation. In so doing, Rzhanitsyn (1949) established the following very important rules enabling one to make a conclusion about the physical meaning of any model of viscoelasticity, namely:

1. The order of the differential equation describing the law of deformation corresponds to the number of viscous elements in the scheme.
2. In the absence of the continuous elastic connection between deformed points (for example, schemes in Figs. 14.1a and 14.4) the law of deformation lacks the elastic part of strain. In such schemes, under prolonged exposure to constant stress the strain ε tends to infinity. In other words, the term $E_0\varepsilon$ is absent in the rheological equation, therefore such an equation describes the behaviour of a viscoelastic fluid.
3. In schemes with continuous elastic connection (schemes in Figs. 14.1b and 14.3), under prolonged exposure to constant stress the strain ε tends to a finite value defined by the prolonged (relaxed) modulus of elasticity E_0 . In other words, rheological equations involving the term $E_0\varepsilon$ describe the behaviour of viscoelastic solids.
4. Under rapidly varying stresses, the deformation of a scheme occurs in such a way if all viscous elements are absolutely rigid. The modulus of elasticity defined under the assumption that viscous elements are absolutely rigid, is called as the instantaneous modulus of elasticity E_∞ .
5. In schemes with continuous viscous connection, the instantaneous modulus of elasticity is equal to infinity.
6. The instantaneous (nonrelaxed) modulus of elasticity is always larger than the prolonged (relaxed) modulus of elasticity $E_\infty > E_0$.

These rules will be used further for defining the type of multi-term models. Similar reasoning could be found in Flugge (1967), wherein the author provided the well-defined classification of viscoelastic models showing that all of them could be divided in two groups: models of solids and models of fluids.

Let us consider first the four-element models consisting of a combination of two springs and two dashpots. A wide variety of these models are described in the literature.

14.2.2.1 Four-Element Models of Viscoelastic Fluids

Figure 14.5 shows the first type of four-element model and its equivalent schemes (Bland, 1960; Flugge, 1967). The four-element model of the first type, also called the Burgers model (Burgers, 1935, 1939; Bogomolov et al, 2016; Kružík and Roubíček, 2019; Mainardi and Spada, 2011; Tschoegl, 1989; Zhou et al, 2016; Malkin and Isayev, 2017), is obtained by serial connection of Maxwell and Kelvin–Voigt elements, which can be denoted as (H-N)-(H|N)=M-KV (Fig. 14.5a). In the literature, this model is also called the Burgers liquid (Kružík and Roubíček, 2019).

The models shown in Fig. 14.5a,b were called by Tschoegl (1989) as the standard four-parameter Voigt and Maxwell models, respectively. Once again we agree with

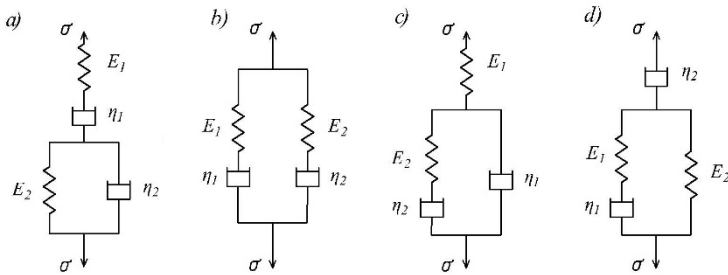


Fig. 14.5 Four-element Burgers models of viscoelastic fluids: a) M-KV-element, b) M|M-element, c) H-(M|N), and d) N-(M|H)

the name of the model in Fig. 14.5b, and completely disagree with the name of the model shown in Fig. 14.5a, since this model and its rheological Eq. (14.10) describe the behaviour of a viscoelastic fluid. Thus, it could not be referred to the Voigt-type model.

Applying the combination rules for series and parallel connected elements and performing the simplest transformations, a general equation that determines the relationship between stress σ and strain ε could be written as

$$\sigma + p_1 D\sigma + p_2 D^2\sigma = q_1 D\varepsilon + q_2 D^2\varepsilon, \tag{14.10}$$

where $p_2 = \frac{\eta_1 \eta_2}{E_1 E_2}$; $p_1 = \frac{E_1 \eta_2 + \eta_1 (E_1 + E_2)}{E_1 E_2}$; $q_2 = \frac{\eta_1 \eta_2}{E_2}$; $q_1 = \eta_1$ for the model in Fig. 14.5a.

It was shown in Alfrey (1948) that the behaviour of any polymer, the viscoelastic properties of which are described by the model shown in Fig. 14.5a, could be equally and accurately described by the model in Fig. 14.5b, in so doing the constants of one model are expressed in terms of equivalent constants of the other. Although mathematically these models are equivalent, but from the point of view of interpreting the physical meaning, the model in Fig. 14.5a has advantages and is more often used.

14.2.2.2 Four-Element Models of Viscoelastic Solids

Four-element models of the second type (Bland, 1960; Flugge, 1967) are shown in Fig. 14.6. Following the rules by Rzhانيتsyn (1949), it could be concluded that all

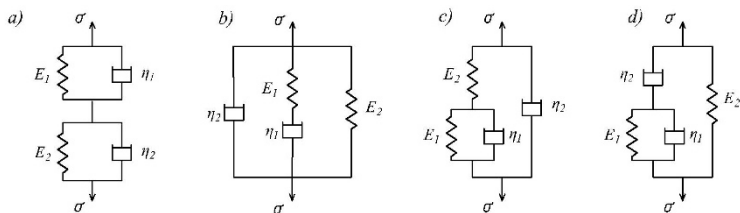


Fig. 14.6 Four-element models of viscoelastic solids: a) KV-KV-element, b) N|M|H-element, c) (H-KV)|N, and d) (N-KV)|H.

four schemes in Fig. 14.6 possess continuous elastic connection between deformed points, thus, describe the behaviour of viscoelastic solids.

Applying the combination rules for series and parallel connected elements and performing the simplest transformations, a general equation that determines the relationship between the stress σ and the strain ε could be written as

$$\sigma + p_1 D\sigma = q_0\varepsilon + q_1 D\varepsilon + q_2 D^2\varepsilon , \tag{14.11}$$

where $p_1 = \frac{\eta_1 + \eta_2}{E_1 + E_2}$; $q_2 = \frac{\eta_1 \eta_2}{E_1 + E_2}$; $q_1 = \frac{\eta_2 E_1 - \eta_1 E_2}{E_1 + E_2}$; $q_0 = \frac{E_1 E_2}{E_1 + E_2}$ for the model in Fig. 14.6a.

The models shown in Fig. 14.6a and Fig. 14.6b were also called in Tschoegl (1989) as non-standard four-parameter Voigt and Maxwell models, respectively. Once again the model in Fig. 14.6b could not be referred to Maxwell-type model, since it describes the behaviour of a viscoelastic solid.

The model in Fig. 14.6c sometimes is also called the generalized four-parameter model of a standard linear solid (Kružík and Roubíček, 2019).

14.2.3 Models with Large Numbers of Elements

Three- or four-element models could describe the observed behaviour of viscoelastic materials with reasonably good approximation. Typically, however, representing the behaviour of most viscoelastic materials requires models with a large or even infinite number of elements. Such models could be easily derived from generalizations of three- or four-element serial-parallel models. Generalized series-parallel models have two forms: generalized Maxwell-type models, which are useful for the analysis

of viscoelastic fluids and rubber-like materials, and generalized Voigt-type models, which should be used for viscoelastic solids.

14.2.3.1 Generalization of the Maxwell Model

By adding Maxwell elements to the standard four-parameter Maxwell model (Fig. 14.5b), a generalized Maxwell model is obtained with the structural formula $GM=M_1|M_2|M_3...|M_n$, where n is the number of Maxwell elements connected in parallel (Christensen, 1971; Tschoegl, 1989; Ferry, 1980; Adolfsson et al, 2005; Fedá, 1992). Such a model (Fig. 14.7) is introduced to describe the so-called “rheodictic” behaviour, when a steady-flow fluidity is present in a viscoelastic material (Tschoegl, 1989). Therefore, in such a formulation, this model describes the behaviour of viscoelastic fluid, and it is not capable of displaying reversible creep, that is why other varieties of the classical Maxwell model are often used (Renaud et al, 2011), which could be applicable for viscoelastic solids (Renaud et al, 2011).

By adding a spring in parallel to the generalized Maxwell element (Fig. 14.7), Wiechert (1893) obtained the model (Fig. 14.8) (Roylance, 2001; Tschoegl, 1989; Knauss et al, 2008; Emri and Gergesova, 2010; Zhou et al, 2016; Morro, 2017), which could describe the so-called “areodictic” behaviour when there is no steady flow in a viscoelastic material (Tschoegl, 1989). In other words, the model shown in Fig. 14.8 is capable to be used for solving problems of dynamics of solids.

Mattei and Ahluwalia (2019) proposed a new analytical method for deriving the constants of this model equation from the strain rate test. Renaud et al (2011) also focused on determining the parameters of this model and wrote down an expression for its transfer function and asymptotes (Renaud et al, 2011).

Another generalization of the Maxwell model (Fig. 14.7) is obtained by adding Maxwell elements in parallel to the Kelvin–Voigt element (Bland, 1960; Flugge, 1967), resulting in a Voigt-type model. This model (Fig. 14.9) was used by Bland (1960) in the stress-relaxation test to study the relaxation function of the material and the spectrum of relaxation times.

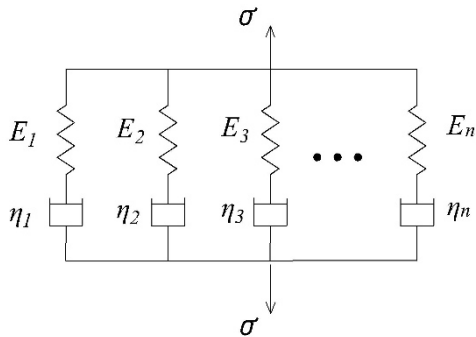


Fig. 14.7 Generalized Maxwell model involving n Maxwell elements: $GM=M_1|M_2|M_3...|M_n$ -element

Fig. 14.8 Wiechert model of a viscoelastic solid: $W=H[M_1|M_2|M_3...|M_n]$ -element

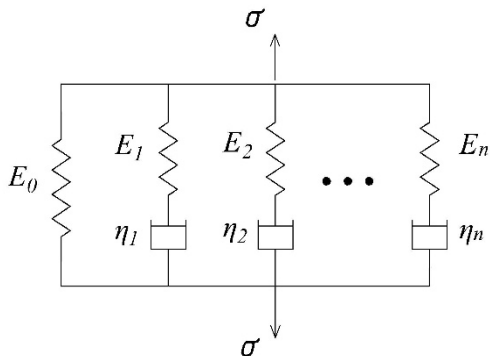
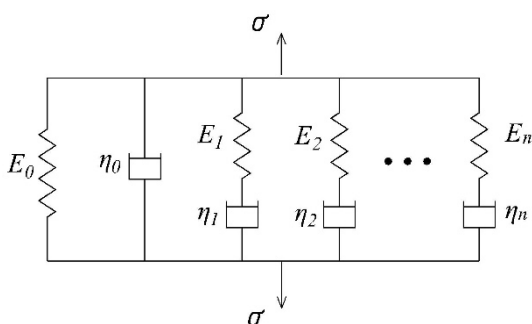


Fig. 14.9 Voigt-type model involving one Kelvin–Voigt element in parallel with n Maxwell elements $KV|M_1|M_2|M_3...|M_n$ -element.



14.2.3.2 Generalization of Voigt or Kelvin Models

Christensen (1971) introduced the generalized Kelvin model obtained by serial connection of a finite number of Kelvin–Voigt elements (Fig. 14.10). This model can be denoted by the structural formula $GKV=KV_1-KV_2-KV_3-...-KV_n$, where n is the number of Kelvin–Voigt elements connected in series (Christensen, 1971; Ferry, 1980; Knauss et al, 2008; Feda, 1992; Steinmann and Ruesson, 2021).

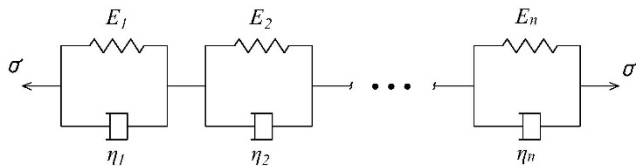


Fig. 14.10 Generalized Kelvin model: $GKV=KV_1-KV_2-KV_3-...-KV_n$ -element.

Adding a Maxwell element or a spring in series with n Kelvin–Voigt elements (Fig. 14.10) results, respectively, in viscoelastic fluid (Fig. 14.11a) and viscoelastic solid (Fig. 14.11b) models (Bland, 1960; Tschoegl, 1989; Emri and Gergesova, 2010) which could describe the so-called rheodictic and areodictic behaviour of a viscoelastic material (Tschoegl, 1989). The model in Fig. 14.11a was used by Bland (1960) in the strain-creep test to investigate the creep function of the material, its compliance and the retardation time spectrum.

This model was also considered by Alfrey (1948) to describe the behaviour of materials with a continuous distribution of retardation times. As special cases of the generalized (continuous) model, the author also singled out models with six and eight elements, which are more accurate than the Burgers model and are used in such a range of experimental conditions under which simpler models no longer provide the required accuracy. He also drew attention to the equivalence of the models in Fig. 14.7 and Fig. 14.11a, the first of which describes the relaxation time dependence of the distribution of elastic moduli, and the second represents the retardation time dependence of elastic compliance.

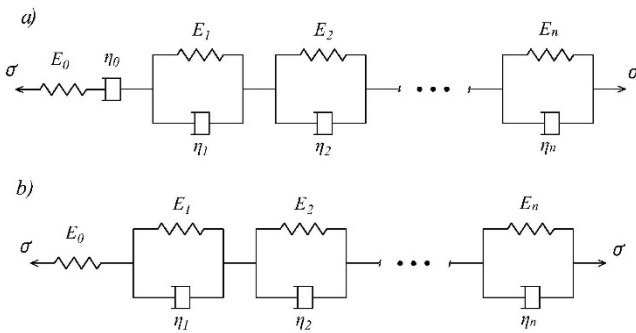

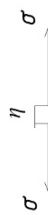

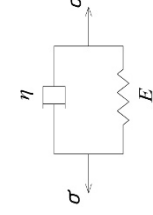
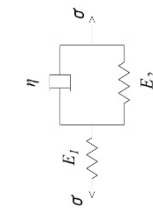
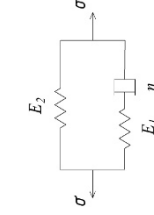
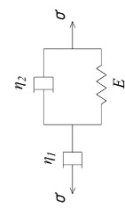
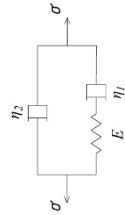
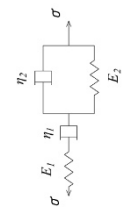
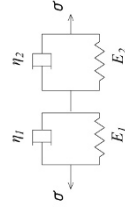


Fig. 14.11 Generalized viscoelastic models: a) M-KV₁-KV₂-KV₃-...-KV_n-element, and b) H-KV₁-KV₂-KV₃-...-KV_n-element.

Formulas for the creep and relaxation functions for the eight basic models of viscoelasticity (Bland, 1960; Flugge, 1967) are given in Table 14.1. The main relations of the models are expressed in terms of the stress and strain, however, these relations can be rewritten in terms of the force F and the elongation a for an element with a cross-sectional area A and a length L , considering that $F = \sigma A$ and $a = \varepsilon L$. Since the rules for series and parallel connection of elements are the same in both cases, then each model describing the relationship between the force and elongation will be the same as the model in terms of stresses and strains.

Table 14.1 The simplest models of viscoelasticity

| Model name | Scheme of the model | Relaxation function | Creep function | Stress-strain relationship |
|---|--|---|---|---|
| Elastic element (Hooke spring) |  | $G(t) = E = const$ | $J(t) = 1/E = const$ | $\sigma = E\varepsilon$ |
| Viscous element (Newtonian dashpot) |  | $G(t) = \eta\delta(t)$ | $J(t) = t/\eta$ | $\sigma = \eta D\varepsilon$ |
| Maxwell element |  | $G(t) = Ee^{-t/\tau_\varepsilon}$, where $\tau_\varepsilon = \eta/E$ | $J(t) = \frac{1}{E} + t/\eta$ | $\sigma + \tau_\varepsilon D\sigma = E\tau_\varepsilon D\varepsilon$ |
| Kelvin-Voigt element |  | $G(t) = E + \eta\delta(t)$ | $J(t) = \frac{1}{E} [1 - e^{-t/\tau_\sigma}]$, where $\tau_\sigma = \eta/E$ | $\sigma = E(\varepsilon + \tau_\sigma D\varepsilon)$ |
| Three-element standard linear solid models: a) Poynting-Thomson-Ishlinsky model; |  | $G(t) = E_0 + \left(\frac{\eta}{\tau_\varepsilon} - E_0\right) e^{-t/\tau_\varepsilon}$, where $\tau_\varepsilon = \eta/(E_1 + E_2)$, $E_0 = \frac{E_1 E_2}{E_1 + E_2}$ | $J(t) = \frac{\tau_\varepsilon}{\eta} + \left(\frac{1}{E_0} - \frac{\tau_\varepsilon}{\eta}\right) [1 - e^{-t/\tau_\sigma}]$, where $\tau_\sigma = \eta/E_2$ | $\sigma + \tau_\varepsilon D\sigma = E_0(\varepsilon + \tau_\sigma D\varepsilon)$ |
| |  | $G(t) = E_0 + \left(\frac{\eta}{\tau_\varepsilon} - E_0\right) e^{-t/\tau_\varepsilon}$, where $\tau_\varepsilon = \eta/E_1$, $E_0 = E_2$ | $J(t) = \frac{\tau_\varepsilon}{\eta} + \left(\frac{1}{E_0} - \frac{\tau_\varepsilon}{\eta}\right) [1 - e^{-t/\tau_\sigma}]$, where $\tau_\sigma = \frac{(E_1 + E_2)\eta}{E_1 E_2}$ | |
| b) Zener-Rzhanitsyn model | | | | |

| | | | | |
|---|---|---|--|---|
| <p>Three-element standard liquid models (Jeffreys models)</p> |  | $G(t) = \frac{\tau_\sigma \eta_0}{\tau_\epsilon} \delta(t) + \left(\frac{\eta_0 - \eta_0 \tau_\sigma}{\tau_\epsilon} \right) e^{-t/\tau_\epsilon},$ <p>where $\tau_\epsilon = (\eta_1 + \eta_2)/E$, $\tau_\sigma = \eta_2/E$, $\eta_0 = \eta_1$</p> | $J(t) = \frac{1}{\eta_0} t + \frac{\tau_\epsilon - \tau_\sigma}{\eta_0} [1 - e^{-t/\tau_\sigma}],$ | $\sigma + \tau_\epsilon D\sigma = \eta_0 (D\epsilon + \tau_\sigma D^2\epsilon)$ |
| <p>Four-element viscoelastic fluid</p> |  | $G(t) = \frac{\tau_\sigma \eta_0}{\tau_\epsilon} \delta(t) + \left(\frac{\eta_0 - \eta_0 \tau_\sigma}{\tau_\epsilon} \right) e^{-t/\tau_\epsilon},$ <p>where $\tau_\epsilon = \eta_1 + \eta_2$, $\tau_\sigma = \eta_2 \eta_1 / (E(\eta_1 + \eta_2))$</p> | $J(t) = \frac{1}{\eta_0} t + \frac{\tau_\epsilon - \tau_\sigma}{\eta_0} [1 - e^{-t/\tau_\sigma}],$ | $\sigma + p_1 D\sigma + p_2 D^2\sigma = q_1 D\epsilon + q_2 D^2\epsilon,$ |
| <p>Four-element viscoelastic solid</p> |  | $G(t) = \frac{1}{\sqrt{p_1^2 - 4p_2}} (q_1 - \alpha q_2) e^{-\alpha t} - (q_1 - \beta q_2) e^{-\beta t},$ <p>$\alpha = \frac{1}{2p_2} (p_1 + \sqrt{p_1^2 - 4p_2})$ $\beta = \frac{1}{2p_2} (p_1 - \sqrt{p_1^2 - 4p_2})$</p> | $J(t) = \frac{t}{q_1} + \frac{p_1 q_1 - q_2}{q_1^2} (1 - e^{\lambda t}) + \frac{p_2}{q_2} e^{-\lambda t}, \lambda = \frac{q_1}{q_2}$ | $\sigma + p_1 D\sigma + p_2 D^2\sigma = q_1 D\epsilon + q_2 D^2\epsilon,$ |
| <p>Four-element viscoelastic solid</p> |  | $G(t) = \frac{q_2}{p_1} \delta(t) + \frac{q_1 p_1 - q_2}{p_1^2} e^{-t/p_1} - \frac{1}{p_1} (q_1 p_1 - q_0 p_1^2 - q_2) (1 - e^{-t/p_1})$ <p>where λ_1, λ_2 are roots of $q_2 \lambda^2 - q_1 \lambda + q_0$</p> | $J(t) = \frac{1 - p_1 \lambda_1}{q_2 \lambda_1 (\lambda_2 - \lambda_1)} (1 - e^{\lambda_1 t}) + \frac{1 - p_1 \lambda_2}{q_2 \lambda_2 (\lambda_1 - \lambda_2)} (1 - e^{\lambda_2 t}),$ <p>where λ_1, λ_2 are roots of $q_2 \lambda^2 - q_1 \lambda + q_0$</p> | $\sigma + p_1 D\sigma = q_0 \epsilon + q_1 D\epsilon + q_2 D^2\epsilon,$ |

Some researchers draw an analogy between the schemes of models of viscoelastic materials and electrical circuits and their elements, despite their different physical meaning (Alfrey, 1948; Gross, 1956; Tschoegl, 1989; Guido et al, 2014). In fact, viscoelastic models involve elastic and viscous elements, which are represented by springs and dashpots. These models can be equivalently considered as electrical circuits, where the spring and dashpot are analogous to the capacitance of a capacitor and the resistance of a resistor, respectively. The application of an electrical analog in viscoelasticity may help to investigate the real behaviour of hereditary materials described by fractional order models of viscoelasticity (Guido et al, 2014).

14.3 Viscoelastic Models with Fractional Derivatives

Fractional differentiation and fractional integration of functions are generalizations of classical differentiation and integration. These generalizations were first proposed in Liouville (1832) and in Riemann (1876) and are easily formulated in the domain of generalized functions, as a result of which the expression for the fractional Riemann–Liouville derivative has the form (Samko et al, 1993):

$${}^{RL}D^\gamma \sigma = \frac{d}{dt} \int_0^t \frac{\sigma(t')}{\Gamma(1-\gamma)(t-t')^\gamma} dt', \quad (14.12)$$

where $0 < \gamma < 1$ is the order of the fractional derivative, and $\Gamma(1-\gamma)$ is the Gamma-function.

Grünwald (1867) and Letnikov (1868) developed an approach to fractional integro-differentiation based on the extension of the Riemann formula $f^{(n)}(x) = \lim_{h \rightarrow 0} \frac{(\Delta_h^n f)(x)}{h^n}$ to the case of non-integer n :

$$D^\alpha f(x) = \lim_{h \rightarrow 0} \frac{(\Delta_h^\alpha f)(x)}{h^\alpha}, \quad (14.13)$$

Letnikov (1868) has shown that the expression for $D^{-\alpha} f$ coincides with the construction of the fractional Riemann–Liouville derivative. The Grünwald–Letnikov approach and its comparison with other definitions of fractional integro-differentiation are presented in Samko et al (1993).

Along with the publications of Liouville, Riemann, Grünwald and Letnikov, at the turn of the 19th and 20th centuries, many other approaches to the description of the fractional derivative appeared, some of which entered into polemics with their predecessors, others developed and supplemented some issues (Hadamard, 1892; Hardy and Riesz, 1916; Weyl, 1917).

One of the nowadays widely used definitions of the fractional derivative is so called Gerasimov–Caputo derivative (Gerasimov, 1948; Caputo, 1967). Thus, the Soviet scientist Gerasimov (1948) introduced a time derivative of order α ($0 < \alpha < 1$) for the strain function $\varepsilon(t)$ in the form (Gerasimov, 1948):

$$\frac{\partial^\alpha \varepsilon(t)}{\partial t^\alpha} = \frac{1}{\Gamma(1-\alpha)} \int_0^\infty \frac{\dot{\varepsilon}(t-\tau) d\tau}{\tau^\alpha}, \quad (14.14)$$

This definition and its properties were not included in the encyclopaedic monograph by Samko et al (1993), it was done in Podlubny (1999) and Diethelm (2004).

It was later shown (Bagley, 2007) that both definitions of the fractional derivative due to the Riemann–Liouville and Gerasimov–Caputo give an equivalent mathematical description of the behaviour of viscoelastic materials if its properties are described by the fractional derivative standard linear solid model.

14.3.1 First Applications of Fractional Calculus in Viscoelasticity

During the twentieth century, many authors have used fractional calculus as an empirical method for describing the properties of viscoelastic materials. The first mention of this new approach in the theory of viscoelasticity could be found in the paper by Nutting (1921), who suggested that the stress relaxation phenomenon could be modelled using fractional orders of time (Bagley and Torvik, 1983; Mainardi, 2012). From a series of experiments for the whole range of materials from an elastic solid to a viscous fluid, Nutting supposed that the general law of deformation, which relates to shear stress, shear strain and time, when shear stress is kept constant, can be expressed as

$$\varepsilon = a\sigma^m t^n, \quad (14.15)$$

where ε is the shear strain, σ is the shear stress, t is time, and a, m, n are constants.

Experimentally Nutting found that the values of n for viscoelastic materials are in the range from 0 to 1. Moreover, for $n = 0$ and $m = 1$ his equation describes the behaviour of a linear elastic solid, and for $n = 1$ and $m = 1$ the behaviour of Newton's viscous fluid (Koeller, 1986). Later Gemant (1936, 1938) substantiated the necessity of using fractional differential operators to calculate the shape of relaxation curves for some viscous elastic fluids.

Scott-Blair (1944, 1949) introduced fractional time derivative, which simultaneously combined observations by Nutting and Gemant. Scott-Blair considered the linear case of the Nutting's equation at $m = 1$, which could be represented as

$$\sigma = KD^n \varepsilon, \quad 0 < n < 1, \quad (14.16)$$

where K is a positive constant, and $D^n \varepsilon$ is a fractional derivative of deformation with respect to time t .

Equation (14.16) is a fractional model of the Newtonian fluid. Scott-Blair and colleagues showed that shear stress is proportional to the fractional derivative of shear strain with respect to time, but they were unable to provide a definition of fractional derivative that would satisfy mathematicians of the time. Dr. J. Scott-Blair wrote the following words in his letter to Dr. Stiassnie (1979): "*I was working on the assessing of firmness of various materials (e.g. Cheese and clay by experts*

handling them) these systems are of course both elastic and viscous but I felt sure that judgements were made not on an addition of elastic and viscous parts but on something in between the two so I introduced fractional differentials of strain with respect to time. I gave up the work eventually, mainly because I could not find a definition of a fractional differential that would satisfy the mathematicians.”

It should be noted that the Soviet scientist Gerasimov (1948) proposed to use a fractional derivative viscoelasticity model similar to the Scott-Blair model, but his work remained unknown to most Western scientists due to the absence of translation of his article into English for a long time (Rossikhin, 2010). Thus, Gerasimov (1948) proposed a linear relationship between the strain $\varepsilon(t)$ and stress functions $\sigma(t)$ in the following form:

$$\sigma(t) = \varkappa \frac{\partial^\alpha \varepsilon(t)}{\partial t^\alpha}, \quad (14.17)$$

which for limiting values of $\alpha = 0$ and $\alpha = 1$ turns over into the Hooke's law of elasticity and Newton's law of internal friction, respectively.

The relationship (14.17) has been also used by Bland (1960) for materials that exhibit neither instantaneous elasticity nor prolonged viscous flow.

Several years later, the same fractional order operator was also discussed in Rabotnov (1969) with reference to Gerasimov (1948) in a monograph published in Moscow.

The simplest element with a fractional derivative, proposed by Scott Blair, was later called a “spring-pot” by Koeller (1984), and the model equation was rewritten as:

$$\sigma = E\tau_\sigma^\gamma D^\gamma \varepsilon, \quad 0 \leq \gamma \leq 1, \quad (14.18)$$

where $\tau_\sigma^\gamma = \eta/E$ is the retardation time, and γ is the memory parameter, whence it is evident that this equation accurately describes two boundary cases, namely: at $\gamma = 0$ the model corresponds to a material with ideal memory (elastic solid), and at $\gamma = 1$ describes a material without memory (viscous liquid).

Koeller (1984) also pointed out that in order to show the connection of fractional calculus to the theory of linear viscoelasticity, he based on the concepts of Rabotnov's theory (Rabotnov, 1980). It was emphasized (Koeller, 1984) that “Rabotnov's theory of Hereditary Solid Mechanics is equivalent to requiring that the stress in the dashpot be proportional to the fractional derivative of the strain in the dashpot”. However, this fact was noted by Rabotnov (1948) himself.

14.3.2 The Simplest Fractional Calculus Viscoelastic Models

In the 60-s of the last century, the simplest models of viscoelasticity with fractional derivatives were proposed. They are based on replacing the derivative of an integer order in classical viscoelastic models by the Riemann–Liouville derivative of the fractional order.

14.3.2.1 Maxwell Model with Fractional Derivatives

The Maxwell model with fractional derivatives (Fig. 14.12a, wherein hereafter a

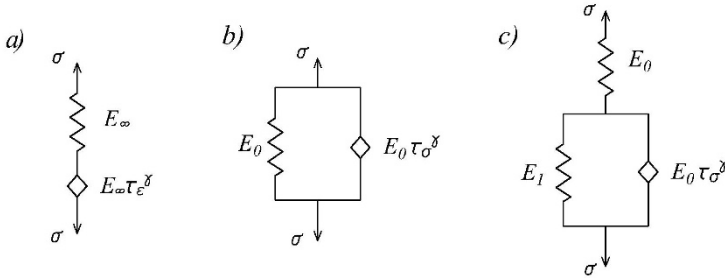


Fig. 14.12 The simplest fractional derivative viscoelastic models: a) Maxwell model, b) Kelvin–Voigt model, and c) standard linear solid model.

spring-pot element is displayed like a diamond as suggested by Bagley and Torvik (1979)) was first presented in Meshkov (1967):

$$\sigma + \tau_\epsilon^\gamma D^\gamma \sigma = E_\infty \tau_\epsilon^\gamma D^\gamma \epsilon, \tag{14.19}$$

where E_∞ is non-relaxed (instantaneous) modulus of elasticity, and τ_ϵ is the relaxation time.

It should be noted that Gemant (1936) was the first to expand the classical Maxwell model proposing a model with a fractional derivative of the order of 1/2, i.e. a semiderivative:

$$\sigma + \tau_\epsilon^{1/2} D^{1/2} \sigma = \eta \dot{\epsilon}, \tag{14.20}$$

The fractional Maxwell model was also independently introduced in Caputo and Mainardi (1971a).

The equation of the fractional derivative Maxwell model could be represented in the form of the Boltzmann–Volterra relations with a fractional exponential function as a weakly singular kernel of heredity (Shermergor, 1966):

$$\sigma = E_\infty \left[\epsilon - \int_0^t \vartheta_\gamma (-t'/\tau_\epsilon) \epsilon(t-t') dt' \right] \tag{14.21}$$

or expressed in terms of the fractional operator (Rossikhin and Shitikova, 2020)

$$\sigma = E_\infty [1 - \vartheta_\gamma^* (t_\sigma^\gamma)] \epsilon(t), \tag{14.22}$$

where $\vartheta_\gamma^* (\tau_\sigma^\gamma) = \frac{1}{1 + \tau_\sigma^\gamma D^\gamma}$ is the Rabotnov’s dimensionless fractional operator (Rossikhin and Shitikova, 2014, 2015), and

$$\mathfrak{z}_\gamma(-t'/\tau_\varepsilon) = \frac{t'^{\gamma-1}}{\tau_\varepsilon^\gamma} \sum_{n=0}^{\infty} \frac{(-1)^n (t'/\tau_\varepsilon)^{\gamma n}}{\Gamma[\gamma(n+1)]}$$

is the Rabotnov fractional exponential function (Rabotnov, 1948), which reduces to the usual exponential function at $\gamma = 1$.

Further Koeller (1984) presented a model consisting of a finite number of fractional Maxwell elements connected in parallel (Fig. 14.13a) and recorded the relationship between the strain and the total stress of the model, which is the sum of the stresses in the individual Maxwell elements. The relationship between the stress and strain of the system expressed in terms of the Rabotnov's dimensionless fractional operator has the form (Rossikhin and Shitikova, 2014):

$$\sigma = \sum_{n=0}^N \sigma_n = E_{\infty n} [1 - \mathfrak{z}_{\gamma_n}^*(t_n^{\gamma_n})] \varepsilon(t). \quad (14.23)$$

14.3.2.2 Kelvin–Voigt Model with Fractional Derivatives

The Kelvin–Voigt model with fractional derivatives (Fig. 14.12b) was first presented by Watanabe (1959) and Shermergor (1966):

$$\sigma = E_0 \varepsilon + E_0 \tau_\sigma^\gamma D^\gamma \varepsilon, \quad (14.24)$$

where E_0 is the relaxed modulus of elasticity and τ_σ is the retardation time. At $\gamma = 1$ the model (14.24) turns over into the classical Kelvin–Voigt model (14.4).

The advantage of this model over the classical Kelvin–Voigt model is in good agreement between the obtained results and experimental data (Eldred et al, 1995).

Almost simultaneously with Shermergor (1966), the fractional Kelvin–Voigt model was presented in Caputo (1967) and Smit and de Vries (1970).

The equation of the Kelvin–Voigt model with fractional derivatives can also be represented in the form of the Boltzmann–Volterra relations with a fractional exponential function as a weakly singular kernel of heredity (Shermergor, 1966)

$$\varepsilon = J_0 \int_0^t \mathfrak{z}_\gamma(-t'/\tau_\sigma) \sigma(t-t') dt' \quad (14.25)$$

or expressed in terms of the fractional operator (Rossikhin and Shitikova, 2020)

$$\varepsilon = J_0 \mathfrak{z}_\gamma^*(\tau_\sigma^\gamma) \sigma(t). \quad (14.26)$$

Koeller (1986) presented a model consisting of a finite number of Kelvin–Voigt elements with fractional derivatives connected in series (Fig. 14.13b), and recorded the relationship between the stress and the total strain of the model, which is the sum of the strains of the individual elements. The relationship between the stress and strain of the system expressed in terms of the Rabotnov's dimensionless fractional operator has the form:

$$\varepsilon = \sum_{n=0}^N \varepsilon_n = J_{0n} \partial_{\gamma_n}^* (\tau_n^{\gamma_n}) \sigma(t), \tag{14.27}$$

where $N + 1$ is the total number of elements in the model.

Katicha and Flintsch (2012) obtained analytical expressions for the creep function for the generalized Maxwell model with fractional derivatives and the relaxation function for the generalized Kelvin–Voigt model with fractional derivatives.

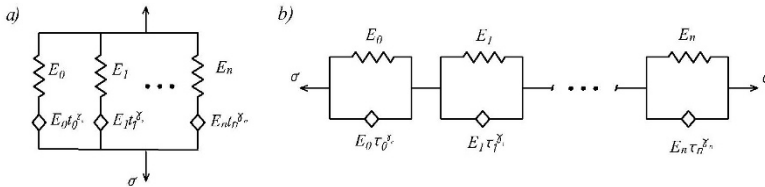


Fig. 14.13 Fractional models of viscoelasticity with a finite number of elements: a) Maxwell model; b) Kelvin–Voigt model.

14.3.2.3 Standard Linear Solid Model with Fractional Derivatives

The model of a standard linear solid with fractional derivatives (Fig. 14.12c) was first presented in Meshkov (1967):

$$\sigma + \tau_\varepsilon^\gamma D^\gamma \sigma = E_0 (\varepsilon + \tau_\sigma^\gamma D^\gamma \varepsilon), \tag{14.28}$$

where

$$\left(\frac{\tau_\varepsilon}{\tau_\sigma} \right)^\gamma = \frac{E_0}{E_\infty} = \frac{J_\infty}{J_0}, \tag{14.29}$$

$J_\infty = E_\infty^{-1}$ is the instantaneous (nonrelaxed) compliance, and $J_0 = E_0^{-1}$ is the prolonged (relaxed) compliance.

This model was also independently introduced into consideration by Caputo and Mainardi (1971b).

The fractional standard linear solid model (14.28) is known to be a four-parameter fractional model, since in order to unambiguously determine the relationship between the stress and strain functions, it is necessary that four parameters (constants) be initially specified: E_0 , E_∞ , τ_ε and γ . The thermodynamic admissibility of this model was analysed in (Bagley and Torvik, 1986). It was shown in (Pritz, 1996) that it is able to describe the change in dynamic modulus and loss factor of real viscoelastic materials over a wide frequency range, provided that there is one symmetric loss peak. The quasi-static viscoelastic behaviour of polymeric materials described by a fractional four-parameter model was studied in (Welch et al, 1999). Huang et al

(2019) applied a standard linear solid model with fractional derivatives to describe the creep of concrete considering its age and duration of load application.

The equation of the standard linear solid model with fractional derivatives could also be represented in the form of the Boltzmann–Volterra relations with a fractional exponential function as a weakly singular kernel of heredity (Rabotnov, 1948; Gross, 1947)

$$\sigma = E_\infty [\varepsilon - \nu_\varepsilon \int_0^t \mathfrak{D}_\gamma (-t'/\tau_\varepsilon) \varepsilon(t-t') dt'] \quad (14.30)$$

or expressed in terms of the fractional operator (Rossikhin and Shitikova, 2020)

$$\sigma = E_\infty [1 - \nu_\varepsilon \mathfrak{D}_\gamma^* (t_\sigma^\gamma)] \varepsilon(t), \quad (14.31)$$

where $\nu_\varepsilon = \Delta E E_\infty^{-1}$ and $\Delta E = E_\infty - E_0$ is the defect of elastic modulus.

The equivalence of the rheological equations of the fractional-derivative viscoelastic models and the equations of the generalized Rabotnov theory was discussed in (Rossikhin and Shitikova, 1997, 2007).

A historical survey of contributions made by Russian and Western researchers in application of Fractional Calculus in problems of Mechanics in the 40-70s of the previous century is presented in Table 2 (Rossikhin, 2010).

The review of applications of the simplest fractional derivative models of viscoelasticity could be found in (Rossikhin and Shitikova, 1997, 2010; Liu and Xu, 2006; Sasso et al, 2011; Zhou et al, 2016), as well as in the recent survey by Bonfanti et al (2020), including such examples as modelling of brain tissue, artery walls, cancerous cells, behaviour of rocks, sandstones and different polymeric materials.

The generalizations of the viscoelastic models of fractional order (14.19), (14.24), (14.28) have been subsequently developed in several ways:

1. by adding additional fractional derivative terms with different fractional orders and/or relaxation/retardation times in rheological equations (Rabotnov, 1969; Rossikhin and Shitikova, 2010);
2. by replacing constant magnitudes of orders of fractional derivatives with time-dependent magnitudes $\gamma_i(t)$ (a review of applications of variable-order fractional operators was recently made in Patnaik et al (2020));
3. by utilizing fractional distributed order models (Ding et al, 2021);
4. by applying fractional derivatives to nonlinear characteristic values (Amabili, 2018, 2019);
5. by using fractional derivatives to describe both types of relaxation: shear and volumetric, resulting in time-dependent operators for all viscoelastic characteristics: Young's modulus, shear modulus, bulk modulus, Lamé's constants and Poisson's ratio (Rossikhin and Shitikova, 2015, 2019, 2020; Shitikova, 2022; Rossikhin et al, 2016).

14.3.3 Viscoelasticity Models with Several Different Fractional Parameters and One Relaxation (Retardation) Time

Viscoelastic models containing fractional derivatives of different orders and other fractional operators with more than one independent fractional parameter have been attracting the attention of researchers for a long time. This is due to the fact that such models make it possible to vary the rheological parameters over a wide range and, more importantly, make it possible to obtain the best agreement between the experimental data and the theoretical result.

Let us consider the simplest types of generalized models using fractional derivatives of different orders with the same retardation (relaxation) time, which are currently used by rheologists to describe experimental data on the rheological properties of various materials and by mechanical engineers to describe the damping properties of structures (Rossikhin and Shitikova, 2010).

14.3.3.1 Maxwell Models with Several Different Fractional Parameters

The following fractional derivative Maxwell models with several different fractional parameters are in use:

- the generalized fractional derivative Maxwell model (Makris et al, 1991)

$$\sigma + \tau_\varepsilon^\alpha D^\alpha \sigma = E_\infty \tau_\varepsilon^\beta D^\beta \varepsilon, \quad (14.32)$$

- the first modified fractional derivative Maxwell model (Friedrich, 1991)

$$\sigma + \tau_\varepsilon^\alpha D^\alpha \sigma = E_\infty (\tau_\varepsilon^\alpha D^\alpha \varepsilon + \tau_\varepsilon^\beta D^\beta \varepsilon), \quad (14.33)$$

- the second modified fractional derivative Maxwell model (Rossikhin and Shitikova, 2001)

$$\sigma + \tau_\varepsilon^\alpha D^\alpha \sigma + \tau_\varepsilon^\beta D^\beta \sigma = E_\infty \tau_\varepsilon^\beta D^\beta \varepsilon, \quad (14.34)$$

- the third modified fractional derivative Maxwell model (Rossikhin and Shitikova, 2001)

$$\sigma + \tau_\varepsilon^\alpha D^\alpha \sigma + \tau_\varepsilon^\beta D^\beta \sigma = E_\infty (\tau_\varepsilon^\alpha D^\alpha \varepsilon + \tau_\varepsilon^\beta D^\beta \varepsilon), \quad (14.35)$$

where $0 < \alpha, \beta < 1$ are the fractional parameters of various orders.

By introducing an additional parameter φ , Su et al (2021) proposed a modified fractional Maxwell model with five-parameters:

$$\sigma \frac{\alpha-\beta}{\varphi} + \tau_\varepsilon^{\alpha-\beta} D^{\alpha-\beta} \sigma = E_\infty \tau_\varepsilon^\alpha D^\alpha \varepsilon, \quad (14.36)$$

where φ is positive and can be larger than 1.

According to Eqs. (14.32)-(14.35), the generalized Maxwell models are four-parameter models, i.e. to determine the relationship between stress and strain, it is necessary to initially set four constants: $E_\infty, \tau_\varepsilon, \alpha$ and β .

14.3.3.2 Kelvin–Voigt Model with Several Different Fractional Parameters

The Kelvin–Voigt model with two different fractional parameters was proposed in (Rossikhin and Shitikova, 2001)

$$\sigma = E_0(\varepsilon + \tau_\sigma^\alpha D^\alpha \varepsilon + \tau_\sigma^\beta D^\beta \varepsilon), \quad (14.37)$$

whence it follows that the generalized Kelvin–Voigt model is also four-parameter model, i.e. to determine the relationship between the stress and strain, it is necessary to initially set four constants: E_0, τ_σ, α and β .

14.3.3.3 Standard Linear Solid Models with Several Different Fractional Parameters

The following standard linear solid models with several different fractional parameters have been proposed:

- the generalized fractional derivative standard linear solid model (Bagley and Torvik, 1983)

$$\sigma + \tau_\varepsilon^\alpha D^\alpha \sigma = E_0(\varepsilon + \tau_\sigma^\beta D^\beta \varepsilon), \quad (14.38)$$

- the first modified fractional derivative standard linear solid model (Friedrich and Braun, 1992)

$$\sigma + \tau_\varepsilon^\alpha D^\alpha \sigma = E_0(\varepsilon + \tau_\sigma^\alpha D^\alpha \varepsilon + \tau_\sigma^\beta D^\beta \varepsilon), \quad (14.39)$$

- the second modified fractional derivative standard linear solid model (Rossikhin and Shitikova, 2001)

$$\sigma + \tau_\varepsilon^\alpha D^\alpha \sigma + \tau_\varepsilon^\beta D^\beta \sigma = E_0(\varepsilon + \tau_\sigma^\alpha D^\alpha \varepsilon + \tau_\sigma^\beta D^\beta \varepsilon). \quad (14.40)$$

According to Eqs. (14.38)-(14.40), generalized standard linear solid models are five-parameter models, i.e. to determine the relationship between the stress and strain, it is necessary to initially set five constants: $E_\infty, E_0, \tau_\varepsilon, \alpha$ and β .

Pritz (2003) showed that the five-parameter model (14.39) is suitable not only for describing the asymmetric peak of losses, but also for describing a peculiar high-frequency change in the dynamic properties of some polymer damping materials. King (2019) compared the application of four- and five-parameter models of a standard linear solid to describe the properties of rubbery polymers commonly used in hearing aids.

Table 14.2 A historical overview of Russian and Western contributors to the use of fractional calculus in the mechanics of solids from the 1940s to the 1970s

| The simplest fractional calculus models | Russian researchers | Western researchers | Applications carried out prior to 1980 |
|---|---------------------|--|--|
| Fractional Newtonian model $\sigma = E_\infty \tau_\varepsilon^\gamma D^\gamma \varepsilon(t)$ $\sigma = E_\infty \tau_\varepsilon^\gamma I^{1-\gamma} d\varepsilon(t)$ | Gerasimov (1948) | Scott-Blair (1944) Bland (1960) | Watanabe (1959) Stiassnie (1979) Gerasimov (1948) Caputo (1976) |
| Standard linear solid model a) via Boltzmann–Volterra relationships $\sigma = E_\infty [\varepsilon - \nu_\varepsilon \int_0^t \partial_\gamma (-t'/\tau_\varepsilon) \varepsilon(t-t') dt']$ $\varepsilon = J_\infty [\sigma + \nu_\sigma \int_0^t \partial_\gamma (-t'/\tau_\sigma) \sigma(t-t') dt']$ | Rabotnov (1948) | Gross (1947) | Rozovskii and Sinaiskii (1966) Meshkov and Rossikhin (1968) Zelenev et al (1970b) Meshkov et al (1971) Gonsovskii and Rossikhin (1972, 1973) |
| b) via fractional derivatives $\sigma + \tau_\varepsilon^\gamma D^\gamma \sigma = E_0 (\varepsilon + \tau_\sigma^\gamma D^\gamma \varepsilon)$ | Meshkov (1967) | Caputo and Mainardi (1971b) | Caputo and Mainardi (1971a,b) |
| c) via fractional operators $\sigma = E_\infty \left[1 - \nu_\varepsilon \frac{\tau_\varepsilon^{-\gamma} I^\gamma}{1 + \tau_\varepsilon^{-\gamma} I^\gamma} \right] \varepsilon$ | Rabotnov (1969) | | |
| Kelvin–Voigt model a) via Boltzmann–Volterra relationships $\varepsilon = J_0 \int_0^t \partial_\gamma (-t'/\tau_\sigma) \sigma(t-t') dt'$ | Shermergor (1966) | | |
| b) via fractional derivatives $\sigma = E_0 \varepsilon + E_0 \tau_\sigma^\gamma D^\gamma \varepsilon$ | Shermergor (1966) | Watanabe (1959) Caputo (1967) Smit and de Vries (1970) | Watanabe (1959) Caputo (1967, 1974) Bagley and Torvik (1979) |
| Maxwell model a) via Boltzmann–Volterra relationships $\sigma = E_\infty [\varepsilon - \int_0^t \partial_\gamma (-t'/\tau_\varepsilon) \varepsilon(t-t') dt']$ | Shermergor (1966) | | Zelenev et al (1970a) |
| b) via fractional derivatives $\sigma + \tau_\varepsilon^{1/2} D^{1/2} \sigma = \eta \dot{\varepsilon}$ $\sigma + \tau_\varepsilon^\gamma D^\gamma \sigma = E_\infty \tau_\varepsilon^\gamma D^\gamma \varepsilon,$ | Meshkov (1967) | Gemant (1936) Caputo and Mainardi (1971a) | Buchen and Mainardi (1975) |
| c) via fractional integral $\varepsilon = J_\infty [\sigma + \tau_\sigma^{-\gamma} I^\gamma \sigma]$ | Shermergor (1966) | | |
| Generalized standard linear solid model $\sigma = E_\infty [\varepsilon - \nu_\varepsilon \int_0^t \sum_{j=1}^n e_j \partial_\gamma (-t'/\tau_{\varepsilon j}) \varepsilon(t-t') dt']$ | Rabotnov (1969) | | |

The general form of the rheological equation with fractional derivatives for the standard linear solid model in the one-dimensional case was presented in Bagley and Torvik (1979, 1983):

$$\sigma + \sum_{i=1}^n \tau_{\varepsilon}^{\alpha_i} D^{\alpha_i} \sigma = E_0 \left(\varepsilon + \sum_{j=1}^m \tau_{\sigma}^{\beta_j} D^{\beta_j} \varepsilon \right), \quad (14.41)$$

where $\alpha_i (i = 1, 2, \dots, n)$ and $\beta_j (j = 1, 2, \dots, m)$ are fractional parameters ($0 < \alpha_i, \beta_j < 1$), and $D^{\alpha_i} \sigma$ and $D^{\beta_j} \varepsilon$ are the Riemann–Liouville fractional derivatives.

14.3.3.4 Burgers Models with Several Different Fractional Parameters

The Burgers model with several different fractional derivative in its general form could be written as

$$\sigma + a_1 D^{\alpha} \sigma + a_2 D^{\beta} \sigma + a_3 D^{\gamma} \sigma = b_1 D^{\mu} \varepsilon + b_2 D^{\nu} \varepsilon, \quad (14.42)$$

where $\alpha_i (i = 1, 2, 3)$ and $b_j (j = 1, 2)$ are the model parameters ($0 < \alpha_i; 0 < b_j$), $\alpha, \beta, \gamma, \mu, \nu$ are the fractional parameters, $\alpha, \beta, \mu \in [0, 1]$ at $\alpha \leq \beta$ and $\gamma, \nu \in [1, 2]$.

However it was shown in Okuka and Zorica (2018) that the orders of fractional differentiation in the generalized Eq. (14.42) could not be arbitrary. In this regard, eight thermodynamically consistent fractional Burgers models with various combinations of fractional parameters containing from five to nine model parameters have been formulated. Expressions were obtained also for the relaxation and creep functions in the integral form for all eight models (Okuka and Zorica, 2020).

14.3.3.5 Fractional Operator Models with Several Different Fractional Parameters

Fractional operator models with two different fractional parameters have been suggested in (Havriliak and Negami, 1967, 1969)

$$\sigma = E_{\infty} [\varepsilon - \nu_{\varepsilon} (1 + \tau_{\varepsilon}^{\alpha} D^{\alpha} \varepsilon)^{-\beta} \varepsilon], \quad \nu_{\varepsilon} = \Delta E E_{\infty}^{-1}, \quad (14.43)$$

$$\varepsilon = J_{\infty} [\sigma + \nu_{\sigma} (1 + \tau_{\sigma}^{\alpha} D^{\alpha} \sigma)^{-\beta} \sigma], \quad \nu_{\sigma} = \Delta J J_{\infty}^{-1}, \quad (14.44)$$

where $\Delta E = (E_{\infty} - E_0)$, and $\Delta J = (J_0 - J_{\infty})$.

Reference to Eqs. (14.43) and (14.44) shows that these fractional operator models are also five-parameter models. For model (14.43), the constants $E_{\infty}, E_0, \tau_{\varepsilon}, \alpha$ and β should be known, and for model (14.44) constants $E_{\infty}, E_0, \tau_{\sigma}, \alpha$ and β .

The application of viscoelastic models with several different fractional parameters and one relaxation (retardation) time has been discussed by many authors, a review of which is presented in Rossikhin and Shitikova (2010).

14.3.4 Viscoelastic Models with One or More Fractional Parameters and Several Relaxation (Retardation) Times

Fractional derivative models of viscoelasticity that include several retardation (relaxation) times make it possible to adequately describe relaxation processes in some polymer materials. The presence of several times of retardation (relaxation) leads to the fact that the distribution function of retardation (relaxation) times includes several maxima. At the molecular level, this can be explained by the simultaneous action of several mechanisms of energy dissipation (Rossikhin and Shitikova, 2010).

14.3.4.1 Rabotnov Model

One of the first mathematical models with several retardation (relaxation) times was proposed by Rabotnov (1969):

$$\begin{aligned}\varepsilon &= J_\infty \left[1 + \sum_{i=1}^n g_i \partial_\gamma (-\tau_i^\gamma) \right] \sigma, \\ \sigma &= E_\infty \left[1 - \sum_{j=1}^n e_j \partial_\gamma^* (-t_j^\gamma) \right] \varepsilon,\end{aligned}\tag{14.45}$$

where g_i and e_i ($i = 1, \dots, n$) are yet unknown coefficients, τ_i and t_i ($i = 1, \dots, n$) are retardation and relaxation times, respectively, and γ ($0 < \gamma < 1$) is the fractional parameter.

Rabotnov (1969) showed that for the kernels in Eqs. (14.45) to be resolvent, it is necessary and sufficient that the following condition to be satisfied:

$$\tau_1^\gamma < t_1^\gamma < \tau_2^\gamma < \dots < t_{n-1}^\gamma < \tau_n^\gamma < t_n^\gamma.\tag{14.46}$$

The properties of the Rabotnov's model (14.45) have been studied in detail in (Rossikhin and Shitikova, 2007, 2010, 2014), and examples of its application could be found in (Rossikhin and Shitikova, 2008).

14.3.4.2 Fractional Calculus Models with Several Different Fractional Parameters

The following polynomial model was suggested in (Koeller, 1986):

$$(\alpha_0 + \alpha_1 D^\gamma + a_2 D^{2\gamma})\varepsilon = (b_0 + b_1 D^\gamma + b_2 D^{2\gamma})\sigma, \tag{14.47}$$

which could be rewritten as

$$E(D^\gamma + \tau_1^{-\gamma})(D^\gamma + \tau_2^{-\gamma})\varepsilon = (D^\gamma + t_1^{-\gamma})(D^\gamma + t_2^{-\gamma})\sigma. \tag{14.48}$$

Some researchers, for example, Welch et al (1999), knowing nothing about Rabotnov’s investigations and later Koeller himself (Koeller, 2007) without any hesitation called this model as Koeller’s model with six parameters: $E, \tau_1, \tau_2, t_1, t_2$ and γ (Fig. 14.14). However, Koeller did not consider the thermodynamic constraints for this model, but Rossikhin and Shitikova (2010) showed that the thermodynamically acceptable Koeller’s model is nothing more than three-term Rabotnov’s model (14.45). Thus, for fairness’ sake, Eqs. (14.45) and (14.47) should be called as Rabotnov–Koeller equations.

A more general case of the polynomial model (14.47) could be presented in the following form:

$$\sum_{i=0}^n \alpha_i D^{i\gamma} \varepsilon = \sum_{j=0}^n b_j D^{j\gamma} \sigma. \tag{14.49}$$

It has been proved by Rossikhin and Shitikova (2014) that the models involving the sums (14.49) or products

$$\prod_{j=1}^n (D^\gamma + \gamma_j) \sigma = E_\infty \prod_{i=1}^n (D^\gamma + \beta_i) \varepsilon \tag{14.50}$$

of fractional derivatives have the physical meaning if and only if they are reduced to the generalized Rabotnov models (14.46), i.e., when the coefficients entering in (14.49) and (14.50) satisfy certain conditions (Rossikhin and Shitikova, 2014), among them (14.46).

The models (14.45) can be easily generalized for the case of n different fractional parameters (Koeller, 1984; Rossikhin et al, 2010) for varying values of γ_i

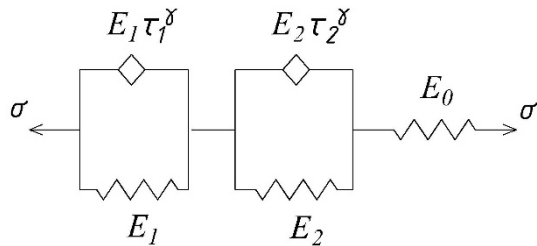


Fig. 14.14 Fractional calculus solid model with six parameters.

$$\begin{aligned}\varepsilon &= J_\infty \left[1 + \sum_{i=1}^n g_j \mathfrak{D}_{\gamma_i}^* (-\tau_i^{\gamma_i}) \right] \sigma, \\ \sigma &= E_\infty \left[1 - \sum_{j=1}^n e_j \mathfrak{D}_{\gamma_j}^* (-t_j^{\gamma_j}) \right] \varepsilon,\end{aligned}\tag{14.51}$$

where $0 < \gamma_i < 1$ are various fractional parameter, but unlike Eqs. (14.45), which are inverses of one another, Eqs. (14.51) do not possess such a feature. Nevertheless, each may be used as a self-contained rheological model. Thus, the application of the generalized Rabotnov–Koeller model (14.51) for analyzing the dynamic behaviour of a hereditarily elastic oscillator with several different relaxation times and different fractional parameters was carried out in (Rossikhin et al, 2010).

Welch et al (1999) reviewed the experimental data of Tobolsky and Catsiff (1956) for polyisobutylene and proposed two models for their description: a five-parameter model with one fractional parameter obtained from Eq. (14.46) at $\alpha_0 = 0$ and a seven-parameter model obtained from Eqs. (14.51) for $n = 2$ and $\gamma_1 = 0,648$, $\gamma_2 = 0,474$. From the comparison of experimental data with the results obtained by the five- and seven-parameter models, it follows that the model with seven parameters gives a more accurate representation of the distribution of times and frequencies than the model with five parameters. It is shown that the seven-parameter model, which involves two different fractional parameters and two relaxation times, accurately simulates glassy and elastic areas, as well as the corresponding transition regions, including the terminal relaxation region.

Heymans (1996) considered modified fractional models of a standard linear solid with five and six parameters and Burgers models with fractional derivatives. Song and Jiang (1998) presented a fractional-order Jeffreys model with five parameters and found a good agreement with experimental data for such materials as xanthan gum and Sesbania gel. Arikoglu (2014) proposed a ten-parameter standard linear solid model for better simulation of viscoelastic properties in the frequency range and showed that this model is consistent with experimental data for several polymer damping materials described in the literature. The author showed that the proposed model could better describe the properties of viscoelastic materials in wide frequency range in comparison with the previously known models of a standard linear solid with four, five and six parameters.

Ding et al (2021) studied in detail the so-called fractional distributed order (DO) models to describe the behaviour of viscoelastic materials with multiple relaxation times. DO statements allow one to visualize multiple relaxation times as individual viscoelastic elements operating simultaneously. Thus, a superposition of several separate fractional operators of constant order (CO) (or, equivalently, several relaxation times) is achieved by defining the DO derivative for viscoelastic solids. Such models are capable of describing such physical phenomena as the memory effect of composite materials or the effect of multiple time scales and have wide practical applications.

14.3.5 Models of Viscoelastic Fluids with Two or More Scott-Blair Fractional Derivative Elements

A variety of fractional derivative models of viscoelastic fluids have been proposed by replacing all springs and dashpots in classical models with Scott-Blair fractional derivative elements of different orders and different relaxation times (Schiessel et al, 1995; Wang and Harris, 2020), as well as considering the schematic arrangement of spring-pots in the form of stairs, trees or fractal structures (Schiessel and Blumen, 1993; Heymans and Bauwens, 1994; Heymans, 1996). Below are some examples:

1. reconstruction of the Maxwell model (Fig. 14.1a) by changing its spring and dashpot by two fractional elements (E_1, τ_1 and α) and (E_2, τ_2 and β) (Fig. 14.15a)

$$\sigma(t) + \frac{E_1 \tau_1^\alpha}{E_2 \tau_2^\beta} \frac{d^{\alpha-\beta} \sigma(t)}{dt^{\alpha-\beta}} = E_1 \tau_1^\alpha \frac{d^\alpha \varepsilon(t)}{dt^\alpha}, \tag{14.52}$$

where $\alpha > \beta$;

2. reconstruction of the Kelvin–Voigt model (Fig. 14.1b) by changing its spring and dashpot by two fractional elements (E_1, τ_1 and α) and (E_2, τ_2 and β) (Fig. 14.15b)

$$\sigma(t) = E \tau^\alpha \frac{d^\alpha \varepsilon(t)}{dt^\alpha} + E \tau^\beta \frac{d^\beta \varepsilon(t)}{dt^\beta}, \tag{14.53}$$

where $\tau = (E_1 \tau_1^\alpha / E_2 \tau_2^\beta)^{1/(\alpha-\beta)}$ and $E = E_1 (\tau_1 / \tau)^\alpha$;

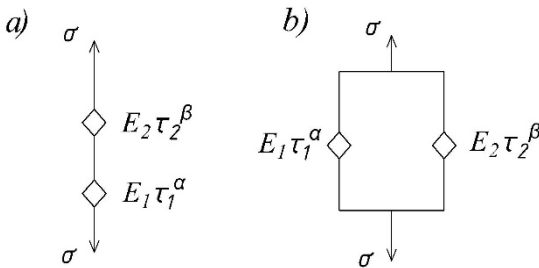


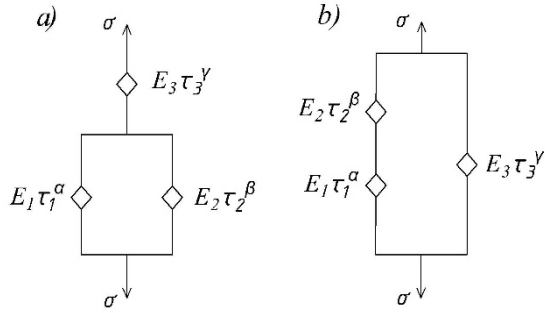
Fig. 14.15 Viscoelastic fluid models with two Scott-Blair elements connected a) in series, and b) in parallel.

3. reconstruction of the Poynting–Thomson–Ishlinsky model (Fig. 14.2a) with three Scott-Blair elements (E_1, τ_1, α), (E_2, τ_2, β) and (E_3, τ_3, γ) (Fig. 14.16a)

$$\sigma(t) + \frac{E_0}{E} \tau^{\alpha-\gamma} \frac{d^{\alpha-\gamma} \sigma(t)}{dt^{\alpha-\gamma}} + \frac{E_0}{E} \tau^{\beta-\gamma} \frac{d^{\beta-\gamma} \sigma(t)}{dt^{\beta-\gamma}} = E_0 \tau^\alpha \frac{d^\alpha \varepsilon(t)}{dt^\alpha} + E_0 \tau^\beta \frac{d^\beta \varepsilon(t)}{dt^\beta}, \tag{14.54}$$

where $\tau = (E_1 \tau_1^\alpha / E_2 \tau_2^\beta)^{1/(\alpha-\beta)}$, $E_0 = E_1 (\tau_1 / \tau)^\alpha$, $E = E_3 (\tau_3 / \tau)^\gamma$, $0 \leq \beta < \alpha \leq 1$, and $0 \leq \gamma \leq 1$;

Fig. 14.16 Three-element models of viscoelastic fluids with Scott-Blair fractional elements.



4. reconstruction of the Zener–Rzhanitsyn model by replacing its elements via three Scott-Blair elements (Fig. 14.16b)

$$\sigma(t) + \tau^{\alpha-\beta} \frac{d^{\alpha-\beta} \sigma(t)}{dt^{\alpha-\beta}} = E_0 \tau^\alpha \frac{d^\alpha \varepsilon(t)}{dt^\alpha} + E_2 \tau^\gamma \frac{d^\gamma \varepsilon(t)}{dt^\gamma} + E_3 \tau^{\gamma+\alpha-\beta} \frac{d^{\gamma+\alpha-\beta} \varepsilon(t)}{dt^{\gamma+\alpha-\beta}}, \tag{14.55}$$

where $\tau_0 = (E_1 \tau_1^\alpha / E_2 \tau_2^\beta)^{1/(\alpha-\beta)}$, $E_0 = E_1 (\tau_1 / \tau_0)^\alpha$, $\tau = \tau_0$, $E = E_3 (\tau_3 / \tau)^\gamma$, $0 \leq \beta < \alpha \leq 1$, and $0 \leq \gamma \leq 1$.

Note that all models presented in Fig. 14.15 and Fig. 14.16 are certain variations of Maxwell-type models.

14.4 Viscoelastic Models with Variable Viscosity

The so-called classical models of viscoelasticity such as Maxwell, Kelvin–Voigt, standard linear solid model models (14.3)-(14.5) and others describe the behaviour of materials, the viscosity of which remains constant over long time scales (Findley, 1976), as well as with time-independent Poisson’s ratio (Shitikova, 2022). But there exist materials with time-dependent viscosity, and/or time-dependent Poisson’s ratios, which could vary from -1 to 1/2.

Yang et al (2020) studied the behaviour of materials, the viscosity of which changes with time or in space under certain conditions. The authors replaced the constant viscosity coefficient of the dashpot in classical viscoelastic models with a time-dependent viscosity function $\eta(t)$ retaining the conventional integer order time-derivative for stress and strain (Fig. 14.17), and also investigated modified models with viscosity varying according to various laws: linear, power, and exponential. Thus, the governing equations for viscoelastic models with variable viscosity have the form:

- Maxwell model

$$\sigma + \frac{\eta(t)}{E} D\sigma = \eta(t) D\varepsilon, \tag{14.56}$$

- Kelvin–Voigt model

$$\sigma = E\varepsilon + \eta(t)D\varepsilon, \tag{14.57}$$

- Zener–Rzhanitsyn model

$$\sigma + \frac{\eta(t)}{E_2} D\sigma = E_1\varepsilon + \frac{\eta(t)(E_1 + E_2)}{E_2} D\varepsilon, \tag{14.58}$$

where E_1 is the modulus of elasticity of the spring in the first branch, and E_2 is the modulus of elasticity of the spring in the branch of the modified Maxwell element (Fig. 17d).

Viscosity $\eta(t)$ varies according to one of the following laws:

- (a) linear law (Buckingham, 2000)

$$\eta(t) = \eta_0 + \theta t, \tag{14.59}$$

where η_0 is the initial viscosity, θ is the strain-hardening coefficient;

- (b) power law (Yang et al, 2020)

$$\eta(t) = \eta_0 + \theta_1 t^\beta, \tag{14.60}$$

where β is an exponent, and θ_1 is pre-factor;

- (c) exponential law (Zhou et al, 2013)

$$\eta(t) = \eta_0 e^{\varphi t}, \tag{14.61}$$

where φ is a constant value.

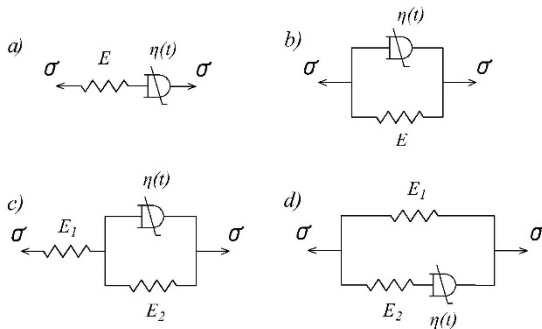


Fig. 14.17 Schemes of viscoelastic elements with variable viscosity: a) Maxwell model, b) Kelvin–Voigt model, and standard linear solid models: c) Poynting–Thomson–Ishlinsky model, d) Zener–Rzhanitsyn model.

Another way of considering time-dependent features of viscoelastic materials was suggested by Rossikhin and Shitikova (2015); Rossikhin et al (2016); Rossikhin

and Shitikova (2019, 2020). It has been proposed to represent two mechanical characteristics of a viscoelastic material (longitudinal and bulk moduli, or shear and bulk moduli, or Lamé parameters) in terms of fractional derivative operators using Kelvin–Voigt, Maxwell or standard linear solid model, and to find other two moduli (Lamé operators, or longitudinal and one Lamé operator, or longitudinal and bulk moduli) and Poisson’s operator in terms of the given two operators using the algebra of fractional Rabotnov’s operators.

The overview of the fractional derivative models involving the time-dependent Poisson’s operators, which allow one to reveal rather interesting features of advanced viscoelastic materials, among them auxetic materials possessing negative Poisson’s ratios (Bhullar, 2015; Carneiro et al, 2013; Gorodtsov and Lisovenko, 2020), has been recently given in Shitikova (2022).

14.5 Nonlinear Viscoelasticity Models with Fractional Derivatives

Nonlinear models of viscoelastic materials have been studied by many authors for a long time. In 1948, Alfrey introduced the concept of nonlinear elasticity and viscosity of elements, which are very common among models for describing the properties of high polymers (Alfrey, 1948). For example, based on the creep curves, a mechanical model describing the behaviour of cellulose acetate must necessarily contain nonlinear elements depicting a non-Newtonian flow. An overview of fluid-type viscoelastic models is presented in (Bird et al, 1987a,b).

Polymer and rubber-like materials are often subjected to significant deformations in engineering applications, therefore, recently, many authors have asked the question of extending linear viscoelastic models based on fractional order derivatives or integrals to the region of finite deformations. The use of fractional order operators in viscoelastic models with finite strains and in nonlinear models was studied in Drozdov (1997, 1998); Bonet (2001); Sjoeborg (2002); Haupt and Lion (2002); Adolfsson and Enelund (2003); Adolfsson (2004); Ramrakhiani et al (2004); Lion and Kadelky (2004); Deng et al (2006); Müller et al (2011); Fukunaga and Shimizu (2011).

Wollscheid and Lion (2014) have shown that constitutive models based on fractional derivatives are suitable for approximating pre-strain and frequency-dependent dynamic behavior of rubber-like materials even at large strains. Zopf et al (2015) presented two approaches for obtaining a fractional Zener–Rzhanitsyn model at large strains, consisting of a nonlinear elastic spring and a fractional Maxwell element connected in parallel. Fukunaga and Shimizu (2015) proposed a method for obtaining fractional derivative models to describe the finite deformations of viscoelastic materials in continuum mechanics. Khajehsaeid (2018) investigated the efficiency of using fractional viscoelasticity models to describe the relaxation behavior of elastomers with different filler contents under finite deformations. King (2019) examined the application of nonlinear fractional derivative models to viscoelastic materials in

hearing aids and sound transducers. Such nonlinear fractional viscoelastic models are used to predict the long-term viscoelastic creep of a loudspeaker suspension over a much longer period of time than is commonly analyzed.

Recently Amabili (2018, 2019) described nonlinear damping for a nonlinear oscillatory system with one degree of freedom using a fractional standard linear solid model with nonlinear springs. A good agreement between the experimental and numerically calculated results was declared.

Singh et al (2020) used a modified standard linear solid model to represent the strain rate dependent response of polylactic acid (PLA) fibers at high strains. Observations based on the experimental data made it possible to conclude that the viscosity coefficients of the model decrease with an increase in the deformation rate, what clearly demonstrates the phenomenon of pseudoplasticity in polymers. This model was previously proposed in Khan et al (2006) to describe the nonlinear finite thermomechanical behavior of viscoelastic polymers.

14.6 Conclusion

For a long time mechanics of solids has been based on Hooke's law, i.e. most of the materials are considered to be elastic. But it is well known that most engineering materials like metals, concrete, wood, soil, are not linearly elastic, that is why starting from the 19th century models of viscoelastic materials began to develop. Mathematical models are commonly used to describe the properties of viscoelastic materials, such as creep and relaxation. According to the review of existing literature in the field, there is a wide variety of names for the same viscoelastic models, and very often many authors incorrectly cite each other without referring to primary sources. In this regard, the main goal of this paper was to understand the origin of all currently known models of viscoelastic materials and also to classify the latest models that have appeared nowadays.

As it turned out, one of the main mistakes in the classification of viscoelastic models was wrong authorship of models of standard linear solid presented in literature. A comparative analysis of the papers by Russian and Western scientists shows that the correct names for the two variants of the standard linear solid should be the following: Poynting–Thomson–Ishlinsky model and Zener–Rzhanitsyn model, since these scientists pioneered in presenting graphical schemes and mathematical equations for the corresponding models.

The models of linear viscoelasticity were generalized by the introduction of fractional derivatives of various orders, resulting in the appearance of viscoelastic models based on fractional order operators. The use of fractional models is largely due to the fact that fewer parameters are required to represent the viscoelastic behaviour of materials than when using traditional integer order models, therefore such models allow rheological parameters to be varied over a wide range. In addition, there is a better agreement of experimental data for models with fractional derivatives than for those with integer-order derivatives. The overview of main early contributions made

by Western and Russian researchers in the field of fractional calculus applications in linear viscoelasticity is presented.

The latest developments in the field of fractional calculus viscoelasticity are also presented, such as modified viscoelastic models with several different fractional parameters, models with variable viscosity and nonlinear viscoelasticity models. All these new classes of models are generalizations of classical models and are introduced for more accurate description of the properties of modern polymer viscoelastic materials, which expands the range of their applicability. Today, a wide variety of viscoelastic models are used to describe the properties of human tissues and cells, various soils and foundations, building materials and structures, polymers, etc. It has been emphasized that all models of viscoelasticity, classical models and fractional calculus models, are divided in two parts, namely: the models which describe the behaviour of viscoelastic solids and viscoelastic fluids, and therefore the choice of this or that model for solving a certain problem should be made very carefully.

Acknowledgements This Survey involves the research results carried out under the financial support of Russian Foundation for Basic Research (Projects Nos. 20-01-00443, 20-51-00008, 20-31-70035), Russian Science Foundation (Project No. 21-19-00634), as well as during fulfilling the projects Nos. 0706-2020-0024, FZGM-2020-0007 from the Russian Ministry of Science and High Education.

References

- Adolfsson K (2004) Nonlinear fractional order viscoelasticity at large strains. *Nonlinear Dynamics* 38:233–246
- Adolfsson K, Enelund M (2003) Fractional derivative viscoelasticity at large deformations. *Nonlinear Dynamics* 33:301–321
- Adolfsson K, Enelund M, Olsson P (2005) On the fractional order model of viscoelasticity. *Mechanics of Time-Dependent Materials* 9:15–34
- Alfrey T (1948) *Mechanical behavior of high polymers*. Interscience Publishers, New York
- Amabili M (2018) Nonlinear damping in large-amplitude vibrations: modelling and experiments. *Nonlinear Dynamics* 93:5–18
- Amabili M (2019) Derivation of nonlinear damping from viscoelasticity in case of nonlinear vibrations. *Nonlinear Dynamics* 97:1785–1797
- Arikoglu A (2014) A new fractional derivative model for linearly viscoelastic materials and parameter identification via genetic algorithms. *Rheologica Acta* 53:219–233
- Bagley RL (2007) On the equivalence of the Riemann–Liouville and the Caputo fractional order derivatives in modeling of linear viscoelastic materials. *Fractional Calculus and Applied Analysis* 10:123–126
- Bagley RL, Torvik PJ (1979) A generalized derivative model for an elastomer damper. *Shock and Vibration* 49:135–143
- Bagley RL, Torvik PJ (1983) A theoretical basis for the application of fractional calculus to viscoelasticity. *Journal of Rheology* 27:201–210
- Bagley RL, Torvik PJ (1986) On the fractional calculus model of viscoelastic behavior. *Journal of Rheology* 30:133–155
- Bhullar SK (2015) Three decades of auxetic polymers: A review. *E-Polymers* 15:205–215
- Bird RB, Armstrong RC, Hassager O (1987a) *Dynamics of Polymeric Liquids*. Vol. 1: Fluid Mechanics, vol 30. Wiley

- Bird RB, Curtiss CF, Armstrong RC, O, Hassager (1987b) *Dynamics of Polymeric Liquids*. Vol.2: Kinetic Theory. Wiley
- Bland DR (1960) *The Theory of Linear Viscoelasticity*. Pergamon Press
- Bogomolov V, Zhdanyuk V, Tsynka A (2016) Viscoelastic structural model of asphalt concrete. *Avtomobil'nyy transport (Khar'kov)* pp 117–125
- Bonet J (2001) Large strain viscoelastic constitutive models. *International Journal of Solids and Structures* 38:2953–2968
- Bonfanti A, Kaplan JL, Charras G, Kabla A (2020) Fractional viscoelastic models for power-law materials. *Soft Matter* 16:6002–6020
- Buchen PW, Mainardi F (1975) Asymptotic expansions for transient viscoelastic waves. *Journal de Mecanique* 14:597–608
- Buckingham MJ (2000) Wave propagation, stress relaxation, and grain-to-grain shearing in saturated, unconsolidated marine sediments. *The Journal of the Acoustical Society of America* 108:2796–2815
- Burgers J (1939) Mechanical considerations—model systems—phenomenological theories of relaxation and viscosity. In: *First Report on Viscosity and Plasticity*, 2nd edn, Nordemann Publishing Company, Inc.
- Burgers JM (1935) *First report on viscosity and plasticity*. Proceedings of the Koninklijke Nederlandse Akademie van Wetenschappen 15
- Caputo M (1967) Linear models of dissipation whose Q is almost frequency independent-II. *Earth* 13:529–539
- Caputo M (1974) Vibrations of an infinite viscoelastic layer with a dissipative memory. *Journal of the Acoustical Society of America* 56:897–904
- Caputo M (1976) Vibrations of an infinite plate with a frequency independent Q. *Journal of the Acoustical Society of America* 60:634–639
- Caputo M, Mainardi F (1971a) Linear models of dissipation in anelastic solids. *La Rivista del Nuovo Cimento* 1:161–198
- Caputo M, Mainardi F (1971b) A new dissipation model based on memory mechanism. *Pure and Applied Geophysics PAGEOPH* 91:134–147
- Carneiro VH, Meireles J, Puga H (2013) Auxetic materials - a review. *Materials Science- Poland* 31:561–571
- Chen YF, Ai ZY (2020) Viscoelastic analysis of transversely isotropic multilayered porous rock foundation by fractional Poyting-Thomson model. *Engineering Geology* 264
- Christensen RM (1971) *Theory of viscoelasticity*. Academic Press
- Christie IF (1964) A re-appraisal of Merchant's contribution to the theory of consolidation. *Geotechnique* 14:309–320
- Deng R, Davies P, Bajaj AK (2006) A nonlinear fractional derivative model for large uni-axial deformation behavior of polyurethane foam. *Signal Processing* 86:2728–2743
- Diethelm K (2004) *The analysis of fractional differential equations: An application-oriented exposition using differential operators of Caputo type*. Springer
- Ding W, Patnaik S, Sidhardh S, Semperlotti F (2021) Applications of distributed-order fractional operators: A review. *Entropy* 23:1–42
- Drozdov AD (1997) Fractional differential models in finite viscoelasticity. *Acta Mechanica* 124:155–180
- Drozdov AD (1998) A model of temporal polymeric networks in nonlinear viscoelasticity. *Mechanics Research Communications* 25:83–90
- Duque-Daza C, Alexiadis A (2021) A simplified framework for modelling viscoelastic fluids in discrete multiphysics. *ChemEngineering* 5
- Eldred LB, Baker WP, Palazotto AN (1995) Kelvin-Voigt versus fractional derivative model as constitutive relations for viscoelastic materials. *AIAA Journal* 33:547–550
- Emri I, Gergesova M (2010) *Time-Dependent Behavior of Solid Polymers*, vol 1. Eolss Publishers Co. Ltd.
- Feda J (1992) *Creep of Soils and Related Phenomena*. Elsevier
- Ferry JD (1980) *Viscoelastic properties of polymers*. John Wiley & Sons, Inc.

- Findley WN (1976) Creep and relaxation of nonlinear viscoelastic materials. Dover publications, Inc.
- Flügge W (1967) Viscoelasticity. Blaisdel Publishing Company
- Friedrich C (1991) Relaxation and retardation functions of the Maxwell model with fractional derivatives. *Rheologica Acta* 30:151–158
- Friedrich C, Braun H (1992) Generalized Cole-Cole behavior and its rheological relevance. *Rheologica Acta* 31:309–322
- Fukunaga M, Shimizu N (2011) Nonlinear fractional derivative models of viscoelastic impact dynamics based on entropy elasticity and generalized Maxwell law. *Journal of Computational and Nonlinear Dynamics* 6:021005
- Fukunaga M, Shimizu N (2015) Fractional derivative constitutive models for finite deformation of viscoelastic materials. *Journal of Computational and Nonlinear Dynamics* 10:1–8
- Fung Y (1981) Biomechanics. Mechanical Properties of Living Tissues. Springer Science+Business Media, LLC
- Fung YC (1965) Foundations of Solid Mechanics. Prentice-hall, inc
- Gemant A (1936) A method of analyzing experimental results obtained from elasto-viscous bodies. *Journal of Applied Physics* 7:311–317
- Gemant A (1938) On fractional differentials. The London, Edinburgh, and Dublin Philosophical Magazine and Journal of Science 25:540–549
- Georgiyevskii DV, Klimov DM, Pobedrya BE (2004) Specific features of the behavior of viscoelastic models. *Mechanics of Solids* 39:88–120
- Gerasimov A (1948) A generalization of linear laws of deformation and its applications to problems of internal friction. *Journal of Applied Mathematics and Mechanics* 12:251–260
- Gonsovskii VL, Rossikhin YA (1972) On the propagation of an impulsive load in a viscoelastic medium. Proceedings of the Scientific-Research Institute of Mathematics of Voronezh University 6:63–66
- Gonsovskii VL, Rossikhin YA (1973) Stress waves in a viscoelastic medium with a singular hereditary kernel. *Journal of Applied Mechanics and Technical Physics* 14:595–597
- Gorodtsov VA, Lisovenko DS (2020) Auxetics among materials with cubic anisotropy. *Mechanics of Solids* 55:461–474
- Gross B (1947) On creep and relaxation. *Journal of Applied Physics* 18:212–221
- Gross B (1956) Electrical analogs for viscoelastic systems. *Journal of Polymer Science* 20:371–380
- Grünwald AK (1867) Über “begrenzte” derivationen und deren anwendung. *Zeitschrift für angewandte Mathematik und Physik* 12:441–480
- Guido A, Paola MD, Francomano E, Li Y, Pinnola FP (2014) Viscoelasticity: An electrical point of view. 2014 International Conference on Fractional Differentiation and Its Applications, ICFDA 2014
- Hadamard J (1892) Essai sur l'étude des fonctions données par leur développement de Taylor. *Journal de Mathématiques Pures et Appliquées* 8:101–186
- Hardy GH, Riesz M (1916) The general theory of Dirichlet's series. *The Mathematical Gazette* 8
- Haupt P, Lion A (2002) On finite linear viscoelasticity of incompressible isotropic materials. *Acta Mechanica* 159:87–124
- Havriliak S, Negami S (1967) A complex plane representation of dielectric and mechanical relaxation processes in some polymers. *Polymer* 8:161–210
- Havriliak S, Negami S (1969) On the equivalence of dielectric and mechanical dispersions in some polymers; e.g. poly(n-octyl methacrylate). *Polymer* 10:859–872
- Heymans N (1996) Hierarchical models for viscoelasticity: Dynamic behaviour in the linear range. *Rheologica Acta* 35:508–519
- Heymans N, Bauwens JC (1994) Fractal rheological models and fractional differential equations for viscoelastic behavior. *Rheologica Acta* 33:210–219
- Hooke R (1676) A description of helioscopes and some other instruments. T.R. for John Martyn Printer

- Huang P, Zhang J, Zhang Q, Damascene NJ, Guo Y (2020) Nonlinear creep model of deep gangue backfilling material and time-dependent characteristics of roof deformation in backfilling mining. *Geofluids* 2020:8816871
- Huang P, Zhang J, Yan X, Spearing AJS, Li M, Liu S (2021) Deformation response of roof in solid backfilling coal mining based on viscoelastic properties of waste gangue. *International Journal of Mining Science and Technology* 31:279–289
- Huang Y, Xiao L, Bao T, Liu Y (2019) Fractional order creep model for dam concrete considering degree of hydration. *Mechanics of Time-Dependent Materials* 23:361–372
- Ishlinskiy AY (1940a) Linear deformation laws of not quite elastic bodies. *Comptes Rendus (Doklady) de l'Academie des Sciences de l'URSS Reports of the USSR Academy of sciences* 24:23–27
- Ishlinskiy AY (1940b) The longitudinal vibrations of a rod in the presence of a linear law aftereffect and relaxation[in Russian]. *Applied Mathematics and Mechanics* 4:79–92
- Ishlinskiy AY (1945) Deformation equations for not completely elastic and viscoplastic solids [in Russian]. *Proceedings of the USSR Academy of sciences, a series of technical sciences* 1-2:34–45
- Jeffreys H (1915) The viscosity of the earth. *Monthly Notices of the Royal Astronomical Society* 75:648–658
- Jeffreys H (1917) The viscosity of the earth (third paper). *Monthly Notices of the Royal Astronomical Society* 77:447–449
- Jeffreys H (1929) *The Earth: Its Origin, History and Physical Constitution*. Cambridge University Press
- Katicha SW, Flintsch GW (2012) Fractional viscoelastic models: Master curve construction, inter-conversion, and numerical approximation. *Rheologica Acta* 51:675–689
- Khajehsaeid H (2018) Application of fractional time derivatives in modeling the finite deformation viscoelastic behavior of carbon-black filled NR and SBR. *Polymer Testing* 68:110–115
- Khan AS, Lopez-Pamies O, Kazmi R (2006) Thermo-mechanical large deformation response and constitutive modeling of viscoelastic polymers over a wide range of strain rates and temperatures. *International Journal of Plasticity* 22:581–601
- King AW (2019) Nonlinear fractional order derivative models of components and materials in hearing aids and transducers. PhD thesis, Technical University of Denmark
- Knauss WG, Emri I, Lu H (2008) Mechanics of polymers: Viscoelasticity. In: Sharpe W (ed) *Springer Handbook of Experimental Solid Mechanics*, Springer, pp 49–95
- Koeller RC (1984) Applications of fractional calculus to the theory of viscoelasticity. *Journal of Applied Mechanics, Transactions ASME* 51:299–307
- Koeller RC (1986) Polynomial operators, Stieltjes convolution, and fractional calculus in hereditary mechanics. *Acta Mechanica* 58:251–264
- Koeller RC (2007) Toward an equation of state for solid materials with memory by use of the half-order derivative. *Acta Mechanica* 191
- Krusser AI, Shitikova MV (2020) Classification of viscoelastic models with integer and fractional order derivatives. *IOP Conference Series: Materials Science and Engineering* 747
- Kružík M, Roubíček T (2019) *Mathematical Methods in Continuum Mechanics of Solids*. Springer Nature Switzerland AG
- Letnikov A (1868) Theory of differentiation with an arbitrary indicator. *Matem Sbornik* 3:1–68
- Liang J, Huang G (2019) Application of a viscoelastic model to creep settlement of high-fill embankments. *Advances in Civil Engineering* 2019:1–8
- Lion A, Kardelky C (2004) The payne effect in finite viscoelasticity: Constitutive modelling based on fractional derivatives and intrinsic time scales. *International Journal of Plasticity* 20:1313–1345
- Liouville J (1832) Mémoire sur quelques questions de géométrie et de mécanique, et sur un nouveau genre de calcul pour résoudre ces questions. *Journal de l'école Polytechnique* 13:1–69
- Liu JG, Xu MY (2006) Higher-order fractional constitutive equations of viscoelastic materials involving three different parameters and their relaxation and creep functions. *Mechanics of Time-Dependent Materials* 10:263–279

- Mainardi F (2012) Short survey : An historical perspective on fractional calculus in linear viscoelasticity. *Fractional Calculus and Applied Analysis* 15:712—717
- Mainardi F, Spada G (2011) Creep, relaxation and viscosity properties for basic fractional models in rheology. *European Physical Journal: Special Topics* 193:133–160
- Makris BN, Constantinou MC, Member A (1991) Fractional-derivative Maxwell model for viscous dampers. *Journal of Structural Engineering* 117:2708–2724
- Malinin NN (1975) Applied theory of plasticity and creep [in Russian], 2nd edn. Mashinostroyeniye
- Malkin AY, Isayev A (2017) Rheology. Concepts, Methods, and Applications: Concepts, Methods, and Applications: 3rd Edition. ChemTec Publishing
- Mattei G, Ahluwalia A (2019) A new analytical method for estimating lumped parameter constants of linear viscoelastic models from strain rate tests. *Mechanics of Time-Dependent Materials* 23:327–335
- Maxwell J (1867) On the dynamical theory of gases. *Philosophical Transactions of the Royal Society of London* 157:49–88
- Merchant W (1939) Some theoretical considerations on the one-dimensional consolidation of clay. PhD thesis, Massachusetts Inst. of Technology
- Meshkov SI (1967) Description of internal friction in the memory theory of elasticity using kernels with a weak singularity. *Journal of Applied Mechanics and Technical Physics* 8:100–102
- Meshkov SI, Rossikhin YA (1968) Propagation of acoustic waves in a hereditary elastic medium. *Journal of Applied Mechanics and Technical Physics* 9:589–592
- Meshkov SI, Pachevskaya GN, Postnikov VS, Rossikhin YA (1971) Integral representations of $\varepsilon\gamma$ -functions and their application to problems in linear viscoelasticity. *International Journal of Engineering Science* 9:387–398
- Meyer OE (1874) Zur theorie der inneren reibung. *Journal fur die Reine und Angewandte Mathematik* 1874:130–135
- Morro A (2017) Modelling of viscoelastic materials and creep behaviour. *Meccanica* 52:3015–3021
- Müller S, Kästner M, Brummund J, Ulbricht V (2011) A nonlinear fractional viscoelastic material model for polymers. *Computational Materials Science* 50:2938–2949
- Newton I (1687) *Philosophiæ naturalis principia mathematica*. Jussu Societatis Regiæ ac Typis Joseph Streater
- Nonnenmacher TF, Glockle WG (1991) A fractional model for mechanical stress relaxation. *Philosophical Magazine Letters* 64:89–93
- Nutting PG (1921) A new general law of deformation. *Journal of the Franklin Institute* 191:679–685
- Okuka AS, Zorica D (2018) Formulation of thermodynamically consistent fractional Burgers models. *Acta Mechanica* 229:3557–3570
- Okuka AS, Zorica D (2020) Fractional Burgers models in creep and stress relaxation tests. *Applied Mathematical Modelling* 77:1894–1935
- Patnaik S, Hollkamp JP, Semperlotti F (2020) Applications of variable-order fractional operators: A review. *Proceedings of the Royal Society A: Mathematical, Physical and Engineering Sciences* 476:0498
- Podlubny I (1999) Fractional differential equations : an introduction to fractional derivatives, fractional differential equations, to methods of their solution and some of their applications, vol 198. Academic Press
- Poynting J, Thomson J (1902) *Properties of Matter*. C. Griffin and Co
- Pritz T (1996) Analysis of four-parameter fractional derivative model of real solid materials. *Journal of Sound and Vibration* 195:103–115
- Pritz T (2003) Five-parameter fractional derivative model for polymeric damping materials. *Journal of Sound and Vibration* 265:935–952
- Rabotnov YN (1948) Equilibrium of an elastic medium with after effect. *Journal of Applied Mathematics and Mechanics* 12:81–91
- Rabotnov YN (1969) *Creep Problems in Structural Members*. North-Holland
- Rabotnov YN (1980) *Elements of Hereditary Solid Mechanics*. Mir Publishers

- Ramrakhiani DS, Lesieutre GA, Smith EC (2004) Modeling of elastomeric materials using non-linear fractional derivative and continuously yielding friction elements. *International Journal of Solids and Structures* 41:3929–3948
- Renaud F, Dion JL, Chevallier G, Tawfiq I, Lemaire R (2011) A new identification method of viscoelastic behavior: Application to the generalized Maxwell model. *Mechanical Systems and Signal Processing* 25:991–1010
- Reyner M (1960) Deformation, strain and flow. An elementary introduction to rheology. H. K. Lewis & Co. Ltd
- Riemann B (1876) Versuch einer allgemeinen Auffassung der Integration und Differentiation. *Gesammelte Mathematische Werke*
- Rossikhin YA (2010) Reflections on two parallel ways in the progress of fractional calculus in mechanics of solids. *Applied Mechanics Reviews* 63:1–12
- Rossikhin YA, Shitikova MV (1997) Applications of fractional calculus to dynamic problems of linear and nonlinear hereditary mechanics of solids. *Applied Mechanics Reviews* 50:15–67
- Rossikhin YA, Shitikova MV (2001) Analysis of rheological equations involving more than one fractional parameters by the use of the simplest mechanical systems based on these equations. *Mechanics Time-Dependent Materials* 5:131–175
- Rossikhin YA, Shitikova MV (2007) Comparative analysis of viscoelastic models involving fractional derivatives of different orders. *Fractional Calculus and Applied Analysis* 10:111–121
- Rossikhin YA, Shitikova MV (2008) Free damped vibrations of a viscoelastic oscillator based on Rabotnov's model. *Mechanics of Time-Dependent Materials* 12:129–149
- Rossikhin YA, Shitikova MV (2010) Application of fractional calculus for dynamic problems of solid mechanics: novel trends and recent results. *Applied Mechanics Reviews* 63:1–52
- Rossikhin YA, Shitikova MV (2014) Centennial jubilee of Academician Rabotnov and contemporary handling of his fractional operator. *Fractional Calculus and Applied Analysis* 17:647–683
- Rossikhin YA, Shitikova MV (2015) Features of fractional operators involving fractional derivatives and their applications to the problems of mechanics of solids. In: Daou R, Xavier M (eds) *Fractional Calculus: History, Theory and Applications*, vol 8, Nova Science Publishers, Inc., pp 165–226
- Rossikhin YA, Shitikova MV (2019) Fractional calculus models in dynamic problems of viscoelasticity. In: *Applications in Engineering, Life and Social Sciences, Part A*, vol 7, De Gruyter, pp 139–158
- Rossikhin YA, Shitikova MV (2020) Fractional operator models of viscoelasticity. *Encyclopedia of Continuum Mechanics* pp 971–982
- Rossikhin YA, Shitikova MV, Shcheglova TA (2010) Analysis of free vibrations of a viscoelastic oscillator via the models involving several fractional parameters and relaxation/retardation times. *Computers and Mathematics with Applications* 59:1727–1744
- Rossikhin YA, Shitikova MV, Krusser AI (2016) To the question on the correctness of fractional derivative models in dynamic problems of viscoelastic bodies. *Mechanics Research Communications* 77:44–49
- Roylance D (2001) Engineering viscoelasticity. Department of Materials Science and Engineering 2139:1–37
- Rozovskii MI, Sinaiskii ES (1966) Vibrations of an oscillator with residual creep. *Journal of Applied Mathematics and Mechanics* 30:696–703
- Rzhanitsyn AR (1949) Some questions of the mechanics of systems deformed in time [in Russian]. State publishing house of technical and theoretical literature
- Samko S, Kilbas A, Marichev O (1993) *Fractional Integrals and Derivatives. Theory and Applications*. Gordon and Breach Science Publishers
- Sasso M, Palmieri G, Amodio D (2011) Application of fractional derivative models in linear viscoelastic problems. *Mechanics of Time-Dependent Materials* 15:367–387
- Schiessel H, Blumen A (1993) Hierarchical analogues to fractional relaxation equations. *Journal of Physics A: Mathematical and General* 26:5057–5069
- Schiessel H, Metzler R, Blumen A, Nonnenmacher TF (1995) Generalized viscoelastic models: Their fractional equations with solutions. *Journal of Physics A: General Physics* 28:6567–6584

- Scott-Blair GW (1944) Analytical and integrative aspects of the stress-strain-time problem. *Journal of Scientific Instruments* 21:80–84
- Scott-Blair GW (1949) A survey of general and applied rheology. Pitman
- Shermergor TD (1966) On the use of fractional differentiation operators for the description of elastic aftereffect properties of materials. *Journal of Applied Mechanics and Technical Physics* 7:85–87
- Shitikova MV (2022) Fractional operator viscoelastic models in dynamic problems of mechanics of solids: A review. *Mechanics of Solids* 57
- Singh A, Guedes RM, Paiva D, Magalhães FD (2020) Experiment and modelling of the strain-rate-dependent response during in vitro degradation of pla fibres. *SN Applied Sciences* 2
- Sjoeborg M (2002) On dynamic properties of rubber isolators. PhD thesis, Royal Institute of Technology
- Smit W, de Vries H (1970) Rheological models containing fractional derivatives. *Rheologica Acta* 9:525–534
- Sobotka Z (1981) Reologie hmot a konstrukci (Rheology of materials and constructions — in Czech). Academia
- Song DY, Jiang TQ (1998) Study on the constitutive equation with fractional derivative for the viscoelastic fluids - modified Jeffreys model and its application. *Rheologica Acta* 37:512–517
- Steinmann P, Runesson K (2021) *Visco-Elasticity*. Springer International Publishing
- Stiassnie M (1979) On the application of fractional calculus for the formulation of viscoelastic models. *Applied Mathematical Modelling* 3:300–302
- Su X, Yao D, Xu W (2021) Processing of viscoelastic data via a generalized fractional model. *International Journal of Engineering Science* 161
- Thompson J (1933) On the theory of visco-elasticity: A thermodynamical treatment of visco-elasticity, and some problems of the vibrations of visco-elastic solids. *Philosophical Transactions of the Royal Society A: Mathematical, Physical and Engineering Sciences* 231(694–70):339–407
- Thomson W (1865) On the elasticity and viscosity of metals. *Proceedings of the Royal Society of London* 14:289–297
- Thomson W (1875) Elasticity. In: *Encyclopaedia Britannica*, vol 7, pp 796–825
- Tobolsky AV, Catsiff E (1956) Elastoviscous properties of polyisobutylene (and other amorphous polymers) from stress–relaxation studies. ix. a summary of results. *Journal of Polymer Science* 19:111–121
- Tschoegl NW (1989) *The Phenomenological Theory of Linear Viscoelastic Behavior*. Springer-Verlag
- Voigt W (1889) Ueber die Beziehung zwischen den beiden Elasticitätsconstanten isotroper Körper. *Annalen Der Physik* 274:573–587
- Voigt W (1892) Ueber innere reibung fester körper, insbesondere der metalle. *Annalen der Physik* 283:671–693
- Wang Y, Harris JM (2020) Seismic attenuation models: Multiple and fractional generalizations. *SEG 2020* pp 2754–2758
- Ward IM, Sweeney J (1983) *Mechanical properties of solid polymers*. John Wiley & Sons, Ltd.
- Watanabe S (1959) An approach to visco-elastic behaviors with a mathematical method. *Journal of the Textile Machinery Society of Japan* 5:10–13
- Welch SW, Rorrer RA, Duren RG (1999) Application of time-based fractional calculus methods to viscoelastic creep and stress relaxation of materials. *Mechanics Time-Dependent Materials* 3:279–303
- Weyl H (1917) Bemerkungen zum Begriff des Differentialquotienten gebrochener Ordnung. *Vierteljahrsschrift der Naturforschenden Gesellschaft in Zürich* 62
- Wiechert E (1893) Gesetze der elastischen Nachwirkung für constante Temperatur. *Annalen der Physik* 286
- Wollscheid D, Lion A (2014) The benefit of fractional derivatives in modelling the dynamics of filler-reinforced rubber under large strains: A comparison with the Maxwell-element approach. *Computational Mechanics* 53:1015–1031

- Yang X, Cai W, Liang Y, Holm S (2020) A novel representation of time-varying viscosity with power-law and comparative study. *International Journal of Non-Linear Mechanics* 119:103,372
- Zelenev VM, Meshkov SI, Rossikhin YA (1970a) Damped vibrations of hereditary-elastic systems with weakly singular kernels. *Journal of Applied Mechanics and Technical Physics* 11:290–293
- Zelenev VM, Meshkov SI, Rossikhin YA (1970b) Effect of the ϑ -function singularity parameters on the damped vibrations of elastic systems with aftereffect. *Mechanics of Solids* 5:92–94
- Zener C (1948) *Elasticity and anelasticity of metals*. University of Chicago press
- Zhou HW, Wang CP, Mishnaevsky L, Duan ZQ, Ding JY (2013) A fractional derivative approach to full creep regions in salt rock. *Mechanics of Time-Dependent Materials* 17:413–425
- Zhou XQ, Yu DY, Shao XY, Zhang SQ, Wang S (2016) Research and applications of viscoelastic vibration damping materials: A review. *Composite Structures* 136:460–480
- Zopf C, Hoque SE, Kaliske M (2015) Comparison of approaches to model viscoelasticity based on fractional time derivatives. *Computational Materials Science* 98:287–296



Chapter 15

Invariance Aspects of $F = F_e F_i$ Representations in Coupled-Field Problems

Marek Werner, Kerstin Weinberg

Abstract In multi-field problems, the free energy contributions of different fields are coupled. For the kinematic of deformation, explicit assumptions on the independent fields are necessary, and the intermediate configurations of composed deformations are not uniquely determined. Here, a thermodynamic free energy potential with two primary variables is analyzed. The two energy representations $\Psi(c, \mathbf{C})$ and $\Psi(c, \mathbf{C}_e)$, based on the concentration c , the right Cauchy-Green tensor \mathbf{C} , and its elastic part \mathbf{C}_e , are studied in full detail. The considerations are specified to the chemomechanical coupling of a regular solution model and two types of elastic energy potentials, but all derivations can be generalized to arbitrary material models.

Keywords: Continuum mechanics · Coupled-field problems · Finite strain · State equations · Intermediate configuration · Finite element method

15.1 Introduction

A continuum mechanical description determines a point of a body \mathcal{B} in the reference configuration at location \mathbf{X} and time t_0 . The deformation mapping to the current configuration, $\chi : \mathbf{X} \rightarrow \mathbf{x}$, defines its position at time $t > t_0$. The corresponding linear approximation of the mapping is the deformation gradient, $\mathbf{F} = \nabla_{\mathbf{X}} \chi$, and the local volume change is described by the Jacobian, $J = \det \mathbf{F}$. For compositions of $n > 1$ deformations, \mathbf{F} is split multiplicatively, $\mathbf{F} = \mathbf{F}_n \cdots \mathbf{F}_2 \mathbf{F}_1$, referring to one or more intermediate configurations, see Fig. 15.1. Such intermediate configurations may be compatible and realistic, but in most cases, an intermediate configuration is

M. Werner, K. Weinberg
Universität Siegen, Lehrstuhl für Festkörpermechanik, Department Maschinenbau, Paul-Bonatz-Str. 9-11, 57076 Siegen, Germany
e-mail: marek.werner@uni-siegen.de, kerstin.weinberg@uni-siegen.de

incompatible and serves as a hypothetical construct to analyze different contributions of a deformation.

In multi-field problems, thermal, chemical, electrical, and other fields contribute with different magnitudes to the resulting deformation, and so \mathbf{F} decomposes with respect to the given fields. In the case of two fields, $\mathbf{F} = \mathbf{F}_2\mathbf{F}_1$, the part \mathbf{F}_2 is usually chosen as the purely elastic part of deformation \mathbf{F}_e , and \mathbf{F}_1 is the non-elastic part. The latter can be related to deformations due to temperature (\mathbf{F}_θ), plasticity (\mathbf{F}_p), viscosity (\mathbf{F}_v), growth (\mathbf{F}_i), or others. The corresponding multiplicative formulations are attributed in the framework of thermoelasticity, $\mathbf{F} = \mathbf{F}_e\mathbf{F}_\theta$, to Stojanović et al (1964), for elastoplasticity, $\mathbf{F} = \mathbf{F}_e\mathbf{F}_p$, to Lee (1969), for viscoelasticity, $\mathbf{F} = \mathbf{F}_e\mathbf{F}_v$, to Sidoroff (1974), for growth modeling, $\mathbf{F} = \mathbf{F}_e\mathbf{F}_i$, to Kondaurov and Nikitin (1987); Takamizawa and Hayashi (1987), and for a combined elastic, viscoelastic and elasto(visco)plastic model to Perić and Dettmer (2003), to name a few.

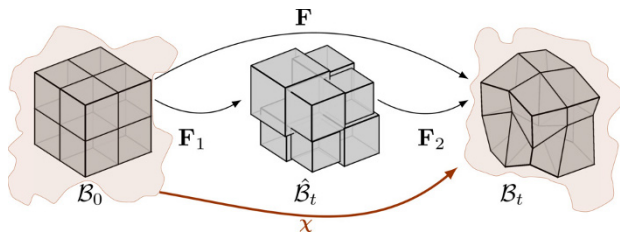


Fig. 15.1 Schematics of a body with reference configuration \mathcal{B}_0 , intermediate configuration $\hat{\mathcal{B}}_t$ and current configuration \mathcal{B}_t . The elastic deformation patches incompatible material elements to a body again.

The most intuitive, generally valid decomposition of the deformation gradient is the polar decomposition, $\mathbf{F} = \mathbf{R}\mathbf{U}$. Assuming a plane uniform deformation for simplicity, it reads $\mathbf{F}(\alpha, \lambda) = \mathbf{R}(\alpha)\mathbf{U}(\lambda)$, and can be understood as a separation of variables, such that the rotation angle α and the stretch λ are independent quantities. The right Cauchy-Green tensor $\mathbf{C}(\lambda) = \mathbf{F}^\top\mathbf{F}$, which is employed to formulate invariant constitutive relations, does *not* depend on the rotation angle.

The intermediate configuration introduced by a multiplicative decomposition is not unique with respect to its rotational part. This is inconsequential for isotropic materials but introduces extended invariance requirements for anisotropy, see e.g. Haupt (2002).

At any stage of deformation, elastic relaxation of the body in the current configuration occurs instantaneously Kelly (2013) and thereby introduces the intermediate configuration as a pointwise-unloaded, stress-free, and therefore incompatible configuration. Isotropic materials, which remain isotropic during deformation, do not depend on local rotation, and so the elastic unloading takes place without rotation Lubarda (2004). A pre-stressed intermediate configuration may also be considered, but then the total stress depends on additional arising strains Sauer et al (2019), e.g., eigen-strains.

For composed deformations, the order of mappings, $\mathbf{F} = \mathbf{F}_n \cdots \mathbf{F}_2 \mathbf{F}_1$, is not uniquely determined. In elastoplasticity, for example, the composition $\mathbf{F} = \mathbf{F}_e \mathbf{F}_p$ is established. The underlying assumption is that the plastic deformations are local; they induce no long-range stress whereas the solid's elastic response is structure insensitive, i.e., invariant under the internal processes. A comparison of different decompositions in the two-field problem of thermoelasticity has been made by Hartmann (2012). The two decompositions, $\mathbf{F} = \mathbf{F}_\theta \mathbf{F}_e$ and $\mathbf{F} = \mathbf{F}_e \mathbf{F}_\theta$, are considered for the case of isotropic material and a purely volumetric temperature response, $\mathbf{F}_\theta = J_\theta^{1/3} \mathbf{1}$. It appears that both formulations yield the same stress state in the current configuration, although the intermediate configuration differs.

The situation is similar for chemomechanical modeling, where inelastic deformations are attributed to the intercalation of species, and elastic deformations result from the local swelling. The diffusing species have a normalized concentration $c \in [0, 1]$, and so the inelastic part of the deformation gradient is a (purely volumetric) function of the concentration field,

$$\mathbf{F}_i(c) = J_i(c)^{1/3} \mathbf{1}. \quad (15.1)$$

Such models are proposed in Anand (2012); Huttin and Kamlah (2012); Weinberg et al (2018); Zhao et al (2015), for example. Here the unknown function $J_i(c)$ is approximated by a Taylor series

$$J_i(c) \approx J_i|_{c=c_0} + \Omega(c - c_0) + \mathcal{O}((c - c_0)^2), \quad (15.2)$$

where the linear slope $\Omega = \partial_c J_i|_{c=c_0}$ matches with the normalized partial molar volume, and c_0 is the species' concentration in the reference concentration, $J_i(c = c_0) = 1$. So in the following we will focus on an isothermal environment and concentrate on the chemical concentration only.

From the multiplicative decomposition $\mathbf{F} = \mathbf{F}_e \mathbf{F}_i$ along with the generally valid relation (15.3) we obtain for the particular case (15.1) the form (15.4)

$$\hat{\mathbf{C}}_e = \mathbf{F}_i^{T-1} \mathbf{C} \mathbf{F}_i^{-1} \quad (15.3)$$

$$\hat{\mathbf{C}}_e = J_i^{-2/3} \mathbf{C}. \quad (15.4)$$

Note that $\hat{\mathbf{C}}_e = \mathbf{F}_e^\top \mathbf{F}_e$ is living in the intermediate configuration (IC), see Fig. 15.1, hence a purely elastic, symmetric, rotation-free deformation measure and therefore the proper argument in the elastic potential, since the IC is the reference configuration for elastic deformation up to the current configuration. However, the attribution of the additional concentration field c to \mathbf{C} and $\hat{\mathbf{C}}_e$ is not that clear. In other words: Is there a concentration dependency of the total right Cauchy-Green tensor, $\mathbf{C}(c)$, or is there an inverse concentration dependency of $\hat{\mathbf{C}}_e(c)$ such that it relaxes \mathbf{C} to be concentration-independent? Formulated in terms of the free energy density Ψ , which determines the constitutive relations, we need to know which consequences are induced by primarily writing $\Psi(c, \mathbf{C})$ or $\Psi(c, \hat{\mathbf{C}}_e)$.

In this paper, we investigate both modeling perspectives and show the consequences stating $\Psi(c, \mathbf{C})$ and $\Psi(c, \hat{\mathbf{C}}_e)$. We remark that our understanding of writing

a function's argument is such that the listed variables are pairwise independent to each other. The notation $\mathbf{F}(\mathbf{C})$ and $\mathbf{F}(\hat{\mathbf{C}}_e)$ is chosen for purpose of illustration; all functions are understood to depend on the corresponding right Cauchy–Green tensor indeed.

To embed the investigation into a chemomechanically coupled framework, we briefly formulate a variational material model and the governing equations in Section 15.2. Then, we study in Section 15.3 the derivatives, which are needed to construct the residual and the tangent of a standard finite element implementation for the two modeling representations. In Section 15.4, we compare both representations, present a numerical example and discuss the results.

15.2 Basic Equations and Free Energy Expressions

The coupled chemomechanical problem's constitutive model is stated in a fully variational form, cf. Weinberg et al (2018). The energy density is additively decomposed according to

$$\Psi = \Psi^{\text{con}} + \Psi^{\text{int}} + \Psi^{\text{el}} \quad (15.5)$$

based on a configurational energy Ψ^{con} , an assigned interfacial energy Ψ^{int} , and an elastic energy Ψ^{el} . For a binary mixture, a configurational energy density of the form

$$\Psi^{\text{con}} = \theta(T)(c \ln(c) + (1 - c) \ln(1 - c)) + \chi c(1 - c) \quad (15.6)$$

is often referred to as the regular solution model, where a temperature function $\theta(T)$ weights the logarithmic entropy term, and where a Flory-Huggins interaction parameter χ scales the second term. The interface-related energy

$$\Psi^{\text{int}} = \frac{\kappa}{2} |\nabla c|^2 \quad (15.7)$$

ensures with $\kappa > 0$ the lowest energy for a vanishing gradient, i.e., minimal interfaces. The elastic energy splits into a volumetric and an isochoric part,

$$\Psi^{\text{el}} = \Psi_{\text{vol}}^{\text{el}} + \Psi_{\text{iso}}^{\text{el}}. \quad (15.8)$$

We assume finite strain elasticity here. For elastic deformations, with components \mathbf{F}_e and $J_e = \det \mathbf{F}_e$, the volumetric part of the energy density reads

$$\Psi_{\text{vol}}^{\text{el}} = \Lambda \beta^{-2} (J_e^{-\beta} - 1 + \beta \ln(J_e)) \quad (15.9)$$

as proposed by Ogden and Hill (1972). In this relation, $\Lambda = K - 2/3 G$ is the first Lamé constant which is expressed here by bulk modulus K and shear modulus G . Different values for β were proposed, e.g., $\beta = -2$ in Simo and Taylor (1991), $\beta = -1$ in Miehe (1994), or $\beta = 1$ together with a Taylor series expansion (see

Appendix). The latter leads to

$$\Psi_{\text{vol}}^{\text{el}} = \frac{\Lambda}{2} (J_e - 1)^2. \tag{15.10}$$

Exemplarily, for the (purely elastic) spherical deformation $\mathbf{F}_e = \lambda \mathbf{1}$, the normalized elastic energy potentials are shown in Fig. 15.2. For moderate volumetric expansion, the expressions for different β are similar and convex.

Pister et al. Simo and Pister (1984) proposed the simple potential

$$\Psi_{\text{iso}}^{\text{el}} = \frac{G}{2} (I_1^e - 3 - 2 \ln(J_e)) \tag{15.11}$$

with $I_1^e = \text{tr}(\hat{\mathbf{C}}_e)$ for the isochoric part of the elastic energy density. Another common model is the classical Neo-Hookean expression for rubber-like materials,

$$\Psi_{\text{iso}}^{\text{el}} = \frac{G}{2} (\bar{I}_1^e - 3), \tag{15.12}$$

where $\bar{I}_1^e = J_e^{-2/3} I_1^e$. Both expressions differ only for large tension or compression, as shown exemplarily in the right plot of Fig. 15.2. For our coupled field model, we state that the Lamé constants to depend on the concentration, $\Lambda = \Lambda(c)$ and $G = G(c)$.

With all energetic contributions at hand, the governing equations comprise the Cahn-Hilliard equation for the chemical diffusion field and the balance of linear momentum for the mechanical field,

$$\dot{c} = \nabla \cdot (\mathbf{M} \nabla \mu) \tag{15.13}$$

$$\mu = \delta_c \Psi, \tag{15.13}$$

$$\mathbf{0} = \nabla \cdot (\mathbf{F} \mathbf{S}) \tag{15.14}$$

$$\mathbf{S} = 2 \partial_c \Psi \tag{15.14}$$

as a coupled set of equations with mobility tensor \mathbf{M} , chemical potential μ , and the second Piola-Kirchhoff stress tensor \mathbf{S} . The variational derivative in Eq. (15.13) reads $\delta_c \bullet = \partial_c \bullet - \nabla \cdot (\partial_{\nabla c} \bullet)$.

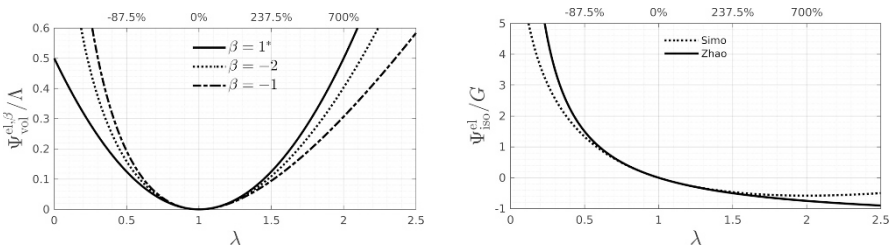


Fig. 15.2 Free energy of elastic material models shown for a spherical expansion $\mathbf{F} = \lambda \mathbf{1}$ without inelasticity, $J_e = J$. A volumetric change of 700% is given for $\lambda = 2$.

15.3 Modeling Representation

Here we will equip the free energy density Ψ with the kinematic assumption of the total or the elastic deformation as a function of the concentration, $\mathbf{F}(c)$ or $\mathbf{F}_e(c)$, respectively. The functional dependency of Ψ on the pairs (c, \mathbf{C}) or $(c, \hat{\mathbf{C}}_e)$ will be studied in full detail.

In particular, the chemical potential μ , i.e., as the derivative with respect to c , Eq. (15.13)₂, and the second Piola-Kirchhoff stress tensor \mathbf{S} , as the derivative of the potential Ψ with respect to \mathbf{C} , Eq. (15.14)₂, will be derived.

15.3.1 First Modeling Representation: $\Psi(c, \mathbf{C})$

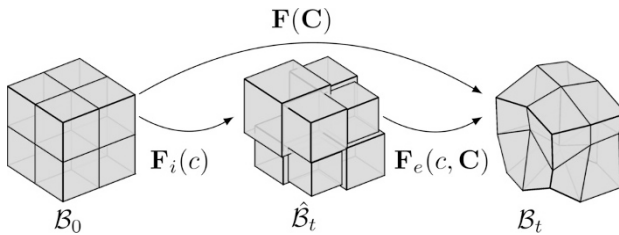


Fig. 15.3 Illustration of the free energy representation $\Psi(c, \mathbf{C})$

In this representation, the two independent variables, c and \mathbf{C} , construct the energy potential $\Psi(c, \mathbf{C})$. Nonetheless, as visualized in Fig. 15.3, the total deformation depends on the right Cauchy-Green tensor only, $\mathbf{F}(\mathbf{C})$. Its inelastic part is a function of concentration, $\mathbf{F}_i(c)$, whereas the elastic response $\mathbf{F}_e(c, \mathbf{C})$ is the mediator between the inelastic deformation and the total deformation.

We start deriving the chemical potential. An application of Jacobi's formula to \mathbf{C} , $\partial_c J^2 = J^2 \operatorname{tr}(\mathbf{C}^{-1} \partial_c \mathbf{C}) = 0$, leads to a concentration-independent total Jacobian,

$$\partial_c J = 0, \quad (15.15)$$

and the explicit expression $J = J(\mathbf{C})$. As illustrated by the arrow between \mathcal{B}_0 and \mathcal{B}_t in Fig. 15.3, the total deformation depends on \mathbf{C} only. The inelastic deformation between \mathcal{B}_0 and $\tilde{\mathcal{B}}_t$ depends on c , and therefore it follows that the elastic relaxation between $\tilde{\mathcal{B}}_t$ and \mathcal{B}_t depends on both, c and \mathbf{C} . Thus, inspection of the elastic Jacobian $J_e(c, \mathbf{C}) = J(\mathbf{C}) J_i^{-1}(c)$ shows that it can be decomposed multiplicatively with separation of variables. The commutator between both derivatives is zero, i.e., $[\partial_c, \partial_c] J_e = \mathbf{0}$, so the chronological order of taking the derivatives is exchangeable, which is known as Schwarz theorem. An expression for the partial derivative $\partial_c \hat{\mathbf{C}}_e$ results from the mutual independence of c and \mathbf{C} ,

$$\mathbf{0} = \partial_c \mathbf{C} = \partial_c (J_i^{2/3} \hat{\mathbf{C}}_e) = 2/3 \Omega J_i^{-1/3} \hat{\mathbf{C}}_e + J_i^{2/3} \partial_c \hat{\mathbf{C}}_e \tag{15.16}$$

$$\Rightarrow \partial_c \hat{\mathbf{C}}_e = -2/3 \Omega J_i^{-1} \hat{\mathbf{C}}_e. \tag{15.17}$$

With Eq. (15.15) it holds further that

$$0 = \partial_c J = (\partial_c J_i) J_e + J_i (\partial_c J_e) \quad \Rightarrow \quad \partial_c J_e = -\Omega J_e J_i^{-1}. \tag{15.18}$$

In this way, an expression for the partial derivative of the elastic Jacobian is found, which enters the derivation of the chemical potential through the elastic energy potential (15.10). Other expressions, which are needed for the gradient of the chemical potential, as well as for the construction of \mathbf{S} , are summarized in Table 15.1.

$$\nabla \mu(c, \mathbf{C}) = (\partial_c \mu) \nabla c + (\partial_{\mathbf{C}} \mu) : \nabla \mathbf{C} = (\partial_c^2 \Psi) \nabla c + (\partial_{\mathbf{C}} \partial_c \Psi) : \nabla \mathbf{C}. \tag{15.19}$$

With the results of Table 15.1, the total gradient of the chemical potential reads

$$\begin{aligned} \nabla \mu(c, \mathbf{C}) &= (\theta(T)c^{-1}(1-c)^{-1} - 2\chi) \nabla c - \kappa \nabla \Delta c \\ &+ (1/2 (\partial_c^2 \Lambda) (J_e - 1)^2) \nabla c \\ &+ (\Omega J_i^{-1} (J_e (J_e - 1) (\Omega J_i^{-1} - 2\partial_c \Lambda) - (2J_e - 1))) \nabla c \\ &+ (1/2 (\partial_c \Lambda) J_e (J_e - 1) - 1/2 \Lambda J_e (2J_e - 1) \Omega J_i^{-1}) \mathbf{C}^{-1} : \nabla \mathbf{C}, \end{aligned} \tag{15.20}$$

where the first line result from the chemical energy density and the remaining expressions from the coupled elasticity. The second Piola-Kirchhoff stress tensor then follows as

$$\mathbf{S} = 2 \partial_{\mathbf{C}} \Psi = \Lambda J_e (J_e - 1) \mathbf{C}^{-1}. \tag{15.21}$$

We remark that this approach has a certain similarity to the “microforce” concept of Anand Anand (2012), used for chemomechanical simulations in Huttin and Kamalah (2012); Zhao et al (2015). However, in opposite to our approach, in Anand (2012), the elastic free energy density refers explicitly to the intermediate configuration, see Werner et al (2021) for a discussion.

Table 15.1 Derivatives of $\Psi(c, \mathbf{C})$ wrt. concentration c and right Cauchy-Green tensor \mathbf{C} ; symbol \mathcal{S} denotes the fourth order super-symmetric identity tensor.

| | J | J_i | J_e | \mathbf{C} | $\hat{\mathbf{C}}_e$ | I_1 | I_1^e | $\bar{I}_1 = \bar{I}_1^e$ |
|------------------------------------|-------------------------------|--------------|---|---------------|--|--------------|---|---|
| ∂_c | 0 | Ω | $-J_e \frac{\Omega}{J_i}$ | $\mathbf{0}$ | $-\frac{2}{3} \frac{\Omega}{J_i} \hat{\mathbf{C}}_e$ | 0 | $-\frac{2}{3} \frac{\Omega}{J_i} I_1^e$ | 0 |
| ∂_c^2 | 0 | 0 | $J_e \frac{\Omega^2}{J_i^2}$ | $\mathbf{0}$ | $\frac{10}{9} \frac{\Omega^2}{J_i^2} \hat{\mathbf{C}}_e$ | 0 | $\frac{10}{9} \frac{\Omega^2}{J_i^2} I_1^e$ | 0 |
| $\partial_{\mathbf{C}}$ | $\frac{J}{2} \mathbf{C}^{-1}$ | $\mathbf{0}$ | $\frac{J_e}{2} \mathbf{C}^{-1}$ | \mathcal{S} | $J_i^{-2/3} \mathcal{S}$ | $\mathbf{1}$ | $J_i^{-2/3} \mathbf{1}$ | $J^{-2/3} (\mathbf{1} - \frac{I_1}{3} \mathbf{C}^{-1})$ |
| $\partial_{\mathbf{C}} \partial_c$ | $\mathbf{0}$ | $\mathbf{0}$ | $-\frac{J_e}{2} \frac{\Omega}{J_i} \mathbf{C}^{-1}$ | $\mathbf{0}$ | $-\frac{2}{3} \frac{\Omega}{J_i} J_i^{-2/3} \mathcal{S}$ | $\mathbf{0}$ | $-\frac{2}{3} \frac{\Omega}{J_i} J_i^{-2/3} \mathbf{1}$ | $\mathbf{0}$ |

15.3.2 Second Modeling Representation: $\Psi(c, \hat{C}_e)$

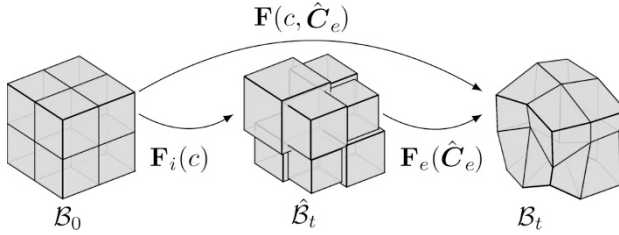


Fig. 15.4 Illustration of the free energy representation $\Psi(c, \hat{C}_e)$

In this representation, the set of independent variables is c and \hat{C}_e . As shown in Fig. 15.4, the inelastic and the elastic processes are coupled in the sense that the inelastic part of deformation is a function of concentration again, $F_i(c)$, and the elastic part is independent of c and just relaxes the intermediate configuration. The total deformation relates both processes to the current configuration. In other words, F is the mediator between the total deformation C and both fields (\hat{C}_e, c) . Consequently, we get $\partial_c \hat{C}_e = \mathbf{0}$ here.

We begin the examination with the derivative $\partial_{\hat{C}_e} C = \partial_{\hat{C}_e} (J_i^{2/3} \hat{C}_e) = J_i^{2/3} \mathcal{S}$, where \mathcal{S} denotes the fourth order super-symmetric identity tensor. With this, we investigate if the concentration depends on the right Cauchy-Green tensor, $c(C)$, and write $\mathbf{0} = \partial_{\hat{C}_e} c = (\partial_C c) : (\partial_{\hat{C}_e} C)$. With $\partial_{\hat{C}_e} C \neq \mathbf{0}$ directly follows that

$$\partial_C c = \mathbf{0}. \quad (15.22)$$

From the application of Jacobi's formula to C , we get the condition

$$2\Omega J_i^{-1} = C^{-1} : \partial_C C. \quad (15.23)$$

Since the left hand side of Eq. (15.23) is greater than zero for any inelastic deformation, the derivative $\partial_C C$ cannot be chosen as zero. However, it is deduced from

$$\partial_C C = \partial_c (J_i^{2/3} \hat{C}_e) = 2/3 \Omega J_i^{-1} C, \quad (15.24)$$

and with this, Eq. (15.23) holds true. At first glance, this result looks strange, since there is a one-way dependency of $C(c)$ and no explicit reverse dependency of the concentration neither on the total deformation $c \neq c(C)$ accordingly to Eq. (15.22) nor on the elastic deformation $c \neq c(\hat{C}_e)$ accordingly to $\Psi(\hat{C}, c)$. Such one-directional dependency has the negative taste that the derivatives ∂_c and ∂_C do not commute. These circumstances require more caution by the calculation of the residuum and the tangent. Consequently, the change of the stress with the concentration $(\partial_c \partial_C \Psi)$ differs from the change of the chemical potential with deformation $(\partial_C \partial_c \Psi)$.

By applying Jacobi's formula this time to $\hat{\mathbf{C}}_e$, we get the expression $\partial_c J_e^2 = J_e^2 \text{tr} \left(\hat{\mathbf{C}}_e^{-1} \partial_c \hat{\mathbf{C}}_e \right) = 0$. With this result, there is no concentration dependency of J_e ,

$$\partial_c J_e = 0, \tag{15.25}$$

which restricts $J_e(\hat{\mathbf{C}}_e)$ only. Moreover, we find an expression for the concentration dependency of the total deformation,

$$\partial_c J = (\partial_c J_i) J_e + J_i (\partial_c J_e) \quad \Rightarrow \quad \partial_c J = \Omega J_e, \tag{15.26}$$

and due to the linear definition of $J_i(c)$, it holds $\partial_c^2 J = 0$. Moreover, with Eq. (15.22) follows that

$$\partial_C J = (\partial_C J_i) J_e + J_i (\partial_C J_e) = \frac{J}{2} \mathbf{C}^{-1} \quad \Rightarrow \quad \partial_C J_e = \frac{J_e}{2} \mathbf{C}^{-1}. \tag{15.27}$$

At this stage, we want to mention, that the explicit dependency is $J_e(\hat{\mathbf{C}}_e)$, and although the expression $\hat{\mathbf{C}}_e = J_i^{-2/3} \mathbf{C}$ is given, it is not possible to write $J_e(\mathbf{C})$ as the following calculation shows:

$$\begin{aligned} 0 &\stackrel{(15.25)}{=} \partial_c J_e(\hat{\mathbf{C}}_e) \stackrel{!}{=} \partial_c J_e(\mathbf{C}) = (\partial_C J_e) : (\partial_c \mathbf{C}) \stackrel{(15.27)}{=} \left(\frac{J_e}{2} \hat{\mathbf{C}}_e^{-1} \right) : \left(\frac{2}{3} \frac{\Omega}{J_i} \mathbf{C} \right) \\ &= J_e \Omega J_i^{-1/3} > 0 \quad \text{!} \end{aligned} \tag{15.28}$$

With this at hand, the elastic part of the gradient of the chemical potential reads

$$\nabla \mu^{\text{el}}(c, \hat{\mathbf{C}}_e) = (\partial_c \mu^{\text{el}}) \nabla c + (\partial_{\hat{\mathbf{C}}_e} \mu^{\text{el}}) : \nabla \hat{\mathbf{C}}_e. \tag{15.29}$$

Table 15.2 summarizes the derivatives of relevant quantities arising in the potential. It can be directly seen that in general they do not commute and therefore the order of taking the derivatives matters. The total gradient of the chemical potential then reads

Table 15.2 Derivatives of $\Psi(c, \hat{\mathbf{C}}_e)$ wrt. concentration c and right Cauchy-Green tensor \mathbf{C} ; symbol \mathbb{S} denotes the fourth order super-symmetric identity tensor.

| | J | J_i | J_e | \mathbf{C} | $\hat{\mathbf{C}}_e$ | I_1 | I_1^e | $\bar{I}_1 = \bar{I}_1^e$ |
|---------------------------------|--|--------------|---|---|---|--|---|--|
| ∂_c | ΩJ_e | Ω | 0 | $\frac{2}{3} \frac{\Omega}{J_i} \mathbf{C}$ | $\mathbf{0}$ | $\frac{2}{3} \frac{\Omega}{J_i} I_1$ | 0 | 0 |
| ∂_c^2 | 0 | 0 | 0 | $-\frac{2}{9} \left(\frac{\Omega}{J_i} \right)^2 \mathbf{C}$ | $\mathbf{0}$ | $-\frac{2}{9} \left(\frac{\Omega}{J_i} \right)^2 I_1$ | 0 | 0 |
| $\partial_{\hat{\mathbf{C}}_e}$ | $\frac{J}{2} \hat{\mathbf{C}}_e^{-1}$ | $\mathbf{0}$ | $\frac{J_e}{2} \hat{\mathbf{C}}_e^{-1}$ | $J_i^{2/3} \mathbb{S}$ | \mathbb{S} | $J_i^{2/3} \mathbf{1}$ | $\mathbf{1}$ | $J_e^{-2/3} \left(\mathbf{1} - \frac{I_1}{3} \hat{\mathbf{C}}_e^{-1} \right)$ |
| $\partial_{\mathbf{C}}$ | $\frac{J}{2} \mathbf{C}^{-1}$ | $\mathbf{0}$ | $\frac{J_e}{2} \mathbf{C}^{-1}$ | \mathbb{S} | $J_i^{-2/3} \mathbb{S}$ | $\mathbf{1}$ | $J_i^{-2/3} \mathbf{1}$ | $J^{-2/3} \left(\mathbf{1} - \frac{I_1}{3} \mathbf{C}^{-1} \right)$ |
| $\partial_C \partial_c$ | $\frac{\Omega}{2} J_e \mathbf{C}^{-1}$ | $\mathbf{0}$ | $\mathbf{0}$ | $\frac{2}{3} \frac{\Omega}{J_i} \mathbb{S}$ | $\mathbf{0}$ | $\frac{2}{3} \frac{\Omega}{J_i} \mathbf{1}$ | $\mathbf{0}$ | $\mathbf{0}$ |
| $\partial_c \partial_C$ | $\frac{\Omega}{6} J_e \mathbf{C}^{-1}$ | $\mathbf{0}$ | $-\frac{J_e}{3} \frac{\Omega}{J_i} \mathbf{C}^{-1}$ | $\mathbf{0}$ | $-\frac{2}{3} \frac{\Omega}{J_i} J_i^{-2/3} \mathbb{S}$ | $\mathbf{0}$ | $-\frac{2}{3} \frac{\Omega}{J_i} J_i^{-2/3} \mathbf{1}$ | $-\frac{2}{3} \frac{\Omega}{J_i} J_e^{-2/3} \left(\mathbf{1} - \frac{I_1}{3} \mathbf{C}^{-1} \right)$ |

$$\begin{aligned}
\nabla\mu(c, \hat{\mathbf{C}}_e) &= (\theta(T)c^{-1}(1-c)^{-1} - 2\chi)\nabla c - \kappa\nabla\Delta c \\
&+ 1/2(\partial_c^2\Lambda)(J_e - 1)^2\nabla c \\
&+ 1/2(\partial_c\Lambda)J_e(J_e - 1)\hat{\mathbf{C}}_e^{-1} : \nabla\hat{\mathbf{C}}_e,
\end{aligned} \tag{15.30}$$

and the second Piola-Kirchhoff stress tensor follows as

$$\mathbf{S} = 2\partial_C\Psi = \Lambda J_e(J_e - 1)\mathbf{C}^{-1}. \tag{15.31}$$

15.3.3 Relation Between Both Representations

In a consistent theory, the results, which are here the stresses and the gradient of the chemical potential, must be independent of the primarily chosen set of arguments. For the stress tensor (15.21) and (15.31), this is obvious. To recover the gradient expression (15.20) from expression (15.30), we write the elastic part of the second representation, Eq. (15.29), at fixed variables

$$\nabla\mu^{\text{el}}(c, \hat{\mathbf{C}}_e) = (\partial_c\mu)|_{\hat{\mathbf{C}}_e, \text{fix}}\nabla c + (\partial_{\hat{\mathbf{C}}_e}\mu)|_{c, \text{fix}} : \nabla\hat{\mathbf{C}}_e. \tag{15.32}$$

We rewrite the third-order tensor as

$$\nabla\hat{\mathbf{C}}_e = \nabla(J_i^{-2/3}\mathbf{C}) = -2/3\Omega J_i^{-1}\nabla c \odot \hat{\mathbf{C}}_e + J_i^{-2/3}\nabla\mathbf{C}. \tag{15.33}$$

Insertion of Eq. (15.33) into Eq. (15.32) leads to

$$\nabla\mu = \left((\partial_c\mu)|_{\hat{\mathbf{C}}_e, \text{fix}} - 2/3\Omega J_i^{-1}(\partial_{\hat{\mathbf{C}}_e}\mu)|_{c, \text{fix}} : \hat{\mathbf{C}}_e \right) \nabla c + J_i^{-2/3}(\partial_{\hat{\mathbf{C}}_e}\mu)|_{c, \text{fix}} : \nabla\mathbf{C}, \tag{15.34}$$

where the relation $(\mathbf{A} \odot \mathbf{B}) : \mathbf{C} = \mathbf{A}(\mathbf{B} : \mathbf{C})$ has been used. The derivatives are fixed at different variables, so we show the two relations

$$(\partial_C\mu(\hat{\mathbf{C}}_e, c))|_{c, \text{fix}} = (\partial_{\hat{\mathbf{C}}_e}\mu)|_{c, \text{fix}} : (\partial_C\hat{\mathbf{C}}_e) = J_i^{-2/3}(\partial_{\hat{\mathbf{C}}_e}\mu)|_{c, \text{fix}}, \tag{15.35}$$

and

$$(\partial_c\mu)|_{\hat{\mathbf{C}}_e, \text{fix}} = (\partial_C\mu)|_{c, \text{fix}} : (\partial_c\mathbf{C}) + (\partial_c\mu)|_{c, \text{fix}} = 2/3\Omega J_i^{-1}(\partial_C\mu)|_{c, \text{fix}} : \mathbf{C} + (\partial_c\mu)|_{c, \text{fix}}. \tag{15.36}$$

One should read Eq. (15.35) backward and insert the first term together with expression of Eq. (15.36) into Eq. (15.34), which gives

$$\nabla\mu = (\partial_c\mu)|_{c, \text{fix}}\nabla c + (\partial_C\mu)|_{c, \text{fix}} : \nabla\mathbf{C}. \tag{15.37}$$

What follows is an expression for $\nabla\mu$ which is known from Eq. (15.20) of the first representation.

15.4 Discussion and Example

The chemomechanical potential is characterized by two independent primary variables, here in the two representations $\Psi(c, \mathbf{C})$ and $\Psi(c, \hat{\mathbf{C}}_e)$. The driving forces of the state equations, i.e., the gradient of the chemical potential and the current stresses, are derived with respect to the concentration and the total deformation \mathbf{C} . Our study shows that the partial derivatives with respect to c and with respect to \mathbf{C} do not commute for the potential $\Psi(c, \hat{\mathbf{C}}_e)$, since the thermodynamic variables have been chosen as c and $\hat{\mathbf{C}}_e$ and fulfill the Maxwell relations to this set of variables. However, both formulations lead to the same gradient chemical potential and the same resulting stresses, although the calculations differ.

Above, we have calculated expressions required for the correct implementation of a chemomechanical coupled-field model within a finite element framework. To illustrate that, we will show here a sample calculation. For the two elasticity models of Sect. 15.2, namely the simplified finite elasticity model with energy density (15.11) and the classical Neo-Hookean model with energy density (15.12), both extended to the volumetric range with density (15.10), we calculate the mechanical deformation of a cylindrical rod under chemical loading.

The elastic rod has a radius of $r = 0.5 \mu\text{m}$ and a length of $l = 7 \mu\text{m}$. It is clamped at both ends, i.e., its longitudinal displacements are constraint. The initial concentration of species is uniform with $c_{\text{ini}} = 0.4$. Without additional loading, the system evolves over time. The material is described by $\Lambda = 10 \text{ GPa}$, $G = 10 \text{ GPa}$, $c_0 = 0.25$. The chosen material parameters result in symmetric equilibrium phases, $c_\alpha = 0.855$ and $c_\beta = 0.145$, whereby these values refer to phase decomposition by diffusion only. For more details on the model and a consistent thermodynamical background, we refer to Weinberg et al (2018); Werner and Weinberg (2019); Werner et al (2021).

In Fig. 15.5, we display the rod radius evolution over the length for five instances of time. Because both representations, $\Psi(c, \mathbf{C})$ and $\Psi(c, \hat{\mathbf{C}}_e)$, deliver essentially the same, the contour curves lay on top of each other. Initially, the rod radius jumps to $r = 0.53 \mu\text{m}$ because $c_{\text{ini}} \neq c_0$. Then three phases evolve, and it can be seen that both elastic potentials result in a similar shape. The maximum volumetric expansion is about 14%, and so the deviation between the curves is small. The average velocity for the swelling process is calculated to be 10^{-11} m/s .

We find that evolution of the radius can be described by simple trigonometric functions. First we fit the contour curves by $r(x) = r_0 + A \cos(\pi kx)$ to get a time dependent amplitude A . Then, the amplitude is fitted by an arctan function, $A = r_A \arctan(a(t - \bar{t}_1)) + b$. To ensure the initial condition $r(x, t = 0) = r_0$, we get the fit function

$$r(x, t) = r_0 + r_A \cos(\pi kx)(\arctan(a\bar{t}_1) - \arctan(a(\bar{t}_1 - \bar{t}))) \quad (15.38)$$

and the specific fit values $r_A = 0.0145$, $k = 0.8569$, $a = 0.1445$ and $\bar{t}_1 = 120.7$. We can estimate the maximum radius $r_{\text{max}} \approx 0.5738$ for $\bar{t} \rightarrow \infty$, which is reached in good approximation after 200 time steps. What we see is that phase decomposition

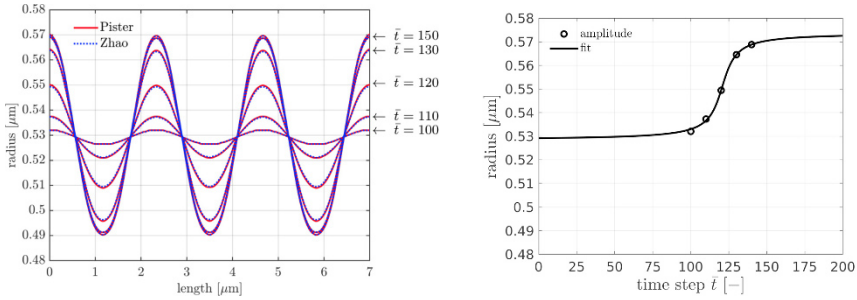


Fig. 15.5 Chemomechanical expansion of a cylindrical rod: contour plot and fitted radius-over-time curve

is a rapid process and might be numerically challenging, in particular with regard to time marching schemes.

15.5 Summary and Conclusion

Field coupling leads to the combination of different energy potentials. Here, an explicit assumption is made for the pairwise independent variables of a two-field problem. An ad-hoc convincing choice is the formulation of the material's potential as a function of the inelastic field and the (superposed) elastic part of the mechanical deformation. The resulting free energy potential depends directly on the elastic variables, like J_e or \hat{C}_e , and so the well-known models of finite elasticity can be used. In the context of coupled problems, such a choice reduces the number of terms in the derivatives required for the state equations. However, a suitable transformation must be found in order to obtain the stresses in the body in its current configuration. Less intuitive but mathematically sound is the formulation of the free energy potential as a function of the total deformation only, where the local elastic deformation \hat{C}_e but not the total deformation C depend implicitly on the inelastic field c . This model gives the elastic response as a function of both inelastic and elastic field. Since the stresses and the chemical potential are defined by the partial derivative with respect to C and c , we prefer the representation $\Psi = \Psi(c, C)$. Here the corresponding derivatives commute. However, our detailed derivation and an illustrating sample calculation show that both formulations yield equivalent results.

Appendix

Ogden Elastic Free Energy Density and its Taylor Series

Ogden elastic free energy density reads

$$\Psi_{\text{vol}}^{\text{el}} = \Lambda \beta^{-2} (J_e^{-\beta} - 1 + \beta \ln(J_e)). \tag{15.39}$$

A Taylor series expansion of the two functions

$$J_e^{-\beta} = J_0^{-\beta} - \beta J_0^{-\beta-1} (J_e - J_0) + \frac{1}{2} (-\beta)(-\beta - 1) J_0^{-\beta-2} (J_e - J_0)^2 - \mathcal{O}(J_e^3) \tag{15.40}$$

$$\ln(J_e) = \ln(J_0) + J_0^{-1} (J_e - J_0) + \frac{1}{2} (-1) J_0^{-2} (J_e - J_0)^2 + \mathcal{O}(J_e^3) \tag{15.41}$$

around $J_e = 1$ leads to

$$\Psi_{\text{vol}}^{\text{el}} = \frac{\Lambda}{2} (J_e - 1)^2. \tag{15.42}$$

Configurational Free Energy Density and its Taylor Series

Also here, a series expansion of the functions $c \ln(c)$ and $(1 - c) \ln(1 - c)$ around the evaluation concentration $c_0 = 1/2$ gives the fourth order potential approximation

$$\Psi_2^{\text{con}} = 4/3 c^2 (1 - c)^2 + (\chi - 8/3) c(1 - c) + 7/12 - \ln(2) \tag{15.43}$$

by exploiting $(c - 1/2)^2 = 1/4 - c(1 - c)$. Both potentials are shown in Fig. 15.6 together with mobilities $M_1 = c(1 - c)$ and $M_2 = 1/8$.

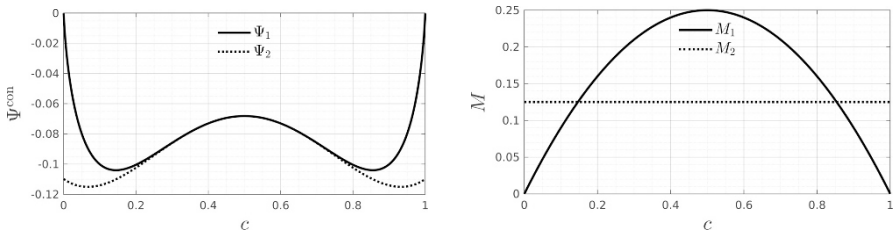


Fig. 15.6 Configurational energy and mobility.

References

- Anand L (2012) A Cahn–Hilliard-type theory for species diffusion coupled with large elastic–plastic deformations. *Journal of the Mechanics and Physics of Solids* 60(12):1983–2002
- Hartmann S (2012) Comparison of the multiplicative decompositions $F = F_{\Theta}F_M$ and $F = F_MF_{\Theta}$ in finite strain thermo-elasticity. Tech. rep., Technical Report Series Fac3-12-01, Faculty of Mathematics/Computer Sciences . . . , Clausthal-Zellerfeld
- Haupt P (2002) *Continuum mechanics and theory of materials*. Springer
- Huttin M, Kamlah M (2012) Phase-field modeling of stress generation in electrode particles of lithium ion batteries. *Applied Physics Letters* 101(13):133,902
- Kelly P (2013) Solid mechanics. part iii. Lecture notes, The University of Auckland pp 371–387
- Kondaurov VI, Nikitin LV (1987) Finite strains of viscoelastic muscle tissue. *Journal of Applied Mathematics and Mechanics* 51(3):346–353
- Lee EH (1969) Elastic-plastic deformation at finite strains. *Journal of Applied Mechanics* 36(1):1–6
- Lubarda VA (2004) Constitutive theories based on the multiplicative decomposition of deformation gradient: Thermoelasticity, elastoplasticity, and biomechanics. *Applied Mechanics Reviews* 57(2):95–108
- Miehe C (1994) Aspects of the formulation and finite element implementation of large strain isotropic elasticity. *International Journal for Numerical Methods in Engineering* 37(12):1981–2004
- Ogden RW, Hill R (1972) Large deformation isotropic elasticity: on the correlation of theory and experiment for compressible rubberlike solids. *Proceedings of the Royal Society of London A Mathematical and Physical Sciences* 328(1575):567–583
- Perić D, Dettmer W (2003) Computational strategies for inelastic solids at large strains: Some recent issues with an industrial application. In: Miehe C (ed) *IUTAM Symposium on Computational Mechanics of Solid Materials at Large Strains*, Springer Netherlands, Dordrecht, pp 425–434
- Sauer RA, Ghaffari R, Gupta A (2019) The multiplicative deformation split for shells with application to growth, chemical swelling, thermoelasticity, viscoelasticity and elastoplasticity. *International Journal of Solids and Structures* 174-175:53–68
- Sidoroff F (1974) Un modèle viscoélastique non linéaire avec configuration intermédiaire. *J Mec* 13(4):679–713
- Simo JC, Pister KS (1984) Remarks on rate constitutive equations for finite deformation problems: computational implications. *Computer Methods in Applied Mechanics and Engineering* 46(2):201–215
- Simo JC, Taylor RL (1991) Quasi-incompressible finite elasticity in principal stretches. *Continuum basis and numerical algorithms*. *Computer methods in applied mechanics and engineering* 85(3):273–310
- Stojanović R, Djurić S, Vujošević L (1964) On finite thermal deformations. *Arch Mech Stosow* 16:103–108
- Takamizawa K, Hayashi K (1987) Strain energy density function and uniform strain hypothesis for arterial mechanics. *Journal of biomechanics* 20(1):7–17
- Weinberg K, Werner M, Anders D (2018) A chemo-mechanical model of diffusion in reactive systems. *Entropy* 20(2):140
- Werner M, Weinberg K (2019) Coupled thermal and electrochemical diffusion in solid state battery systems. In: et al A (ed) *New Achievements in Continuum Mechanics and Thermodynamics, Advanced Structured Materials*, vol 108, Springer, chap 35, pp 519–535
- Werner M, Pandolfi A, Weinberg K (2021) A multi-field model for charging and discharging of lithium-ion battery electrodes. *Continuum Mechanics and Thermodynamics* 33(3):661–685
- Zhao Y, Stein P, Xu BX (2015) Isogeometric analysis of mechanically coupled Cahn–Hilliard phase segregation in hyperelastic electrodes of Li-ion batteries. *Computer Methods in Applied Mechanics and Engineering* 297:325–347

Part II

Computations



Chapter 16

Strain-Gradient Modeling and Computation of 3-D Printed Metamaterials for Verifying Constitutive Parameters Determined by Asymptotic Homogenization

Gokhan Aydin, M. Erden Yildizdag, Bilen Emek Abali

Abstract Metamaterials exhibit significantly different mechanical deformation than in classical “first-order” theory. One possible modeling approach is to use a “strain-gradient” theory by incorporating also higher gradients of displacements into the formulation. This procedure clearly brings in additional constitutive parameters. In this study, a numerical framework is presented by applying strain-gradient theory to 3-D printed structures with an infill ratio used frequently in additive manufacturing for weight reduction. This choice causes metamaterials; the additional constitutive parameters in the strain-gradient model are determined by an asymptotic homogenization. In order to demonstrate the reliability of this methodology, we verify the accuracy by computations using the finite element method.

Keywords: Generalized mechanics · Asymptotic homogenization · Finite element method · 3-D printing · Infill pattern · Mechanical metamaterials

G. Aydin
Istanbul Technical University, Faculty of Naval Architecture and Ocean Engineering, Istanbul, Turkey
e-mail: aydingo18@itu.edu.tr

M. E. Yildizdag
University of L'Aquila, International Research Center on Mathematics and Mechanics of Complex Systems, L'Aquila, Italy
Istanbul Technical University, Faculty of Naval Architecture and Ocean Engineering, Istanbul, Turkey
e-mail: yildizdag@itu.edu.tr

B. E. Abali
Uppsala University, Division of Applied Mechanics, Department of Materials Science and Engineering, Uppsala, Sweden
e-mail: bilenemek@abali.org

16.1 Introduction

Recently, the usage of additive manufacturing (AM) has considerably increased effected by its ability to construct sophisticated geometries not possible in conventional manufacturing techniques like casting or milling. AM techniques build 3-D objects in a layer-by-layer fashion by using virtual models created in a CAD software. As its layer-wise approach eliminates dependency on many constraints in terms of design and manufacturing, AM techniques are able to provide suitable solutions for complex manufacturing requirements in different industrial applications. Indeed, in the last decade, additive manufacturing techniques have substantially changed the viewpoint of designers and engineers in terms of geometric complexity, topology optimization, multifunctionality and customization. Presently, fabrication of materials with complex microstructures exhibiting exotic properties is not an unlikely effort with the inexorable progress in additive manufacturing and material technology (Yildizdag et al, 2019). Therefore, design of metamaterials has become a popular research subject with increasing advanced manufacturing techniques to obtain unique application-tailored responses, and many new ideas from biomechanics (Lekszycki and dell'Isola, 2012; Giorgio et al, 2016, 2017; George et al, 2018; Giorgio et al, 2019, 2021; Scerrato et al, 2021) to micrometer length scale designs (Kwon et al, 2020; Vangelatos et al, 2021a; Casalotti et al, 2020) have been promulgated relying on sophisticated microstructure based designs.

Matematerials belong to a class of materials showing unconventional overall behavior due to their complex microstructures, and in general, metamaterials are categorized based on the main interaction phenomena occurring in their microstructures. This study is concerned with one of the most popular metamaterials, namely mechanical metamaterials. In mechanical metamaterials, the overall behavior is obtained via mechanical interaction between micro-structural constituents of the material. Obviously, they are the most suitable type of metamaterials, which are designed and fabricated even with regular 3-D printers. For instance, among different mechanical metamaterials, pantographic metamaterials have garnered a lot of attention in the recent literature as reviewed by Barchiesi et al (2019) due to their distinct properties and have been investigated numerically and experimentally in various studies (for example, see dell'Isola et al, 2019c; Yildizdag et al, 2020; Vangelatos et al, 2021b; Spagnuolo et al, 2021; Hild et al, 2021). In fact, studies on pantographic metamaterials have had an important role to initiate the concept of higher-gradient mathematical modeling for materials with complex microstructures (see dell'Isola et al, 2019b,a, 2016). Although this is not a new concept in theoretical mechanics, fabrication of materials showing higher-gradient effects has been enabled by advanced 3-D printing techniques as discussed in Alibert et al (2003); dell'Isola et al (2015); Giorgio et al (2018); Ciallella et al (2021). Actually, development of new mathematical models is inevitable from a theoretical point of view, while tremendous effort made in additive manufacturing and material technology enables fabrication of complex structures. In addition, these novel mathematical models may play an important role for exploring new potential metamaterials (Skrzat and Eremeyev, 2020; Rahali et al, 2015; Eremeyev and Turco, 2020). For interested readers, we

refer to the recently published works of Turco et al (2016); Berezovski et al (2020); Desmorat et al (2020); Barchiesi et al (2021); Laudato et al (2021); Shekarchizadeh et al (2021a,b) on different aspects of higher-gradient theories and their applications.

In this study, a numerical framework is presented, which is suitable to identify the second-gradient mathematical model for 3-D printed specimens with different infill patterns and ratios. This infill ratio is a standard feature in slicer software that is used to construct numerical control code (G-code) defining how to manufacture the structure. Hence, it is frequently used in AM and we examine the metamaterials parameters in one possible infill pattern. To this end, a representative volume element (RVE) is first formed by using the periodicity of the internal structure of specimen, i.e. infill pattern. Then, second-gradient constitutive parameters are determined by using an asymptotic homogenization technique. The mechanical behavior of specimen as a cantilever is investigated by means of simulations for the second-gradient model by using the determined constitutive parameters. In order to examine the accuracy of the numerical framework, the solution based on classical 1st-gradient model, i.e. CAUCHY continuum, is used as a reference solution. Compared with this reference solution, we obtain adequate results by means of the 2nd-gradient model, which indeed decreases the computational cost significantly. As a target problem, a specimen with “grid” infill pattern is selected, since this pattern is one of the mostly used microstructure in AM. Albeit the computational formulation is readily available in 3-D continuum, we present a 2-D analysis for the sake of simplicity.

The rest of the manuscript is as follows. In Section 16.2, the numerical framework based on an asymptotic homogenization technique is briefly reviewed. Then, numerical results are presented for the target specimen and verified comparing with the results of classical 1st-gradient theory in Section 16.4. Finally, in Section 16.5, conclusions are drawn. All the computations for the parameter determination as well as simulations are employed by means of open-source packages under license of Gnu Public (2007) from the FEniCS project (Logg et al, 2011; Hoffman et al, 2005) and we make the code publicly available in Abali (2021) in order to increase the scientific exchange.

16.2 Asymptotic Homogenization

We follow the homogenization method and its implementation in Abali and Barchiesi (2021) that is verified and applied in Vazic et al (2021); Yang et al (2022). Homogenization method starts with a microstructure expressed in \mathbf{y} and with a given material model, we use linear elastic isotropic model with the known stiffness tensor, \mathbf{C}^m . At the microscale, the deformation energy is quadratic,

$$e^m = \frac{1}{2} \varepsilon_{ij}^m C_{ijkl}^m \varepsilon_{kl}^m. \quad (16.1)$$

Herein we use standard continuum mechanics formulation and understand summation convention over repeated indices. For the sake of simplicity, we use linearized

displacement gradients as a strain measure,

$$\varepsilon_{ij}^m = \frac{1}{2} \left(\frac{\partial u_i}{\partial y_j} + \frac{\partial u_j}{\partial y_i} \right). \quad (16.2)$$

In the homogenized continuum, modeled by the strain-gradient modeling approach, the energy reads

$$e^M = \frac{1}{2} \varepsilon_{ij}^M C_{ijkl}^M \varepsilon_{kl}^M + \varepsilon_{ij}^M G_{ijklm}^M \varepsilon_{kl,m}^M + \frac{1}{2} \varepsilon_{ij,k}^M D_{ijklmn}^M \varepsilon_{lm,n}^M. \quad (16.3)$$

A comma notation denotes a partial derivative in \boldsymbol{x} . We aim for obtaining the numerical values of metamaterials tensors, \boldsymbol{C}^M and \boldsymbol{D}^M . The only assertion of the whole method is that the deformation energy is equal in a representative volume element (RVE), Ω , leading to

$$\int_{\Omega} e^m dV = \int_{\Omega} e^M dV. \quad (16.4)$$

In the asymptotic homogenization, the displacement field is expanded by using additional unknowns, φ and ψ . Then by comparing coefficients out of Eq. (16.4), we obtain differential equations to solve and calculate φ and ψ . By means of the finite element method, we obtain the numerical solution for φ by solving

$$\frac{\partial}{\partial y_j} \left(C_{ijkl}^m L_{abkl} \right) = 0, \quad L_{abkl} = \delta_{ak} \delta_{bl} + \frac{\partial \varphi_{abk}}{\partial y_l}. \quad (16.5)$$

With the solution of φ , we determine

$$C_{abcd}^M = \frac{1}{V} \int_{\Omega} C_{ijkl}^m L_{abij} L_{cdkl} dV. \quad (16.6)$$

The macroscale stiffness tensor, \boldsymbol{C}^M , is used in order to solve ψ by the following governing equation:

$$-\frac{\rho^m}{\rho^M} C_{icab}^M + C_{ickl}^m L_{abkl} + \frac{\partial}{\partial y_j} \left(C_{ijkl}^m N_{abckl} \right) = 0, \quad N_{abckl} = \varphi_{abk} \delta_{cl} + \frac{\partial \psi_{abck}}{\partial y_l}. \quad (16.7)$$

With this solution, we construct

$$M_{abcij} = y_c L_{abij} + N_{abcij}, \quad \bar{I}_{kn} = \epsilon^2 \int_{\Omega^P} y_k y_n dV, \quad (16.8)$$

and obtain all strain-gradient parameters

$$\begin{aligned}
G_{abcde}^M &= \frac{\epsilon}{V} \int_{\Omega} C_{ijkl}^m L_{abij} M_{cdekl} dV, \\
D_{ijklmn}^M &= \frac{\epsilon^2}{V} \int_{\Omega} C_{ijkl}^m M_{abcij} M_{defkl} dV - C_{ijlm}^M \bar{I}_{kn}.
\end{aligned} \tag{16.9}$$

16.3 Computation

For the numerical solution of Eq. (16.5) as well as Eq. (16.7), we utilize the finite element method (Zohdi, 2018) and span a finite dimensional HILBERTIAN SOBOLEV space for trial functions. The same space is used for the test functions, known as the GALERKIN procedure. The triangulation of the RVE is generated by NetGen algorithms in Salome. We solve the discrete problem by minimizing the weak form obtained after a standard variational formulation with an implementation in the FEniCS platform, we refer to Abali (2017) for an introduction with examples. Specifically in strain-gradient method, we refer to Abali et al (2015); Reiher et al (2017); Khakalo and Niiranen (2020). The weak form is obtained after integrating by parts; periodic boundary conditions vanish boundary integrals. Determining C^M , G^M , and D^M necessitates linear form functions for φ and ψ .

For verification purposes, we solve the same application for a continuum body \mathcal{B} at microscale as well as at macroscale. At the microscale, the problem is linear elastic problem with the weak form

$$\int_{\mathcal{B}} C_{jikl}^m \varepsilon_{kl}^m \delta u_{i,j} dV = \int_{\partial \mathcal{B}_N} \hat{t}_i \delta u_i dA. \tag{16.10}$$

On DIRICHLET boundaries, the displacement is given such that the test function vanishes. Hence, only on NEUMANN boundaries, $\partial \mathcal{B}_N$, traction vector, \hat{t} , is defined. We solve the displacement at the microscale, u^m , again by using linear form functions within the elements. The discrete nature of the finite element method allows a continuous displacement function across elements.

At the macroscale, we minimize the energy involving second gradient of displacement at the macroscale, u^M . Hence, for the computation, we use quadratic form functions. In order to enforce a continuous and differentiable field across the elements, we use a mixed formulation and solve derivative of displacement as an additional unknown, ∇u . For ensuring consistency, $u_{i,j}^M = \nabla u_{ij}$, we use a LAGRANGE multiplier, λ , as an additional unknown. For the multiplier, we use a constant (discontinuous) form functions. In this way, we employ strain and its gradient from two unknown fields,

$$\varepsilon_{ij}^M = \frac{1}{2} (u_{i,j}^M + u_{j,i}^M), \quad \nabla \varepsilon_{ijk} = \frac{1}{2} (\nabla u_{ij,k} + \nabla u_{ji,k}), \tag{16.11}$$

and generate the weak form, as follows:

$$\int_{\mathcal{B}} \left(C_{jikl}^M \varepsilon_{kl}^M \delta u_{i,j} + D_{ijklmn}^M \nabla \varepsilon_{lmn} \delta \nabla u_{ij,k} + \lambda_{ij} (\delta \nabla u_{ij} - \delta u_{i,j}) + (\nabla u_{ij} - u_{i,j}) \delta \lambda_{ij} \right) dV = \int_{\partial \mathcal{B}_N} \hat{t}_i \delta u_i dA . \tag{16.12}$$

We refer for technical details to an analogous implementation in Abali et al (2021). In each node, displacement, \mathbf{u}^M , gradient of displacement, $\nabla \mathbf{u}$, and multiplier, $\boldsymbol{\lambda}$, are solved in a coupled manner. The unknowns are tensor rank 1, 2, and 2, respectively. Therefore, the computational cost is high. Specifically, for a 2-D problem $2 + 4 + 4 = 10$ degrees of freedom (DOFs) and for a 3-D problem $3 + 9 + 9 = 21$ DOFs are used in each node. This method is a method to ensure C^1 continuity, which ensures a monotonous convergence in strain-gradient solved by the finite element method.

16.4 Results and Verification

In this study, a 3-D printed structure is considered for the verification. The specimen has length $L = 110$ mm and height $H = 22$ mm, with a grid infill pattern which corresponds to a 70.25% infill ratio as shown in Fig. 16.1 and 16.2. We model the specimen out of PLA, poly(lactic acid), which is a thermoplastic polyester. By using YOUNG’S modulus $E = 3500$ MPa and Poisson’s ratio $\nu = 0.3$, we use an isotropic material model at the microscale,

$$\lambda = \frac{E\nu}{(1 + \nu)(1 - 2\nu)}, \mu = \frac{E}{2(1 + \nu)}, \tag{16.13}$$

$$C_{ijkl}^m = \lambda \delta_{ij} \delta_{kl} + \mu \delta_{ik} \delta_{jl} + \mu \delta_{il} \delta_{jk} .$$

KRONECKER delta, δ_{ij} , is the identity (unit tensor of rank 2). Also, in order to apply boundary conditions properly, additional parts are added to the left and right of the beam, see the CAD shown Fig. 16.1, the computational domain is the orange domain (of interest) and gray supports on left and right for clamping.

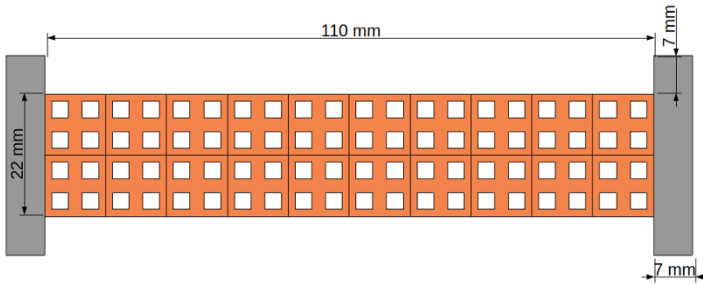
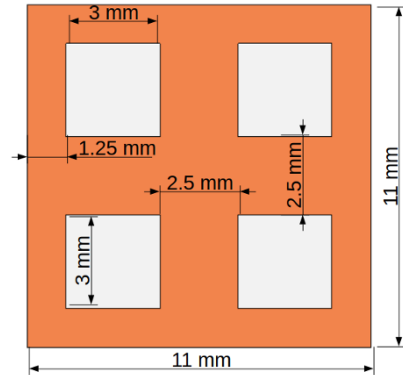


Fig. 16.1 Dimensions of 3-D printed of approx. 70% infill ratio structure with “rigid” left and right parts for clamping to a machine.

Fig. 16.2 Dimensions of selected RVE of the specimen.



16.4.1 Reference Solution Based on 1st-Gradient Theory

The structure has been analyzed by a 1st-gradient model in the context of linearized elasticity theory in order to have a reference solution. In the analysis, a vertical traction vector of 0.1 MPa is applied along the free end of the specimen as shown in Fig. 16.3. For acquiring the numerical accuracy of the reference solution, a posteriori error analysis is employed. For this purpose, an h -convergence is conducted by using discretizations with local mesh lengths of 0.2, 0.1, and 0.05 mm, respectively (see Fig. 16.3 for a mesh sample). The error is measured by the deflection change occurring at the tip of the specimen as a consequence of h -convergence. Herein we use the well-known feature of monotonous convergence of the finite element method (by using adequate shape functions). In Table 16.1, for each discretization, the

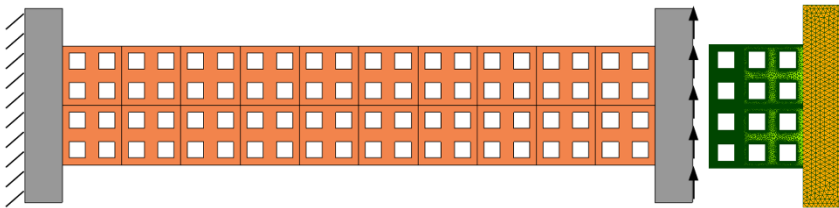


Fig. 16.3 Boundary conditions and a mesh sample used in the simulations based on 1st-gradient theory.

obtained deflection is presented along with the number of nodes and computational time required (using one Intel Xeon E7-4850 with 40 MB cache). Obviously, achieved convergence with the most refined discretization is adequate as a reference solution with a predicted numerical error of 0.3%. In Fig. 16.4, the obtained deformation with the 1st-gradient theory is presented. Here, the contour plot shows the deformation in the vertical direction, and the result is given with scale factor of 16 to obtain a better

Table 16.1 Convergence study with the simulations based on 1st-gradient model.

| Mesh length in mm | Deflection in mm | Number of nodes | Computation time in s |
|-------------------|------------------|-----------------|-----------------------|
| 0.2 | 1.135 | 45 029 | 1.46 |
| 0.1 | 1.143 | 160 887 | 7.49 |
| 0.05 | 1.146 | 606 293 | 57.93 |

illustration. As expected, bending occurs due to the applied shear stress at the short side of the specimen.

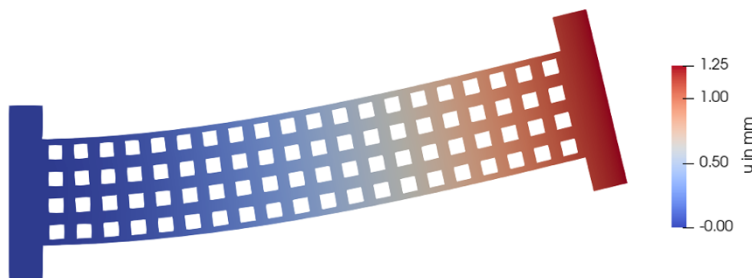
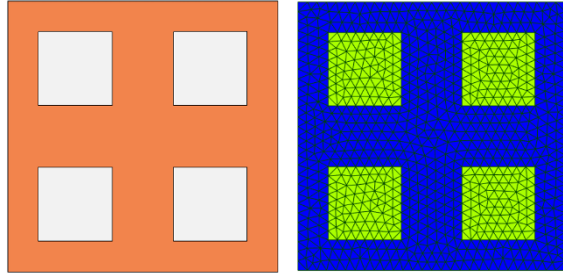


Fig. 16.4 Deformation obtained by 1st-gradient theory, colors denote the magnitude of displacement, deformation is shown by scaling 16 times.

16.4.2 Determination of Constitutive Parameters in the Strain-Gradient Model

To conduct simulations with the strain-gradient model, the constitutive parameters are first obtained through the aforementioned asymptotic homogenization procedure. To this end, in this study, an appropriate representative volume element (RVE) was extracted from the geometry of specimen by the periodicity of its microstructure. The choice of RVE is to be depicted in Fig. 16.5. For the asymptotic homogenization process, this selected RVE is discretized and periodic boundary conditions are applied on all boundaries. For voids inside RVE, we choose a “numerical zero” for their YOUNG’s modulus of 0.01 MPa. Therefore, the whole RVE domain is discretized. Asymptotic homogenization generates the parameters, for writing the results, we use an extended VOIGT notation, where A, B indicate $\{11, 22, 12\}$ and α, β denote $\{111, 221, 121, 112, 222, 122\}$, as follows:

Fig. 16.5 Selected RVE with 4 unit cells (left) and its mesh as the homogenized body (right).



$$\begin{aligned}
 C_{AB}^M &= \begin{pmatrix} C_{1111}^M & C_{1122}^M & C_{1112}^M \\ C_{2211}^M & C_{2222}^M & C_{2212}^M \\ C_{1211}^M & C_{1222}^M & C_{1212}^M \end{pmatrix}, \\
 G_{A\alpha}^M &= \begin{pmatrix} G_{11111}^M & G_{11221}^M & G_{11121}^M & G_{11112}^M & G_{11222}^M & G_{11122}^M \\ G_{22111}^M & G_{22221}^M & G_{22121}^M & G_{22112}^M & G_{22222}^M & G_{22122}^M \\ G_{12111}^M & G_{12221}^M & G_{12121}^M & G_{12112}^M & G_{12222}^M & G_{12122}^M \end{pmatrix}, \\
 D_{\alpha\beta}^M &= \begin{pmatrix} D_{111111}^M & D_{111221}^M & D_{111121}^M & D_{111112}^M & D_{111222}^M & D_{111122}^M \\ D_{221111}^M & D_{221221}^M & D_{221121}^M & D_{221112}^M & D_{221222}^M & D_{221122}^M \\ D_{121111}^M & D_{121221}^M & D_{121121}^M & D_{121112}^M & D_{121222}^M & D_{121122}^M \\ D_{112111}^M & D_{112221}^M & D_{112121}^M & D_{112112}^M & D_{112222}^M & D_{112122}^M \\ D_{222111}^M & D_{222221}^M & D_{222121}^M & D_{222112}^M & D_{222222}^M & D_{222122}^M \\ D_{122111}^M & D_{122221}^M & D_{122121}^M & D_{122112}^M & D_{122222}^M & D_{122122}^M \end{pmatrix}.
 \end{aligned} \tag{16.14}$$

The convergence characteristics of the parameters are not known. Hence, another *h*-convergence study has been conducted to check the estimated constitutive parameters and their mesh dependency. Five different local mesh lengths, namely 0.4, 0.2, 0.1, 0.05, and 0.025 mm, have been utilized. The convergence of two constitutive parameters, namely C_{11}^M and D_{11}^M , are presented in Fig. 16.6. The monotonic

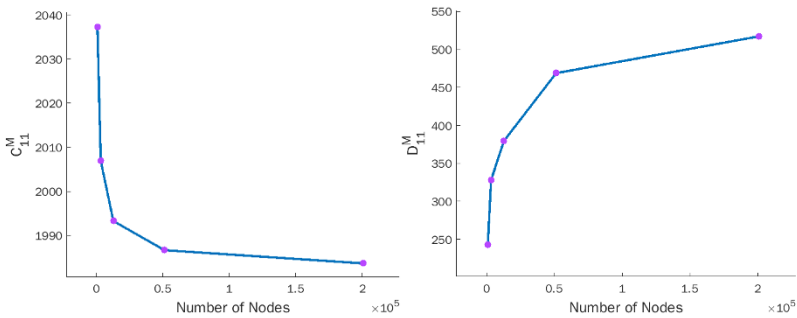


Fig. 16.6 Convergence of constitutive parameters C_{11}^M (left) and D_{11}^M (right).

convergence is obviously showing the robustness of the methodology. Parameters

obtained by the mesh with local mesh length length of 0.025 mm may be used in the strain-gradient simulations. With the most refined mesh, the predicted constitutive parameters read

$$\begin{aligned}
 C_{AB}^M &= \begin{pmatrix} 1987 & 475 & 0 \\ 475 & 1987 & 0 \\ 0 & 0 & 281 \end{pmatrix} \text{ MPa}, \quad G_{A\alpha}^M = \begin{pmatrix} 0 & 0 & 0 & 0 & 0 \\ 0 & 0 & 0 & 0 & 0 \\ 0 & 0 & 0 & 0 & 0 \end{pmatrix} \text{ N/mm}, \\
 D_{\alpha\beta}^M &= \begin{pmatrix} 469 & 634 & 1 & 3 & 1 & -75 \\ 634 & 4078 & 0 & 1 & -2 & 1473 \\ 1 & 0 & 1142 & 1473 & -75 & 0 \\ 3 & 1 & 1473 & 4079 & 636 & 1 \\ 1 & -2 & -75 & 636 & 469 & -1 \\ -75 & 1473 & 0 & 0 & 0 & 1143 \end{pmatrix} \text{ N}.
 \end{aligned} \tag{16.15}$$

Here, it must be remarked that the computed constitutive matrix $G_{A\alpha}^M$ becomes zero, as expected from the RVE that is centro-symmetric. Albeit some components are negative, the total energy is positive since the homogenization is achieved by using the microscale energy with a quadratic form and a positive definite stiffness tensor at the microscale. The positive-definiteness is an important feature for defining a 2nd-gradient problem with a unique solution as studied in Nazarenko et al (2021a,b); Eremeyev (2021).

16.4.3 Simulations with 2nd-Gradient Theory and Validation

To investigate the validity of determined strain-gradient constitutive parameters, the same specimen as a homogenized continuum has been simulated. As shown in Fig. 16.7, for strain-gradient simulations, a rectangular domain is assigned as the computational domain, and the same boundary conditions are applied to both ends. The numerical simulations have been conducted by discretizing the computational



Fig. 16.7 Boundary conditions of computational domain used in the 2nd-gradient theory simulations.

domain with five different local mesh lengths, namely 4, 3, 2, 1, and 0.5 mm. In

Table 16.2, the obtained tip deflection, error with respect to the reference (1st-gradient) solution, and computation time with the same machine are presented for each simulation. Also in Fig. 16.8, error obtained by the strain-gradient model with

Table 16.2 Convergence study and calculated accuracy by using the reference solution by 2nd-gradient simulations

| Mesh Length in mm | Deflection in mm | Error in % | Computation time in s |
|-------------------|------------------|------------|-----------------------|
| 4 | 1.112 | 2.95 | 0.39 |
| 3 | 1.118 | 2.43 | 0.60 |
| 2 | 1.124 | 1.97 | 1.16 |
| 1 | 1.128 | 1.60 | 6.94 |
| 0.5 | 1.130 | 1.37 | 69.36 |

respect to the reference solution is given as a function of number of nodes. This plot is on logarithmic axes such that a linear convergence is expected from an adequate implementation by using proper form functions. Obviously, the results given in Table 16.2 and Fig. 16.8 demonstrate the robustness and reliability of the acquired parameters as well as simulations by the strain-gradient model. Also, as expected, the computational cost is greatly reduced by the strain-gradient modeling. In short, when both results are compared, it is apparent that strain-gradient model can have a robust prediction of mechanical behavior in a shorter time period with a sufficiently small margin of error. In addition, deformed configurations obtained by 1st-gradient and 2nd-gradient models are compared in Fig. 16.9. It is seen that the error is not only low on the chosen point for error calculation, but the same trend is visible in the whole displacement field. Therefore, constitutive parameters are suitable to investigate the mechanical behavior of homogenized continuum at a significantly lower computational cost.

16.5 Conclusion

In conclusion, a numerical framework has been presented in this study in order to determine strain-gradient model of 3-D printed metamaterials. As a result of a long term study in strain-gradient modeling and parameter determination, we have acquired a robust implementation with an adequate accuracy and monotonous convergence. Specifically, an easy-to-print specimen with grid infill has been considered and its strain-gradient constitutive parameters have been determined by using asymptotic homogenization. Then, the determined parameters have been verified by using the reference solution obtained by computations based on the classical 1st-gradient theory. The obtained results in this study show that the proposed numerical framework

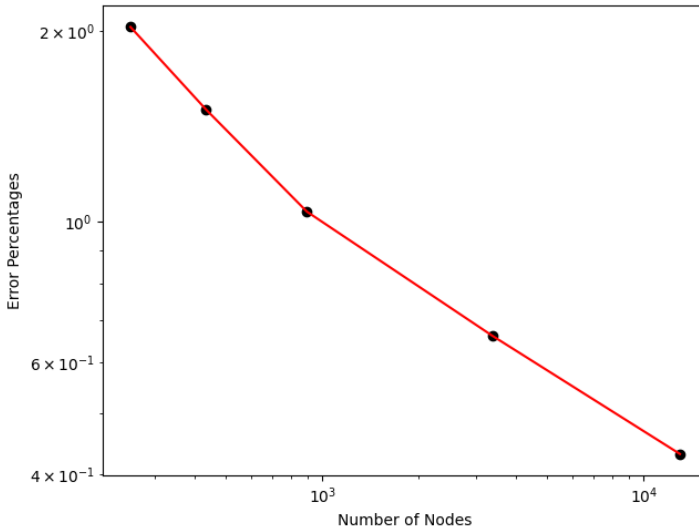


Fig. 16.8 Convergence of strain-gradient solutions.

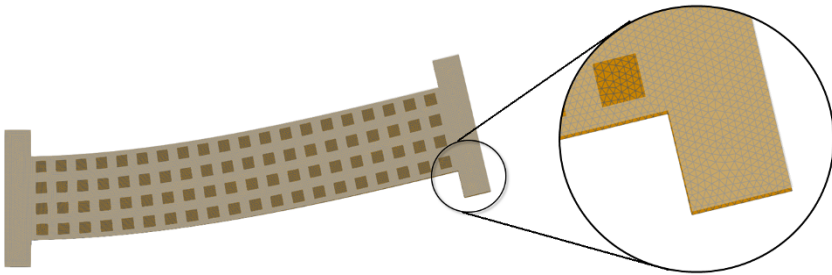


Fig. 16.9 Comparison between 1st-gradient model (orange, with mesh) and strain-gradient model (white, transparent).

is suitable to determine strain-gradient constitutive parameters and can be applied to materials with different infill ratios and a more complex microstructure. We emphasize that the 3-D printed structures possess the effect of microstructure generated by infill ratio. The mechanical response deviation may be significant between a CAD model designed with 100% material and its 3-D printed structure with only 70% infill ratio.

References

Abali BE (2017) Computational Reality, Solving Nonlinear and Coupled Problems in Continuum Mechanics. Advanced Structured Materials, Springer

- Abali BE (2021) Supply code for computations. <http://bilenemek.abali.org/>
- Abali BE, Barchiesi E (2021) Additive manufacturing introduced substructure and computational determination of metamaterials parameters by means of the asymptotic homogenization. *Continuum Mechanics and Thermodynamics* 33:993–1009
- Abali BE, Müller WH, Eremeyev VA (2015) Strain gradient elasticity with geometric nonlinearities and its computational evaluation. *Mechanics of Advanced Materials and Modern Processes* 1(1):1–11
- Abali BE, Klunker A, Barchiesi E, Placidi L (2021) A novel phase-field approach to brittle damage mechanics of gradient metamaterials combining action formalism and history variable. *ZAMM-Journal of Applied Mathematics and Mechanics/Zeitschrift für Angewandte Mathematik und Mechanik* 101(9):e202000,289
- Alibert JJ, Seppecher P, Dell'Isola F (2003) Truss modular beams with deformation energy depending on higher displacement gradients. *Mathematics and Mechanics of Solids* 8(1):51–73
- Barchiesi E, Spagnuolo M, Placidi L (2019) Mechanical metamaterials: a state of the art. *Mathematics and Mechanics of Solids* 24(1):212–234
- Barchiesi E, Yang H, Tran C, Placidi L, Müller WH (2021) Computation of brittle fracture propagation in strain gradient materials by the fenics library. *Mathematics and Mechanics of Solids* 26(3):325–340
- Berezovski A, Yildizdag ME, Scerrato D (2020) On the wave dispersion in microstructured solids. *Continuum Mechanics and Thermodynamics* 32(3):569–588
- Casalotti A, D'Annibale F, Rosi G (2020) Multi-scale design of an architected composite structure with optimized graded properties. *Composite Structures* 252:112,608
- Ciallella A, Pasquali D, Gofaszewski M, D'Annibale F, Giorgio I (2021) A rate-independent internal friction to describe the hysteretic behavior of pantographic structures under cyclic loads. *Mechanics Research Communications* 116:103,761
- dell'Isola F, Andreaus U, Placidi L (2015) At the origins and in the vanguard of peridynamics, non-local and higher-gradient continuum mechanics: an underestimated and still topical contribution of gabrio piola. *Mathematics and Mechanics of Solids* 20(8):887–928
- dell'Isola F, Giorgio I, Pawlikowski M, Rizzi NL (2016) Large deformations of planar extensible beams and pantographic lattices: heuristic homogenization, experimental and numerical examples of equilibrium. *Proceedings of the Royal Society A: Mathematical, Physical and Engineering Sciences* 472(2185):20150,790
- dell'Isola F, Seppecher P, Alibert JJ, Lekszycki T, Grygoruk R, Pawlikowski M, Steigmann D, Giorgio I, Andreaus U, Turco E, et al (2019a) Pantographic metamaterials: an example of mathematically driven design and of its technological challenges. *Continuum Mechanics and Thermodynamics* 31(4):851–884
- dell'Isola F, Seppecher P, Spagnuolo M, Barchiesi E, Hild F, Lekszycki T, Giorgio I, Placidi L, Andreaus U, Cuomo M, Eugster SR, Pfaff A, Hoschke K, Langkemper R, Turco E, Sarikaya R, Misra A, De Angelo M, D'Annibale F, Bouterf A, Pinelli X, Misra A, Desmorat B, Pawlikowski M, Dupuy C, Scerrato D, Peyre P, Laudato M, Manzari L, Göransson P, Hesch C, Hesch S, Franciosi P, Dirrenberger J, Maurin F, Vangelatos Z, Grigoropoulos C, Melissinaki V, Farsari M, Muller W, Abali BE, Liebold C, Ganzosch G, Harrison P, Drobnicki R, Igumnov L, Alzahrani F, Hayat T (2019b) Advances in pantographic structures: design, manufacturing, models, experiments and image analyses. *Continuum Mechanics and Thermodynamics* 31(4):1231–1282
- dell'Isola F, Turco E, Misra A, Vangelatos Z, Grigoropoulos C, Melissinaki V, Farsari M (2019c) Force–displacement relationship in micro-metric pantographs: Experiments and numerical simulations. *Comptes Rendus Mécanique* 347(5):397–405
- Desmorat B, Spagnuolo M, Turco E (2020) Stiffness optimization in nonlinear pantographic structures. *Mathematics and Mechanics of Solids* 25(12):2252–2262
- Eremeyev VA (2021) Strong ellipticity conditions and infinitesimal stability within nonlinear strain gradient elasticity. *Mechanics Research Communications* 117:103,782
- Eremeyev VA, Turco E (2020) Enriched buckling for beam-lattice metamaterials. *Mechanics Research Communications* 103:103,458

- George D, Allena R, Remond Y (2018) A multiphysics stimulus for continuum mechanics bone remodeling. *Mathematics and Mechanics of Complex Systems* 6(4):307–319
- Giorgio I, Andreaus U, Scerrato D, dell'Isola F (2016) A visco-poroelastic model of functional adaptation in bones reconstructed with bio-resorbable materials. *Biomechanics and modeling in mechanobiology* 15(5):1325–1343
- Giorgio I, Andreaus U, dell'Isola F, Lekszycki T (2017) Viscous second gradient porous materials for bones reconstructed with bio-resorbable grafts. *Extreme Mechanics Letters* 13:141–147
- Giorgio I, Harrison P, dell'Isola F, Alsayednoor J, Turco E (2018) Wrinkling in engineering fabrics: a comparison between two different comprehensive modelling approaches. *Proceedings of the Royal Society A: Mathematical, Physical and Engineering Sciences* 474(2216):20180,063
- Giorgio I, dell'Isola F, Andreaus U, Alzahrani F, Hayat T, Lekszycki T (2019) On mechanically driven biological stimulus for bone remodeling as a diffusive phenomenon. *Biomechanics and modeling in mechanobiology* 18(6):1639–1663
- Giorgio I, Spagnuolo M, Andreaus U, Scerrato D, Bersani AM (2021) In-depth gaze at the astonishing mechanical behavior of bone: A review for designing bio-inspired hierarchical metamaterials. *Mathematics and Mechanics of Solids* 26(7):1074–1103
- Gnu Public (2007) Gnu general public license. <http://www.gnu.org/copyleft/gpl.html>
- Hild F, Misra A, dell'Isola F (2021) Multiscale dic applied to pantographic structures. *Experimental Mechanics* 61(2):431–443
- Hoffman J, Jansson J, Johnson C, Knepley M, Kirby R, Logg A, Scott LR, Wells GN (2005) Fenics. <http://www.fenicsproject.org/>
- Khakalo S, Niiranen J (2020) Anisotropic strain gradient thermoelasticity for cellular structures: Plate models, homogenization and isogeometric analysis. *Journal of the Mechanics and Physics of Solids* 134:103,728
- Kwon J, Evans K, Ma L, Arnold D, Yildizdag ME, Zohdi T, Ritchie RO, Xu T (2020) Scalable electrically conductive spray coating based on block copolymer nanocomposites. *ACS applied materials & interfaces* 12(7):8687–8694
- Laudato M, Manzari L, Giorgio I, Spagnuolo M, Göransson P (2021) Dynamics of pantographic sheet around the clamping region: experimental and numerical analysis. *Mathematics and Mechanics of Solids* p 1081286521992646
- Lekszycki T, dell'Isola F (2012) A mixture model with evolving mass densities for describing synthesis and resorption phenomena in bones reconstructed with bio-resorbable materials. *ZAMM-Journal of Applied Mathematics and Mechanics/Zeitschrift für Angewandte Mathematik und Mechanik* 92(6):426–444
- Logg A, Mardal KA, Wells GN (2011) Automated Solution of Differential Equations by the Finite Element Method, The FEniCS Book, *Lecture Notes in Computational Science and Engineering*, vol 84. Springer
- Nazarenko L, Glüge R, Altenbach H (2021a) Positive definiteness in coupled strain gradient elasticity. *Continuum Mechanics and Thermodynamics* 33(3):713–725
- Nazarenko L, Glüge R, Altenbach H (2021b) Uniqueness theorem in coupled strain gradient elasticity with mixed boundary conditions. *Continuum Mechanics and Thermodynamics* pp 1–14
- Rahali Y, Giorgio I, Ganghoffer J, dell'Isola F (2015) Homogenization à la Piola produces second gradient continuum models for linear pantographic lattices. *International Journal of Engineering Science* 97:148–172
- Reiher JC, Giorgio I, Bertram A (2017) Finite-element analysis of polyhedra under point and line forces in second-strain gradient elasticity. *Journal of Engineering Mechanics* 143(2):04016,112
- Scerrato D, Bersani AM, Giorgio I (2021) Bio-inspired design of a porous resorbable scaffold for bone reconstruction: A preliminary study. *Biomimetics* 6(1):18
- Shekarchizadeh N, Abali BE, Barchiesi E, Bersani AM (2021a) Inverse analysis of metamaterials and parameter determination by means of an automatized optimization problem. *ZAMM-Journal of Applied Mathematics and Mechanics/Zeitschrift für Angewandte Mathematik und Mechanik* p e202000277

- Shekarchizadeh N, Laudato M, Manzari L, Abali BE, Giorgio I, Bersani AM (2021b) Parameter identification of a second-gradient model for the description of pantographic structures in dynamic regime. *Zeitschrift für angewandte Mathematik und Physik* 72(6):1–24
- Skrzatz A, Eremeyev VA (2020) On the effective properties of foams in the framework of the couple stress theory. *Continuum Mechanics & Thermodynamics* 32(6)
- Spagnuolo M, Yildizdag ME, Andraus U, Cazzani AM (2021) Are higher-gradient models also capable of predicting mechanical behavior in the case of wide-knit pantographic structures? *Mathematics and Mechanics of Solids* 26(1):18–29
- Turco E, dell'Isola F, Cazzani A, Rizzi NL (2016) Hencky-type discrete model for pantographic structures: numerical comparison with second gradient continuum models. *Zeitschrift für angewandte Mathematik und Physik* 67(4):1–28
- Vangelatos Z, Sheikh HM, Marcus PS, Grigoropoulos CP, Lopez VZ, Flamourakis G, Farsari M (2021a) Strength through defects: A novel bayesian approach for the optimization of architected materials. *Science advances* 7(41):eabk2218
- Vangelatos Z, Yildizdag ME, Giorgio I, dell'Isola F, Grigoropoulos C (2021b) Investigating the mechanical response of microscale pantographic structures fabricated by multiphoton lithography. *Extreme Mechanics Letters* 43:101,202
- Vazic B, Abali BE, Yang H, Newell P (2021) Mechanical analysis of heterogeneous materials with higher-order parameters. *Engineering with Computers* pp 1–17
- Yang H, Abali BE, Müller WH, Barboura S, Li J (2022) Verification of asymptotic homogenization method developed for periodic architected materials in strain gradient continuum. *International Journal of Solids and Structures* 238:111,386
- Yildizdag ME, Tran CA, Barchiesi E, Spagnuolo M, dell'Isola F, Hild F (2019) A multi-disciplinary approach for mechanical metamaterial synthesis: a hierarchical modular multiscale cellular structure paradigm. In: *State of the art and future trends in material modeling*, Springer, pp 485–505
- Yildizdag ME, Barchiesi E, dell'Isola F (2020) Three-point bending test of pantographic blocks: numerical and experimental investigation. *Mathematics and Mechanics of Solids* 25(10):1965–1978
- Zohdi TI (2018) *Finite Element Primer for Beginners*. Springer



Chapter 17

On Boundary Layers Observed in Some 1D Second-Gradient Theories

Emilio Barchiesi, Alessandro Ciallella, Ivan Giorgio

Abstract Boundary layers are regions into a material domain where gradients localize. They often arise in non-local theories such as second gradient ones, which introduce various internal length scales. This work aims at exploring the properties linked to boundary layers for a few typologies of one-dimensional continua moving in plane. More particularly, three cases are explored: the deflection of an extensible Euler–Bernoulli beam, and the axial deformation of a pantographic beam with nonlinear first gradient and second gradient effects. It is concluded that the size of boundary layers depends on the internal lengths and, when nonlinearities are considered, on the external load.

Keywords: Non-linear extensible beam · Pantographic beam · Second gradient continua

E. Barchiesi

École Nationale d'Ingénieurs de Brest, UMR CNRS 6027, IRDL, Brest, France.

Université de Bretagne Sud, IRDL-UBS - UMR CNRS 6027, Centre de Recherche, Rue de Saint Maudé - BP 92116 56321, Lorient, Cedex, France

International Research Center on the Mathematics and Mechanics of Complex Systems (M&MoCS), University of L'Aquila, Italy.

e-mail: emilio.barchiesi@enib.fr

A. Ciallella, I. Giorgio

Department of Civil, Construction-Architectural and Environmental Engineering (DICEAA), University of L'Aquila, Italy

International Research Center on the Mathematics and Mechanics of Complex Systems (M&MoCS), University of L'Aquila, Italy.

e-mail: alessandro.ciallella@univaq.it, ivan.giorgio@univaq.it

17.1 Introduction

Research in materials exceeding mechanical performances of conventional materials is nowadays incredibly audacious. Defined by renowned engineers Gibson and Ashby as ‘*an interconnected network of solid struts or plates which form the edges and faces of cells*’ (Ashby and Gibson, 1997; Ashby, 2006), architected materials are periodical structures that can take either stochastic or non-stochastic forms, depending on the arrangement of their unit cells. Recent developments in experimental Science enabling the examination of defects at very low scales provide an unprecedented possibility to link the structure with the properties of materials (Spanos et al, 2021). Techniques ranging from high-resolution electron microscopy to atomic-force microscopy reveal new insights into the micro-mechanical foundations of material behaviors, but also pose deep challenges concerning theory, modeling and simulation (dell’Isola et al, 2019c). Indeed, the link between the structure and the observed behaviors is still often a difficult one to forge theoretically or computationally, and remains an active area of research (Misra et al, 2020; Abdoul-Anziz et al, 2019; Abali et al, 2019; Abali and Barchiesi, 2021; Mandadapu et al, 2021; Falsone and La Valle, 2019). Establishing such a link is of utmost importance in advancing the design and fabrication of improved engineering materials. Indeed, properly designed architected materials can exhibit extremely favorable performances like low weight-to-stiffness ratios (De Angelo et al, 2019), high element-failure tolerance (Turco et al, 2016b), and high energy-absorption capability (Barchiesi et al, 2021b).

The significance of micro-scale mechanisms in influencing macro-scale material behaviors has been nowadays largely recognized in the context of mechanics (Nejad-sadeghi et al, 2019; Greco, 2020). Micro-scale mechanisms can be extremely interesting, being a complex combination of local buckling phenomena (Vangelatos et al, 2019), folding (Lin et al, 2020), snapping (Barchiesi et al, 2021a), and many others. At the architecture element scale, many modeling approaches in the literature make use of fine-geometry finite element models based on Cauchy continuum and elastoplastic constitutive laws. Many micro-structures have been investigated in the existing literature. It is particularly worth to remark, also in view of the topics presented in this paper, that special emphasis has been placed on those micro-structures based on the pantographic motif (dell’Isola et al, 2019b,a; Ciallella, 2020), i.e., a mechanism which is well known from everyday life (pantographic mirrors, expanding fences, scissor lifts, etc.), which is characterized by a zero-energy accordion-like homogeneous extension/compression deformation mode. These materials can be suitably designed to show strong anisotropic effects, namely to be extremely compliant in some directions and extremely stiff in others. Owing to the otherwise unbearable computational complexity, properly identified coarse-geometry continuum models are the go-to choice when dealing with the macro-scale (Eremeyev and Morozov, 2010; Niiranen et al, 2019; Tran and Niiranen, 2020). It is nowadays well-established that, when the micro-structure is not resolved spatially, so-called generalized continua (including also higher gradient theories (Germain, 2020; Alibert et al, 2003; dell’Isola et al, 2015)), as opposed to Cauchy continuum, are the proper tool to capture relevant micro-scale deformation mechanisms originating from non-local

interactions and strong local stiffness contrast, especially below the threshold for a sufficient length scale difference allowing a scale separation (Rosi et al, 2018).

Indeed, it is well known that continuum descriptions based on Cauchy continuum, due to the dependence of the strain energy density on the first space gradient of the displacement field only, cannot correctly deal with energy localizations due to strong local stiffness contrast (as in micro-structured materials) or due to localized loading (as in impact dynamics), leading to numerical instabilities and severe mesh sensitivity in computations, thus giving physically unrealistic results with increasing mesh refinement (Abali et al, 2017). Despite several attempts, mainly based upon ad hoc enhancements, no satisfactory solution to the above problems has been achieved within the framework of Cauchy continuum. A satisfactory mitigation of these issues can be obtained by non-local continuum formulations, like enriched-kinematics and higher-gradient theories, that introduce internal characteristic lengths that manifest as the formation of boundary layers, i.e. layers where gradients are concentrated. When these theories must be addressed numerically by the Finite Element Method, one should employ suitably smooth test functions (Placidi et al, 2018; Greco and Cuomo, 2013; Greco et al, 2017; Greco and Cuomo, 2016; Cazzani et al, 2016a,b; Yildizdag et al, 2020). At the architecture scale, many approaches in the literature make use of discrete *à la* Hencky spring models (Turco et al, 2016a; Giorgio, 2020). Aimed at bridging the gap between discrete and continuum, variational asymptotic homogenization technique (Barchiesi et al, 2020b,a) (*à la* Piola) are exploited transferring the discrete description of a self-similar finite-dimensional system into a continuous formulation when the degrees of freedom tend to infinity.

The main objective of this paper is to explore the properties linked to boundary layers for a few typologies of one-dimensional continua moving in plane. Only a few simple theories are explored to avoid being distracted by very complex circumstances. Three cases are considered: the deflection of an extensible Euler–Bernoulli beam, and the axial deformation of a pantographic beam with nonlinear first gradient effects and with nonlinear second gradient effects. While all the beam theories considered in this contribution are second gradient ones, unlike the pantographic beam, Euler–Bernoulli beam is an incomplete second gradient 1D continuum in plane. These theories can all be obtained by means of homogenization procedures, including variational asymptotic homogenization, applied to Hencky spring models (Placidi et al, 2020). The plan of the work is the following one. In Sect. 17.2, the properties of boundary layers arising in the solution of an Euler–Bernoulli beam problem are explored, while Sect. 17.3 addresses the case of a pantographic beam, at first with nonlinear first gradient effects and, then, with nonlinear second gradient effects. Finally, some conclusions are presented.

17.2 Euler–Bernoulli Beam

The first case which is considered deals with an extensible planar Euler–Bernoulli beam (Eugster and Harsch, 2020; Harsch and Eugster, 2020; Harsch et al, 2021; Della Corte et al, 2017; Greco and Cuomo, 2015). Such a beam is assumed to be straight in the reference configuration. To represent the axis line of the beam in the current configuration in the framework of a Lagrangian description, we introduce a ‘material’ abscissa $X \in [0, 1]$ and then the following parametrization

$$\begin{cases} x_1(X) = X + u_1(X) \\ x_2(X) = u_2(X) \end{cases} \quad (17.1)$$

where u_i stand for the coordinates of the displacement field in the given right-hand reference frame whose x_1 -axis is directed along the beam-axis prior to the deformation. The static behavior of this one-dimensional nonlinear mechanical system is characterized by the elastic energy:

$$\mathcal{W}[u'_i(\cdot), u''_i(\cdot)] = \frac{1}{2} \int_0^1 K_e (\rho - 1)^2 dX + \frac{1}{2} \int_0^1 K_b (\theta')^2 dX \quad (17.2)$$

which is a quadratic form of the two measures of deformation: i) the elongation $\rho - 1$; ii) and the curvature θ' (Spagnuolo and Andreaus, 2019). Specifically, the considered quantities can be expressed as a function of the displacement as follows:

$$\rho = \sqrt{(1 + u'_1)^2 + (u'_2)^2}, \quad \theta' = \frac{u''_2(1 + u'_1) - u''_1 u'_2}{\rho^2} \quad (17.3)$$

where the symbol $'$ denotes differentiation with respect to X . The two stiffnesses K_e and K_b can be regarded as the reluctance of the system to be deformed, respectively, with stretching and bending. The current shape of the beam is the curve (17.1) that minimizes the energy (17.2) and satisfies the given boundary conditions. To avoid an excessive variety of scenarios, we consider from this point forth only essential boundary conditions; therefore, without losing generality, we can afford the lack of introduction on the boundary of an external elastic potential to complete the characterization of the system. The results presented herein are obtained by a finite element formulation implemented in the commercial software COMSOL Multiphysics with the weak form tool, which simply requires the specification of the deformation energy.

In this system, the boundary layers are a direct consequence of a possible interaction of the two kinds of energy considered (first and second gradient), the relative weight bestowed to them by their stiffnesses, and the necessity of satisfying the boundary conditions.

As a matter of fact, in the linearized case:

$$\mathcal{W}_{\text{lin}} [u'_i(\cdot), u''_i(\cdot)] = \frac{1}{2} \int_0^1 K_e (u'_1)^2 dX + \frac{1}{2} \int_0^1 K_b (u''_2)^2 dX \quad (17.4)$$

the two energetic terms of the first and second gradient are utterly decoupled, and then there is no possibility of having a boundary layer. Indeed, the two solutions for the longitudinal displacement u_1 and the transverse one u_2 are completely independent. In the absence of an external bulk potential, the longitudinal displacement is uniform within the span of the beam to minimize the current length. At the same time, the transverse displacement is characterized by the minimum (linearized) curvature compatibly with the boundary conditions. These circumstances do not lead to a localization of the deformation energy near the boundary conditions; therefore, no boundary layers are detected.

Clearly, the two energy contributions can have some possible interactions only in the nonlinear case. Therefore, we deal with this instance. In the most general nonlinear case, the two components of the displacement are linked since they appear simultaneously in both deformation measures. Consequently, the energy related to the second gradient deformation, namely the term incorporating the curvature, and the term of the first gradient, involving the elongation, can exhibit a certain level of interaction depending on the specific boundary conditions considered. Particularly, in the case in which the boundary conditions are chosen in such a way that no extension is involved, this interaction is not triggered, and consequently, the solution is only governed by the second gradient deformation measure (the curvature). See Fig. 17.1 where a shear test with fixed orientations at ends are considered and the longitudinal displacement is kept free on the right end in order to avoid any elongation of the beam. In this picture, the boundary layers are clearly absent. Of course, even in the inextensible case, we have the same behavior: The solutions are governed by the curvature only. Indeed, the energy becomes

$$\mathcal{W}_{\text{inx}} [u'_i(\cdot), u''_i(\cdot)] = \int_0^1 \lambda (\rho - 1) dX + \frac{1}{2} \int_0^1 K_b (\theta')^2 dX \quad (17.5)$$

where λ is the Lagrange multiplier that ensures the constraint $\rho = 1$ and thus represents the axial contact force.

On the contrary, if we consider a shear test with orientations at ends fixed and we also set to zero the longitudinal displacement u_1 in both the ends, the two energies interact, and the level of this interaction depends on the ratio between the stiffnesses K_b and K_e , as well as on the transverse displacement imposed during the test at one end. The ratio between the aforementioned stiffnesses has the dimensions of a squared length; therefore, we can define a characteristic length as

$$\alpha = \sqrt{\frac{K_b}{K_e}} \quad (17.6)$$

If K_b is very small with respect to K_e , as it occurs in common applications, bending the beam is easier than stretching it. Thus, the current shape of the beam is characterized by the minimum possible length, and the boundary conditions are satisfied via localization of curvature strain occurring because of the small work

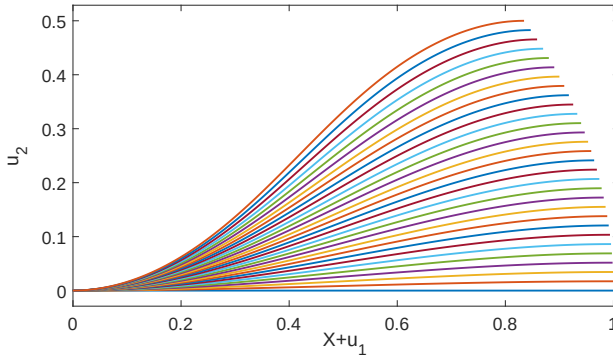


Fig. 17.1 Equilibrium shapes varying the assigned displacement u_0 where no extension is involved.

needed to have higher curvatures. Clearly, this mechanism of deformation that leads to the formation of boundary layers strongly depends on the characteristic length, namely the ratio between the stiffnesses and how the two deformations of the first and second gradient are prone to be activated in the particular case examined. See Fig. 17.2, where the current shapes of the beam for different displacements and characteristic lengths ($\alpha = 0.01$, $\alpha = 0.03$, $\alpha = 0.06$) are shown. Increasing K_b with respect to K_e , indeed, the boundary layer width changes giving growing importance to the second gradient term.

To illustrate the dependence of the boundary layer width on the characteristic length α and the level of the deformation, we have performed different numerical simulations changing them. The boundary layer width is evaluated as follows. Firstly, we normalize the deformation energy density to its maximum value; secondly, considering as a reference, the value of the energy density at the middle, namely in the farthest place from the boundaries, the width of the boundary layer is defined as the interval in which the energy density localizes itself deviating from the reference value of a threshold of 1% (see, Fig. 17.3).

In particular, considering a parametric study on shear tests, Fig. 17.4a displays that independently by α , when the imposed displacement u_0 at the right side of the beam is very small, namely the linear approximation holds, there is no boundary layer as expected. As u_0 increases, instead, the boundary layer width decreases because the share of the deformation energy due to the elongation grows, and hence the possibility of localizing curvature near the ends waxes as well. Moreover, as shown in Fig. 17.4b for a given displacement, the boundary layer width rises, naturally with different ratios for each displacement, because the relative importance of the second gradient term in the energy becomes increasingly important with the growing of α . When α increases and goes beyond 0.1, the boundary layer invades the whole structure. Therefore, it loses its importance.

In common applications, we have

$$\alpha^2 = \frac{K_b}{K_e} = \frac{Y_b J}{Y_b A} \simeq d^2 \tag{17.7}$$

where Y_b is the Young modulus of the material employed, J the second moment of area of the beam cross-section, A is the area of the beam cross-section, and d can be interpreted as a characteristic transverse size of the beam. Namely, the characteristic length α and the transverse size d , which is negligible with respect to the length of the beam, are of the same order of magnitude. Having said this, the boundary layer has meaning at the macroscopic level of observation if and only if its width is much greater than the characteristic length α . In this context, this is verified as it is shown in Fig. 17.4. This aspect is quite crucial since the boundary layer width should always have a non-negligible size at the macro-scale to be of some relevance. Besides, if the continuum model considered is the result of a homogenization procedure, the boundary layer width never shall be smaller than the size of the characteristic length of the unit cell at the microlevel of observation. Otherwise, the considered model is inconsistent and must be reformulated.

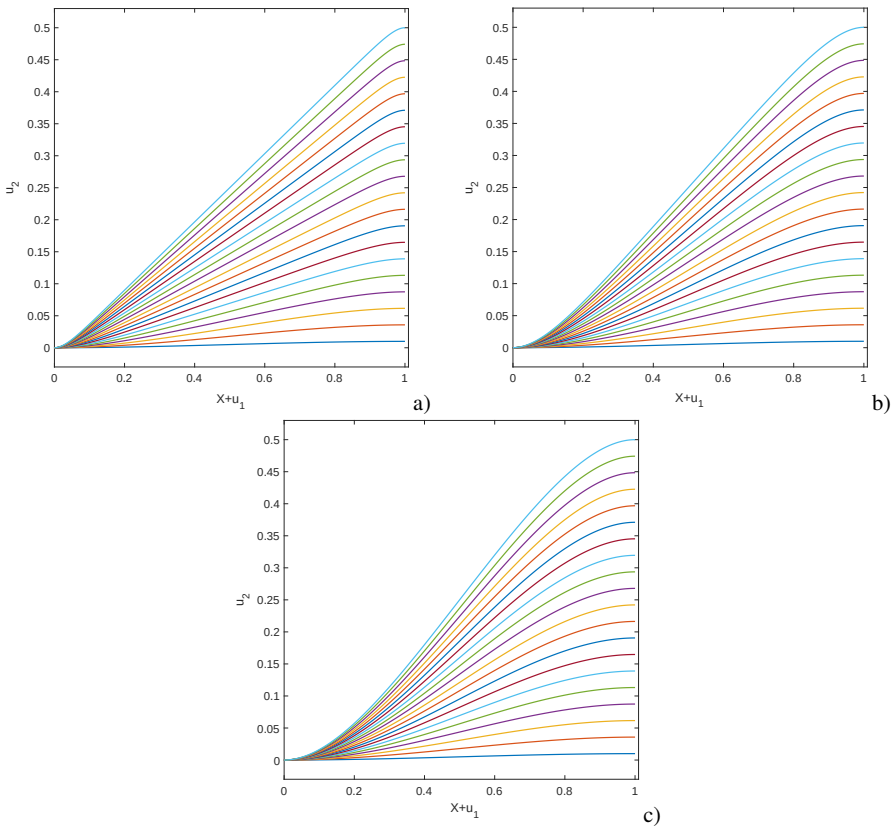


Fig. 17.2 Equilibrium shapes varying u_0 : a) $\alpha = 0.01$; b) $\alpha = 0.03$; c) $\alpha = 0.06$.

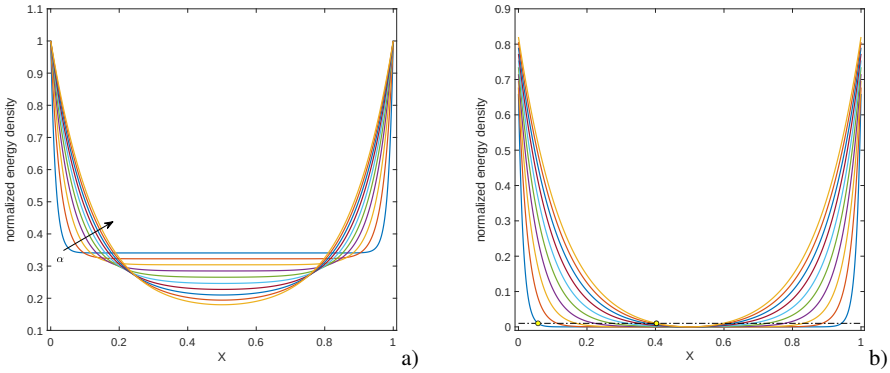


Fig. 17.3 Normalized energy densities varying $\alpha = \{0.01 - 0.1\}$, $u_0 = 0.5$ a). Graphic display of the boundary layer widths b); the two markers highlight the extreme cases for $\alpha = 0.01$ and $\alpha = 0.1$.

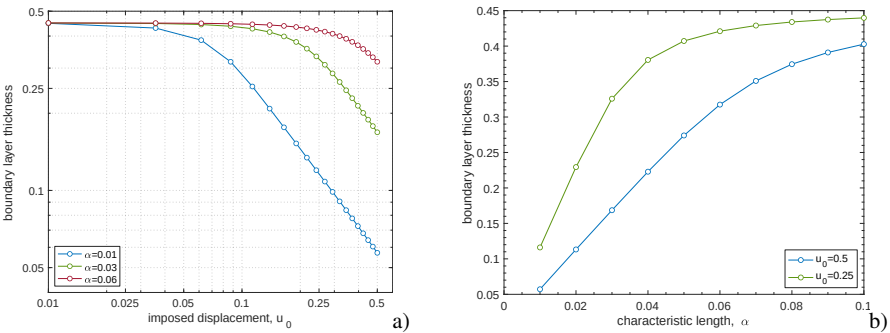


Fig. 17.4 Some boundary layer widths as function of α and u_0 .

A final comment on the buckling of a beam under a compressive load deserves to be made to fully understand the link between the characteristic length and the behavior of the beam. Albeit, the buckling modes of a beam loaded at the tip are almost indistinguishable for different values of α . They mostly depend on the boundary conditions. See, for example, the clamped-clamped beam case in Fig. 17.5. The critical values of the imposed displacement or compressive force change drastically with it (see Figs. 17.6 and 17.7). The reason for that lies in the ratio between the two stiffnesses, i.e., bending and stretching. Indeed, a very small bending stiffness allows the lateral deviation of the beam much earlier since the work done for have higher curvature is in turn reduced.

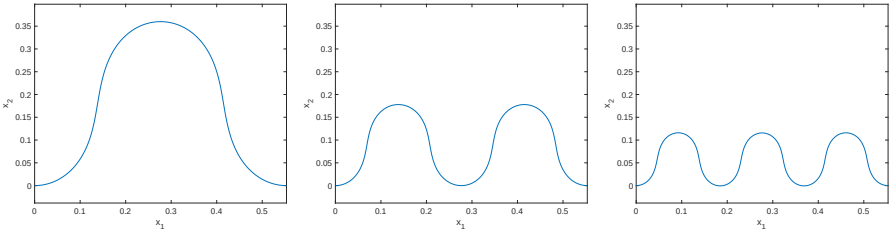


Fig. 17.5 The first three buckling shapes of the clamped-clamped beam.

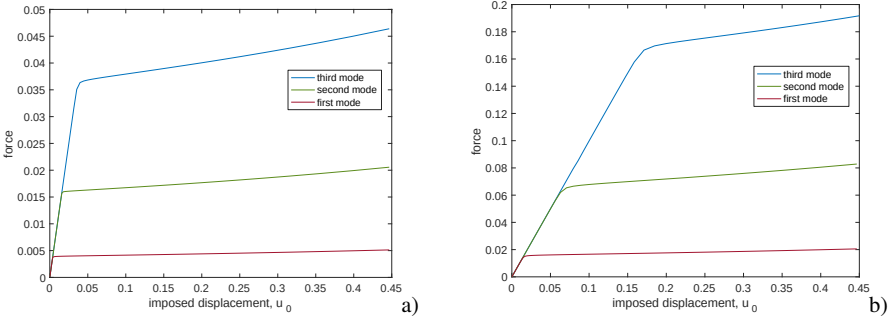


Fig. 17.6 Force vs displacement: a) $\alpha = 0.01$; b) $\alpha = 0.02$.

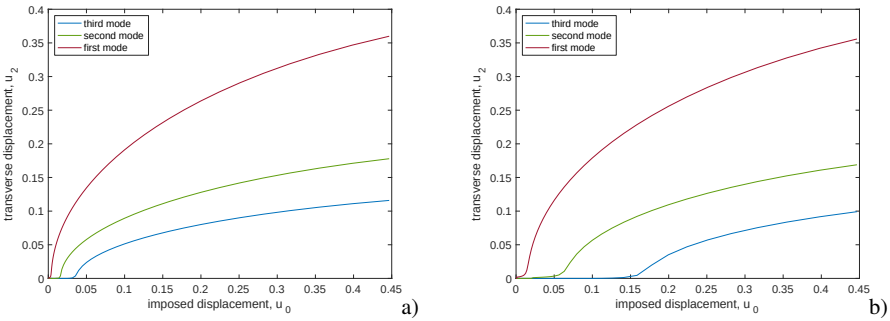


Fig. 17.7 Pitchfork bifurcation: a) $\alpha = 0.01$; b) $\alpha = 0.02$.

17.3 Pantographic Beam

17.3.1 Longitudinal Pantographic Beam with Nonlinear First Gradient Term

The second example taken into account is the so-called pantographic beam. The continuum one-dimensional model capable of describing the behavior of such a complex system is characterized by the presence in the deformation energy of a

term with the second derivative of the displacement with respect to its abscissa (see, e.g., Giorgio et al (2017); Alibert et al (2003); Seppecher et al (2011)). The microstructure of the considered system is constituted by a unit cell of two inextensible flexible elastic elements connected through one hinge, say *principal nodes* (the blue circles in Fig. 17.8). All these unit cells are then connected to compose a *pantographic mechanism* employing other hinges, namely *auxiliary nodes* (the red circles in Fig. 17.8). This particular ‘mechanism’ is the responsible for the presence of the second-gradient term in the deformation energy because each principal node has a ‘long’ range interaction which involves three adjacent nodes (therefore, not only the first nearest neighbors but also the second neighbors in the chain) differently from the first-gradient case where the elastic interaction is defined only for a couple of nodes. The microstructure is completed by springs connecting two adjacent principal nodes. These last elements provide the presence in the energy of a term related to the first gradient of the displacement.

For the sake of simplicity, in what follows, we consider deformation modes in which the principal nodes can have only longitudinal displacements, namely u .



Fig. 17.8 Kinematical scheme of a pantographic beam with nonlinear first gradient term.

Considering Piola’s ansatz that identifies the principal nodes in the discrete microstructure with the points of the continuum system and under the hypothesis of small deformations of the pantographic microstructure, the homogenized 1D model can be characterized by the following deformation energy:

$$\mathcal{W}_a [u'(\cdot), u''(\cdot)] = \frac{1}{2} \int_0^1 K_I \left[(u')^2 + \frac{\beta}{2} (u')^4 \right] dX + \frac{1}{2} \int_0^1 K_{II} (u'')^2 dX \tag{17.8}$$

where K_I and K_{II} are the stiffnesses related to the first and second gradient contribution of the deformation energy, respectively. The parameter β is introduced to consider also possibly nonlinear effects (a material nonlinearity) coming from the first-gradient interaction. Similarly to the previous case, we have the characteristic length

$$\alpha = \sqrt{\frac{K_{II}}{K_I}} \tag{17.9}$$

To activate the formation of a boundary layer in this system, we consider a tensile test controlled in displacement, i.e., we fixed the displacement of the left end of the continuum 1D system and imposed a given displacement in the opposite end. Furthermore, since this is a second-gradient continuum model, we impose boundary

conditions on the first derivative of the displacement at both ends. Indeed, if we set to zero such derivatives, a boundary layer occurs due to the interaction between the two contributions of the deformation energy of the first and second gradient.

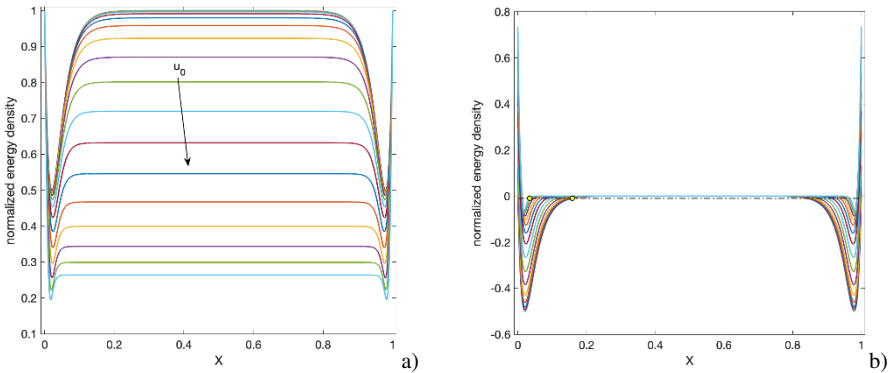


Fig. 17.9 Normalized energy densities varying $u_0 = \{0.01 - 0.5\}$, $\alpha = 0.03$, $\beta = 100$ a). Graphic display of the boundary layer widths b); the two markers highlight the extreme cases for $u_0 = 0.01$ and $u_0 = 0.5$.

Figure 17.9 shows the normalized distributions of deformations energy for different values of the imposed displacement and for a fixed value of $\alpha = 0.03$ and $\beta = 100$. In this case, the boundary layer has a profile where the deformation energy presents a peak near the external edge and then slowly asymptotes to the reference value at the middle of the pantographic beam.

Moreover, contrary to the previous case, the linear approximation experiences a boundary layer since the energy of the first and second gradient contribution can interact with each other (see Fig. 17.10a). As expected, as α grows, the boundary layer width increases. The reason for that is quite clear since increasing α involves a second-gradient term in the energy with a more influential weight with respect to the first-gradient term, and then the localization of the deformation energy becomes increasingly inconvenient for an energetic viewpoint. Figure 17.10b exhibits the effect of the nonlinear term in the first gradient energy term. For small displacements the non linear effect is negligible and the boundary layer width is almost insensitive to the imposed displacement. However, when the imposed displacement becomes sufficiently high, the nonlinear effect manifests itself with decreasing width, and the ratio of the decrease is larger for higher α . This behavior is because, in the model, the nonlinear contribution is attributed only to the first-gradient energy; therefore, when large imposed displacements activate it, the weight of this energy contribution becomes increasingly significant, and then it is like there is an ‘effective’ characteristic length that decreases.

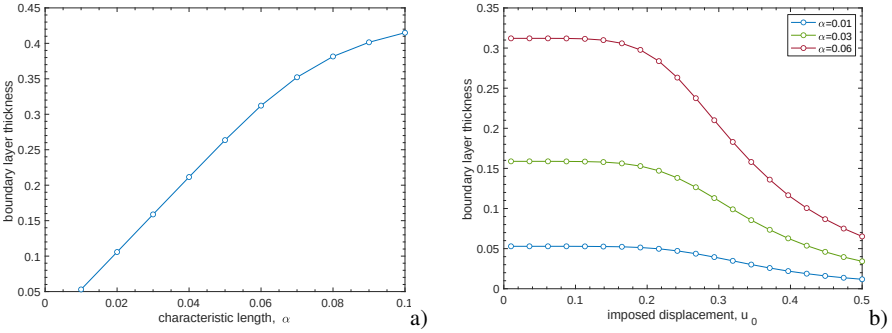


Fig. 17.10 Boundary layer widths as function of α and u_0 : a) $\beta = 0$; b) $\beta = 100$.

17.3.2 Longitudinal Pantographic Beam with Nonlinear Second Gradient Term

Finally, we examine a variant of the longitudinal pantographic beam that could be described by a continuum model with a nonlinear second-gradient energy contribution (see, for more details, Barchiesi et al (2019)). In the microstructure, we assume that the arms of the pantograph are extensible and flexible elastic elements then they can be represented in a lumped discrete model as extensional and rotational springs, all connected by hinges. In this case, the principal nodes related to the scissor-like mechanism of the pantograph are also connected by extensional springs to provide a first-gradient contribution of the energy (see Fig. 17.11).

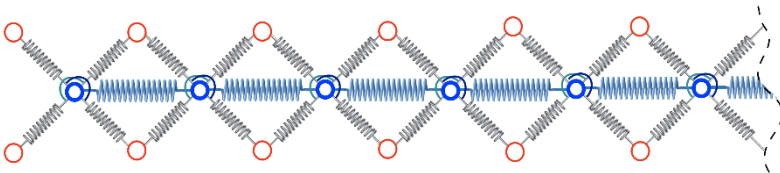


Fig. 17.11 Kinematical scheme of a pantographic beam with nonlinear second gradient term.

The homogenized model resulting from this scheme can be expressed in terms of longitudinal displacement u as follows:

$$\mathcal{W}_b [u'(\cdot), u''(\cdot)] = \frac{1}{2} \int_0^1 K_I (\rho - 1)^2 dX + \frac{1}{2} \int_0^1 K_E K_F \frac{\rho^2}{(2 - \rho^2) [(K_E - 4K_F) \rho^2 + 8K_F]} (\rho')^2 dX \quad (17.10)$$

where the variable ρ is defined as

$$\rho = 1 + u' \tag{17.11}$$

The stiffnesses K_I , K_E , and K_F are material parameters obtained by rescaling the rigidities at the micro-level associated with the extensional springs of the first-gradient term, the extensional and rotational springs of the arms of the pantograph, respectively.

Defining the characteristic length as the ratio between the linearized coefficient of the second-gradient energy and the first-gradient linear rigidity as follows

$$\frac{K_E K_F}{K_I (K_E + 4K_F)} = \alpha^3 \tag{17.12}$$

we can study the influence of this parameter on the width of the boundary layer. In this case, we consider a tensile test with one end fixed, namely ($u(0) = 0$, $u'(0) = 0$), and a given imposed displacement u_0 at the opposite end ($u(1) = u_0$) with the clamped condition $u'(1) = 0$. Fig. 17.12 shows the distributions of the deformation energy density changing α for a moderate value of the displacement u_0 . The qualitative behavior is very similar to the previous case, albeit the boundary layer widths are larger. This property is expected since, for small displacement, the two pantographic models tend to act in a similar way.

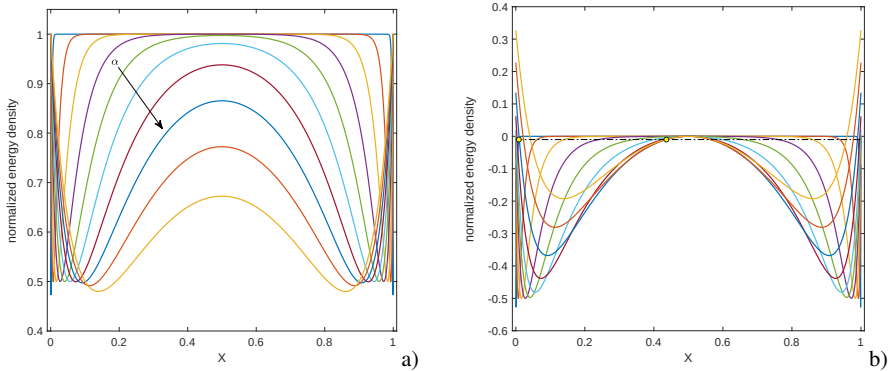


Fig. 17.12 Normalized energy densities varying $\alpha = \{0.01 - 0.25\}$, $u_0 = 0.15$ a). Graphic display of the boundary layer widths b); the two markers highlight the extreme cases for $\alpha = 0.01$ and $\alpha = 0.25$.

However, the nonlinear behavior of the second-gradient term in the energy produces some differences when the imposed displacement increases beyond a certain threshold (see Fig. 17.13). Figure 17.13, indeed, displays a typical behavior for small displacements. On the contrary, the boundary layer width changes drastically when the displacement is sufficiently large, i.e., $u_0 = 0.35$. In fact, after a first positive slope, the boundary layer width has a maximum, and subsequently, it decreases,

and finally, after a minimum it returns to grow. We remark that near the minimum value of the boundary layer, there is a transition behavior for which the shape of the localized deformation energy changes, as shown in Fig. 17.14, from the shape with the swelling to the monotonic one.

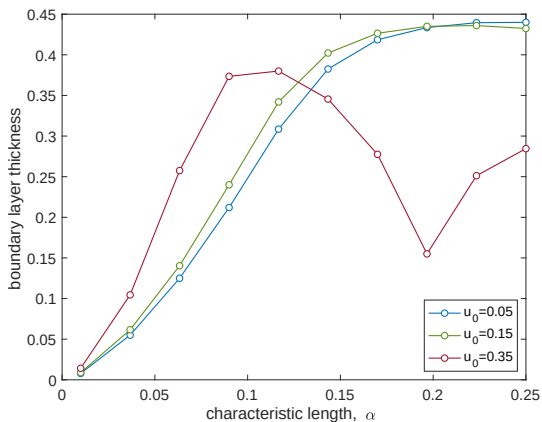


Fig. 17.13 Some boundary layer thicknesses as function of α and u_0 .

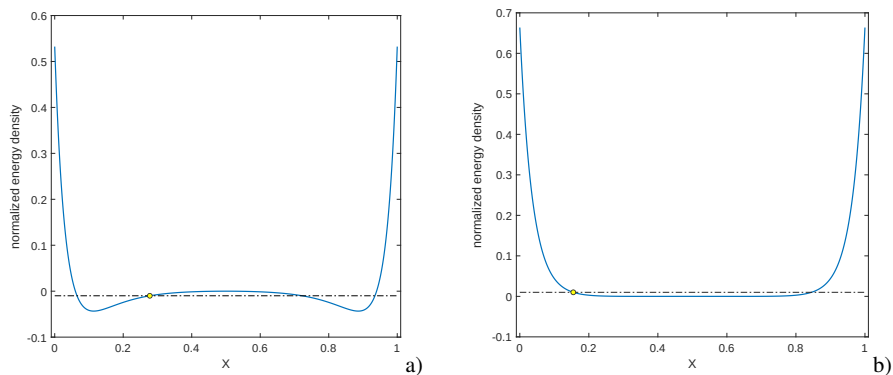


Fig. 17.14 Normalized energy densities $u_0 = 0.35$: a) $\alpha = 0.17$, b) $\alpha = 0.1966$.

This peculiar characteristic is related to the specific distribution of the two energy contributions, i.e., first and second gradient (see Fig. 17.15). Indeed, the two distributions exhibit a complementary trend, and the variability ratio with the characteristic length α is sensibly diverse for the two energetic contributions.

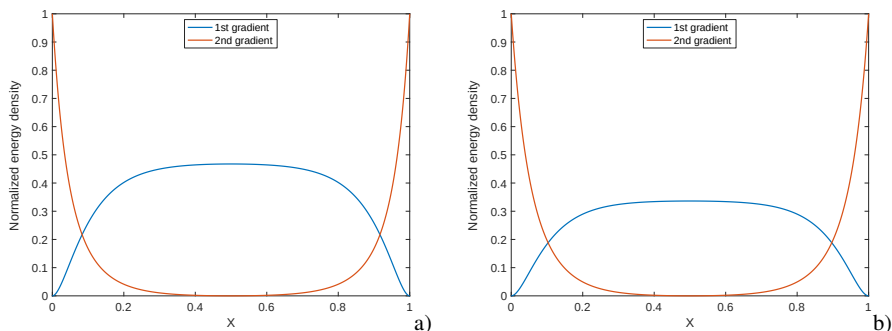


Fig. 17.15 Normalized energy densities $u_0 = 0.35$: a) $\alpha = 0.17$, b) $\alpha = 0.1966$. Energy distribution of the first and second gradient contributions.

17.4 Concluding Remarks

In this paper we have explored the properties linked to boundary layers for a few typologies of one-dimensional continua moving in plane. As expected from previous works in the literature Andreaus et al (2016) it is possible to conclude that whenever there are interacting first-gradient and second-gradient deformation modes, it is possible to observe boundary layers.

Acknowledgements This project has received funding from the European Union's Horizon 2020 research and innovation programme under the Marie Skłodowska-Curie grant agreement No 899546.

References

- Abali BE, Barchiesi E (2021) Additive manufacturing introduced substructure and computational determination of metamaterials parameters by means of the asymptotic homogenization. *Continuum Mechanics and Thermodynamics* 33:993–1009
- Abali BE, Müller WH, dell'Isola F (2017) Theory and computation of higher gradient elasticity theories based on action principles. *Archive of Applied Mechanics* 87(9):1495–1510
- Abali BE, Yang H, Papadopoulos P (2019) A computational approach for determination of parameters in generalized mechanics. In: Altenbach H, Müller WH, Abali BE (eds) *Higher Gradient Materials and Related Generalized Continua*, *Advanced Structured Materials*, vol. 120, Springer, Cham, chap 1, pp 1–18
- Abdoul-Anziz H, Seppecher P, Bellis C (2019) Homogenization of frame lattices leading to second gradient models coupling classical strain and strain-gradient terms. *Mathematics and Mechanics of Solids* 24(12):3976–3999
- Alibert JJ, Seppecher P, dell'Isola F (2003) Truss modular beams with deformation energy depending on higher displacement gradients. *Mathematics and Mechanics of Solids* 8(1):51–73
- Andreaus U, dell'Isola F, Giorgio I, Placidi L, Lekszycki T, Rizzi NL (2016) Numerical simulations of classical problems in two-dimensional (non) linear second gradient elasticity. *International Journal of Engineering Science* 108:34–50

- Ashby MF (2006) The properties of foams and lattices. *Philosophical Transactions of the Royal Society A: Mathematical, Physical and Engineering Sciences* 364(1838):15–30
- Ashby MF, Gibson LJ (1997) *Cellular solids: structure and properties*. Press Syndicate of the University of Cambridge, Cambridge, UK pp 175–231
- Barchiesi E, Eugster SR, Placidi L, dell’Isola F (2019) Pantographic beam: A complete second gradient 1D-continuum in plane. *Zeitschrift für angewandte Mathematik und Physik* 70(5):135
- Barchiesi E, dell’Isola F, Hild F, Seppecher P (2020a) Two-dimensional continua capable of large elastic extension in two independent directions: asymptotic homogenization, numerical simulations and experimental evidence. *Mechanics Research Communications* 103:103,466
- Barchiesi E, Eugster SR, dell’Isola F, Hild F (2020b) Large in-plane elastic deformations of bi-pantographic fabrics: asymptotic homogenization and experimental validation. *Mathematics and Mechanics of Solids* 25(3):739–767
- Barchiesi E, dell’Isola F, Bersani AM, Turco E (2021a) Equilibria determination of elastic articulated duoskelion beams in 2D via a Riks-type algorithm. *International Journal of Non-Linear Mechanics* 128:1–24
- Barchiesi E, dell’Isola F, Hild F (2021b) On the validation of homogenized modeling for bi-pantographic metamaterials via digital image correlation. *International Journal of Solids and Structures* 208:49–62
- Cazzani A, Malagù M, Turco E (2016a) Isogeometric analysis of plane-curved beams. *Mathematics and Mechanics of Solids* 21(5):562–577
- Cazzani A, Malagù M, Turco E, Stochino F (2016b) Constitutive models for strongly curved beams in the frame of isogeometric analysis. *Mathematics and Mechanics of Solids* 21(2):182–209
- Ciallella A (2020) Research perspective on multiphysics and multiscale materials: a paradigmatic case. *Continuum Mechanics and Thermodynamics*
- De Angelo M, Spagnuolo M, D’Annibale F, Hoschke K, Misra A, Dupuy C, Peyre P, Dirrenberger J, Pawlikowski M (2019) The macroscopic behavior of pantographic sheets depends mainly on their microstructure: experimental evidence and qualitative analysis of damage in metallic specimens. *Continuum Mechanics and Thermodynamics* 31(4):1181–1203
- Della Corte A, dell’Isola F, Esposito R, Pulvirenti M (2017) Equilibria of a clamped Euler beam (Elastica) with distributed load: Large deformations. *Mathematical Models and Methods in Applied Sciences* 27(08):1391–1421
- dell’Isola F, Andreaus U, Placidi L (2015) At the origins and in the vanguard of peridynamics, non-local and higher-gradient continuum mechanics: an underestimated and still topical contribution of Gabrio Piola. *Mathematics and Mechanics of Solids* 20(8):887–928
- dell’Isola F, Seppecher P, Alibert JJ, et al (2019a) Pantographic metamaterials: an example of mathematically driven design and of its technological challenges. *Continuum Mechanics and Thermodynamics* 31(4):851–884
- dell’Isola F, Seppecher P, Spagnuolo M, et al (2019b) Advances in pantographic structures: design, manufacturing, models, experiments and image analyses. *Continuum Mechanics and Thermodynamics* 31(4):1231–1282
- dell’Isola F, Turco E, Misra A, Vangelatos Z, Grigoropoulos C, Melissinaki V, Farsari M (2019c) Force–displacement relationship in micro-metric pantographs: Experiments and numerical simulations. *Comptes Rendus Mécanique* 347(5):397–405
- Eremeyev V, Morozov N (2010) The effective stiffness of a nanoporous rod. In: *Doklady Physics*, vol 55, pp 279–282
- Eugster SR, Harsch J (2020) A variational formulation of classical nonlinear beam theories. In: *Developments and Novel Approaches in Nonlinear Solid Body Mechanics*, Springer, pp 95–121
- Falson G, La Valle G (2019) A homogenized theory for functionally graded Euler–Bernoulli and Timoshenko beams. *Acta Mechanica* 230(10):3511–3523
- Germain P (2020) The method of virtual power in the mechanics of continuous media, I: Second-gradient theory. *Mathematics and Mechanics of Complex Systems* 8(2):153–190
- Giorgio I (2020) A discrete formulation of Kirchhoff rods in large-motion dynamics. *Mathematics and Mechanics of Solids* 25(5):1081–1100

- Giorgio I, Della Corte A, dell'Isola F (2017) Dynamics of 1D nonlinear pantographic continua. *Nonlinear Dynamics* 88(1):21–31
- Greco L (2020) An iso-parametric G^1 -conforming finite element for the nonlinear analysis of Kirchhoff rod. Part I: the 2D case. *Continuum Mechanics and Thermodynamics* pp 1–24
- Greco L, Cuomo M (2013) B-spline interpolation of kirchhoff-love space rods. *Computer Methods in Applied Mechanics and Engineering* 256:251–269
- Greco L, Cuomo M (2015) Consistent tangent operator for an exact Kirchhoff rod model. *Continuum Mechanics and Thermodynamics* 27(4):861–877
- Greco L, Cuomo M (2016) An isogeometric implicit G^1 mixed finite element for Kirchhoff space rods. *Computer Methods in Applied Mechanics and Engineering* 298:325–349
- Greco L, Cuomo M, Contrafatto L, Gazzo S (2017) An efficient blended mixed B-spline formulation for removing membrane locking in plane curved Kirchhoff rods. *Computer Methods in Applied Mechanics and Engineering* 324:476–511
- Harsch J, Eugster SR (2020) Finite element analysis of planar nonlinear classical beam theories. In: *Developments and Novel Approaches in Nonlinear Solid Body Mechanics*, Springer, pp 123–157
- Harsch J, Capobianco G, Eugster SR (2021) Finite element formulations for constrained spatial nonlinear beam theories. *Mathematics and Mechanics of Solids* p 10812865211000790
- Lin Z, Novelino LS, Wei H, Alderete NA, Paulino GH, Espinosa HD, Krishnaswamy S (2020) Folding at the microscale: Enabling multifunctional 3D origami-architected metamaterials. *Small* 16(35)
- Mandadapu KK, Abali BE, Papadopoulos P (2021) On the polar nature and invariance properties of a thermomechanical theory for continuum-on-continuum homogenization. *Mathematics and Mechanics of Solids* pp 1–18
- Misra A, NejadSadeghi N, De Angelo M, Placidi L (2020) Chiral metamaterial predicted by granular micromechanics: verified with 1d example synthesized using additive manufacturing. *Continuum Mechanics and Thermodynamics* pp 1–17
- NejadSadeghi N, De Angelo M, Drobnicki R, Lekszycki T, dell'Isola F, Misra A (2019) Parametric experimentation on pantographic unit cells reveals local extremum configuration. *Experimental Mechanics* 59(6):927–939
- Niiranen J, Balabanov V, Kiendl J, Hosseini SB (2019) Variational formulations, model comparisons and numerical methods for Euler–Bernoulli micro- and nano-beam models. *Mathematics and Mechanics of Solids* 24(1):312–335
- Placidi L, Barchiesi E, Misra A (2018) A strain gradient variational approach to damage: a comparison with damage gradient models and numerical results. *Mathematics and Mechanics of Complex Systems* 6(2):77–100
- Placidi L, dell'Isola F, Barchiesi E (2020) Heuristic homogenization of euler and pantographic beams. In: *Mechanics of Fibrous Materials and Applications*, Springer, pp 123–155
- Rosi G, Placidi L, Auffray N (2018) On the validity range of strain-gradient elasticity: a mixed static-dynamic identification procedure. *European Journal of Mechanics-A/Solids* 69:179–191
- Seppacher P, Alibert JJ, dell'Isola F (2011) Linear elastic trusses leading to continua with exotic mechanical interactions. In: *Journal of Physics: Conference Series*, IOP Publishing, vol 319, p 012018
- Spagnuolo M, Andraus U (2019) A targeted review on large deformations of planar elastic beams: extensibility, distributed loads, buckling and post-buckling. *Mathematics and Mechanics of Solids* 24(1):258–280
- Spanos I, Vangelatos Z, Grigoropoulos C, Farsari M (2021) Design and characterization of microscale auxetic and anisotropic structures fabricated by multiphoton lithography. *Nanomaterials* 11(2):446
- Tran LV, Niiranen J (2020) A geometrically nonlinear Euler–Bernoulli beam model within strain gradient elasticity with isogeometric analysis and lattice structure applications. *Mathematics and Mechanics of Complex Systems* 8(4):345–371

- Turco E, dell'Isola F, Cazzani A, Rizzi NL (2016a) Hencky-type discrete model for pantographic structures: numerical comparison with second gradient continuum models. *Zeitschrift für angewandte Mathematik und Physik* 67(4):85
- Turco E, dell'Isola F, Rizzi NL, Grygoruk R, Müller WH, Liebold C (2016b) Fiber rupture in sheared planar pantographic sheets: numerical and experimental evidence. *Mechanics Research Communications* 76:86–90
- Vangelatos Z, Gu GX, Grigoropoulos CP (2019) Architected metamaterials with tailored 3D buckling mechanisms at the microscale. *Extreme Mechanics Letters* 33:100,580
- Yildizdag ME, Demirtas M, Ergin A (2020) Multipatch discontinuous galerkin isogeometric analysis of composite laminates. *Continuum Mechanics and Thermodynamics* 32(3):607–620



Chapter 18

Design and Parametric Enhancement of a Flexible Planar TEG - Numerical Study

Maria Carolina Fernandes, Cristina Furtado, Daniela Campanhã,
Sónia Isabel Silva Pinto

Abstract A thermoelectric generator (TEG) can recover waste energy and convert it into electricity. Therefore, a TEG is a sustainable and reliable device that can be applied in several fields. The current work aims to go further in the design and enhancement of a flexible planar TEG made with bismuth telluride. For this purpose, ANSYS® software was used. An initial design of the generator was created, and a sensitivity analysis was carried out to understand which parameters most impact its performance. Setting a satisfactory mesh, numerical simulations of the TEG were performed in its operating conditions to obtain the corresponding output properties. The device was enhanced for an industrial application through a numerical model based on the parametric enhancement of the most relevant design parameters, namely the height and width of the semiconductor components and the number of thermocouples. A theoretical model was used for comparison of the numerical model, and both models were validated with experimental data from literature. The numerical simulations produced more complete results, such as contours of temperature and voltage in the TEG and led to an optimal design capable of reaching a maximum of 0.10W and an output voltage of 9.973V when exposed to a temperature gradient of 130°C. Additionally, the generator fit within the desired area of this specific in-

M. C. Fernandes

Engineering Faculty, University of Porto, Rua Dr. Roberto Frias, s/n, 4200 – 465 Porto, Portugal
e-mail: up201506004@fe.up.pt

C. Furtado, D. Campanhã

Centre for Nanotechnology and Smart Materials, Rua Fernando Mesquita, 2785, 4760-034 Vila Nova de Famalicão, Portugal
e-mail: cfurtado@centi.pt, dcampanha@centi.pt

S. I. S. Pinto

Engineering Faculty, University of Porto, Rua Dr. Roberto Frias, s/n, 4200 – 465 Porto, Portugal
Institute of Science and Innovation in Mechanical and Industrial Engineering, LAETA-INEGI, Rua Dr. Roberto Frias, 400, 4200 – 465 Porto, Portugal
e-mail: spinto@fe.up.pt

dustrial application and exhibited an efficiency of approximately 5%. This research study is expected to encourage TEG manufacturing in industrial applications.

Keywords: Thermoelectricity · Flexible planar device · Energy harvesting · Numerical simulation · Additive manufacturing · Power generation

18.1 Introduction

The growth of the world's population led to the increase of energy needs, and due to the rising efforts of reducing global warming, this growth is accompanied by an increase of the employment of more sustainable methods of energy production, that utilize natural and renewable resources (International Energy Agency, 2020). Besides the clear environmental advantages, the current evolution of the energy paradigm can also bring political and economical advantages, such as the reduction of the strong dependency on the small group of countries that possess reserves of fossil fuels, the increase of qualified professionals in the renewable energy fields and the consequent obsolescence of non-sustainable energy facilities (Sztekler et al, 2017). However, the transport sector, one of the main contributors of pollutant gas emissions to the atmosphere, requires a mobile energy source, and, therefore, cannot be easily powered by resources such as the wind or the sun (International Energy Agency, 2020). Thus, alternative technologies are being developed for recovery and generation of useful energy through less conventional methods. Semiconductors can produce electricity recovered from waste heat associated, for instance, for industrial processes, and produce electricity to power other machines and devices, increasing the overall efficiency of the energy cycle (Sztekler et al, 2017).

Thermoelectric generators (TEG) use these materials, and, because they have several advantages, they are currently being researched and developed in a wide range of applications, such as automotive (Lan et al, 2018; Khan et al, 2018; Pandit et al, 2014), aeronautic (Lan et al, 2018; Khan et al, 2018; Pandit et al, 2014; Gusev et al, 2011), electronics (Suarez et al, 2016; Zhang et al, 2019) and medicine (Suarez et al, 2016; Zhang et al, 2019; Siddique et al, 2016). In fact, thermoelectric generators do not emit any pollutants to the atmosphere (Jia and Gao, 2014), and do not have any moving parts, granting it low maintenance levels, low operational costs, and the absence of noise pollution (Lan et al, 2018; Jia and Gao, 2014; Liao et al, 2018; Fan et al, 2016). Furthermore, they are wireless, lightweight (Wu and Yu, 2014), portable and highly customisable, meaning that they can be easily adapted to specific situations (Zhang et al, 2019; Jia and Gao, 2014). Moreover, due to the Peltier effect, these machines, which take advantage of a thermal gradient to produce electricity, can be reversed and turned into a heating or cooling machine which preserves a temperature gradient by consuming electricity, becoming a Peltier heater or cooler, respectively (Twaha et al, 2016; Snyder and Toberer, 2008).

However, the biggest disadvantage of TEGs is their low efficiency when compared to other well-established heat engines (Zhang et al, 2019; Dhoopagunta, 2016), which

is usually below 10% (Twaha et al, 2016; He and Tritt, 2017). Yet, since the intent of these devices is the recovery of waste energy, they are still valuable and sustainable tools to obtain useful energy, and should continue to be studied, researched, and improved to become competitive energy conversion devices. Looking at some of the existing literature (Sztekler et al, 2017; Lan et al, 2018; Pandit et al, 2014; Gusev et al, 2011; Liao et al, 2018; Wu and Yu, 2014; Snyder and Toberer, 2008; Kishore et al, 2018; Teichert et al, 2015; Goldsmid, 2014; Brostow et al, 2012; Lowhorn et al, 2011; Chen and Lee, 2016; Stuban and Torok, 2010), research regarding thermoelectric generators is more focused on the output properties they can achieve, such as output power or efficiency, and not on the process of the design of the thermoelectric generators which leads to these outcome properties. This part of the manufacturing process of TEGs is of great importance, because a generator is composed of expensive materials, synonymous of their great potential, and the appropriate materials and geometry needs to be set a priori to avoid unnecessary costs and material waste (He and Tritt, 2017). In addition, these devices can have smaller dimensions, in order of magnitude of micro and nano meters (Kao et al, 2010), when they are inserted into small components like microsensors. Thus, manufacturing processes with low levels of geometrical resolution would not be adequate. Additionally, the analysis of TEG manufacturing processes and their suitability to produce generators are not significantly researched in literature. In fact, additive manufacturing methods would be ideal to manufacture these devices since they do not promote material waste and have high printing resolution (He and Tritt, 2017). Specifically, methods like dispenser printing or screen printing, used in the textile industry, have been successfully employed to print planar thermoelectric generators (Siddique et al, 2016; Chen et al, 2011; Madan et al, 2011), since their thickness is negligible, and show great potential.

Going further than the available literature, the present study intends to analyze the design process of planar thermoelectric generators, by the definition of the most significant parameters involved in the design process of the generator and the development of a theoretical and a numerical tool used to generate an optimal design. Through the definition of the conditions in which the generator is meant to work, the initial design of the generator, based on the design of Chen et al (2011), was analyzed through numerical simulations using ANSYS® software. Then, its dimensions were parametrically altered until an optimal design of the generator was achieved, guaranteeing a maximum power condition. A theoretical model, based on equations found in literature, was created with the same purpose and to act as comparison of the numerical results. Then, both numerical and theoretical models were validated with experimental data of Chen et al (2011). Subsequent to the developed models was the study of the state-of-the-art device materials, since the choice of the semiconductor materials, which are separated into different material families, is conditioned by the operating temperatures and the configuration that the generator assumes according to its desired application.

The created tools are expected to encourage distinct industries to easily design thermoelectric generators that fit specific requirements and increase their manufacturing and application, promoting sustainable energy recovery in industrial settings.

18.2 Materials and Methodology

To find an optimal design of a thermoelectric generator, it is essential to first understand the theoretical basis regarding the thermoelectric effect, composed of the Seebeck, Peltier and Thomson effects. Defining the involved physical processes, geometrical parameters and materials, the initial generator design can be attained. To perform numerical simulations in ANSYS® software, a mesh capable of balancing a greater mesh detail with low computational time needs to be chosen. Afterwards, the boundary conditions can be defined in ANSYS® software to numerically simulate the generator in its practical operating conditions. Then, a sensitivity analysis is carried out to study the different parameters involved and their influence on the output properties. Finally, the parameters which most impact the performance can be parameterized in ANSYS® and altered until an optimal design is found.

Parallely, equations from literature were used to develop a model which returns a theoretical optimal design to act as validation to the results obtained through the numerical analysis.

18.2.1 Theoretical Analysis

Generically, a thermoelectric generator can be analyzed as a heat engine producing power while working in a power cycle between a hot and cold source, as illustrated in Fig. 18.1a (Twaha et al, 2016; Chen et al, 2018). Through the First Law of Thermodynamics, the output electrical power, \dot{W} [W], is the subtraction of \dot{Q}_h [W] and \dot{Q}_ℓ [W], the rates of heat flow from the heat source and to the heat sink, respectively.

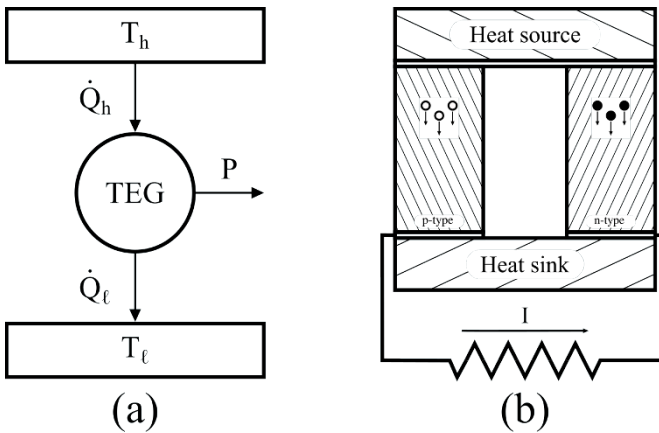


Fig. 18.1 Thermoelectric generator (a) as a generic power cycle, (b) in a closed circuit. Adapted from Twaha et al (2016).

A thermoelectric generator is composed of one or more thermocouples comprised of “legs” made from semiconductor material (Snyder and Toberer, 2008), connected to each other with contact made from a conductive material. Each thermocouple possesses two legs made with different materials, the p-type with positive charges, called holes (h^+), and the n-type with negative particles such as electrons (e^-) (Snyder and Toberer, 2008), represented with white and black circles in Fig. 18.1b, respectively (Twaha et al, 2016). The different thermocouples are connected electrically in series, while they are thermally in parallel with the heat source and heat sink (Twaha et al, 2016).

According to the Seebeck effect, when placed between a heat source and a heat sink, the carriers migrate and accumulate near the colder junction, creating a voltage, V [V], calculated by

$$V = -n \int_{T_\ell}^{T_h} S(T) dT \quad (18.1)$$

where n is the number of thermocouples present in the TEG, T_h [K] and T_ℓ [K] are the temperatures of the heat source and heat sink, respectively, and S [$V K^{-1}$] is the Seebeck coefficient of the whole thermocouple, calculated through the subtraction of the Seebeck coefficients of each leg (Lan et al, 2018; Dhoopagunta, 2016). S is temperature dependent (Dhoopagunta, 2016; Goldsmid, 2014). The Peltier effect suggests that when a voltage is applied to two dissimilar materials connected in two junctions, the temperature of one of the junctions rises while the temperature of the other decreases (Liao et al, 2018; Wu and Yu, 2014; Twaha et al, 2016; Dhoopagunta, 2016; Szczech et al, 2011). Moreover, through Joule’s First Law, the output power can be calculated by

$$\dot{W} = RI^2, \quad (18.2)$$

where R [Ω] is the internal resistance of the generator and I [A] is the current (Watt, P. J., 2009). The performance of thermoelectric materials is measured through the figure of merit, zT , a non-dimensional number calculated through

$$zT = \frac{S^2 T}{\rho k}; \quad (18.3)$$

where T [K] is the absolute temperature, ρ [Ωm] is the electric resistivity and k [$W m^{-1} K^{-1}$] is the thermal conductivity (Liao et al, 2018; Fan et al, 2016; Twaha et al, 2016; Dhoopagunta, 2016; He and Tritt, 2017; Goldsmid, 2014). It is possible to correlate thermal and electrical equations, consequently linking geometrical, thermal, and electrical parameters. In fact, \dot{Q}_h and \dot{Q}_ℓ can be calculated by

$$\dot{Q}_h = -\frac{1}{2} I^2 R + (T_h - T_\ell) K + SIT_h, \quad (18.4)$$

$$\dot{Q}_\ell = \frac{1}{2} I^2 R + (T_h - T_\ell) K + SIT_\ell, \quad (18.5)$$

where the internal resistance and the thermal conductance K [$W K^{-1}$] of a thermocouple are obtained, respectively, through

$$R = \frac{\rho_p L_p}{A_p} + \frac{\rho_n L_n}{A_n}, \quad (18.6)$$

$$K = \frac{k_p L_p}{A_p} + \frac{k_n L_n}{A_n}, \quad (18.7)$$

where L [m] is the leg length, A [m²] is its cross-sectional area and the indexes n and p are relative to the n -type and p -type legs, respectively (Lan et al, 2018; Suarez et al, 2016).

In fact, the generator is meant to power a load, which has an internal resistance, in a closed-circuit. Defining m as the ratio between the load resistance, R_{load} [Ω] and the internal resistance,

$$m = \frac{R_{load}}{R}, \quad (18.8)$$

the output power can be determined by replacing Eq. (18.4), Eq. (18.5) and Eq. (18.8) in the First Law of Thermodynamics equation:

$$\dot{W} = \frac{S^2(T_h - T_\ell)^2}{R} \frac{m}{(1 + m)^2}. \quad (18.9)$$

In heat recovery, the TEG must extract as much energy as possible and, therefore, should be set to work in maximum power conditions (Kempf and Zhang, 2016). The optimum resistance ratio, m_{opt} , that leads to the maximum power, \dot{W}_{max} [W] is achieved when

$$m_{opt} = 1, \quad (18.10)$$

$$\dot{W}_{max} = \frac{S^2(T_h - T_\ell)^2}{4R}, \quad (18.11)$$

From Eq. (18.10), it is concluded that the optimal internal resistance is the load resistance (Liao et al, 2018; Wu and Yu, 2014; Dhoopagunta, 2016; Chen et al, 2011), and this condition is accounted for in the TEG design enhancement.

18.2.2 Numerical Analysis

The numerical simulation software is based on two general equations regarding the heat flux vector, $\{q\}$ [W m⁻²], and the current density vector, $\{J\}$ [A m⁻²], as follows:

$$\{q\} = T[S]\{J\} - [K]\{\nabla T\}, \quad (18.12)$$

$$\{J\} = [\sigma](\{E\} - [S]\{\nabla T\}), \quad (18.13)$$

where $[S]$ is the matrix of the Seebeck coefficients, $[K]$ represents, for a null current density state, the matrix of thermal conductivity, $\{\nabla T\}$ [K] is the vector for the thermal gradient, $[\sigma]$ [S m⁻¹] represents the electrical conductivity matrix for a null thermal gradient, and $\{E\}$ [V m⁻¹] is the electric field vector. Moreover, $[S]$, $[K]$ and

$[\sigma]$ are diagonal matrices that contain the respective properties in each direction xx , yy and zz . Applying the principles of the conservation of energy and electric charge, Eq. (18.12) and Eq. (18.13) can be compiled, and ANSYS® utilizes the following finite element matrix equation to perform the numerical analysis of thermoelectric processes:

$$\begin{bmatrix} [C^t] & [0] \\ [0] & [C^v] \end{bmatrix} \begin{Bmatrix} \{\dot{T}\} \\ \{\dot{V}\} \end{Bmatrix} + \begin{bmatrix} [K^t] & [0] \\ [K^{vt}] & [K^v] \end{bmatrix} \begin{Bmatrix} \{T\} \\ \{V\} \end{Bmatrix} = \begin{Bmatrix} \{Q\} + \{Q^p\} \\ \{I\} \end{Bmatrix} \quad (18.14)$$

where $[C^t]$ is the specific heat matrix, $[C^v]$ represents the matrix of the dielectric permittivity coefficients, $\{\dot{T}\}$ [K s^{-1}] and $\{\dot{V}\}$ [V s^{-1}] are the time derivative vectors of temperature $\{T\}$ [K] and voltage $\{V\}$ [V], respectively, $[K^t]$ is the diffusion conductivity matrix, $[K^{vt}]$ is the finite element coupling matrix of Seebeck coefficients, and $[K^v]$ is the thermal conductivity matrix. Moreover, the vector $\{Q\}$ [W] is the sum of the finite element heat generation load vector and the convection surface heat flow vector, $\{Q^p\}$ [W] is the load vector of Peltier heat, and $\{I\}$ [A] is the nodal current load vector (Chen et al, 2011).

18.2.3 Geometrical Parameters

To design the generator of the present work, the geometrical parameters were defined according to the design of a standard planar thermoelectric generator, which can be observed in Fig. 18.2. The parameters c , h_c , h_l , p , t , t_s and w_l are, respectively, half the distance between thermocouples, contacts' height, leg height, pitch (distance between consecutive legs in a thermocouple), generator thickness, substrate thickness and leg width.

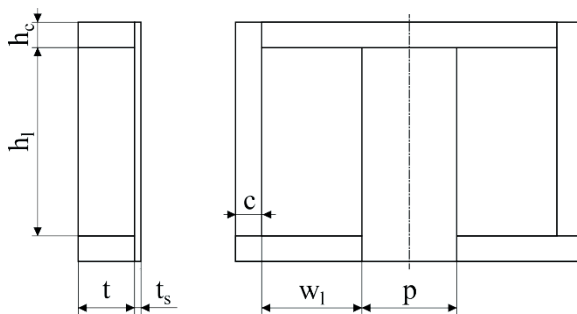


Fig. 18.2 Technical drawing of a planar thermocouple.

Thus, by replicating the planar thermoelectric generator developed by Chen et al (2011), since it proved to have a notable thermoelectric performance, and following

the created nomenclature, the initial design of a one-thermocouple generator was created.

18.2.4 Boundary Conditions

The thermoelectric generator is meant to work in conditions which are applied in ANSYS® software, avoiding the need for an experimental set-up to enhance the prototype and to obtain the output properties with larger costs. Firstly, the temperature of the heat source was defined as 150°C (423.15K), while the heat sink was deemed as the environment at a constant temperature of 20°C (293.15K). In ANSYS® software, T_h was applied to the top surface of the top contact, whereas T_l was applied to the bottom surfaces of the two bottom contacts, as visible in Fig. 18.3a and Fig. 18.3b, respectively. Additionally, the remaining surfaces of the generator were considered to have a null heat flux and be thermally insulated, as observed in Fig. 18.3c. Finally, an electrical condition of null voltage was applied on the leftmost surface of the generator, shown in Fig. 18.3d.

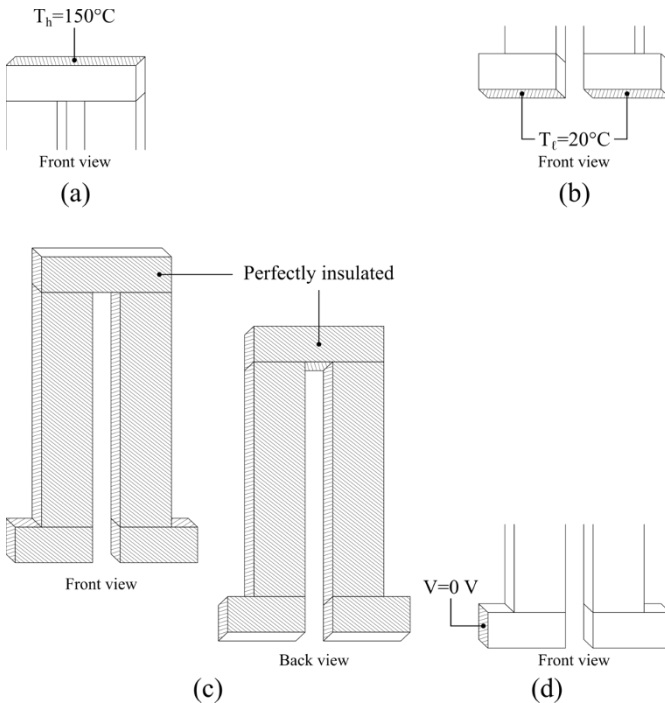


Fig. 18.3 Boundary conditions (a) heat source temperature, (b) heat sink temperature, (c) thermal insulation condition, (d) null voltage.

It is worth mentioning that the boundary conditions are equally applied to every thermocouple, guaranteeing that the heat source and sink are connected to the top and bottom surfaces of the generator respectively; and that the TEG is completely insulated, with the exception being the electrical boundary condition, which only applies to the leftmost thermocouple.

18.2.5 Material Choice

The boundary conditions impact the material choice, since thermoelectric materials excel in different temperature ranges, as well as the TEG output properties. The thermoelectric generator is composed of semiconductor legs, where the thermoelectric effect occurs, metallic contacts, which connect consecutive legs electrically in series and connect the legs to the heat source and heat sink, and a polymeric substrate, where the generator is printed onto.

In general, semiconductors are ideal thermoelectric materials, since the conflicting properties of elevated electric conductivity and reduced thermal conductivity are better in these materials than polymers or metals (Fraisse et al, 2013; Lu et al, 2016; Park et al, 2017). The chosen material for the two legs of the TEG is Bi_2Te_3 (bismuth telluride).

Semiconductor materials have temperature dependent properties, such as the Seebeck coefficient, thermal conductivity, and electrical conductivity. Fraisse et al (2013) was able to interpolate experimental data into the theoretical equations

$$S_p(T) = -S_n(T) = (22224 + 930.6T - 0.9905T^2)10^{-9} [VK^{-1}], \quad (18.15)$$

$$k_p(T) = k_n(T) = (62605 + 277.7T - 0.94131T^2)10^{-4} [Wm^{-1}K^{-1}], \quad (18.16)$$

$$\sigma_p(T) = \sigma_n(T) = (5112 + 163.4T - 0.6279T^2)^{-1}10^{10} [Sm^{-1}], \quad (18.17)$$

where the n-type leg was considered to have a negative p-type Seebeck coefficient, but identical thermal and electrical conductivities (Omnexus, 2020).

Regarding the contacts, silver was the material of choice for having high thermal and electrical conductivities. The thermal conductivity is $406 \text{ W m}^{-1} \text{ K}^{-1}$ and the electrical resistivity equal to $1.59 \times 10^{-8} \Omega \text{ m}$.

The substrate should be flexible, lightweight, and insulating to withstand the inherent mechanical and thermal stresses. Fabrics, paper, and polymers have been used as substrate for generators in literature (Lu et al, 2016; Park et al, 2017; Yuan et al, 2019). For the current TEG, polyimide was chosen because, despite its elevated cost, the material complies with the mechanical, electrical, and chemical demands of the device.

Finally, to simulate the TEG in a closed circuit with the load, a fourth generic material with a customisable electrical resistivity was created. The geometry of this new component is known, since it can be related to dimensions of the TEG, and, therefore, it is possible to relate the load resistance with its resistivity:

$$R_{load} = \frac{\rho_{load} L_{load}}{A_{load}}, \quad (18.18)$$

where L_{load} [m] is the medium length of the load object and A_{load} [m²] is its cross-sectional area. The current, I [A], combining Ohm's Law and Joule's First Law, is given by

$$I = \frac{S(T_h - T_\ell)}{R + R_{load}} \quad (18.19)$$

representing the ratio between the open-circuit voltage and the sum of the existing resistances.

18.2.6 Mesh Convergence Analysis

The definition of the mesh is a necessary part of a numerical study. Since a detailed mesh generates more accurate results, but also higher computational times, a balance needs to be set between refinement and computational time in the simulations. For the initial TEG design, ten different cubic mesh sizes were applied to the model. In Fig. 18.4, keeping T_ℓ as 20°C (293.15K), T_h was set at 260°C (533.15K), and measuring the computational times for the mesh sizes, the open-circuit voltage, V_{oc} , was obtained.

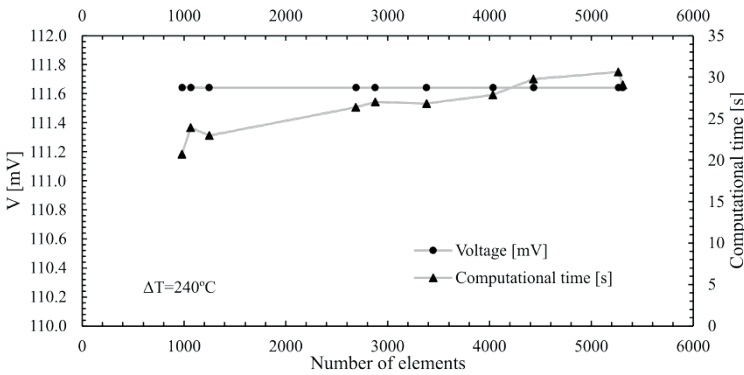


Fig. 18.4 V_{oc} , computational time and mesh size.

Looking at the results, the voltage was not impacted by the increase of the number of elements, but the computational time increased. It is possible to conclude that, since the computational times are very low for all meshes, a 59 μm cubic mesh should be chosen.

18.2.7 Sensitivity Analysis

A sensitivity analysis allows researchers to find the most relevant aspects concerning the TEG, by imposing small changes and analyzing their degree of influence in the simulated results. Thus, a parametric change took place by holding all parameters but one, whose impact was measured through the comparison of the TEG output properties.

18.2.7.1 Number of Thermocouples

Firstly, the number of thermocouples was changed, since its growth increases the number of legs in which the thermoelectric phenomena occur. However, the internal resistance also increases, so an optimal number of thermocouples should be found for the final TEG. In this section, the number of thermocouples studied ranged from one to nine. In an open circuit, the voltage was measured, and, in a closed circuit, the nine TEGs were linked to the load material, and its resistivity was altered to find the optimum R_{load} value that maximizes the produced power. The output open-circuit voltage and the maximum electrical power were plotted as a function of the number of thermocouples (Fig. 18.5).

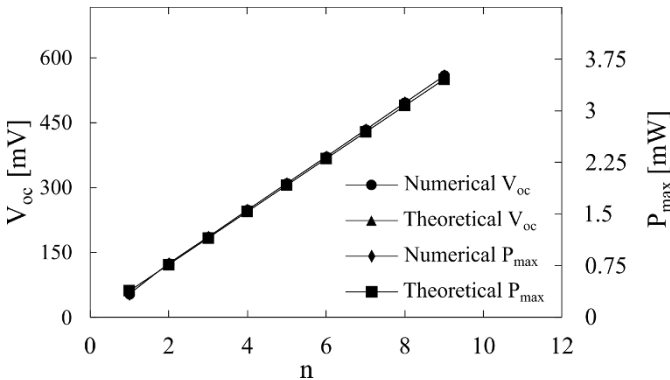


Fig. 18.5 Theoretical and numerical values of V_{oc} and P_{max} as a function of the number of thermocouples.

All the measured properties changed linearly with the increase of n , meaning that, for the same temperature gradient, V_{oc} [V] is directly proportional to the number of thermocouples, as well as P_{max} [W] when the load resistance corresponds to the optimal value (equal to the internal resistance of the device).

18.2.7.2 Presence of Protective Coating

The insulation of a single thermocouple TEG, to prevent oxidation at higher temperatures, was numerically studied (Fig. 18.6). Since it is widely available, a boron nitride coating of varying thicknesses, equal to 0 μm , 30 μm , and 60 μm was chosen, with an estimated thermal conductivity of $500 \text{ W m}^{-1} \text{ K}^{-1}$ (Final Advanced Engineering, 2020) and an electrical resistivity equal to $1014 \Omega \text{ m}$ (Suarez et al, 2016; Siddique et al, 2016). Moreover, heat transfer through natural convection was established between the TEG and three different environments at 0°C (273.15K), 20°C (293.15K) and 40°C (313.15K), with a natural convection coefficient of $5 \text{ W m}^{-2} \text{ K}^{-1}$ for all coating thicknesses. The thermal insulation boundary condition was not applied in the coating of the TEG. The load needs to be equal in all simulations and, thus, the convection boundary condition was not implemented in this component. Recovering the data for the optimum load resistance value, the maximum output power, absorbed heat and efficiency (η) were obtained and the results are presented in Tab. 18.1.

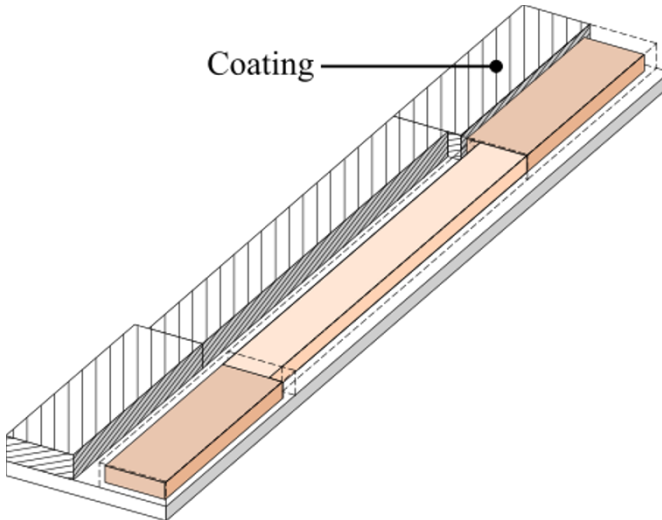


Fig. 18.6 New boundary conditions for the coating analysis numerical simulations.

Coating a thermoelectric device may prolong its useful life, but negatively impacts its performance and, looking at the obtained results, the thickness of the coating should be as minimal as possible. Moreover, with the increase of heat transfer processes with the environment, the TEG produces less electrical power.

Table 18.1 Coating of TEG and its output properties.

| Coat thickness [μm] | T [$^{\circ}\text{C}$] | P_{max} [mW] | $\dot{Q}_{h,P_{max}}$ [mW] | $\eta_{P_{max}}$ [%] |
|----------------------------------|--------------------------|----------------|----------------------------|----------------------|
| 0 | 0 | 0.366 | 14.89 | 2.46 |
| | 20 | 0.362 | 13.73 | 2.63 |
| | 40 | 0.357 | 12.57 | 2.84 |
| 30 | 0 | 0.343 | 79.20 | 0.43 |
| | 20 | 0.343 | 78.05 | 0.44 |
| | 40 | 0.340 | 76.58 | 0.44 |
| 60 | 0 | 0.325 | 142.4 | 0.23 |
| | 20 | 0.325 | 141.1 | 0.23 |
| | 40 | 0.325 | 139.8 | 0.23 |

18.2.7.3 Substrate Material and Dimensions

Given its small dimensions, a thermoelectric generator could be applied in wearable parts, taking advantage of the metabolism to produce useful power (Jiao, 2020). Hence, since polyimide could be uncomfortable for the individual, a softer material should be used, preferably one that is commonly used in wearables.

In this section, a cotton substrate was analyzed and compared to polyimide and, to simulate different environmental conditions the person may be inserted in. Like the previous subsection, the environment temperature was changed to 0°C , 20°C and 40°C , and a convection coefficient was set at $5 \text{ W m}^{-2} \text{ K}^{-1}$. Moreover, two thickness values were studied, 0.0508 mm and 0.1016 mm. The material properties of the two substrate materials were already defined in the material library of ANSYS® software. The heat flux between the environment and the TEG was measured for both substrates and the results are represented in Tab. 18.2.

Table 18.2 Influence of the ambient temperature and substrate thickness in the heat flux.

| t_s [mm] | T [$^{\circ}\text{C}$] | \dot{q}_{pol} [W m^{-2}] | \dot{q}_{cot} [W m^{-2}] |
|------------|--------------------------|---------------------------------------|---------------------------------------|
| 0.0508 | 0 | 1935.64 | 1647.30 |
| | 20 | 1704.54 | 1431.32 |
| | 40 | 1619.04 | 1215.43 |
| 0.1016 | 0 | 1935.64 | 1647.30 |
| | 20 | 1704.54 | 1431.32 |
| | 40 | 1619.04 | 1215.43 |

It is evident that the heat flux for each temperature is independent of the thickness of the substrate, although it is harmed by the increase of the ambient temperature.

Therefore, it is possible to conclude that it does not impact the electrical properties of the device. The results could be complemented by considering the heat produced by the individual, but since this value changes according to the location where the wearable is placed (Chen et al, 2011; Madan et al, 2011), as well as the metabolism levels of each person, it was not analyzed in this study.

18.2.7.4 Generator Thickness

A planar generator is, as indicated by its name, a very thin device, and the thickness of the materials depends mostly on the precision of the manufacturing equipment. The generator in question is meant to be fabricated through dispensing, an additive manufacturing known for its high printing precision and ability to print materials at room temperature (Yang et al, 2017). However, the dimension of the extrusion nozzle determines the thickness of the filament (Kramer et al, 2019).

Ten generator thickness values, between 100 μm and 500 μm , were examined in an open and closed circuit. The open-circuit voltage and the maximum electrical power are registered in Fig. 18.7.

The numerical simulation reveals the independence between the thickness of the generator and the voltage in its terminals. In addition, the increase of the thickness is responsible for the increase of the cross-sectional area of the semiconductor legs, consequently increasing the maximum power.

18.2.7.5 Leg Dimensions

The semiconductor legs have two in-plane dimensions, namely the width and the height (w_l and h_l , respectively) which should be analyzed. Once more, one thermocouple was analyzed, and, firstly, its height was changed from 1 mm to 10 mm, to understand the impact on the output voltage, maximum power. Those results are shown, respectively, in Fig. 18.8.

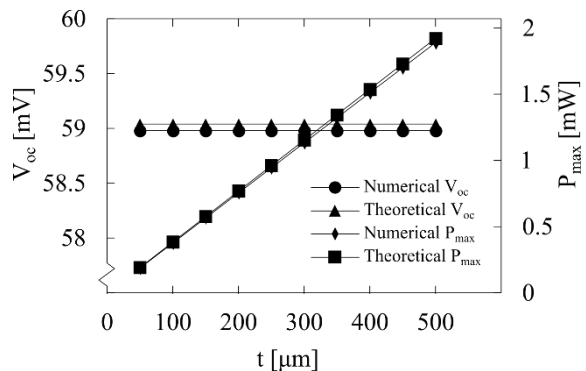
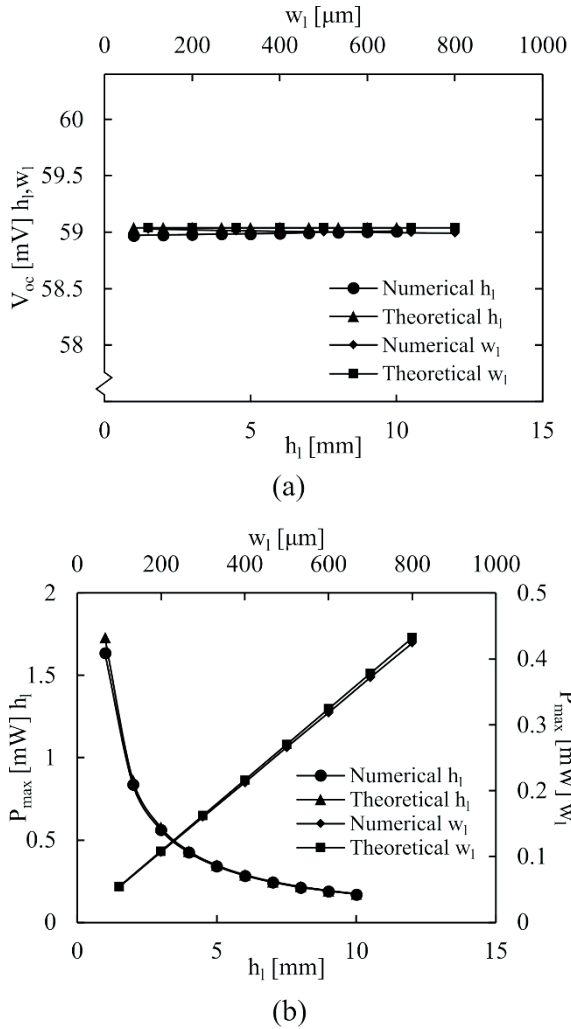


Fig. 18.7 Theoretical and numerical values of V_{oc} and P_{max} as a function of the thickness of generator.

Fig. 18.8 Output properties as a function of h_l (bottom horizontal axis) and w_l (top horizontal axis) (a) open-circuit voltage, (b) maximum power.



Once again, the open-circuit voltage did not change when geometric variations were imposed. However, the output power decreased and, when the height tends to infinity, this electrical property tends to zero. In fact, since the direction of the heat flow is parallel to the direction of the height of the legs, an increase of these dimensions inevitably leads to the increase of the internal thermal resistance and, consequently, the decrease of the current, given that V_{oc} continued unchanged. Since the maximum output power depends on the square of I , from Eq. (18.2), this property is vastly affected by changes of the current.

Likewise, the width of the legs was altered between the values of 100 μm and 800 μm , and V_{oc} and P_{max} were obtained. The results can also be seen in Fig. 18.8. The differing conclusion from the previous analysis is that the increase of the width of the

legs increased the cross-sectional area, decreasing the internal resistance. Therefore, the output power, as well as the absorbed heat rate, are benefited by the increase of the leg width in a linear manner.

18.2.7.6 Contact Dimensions

Finally, a study of the height and width (w_c [mm]) of the contact components, which connect the legs and conduct the heat to the heat sink and from the heat source, was carried out. To analyze the impact of the width, the parameters p (pitch) and c (half of the distance between thermocouples) were changed, and V_{oc} and $Q_{h,oc}$ were obtained. For all cases, the open-circuit voltage and absorbed heat rate were practically constant and equal to 59.04 mV and 5.002 mW, respectively. Since silver has large values for thermal and electrical conductivities, h_c and w_c have a negligible impact on the performance of the TEG.

18.2.8 Enhancement Methodology

From the conducted sensitivity analysis, it is possible to conclude that, to increase the maximum power, the number of thermocouples and the dimensions of their legs are the properties to optimize, since properties such as the temperature gradient are set by existing conditions. This enhancement was done through theoretical and numerical methods, the former acting as validation for the latter.

18.2.8.1 Constraints

The generator has thermal, geometrical, and electrical constraints that ought to be defined to mimic the real operating conditions in the theoretical and numerical methods. The imposed constraints correspond to the needs and restraints of a specific industrial application defined by the company CeNTI.

The goal of the enhancement of the design can be expressed as the minimization of the difference between the internal and the load resistances, for m to be as close to the unit as possible. The operating conditions are the constraints of the enhancement problem, which can be formulated with

$$\begin{aligned}
& \text{minimize } R - R_{load} \\
& \text{subject to } T_h = 150^\circ\text{C}(423.15 \text{ K}) \\
& \quad T_\ell = 20^\circ\text{C}(293.15 \text{ K}) \\
& \quad A \leq 100 \text{ mm} \times 100 \text{ mm} \\
& \quad t = 90 \mu\text{m} \\
& \quad t_s = 50.8 \mu\text{m} \\
& \quad c = 0.28125w_l \\
& \quad P = 2c \\
& \quad V_{load} = 5 \text{ V} \\
& \quad P \geq 0.1 \text{ W}
\end{aligned} \tag{18.20}$$

The geometrical parameter γ [mm] was created and it is defined as the ratio between the cross-sectional area of the legs and their height. This parameter allows the simplification of theoretical formulas and, on the other hand, since the thickness of the generator is constant, it can be used to linearly relate the width and the height of the semiconductor legs.

18.2.8.2 Numerical Parametrization

While the theoretical model was created using equations, the used numerical model was developed in ANSYS® in a particular manner. Firstly, the dimensions of the TEG were parameterized in SpaceClaim, an application of the software employed in the modeling of the geometries, and the assembly tool of surface alignment was used to preserve the arrangement of all the different parts that compose the generator. Therefore, ANSYS® software was able to update the geometry at every parametric alteration made. In addition, this application also allows the parametrization of the number of components in an array, for instance the number of thermocouples in the generator. However, the load component would need to stretch with the increase of n . So, given the complexity of this process, the number of thermocouples was not parameterized, and the load geometry and resistivity values were changed manually.

In ANSYS® software, the height of the legs was set to change from 1 μm to 10 mm in regular increments of 1 μm and, similarly, it was determined that the width would alter from 1 μm to 5 mm in steps of 1 μm . Finally, as mentioned, the number of thermocouples was manually altered, from 100 to 800, in increments of 70.

18.3 Results and Discussion

18.3.1 Parametric Theoretical Enhancement

The voltage consumed by the load is not the same as the open-circuit voltage, but the parameters can be related with

$$V_{load} = \frac{V_{oc} R_{load}}{R + R_{load}}. \quad (18.21)$$

Since the load resistance and the internal resistance need to be identical, it can be deduced that the load consumed by the voltage is half of V_{oc} (Kramer et al, 2019) and equal to 10V. From Eq. (18.11) and the defined constraints, the internal resistance is equal to 250 Ω .

From this result, since V_{oc} is independent of the geometry, it is possible to calculate the minimum number of thermocouples the generator should have. From Eq. (18.1), n is obtained and, approximating to the closest integer, should be equal to 170. Then, the resistivity of the Bi_2Te_3 legs is calculated through

$$\rho_{\text{Bi}_2\text{Te}_3} = \frac{n}{T_h - T_\ell} \int_{T_\ell}^{T_h} \frac{dT}{\sigma(T)}, \quad (18.22)$$

and its value is $2.456041 \times 10^{-3} \Omega \text{ m}$. Moreover, using Eq. (18.6), the parameter γ can be obtained considering that this parameter is the same for both p type and n-type legs, to preserve the symmetry and to harmonize the geometry of the legs, γ is equal to $1.96563 \times 10^{-5} \text{ m}$. Then, looking at Fig. 18.2 and Eq. (18.20), the enhanced dimensions of the TEG can be discovered through

$$\begin{cases} w_{TEG} = n(2w_l + 2c + p) \\ w_{TEG} \leq 0.1 \text{ m} \end{cases} \quad (18.23)$$

From Eq. (18.23), the maximum possible values for the height and width of the legs are 0.8619 mm and 0.1882 mm, respectively. Then, the theoretical linear equation that relates h_l and w_l is

$$h_l(w_l) = 4.5790w_l ; w_l \leq 0.1882 \text{ mm}. \quad (18.24)$$

18.3.2 Parametric Numerical Enhancement

The numerical analysis took place in ANSYS® software. Firstly, all the different models were simulated in an open circuit; then, the load component was introduced and set as equal to 250 Ω . The retrieved variables, namely V_{oc} and the absorbed and rejected heat rates in a closed-circuit, were examined in EXCEL. After handling

the data, scatter plots of the open-circuit voltage and the output power results were made, by interpolating the different points into surfaces.

In Fig. 18.9a, the numerical open-circuit voltage is plotted as a function of the parameter γ and n . A plane represented in gray marks the required 10V, and the intersection of this plane with the interpolated surface is the line represented in black. Therefore, similarly to the theoretical model, 170 is the closest integer value for the number of thermocouples.

Moreover, the values for \dot{Q}_h and \dot{Q}_ℓ of the models in a closed circuit were used to obtain the relation between the power, γ and n , visible in Fig. 18.9b. The interpolated surface indicates that the obtained power increases with the increase of the number of thermocouples and γ . Intercepting the surface with the plane, represented in gray, where the power is equal to the desired value of 0.1W, it becomes clear that γ evolves in an inversely proportional manner to the number of thermocouples. Thus, it can be observed from Fig. 18.9c that, for 170 thermocouples, γ is 2.23472×10^{-5} m.

Considering only the values of the power for a TEG with 170 thermocouples, the power was plotted as a function of the width and the height of the legs, visible in Fig. 18.9c.

The power evolved linearly with the width, but inversely proportional to the height. The interception of the surface with the plane of $P = 0.1$ W, in gray, is represented in black and it represents the numerical linear relation between h_l and w_l , equal to

$$h_l(w_l) = 4.0266w_l ; w_l \leq 0.1882\text{mm}. \quad (18.25)$$

18.3.3 Validation with the Literature

To assess the tools with other TEGs, the material data, design, and experimental results of the 50-unit TEG of Chen et al (2011) were introduced in the developed tools without optimizing the dimensions, and V_{load} , I and P_{max} for a load resistance equal to the internal resistance were computed and collected (Tab. 18.3).

Table 18.3 Comparison of numerical and theoretical results with experimental data from the literature Chen et al (2011).

| Property | Results of Chen et al (2011) | Numerical results | Theoretical results |
|-------------------------|------------------------------|-------------------|---------------------|
| V_{load} [mV] | 171.6 | 178.5 | 157.0 |
| R_{int} [k Ω] | 2.79 | 2.36 | 1.736 |
| I [μ A] | 61.3 | 75.6 | 90.4 |
| P_{max} [μ W] | 10.5 | 13.5 | 14.2 |

As expected, the theoretical and numerical properties are improved over the experimental ones since the tools do not consider environmental losses. The theoretical model is simpler and more optimistic than the numerical method, whose properties

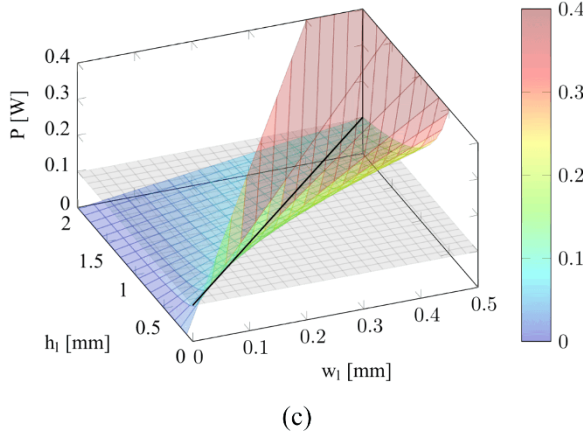
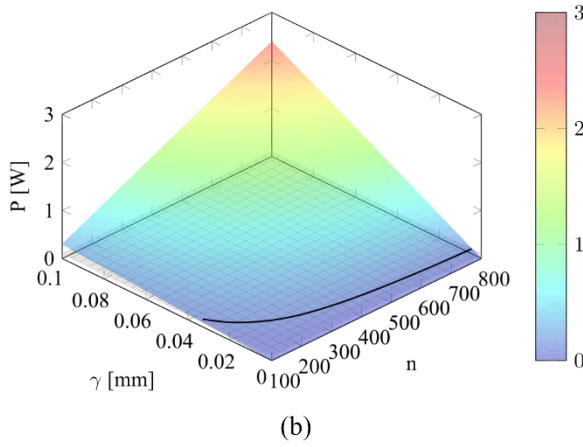
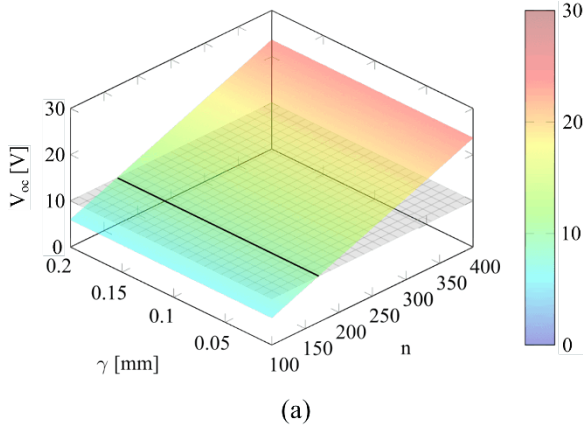


Fig. 18.9 Numeric results as a function of γ and n (a) open-circuit voltage, (b) output power as a function of γ and n , (c) output power as a function of the legs dimensions h_l and w_l .

lie closer to the expected experimental results. Yet, the theoretical and numerical electrical properties are similar and seem accurate enough to validate the precision of the created numerical tool.

18.3.4 Final TEG design

It is possible to conclude that the theoretical model attests the results of the numerical model. Since the dimensions of the generator should be as big as possible, to ensure a higher manufacturing resolution, the chosen width should be as close to the maximum 0.1882mm allowed. For being rounder numbers, a width of 0.188mm and a height of 0.757mm were chosen. The thermocouple design is represented in Fig. 18.10.

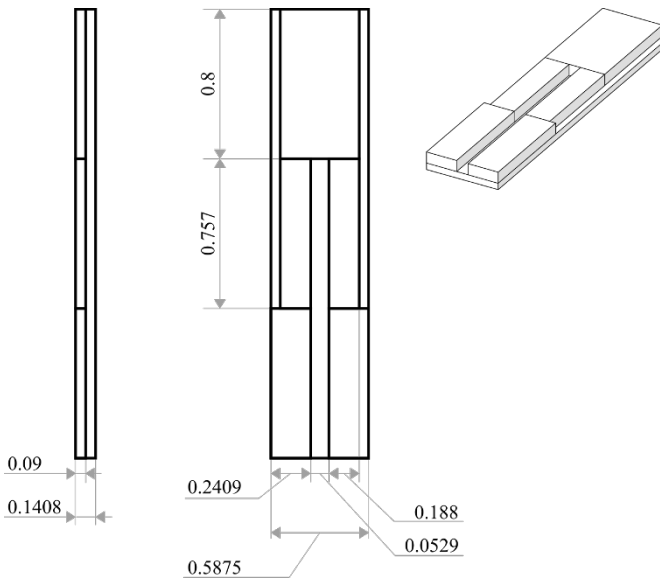
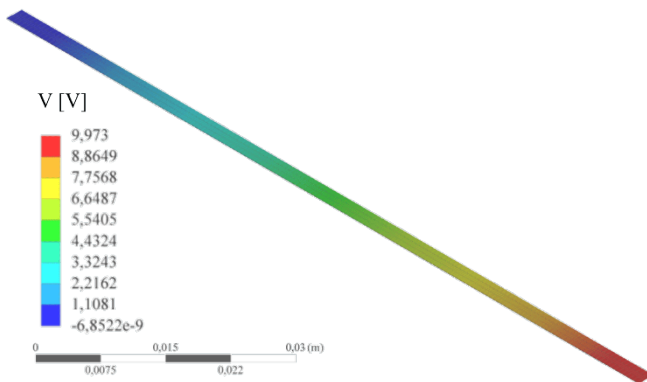


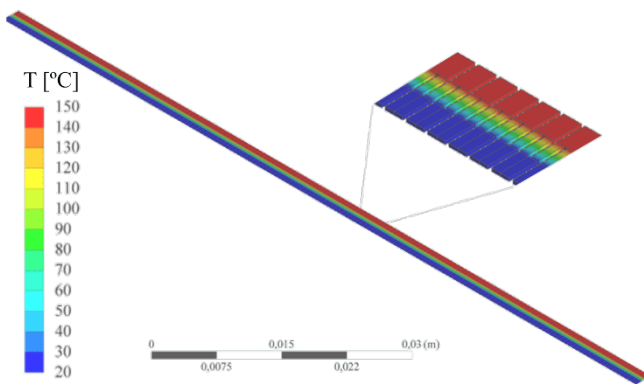
Fig. 18.10 2D drawing of a thermocouple of the enhanced TEG (dimensions in millimeters) and its 3D representation.

Through the numerical simulations carried in the ANSYS® software, it is possible to obtain the voltage and the temperature profile of the enhanced TEG, represented in Fig. 18.11.

The voltage increased in the direction of the width of the legs, from a null value (defined in the boundary conditions) to the maximum value, whereas the temperature varied in parallel to the legs of the generator. In Tab. 18.4, the output properties of the final TEG are displayed.



(a)



(b)

Fig. 18.11 3D profile of (a) voltage, (b) temperature.

Table 18.4 Output properties of the enhanced TEG.

| Property | Value |
|-----------|---------------------|
| n | 170 |
| A_{TEG} | 99.88 mm × 2.357 mm |
| V_{oc} | 9.973 V |
| I | 0.020 A |
| R_{int} | 250.91 Ω |
| P | 0.1 W |
| η | 4.99% |

18.4 Conclusions

The main goal of finding an optimal design of the planar thermoelectric generator, for the established constraints of utility, was achieved. First, the obtained results indicate that the number of thermocouples and the dimensions of the semiconductor legs were the parameters that were the most impactful on the power and on the open-circuit voltage. Additionally, the chosen material needs to have excellent thermoelectric properties in the defined temperature range, so bismuth telluride was a suitable selection.

Moreover, the theoretical and the numerical models were validated through the experimental data of Chen et al (2011). Since the models produced similar results in the optimization of the TEG for the proposed industrial application, it is concluded that the numerical model led to realistic results and it is a tool that could be used in the development of an optimal design of the generator, as well as in the prediction of the output properties of any TEG when restricted to specific thermal and geometrical conditions. Moreover, the complete voltage and temperature contours of the final TEG were obtained through numerical simulations. This is the advantage of using a numerical software instead of using theoretical approach, which is more restricted and only serves for comparison.

The attained enhanced design of the generator corresponded to a TEG with 170 thermocouples, each with a thickness of $90\mu\text{m}$, and with semiconductor legs with a width of 0.188mm and height of 0.757mm , leading to an overall area of $99.88\text{mm} \times 2.357\text{mm}$. The final generator was able to produce an open-circuit voltage of 9.973V and a power of 0.1W when connected to a load with an internal resistance of 250Ω , and while exposed to a temperature gradient of 130K .

The generator should be manufactured resorting to additive manufacturing procedures such as dispensing since it would generate a device with appropriate dimension resolution for the given geometry. With this work, the optimization and validation tools created are expected to be used by industries from various areas which consider that there are conditions for energy recovery. This way, there is an effort in stimulating the production of TEGs. In fact, the restrictions imposed by the enhancement problem can be altered, and thus each user can build a TEG that suits their operating conditions.

Acknowledgements Authors gratefully acknowledge the Engineering Faculty of University of Porto (FEUP), the Department of Mechanical Engineering (DEMec) of FEUP, the Institute of Science and Innovation in Mechanical and Industrial Engineering (LAETA-INEGI) and the Centre for Nanotechnology and Smart Materials (CeNTI).

References

Brostow W, Datashvili T, Lobland HE, Hilbig T, Su L, Vinado C, White J (2012) Bismuth telluride-based thermoelectric materials: Coatings as protection against thermal cycling effects. *Journal*

- of Materials Research 27(22):2930–2936
- Chen A, Madan D, Wright PK, Evans JW (2011) Dispenser-printed planar thick-film thermoelectric energy generators. *Journal of Micromechanics and Microengineering* 21(10)
- Chen L, Lee J (2016) Efficiency enhancement of an industrial-scale thermoelectric generator system by periodically inputting thermal power. *Energy Conversion and Management* 119:75–80
- Chen Y, Hou X, Ma C, Dou Y, Wu W (2018) Review of Development Status of Bi₂Te₃-Based Semiconductor Thermoelectric Power Generation. *Advances in Materials Science and Engineering* 2018:1210,562
- Dhoopagunta S (2016) Analytical modeling and numerical simulation of a thermoelectric generator including contact resistances. Master thesis, Western Michigan University
- Fan L, Zhang G, Wang R, Jiao K (2016) A comprehensive and time-efficient model for determination of thermoelectric generator length and cross-section area. *Energy Conversion and Management* 122:85–94
- Final Advanced Engineering (2020) Boron Nitride Coating. URL <https://www.final-materials.com/gb/177-boron-nit%0Aride-coating>
- Fraisse G, Ramousse J, Sgorlon D, Goupil C (2013) Comparison of different modeling approaches for thermoelectric elements. *Energy Conversion and Management* 65:351–356
- Goldsmid HJ (2014) Bismuth telluride and its alloys as materials for thermoelectric generation. *Materials* 7(4):2577–2592
- Gusev VV, Pustovalov AA, Rybkin NN, Anatyshuk LI, Demchuk BN, Ludchak IY (2011) Milliwatt-power radioisotope thermoelectric generator (RTG) based on plutonium-238. *Journal of Electronic Materials* 40(5):807–811
- He J, Tritt TM (2017) Advances in thermoelectric materials research: Looking back and moving forward. *Science* 357(6358)
- International Energy Agency (2020) Electricity generation by source, World 1990–2018. URL <https://www.iea.org/>
- Jia X, Gao Y (2014) Estimation of thermoelectric and mechanical performances of segmented thermoelectric generators under optimal operating conditions. *Applied Thermal Engineering* 73(1):335–342
- Jiao F (2020) Flexible Thermoelectrics and Thermoelectric Textiles. In: *Flexible and Wearable Electronics for Smart Clothing*, John Wiley & Sons, Ltd, Tianjin, China, chap 3, pp 49–66
- Kao PH, Shih PJ, Dai CL, Liu MC (2010) Fabrication and characterization of CMOS-MEMS thermoelectric micro generators. *Sensors* 10(2):1315–1325
- Kempf N, Zhang Y (2016) Design and optimization of automotive thermoelectric generators for maximum fuel efficiency improvement. *Energy Conversion and Management* 121:224–231
- Khan MQ, Malarmannan S, Manikandaraja G (2018) Power generation from waste heat of vehicle exhaust using thermoelectric generator: A review. *IOP Conference Series: Materials Science and Engineering* 402(1)
- Kishore RA, Kumar P, Priya S (2018) A comprehensive optimization study on Bi₂Te₃-based thermoelectric generators using the Taguchi method. *Sustainable Energy and Fuels* 2(1):175–190
- Kramer LR, Maran ALO, De Souza SS, Ando OH (2019) Analytical and numerical study for the determination of a thermoelectric generator's internal resistance. *Energies* 12(16)
- Lan S, Yang Z, Chen R, Stobart R (2018) A dynamic model for thermoelectric generator applied to vehicle waste heat recovery. *Applied Energy* 210(November 2017):327–338
- Liao M, He Z, Jiang C, Fan X, Li Y, Qi F (2018) A three-dimensional model for thermoelectric generator and the influence of Peltier effect on the performance and heat transfer. *Applied Thermal Engineering* 133(September 2017):493–500
- Lowhorn ND, Wong-Ng W, Lu ZQ, Martin J, Green ML, Bonevich JE, Thomas EL, Dilley NR, Sharp J (2011) Development of a Seebeck coefficient Standard Reference MaterialTM. *Journal of Materials Research* 26(15):1983–1992
- Lu Z, Zhang H, Mao C, Li CM (2016) Silk fabric-based wearable thermoelectric generator for energy harvesting from the human body. *Applied Energy* 164:57–63

- Madan D, Chen A, Wright PK, Evans JW (2011) Dispenser printed composite thermoelectric thick films for thermoelectric generator applications. *Journal of Applied Physics* 109(3)
- Omnexus (2020) Flexibility: Flexural modulus. URL <https://omnexus.specialchem.com/polymer-properties/properties/flexibility?id=307>
- Pandit J, Thompson M, Ekkad SV, Huxtable ST (2014) Effect of pin fin to channel height ratio and pin fin geometry on heat transfer performance for flow in rectangular channels. *International Journal of Heat and Mass Transfer* 77:359–368
- Park T, Lim H, Hwang JU, Na J, Lee H, Kim E (2017) Roll type conducting polymer legs for rigid-flexible thermoelectric generator. *APL Materials* 5(7)
- Siddique ARM, Rabari R, Mahmud S, Heyst BV (2016) Thermal energy harvesting from the human body using flexible thermoelectric generator (FTEG) fabricated by a dispenser printing technique. *Energy* 115:1081–1091
- Snyder GJ, Toberer ES (2008) Complex thermoelectric materials. *Nature Materials* 7(2):105–114
- Stuban N, Torok A (2010) Utilization of exhaust gas thermal energy - Theoretical investigation. ISSE 2010 - 33rd International Spring Seminar on Electronics Technology: Polymer Electronics and Nanotechnologies: Towards System Integration - Conference Proceedings pp 268–272
- Suarez F, Nozariasbmarz A, Vashaee D, Öztürk MC (2016) Designing thermoelectric generators for self-powered wearable electronics. *Energy and Environmental Science* 9(6):2099–2113
- Szzech JR, Higgins JM, Jin S (2011) Enhancement of the thermoelectric properties in nanoscale and nanostructured materials. *Journal of Materials Chemistry* 21(12):4037–4055
- Sztekler K, Wojciechowski K, Komorowski M (2017) The thermoelectric generators use for waste heat utilization from conventional power plant. *E3S Web of Conferences* 14
- Teichert S, Bochmann A, Reimann T, Schulz T, Dreßler C, Töpfer J (2015) An oxide-based thermoelectric generator: transversal thermoelectric strip-device. *AIP Advances* 5(7)
- Twaha S, Zhu J, Yan Y, Li B (2016) A comprehensive review of thermoelectric technology: Materials, applications, modelling and performance improvement. *Renewable and Sustainable Energy Reviews* 65:698–726
- Watt, P J (2009) The critical need for closer ties between physics and industry. URL <https://www.aps.org/publications/apsnews/200912/physicshistory.cfm>
- Wu G, Yu X (2014) A holistic 3D finite element simulation model for thermoelectric power generator element. *Energy Conversion and Management* 86:99–110
- Yang L, Hsu K, Baughman B, Godfrey D, Medina F, Menon M, Wiener S (2017) *Additive Manufacturing of Metals: The Technology, Materials, Design and Production*. Springer, Cham, Switzerland
- Yuan C, Li J, Lindsay L, Cherns D, Pomeroy JW, Liu S, Edgar JH, Kuball M (2019) Modulating the thermal conductivity in hexagonal boron nitride via controlled boron isotope concentration. *Communications Physics* 2(1):1–8
- Zhang D, Wang Y, Yang Y (2019) Design, performance, and application of thermoelectric nano-generators. *Small* 15(32):1–13



Chapter 19

Implementation and Comparison of Non-Newtonian Viscosity Models in Hemodynamic Simulations of Patient Coronary Arteries

Maria Carolina Fernandes, Luísa Costa Sousa, Catarina Ferreira de Castro, José Manuel Laginha Mestre da Palma, Carlos Conceição António, Sónia Isabel Silva Pinto

Abstract Realistic numerical simulations of blood flow in patient-specific coronary arteries constitute a challenge in the study of hemodynamics. Several blood viscous models are available; yet their direct comparison has not been carried out. This work innovates by programming and implementing six viscosity models (Carreau, Carreau-Yasuda, Casson, Cross, generalized power-law and power law) as user-defined functions in ANSYS® Fluent to compare the major hemodynamic parameters, the time-averaged wall shear, the oscillatory shear index and the relative residence time, and to evaluate atherosusceptibility in coronary arteries. The study used the left coronary arteries of an apparently healthy patient and an unhealthy patient, with 40% stenosis in the left anterior descending. Flow simulations comprised two sets (steady-state and pulsatile flows), each based on Newtonian and non-Newtonian fluid, i.e., a total of four cases. Results indicate that the Casson model originates larger areas of atherosusceptibility and the generalized power-law models returns the most healthy results. The non-Newtonian pulsatile cases show less critical areas than the remaining studied regimes.

Keywords: Non-Newtonian viscosity · Hemodynamics · Blood flow · Numerical simulation · atherosclerosis · CFD

M. C. Fernandes, L. C. Sousa, C. F. Castro, C. C. António, S. I. S. Pinto
Engineering Faculty, University of Porto, Rua Dr. Roberto Frias, s/n, 4200 – 465 Porto, Portugal
Institute of Science and Innovation in Mechanical and Industrial Engineering, LAETA-INEGI,
Rua Dr. Roberto Frias, 400, 4200 – 465 Porto, Portugal
e-mail: up201506004@fe.up.pt, lcsousa@fe.up.pt, ccastro@fe.up.pt, cantonio@fe.up.pt, spinto@fe.up.pt

J. M. L. M. Palma
Engineering Faculty, University of Porto, Rua Dr. Roberto Frias, s/n, 4200 – 465 Porto, Portugal
e-mail: jpalma@fe.up.pt

19.1 Introduction

Cardiovascular diseases have been a major cause of death in developed countries (Mozaffarian et al, 2015). Clinical practice indicates that arterial curves and bifurcations are more sensitive to the accumulation of fat, calcium, and other substances, and the development of a stenosis (narrowing of the artery) precludes normal blood flow circulation, and the onset of eventual health problems, like atherosclerosis, must be prevented (Barquera et al, 2015).

Hemodynamic simulation is an auxiliary tool that can be used for the prevention and diagnosis of cardiovascular diseases. Computed tomography angiography (CTA) images of coronary arteries provide information about the geometry and location of the stenosis, but the images alone do not explain the hemodynamic properties. Thus, to better assist in research and clinical practice, a numerical tool of computational fluid dynamics (CFD) is needed to simulate hemodynamic flow as close to reality as possible. The complex geometries of patient-specific coronary arteries, fluid properties and simulation settings are essential in ensuring the similarities between the actual and numerical blood flow. However, utilizing more complex and time-consuming models may not produce significant differences, unnecessarily increasing the required computational power.

According to Ballyk et al (1994); Chaichana et al (2012), there were some similarities in the wall shear stress measured in Newtonian and non-Newtonian blood flow numerical simulations in a simplified artery geometry, and Marossy et al (2009) states that, since the rheological properties of blood in large vessels are linear, blood can be modeled as a Newtonian fluid. Yet, other authors (Jonášová and Vimmr, 2018; Varchanis et al, 2018; Jonášová and Vimmr, 2021) concluded that Newtonian models do not accurately represent the blood's rheology, and non-Newtonian viscosity models should be used instead. Since there are multiple experimental methods of measuring the viscosity of blood, many theoretical viscosity models are used to model blood (Chien et al, 1966; Merrill and Pelletier, 1967; Sandeep and Shine, 2021). For instance, Soulis et al (2008) and Husain et al (2020) concluded that the generalized power-law model led to more satisfactory results for wall shear stress in right coronary arteries and simplified aneurysms, respectively, while Apostolidis and Beris (2014) claims Casson is the more accurate viscosity model for blood. The majority of studies which aim at studying the different viscosity models do so with heavily simplified geometries of blood vessels and simplified boundary conditions, distancing the numerical simulations from real circulatory system conditions, and do not analyze relevant hemodynamic parameters like the time-averaged wall shear stress (TAWSS), the oscillatory shear index (OSI) and the relative residence time (RRT) to evaluate the regions prone to develop atherosclerosis.

Going beyond the current literature (Apostolidis et al, 2016; Jonášová and Vimmr, 2018; Varchanis et al, 2018; Jonášová and Vimmr, 2021), this study aims to compare a wide range of viscosity models used in literature to model blood's rheology, specifically Carreau, Carreau-Yasuda, Casson, Cross, generalized power-law and power law. Thus, these models were implemented in ANSYS® Fluent as user-defined functions (UDFs). Different types of fluid flow, steady-state and transient, in patient-

specific left coronary arteries were also analyzed. This study helps the analysis of the impact of the choice of flow regime and blood properties on hemodynamic descriptors (OSI, RRT and TAWSS), wall shear stress and pressure drop in patient arteries, and contribute to medical intervention.

Therefore, blood flow simulations in coronary arteries of two patients, one with atherosclerotic disease and another with no apparent disease, were carried out for steady-state and transient flows, i. e. one with an average velocity value and another with estimated velocity and pressure profiles (Pinho et al, 2019). Then, they were arranged into four combinations:

- (1) steady-state flow of Newtonian fluid,
- (2) steady-state flow of non-Newtonian fluid,
- (3) pulsatile flow of Newtonian fluid, and
- (4) pulsatile flow of non-Newtonian fluid.

19.2 Methodology

19.2.1 Theoretical Analysis

19.2.1.1 Hemodynamic Indices

The hemodynamic descriptors (TAWSS, OSI and RRT) are empiric. TAWSS measures the average shear stress in the artery wall over a cardiac cycle with a period T . It is considered that individuals with TAWSS inferior to 0.4 Pa have a higher probability of developing atherosclerosis (Malek et al, 1999). This parameter can be calculated through Eq. (19.1) (Jonášová and Vimmr, 2021), where τ_{wall} is the wall shear stress (WSS), t is time and s is the artery wall location. It is considered that the WSS is proportional to the radial gradient of the velocity along x direction, u , in the wall and the viscosity μ . The WSS was calculated through the linear model of incompressible Newtonian fluids (Eq. (19.2)), as considered by others in the literature (Sandeep and Shine, 2021).

$$TAWSS = \frac{1}{T} \int_0^T |\tau_{wall}(s, t)| dt \quad (19.1)$$

$$\tau_{wall} = \mu \left. \frac{\partial u}{\partial r} \right|_{r=R} \quad (19.2)$$

Moreover, there is the oscillatory shear index. This is a non-dimensional value that indicates whether the vector of the wall shear stress suffers any changes in direction. It is measured like an angle, and, following Eq. (19.3), it belongs to the interval $[0, 0.5]$. When OSI is null, there is no directional change (0°), while when it is equal to the maximum value of 0.5, the blood flow is oscillatory and the vector changes 180° . For values of OSI above 0.1, the patient is more prone to develop neointimal

hyperplasia, a condition in which the arterial layers thicken and the lumen narrows (Chiastra et al, 2013).

$$OSI = \frac{1}{2} \left(1 - \frac{\left| \int_0^T \tau_{\text{wall}}(\mathbf{s}, \mathbf{t}) \right|}{\int_0^T |\tau_{\text{wall}}|(\mathbf{s}, \mathbf{t})} \right) \tag{19.3}$$

Additionally, RRT is an indicative of blood flow disturbance. According to Lagache et al (2021), there is greater atherosusceptibility when this parameter is greater than 8 Pa^{-1} . The relative residence time results from the combination of TAWSS and OSI (Eq. (19.4)).

$$RRT = \frac{1}{TAWSS (1 - 2 OSI)} \tag{19.4}$$

19.2.1.2 Blood Rheology

The viscosity of a Newtonian fluid is a thermodynamic property which varies with temperature and pressure (Munson et al, 2012). For these fluids, the shear stress is linearly related to the rate of shearing strain. However, Non-Newtonian blood has a shear-thinning evolution, meaning blood gets less viscous with the increase of the shear rate, $\dot{\gamma}$. Usually, the viscosity has a lower and an upper bound, μ_0 and μ_∞ , which are the zero-shear viscosity and the infinite-shear viscosity, respectively. For low shear rate values, it is also important to know the power-law index, n , and the time constant, λ . The Casson viscosity model measures μ through N_∞ , the consistency index, μ_∞^2 , the square of the yield stress, μ_p , the plasma viscosity and Hct, hematocrit, the volume percentage of red blood cells. The used viscosity models are shown in Fig. 19.1 and described in Table 19.1. Theoretically, the Casson and the generalized power-law viscosity models diverge from the other models, which are similar to each other.

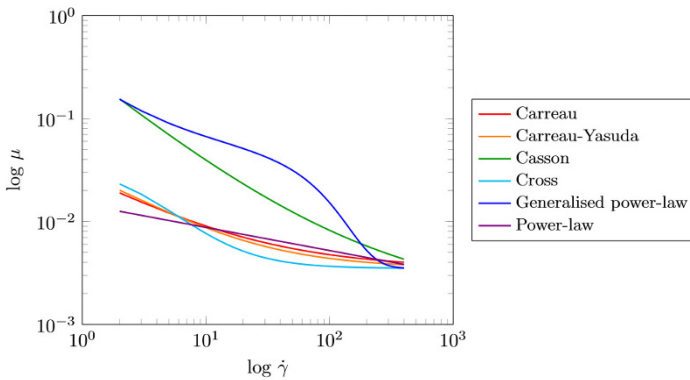


Fig. 19.1 Representation of the used viscosity models.

Table 19.1 Studied viscosity models (Sandeep and Shine, 2021).

| Name | Equation | Constants |
|-----------------------|--|---|
| Carreau | $\mu = \mu_{\infty} + (\mu_0 - \mu_{\infty})(1 + (\lambda\dot{\gamma})^2)^{\frac{n-1}{2}}$ | $\mu_{\infty} = 0.0035 \text{ Pa s,}$ $\mu_0 = 0.056 \text{ Pa s,}$ $\lambda = 3.313 \text{ s,}$ $n = 0.3568.$ |
| Carreau-Yasuda | $\mu = \mu_{\infty} + (\mu_0 - \mu_{\infty})(1 + (\lambda\dot{\gamma})^a)^{\frac{n-1}{a}}$ | $\mu_{\infty} = 0.0035 \text{ Pa s,}$ $\mu_0 = 0.056 \text{ Pa s,}$ $\lambda = 1.902 \text{ s,}$ $n = 0.22,$ $a = 1.25.$ |
| Casson | $\mu = \frac{\mu_{\infty}^2}{\dot{\gamma}} + \frac{2\mu_{\infty}N_{\infty}}{\sqrt{\dot{\gamma}}} + N_{\infty}^2$ $N_{\infty} = \frac{\sqrt{\mu_p}}{\sqrt[8]{1 - Hct}}$ $\mu_{\infty} = \sqrt{0.625 Hct}$ | Hct = 0.4, $\mu_p = 0.00145.$ |
| Cross | $\mu = \mu_{\infty} + \frac{\mu_0 - \mu_{\infty}}{1 + \left(\frac{\dot{\gamma}}{\gamma_c}\right)^n}$ | $\mu_{\infty} = 0.0035 \text{ Pa s,}$ $\mu_0 = 0.0364 \text{ Pa s,}$ $\gamma_c = 2.63 \text{ s}^{-1},$ $n = 1.45.$ |
| Generalized power-law | $\mu = \lambda(\dot{\gamma}) \dot{\gamma} ^{n(\dot{\gamma})-1}$ $\lambda(\dot{\gamma}) = \mu_{\infty} + \Delta\mu e^{-\left(1 + \frac{ \dot{\gamma} }{a}\right)e^{\frac{-b}{ \dot{\gamma} }}}$ $n(\dot{\gamma}) = n_{\infty} - \Delta n e^{-\left(1 + \frac{ \dot{\gamma} }{c}\right)e^{\frac{-d}{ \dot{\gamma} }}}$ | $\Delta\mu = 0.25,$ $\Delta n = 0.45,$ $\mu_{\infty} = 0.0035 \text{ Pa s,}$ $n_{\infty} = 1,$ $a = 50, b = 3,$ $c = 50, d = 4.$ |
| Power-law | $\mu_{min} < \mu = \lambda \dot{\gamma} ^{n-1} < \mu_{max}$ | $\mu_{max} = 0.025 \text{ Pa s,}$ $\mu_{min} = 0.00345 \text{ Pa s,}$ $\lambda = 0.01467,$ $n = 0.7755.$ |

19.2.2 Patients Data and Artery Models

The coronary artery models used in the numerical simulations were obtained through a series of steps. The patients were selected from a database of the Hospital Center of Vila Nova de Gaia/Espinho (CHVNG/E). A case of a clearly unhealthy patient, a 63 year-old male with a heartbeat rate, HBR, of 59 bpm, was chosen for this study, as well as an apparently healthy patient, who is a 29 year-old male with a HBR of 80 beats per minute. The two patients included in the study gave informed consent and the current study was approved by the local institutional ethics committee.

From CTA image sequences, all of the visible arterial branches' start and end points were manually selected. The aorta, as well as the left main stem, left anterior descending (LAD) artery, and the left circumflex (LCx) artery were picked from an axial view of the heart using MIMICS® (Materialize Interactive Medical Image Control System), an image processing software. This program then automatically established the centerline of the artery and the lumen frontier, producing the 3D shell of the artery of the patient. The arteries were then truncated, and the final models were created (Fig. 19.2). The unhealthy patient has a visible stenosis of 40% in the LAD, and the LCx did not exhibit any obstruction.

19.2.3 Boundary Conditions

The necessary boundary conditions for the numerical simulations are the profiles of the blood pressure and velocity, conditioned by many biological and physiological parameters, including body weight, gender, and overall health. The fluid properties must also be selected.

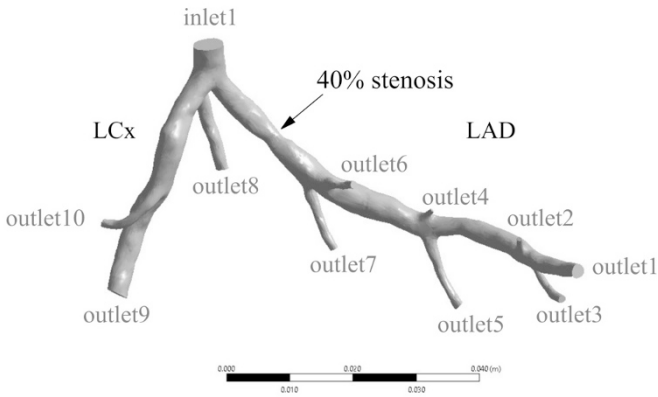
19.2.3.1 Pressure Boundary Condition

For transient flow, the pressure of blood was first measured by Dong et al (2015) in the outlets of the arteries during a cardiac cycle, and the generated profile was approximated by a Fourier series in MATLAB® (Eq. (19.5)). The series was truncated after 8 terms (Table 19.2).

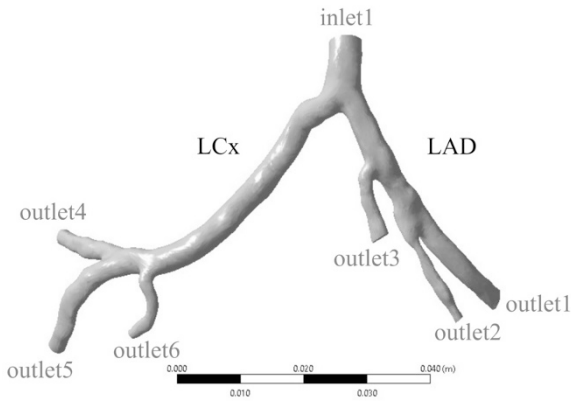
$$f(t) = a_0 + \sum_{i=1}^{\infty} (a_i \cos i\omega t + b_i \sin i\omega t) \quad (19.5)$$

The shape of the pressure profile was considered identical for both patients, but the angular cardiac frequency, ω , determined by the HBR, is specific to each patient. The period, T depends on ω and HBR:

$$\omega = \frac{2\pi HBR}{60} \quad (19.6)$$



(a)



(b)

Fig. 19.2 3D models of the left coronary artery of the two patients.

Table 19.2 Parameters of Fourier series of the pressure profiles.

| Index i | 0 | 1 | 2 | 3 | 4 | 5 | 6 | 7 | 8 |
|-----------|-------|--------|---------|---------|--------|--------|--------|---------|---------|
| a_i | 22.19 | -14.12 | -6.355 | -0.5552 | 2.077 | 0.9805 | 0.3492 | 0.07955 | -0.5758 |
| b_i | 0 | 5.662 | -0.8518 | -4.236 | -1.853 | 0.5314 | 0.6549 | 0.6130 | 0.1042 |

$$T = 2\pi \omega \quad (19.7)$$

In Fluent®, the pressure distribution was implemented through an interpreted UDF and applied to all outlets.

In the transient simulations, the temporal average outlet pressure was determined with the previous data, being equal to 2932.12 Pa for the healthy patient and 2962.18 Pa for the unhealthy one.

19.2.3.2 Velocity Boundary Condition

The shape of the velocity profile at the inlet can be considered identical for both patients (Dong et al, 2015), depending on circulatory properties of each patient, specifically the duration of the cardiac cycle, T , and the Womersley number, α . This non-dimensional parameter measures the change of the velocity profile's shape, and it represents the ratio between transient inertial forces and viscous forces (Eq. (19.8)). It depends on the cardiac frequency, ω , the radius of the artery, R , and properties such as viscosity and density of blood (Womersley, 1955).

$$\alpha = R \sqrt{\frac{\rho \omega}{\mu}} \quad (19.8)$$

To calculate the latter parameter in the entrance of the artery, the inlet area was measured for both models in SpaceClaim®, an application of ANSYS®, and equivalent radii, R_{eq} , of circles with those areas were calculated. α was calculated considering blood as a Newtonian fluid with constant viscosity. These parameters are represented in Table 19.3.

Table 19.3 Parameters used for transient blood flow.

| Parameters for blood flow | Unhealthy patient | Healthy patient |
|--|-----------------------|-----------------------|
| Womersley number, α | 3.265 | 3.941 |
| Cardiac pulse frequency, ω [rad s ⁻¹] | 6.178 | 8.378 |
| Period, T [s] | 1.017 | 0.7500 |
| Inlet area, A_{inlet} [mm ²] | 17.64 | 18.95 |
| Equivalent radius, R_{eq} [mm] | 2.370 | 2.456 |
| Blood density, ρ [kg m ⁻³] | 1060 | 1060 |
| Newtonian blood viscosity, μ [kg m ⁻¹ s ⁻¹] | 3.45×10^{-3} | 3.45×10^{-3} |

Numerically, the Womersley velocity profile is created from a flow waveform (Womersley, 1955) (Eq. (19.9)) and approximating it through a Fourier transform using MATLAB®. Thus, the first six harmonic coefficients, a_n and b_n , were obtained

(Table 19.4). The longitudinal velocity was implemented in a compiled UDF as a function of time and radial position, where i is the index of the $N = 5$ harmonic coefficients and the index of the Fourier's series terms, and J_0 and J_1 are Bessel functions. Only the real part of the equation is considered:

$$u(r, t) = \frac{a_o}{\pi R^2} \left[1 - \left(\frac{r}{R} \right)^2 \right] + \frac{1}{\pi R^2} \sum_{n=1}^N \left[\frac{1 - \frac{J_0\left(\alpha \frac{r}{R} i^{\frac{3}{2}}\right)}{J_0\left(\alpha i^{\frac{3}{2}}\right)}}{1 - \frac{2J_1\left(\alpha i^{\frac{3}{2}}\right)}{\alpha i^{\frac{3}{2}} J_0\left(\alpha i^{\frac{3}{2}}\right)}} \right] (a_n \cos \omega n t + b_n i \sin \omega n t) \quad (19.9)$$

Table 19.4 Parameters of Fourier series of the velocity profiles.

| Index n | 0 | 1 | 2 | 3 | 4 | 5 |
|---------|-------|--------|---------|--------|-------|---------|
| a_n | 26.16 | 5.282 | -0.9090 | -2.733 | 2.509 | -0.2680 |
| b_n | 0 | -4.866 | -1.040 | 0.2598 | 2.111 | -1.372 |

Additionally, it is assumed that there is a no-slip condition in the wall, meaning the blood velocity in the vicinity of the wall is null.

In the steady-state simulations, the velocity profiles were considered uniform with an amplitude of 0.12495 m s^{-1} for the healthy patient and 0.10313 m s^{-1} for the unhealthy one (the average values of the transient velocity distributions).

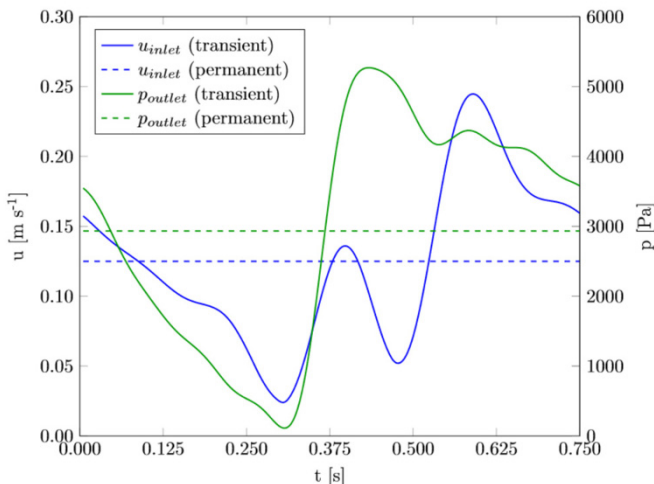
As a result, the implemented profiles of velocity, u , and pressure, p , are represented (see Fig. 19.3).

The viscosity models described in Table 19.1 were implemented as UDFs (See Fig. 19.17 in Appendix 19.5).

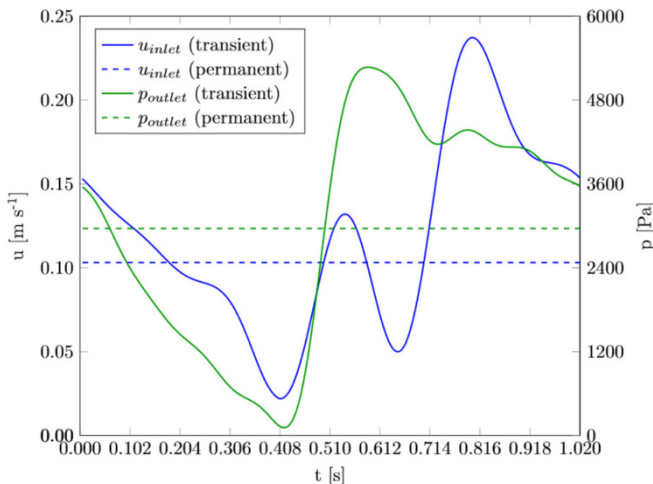
19.2.4 Mesh Convergence Analysis

To find the most appropriate mesh size, a mesh convergence test was done for transient flow and with the model of the unhealthy patient, since the conclusions apply to both models. To perform the mesh convergence test, the maximum element size (MES) of the elements was changed from $3.5 \times 10^{-4} \text{ m}$ to $4.0 \times 10^{-4} \text{ m}$, in intervals of $0.1 \times 10^{-4} \text{ m}$ and the maximum values of TAWSS and OSI were measured (Fig. 19.4).

Looking at the results, the ideal maximum mesh size is $3.9 \times 10^{-4} \text{ m}$ because the differences in the measured hemodynamic parameters are no longer substantial after refinement (the error between this mesh and the most refined one was 0.97% for the TAWSS and 2.07% for the OSI). Properties of the created meshes are shown



(a)



(b)

Fig. 19.3 Velocity and pressure profiles in steady-state and pulsatile regime flow (a) healthy patient, (b) unhealthy patient.

(Table 19.5). According to ANSYS Inc. (2009), the maximum skewness should never be greater than 0.95 and the average skewness should be below 0.33. The results indicate that the orthogonality of the tetrahedral elements of the geometries of both patients is not compromised.

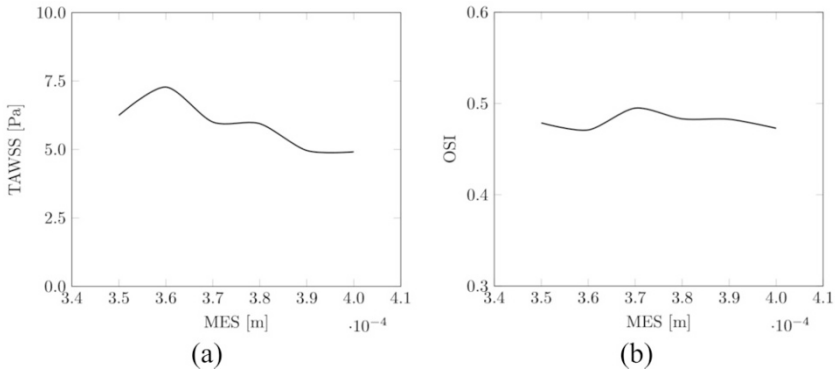


Fig. 19.4 Hemodynamic indicators for different mesh sizes (a) TAWSS, (b) OSI.

Table 19.5 Final mesh properties.

| Mesh property | Unhealthy patient | Healthy patient |
|--------------------|----------------------|----------------------|
| MES [m] | 3.9×10^{-4} | 3.9×10^{-4} |
| Number of nodes | 66238 | 75490 |
| Number of elements | 336765 | 388782 |
| Maximum skewness | 0.72273 | 0.65364 |
| Average skewness | 0.13981 | 0.13384 |

19.2.5 Numerical Simulation Definitions

The SIMPLE scheme of pressure-velocity coupling was chosen to obtain the pressure field while assuring mass conservation (Patankar and Spalding, 1972). For spatial discretization, the preferred solution method for gradients was the Green-Gauss node based, for pressure the second order solution method, while second order upwind solution method was chosen for the calculations of momentum. The transient formulation was solved through first order implicit solution method. A node-based approach was selected for the evaluation of gradients and derivatives over a cell-based one because it has been proven to be more accurate (ANSYS Inc., 2009). An absolute convergence criterion of 1×10^{-18} was used for the computation of all the necessary equations. Moreover, the flows were considered laminar.

In transient flow simulations, assuming a maximum of 20 iterations for each time step and selecting a time step size of 5×10^{-3} s, the number of time steps was defined as the division of T by the time step size. The total number of iterations was defined by the product of the number of time steps with the maximum number of iterations per time step. Hence, the numerical simulations for the unhealthy patient required 204 time steps and 4080 iterations, while the healthy patient simulations took 150 time steps and 3000 iterations.

In steady-state flow simulations, the number of iterations was set to 200 for both patients, considered a large enough number to allow a satisfactory convergence of the results without requiring much computational time. For steady-state and transient simulations, the used reference values for inlet area and density of blood are displayed in Table 19.3.

19.2.6 Validation of Numerical Method with the Literature

To validate the chosen methods and settings with literature, an ANSYS® course (ANSYS Inc., 2014), which used a coronary artery obtained from GrabCAD (2012) and specific boundary conditions, was followed, but applying the numerical method defined in this paper. The pressure gradient and wall shear stress of the tutorial course and the ones obtained through the application of the presented numerical settings were measured and are displayed in Table 19.6. The calculated relative error values are very low and, therefore, the utilized numerical methodology can be considered valid.

Table 19.6 Validation of the numerical methods and settings by comparison with results of ANSYS Inc. (2014).

| Property | Present work results | Literature results | Relative error |
|--------------------|----------------------|--------------------|----------------|
| Δp [Pa] | 13385.5 | 13384.5 | 0.0067 % |
| τ_{wall} [Pa] | 4.0290 | 4.1814 | 3.82 % |

19.3 Results and Discussion

The pulsatile nature of the blood flow and the elasticity of the arterial walls could mean the control volume changes in each instance, with the expansion and contraction of the blood vessel. However, according to the findings of Pinho et al (2018), WSS, OSI, TAWSS and RRT were not significantly affected by the existence of elastic boundary walls and, therefore, a fluid-solid interaction (FSI) was not taken into consideration.

19.3.1 Steady-State Flow of Newtonian Blood

The average mass flow rate of blood entering the arteries is constant and equal to 1.921 g s^{-1} and 2.504 g s^{-1} , for the unhealthy and healthy patient, respectively. The maximum wall shear stress is equal to 7.419 Pa and to 7.520 Pa , accordingly. The maximum pressure drop, Δp , of the healthy patient is 82.6 Pa , larger than the Δp of the unhealthy patient, equal to 72.1 Pa . The spatial and temporal data regarding WSS was collected in order to calculate OSI, RRT and TAWSS. CFD-Post® was used to plot RRT and TAWSS (Fig. 19.5 and Fig. 19.6), while the oscillatory shear index is null in the artery of both patients.

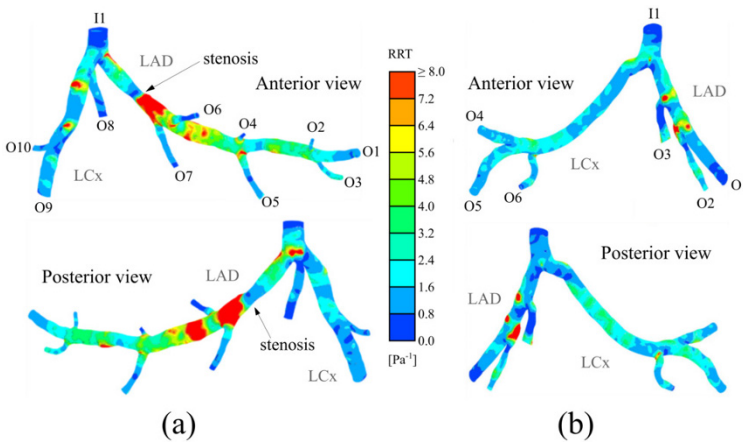


Fig. 19.5 RRT distribution in LCA in Newtonian steady-state flow (a) unhealthy patient, (b) healthy patient.

The unhealthy patient possesses higher values of RRT, being more prone to plaque formation in the regions represented in red. The time-averaged wall shear stress is lower for the unhealthy patient, being the lowest in the same location as the elevated RRT, before and after outlet6 and outlet7.

This section of the artery jeopardizes the blood flow to the myocardium in outlet1 through outlet7, whereas the healthy patient does not possess such areas of urgent concern, like the bifurcation area between outlet1 and outlet2. So, the results show that the healthy patient has lower risk of developing atherosclerosis despite having a greater Δp .

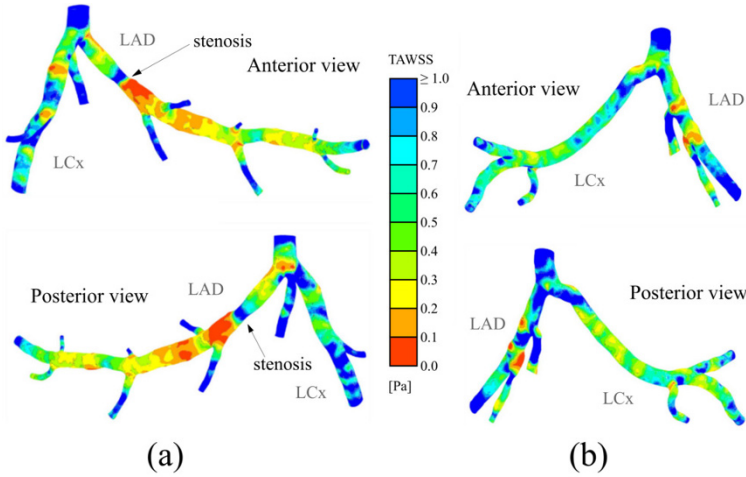


Fig. 19.6 TAWSS distribution in LCA in Newtonian steady-state flow (a) unhealthy patient, (b) healthy patient.

19.3.2 Transient Flow of Newtonian Blood

The maximum wall shear stress was measured (Fig. 19.7). Its evolution over time is shaped similarly to the velocity, since τ_{wall} is a function of the flow speed adjacent to the wall. The initial peak of the wall shear stress in both patients results from the initialization of the computation process, and it should be disregarded.

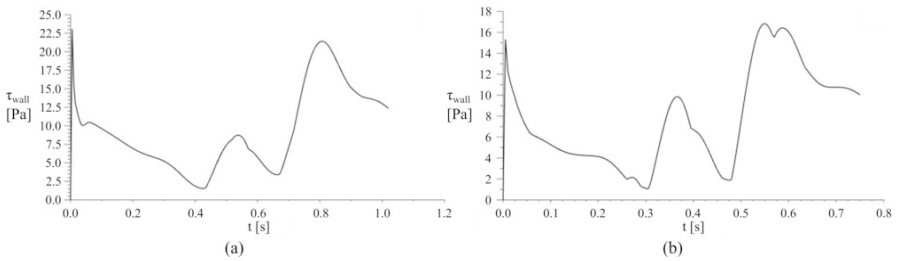


Fig. 19.7 Max. WSS in LCA in Newtonian transient flow (a) unhealthy patient, (b) healthy patient.

In the velocity peak (0.6 s in the healthy patient, and 0.725 s for the unhealthy patient), the maximum pressure gradients increases significantly, equal to 189.55 Pa for the unhealthy patient and 185.19 Pa to the healthy one.

Then, a three-dimensional distribution of OSI, RRT and TAWSS was obtained in order to evaluate the atherosusceptibility in both arteries (Fig. 19.8 - Fig. 19.10).

In comparison to the results of the steady-state flow, the introduction of the realistic transient blood flow condition increases the concern over the occurrence of

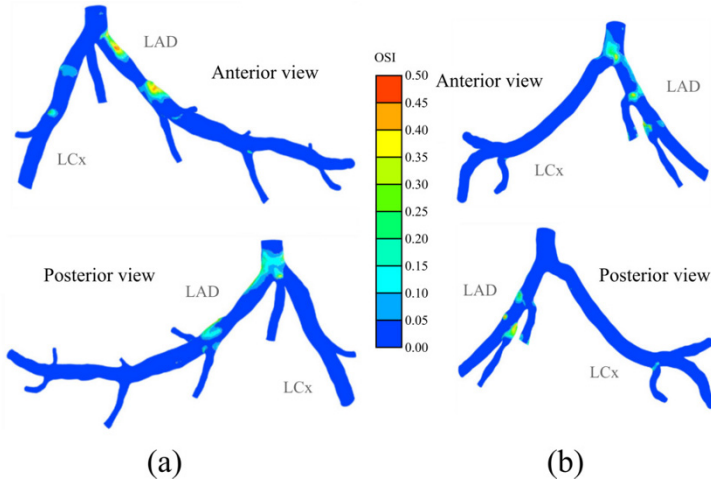


Fig. 19.8 OSI distribution in LCA in transient flow of Newtonian blood (a) unhealthy patient, (b) healthy patient.

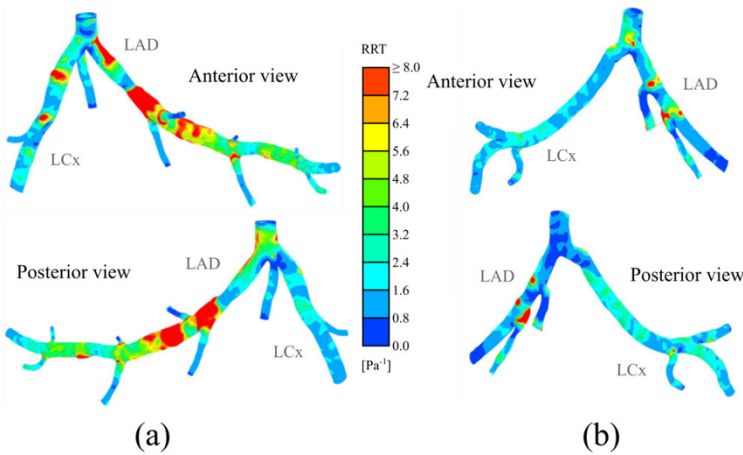


Fig. 19.9 RRT distribution in LCA in transient flow of Newtonian blood (a) unhealthy patient, (b) healthy patient.

plaque formation for the unhealthy individual. OSI become greater than zero near bifurcations (See Fig. 19.8) and, in relation to the steady-state flow, the critical area of atherosusceptibility increases from 0% to 3.87% in the healthy patient and to 6.40% in the unhealthy patient. Additionally, there is a change in the areas where RRT is equal or greater than 8 Pa^{-1} from 1.36% in the steady-state flow to 1.38% in the healthy patient and from 5.88% to 5.40% in the unhealthy patient. The regions where TAWSS is lower than 0.4 Pa decrease (from 17.95% to 16.53% in the healthy patient and from 38.55% to 27.12% in the unhealthy patient). The results suggest

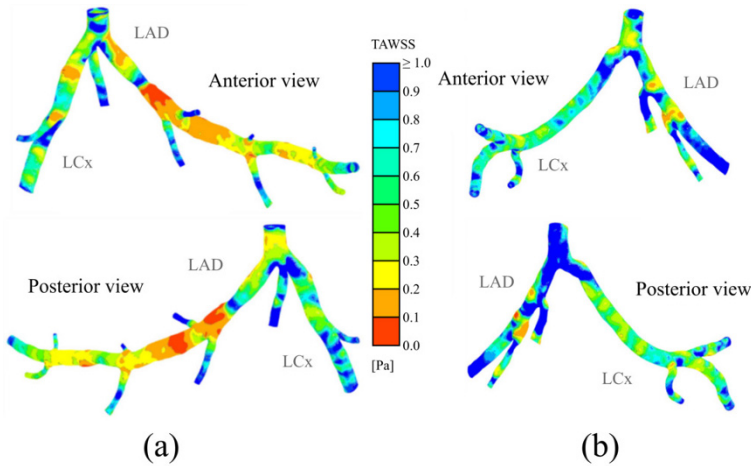


Fig. 19.10 TAWSS distribution in LCA in transient flow of Newtonian blood (a) unhealthy patient, (b) healthy patient.

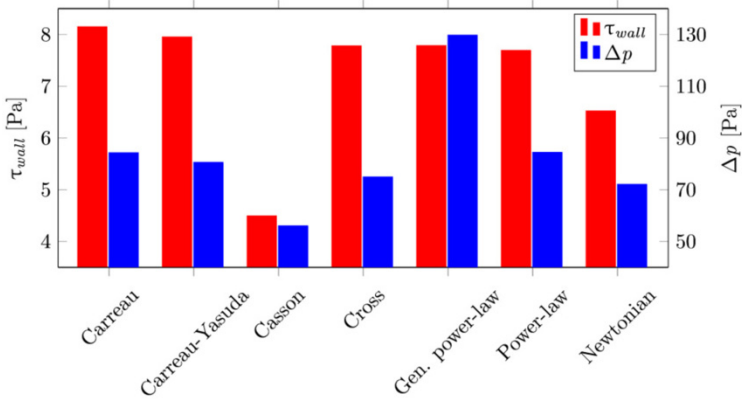
that the healthy patient is less prone to having atherosclerosis when compared to the results of the unhealthy patient.

19.3.3 Steady-State Flow of Non-Newtonian Blood

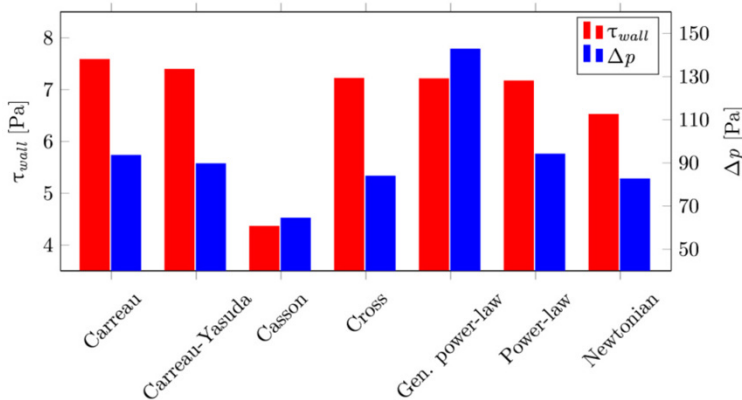
The velocity and the mass flow rate are not altered by the viscosity models in both patients, being equal to the values of the Newtonian model, however, there is a larger discrepancy in the obtained values of the maximum Δp and maximum τ_{wall} (Fig. 19.11).

With the exception of the Casson viscosity model, the pressure drop and the maximum wall shear stress of the non-Newtonian models are greater than the ones where blood was considered a Newtonian fluid. The generalized power-law model leads to the biggest pressure gradients in both patients, which is in accordance with the results of Sandeep and Shine (2021), while the Carreau model led to the largest shear stress in the artery walls of the two patients. The pressure gradients of the Carreau, Carreau-Yasuda, Cross and Power-law viscosity models are relatively similar to each other.

The RRT and TAWSS distribution of the unhealthy patient were plotted (Fig. 19.12). OSI is null for all models. The results considering the Carreau, Carreau-Yasuda, Cross and the power-law model for blood are very similar. The Casson model leads to more critical regions of atherosusceptibility (49.09% of the area distribution of TAWSS is below 0.4 Pa and 6.46% of the RRT distribution is above 8 Pa^{-1}), while the generalized power-law model returns more healthy results (the critical regions of TAWSS are only 8.33% and RRT values do not surpassed 8 Pa^{-1}). Comparing all



(a)



(b)

Fig. 19.11 Maximum Δp and τ_{wall} for non-Newtonian blood in steady-state flow in LCA (a) unhealthy patient, (b) healthy patient.

the studied viscosity models, the generalized power-law provides the furthest values of RRT and TAWSS from the results of the remaining viscosity models.

19.3.4 Transient Flow of Non-Newtonian Blood

In transient flow, the flow properties of mass flow rate and velocity are not affected by the viscosity models. At the velocity peak, the same properties are computed (Fig. 19.13).

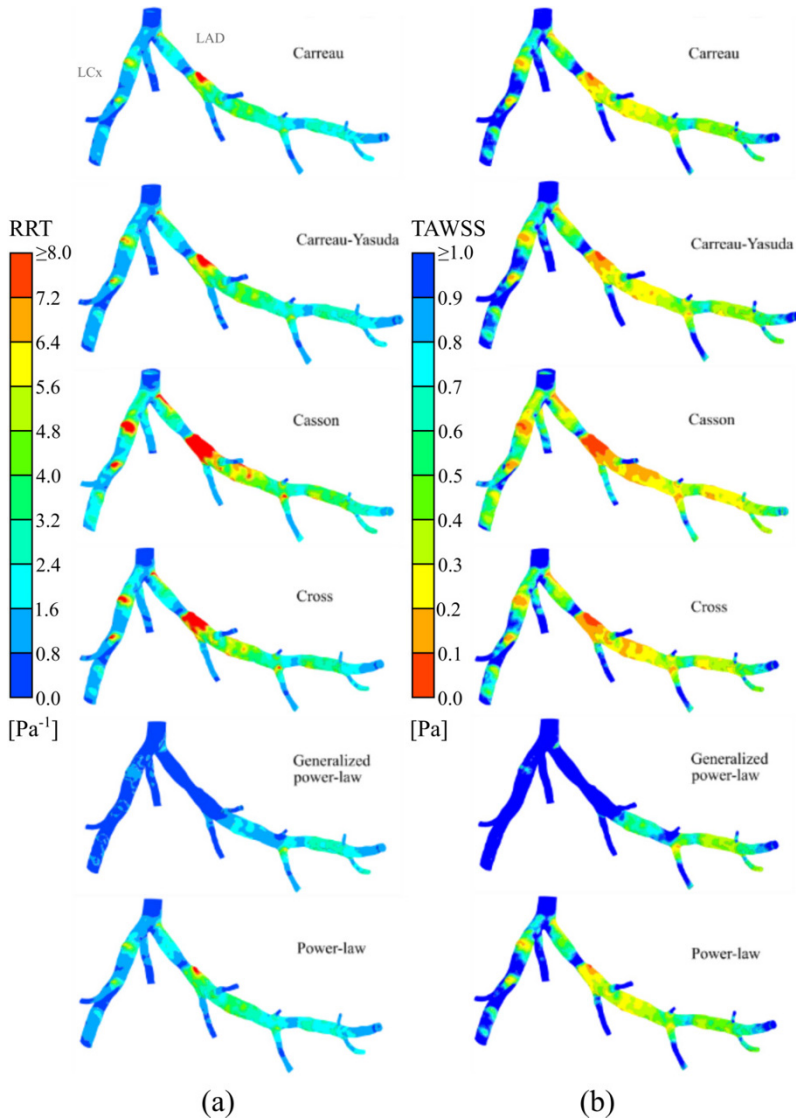
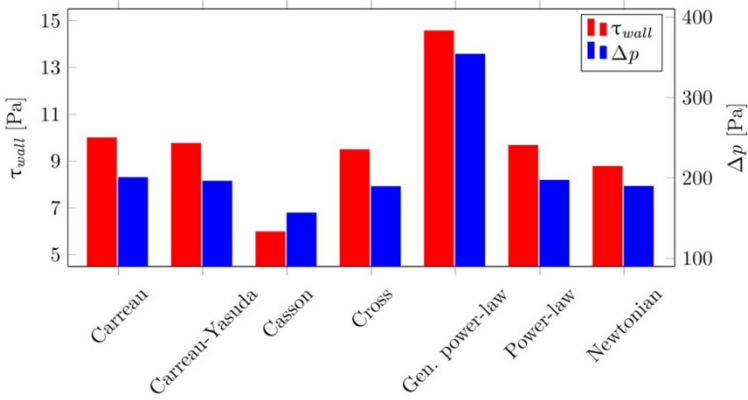
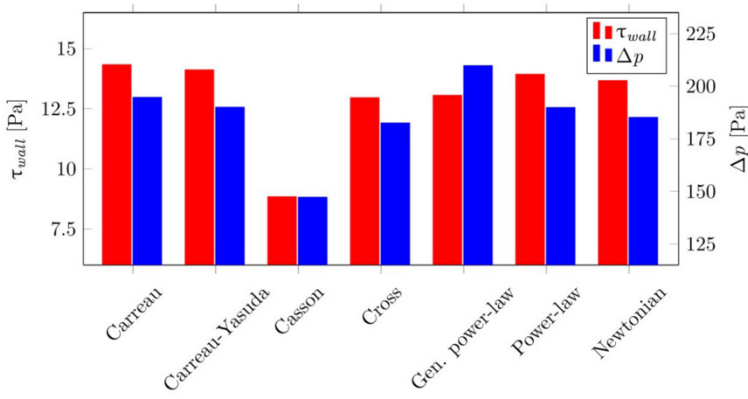


Fig. 19.12 Hemodynamic indicators of the non-Newtonian steady-state blood flow for the unhealthy patient (a) RRT, (b) TAWSS.

Similarly to the non-Newtonian steady-state flow, the pressure drop in the unhealthy patient is greater than the one of the healthy patient for all viscosity models. In addition, the Casson model returns reduced values of maximum Δp and τ_{wall} . The application of generalized power-law model led to the highest values of pressure drop, the imposition of the Carreau model returns the highest values of wall shear stress, and the results of the remaining viscosity models are very close to one another.



(a)



(b)

Fig. 19.13 Maximum Δp and τ_{wall} in the velocity peaks for non-Newtonian blood in transient flow in LCA (a) unhealthy patient, (b) healthy patient.

RRT and TAWSS of the unhealthy model were plotted (Fig. 19.14).

The generalized power-law viscosity model shows the most distant results and, once more, the Casson viscosity model results present more critical regions than the remaining results. In fact, the Casson viscosity model returns critical regions of OSI,

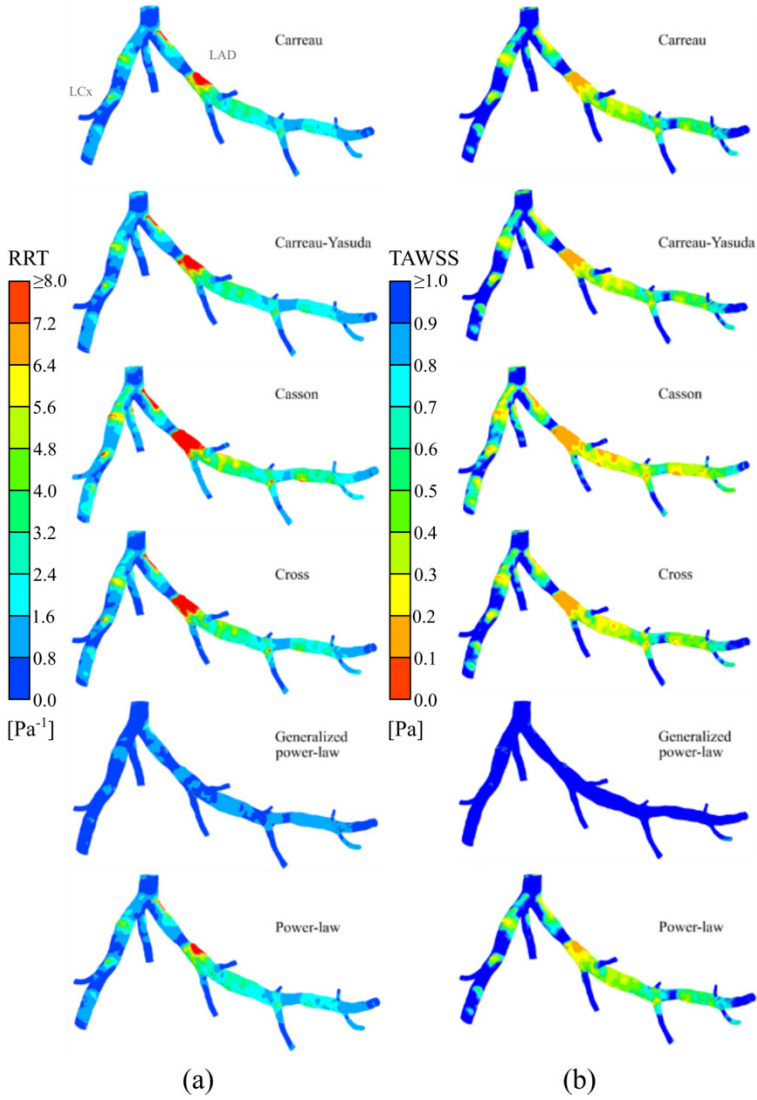


Fig. 19.14 Hemodynamic indicators of the transient flow of non-Newtonian blood flow for the unhealthy patient (a) RRT, (b) TAWSS.

RRT and TAWSS occupying an area of 8.31%, 6.10% and 35.76%, respectively, while in the generalized power-law model, these areas are 2.60%, 0.01% and 0%, accordingly.

In comparison to the steady-state flow (Fig. 19.12), the RRT of both patients increases with the application of the transient boundary conditions (with the exception of the Casson viscosity model), as well as the OSI. Yet, all the TAWSS values at the velocity peak in the transient flow decrease for all the studied non-Newtonian models when in comparison to the steady-state flow (See Table 19.7).

Table 19.7 Atherosusceptible area comparison through hemodynamic descriptors between patients and between flow regimes for all the studied non-Newtonian viscosity models.

| Patient | Flow regime | Viscosity model | Critical OSI (%) | Critical RRT (%) | Critical TAWSS (%) |
|-----------|--------------|-----------------|------------------|------------------|--------------------|
| Healthy | Steady-state | Carreau | 0 | 0.60 | 6.21 |
| | | Carreau-Yasuda | 0 | 0.70 | 8.53 |
| | | Casson | 0 | 1.44 | 31.66 |
| | | Cross | 0 | 1.06 | 14.95 |
| | | Gen. power-law | 0 | 0 | 0.01 |
| | | Power-law | 0 | 0.48 | 4.52 |
| | | Newtonian | 0 | 1.36 | 17.95 |
| | Transient | Carreau | 1.84 | 0.64 | 5.99 |
| | | Carreau-Yasuda | 2.19 | 0.72 | 7.80 |
| | | Casson | 6.34 | 2.33 | 29.92 |
| | | Cross | 3.04 | 1.06 | 13.95 |
| | | Gen. power-law | 0.57 | 0 | 0 |
| | | Power-law | 1.61 | 0.53 | 4.63 |
| | | Newtonian | 3.87 | 1.38 | 16.54 |
| Unhealthy | Steady-state | Carreau | 0 | 0.44 | 27.24 |
| | | Carreau-Yasuda | 0 | 0.86 | 30.83 |
| | | Casson | 0 | 6.46 | 49.09 |
| | | Cross | 0 | 3.86 | 36.57 |
| | | Gen. power-law | 0 | 0 | 8.33 |
| | | Power-law | 0 | 0.22 | 23.05 |
| | | Newtonian | 0 | 5.88 | 38.55 |
| | Transient | Carreau | 3.08 | 1.51 | 17.17 |
| | | Carreau-Yasuda | 3.63 | 2.14 | 19.17 |
| | | Casson | 8.31 | 6.10 | 35.76 |
| | | Cross | 5.25 | 4.15 | 24.38 |
| | | Gen. power-law | 2.60 | 0.01 | 0 |
| | | Power-law | 2.68 | 0.99 | 14.88 |
| | | Newtonian | 6.40 | 5.40 | 27.12 |

A volumetric rendering and a vector distribution of the velocity were generated in CFD-Post® at the velocity peak (Fig. 19.15). In all viscosity models except for the generalized power-law one there is an increase in velocity after the obstruction in the LAD of the unhealthy patient.

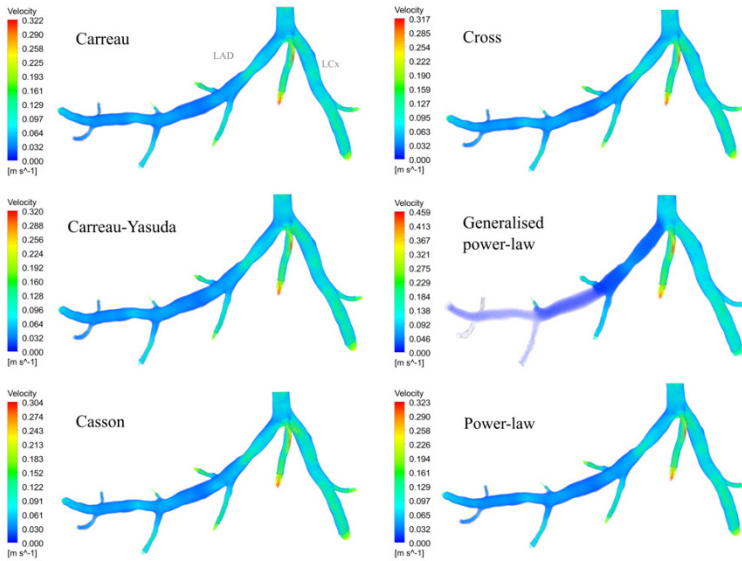


Fig. 19.15 Velocity distribution during the velocity peak (at 0.725s) in the transient flow in LCA of the unhealthy patient.

It is found that, from $t = 0.375$ s until $t = 0.450$ s, the blood velocity at the stenosis is almost null in every viscosity model (Fig. 19.16). Therefore, there are instances where the blood is primarily flowing through the LCx during the velocity peak. No recirculation regions are found in the illustrated area, yet the results indicate that this zone is prone to the development of atheroma plaque.

Thus, the majority of the results substantiate the negative impact the obstruction in the LCA has on the blood flow of the patient.

19.4 Conclusions

Blood flow in three-dimensional models of coronary arteries of two patients with varying degrees of stenosis, one with clear evidence of disease development and the other seemingly healthy, was studied through computational fluid dynamics. The numerical simulations allowed the quantification of parameters that could not be measured *in vivo* and should be used to aid doctors in diagnosing and treating atherosclerosis.

The velocity and pressure fields were analyzed, as well as the main hemodynamic descriptors, OSI, RRT and TAWSS, which can be used to identify problematic areas linked to the creation and development of atherosclerotic plaque. Moreover, since there is not a global consensus on the theoretical model that best describes the

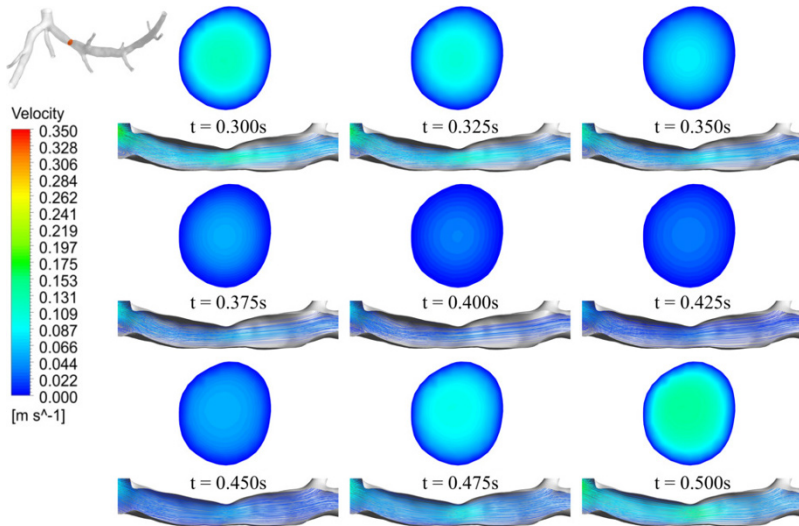


Fig. 19.16 Time instances from $t = 0.300$ s until $t = 0.500$ s where blood flow was almost stagnated.

viscosity of blood, the Carreau, Carreau-Yasuda, Casson, Cross, generalized power-law and power-law viscosity models in patient-specific arteries were compared.

The numerical results showed that the most problematic areas of the arteries were the bifurcations and the sudden changes in diameter in obstructions, where there were signs of stagnation and sometimes absence of blood flow. The Casson viscosity model is the only one that considers blood properties such as hematocrit and plasma viscosity, and it produced greater critical areas of hemodynamic descriptors. Thus, critical values of TAWSS, OSI and RRT strongly depend on the model. The generalized power-law viscosity model produced the most healthy and most distant results when compared to the remaining studied models, which produced similar results. Apart from the generalized power-law viscosity model, the implementation of the transient flow and the non-Newtonian viscosity models generally decreased the critical regions of atherosusceptibility in both patients in comparison with the steady-state model, since properties such as wall shear stress and pressure gradient at the velocity peak decreased and, therefore, diminished the probability of the patients developing future health problems. For the steady-state regime and Newtonian blood flow simulations, the opposite behavior was observed and, this disparity highlights the fact that blood should be correctly modeled and, therefore, not considered a Newtonian fluid and be simulated under more realistic boundary conditions.

All in all, from the collected results, it became evident that the unhealthy patient should be performing treatment to prevent possibly deadly repercussions of non-normal blood flow, yet the healthy patient showed that it too could develop serious health problems in the future. Therefore, routine analysis and an improvement of the overall lifestyle could prevent impending complications.

Acknowledgements Authors gratefully acknowledge the Engineering Faculty of University of Porto (FEUP), the Department of Mechanical Engineering (DEMec) of FEUP and the Institute of Science and Innovation in Mechanical and Industrial Engineering (LAETA-INEGI), the Faculty of Medicine of the University of Porto (FMUP) and Vila Nova de Gaia / Espinho Hospital Center (CHVNG/E).

19.5 Appendix I

```

1  /* Carreau-Yasuda viscosity model */
2  #include "udf.h"
3  DEFINE_PROPERTY(cy_viscosity, c, t)
4  {
5      real mu_inf = 0.0035;
6      real mu_zero = 0.056;
7      real lambda = 1.902;
8      real a = 1.25;
9      real n = 0.22;
10     real mu_cy;
11     real gamma =
12     (C_STRAIN_RATE_MAG(c,t));
13     mu_cy = mu_inf + (mu_zero -
14     mu_inf) * pow(1.0 + pow(lambda *
15     gamma , a), (n - 1)/a);
16 }

```

(a)

```

1  /* Generalized power-law viscosity
2  model */
3  #include "udf.h"
4  #include <math.h>
5  #define mu_inf 0.0035
6  #define delta_mu 0.25
7  #define delta_n 0.45
8  #define a 50
9  #define b 3
10 #define cons 50
11 #define d 4
12 DEFINE_PROPERTY(gpl_viscosity, c, t)
13 {
14     real mu_gpl;
15     real gamma =
16     C_STRAIN_RATE_MAG(c, t);
17     if(gamma!=0){
18         real lambda = mu_inf +
19         delta_mu * exp(-1*( 1 + abs(gamma) / a)
20         * exp(-1 * (b / abs(gamma))));
21         real n = n_inf + delta_n *
22         exp( -1 * (1 + abs(gamma) / cons) *
23         exp(-1 * (d / abs(gamma))));
24         mu_gpl = lambda *
25         pow(abs(gamma),(n - 1));
26     }
27     else{
28         mu_gpl = mu_inf;
29     }
30 }

```

(d)

```

1  /* Casson viscosity model */
2  #include "udf.h"
3  #define Hct 0.4
4  #define mu_p 0.00145
5  DEFINE_PROPERTY(casson_viscosity,c,t)
6  {
7      real mu_casson;
8      real gamma =
9      C_STRAIN_RATE_MAG(c,t);
10     real N_inf = sqrt(mu_p * pow((1
11     - Hct), -0.25));
12     real mu_inf = sqrt(pow((0.625 *
13     Hct), 3));
14     if(gamma!=0){
15         mu_casson = pow(mu_inf,
16         2)/gamma + 2 * mu_inf *
17         N_inf / sqrt(gamma) +
18         pow(N_inf, 2);
19     }
20     else{
21         mu_casson = 0.0035;
22     }
23 }

```

(b)

```

1  /* Cross viscosity model */
2  #include "udf.h"
3  #define mu_inf 0.0035
4  #define mu_zero 0.0364
5  #define gamma_c 2.63
6  #define n 1.45
7  DEFINE_PROPERTY(cross_viscosity, c, t)
8  {
9      real mu_cross;
10     real gamma =
11     (C_STRAIN_RATE_MAG(c, t));
12     if(gamma!=0){
13         mu_cross = mu_inf +
14         (mu_zero - mu_inf) / (1 + pow(
15         gamma / gamma_c, n));
16     }
17     else{
18         mu_cross = mu_inf;
19     }
20 }

```

(c)

Fig. 19.17 Definition of the viscosity models in UDFs (a) Carreau-Yasuda, (b) Casson, (c) Cross, (d) Generalized power-law.

References

- ANSYS Inc (2009) ANSYS Inc. Fluent Guide 12.0. URL <https://www.afs.enea.it/project/neptunius/docs/fluent/html/ug/node167.htm>
- ANSYS Inc (2014) ANSYS Innovation Courses. URL <https://courses.ansys.com/index.php/courses/fluent-3d-bifurcating-artery/>
- Apostolidis AJ, Beris AN (2014) Modeling of the blood rheology in steady-state shear flows. *Journal of Rheology* 58(3):607–633
- Apostolidis AJ, Moyer AP, Beris AN (2016) Non-Newtonian effects in simulations of coronary arterial blood flow. *Journal of Non-Newtonian Fluid Mechanics* 233:155–165
- Ballyk PD, Steinman DA, Ethier CR (1994) Simulation of non-Newtonian blood flow in an end-to-side anastomosis. *Biorheology* 31(5):565–586
- Barquera S, Pedroza-Tobías A, Medina C, Hernández-Barrera L, Bibbins-Domingo K, Lozano R, Moran AE (2015) Global Overview of the Epidemiology of Atherosclerotic Cardiovascular Disease. *Archives of Medical Research* 46(5):328–338
- Chaichana T, Sun Z, Jewkes J (2012) Computational fluid dynamics analysis of the effect of plaques in the left coronary artery. *Computational and Mathematical Methods in Medicine* 2012:504,367
- Chiastra C, Morlacchi S, Gallo D, Morbiducci U, Cárdenes R, Larrabide I, Migliavacca F (2013) Computational fluid dynamic simulations of image-based stented coronary bifurcation models. *Journal of the Royal Society Interface* 10(84)
- Chien S, Usami S, Taylor HM, Lundberg JL, Gregersen MI (1966) Effects of hematocrit and plasma proteins on human blood rheology at low shear rates. *Journal of applied physiology* 21(1):81–87
- Dong J, Sun Z, Inthavong K, Tu J (2015) Fluid–structure interaction analysis of the left coronary artery with variable angulation. *Computer Methods in Biomechanics and Biomedical Engineering* 18(14):1500–1508
- GrabCAD (2012) Free CAD Designs, Files & 3D Models: The GrabCAD Community Library. URL <https://grabcad.com/library/carotid-bifurcation>
- Husain I, Labropulu F, Langdon C, Schwark J (2020) A comparison of Newtonian and non-Newtonian models for pulsatile blood flow simulations. *Journal of the Mechanical Behaviour of Materials* 21(5-6):147–153
- Jonášová A, Vimmr J (2018) Noninvasive assessment of carotid artery stenoses by the principle of multiscale modelling of non-Newtonian blood flow in patient-specific models. *Applied Mathematics and Computation* 319:598–616
- Jonášová A, Vimmr J (2021) On the relevance of boundary conditions and viscosity models in blood flow simulations in patient-specific aortocoronary bypass models. *International Journal for Numerical Methods in Biomedical Engineering* 37(4):32
- Lagache M, Coppel R, Finet G, Derimay F, Pettigrew RI, Ohayon J, Malvè M (2021) Impact of Malapposed and Overlapping Stents on Hemodynamics: A 2D Parametric Computational Fluid Dynamics Study. *Mathematics* 9(8)
- Malek AM, Alper SL, Izumo S (1999) Hemodynamic Shear Stress and Its Role in Atherosclerosis. *Stress: The International Journal on the Biology of Stress* 282(21):2035–2042
- Marossy A, Švorc P, Kron I, Grešová S (2009) Hemorheology and circulation. *Clinical Hemorheology and Microcirculation* 42(4):239–258
- Merrill EW, Pelletier GA (1967) Viscosity of human blood: transition from Newtonian to non-Newtonian. *Journal of applied physiology* 23(2):178–182
- Mozaffarian D, Benjamin EJ, Go AS, Arnett DK, Blaha MJ, Cushman M, de Ferranti S, Després JP, Fullerton HJ, Howard VJ, et al (2015) Heart Disease and Stroke Statistics—2015 Update. *Circulation* 131(4)
- Munson B, Rothmayer A, Okiishi T (2012) *Fundamentals of Fluid Mechanics*, 7th Edition. Wiley
- Patankar S, Spalding D (1972) A calculation procedure for heat, mass and momentum transfer in three-dimensional parabolic flows. *International Journal of Heat and Mass Transfer* 15(10):1787–1806

- Pinho N, Bento M, Sousa LC, Pinto S, Castro CF, António CC, Azevedo E (2018) Patient-Specific Study of a Stenosed Carotid Artery Bifurcation Using Fluid–Structure Interactive Simulation. In: Tavares JMR, Natal Jorge R (eds) *VipIMAGE 2017*, Springer International Publishing, pp 495–503
- Pinho N, Castro CF, António CC, Bettencourt N, Sousa LC, Pinto SI (2019) Correlation between geometric parameters of the left coronary artery and hemodynamic descriptors of atherosclerosis: FSI and statistical study. *Medical and Biological Engineering and Computing* 57(3):715–729
- Sandeep S, Shine SR (2021) Effect of stenosis and dilatation on the hemodynamic parameters associated with left coronary artery. *Computer Methods and Programs in Biomedicine* 204
- Soulis JV, Giannoglou GD, Chatzizisis YS, Seralidou KV, Parcharidis GE, Louridas GE (2008) Non-Newtonian models for molecular viscosity and wall shear stress in a 3D reconstructed human left coronary artery. *Medical Engineering and Physics* 30(1):9–19
- Varchanis S, Dimakopoulos Y, Wagner C, Tsamopoulos J (2018) How viscoelastic is human blood plasma? *Soft Matter* 14(21):4238–4251
- Womersley JR (1955) Method for the calculation of velocity, rate of flow and viscous drag in arteries when the pressure gradient is known. *The Journal of Physiology* 127(3):553–563



Chapter 20

Bending/Tension of Plate Reinforced by a System of Parallel Fiber

Alexander G. Kolpakov, Sergei I. Rakin

Abstract We present a 3-D to 2-D dimension reduction procedure as applied to the periodicity cell problem (PCP) of the homogenization theory for plates reinforced with a unidirectional system of fibers. The original 3-D PCP is reduced to several 2-D problems. The reduction procedures are not trivial, in one case we encounter the incompatibility condition, which makes impossible to transform the 3-D elasticity problem to the 2-D elasticity problem (only the transformation to 2-D thermoelasticity problem is possible). Numerical analysis of 2-D periodicity cell problems demonstrates new phenomena: the boundary layers on the top and bottom surfaces of the plate and, as a result, the wrinkling of the top and bottom surfaces of the plate. Note that these phenomena never occur in uniform plates or plates made of uniform layers.

Keywords: Fiber-reinforced plates · Homogenization · Dimensional reduction

20.1 Introduction

We consider a plate reinforced by a periodic system of parallel fibers, see Fig.20.1. Assume the fibers are parallel to the Oy -axis and form a periodic structure in the Oxz -plane. The periodicity cell (PC) $P_3 = [0, L] \times [0, 1] \times [-h, h]$ of such structure and its 2-D cross-sections $P = [0, L] \times [-h, h]$ are displayed in Fig.20.1.

Since the plate under consideration is invariant with respect to translation along the Oy -axis, there is a reason to look for a 2-D model of the plate. The procedure

A. G. Kolpakov
SysAn, A Nevskogo street 12-a, 34, Novosibirsk, Russia
e-mail: algk@ngs.ru

S. I. Rakin
Siberian Transport University, D. Koval'chuk st., 191, Novosibirsk, Russia
e-mail: rakinsi@ngs.ru

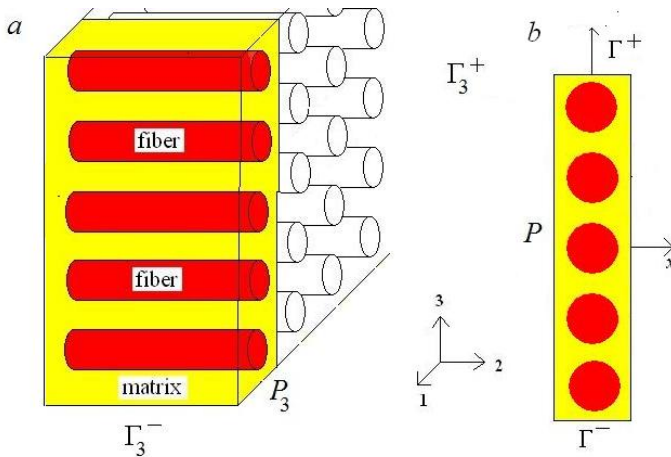


Fig. 20.1 a - fiber-reinforced plate, b - its 2-D periodicity cells

of dimension reduction is known for the solids with periodic systems of fibers or channels (Sendecyj, 1974; Grigolyuk and Fil'Shtinskii, 1966; Grigolyuk and Fil'shtinskij, 1992; Lu, 1995; Mityushev and Rogosin, 2000; Gluzman et al, 2018; Drygaś et al, 2019) and for plates of complex geometry made of homogeneous materials (Annin et al, 2017; Kolpakov and Kolpakov, 2020; Grigolyuk et al, 1991).

The specific features of plates are:

- the free (top and bottom) surfaces;
- the bending/torsion modes of deformation.

These features distinguish the plates from the solids with the periodic structure considered in Sendecyj (1974); Grigolyuk and Fil'Shtinskii (1966); Grigolyuk and Fil'shtinskij (1992); Lu (1995); Mityushev and Rogosin (2000); Gluzman et al (2018); Drygaś et al (2019). The inhomogeneity also brings some new effects.

There exists a great variety of approaches to the analysis of thin plates. In order to mention the recent papers, see Barchiesi and Khakalo (2019); Franciosi et al (2019); Yang et al (2020); Placidi and El Dhaba (2017); Altenbach et al (2010); Wang et al (2021) as well as references in them. As follows from the literature, the classical (Kirchoff–Love, Timoshenko, etc.) approaches work well for homogeneous plates or plates made of uniform layers. The classical theories do not work as applied to the inhomogeneous plates of general structure (for example, fiber-reinforced plates or plates with high-porous core). In some cases, even the basic notions of the classical theories are not well defined as applied to the inhomogeneous plates of general structure (for example, the inhomogeneous plate may have several "neutral" planes). The problem of construction of plate model was solved in the homogenization theory. The rigor homogenization theories as applied to elastic thin plates were developed first in Caillerie (1984); Kohn and Vogelius (1984). The papers (Caillerie, 1982, 1984) were devoted to the investigation of 3-D model of thin elastic periodic plate

when the thickness of the plate and the size of the periods are small. In the paper (Kohn and Vogelius, 1984), the elastic thin body with rapidly varying thickness was considered.

Note that the homogenization theory is a mathematical theory and it does not answer the questions of mechanical nature on its own.

The homogenization theory justifies that solution of the elasticity theory problem in a thin inhomogeneous layer of complex geometry has the form ($A, B = 1, 2$)

$$\mathbf{u}^\varepsilon = u_A(x, z)\mathbf{e}_A + yw(x, z)_{,A}\mathbf{e}_A + \varepsilon\mathbf{N}^{AB0}(\mathbf{x}/\varepsilon)u_{A,B}(x, z) + \varepsilon\mathbf{N}^{AB1}(\mathbf{x}/\varepsilon)w_{,AB}(x, z), \tag{20.1}$$

where ε is the characteristic thickness of the plate; $u_A(x, z)$ are the global in-plane displacements, $w(x, z)$ is the global normal deflection; $e_{AB} = u_{A,B}$ are global in-plane strains and $\rho_{AB} = w_{,AB}$ are global curvatures/torsion ($A, B = 1, 2$). These functions have the same meaning as in the classical theory. We use the notations $f_{,i}(\mathbf{x}) = \partial f(\mathbf{x})/\partial x_i$ and $f_{,i}(\mathbf{y}) = \partial f(\mathbf{y})/\partial y_i$ for the partial derivatives and assume summation with respect the repeating indices.

The term $\varepsilon\mathbf{N}^{AB0}(\mathbf{x}/\varepsilon)u_{A,B}(x, z) + \varepsilon\mathbf{N}^{AB1}(\mathbf{x}/\varepsilon)w_{,AB}(x, z)$ (known in the homogenization theory as “corrector” (Caillerie, 1984; Kohn and Vogelius, 1984) has the order of the thickness ε of the plate. Note that the plate may have rapidly varying thickness (top and/or bottom surfaces of the plate may be wavy). Therefore, the corrector has little effect on the global shape of the deformed plate. On the contrary, the derivatives of the functions $\varepsilon\mathbf{N}^{AB0}(\mathbf{x}/\varepsilon)$ and $\varepsilon\mathbf{N}^{AB1}(\mathbf{x}/\varepsilon)$ in \mathbf{x} are not small and may strongly influence the local stress-strain state of the plate.

It is known from the homogenization theory (Caillerie, 1984; Kohn and Vogelius, 1984) that the functions $\mathbf{N}^{AB\mu}$ are solutions to the following so-called periodicity cell problems:

$$\begin{cases} (a_{ijkl}(x, z)N_{k,l}^{AB\mu} + (-1)^\mu a_{ijAB}(x, z)z^\mu)_{,j} = 0 \text{ in } P_3, \\ (a_{ijkl}(x, z)N_{k,l}^{AB\mu} + (-1)^\mu a_{ijAB}(x, z)z^\mu)n_j = 0 \text{ on } \Gamma_3, \\ \mathbf{N}^{AB\mu} \text{ is periodic in } x, y, \end{cases} \tag{20.2}$$

$\Gamma_3 = \Gamma_3^- \cup \Gamma_3^+$. Hereafter, $\mathbf{y} = (x, y, z) = \mathbf{x}/\varepsilon$. The variable-index correspondence: $x \leftrightarrow 1, y \leftrightarrow 2, z \leftrightarrow 3$. The Latin indices take values 1, 2, 3; the capital Greek indices takes values 1, 2; the indices μ, ν take values 0, 1. Γ_3 means the top and the bottom surfaces of the PC P_3 .

The local stresses in the PC are (Caillerie, 1984; Kohn and Vogelius, 1984)

$$\sigma_{ij} = a_{ijkl}(x, z)N_{k,l}^{AB\mu} + (-1)^\mu a_{ijAB}(x, z)z^\mu$$

correspond to the in-plane strains ($\mu = 0$) of the unit magnitude or the bending/torsion ($\mu = 1$) of the unit magnitude.

In the plates subjected to the macroscopic stress-strain state (SSS) e_{AB}, ρ_{AB} , the local stresses are computed as

$$\begin{aligned} \sigma_{ij} = & (a_{ijkl}(x, z)N_{k,l}^{AB0} + a_{ijAB}(x, z))e_{AB} + \\ & (a_{ijkl}(x, z)N_{k,l}^{AB1} - a_{ijAB}(x, z)z)\rho_{AB}. \end{aligned} \quad (20.3)$$

This formula may be used for analysis of the local strength of plates, local stability of the constitutive elements of plate, etc. The effective rigidities of the plate are computed in accordance with the formulas (Caillerie, 1984; Kohn and Vogelius, 1984)

$$\begin{aligned} S_{\alpha\beta AB}^{\nu+\mu} = & \frac{1}{|PrP_3|} \int_{P_3} (a_{\alpha\beta kl}(\mathbf{y})N_{k,l}^{AB\nu} + (-1)^\nu z^\nu a_{ijAB}(\mathbf{y})(-1)^\mu z^\mu d\mathbf{y} = \\ & \frac{1}{L} \int_P (a_{\alpha\beta k\delta}(x, z)N_{k,\delta}^{AB\nu} + (-1)^\nu z^\nu a_{ijAB}(x, z))(-1)^\mu z^\mu dx dz. \end{aligned} \quad (20.4)$$

2-D PC $P = [0, L] \times [-h, h]$ is projection PrP_3 of 3-D PC P_3 on Oxz -plane; $|PrP_3| = L \times 1$; L is the width of the 2-D periodicity cell P ; Γ^+ and Γ^- are the top and the bottom of the PC P , correspondingly; $\Gamma = \Gamma^- \cup \Gamma^+$.

One can conclude that the functions $N^{AB\mu}$ are the key to the analysis of the macro and microscopic properties of the inhomogeneous plate.

The homogenization theory itself provides us with no information about the solution to the PCP (20.2). One can see that the PCP (20.2) is a special type of 3-D elasticity theory problem, which is the subject of the elasticity theory. It would be reasonable to regard the PCP as the point of torch transfer from the homogenization theory to the elasticity theory. In particular, it would be reasonable to apply the methods developed in the elasticity theory to the analysis of PCP.

20.2 Reduction of 3-D PCP (20.2) to 2-D problems

Although the dimension reduction procedures have a longstanding history, the first work (to the best knowledge of the authors) devoted to the dimension reduction in the bending problem for the 3-D elastic body of the periodic structure is in Grigolyuk et al (1991). Grigolyuk et al (1991) was devoted to the bending of an elastic layer with the periodic systems of tunnel cuts. Grigolyuk et al (1991) used the double periodic function technique, thus treated the body as a layer of “infinite” thickness. It means that Grigolyuk et al (1991) is not the case of the plate, which thickness is small in the original variables \mathbf{x} or finite in the fast variables $\mathbf{y} = \mathbf{x}/\varepsilon$. The results in Grigolyuk et al (1991) can be used to predict the SSS inside the plate, but not near-surface phenomena. Do not confuse the dimension reductions in Grigolyuk et al (1991) and one discussed in this paper with the traditional dimensional reduction in the plane of the plate (Love, 2013). The dimensional reduction discussed in this paper is based on the transition to the problems on the cross-section of the plate.

Our starting point is the PCP (20.2) of the homogenization theory as applied to thin plates. The PC P is a cylinder parallel to the Oy -axis, see Fig.20.1, and the elastic constants a_{ijkl} do not depend on the variable y . In this case, the solution to

the problem (20.2) does not depend on y and has the form $\mathbf{N}^{AB\mu} = \mathbf{N}^{AB\mu}(x, z)$. Substituting into (20.2), we arrive at the following 2-D PCP:

$$\begin{cases} (a_{i\alpha k\beta}(x, z)N_{k,\beta}^{AB\mu} + (-1)^\mu a_{i\alpha AB}(x, z)z^\mu)_{,\alpha} = 0 \text{ in } P, \\ (a_{i\alpha k\beta}(x, z)N_{k,\beta}^{AB\mu} + (-1)^\mu a_{i\alpha AB}(x, z)z^\mu)n_\alpha = 0 \text{ on } \Gamma, \\ \mathbf{N}^{AB\mu}(x, z) \text{ is periodic in } x. \end{cases} \quad (20.5)$$

Hereafter $\alpha, \beta=1,3; i,k=1,2,3; AB=11, 22, 12,21$.

In the equations (20.5)

$$\begin{aligned} & a_{i\alpha k\beta}(x, z)N_{k,\beta}^{AB\mu} + (-1)^\mu a_{i\alpha AB}(x, z)z^\mu = \\ & a_{i\alpha\theta\beta}(x, z)N_{\theta,\beta}^{AB\mu} + a_{i\alpha 2\beta}(x, z)N_{2,\beta}^{AB\mu} + (-1)^\mu a_{i\alpha AB}(x, z)z^\mu. \end{aligned} \quad (20.6)$$

The boundary-value problem (20.5) decomposes into several 2-D problems. The form of the 2-D problems depends on the index i in (20.5). For $i = 2$, the original problems are reduced to scalar 2-D problems. For $i = \xi = 1, 3$ the original problems are reduced to 2-D elasticity or thermoelasticity problems.

For this reason, we consider problem (20.2) for $i = 2$ and $i = \xi = 1, 3$, separately. In this paper, we pay the main attention to the case $i = 2$, which leads to the analogs of the anti-plane elasticity problem. The case $i = \xi = 1, 3$, leads to the analogs of the planar elasticity problem.

Problem (20.2) with index $i = 2$. We assume the fibers and matrix are made of isotropic materials. It is convenient to save the notations a_{ijkl} for the elastic constants in our analysis. In special cases below, we will use the technical constants, see formulas (20.31) below.

In the case, under consideration $a_{2\alpha\theta\beta} = 0, a_{2\alpha AB} = 0$ (Love, 2013) and expression in (20.6) takes the form ($\alpha = 1, 3$)

$$\begin{aligned} & a_{2\alpha\theta\beta}(x, z)N_{\theta,\beta}^{AB\mu} + a_{2\alpha 2\beta}(x, z)N_{2,\beta}^{AB\mu} + (-1)^\mu a_{i\alpha AB}(x, z)z^\mu = \\ & a_{2\alpha 2\alpha}(x, z)N_{2,\alpha}^{AB\mu} + \begin{cases} (-1)^\mu a_{2121}(x, z)z^\mu \text{ if } AB = 12, 21, \\ 0 \text{ else.} \end{cases} \end{aligned} \quad (20.7)$$

By virtue of (20.7), the solution to (20.2) $N_2^{AB\mu}(x, z) = 0$ if $AB \neq 12, 21$. Only $N_2^{AB\mu}(x, z) \neq 0$. This is the case of in-plane shift (if $\mu = 0$) or torsion (if $\mu = 1$). The in-plane shift is also called anti-plane deformation (Love, 2013).

The problem for $N_2^{21\mu}(x, z)$ takes the form

$$\begin{cases} (a_{2\alpha 2\alpha}(x, z)N_{2,\alpha}^{21\mu} + (-1)^\mu a_{2121}(x, z)z^\mu \delta_{\alpha 1})_{,\alpha} = 0 \text{ in } P, \\ (a_{2\alpha 2\alpha}(x, z)N_{2,\alpha}^{21\mu} + (-1)^\mu a_{2121}(x, z)z^\mu \delta_{\alpha 1})n_\alpha = 0 \text{ on } \Gamma, \\ N_2^{21\mu}(x, z) \text{ periodic in } x. \end{cases} \quad (20.8)$$

It is convenient to eliminate the "mass" and "surface" forces in (20.8). It may be done if there exists a function w , such that ($\nu = 0, 1$)

$$a_{2\delta 2\delta}(x, z)w_{,\delta} = (-1)^\mu a_{2121}(x, z)z^\mu. \quad (20.9)$$

For $\delta = 2$ and $\delta = 2$, we obtain from (20.9) $a_{2\delta 2\delta}(x, z)w_{,1} = (-1)^\mu a_{2121}z^\mu$ and $a_{2\delta 2\delta}w_{,2} = (-1)^\mu a_{2121}(x, z)z^\mu$, correspondingly. From these equalities, we obtain the following system of differential equations

$$w_{,1} = (-1)^\mu, w_{,3} = 0. \quad (20.10)$$

In-plane shift ($\mu = 0$). For $\mu = 0$, the system (20.9) takes the form $w_{,1} = 1, w_{,3} = 0$. The solution to this system is $w(x, z) = x$. Introduce function

$$M(x, z) = N_2^{120}(x, z) + x,$$

and write (20.8) in the form of a boundary-value problem without "mass" and "surface" forces:

$$\begin{cases} (a_{2\alpha 2\alpha}(x, z)M_{,\alpha})_{,\alpha} = 0 \text{ in } P, \\ a_{2\alpha 2\alpha}(x, z)M_{,\alpha}n_\alpha = 0 \text{ on } \Gamma, \\ M(x, z) - x \text{ periodic in } x. \end{cases} \quad (20.11)$$

The problem (20.11) is the anti-plane elasticity theory problem.

After some algebra, we obtain the following formulas for the local stresses:

$$\sigma_{ij} = a_{ij2\alpha}(x, z)N_{2,\alpha}^{120} + a_{ij21}(x, z) = a_{ij2\alpha}(x, z)M_{,\alpha}, \quad (20.12)$$

and the homogenized shift rigidity

$$\begin{aligned} S_{2121}^0 &= \frac{1}{L} \int_P (a_{212\alpha}(x, z)N_{2,\alpha}^{210} + a_{2121}(x, z)) dx dz = \\ &\quad \frac{1}{L} \int_P (a_{212\alpha}(x, z)M_{,\alpha}) dx dz, \\ S_{2121}^1 &= \frac{1}{L} \int_P (a_{212\alpha}(x, z)N_{2,\alpha}^{210} + a_{2121}(x, z)) z dx dz = \\ &\quad \frac{1}{L} \int_P (a_{212\alpha}(x, z)M_{,\alpha} z) dx dz. \end{aligned} \quad (20.13)$$

The local stresses (20.12) and the homogenized shift rigidity (20.13) depend on the elastic constants of the composite plate.

These formulas may be used for the analysis of the local strength of the plates, local stability of the constitutive elements of the plate, etc. The effective rigidities of the plate are computed in accordance with the formulas (Caillerie, 1984; Kohn and Vogelius, 1984).

Torsion ($\mu = 1$). In this case, we meet a problem, which has no analog in the classical theory of elasticity or classical plate theory.

For $\mu = 1$, the system (20.10) takes form $w_{,1} = -z, w_{,3} = 0$. This system is not integrable. Really, the necessary integrability condition (Love, 2013) is not satisfied for this system because $w_{,13} = -z_{,3} = -1 \neq w_{,31} = 0$.

For $\mu = 1$, (20.8) takes the form

$$\begin{cases} (a_{2\alpha 2\alpha}(x, z)N_{2,\alpha}^{211} - a_{2121}(x, z)z\delta_{\alpha 1}),_{\alpha} = 0 \text{ in } P, \\ (a_{2\alpha 2\alpha}(x, z)N_{2,\alpha}^{211} - a_{2121}(x, z)z\delta_{\alpha 1})n_{\alpha} = 0 \text{ on } \Gamma, \\ N^{211}(x, z) \text{ is periodic in } x. \end{cases} \quad (20.14)$$

To write (20.14) in compact form, we introduce function as

$$\varphi_{,3} = a_{2121}(x, z)(N_{2,1}^{211} - z), \varphi_{,1} = -a_{2323}(x, z)N_{2,3}^{211}. \quad (20.15)$$

The function $\varphi(x, z)$ introduced by (20.15) is similar to the conjugate function (Sedov, 1971). The equality

$$\varphi_{,31} - \varphi_{,13} = (a_{2121}(x, z)(N_{2,1}^{211} - z))_{,1} + (a_{2323}(x, z)N_{2,3}^{211})_{,3} = 0, \quad (20.16)$$

follows from (20.14). This equality justifies the existence of the function $\varphi(x, z)$.

Express $N_{2,1}^{211}(x, z)$ from (20.15)

$$N_{2,1}^{211} = \frac{1}{a_{2121}(x, z)}\varphi_{,3} + z, N_{2,3}^{211} = -\frac{1}{a_{2323}(x, z)}\varphi_{,1}. \quad (20.17)$$

Differentiation of (20.17) yields

$$0 = N_{2,13}^{211} - N_{2,31}^{211} = \left(\frac{1}{a_{2121}(x, z)}\varphi_{,3} + z\right)_{,3} + \left(\frac{1}{a_{2323}(x, z)}\varphi_{,1}\right)_{,1}. \quad (20.18)$$

Taking into account that for the isotropic materials $a_{2121} = a_{2323}$, we obtain

$$\left(\frac{1}{a_{2121}(x, z)}\varphi_{,3}\right)_{,3} + \left(\frac{1}{a_{2121}(x, z)}\varphi_{,1}\right)_{,1} = 1. \quad (20.19)$$

With the use of the function $\varphi(x, z)$, the boundary conditions on the top and bottom boundaries Γ^+ and Γ^- (20.8) can be written as

$$\begin{aligned} (a_{2121}(x, z)N_{2,1}^{21\nu} - a_{2121}(x, z)zn_1 + a_{2323}(x, z)N_{2,3}^{21\nu}n_3 = \\ \varphi_{,3}n_1 - \varphi_{,1}n_3 = \frac{\partial\varphi}{\partial s} = 0 \text{ on } \Gamma, \end{aligned} \quad (20.20)$$

where $\partial\varphi/\partial s$ is the derivative along the boundary Γ^+ or Γ^- . Because of (20.20), the function $\varphi(x, z)$ takes constant values on the top and bottom boundaries Γ^+ and Γ^- :

$$\varphi(x, z) = \text{const}_{\pm} \text{ on } \Gamma^{\pm}. \quad (20.21)$$

Without loss of generality, we can assume that $\varphi(x, z) = 0$ at the bottom boundary Γ^- .

Integrating the first equality in (20.15) over z from $-h$ to h , we have

$$\varphi(x, L) = \varphi(x, -L) + \int_{-h}^h a_{2121}(x, z)(N_{2,1}^{211} - z)dz. \tag{20.22}$$

Integrating the (20.23) over x from 0 to L , we have

$$\varphi(-h, L)L = \varphi(-h, -L)L + \int_P a_{2121}(x, z)(N_{2,1}^{211} - z)dx dz. \tag{20.23}$$

Writing (20.23), we take into account that $\varphi(x, L)$ and $\varphi(x, -L)$ are constants.

Multiplying (20.14) by x and integrating by parts, we have

$$\int_P a_{2121}(x, z)(N_{2,1}^{211} - z)dx dz = \int_P \varphi_{,3} dx dz.$$

As the result

$$S_{2121}^1 = \frac{1}{L} \int_P a_{2121}(x, z)(N_{2,1}^{211} - z)dx dz = \frac{1}{L} \int_P \varphi_{,3} dx dz. \tag{20.24}$$

Comparing (20.23) and (20.24), we find that the RHP (20.23) is equal to

$$\varphi(h, -L) = \phi(-h, -L) + S_{2121}^1.$$

We have assumed that $\varphi(x, z) = 0$ on the bottom boundary Γ^+ , in particular, $\varphi(-h, -L) = 0$ and $\varphi(x, z) = S_{2121}^1$ on the top boundary Γ^+ . As a result, we arrive at the following boundary value problem:

$$\begin{cases} (\frac{1}{a_{2121}(x, z)}\varphi_{,1})_{,1} + (\frac{1}{a_{2121}(x, z)}\varphi_{,3})_{,3} = 1 \text{ in } P, \\ \varphi = 0 \text{ on } \Gamma^-, \varphi = S_{2121}^1 \text{ on } \Gamma^+, \\ \varphi(x, z) \text{ is periodic in } x. \end{cases} \tag{20.25}$$

The problem (20.25) involves the asymmetric effective stiffness S_{2121}^1 of the plate, which has been expressed in (20.24) through the solution φ to the BVP (20.25). The problem (20.25) with the condition (20.24) has a not usual form. This is lucky for us that the asymmetric effective stiffness S_{2121}^1 also may be computed by using the second formula in (20.13). As a result, we have the problem (20.25) with S_{2121}^1 known after the BVP (20.11) be solved.

The local stresses, corresponding to the case under consideration, are expressed in the form

$$\sigma_{ij} = a_{ij2\alpha}(x, z) + a_{ij21}(x, z)z = \frac{a_{ij21}(x, z)}{a_{2121}(x, z)}(\varphi_{,3} - \varphi_{,1}),$$

and the homogenized torsion rigidity is expressed in the form

$$S_{2121}^2 = - \int_P (\varphi_{,3} - \varphi_{,1})z dx dz. \tag{20.26}$$

Problem (20.2) with index $i = \xi = 1, 3$. Deformation perpendicular to the fibers. In this case, $a_{\xi\alpha 2\beta}(\mathbf{y}) = 0$ and expression in (20.6) takes the form $(\alpha, \beta, \theta, \xi = 1, 1)$.

In the equations (20.5)

$$\begin{aligned} & a_{i\alpha k\beta}(\mathbf{y})N_{k,\beta}^{AB\mu} + (-1)^\mu a_{i\alpha AB}(x, z)z^\mu = \\ & a_{\xi\alpha\theta\beta}(x, z)N_{\theta,\beta}^{AB\mu} + a_{\xi\alpha 2\beta}(x, z)N_{2,\beta}^{AB\mu} + (-1)^\mu a_{\xi\alpha AB}(x, z)z^\mu = \\ & a_{\xi\alpha\theta\beta}(x, z)N_{\theta,\beta}^{AB\mu} + (-1)^\mu a_{\xi\alpha AB}(x, z)z^\mu. \end{aligned} \quad (20.27)$$

Here $AB = 11, 22, 12, 21$. Then the PCP (20.5) takes the form

$$\begin{cases} (a_{\xi\alpha\theta\beta}(x, z)N_{\theta,\beta}^{AB\mu} + (-1)^\mu a_{\xi\alpha AB}(x, z)z^\mu)_{,\alpha} = 0 \text{ in } P, \\ a_{\xi\alpha\theta\beta}(x, z)N_{\theta,\beta}^{AB\mu} + (-1)^\mu a_{\xi\alpha AB}(x, z)z^\mu n_\alpha = 0 \text{ on } \Gamma, \\ (N_1^{AB\mu}, N_3^{AB\mu})(x, z) \text{ periodic in } x. \end{cases} \quad (20.28)$$

Note that $a_{\xi\alpha 12} = 0$ and $a_{\xi\alpha 21} = 0$ for $i = \xi = 1, 3$, then $(N_1^{21\mu}, N_3^{21\mu})=0$ and $(N_1^{12\mu}, N_3^{12\mu})=0$. The problem (20.28) is non-trivial for $AB = 11, 22$.

In some cases, (20.28) for $AB = 11, 22$ may be transformed into problems without free terms. We shall check if it is possible to represent the free term $(-1)^\mu a_{\xi\alpha AB}(x, z)z^\mu$ in (20.28) in the form $(-1)^\mu a_{\xi\alpha\theta\beta}(x, z)e_{\theta\beta}^{AB\mu}$ with the strains $e_{\theta\beta}^{AB\mu} = v_{\theta,\beta}^{AB\mu}$ corresponding proper displacements $\mathbf{v}_{\theta,\beta}^{AB\mu}$ ($\mu=0, 1$):

$$a_{\xi\alpha\theta\beta}(x, z)v_{\theta,\beta}^{AB\mu} = a_{\xi\alpha AB}(x, z)z^\mu. \quad (20.29)$$

Index $AB = 22$. Tension and bending along the fibers. Equation (20.29) takes the form $a_{\xi\alpha\theta\beta}(x, z)e_{\theta,\beta} = a_{\xi\alpha 22}(x, z)z^\mu$. In the coordinate-wise form, it is

$$\begin{aligned} & a_{1111}e_{11} + a_{1133}e_{33} = -a_{1122}z^\mu, \\ & a_{3311}e_{11} + a_{3333}e_{33} = -a_{1122}z^\mu, \\ & a_{1313}e_{13} = 0, a_{1111}e_{31} = 0. \end{aligned} \quad (20.30)$$

Write the elastic constants in terms of Young's E modulus and Poisson's ratio ν (Love, 2013)

$$\begin{aligned} & a_{1111} = a_{1111} = \frac{E(1-\nu)}{(1+\nu)(1-2\nu)}, \\ & a_{1133} = a_{3311} = a_{1122} = a_{3322} \frac{E(1-\nu)}{(1+\nu)(1-2\nu)}. \end{aligned} \quad (20.31)$$

In this case, the first two equations in (20.30) take the form

$$\begin{aligned} & (1-\nu)e_{11} + \nu e_{33} = -\nu(x, z)z^\mu, \\ & \nu e_{11} + (1-\nu)e_{33} = -\nu(x, z)z^\mu. \end{aligned} \quad (20.32)$$

The solution to (20.32) is

$$e_{11} = e_{33} = -\nu(x, z)z^\mu. \quad (20.33)$$

Taking into account that $e_{13} = e_{31} = 0$, we arrive at the following system:

$$\frac{\partial v_1}{\partial x} = -\nu(x, z)^\mu, \quad \frac{\partial v_3}{\partial z} = -\nu(x, z)^\mu, \quad \frac{\partial v_1}{\partial z} + \frac{\partial v_3}{\partial x} = 0. \quad (20.34)$$

Generally, the compatibility condition (Love, 2013) is not satisfied for the system (20.34) for arbitrary $\nu(x, z)$.

This incompatibility indicates that a simple transfer from 3-D to the 2-D problem is impossible in the general case.

The case $\nu(x, z) = const$. If $\nu(x, z) = \nu = const$, the system (20.34) is compatible. In this case, the solution to (20.34) may be obtained in the explicit form. For $\mu = 0$, $v_1 = -\nu x$ and $v_3 = -\nu z$.

Introduce $M_1^{22\mu} = N_1^{22\mu} + v_1$ and $M_2^{22\mu} = N_2^{22\mu} + v_2$. By using these functions, we can transform the problem (20.28) to the following:

$$\begin{cases} (a_{\xi\alpha\theta\beta}(x, z)M_{\theta,\beta}^{22\mu})_{,\alpha} = 0 \text{ in } P, \\ a_{\xi\alpha\theta\beta}(x, z)M_{\theta,\beta}^{22\mu}n_\alpha = 0 \text{ in } \Gamma, \\ [M_1^{22\mu}]_x = -\nu z^\mu [x]_x, [M_3^{22\mu}]_x = 0, \end{cases} \quad (20.35)$$

where $\llbracket \cdot \rrbracket_x$ means the jump of the function value at the opposite sides of the PC in the direction Ox .

The case $\nu(x, z) \neq const$. In this general case, we can transform the problem (20.28) into a thermoelasticity problem.

In (20.28)

$$a_{\xi\alpha\theta\beta}(x, z)N_{\theta,\beta}^{AB\mu} + (-1)^\mu a_{\xi\alpha AB}(\mathbf{y})z^\mu = a_{\xi\alpha\theta\beta}(x, z)N_{\theta,\beta}^{AB\mu} + a_{\xi\alpha\theta\beta}e_{\theta\beta} = a_{\xi\alpha\theta\beta}(x, z)(N_{\theta,\beta}^{AB\mu} + e_{\theta\beta}),$$

where $e_{\theta\beta}$ are given by (20.33). Then (20.28) may be written in the form

$$\begin{cases} (a_{\xi\alpha\theta\beta}(x, z)(N_{\theta,\beta}^{AB\mu} + e_{\theta\beta}))_{,\alpha} = 0 \text{ in } P, \\ a_{\xi\alpha\theta\beta}(x, z)(N_{\theta,\beta}^{AB\mu} + e_{\theta\beta})n_\alpha = 0 \text{ on } \Gamma, \\ (N_1^{AB\mu}, N_3^{AB\mu})(x, z) \text{ periodic in } x. \end{cases} \quad (20.36)$$

Problem (20.36) is the thermoelasticity problem with the coefficients of thermal expansion $e_{\theta\beta}$. Since $e_{11} = e_{22} = -\nu(x, z)z^\mu$ and $e_{13} = e_{31} = 0$, this tensor is isotropic. For $\nu = 1$, coefficients $e_{11} = e_{22} = -\nu(x, z)z$, where $\nu(x, z)$ takes constant values in the fibers and the matrix. Some ANSYS APDL programming is required to input such kind coefficients. The local stresses are

$$\sigma_{\xi\alpha} = a_{\xi\alpha\theta\beta}(x, z)(N_{\theta,\beta}^{AB\mu} + e_{\theta\beta})n_\alpha. \quad (20.37)$$

The effective rigidities are

$$S_{\xi\alpha\theta\beta}^{\mu+\nu} = \frac{1}{L} \int_P (a_{\xi\alpha\theta\beta}(x, z) N_{\theta,\beta}^{AB\mu} + a_{\xi\alpha AB}(x, z)) z^\nu dx dy = \\ \frac{1}{L} \int_P (a_{\xi\alpha\theta\beta}(x, z) (N_{\theta,\beta}^{AB\mu} + e_{\theta\beta}(x, z))) z^\nu dx dy.$$

Index $AB = 11$. Tension and bending perpendicular to the fibers. In this case, we arrive at the problem

$$\frac{\partial v_1}{\partial x} = -z^\mu, \quad \frac{\partial v_3}{\partial z} = 0, \quad \frac{\partial v_1}{\partial z} + \frac{\partial v_3}{\partial x} = 0. \quad (20.38)$$

The problem (20.38) may be solved in the explicit form. Its solution is

$$v_1 = -x, v_1 = 0 \text{ for } \mu = 0,$$

$$v_1 = -xz, v_1 = x^2/2 \text{ for } \mu = 1.$$

Introduce $M_1^{11\mu} = N_1^{11\mu} + v_1$ and $M_2^{11\mu} = N_2^{11\mu} + v_2$. By using the functions, we can transform the problem (20.28) to the following:

$$\begin{cases} (a_{\xi\alpha\theta\beta}(x, z) M_{\theta,\beta}^{11\mu})_{,\alpha} = 0 \text{ in } P, \\ a_{\xi\alpha\theta\beta}(x, z) M_{\theta,\beta}^{11\mu} n_\alpha = 0 \text{ on } \Gamma, \\ [M_1^{11\mu}]_x = -\nu z^\mu [x]_x, [M_3^{11\mu}]_x = 0. \end{cases} \quad (20.39)$$

Index $AB = 12, 21$. Shift/torsion. For $AB = 12, 21$, equation (20.29) takes the form $a_{\xi\alpha\theta\beta} e_{\theta,\beta} = a_{\xi\alpha 12} z^\mu = 0$, $\xi, \alpha = 1, 3$. Its solution is $e_{\theta\beta} = 0$. Then $v_1 = v_3 = 0$ and solution to (20.28) is trivial.

20.3 Numerical Computations

In this section, we present several numerical solutions interesting from mechanic's point of view. In our computations the fibers Young's modulus $E=170\text{GPa}$ and Poisson's ratio $\nu=0.3$; and the matrix $E=2\text{GPa}$ and Poisson's ratio $\nu=0.36$. These values correspond to carbon/epoxy composite (Agarwal et al, 2017).

The computer program was developed by using the APDL programming language (Thompson and Thompson, 2017). The finite elements PLANE183 are used for the fibers and the matrix, the characteristic size of the finite elements is 0.03, the total number of finite elements is about 10000.

Figure 20.2 displays the solution to the PCP corresponding to the bending in the direction perpendicular to the fibers. We have observed edge effects near the top and the bottom surfaces of the plate. The edge effect zone thickness is less than the thickness of one structural layer (fiber + surrounding matrix). To the best knowledge of the authors, such kind edge effect was not reported before.

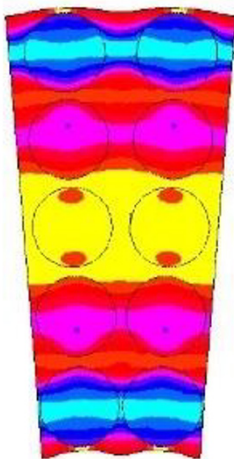


Fig. 20.2 PC formed of two adjacent PCs of 5-layer fiber-reinforced plate

If the plate is thick, these top/bottom edge layers do not influence the effective rigidity of the plate. But they influence the local SSS, thus, the strength of the plate.

An analysis of Fig.20.2 leads to the conclusion that the found edge effect does not lead to a stress concentration in the edge effect zone. In Fig.20.2, we observe the von Mises stress decrease in the edge effect zone. The stress concentration between the fibers is the result of the dense packing on the fibers (Flaherty and Keller, 1973; Kolpakov and Kolpakov, 2009; Kang and Yu, 2020; Kolpakov, 2007; Rakin, 2014).

One result of the edge effect is the wrinkling of the top/bottom boundaries of the plate. The wrinkling is especially good seen for the PCP formed of two adjacent PCs, see Fig.20.2. The wrinkling may influence the plate-to-surrounding media interaction. The various kinds of wrinkling were discussed in the literature on the composite materials (Boisse et al, 2018, 2021; Giorgio et al, 2018). The authors find no analogs between the wrinkling effects describer early and the wrinkling described in this paper.

The top/bottom edge effect (including wrinkling) described above never occurs in uniform plates or plates made of uniform layers. The solutions to the PCPs for the homogeneous plates and plates made of uniform layers are well known and may be easily computed.

20.4 Conclusion

We developed a procedure of transition from the original 3-D PCP (20.2) in a thin domain with a system of parallel cylindrical inhomogeneities to 2-D boundary-value problems. We arrive at 2-D boundary-value problems (20.11) and (20.25)

corresponding to the shift and torsion of the plate. These problems have the forms of the anti-plane elasticity problems with and without mass forces (Laplace-type and Poisson-type problems). 2-D boundary-value problem (20.25) is a new problem. 2-D boundary-value problems (20.35) and (20.36) correspond to the tension/bending. They have the forms of planar elasticity and thermo-elasticity problems.

Our numerical analysis of the obtained 2-D problems demonstrates the existence of boundary layers near the top and bottom surfaces of the plate. The boundary layer thickness is less than the thickness of one structural layer (the diameter of the fiber + the thickness of the surrounding matrix).

One of the manifestations of the found boundary layer is the wrinkling of the top and the bottom of the plate. To the best knowledge of the authors, such kind boundary layers and the wrinkling effect did not refer earlier. Note that the boundary layers and the wrinkling effect described in this paper cannot occur in uniform plates or plates made of homogeneous layers.

References

- Agarwal BD, Broutman LJ, Chandrashekhara K (2017) Analysis and performance of fiber composites. John Wiley & Sons, Hoboken, NJ
- Altenbach J, Altenbach H, Eremeyev VA (2010) On generalized Cosserat-type theories of plates and shells: a short review and bibliography. *Archive of Applied Mechanics* 80(1):73–92
- Annin BD, Kolpakov AG, Rakin SI (2017) Homogenization of corrugated plates based on the dimension reduction for the periodicity cell. In: Altenbach H, et al (eds) *Problem Mechanics for Materials and Technologies*, Springer, pp 30–72
- Barchiesi E, Khakalo S (2019) Variational asymptotic homogenization of beam-like square lattice structures. *Mathematics and Mechanics of Solids* 24(10):3295–3318
- Boisse P, Colmars J, Hamila N, Naouar N, Steer Q (2018) Bending and wrinkling of composite fiber preforms and prepregs. A review and new developments in the draping simulations. *Composites Part B: Engineering* 141:234–249
- Boisse P, Huang J, Guzman-Maldonado E (2021) Analysis and modeling of wrinkling in composite forming. *Journal of Composites Science* 5(3):81–95
- Caillerie D (1982) Plaques élastiques minces à structure périodique de période et d'épaisseur comparables. *Comptes Rendus de l'Académie des Sciences de Paris, série II* 294:159–162
- Caillerie D (1984) Thin elastic and periodic plates. *Mathematical Methods in the Applied Sciences* 6(1):159–191
- Drygaś P, Gluzman S, Mityushev V, Nawalaniec W (2019) *Applied Analysis of Composite Media: Analytical and Computational Results for Materials Scientists and Engineers*. Woodhead Publishing
- Flaherty JE, Keller JB (1973) Elastic behavior of composite media. *Communications on Pure and Applied Mathematics* 26(4):565–580
- Franciosi P, Spagnuolo M, Salman OU (2019) Mean Green operators of deformable fiber networks embedded in a compliant matrix and property estimates. *Continuum Mechanics and Thermodynamics* 31(1):101–132
- Giorgio I, Harrison P, dell'Isola F, Alsayednoor J, Turco E (2018) Wrinkling in engineering fabrics: a comparison between two different comprehensive modelling approaches. *Proceedings of the Royal Society A: Mathematical, Physical and Engineering Sciences* 474(2216):20180,063
- Gluzman S, Mityushev V, Nawalaniec W (2018) *Computational analysis of structured Media*. Academic Press, Amsterdam

- Grigolyuk EI, Fil'Shtinskii LA (1966) Elastic equilibrium of an isotropic plane with a doubly periodic system of inclusions. *Soviet Applied Mechanics* 2(9):1–5
- Grigolyuk EI, Fil'shtinskij LA (1992) Periodic piecewise homogeneous elastic structures. Nauka, Moscow
- Grigolyuk ÉI, Kovalev YD, Fil'Shtinskii LA (1991) Bending of a layer weakened by through tunnel cuts. In: *Doklady Akademii Nauk SSSR*, vol 317, pp 51–53
- Kang H, Yu S (2020) A proof of the Flaherty–Keller formula on the effective property of densely packed elastic composites. *Calculus of Variations and Partial Differential Equations* 59(1):1–13
- Kohn RV, Vogelius M (1984) A new model for thin plates with rapidly varying thickness. *International Journal of Solids and Structures* 20(4):333–350
- Kolpakov AA (2007) Numerical verification of the existence of the energy-concentration effect in a high-contrast heavy-charged composite material. *Journal of Engineering Physics and Thermophysics* 80(4):812–819
- Kolpakov AA, Kolpakov AG (2009) Capacity and transport in contrast composite structures: Asymptotic analysis and applications. CRC Press, Boca Raton, FL
- Kolpakov AA, Kolpakov AG (2020) On the effective stiffnesses of corrugated plates of various geometries. *International Journal of Engineering Science* 154:103,327
- Love AEH (2013) A treatise on the mathematical theory of elasticity. Cambridge university press
- Lu Jk (1995) Complex variable methods in plane elasticity, vol 22. World Scientific, Singapore
- Mityushev V, Rogosin SV (2000) Constructive Methods for Linear and Nonlinear Boundary Value Problems for Analytic Function Theory. Chapman Hall/CRC, Boca Raton, FL
- Placidi L, El Dhaba AR (2017) Semi-inverse method à la Saint-Venant for two-dimensional linear isotropic homogeneous second-gradient elasticity. *Mathematics and Mechanics of Solids* 22(5):919–937
- Rakin SI (2014) Numerical verification of the existence of the elastic energy localization effect for closely spaced rigid disks. *Journal of Engineering Physics and Thermophysics* 87(1):246–253
- Sedov LI (1971) A course in continuum mechanics. Wolters-Noordhoff Groningen, Netherlands
- Sendeckyj GP (1974) Elastic behavior of composites. *Composite materials* 2:45–83
- Thompson MK, Thompson JM (2017) ANSYS mechanical APDL for finite element analysis. Butterworth-Heinemann, Oxford
- Wang FF, Dai HH, Giorgio I (2021) A numerical comparison of the uniformly valid asymptotic plate equations with a 3D model: Clamped rectangular incompressible elastic plates. *Mathematics and Mechanics of Solids* p doi: 10.1177/10812865211025583
- Yang H, Abali BE, Timofeev D, Müller WH (2020) Determination of metamaterial parameters by means of a homogenization approach based on asymptotic analysis. *Continuum mechanics and thermodynamics* 32(5):1251–1270



Chapter 21

Semi-Automatic Method of Stent Development for Hemodynamic Simulations in Patient Coronary Arteries with Disease

Luís Matias, Catarina Ferreira de Castro, Carlos Conceição António,
Luísa Costa Sousa, Sónia Isabel Silva Pinto

Abstract Atherosclerosis contributes to the development cardiovascular diseases, the leading cause of death in the world. Complications arising from atherosclerosis, such as stenosis (an abnormal narrowing of a blood vessel, which can lead to its clogging) exacerbate the risk of cardiovascular disorders. Besides aging, sedentary lifestyle, unhealthy diet and tobacco consumption are among the risk factors which increase the likelihood of developing atherosclerosis overtime. One way to prevent stenosis development, due to atherosclerosis, is by inserting stents inside the relevant blood vessels. Stents are small metal tubes which can be expanded to keep the passageway open and improve blood flow, essentially resulting in an arterioplasty. The achievement of an accurate stent, such as accurate mesh, length and other features, specific for a patient coronary artery with atherosclerosis, is still a challenge in clinical practice. Therefore, after developing numerical based coding solution that simulate hemodynamic conditions as close as possible to reality, the goal of the present work is to develop a semi-automatic method to create a stent in the stenotic location of patient-specific coronary arteries. As far as we know, no authors have been able to quickly and effectively place the stent in a model of a patient's artery, which is subject to the complex geometry of the coronary such as curvature, tortuosity, etc. The impact of stent length was considered, in order to verify which is the ideal, for a patient case, avoiding restenosis occurrence. After hemodynamic simulations in the model artery with stenosis and in the model artery with stent, it is observed that strong atherosusceptible regions just after the stenosis are eliminated after stent insertion.

L. Matias

Engineering Faculty, University of Porto, Rua Dr. Roberto Frias, s/n, 4200 – 465 Porto, Portugal
e-mail: up201502891@edu.fe.up.pt

C. F. Castro, C. C. António, L. C. Sousa, S. I. S. Pinto

Engineering Faculty, University of Porto, Rua Dr. Roberto Frias, s/n, 4200 – 465 Porto, Portugal
Institute of Science and Innovation in Mechanical and Industrial Engineering, LAETA-INEGI, Rua Dr. Roberto Frias, 400, 4200 – 465 Porto, Portugal
e-mail: ccastro@fe.up.pt, cantonio@fe.up.pt, lcsousa@fe.up.pt, spinto@fe.up.pt

Keywords: Stent development · Hemodynamic simulations · Coronary arteries · Atherosclerosis

21.1 Introduction

Cardiovascular diseases have been one of the main causes of death in developed countries (Mozaffarian et al, 2015). The clinical practice highlights that specific locations in the human circulatory system, such as arterial curvatures and bifurcations, are sensitive to the development of cardiovascular diseases such as atherosclerosis, caused by a stenosis – accumulation of lipoproteins, calcium and other (fat) substances in the arterial wall. The stenosis blocks the normal circulation of blood flow. Therefore, in clinical practice, a stent is inserted in the stenotic location of the artery for its enlargement. From there, the hemodynamics occurs in a best way.

The stent is an endoprosthesis composed by a metallic tube in a mesh format. According to Nikolic and Filipovic (2020), stents can be divided into three categories: (1) Method of Spread: balloon-expanding or self-expanding stents; (2) Coating: with or without drug coating; (3) Persistence in the body: permanent or bioabsorbable. As for materials, in balloon-expandable stents the most used is stainless steel 316L and in self-expanding stents, nitinol. Despite their ability to restore normal blood flow, stents have some limitations. The biggest obstacle encountered is restenosis. This, as the name implies, is the reappearance of stenosis in the stent area.

The hemodynamic simulation is an important and auxiliary tool for the prevention, diagnostic and treatment of cardiovascular diseases. Computed tomography images of coronary arteries can give information about the geometry of the artery and location and degree of the stenosis. However, they do not explain the hemodynamics with detail. Thus, for better assistance in research and clinical practice, a numerical tool to simulate the hemodynamics, as close as possible to the reality, is of extreme necessity. This numerical tool has been developed, recently, by the present authors (Pinho et al (2018); Pinho et al (2019), Pinto et al (2020)). The Simplified Phan-Thien/Tanner (sPTT) model implemented as an user-defined function (UDF), in Ansys® software, takes into account the viscoelastic property of blood (Bodnár et al (2011); Campo-Deaño et al (2013)). The sPTT model was achieved as efficient by Pinto et al (2020). The hemodynamic results using sPTT model were in accordance with the literature (Good et al, 2016). Moreover the arterial walls are assumed to be rigid. Another type of blood flow analysis is the fluid-structure interaction (FSI) which has into account the deformability of the arterial wall. It was concluded in Miranda et al (2020), that FSI requires more computational time and the results do not differ from the case where the arterial wall movement is neglected. Hemodynamic descriptors, based in the wall shear stress (WSS) are used to predict the areas of the arteries that are more susceptible to the appearance of stenosis (Miranda et al (2020); Pinto et al (2020)).

Regarding stent creation, David Chua et al (2003) and Gay et al (2006), modeled a crimped stent, uniquely in a straight cylindrical format, analyzed his expansion

with a balloon applying a radial force. Bonsignore (2010) starting with an unit cell, projected and embossed it to a cylinder obtaining a circular unit cell. Repeating that circular cell, he obtains the final crimped stent model. Using previous method, Hsiao et al (2012), Amin et al (2015), Wang et al (2019) and Chen et al (2019) analyzed the mechanical performance of different stent designs. Migliavacca et al (2007) studied the expansion and drug elution of a coronary stent in an ideal straight artery. Recently, Okereke et al (2021), using Bonsignore method, show a virtual testing approach for the development of 3D printable artery stents based on biomaterials. Besides the advances that these studies contribute for the cardiovascular engineering field, none of them have created a stent inside the complex geometry of a patient coronary artery.

Thus, going further than the available literature, the goal of the present work is to develop a semi-automatic method of an expanded stent creation in a patient-specific coronary artery with stenosis, in order to perform hemodynamic simulations in patients with stents. Then, using numerical simulation we can predict the hemodynamic performance of a stent in the main branch of a coronary artery.

21.2 Methodology

Computed tomography (CT) is becoming an emerging role in coronary ischemia diagnosis, by enabling a 3D visualization of arteries and their geometries, and even providing the means for identifying the presence of atheromatous plaque buildup, which constrains blood flow. When analyzed via computational fluid dynamics, the 3D models obtained from CT enable a more detailed study of the respective hemodynamics.

The following method makes it possible to place a stent in the damaged area of the artery for further hemodynamic analysis: (1) obtaining the three-dimension model of artery lumen from CT images, (2) designing stent and combine artery lumen with it (3) analyzing the 3D model obtained, using computational fluid dynamics (CFD). This method can be observed with more detail in Fig. 21.1.

For this study, it was selected a patient-specific case (male, with 55 years old) with atherosclerotic disease (degree of 50% stenosis) in the left circumflex artery (LCx) of the left coronary artery (LCA). DICOM images, obtained with CT by the Vila Nova de Gaia/Espinho (CHVNG/E) Hospital Center, were segmented, using MIMICS®, to obtain the contours of the LCA, Fig. 21.2. The patient subject to the study gave informed consent and the present research was approved by the local institutional ethics committee.

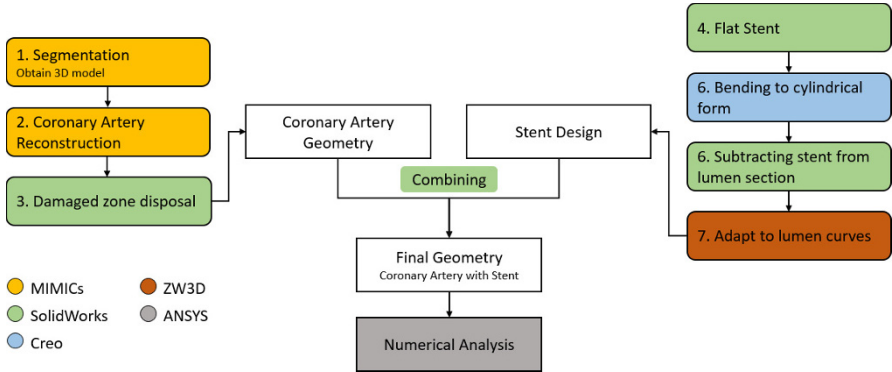


Fig. 21.1 Diagram of the semi-automatic method used with the software references.

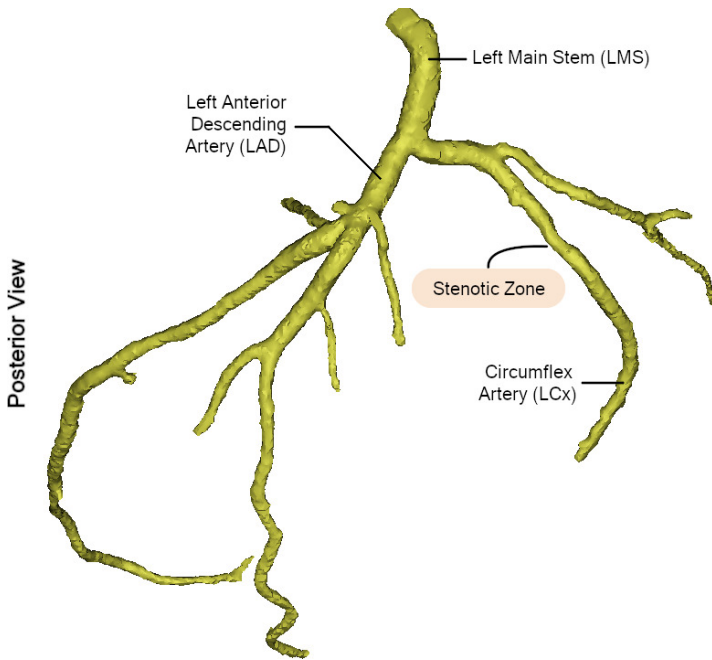


Fig. 21.2 Left coronary artery contours obtained after DICOM images segmentation.

21.2.1 Left Coronary Artery Geometry and Stent Design

21.2.1.1 Stenotic Zone Reconstruction

Using MIMICs®, the model is softened and the limits of the artery branches are defined. The damaged area of the LCA is recovered in an approximate way. Although

the result of this recovery corresponds to a healthy artery without a stent, the objective is to obtain the line that passes through the center of the artery. Figure 21.3(a) illustrates all the modifications and it is possible to observe the differences between the damaged artery and the recovery made (with transparency).

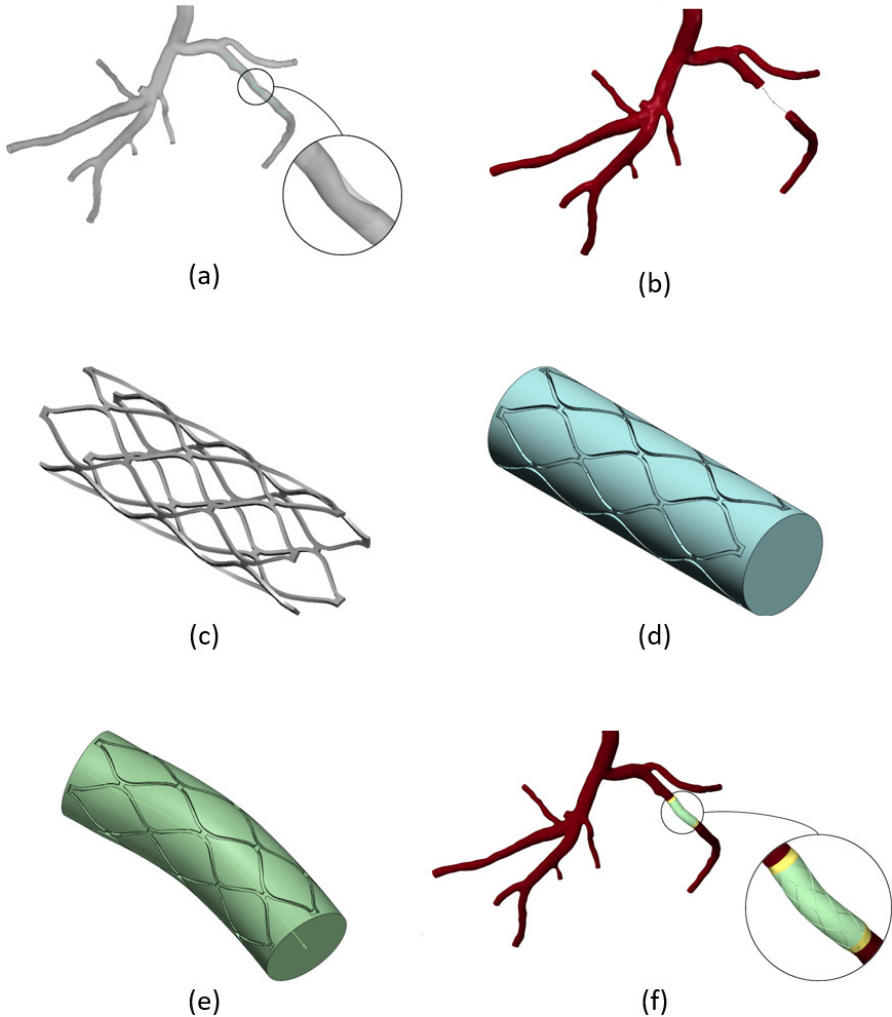


Fig. 21.3 Stent design: (a) Softened coronary artery with branches limits defined; (b) Coronary artery model after removing damaged zone; (c) Final stent with cylindrical shape; (d) Stent subtracted from a cylinder - stent-lumen; (e) Curved stent-lumen; (f) Final model obtained after combining coronary artery model (red), the curved stent-lumen (green) and transition zone (yellow).

21.2.1.2 Stenotic Zone Disposal

Using the softened LCA model and centerline, the damaged zone is removed, Fig. 21.3(b), and the minimum dimensions of the sent, diameter (2.9 mm) and length (9.0 mm), are obtained. For this the IGS model obtained in MIMICs® was imported to SolidWorks®. The centerline was imported indicating the set of points that describe it. In addition a small portion of the LCA was also removed at the ends. In this way, when the stent is placed, it is possible to make a smooth connection to the rest of the artery, avoiding creating turbulence zones and bringing the results closer to reality. Model was saved in SolidWorks® format (.SLDRPT) for further assembly with stent.

21.2.1.3 Flat Stent Design

Stents can be divided into three categories regarding: (1) form of expansion (self-expanding or balloon expanding); (2) coating (with or without drug coating); (3) permanence in the body (permanent or biodegradable). Concerning biocompatibility, 316L stainless steel is the most used material in balloon expanding stent. To develop the semi-automatic method of stent placement in real arteries, an uncoated, permanent and balloon expanding stent was used. Patents associated with stents make it difficult to define their dimensions. The chosen stent, taken from the literature (Lee et al, 2020), is an adaptation of the Palmaz-Schatz stent. Based on the following authors, (Hall and Kasper (2006); Kioussis et al (2007); Migliavacca et al (2007); Bekal et al (2018); Lee et al (2020)), the dimensions of the stent structure were defined, see Fig. 21.4(a). The final diameter and length will depend

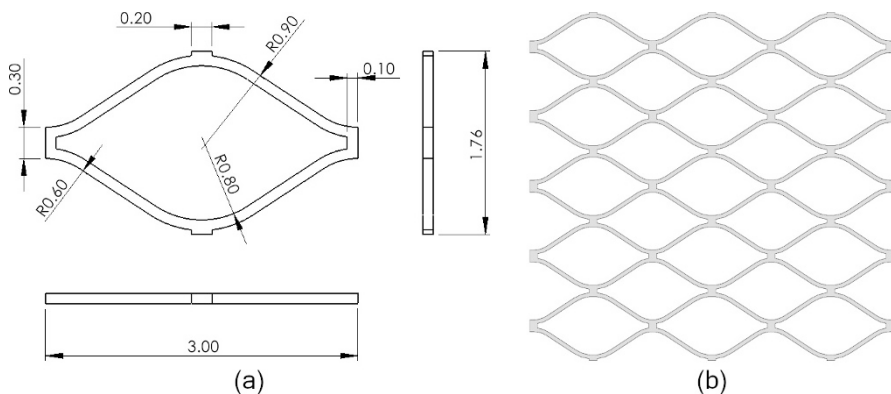


Fig. 21.4 (a) Stent structure dimensions (mm); (b) Flat stent (9 mm).

on the size of this structure. To increase/decrease the diameter, a simple structure in the vertical direction is removed/added. The same is true for the length, in the

horizontal direction. Considering the dimensions taken from Section 21.2.1.2, using Solidworks®, structures were added in both directions to obtain the flattened stent mesh in illustrated in Fig. 21.4(b). Final stent dimensions are indicated in Table 21.1. SolidWorks® uses geometric modeling kernel, for that reason Parasolid format was used to import/export in the different used software.

Table 21.1 Final stent dimensions.

| | Length | Diameter |
|-------------|--------|----------|
| 9 mm stent | 9 mm | 1.4 mm |
| 12 mm stent | 12 mm | 1.4 mm |

21.2.1.4 Bending to Cylindrical Form and Curve Adaptation

Flat stent was imported into Creo® and rolled 360 degrees to obtain a cylindrical shape as shown in Fig. 21.3(c).

In simulations, the artery wall thickness will not taken into account, as explained previously. For this reason, using SolidWorks® , the stent was subtracted from a cylinder to simulate the blood surrounding the device and to obtain the stent-lumen, Fig. 21.3(d). Artery central line, previously obtained, is now used to adapt the stent-lumen to artery curves, Fig. 21.3(e), using ZW3D® software.

21.2.1.5 Combining Artery Geometry with Stent-Lumen

Using SolidWorks®, the artery geometry obtained in Section 21.2.1.2 and the stent-lumen obtained in Section 21.2.1.4 were combined. Transition zone was constructed and the final geometry, illustrated in Fig. 21.3(f) was obtained.

21.2.2 Mesh Generation

The mesh was automatically generated with the algorithm implemented in the Ansys Meshing, Tetrahedrons Patch Independent Model. To verify mesh quality, skewness was obtained for all mesh elements. Skewness is defined as the difference between the shape of the element and the shape of an equilateral element of equivalent volume. It allows checking homogeneity and orthogonality of the mesh. For a tetrahedral mesh, a maximum skewness should be kept bellow 0.95 to avoid convergence difficulties (ANSYS, 2016). In addition to the quality indicator presented, a mesh test was performed for different element sizes with the objective of reducing the number of elements, without decreasing the precision of the results. This test compares the

maximum values at peak systolic (maximum velocity of flow) with the number of elements. According to the Fig. 21.5 a number of elements of 400000 should be used. Thus, this mesh is represented in Fig. 21.6.

21.2.3 Blood Properties

Blood was considered as a non-Newtonian, isotropic and homogeneous viscoelastic fluid. The density of blood used in the equations was 1060 kg/m^3 . The user defined functions (UDFs) for the sPTT model, implemented by Pinto et al (2020), take into account the viscoelastic property of blood. These properties are introduced in Ansys as differential equations to obtain results close to reality. sPTT model is given by

$$\left[1 + \frac{\lambda_k \epsilon_k}{\mu_{e_k}} \text{tr}(\boldsymbol{\tau}_{e_k}) \right] \boldsymbol{\tau}_{e_k} + \lambda_k \overset{\nabla}{\boldsymbol{\tau}}_{e_k} = 2\mu_{e_k} \boldsymbol{D}, \quad (21.1)$$

where k represents each mode number, λ is the relaxation time, ϵ the extensibility coefficient, μ_e the elastic viscosity, $\boldsymbol{\tau}_e$ the elastic contribution of the extra stress tensor, $\overset{\nabla}{\boldsymbol{\tau}}_e$ the upper convective derivative and \boldsymbol{D} the velocity gradient. The parameters of sPTT model are defined in Table 21.2.

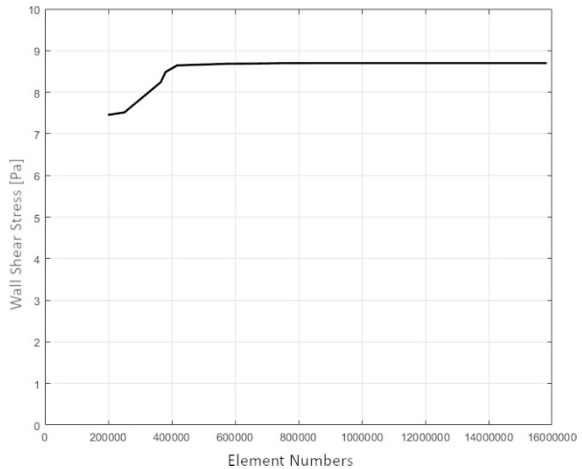


Fig. 21.5 Maximum WSS during systolic peak vs. Number of mesh elements for the patient specific case under study.

Fig. 21.6 Generated mesh for LCA domain.

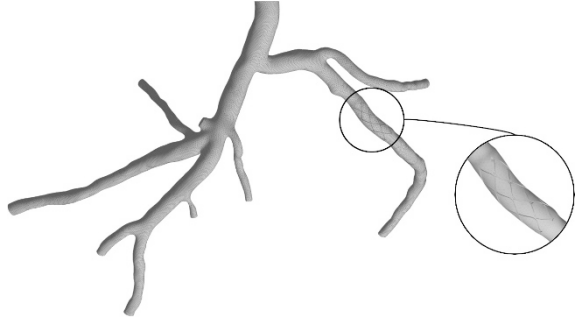


Table 21.2 Parameters of sPTT model (Campo-Deaño et al, 2013).

| Mode | μ_{e_k} [Pa s] | λ_k [s] | ϵ_k |
|---------|-----------------------|-----------------|--------------|
| 1 | 0.05 | 7 | 0.2 |
| 2 | 0.001 | 0.4 | 0.5 |
| 3 | 0.001 | 0.4 | 0.5 |
| 4 | 0.0016 | 0.06 | 0.5 |
| Solvent | $\mu_s = 0.0012$ Pa s | | |

21.2.4 Boundary Conditions

As boundary conditions, it is necessary to define the inlet blood velocity at the entrance of the artery and the pressure at the outlet of all the branches. The arterial wall was considered rigid as explained with detail in previous section.

Blood is pumped by the heart in a pulsatile and complex way. However, it can be approximated to a sinusoidal periodic movement and heart rate ω , (Dong et al, 2015) based on the pulsatile flow rate. Thus, the mean inlet velocity and outlet pressure were obtained using Fourier series in Matlab, Fig. 21.7.

One way of representing the evolution of the average input velocity is the Womersley velocity profile. Taking into account the inlet radius of the artery, R , and the heart rate, ω , the Poiseuille profile is adapted to obtain the Womersley profile described in Eq. (21.2):

$$v(r_d, t) = \frac{AR^2}{i\mu_f W_o^2} \left[1 - \frac{J_0(i^{3/2} W_o \frac{r_d}{R})}{J_0(i^{3/2} W_o)} \right] e^{i\omega t} \quad (21.2)$$

Womersley velocity is given as a function of time, t , and the radial distance from the central axis of the artery to a given point, r_d , within the arterial wall. The dynamic viscosity of blood is considered constant, equal to 0.00345 Pa \cdot s, and is represented by μ_f , i represents the imaginary unit, J_0 the first order Bessel function, A the pressure gradient and W_o the Womersley number. Only the real part of the equation is considered.

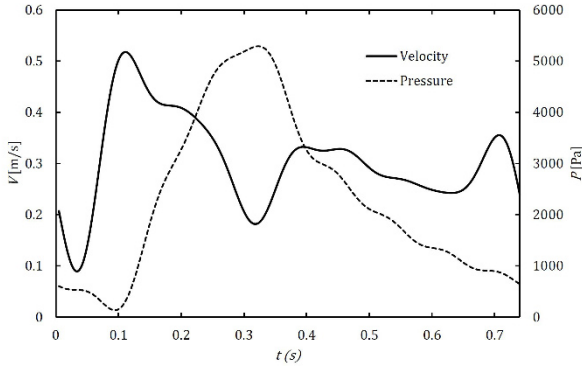


Fig. 21.7 Mean inlet velocity in the LCA and the outlet pressure profile in its branches (Pinto et al, 2020).

The number of Womersley is given by the Eq. (21.3) and relates the inertia forces to the viscosity forces, in transient flows. The parameters used to calculate the Womersley number are shown in Table 21.3.

$$Wo = R \sqrt{\frac{\rho \omega}{\mu}} \quad (21.3)$$

Table 21.3 Womersley number parameters.

| | |
|--------------|------------------------|
| Inlet radius | 2.36 mm |
| Viscosity | 0.00345 Pa s |
| Frequency | 8.49 s ⁻¹ |
| Density | 1060 kg/m ³ |

21.2.5 Numerical Method

The CFD model was defined as transient and calculations were performed with a time step equal to 0.005 s. Thus, 148 time steps were necessary in order to achieve the total time of the cardiac cycle, 0.74 s. The algorithm chosen to solve the Navier-Stokes equations, SIMPLE (Semi-Implicit Method for Pressure Linked Equations), is implemented in Ansys Fluent and uses a relationship between velocity and pressure corrections to enforce mass conservation and to obtain the pressure field. For compressible flow calculations, Ansys Fluent applies upwind interpolation of density at cell faces. There are several schemes for the density upwinding at cell

faces: first-order upwind, second-order upwind, QUICK, etc. Second-order upwind discretization was used with a convergence criterion equal to 1×10^{-4} and provides stability for supersonic flows and capture shocks better than the first-order upwind interpolation scheme. This numerical method was used and tested by Pinto et al (2020).

21.2.6 Hemodynamic Descriptors

Hemodynamic descriptors (Pinto et al, 2020), based on the wall shear stress (WSS), predict the areas of the arteries that are more prone to the atherosclerosis appearance. The Time Averaged Wall Shear Stress (TAWSS) evaluates the mean value of the WSS magnitude along the cardiac cycle, Eq. (21.4):

$$TAWSS(s) = \frac{1}{T} \int_0^T |WSS(s, t)| dt \quad (21.4)$$

where T is the duration of the cardiac cycle and s is the location in the wall. The units are in Pa and values less than 0.4 Pa indicate a higher probability of plaque formation.

The Oscillatory Shear Index (OSI), Eq. (21.5), is a dimensionless parameter that describes the flow along the wall, taking into account the variation of the WSS throughout the cardiac cycle:

$$OSI(s) = 0.5 \left[1 - \frac{|\int_0^T WSS(s, t) dt|}{\int_0^T |WSS(s, t)| dt} \right] \quad (21.5)$$

This parameter can range between 0 and 0.5. The minimum value corresponds to zero deflection and the maximum value corresponds to highly disturbed flow with 180° deflections.

Relative Residence Time (RRT), Eq. (21.6), estimates the residence time of blood particles in the arterial wall. The RRT descriptor results from the combination of the OSI and TAWSS descriptors. It is directly dependent on OSI and inversely dependent on TAWSS. Thus, RRT, is the one that best assesses the tendency of atherosclerosis appearance:

$$RRT(s) = \frac{1}{(1 - 2 \times OSI) \times TAWSS} \quad (21.6)$$

RRT values greater than 8 Pa^{-1} indicate zones susceptible to atherosclerosis.

21.3 Results and Discussion

Three simulations were made: (1) left coronary artery with stenosis; (2) left coronary artery with 9 mm stent (length of the stent); (3) left coronary artery with 12 mm stent.

The hemodynamic descriptors (OSI, RRT and TAWSS) were obtained. The hot spots (red) are areas favorable to the onset of atherosclerosis. These regions are the ones which OSI is equal or greater than 0.2, RRT higher than 8.0 Pa^{-1} and TAWSS close to 0 Pa. Figures 21.8, 21.9 and 21.10 show the spatial distribution of the

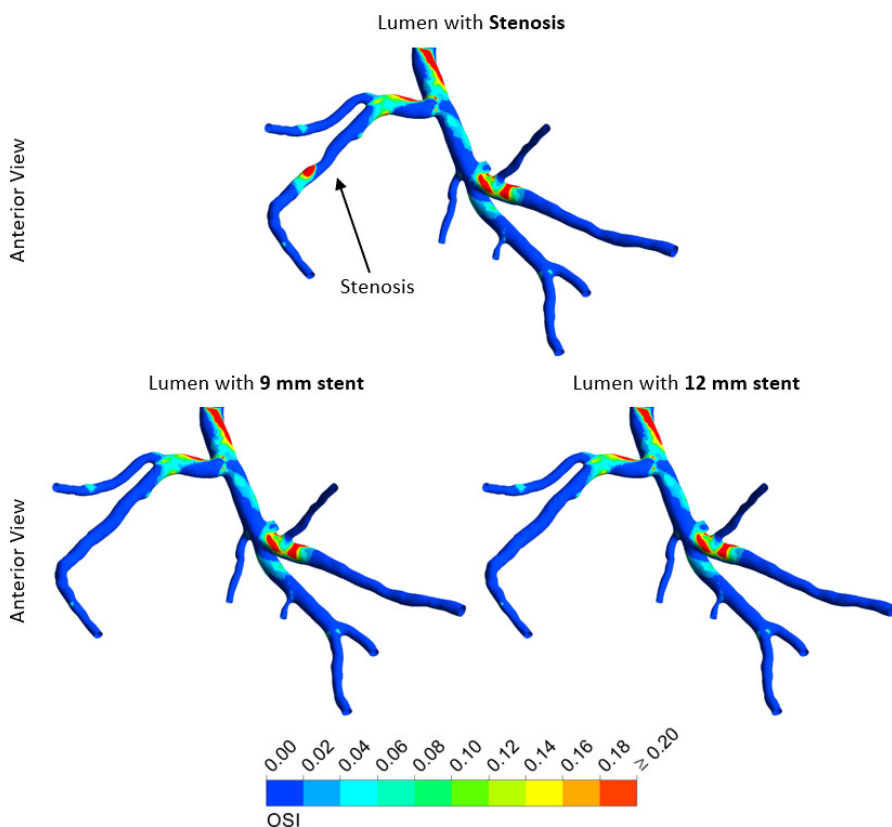


Fig. 21.8 OSI spatial distribution for the patient-specific case.

descriptors for the patient-specific case. We can observe that the stent eliminates strong atherosusceptible regions after the stenosis.

For a quantitative analysis the maximum values of the descriptors in the area after the stent were obtained, Table 21.4. The relative difference of the OSI between the model with stenosis in relation to the 9 mm stent is 83.33%; in TAWSS the difference

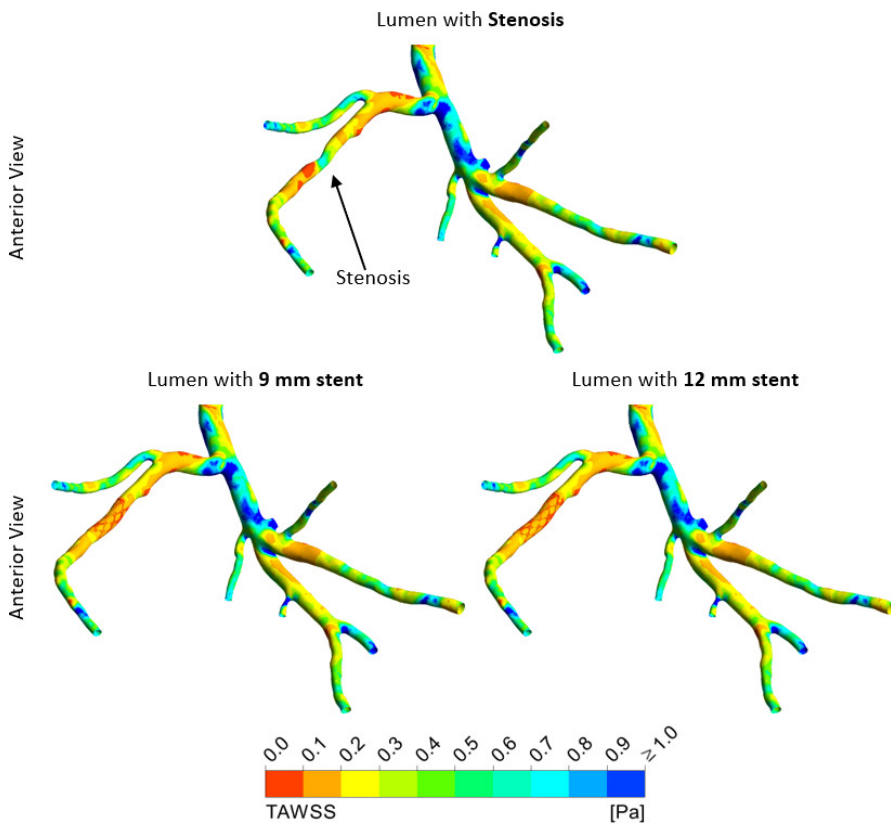


Fig. 21.9 TAWSS spacial distribution for the patient-specific case.

is 18.35%; in the RRT the difference is 83.84%. The relative difference, for the same descriptors, between the models with different stent sizes does not exceed 3%. Thus, it can be verified, quantitatively, that there is a great decrease in the OSI and RRT values, that is, a decrease in atherosusceptibility, when a stent is introduced.

However, we can verify a tendency to occur restenosis in the stent location.

Table 21.4 Maximum value for hemodynamic descriptors after stent.

| Model | OSI | TAWSS [Pa] | RRT [Pa^{-1}] |
|-------------|------|------------|--------------------------|
| Stenosis | 0.48 | 1.09 | 129.3 |
| 9 mm stent | 0.08 | 1.29 | 20.89 |
| 12 mm stent | 0.07 | 1.29 | 18.90 |

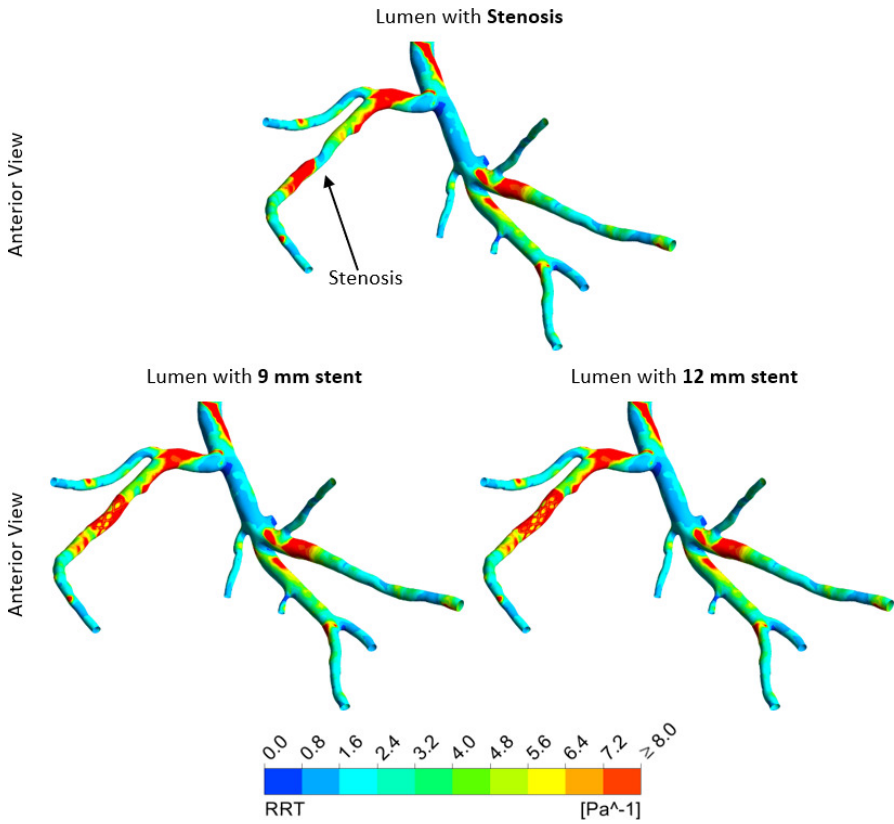


Fig. 21.10 RRT spatial distribution for the patient-specific case.

21.4 Conclusion

After analyzing the results, it is concluded that the implantation of stents in the left coronary arteries improves blood flow. After the stented area, the blood flow approaches of a normal flow situation, with no great propensity for atherosclerotic plaque formation. Atherosusceptible zones in the stent zone were expected and are related to the increase in shear stresses due to the stent own geometry. At a clinical level, this increase in stress is related to the reappearance of the stenosis, the restenosis. Increasing the length of the stent did not result in improvements, on the opposite, the susceptible zone to restenosis is greater the larger is the stent. Thus, according to this study, the shortest stent is the best choice.

Acknowledgements Authors gratefully acknowledge the Engineering Faculty of University of Porto (FEUP), the Department of Mechanical Engineering (DEMec) of FEUP, the Institute of Science and Innovation in Mechanical and Industrial Engineering (LAETA-INEGI) and Vila Nova de Gaia/Espinho Hospital Center (CHVNG/E).

References

- Amin F, Ali DMN, Ansari U, Mir M, Minhas MA, Shahid W (2015) Auxetic coronary stent endoprosthesis: Fabrication and structural analysis. *Journal of Applied Biomaterials & Functional Materials* 13(2):127–135
- ANSYS (2016) ANSYS FLUENT 12.0 User's Guide. ANSYS Inc.
- Bekal C, Shetty R, Shenoy S (2018) Numerical investigation of influence of number of stent cells and type of link on expansion and haemodynamic behaviour of balloon-expandable coronary stent. *Sādhanā* 43(88)
- Bodnár T, Sequeira A, Prosi M (2011) On the shear-thinning and viscoelastic effects of blood flow under various flow rates. *Applied Mathematics and Computation* 217(11):5055–5067
- Bonsignore C (2010) Open Stent Design. Nitinol Devices & Components, Inc.
- Campo-Deaño L, Dullens R, Aarts D, Pinho FT, Oliveira MSN (2013) Viscoelasticity of blood and viscoelastic blood analogues for use in polydimethylsiloxane in vitro models of the circulatory system. *Biomicrofluidics* 7:1–11
- Chen C, Xiong Y, Jiang W, Wang Y, Wang Z, Chen Y (2019) Experimental and numerical simulation of biodegradable stents with different strut geometries. *Cardiovascular Engineering and Technology* 11(1):36–46
- David Chua SN, Mac Donald BJ, Hasmi MSJ (2003) Finite element simulation of stent and balloon interaction. *Journal of Materials Processing Technology* 143-144(1):591–597
- Dong J, Sun Z, Inthavong K, Tu J (2015) Fluid-structure interaction analysis of the left coronary artery with variable angulation. *Computer Methods in Biomechanics and Biomedical Engineering* 18:1500–1508
- Gay M, Zhang L, Liu WK (2006) Stent modeling using immersed finite element method. *Computer Methods in Applied Mechanics and Engineering* 195(33):4358–4370
- Good B, Deutsch S, Manning K (2016) Hemodynamics in a pediatric ascending aorta using a viscoelastic pediatric blood model. *Annals of Biomedical Engineering* 44:1019–1035
- Hall GJ, Kasper EP (2006) Comparison of element technologies for modeling stent expansion. *Journal of Biomechanical Engineering* 128(5)
- Hsiao HM, Chiu YH, Lee KH, Lin CH (2012) Computational modeling of effects of intravascular stent design on key mechanical and hemodynamic behavior. *Computer-Aided Design* 44(8):757–765
- Kiousis DE, Gasser TC, Holzapfel GA (2007) A numerical model to study the interaction of vascular stents with human atherosclerotic lesions. *Annals of Biomedical Engineering* 43(11)
- Lee W, Cho SW, Allahwala UK, Bhindi R (2020) Numerical study to identify the effect of fluid presence on the mechanical behavior of the stents during coronary stent expansion. *Computer Methods in Biomechanics and Biomedical Engineering* 23(11):744–754
- Migliavacca F, Gervaso F, Prosi M, Zunino P, Minisini S, Formaggia L, Dubini G (2007) Expansion and drug elution model of a coronary stent. *Computer Methods in Biomechanics and Biomedical Engineering* 10(1):63–73
- Miranda E, Sousa LC, António CC, Castro CF, Pinto SIS (2020) On the impact of using the non-linear viscoelastic property of blood and fsi simultaneously for arterial hemodynamic simulations. *IRF2020-7th International Conference Integrity-Reliability-Failure* pp 1017–1022
- Mozaffarian D, Benjamin EJ, Go AS, Arnett DK, Blaha MJ, Cushman M, Ferranti S, Després J, Fullerton H, Howard VJ, Huffman MD, Judd SE, Kissela BM, Lackland DT, Lichtman JH, Lisabeth LD, Liu S, Mackey RH, Matchar DB, McGuire DK, Mohler ER, Moy CS, Muntner P, Mussolino ME, Nasir K, Neumar RW, Nichol G, Palaniappan L, Pandey DK, Reeves MJ, Rodriguez CJ, Sorlie P, Stein J, Towfighi A, Turan TN, Virani SS, Willey JZ, Woo D, Yeh RW, Turner MB (2015) Heart disease and stroke statistics–2015 update: a report from the american heart association. *Circulation* 131:e29–322
- Nikolic DD, Filipovic N (2020) Chapter 3 - topological and parametric optimization of stent design based on numerical methods. In: Filipovic N (ed) *Computational Modeling in Bioengineering and Bioinformatics*, Academic Press, pp 69–103

- Okereke MI, Khalaj R, Tabriz AG, Douroumis D (2021) Development of 3d printable bioresorbable coronary artery stents: A virtual testing approach. *Mechanics of Materials* 163:104,092
- Pinho N, Castro CF, António CC, Bettencourt N, Sousa LC, Pinto SIS (2018) Heart disease and stroke statistics–2015 update: a report from the american heart association. *Medical & Biological Engineering & Computing* 57:715–729
- Pinho N, Sousa LC, Castro CF, António CC, Carvalho C, Ferreira W, Ladeiras-Lopes R, Ferreira ND, Braga P, Bettencourt N, SIS P (2019) The impact of the right coronary artery geometric parameters on hemodynamic performance. *cardiovascular engineering and technology. Cardiovascular Engineering and Technology* 10:257–270
- Pinto SIS, Romano E, António CC, Sousa LC, Castro CF (2020) The impact of non-linear viscoelastic property of blood in right coronary arteries hemodynamics — a numerical implementation. *International Journal of Non-Linear Mechanics* 123:1–14
- Wang XM, Liu P, Liang H, Zhang MC, Li L, Yue ZF (2019) Analysis of the whole implementation process and optimization of a nitinol superelastic stent. *Materials Science & Engineering Technology* 50(1):44–51



Chapter 22

The Efficient Trabecular Bone Remodeling Numerical Tool Enabling Multiple Load Case Simulation

Jan Polak, Michał Nowak

Abstract Paper concerns a simulation of the trabecular bone remodeling process taking into account its real geometric form. The efficient trabecular bone remodeling numerical tool enabling multiple load case simulation is presented. The observation proposed by Julius Wolff - called the Wolff's law - can be described as a structural adaptation of the bone to the external forces. Thus the trabecular bone remodeling process numerical simulation has to include the very important aspect of external load, namely the variable loads. For simulation purposes it means, that the numerical tool must be able to simulate multiple load case and the geometric form of the bone must correspond to these loads. Technically the numerical system is .Net C# project designed with Inversion of Control paradigm design pattern that provides pluggable and extensible platform.

Keywords: Trabecular bone remodeling · Multiple load case

22.1 Introduction

The trabecular bone structure is continually rebuilt. This process is the subject of intensive research due to its high medical significance (Parfitt et al, 1983; Ehrlich and Lanyon, 2002; Müller, 2005; Giorgio et al, 2021). The observation proposed by Julius Wolff - called the Wolff's law (Wolff, 1892) - can be described as a structural adaptation of the bone to the external forces. Thus, the trabecular bone remodeling process numerical simulation has to include the very important aspect of external load, namely the variable loads. For simulation purposes it means, that the numerical tool must be able to simulate multiple load case and the geometric form

J. Polak, M. Nowak

Poznan University of Technology, Department of Virtual Engineering, Poland, ul. Jana Pawla II 24 60-965 Poznan, Poland

e-mail: Jan.Polak@put.poznan.pl, Michal.Nowak@put.poznan.pl

© The Author(s), under exclusive license to Springer Nature Switzerland AG 2022

459

I. Giorgio et al. (eds.), *Theoretical Analyses, Computations,*

and Experiments of Multiscale Materials, Advanced Structured Materials 175,

https://doi.org/10.1007/978-3-031-04548-6_22

of the bone must correspond to these loads. The second, equally important aspect of the trabecular bone remodeling phenomenon is the fact, that this process takes place on the bone surface. The need to build models and simulate the trabecular bone structure evolution taking into account the actual geometric form has been recognized already. Consequently, a number of scientific research has appeared that's this fact the center of attention (Huiskes, 2000; Huiskes et al, 2000; Van Oers et al, 2008; Müller et al, 2014; Callens et al, 2021). Including the real structural surface into the consideration provides significant approximation of numerical simulations and allows for the introduction of modeling on cells scale to the numerical models (Adachi et al, 2009; Hemmatian et al, 2021). Any attempts to correlate the developed models and theories with actual observations requires an accurate model of the trabecular bone structure for each problem under consideration. An accurate model of the trabecular bone structure will also be needed to verify multi-scale simulation approaches (Hamed et al, 2012; Fernandes et al, 2012; Wierszycki et al, 2014).

Mechanical aspects of the trabecular bone remodeling phenomenon are not the only ones that should be used to correctly build numerical models and predict trabecular bone evolution. In addition to considering the mechanical aspects, it is also necessary to take into account other factors, such as purely biological aspects of tissue growth or, for example, issues related to electrical interactions. This is of particular importance when the task is not only to model the trabecular bone remodeling phenomenon itself, but to design an appropriate materials to replace damaged or diseased bone tissue (Giorgio et al, 2016, 2017).

The assumptions concerning the modeled phenomenon of bone remodeling used to create the simulation environment will be presented below in this paper.

22.2 The Trabecular Bone Remodeling Regulatory Model with the Lazy Zone Concept

A model of the trabecular bone remodeling phenomenon is based on the idea of a regulatory model presented by Huiskes et al (1987, 2000). The lazy zone concept - proposed by Carter (1984) - is also included in the presented model, but this issue will be discussed in a section devoted to the simulation approach.

It was also assumed that the geometry of the bone structure would be reproduced as accurately as possible by medical imaging methods. The tissue of trabecular bone has a very sophisticated structure which is capable of handling a wide range of loads. The network of beams called trabeculae with lengths of 100 or 200 μm , and diameters of ca. 50 μm . is continually rebuilt so that the whole bone tissue is replaced in the course of a few years. The process is called trabecular bone adaptation or remodeling and is responsible for self-optimization of the trabecular bone structures. The phenomenon of trabecular bone adaptation has two important attributes. First, mechanical stimulation is needed to conserve the rebuilding balance. Second, the process of resorption and formation occurs only on the trabecular bone

surface. The process takes place within Basic Multicellular Unit (BMU), areas with a smaller volume, but comparable to a small part of a single trabecula.

This is where the sequence of resorption and new tissue formation takes place. Adding the ability to determine the level of local mechanical stimulation, all the actors needed to build the model are now present. The model consists of a regulatory mechanism (on the bone surface only) between bone resorption and formation, corresponding to the intensity of mechanical stimulation and this is the main assumption of the discussed model. The regulatory mechanism depends, in turn, on the mechanical stimulation of the entire bone structure.

The assumption based on clinical observations is that, if the strain energy density is close to observed equilibrium, there is no change in the bone mass during the bone remodeling process. In this way, if the intensity of mechanical stimulation differs slightly from the homeostatic value of the strain energy density, bone mass does not change. However when the intensity of mechanical stimulation is larger or smaller than the reference value, the bone mass increases or decreases respectively. Modeling the actual bone geometry allows the simulation of the bone remodeling phenomenon in the most similar way to the process occurring on the surface of the BMU's. Hence the necessity of geometrical modeling of the real geometry of the reconstructed structure becomes clear.

22.3 Multiple Loading Conditions

The physical activity is only one source for mechanical stimulation of bone. Different activities result in different distribution of bone mass density. There is no possibility to investigate experimentally the change in bone mass distribution as a response for the different loading conditions. But it is possible using the numerical simulation methods. Experiments show clearly, that the bone structure is not isotropic and it is the result of bone mechanosensation.

Studies dedicated to multiple load cases representing different activities of daily living has been published already in Miller et al (2002); Geraldes et al (2016). The used adaptation algorithms usually assume orthotropic material properties and try to obtain information about the bone density. In this kind of simulations, the computational system remains at the level of continuous material model. The change in bone structure is represented by the modification of the Young's modulus and the isotropic material model is replaced, for example, with an orthotropic one.

The purpose of the computing environment presented in this paper is to go down to the level of analysis of the actual structure of the trabecular bone. Multiple loading conditions have a different dimension in the presented approach, because they not only determine the material properties (expressed globally, for example, by Young's modulus distribution), but also allow the observation of the actual evolution of the bone structure.

22.4 The Simulation Approach Including the Postulates based on Shape Optimization Studies

Continuous models, although they currently dominate the area of modeling the evolution of the trabecular bone structure, are not sufficient to simulate real processes on the surface of the bone structure (George et al, 2019; Giorgio et al, 2019; Lekszycki and dell'Isola, 2012). The microarchitecture of bone tissue has a major influence on the mechanical properties and must also be considered when trying to explain disease processes.

In order to be able to provide general relationships between the geometric form of the structure observed in imaging studies and its mechanical properties, an accurate, three-dimensional simulation model of the trabecular bone structure is necessary. As indicated above, there are two elements necessary to build a computing environment - the inclusion of multiple load cases and an accurate geometric model of the trabecular tissue. The simulation approach presented in this paper uses two postulates (Nowak, 2020) concerning the trabecular bone remodeling regulatory model, based on shape optimization studies in Nowak et al (2018, 2020).

These studies show that the remodeling of the trabecular bone can be treated as a simultaneous optimization of shape and topology. The similarity between the phenomenon of trabecular bone remodeling and topology optimization has been recognized and it is used in two opposite research approaches. The first approach is to use exact mathematical results from the optimization area (maximization or minimization of a function) to predict the evolution of the bone structure (Sigmund, 1999; Wu et al, 2017; Lee et al, 2015).

And the second approach which is presented also in the paper is to apply the bio-mechanical observations and models to the structural optimization issues (Nutu, 2015; Klarbring and Torstenfelt, 2012; Nowak et al, 2018). In the latter paper we proved with use of shape derivative, that the maximization of a structure stiffness needs the structural form, having on the part of the boundary, subject to modification, constant value of the strain energy density. This is also the purpose of the trabecular bone remodeling phenomenon.

The postulates are as follows:

Postulate 1.: during the remodeling process, the trabecular bone tends to maximize the stiffness of a structure (i.e. to find the stiffest design) by the strain energy density equalization on the structural surface of the trabecular tissue. According to formula

$$\sigma(\mathbf{u}) : \varepsilon(\mathbf{u}) = \lambda = \text{const.} \quad (22.1)$$

where

- $\sigma(\mathbf{u}) : \varepsilon(\mathbf{u})$ - strain energy density at the point on structural surface
- λ - homeostatic value of strain energy density (surrounded by the lazy zone)

mean that the bone remodeling phenomenon can be interpreted as structural optimization process. It means that for the stiffest design, the strain energy density on the part of the boundary subject to modification must be constant. Comparing this

result with the regulatory model of bone remodeling, it can be deduced that the mechanical stimulation (measured by strain energy density distribution on structural surface) has to be between the values determined by the lazy zone. In other words, at each point of the surface of the trabecular bone, the strain energy density should be similar, and this can be achieved by remodeling the bone structure.

Postulate 2.: the regulatory model of the trabecular bone remodeling can be applied to the multiple load problem maintaining its character and the basic assumptions about the existence of the homeostatic value of the strain energy density. The 'lazy zone' is an important element of the model which provides the opportunity to find a solution for many load cases. The local change (in this case related to different loads) on the structural surface leads to global minimization of the strain energy for the whole structure.

According to formula

$$\alpha_1\sigma(\mathbf{u}_1) : \varepsilon(\mathbf{u}_1) + \alpha_2\sigma(\mathbf{u}_2) : \varepsilon(\mathbf{u}_2) = \lambda = \text{const.} \quad (22.2)$$

where $\alpha_1\sigma(\mathbf{u}_1) : \varepsilon(\mathbf{u}_1) + \alpha_2\sigma(\mathbf{u}_2) : \varepsilon(\mathbf{u}_2)$ - weighted sum of strain energy density at the point on structural surface for different load cases, λ - homeostatic value of strain energy density (surrounded by the lazy zone), the regulatory model can be directly used for the simulation of the multiple load problem.

22.5 The Numerical Implementation and Mesh Generation Parallelization

To carry out the simulation of trabecular bone structure it is necessary to combine two areas - numerical simulation of deformation of the bone structure under load and structural evolution. Finite Element Method will be used for this purpose. In terms of structural calculations, there is no alternative but to use the already existing FEM systems. The presented implementation uses the Elmer open source multiphysical simulation software (<http://www.elmerfem.org>). Tetrahedral, 10-node volume elements were used for computational purposes.

The more difficult task is to plan how to reflect the evolution of the structure. Based on previous experience Nowak (2006), it was decided to build separate computational meshes for each simulation step. The idea of building a volumetric mesh based on data in the form of two-dimensional images containing the cross-sections of tissue is presented schematically in Fig.22.1. This is a natural way of mesh generation since the visualization for the biological entities is based on the digital images e.g. Computer Tomography. Also the evolution of the structure is based on the two-dimensional images modification, which is depicted schematically in Fig.22.2. According to remodeling scenario described by regulatory model, depending on the calculated value of the energy density, the surface of the structure is modified by adding or removing material on its surface.

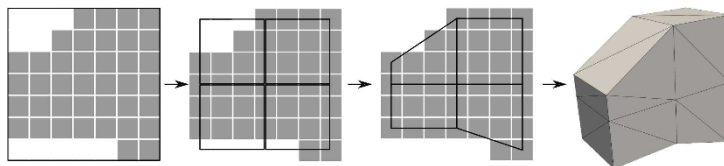


Fig. 22.1 Data Discretization and Volumetric Mesh Building algorithms applied for sample image. Image is divided into squares, in this particular example size of 3 was selected. For each square, four points are selected and used for volumetric mesh building. Last image shows volumetric mesh created from two identical images.

System was implemented using .Net platform, activity diagram is depicted in Fig.22.3. System created has been designed with two main goals: high performance and flexibility for future enhancements and modifications. Underlying phenomenon of trabecular bone remodeling is a process that happens over time hence the algorithm works in iterations, each run is a full remodeling cycle. Single loop consists of a series of steps. First step is data discretization to reduce the size of data used to build mesh.

Scale factor is input parameter for algorithm and allows choosing between fine and coarse meshes and consequent trade-off between solution resolution and resources required to perform calculations. Each two-dimensional image (slice) is divided into squares of size depending on scale factor that are used as an input for Volumetric

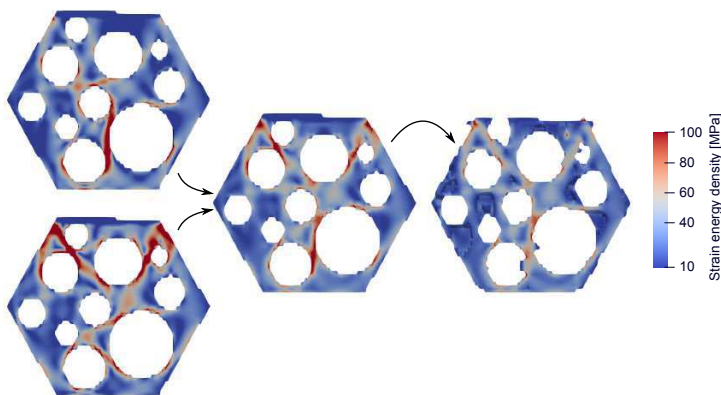


Fig. 22.2 Showcase of the multiple load case and mesh evolution algorithm. On the left element with random holes subjected to shear stress (top) and compression (bottom). In the middle both cases aggregated using formula 22.2. On the right the same element after the evolution algorithm has been applied and then both load cases calculated and aggregated together. New material 'grows' in high and is removed from low strain energy density areas. Material with strain energy density values inside the lazy zone is left intact.

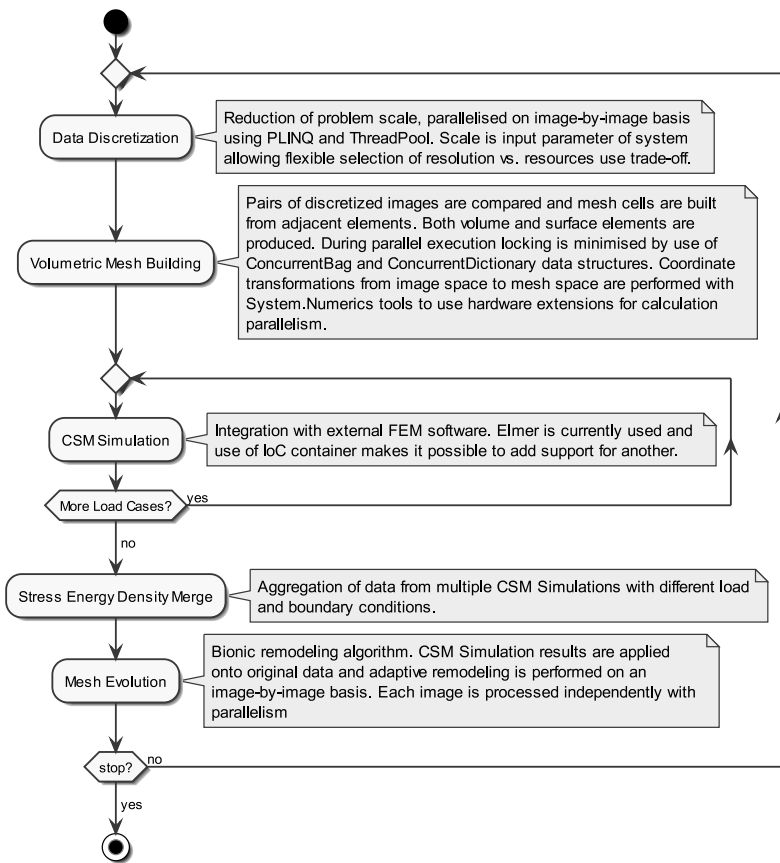


Fig. 22.3 Activity diagram of system for efficient trabecular bone remodeling numerical simulation enabling multiple load case analysis.

Mesh Building. For each square up to 4 points on edges are selected in such a way that the resulting tetragon approximates material inside each square.

Second step is the Volumetric Mesh Building and it consists of three operations. First, pairs of adjacent discretized images are converted into layers of mesh cells – squares from adjacent two-dimensional images are paired and for each pair, mesh cells are created, each consists of 6 tetrahedral elements spanned between points from adjacent squares. Data is filtered to remove mesh items that are not eligible for strain energy density (SED) calculation, mesh items that are connected only by a single point or single edge.

Filtered data is collected and merged into a single mesh – each cell and vertex gets assigned a number and boundary faces are computed. Prepared mesh is saved and FEM software is used to calculate displacement and SED values. To support multiple load scenarios, for each load case, separate simulation is executed in a loop.

Results of all calculations are merged together according to equation 22.2. Provided formula is not limited to two cases and thus implementation supports any amount of load cases, each allowing a different set of forces and boundary conditions.

The only limiting factor is time - each load case requires a separate SED calculation which is the most time consuming part of the whole process. After all load cases are evaluated, the stop criterion is evaluated - if surface SED values are all inside the lazy zone or maximum allowed number of iteration is exceeded, algorithm stops. SED data is passed to the Mesh Evolution algorithm where it is applied onto two-dimensional images used for mesh building. Each image is remodelled depending on a surface SED - areas where SED exceeds the upper bound of lazy zone grow and those where SED is below the lower bound shrink. Remodeled stack of images is input for the next iteration.

Slices Discretization, Volumetric Mesh Building and Mesh Evolution algorithms are optimised for execution speed in a multithreaded environment. Slices Discretization and Mesh Evolution steps operate on two-dimensional images (slices) directly without the need for exchanging information between workers hence parallelism is achieved by executing parallel processing of each item independently. To maximise efficiency of parallel operations Parallel LINQ (PLINQ) and .Net ThreadPool are used. It utilizes a hill climbing algorithm to dynamically control an optimal amount of thread running in the system to maximise processing throughput (Hellerstein et al, 2010).

Each of three phases of the Volumetric Mesh Building algorithm is executed using ThreadPool in sequence. Unlike two other algorithms, Volumetric Mesh Building was challenging to scale horizontally because the last phase - data collection - requires collecting all mesh data into the single data structure. Data structures provided by .Net framework, ConcurrentDictionary and ConcurrentBag in particular, were used to provide capabilities of writing data from multiple threads without need to use any additional critical section locking.

During development, the system was analysed with a .Net profiler to find non performing parts. Because this created system contains multiple source code micro-optimisations, i.e. commonly used LINQ extensions were replaced with classic *for* loops for data iteration to speed up execution by order of magnitude. All mathematical operations such as geometric transformations or vector operations are performed using System.Numerics library that provides SIMD (single instruction, multiple data) capabilities enabling hardware parallelisation of those operations. Data lookups were used when possible to save CPU time (and increase RAM consumption as a trade-off) for frequently run operations, i.e. the Volumetric Mesh Building algorithm builds tetrahedral elements based on pre-computed vertex tables and produces both volume and surface elements at the same time.

Important part of system design is the use of the Inversion of Control principle using Castle.Windsor dependency injection container (Burns, 2012). Each algorithm is an independent project and is able to operate independently of other system components. Core system parts, like an orchestrator that is responsible for the main loop and executing described algorithms, references class interfaces, not concrete implementations which are instead injected by Castle container. Main application

executable is a place where concrete implementations are loaded, depending on application configuration. System described above consists of the set of the best of algorithms explored during research, but can be run with implementations that yielded less promising results such as mesh discretization based on fuzzy logic approach or hexahedral volumetric mesh generator. In future research it will be possible to extend the platform with new algorithms and approaches whilst keeping the baseline system intact as a reference.

22.6 The Sample Simulation Results

Sample simulation was run on micro CT of rat bone. Input data set consisted of 400 black-and-white images with resolution of 1024x911px. A single step of the system was executed using a scale factor of 2 and produced a mesh with 54 million elements, 10 million vertices and additional 67 million points located on element's edges required for T10 structural elements. The cross section of produced mesh and results of stress simulation are visible on Fig.22.4.

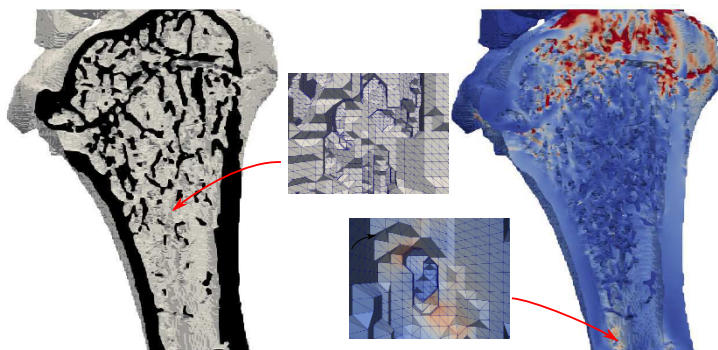


Fig. 22.4 Left: Cross-section view of mesh with 54 millions of elements showing trabecula network of the bone (Cross-section plane in black). Insets show detailed structure of highlighted mesh fragments with edges of tetrahedral cells highlighted. Right: The same bone fragment after FEM simulation of shear stress applied to top part. Nonlinear coloring scale was used to increase contrast between trabeculae. Data from the MIAB project (Waarsing et al, 2004).

22.7 The System Efficiency and Scalability

All tests were run on a PC with Ryzen 7 5800x CPU with 8 physical cores and 64GB of DDR4 3600Mhz RAM. Two series of tests were conducted: scalability tests and

resource utilization in function of input data size. Scalability tests were run using CPU affinity settings in the operating system. Dataset used was the same as in chapter 22.7. Physical CPU cores were selected for testing and tests were run on 1, 2, 4, 6 and 8 processors. Processor affinity was selected in such a way that each processor was a different physical core – CPU used for tests has 8 physical and 16 logical cores - each physical core has two sets of registers allowing the running of two threads at once without switching context. Running CPU-bound code on both virtual cores of a single physical core would not increase performance and lead to invalid results.

Plot 22.5 shows speedup, defined as in Eager et al (1989)

$$S_p = \frac{T_1}{T_p} \quad (22.3)$$

where T_1 is real time used to run calculations on a single core and T_p is real time used at p processors. Optimal value is observed when $S_p = p$. Speedup for each of the three main algorithms was calculated separately. Data discretization algorithm exhibits suboptimal speedup. This particular algorithm has no critical sections or locking, but reads and writes big amounts of data into memory - creates scaled down copies of input data. Volumetric Mesh Building exhibits little speedup - current implementation is I/O bound and data processing is no longer a bottleneck. Mesh Evolution algorithm, that works on structures established by previous steps scales nearly optimally with more processors, exhibiting optimal behaviour up to 4 cores.

Table 22.1 contains results of resource utilization tests. Tests were run for input data of different size to measure resource utilization - real time, RAM and disk space - by system during end-to-end tests, excluding FEM (Finite Element Method) calculations (this also excludes writing input files for Elmer). Mesh points counts list are tetrahedron vertices – to save memory 6 of T10 tetra points that are on edges are calculated as average of vertex positions during writing input file for FEM software. The biggest case analysed – creation of a mesh with 56 million elements took less than a minute and required less than 16GB of RAM which is very little compared to

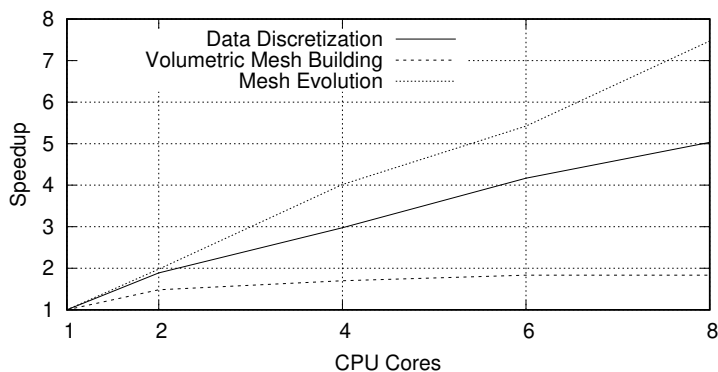


Fig. 22.5 The results of scalability tests of three core components of system.

Table 22.1 Comparison of output mesh size and resources utilization for different sizes of input data. Data from the MIAB project (Waarsing et al, 2004).

| Input Images | Mesh Elements | Mesh Points | Peak RAM Use | Total Real Time | Elmer Input Size |
|--------------|---------------|-------------|--------------|-----------------|------------------|
| 50 | 5.6M | 1.0M | 1.56GB | 6.2s | 816MB |
| 100 | 14.5M | 2.7M | 3.83GB | 13.7s | 2.2GB |
| 200 | 32.6M | 6.2M | 8.44GB | 30.6s | 5.1GB |
| 300 | 45.2M | 8.5M | 11.08GB | 41.9s | 7.2GB |
| 400 | 54.6M | 10.2M | 14.74GB | 58.3s | 8.6GB |

the amount of resources used by FEM calculations. Moreover Elmer, FEM software used by the system, uses text file format as an input.

This requires creation of very big input files and with storage devices reaching write speeds over 100MB/s writing data takes the same amount of time as data generation making any efforts to optimise current system even more unnecessary because the bottleneck is data transfer. To enable processing of bigger meshes some optimisation might be removed in future. When time is no longer a priority some auxiliary data structures maintained for fast data lookups might be removed to save RAM instead.

22.8 Conclusions

The presented trabecular bone remodeling numerical tool enables multiple load case simulation taking into account the postulates regarding the evolution of the trabecular bone. The trabecular bone remodeling regulatory model applied to an actual three-dimensional trabecular structure requires the preparation of an appropriate numerical approach. Since the local change on the structural surface leads to global minimization of the strain energy for the whole structure, the fulfillment of both postulates requires energy distribution analysis on the structural surface. Thus, the most important role in such an approach must be played by a very efficient finite element mesh generator for structural computations as well as an efficient computational environment. In both cases, it becomes necessary to use parallel processing. Such a numerical tool is able to mimic the trabecular bone remodeling process by structural surface evolution. So, on the one hand it will be possible to repeat virtually the observations recorded on the micro-CT scans, and on the other hand, to better adjust the continuous models of the trabecular bone remodeling phenomenon.

The developed software promises to simulate significant fragments of trabecular bone tissue, and as equipment develops, also structures covering the entire bone. Mesh generator performance is no longer a limiting factor nor is computing power. Created algorithms are I/O-bound and the main challenge in large-scale simulations is handling of very large amounts of physical data that needs to be transferred to the

FEM software. Highly optimised code enables using system on a single high-end PC while HPC grid is required only for FEM simulations.

Acknowledgements This work was supported by the Polish National Centre for Research and Development under the grant – decision no. DWP/TECHMATSTRATEG-III/136/2020 and the computational grant no. 362 – Biomimetic approach to compliance optimization and multiple load cases – of Poznan Super computing and Networking Center (PCSS), Poznan, Poland.

References

- Adachi T, Aonuma Y, Ito Si, et al (2009) Osteocyte calcium signaling response to bone matrix deformation. *Journal of biomechanics* 42(15):2507–2512
- Burns K (2012) *Inversion of Control in Beginning Windows 8 Application Development XAML Edition*. Apress, Berkeley
- Callens SJP, né Betts DCT, Müller R, Zadpoor AA (2021) The local and global geometry of trabecular bone. *Acta Biomaterialia* 130:343–361
- Carter DR (1984) Mechanical loading histories and cortical bone remodeling. *Calcified tissue international* 36(1):S19–S24
- Eager DL, Zahorjan J, Lazowska ED (1989) Speedup versus efficiency in parallel systems. *IEEE transactions on computers* 38(3):408–423
- Ehrlich PJ, Lanyon LE (2002) Mechanical strain and bone cell function: a review. *Osteoporosis international* 13(9):688–700
- Fernandes PR, Rodrigues HC, Guedes JM, Coelho PG (2012) Multiscale modelling on bone mechanics—application to tissue engineering and bone quality analysis. *IFAC Proceedings Volumes* 45(2):1013–1017
- George D, Allena R, Remond Y (2019) Integrating molecular and cellular kinetics into a coupled continuum mechanobiological stimulus for bone reconstruction. *Continuum Mechanics and Thermodynamics* 31(3):725–740
- Geraldes DM, Modenese L, Phillips ATM (2016) Consideration of multiple load cases is critical in modelling orthotropic bone adaptation in the femur. *Biomechanics and modeling in mechanobiology* 15(5):1029–1042
- Giorgio I, Andreaus U, Scerrato D, dell’Isola F (2016) A visco-poroelastic model of functional adaptation in bones reconstructed with bio-resorbable materials. *Biomechanics and modeling in mechanobiology* 15(5):1325–1343
- Giorgio I, Andreaus U, dell’Isola F, Lekszycki T (2017) Viscous second gradient porous materials for bones reconstructed with bio-resorbable grafts. *Extreme Mechanics Letters* 13:141–147
- Giorgio I, dell’Isola F, Andreaus U, Alzahrani F, Hayat T, Lekszycki T (2019) On mechanically driven biological stimulus for bone remodeling as a diffusive phenomenon. *Biomechanics and modeling in mechanobiology* 18(6):1639–1663
- Giorgio I, Spagnuolo M, Andreaus U, Scerrato D, Bersani AM (2021) In-depth gaze at the astonishing mechanical behavior of bone: A review for designing bio-inspired hierarchical metamaterials. *Mathematics and Mechanics of Solids* 26(7):1074–1103
- Hamed E, Jasiuk I, Yoo A, Lee Y, Liszka T (2012) Multi-scale modelling of elastic moduli of trabecular bone. *Journal of The Royal Society Interface* 9(72):1654–1673
- Hellerstein JL, Morrison V, Eilebrecht E (2010) Applying control theory in the real world: experience with building a controller for the. net thread pool. *ACM SIGMETRICS Performance Evaluation Review* 37(3):38–42
- Hemmatian H, Bakker AD, Klein-Nulend J, van Lenthe GH (2021) Alterations in osteocyte lacunar morphology affect local bone tissue strains. *Journal of the Mechanical Behavior of Biomedical Materials* 123:104,730

- Huiskes R (2000) If bone is the answer, then what is the question? *The Journal of Anatomy* 197(2):145–156
- Huiskes R, Weinans HHJG, Grootenboer HJ, Dalstra M, Fudala B, Slooff TJ (1987) Adaptive bone-remodeling theory applied to prosthetic-design analysis. *Journal of biomechanics* 20(11-12):1135–1150
- Huiskes R, Ruimerman R, Van Lenthe GH, Janssen JD (2000) Effects of mechanical forces on maintenance and adaptation of form in trabecular bone. *Nature* 405(6787):704–706
- Klarbring A, Torstenfelt B (2012) Lazy zone bone remodeling theory and its relation to topology optimization. *Annals of Solid and Structural Mechanics* 4(1):25–32
- Lee YH, Kim Y, Kim JJ, Jang IG (2015) Homeostasis-based aging model for trabecular changes and its correlation with age-matched bone mineral densities and radiographs. *European journal of radiology* 84(11):2261–2268
- Lekszycki T, dell’Isola F (2012) A mixture model with evolving mass densities for describing synthesis and resorption phenomena in bones reconstructed with bio-resorbable materials. *ZAMM-Zeitschrift für Angewandte Mathematik und Mechanik* 92(6):426–444
- Miller Z, Fuchs MB, Arcan M (2002) Trabecular bone adaptation with an orthotropic material model. *Journal of biomechanics* 35(2):247–256
- Müller R (2005) Long-term prediction of three-dimensional bone architecture in simulations of pre-, peri- and post-menopausal microstructural bone remodeling. *Osteoporosis International* 16(2):S25–S35
- Müller R, Kampschulte M, El Khassawna T, et al (2014) Change of mechanical vertebrae properties due to progressive osteoporosis: combined biomechanical and finite-element analysis within a rat model. *Medical & biological engineering & computing* 52(4):405–414
- Nowak M (2006) A generic 3-dimensional system to mimic trabecular bone surface adaptation. *Computer methods in biomechanics and biomedical engineering* 9(5):313–317
- Nowak M (2020) New aspects of the trabecular bone remodeling regulatory model—two postulates based on shape optimization studies. In: Abali B GI (ed) *Developments and Novel Approaches in Biomechanics and Metamaterials, Advanced Structured Materials*, vol 132, Springer, Cham., pp 97–105
- Nowak M, Sokołowski J, Zochowski A (2018) Justification of a certain algorithm for shape optimization in 3D elasticity. *Structural and Multidisciplinary Optimization* 57(2):721–734
- Nowak M, Sokołowski J, Zochowski A (2020) Biomimetic approach to compliance optimization and multiple load cases. *Journal of Optimization Theory and Applications* 184(1):210–225
- Nutu E (2015) Interpretation of parameters in strain energy density bone adaptation equation when applied to topology optimization of inert structures. *Mechanika* 21(6):443–449
- Parfitt AM, Mathews CH, Villanueva AR, et al (1983) Relationships between surface, volume, and thickness of iliac trabecular bone in aging and in osteoporosis. Implications for the microanatomic and cellular mechanisms of bone loss. *The Journal of clinical investigation* 72(4):1396–1409
- Sigmund O (1999) On the optimality of bone microstructure. In: *IUTAM symposium on synthesis in bio solid mechanics*, Springer, pp 221–234
- Van Oers RFM, Ruimerman R, Tanck E, Hilbers PAJ, Huiskes R (2008) A unified theory for osteonal and hemi-osteonal remodeling. *Bone* 42(2):250–259
- Waarsing JH, Day JS, Weinans H (2004) An improved segmentation method for in vivo μ CT imaging. *Journal of Bone and Mineral Research* 19(10):1640–1650
- Wierszycki M, Szajek K, Lodygowski T, Nowak M (2014) A two-scale approach for trabecular bone microstructure modeling based on computational homogenization procedure. *Computational Mechanics* 54(2):287–298
- Wolff J (1892) *Das Gesetz der Transformation der Knochen*, Berlin, A. Hirschwald. *The Law of Bone Remodeling*
- Wu J, Aage N, Westermann R, Sigmund O (2017) Infill optimization for additive manufacturing—approaching bone-like porous structures. *IEEE transactions on visualization and computer graphics* 24(2):1127–1140



Chapter 23

Modeling the Magnetic Relaxation Behavior of Micropolar Ferrofluids by Means of Homogenization

Wilhelm Rickert, Max Winkelmann, Wolfgang H. Müller

Abstract In this paper a simple particle population homogenization approach is used in order to estimate the magnetic relaxation time of a ferrofluid by means of a microscopic analysis. At a macroscopic level the ferrofluid is modeled as a micropolar fluid with rotational degrees of freedom. The governing equations for these degrees of freedom are the spin balance and the magnetic relaxation equation. They are solved analytically for a simple unidirectional magnetic setup. On a microscopic level the ferrofluid is considered to consist of rigid spherical permanent magnets suspended in a non-magnetic carrier fluid. Due to both, the friction of the micro magnets with the carrier fluid and their own inertia, the alignment of the magnets with an applied external field is retarded. By neglecting thermal effects and therefore the Brownian motion, it is possible to reduce the equations of motion to a nonlinear pendulum equation, which is readily solved using numerical methods for ordinary differential equations. By averaging over all possible initial configurations of the micro magnets, a pseudo homogenization is obtained, which can then be compared to the macroscopic solution. From this comparison the relaxation time at a continuum level can be estimated.

Keywords: Micropolar fluids · Magnetic relaxation · Homogenization · Parameter identification

W. Rickert, W. H. Müller

Institute of Mechanics, Chair of Continuum Mechanics and Constitutive Theory, Technische Universität Berlin, Einsteinufer 5, 10587 Berlin, Germany
e-mail: rickert@tu-berlin.de, wolfgang.h.mueller@tu-berlin.de

M. Winkelmann

Multiscale Mechanics, Department of Thermal and Fluid Engineering, Faculty of Engineering Technology, University of Twente, PO Box 217, 7500AE Enschede, the Netherlands
e-mail: m.winkelmann@utwente.nl

23.1 Introduction

The theory as well as almost all experimental considerations regarding ferrofluids are outlined in Rosensweig (1997), see also the references therein. In short, ferrofluids are a suspension of magnetic nanoparticles in a carrier fluid. Magnetite (Fe_3O_4) is commonly used for the particles and fluids like water, kerosene and other oils are used as a carrier. At a continuum level ferrofluids can be modeled as micropolar fluids. In addition to the translational degrees of freedom of material points, their intrinsic rotation is represented by a local angular velocity field, $\boldsymbol{\omega}$. Ferrofluids exhibit a complex magnetic behavior. They can be approximated as linear magnets, but with additional viscous behavior, *i.e.*, the magnetization undergoes the process of relaxation, Torres-Diaz and Rinaldi (2014). This is captured by the magnetic relaxation equation,

$$\frac{d\mathbf{M}}{dt} = \boldsymbol{\omega} \times \mathbf{M} - \frac{1}{\tau_r}(\mathbf{M} - \mathbf{M}_{\text{eq}}), \quad (23.1)$$

where \mathbf{M} is the (MINKOWSKIAN) magnetization vector and τ_r is the magnetic relaxation time. The equilibrium magnetization $\mathbf{M}_{\text{eq}} = \hat{\mathbf{M}}_{\text{eq}}(\boldsymbol{\mathfrak{H}})$ is usually modeled using a linear approximation, $\mathbf{M}_{\text{eq}} = \chi \boldsymbol{\mathfrak{H}}$, where $\boldsymbol{\mathfrak{H}}$ is the magnetic field. This evolution equation is motivated in (Rosenweig, 1997) and derived using rational thermodynamics in (Felderhof and Kroh, 1999).

The goal of this paper is to use a simple homogenization approach in order to obtain the relaxation time τ_r of the ferrofluid by means of analyzing the suspension at a microscopic level. It is assumed that the material parameters of both the carrier fluid and the magnetic particles are known. The procedure from Vilchevskaya and Müller (2021) is followed closely.

23.2 Problem Setup and Homogenization Procedure

Consider an infinitely large domain of resting ferrofluid that is subjected to a homogeneous magnetic field $\boldsymbol{\mathfrak{H}}_M(t)$, which is only a function of time. This is depicted schematically in Fig. 23.1 (left). At a continuum level the fluid is modeled by means of micropolar theory. Hence, each material point has both a translational velocity \mathbf{v}_M and an angular velocity $\boldsymbol{\omega}_M$. The index “M” indicates that these are macroscopic quantities, *i.e.*, they are defined at a continuum level. The ferrofluid is considered to be incompressible and therefore its mass density ρ_M is constant. Furthermore, the rotational inertia, given by the micropolar inertia tensor \mathbf{J}_M , is also assumed to be constant. In this idealized scenario, no field is expected to have a spatial dependence. In particular, there is no translational velocity, $\mathbf{v}_M \equiv \mathbf{0}$. The quantities of interest are both the magnetization, \mathbf{M}_M , as well as the angular velocity field, $\boldsymbol{\omega}_M$. For a comprehensive review of micropolar theory see (Cowin, 1974).

In order to find the magnetic relaxation time τ_r in Eq. (23.1), the scenario described above is additionally analyzed from a microscopic point of view. At a microscopic level the particles suspended in the carrier fluid are assumed to be spherical magnets. Their magnetization M_m is approximately constant, which is referred to as permanent magnetization. The index “m” indicates a quantity at the microscopic level. The view onto a single particle at the microlevel is depicted schematically in Fig. 23.1. The suspended particles are assumed to be far enough away from each other such

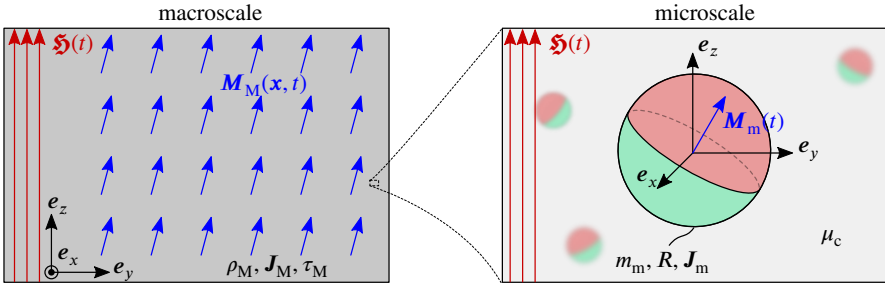


Fig. 23.1 Schematic depiction of both the macroscale and the microscopic view of a ferrofluid. Left: Section of a ferrofluid bath at a continuum level. Right: Zoom into the microstructure of the ferrofluid.

that their mutual interaction can be neglected. Furthermore, these micro magnets are assumed to be rigid. Therefore, rigid body mechanics is used to determine their motion. In addition to the mass of a rigid body, its moment of inertia tensor J_m is required. For a spherical rigid body the moment of inertia tensor is spherical, *i.e.*, $J_m = J_m \mathbf{1}$, where $\mathbf{1}$ is the unit tensor.

Note that the micropolar inertia tensor J_M and the moment of inertia tensor J_m are different quantities. In general, $J_M = \hat{J}_M(x, t)$ is a field quantity in the context of a continuum similar to the mass density. It connects the micropolar angular velocity ω_M with the specific spin field and has the unit m^2 . In contrast, the tensor $J_m = \hat{J}_m(t)$ may be a function of time only and represents a property of a rigid body as a whole similar to its mass. The moment of inertia tensor connects the angular velocity of a rigid body with its angular momentum and has the unit $kg \cdot m^2$.

At the microscopic level all particles are considered to be equal, *i.e.*, they have the same radius, mass and magnetization, namely R , m_m and M_m , respectively. As the micro magnets are assumed to have a permanent magnetization, its temporal change is solely given by the rotation of the magnet,

$$\frac{dM_m}{dt} = \omega_m \times M_m, \tag{23.2}$$

where ω_m is the rigid body angular velocity at the microscale.

The connections between the microscale and the macroscale are found by means of a particle population homogenization approach. The particle population average

operator is defined via, see Vilchevskaya and Müller (2021),

$$\langle \mathbf{M}_m \rangle := \int_{\varphi=0}^{2\pi} \int_{\vartheta=0}^{\pi} \mathbf{M}_m P(\vartheta, \varphi) \sin(\vartheta) \, d\vartheta \, d\varphi, \quad (23.3)$$

where $P(\vartheta, \varphi)$ is a probability density, ϑ and φ are the azimuthal angle and polar angle, respectively. Initially, a micro magnet may have an orientation that deviates from the external magnetic field. This difference in orientation is captured by the two angles ϑ and φ . The function $P(\vartheta, \varphi)$ returns the probability of finding a micro magnet with the orientation specified by ϑ and φ . The integration with respect to all possible orientations yields an averaged magnetization $\langle \mathbf{M}_m \rangle$. It is assumed that the application of the same averaging procedure to other quantities yields their counterpart at the continuum level, *e.g.*,

$$\boldsymbol{\omega}_M = \langle \boldsymbol{\omega}_m \rangle, \quad \mathbf{J}_M = \left\langle \frac{\mathbf{J}_m}{m_m} \right\rangle. \quad (23.4)$$

Note that since all microparticles are assumed to be identical spheres, it follows that $\mathbf{J}_M = m_m^{-1} \mathbf{J}_m$, see (Vilchevskaya and Müller, 2021). Furthermore, the external magnetic field does not depend upon the scale and hence $\mathfrak{H}(t) := \mathfrak{H}_m(t) = \mathfrak{H}_M(t)$. For the magnetization, however, the identification of the macroscopic version, \mathbf{M}_M , by means of the microscopic one, $\langle \mathbf{M}_m \rangle$, is *not* given by the particle population average. This is due to the fact that the magnetization vector is a volume density, *i.e.*, the magnetic moment per volume. Hence, a volumetric average is more appropriate which requires knowledge of the spatial particle distribution, see the comments in Nicot et al (2017). In order to simplify the analysis we assume that the macroscopic magnetization and the averaged microscopic magnetization are at least proportional,

$$\mathbf{M}_M \sim \langle \mathbf{M}_m \rangle. \quad (23.5)$$

In order to perform the comparison between the two magnetization representations, solutions to the corresponding microscopic and macroscopic problems for *one* process are to be found. At both scales the external magnetic field $\mathfrak{H}(t)$ is the process defining quantity. Two simple field evolutions could be considered. First, a ramping magnetic field in one direction is considered. A second process that seems natural to analyze is a rotating magnetic field. The latter may reveal the influence of the micropolar rotational shear viscosity. However, the ramping magnetic field is easier to analyze. Furthermore, an experimental investigation is easier to perform for a non-rotating field. In short, the following magnetic field strength will be used:

$$\mathfrak{H} = \begin{cases} \mathfrak{H}_0 \frac{t}{t_0} \mathbf{e}_z, & t \leq t_0, \\ \mathfrak{H}_0 \mathbf{e}_z, & t > t_0. \end{cases} \quad (23.6)$$

The starting time interval is defined by $t_0 = 1$ s.

23.3 The Governing Equations

At the continuum level, the ferrofluid is modeled as a micropolar fluid. The governing equation for the micropolar angular velocity ω_M is given by the spin balance, see (Eringen and Maugin, 1990),

$$\rho_M \frac{d}{dt} (\mathbf{J}_M \cdot \omega_M) = \nabla \cdot \boldsymbol{\mu} + \boldsymbol{\sigma} \cdot \overset{(3)}{\boldsymbol{\epsilon}} + \mathbf{m}, \quad (23.7)$$

where the constitutive equations for the stress tensor, the couple stress tensor and the volumetric moment density are given by:

$$\begin{aligned} \boldsymbol{\sigma} &= -p_M \mathbf{1} + 2\mu_M \text{sym}(\nabla \otimes \mathbf{v}_M) - 2\tau_M (\text{skw}(\nabla \otimes \mathbf{v}_M) + \overset{(3)}{\boldsymbol{\epsilon}} \cdot \omega_M), \\ \boldsymbol{\mu} &= \alpha_M (\nabla \cdot \omega_M) \mathbf{1} + 2\beta_M \text{sym}(\nabla \otimes \omega_M) + 2\gamma_M \text{skw}(\nabla \otimes \omega_M), \\ \mathbf{m} &= \mathbf{M}_M \times \mathbf{B}. \end{aligned} \quad (23.8)$$

Therein, ρ_M is the mass density, p_M denotes the pressure and \mathbf{B} is the magnetic flux density. The latter is connected to the magnetization \mathbf{M}_M and the magnetic field $\boldsymbol{\mathfrak{H}}$ via $\mathbf{B} = \mu_0 (\mathbf{M}_M + \boldsymbol{\mathfrak{H}})$, where μ_0 is the magnetic field constant. The operators $\text{sym}(\mathbf{A}) = \frac{1}{2}(\mathbf{A} + \mathbf{A}^T)$ and $\text{skw}(\mathbf{A}) = \frac{1}{2}(\mathbf{A} - \mathbf{A}^T)$ yield the symmetric and skew-symmetric part of a tensor. The symbol $\overset{(3)}{\boldsymbol{\epsilon}}$ denotes the LEVI-CIVITA tensor. The various coefficients in the constitutive equations represent viscosities of different kinds. The parameter μ_M is the classical shear viscosity and α_M, β_M as well as γ_M represent generalized viscosities. A comprehensive review of micropolar theory is given in (Cowin, 1974).

For the following analysis, however, only the rotational shear viscosity τ_M is relevant. This is due to the specialized setting of an infinitely large domain. It is assumed that there are no spatial dependencies, *i.e.*, all fields are functions of time only. In particular, we have $\omega = \hat{\omega}(t)$. Hence, all gradients vanish and the spin balance in Eq. (23.7) reduces to

$$\rho_M \mathbf{J}_M \cdot \frac{d\omega_M}{dt} = -4\tau_M \omega_M + \mathbf{M}_M \times \mu_0 \boldsymbol{\mathfrak{H}}, \quad (23.9)$$

where $\mathbf{J}_M = J_M \mathbf{1}$ is assumed to be constant. Note that ρ_M is the mass density on the macroscale, *i.e.*, of the suspended particles and the carrier fluid combined. This equation is to be solved together with the relaxation relation in Eq. (23.1).

By assuming a planar setting with $\omega_M = \omega_M e_x$ and the magnetic field from Eq. (23.6) as well as $\mathbf{M}_M = M_y^M e_y + M_z^M e_z$, the system of equations reduces to

$$\begin{aligned} \rho_M J_M \dot{\omega}_M &= -4\tau_M \omega_M + \mu_0 \boldsymbol{\mathfrak{H}} M_y^M, \\ \dot{M}_y^M &= -\omega_M M_z^M - \frac{1}{\tau_r} M_y^M, \\ \dot{M}_z^M &= \omega_M M_y^M - \frac{1}{\tau_r} (M_z^M - \chi \boldsymbol{\mathfrak{H}}). \end{aligned} \quad (23.10)$$

At the microscopic level the scenario depicted in Fig. 23.1 (right) is considered. The rigid permanent magnet experiences a moment similar to the moment density in Eq. (23.9). Since the micro magnetization \mathbf{M}_m may not be aligned with the applied magnetic field $\mathfrak{H}(t)$, a rotation is initiated. Consequently, friction occurs between the magnet and the initially resting carrier fluid. Together, the balance of moment of momentum for the spherical magnet Ω with respect to its center of mass reads

$$\frac{d}{dt}(\mathbf{J}_m \cdot \boldsymbol{\omega}_m) = \int_{\Omega} \mathbf{M}_m \times \mathbf{B} \, dV + \int_{\partial\Omega} \mathbf{x} \times \mathbf{t} \, dA. \quad (23.11)$$

Therein, the microscopic moment of inertia is given by $\mathbf{J}_m = J_m \mathbf{1} = \frac{2}{5} m_m R^2 \mathbf{1}$. Furthermore, the stress vector exerted by the surrounding fluid is obtained from the corresponding stress tensor *in the carrier fluid*,

$$\mathbf{t} = -p_c \mathbf{n} + 2\mu_c \mathbf{n} \cdot \mathbf{D}, \quad \mathbf{D} = \frac{1}{2}(\nabla \otimes \mathbf{v}_c + \mathbf{v}_c \otimes \nabla), \quad (23.12)$$

where p_c and \mathbf{v}_c are the pressure and the velocity field in the carrier fluid, respectively, μ_c is its shear viscosity and $\mathbf{n} = \mathbf{e}_r$ is the outward normal vector of the rigid sphere, see Fig. 23.1 (right). In spherical coordinates the position vector at the surface of the sphere is given by $\mathbf{x} = R\mathbf{e}_r$. It turns out that only the φ - r component of the symmetric velocity gradient is relevant. Hence, the moment density due to friction is given by $\mathbf{x} \times \mathbf{t} = -2R\mu_c D_{\varphi r} \mathbf{e}_{\vartheta}$.

In order to obtain the velocity field of the carrier fluid, the NAVIER–STOKES equations are solved. To this end a simplified scenario is considered. Assume that there is no magnetic field and the rigid sphere spins with a constant angular velocity $\boldsymbol{\omega}_0 = \omega_0 \mathbf{e}_z$. At the sphere's interface a no-slip condition is used, *i.e.*,

$$\mathbf{v}_c(r = R) = \boldsymbol{\omega}_0 \times \mathbf{x} = \omega_0 R \sin(\vartheta) \mathbf{e}_{\varphi}. \quad (23.13)$$

Additionally, it is assumed that the velocity disturbance due to the motion of the magnet vanishes as $\|\mathbf{x}\| \rightarrow \infty$. By means of BERNOULLI's separation method one obtains an analytical solution for the velocity field of the carrier fluid,

$$\mathbf{v}_c = \omega_0 R^3 r^{-2} \sin(\vartheta) \mathbf{e}_{\varphi} \quad \Rightarrow \quad D_{\varphi r} = -\frac{3\omega_0 R^3}{2r^3} \sin(\vartheta). \quad (23.14)$$

Consequently, the mechanical moment due to friction can be written as

$$\int_{\partial\Omega} \mathbf{x} \times \mathbf{t} \, dA = -4\mu_c R^3 \boldsymbol{\omega}_0. \quad (23.15)$$

This shows that the mechanical moment acting on the sphere is proportional to its (constant) angular velocity. A key simplification of Eq. (23.11) is obtained by adopting this relation also for the case of non constant angular velocities. We replace $\boldsymbol{\omega}_0 \rightarrow \boldsymbol{\omega}_m(t)$, where $\boldsymbol{\omega}_m(t)$ is the time dependent angular velocity of the magnet

that is subjected to an external field. The resulting representation for the mechanical moment due to friction was also suggested in (Shliomis, 1971).

Finally, the balance of moment of momentum for the spherical permanent magnet subjected to an external magnetic field $\mathfrak{H}(t)$ is given by

$$J_m \dot{\omega}_m = \frac{4}{3} \pi R^3 \mu_0 \mathbf{M}_m \times \mathfrak{H}(t) - 4 \mu_c R^3 \omega_m . \tag{23.16}$$

Note that the magnetic field disturbance caused by the magnet itself does not contribute to the moment. This is due to the fact that a magnet does not accelerate on its own.

All relevant parameters are given in Tab. 23.1. A value for the rotational shear viscosity τ_M was not found in the literature. Instead, an estimate is used based on the results from (Kolpashchikov et al, 1983) for water. One should note that the

Table 23.1 Material parameters on the micro and macroscale for magnetite particles suspended in kerosene.

| parameter | symbol | value | reference |
|----------------------------|----------------------------------|---|---|
| micro mass density | ρ_m | 5170 kg/m ³ | Kampf et al (2001) |
| radius of one particle | R | 2.5 – 10 nm | Torres-Diaz and Rinaldi (2014) |
| carrier fluid viscosity | μ_c | 2.2×10^{-3} Pa s | Rosensweig (1997) |
| micromagnetization | $M_m = \frac{m_{\text{mag}}}{V}$ | $2.2 \times 10^5 - 1.4 \times 10^6$ A/m | Odenbach (2004); Torres-Diaz and Rinaldi (2014) |
| mass density | ρ_M | 1330 kg/m ³ | estimated |
| shear viscosity | μ_M | 2.9×10^{-3} Pa s | (Rosensweig, 1997, Tab. 8.1) |
| rotational shear viscosity | τ_M | (1 to 2) μ_M | estimated |
| susceptibility | χ | 0.37 | (Rosensweig et al, 1969, Tab. 1) |

macroscopic material parameters can vary significantly with the magnetic field. In (Rosensweig, 1997, Tab. 8.1) the relative change of the shear viscosity due to an external magnetic field ranges from 13% for moderate field strengths up to 77% for strong fields. Hence, our assumption of constant material parameters in Tab. 23.1 is questionable. However, as will be seen later, several parameters do not influence the analysis, *e.g.*, τ_M is not contained in the magnetization solution. Additionally, from the table it follows that the mass of one microparticle can be obtained by $m_m \approx \rho_m \frac{4}{3} \pi R^3 \approx 2.7 \times 10^{-21}$ kg.

23.4 Solution to the Microscopic Problem

First, the problem is reformulated by using nondimensional quantities. By introducing

$$\boldsymbol{\omega}_m = \frac{1}{t_{\text{ref}}} \tilde{\boldsymbol{\omega}}_m, \quad \mathbf{M}_m = M_m \tilde{\mathbf{M}}_m, \quad \boldsymbol{\mathfrak{H}} = \mathfrak{H}_0 \tilde{\boldsymbol{\mathfrak{H}}}, \quad (23.17)$$

the problem on the microscale from Eq. (23.16) is written as

$$\frac{d\tilde{\boldsymbol{\omega}}_m}{d\tilde{t}} = \tilde{\mathbf{M}}_m \times \tilde{\boldsymbol{\mathfrak{H}}} - D_m \tilde{\boldsymbol{\omega}}_m, \quad (23.18)$$

where the reference time was chosen in order to emphasize the moment due to magnetic misalignment, *i.e.*,

$$t_{\text{ref}} = \sqrt{\frac{3m_m}{10\mu_0 M_m \mathfrak{H}_0 \pi R}}, \quad D_m = \frac{10t_{\text{ref}} \mu_c R}{m_m}. \quad (23.19)$$

The newly introduced parameter D_m characterizes the damping due to friction. Both the reference time and the damping parameter depend strongly upon the magnitude of the applied magnetic field. In particular, since very small field strengths could be applied, the damping parameter could become very large as $D_m \rightarrow \infty$ as $\mathfrak{H}_0 \rightarrow 0$. For commonly used solenoids and their corresponding magnetic field strengths a lower bound for the damping parameter of $100 \leq D_m$ can be estimated.

The differential Eq. (23.18) is supplemented with the following initial conditions:

$$\tilde{\mathbf{M}}_m(\tilde{t} = 0) = \tilde{\mathbf{M}}_m^0 = \mathbf{e}_r(\vartheta_0, \varphi_0), \quad \tilde{\boldsymbol{\omega}}_m(\tilde{t} = 0) = \mathbf{0}. \quad (23.20)$$

Therein, \mathbf{e}_r is the radial base vector in spherical coordinates and ϑ_0 and φ_0 are the polar and azimuthal angle of the initial magnetization with respect to a coordinate system for which the z axis is aligned with $\tilde{\boldsymbol{\mathfrak{H}}}$. The magnetization vector $\tilde{\mathbf{M}}_m$ represents the orientation of the magnet, from which the angular velocity $\tilde{\boldsymbol{\omega}}_m$ can be obtained. Hence, Eq. (23.18) can be formulated solely in terms of the magnet's orientation. In general, the orientation can be described by, *e.g.*, EULER angles, BYRANT angles or EULER parameters, see (Wittenburg, 1977). Then, the orientation parameters are connected to the angular velocity via a coupled linear system of differential equations.

However, due to the azimuthal symmetry of the problem and due to the simple magnetic excitation in z direction only, the scenario simplifies significantly. If the micro magnet is initially at rest, its motion is restricted to the plane spanned by the vectors \mathbf{e}_z and $\tilde{\mathbf{M}}_m^0$. The current magnetization is obtained by means of a rotation about the z axis

$$\tilde{\mathbf{M}}_m(\tilde{t}) = \cos(\vartheta) \mathbf{e}_z + \sin(\vartheta) \mathbf{d} \times \mathbf{e}_z + (1 - \cos(\vartheta)) (\mathbf{d} \cdot \mathbf{e}_z) \mathbf{d}, \quad (23.21)$$

where $\vartheta = \hat{\vartheta}(\tilde{t})$ is the angle of rotation and \mathbf{d} is the normalized axis of rotation, which is constant in this scenario. Note that the angle of rotation coincides with the

polar angle in spherical coordinates. Hence, the same symbol is used. Furthermore, one has

$$\hat{\vartheta}(\tilde{t} = 0) = \vartheta_0, \quad \mathbf{d} = \frac{\mathbf{e}_z \times \tilde{\mathbf{M}}_m^0}{\|\mathbf{e}_z \times \tilde{\mathbf{M}}_m^0\|} = \text{const.} \quad (23.22)$$

Note that every vector perpendicular to the z axis can be used as the axis of rotation. Hence, without loss of generality we put $\mathbf{d} = -\mathbf{e}_x$ and obtain

$$\tilde{\mathbf{M}}_m(\tilde{t}) = \sin(\vartheta)\mathbf{e}_y + \cos(\vartheta)\mathbf{e}_z. \quad (23.23)$$

Since the axis of rotation is constant, the angular velocity is simply proportional to this axis and it follows from Eq. (23.18) that

$$\tilde{\omega}_m = \frac{d\vartheta}{d\tilde{t}}\mathbf{d} \Rightarrow \frac{d^2\vartheta}{d\tilde{t}^2} + D_m \frac{d\vartheta}{d\tilde{t}} + \tilde{\mathcal{H}}(\tilde{t}) \sin(\vartheta) = 0, \quad (23.24)$$

which is a nonlinear pendulum equation that is solved numerically using MATHEMATICA’s build in function “NDSolve,” (Inc., 2015). The resulting solutions for different values of D_m are depicted in Fig. 23.2. From the figure it can be seen that for small

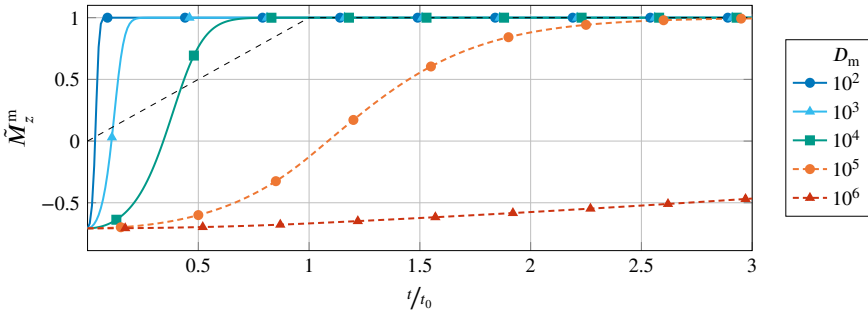


Fig. 23.2 Time evolution of the microscopic magnetization for different damping parameters. The initial direction of the magnetization is characterized by $\vartheta_0 = \frac{3}{4}\pi$. The black dashed line represents the evolution of the external magnetic field.

values of the damping parameter the stationary state, *i.e.*, alignment with the z axis is achieved even before the external field reached its maximum value. With increasing damping in this system the alignment of the magnetization lags behind further and further.

23.5 Solution to the Macroscopic Problem

The equations on the macroscopic scale are also normalized, but in a slightly different manner:

$$\omega_M = \frac{1}{t_{\text{ref}}} \tilde{\omega}_M, \quad \mathfrak{H} = \mathfrak{H}_0 \tilde{\mathfrak{H}}, \quad M_i^M = \mathfrak{H}_0 \tilde{M}_i^M. \quad (23.25)$$

Both the micro and macroproblem should be considered on the same timescale. Therefore, t_{ref} from Eq. (23.19) is used. Note, however, that the normalization factors for the magnetization on both scales are different. Subsequently, the system in Eq. (23.10) reads

$$\begin{aligned} I \frac{d\tilde{\omega}_M}{d\tilde{t}} &= -D_M \tilde{\omega}_M + \tilde{\mathfrak{H}} \tilde{M}_y^M, \\ \frac{d\tilde{M}_y^M}{d\tilde{t}} &= -\tilde{\omega}_M \tilde{M}_z^M - \frac{1}{\tilde{\tau}_r} \tilde{M}_y^M, \\ \frac{d\tilde{M}_z^M}{d\tilde{t}} &= \tilde{\omega}_M \tilde{M}_y^M - \frac{1}{\tilde{\tau}_r} (\tilde{M}_z^M - \chi \tilde{\mathfrak{H}}). \end{aligned} \quad (23.26)$$

with

$$I := \frac{\rho_M}{\rho_m} \frac{M_m}{\mathfrak{H}_0}, \quad D_M := \frac{4\tau_M}{\mu_0 \mathfrak{H}_0^2 t_{\text{ref}}}, \quad \tilde{\tau}_r := \frac{\tau_r}{t_{\text{ref}}}. \quad (23.27)$$

With the parameters from Tab. 23.1 one can estimate the dimensionless parameters as

$$I \approx 69, \quad D_M \approx 798\,036. \quad (23.28)$$

In general, the system in Eq. (23.26) needs to be solved numerically, *e.g.*, for a rotating \mathfrak{H} field both components \tilde{M}_y^M and \tilde{M}_z^M are expected to be present. Due to the simple form of the exciting magnetic field, however, a rotational motion never start to develop from the zero initial conditions for all fields,

$$\tilde{\omega}_M(\tilde{t} = 0) = 0, \quad \tilde{M}_y^M(\tilde{t} = 0) = 0, \quad \tilde{M}_z^M(\tilde{t} = 0) = 0. \quad (23.29)$$

Hence, one finds $\tilde{\omega}_M \equiv 0$ as well as $\tilde{M}_y^M \equiv 0$ and

$$\tilde{M}_z^M(\tilde{t}) = \frac{\chi}{\tilde{\tau}_r} \int_{T=0}^{T=\tilde{t}} \exp\left(-\frac{T-\tilde{t}}{\tilde{\tau}_r}\right) \tilde{\mathfrak{H}}(T) dT. \quad (23.30)$$

For the magnetic field in Eq. (23.6) the integration yields with $\tilde{t}_0 = t_0/t_{\text{ref}}$

$$\tilde{M}_z^M(\tilde{t}) = \frac{\chi}{\tilde{t}_0} \begin{cases} (\tilde{t} - \tilde{\tau}_r) + \tilde{\tau}_r \exp\left(-\frac{\tilde{t}}{\tilde{\tau}_r}\right), & \tilde{t} < \tilde{t}_0 \\ \tilde{t}_0 + \tilde{\tau}_r \exp\left(-\frac{\tilde{t}}{\tilde{\tau}_r}\right) - \tilde{\tau}_r \exp\left(-\frac{\tilde{t} - \tilde{t}_0}{\tilde{\tau}_r}\right), & \tilde{t} \geq \tilde{t}_0. \end{cases} \quad (23.31)$$

Note that in contrast to the microscopic problem, the *dimensionless* solution to the macroscopic problem does not depend upon the magnitude of the external field. The time evolution of this field is depicted in Fig. 23.3. As expected, the lag of the alignment with the external field decreases with decreasing relaxation time.

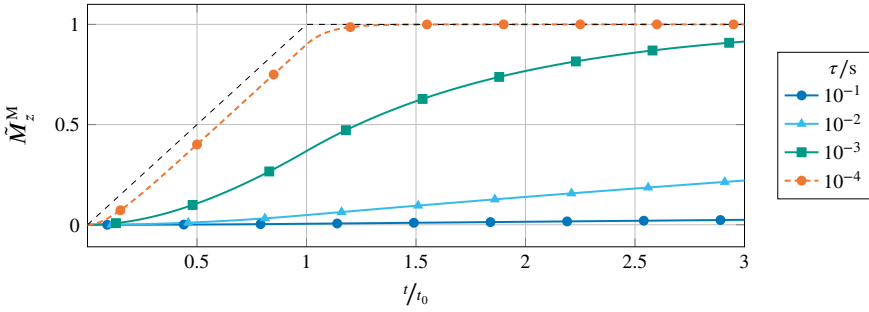


Fig. 23.3 Time evolution of the macroscopic magnetization for different relaxation times. The black dashed line represents the evolution of the external magnetic field.

23.6 Homogenization and Parameter Identification

In order to compare the microscopic fields with the macroscopic ones, a homogenization is to be performed. Following (Vilchevskaya and Müller, 2021) a transversally isotropic probability density function

$$P(\xi, \vartheta) = \frac{1}{2\pi} \left((1 + \xi^2) \exp(-\xi\vartheta) - \frac{1}{2} \exp(-\xi\pi) \right), \quad 0 \leq \vartheta \leq \pi, \quad (23.32)$$

is introduced, where ξ is a dimensionless scatter parameter. This function represents transversally isotropic behavior since the azimuthal dependence is removed, *i.e.*, the angle φ has no influence. Therefore, any two micro magnetizations that differ only by a rotation about the z axis are treated equally. The macroscopic magnetization is subsequently found via homogenization of the microscopic function with respect to the different initial configurations, *i.e.*, the angles ϑ_0 and φ_0 . If the solution to the microscopic problem is denoted as being parametrically dependent upon these initial angles, its homogenization reads

$$\langle \tilde{M}_z^m \rangle := \int_{\varphi_0=0}^{2\pi} \int_{\vartheta_0=0}^{\pi} \tilde{M}_z^m(\tilde{t}; \vartheta_0, \varphi_0) P(\xi, \vartheta) \sin(\vartheta_0) d\vartheta_0 d\varphi_0. \quad (23.33)$$

Since the microscopic field is only available numerically, this integral is approximated numerically by means of RIEMANN sums. There is, however, one analytical simplification that can be employed. As mentioned earlier, a difference in the initial azimuthal orientation φ_0 has no influence on the resulting z component of the micro magnetization. Therefore, the φ integration is readily performed resulting in a factor of 2π . Furthermore, the initial distribution of the micro magnetizations is assumed to be completely randomized, *i.e.*, a fully isotropic configuration is considered. Then, following (Vilchevskaya and Müller, 2021), one has $\xi = 0$ and the probability density reduces to $P(\xi, \vartheta) = \frac{1}{4\pi}$. Hence, without loss of generality we

set

$$\langle \tilde{M}_z^m \rangle = \frac{1}{2} \int_{\vartheta_0=0}^{\pi} \tilde{M}_z^m(\tilde{t}; \vartheta_0, \varphi_0 = 0) \sin(\vartheta_0) d\vartheta_0 . \quad (23.34)$$

The resulting time evolution is depicted in Fig. 23.4 for different damping parameters. The solutions look very similar to the results in Fig. 23.2 with the important difference, that there is no magnetization present in the initial state.

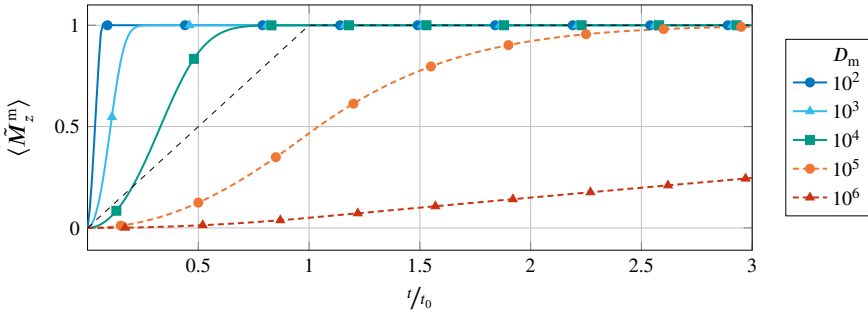


Fig. 23.4 Time evolution of the homogenized microscopic magnetization for different damping parameters. The black dashed line represents the evolution of the external magnetic field.

The goal function f that is to be minimized with respect to the relaxation time $\tilde{\tau}_r$ is given by the difference between the macroscopic magnetization \tilde{M}_z^M and the averaged microscopic solution $\langle \tilde{M}_z^m \rangle$:

$$\underset{\tilde{\tau}_r}{\text{minimize}}(f) , \quad f = |\tilde{M}_z^M - \langle \tilde{M}_z^m \rangle| . \quad (23.35)$$

It should be noted that both magnetization functions are normalized differently such that both fields assume a value of one when the relaxation is complete. Since the microscopic solution does not depend upon the relaxation time, it only has to be calculated once. Furthermore, as the macroscopic solution is given analytically, this minimization problem is rather a nonlinear model fit.

23.7 Results and Conclusion

By solving Eq. (23.35) numerically, one obtains a relaxation time of

$$\tau_r \approx 0.185 \times 10^{-3} \text{ s} . \quad (23.36)$$

The corresponding homogenized microscopic and macroscopic solutions are shown in Fig. 23.5. The fit is not perfect, but the time at which the stationary solution is reached is predicted equally by both models. The magnitude of the applied mag-

netic field $\mathfrak{H}_0 \approx 1800 \frac{\text{A}}{\text{m}}$ results in a damping parameter of $D_m = 0.5 \times 10^5$, see Eq. (23.19). The relaxation time in Eq. (23.36) is not in agreement with values for

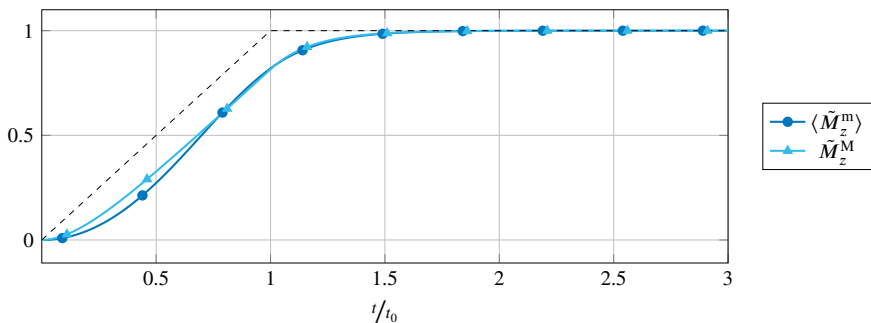


Fig. 23.5 Time evolution of both the homogenized microscopic as well as the macroscopic magnetization solution. The black dashed line represents the evolution of the external magnetic field.

the relaxation time in the literature. For example in (Rosensweig, 1997) the order of magnitude of the relaxation time is 10^{-7} to 10^{-6} . In (Torres-Diaz and Rinaldi, 2014) a similar range of 10^{-7} to 10^{-5} is given. This discrepancy may arise due to the simplicity of the models in our paper. First of all the applied magnetic process $\mathfrak{H}(t)$ is unidirectional such that, *e.g.*, the rotational shear viscosity and therefore the damping parameter D_M become irrelevant. Additionally, our “microscale” is actually a nanoscale when the radius of the particles $R \approx 10 \text{ nm}$ is considered. Hence, this problem cannot be analyzed using only mechanical considerations. The BROWNIAN motion becomes relevant at these scales. This may be the most significant influences that is missing in our simple analysis. Furthermore, the assumption of permanent magnets on the microscale is questionable and a linear magnetic behavior would be more appropriate. Last, a probably minor error is introduced by the assumption of constant material parameters at both levels.

With little effort the presented method could be extended to incorporate also thermal effects and thus to account for the BROWNIAN motion. It would be interesting to see how the macroscopic system reacts to a rotating external magnetic field, which would trigger the $\omega \times M$ term in the relaxation equation. However, the resulting system of differential equations probably does not permit an analytical solution, which in turn renders the parameter identification more complex. Finally, one could restrict the computational domain such that boundary conditions are to be imposed. This would allow for a comparison with real experiments, but requires additional numerical effort as, *e.g.*, the spin balance becomes a partial differential equation and gradients of all fields have to be considered.

References

- Cowin SC (1974) The theory of polar fluids. In: *Advances in Applied Mechanics*, vol. 14, Academic Press, Inc., New York, pp 279–347
- Eringen AC, Maugin GA (1990) *Electrodynamics of Continua II*. Springer New York
- Felderhof U, Kroh H (1999) Hydrodynamics of magnetic and dielectric fluids in interaction with the electromagnetic field. *The Journal of chemical physics* 110:7403–7411
- Inc WR (2015) *Mathematica*, Version 10.2
- Kampf R, Anthony JW, Bideaux RA, Bladh KW, Nichols MC (2001) Handbook of mineralogy. *American Mineralogist* 86(7-8):954–954
- Kolpashchikov V, Migun N, Prokhorenko P (1983) Experimental determination of material micropolar fluid constants. *International Journal of Engineering Science* 21(4):405–411
- Nicot F, Kruyt NP, Millet O (2017) On Hill's lemma in continuum mechanics. *Acta Mechanica* 228(5):1581–1596
- Odenbach S (2004) Recent progress in magnetic fluid research. *J Phys: Condens Matter* 16:1135–1150
- Rosensweig RE (1997) *Ferrohydrodynamics*. Dover Books on Physics, Dover Publications
- Rosensweig RE, Kaiser R, Miskolczy G (1969) Viscosity of magnetic fluid in a magnetic field. *Journal of Colloid and Interface Science* 29(4):680–686
- Shliomis MI (1971) Effective viscosity of magnetic suspensions. *Zh Eksp Teor Fiz* 61(2411):s1971d–1971
- Torres-Diaz I, Rinaldi C (2014) Recent progress in ferrofluids research: Novel applications of magnetically controllable and tunable fluids. *Soft Matter* 10
- Vilchevskaya EN, Müller WH (2021) Modeling of orientational polarization within the framework of extended micropolar theory. *Continuum Mechanics and Thermodynamics* 33(4):1263–1279
- Wittenburg J (1977) *Dynamics of Systems of Rigid Bodies*. Vieweg + Teubner Verlag



Chapter 24

Numerical Homogenisation of Gradient Materials

Felix Schmidt, Melanie Krüger, Christian Hesch

Abstract In this contribution, we present a numerical homogenization procedure for gradient materials. In particular, we investigate the prototypical example of fiber reinforced materials and demonstrate, that even at a typical microscale we obtain second order continuum. In particular, we make use of immersed technologies to embed the fibers within the matrix material. Introducing a novel approach IGA² using spline based approximations on both, the micro- and the macroscale, allows for the numerical homogenisation of complex microstructures with anisotropic second gradient contributions of the fibers as shown in a representative example.

Keywords: Numerical homogenization · Gradient materials · IGA² approach · Fiber reinforced polymers

24.1 Introduction

In this contribution we focus on second gradient materials on the microscale with respect to the particular example of fiber reinforced materials with high stiffness ratio. Hence, the constitutive relation of this class of materials is governed by the given microstructure. In Giorgio (2016) a detailed analysis demonstrates that a model using a Cauchy continuum on the finest scale can be homogenized using a macro second gradient model. In Kouznetsova (2002) and Kouznetsova et al (2002) a homogenization method using a representative volume element for the microscopic first order Cauchy continuum leads also to a second order macroscopic continuum.

However, we consider the length scales of the embedded fibers on the microscale as small compared to the surrounding continuum. Hence, the diameter of the em-

F. Schmidt, M. Krüger, C. Hesch
University of Siegen, Paul-Bonatz-Straße 9-11, Siegen, Germany
e-mail: felix.schmidt@uni-siegen.de, melanie.krueger@uni-siegen.de,
christian.hesch@uni-siegen.de

bedded fibers is even small compared to the size of the microstructure, such that there exist also a 'nanostructure', resolving the structure of the fibers, such that the microstructure only represents an intermediate scale model. In dell'Isola et al (2019), pantographic mechanisms as prototypical material with dedicated microstructure have been investigated, see also dell'Isola et al (2016) for a suitable Piola homogenization of rod-like structures. We refer also to Asmanoglo and Menzel (2017) for higher-order formulations used in the context of composites based on the early work of Spencer and Soldatos (2007).

Attached unit cells or representative volume elements (\mathcal{RVE}) are used in Keip et al (2014) and Schröder and Keip (2012) for electro-mechanically coupled boundary value problems. Here, first gradient theories are applied for the displacement and the electric potential. Furthermore, a two-scale homogenization approach is implemented with the FE^2 -method using a consistent linearization of the macroscopic stresses, see Schröder (2014). Fundamentals on homogenisation based on energy criteria for first order continua can be found in Hill (1963, 1972) and Mandel (1972), along other homogenisation techniques, i.e. in Barboura and Li (2018); Abali and Barchiesi (2021).

To deal with higher-order continuity requirements, isogeometrical analysis (IGA) has become popular in recent years. IGA employs the same NURBS basis functions for the geometric design as well as for the analysis and was introduced in Hughes et al (2005). It allows for the construction of finite element basis functions with adjustable continuity across the element boundaries, in contrast to classical Lagrangian basis functions, which are always C^0 continuous at the element boundaries. This enables the numerical treatment of higher-order partial differential equations, e.g. for Cahn–Hilliard or Cahn–Hilliard like formulations (see Gomez et al, 2008; Hesch et al, 2016), for the application on fracture mechanics (see Borden et al, 2014; Dittmann et al, 2018), in structural mechanics (see, e.g., Benson et al, 2010; Kiendl et al, 2009; Reali and Gomez, 2015), and for generalized continua (see Fischer et al, 2011).

In this work, we introduce first the basic concepts in Section 24.2, 24.3 and 24.3.2. Afterwards, in Section 24.4 a continuous distribution of fibers is taken into account using a homogeneous second gradient model. The corresponding homogenisation procedure of this gradient material on the microscale is shown in Section 24.5. A final example is given in Section 24.6 and conclusion are drawn in Section 24.7.

24.2 Basic Notation

In the following, we briefly summarize the basic notation used throughout the article. The scalar product of two vectors \mathbf{a} , \mathbf{b} , two second order tensors \mathbf{A} , \mathbf{B} , two third order tensors \mathfrak{A} , \mathfrak{B} and two fourth order tensors \mathbb{A} , \mathbb{B} is given by

$$\begin{aligned} [\mathbf{a} \cdot \mathbf{b}] &= a_i b_i, & [\mathbf{A} : \mathbf{B}] &= A_{ij} B_{ij}, \\ [\mathfrak{A} \dot{\mathfrak{B}}] &= A_{ijk} B_{ijk}, & [\mathbb{A} :: \mathbb{B}] &= A_{ijkl} B_{ijkl}. \end{aligned} \tag{24.1}$$

Here, Latin indices range in the set $\{1, 2, 3\}$. We will make use of the Einstein summation convention on repeated indices. Other multiplications of two tensors of different order are given in the following way, here for example, for a fourth order tensor \mathbb{A} with a third order tensor \mathfrak{B} , second order \mathbf{B} and vector \mathbf{b}

$$[\mathbb{A}\mathbf{b}]_{ijkl} = A_{ijkl} b_l, \quad [\mathbb{A} : \mathbf{B}]_{ij} = A_{ijkl} B_{kl}, \quad [\mathbb{A} : \mathfrak{B}]_i = A_{ijkl} B_{jkl}. \quad (24.2)$$

All other combinations follow analogously. The dyadic product \otimes increases the order of the tensor. For example, a dyadic product of two vectors \mathbf{a}, \mathbf{b} is given by $\mathbf{A} = \mathbf{a} \otimes \mathbf{b}$ with $A_{ij} = a_i b_j$. Next, we define the macroscopic gradient with respect to the macroscopic reference $\bar{\nabla}(\bullet)$ of a vector field $\bar{\mathbf{a}}$ and of a second order tensor field $\bar{\mathbf{A}}$ as

$$[\bar{\nabla}\bar{\mathbf{a}}]_{iJ} = \frac{\partial[\bar{\mathbf{a}}]_i}{\partial[\bar{\mathbf{X}}]_J} \quad \text{and} \quad [\bar{\nabla}\bar{\mathbf{A}}]_{iJK} = \frac{\partial[\bar{\mathbf{A}}]_{iJ}}{\partial[\bar{\mathbf{X}}]_K}. \quad (24.3)$$

For the macroscopic divergence operator it follows

$$[\bar{\nabla} \cdot \bar{\mathbf{A}}]_i = \frac{\partial[\bar{\mathbf{A}}]_{iJ}}{\partial[\bar{\mathbf{X}}]_J} \quad \text{and} \quad [\bar{\nabla} \cdot \bar{\mathfrak{A}}]_{iJ} = \frac{\partial[\bar{\mathfrak{A}}]_{iJK}}{\partial[\bar{\mathbf{X}}]_K}. \quad (24.4)$$

The microscopic gradient $\nabla\mathbf{a}$ and $\nabla\mathbf{A}$ as well as the divergence operators $\nabla \cdot \mathbf{A}$ and $\nabla \cdot \mathfrak{A}$ are given analogously to (24.3) and (24.4) omitting the overlined symbol “-”.

24.3 Second Gradient Macroscopic Continuum and First Gradient Microscopic Continuum

In this first section, we start with a short summary of a homogenization technique for a second gradient continuum in the macroscale and a first gradient continuum in the microscale. In particular, we follow the work of Kouznetsova et al (2002, 2004), introducing the fundamental equations and settings for a numerical two-scale homogenisation problem.

24.3.1 Macroscopic Boundary Value Problem

At first, we introduce a reference configuration $\bar{\Omega}_0 \subset \mathbb{R}^3$ with boundary $\partial\bar{\Omega}_0$ and outward unit normal $\bar{\mathbf{N}}$ and a current configuration $\bar{\Omega} \subset \mathbb{R}^3$ with boundary $\partial\bar{\Omega}$ and outward unit normal $\bar{\mathbf{n}}$. The deformation mapping $\bar{\varphi} : \bar{\Omega}_0 \rightarrow \bar{\Omega}$ relates the reference and current configuration to each other, $\bar{\Omega} = \bar{\varphi}(\bar{\Omega}_0)$. Furthermore, the vector to an arbitrary material point P is labeled by $\bar{\mathbf{X}} \in \bar{\Omega}_0$. In the current configuration, the corresponding point p is given by $\bar{\mathbf{x}} = \bar{\varphi}(\bar{\mathbf{X}})$, see Fig. 24.1.

The first order deformation measure $\bar{\mathbf{F}} : \bar{\Omega}_0 \rightarrow \mathbb{R}^{3 \times 3}$ and the second order deformation measure $\bar{\mathfrak{F}} : \bar{\Omega}_0 \rightarrow \mathbb{R}^{3 \times 3 \times 3}$ are given by the first and second derivative of the mapping $\bar{\varphi}(\bar{\mathbf{X}})$

$$\bar{\mathbf{F}} = \bar{\nabla} \bar{\varphi} \quad \text{and} \quad \bar{\mathfrak{F}} = \bar{\nabla}^2 \bar{\varphi}, \tag{24.5}$$

where $\bar{\nabla}$ refers to the gradient with respect to $\bar{\mathbf{X}}$, see (24.3). Following Kouznetsova (2002), Javili et al (2013) and Dittmann et al (2021), we postulate the virtual work of the internal contributions as follows

$$\delta \bar{\Pi}^{\text{int}} = \int_{\bar{\Omega}_0} \left(\bar{\mathbf{P}} : \delta \bar{\mathbf{F}} + \bar{\mathfrak{P}} : \delta \bar{\mathfrak{F}} \right) dV, \tag{24.6}$$

where $\bar{\mathbf{P}}$ denotes the macroscopic two-point first Piola-Kirchhoff stress tensor and $\bar{\mathfrak{P}}$ the macroscopic two-point third order stress tensor, conjugate to $\bar{\mathfrak{F}}$. Moreover,

$$\delta \bar{\mathbf{F}} = \bar{\nabla} \delta \bar{\varphi} \quad \text{and} \quad \delta \bar{\mathfrak{F}} = \bar{\nabla}^2 \delta \bar{\varphi}, \tag{24.7}$$

where the space of virtual or admissible test functions is given by

$$\mathcal{V} = \{ \delta \bar{\varphi} \in \mathcal{H}^2(\bar{\Omega}) \mid \delta \bar{\varphi} = \mathbf{0}, \bar{\nabla} \delta \bar{\varphi} \bar{\mathbf{N}} = \mathbf{0} \text{ on } \bar{\Gamma}^{\varphi} \} \tag{24.8}$$

with boundary $\bar{\Gamma}^{\varphi}$, see Fig. 24.2. The external contributions to the virtual work are given by

$$\delta \bar{\Pi}^{\text{ext}} = \int_{\bar{\Omega}_0} \bar{\mathbf{B}}_{\text{ext}} \cdot \delta \bar{\varphi} dV + \int_{\bar{\Gamma}^{\sigma}} \bar{\mathbf{T}}_{\text{ext}} \cdot \delta \bar{\varphi} dA + \int_{\bar{\Gamma}^{\nabla \sigma}} \bar{\mathbf{M}}_{\text{ext}} : \bar{\nabla} \delta \bar{\varphi} dA \tag{24.9}$$

with the common body force per unit volume $\bar{\mathbf{B}}_{\text{ext}}$, the traction forces $\bar{\mathbf{T}}_{\text{ext}}$ on boundary $\bar{\Gamma}^{\sigma}$ and the hyperstress traction force $\bar{\mathbf{M}}_{\text{ext}}$ on boundary $\bar{\Gamma}^{\nabla \sigma}$, see once again Fig. 24.2.

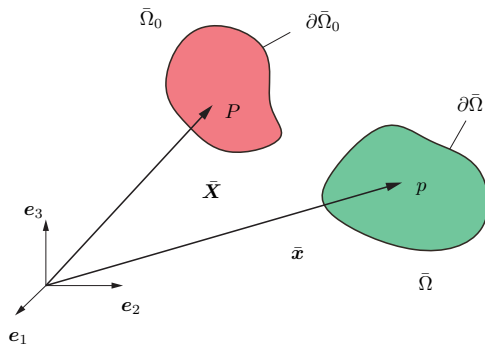


Fig. 24.1 Reference and current configuration.

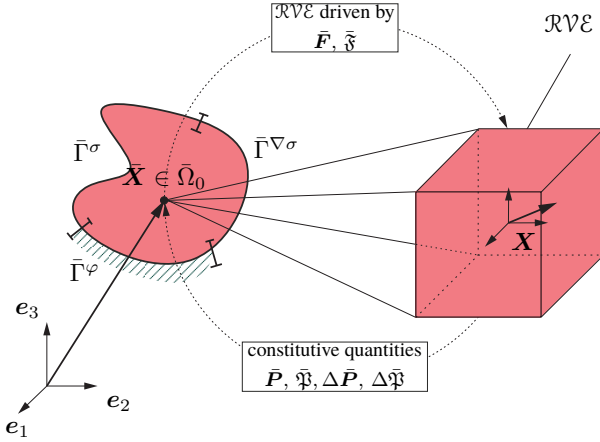


Fig. 24.2 Micro-macro transition of the mechanical boundary value problem. Left: Boundary decomposition of the macro continuum in Dirichlet boundaries $\bar{\Gamma}^\varphi$ and Neumann boundaries $\bar{\Gamma}^\sigma$, $\bar{\Gamma}^{\nabla\sigma}$ of the traction force and the hyperstress traction force. Right: \mathcal{RVE} as defined for every macroscopic point.

The principle of virtual work reads now

$$\delta \bar{\Pi}^{\text{int}} - \delta \bar{\Pi}^{\text{ext}} = 0, \quad \forall \delta \bar{\varphi} \in \mathcal{V}. \quad (24.10)$$

The internal contributions can be related by applying partial integration and the Gaussian integral theorem to the external contributions, see Javili et al (2013)

$$\begin{aligned} \bar{\mathbf{T}}_{\text{ext}} &= (\bar{\mathbf{P}} - \bar{\nabla} \cdot \bar{\mathfrak{P}}) \bar{\mathbf{N}}, \\ \bar{\mathbf{M}}_{\text{ext}} &= \bar{\mathfrak{P}} \bar{\mathbf{N}}. \end{aligned} \quad (24.11)$$

Note, that the last equation can be decomposed in tangential and normal components, see Madeo et al (2016) for details. Taking the balance equation

$$\bar{\nabla} \cdot (\bar{\mathbf{P}} - \bar{\nabla} \cdot \bar{\mathfrak{P}}) + \bar{\mathbf{B}}_{\text{ext}} = \mathbf{0} \quad (24.12)$$

into account, completes the set of equations for the strong form of the second gradient boundary value problem. In the following, we omit volumetric body forces as gravity forces, thereby $\bar{\mathbf{B}}_{\text{ext}} = \mathbf{0}$.

24.3.2 Microscopic Boundary Value Problem (First Gradient)

In every material point P , we assume the existence of a representative finite domain \mathcal{RVE} containing the information on the microscopic continuum, see Fig. 24.2. To be specific, we postulate a first gradient material in the domain \mathcal{RVE} .

We start with the mapping for the microscopic relative position of the material points $\mathbf{x} = \varphi(\mathbf{X})$

$$\varphi(\mathbf{X}) = \bar{\mathbf{F}} \mathbf{X} + \frac{1}{2} \bar{\mathfrak{F}} : (\mathbf{X} \otimes \mathbf{X}) + \tilde{\mathbf{w}}. \tag{24.13}$$

Here, $\tilde{\mathbf{w}}$ describes the unknown microscopic fluctuation field, which includes all higher-order terms of the Taylor series expansion, see Kouznetsova et al. Kouznetsova et al (2002). For consistency, we require $\int_{\mathcal{RVE}} \tilde{\mathbf{w}} \, dV = \mathbf{0}$. In analogy to the macroscopic quantities, we obtain the microscopic first order deformation measure $\mathbf{F} = \nabla \varphi$

$$\mathbf{F} = \bar{\mathbf{F}} + \bar{\mathfrak{F}} \mathbf{X} + \tilde{\mathbf{F}}, \tag{24.14}$$

where $\tilde{\mathbf{F}} := \nabla \tilde{\mathbf{w}}$. The averaged microscopic deformations over the volume of the \mathcal{RVE} can be connected to the macroscopic counterpart of $\bar{\mathbf{F}}$ via

$$\frac{1}{V} \int_{\mathcal{RVE}} \mathbf{F} \, dV = \bar{\mathbf{F}}, \tag{24.15}$$

if the fluctuations fulfill the following restrictions on the boundary¹

$$\frac{1}{V} \int_{\partial \mathcal{RVE}} \tilde{\mathbf{w}} \otimes \mathbf{N} \, dA = \mathbf{0} \quad \text{and} \quad \frac{1}{V} \int_{\partial \mathcal{RVE}} \nabla \tilde{\mathbf{w}} \otimes \mathbf{N} \, dA = \mathbf{0}. \tag{24.19}$$

¹ Placing the coordinate system in the center of the \mathcal{RVE} , yielding $\int_{\mathcal{RVE}} \vec{X} \, dV = \vec{0}$, and inserting the kinematic 24.13 into the volume averages, it follows

$$\frac{1}{V} \int_{\mathcal{RVE}} \mathbf{F} \, dV = \frac{1}{V} \int_{\mathcal{RVE}} (\bar{\mathbf{F}} + \bar{\mathfrak{F}} \vec{X} + \nabla \tilde{\mathbf{w}}) \, dV = \bar{\mathbf{F}} + \frac{1}{V} \int_{\mathcal{RVE}} \nabla \tilde{\mathbf{w}} \, dV \tag{24.16}$$

and

$$\frac{1}{V} \int_{\mathcal{RVE}} \bar{\mathfrak{F}} \, dV = \frac{1}{V} \int_{\mathcal{RVE}} (\bar{\mathfrak{F}} + \nabla^2 \tilde{\mathbf{w}}) \, dV = \bar{\mathfrak{F}} + \frac{1}{V} \int_{\mathcal{RVE}} \nabla^2 \tilde{\mathbf{w}} \, dV. \tag{24.17}$$

Since the macroscopic values are exactly the volume averages of the microscopic values and do not depend on the fluctuations, we require

$$\frac{1}{V} \int_{\mathcal{RVE}} \nabla \tilde{\mathbf{w}} \, dV = \vec{0} \quad \text{and} \quad \frac{1}{V} \int_{\mathcal{RVE}} \nabla^2 \tilde{\mathbf{w}} \, dV = \mathbf{0}, \tag{24.18}$$

which can be rewritten into surface integrals.

The local balance equation of the microscopic first gradient continuum is given by

$$\nabla \cdot \mathbf{P} = \mathbf{0}, \quad (24.20)$$

where $\mathbf{P} := \partial_{\mathbf{F}} \Psi(\mathbf{F})$ is defined in terms of a Helmholtz energy function Ψ .

The macro-homogeneity condition as given by a suitable energy criterion, stating that the virtual work applied to the system in the material point P is equal to the virtual work in the domain \mathcal{RVE} , hence we assume

$$\frac{1}{V} \int_{\mathcal{RVE}} \mathbf{P} : \nabla \delta \varphi \, dV = \bar{\mathbf{P}} : \delta \bar{\mathbf{F}} + \bar{\mathfrak{P}} : \delta \bar{\mathfrak{F}}. \quad (24.21)$$

Note, that this assumption excludes Neumann conditions with an effective contribution to the virtual work.

After inserting the variations of the material points φ

$$\delta \varphi = \delta \bar{\mathbf{F}} \mathbf{X} + \frac{1}{2} \delta \bar{\mathfrak{F}} : (\mathbf{X} \otimes \mathbf{X}) + \delta \tilde{\mathbf{w}} \quad (24.22)$$

and

$$\nabla \delta \varphi = \delta \bar{\mathbf{F}} + \delta \bar{\mathfrak{F}} \mathbf{X} + \delta \tilde{\mathbf{F}} \quad (24.23)$$

into 24.21 along with partial integration and separation towards $\delta \bar{\mathbf{F}}$ and $\delta \bar{\mathfrak{F}}$, the left side of the energy criteria can be rewritten as follows

$$\frac{1}{V} \int_{\mathcal{RVE}} \mathbf{P} \, dV : \delta \bar{\mathbf{F}} + \frac{1}{V} \int_{\mathcal{RVE}} \mathbf{P} \otimes \mathbf{X} \, dV : \delta \bar{\mathfrak{F}} = \bar{\mathbf{P}} : \delta \bar{\mathbf{F}} + \bar{\mathfrak{P}} : \delta \bar{\mathfrak{F}}. \quad (24.24)$$

Comparing the left and right sides of the last equation, yields

$$\bar{\mathbf{P}} = \frac{1}{V} \int_{\mathcal{RVE}} \mathbf{P} \, dV \quad \text{and} \quad \bar{\mathfrak{P}} = \frac{1}{V} \int_{\mathcal{RVE}} \mathbf{P} \otimes \mathbf{X} \, dV. \quad (24.25)$$

Here, the macroscopic third order stress tensor $\bar{\mathfrak{P}}$ is given by the volume average of the first moment of the microscopic stresses \mathbf{P} . To obtain information about the boundary conditions, (24.21) can be rewritten as:

$$\frac{1}{V} \int_{\mathcal{RVE}} [\bar{\mathbf{P}} - \mathbf{P}] : [\delta \bar{\mathbf{F}} + \delta \bar{\mathfrak{F}} \mathbf{X} - \delta \mathbf{F}] \, dV = 0. \quad (24.26)$$

An alternative expression of (24.26) yields:

$$\frac{1}{V} \int_{\partial \mathcal{RVE}} ([\bar{\mathbf{P}} - \mathbf{P}] \mathbf{N}) \cdot \left[\delta \bar{\mathbf{F}} \mathbf{X} + \frac{1}{2} \delta \bar{\mathfrak{F}} : (\mathbf{X} \otimes \mathbf{X}) - \delta \varphi \right] \, dA = 0. \quad (24.27)$$

Thus, regarding a deformation driven approach, we derive two different sets of boundary conditions. Either we set the whole boundary as Dirichlet or we apply a periodicity condition on $\partial\mathcal{RVE}$. A suitable Dirichlet boundary condition on the boundary $\partial\mathcal{RVE}$ is

$$\bar{\mathbf{F}} \mathbf{X} + \frac{1}{2} \bar{\mathfrak{F}} : (\mathbf{X} \otimes \mathbf{X}) - \boldsymbol{\varphi} = \mathbf{0}, \quad (24.28)$$

satisfying (24.27). A comparison of the Dirichlet boundary conditions with (24.13) yields $\tilde{\mathbf{w}} = \mathbf{0}$ on the boundary. Furthermore, periodic boundary conditions can be used via the enforcement of

$$\tilde{\mathbf{w}}(\mathbf{X}^+) = \tilde{\mathbf{w}}(\mathbf{X}^-), \quad \mathbf{T}_{\text{ext}}(\mathbf{X}^+) = -\mathbf{T}_{\text{ext}}(\mathbf{X}^-), \quad (24.29)$$

satisfying again the energetic criteria (24.21).

In Kouznetsova (2002) is noted, that (24.19)₂ yields higher-order boundary conditions and as a consequence the microstructural formulation becomes higher-order. This contradicts the intention to solve the microstructural \mathcal{RVE} problem as a classical boundary value problem, where the Dirichlet boundaries are given by (24.28). As a remedy of this drawback, we will next investigate suitable reasons to introduce a second gradient material on the microscale.

24.4 Continuous Strain Energy Formulation for Fibers

In Schulte et al (2020) we investigated fiber-reinforced materials. In particular, glass-fibers embedded within a thermoplastic is analysed; due to the large differences in the Young's modulus (about 1.5 [GPa] for the matrix material and 71 [GPa] for the glass-fiber) a linear deformation within the cross section is reasonable leading to bending and torsional stress contributions. For a detailed investigation, an overlapping domain decomposition model for fiber-reinforced material is proposed in Khristenko et al (2021), using a dimensional reduction of the thin fibers within the threedimensional model for the matrix material. This is resonable even within a microscale \mathcal{RVE} due to the length-to-diameter ratio of 20 in the scale of [μm] of the fibers. The contribution of a single fiber may be negligible, however, industrial composites uses more then 50 volume percentage of fiber within the material. Hence, we have to formulate a continuous second gradient formulation next.

Concerning the fiber material, we introduce

$$\lambda_L = \|\mathbf{l}\| = \|\mathbf{FL}\| \quad \text{and} \quad \lambda_M = \|\mathbf{m}\| = \|\mathbf{FM}\| \quad (24.30)$$

as stretch of the respective fiber and

$$\begin{aligned} \varphi &= \text{acos}(\mathbf{l} \cdot \mathbf{m}) - \frac{\pi}{2} \\ &= \text{acos}\left(\frac{(\mathbf{FL}) \cdot (\mathbf{FM})}{\|\mathbf{FL}\| \|\mathbf{FM}\|}\right) - \frac{\pi}{2} \end{aligned} \quad (24.31)$$

as change of the angle between two fibers. Here $\mathbf{l} = \lambda_L \mathbf{l}$ and $\mathbf{m} = \lambda_M \mathbf{m}$ are deformed fiber configurations decomposed into fiber stretches and normalized fiber directions. To describe fiber bending directly for the continuum, the gradients of the deformed fiber vectors, i.e. $\nabla \mathbf{l} = \nabla \mathbf{FL}$ and $\nabla \mathbf{m} = \nabla \mathbf{FM}$, have to be taken into account. In particular, we consider

$$\nabla \mathbf{lL} = \lambda_L \nabla \mathbf{lL} + (\nabla \lambda_L \cdot \mathbf{L}) \mathbf{l} \quad \text{and} \quad \nabla \mathbf{mM} = \lambda_M \nabla \mathbf{mM} + (\nabla \lambda_M \cdot \mathbf{M}) \mathbf{m} \quad (24.32)$$

which are projections of the fiber configuration gradients onto the initial fiber direction, cf. Asmanoglo and Menzel (2017). These expressions include terms related to stretch gradients of the fibers as well as fiber curvatures. We introduce the curvature measure for the fiber initially aligned in \mathbf{L} -direction as

$$\begin{aligned} \kappa_L &= \frac{1}{\lambda_L} \nabla \mathbf{lL} \\ &= \frac{1}{\lambda_L^2} (\nabla \mathbf{l} - \mathbf{l} \otimes \nabla \lambda_L) \mathbf{L} \\ &= \frac{1}{\|\mathbf{FL}\|^2} \left(\nabla \mathbf{FL} - \frac{\mathbf{FL}}{\|\mathbf{FL}\|} \otimes \left(\frac{\mathbf{FL}}{\|\mathbf{FL}\|} \otimes \mathbf{L} \right) : \nabla \mathbf{F} \right) \mathbf{L} \end{aligned} \quad (24.33)$$

and for the fiber initially aligned in \mathbf{M} -direction as

$$\begin{aligned} \kappa_M &= \frac{1}{\lambda_M} \nabla \mathbf{mM} \\ &= \frac{1}{\lambda_M^2} (\nabla \mathbf{m} - \mathbf{m} \otimes \nabla \lambda_M) \mathbf{M} \\ &= \frac{1}{\|\mathbf{FM}\|^2} \left(\nabla \mathbf{FM} - \frac{\mathbf{FM}}{\|\mathbf{FM}\|} \otimes \left(\frac{\mathbf{FM}}{\|\mathbf{FM}\|} \otimes \mathbf{M} \right) : \nabla \mathbf{F} \right) \mathbf{M}. \end{aligned} \quad (24.34)$$

Note that the latter form is equivalent to a Piola homogenisation approach as demonstrated in dell'Isola et al (2016) Assuming that the fiber portion in both directions is identical, the corresponding elastic contribution of the fiber material is defined by

$$\begin{aligned} \Psi_{\text{fib}}^e &= \frac{1}{2} a \left((\lambda_L - 1)^2 + (\lambda_M - 1)^2 \right) + b \phi^2 \\ &\quad + \frac{1}{2} (\kappa_L \cdot \mathbf{c} \kappa_L + \kappa_M \cdot \mathbf{c} \kappa_M) \end{aligned} \quad (24.35)$$

where a and b are stiffness parameters related to stretch and shear of the fiber material. Moreover, the stiffness tensor related to fiber curvature is given as

$$\mathbf{c} = c_{\#} (\mathbf{l} \otimes \mathbf{l} + \mathbf{m} \otimes \mathbf{m}) + c_{\perp} \mathbf{n} \otimes \mathbf{n} \quad \text{with} \quad \mathbf{n} = \mathbf{l} \times \mathbf{m} \quad (24.36)$$

taking into account a geometric dependency via the stiffness parameters $c_{\#}$ and c_{\perp} , which can be interpreted as the in-plane and out-of-plane bending stiffness, see

Schulte et al (2020), Asmanoglo and Menzel (2017), and dell’Isola et al (2016) for details.

This model allows now for large volume fractions of directed fibers to introduce a homogeneous second gradient model within the $\mathcal{RV}\mathcal{E}$. It is obvious, that extremely fine meshes resolving every fiber using elements in the nanoscale (typical glass fibers have a diameter of 10 [μm]) allows us to circumvent the usage of second gradient formulations within the microscale $\mathcal{RV}\mathcal{E}$. However, in our opinion this is even in the microscale highly inefficient. Hence, we need a homogenisation procedure for second gradient materials, which we introduced in Schmidt et al (2021) as IGA² method, outlined in the following section.

24.5 Second Gradient Macroscopic Continuum and Second Gradient Microscopic Continuum

In Schmidt et al (2021), we extended the formulation of Kouznetsova et al (2002, 2004) and reformulate the FE² method (see, e.g., Schröder (2014)) on higher order continua using a spline based approach in the context of isogeometric analysis (IGA) for the discretisation, introducing the IGA² method. Here, we will briefly summarize the application on second gradient microscopic continua to be homogenized on a second gradient macroscopic continuum.

24.5.1 Microscopic Boundary Value Problem (Second Gradient)

For a second gradient microscopic continuum the equations (24.13) to (24.19) remain valid. The local balance equation of the microscopic second gradient continuum is given analogously to (24.12) by:

$$\nabla \cdot [\mathbf{P} - \nabla \cdot \mathfrak{P}] = \mathbf{0}, \quad (24.37)$$

where $\mathbf{P} := \partial_{\mathbf{F}}\Psi(\mathbf{F}, \mathfrak{F})$ and $\mathfrak{P} := \partial_{\mathfrak{F}}\Psi(\mathbf{F}, \mathfrak{F})$ are defined in terms of a Helmholtz energy function Ψ .

The macro-homogeneity condition as given by energetic criteria states that the virtual work applied to the system in the material point P is equal to the virtual work in the domain $\mathcal{RV}\mathcal{E}$, hence we assume

$$\frac{1}{V} \int_{\mathcal{RV}\mathcal{E}} (\mathbf{P} : \nabla \delta \varphi + \mathfrak{P} \dot{=} \nabla^2 \delta \varphi) \, dV = \bar{\mathbf{P}} : \delta \bar{\mathbf{F}} + \bar{\mathfrak{P}} \dot{=} \delta \bar{\mathfrak{F}}. \quad (24.38)$$

After again inserting the variations for φ in 24.22 to 24.23, partial integration and separation towards $\delta \bar{\mathbf{F}}$ and $\delta \bar{\mathfrak{F}}$, the left side of the energetic criteria can be rewritten as follows

$$\frac{1}{V} \int_{\mathcal{RVE}} \mathbf{P} \, dV : \delta \bar{\mathbf{F}} + \frac{1}{V} \int_{\mathcal{RVE}} (\mathbf{P} \otimes \mathbf{X} + \mathfrak{P}) \, dV : \delta \bar{\mathfrak{F}} = \bar{\mathbf{P}} : \delta \bar{\mathbf{F}} + \bar{\mathfrak{P}} : \delta \bar{\mathfrak{F}}, \quad (24.39)$$

Comparing the left and right sides of the last equation, yields

$$\bar{\mathbf{P}} = \frac{1}{V} \int_{\mathcal{RVE}} \mathbf{P} \, dV \quad \text{and} \quad \bar{\mathfrak{P}} = \underbrace{\frac{1}{V} \int_{\mathcal{RVE}} \mathbf{P} \otimes \mathbf{X} \, dV}_{\bar{\mathfrak{P}}^P} + \underbrace{\frac{1}{V} \int_{\mathcal{RVE}} \mathfrak{P} \, dV}_{\bar{\mathfrak{P}}^{\mathfrak{P}}}. \quad (24.40)$$

Now, the macroscopic third order stress tensor $\bar{\mathfrak{P}}$ is split into $\bar{\mathfrak{P}}^P$, which is once again given by the volume average of the first moment of the microscopic stresses \mathbf{P} , and $\bar{\mathfrak{P}}^{\mathfrak{P}}$, which is a volume average of the microscopic third order stress tensor \mathfrak{P} . Rewriting (24.38), we receive information about the boundary conditions:

$$\frac{1}{V} \int_{\mathcal{RVE}} \left([\bar{\mathbf{P}} - \mathbf{P}] : [\delta \bar{\mathbf{F}} + \delta \bar{\mathfrak{F}} \mathbf{X} - \delta \mathbf{F}] + [\bar{\mathfrak{P}}^{\mathfrak{P}} - \mathfrak{P}] : [\delta \bar{\mathfrak{F}} - \delta \mathfrak{F}] \right) dV = 0, \quad (24.41)$$

In this case, the simplest assumption for all points of the microscopic scale, that fulfills the last equation is given by postulating the constraints $\bar{\mathbf{P}} := \mathbf{P}$ or $\delta \bar{\mathbf{F}} + \delta \bar{\mathfrak{F}} \mathbf{X} := \delta \mathbf{F}$ and additionally $\bar{\mathfrak{P}}^{\mathfrak{P}} := \mathfrak{P}$ or $\delta \bar{\mathfrak{F}} := \delta \mathfrak{F}$, compare Schröder (2014). An alternative expression of (24.41) yields

$$\begin{aligned} & \frac{1}{V} \int_{\partial \mathcal{RVE}} ([\bar{\mathfrak{P}}^{\mathfrak{P}} - \mathfrak{P}] \mathbf{N}) : [\delta \bar{\mathbf{F}} + \delta \bar{\mathfrak{F}} \mathbf{X} - \delta \mathbf{F}] \, dA \\ & + \frac{1}{V} \int_{\partial \mathcal{RVE}} ([\bar{\mathbf{P}} - (\mathbf{P} - \nabla \cdot \mathfrak{P})] \mathbf{N}) \cdot \left[\delta \bar{\mathbf{F}} \mathbf{X} + \frac{1}{2} \delta \bar{\mathfrak{F}} : (\mathbf{X} \otimes \mathbf{X}) - \delta \boldsymbol{\varphi} \right] \, dA = 0. \end{aligned} \quad (24.42)$$

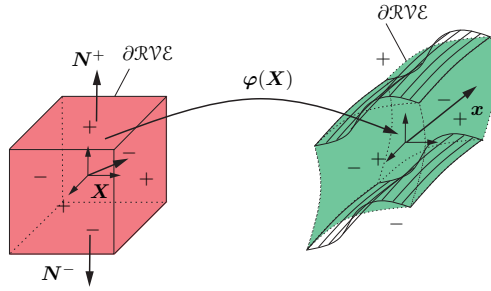
Thus, regarding a deformation driven approach, suitable Dirichlet boundary conditions on the boundary $\partial \mathcal{RVE}$ are

$$\begin{aligned} \bar{\mathbf{F}} \mathbf{X} + \frac{1}{2} \bar{\mathfrak{F}} : (\mathbf{X} \otimes \mathbf{X}) - \boldsymbol{\varphi} &= \mathbf{0}, \\ \bar{\mathbf{F}} + \bar{\mathfrak{F}} \mathbf{X} - \mathbf{F} &= \mathbf{0}, \end{aligned} \quad (24.43)$$

satisfying (24.42). Note that due to $\bar{\mathfrak{F}}$ the boundaries are quadratic functions.

For a stress driven approach, (24.42) yields possible Neumann boundary conditions, however, that would render an inherently complex implementation for large deformations, see Kouznetsova (2002). A comparison of the Dirichlet boundary conditions with the mappings (24.13) and (24.14)₁ provides the following relationship for these conditions, $\tilde{\boldsymbol{\omega}} = \mathbf{0}$ and $\nabla \tilde{\boldsymbol{\omega}} = \mathbf{0}$ on the boundary. Furthermore, the microscopic stress tractions are $\mathbf{T}_{\text{ext}} = (\mathbf{P} - \nabla \cdot \mathfrak{P}) \mathbf{N}$ and the hyperstress tractions are given by $\mathbf{M}_{\text{ext}} = \mathfrak{P} \mathbf{N}$, periodic boundary conditions as shown in Fig. 24.3 require

Fig. 24.3 Microscopic boundary value problem, periodic boundary conditions on $\partial\mathcal{R}\mathcal{V}\mathcal{E}$, here only displayed for top and bottom for better understanding.



$$\begin{aligned} \tilde{w}(\mathbf{X}^+) &= \tilde{w}(\mathbf{X}^-), & \mathbf{T}_{\text{ext}}(\mathbf{X}^+) &= -\mathbf{T}_{\text{ext}}(\mathbf{X}^-), \\ \nabla \tilde{w}(\mathbf{X}^+) &= \nabla \tilde{w}(\mathbf{X}^-), & \mathbf{M}_{\text{ext}}(\mathbf{X}^+) &= -\mathbf{M}_{\text{ext}}(\mathbf{X}^-), \end{aligned} \quad (24.44)$$

satisfying the energetic criteria (24.38).

Note that the periodicity is given in term of the fluctuation \tilde{w} , thus, the boundary deformation emanating from \vec{F} is periodic whereas the deformation emanating from $\vec{\mathfrak{F}}$ may not due to the quadratic formulation in \mathbf{X} , see (24.13). A consistent linearisation is presented in Schmidt et al (2021), such that a Newton-Raphson iteration can be used on the macroscale for non-linear materials on the microscale.

24.6 Numerical Example: Cook Membrane

To demonstrate the applicability of the proposed homogenisation, we examine a Cook’s membrane as macroscopic system, see Fig. 24.4 left, using a second gradient model for the microscopic system. As first order material model for the matrix, we apply a classical Mooney Rivlin material,

$$\Psi(J, I_1, I_2) = c(J - 1)^2 - d \ln(J) + c_1(I_1 - 3) + c_2(I_2 - 3). \quad (24.45)$$

where $J = \det(\vec{F})$, $I_1 = \text{tr}(\vec{F}^T \vec{F}) = \vec{F} : \vec{F}$ and $I_2 = \text{tr}(\text{cof}(\vec{F}^T \vec{F}))$. For the second order unidirectional fibers we use

$$\Psi_{\text{fib}} := \frac{1}{2} \left[a(\lambda - 1)^2 + b \boldsymbol{\kappa} \cdot (\mathbf{F} \mathbf{F}^T \boldsymbol{\kappa}) \right], \quad (24.46)$$

where the stretch of the fibers λ in direction \mathbf{L} reads $\lambda^\alpha = \|\mathbf{l}\| = \|\mathbf{F} \mathbf{L}\|$ and the curvature measure for the fiber initially aligned in \mathbf{L} -direction is introduced as follows

$$\boldsymbol{\kappa} = \frac{1}{(\lambda)^2} \left(\mathbf{I} - \tilde{\mathbf{l}} \otimes \tilde{\mathbf{l}} \right) \vec{\mathfrak{F}} : (\mathbf{L} \otimes \mathbf{L}). \quad (24.47)$$

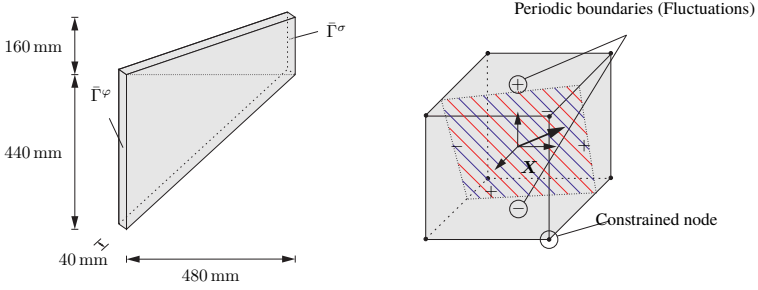


Fig. 24.4 Cook’s membrane. Left: Cook’s membrane with Dirichlet boundaries $\bar{\Gamma}^\varphi$ on the left side and Neumann boundaries $\bar{\Gamma}^\sigma$ on the right side. Right: \mathcal{RVE} of the Cook’s membrane with a second gradient material for fiber-reinforced polymers with parallel oriented fibers for anisotropic behavior and periodic boundary conditions.

The full model reads

$$\Psi_{\text{frp}} := \zeta \Psi_{\text{mat}} + \frac{1 - \zeta}{2} \Psi_{\text{fib}}, \tag{24.48}$$

where $\zeta \in [0, 1]$ is the volume fraction of the matrix material. For the macroscopic system, the Cook’s membrane is clamped on the left side, i.e. $\bar{\varphi} = \vec{0}$ mm on $\bar{\Gamma}^\varphi$. On the right hand side, the Cook’s membrane a constant traction force $\bar{\mathbf{T}}_{\text{ext}} = [0; 50; 0]$ N on $\bar{\Gamma}^\sigma$ is applied. Periodic boundary conditions are applied on the RVE and the material values are given in table 24.1.

For the results shown in Fig. 24.5 $24 \times 24 \times 6$ Elements using quadratic B-Splines are used. For 27 Gauss points per Element, a total of 93312 \mathcal{RVE} have to be evaluated in every Newton–Raphson iteration, using 64 nodes on the OMNI cluster of the University of Siegen with each 64 cores (AMD EPYC 7452). The von Mises stress distribution of the first order stresses and the Fröbenius norm of the second order hyperstresses are displayed. Note that the deformation is scaled by a factor of 5. Note that the second order hyperstresses concentrate on the notching effect at the left boundary. Moreover, the anisotropic effects of the fibers are clearly visible. Although the \mathcal{RVE} is geometrically homogeneous, more advanced models using geometrical inhomogeneities as they are common nowadays in additive manufacturing for lightweight design can be easily applied using the proposed formulation, see (Schmidt et al, 2021) for details.

24.7 Conclusion

In this contributions, we motivate the usage of second gradient material models on a microscale with application to fiber reinforced materials. The high stiffness ratio of the fibers on the microscale allows to assume a rigid cross section, such that we obtain a torsional-bending strain vector. For large volume fractions of fibers, a three

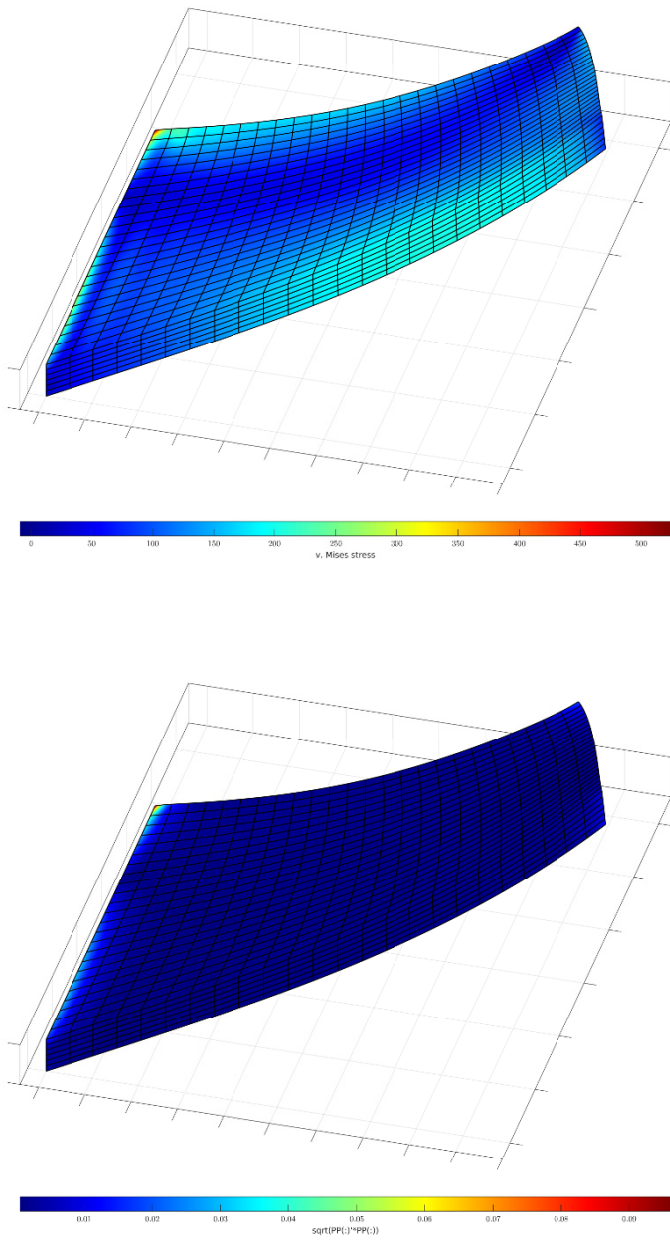


Fig. 24.5 Cook's membrane. Up: von Mises stress distribution of the first order Cauchy stresses. Down: Fröbenius norm of the second order hyperstresses.

Table 24.1 Second gradient material. Material setting of the fiber-reinforced polymere.

| | | | |
|---------------------------------------|--------------|---------------------------------------|-----|
| | c_1 | 2000 | MPa |
| parameter of matrix material | c_2 | 1000 | MPa |
| | c | $1/3(c_1 + c_2)$ | MPa |
| | d | $2(c_1 + 2c_2)$ | MPa |
| volume fraction of matrix material | ζ | 0.5 | – |
| stretch parameter of fiber material | a | 3000 | MPa |
| curvature parameter of fiber material | b | 1.25 | N |
| orientation | \mathbf{L} | $\frac{1}{\sqrt{4.25}} [-1; -1; 1.5]$ | – |

dimensional model has been derived as well. This model penalizes the curvature contributions in fiber directions and leads to a full three dimensional second order model on the microscale.

The necessary homogenisation step is build on an energetic criteria, i.e. on both scales the same virtual work is enforced. With this assumption Dirichlet and periodic boundary conditions can be defined for the microscale, such that a finite element discretisation using IGA to account for the higher regularity of the second order terms can be applied. This novel IGA² approach allows now for arbitrary complex geometries and materials on the microscale, as demonstrated in the final example.

Acknowledgements Support for this research was provided by the ZIMT (Zentrum für Informations- und Medientechnologie) and the OMNI Cluster at the University of Siegen. This support is gratefully acknowledged.

References

- Abali BE, Barchiesi E (2021) Additive manufacturing introduced substructure and computational determination of metamaterials parameters by means of the asymptotic homogenization. *Continuum Mechanics and Thermodynamics* 33(4):993–1009
- Asmanoglo T, Menzel A (2017) A finite deformation continuum modelling framework for curvature effects in fibre-reinforced nanocomposites. *Journal of the Mechanics and Physics of Solids* 107:411–432
- Barboura S, Li J (2018) Establishment of strain gradient constitutive relations by using asymptotic analysis and the finite element method for complex periodic microstructures. *International Journal of Solids and Structures* 136-137:60–76
- Benson D, Bazilevs Y, Hsu M, Hughes T (2010) Isogeometric shell analysis: The Reissner–Mindlin shell. *Computer Methods in Applied Mechanics and Engineering* 199:276–289
- Borden M, Hughes T, Landis C, Verhoosel C (2014) A higher-order phase-field model for brittle fracture: Formulation and analysis within the isogeometric analysis framework. *Computer Methods in Applied Mechanics and Engineering* 273:100–118

- dell'Isola F, Giorgio I, Pawlikowski M, Rizzi NL (2016) Large deformations of planar extensible beams and pantographic lattices: heuristic homogenization, experimental and numerical examples of equilibrium. *Proceedings of the Royal Society of London A: Mathematical, Physical and Engineering Sciences* 472(2185)
- dell'Isola F, Seppecher P, Spagnuolo M, Barchiesi E, Hild F, Lekszycki T, Giorgio I, Placidi L, Andreas U, Cuomo M, Eugster S, Pfaff A, Hoshcke K, Langkemper R, Turco E, Sarikaya R, Misra A, De Angelo M, D'Annibale F, Bouterf A, Pinelli X, Misra A, Desmorat B, Pawlikowski M, Dupuy C, Scerrato D, Peyre P, Laudato M, Manzari L, Göransson P, Hesch C, Hesch S, Franciosi P, Dirrenberger J, Maurin F, Vangelatos Z, Grigoropoulos C, Melissinaki V, Farsari M, Muller W, Abali B, Liebold C, Ganzosch G, Harrison P, Drobnicki R, Igunmov L, Alzahrani F, Hayat T (2019) Advances in pantographic structures: design, manufacturing, models, experiments and image analyses. *Continuum Mechanics and Thermodynamics* 31:1231–1282
- Dittmann M, Aldakheel F, Schulte J, Wriggers P, Hesch C (2018) Variational Phase-Field Formulation of Non-Linear Ductile Fracture. *Computer Methods in Applied Mechanics and Engineering* 342:71–94
- Dittmann M, Schulte J, Schmidt F, Hesch C (2021) A strain-gradient formulation for fiber reinforced polymers: Hybrid phase-field model for porous-ductile fracture. *Computational Mechanics* 67:1747–1768
- Fischer P, Klassen M, Mergheim J, Steinmann P, Müller R (2011) Isogeometric analysis of 2D gradient elasticity. *Computational Mechanics* 47(3):325–334
- Giorgio I (2016) Numerical identification procedure between a micro-Cauchy model and a macro-second gradient model for planar pantographic structures. *Zeitschrift für angewandte Mathematik und Physik* 67:95:1–17
- Gomez H, Calo V, Bazilevs Y, Hughes T (2008) Isogeometric analysis of the Cahn–Hilliard phase-field model. *Computer Methods in Applied Mechanics and Engineering* 197:4333–4352
- Hesch C, Schuß S, Dittmann M, Franke M, Weinberg K (2016) Isogeometric analysis and hierarchical refinement for higher-order phase-field models. *Computer Methods in Applied Mechanics and Engineering* 303:185–207
- Hill R (1963) Elastic properties of reinforced solids: Some theoretical principles. *Journal of the Mechanics and Physics of Solids* 11(5):357–372
- Hill R (1972) On constitutive macro-variables for heterogeneous solids at finite strain. *Proceedings of the Royal Society of London A Mathematical and Physical Sciences* 326:131 – 147
- Hughes T, Cottrell J, Bazilevs Y (2005) Isogeometric analysis: CAD, finite elements, NURBS, exact geometry and mesh refinement. *Computer Methods in Applied Mechanics and Engineering* 194(39–41):4135–4195
- Javili A, dell'Isola F, Steinmann P (2013) Geometrically nonlinear higher-gradient elasticity with energetic boundaries. *Journal of the Mechanics and Physics of Solids* 61(12):2381–2401
- Keip MA, Steinmann P, Schröder J (2014) Two-scale computational homogenization of electro-elasticity at finite strains. *Computer Methods in Applied Mechanics and Engineering* 278:62–79
- Khrstenko U, Schuß S, Krüger M, Schmidt F, Wohlmuth B, Hesch C (2021) Multidimensional coupling: A variationally consistent approach to fiber-reinforced material. *Computer Methods in Applied Mechanics and Engineering* 382:113,869
- Kiendl J, Bletzinger K, Linhard J, Wüchner R (2009) Isogeometric shell analysis with Kirchhoff–Love elements. *Computer Methods in Applied Mechanics and Engineering* 198:3902–3914
- Kouznetsova V (2002) Computational homogenization for the multi-scale analysis of multi-phase materials. Ph.D. thesis. Technische Universiteit Eindhoven
- Kouznetsova V, Geers M, Brekelmans W (2002) Multi-scale constitutive modelling of heterogeneous materials with a gradient-enhanced computational homogenization scheme. *International Journal for Numerical Methods in Engineering* 54:1235–1260
- Kouznetsova V, Geers M, Brekelmans W (2004) Multi-scale second-order computational homogenization of multi-phase materials: a nested finite element solution strategy. *Computer Methods in Applied Mechanics and Engineering* 193(48-51):5525–5550

- Madeo A, Ghiba ID, Neff P, Münch I (2016) A new view on boundary conditions in the Grioli–Koiter–Mindlin–Toupin indeterminate couple stress model. *European Journal of Mechanics A* 59:294–322
- Mandel J (1972) *Plasticité classique et viscoplasticité* 97
- Reali A, Gomez H (2015) An isogeometric collocation approach for Bernoulli–Euler beams and Kirchhoff plates. *Computer Methods in Applied Mechanics and Engineering* 284:623–636
- Schmidt F, Krüger M, Hesch C (2021) Homogenization of higher-order continua. *International Journal for Numerical Methods in Engineering*, submitted for publication
- Schröder J (2014) A numerical two-scale homogenization scheme: the FE2-method. In: Schröder J., Hackl K. (eds) *Plasticity and Beyond*. CISM International Centre for Mechanical Sciences, vol 550. Springer, Vienna. *Journal of Applied Mechanics*
- Schröder J, Keip MA (2012) Two-scale homogenization of electromechanically coupled boundary value problems. *Computational Mechanics* 50:229–244
- Schulte J, Dittmann M, Eugster S, Hesch S, dell’Isola F, Hesch C (2020) Isogeometric analysis of fiber reinforced composites using Kirchhoff–Love shell elements. *Computer Methods in Applied Mechanics and Engineering* 362:112,845
- Spencer A, Soldatos K (2007) Finite deformations of fibre-reinforced elastic solids with fibre bending stiffness. *International Journal of Non-Linear Mechanics* 42:355–368



Chapter 25

Modeling the Slow Crack Growth of an Edge Crack within the Cohesive Zone Model Approach

Mikhailo Selivanov, Lidiia Nazarenko, Holm Altenbach

Abstract The problem of quasi-static growth of the mode I edge crack in a viscoelastic material is solved. The stages of analysis are indicated, namely (i) choice of rheological model, (ii) choice of crack model and fracture criterion, (iii) solution of the elastic problem of crack mechanics within the chosen model approach, (iv) constructing the viscoelastic solution of the problem and equations of crack propagation. The last two of these stages were given particular attention. The proposed algorithm for determining the crack opening in the framework of the cohesive zone model approach is based on the methodology developed in previous papers of the authors. A regularized singular integral equation is used to obtain an elastic crack opening. When modeling the quasi-static crack growth, the hypothesis of the independence of the cohesive law on the rate of slow crack propagation is assumed to be true. To construct numerical solutions, the exponential kernel of the slow crack growth equations is utilized. The smoothed triangular traction–separation law with the hardening segment ensures smooth crack closure. Auxiliary solutions of the problem that are obtained at each step and should be used to describe hereditary viscoelastic behavior are illustrated. The dependence of crack length on time is obtained for some numerical values of model parameters. The proposed methodology for modeling slow crack growth has demonstrated its effectiveness by fast convergence of solutions at each iteration of the algorithm.

Keywords: Edge crack · Cohesive zone model · Slow crack growth

M. Selivanov

S.P. Timoshenko Institute of Mechanics, National Academy of Sciences, Nesterov St., 3, 03057, Kyiv, Ukraine

e-mail: mfs@ukr.net

L. Nazarenko, H. Altenbach

Otto-von-Guericke-Universität Magdeburg, Lehrstuhl für Technische Mechanik, Institut für Mechanik, Fakultät für Maschinenbau, Universitätsplatz 2, 39106 Magdeburg, Germany

e-mail: lidiia.nazarenko@ovgu.de, holm.altenbach@ovgu.de

© The Author(s), under exclusive license to Springer Nature Switzerland AG 2022

505

I. Giorgio et al. (eds.), *Theoretical Analyses, Computations,*

and Experiments of Multiscale Materials, Advanced Structured Materials 175,

https://doi.org/10.1007/978-3-031-04548-6_25

25.1 Introduction

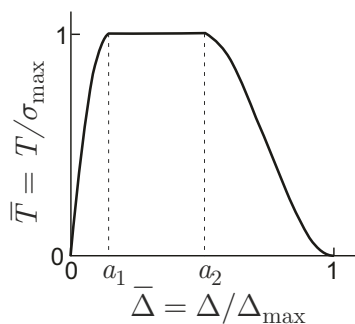
Slow propagation of cracks due to creep of the material is one of the most common types of fracture. This phenomenon has led to numerous theoretical and experimental studies over the past forty six years beginning with the pioneering work (Schapery, 1975). It was established that this type of fracture cannot be described in the framework of classical fracture mechanics, which cannot predict the rate of crack propagation, and a cohesive model (Dugdale, 1960; Barenblatt, 1962; Hillerborg et al, 1976; Needleman, 1987; Hui et al, 2011) must be used (Ciavarella et al, 2021a). Another approach to treat the crack propagation in viscoelastic materials is proposed in (Persson and Brener, 2005) and gives similar results. Using the cohesive zone model, the crack propagation can be treated not only for homogeneous materials. For example, in (Ciavarella et al, 2021b), this model was used to investigate the subcritical crack growth along the interface between an elastic and a viscoelastic material. A review of the basic concepts of modeling the slow propagation of cracks in viscoelastic materials is made in (Kaminskii, 2014; Knauss, 2015). The three important stages of crack growth were considered: initiation, slow steady growth, and the onset of rapid unstable propagation. It is believed that the initiation of fracture from a crack preexisting in a viscoelastic body requires some time (incubation time), which depends on the geometry, the scheme of the applied load, and the hereditary viscoelastic properties of the material. The load level can be significantly lower than the critical level in the absence of hereditary viscoelastic properties of the material. During the initial stage, the material at the crack tip gradually loses the ability to resist crack propagation. The second stage of fracture is the subcritical growth of the crack, which occurs even at a constant level of external loading and can be characterized by a slight change in the rate of propagation. The state of instability is characterized by a significant increase in the velocity of the crack tip. The time when critical growth initiates is important because it determines the time of failure of the structural member with a crack.

Building a model of quasi-static crack growth in viscoelastic bodies is a multilayered process. At each level, modeling concepts or solution methods are developed and combined into a common model. In the first step, a rheological model is selected and the relaxation functions of the viscoelastic material are determined. These functions can be obtained both experimentally and by modeling using the mechanics of composite materials from the viscoelastic properties of the composite phases if the fracture of such materials is studied (Kaminskii, 2021). Although this approach does not take into account many of the factors accompanying composite failure (Nazarenko et al, 2019; Khoroshun and Nazarenko, 2013), it can provide satisfactory results for engineering applications. Fractional constitutive equations (Peng et al, 2019) can be used as well as classical viscoelastic models. In the second step, the crack model and the fracture criterion are selected. When modeling the slow propagation of cracks, the cohesive zone model is often used. According to this model, a fictitious crack is introduced on the continuation of the physical crack. The cohesive traction is applied to the faces of the fictitious crack. This traction is assumed to be the function of displacement of the fictitious crack faces, thus establishing the traction–

separation law. The crack faces are assumed to close smoothly at the fictitious crack tip. In the last two decades, an alternative approach has been proposed to eliminate the singularity at the crack tip (e.g. (Gourgiotis and Georgiadis, 2009; Mousavi and Aifantis, 2016) among others). Within the framework of the gradient theory of elasticity, it was possible to describe the smooth crack closure without introducing a cohesive zone. When the velocity of crack propagation is low, it is natural to assume the time-independence of fracture parameters (the fracture energy, cohesive strength, and shape parameters of the cohesive law). Thus, the traction–separation law must be satisfied at every moment of time. The rate-dependent cohesive law can be implemented using the models proposed in (Bažant and Li, 1997; Musto and Alfano, 2015; Nordmann et al, 2020). At the third stage, the problem of crack mechanics within the chosen model is solved. Analytical, semi-analytical, and numerical methods can be used. In the first two cases, it is sometimes possible to present a solution in the form of product of elastic moduli and function of coordinate. When the cohesive zone model is implemented, it is necessary to determine the displacement of the fictitious crack faces (this solution is necessary to construct the equations of slow crack growth). In the case of isotropic material, the multiplier is the compliance function. In the case of orthotropic material, the multiplier with orthotropic moduli can be obtained utilizing the elastic–viscoelastic correspondence principle. If this factorization is possible, the solution can be presented in an integral form, which is the basis of the theory of slow crack propagation in the hereditary solid. The obtained equations are solved in the fourth, last step of solving the problem. We find the solution in the form of dependence of crack length on time. Additionally, the cohesive length also varies with time (Hakim and Mikhailov, 2015, 2018). The smooth crack closure condition embedded in the cohesive zone model defines the position of the cohesive zone tip.

This paper illustrates an example of modeling the quasi-static propagation of an edge crack normal to the boundary due to the hereditary viscoelastic properties of the material. It develops the theory of the long-term failure of cracked viscoelastic solids, which was experimentally tested for some polymeric and composite materials (Kaminskii, 1998). In Section 25.2, the crack opening displacement is obtained as the solution of the singular integral equation of the first kind. The example is illustrated for the critical state of a crack. The shortcomings of this solution are noted and eliminated in Section 25.3. The regularization of the first kind integral equation allowed us to obtain the correct solutions corresponding to the subcritical crack state in Section 25.4. We pay particular attention to solving the equation of slow crack growth in Section 25.5. We propose the algorithm at each step of which the auxiliary elastic solution of the problem and the corresponding time are being obtained. The paper ends with conclusions in Section 25.6.

Fig. 25.1 The effective traction–separation law (T and Δ are the cohesive traction and the separation respectively, σ_{\max} and Δ_{\max} are their maximum values, a_1 and a_2 are the shape parameters of the traction–separation law).



25.2 An Edge Crack with Cohesive Zone

The fracture in quasi-brittle materials can occur due to the propagation of a crack, near the tip of which a failure zone is formed. The cohesive zone model is successfully used to simulate the failure zone. According to this model, the crack tip is represented by a fictitious cut on the continuation of the crack line with the cohesive traction applied to its faces. This traction is assumed to be dependent on the opening displacement along a fictitious crack according to a traction–separation law, which can take into account the various effects that take place around the tip of a physical crack. The model received its main features in (Dugdale, 1960; Barenblatt, 1962; Hillerborg et al, 1976; Needleman, 1987) and is widely used in the study of crack resistance of structures made of various materials. Despite the widespread use of the model, there are not many analytical and semi-analytical solutions obtained within the model. With the help of such solutions, it is possible to make quantitative conclusions about the application of the model.

An important step in solving problems within the cohesive zone model approach is to satisfy the smooth crack closure, which ensures the absence of stress discontinuity along the crack line, and, in the case of constructing an analytical solution, satisfies the requirement of finite stress in the body. For the traction–separation law with the maximum cohesive traction corresponding to zero separation, the condition of smooth closure can be provided by the iterative procedure (Selivanov and Chornoivan, 2018; Selivanov et al, 2018). The solution can be obtained by a small number of iterations, on each of which a system of nonlinear equations is solved by a fast-convergent iterative method. The smooth crack closure can also be ensured by modifying the traction–separation law by assigning zero cohesion to zero separation (Fig. 25.1) with small interval for the ascending branch (a_1 is close to zero), thus representing the model without the cohesive zone tip (Hui et al, 2011). In this case, the rate of convergence of the iterative method decreases significantly, but the solution can be obtained by solving a single system of nonlinear equations. In this section, in the framework of the first approach, we investigate the solution of the problem for the critical state of the edge crack modeled using the cohesive zone model. The second approach is used in Section 25.4 to model the subcritical crack mode.

If an edge crack (Fig. 25.2) is perpendicular to the boundary of a half-infinite

plane, the following equation embodies the solution of the boundary value problem ((Broberg, 1999), p. 155)

$$\frac{1}{\pi} \int_0^\delta K(\xi, \tau) \varphi(\tau) d\tau = \Lambda \tilde{\sigma}(\xi), \quad 0 \leq \xi \leq \delta, \tag{25.1}$$

where δ is the crack length, $\tilde{\sigma}(x)$ is the traction along the crack line in an uncracked solid, $\Lambda = (\nu + 1)/(2\mu)$ is the elastic parameter (ν and μ are the Kolosov’s parameter (Muskhelishvili, 1977) and the shear modulus respectively),

$$K(\xi, \tau) = \frac{1}{\tau - \xi} + h(\xi, \tau), \tag{25.2}$$

$$h(\xi, \tau) = \sum_{i=1}^3 \frac{C_i(\xi)}{(\tau + \xi)^i}, \quad C_1 = -1, \quad C_2 = 6\xi, \quad C_3 = -4\xi^2.$$

The idea behind the solution is to represent the sought function as a shape function with unknown parameters that need to be found from the boundary conditions. We have chosen a piecewise linear shape function. In contrast to the expansion in Chebyshev polynomials, this choice makes it possible to better account for the discontinuity of the boundary conditions on the contour of a fictitious crack (conditions of this type will be considered in Section 25.4). In Selivanov et al (2018), a similar approach was used to find a solution to the problem for a central crack in an infinite plane. In this case, the calculations are quite simple in comparison with the solution given below.

Thus, the solution of (25.1) can be obtained by the collocation method (Erdogan et al, 1973). We find the unknown function $\varphi(x)$ as the product of the piecewise linear function $g(x)$ and weight function $w(t)$ selected according to the results of (Savruk et al, 1999)

$$g(t) = g_k q_k(t) + g_{k+1} [1 - q_k(t)], \quad t \in (t_k, t_{k+1}), \tag{25.3}$$

$$g_k = g(t_k), \quad q_k(t) = (t_{k+1} - t) / \Delta t_k, \quad \Delta t_k = t_{k+1} - t_k.$$

Further, we consider the change of variables

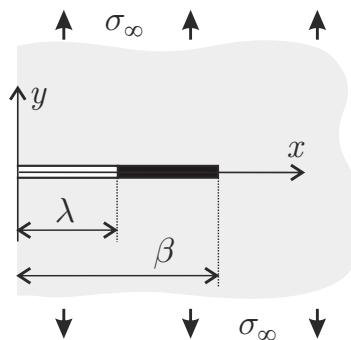


Fig. 25.2 The edge crack (λ and β correspond to the tips of physical and fictitious cracks respectively).

$$\tau = \delta t, \quad \xi = \delta x, \quad 0 \leq t, x \leq 1 \tag{25.4}$$

in (25.1) and use $g(\delta t)$ instead of $g(t)$ and $\tilde{\sigma}(\delta t)$ instead of $\tilde{\sigma}(t)$. Then, the integral in (25.1) can be written in the form

$$\int_0^1 K(x, t)w(t)g(t)dt = \sum_{k=1}^n g_k J_k(x), \tag{25.5}$$

where

$$\begin{aligned} J_1(x) &= T'_1(x) - Q_1(x), & J_n(x) &= -T'_{n-1}(x), \\ J_k(x) &= T'_k(x) - T'_{k-1}(x), & k &= 2, \dots, n-1; \end{aligned} \tag{25.6}$$

$$Q_k(x) = Q(x, t_k), \quad T'_k(x) = \frac{T_{k+1}(x) - T_k(x)}{\Delta t_k}, \quad T_k(x) = T(x, t_k); \tag{25.7}$$

$$\begin{aligned} Q(x, t) &= \hat{Q}(x, t) + \check{Q}(x, t), \\ \hat{Q}(x, t) &= \int \frac{w(t)}{t-x} dt = w(x) \ln \left| \frac{w(t) - w(x)}{w(t) + w(x)} \right|, \\ \check{Q}(x, t) &= \int h(x, t)w(t)dt = \sum_{i=1}^3 P_i(x)I_i(x, t), \end{aligned} \tag{25.8}$$

$w(t) = (1-t)^{-1/2}$. After the integration, the functions $I_i(x, t) = \int w(t)/(t+x)^i dt$ can be rewritten as follows

$$\begin{aligned} I_1(x, t) &= v(x) \ln \left| \frac{w(t) - v(x)}{w(t) + v(x)} \right|, & v(x) &= (1+x)^{-1/2}, \\ I_2(x, t) &= v^2(x) \left[\frac{1}{2} I_1(x, t) - H_1(x, t) \right], & H_1(x, t) &= \frac{w(t)}{t+x}, \\ I_3(x, t) &= v^2(x) \left[\frac{3}{4} I_2(x, t) - \frac{1}{2} H_2(x, t) \right], & H_2(x, t) &= \frac{H_1(x, t)}{t+x}. \end{aligned} \tag{25.9}$$

The function $T(x, t)$ in (25.7) takes the form

$$\begin{aligned} T(x, t) &= \hat{T}(x, t) + \check{T}(x, t), \\ \hat{T}(x, t) &= \int \hat{Q}(x, t)dt = (t-x)\hat{Q}(x, t) + 2w^{-1}(t), \\ \check{T}(x, t) &= \int \check{Q}(x, t)dt = \sum_{i=1}^3 P_i(x)\check{I}_i(x, t). \end{aligned} \tag{25.10}$$

Integration in $\check{I}_i(x, t) = \int I_i(x, t)dt$ gives

$$\begin{aligned} \check{I}_1(x, t) &= (t+x)I_1(x, t) + 2w^{-1}(t), \\ \check{I}_2(x, t) &= v^2(x) \left[\frac{1}{2} \check{I}_1(x, t) - \check{H}_1(x, t) \right], \\ \check{I}_3(x, t) &= v^2(x) \left[\frac{3}{4} \check{I}_2(x, t) - \frac{1}{2} \check{H}_2(x, t) \right], \\ \check{H}_1(x, t) &= v^{-2}(x)I_1(x, t) + 2w^{-1}(t), \\ \check{H}_2(x, t) &= -\frac{1}{2}I_1(x, t) - H_1(x, t). \end{aligned} \tag{25.11}$$

We write the function Q_1 from (25.7) in detail

$$Q_1(x) = \frac{1}{\sqrt{1-x}} \ln \frac{1 - \sqrt{1-x}}{1 + \sqrt{1-x}} + \frac{1}{(x+1)^2} \left(\frac{x^2 + 2x - 2}{2\sqrt{1+x}} \ln \frac{\sqrt{1+x} - 1}{\sqrt{1+x} + 1} - 4 - x \right); \quad (25.12)$$

it has two singular addends (see (25.8)) at $x = 0$. Using their asymptotic properties, we can find

$$Q_1(0) = -4, \quad Q_1(1) = -\frac{13}{4} - \frac{\sqrt{2}}{16} \ln \frac{\sqrt{2} + 1}{\sqrt{2} - 1} \approx -3.4. \quad (25.13)$$

In Fig. 25.3, the function $T(x, t)$ is illustrated. To satisfy continuity, it is assumed that

$$\hat{T}(t, t) = 2\sqrt{1-t}, \quad \hat{T}(1, t) = 4\sqrt{1-t}. \quad (25.14)$$

If the functions $Q_1(x)$ and $T_k(x)$ are bounded, then $J_k(x)$ are also bounded.

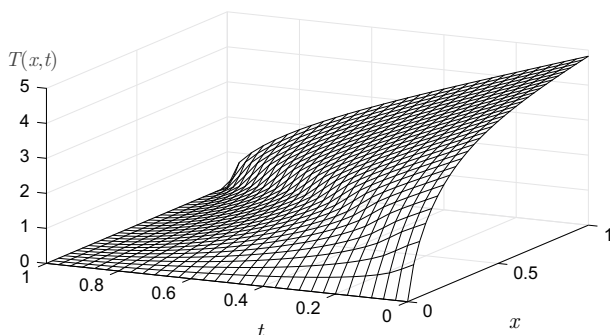


Fig. 25.3 Geometrical characteristics of the problem.

The discretization of (25.1) yields

$$\mathbf{Jg} = \mathbf{b}, \quad (25.15)$$

$$\mathbf{J} = [j_{mk}], \quad m, k = 1, \dots, n, \quad j_{mk} = \frac{1}{\pi} J_k(x_m), \quad (25.16)$$

$$\mathbf{g} = \{g_1, \dots, g_n\}^T, \quad \mathbf{b} = \{b_1, \dots, b_n\}^T, \quad b_m = \delta \Delta \tilde{\sigma}(x_m).$$

Numerical implementation of the technique for determining the stress intensity factor in the case of $\tilde{\sigma}(x) = \sigma_\infty$ gives $\bar{K}_I = \sqrt{2} \cdot g(1) = 1.12146$ when $n = 11$ ($\bar{K}_I = K_I / (\sigma_\infty \sqrt{\pi \delta})$). The exact stress intensity factor value of this problem is $\bar{K}_I = 1.12152$ ((Broberg, 1999), p. 169). Thus, the error is $5.5 \cdot 10^{-5}$. In numerical calculations, we choose evenly spaced quadrature points t_k that coincide with the collocation points x_m .

The crack opening displacement

$$\Delta(x) = \delta\Lambda \int_x^1 \omega(t)g(t)dt \quad (25.17)$$

after discretization takes the following form

$$\Delta(\mathbf{x}) = \delta\Lambda \cdot \mathbf{V}\mathbf{g}, \quad \mathbf{x} = \{x_1, \dots, x_n\}^T, \quad (25.18)$$

$$\mathbf{V} = \begin{pmatrix} N_1 & N_2 & N_3 & \dots & N_{n-1} & N_n \\ 0 & G'_2 - R_2 & N_3 & \dots & N_{n-1} & N_n \\ 0 & 0 & G'_3 - R_3 & \dots & N_{n-1} & N_n \\ & & & \dots & & \\ 0 & 0 & 0 & \dots & G'_{n-1} - R_{n-1} & N_n \\ 0 & 0 & 0 & \dots & 0 & 0 \end{pmatrix}, \quad (25.19)$$

$$\begin{aligned} N_1 &= G'_1 - R_1, & N_n &= R_n - G'_{n-1} \\ N_k &= G'_k - G'_{k-1} & (k &= 2, \dots, n-1) \\ R_k &= R(t_k), & G_k &= G(t_k), & G'_k &= (G_{k+1} - G_k)/\Delta t_k \\ R(t) &= \int \omega(t)dt, & G(t) &= \int R(t)dt. \end{aligned} \quad (25.20)$$

The equation in (25.1) can be written for the given boundary conditions as follows

$$\begin{aligned} \frac{1}{\pi} \int_0^\beta K(\xi, \tau)\varphi(\tau)dt &= \Lambda\tilde{\sigma}(\xi) \\ \tilde{\sigma}(\xi) &= \sigma_\infty - T[\Delta(\xi)]. \end{aligned} \quad (25.21)$$

This equation has to be satisfied together with the smooth crack closure condition

$$\Delta'(\beta) = 0. \quad (25.22)$$

The equations (25.21) and (25.22) determine the stress state of the edge crack with cohesive zones (Fig. 25.4 *a*). The function $T(\Delta)$ describes the traction–separation law. The position of the cohesive zone tip β is the problem unknown that must meet the condition (25.22). When studying the critical state, the following condition is added to the governing system

$$\Delta(\lambda) = \Delta_{\max}. \quad (25.23)$$

We consider the modified problem statement (Fig. 25.4 *b*), which lead to the governing equations that do not contain the unknown cohesive length. According to this statement, the cohesive traction is to be found in the form

$$\sigma(\xi) = \hat{T}[\Delta(\xi)] - \hat{\sigma}(\xi), \quad \lambda < \xi < \delta, \quad (25.24)$$

where

$$\hat{T}(\Delta) = \begin{cases} T(\Delta), & \Delta \geq 0 \\ P(\Delta), & \Delta < 0 \end{cases} \quad (25.25)$$

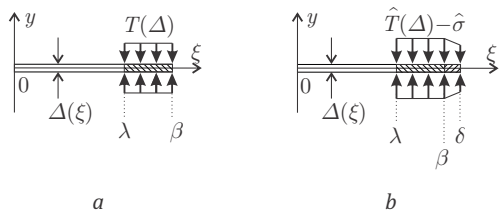


Fig. 25.4 Parameters of the problem statement (a) and modified problem statement (b); \hat{T} is the traction extended to negative separation.

is the cohesive traction extended to a negative separation, $\hat{\sigma}(\xi)$ is the auxiliary traction, which is determined by the condition $\Delta(\xi) \geq 0$. The proposed technique does not give an exact value for the cohesive length but provides a smooth crack closure and allows us to determine the parameters of the critical state accurately.

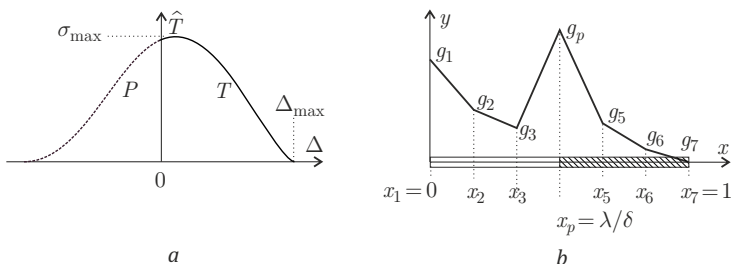


Fig. 25.5 The traction–separation law extended to negative separation (a) and discrete displacement density (b).

The unknown function $g(\xi)$ ($0 < \xi < \delta$) is found for the cohesive traction in the form (25.24); the mentioned interval has to contain the position of the cohesive zone tip, which is as well unknown. The solution of the problem at hand is given by the integral equation (25.1). For the subcritical state, the solution is determined by the following set of integral equations and inequalities

$$\frac{1}{\pi} \int_0^1 K(x, t)w(t)g(t)dt = \sigma_\infty - \hat{T} \left[\delta \Lambda \int_x^1 \omega(t)g(t)dt \right] + \hat{\sigma}(x) \tag{25.26}$$

$$\int_x^1 \omega(t)g(t)dt \geq 0.$$

To solve this system of equations, we construct its discretization and iterative procedure, at each step of which the system of linear algebraic equations is solved. The set (25.26) coupled with the condition (25.23) can be written in the form

$$\begin{aligned} \mathbf{Jg} &= \sigma_\infty \mathbf{1} - \hat{T}(\delta\Lambda \mathbf{Vg}) + \hat{\sigma} \\ \mathbf{V}_i \mathbf{g} &\geq 0, \quad i = 1, \dots, n \\ \delta\Lambda \mathbf{V}_p \mathbf{g} &= \Delta_{\max}, \end{aligned} \quad (25.27)$$

where \mathbf{V}_p is the row-vector constructed from the elements of p th row of the matrix \mathbf{V} , $\mathbf{1}$ is the column vector of ones. The collocation point x_p corresponds to the position of the physical crack tip (Fig. 25.5 *b*). The elements of $\hat{\sigma}$ are $\hat{\sigma}(x_k)$, $k = 1, \dots, n$.

The set of equations and inequalities (25.27) can be solved using the iterative procedure. To construct the procedure, we define the function T for negative values of argument:

$$P(\Delta) = \begin{cases} 0, & \Delta < -1 \\ P_3(\Delta), & -1 \leq \Delta < 0 \end{cases}, \quad (25.28)$$

where the polynomial $P_3(x)$ is defined by the following boundary conditions $P_3(0) = T(0)$, $P_3'(0) = T'(0)$, $P_3(-1) = P_3'(-1) = 0$.

In the first step of the procedure, we introduce two sets of indices S and M . The first set corresponds to collocation points ξ_s that satisfy the condition $0 \leq \xi_s < \beta$, the second one corresponds to all other collocation points. In the first step of the iterative procedure, we can assume

$$S = \{s : \xi_s < \lambda + \ell\}, \quad \ell = \frac{\pi}{8} \frac{E\phi}{\sigma_{\max}^2}, \quad (25.29)$$

where ϕ and σ_{\max} are the fracture energy and the cohesive strength respectively.

Next, we solve the system of equations

$$\begin{aligned} \mathbf{J}_s \mathbf{g} &= \sigma_\infty^* \mathbf{1} - \hat{T}(\delta\Lambda \mathbf{V}_s \mathbf{g}) \\ \mathbf{V}_m \mathbf{g} &= \mathbf{0} \\ \delta\Lambda \mathbf{V}_p \mathbf{g} &= \Delta_{\max}, \end{aligned} \quad (25.30)$$

$s \in S$, $m \in M$. The elements of the row vectors \mathbf{J}_k and \mathbf{V}_k are the elements of the k th row of the corresponding matrix. The defining system (25.30) is nonlinear but its Jacobi matrix is calculated quite easily if it is easy to find the derivative of \hat{T} .

Now we can determine \mathbf{g} and the critical load parameter σ_∞^* using (25.30) and estimate the elements of the auxiliary vector that prevents negative separation. The following system of equations gives the solution

$$\hat{\sigma} = \mathbf{Jg} - \sigma_\infty + \hat{T}(\delta\Lambda \mathbf{Vg}). \quad (25.31)$$

In the second step, we reassign the indices $S = \{s : \hat{\sigma}_s \geq 0\}$ and continue the iterative procedure until all the elements $\hat{\sigma}$ are non-negative.

In the numerical example, the traction–separation law with a hardening branch is used

$$\bar{T}(\bar{\Delta}) = (\bar{\sigma}_l \bar{\Delta} + \bar{\sigma}_n)(1 - \bar{\Delta})^2, \quad \Delta_{\max} = \frac{12\phi}{\sigma_{\max}(\bar{\sigma}_l + 4\bar{\sigma}_n)}, \quad (25.32)$$

$\bar{T} = T/\sigma_{\max}$, $\bar{\Delta} = \Delta/\Delta_{\max}$ are the relative tractions and displacements respectively, the first shape parameter $\bar{\sigma}_n$ defines the traction for zero separation, the second shape parameter, $\bar{\sigma}_l$ is defined by the equation $\max\{\bar{T}(\bar{\Delta})\} = 1$, which takes the form

$$\frac{4}{27}\bar{\sigma}_l \left(1 + \frac{\bar{\sigma}_n}{\bar{\sigma}_l}\right)^3 = 1 \tag{25.33}$$

for the law (25.32).

The polynomial that determine the law for negative displacements is taken in the following form: $P_3(\bar{\Delta}) = (\bar{\sigma}_l - 4\bar{\sigma}_n)\bar{\Delta}^3 + (2\bar{\sigma}_l - 7\bar{\sigma}_n)\bar{\Delta}^2 + (\bar{\sigma}_l - 2\bar{\sigma}_n)\bar{\Delta} + \bar{\sigma}_n$ (see Fig. 25.5 a).

Figure 25.6 illustrates the solution for the specified parameters. The plane stress state is considered, so $\Lambda = 4/E$. The value of β corresponds to the smallest ξ_l , such that $\bar{g}_l = 0$. The critical value of the external load is $\sigma_{\infty}^* = 0.619\sigma_{\max}$.

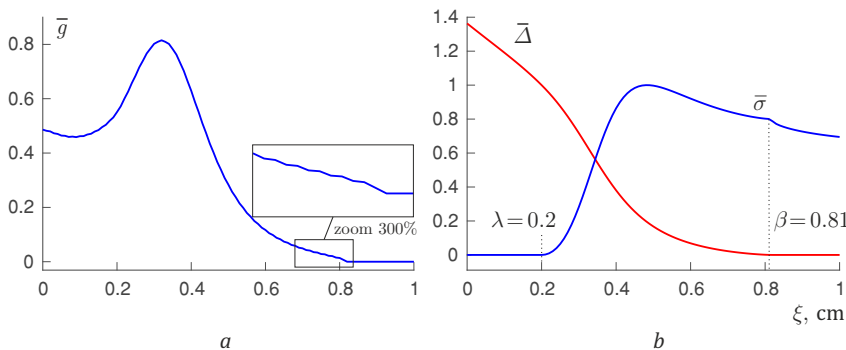


Fig. 25.6 The relative displacement density $\bar{g}(\xi) = g(\xi)/(\Lambda\sigma_{\max})$ (a), the relative traction $\bar{\sigma}(\xi) = \{\hat{T}[\Delta(\xi)] - \hat{\sigma}(\xi)\}/\sigma_{\max}$ and the crack opening displacement $\bar{\Delta}(\xi)$ (b) obtained for $\delta = 1$ cm, $\bar{\sigma}_n = 0.8$, $\bar{\sigma}_l = 3.8109$, $E = 40$ GPa ($\Lambda = 4/E$), $\phi = 200$ N/m, $\sigma_{\max} = 35$ MPa, $n = 101$ (mesh parameter).

Thus, in this section, a semi-analytical method of crack mechanics based on the cohesive zone model approach is constructed and illustrated for the case of an edge crack. The method uses the iterative procedure at each step of which the integral equation with the generalized Cauchy kernel is solved by the collocation method without regularization. Quadrature formulas are constructed taking into account the stationary singularity of the specified kernel. A numerical solution corresponding to the critical condition is obtained. The solution is constructed for the traction–separation law according to which the zero opening displacement corresponds to the traction that is close to the cohesive strength. This allowed us to obtain a continuous force function (the right part of the singular equation associated with the boundary conditions). When studying the subcritical state or even the critical state with a larger initial cohesion ($\bar{\sigma}_n > 0.8$), the presented technique gives the solution $g(x)$ with pronounced oscillation (Fig. 25.7). To obtain a physically correct solution, the

regularization of the initial integral equation is necessary, which is the subject of Section 25.3.

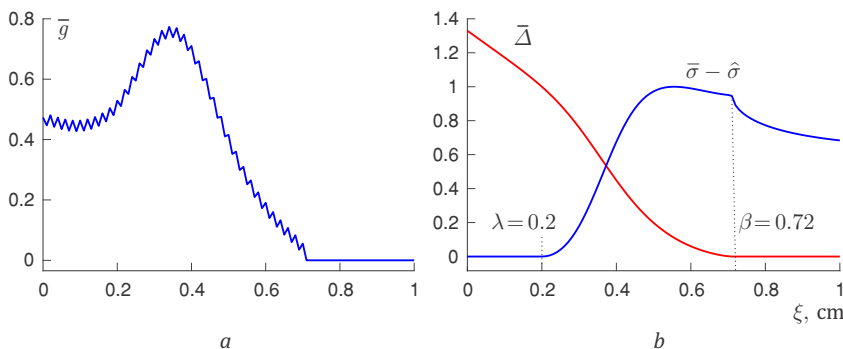


Fig. 25.7 The relative displacement density (*a*), the relative traction and separation (*b*) for $\bar{\sigma}_n = 0.95$ and other parameters used to obtain the results shown in Fig. 25.6.

25.3 Solving a Problem on an Edge Crack with Cohesive Zone by the Regularization of Singular Integral Equation

This section is a continuation of the study presented in Section 25.2, where the integral equation with the generalized Cauchy kernel, which determines the solution of the boundary crack problem, is solved without regularization. This direct approach lead to the oscillation of the solution under some traction–separation laws.

We consider the same problem of determining the stress state of a semi-infinite plane with an edge crack in the presence of a failure zone near its front (Fig. 25.2). The crack lies along the normal to the half-plane boundary; the distributed tensile load is applied perpendicular to crack plane at a considerable distance from it.

The problem solution, the function $\varphi(t)$ is defined by the generalized Cauchy integral equation and the condition of smooth crack closure:

$$\begin{aligned} \frac{1}{\pi} \int_0^\beta K(\xi, \tau)\varphi(\tau)d\tau &= \Lambda \psi(\xi), \quad 0 < \xi < \beta, \\ \psi(\xi) &= \sigma_\infty - \sigma_{\max} \bar{T}[\bar{\Delta}(\xi)], \quad \Delta(\xi) = \int_\xi^\beta \varphi(\tau)d\tau, \\ \Delta'(\beta) &= 0, \end{aligned} \tag{25.34}$$

where $\bar{T}(\Delta)$ is the given traction–separation law, $\bar{\Delta} = \Delta/\Delta_{\max}$ is the relative separation. Fig. 25.4 *a* illustrates the notations introduced above. As before, the cohesive strength σ_{\max} and critical separation Δ_{\max} are the main parameters of crack resistance,

$$\begin{aligned}
 K(\xi, \tau) &= \frac{1}{\tau - \xi} - h(\xi, \tau), \\
 h(\xi, \tau) &= \sum_{r=0}^2 d_r \xi^r \frac{\partial^r}{\partial \xi^r} \frac{1}{\tau + \xi}, \quad d_0 = 1, \quad d_1 = 6, \quad d_2 = 2.
 \end{aligned}
 \tag{25.35}$$

Point out that in addition to the function φ in the problem (25.34), the value of β is also unknown. When studying the critical state, the equation $\Delta(\lambda) = \Delta_{\max}$ is to be added to the governing system (25.34). The analytical expression of the function h is chosen for the convenience of further analysis. A more common form for this function is as follows

$$h(\xi, \tau) = \frac{\tau^2 - 4\xi\tau - \xi^2}{(\tau + \xi)^3}.
 \tag{25.36}$$

After dividing of the first equation in (25.34) by $\Lambda\sigma_{\max}$ and replacement $\tau = \beta t$, $\xi = \beta x t$, $x \in [0, 1]$, we obtain

$$B(f, x) = \tilde{\sigma}(x),
 \tag{25.37}$$

$$f(t) = \frac{\varphi(\beta t)}{\Lambda\sigma_{\max}}, \quad \tilde{\sigma}(x) = \frac{\psi(\beta x)}{\sigma_{\max}}, \quad B(f, x) = \frac{1}{\pi} \int_0^1 K(x, t) f(t) dt.
 \tag{25.38}$$

To regularize (25.37), we solve the equation

$$\frac{1}{\pi} \int_0^1 \frac{f(t)}{t - x} dt = y(x),
 \tag{25.39}$$

with the function

$$y(x) = \tilde{\sigma}(x) + \frac{1}{\pi} \int_0^1 h(x, t) f(t) dt
 \tag{25.40}$$

assumed to be known. The solution of (25.39) is well-known (Muskhelishvili, 1977):

$$f(x) = -\frac{1}{\pi \tilde{X}(x)} \int_0^1 \frac{\tilde{X}(t) y(t)}{t - x} dt, \quad \tilde{X}(t) = \frac{(1 - t)^{1/2}}{t^{1/2}}.
 \tag{25.41}$$

Substituting

$$y(t) = \tilde{\sigma}(t) + \frac{1}{\pi} \int_0^1 h(t, s) f(s) ds
 \tag{25.42}$$

into the expression for $f(x)$ and taking into account that

$$\begin{aligned}
 \frac{1}{\pi} \int_0^1 \frac{\tilde{X}(t) h(t, s)}{t - x} dt &= -\frac{R(x, s)}{s^{1/2}(1 + s)^{3/2}}, \\
 R(x, s) &= 5 - 7x + s + R_s(x, s), \quad R_s(x, s) = \sum_{r=0}^2 c_r(x) x^r \frac{\partial^r}{\partial x^r} \frac{1}{s + x}, \\
 c(x) &= \{17x^2 - 19x + 3.5, 2(7x - 4)(x - 1), 2(x - 1)^2\},
 \end{aligned}
 \tag{25.43}$$

we obtain

$$f(x) = \frac{1}{\check{X}(x)} \left\{ \tilde{P}(x) + \frac{1}{\pi} \int_0^1 \frac{R(x, s)f(s)}{s^{1/2}(1+s)^{3/2}} ds \right\}, \tag{25.44}$$

where

$$\tilde{P}(x) = -\frac{1}{\pi} \int_0^1 \frac{\check{X}(t)\tilde{\sigma}(t)}{t-x} dt. \tag{25.45}$$

Note that when $\tilde{\sigma}(x) = \tilde{\sigma}_0$ we have $\tilde{P}(x) = \tilde{\sigma}_0$.

In the kernel $R(x, t)$, the term $R_s(x, t)$ is called the generalized Cauchy kernel, and it has a stationary singularity at the left end of the interval $(0, 1)$. The kernel R is also can be written as follows

$$R(x, s) = \frac{s^2(2s^2 + 10s + 7) - 2xs(4s^2 + 4s + 1) - x^2(2s^2 + 2s + 1)}{2(s+x)^3}. \tag{25.46}$$

We next rewrite (25.44):

$$\check{X}(x)f(x) - \frac{1}{\pi} \int_0^1 \frac{R(x, t)f(t)}{t^{1/2}(1+t)^{3/2}} dt = \tilde{P}(x). \tag{25.47}$$

This equation can also be rewritten as

$$a(x)u(x) - \frac{1}{\pi} \int_0^1 R(x, t)u(t)dt = \tilde{P}(x), \tag{25.48}$$

where

$$a(x) = (1-x)^{1/2}(1+x)^{3/2}, \quad u(x) = \frac{f(x)}{x^{1/2}(1+x)^{3/2}}. \tag{25.49}$$

Further, we introduce the weigh function x^b in (25.48) and write down the characteristic equation to determine b (see equation (25b) in (Savruk et al, 1999)):

$$1 + \frac{1}{\sin \pi b} \{c_0(0) + c_1(0)b + c_2(0)b(b-1)\} = 0, \tag{25.50}$$

whence $b = -1/2$. Thus, to distinguish the singularity in (25.48), the unknown function must be sought in the form $u(x) = q(x)/x^{1/2}$, where q is a regular function. To take into account this conclusion as well as the singularity at the right end of the interval $(0, 1)$, we find the unknown function in the form

$$u(x) = \frac{q(x)}{\hat{X}(x)}, \quad \hat{X}(x) = [x(1-x)]^{1/2}. \tag{25.51}$$

To take into account the condition of smooth crack closure (the third line in (25.34)), we increase the length of the fictitious crack from β to δ and rewrite the force function in the form (Fig. 25.4 b)

$$\tilde{\sigma}(x) = \tilde{\sigma}_\infty - \hat{T}[\bar{\Delta}(x)] + \hat{\sigma}(x), \tag{25.52}$$

where $\bar{\sigma}_\infty = \sigma_\infty/\sigma_{\max}$ and $\hat{T}(\bar{\Delta})$ is the relative traction extended to negative separation

$$\hat{T}(\bar{\Delta}) = \begin{cases} \bar{T}(\bar{\Delta}), & \bar{\Delta} \geq 0 \\ P(\bar{\Delta}), & \bar{\Delta} < 0 \end{cases}, \quad \bar{\Delta}(x) = w \int_{x/\delta}^1 f(t)dt, \quad w = \frac{\delta \Delta \sigma_{\max}}{\Delta_{\max}}, \quad (25.53)$$

The equation (25.48) takes the form

$$A(q, x) = \tilde{P}(x), \quad (25.54)$$

with the left-hand side

$$A(q, x) = \frac{(1+x)^{3/2}}{x^{1/2}}q(x) - \frac{1}{\pi} \int_0^1 R(x, t) \frac{q(t)}{\hat{X}(t)} dt, \quad (25.55)$$

$$q(t) = \frac{f(t)}{\omega_1(t)}, \quad \omega_1(t) = \frac{(1+t)^{3/2}}{(1-t)^{1/2}},$$

and the force function

$$\tilde{P}(x) = \bar{\sigma}_\infty - \bar{P}(x) + \hat{P}(x),$$

$$\bar{P}(x) = -\frac{1}{\pi} \int_{\lambda/\delta}^1 \frac{\check{X}(t)\hat{T}[\bar{\Delta}(t)]}{t-x} dt, \quad \hat{P}(x) = -\frac{1}{\pi} \int_{\beta/\delta}^1 \frac{\check{X}(t)\hat{\sigma}(t)}{t-x} dt. \quad (25.56)$$

The unknown regular function q can be defined from (25.54) in the piecewise-linear form. To find the parameters of q , we rewrite the left side of (25.54) as follows:

$$A(q, x) = \frac{(1+x)^{3/2}}{x^{1/2}}q(x) - \frac{1}{\pi} \sum_{k=1}^n J_k(x)q_k, \quad (25.57)$$

where q_k are the values of $q(x)$ at the quadrature points t_k ,

$$Q'_k(x) = [Q(x, t_{k+1}) - Q(x, t_k)] / \Delta t_k, \quad (25.58)$$

$$S'_k(x) = [S(x, t_{k+1}) - S(x, t_k)] / \Delta t_k, \quad \Delta t_k = t_{k+1} - t_k,$$

$$Q(x, t) = \int \frac{R(x, t)}{\hat{X}(t)} dt = (7x - \frac{11}{2}) I(t) - \hat{X}(t) + \sum_{r=0}^2 c_r(x) I_{0r}(x, t),$$

$$S(x, t) = \int \frac{tR(x, t)}{\hat{X}(t)} dt = (7x - \frac{23}{4}) \left\{ \frac{1}{2} I(t) + \hat{X}(t) \right\} \quad (25.59)$$

$$- \frac{1}{2} t \hat{X}(t) + \sum_{r=0}^2 c_r(x) I_{1r}(x, t).$$

The integrals that define functions $Q(x, t)$ and $S(x, t)$ are as follows

$$I_{kr}(x, t) = \frac{\partial^r}{\partial x^r} \int \frac{t^k dt}{\hat{X}(t)(t+x)}, \quad k = 0, 1, \quad r = 0, 1, 2. \quad (25.60)$$

After integration, we can rewrite the functions I_{kr} ,

$$\begin{aligned}
 I_{00}(x, t) &= -\frac{2}{[x(1+x)]^{1/2}} \arctan \frac{x^{1/2} \check{X}(t)}{(1+x)^{1/2}}, \\
 I_{01}(x, t) &= -\frac{1}{x+1} \left\{ \left(x + \frac{1}{2}\right) I_{00}(x, t) + \frac{\hat{X}(t)}{t+x} \right\}, \\
 I_{02}(x, t) &= \frac{1}{(x+1)^2} \left\{ \left(2x^2 + 2x + \frac{3}{4}\right) I_{00}(x, t) \right. \\
 &\quad \left. + \frac{8x^2 + 6tx + 3t + 5x}{2(t+x)^2} \hat{X}(t) \right\};
 \end{aligned}
 \tag{25.61}$$

$$\begin{aligned}
 I_{10}(x, t) &= -xI_{00}(x, t) - I(t), \quad I(t) = 2 \arctan \check{X}(t), \\
 I_{11}(x, t) &= \frac{x}{1+x} \left\{ -\frac{1}{2} I_{00}(x, t) + \frac{1}{t+x} \hat{X}(t) \right\}, \\
 I_{12}(x, t) &= \frac{x}{(1+x)^2} \left\{ \left(x + \frac{1}{4}\right) I_{00}(x, t) - \frac{4x^2 + 2tx - t + x}{2(t+x)^2} \hat{X}(t) \right\}.
 \end{aligned}
 \tag{25.62}$$

It is easy to see that $S(x, t_k)$ ($k = 1, \dots, n$) and $Q(x, t_k)$ ($k = 2, \dots, n$) are bounded when $x \rightarrow 0$, and

$$Q(x, t_1) = -\frac{\pi}{x^{1/2}} + O(1),
 \tag{25.63}$$

thus

$$J_1(x) = \frac{\pi}{x^{1/2}} + O(1), \quad J_k(x) = O(1), \quad k = 2, \dots, n.
 \tag{25.64}$$

The right-hand part of (25.54) contains the expression (see (25.56))

$$\bar{P}(x) = -\frac{1}{\pi} \int_{\lambda/\delta}^1 \frac{\check{X}(t) \hat{T}[\bar{\Delta}(t)]}{t-x} dt, \quad \bar{\Delta}(t) = w \int_{t/\delta}^1 \omega_1(s) q(s) ds,
 \tag{25.65}$$

where it is difficult to perform integration. Instead, consider the function $\hat{T}[\bar{\Delta}(x)] - \hat{\sigma}(x)$ ($\lambda < x < \delta$) which is linear on each quadrature interval, then

$$\tilde{P}(x) = \bar{\sigma}_\infty - \sum_{k=1}^{n-p} Z_k(x) (\bar{\sigma}_k - \hat{\sigma}_k), \quad \bar{\sigma}_k = \hat{T}[\bar{\Delta}(x_{p+k})],
 \tag{25.66}$$

$$\begin{aligned}
 Z_1(x) &= B'_1(x) - A_1(x), \quad Z_n(x) = -B'_{n-1}(x) + A_n(x), \\
 Z_k(x) &= B'_k(x) - B'_{k-1}(x), \quad k = 2, \dots, n-1,
 \end{aligned}
 \tag{25.67}$$

where

$$\begin{aligned}
 A_k(x) &= A(x, t_k), \quad B'_k(x) = [B_{k+1}(x) - B_k(x)]/\Delta t_k, \\
 B_k(x) &= B(x, t_k);
 \end{aligned}
 \tag{25.68}$$

$$\begin{aligned}
 A(x, t) &= \tilde{X}(x) \ln \left| \frac{\tilde{X}(t) - \tilde{X}(x)}{\tilde{X}(t) + \tilde{X}(x)} \right| + I(t), \\
 B(x, t) &= \tilde{A}(x, t) + \frac{1}{2}I(t) - \tilde{X}(t), \\
 \tilde{A}(x, t) &= (t - x)A(x, t) = \begin{cases} 0, & x = t \\ -\pi x, & t = 0 \\ tI(t) - 2\hat{X}(t), & x = 0 \end{cases} .
 \end{aligned} \tag{25.69}$$

The quadrature formulae for $\bar{\Delta}(x)$ is as follows

$$\bar{\Delta}(\mathbf{x}) = w\mathbf{V}\mathbf{q}, \quad \mathbf{x} = \{x_1, \dots, x_n\}^T, \tag{25.70}$$

where the matrix \mathbf{V} is given in (25.19); to define \mathbf{V} , it is necessary to replace the function ω in (25.20) with ω_1 and to calculate the integrals

$$\begin{aligned}
 R(t) &= \frac{3}{2}U(t) - \left(\frac{1}{2}t + 2\right)Y(t), \\
 G(t) &= \left(\frac{3}{2}t - 1\right)U(t) - \frac{1}{6}(t^2 + 6t - 10)Y(t),
 \end{aligned} \tag{25.71}$$

where

$$U(t) = 2 \arctan \alpha^{-1}(t), \quad \alpha(t) = \frac{(1 - t)^{1/2}}{(1 + t)^{1/2}}, \quad Y(t) = (1 - t^2)^{1/2}. \tag{25.72}$$

The discretization of (25.54) takes the following form:

$$\mathbf{J}\mathbf{q} = \bar{\sigma}_\infty \mathbf{1} - \mathbf{Z}[\hat{T}(w\mathbf{V}\mathbf{q}) - \hat{\sigma}], \tag{25.73}$$

where $\mathbf{1}$ is $n \times 1$ vector of ones,

$$\begin{aligned}
 \mathbf{J} &= [j_{mk}], \quad m, k = 1, \dots, n, \\
 \mathbf{Z} &= [z_{mk}], \quad z_{mk} = Z_m(x_k), \quad m = 1, \dots, n, \quad k = 1, \dots, n - p,
 \end{aligned} \tag{25.74}$$

$$\begin{aligned}
 \mathbf{q} &= \{q_1, \dots, q_{n-s}, \underbrace{0, \dots, 0}_s\}^T, \\
 \hat{T}(w\mathbf{V}\mathbf{q}) &= \{\bar{\sigma}_1, \dots, \bar{\sigma}_{n-p}\}^T, \quad \bar{\sigma}_k = \hat{T}(w\mathbf{V}_{p+k}\mathbf{q}), \\
 \hat{\sigma} &= \{\underbrace{0, \dots, 0}_{n-p-s}, \hat{\sigma}_1, \dots, \hat{\sigma}_s\}^T,
 \end{aligned} \tag{25.75}$$

the row vector \mathbf{V}_k is defined by the k th row of the matrix \mathbf{V} , the index p corresponds to the quadrature point $x_p = \lambda/\delta$.

The nonlinear system (25.34) contains n unknowns: $n - s$ nonzero components of \mathbf{q} and s nonzero components of $\hat{\sigma}$. To satisfy the condition of smooth crack closure, it is necessary to choose the index s so that for the corresponding solution of the system (25.34) the inequality holds

$$\mathbf{V}_{n-s}\mathbf{q} \geq 0. \tag{25.76}$$

The position of the cohesive zone tip is determined with the accuracy of Δt : $\beta = \delta x_{n-s}$.

When studying the critical state, it is necessary to include into the governing system (25.34) the equation that meets the fracture criterion

$$w \nabla_p \mathbf{q} = 1. \tag{25.77}$$

This condition add one more unknown $\sigma_\infty = \sigma_\infty^*$ into the governing system.

In the numerical example, the stress state under the critical state condition is determined. According to the used traction–separation law, the maximum separation corresponds to zero cohesive traction, and we have $\hat{T}[\bar{\Delta}(x_p)] = 0$, which is taken into account in (25.66).

The stresses on the crack faces is determined by the integral

$$\sigma(x) = -\frac{\Lambda \sigma_{\max}}{\pi} \int_0^1 K(x, t) \omega_1(t) q(t) dt = -\frac{\Lambda \sigma_{\max}}{\pi} \sum_{k=1}^n q_k J_k(x), \tag{25.78}$$

the functions $J_k(x)$ can be written in similar to (25.67) way, where it is assumed that

$$\begin{aligned} Q(x, t) &= \hat{Q}(x, t) + \check{Q}(x, t), \\ \hat{Q}(x, t) &= \int \frac{\omega_1(t)}{t-x} dt = \\ &\quad \omega_1(x) \ln \left| \frac{\alpha(x) - \alpha(t)}{\alpha(x) + \alpha(t)} \right| + (x+2)U(t) - Y(t), \\ \check{Q}(x, t) &= \int h(x, t) \omega_1(t) dt = \sum_{r=0}^2 d_r x^r \hat{I}_r(x, t); \end{aligned} \tag{25.79}$$

and the functions

$$\hat{I}_r(x, t) = \frac{\partial^r}{\partial x^r} \int \frac{\omega_1(t)}{t+x} dt \tag{25.80}$$

after integration take the form

$$\begin{aligned} \hat{I}_0(x, t) &= \alpha(x)W(x, t)(1-x) + (2-x)U(t) - Y(t), \\ \hat{I}_1(x, t) &= -\alpha(x)W(x, t) \frac{x+2}{x+1} - U(t) + \frac{\alpha^2(x)}{x+t} Y(t), \\ \hat{I}_2(x, t) &= \frac{1}{x+1} \left(\frac{3W(x, t)}{\alpha(x)(x+1)^2} - \left(\frac{x+4}{x+1} + \frac{1-x}{x+t} \right) \frac{Y(t)}{x+t} \right), \end{aligned} \tag{25.81}$$

where

$$W(x, t) = \ln \frac{1 - \alpha(x)\alpha(t)}{1 + \alpha(x)\alpha(t)}. \tag{25.82}$$

The second function from (25.67) can be written as

$$\begin{aligned}
 T(x, t) &= \hat{T}(x, t) + \check{T}(x, t), \\
 \hat{T}(x, t) &= \frac{x+1}{\alpha(x)}(t-x) \ln \left| \frac{\alpha(t) - \alpha(x)}{\alpha(t) + \alpha(x)} \right| \\
 &\quad + \left[(x+2)t - (x+1)^2 - \frac{1}{2} \right] U(t) + (x+2 - \frac{1}{2}t) Y(t), \quad (25.83) \\
 \check{T}(x, t) &= \int \check{Q}(x, t) dt = \sum_{r=0}^2 d_r x^r \check{I}_r(x, t).
 \end{aligned}$$

$$\begin{aligned}
 \check{I}_0(x, t) &= \alpha(x)W(x, t)(1-x)(t+x) \\
 &\quad + \left[(2-x)t - (1-x)^2 - \frac{1}{2} \right] U(t) \\
 &\quad + (2-x - \frac{1}{2}t) Y(t), \\
 \check{I}_1(x, t) &= \alpha(x)W(x, t) \left[1-x - \frac{x+2}{x+1}(t+x) \right] \\
 &\quad + (2(1-x) - t)U(t) - \frac{2x}{x+1} Y(t), \quad (25.84) \\
 \check{I}_2(x, t) &= \alpha(x)W(x, t) \frac{3t - 4 + x + 4x^2 + 2x^3}{(x+1)^2(1-x)} \\
 &\quad - 2U(t) + \left(\frac{1-x}{x+t} - \frac{x+4}{x+1} \right) \frac{Y(t)}{x+1}.
 \end{aligned}$$

Write down the functions from (25.67),

$$\begin{aligned}
 Q_1(x) &= \frac{1}{(x+1)^2} \left\{ - \frac{2x(3x^3 + 4x^2 - 4x - 8)}{Y(x)} \ln \frac{1 - \alpha(x)}{1 + \alpha(x)} \right. \\
 &\quad \left. + 4 \left(\pi x^3 + \left(2\pi + \frac{3}{2} \right) x^2 + (\pi + 2)x - 1 \right) \right\}, \quad Q_n(x) = 8\pi x. \quad (25.85)
 \end{aligned}$$

The two terms in the expression of Q_1 (see (25.79)) are singular. Using asymptotic properties, we can assume that $Q_1(0) = -4$ and $Q_1(1) = 4\pi$. It is also easy to obtain the asymptotic behavior of $T_k(x)$.

To obtain the numeric solution, we use the traction–separation law with hardening segment

$$\begin{aligned}
 \bar{T}(\bar{\Delta}) &= (\bar{\sigma}_l \bar{\Delta} + \bar{\sigma}_n)(1 - \bar{\Delta})^2, \\
 \Delta_{\max} &= \frac{12\phi}{\sigma_{\max}(\bar{\sigma}_l + 4\bar{\sigma}_n)}, \quad \frac{4}{27} \bar{\sigma}_l \left(1 + \frac{\bar{\sigma}_n}{\bar{\sigma}_l} \right)^3 = 1. \quad (25.86)
 \end{aligned}$$

The dashed line in Fig. 25.8 *b* shows the discretized function $\hat{T}[\bar{\Delta}(\xi)] - \hat{\sigma}(\xi)$ (stress on the crack line). Here, the oscillation about $\sigma(x)$ on the interval $\beta < \xi < \delta$ takes place. Though, the function $\hat{\sigma}(\xi)$ is auxiliary and has no physical meaning. Instead, the opening displacement density $q(x)$ has no oscillation in contrast to the solution without regularization. It is shown for some other values of shape parameter $\bar{\sigma}_n$ in Fig. 25.8 *c*.

The critical value of the external load $\sigma_{\infty}^* = 0.6021\sigma_{\max}$. We obtained $0.6023\sigma_{\max}$ when solving the problem without regularization in Section 25.2. The

corresponding solution \bar{g} illustrated in Fig. 25.7 of the mentioned section is also shown in Fig. 25.8 *a* for the comparison.

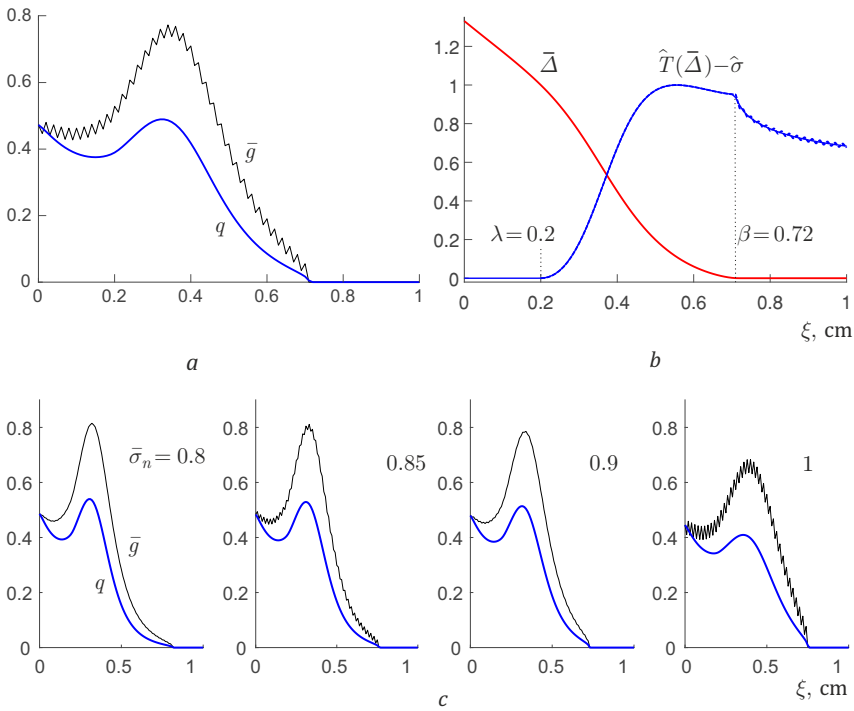


Fig. 25.8 The relative displacement density $q(\xi)$ (a), corresponding cohesive traction $\hat{T}[\bar{\Delta}(\xi)] - \hat{\sigma}(\xi)$ and separation $\bar{\Delta}(\xi)$ (b) for $\delta = 1$ cm, $\bar{\sigma}_n = 0.95$, $\bar{\sigma}_l = 2.8406$, $E = 40$ GPa, $\phi = 200$ N/m, $\sigma_{\max} = 35$ MPa, $n = 101$ (discretization parameter). The comparison of regularized solutions with non-regularized ones for some additional values of shape parameter $\bar{\sigma}_n$ (c).

Thus, in this section, a semi-analytical technique is developed to solve the problem of crack mechanics for an edge crack. The integral equation with the generalized Cauchy kernel, which gives the solution of the problem, after regularization is solved by the collocation method. The solution is constructed taking into account the stationary singularity of the specified kernel. The use of regularization allowed us to obtain a physically correct (without oscillation) solution for the density of opening displacement (the function φ in (25.34)). It is established that both solutions (with and without regularization) give very close values of the critical load, which due to the simplicity of implementation makes the semi-analytical algorithm presented in the previous section more attractive.

25.4 Subcritical State of a Crack

Consider the problem of the subcritical state of an edge crack with a failure zone near its front in a semi-infinite plane (Fig. 25.2). The crack is located along the normal to the boundary of the half-plane, the distributed tensile load is applied at a considerable distance from the crack along the normal to its plane.

For this problem, the governing system of the equations is given in Section 25.2 (see (25.34)) and regularized in Section 25.3. When studying the subcritical state, the mentioned equation have be solved together with the condition $\Delta(\lambda) = \Delta_0$ ($\Delta_0 < \Delta_{\max}$).

In Section 25.3, the integral equation of the first kind (25.1) is transformed into the following second kind equation

$$\frac{(1+x)^{3/2}}{x^{1/2}}q(x) - \frac{1}{\pi} \int_0^1 R(x,t) \frac{q(t)}{\hat{X}(t)} dt = \bar{\sigma}_\infty + \frac{1}{\pi} \int_{\lambda/\delta}^1 \frac{\check{X}(t)\bar{T}[\bar{\Delta}(t)]}{t-x} dt, \tag{25.87}$$

where

$$\hat{X}(t) = t^{1/2}(1-t)^{1/2}, \quad \check{X}(t) = \frac{(1-t)^{1/2}}{t^{1/2}}, \tag{25.88}$$

$$\bar{\Delta}(t) = w \int_{t/\delta}^1 \omega_1(s)q(s)ds, \quad w = \frac{\delta\Lambda\sigma_{\max}}{\Delta_{\max}}, \quad \omega_1(t) = \frac{(1+t)^{3/2}}{(1-t)^{1/2}}$$

(δ is a constant, which is greater than the unknown characteristic β (Fig. 25.4 b)),

$$R(x,s) = 5 - 7x + s + R_s(x,s), \quad R_s(x,s) = \sum_{r=0}^2 c_r(x)x^r \frac{\partial^r}{\partial x^r} \frac{1}{s+x},$$

$$c(x) = \{17x^2 - 19x + 3.5, 2(7x - 4)(x - 1), 2(x - 1)^2\}.$$

The unknown functions $q(x)$ and $\bar{\sigma}(x) = \bar{T}[\bar{\Delta}(x)]$ can be defined from (25.87) in piece-wise linear form. We rewrite (25.87) according with results of the previous section,

$$\frac{(1+x)^{3/2}}{x^{1/2}}q(x) - \frac{1}{\pi} \sum_{k=1}^n J_k(x)q_k = \bar{\sigma}_\infty + \frac{1}{\pi} \sum_{k=p}^n Z_k(x)\bar{\sigma}_k, \tag{25.89}$$

$$q_k = q(x_k), \quad \bar{\sigma}_k = \bar{\sigma}(x_k).$$

To satisfy (25.89) at the collocation points, we solve the following system of equations

$$\sum_{k=1}^n j_{mk}q_m = \bar{\sigma}_\infty - \sum_{k=p}^n z_{mk}\bar{\sigma}_k, \tag{25.90}$$

the coefficients of which are defined in Section 25.3.

Similarly, we can determine the displacement at the collocation points

$$\bar{\Delta} = w\mathbf{V}\mathbf{q}, \quad \bar{\Delta} = \{\Delta_1, \Delta_2, \dots, \Delta_n\}^T, \quad \bar{\Delta}_k = \bar{\Delta}(x_k), \quad (25.91)$$

and using this expression, rewrite the system of equations (25.90) in the matrix form

$$\mathbf{J}\mathbf{q} = \bar{\sigma}_\infty \mathbf{1} - \mathbf{Z}\bar{T}(w\mathbf{V}\mathbf{q}), \quad (25.92)$$

where $\mathbf{1}$ is the $n \times 1$ vector of ones,

$$\mathbf{q} = \{q_1, q_2, \dots, q_n\}^T, \quad \mathbf{J} = [j_{mk}], \quad \mathbf{Z} = [z_{mk}], \quad m, k = 1, \dots, n. \quad (25.93)$$

The system of equations (25.92) contains n nodal values of the unknown function $q(x)$. The standard iterative process of the numerical method for solving a system of nonlinear equations often does not converge to the solution. This is due to the presence of two solutions for load values close to their critical value (Selivanov and Chornoivan, 2018). This inconvenience can be avoided by assuming quantity $\bar{\sigma}_\infty$ unknown and supplementing the system (25.92) with the equation

$$w\mathbf{V}_p\mathbf{q} = \Delta(\lambda), \quad (25.94)$$

where $\Delta(\lambda)$ is the given crack tip opening displacement. The components of the row vector \mathbf{V}_p are the elements of the p th row of \mathbf{V} , the index p corresponds to the quadrature point $x_p = \lambda/\delta$.

We construct a numerical example for the smoothed trapezoidal traction–separation law (the effective law is illustrated in Fig. 25.1).

$$\bar{T}(\bar{\Delta}) = \begin{cases} a_1^{-1}\bar{\Delta}(2 - a_1^{-1}\bar{\Delta}), & \bar{\Delta} \in [0, a_1) \\ 1, & \bar{\Delta} \in [a_1, a_2] \\ (1 - \bar{\Delta})^2(1 + 2\bar{\Delta} - 3a_2)(1 - a_2)^{-3}, & \bar{\Delta} \in (a_2, 1] \end{cases} \quad (25.95)$$

After introducing the constant $\omega = \int_0^1 \bar{T}(\bar{\Delta})d\bar{\Delta} = \frac{1}{6}(3 - 2a_1 + 3a_2)$, the inner model parameter $\Delta_{\max} = \phi/(\omega\sigma_{\max})$ can be determined. The quantity $\omega \in (0, 1)$ is one of the measures of deviation of the traction–separation law from the uniform one, which corresponds to the Dugdale model (Dugdale, 1960).

In Fig. 25.9, the problem solution $q(x)$ is illustrated. On the second plot, nondimensional cohesive traction $\bar{\sigma}(x)$ and corresponding separation $\bar{\Delta}(x)$ are shown. The solution is obtained for the following values of the problem parameters: $\delta = 1$ cm, $a_1 = a_2 = 10^{-3}$, $E = 40$ GPa, $\phi = 200$ N/m, $\sigma_{\max} = 35$ MPa, $n = 500$ (discretization parameter). Thus, the oscillation is not observed both for the solution of the critical state problem ($\Delta(\lambda) = \Delta_{\max}$) and the subcritical state solution ($\Delta(\lambda) < \Delta_{\max}$). In the second case, with a decrease in the crack tip opening displacement, the influence of the discontinuity of the contour conditions begins to appear, which causes the singularity of the solution. Taking into account this feature may be the subject of further research.

In Fig. 25.10, the solutions of the equations of the first and second kind are compared and the levels of external load corresponding to these solutions are indicated. For small cohesive lengths (small levels of subcritical load), there are differences

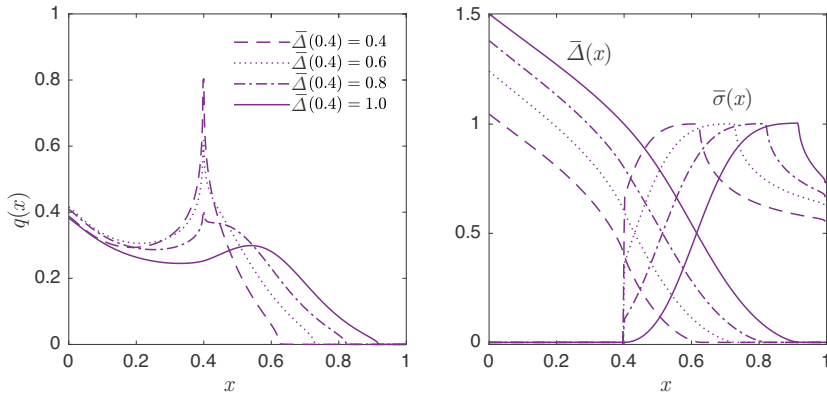


Fig. 25.9 Solution of the problem for the edge crack within the cohesive zone model approach.

in the two solutions. For load levels close to critical, these discrepancies are within graphical accuracy. The parameters of the previous example were used to construct numerical solutions, except for E , which is taken to be equal to 4 GPa.

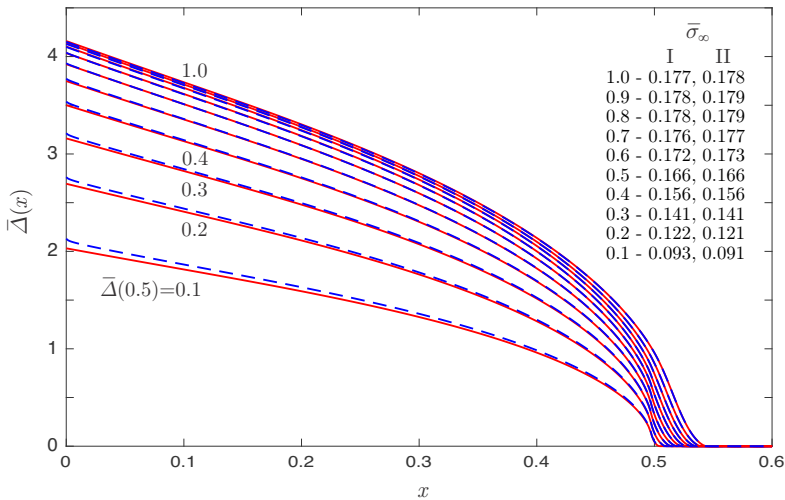


Fig. 25.10 Comparison of solutions that equations of the first (dashed curves) and second (solid curves) kind yield.

25.5 Modeling the Slow Crack Growth

According to the results of Section 25.2, the elastic solution of the boundary problem for a crack in an infinite half-plane is given by a singular integral equation

$$\frac{1}{\pi\Lambda} \int_0^1 K(x, \xi)\psi(\xi)d\xi = \bar{\sigma}_\infty - \bar{T} \left(\underbrace{\delta \frac{\Lambda\sigma_{\max}}{\Delta_{\max}} \int_{x/\delta}^1 \psi(\xi)d\xi}_{\bar{\Delta}(x)} \right), \quad (25.96)$$

where $\psi(x)$ is the sought solution, \bar{T} is the effective traction–separation law ($\bar{T}(\bar{\Delta}) = 0$ for $\bar{\Delta} < 0$ and $\bar{\Delta} > 1$), which lies in the base of the cohesive zone model, σ_{\max} and Δ_{\max} are the cohesive strength and the critical crack tip opening displacement, respectively. These parameters along with shape parameters of the law \bar{T} are the fracture characteristics of the material, $\bar{\sigma}_\infty$ is the remote stress divided by σ_{\max} , Λ is the function of elastic moduli (when the isotropic material is studied and plane stress is under consideration $\Lambda = 4/E$, where E is Young's modulus), the kernel $K(x, \xi)$ is given in (25.2), δ is the tip of fictitious crack, and $\bar{\Delta}(x)$ is the crack opening displacement divided by Δ_{\max} . Thus, elastic moduli and functions of coordinates are separated.

The disadvantages of the solution of (25.96) are discussed in Section 25.2, and in Section 25.3, the following regularized equation is obtained

$$a(x)q(x) - \frac{1}{\pi} \int_0^1 J(x, \xi)q(\xi)d\xi = \bar{\sigma}_\infty + \frac{1}{\pi} \int_0^1 Z(x, \xi)\bar{T} \left(\underbrace{\delta \frac{\Lambda\sigma_{\max}}{\Delta_{\max}} \int_{\xi/\delta}^1 \omega(\eta)q(\eta)d\eta}_{\bar{\Delta}(\xi)} \right) d\xi. \quad (25.97)$$

In the case of the subcritical state, the solution of this equation is analyzed in Section 25.5. In (25.97), $q(x)$ is the sought solution, the functions $a(x)$, $J(x, \xi)$, $Z(x, \xi)$ and $\omega(x)$ are listed in Section 25.3. To solve (25.97), we use the collocation method, which requires finding the function $q(x)$ at the collocation points \mathbf{x} : $q(\mathbf{x}) = \mathbf{q}$. The piece-wise linear form for $q(x)$ is used. The equation (25.97) thus can be reduced to the system of nonlinear equations:

$$\mathbf{J}\mathbf{q} = \bar{\sigma}_\infty \mathbf{1} - \mathbf{Z}\bar{T}(l \cdot \underbrace{w \cdot \mathbf{V}\mathbf{q}}_{\bar{\Delta}(\mathbf{x})}), \quad (25.98)$$

where

$$w = \delta \frac{\Lambda_0\sigma_{\max}}{\Delta_{\max}}, \quad l = \frac{\Lambda}{\Lambda_0}, \quad (25.99)$$

$$\mathbf{q} = \{q_1, q_2, \dots, q_n\}^T, \quad \mathbf{J} = [j_{mk}], \quad \mathbf{Z} = [z_{mk}], \quad m, k = 1, \dots, n, \quad (25.100)$$

$\mathbf{1}$ is the $n \times 1$ vector of ones, \mathbf{J} , \mathbf{Z} and \mathbf{V} are listed in Section 25.3, the nondimensional elastic constant l is introduced for the further determination of viscoelastic analogues of displacement $\Delta(x, t)$ (it is obvious that in the elastic problem solution $l = 1$).

We study the quasi-static stable growth of the preexisting mode I crack in a semi-infinite plate made of viscoelastic non-aging material in isothermal conditions. The propagation initiates under the constant subcritical external load applied at infinity, σ_∞ due to the viscoelastic properties of the material. We consider the growth of a crack along the predefined path.

At the time of load application, the crack is in a subcritical state. The crack tip opening displacement does not exceed the maximum level:

$$\Delta(\lambda, t = 0) < \Delta_{\max}. \tag{25.101}$$

Due to the creep, the value of $\Delta(\lambda, t)$ reaches with time its critical value Δ_{\max} , ending the incubation period and initiating the beginning of growth. Both during the incubation period and quasi-static propagation, the traction–separation law holds true (Fig. 25.11 a):

$$\bar{\sigma}(x, t) = \bar{T} [\bar{\Delta}(x, t)], \tag{25.102}$$

where $\bar{\sigma}(x, t) = \sigma(x, t) / \sigma_{\max}$.

Due to the isotropy of the material, the function of viscoelastic moduli in the factorized solution (25.96) coincides with the compliance function up to the constant multiplier. Thus, the crack opening displacement can be represented in the same form as the constitutive equations:

$$\bar{\Delta}(x, t) = \int_{-\infty}^t l(t - \tau) \tilde{\Delta}'_\tau(x, \tau) d\tau, \tag{25.103}$$

where $\tilde{\Delta}(x, t)$ is nondimensional solution of the problem for instantaneous values of viscoelastic moduli:

$$\tilde{\Delta}(x, t) = w \int_{x/\delta}^1 \omega(\eta) q(\eta, t) d\eta. \tag{25.104}$$

If an external load is applied instantaneously at time $t = 0$,

$$\bar{\Delta}(x, t) = l(t) \tilde{\Delta}(x, 0) + \int_0^t l(t - \tau) \tilde{\Delta}'_\tau(x, \tau) d\tau. \tag{25.105}$$

Next, an algorithm for determining the length of a crack that increases with time will be constructed. There are two methodologies to build the algorithm. According to the first one, the points on the crack path that the crack tip passes have to be found for the given moments of time. In the present paper we use another approach: the moments when the crack tip passes the given points on its path are found at each step.

Thus, at each step, we find the value of $\tilde{\Delta}_m(x)$ and time t_m that determine the solution from the equation

$$\underbrace{\bar{T}\left(l(t_m)\tilde{\Delta}_0(x) + \sum_{i=1}^m \Lambda_i(t_m) \left[\tilde{\Delta}_i(x) - \tilde{\Delta}_{i-1}(x)\right]\right)}_{\bar{\Delta}(x, t_m)} = \bar{\sigma}(x, t_m), \quad (25.106)$$

where $\tilde{\Delta}_i(x) = \tilde{\Delta}(x, t_i)$, $\bar{\sigma}(x, t_m)$ is nondimensional cohesive traction that causes the displacement $\bar{\Delta}(x, t_m)$, and nondimensional creep function is as follows

$$\Lambda_i(t_n) = \frac{1}{\Delta t_i} \int_{t_{i-1}}^{t_i} l(t_n - \tau) d\tau. \quad (25.107)$$

At each step of the algorithm, we solve (25.106) with the following condition

$$\bar{\Delta}(\lambda_m, t_m) = \bar{\Delta}^{(m)}. \quad (25.108)$$

During the incubation, $\lambda_m = \lambda_0$ (λ_0 is the initial length of a crack), $\bar{\Delta}^{(m)} < \bar{\Delta}^{(m+1)} < 1$. When modeling the crack growth, the crack length is given at each step, $\lambda_{m+1} > \lambda_m$ and $\bar{\Delta}^{(m)} = 1$ (Fig. 25.11 b). We next illustrate solving the

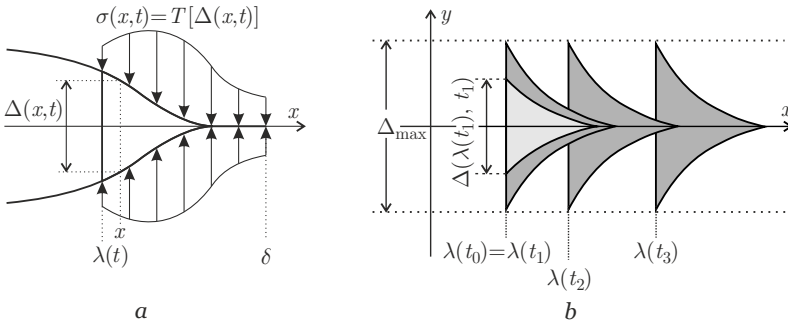


Fig. 25.11 Dependence of cohesive traction on opening displacement (a), and modeling the slow crack growth within the cohesive zone model approach (b).

equations of quasi-static crack growth in the first steps of the algorithm. The solution $\tilde{\Delta}_0(x) = \tilde{\Delta}(x)$ at the moment $t_0 = 0$ is defined by (25.98). The argument of \bar{T} is the instantaneous opening displacement at the collocation points, $\tilde{\Delta}_0(\mathbf{x})$.

The solution $\{\mathbf{q}^{(1)}, t_1\}$ in the second step is defined by the following system of equations:

$$\mathbf{Jq}^{(1)} = \bar{\sigma}_\infty \mathbf{1} - \mathbf{Z}\bar{T} \left\{ \underbrace{l(t_1)\tilde{\Delta}_0(\mathbf{x}) + \left[w\mathbf{Vq}^{(1)} - \tilde{\Delta}_0(\mathbf{x})\right] \Lambda_1(t_1)}_{\bar{\Delta}(\mathbf{x}, t_1)} \right\} \quad (25.109)$$

$$\bar{\Delta}(\lambda_1, t_1) = \bar{\Delta}^{(1)}$$

For the found solution $\mathbf{q}^{(1)}$, it is necessary to obtain the displacement $\tilde{\Delta}_1(\mathbf{x}) = w\mathbf{V}\mathbf{q}^{(1)}$ that is used in the following steps.

In the third step, solving the system of equations

$$\mathbf{J}\mathbf{q}^{(2)} = \bar{\sigma}_\infty \mathbf{1} - \underbrace{\mathbf{Z}\bar{T} \left\{ l(t_2)\tilde{\Delta}_0(\mathbf{x}) + \left[\tilde{\Delta}_1(\mathbf{x}) - \tilde{\Delta}_0(\mathbf{x}) \right] A_1(t_2) + \left[w\mathbf{V}\mathbf{q}^{(2)} - \tilde{\Delta}_1(\mathbf{x}) \right] A_2(t_2) \right\}}_{\tilde{\Delta}(\mathbf{x}, t_2)}$$

$$\bar{\Delta}(\lambda_2, t_2) = \bar{\Delta}^{(2)} \tag{25.110}$$

yields a solution $\mathbf{q}^{(2)}$ and t_2 . For the obtained $\mathbf{q}^{(2)}$, it is necessary to calculate $\tilde{\Delta}_2(\mathbf{x}) = w\mathbf{V}\mathbf{q}^{(2)}$ and continue the algorithm until the solution of (25.98) exists.

We find the numerical solution for the classical Kelvin–Voigt material model

$$l(t) = l_\infty - (l_\infty - 1) \exp(-t/\eta). \tag{25.111}$$

In this case, the nonlinear equations (25.109) and (25.110) can be easily linearized.

To obtain numerical results, we use the following effective traction–separation law

$$\bar{T}(\bar{\Delta}) = \begin{cases} \bar{\Delta}/a (2 - \bar{\Delta}/a), & \bar{\Delta} \in (0, a) \\ (1 - \bar{\Delta})^2(1 + 2x - 3a)/(1 - a)^3, & \bar{\Delta} \in (a, 1) \end{cases} \tag{25.112}$$

The function \bar{T} is zero outside the interval $(0, 1)$. The initial hardening segment is introduced to ensure the smooth crack closure that lies in the base of the cohesive zone model approach. The length of this segment should be small enough. When a is small, on the other hand, it is observed a significant increase in iterations when solving nonlinear equations in the implementation of the proposed algorithm.

In Fig. 25.12, the problem solution is illustrated for $l_\infty = 4$, $\eta = 100$ sec (creep function parameters), $a = 1/1000$ (parameter of hardening segment in the effective traction–separation law (25.112)), $\lambda_0 = 2/5$ cm, $\delta = 4/5$ cm (geometric parameters), $w = 28/5$, $\bar{\sigma}_\infty = 11/35$ (relationship between the elastic moduli, crack resistance characteristics and geometric parameters) and $n = 500$ (discretization parameter). The incubation period is described by two subcritical values of the nondimensional crack tip opening displacement: $\bar{\Delta}^{(1)} = 1/3$, $\bar{\Delta}^{(2)} = 2/3$. Thus, the duration of the incubation period is determined by the time t_3 . The bold curves correspond to the instantaneous solution and the beginning of crack propagation. The circles indicate the crack tip position.

Fig. 25.13 illustrates auxiliary solutions of the problem for the moments of time t_m calculated during the solving process. Note that all values of $\bar{\Delta}_i(\mathbf{x})$ must be preserved when solving the equations of slow crack growth.

In Fig. 25.14 *a*, the selected creep function is shown. The circles at the curve correspond to the found moments of time t_m . In Fig. 25.14 *b*, the dependence of crack length on time (t_m, λ_m) is illustrated.

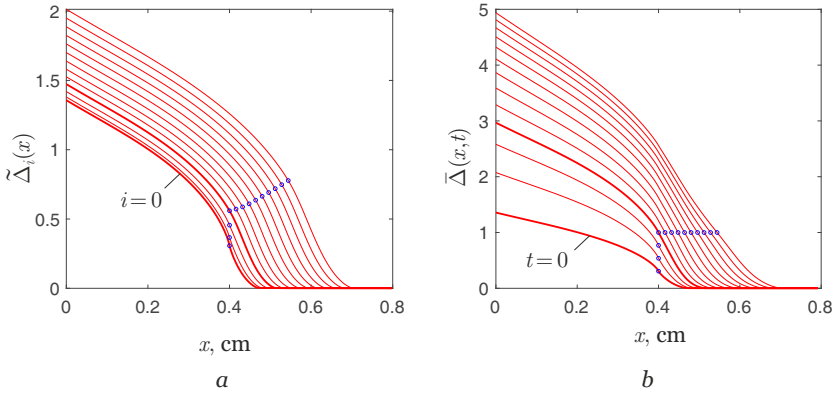


Fig. 25.12 The auxiliary solutions (a) and the crack opening displacement for some moments of time after applying loads (b).

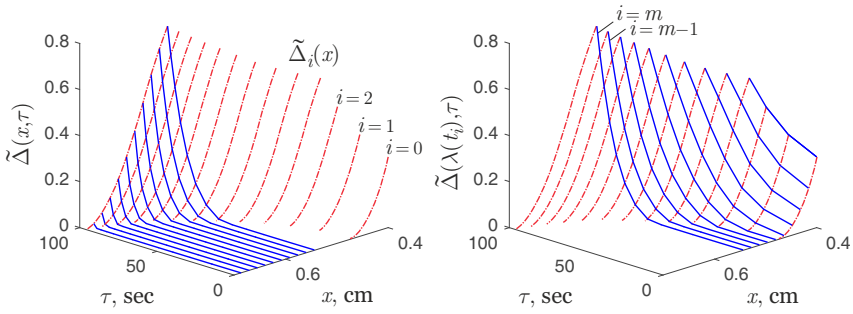


Fig. 25.13 The auxiliary solutions: $\tilde{\Delta}_i(x)$ are dot-dash curves, $\tilde{\Delta}(x, \tau)$ are solid curves (the partial time derivative of this function is integrated in (25.103) and (25.105) to find the solution on the m th step).

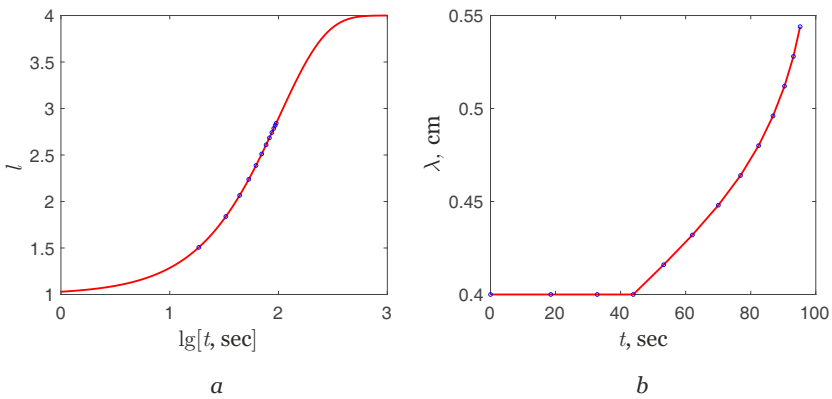


Fig. 25.14 The nondimensional creep function (a) and the crack length (b).

Thus, this section illustrates solving the problem of slow propagation of an edge crack along a known path. Particular attention is paid to the transition from elastic to viscoelastic opening displacement and solving the equations of slow crack growth. Numerical solution demonstrated the effectiveness of the proposed methodology for modeling quasi-static crack growth due to the hereditary viscoelastic properties of the material.

25.6 Conclusion

The present work is related to the problem of the critical and subcritical states of a semi-infinite plane with a mode I crack and its slow growth due to the hereditary viscoelastic properties of the material. The problem was solved within the framework of the cohesive zone model approach. The integral equation with the generalized Cauchy kernel, which determines the solution of this problem, is solved without regularization. It is established that the solution of the problem—the density of crack opening displacement—oscillates. This oscillation is due to the fact that the cohesive traction applied to the fictitious crack faces within the model are not continuous functions and can have a jump at the point corresponding to the tip of the physical crack. This feature of the formulation can be taken into account by introducing an additional weight function, but such an approach makes it impossible to find the obtained integrals analytically. The mentioned oscillation consequently was eliminated by regularizing the singular integral equation of the first kind. First, the solution corresponding to the conditions of the critical state was obtained, i.e. when the cohesive traction is zero provided that the maximum possible separation in the zone is reached (boundary conditions are not a jump function at the transition to the faces of a physical crack). It was shown that the oscillation disappears. The question arises as to how the solution of the problem behaves in the study of the subcritical state in the absence of weight functions. It was illustrated that the oscillation is absent in this case as well. Moreover, the crack opening displacement obtained using the regularized equation is more adequate than the one obtained from the first-kind integral equation (see Fig. 25.10), especially for the small cohesive lengths. Based on the methodology of finding the solution for the elasticity problem, the algorithm for modeling the slow crack growth in viscoelastic material was described and illustrated.

References

- Barenblatt G (1962) The mathematical theory of equilibrium cracks in brittle fracture. *Advances in Applied Mechanics* 7:55–129
- Bažant Z, Li YN (1997) Cohesive crack model with rate-depending opening and viscoelasticity: I. Mathematical model and scaling. *International Journal of Fracture* 86:247–265
- Broberg K (1999) *Cracks and Fracture*. Academic Press

- Ciavarella M, Cricri G, McMeeking R (2021a) A comparison of crack propagation theories in viscoelastic materials. *Theoretical and Applied Fracture Mechanics* 116:103,113
- Ciavarella M, Papangelo A, McMeeking R (2021b) Crack propagation at the interface between viscoelastic and elastic materials. *Engineering Fracture Mechanics* 257:108,009
- Dugdale D (1960) Yielding of steel sheets containing slits. *Journal of the Mechanics and Physics of Solids* 8:100–104
- Erdogan F, Gupta G, Cook T (1973) Numerical solution of singular integral equations. In: Sih G (ed) *Methods of analysis and solutions of crack problems. Mechanics of Fracture*, vol 1, Springer, Dordrecht, pp 368–425
- Gourgiotis P, Georgiadis H (2009) Plane-strain crack problems in microstructured solids governed by dipolar gradient elasticity. *Journal of the Mechanics and Physics of Solids* 57(11):1898–1920
- Hakim L, Mikhailov S (2015) Numerical implementation of a cohesive zone model in history-dependent materials. *The Quarterly Journal of Mechanics and Applied Mathematics* 68:387–341
- Hakim L, Mikhailov S (2018) A history-dependent cohesive zone model in elastic and visco-elastic materials under constant and variable loading. *International Journal of Mechanical Sciences* 144:518–525
- Hillerborg A, Modeer M, Petersson P (1976) Analysis of crack formation and crack growth in concrete by means of fracture mechanics and finite elements. *Cement and Concrete Research* 6:773–781
- Hui C, Ruina A, Long R, Jagota A (2011) Cohesive zone models and fracture. *The Journal of Adhesion* 87:1–52
- Kaminskii A (2014) Mechanics of the delayed fracture of viscoelastic bodies with cracks: theory and experiment (review). *International Applied Mechanics* 50:485–548
- Kaminskii A (2021) Studies of subcritical crack growth in viscoelastic anisotropic bodies using the continued fraction operator method: synthesis and summary. *International Applied Mechanics* 144:518–525
- Kaminskii AA (1998) Fundamentals of the theory of the long-term failure of cracked viscoelastic anisotropic bodies under varying external loads. *International Applied Mechanics* 34:1573–8582
- Khoroshun L, Nazarenko L (2013) Deformation and damage of composite materials with anisotropic components (review). *International Applied Mechanics* 49:388–455
- Knauss W (2015) A review of fracture in viscoelastic materials. *International Journal of Fracture* 196:99–146
- Mousavi S, Aifantis E (2016) Dislocation-based gradient elastic fracture mechanics for in-plane analysis of cracks. *International Journal of Fracture* 202:93–110
- Muskhelishvili N (1977) *Some Basic Problems of the Mathematical Theory of Elasticity*. Springer
- Musto M, Alfano G (2015) A fractional rate-dependent cohesive-zone model. *International Journal for Numerical Methods in Engineering* 103:313–341
- Nazarenko L, Stolarski H, Altenbach H (2019) A statistical interphase damage model of random particulate composites. *International Journal of Plasticity* 116:118–142
- Needleman A (1987) A continuum model for void nucleation by inclusion debonding. *Journal of Applied Mechanics* 54:525–531
- Nordmann J, Naumenko K, Altenbach H (2020) Cohesive zone models — theory, numerics and usage in high-temperature applications to describe cracking and delamination. In: Naumenko K, Krüger M (eds) *Advances in mechanics of high-temperature materials*, Springer Nature Switzerland AG, pp 131–168
- Peng Y, Zhao J, Sephrnoori K, Li Z, Xu F (2019) Study of delayed creep fracture initiation and propagation based on semi-analytical fractional model. *Applied Mathematical Modelling* 72:700–715
- Persson B, Brener E (2005) Crack propagation in viscoelastic solids. *Physical Review E* 71:036,123
- Savruk M, Madenci E, Shkarayev S (1999) Singular integral equations of the second kind with generalized cauchy-type kernels and variable coefficients. *International Journal for Numerical Methods in Engineering* 45:1457–1470

- Schapery R (1975) A theory of crack initiation and growth in viscoelastic media. *International Journal of Fracture* 11(1):141–159
- Selivanov M, Chornoivan Y (2018) A semi-analytical solution method for problems of cohesive fracture and some of its applications. *International Journal of Fracture* 212(1):113–121
- Selivanov M, Chornoivan Y, Kononchuk O (2018) Determination of crack opening displacement and critical load parameter within a cohesive zone model. *Continuum Mechanics and Thermo-dynamics* 31(2):569–586



Chapter 26

An Insight into Computational Challenges in Damage Mechanics: Analysis of a Softening Hooke's Spring

Salvatore Sessa, Emilio Barchiesi, Luca Placidi, Massimo Paradiso,
Emilio Turco, Nahiene Hamila

Abstract While many efforts are being currently spent to forge reliable damage laws based on the physics of the materials to be studied, damage modeling is still addressed numerically too naively in many situations. This article highlights some topical conceptual aspects that have been up to now dealt with too superficially by comparing the performances of different numerical algorithms in solving Karush–Kuhn–Tucker conditions for a simple linearly softening Hooke's spring. It is concluded that even such a primitive model, because of the multiplicity of solutions satisfying simultaneously equilibrium, damage law and irreversibility conditions, actually requires well-established numerical algorithms to face unexpected challenges. A comparison between different numerical strategies, beyond highlighting critical behaviors of traditional algorithms, permitted to observe an appealing robustness shown by an iterative strategy based on the fixed-point theorem. As a closure remark, evidences collected within this contribution naturally lead to the following question, which is left open for future studies: Is it possible to envisage the formulation of a criterion

S. Sessa, M. Paradiso

Department of Structures for Engineering and Architecture, University of Naples Federico II, via Claudio, 21, 80124, Naples, Italy
e-mail: salvatore.sessa2@unina.it, massimo.paradiso@unina.it

E. Barchiesi

Université de Bretagne Sud, Rue de Saint Maudé - BP 92116 56321, Lorient, Cedex, France
e-mail: emilio.barchiesi@enib.fr

L. Placidi

International Telematic University UNINETTUNO, Italy
e-mail: luca.placidi@uninettunouniversity.net

E. Turco

Department of Architecture, Design and Urban planning (DADU), University of Sassari, Italy
e-mail: emilio.turco@uniss.it

N. Hamila

École Nationale d'Ingénieurs de Brest, France
e-mail: nahiene.hamila@enib.fr

– possibly an energetic one, like that distinguishing stable and unstable solutions in elasticity – to establish which solution should be considered as valid in a given situation?

Keywords: Damage mechanics · Karush–Kuhn–Tucker conditions · Irreversibility

26.1 Introduction

Despite modeling of damage represents one of the most investigated topics of continuum mechanics (Auffray et al, 2015; Cazzani et al, 2017; Cuomo et al, 2014; dell’Isola et al, 2015, 2012), it still represents an open problem characterized by unsolved issues. Moreover, its importance fostered the development of different approaches depending on the fact that the significance of micro-scale mechanisms in influencing macro-scale material behaviors is nowadays largely recognized in the context of mechanics (dell’Isola et al, 2019a,b; Eremeyev et al, 2018; Grazioso et al, 2021).

The seminal ideas at the base of such a scientific paradigm can be traced back to the early developments of continuum mechanics (dell’Isola et al, 2017; Eugster and dell’Isola, 2017a,b, 2018). To incorporate structural information into models for predicting material behaviours, many approaches applicable at different scales can be contemplated.

At the smallest scale, one can conceive atomistic models which investigate material behaviours by considering atomic interactions (Ching et al, 2010; Dharmawardhana et al, 2013, 2016; Poudel et al, 2017). These models are practically infeasible at scales larger than a few hundred atoms for complex material systems. Moreover, their difficulty is not only confined to their high computational cost but, more importantly, it is due to the difficulty of specifying the atomic structures of the myriad of material phases and interphases, including also their defects. As a matter of fact, for such models, classic mechanics may be not feasible while quantum mechanics should be considered.

Alternative approaches introduce large scale formulation of such constitutive behavior. Within such approaches, coarse graining ideas have been prevalent and widely applied. Indeed, several coarse grained methods of incorporating micro-scale effects can be conceived, such as molecular models (Misra and Poorsolhjouy, 2017, 2020) and bead-spring models (dell’Isola et al, 2020; Turco, 2020; Turco and Barchiesi, 2019; Turco et al, 2020, 2016, 2019).

Challenges encountered in using these models include defining particles, their shapes and sizes, their contacts and interaction relationships, the evolution of their contacts during loading, surface properties and their change during loading, and many more which are extremely difficult to define experimentally. For this reason, the description of coarse graining materials is often provided by means of phenomenological models (Gibson et al, 1989; Triantafillou et al, 1989) addressing continuous homogeneous mediums (Serpieri et al, 2018; Sessa et al, 2019a, 2017).

Damage phenomena in materials take place through a wide range of mechanisms (Spagnuolo et al, 2017) which are generally complex and interactions between micro-constituents at different intervening scales should be considered for their understanding. In the past twenty years, several modelling strategies, including plasticity-based (Valoroso and Rosati, 2009a,b), probabilistic (Sessa et al, 2019b), phenomenological (Formica et al, 2021; Losanno et al, 2020, 2021) and algebraic approaches (Vaiana et al, 2017, 2018, 2019, 2021c,b,a), have been developed to simulate damage and failure processes, and more in general nonlinear behaviors, in materials.

Among these strategies, the continuum damage mechanics approach (Placidi et al, 2018a, 2020a, 2019) is particularly attractive because it provides a computationally and experimentally viable framework for the description of distributed damage, including material stiffness degradation, initiation, growth and coalescence of microcracks and voids. Various continuum damage models for brittle, quasi-brittle (Valoroso and Stolz, 2020) and ductile materials (Valoroso and Fedele, 2010) have been proposed in the literature (Barchiesi et al, 2021b; Dittmann et al, 2018; Placidi and Barchiesi, 2018). They can roughly classified into micro-mechanical (Ju, 1991) and macro-mechanical (Barchiesi et al, 2021a; Boutin et al, 2017; Giorgio et al, 2017) approaches.

In the macro-mechanical damage approach, a material is idealized as a homogeneous medium and damage is introduced via an internal variable whose tensorial nature depends on assumptions about crack/damage orientation induced by the micro-structure (Ju, 1990; Wu et al, 2020). The micro-mechanical damage approach, on the other hand, treats each micro-constituent as a statistically homogeneous medium. Local damage variables are defined to represent the state of damage in each micro-constituent and the overall response is subsequently obtained by homogenization (Barchiesi et al, 2020a,b; dell’Isola et al, 2016; Placidi et al, 2020b; Rahali et al, 2015). Both approaches can be viewed as the result of a two-step procedure. The main difference between the two approaches lies in the fact that in the macro-mechanical approach, homogenization is performed first and then is followed by the application of damage mechanics principles to the homogeneous medium, while in the micro-mechanical approach damage mechanics is applied to each micro-constituent followed by homogenization.

A pivotal aspect concerning most of the damage models is related to the existence and uniqueness of the solution of the mechanical problem. Such an issue has been widely investigated for plasticity and large-displacement problems while applications to damage still present unsolved questions.

In particular, both non-existence and the presence of multiple solutions may be related both to numerical or analytical issues of the mathematical model, as well as to the physical behavior of the material. The latter case is rather significant since it involves possible bifurcations of the equilibrium path of the material.

This article takes its steps from the numerical pitfalls experienced by the authors in addressing large discrete systems, i.e. models made of a large number of elements, exploiting the multi-level micro-mechanical approach to continuum damage mechanics presented in Timofeev et al (2020).

Rather surprisingly, in scoping the specialized literature on the topic, neither specific examples related to damage models nor a detailed assessment of the numerical properties of iterative strategies used in nonlinear analysis applied to damage modelling could be found if not vague statements, yet well-known, on the possibility that such methods cannot discriminate between two or more competing solutions.

For this reason we have decided to pinpoint a simple softening Hooke's spring in order to a-priori exclude phenomena related to the collective interaction of particles at microscale, complex loading conditions and more realistic damage laws as to investigate in depth the actual numerical properties of celebrated numerical procedures that, as a matter of fact, still present some obscure aspect that we hope to clarify.

The study is organized as follows. The mechanical formulation is introduced in Section 26.2 by means of a variational inequality and then specialized to the case under study. Analytical solutions are then derived in Section 26.3 for monotonous load and displacement control conditions. Subsequently, in Section 26.4, three different classes of explicit and implicit algorithms, based on displacement, force, and arc-length control, respectively, are introduced and adapted to the case under study. In Section 26.5, numerical results are presented allowing their performances in recovering the structural response of the previously introduced model to be assessed. Finally, conclusions are discussed along with some outlooks.

26.2 Formulation of the Problem

We begin by considering a finite dimensional Lagrangian system, whose state is univocally described by the displacement $u \in \mathbb{R}$ and the damage $d \in [0, 1]$ – $d = 0$ is the undamaged state, while $d = 1$ corresponds to failure – namely the two fundamental kinematic quantities, which are both functions of the time $t \in [0, T]$, with $T \in \mathbb{R}^+$ being the time horizon

$$\begin{aligned} u &= u(t) \\ d &= d(t). \end{aligned} \tag{26.1}$$

In a variational framework, constitutive relationships, which determine the response of the system as the result of an external action, are encoded in terms of an energy functional $E = \mathcal{E}(u, d)$, which will be referred to as the *total energy*. As customarily done in the mechanics, let us henceforth assume that the following additive decomposition holds for such an energy functional

$$E = U + W - U^{ext}. \tag{26.2}$$

In other words, we require it to be expressed as the sum of the elastic $U = \mathcal{U}(u, d)$, dissipated $W = \mathcal{W}(d)$, and external $U^{ext} = \mathcal{L}(u)$ energies. Remark that the previous formula should be amended to deal with loading processes that do not meet the quasi-static assumption, as a non-negligible kinetic energy should be then consid-

ered, thus requiring to define a time-integral functional – customarily called *action functional* – in terms of the energy functionals. For the considered finite dimensional system, a motion is defined as a family of pairs made up by the displacement u and the associated damage d , i.e. $(u(t), d(t))$. To make the evolution problem well-posed, namely the problem of determining the dependence – be it numerically or analytically – of u and d upon the time t , initial data on damage should be given at $t = 0$, namely $d(t = 0) = d_0$.

Let us denote with $AM_t \subset \mathbb{R}$ and $AV_t \subset \mathbb{R}$, respectively, the set of kinematically admissible displacements and the linear space of kinematically admissible displacement variations at time t . The generic element of AV_t will be denoted with δu . To lighten the discussion, we omit to introduce analogous symbols for the damage variable. We only declare that admissible variations of the damage variable d will be denoted with δd . Remark that, because of a non-healing constraint on the damage variable, i.e. $d(t_2) \geq d(t_1)$ for $t_2 > t_1$, that makes the system irreversible without the need for any thermodynamic quantity such as temperature and entropy to be introduced – namely the formulation is purely mechanical – the quantity δd must be non-negative, i.e. $\delta d \in \mathbb{R}^+ \cup 0$. At the generic time instant t , the forward variation $\delta \mathcal{E}$ of the energy functional evaluated in (u, d) along the directions $(\delta u, \delta d)$ is defined as

$$\delta \mathcal{E}(u, d) = \lim_{|\delta u|, \delta d \rightarrow 0^+} \mathcal{E}(u + \delta u, d + \delta d) - \mathcal{E}(u, d). \quad (26.3)$$

The variational principle, modernly referred to as *maximum energy release rate principle* (Hill, 1948), which characterizes the motions $(u(t), d(t))$ of the finite-dimensional Lagrangian system, consists in the following inequality, that should be fulfilled for all $t \in [0, T]$

$$\dot{\mathcal{E}}(t) dt \leq \delta \mathcal{E}(u(t), d(t)) \quad (26.4)$$

for any admissible variation $\delta u \in AV_t$ and $\delta d \in \mathbb{R}^+$. The dot in Eq. (26.4) stands for the total time derivative.

Aiming at utilising numerical algorithms, it is convenient to introduce a discrete set of time instants spanning the whole time domain $[0, T]$. For the sake of simplicity, uniformly spaced time instants are chosen as

$$t_i = i\Delta t, \quad i \in [0; N], \quad (26.5)$$

where $\Delta t = T/N \in \mathbb{R}^+$ is the amplitude of the time step. We make use of the time discretization above to define the discrete forward increments of the displacement and damage variables at the generic i -th time instant

$$\begin{aligned} (\Delta u)(t_i) &= u(t_{i+1}) - u(t_i) \\ (\Delta d)(t_i) &= d(t_{i+1}) - d(t_i), \end{aligned} \quad (26.6)$$

which entail the following forward increment $\Delta E(t_i)$ of the energy functional $E = \mathcal{E}(u, d)$ at the generic i -th time instant

$$\begin{aligned}\Delta\mathcal{E}(t_i) &= \mathcal{E}(u(t_i) + \Delta u, d(t_i) + \Delta d) - \mathcal{E}(u(t_i), d(t_i)) = \\ &= \mathcal{E}(u(t_{i+1}), d(t_{i+1})) - \mathcal{E}(u(t_i), d(t_i)).\end{aligned}\quad (26.7)$$

We have now introduced all the ingredients needed to state the variational principle that characterizes the motions $(u(t), d(t))$ of the finite-dimensional Lagrangian system under study in time-discrete form. The following inequality should be fulfilled for all $i \in [1; N]$

$$\Delta\mathcal{E}(t_i) \leq \delta\mathcal{E}(u(t_i), d(t_i)) \quad (26.8)$$

for any admissible variation $\delta u \in AV_{t_i}$ and $\delta d \in \mathbb{R}^+$. Henceforth, for the sake of brevity, we shall use the notations $u_i = u(t_i)$ and $d_i = d(t_i)$.

26.2.1 Linearly Softening Hooke's Spring

Let us specialize the constitutive relationships encoded in terms of the energy functional $E = \mathcal{E}(u, d)$, see Eq. (26.2), to the most simple case that can be considered in damage mechanics, which is the linearly softening extensional Hooke's spring without pre-stress, namely a zero-dimensional mechanical element in space. Without any loss of generality, one end of the spring will be always considered to be fixed. We also introduce the external force $F = \hat{F}(t)$ that may be applied at the other end of the spring (free-boundary condition). Henceforth, for the sake of brevity, we shall use the notation $F_i = F(t_i)$.

We aim to define a constitutive model presenting a linear-elastic behavior in the undamaged state by means of a limited set of parameters. This can be done by adopting an elastic energy functional defined as:

$$U = \frac{1}{2}k_{el}(1-d)u^2 \quad (26.9)$$

where k_{el} is the stiffness at the undamaged state and d is the damage. Such an expression is conceptually similar to the classic formulation of the Clapeyron's theorem with the sole difference that the tangent stiffness linearly decreases with the damage.

The dissipated energy is defined by a similar functional:

$$W = \frac{1}{2}k_d d^2 + k_t d, \quad (26.10)$$

where k_d is the resistance to damage and k_t serves as a threshold for specifying the damage-yielding point.

External energy yields

$$U^{ext} = Fu, \quad (26.11)$$

so that, recalling Eq. (26.2), the energy functional becomes

$$E = (1/2)k_{el}(1-d)u^2 + (1/2)k_d d^2 + k_t d - Fu \quad (26.12)$$

while its variation $\delta\mathcal{E}$ and increment $\Delta\mathcal{E}$ respectively read as

$$\delta\mathcal{E} = [k_{el}(1-d)u - F]\delta u + [k_t + k_d d - (1/2)k_{el}u^2]\delta d \quad (26.13)$$

and

$$\dot{\mathcal{E}} = [k_{el}(1-d)u - F]\dot{u} + [k_t + k_d d - (1/2)k_{el}u^2]\dot{d}. \quad (26.14)$$

A first Euler–Lagrange equation can be obtained by choosing $(\delta u, \delta d) = (\dot{u} + v, \dot{d})$ and then $(\delta\dot{u}, \delta\dot{d}) = (\dot{u} - v, \dot{d})$, so that, for arbitrary v , exploiting the linearity of $\delta\mathcal{E}$ with respect to δu and δd , we obtain from Eq. (26.4) two inequalities implying the following relationship (Placidi et al, 2018b)

$$[k_{el}(1-d)u - F]\delta u = 0, \quad \forall \delta u \in AV_t, \quad (26.15)$$

which, when no displacement is applied at the non-fixed end of the spring (free-boundary condition, hence no restriction on u and, subsequently, on δu), implies

$$k_{el}(1-d)u = F \quad (26.16)$$

A second Euler–Lagrange equation can be obtained by choosing $(\delta u, \delta d) = (\dot{u}, 2\dot{d})$ and then $(\delta\dot{u}, \delta\dot{d}) = (\dot{u}, 0)$, so that, exploiting the linearity of $\delta\mathcal{E}$ with respect to δu and δd , we obtain from Eq. (26.4) two inequalities implying the following relationship (Placidi et al, 2018b)

$$[k_t + k_d d - (1/2)k_{el}u^2]\dot{d} = 0, \quad (26.17)$$

which is customarily referred to as *Karush–Kuhn–Tucker* condition.

26.3 Analytical Solutions

Clearly, the main reason which led us to study a simple linearly softening Hooke’s spring, is that analytical solutions are at hand. This is particularly beneficial to get an insight into the issue we aim at studying as, provided the non-triviality of the chosen example, unnecessary complexities are avoided allowing to emphasize only the salient points.

26.3.1 Displacement Control Solution

The response $\hat{F}(t)$ associated with a time-varying applied displacement $u(t)$, namely – by Castigliano’s first theorem – the force that one should apply on the non-fixed spring end to get such displacement, or equivalently the reaction force that the spring exerts on the external world, can be computed in closed form. We study a linear displacement control defined as

$$\hat{u}(t) = \alpha t, \quad (26.18)$$

where the parameter α is a real coefficient, namely the rate of the applied strain. In such a case, the first Euler-Lagrange equation (26.15) is automatically satisfied, because $\delta u = 0$, while the second one (26.17) has the following analytical solution

$$d(t) = \left(\frac{k_{el}\alpha^2 t^2}{2k_d} - \frac{k_t}{k_d} \right) H \left(\frac{k_{el}\alpha^2 t^2}{2k_d} - \frac{k_t}{k_d} \right), \quad (26.19)$$

where $H(x)$ is the Heaviside function

$$H(x) = \begin{cases} 1 & x \geq 0 \\ 0 & x < 0. \end{cases} \quad (26.20)$$

Remark that the irreversibility condition $\dot{d} \geq 0$ has been already taken into account in (26.19) and (26.20). Hence, the force corresponding to the displacement control (26.18) is computed by Eqs. (26.16) and (26.19) as

$$F = \hat{F}(t) = k_{el}(1-d)u = k_{el}\alpha t + \left(\frac{k_t k_{el}}{k_d} \alpha t - \frac{k_{el}^2 \alpha^3 t^3}{2k_d} \right) H \left(-\frac{k_t}{k_d} + \frac{k_{el}\alpha^2 t^2}{2k_d} \right), \quad (26.21)$$

which can be expressed by two different continuous solutions depending on the argument of the Heaviside function. Specifically, the response turns out to be

$$\hat{F}(t) = \begin{cases} k_{el}\alpha t & \text{for } t \leq t_{yp} \\ k_{el}\alpha t + \frac{k_t k_{el}}{k_d} \alpha t - \frac{k_{el}^2 \alpha^3 t^3}{2k_d} & \text{for } t > t_{yp} \end{cases} \quad (26.22)$$

where

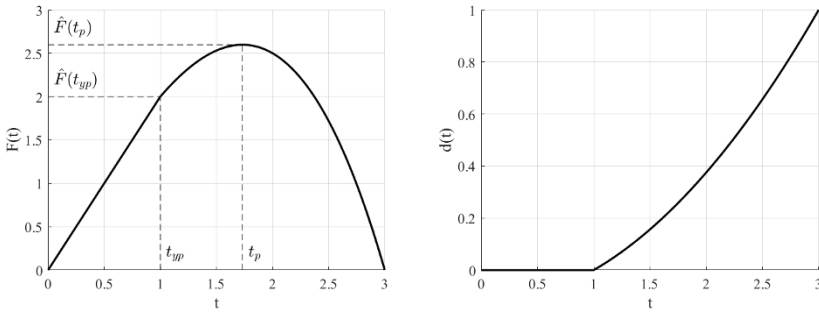
$$t_{yp} = \frac{1}{\alpha} \sqrt{\frac{2k_t}{k_{el}}}. \quad (26.23)$$

It is worth being emphasized that the condition $t \leq t_{yp}$ holds when the condition

$$-\frac{k_t}{k_d} + \frac{k_{el}\alpha^2 t^2}{2k_d} < 0 \quad (26.24)$$

is satisfied; in such a case, the Heaviside function in Eq. (26.21) attains a null value and the response turns out to be linear elastic. On the other hand, for $t > t_{yp}$, because of the onset of softening, the response is cubic with respect to the time variable.

The time instant t_{yp} represents the time yielding point of the spring and determines the transition between undamaged and damaged states of the spring. Plots of the analytically computed reaction force and damage as functions of time are reported, respectively, in Figs. 26.1a and 26.1b, where the parameters' values $k_t = 1$, $k_d = 8$, $k_{el} = 2$, and $\alpha = 1$ have been considered. As mentioned above, Fig. 26.1a shows that, as time increases, following the purely elastic phase, onset of damage occurs and the spring softens. Subsequently, the reaction force reaches a stationary maximum



(a) Reaction force vs. time (b) Damage vs. time

Fig. 26.1 Plots of the analytically computed reaction force and damage as functions of time for a linearly softening extensional Hooke’s spring subjected to linear displacement control.

value and then decreases until failure. The response and displacement at the time yielding point are, respectively,

$$\hat{F}(t_{yp}) = k_{el}\alpha t_{yp} = \sqrt{2k_{el}k_t}, \quad u(t_{yp}) = \sqrt{\frac{2k_t}{k_{el}}}. \tag{26.25}$$

The complete failure of the spring occurs when the damage variable attains the value $d = 1$ and, from Eq. (26.19), it is determined by the condition

$$-\frac{k_t}{k_d} + \frac{k_{el}\alpha^2 t^2}{2k_d} = 1, \tag{26.26}$$

which is met when the time

$$t_c = \frac{1}{\alpha} \sqrt{\frac{2k_t}{k_{el}} \left(1 + \frac{k_d}{k_t}\right)}$$

is reached. The peak of the reaction force F_p , attained at $t = t_p$, can be computed by enforcing the stationarity condition, in terms of vanishing first derivative, on the reaction force (26.21). In formulas, such a stationarity condition reads as

$$k_{el}\alpha + \frac{k_t k_{el}}{k_d} \alpha - 3 \frac{k_{el}^2 \alpha^3 t^2}{2k_d} = 0,$$

which is fulfilled for

$$t_p = \frac{1}{\alpha} \sqrt{\frac{2}{3} \left(\frac{k_d + k_t}{k_{el}}\right)}. \tag{26.27}$$

The peak force thus reads

$$\hat{F}(t_p) = k_{el} \frac{2}{3} \left(\frac{k_d + k_t}{k_d} \right) \sqrt{\frac{2}{3} \left(\frac{k_d + k_t}{k_{el}} \right)}. \quad (26.28)$$

An essential aspect concerning the derived solution consists in the fact that, as long as a displacement control is applied, the model has a unique solution. This is because the damage due to a monotonic displacement law is univocally determined, see Eq. (26.19).

26.3.2 Force Control Solution

Let us now apply an external force $F = \hat{F}(t)$, rather than a displacement, on the non-fixed spring end. We anticipate that, in such a case, the solution lacks of uniqueness. We study a linear force control defined as

$$\hat{F}(t) = \beta t, \quad (26.29)$$

where the parameter β is a real coefficient, namely the rate of the applied stress. Displacement and damage are given by Eqs. (26.16) and (26.17), that specialize to

$$\begin{cases} k_{el} (1 - d) u = \beta t \\ [k_t + k_d d - \frac{1}{2} k_{el} u^2] \dot{d} = 0. \end{cases} \quad (26.30)$$

Thus, damage can be analytically retrieved as

$$d = H \left(\frac{1}{2} \frac{k_{el}}{k_d} u^2 - \frac{k_t}{k_d} \right) \left(\frac{1}{2} \frac{k_{el}}{k_d} u^2 - \frac{k_t}{k_d} \right) \quad (26.31)$$

or, equivalently, as

$$d = \begin{cases} 0 & u^2 < \frac{2k_t}{k_{el}} \\ -\frac{k_t}{k_d} + \frac{1}{2} \frac{k_{el}}{k_d} u^2 & u^2 \geq \frac{2k_t}{k_{el}}, \end{cases} \quad (26.32)$$

thus indicating that the yielding condition reads as

$$u^2 < \frac{2k_t}{k_{el}}. \quad (26.33)$$

Therefore, before that the yielding condition is reached, the displacement linearly depends upon time.

$$u(t) = \frac{\beta}{k_{el}} t \quad (26.34)$$

while, after that, it is given by the solution of the cubic equation

$$k_{el} \left(1 + \frac{k_t}{k_d} - \frac{1}{2} \frac{k_{el}}{k_d} u^2 \right) u = \beta t, \quad (26.35)$$

that is derived by the insertion of (26.32)₂ in (26.30)₂. Such an equation presents three solutions in the complex plane, namely

$$\begin{aligned}
 u_1 &= \frac{2\sqrt[3]{3k_{el}}(k_d + k_t) + x^2}{(3k_{el})^{2/3}x} \\
 u_2 &= \frac{-2(3i + \sqrt{3})\sqrt[3]{k_{el}}(k_d + k_t) + i\sqrt[6]{3}(i + \sqrt{3})x^2}{2 \cdot 3^{5/6}(k_{el})^{2/3}x} \\
 u_3 &= \frac{-2(-3i + \sqrt{3})\sqrt[3]{k_{el}}(k_d + k_t) + \sqrt[6]{3}(-1 - i\sqrt{3})x^2}{2 \cdot 3^{5/6}(k_{el})^{2/3}x},
 \end{aligned} \tag{26.36}$$

where

$$x = \hat{x}(t) = \sqrt[3]{-9k_d\hat{F}(t)} + \sqrt{-24k_{el}(k_d + k_t)^3 + 81k_d^2[\hat{F}(t)]^2}. \tag{26.37}$$

The real and imaginary parts of these three solutions, computed with $\alpha = 1, k_{el} = 1$,

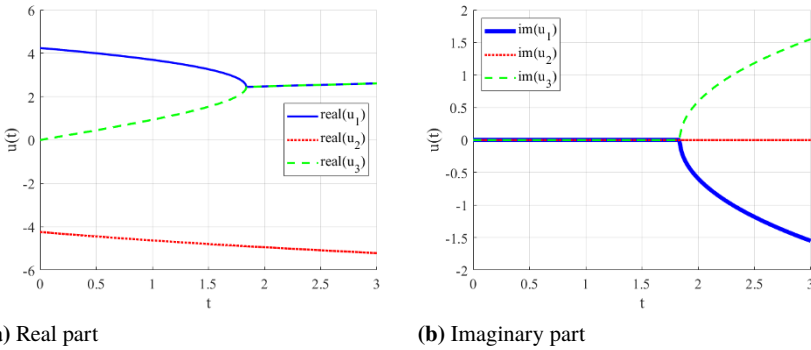


Fig. 26.2 Plots of the analytically computed displacement as function of time for a linearly softening extensional Hooke's spring subjected to linear force control.

$k_t = 1$ and $k_d = 8$, are plotted in Figs. 26.2a and 26.2b, respectively. Among these solutions, u_3 represents the correct load-control analytical solution as long as its imaginary part remains zero. In fact, u_2 is not physically meaningful since it is associated with a negative virtual work.

On the contrary, although not consistent with the load path of Eq. (26.29), u_1 represents a solution associated with the softening branch which the material can activate after that the peak force has been attained. Specifically, denoting by t_{yp} the time yielding point (attained at $t = \sqrt{2}$ in Fig. 26.2), for each load state in which $t < t_{yp}$, the force βt is associated with two possible displacement values, one on the loading curve and belonging to u_3 and a further one on the softening branch, and belonging to u_1 .

Obviously, the latter solution is purely numerical because of the initial conditions of the load path, belonging to u_3 .

In order to compute t_{yp} , we plug the selected displacement solution in the yielding condition (26.33) allows to retrieve

$$t_{yp} = \frac{1}{\beta} \sqrt{2k_{el}k_t}. \quad (26.38)$$

The displacement and force at the time yielding point can thus be computed as

$$u(t_{yp}) = \sqrt{\frac{2k_t}{k_{el}}}, \quad \hat{F}(t_{yp}) = \sqrt{2k_{el}k_t}, \quad (26.39)$$

which are the same calculated in Eq. (26.25). The motion obtained by the force control (26.29) is such that the damage variable cannot reach the unitary maximum value, because the strain rate reaches an infinite value before complete failure. This is clear by looking at the analytically computed damage and displacement plotted as functions of time, respectively, in Figs. 26.3a and 26.3b, where the parameters' values $k_t = 1$, $k_d = 8$, $k_{el} = 2$, and $\alpha = 1$ have been considered. We remark that this issue can be overcome by considering a non-negligible kinetic energy.

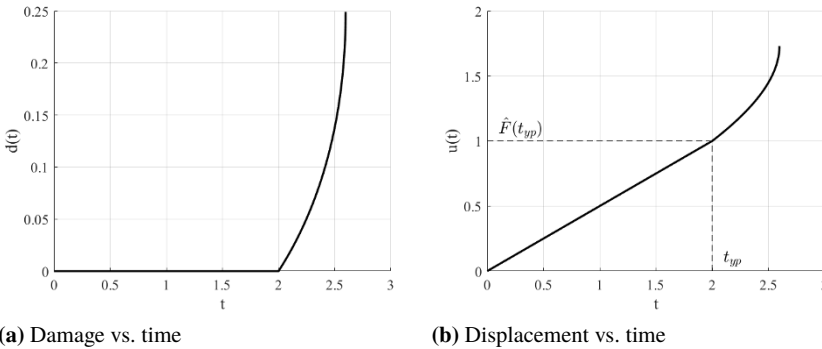


Fig. 26.3 Plots of the analytically computed damage and displacement as functions of time for a linearly softening extensional Hooke's spring subjected to linear force control.

26.4 Numerical Integration Algorithms

Within the context of computational analysis, the determination of the structural response predicted by a given model is usually performed by integration algorithms. In general, such procedures are formulated according to different philosophies (Cr-

isfield, 2001) which can be grouped in three main classes. The first class consists of displacement control strategies, which, conceptually, are equivalent to the solution reported in Subsection 26.3.1. They are all based on prescribing the evolution of a subset of nodal displacements and the subsequent determination of the corresponding external force. Displacement control strategies are used both in dynamic analyses, where the displacement is governed by a differential equation of motion, and static ones. A second approach consists in the load-control technique, analogous to the force-control solution reported in Subsection 26.3.2, which determines the displacement corresponding to a prescribed external force. The third class includes approaches, such as the arc-length, where we do not prescribe neither displacement alone nor external force alone, but adopt conditions involving both variables. It is worth to mention that a possible classification consists also in distinguishing *explicit* strategies, i.e. strategies where the solution at a generic step $i + 1$ is computed in closed-form as a function of the solution at the time step i , and *implicit* strategies which, on the contrary, are such that each step requires in turn an additional iterative procedure.

Since existence and uniqueness of the solution of the considered problem, as we have previously seen, are not guaranteed, it is possible that numerical integration may lack of convergence and robustness. The following subsections investigate the performance of the most popular strategies used in common practice.

26.4.1 Displacement Control Integration

The damage variable at step $i + 1$ can be computed by Eq. (26.17) as

$$d_{i+1} = \begin{cases} -\frac{k_t}{k_d} + \frac{k_{el}u_{i+1}}{2k_d} & \text{for } -\frac{k_t}{k_d} + \frac{k_{el}u_{i+1}}{2k_d} > d_i \\ d_i & \text{otherwise,} \end{cases} \quad (26.40)$$

so that the external force can be computed by Eq. (26.16) as

$$F_{i+1} = \begin{cases} k_{el}(1 - d_{i+1})u_{i+1} & \text{for } d_{i+1} < 1 \\ 0 & \text{for } d_{i+1} \geq 1, \end{cases} \quad (26.41)$$

where the second equation (26.41)₂ represents failure since the damage reached its maximum admissible value $d = 1$. Equations (26.40) and (26.41) can be computed in succession for $i = 1, \dots, N$ in order to determine the complete solution. In this sense, the displacement control procedure is an explicit strategy capable of determining the exact solution of the considered problem.

26.4.2 Load Control Integration

Load control strategies are based on the definition of an arbitrary path of the external force assigned to the model. Differently from the case of the displacement control strategy, within a load control context, if the equilibrium state (u_i, F_i) and its corresponding damage d_i at the generic step i are known, the determination of the solution associated with an arbitrary value F_{i+1} of the external force is not straightforward. In fact, in such a case, the value F_{i+1} is fixed, while u_{i+1} needs to be determined so that its relationship with d_{i+1} is satisfied. This implies that, once fixed the force F_{i+1} , the displacement u_{i+1} is a solution of the cubic equation (26.35). As shown in Subsection 26.3.2, in such a case, the solution is not unique in the complex space and its existence in the real space is not even guaranteed.

In order to determine the load control solution, it is necessary to adopt appropriate algorithms to address the non-linear relationship between external force, damage and displacement at each step of the analysis.

26.4.2.1 Explicit Algorithm

One of the most intuitive strategies consists in computing at time step $i + 1$ the linear solution associated with the values of damage and stiffness computed at the previous time step. Specifically, given the triple (F_i, u_i, d_i) at step i and the external force F_{i+1} , the displacement u_{i+1} is computed by a simplification of Eq. (26.16) as

$$u_{i+1} = \frac{F_{i+1}}{k_{el}(1 - d_i)}, \quad (26.42)$$

being $k_{el}(1 - d_i)$ the tangent stiffness at the previous step i , and the damage d_{i+1} is computed:

$$d_{i+1} = \begin{cases} -\frac{k_t}{k_d} + \frac{k_{el}u_{i+1}^2}{2k_d} & \text{for } -\frac{k_t}{k_d} + \frac{k_{el}u_{i+1}}{2k_d} > d_i \\ d_i & \text{otherwise.} \end{cases} \quad (26.43)$$

Such a procedure is actually an explicit strategy. It is worth being emphasized that, analogously to similar algorithms such as the *central difference method* in dynamics (Chopra, 2007), the accuracy of the explicit algorithm strongly depends on the time discretization of the load control algorithm. The smaller the time step is adopted, the more accurate will the solution be. Moreover, since the displacement in Eq. (26.42) is computed by adopting stiffness and damage of a different time step, such explicit approach may provide numerical solutions even for those states for which no theoretical solution exists.

26.4.2.2 Newton–Raphson Algorithm

One of the most popular implicit strategies to assess quantitatively the non-linear behaviour of a system is the Newton–Raphson algorithm. It consists of an iterative procedure aiming to determine, for a given time step i , a sequence of trials $u_{i+1,j}$, where $j \in \mathbb{N}$ is the iteration index, so that the following residual

$$R_{i+1,j} = \frac{u_{i+1,j}k_{el}(1 - d_{i+1,j}) - F_{i+1}}{F_{i+1}} \quad (26.44)$$

with

$$d_{i+1,j} = \max \left\{ d_i, \frac{k_{el}u_{i+1,j}^2}{2k_d} - \frac{k_t}{k_d} \right\}. \quad (26.45)$$

tends to zero for increasing values of the iteration index j . The recurrence function is obtained by linearisation of the residual function. To fix ideas, let us consider Fig. 26.4, where a generic residual function, represented by the black curve, is plotted with respect to the displacement. The point at u^* represents the target solution since it corresponds to the zero of the residual function and the point with coordinates $(u_{i+1,j}, R_{i+1,j})$ is the equilibrium state relevant to the j -th iteration of the algorithm. The subsequent trial displacement $u_{i+1,j+1}$ is estimated by a linear approximation of the residual function. Specifically, we have

$$u_{i+1,j+1} = u_{i+1,j} + \Delta u_j \quad (26.46)$$

where the trial increment Δu_j is computed by

$$\Delta u_j = - \frac{R_{i+1,j}}{\tan(\theta_j)}. \quad (26.47)$$

Recalling that the tangent of θ_j is the first derivative of the residual with respect to the displacement, the Newton–Raphson recurrence function turns out to be

$$u_{i+1,j+1} = u_{i+1,j} - \left(\frac{dR_{i+1,j}}{du_{i+1,j}} \right)^{-1} R_{i+1,j} \quad (26.48)$$

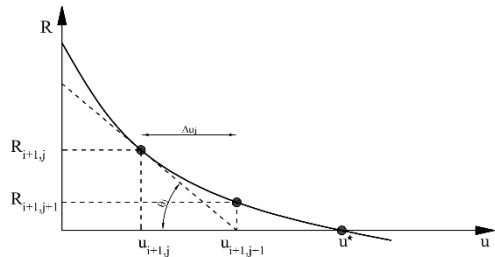


Fig. 26.4 Recurrence scheme of the Newton–Raphson algorithm.

For the case of the elastic damage spring defined in Section 26.2, the residual derivative is computed as

$$\frac{dR_{i+1,j}}{du_{i+1,j}} = \frac{k_{el}(1-d_{i+1,j})}{F_{i+1}} - \frac{u_{i+1,j}k_{el}}{F_{i+1}} \frac{d}{du_{i+1,j}}(d_{i+1,j}) \quad (26.49)$$

where the latter term is the derivative of the damage with respect to the displacement

$$\frac{d}{du_{i+1,j}}(d_{i+1,j}) = \begin{cases} 0 & \text{for } d_{i+1,j} - d_i = 0 \\ \frac{k_{el}u_{i+1,j}}{k_d} & \text{for } d_{i+1,j} - d_i > 0 \end{cases} \quad (26.50)$$

Initial trial values with $j = 0$ of the involved variables $u_{i+1,0}$ and $d_{i+1,0}$ for the time step $i + 1$ are assumed to be equal to the convergence values determined at the previous time step i :

$$j = 0; \quad u_{i+1,0} = u_i; \quad d_{i+1,0} = d_i, \quad (26.51)$$

so that the initial trial values with $j = 0$ of the residual and of its derivative are:

$$R_{i+1,0} = \frac{F_i - F_{i-1}}{F_{i-1}}, \quad \nabla R_{i,0} = \nabla R_{i-1}. \quad (26.52)$$

The computation of the points of the sequence is stopped when the residual becomes smaller than a fixed tolerance: $|R_{i+1,j}| \leq \delta$. Hence, the accuracy of the algorithm can be directly controlled. The Newton–Raphson algorithm is one of the fastest iterative strategies to determine the zeros of nonlinear functions and can be generalized for multi-dimensional problems. In such a case, the variables are defined in vectorial spaces and the derivative is replaced by the gradient – or Jacobian matrix – of the residual vector with respect to the displacement vector.

Despite of its fast convergence, the Newton–Raphson algorithm presents some drawbacks. A first one concerns the value of the tolerance δ : it influences the number of iterations required to reach accurate enough solutions, and even the chance that the algorithm may fail in finding a solution or it may converge on incorrect ones. A further aspect concerns the dependency of the trials on the residual gradient. As a first consideration, if the gradient is null, then the algorithm may not converge since it cannot update the trials. As a further consideration, if such a procedure is applied to multi-dimensional problems, the determination of the gradient can be very complex.

26.4.2.3 Fixed-Point Iterative Method

To overcome the drawbacks of the Newton–Raphson algorithm, alternative strategies are available in the literature most of them based on the fixed-point theorem (Reed and Simon, 1980). A possible implementation of an iterative strategy belonging to the fixed-point class is based on the recurrence relationship

$$u_{i+1,j+1} = g(u_{i+1,j}) = \frac{F_{i+1}}{k_{el}(1 - d_{i+1,j})} \quad (26.53)$$

where the trial displacement at iteration $j + 1$ is computed as a function of the current force F_{i+1} and of the damage $d_{i+1,j}$ computed at the previous trial iteration j . The latter quantity is

$$d_{i+1,j} = \max \left\{ d_i, \frac{k_{el}u_{i+1,j}^2}{2k_d} - \frac{k_t}{k_d} \right\}. \quad (26.54)$$

The strategy adopts as initial conditions the displacement and damage values relevant to the last converged state at time step i

$$j = 0; \quad u_{i+1,0} = u_i; \quad d_{i+1,0} = d_i \quad (26.55)$$

while the stopping criterion consists in checking that the norm of a residual $R_{i+1,j+1}$ is smaller than a suitable tolerance δ . Hence, as for the case of the Newton–Raphson algorithm, the accuracy of the iterative procedure can be set by the analyst. Within the scopes of this research, two different residuals are investigated. Both are expressed as relative increment between two subsequent iterations; the first residual $R_{i+1,j+1}^d$ determines the variation of the damage while the second residual $R_{i+1,j+1}^e$ computes the energy increment

$$R_{i+1,j+1}^d = \frac{d_{i+1,j+1} - d_{i+1,j}}{d_{i+1,j}} \quad (26.56)$$

$$R_{i+1,j+1}^e = \frac{[1 - d_{i+1,j+1}]u_{i+1,j+1}^2 - [1 - d_{i+1,j}]u_{i+1,j}^2}{[1 - d_{i+1,j}]u_{i+1,j}^2}. \quad (26.57)$$

An essential property of the iterative procedures based on the fixed-point theorem consists in the fact that the procedure has a sufficient condition for the convergence of the trial sequence. It is expressed by means of the derivative of function $g(u_i)$ of Eq. (26.53) and turns out to be

$$\left| \frac{dg(u_{i+1,j})}{du_{i+1,j}} \right| \leq 1 \quad (26.58)$$

which, accounting for Eqs. (26.53) and (26.54), becomes

$$\frac{dg(u_i)}{du_i} = \begin{cases} 0 & \text{for } d_{i,j} - d_{i-1} = 0 \\ \frac{F_i u_i}{k_d \left[\frac{k_t}{k_d} - \frac{k_{el} u_i^2}{2k_d} + 1 \right]^2} & \text{for } d_{i,j} - d_{i-1} > 0 \end{cases} \quad (26.59)$$

This issue represents a pivotal aspect of the robustness of iterative strategies. As it is discussed in details in Section 26.5, the Newton–Raphson algorithm, besides of its

fast convergence, often presents issues in determining the correct root. In this sense, a convergence condition permits to control the robustness of the fixed-point strategy.

26.4.3 Arc-Length Control Integration

In order to address non linear problems whose equilibrium path, i.e. load-displacement response, presents limit points, namely local maxima/minima, or snap-back/snap-through regions, integration strategies different from those presented previously are required since the algorithms introduced in the previous subsections are not capable of determining the correct solution. To fix ideas, let us consider the load-displacement curve represented in Figure 26.5. Once that the equilibrium state of point A has been reached, load control strategies are not capable of determining the states belonging to the descending branch; indeed, the response will present a snap-through to point A'. Analogously, a displacement control strategy is not capable of determining the backward branch after point B so that the response will present a snap-back to point B'. A very popular technique utilised to solve such issues is the Arc-length integration control proposed by Riks (1979) and extended by several researchers, including Crisfield (1981).

Referring to the original papers for its formulation, which is omitted for brevity, the arc-length control determines the increments Δu and ΔF of the displacement and of the external force, respectively, so that the normalized distance between two subsequent equilibrium states remains constant

$$\alpha \Delta u^2 + \beta \Delta F^2 = \alpha (u_{i+1} - u_i)^2 + \beta (F_{i+1} - F_i)^2 = \lambda^2. \quad (26.60)$$

In the latter relationship, α and β are scale coefficient introduced to ensure compatibility between the units of displacement and force and λ is the *arc length*. Such a strategy is capable of determining the correct sequence of equilibrium states even in presence of limit points, softening and backward branches. Nevertheless, it presents a serious drawback since the relationship between force and displacement increments depends on a quadratic condition and, thus, multiple roots may be obtained. In some cases, such an issue compromises the chance of determining the correct solution.

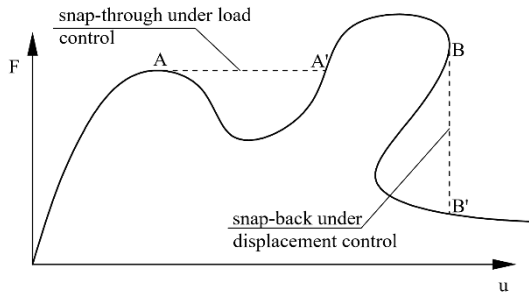
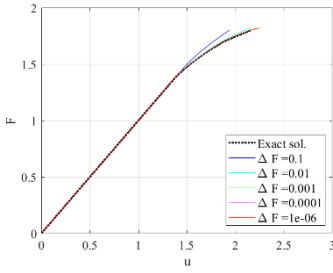
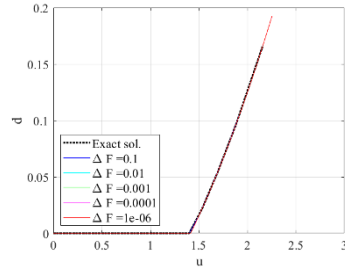


Fig. 26.5 Critical points of a load-displacement response in increasing displacement/load control.

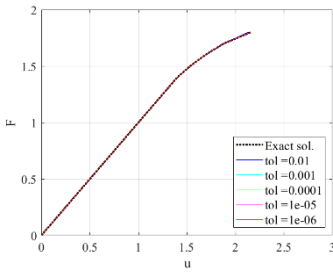


(a) Load vs. displacement

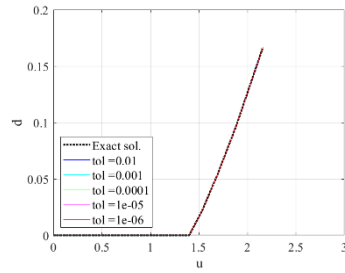


(b) Damage vs. displacement

Fig. 26.6 Explicit method, monotonic load.

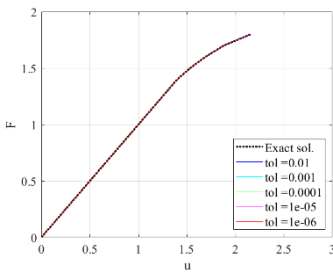


(a) Load vs. displacement

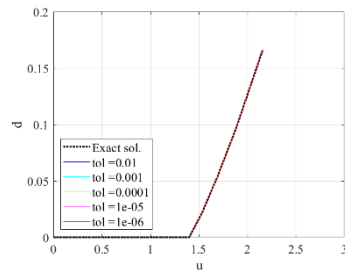


(b) Damage vs. displacement

Fig. 26.7 Newton-Raphson method, monotonic load, $\Delta F = 0.1$

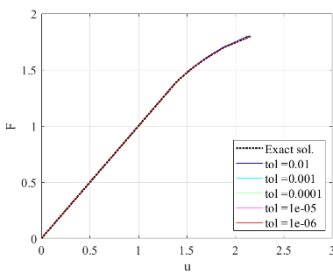


(a) Load vs. displacement

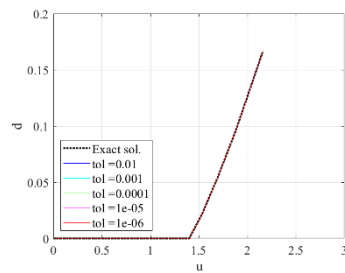


(b) Damage vs. displacement

Fig. 26.8 Fixed-point method (damage residual), monotonic load, $\Delta F = 0.1$



(a) Load vs. displacement



(b) Damage vs. displacement

Fig. 26.9 Fixed-point method (energy residual), monotonic load, $\Delta F = 0.1$

26.5 Numerical Results

The algorithms discussed in Section 26.4 have been implemented in MatLab®v. R2020b and are hereby compared in terms of robustness, speed and accuracy. While robustness is analysed by a qualitative point of view by checking if the algorithm presents convergence issues, the computational speed is determined by reporting, for each analysis, the number of the performed computations. This consists in the sum of all the trial computations eventually performed for each time step. Algorithmic accuracy is investigated by determining the error θ defined by means of (squared) mean-square of the relative error between the algorithmic response and the theoretical solution. For the case of force control integration, the error is

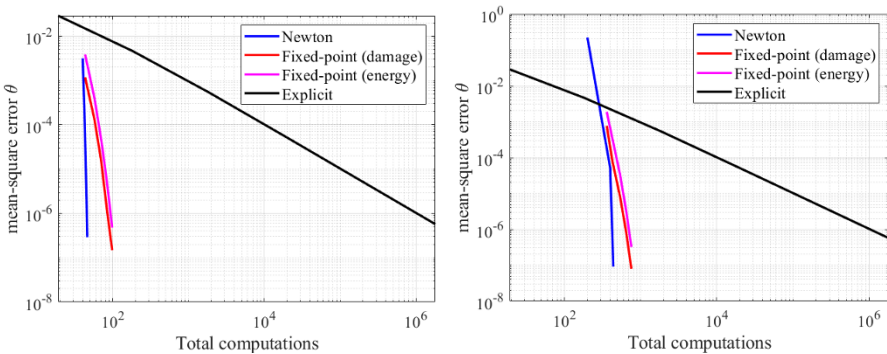
$$\theta^2 = \frac{1}{n} \sum_{i=1}^n \left[\frac{u_i - \hat{u}_i}{\hat{u}_i} \right]^2 \tag{26.61}$$

where u_i is the algorithmic displacement and \hat{u}_i is the exact solution, computed at time step i .

Numerical tests take into account a spring with $k_t = 1$, $k_d = 8$ and $k_{el} = 1$ and, according to (26.38), reaching yielding at

$$u(t_{yp}) = \sqrt{\frac{2k_t}{k_{el}}} = \sqrt{2}; \quad \hat{F}(t_{yp}) = k_{el}u(t_{yp}) = \sqrt{2}. \tag{26.62}$$

A first investigation concerns the load-control analysis with monotonically increasing external force until collapse. In general, all the approaches introduced in Subsection 26.4.2 provide sufficiently accurate results (see Figs. 26.6–26.9). The explicit algorithm, whose load-displacement response is reported in Figure 26.6, presents a



(a) Implicit schemes' force increment: $\Delta F = 0.1$.

(b) Implicit schemes' force increment: $\Delta F = 0.01$.

Fig. 26.10 Error θ , load-control integration, monotonic load.

significant drift as long as the force increment increases. The remaining strategies present responses which are almost indistinguishable by the exact solution. Figures 26.10a and 26.10b show the mean-square error θ vs. the overall number of computations performed by the load control strategies. Specifically, results of Fig. 26.10a have been computed by adopting a force increment $\Delta F = 0.1$ for the implicit algorithms, while Fig. 26.10b assumes $\Delta F = 0.01$. Obviously, the explicit strategy, where no iterations are necessary, adopts different force increments in order to improve accuracy. Such curves show that, in general, the Newton–Raphson algorithm is the one presenting the best compromise between computational burden and accuracy: fixed-point algorithms require a higher number of iterations in order to get the same errors, while accuracy of the explicit method is far worse. A further set of analyses concerns cyclic loads where the external force is monotonically increased with step $\Delta F = 0.1$ up to a maximum value of $F_{max} = 1.8 < F_m$, slightly smaller than its theoretical peak of Eq. (26.28). Then, the external force is monotonically reduced to zero.

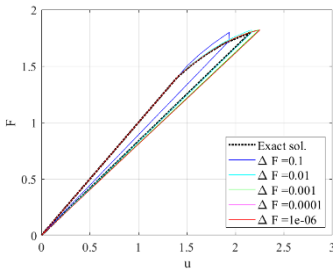
Figures 26.11 and 26.12 present the responses computed by the explicit strategy and the fixed-point algorithm, respectively. In both figures, the black-dotted curve represents the exact solution of the force–path problem discussed in Subsection 26.3.2: since the peak F_m has not been reached, then the response is linearly decreasing till the origin. As expected, responses computed by the explicit algorithm present a significant drift from the exact solution while the Fixed-point strategy provides accurate results. Both strategies do not present any convergence issue. Concerning the fixed-point algorithm, Fig. 26.14 reports the value of the derivative $dg(u_i)/du_i$, used in the convergence criterion of Eq. (26.59), vs. the displacement. Remarkably, such a derivative remains smaller than one during all the analysis, this meaning that convergence of the fixed-point algorithm is ensured.

In order to check the stability of the algorithms implemented in finite element codes, further analyses have been performed in OpenSees 3.0.3, an open source framework for finite element analysis released by the University of California, Berkeley McKenna (2011), in which the investigated damage model has been implemented. The modified release and the input file relevant to the shown example can be downloaded at Sessa (2021).

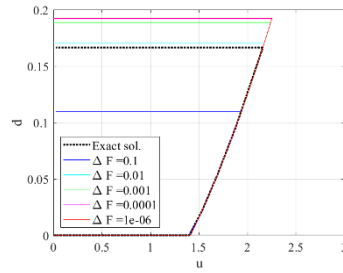
In particular, while the Newton–Raphson algorithm provides solutions similar to the fixed-point procedure discussed above, the test has been focused on the well known Arc-Length control.

In such a case, the presence of multiple solutions is a significant drawback affecting the results, as shown in Fig. 26.15. In particular, once considered a generic equilibrium state A, the arc-length algorithm tries to determine a point belonging to the equilibrium path lying at a prescribed distance (i.e. the arc-length) from point A.

After that yielding has been achieved, the system presents two possible equilibrium paths starting from point A so that both points B and B' are possible solutions. As a matter of fact, it is not possible to make any physical discrimination between them. Such a behaviour is confirmed by the analysis reported in Fig. 26.16, where the blue curve is the displacement control response and the red curve has been computed by the arc length control integrator.

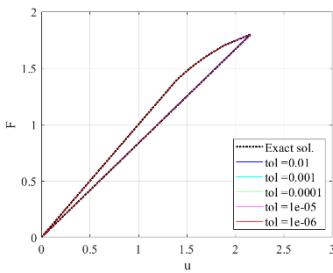


(a) Load vs. displacement

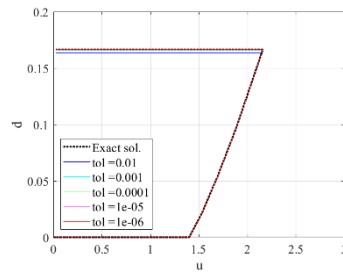


(b) Damage vs. displacement

Fig. 26.11 Explicit method, cyclic load.

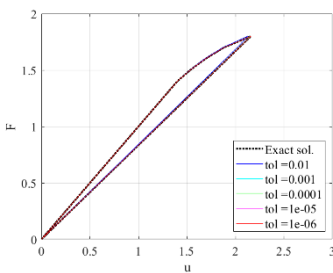


(a) Load vs. displacement

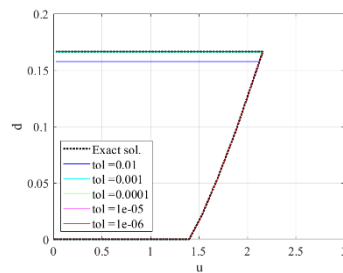


(b) Damage vs. displacement

Fig. 26.12 Fixed-point algorithm (damage residual), cyclic load, $\Delta F = 0.1$



(a) Load vs. displacement



(b) Damage vs. displacement

Fig. 26.13 Fixed-point algorithm (energy residual), cyclic load, $\Delta F = 0.1$

As a matter of fact, in such problems, arc-length control is expected to determine the softening branch (Crisfield, 2001) even in presence of snap-through or snap-back behaviors. On the contrary, as previously discussed in commenting Fig. 26.15, after the response reaches the peak force, the arc length procedure fails in determining the softening branch and converges to the unloading linear branch.

It is worth being emphasized that the states belonging to the arc length solution are all correct equilibrium states. Moreover, an essential aspect concerns the physical

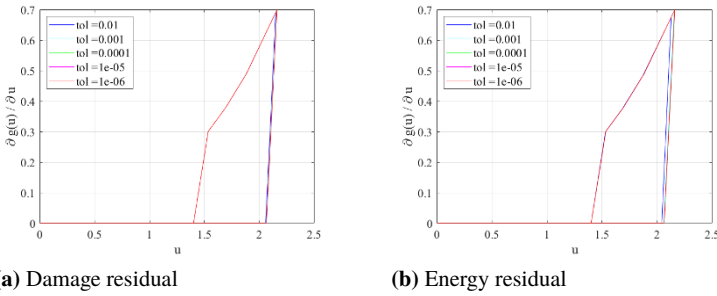


Fig. 26.14 Convergence criterion of the fixed-point algorithm.

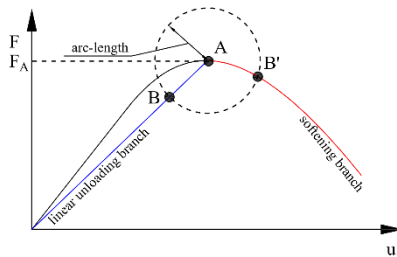


Fig. 26.15 Examples of unloading multiple solutions in Arc-length control.

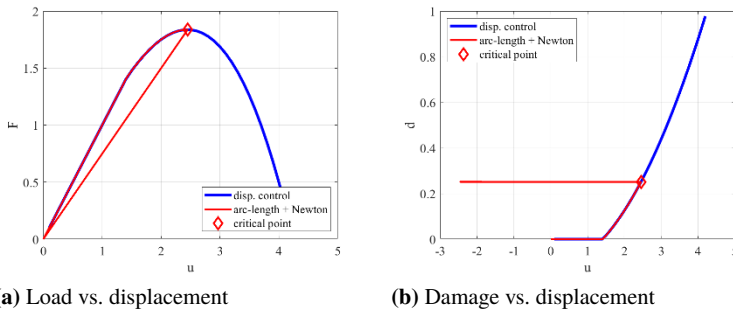


Fig. 26.16 Load-displacement response for a cyclic loading-unloading analysis via arc-length integration.

meaningfulness of the solution. In fact, considering the analysis reported in Fig. 26.16a, once that the algorithm reaches the peak force (i.e. the limit point), there are two possible equilibrium states fulfilling the prescribed arc length condition, belonging to the softening curve and to the unloading branch, respectively. The critical issue consists in the fact that both points are meaningful solutions and there is no reason for which one of them should be preferred. We emphasize that such a circumstance for which the problem presents multiple solutions occurs for all points

whose displacement is greater than the yielding value. For this reason, the arc length algorithm naturally may present several bifurcations.

26.6 Conclusions

In this contribution we investigated the performances of different algorithms in analyzing a simple uniaxial linearly damaging spring with quadratic dissipation energy.

Analyses have proved that, because of the multiplicity of solutions satisfying at once equilibrium, damage law and irreversibility conditions, well-established numerical algorithms may face unexpected pitfalls and failures even in studying simple damage problems. The reported evidence should stimulate future research dealing with the problem of discriminating – among physically meaningful (and meaningless, albeit this seems a more easy task) solutions – the one that is actually occurring experimentally in damaging systems.

Concerning load-control integration, among the considered algorithms, the fixed-point algorithm provided stable results confirmed by a convergence criterion. Hence, it could be preferential in using damage constitutive relationships in more complex applications such as coarse graining continuum (dell’Isola et al, 2020).

The non-uniqueness issue arised for the arc-length algorithm is well known for the case of some classic topics in structural analysis, such as buckling and bifurcation. In such cases, different solutions are discriminated by energetic criteria, hence, we conjecture that a kind of second order energy criterion – like that distinguishing stable and unstable solutions in elasticity – may serve to the scope. A variational formulation may thus provide a fertile ground to profitably explore the subject, which is the reason why, in this contribution, albeit for a very simple system, a variational inequality, known as the maximum energy release rate principle, has been used as a postulate. Moreover, a variational approach may ensure that the fulfillment of the thermodynamic principles in analyzing those materials for which the Karush–Kuhn–Tucker condition is not directly enforced (Sessa, 2022).

A further aspect worth of investigation concerns the determination of alternative equilibrium paths after bifurcation points. While computation of such paths was straightforward for the Hooke’s spring analyzed in this research, it may become very complex when the considered damage formulation models multi-dimensional systems such as continuum media. In such cases, alternative equilibrium paths may be substantially unknown.

Future research directions will investigate both aspects in order to exploit computational strategies for analyzing generalized finite element models.

Acknowledgements This project has received funding from the University of Naples Federico II and the *Compagnia di San Paolo*, FRA grants, CUP E69C21000250005, and from the European Union’s Horizon 2020 research and innovation programme under the Marie Skłodowska-Curie grant agreement No 899546. These contributions are gratefully acknowledged.

References

- Auffray N, dell'Isola F, Eremeyev VA, Madeo A, Rosi G (2015) Analytical continuum mechanics à la hamilton–piola least action principle for second gradient continua and capillary fluids. *Mathematics and Mechanics of Solids* 20(4):375–417
- Barchiesi E, dell'Isola F, Hild F, Seppecher P (2020a) Two-dimensional continua capable of large elastic extension in two independent directions: asymptotic homogenization, numerical simulations and experimental evidence. *Mechanics Research Communications* 103:103,466
- Barchiesi E, Eugster SR, dell'Isola F, Hild F (2020b) Large in-plane elastic deformations of bipantographic fabrics: asymptotic homogenization and experimental validation. *Mathematics and Mechanics of Solids* 25(3):739–767
- Barchiesi E, dell'Isola F, Hild F (2021a) On the validation of homogenized modeling for bipantographic metamaterials via digital image correlation. *International Journal of Solids and Structures* 208:49–62
- Barchiesi E, Yang H, Tran C, Placidi L, Müller WH (2021b) Computation of brittle fracture propagation in strain gradient materials by the FEniCS library. *Mathematics and Mechanics of Solids* 26(3):325–340
- Boutin C, Giorgio I, Placidi L, et al (2017) Linear pantographic sheets: asymptotic micro-macro models identification. *Mathematics and Mechanics of Complex Systems* 5(2):127–162
- Cazzani A, Rosati L, Ruge P (2017) The contribution of Gustav R. Kirchhoff to the dynamics of tapered beams. *ZAMM Zeitschrift für Angewandte Mathematik und Mechanik* 97(10):1174–1203
- Ching WY, Rulis P, Ouyang L, Aryal S, Misra A (2010) Theoretical study of the elasticity, mechanical behavior, electronic structure, interatomic bonding, and dielectric function of an intergranular glassy film model in prismatic β -Si₃N₄. *Physical Review B* 81(21):214,120
- Chopra AK (2007) *Dynamics of Structures*, 3rd edition. Pearson Prentice Hall, Upper Saddle River, NJ 07458, USA
- Crisfield M (1981) A fast incremental/iterative solution procedure that handles "snap-through". *Computers & Structures* 13(1):55–62
- Crisfield MA (2001) *Non-Linear Finite Element Analysis of Solids and Structures: Volume 1: Essentials*. John Wiley & Sons, Ltd., The Atrium, Southern Gate, Chichester, West Sussex PO19 8SQ, United Kingdom
- Cuomo M, Contrafatto L, Greco L (2014) A variational model based on isogeometric interpolation for the analysis of cracked bodies. *International Journal of Engineering Science* 80:173–188
- dell'Isola F, Seppecher P, Madeo A (2012) How contact interactions may depend on the shape of Cauchy cuts in Nth gradient continua: approach "à la D'Alembert". *Zeitschrift für angewandte Mathematik und Physik* 63(6):1119–1141
- dell'Isola F, Andreaus U, Placidi L (2015) At the origins and in the vanguard of peridynamics, non-local and higher-gradient continuum mechanics: an underestimated and still topical contribution of Gabrio Piola. *Mathematics and Mechanics of Solids* 20(8):887–928
- dell'Isola F, Giorgio I, Pawlikowski M, Rizzi NL (2016) Large deformations of planar extensible beams and pantographic lattices: heuristic homogenization, experimental and numerical examples of equilibrium. *Proceedings of the Royal Society A: Mathematical, Physical and Engineering Sciences* 472(2185):20150,790
- dell'Isola F, Corte AD, Giorgio I (2017) Higher-gradient continua: The legacy of Piola, Mindlin, Sedov and Toupin and some future research perspectives. *Mathematics and Mechanics of Solids* 22(4):852–872
- dell'Isola F, Seppecher P, Alibert JJ, Lekszycki T, Grygoruk R, Pawlikowski M, Steigmann D, Giorgio I, Andreaus U, Turco E, et al (2019a) Pantographic metamaterials: an example of mathematically driven design and of its technological challenges. *Continuum Mechanics and Thermodynamics* 31(4):851–884
- dell'Isola F, Seppecher P, Spagnuolo M, Barchiesi E, Hild F, Lekszycki T, Giorgio I, Placidi L, Andreaus U, Cuomo M, et al (2019b) *Advances in pantographic structures: design, manufac-*

- turing, models, experiments and image analyses. *Continuum Mechanics and Thermodynamics* 31(4):1231–1282
- dell'Isola F, Turco E, Barchiesi E (2020) Lagrangian discrete models: Applications to metamaterials. *Discrete and Continuum Models for Complex Metamaterials* p 197
- Dharmawardhana C, Misra A, Aryal S, Rulis P, Ching W (2013) Role of interatomic bonding in the mechanical anisotropy and interlayer cohesion of csh crystals. *Cement and Concrete Research* 52:123–130
- Dharmawardhana C, Bakare M, Misra A, Ching WY (2016) Nature of interatomic bonding in controlling the mechanical properties of calcium silicate hydrates. *Journal of the American Ceramic Society* 99(6):2120–2130
- Dittmann M, Aldakheel F, Schulte J, Wriggers P, Hesch C (2018) Variational phase-field formulation of non-linear ductile fracture. *Computer Methods in Applied Mechanics and Engineering* 342:71–94
- Eremeyev VA, dell'Isola F, Boutin C, Steigmann D (2018) Linear pantographic sheets: existence and uniqueness of weak solutions. *Journal of Elasticity* 132(2):175–196
- Eugster SR, dell'Isola F (2017a) Exegesis of the Introduction and Sect. I from "Fundamentals of the Mechanics of Continua" by e. hellinger. *ZAMM-Journal of Applied Mathematics and Mechanics/Zeitschrift für Angewandte Mathematik und Mechanik* 97(4):477–506
- Eugster SR, dell'Isola F (2017b) Exegesis of the Introduction and Sect. I from "Fundamentals of the Mechanics of Continua" by E. Hellinger. *ZAMM-Journal of Applied Mathematics and Mechanics/Zeitschrift für Angewandte Mathematik und Mechanik* 97(4):477–506
- Eugster SR, dell'Isola F (2018) Exegesis of Sect. II and III. A from "Fundamentals of the Mechanics of Continua" by E. Hellinger. *ZAMM-Journal of Applied Mathematics and Mechanics/Zeitschrift für Angewandte Mathematik und Mechanik* 98(1):31–68
- Formica G, Vaiana N, Rosati L, Lacarbonara W (2021) Pathfollowing of high-dimensional hysteretic systems under periodic forcing. *Nonlinear Dynamics* 103(4):3515–3528
- Gibson L, Ashby M, Zhang J, Triantafyllou T (1989) Failure surfaces for cellular materials under multiaxial loads-i.modelling. *International Journal of Mechanical Sciences* 31(9):635–663
- Giorgio I, Rizzi N, Turco E (2017) Continuum modelling of pantographic sheets for out-of-plane bifurcation and vibrational analysis. *Proceedings of the Royal Society A: Mathematical, Physical and Engineering Sciences* 473(2207):20170,636
- Grazioso S, Di Gironimo G, Rosati L, Siciliano B (2021) Modeling and simulation of hybrid soft robots using finite element methods: Brief overview and benefits. vol 15, pp 335–340
- Hill R (1948) A variational principle of maximum plastic work in classical plasticity. *The Quarterly Journal of Mechanics and Applied Mathematics* 1(1):18–28
- Ju J (1990) Isotropic and anisotropic damage variables in continuum damage mechanics. *Journal of Engineering Mechanics* 116(12):2764–2770
- Ju J (1991) On two-dimensional self-consistent micromechanical damage models for brittle solids. *International Journal of Solids and Structures* 27(2):227–258
- Losanno D, Madera Sierra I, Spizzuoco M, Marulanda J, Thomson P (2020) Experimental performance of unbonded polyester and carbon fiber reinforced elastomeric isolators under bidirectional seismic excitation. *Engineering Structures* 209
- Losanno D, Palumbo F, Calabrese A, Barrasso T, Vaiana N (2021) Preliminary investigation of aging effects on recycled rubber fiber reinforced bearings (RR-FRBs). *Journal of Earthquake Engineering*
- McKenna F (2011) OpenSees: A framework for earthquake engineering simulation. *Computing in Science and Engineering* 13(4):58–66
- Misra A, Poorsolhjoui P (2017) Grain-and macro-scale kinematics for granular micromechanics based small deformation micromorphic continuum model. *Mechanics Research Communications* 81:1–6
- Misra A, Poorsolhjoui P (2020) Granular micromechanics model for damage and plasticity of cementitious materials based upon thermomechanics. *Mathematics and Mechanics of Solids* 25(10):1778–1803

- Placidi L, Barchiesi E (2018) Energy approach to brittle fracture in strain-gradient modelling. *Proceedings of the Royal Society A: Mathematical, Physical and Engineering Sciences* 474(2210):20170,878
- Placidi L, Barchiesi E, Misra A (2018a) A strain gradient variational approach to damage: a comparison with damage gradient models and numerical results. *Mathematics and Mechanics of Complex Systems* 6(2):77–100
- Placidi L, Misra A, Barchiesi E (2018b) Two-dimensional strain gradient damage modeling: a variational approach. *Zeitschrift für angewandte Mathematik und Physik* 69(3):1–19
- Placidi L, Misra A, Barchiesi E (2019) Simulation results for damage with evolving microstructure and growing strain gradient moduli. *Continuum Mechanics and Thermodynamics* 31(4):1143–1163
- Placidi L, Barchiesi E, Misra A, Andreaus U (2020a) Variational methods in continuum damage and fracture mechanics. *Encyclopedia of Continuum Mechanics* pp 2634–2643
- Placidi L, dell’Isola F, Barchiesi E (2020b) Heuristic homogenization of euler and pantographic beams. In: *Mechanics of Fibrous Materials and Applications*, Springer, pp 123–155
- Poudel L, Tamerler C, Misra A, Ching WY (2017) Atomic-scale quantification of interfacial binding between peptides and inorganic crystals: The case of calcium carbonate binding peptide on aragonite. *The Journal of Physical Chemistry C* 121(51):28,354–28,363
- Rahali Y, Giorgio I, Ganghoffer J, dell’Isola F (2015) Homogenization à la piola produces second gradient continuum models for linear pantographic lattices. *International Journal of Engineering Science* 97:148–172
- Reed M, Simon B (1980) *Methods of Modern Mathematical Physics, Vol. 1: Functional Analysis*, 2nd ed. Academic press inc., San Diego, CA, USA
- Riks E (1979) An incremental approach to the solution of snapping and buckling problems. *International Journal of Solids and Structures* 15(7):529–551
- Serpieri R, Sessa S, Rosati L (2018) A mitc-based procedure for the numerical integration of a continuum elastic-plastic theory of through-the-thickness-jacketed shell structures. *Composite Structures* 191:209–220
- Sessa S (2021) Modified OpenSees v.3.0.3 executable <https://bit.ly/3rupjrr>. URL <https://bit.ly/3rUPJrr>, last visited: August 2021
- Sessa S (2022) Thermodynamic compatibility conditions of a new class of hysteretic materials. *Continuum Mechanics and Thermodynamics* 34(1):61–79
- Sessa S, Serpieri R, Rosati L (2017) A continuum theory of through-the-thickness jacketed shells for the elasto-plastic analysis of confined composite structures: Theory and numerical assessment. *Composites Part B: Engineering* 113:225–242
- Sessa S, Marmo F, Vaiana N, De Gregorio D, Rosati L (2019a) Strength hierarchy provisions for transverse confinement systems of shell structural elements. *Composites Part B: Engineering* 163:413–423
- Sessa S, Marmo F, Vaiana N, Rosati L (2019b) Probabilistic assessment of axial force–biaxial bending capacity domains of reinforced concrete sections. *Meccanica* 54(9):1451–1469
- Spagnuolo M, Barcz K, Pfaff A, dell’Isola F, Franciosi P (2017) Qualitative pivot damage analysis in aluminum printed pantographic sheets: numerics and experiments. *Mechanics Research Communications* 83:47–52
- Timofeev D, Barchiesi E, Misra A, Placidi L (2020) Hemivariational continuum approach for granular solids with damage-induced anisotropy evolution. *Mathematics and Mechanics of Solids* p 1081286520968149
- Triantafyllou T, Zhang J, Shercliff T, Gibson L, Ashby M (1989) Failure surfaces for cellular materials under multiaxial loads-ii. comparison of models with experiment. *International Journal of Mechanical Sciences* 31(9):665–678
- Turco E (2020) Modelling of two-dimensional Timoshenko beams in Hencky fashion. In: *Developments and Novel Approaches in Nonlinear Solid Body Mechanics*, Springer, pp 159–177
- Turco E, Barchiesi E (2019) Equilibrium paths of Hencky pantographic beams in a three-point bending problem. *Mathematics and Mechanics of Complex Systems* 7(4):287–310

- Turco E, dell'Isola F, Cazzani A, Rizzi NL (2016) Hencky-type discrete model for pantographic structures: numerical comparison with second gradient continuum models. *Zeitschrift für angewandte Mathematik und Physik* 67(4):1–28
- Turco E, dell'Isola F, Misra A (2019) A nonlinear Lagrangian particle model for grains assemblies including grain relative rotations. *International Journal for Numerical and Analytical Methods in Geomechanics* 43(5):1051–1079
- Turco E, Barchiesi E, Giorgio I, dell'Isola F (2020) A Lagrangian Hencky-type non-linear model suitable for metamaterials design of shearable and extensible slender deformable bodies alternative to timoshenko theory. *International Journal of Non-Linear Mechanics* 123:103,481
- Vaiana N, Spizzuoco M, Serino G (2017) Wire rope isolators for seismically base-isolated lightweight structures: Experimental characterization and mathematical modeling. *Engineering Structures* 140:498–514
- Vaiana N, Sessa S, Marmo F, Rosati L (2018) A class of uniaxial phenomenological models for simulating hysteretic phenomena in rate-independent mechanical systems and materials. *Nonlinear Dynamics* 93(3):1647–1669
- Vaiana N, Sessa S, Paradiso M, Rosati L (2019) Accurate and efficient modeling of the hysteretic behavior of sliding bearings. vol 3, pp 5291–5303
- Vaiana N, Capuano R, Sessa S, Marmo F, Rosati L (2021a) Nonlinear dynamic analysis of seismically base-isolated structures by a novel openseees hysteretic material model. *Applied Sciences* 11(3):900
- Vaiana N, Losanno D, Ravichandran N (2021b) A novel family of multiple springs models suitable for biaxial rate-independent hysteretic behavior. *Computers and Structures* 244
- Vaiana N, Sessa S, Rosati L (2021c) A generalized class of uniaxial rate-independent models for simulating asymmetric mechanical hysteresis phenomena. *Mechanical Systems and Signal Processing* 146
- Valoroso N, Fedele R (2010) Characterization of a cohesive-zone model describing damage and de-cohesion at bonded interfaces. sensitivity analysis and mode-i parameter identification. *International Journal of Solids and Structures* 47(13):1666–1677
- Valoroso N, Rosati L (2009a) Consistent derivation of the constitutive algorithm for plane stress isotropic plasticity. part i: Theoretical formulation. *International Journal of Solids and Structures* 46(1):74–91
- Valoroso N, Rosati L (2009b) Consistent derivation of the constitutive algorithm for plane stress isotropic plasticity. part ii: Computational issues. *International Journal of Solids and Structures* 46(1):92–124
- Valoroso N, Stolz C (2020) Progressive damage in quasi-brittle solids. *Lecture Notes in Mechanical Engineering* pp 408–418
- Wu JY, Nguyen VP, Zhou H, Huang Y (2020) A variationally consistent phase-field anisotropic damage model for fracture. *Computer Methods in Applied Mechanics and Engineering* 358



Chapter 27

Thermodynamic Compatibility of the Hysteretic Poly Uniaxial Material Implemented in OpenSees

Salvatore Sessa, Nicoló Vaiana, Massimo Paradiso, Luciano Rosati

Abstract The fulfillment of the Drucker postulate applied to a phenomenological hysteretic constitutive model is hereby investigated. Such a material is defined in terms of analytical functions so that it is capable of determining the response and its tangent operator in closed form and does not require any iterative algorithm. Hence, the constitutive model is very appealing for several applications, including structural analysis and homogenization techniques. Within this context, the thermodynamic compatibility implied by the Drucker's postulate aims to ensure that the model does not provide responses associated with negative values of the dissipated energy, this in order to fulfill the 2nd law of thermodynamics. In particular, the research is focused on two peculiar phenomena associated with non-consistent energy dissipations: the *negative softening* and the *hysteretic crossing paths*. It is shown that the thermodynamic compatibility may be violated because of negative softening although it is possible to determine a displacement range for which the material preserves its physical significance. On the contrary, it is proved that the analytical formulation of the investigated model avoids the crossing path phenomenon thus ensuring the fulfillment of the Drucker's postulate.

Keywords: Drucker postulate · Thermodynamic compatibility · Plasticity

27.1 Introduction

Within the context of structural analysis and continuum mechanics, uniaxial constitutive models describing hysteretic behaviors play an important role (Dimian and

S. Sessa, N. Vaiana, M. Paradiso, L. Rosati

Department of Structures for Engineering and Architecture, University of Naples Federico II, via Claudio, 21, 80124, Naples, Italy

e-mail: salvatore.sessa2@unina.it, nicolo.vaiana@unina.it, massimo.paradiso@unina.it, rosati@unina.it

Andrei, 2008). In particular, such models are capable of reproducing the behavior of fragile (Bahn and Hsu, 1998) and ductile materials (Nuzzo et al, 2018) as well as seismic devices (Castellano et al, 2014; Kikuchi and Aiken, 1997; Losanno et al, 2020, 2021; Vaiana et al, 2017).

An essential aspect of these applications consists in the fact that such uniaxial relationships may be used in more complex models, based on homogenization techniques (De Angelo et al, 2020; Placidi et al, 2020) addressing continuum and multiaxial problems, including micromechanic approaches (Barchiesi et al, 2021; Maksimov et al, 2021; Misra et al, 2021; Placidi et al, 2019), metamaterials (Abali et al, 2021; Ciallella et al, 2021; dell'Isola et al, 2019; Turco and Barchiesi, 2019; Turco et al, 2020), and multiscale approaches (Giorgio and Scerrato, 2017). Within this context, it is convenient if hysteresis loops are characterized by smooth load-displacement relationships so that both the response and its first derivative are continuous.

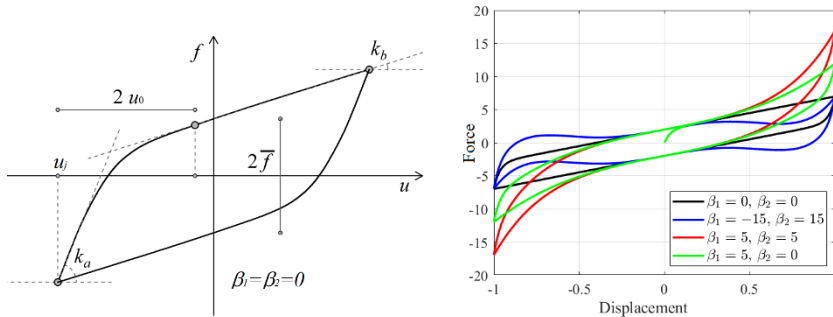
To this end, the use of analytical expressions is a very popular technique and several models are available in the literature. One of the most popular ones was proposed by Bouc (1971) and extended by Wen (1976, 1980). Its popularity is due to its capability of reproducing complex and smooth hysteresis loops by means of a limited set of parameters and a simple analytical function.

On the other hand, most of these models, including the Bouc–Wen material, are based on differential relationships involving both the response and its first derivative in time. For this reason, the computation of the structural response must be performed by adopting iterative algorithms, hence increasing the computational burden, since no closed form solutions is available.

To avoid such a drawback, a new class of hysteretic models has been recently proposed (Vaiana et al, 2018). Such materials are characterized by closed-form expressions determining the constitutive response (Vaiana et al, 2021). In particular, the model proposed by Vaiana et al (2019), defined by means of five constitutive parameters, is particularly appealing since it provides smooth hysteresis loops with hardening and softening behaviors. Moreover, since its parameters can be directly related to quantities deduced from experimental data, their identification is straightforward (Sessa et al, 2020). The model, addressed as *HystereticPoly* uniaxial material, has been implemented in OpenSees (Sessa, 2019), an open-source framework for finite element analysis.

An essential aspect in order to use such a constitutive model in structural analyses consists in investigating the fulfillment of the Drucker's postulate (Drucker, 1959). Specifically, such a condition prescribes that the increments of the dissipated energy must always be non-negative in order to fulfill the second law of thermodynamics and to avoid physically impossible energy balances.

A general purpose condition for hysteretic models belonging to the class introduced in Vaiana et al (2018) has been proposed in Sessa (2022) where it has been also specialized for the *HystereticPoly* material. In particular, it is shown that, depending on the values of the constitutive parameters, thermodynamic compatibility may not be always fulfilled by the model. Nevertheless, it is possible to determine a compatibility range in terms of displacement/strain where the response fulfills the Drucker's postulate.



(a) Physical interpretation of k_a , k_b , \bar{f} and u_0 with $\beta_1 = \beta_2 = 0$ (b) Influence of β_1 and β_2 with $k_a = 120$, $k_b = 5$ and $\alpha = 30$

Fig. 27.1 Physical interpretation of the constitutive parameters

Such an interval was computed in Sessa (2022) by means of a strongly conservative condition. Hence, numerical tests have shown that, in general, the response may be thermodynamically consistent even for equilibrium states located outside the compatibility range.

The present research aims to illustrate further insights about the thermodynamic compatibility of the *HystereticPoly* constitutive model presented in Vaiana et al (2019). In particular, two peculiar behaviors of the hysteresis loop are investigated in order to get more accurate compatibility conditions depending on the constitutive parameters.

In particular, the first investigated behavior, i.e. the *negative softening*, consists in the fact that, because of negative stiffness, the model provides responses associated with negative work. A further behavior, i.e., the *hysteresis crossing paths*, consists in loops in which loading and unloading branches present anomalous intersections. Both the cases are discussed in order to identify suitable compatibility ranges ensuring the fulfillment of the second law of thermodynamics.

Numerical tests are provided in order to prove the effectiveness of the discussed conditions and to show the stability of the *HystereticPoly* constitutive model.

27.2 A Review of the HystereticPoly Constitutive Model

The *HystereticPoly* uniaxial material proposed in Vaiana et al (2019) is a constitutive model, defined by five parameters, capable of reproducing complex hysteresis loops with various shapes.

In particular, it is defined by two stiffness coefficients k_a and k_b associated with the elastic and inelastic region, respectively, a transition parameter α ruling a

smooth passage from elastic to inelastic states, and two shape parameters, β_1 and β_2 , governing hardening, softening, and pinching behaviors.

It is worth being emphasized that, being the constitutive model completely phenomenological, it can express both displacement/force and strain/stress relationships as well as any different couple of energetically associated structural quantities. Nevertheless, we will hereby refer to displacement and forces to avoid needless complexity.

For convenience, two auxiliary parameters, schematized in Fig. 27.1a, are introduced:

$$u_0 = \frac{1}{2} \left[\left(\frac{k_a - k_b}{\delta} \right)^{\frac{1}{\alpha}} - 1 \right] \quad (27.1)$$

$$\bar{f} = \frac{k_a - k_b}{2} \left[\frac{(1 + 2u_0)^{1-\alpha} - 1}{1 - \alpha} \right] \quad (27.2)$$

Specifically, u_0 measures the displacement needed to reach the complete inelastic state while \bar{f} is the hysteretic response with zero displacement and δ is a tolerance.

A few realizations of the hysteresis loops that it is possible to reproduce with such a constitutive model are represented in Fig. 27.1b.

In order to introduce the closed form expression of the material's response, we make reference to the symbology usually adopted by the finite element method. Specifically, we denote by u_c and f_c , respectively, the displacement and force of a generic equilibrium state which has been reached during the analysis. Moreover, s_c is the sign of the velocity associated with u_c .

The analysis algorithms typical of the finite element method use a trial value u_t of the displacement that perturbs the equilibrium state. The constitutive model must compute the force f_t associated with such perturbation and its first derivative.

To this end, it is necessary to introduce the history variable:

$$u_j = u_c + s_t (1 + 2u_0) - s_t (\Delta_1 \Delta_2)^{\frac{1}{1-\alpha}} \quad (27.3)$$

where

$$\Delta_1 = \frac{s_t (1 - \alpha)}{k_a - k_b} \quad (27.4)$$

$$\Delta_2 = f_c - \beta_1 u_c^3 - \beta_2 u_c^5 - k_b u_c - s_t \bar{f} + \Delta_3 \quad (27.5)$$

and

$$\Delta_3 = (k_a - k_b) \frac{(1 + 2u_0)^{1-\alpha}}{s_t (1 - \alpha)} \quad (27.6)$$

As shown in Fig. 27.1a, the history variable u_j represents the displacement relevant to the latest inversion of the displacement path. In particular, Equation (27.3) takes advantage by the fact that, for a known equilibrium state (u_c, f_c) , the relevant hysteresis curve can be univocally determined and u_j represents the maximum displacement associated with the current hysteresis loop.

Eventually, the trial force is computed as

$$f_t = \beta_1 u_t^3 + \beta_2 u_t^5 + k_b u_t + (k_a - k_b) (\Delta_4 - \Delta_5) + s_t \bar{f} \quad (27.7)$$

with

$$\Delta_4 = \frac{(1 + s_t u_t - s_t u_j + 2u_0)^{1-\alpha}}{s_t (1 - \alpha)} \quad (27.8)$$

and

$$\Delta_5 = \frac{(1 + 2u_0)^{1-\alpha} - 1}{1 - \alpha} \quad (27.9)$$

The tangent operator, defined as the derivative of the force with respect to the displacement, is:

$$k(u_t) = \frac{df_t}{du_t} = 3\beta_1 u_t^2 + 5\beta_2 u_t^4 + k_b + s_t (k_a - k_b) (1 + s_t u_t - s_t u_j + 2u_0)^{-\alpha} \quad (27.10)$$

An important aspect concerning the definition of the tangent operator is relevant to the fact that this may be expressed by the combination of two quantities:

$$k(u_t) = k_e(u_t) + k_h(u_t) \quad (27.11)$$

where k_e does not depend on the history variable

$$k_e(u_t) = 3\beta_1 u_t^2 + 5\beta_2 u_t^4 + k_b \quad (27.12)$$

while k_h is

$$k_h(u_t) = s_t (k_a - k_b) (1 + s_t u_t - s_t u_j + 2u_0)^{-\alpha} \quad (27.13)$$

An essential property of $k_h(u_t)$ consists in the fact that it is a symmetric decaying function univocally defined by the difference between the current displacement u and the history variable u_j , as shown in Fig. 27.2.

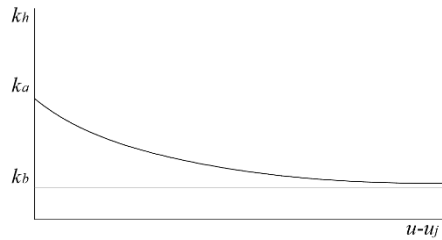


Fig. 27.2 History-dependent stiffness k_h typical trend

27.3 The Thermodynamic Compatibility

Within the context of nonlinear mechanics, the Drucker's postulate Drucker (1959) states that, for any possible equilibrium state and assumed an arbitrary displacement increment, the variation of the inelastic work must be non-negative.

Such a condition, often addressed as *thermodynamic compatibility*, is of exceptional importance because it states that the energy dissipated by the constitutive model is never negative, according to the second law of thermodynamics. Hence, the Drucker's postulate represents a fundamental condition to be fulfilled in order to reproduce physically meaningful constitutive responses.

To investigate the fulfillment of such a postulate in the case of the *HystereticPoly* material, let us assume a generic equilibrium state, represented in Fig. 27.3, defined by the current displacement value u , by the associated force value $f(u)$, both supposed positive for simplicity, and by the tangent stiffness $k(u) = df(u)/du$. The blue curve represents the equilibrium path followed before the attainment of the current state.

Moreover, let the red curve be the unloading path, i.e., the path that the constitutive response follows if the current force is reduced to zero, so that the value $u^*(u)$ represents the *residual displacement* associated with the state $(u, f(u))$. Let us also denote by $k^*(u)$ the tangent stiffness associated with the unloading branch at $u^*(u)$.

The integral of the unloading curve in the interval $[u, u^*]$, represented by the yellow area in Fig. 27.4, is the energy that the system releases if the force is suppressed. For simplicity and following the classic nomenclature of structural mechanics, such a quantity will be addressed as *elastic energy* \mathcal{W}_{el} below. Hence, a simple thermodynamic balance permits to define the *inelastic work* \mathcal{W}_{in} , i.e. the energy dissipated by the constitutive model, as difference between the total work \mathcal{W}_{tot} and the elastic energy \mathcal{W}_{el} :

$$\mathcal{W}_{in} = \mathcal{W}_{tot} - \mathcal{W}_{el} \quad (27.14)$$

A previous research Sessa (2022) investigated the fulfillment of such a condition for all the constitutive models belonging to the class proposed by Vaiana et al. Vaiana et al (2018), including the *HystereticPoly* material Vaiana et al (2019). In particular,

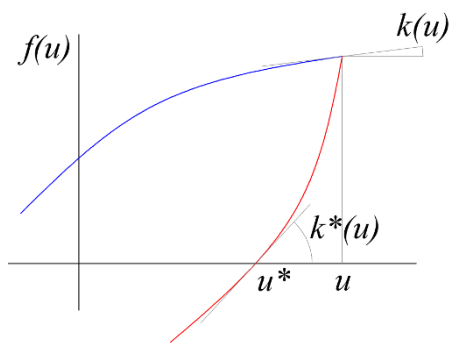
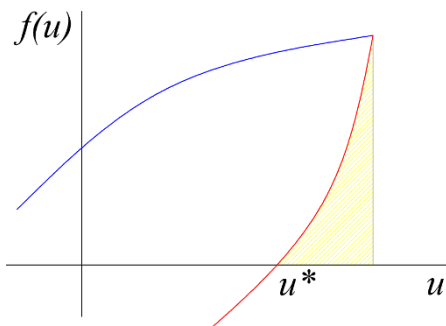


Fig. 27.3 Generic initial stress-strain state

Fig. 27.4 Elastic energy associated with the state $[u, f(u)]$



the research provided the general-purpose relationship:

$$\frac{\min [k_s(u)|\forall u]}{\max [k(u)|\forall u]} \geq \frac{1}{2} \quad (27.15)$$

where $k_s(u) = f(u)/u$ denotes the secant stiffness.

It is worth being emphasized that such a condition was developed regardless of the peculiar computational model and has a conservative nature that has been observed numerically. Actually, it is possible to provide further insights about the energetic balances of the *HystereticPoly* material so that less conservative conditions for the fulfillment of the thermodynamic compatibility can be determined. In particular, we will focus on two thermodynamically non-consistent phenomena that will be addressed as *negative softening* and *hysteresis crossing paths* below.

27.3.1 Negative Softening

Let us denote by $\hat{f}^+(u)$ and $\hat{f}^-(u)$, respectively, the top and bottom boundaries of the hysteresis loops. These functions are defined as:

$$\hat{f}^+(u) = \max [f(u, u_j)] \forall u_j \quad (27.16)$$

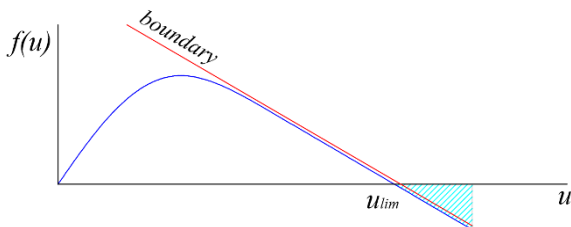
$$\hat{f}^-(u) = \min [f(u, u_j)] \forall u_j \quad (27.17)$$

where the explicit dependency on the history variable u_j has been specified. Such boundaries are the maximum and minimum value that the force f can attain at a specific displacement u for any possible load history of the material.

The phenomenological characterization of the *HystereticPoly* material provides that $k_a > k_b$ as unique analytical condition on the values of the constitutive parameter. For this reason, the top and bottom boundaries of the hysteresis loops are defined by 5th degree polynomial functions:

$$\hat{f}^\pm(u) = \pm \bar{f} + \beta_1 u^3 + \beta_2 u^5 + k_b u \quad (27.18)$$

Fig. 27.5 Example of thermodynamically non-compatible softening



In general, such boundary curves may cross the horizontal axis thus determining states for which the total work \mathcal{W}_{tot} turns out to be negative, as for the example reported in Fig. 27.5 in which the negative work increment is represented by the cyan area.

The Drucker's postulate is not fulfilled for displacements greater than u_{lim} , i.e., the displacement for which the boundary function crosses the horizontal axis. The computation of u_{lim} cannot be solved in closed form if $\beta_2 \neq 0$ but it can be easily determined numerically.

The latter represents the boundary of a compatibility range of the displacements, already discussed in Sessa (2022). It does not depend on the past load history of the material and can be used as a limit state condition of the response.

27.3.2 Hysteresis Crossing Paths

A further circumstance for which thermodynamic not-consistent states may occur consists in the fact that, in case of load inversion, the unloading path crosses the previous loading curve, as schematized in Fig. 27.6.

To better clarify the reason of possible thermodynamic violations, let us consider an initial state relevant to an unloaded state with non-zero residual displacement as the one represented by the point $(u^*, 0)$ in Fig. 27.7. The elastic energy associated with such an equilibrium state is obviously zero.

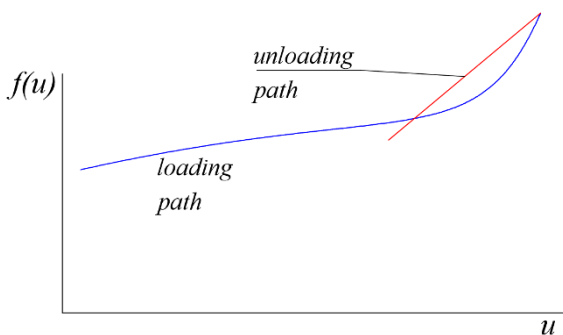


Fig. 27.6 Example of hysteresis crossing paths

Let us assume that the material response, because of a displacement increment Δu , follows the blue curve in the figure. Moreover, let the red curve be the unloading branch associated with the equilibrium state at $u^* + \Delta u$.

Actually, the total work increment is represented by the area underneath the blue curve while the elastic energy increment is equal to the area underneath the red one. As a matter of fact, if the unloading path crosses the loading one, the increment of elastic energy may result greater than the total work increment thus violating the Drucker’s postulate since such a condition corresponds to negative dissipated energy.

To investigate the existence of possible crossings in the responses of the *HystereticPoly* model, let us consider the analytical expressions of the loading and unloading curves as functions of the stiffness. Specifically, assuming that the value of the force $f(u^* + \Delta u)$ at $u^* + \Delta u$ is known.

Following the loading branch, the force $f(u_c)$ at the crossing displacement u_c is:

$$f(u_c) = f(u^* + \Delta u) - \int_{u_c}^{u^* + \Delta u} k_e(v) dv - \int_{u_c}^{u^* + \Delta u} k_h(v, u_j) dv \quad (27.19)$$

while the force $f_u(u_c)$ at u_c obtained by following the unloading path turns out to be:

$$f_u(u_c) = f(u^* + \Delta u) - \int_{u_c}^{u^* + \Delta u} k_e(v) dv - \int_{u_c}^{u^* + \Delta u} k_h(v, u^* + \Delta u) dv \quad (27.20)$$

in fact, assuming for simplicity that the response has reached the top boundary curve, the history variable u_j must be updated because of the load inversion and becomes equal to the displacement where the load is inverted.

Eventually, since at the crossing point $f(u_c) = f_u(u_c)$ and considering Equations (27.19) and (27.20), it yields:

$$\int_{u_c}^{u^* + \Delta u} k_h(v, u_j) dv = \int_{u_c}^{u^* + \Delta u} k_h(v, u^* + \Delta u) dv \quad (27.21)$$

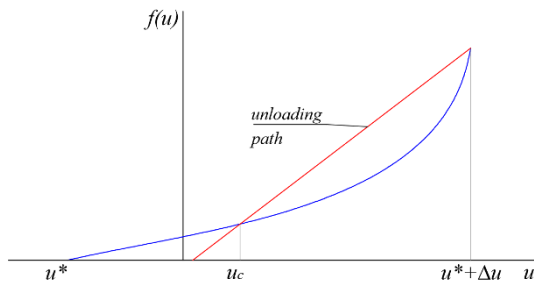


Fig. 27.7 Thermodynamically non-consistent increments

Because of the symmetry and the monotonic trend of k_h , such an equality is fulfilled only if $u_c = u_j$, i.e., if the response reaches the symmetric (negative) boundary of the hysteresis loops. Hence, regardless of the values of the constitutive parameters, the unloading response of the *HystereticPoly* material (i.e. the response obtained by dropping the force to zero) cannot cross the relevant loading path since the latter condition $u_c = u_j$ is attained for negative values of the force.

In conclusion, the analytical formulation of the *HystereticPoly* material intrinsically prevents the chance of getting equilibrium states violating the thermodynamic compatibility because of the crossing path phenomenon.

27.4 Numerical Applications

To exploit the thermodynamic compatibility of the investigated material from the numerical point of view, two sets of constitutive parameters have been used to determine the energetic quantities of interest.

In particular, such models have been calibrated on experimental responses of real devices by the procedure described in Sessa et al (2020); the first one is relevant to the Fiber Reinforced Rubber Bearer (FREB) tested by Kelly and Takhirov Kelly and Takhirov (2001) while the second one (test PW16010L) reproduces the longitudinal response of the wire-rope isolator type PWHS 16010 tested in Vaiana et al (2017).

Analyses have been performed in Matlab by means of a displacement-control algorithm and the considered sets of parameters are reported in Table 27.1.

Table 27.1 Values of the constitutive parameters relevant to the investigated models ($\delta = 10^{-8}$)

| Test | k_a | k_b | α | β_1 | β_2 | u^* | u_{max} |
|----------|------------------|------------------|----------|-------------------|---------------------|---------|-----------|
| FREB | $5.3 \cdot 10^6$ | $3.7 \cdot 10^5$ | 280.43 | $-2.4 \cdot 10^7$ | $9.8 \cdot 10^8$ | -0.0248 | 0.15 |
| PW16010L | $1.8 \cdot 10^6$ | $2.6 \cdot 10^5$ | 704.96 | $1.0 \cdot 10^8$ | $5.0 \cdot 10^{11}$ | -0.0042 | 0.03 |

The numerical investigations consist in a displacement-control path-following analysis with monotonic increasing load starting from different initial equilibrium states. To define such starting points, we recall the nature of the investigated phenomenological model and schematized in Fig. 27.1a.

The model is defined by means of the two boundary curves reported in Equations (27.16) and (27.17) which do not depend on the previous load history of the material. Moreover, each equilibrium state is associated with a transition curve of which u_j denotes the initial displacement. To fix ideas, if we assume positive displacement increments, u_j represents the displacement at which the transition curve, associated with the current response, intersects the bottom boundary curve while it reaches the top bound at the displacement $u_j + 2u_0$.

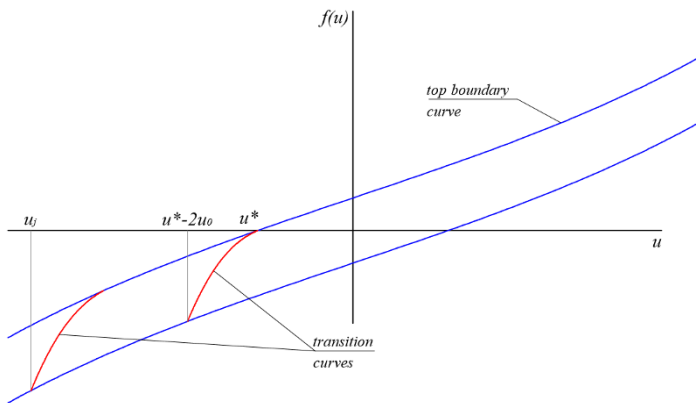


Fig. 27.8 Example of transition curves for $u_j \leq u^* - 2u_0$

In order to account for all possible equilibrium states, the analyses adopt different values of the history variable. In particular, u_j spans within the interval $[u^* - 2u_0, u_{max}]$. The upper limit u_{max} , reported in the last column of Table 27.1, is the maximum value of the displacement for which the response of the analyzed devices preserves physical significance.

The lower limit has been computed as function of the residual displacement u^* , i.e. the displacement for which the upper boundary curve intersects the horizontal axis. As schematized in Fig. 27.8, the transition curve associated with $u_j = u^* - 2u_0$ reaches the top boundary at u^* with $f = 0$. We emphasize that the increments of the inelastic energy are non-zero only for those equilibrium states for which $u > u^*$ since all those with $u < u^*$ are associated with increments of the total work that are in perfect balance with the decrease of the elastic energy. As a matter of fact, all loops with $u_j \leq u^* - 2u_0$ coincide in the region $u \geq u^*$; hence, the energy dissipated for $u_j \leq u^* - 2u_0$ and $u > u^*$ depends on the top boundary curve only and is equal to its value computed with $u_j = u^* - 2u_0$.

Finally, the numerical analyses computed inelastic energy \mathcal{W}_{in} dissipated by the model for equilibrium states associated with $u_j \in [u^* - 2u_0, u_{max}]$, $u \in [u_j, u_{max}]$, and $du > 0$. The outcomes of the computations are reported in Figures 27.9 and 27.10 reporting the first derivative $d\mathcal{W}_{in}/du$ of the inelastic energy vs. u_j and u , relevant to the parameter sets FREB and PW1610L, respectively.

As a matter of fact, the derivative of the inelastic energy dissipated by the analyzed models turns out to be non-negative for positive increments du of the displacement, thus confirming the fulfillment of the Drucker’s postulate by the *HystereticPoly* hysteretic material. Analyses relevant to negative increments of the displacement have been omitted for brevity because of the symmetry of the constitutive response.

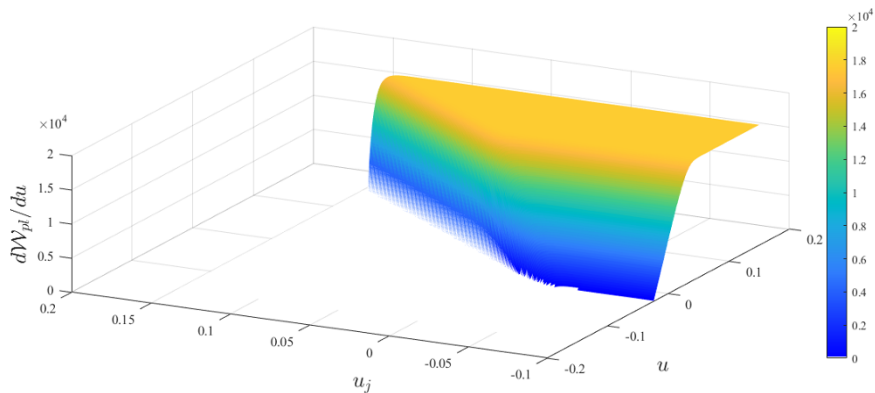


Fig. 27.9 First derivative dW_{in}/du of the inelastic energy vs. the history variable u_j and the displacement u relevant to the FREB model

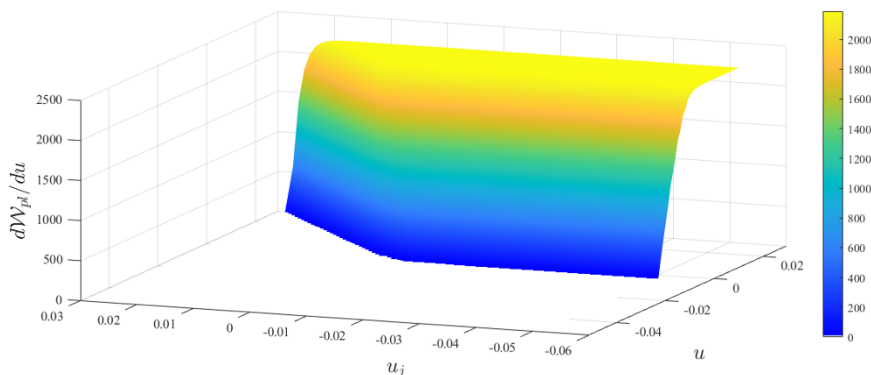


Fig. 27.10 First derivative dW_{in}/du of the inelastic energy vs. the history variable u_j and the displacement u relevant to the PW1610L model

To provide a further insight of the energetic balances relevant to the analyzed models, two further analyses have been performed. Both consist in adopting the cyclic, quasi-static displacement path represented in Fig. 27.11.

Figures 27.12a and 27.13a report the load-displacement hysteresis responses of materials FREB and PW16010L, respectively, while Figures 27.12b and 27.13b report their total, inelastic, and elastic energy vs. the displacement.

The two latter figures clearly confirm that, while the total and elastic energy present decreasing regions, the inelastic energy dissipated by the models is always non-decreasing.

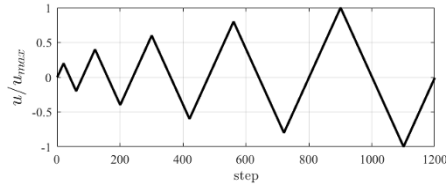
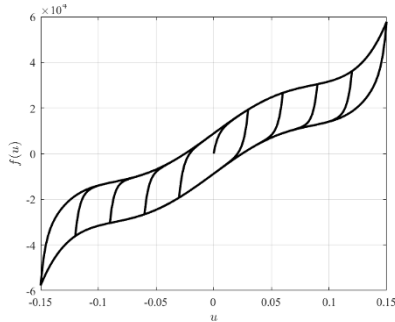
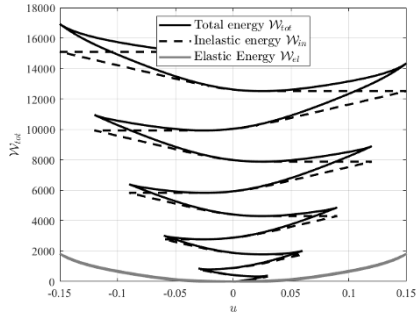


Fig. 27.11 Normalized displacement path

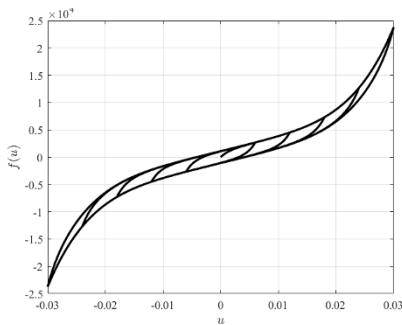


(a) Load-displacement response

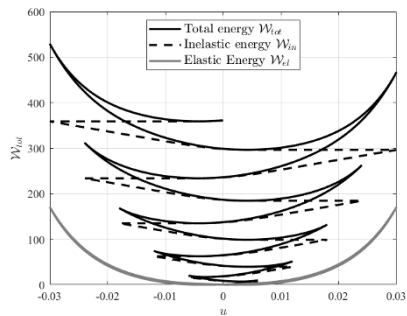


(b) Total and inelastic work

Fig. 27.12 Load-displacement response and energy of material FREB



(a) Load-displacement response



(b) Total and inelastic work

Fig. 27.13 Load-displacement response and energy of material PW16010L

27.5 Discussion and Conclusions

The fulfillment of the Drucker’s postulate Drucker (1959) by the phenomenological material *HystereticPoly* presented by Vaiana et al. Vaiana et al (2019), and thus its

thermodynamic compatibility, have been investigated. Such a condition provides that the inelastic energy dissipated by the model is non-decreasing according to the second law of thermodynamics.

In particular, the presented research focused on two possible behaviors associated with non-compatible energetic rates and specifically the *negative softening* and the *hysteresis crossing paths*.

The first behavior is associated with hysteresis loops presenting softening regions in which the response becomes negative for positive displacements, thus providing negative increments of the total work. Such a behavior is not intrinsically prevented by the analyzed model since and can be obtained by adopting inappropriate parameter sets. Nevertheless, it is possible to determine the maximum displacement range for which the model provides physically significant outcomes by numerically solving a 5th degree polynomial equation.

Conversely, it has been proved that the analytical formulation of the *HystereticPoly* material intrinsically avoids the phenomenon of crossing paths thus providing outcomes that are always thermodynamically consistent and fulfill the Drucker's postulate.

The latter property is of the outmost importance for several applications since the event of crossing path is far more difficult to control during nonlinear analyses especially if the uniaxial hysteretic relationship is used within a context of more complex homogeneized materials, such as the ones described in Barchiesi et al (2021). In fact, the case of negative softening does not depend on the load history but on the constitutive parameters only. For this reason, it is possible to determine the maximum displacement range, for which the response preserves its physical significance, and to use such a boundary as a limit state condition of the uniaxial response.

On the contrary, the event of crossing paths, if possible, may occur at equilibrium states that are difficult to determine *a priori*. This implies to include computationally demanding checks while the analysis is performed in order to compare the evolution of the dissipated energy. As a matter of fact, such a task could even be impossible to be done in case of homogeneization procedures.

The fact that circumstances in which crossing paths compromise the fulfillment of the Drucker's postulate are prevented by the *HystereticPoly* material, opens appealing perspectives for its diffusion within the scientific and professional communities. With this respect, future research directions will take advantage of the fact that each possible equilibrium state is univocally associated with a value of the elastic energy regardless of the load history. For this reason, authors are confident that the inelastic energy can be expressed as function of some history variable, such as the residual displacement and/or some sort of plastic multiplier, so that the analytical model can be defined by means of an energetic formulation. This would foster the implementation of the analytical model in hemivariational models Timofeev et al (2021) and would permit its generalization for multiaxial responses.

Acknowledgements The present research was supported by the University of Naples Federico II and the *Compagnia di San Paolo*, which are gratefully acknowledged by the author, as part of

the Research Project *MuRA – Multi-risk assessment and structural protection of archaeological vestiges in volcanic scenarios*, FRA grants, CUP E69C21000250005.

References

- Abali B, Klunker A, Barchiesi E, Placidi L (2021) A novel phase-field approach to brittle damage mechanics of gradient metamaterials combining action formalism and history variable. *ZAMM Zeitschrift für Angewandte Mathematik und Mechanik* 101(9):e202000,289
- Bahn B, Hsu CT (1998) Stress-strain behavior of concrete under cyclic loading. *ACI Materials Journal* 95(2):178–193
- Barchiesi E, Misra A, Placidi L, Turco E (2021) Granular micromechanics-based identification of isotropic strain gradient parameters for elastic geometrically nonlinear deformations. *ZAMM Zeitschrift für Angewandte Mathematik und Mechanik* p e202100059
- Bouc R (1971) Modele mathematique d'hysteresis. *Acustica* 24:16–25
- Castellano A, Foti P, Fraddosio A, Marzano S, Mininno G, Piccioni M (2014) Seismic response of a historic masonry construction isolated by stable unbonded fiber-reinforced elastomeric isolators (su-frei). *Key Engineering Materials* 628:160–167
- Ciallella A, Pasquali D, Gołaszewski M, D'Annibale F, Giorgio I (2021) A rate-independent internal friction to describe the hysteretic behavior of pantographic structures under cyclic loads. *Mechanics Research Communications* 116
- De Angelo M, Placidi L, NejadSadeghi N, Misra A (2020) Non-standard timoshenko beam model for chiral metamaterial: Identification of stiffness parameters. *Mechanics Research Communications* 103
- dell'Isola F, Seppacher P, Alibert J, Lekszycki T, Grygoruk R, Pawlikowski M, Steigmann D, Giorgio I, Andreaus U, Turco E, Gołaszewski M, Rizzi N, Boutin C, Eremeyev V, Misra A, Placidi L, Barchiesi E, Greco L, Cuomo M, Cazzani A, Corte A, Battista A, Scerrato D, Eremeeva I, Rahali Y, Ganghoffer JF, Müller W, Ganzosch G, Spagnuolo M, Pfaff A, Barcz K, Hoschke K, Neggers J, Hild F (2019) Pantographic metamaterials: an example of mathematically driven design and of its technological challenges. *Continuum Mechanics and Thermodynamics* 31(4):851–884
- Dimian M, Andrei P (2008) *Phenomena in hysteretic systems*. Springer, New York, USA
- Drucker D (1959) A definition of a stable inelastic material. *ASME Journal of Applied Mechanics* 26:101–195
- Giorgio I, Scerrato D (2017) Multi-scale concrete model with rate-dependent internal friction. *European Journal of Environmental and Civil Engineering* 21(7-8):821–839
- Kelly J, Takhirov S (2001) Analytical and experimental study of fiber-reinforced elastomeric isolators. PEER Report 2001/11, University of California, Berkeley, CA, USA
- Kikuchi M, Aiken ID (1997) An analytical hysteresis model for elastomeric seismic isolation bearings. *Earthquake Engineering & Structural Dynamics* 26(2):215–231
- Losanno D, Calabrese A, Madera-Sierra I, Spizzuoco M, Marulanda J, Thomson P, Serino G (2020) Recycled versus natural-rubber fiber-reinforced bearings for base isolation: Review of the experimental findings. *Journal of Earthquake Engineering*
- Losanno D, Palumbo F, Calabrese A, Barrasso T, Vaiana N (2021) Preliminary investigation of aging effects on recycled rubber fiber reinforced bearings (RR-FRBs). *Journal of Earthquake Engineering*
- Maksimov V, Barchiesi E, Misra A, Placidi L, Timofeev D (2021) Two-dimensional analysis of size effects in strain-gradient granular solids with damage-induced anisotropy evolution. *Journal of Engineering Mechanics* 147(11)
- Misra A, Placidi L, dell'Isola F, Barchiesi E (2021) Identification of a geometrically nonlinear micromorphic continuum via granular micromechanics. *Zeitschrift für Angewandte Mathematik und Physik* 72(4)

- Nuzzo I, Losanno D, Caterino N, Serino G, Bozzo Rotondo L (2018) Experimental and analytical characterization of steel shear links for seismic energy dissipation. *Engineering Structures* 172:405–418
- Placidi L, Misra A, Barchiesi E (2019) Simulation results for damage with evolving microstructure and growing strain gradient moduli. *Continuum Mechanics and Thermodynamics* 31(4):1143–1163
- Placidi L, dell’Isola F, Barchiesi E (2020) Heuristic homogenization of euler and pantographic beams. CISM International Centre for Mechanical Sciences, Courses and Lectures 596:123–155
- Sessa S (2019) Modified OpenSees v.3.0.3 executable. URL <http://bit.ly/2OTHiLE>, last visited: December 2020
- Sessa S (2022) Thermodynamic compatibility conditions of a new class of hysteretic materials. *Continuum Mechanics and Thermodynamics* 34(1):61–79
- Sessa S, Vaiana N, Paradiso M, Rosati L (2020) An inverse identification strategy for the mechanical parameters of a phenomenological hysteretic constitutive model. *Mechanical Systems and Signal Processing* 139:106,622
- Timofeev D, Barchiesi E, Misra A, Placidi L (2021) Hemivariational continuum approach for granular solids with damage-induced anisotropy evolution. *Mathematics and Mechanics of Solids* 26(5):738–770
- Turco E, Barchiesi E (2019) Equilibrium paths of hencky pantographic beams in a three-point bending problem. *Mathematics and Mechanics of Complex Systems* 7(4):287–310
- Turco E, Barchiesi E, Giorgio I, dell’Isola F (2020) A lagrangian hencky-type non-linear model suitable for metamaterials design of shearable and extensible slender deformable bodies alternative to timoshenko theory. *International Journal of Non-Linear Mechanics* 123:103,481
- Vaiana N, Spizzuoco M, Serino G (2017) Wire rope isolators for seismically base-isolated lightweight structures: Experimental characterization and mathematical modeling. *Engineering Structures* 140:498–514
- Vaiana N, Sessa S, Marmo F, Rosati L (2018) A class of uniaxial phenomenological models for simulating hysteretic phenomena in rate-independent mechanical systems and materials. *Nonlinear Dynamics* 93(3):1647–1669
- Vaiana N, Sessa S, Marmo F, Rosati L (2019) An accurate and computationally efficient uniaxial phenomenological model for steel and fiber reinforced elastomeric bearings. *Composite Structures* 211:196–212
- Vaiana N, Losanno D, Ravichandran N (2021) A novel family of multiple springs models suitable for biaxial rate-independent hysteretic behavior. *Computers and Structures* 244:106,403
- Wen Y (1980) Equivalent linearization for hysteretic systems under random excitation. *Journal of Applied Mechanics, Transactions ASME* 47(1):150–154
- Wen YK (1976) Method for random vibration of hysteretic systems. *ASCE J Eng Mech Div* 102(2):249–263



Chapter 28

Studying the Higher-Order Inertia in the Second-Order Theory of Elasticity for Modeling Metamaterials

Navid Shekarchizadeh, Alberto Maria Bersani

Abstract Modeling the materials with a complex microstructure, such as metamaterials, is challenging especially in the dynamic regime. Higher-gradient models have been widely used for modeling the mechanical behavior of metamaterials. In dynamic loading problems, the inertia plays an important role. Including higher-order inertia in the model could possibly improve the accuracy of the model close to the eigenfrequencies of the structure. Such inertial terms have been presented in theory but they are not understood experimentally, therefore it has not been possible to quantify their value. Herein, we consider a macro-scale model for a pantographic structure and simulate a dynamic loading on it. We run the simulation for a range of frequencies of loading and for a number of arbitrary values for a higher-order inertial term that we have added to the model. The results show a clear relation between the value considered for the inertial term and the eigenfrequency of the structure that we get from the model. This result sheds light on finding an algorithm for determining the higher-order inertial terms experimentally in further studies.

Keywords: Higher-order inertia · Finite element method · Dynamic loading · Metamaterials

N. Shekarchizadeh

Department of Basic and Applied Sciences for Engineering, Sapienza University of Rome, Via Antonio Scarpa, 16, 00161 Rome, Italy
e-mail: navid.shekarchizadeh@uniroma1.it

A. M. Bersani

Department of Mechanical and Aerospace Engineering, Sapienza University of Rome, Via Eudossiana, 18, 00184 Rome, Italy
e-mail: alberto.bersani@uniroma1.it

28.1 Introduction

The structures with a complex substructure show specific mechanical behaviors that make it challenging to model them. The classical continuum mechanics usually is not a suitable candidate for describing such structures since it considers only a close vicinity of the material point unless we use a very fine mesh which results in high computational cost. An approach to overcome this issue is utilizing generalized continuum mechanics such as models which include higher gradients of displacement and additional material parameters. By using higher-gradient models, it is possible to model the structure as a homogenized domain and with a rather coarse mesh. Therefore, such a macro-scale model is capable of correctly modeling a complex structure at a low computational cost.

Metamaterials are a group of architected materials with peculiar properties (Barchiesi et al, 2019; Eugster et al, 2019; Surjadi et al, 2019). They usually have a complex and detailed microstructure. The behavior of metamaterials in macro-scale is a result of their underlying microstructure. This microstructure is purposely designed to result in a specific performance in the structure. This performance is usually independent of the material from which the microstructure is made (Giorgio et al, 2021). Examples of metamaterials are structures with negative Poisson's ratio (Larsen et al, 1997; Jafari Nedoushan et al, 2021), locally resonant plates (Russillo and Failla, 2021), and pantographic structures which are capable of undergoing large deformations in the elastic regime (dell'Isola et al, 2015, 2019a,b).

In the literature, many models have been presented for modeling pantographic structures (for a review, see Placidi et al, 2016; Barchiesi and Placidi, 2017). An important issue is determining the parameters of a model for a specific structure. Numerical parameter identification studies have been carried out in Giorgio (2016); De Angelo et al (2019); Shekarchizadeh and Abedi (2019). In Abali and Barchiesi (2021), an asymptotic homogenization is used to determine the parameters for describing a material on a macroscopic level.

In a recent study (Shekarchizadeh et al, 2021a), a method is proposed for inverse analysis and numerical parameter determination of metamaterials through an automated optimization algorithm. In this algorithm, the parameters of a macroscopic model are determined by fitting the strain energy of the macro-scale model with that of the microscopic solution of the problem. With the determined parameters, the model predicts the deformation of a pantographic structure in a tensile test accurately. In that paper, the loading is quasi-static.

In a subsequent research (Shekarchizadeh et al, 2021b), the identified parameters are validated for the dynamic regime. The displacement plots are compared with experimental results which are obtained by applying forced oscillations to pantographic specimens made by 3D-printing technology. The cyclic loading is simulated in the computations for different frequency ranges. The outcome is that the simulations are matching the dynamic experimental tests in some frequency ranges while in some other ranges, especially close to the eigenfrequencies, the computations are deviating.

In the problems in the dynamic regime, the higher-order inertia is usually ignored since the experimental characterization of such inertial terms is not yet understood. Hence, so far there is no clear algorithm for determining the values of higher-order inertial parameters. The theory of including such terms is presented in Polizzotto (2013a,b); Abali (2018). In Shekarchizadeh et al (2021b), a higher-order term is included in the model to investigate the effect. The values of the new term are chosen arbitrarily. The results show that the new term introduced in the model has a noticeable effect and in some cases, it makes the results closer to the experimental data.

We herein consider a homogenized second-gradient model for pantographic structures. We study the behavior of the model with the identified parameters in a range of frequencies of sinusoidal loading. The frequency range includes the eigenfrequency of the structure. Furthermore, the effect of adding a higher-order inertial term to the model is investigated more deeply by considering different values for it. We try to perceive the behavior of the model with respect to the value considered for the new inertial term. We aim to gain an insight into the characterization of such complex inertial parameters.

28.2 Model Implementation

The macroscopic model presented in dell’Isola et al (2016) is a 2D description of planar pantographic structures. The pantographic structure consists of two families of parallel beams and cylindrical pivots which connect the beams together as shown in Fig. 28.1. The reduced-order model considers the structure as a homogenized plate. Second-gradients of displacement are present in the model. The energy definition takes into account the deformation energy of the elongation of the beams, the in-plane bending of the beams, and the twisting shear of the pivots. The stored energy density is expressed as

$$W_M(\boldsymbol{\varepsilon}, \boldsymbol{\kappa}, \gamma) = \frac{1}{2}K_e(\varepsilon_1^2 + \varepsilon_2^2) + \frac{1}{2}K_g(\kappa_1^2 + \kappa_2^2) + \frac{1}{2}K_s\gamma^2, \quad (28.1)$$

where $\boldsymbol{\varepsilon}$, $\boldsymbol{\kappa}$, γ are the “stretch of fibers”, the “beam geodesic curvature”, and the shear distortion of the pivots, respectively. The term $\boldsymbol{\kappa}$ includes second-gradient of displacement terms. For the detailed formulation of the above-mentioned parameters, see Shekarchizadeh et al (2021a). The model has three parameters, K_e , K_g , K_s , namely the stretching, the geodesic bending, and the shear stiffness values.

By using the variational principle, the discretized weak form of the governing equation of the problem is obtained as

$$\int_{\mathcal{B}_0} \left(-\rho_0 \frac{u_i - 2u_i^0 + u_i^{00}}{\Delta t \Delta t} \delta u_i - \frac{\partial W_M(\varepsilon, \boldsymbol{\kappa}, \gamma)}{\partial u_{i,j}} \delta u_{i,j} - 2\rho_0 d^2 \frac{u_{i,j} - 2u_{i,j}^0 + u_{i,j}^{00}}{\Delta t \Delta t} \delta u_{i,j} \right) dV + \int_{\partial \mathcal{B}_0^N} \hat{t}_i \delta u_i dA = 0, \quad (28.2)$$

where u_i is the primary variable of the equation, i.e. the displacement field over the domain \mathcal{B}_0 , δu_i is the test function, Δt is the time increment, \hat{t}_i is the traction applied on the Neumann boundary $\partial \mathcal{B}_0^N$, ρ_0 is the structure's surface mass density, and d is the added higher-order inertial term, which is a length scale (unit of length).

The geometrical parameters and the material of the pantographic structure are the same as the ones used in Shekarchizadeh et al (2021b). By following the procedure elaborated in Shekarchizadeh et al (2021a), the three unknown stiffnesses in Eq. (28.1) are determined for the considered pantographic structure as $K_e = 2.847 \times 10^5$ N/m, $K_g = 3.697 \times 10^{-2}$ Nm, and $K_s = 8.160 \times 10^2$ N/m.

For the numerical implementation of the model, we employ the finite element method in the FEniCS open-source package (Logg et al, 2012). For a discussion on the engineering applications of FEniCS, see Abali (2017). The domain is a rectangular plate meshed with standard FEM elements with quadratic polynomial form functions constituting the vector space

$$\mathcal{V} = \left\{ \{u_x, u_y\} \in [\mathcal{H}^2(\mathcal{B})]^2 : \{u_x, u_y\} \Big|_{\partial \mathcal{B}_0^D} = \text{given} \right\}, \quad (28.3)$$

where the displacement is given on the so-called DIRICHLET boundaries, $\partial \mathcal{B}_0^D$. After an h -convergence analysis, the FEM mesh of 308,482 degrees of freedom has been used. For time discretization, each sinusoidal period of loading is applied in 48 time increments.

As shown in Fig. 28.1, the lower side of the rectangular domain is fixed in x and y directions, and the upper edge is fixed in the x direction while a sinusoidal forced oscillation is applied on it to simulate a cyclic loading as

$$u_y = A \sin(2\pi ft), \quad (28.4)$$

where A is the amplitude of loading, f is the frequency of loading over time, t . We set the amplitude of loading, $A = 3.0 \times 10^{-4}$ m for all the simulations. The loading is continued for five cycles to make sure that the solution has reached a steady state.

We run the simulations separately for all the frequencies of the range, $f = \{80, 81, 82, \dots, 198, 199, 200\}$ Hz. In addition, the same simulations are repeated with different values for the higher-order inertial term d in Eq. (28.2). We choose the arbitrary values for d as $d = \{0.0, 0.005, 0.01, 0.015, 0.02\}$ m. Based on the eigenfrequency identification study in Laudato et al (2020), we expect that the selected frequency range (80-200 Hz) includes one or more eigenfrequencies of the structure. Our goal is to determine the behavior of the model in detecting the eigenfrequencies and also the effect of the value of the higher-order inertia on the observed eigenfrequency. This study is an effort to acquire an understanding of the

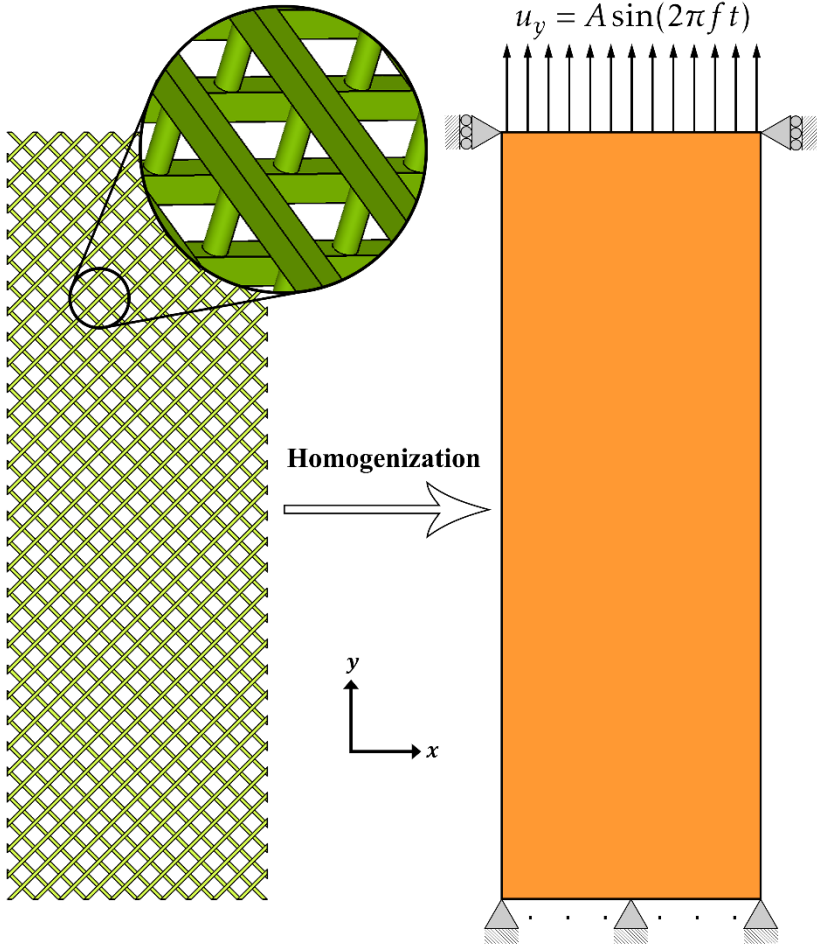


Fig. 28.1 The pantographic structure (left), and the boundary conditions applied on the homogenized plate (right)

characterization of the higher-order inertial terms and their role in a process since the experimental characterization of such inertial terms is not yet resolved.

28.3 Results and Discussion

In the following, the results of the simulations are presented. The solutions of the numerical analyses are saved in PVD files. For visualization and post-processing

the results, we utilize the Paraview open-source package (Ahrens et al, 2005). A python script is generated for post-processing of all the PVD files in Paraview. Each solution file includes the displacement field for a specific frequency of loading and a higher-order inertial term. For each case, the so-called gain is extracted in x and y directions separately. We define the gain- x and gain- y as the maximum displacement that has happened in the domain \mathcal{B} in x and y directions, respectively.

We plot the gain versus the frequency of the dynamic loading. The plotted gain is normalized with respect to the starting point of the graph therefore each graph begins from the value 1. Figure 28.2 shows the gain- y for five different values of the higher-order inertial term d in Eq. (28.2). The first case is $d = 0.0$ m, which is equivalent to not considering any higher-order inertia in the model. Two peaks are visible for each d which are known as the eigenfrequencies of the structure given by the computations. In fact, in the eigenfrequencies, the gain is expected to go to infinity but here we see finite peak values which is due to the numerical viscosity as a matter of the time discretization.

The values of the frequencies of the first and second peaks of the plot in Fig. 28.2, denoted by f_1 and f_2 , respectively, are compiled in Table 28.1. A noticeable pattern is visible in Fig. 28.2 and Table 28.1: the larger the term d is, the less the eigenfrequencies are. This meaningful relation can lead to an approach for detecting the higher-order inertial term experimentally in future studies. Figure 28.3 shows the gain- x for five different values of the higher-order inertial term d . Comparing Fig. 28.3 with Fig. 28.2, the same pattern is seen for the relation between the eigenfrequency and the term d .

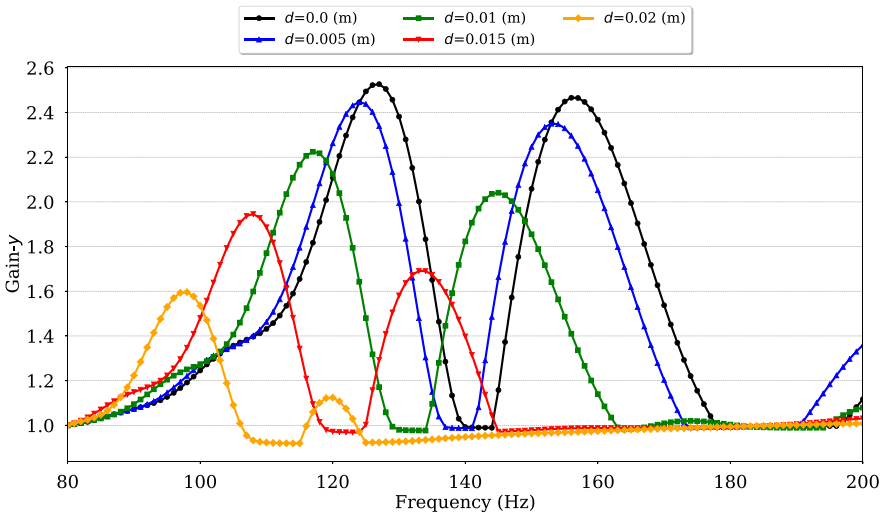


Fig. 28.2 The gain in y direction versus the frequency of loading for different values of the higher-order inertial term d in Eq. 28.2

Table 28.1 The first, f_1 , and second, f_2 , eigenfrequencies from Figs. 28.2 and 28.3 and their ratio, f_2/f_1

| d (m) | f_1 (Hz) | f_2 (Hz) | f_2/f_1 |
|---------|------------|------------|-----------|
| 0.0 | 127 | 156 | 1.23 |
| 0.005 | 124 | 153 | 1.23 |
| 0.01 | 117 | 145 | 1.24 |
| 0.015 | 108 | 133 | 1.23 |
| 0.02 | 98 | 120 | 1.22 |

The ratio of the second eigenfrequency to the first one (f_2/f_1) from Figs. 28.2 and 28.3 is reported in Table 28.1. The change in the eigenfrequency ratio is less than 1% for different values of d . This change might be due to the numerical discretization. We consider the hypothesis that the f_2/f_1 is constant, and we make a deeper study around the eigenfrequencies to see if this hypothesis is proved. We repeat the simulations with a finer step of frequency (0.25 Hz) around the f_1 and f_2 values. Therefore, we obtain more precise values for the eigenfrequencies f_1 and f_2 . The results are presented in Table 28.2.

In Table 28.2, for each d value, the eigenfrequencies are equal in x and y directions except in some cases that we see minor differences. Moreover, there still exists slight variation in the f_2/f_1 ratio. We need to investigate more deeply these two intriguing aspects, either from a theoretical point of view, or from a numerical one. For example, we may choose a finer discretization of time in the simulations, in order to understand if the peaks appear exactly at same frequencies in x and y directions and if the f_2/f_1 ratio is constant with respect to d . The equality of eigenfrequencies in x and y directions could match what we expect, since all the displacement components are simultaneously affected by the vibrations happening in the structure close to the eigenfrequencies.

Table 28.2 The first, f_1 , and second, f_2 eigenfrequencies, in x and y directions, with higher precision, and their ratio, f_2/f_1

| d (m) | x direction | | | y direction | | |
|---------|---------------|------------|-----------|---------------|------------|-----------|
| | f_1 (Hz) | f_2 (Hz) | f_2/f_1 | f_1 (Hz) | f_2 (Hz) | f_2/f_1 |
| 0.0 | 126.75 | 156.50 | 1.235 | 126.75 | 156.50 | 1.235 |
| 0.005 | 124.00 | 153.25 | 1.236 | 124.25 | 153.25 | 1.233 |
| 0.01 | 117.00 | 144.75 | 1.237 | 117.25 | 144.75 | 1.234 |
| 0.015 | 107.75 | 133.50 | 1.239 | 107.75 | 133.25 | 1.237 |
| 0.02 | 97.50 | 120.25 | 1.233 | 97.75 | 120.00 | 1.228 |

We should mention that in this study we have not studied the phase shift between the input and output of the model. For all the frequencies, the gain values are read at the same time step, i.e. at the peak of the last cycle of loading. The discussion of the phase shift is left to further studies.

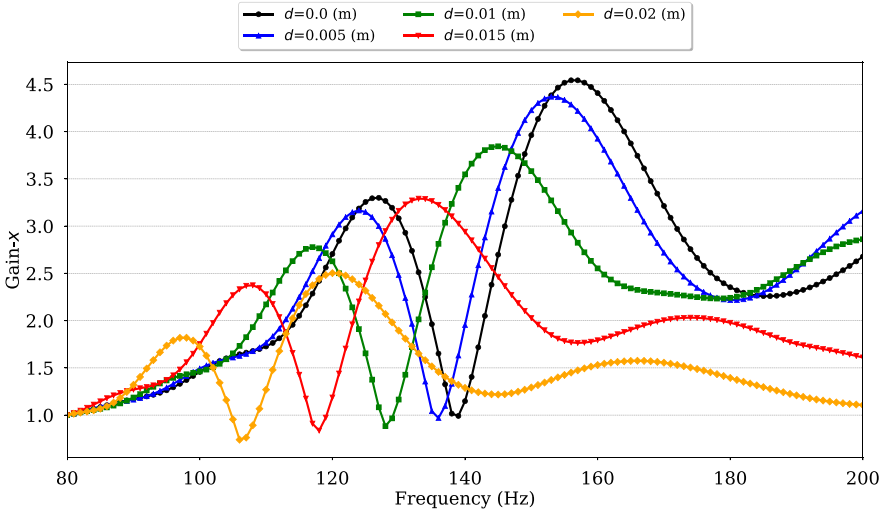


Fig. 28.3 The gain in x direction versus the frequency of loading for different values of the higher-order inertial term d in Eq. 28.2

28.4 Conclusion

In this work, a macro-scale homogenized model is considered for a metamaterial and the parameters of the model are identified through an optimization algorithm. Then, the model is utilized for simulating a dynamic loading on the structure. Moreover, the effect of adding a higher-order inertial term to the formulation is studied. The simulations are carried out for a range of frequencies of loading and also for a number of arbitrary values for the higher-order inertial term. From the results, we perceive that the larger the value of the higher-order inertial term is assumed, the lower the eigenfrequencies are seen in the plots. This result sheds light on the topic of higher-order inertia which still has not been characterized experimentally in the literature.

Acknowledgements The work illustrated in this paper is part of N. Shekarchizadeh's thesis for the Ph.D. course in "Mathematical Models for Engineering, Electromagnetism and Nanosciences" at Sapienza University of Rome.

References

- Abali BE (2017) Computational Reality, *Advanced Structured Materials*, vol 55. Springer Nature, Singapore
- Abali BE (2018) Revealing the physical insight of a length scale parameter in metamaterials by exploring the variational formulation. *Continuum Mechanics and Thermodynamics* 31(4):885–894
- Abali BE, Barchiesi E (2021) Additive manufacturing introduced substructure and computational determination of metamaterials parameters by means of the asymptotic homogenization. *Continuum Mechanics and Thermodynamics* 33(4):993–1009
- Ahnes J, Geveci B, Law C (2005) ParaView: An end-user tool for large data visualization. *The visualization handbook* 717
- Barchiesi E, Placidi L (2017) A review on models for the 3d statics and 2d dynamics of pantographic fabrics. In: Sumbatyan MA (ed) *Wave Dynamics and Composite Mechanics for Microstructured Materials and Metamaterials*, Springer Singapore, Singapore, pp 239–258
- Barchiesi E, Spagnuolo M, Placidi L (2019) Mechanical metamaterials: a state of the art. *Mathematics and Mechanics of Solids* 24(1):212–234
- De Angelo M, Barchiesi E, Giorgio I, Abali BE (2019) Numerical identification of constitutive parameters in reduced-order bi-dimensional models for pantographic structures: application to out-of-plane buckling. *Archive of Applied Mechanics* 89(7):1333–1358
- dell'Isola F, Lekszycki T, Pawlikowski M, Grygoruk R, Greco L (2015) Designing a light fabric metamaterial being highly macroscopically tough under directional extension: first experimental evidence. *Zeitschrift für angewandte Mathematik und Physik* 66(6):3473–3498
- dell'Isola F, Giorgio I, Pawlikowski M, Rizzi NL (2016) Large deformations of planar extensible beams and pantographic lattices: heuristic homogenization, experimental and numerical examples of equilibrium. *Proceedings of the Royal Society A: Mathematical, Physical and Engineering Sciences* 472(2185):20150,790
- dell'Isola F, Sepecher P, Alibert JJ, Lekszycki T, Grygoruk R, Pawlikowski M, Steigmann D, Giorgio I, Andraus U, Turco E, Golaszewski M, Rizzi N, Boutin C, Eremeyev VA, Misra A, Placidi L, Barchiesi E, Greco L, Cuomo M, Cazzani A, Corte AD, Battista A, Scerrato D, Eremeeva IZ, Rahali Y, Ganghoffer JF, Müller W, Ganzosch G, Spagnuolo M, Pfaff A, Barcz K, Hoschke K, Neggens J, Hild F (2019a) Pantographic metamaterials: an example of mathematically driven design and of its technological challenges. *Continuum Mechanics and Thermodynamics* 31(4):851–884
- dell'Isola F, Sepecher P, Spagnuolo M, Barchiesi E, Hild F, Lekszycki T, Giorgio I, Placidi L, Andraus U, Cuomo M, Eugster SR, Pfaff A, Hoschke K, Langkemper R, Turco E, Sarikaya R, Misra A, De Angelo M, D'Annibale F, Bouterf A, Pinelli X, Misra A, Desmorat B, Pawlikowski M, Dupuy C, Scerrato D, Peyre P, Laudato M, Manzari L, Göransson P, Hesch C, Hesch S, Franciosi P, Dirrenberger J, Maurin F, Vangelatos Z, Grigoropoulos C, Melissinaki V, Farsari M, Muller W, Abali BE, Liebold C, Ganzosch G, Harrison P, Drobnicki R, Igunnov L, Alzahrani F, Hayat T (2019b) Advances in pantographic structures: design, manufacturing, models, experiments and image analyses. *Continuum Mechanics and Thermodynamics* 31(4):1231–1282
- Eugster SR, dell'Isola F, Steigmann D (2019) Continuum theory for mechanical metamaterials with a cubic lattice substructure. *Mathematics and Mechanics of Complex Systems* 7(1):75–98
- Giorgio I (2016) Numerical identification procedure between a micro-cauchy model and a macro-second gradient model for planar pantographic structures. *Zeitschrift für angewandte Mathematik und Physik* 67(4):95
- Giorgio I, Spagnuolo M, Andraus U, Scerrato D, Bersani AM (2021) In-depth gaze at the astonishing mechanical behavior of bone: A review for designing bio-inspired hierarchical metamaterials. *Mathematics and Mechanics of Solids* 26(7):1074–1103
- Jafari Nedoushan R, An Y, Yu WR, Abghary MJ (2021) Novel triangular auxetic honeycombs with enhanced stiffness. *Composite Structures* 277:114,605

- Larsen U, Sigmund O, Bouwstas S (1997) Design and fabrication of compliant micromechanisms and structures with negative poisson's ratio. *Journal of Microelectromechanical Systems* 6(2):99–106
- Laudato M, Manzari L, Scerrato D, Göransson P, Giorgio I (2020) Spectral properties of 2d pantographic metamaterial: Experimental results. *Mechanics Research Communications* 109:103,613
- Logg A, Mardal KA, Wells G (2012) Automated solution of differential equations by the finite element method: The FEniCS book, vol 84. Springer
- Placidi L, Barchiesi E, Turco E, Rizzi NL (2016) A review on 2d models for the description of pantographic fabrics. *Zeitschrift für angewandte Mathematik und Physik* 67(5):121
- Polizzotto C (2013a) A second strain gradient elasticity theory with second velocity gradient inertia—part i: Constitutive equations and quasi-static behavior. *International Journal of Solids and Structures* 50(24):3749–3765
- Polizzotto C (2013b) A second strain gradient elasticity theory with second velocity gradient inertia—part ii: Dynamic behavior. *International Journal of Solids and Structures* 50(24):3766–3777
- Russillo AF, Failla G (2021) A novel reduced-order dynamic-stiffness formulation for locally resonant metamaterial plates. *Composite Structures* p 114811
- Shekarchizadeh N, Abedi M (2019) Determining the constitutive parameters of a macro-scale second-gradient model for planar pantographic structures by using optimization algorithms. *Proceedings of 8th GACM Colloquium on Computational Mechanics: For Young Scientists From Academia and Industry* pp 31–34
- Shekarchizadeh N, Abali BE, Barchiesi E, Bersani AM (2021a) Inverse analysis of metamaterials and parameter determination by means of an automatized optimization problem. *ZAMM - Journal of Applied Mathematics and Mechanics / Zeitschrift für Angewandte Mathematik und Mechanik* 101(8):e202000,277
- Shekarchizadeh N, Laudato M, Manzari L, Abali BE, Giorgio I, Bersani AM (2021b) Parameter identification of a second-gradient model for the description of pantographic structures in dynamic regime. *Zeitschrift für angewandte Mathematik und Physik* 72(6):190
- Surjadi JU, Gao L, Du H, Li X, Xiong X, Fang NX, Lu Y (2019) Mechanical metamaterials and their engineering applications. *Advanced Engineering Materials* 21(3):1800,864



Chapter 29

Structural Analysis of Doubly-Curved Shells with General Boundary Conditions

Francesco Tornabene, Matteo Viscoti, Rossana Dimitri

Abstract The paper focuses on a bi-dimensional (2D) formulation for the dynamic and static analysis of arbitrary shaped laminated doubly-curved shells enforced with general boundary conditions via the Generalized Differential Quadrature (GDQ). Following the Equivalent Single Layer approach, a 2D theory based on a miscellaneous assessment of the displacement field variable is provided, accounting for different higher order theories. The geometry of the structure is described with a set of principal coordinates. The fundamental equations are derived from the Hamiltonian principle, together with the natural boundary conditions. Unconventional constraints are assessed by means of in-plane and out-of-plane sets of linear elastic springs distributed along the shell edges. The accuracy of the formulation is outlined by means of a series of validating examples. Doubly-curved shells of variable thickness and different curvatures enforced with non-conventional boundary conditions are investigated. In particular, mode frequencies and shapes, as well as the static three-dimensional deflection of the structure, have been calculated employing different kinematic assumptions. The results have been successfully compared to predictions by high-computationally demanding Finite Element simulations. The methodology outlined in this chapter well predicts with a reduced computational effort both the static and the dynamic response of generally anisotropic laminated structures embedding all the effects that are usually depicted by 3D formulations.

Keywords: Doubly-curved shells · Anisotropic materials · Generalized Differential Quadrature (GDQ) · General boundary conditions

F. Tornabene, M. Viscoti, R. Dimitri
School of Engineering, University of Salento, Via per Monteroni, Lecce, Italy
e-mail: francesco.tornabene@unisalento.it, matteo.viscoti@unisalento.it,
rossana.dimitri@unisalento.it

29.1 Introduction

In the last years new insights in many engineering fields have been endeavoured, and even more complex structures have been usually required in disparate applications (Pilato and Michno, 1994). In this perspective, new issues have found their way in the scientific debate, namely to the structural assessment of generally-shaped structures with various geometric features, as well as non conventional mechanical properties (Vasiliev and Morozov, 2018). It is well-known that doubly-curved shell structural theories are the most comprehensive modelling strategies for a wide range of applications (Reddy et al, 1997). Among literature, they are commonly developed essentially following three-different main approaches: the three-dimensional strategy (Sokolnikoff et al, 1956), the bi-dimensional Layer-Wise model (Li, 2021; Tornabene et al, 2022), and the bi-dimensional Equivalent Single Layer (ESL) approach (Reddy, 1993; Demasi et al, 2017). With particular reference to ESL, all the geometric, kinematic and mechanical parameters are reduced to a 2-manifold located at the middle thickness of the structure (Tu, 2017). The accuracy of the simulation lies on a proper selection of the field variables along the normal direction to the middle surface. As a matter of fact, classical approaches like the First Order Shear Deformation Theory (FSDT) developed by Reissner (1945) and Mindlin (1951), as well as the Third Order Shear Deformation Theory (TSDT) by Reddy (1984) assume a linear and a cubic expression for in-plane displacement components, respectively, whereas a constant out-of-plane one is assessed. It has been shown that such axiomatic assumptions are very likely to yield erroneous results when innovative and pantographic materials (Giorgio, 2021; Giorgio et al, 2017) are embedded in the structure employing the continuum hypothesis (Tornabene et al, 2021b), since lattice elements behave like a softcore in the lamination sequence (Ganzosch et al, 2017). Actually, significant warping and stretching phenomena can be seen in the bending deflection, as it has been shown by dell'Isola et al (2015); Giorgio et al (2021) following both numerical and experimental approaches. Nevertheless, formulations with a higher order description of the displacement field components have been provided. Moreover, the definition of the shape function can be done starting from the actual lamination scheme shear properties that has been adopted in the shell object of analysis (Tessler et al, 2009) in order to seek the actual shear mechanical behaviour of the structure.

In Wang et al (2021) a comprehensive weak formulation employing a power series expansion of the kinematic field variables accounts for the static behaviour of rectangular plates of uncompressive Hookean materials. Another interesting issue is the assessment of the coupling effects occurring between two adjacent laminae within an ESL framework, since interlaminar effects are determining during the design of laminated structures in order to avoid the delamination phenomenon (Gürdal et al, 1999). Generally speaking, both classical and higher order approaches are not capable of well predicting the structural response in the interlaminar region as abrupt variations of stiffnesses occur at the interface between two layers. As a matter of fact, a layer coupling cannot be properly described unless a significative higher order power expansion of smooth functions is performed. To solve this issue, the so-called zigzag functions have been proposed in literature, accounting for a discontinuous

variation of the field variable. In this way, all these very complex issues can be well described employing a reduced number of Degrees of Freedom (DOFs). In the work by Toledano and Murakami (1987) and Murakami (1986) it is shown that this trick allows to catch very complex shear effects occurring in laminated structures, which can be prominent in many laminated appliances (the interested reader can refer to Whitney, 1969; Whitney and Pagano, 1970). Apart from first pioneering works concerning isotropic and non-homogeneous stacking sequences, several works can be found in literature where formulations for orthotropic materials have been presented, like that of Wang and Redekop (2005). On the other hand, there are few works investigating the problem of laminated structures infilled with generally anisotropic materials, accounting for all the possible coupling effects between static and kinematic quantities. In Tornabene et al (2011) a bi-dimensional model has been developed for the dynamic analysis of doubly-curved shells accounting for very innovative materials. Actually, we mention some research referred to FGM (Tornabene and Reddy, 2013; Ansari and Darvizeh, 2008) CNTs (Tornabene et al, 2019), honeycomb and lattice structures (Tornabene et al, 2021a). In particular, it is shown that the employment of very complex infills within the stacking sequence can dramatically orient both the local and global structural response of the structure. Moreover, when a suitable formulation for generally anisotropic materials is provided, disparate homogenized material syngonies can be easily modelled employing a reduced number of design parameters since the formulation turns out to be a particular case of the generalized one. As a matter of fact, when very complex shapes and materials are considered, the proper selection of the thickness functions set allows to catch with success typically three-dimensional effects even with a 2D ESL formulation (Tornabene et al, 2021c).

Once the structural model is developed, the accuracy of the simulation is dramatically affected by the numerical assessment of the developed theoretical formulation. The classical Finite Element Method (FEM) has largely demonstrated to be very reliable in many applications, due to its high efficiency and stability (Zienkiewicz et al, 1977). Belonging to the class of the weighted residual numerical technique (Finlayson and Scriven, 1966), it provides a weak formulation of the differential problem based on a local a-priori interpolation of the unknown field variable. On the other hand, no higher order continuity is contemplated between two adjacent elements. In addition, the discretization of the physical continuum model accounts for a discrepancy between the designed object shape and that of the computational model. Besides, the class of spectral collocation methods (Tornabene et al, 2015b) accounts for an interpolation procedure of the unknown field variable performed alongside the entire computational domain. Among these, the Generalized Differential Quadrature (GDQ) Method is the best performing algorithm for the numerical assessment of structural problems concerning laminated anisotropic doubly-curved shells. Based on a higher order Lagrange polynomials-based procedure (Tornabene and Bacciocchi, 2018), it has been applied to a series of doubly-curved structures of complex shapes and stacking sequences. It has been shown that it can provide very accurate results with respect to refined model employing a significative reduced number of DOFs with respect to other numerical techniques (Fazzolari et al, 2021). Since the GDQ Method accounts for a squared computational domain, when shells

of arbitrary shape are investigated it is possible to perform a distortion of the geometry via the implementation of a proper set of blending functions employing a Non Uniform Rational B-Spline (NURBS) formulation, as extensively adopted in the Computer Aided Design (CAD) methodology (Piegl, 1991). In the case of structural problems with singularities (Dimitri et al, 2018), the local version of the GDQ Method (Tornabene et al, 2016b) has been demonstrated to be an appropriate tool. We recall some works on fracture mechanics (Dimitri and Tornabene, 2018) and discontinuities (Dimitri et al, 2016), among others, where a GDQ formulation has been adopted. Last but not least, this innovative computational model is applied also for time-stepping analyses (see among others Bellman and Casti, 1971; Tornabene et al, 2016a). It has been demonstrated that the accuracy of the GDQ numerical technique comes from the computation of the quadrature weighted coefficients (Shu and Richards, 1992), as well as the selection of the computational grid (Shu et al, 2001). In the case of bi-dimensional domains, some considerations should be taken on the implementation of the natural boundary conditions at the corners (see Shu and Du, 1997b; Brischetto et al, 2017). In the case of structural problems embedding very complex shapes, sometimes the computational domain should be properly patched (Viola et al, 2013), therefore the compatibility conditions should be fulfilled between two adjacent elements as well. As far as the external constraints on bi-dimensional curved structures is concerned, a general methodology is required for the assessment of the boundary conditions of the structural problem. The FEM procedure simply accounts for the limitation of the desired DOFs in a selected set of nodes. In Wang et al (2018), some cylindrical panels have been considered with a localized clamped boundary condition. Accordingly, in the work by Shu and Du (1997a) an innovative method is proposed for the assessment of external elastic constraints by means of a set of linear elastic springs within the GDQ implementation. In this way it is possible to assess generalized external constraints, accounting for a clamping only of a portion of the structure, or providing a smooth continuous variation of the external bonding in-plane and out-of-plane stiffness.

Generally speaking, when the static performance is studied by means of bi-dimensional models, the exact three-dimensional structural response is not well predicted in terms of both kinematic and mechanical quantities due to the approximating hypothesis hold on the through-the-thickness field variable. For this reason, a reconstruction of both stresses and strains is generally introduced. In Paton et al (2021) a stress recovery methodology based on the equilibrium equations is performed employing a composite trapezoidal rule for the numerical integration throughout the structure width. In Katili et al (2017) the three-dimensional profiles of stresses has been recovered employing various procedures from the outcomes of a Finite Element formulation employing bi-dimensional elements developed for the analysis of thin and thick plates and shells via the Naghdi shell model (Chapelle and Bathe, 1998). In particular, the Averaging Method, the Projection Method and the Superconvergent Patch Recovery have been checked for the continuity assessment of stresses from one element to the other. In Rah et al (2012) a very accurate method for the reconstruction of stresses and strains profiles is developed employing solid-shell elements. On the other hand, in classical Finite Element simulations employing brick

elements, stresses are calculated at the internal integration points and then they are extrapolated at the interface between two adjacent elements, which usually coincides with the interface between two adjacent laminae. On the other hand, in the work by Tornabene et al (2015a) an innovative recovery procedure has been developed for a bi-dimensional layerwise simulation held on doubly-curved structures, whereas in Tornabene et al (2012) the same procedure has been presented in a ESL framework.

In the present Chapter an ESL formulation is presented for the static and the free vibration analysis of doubly-curved shell structures with variable thickness. The geometry of the structure is described in terms of principal curvilinear coordinates defined from the geometric properties of the reference middle surface. Moreover, a generalized NURBS-based mapping procedure is implemented so that arbitrary shaped structures can be taken into account as well. A displacement field-based theory has been presented, accounting for a unified formulation of each three-dimensional field variable component. Namely, a higher order polynomial assumption has been adopted, as well as classical approaches like FDST and TSDT. The fundamental governing equations, derived from the variational form of the Hamiltonian principle, are numerically tackled with the GDQ Method, setting a rectangular non-uniform grid alongside the computational domain. A lamination scheme characterized by a generic orientation of each lamina is accounted in the model. In the same way, within each layer a three-dimensional generally anisotropic stiffness matrix has been implemented. A generalized set of external boundary conditions has been developed, employing a non-uniform dispersion of linear elastic springs that can be effectively assessed in both in-plane and out-of-plane components. Moreover, natural external constraints have been considered too. Despite the formulation is provided for the dynamic problem, the static formulation eventually comes out by neglecting the inertial properties of the structure object of analysis. An efficient reconstruction of the through-the-thickness stress distribution has been considered, accounting for the exact fulfilment of the compatibility between stresses and applied external loads. A series of validating examples have been presented, in which mode frequencies and the corresponding mode shapes have been calculated for structures characterized by different curvatures and lamination schemes under different external boundary conditions. The influence of the shell distortion via NURBS curves has been considered too, accounting for different shapes of the physical domain. After that, the same structures have been subjected to surface elastic loads, and the deflection of the shell has been outlined. An efficient reconstruction of the three-dimensional stress and strain distributions along the three-dimensional solid led to a three-dimensional assessment of the proposed bi-dimensional static formulation. The results have been compared to that provided by a refined FEM simulation developed with 20 nodes brick elements, showing an excellent agreement between predictions from different approaches. Last but not least, the GDQ formulation accounts for an efficient model involving a reduced number of DOFs, such that it can be considered as a valid alternative to many common commercial software packages for the static and dynamic analysis of curved and layered structures. The research work is included within the DiQuMASPAB project (Tornabene et al, 2018), a research software which embeds

several GDQ tools for the static and dynamic analysis of shell structures infilled with innovative laminated materials.

29.2 Geometrical Representation of Shells in Principal Coordinates

A doubly-curved shell is a three-dimensional structure, whose arbitrary point can be defined by its position vector \mathbf{R} . If we denote with $Ox_1x_2x_3$ the global coordinate system of the Euclidean space defined from the unit vectors $\mathbf{e}_1, \mathbf{e}_2, \mathbf{e}_3$, the following relation can be assessed (Fig. 29.1)

$$\mathbf{R}(\alpha_1, \alpha_2, \alpha_3) = \sum_{i=1}^3 f_i(\alpha_1, \alpha_2, \alpha_3) \mathbf{e}_i \quad (29.1)$$

where $\alpha_1, \alpha_2, \alpha_3$ accounts for the three parameters required for the representation of the three-dimensional solid. If we introduce the so-called reference surface $\mathbf{r}(\alpha_1, \alpha_2)$, it is possible to turn Eqn. (29.1) as follows (Tornabene and Bacciocchi, 2018):

$$\mathbf{R}(\alpha_1, \alpha_2, \alpha_3) = \mathbf{r}(\alpha_1, \alpha_2) + \frac{h(\alpha_1, \alpha_2)}{2} z \mathbf{n}(\alpha_1, \alpha_2) \quad (29.2)$$

Thus, the parametrization of Eqn. (29.1) can be identified with the in-plane principal coordinates α_1, α_2 of the reference surface \mathbf{r} , whereas the remaining one can be taken along the thickness of the shell, setting the dimensionless parameter $z = 2\zeta/h(\alpha_1, \alpha_2)$ where $\alpha_3 = \zeta$. Actually, it should be noticed that $z \in [-1, 1]$. For the sake of completeness, a graphic representation of what exerted in Eqn. (29.2) can be found in Fig. 29.1. A physical significance is provided to the ESL shell description outlined in Eqn. (29.2) setting $(\alpha_1, \alpha_2) \in [\alpha_1^0, \alpha_1^1] \times [\alpha_2^0, \alpha_2^1]$ and $\zeta \in [-h/2, h/2]$. Accordingly, the normal unit vector $\mathbf{n}(\alpha_1, \alpha_2)$ can be defined starting from the partial derivatives of $\mathbf{r}(\alpha_1, \alpha_2)$ with respect to in-plane coordinates, setting $\partial \mathbf{r} / \partial \alpha_i = \mathbf{r}_{,i}$ for $i = 1, 2$,

$$\mathbf{n} = \frac{\mathbf{r}_{,1} \times \mathbf{r}_{,2}}{|\mathbf{r}_{,1} \times \mathbf{r}_{,2}|} \quad (29.3)$$

The geometric assessment of the shell according to Eqn. (29.1) is referred to a set of coordinates taken along the principal parametric lines of $\mathbf{r}(\alpha_1, \alpha_2)$. Accordingly, the main curvature radii R_1, R_2 can be computed in each (α_1, α_2) point of \mathbf{r} as follows:

$$R_i(\alpha_1, \alpha_2) = -\frac{\mathbf{r}_{,i} \cdot \mathbf{r}_{,i}}{\mathbf{r}_{,ii} \cdot \mathbf{n}} \quad \text{for } i = 1, 2 \quad (29.4)$$

where $\mathbf{r}_{,ij} = \partial^2 \mathbf{r} / (\partial \alpha_i \partial \alpha_j)$ for $i, j = 1, 2$ denotes the second order derivatives with respect to in-plane coordinates α_1, α_2 . Moreover, the thickness parameter $H_i(\alpha_1, \alpha_2, \zeta)$ for $i = 1, 2$ accounts for the curvature effects coming into the varia-

tion of out-of-plane quantities

$$H_i = 1 + \frac{\zeta}{R_i} \quad \text{for } i = 1, 2 \quad (29.5)$$

where $H_i = 1$ for straight structures like rectangular plates. Moreover, Lamè parameters A_1, A_2 of the reference surface $\mathbf{r}(\alpha_1, \alpha_2)$ can be expressed in terms of first order derivatives $\mathbf{r}_{,i}$ for $i = 1, 2$ according to the following expressions:

$$A_1 = \sqrt{\mathbf{r}_{,1} \cdot \mathbf{r}_{,1}}, \quad A_2 = \sqrt{\mathbf{r}_{,2} \cdot \mathbf{r}_{,2}} \quad (29.6)$$

Based on Eqn. (29.2), the shell thickness $h(\alpha_1, \alpha_2)$ can be varied throughout the whole physical domain via the introduction of some analytical expressions $\phi_j(\alpha_1, \alpha_2)$ for $j = 1, \dots, 4$ associated to a set of scaling parameters δ_j and a shift $\bar{\delta}$. Eventually, the dimensionless thickness variation $\bar{\Delta}(\alpha_1, \alpha_2)$ can be assessed to this end, being \bar{h} the reference width of the structure defined directly from the lamination scheme

$$h(\alpha_1, \alpha_2) = \bar{h}\bar{\Delta}(\alpha_1, \alpha_2) = \bar{h} \left(1 + \bar{\delta} + \sum_{j=1}^4 \delta_j \phi_j(\alpha_1, \alpha_2) \right) \quad (29.7)$$

As far as the univariate expressions of $\phi_j(\alpha_1, \alpha_2)$ for $j = 1, \dots, 4$ are concerned, a dimensionless coordinate $\bar{\alpha}_i$ is introduced. In this way, thickness univariate expressions can be written in a consistent way regardless the effective dimensions of shells

$$\bar{\alpha}_i = \frac{\alpha_i - \alpha_i^0}{\alpha_i^1 - \alpha_i^0} \quad \text{for } i = 1, 2 \quad (29.8)$$

In the following, some expressions for each $\phi_j(\alpha_1, \alpha_2)$ are provided. Accordingly, a power and a sinusoidal thickness variation have been considered, setting $n_j \in \mathbb{N}$, $\alpha_{jm} \in [0, 1]$ and $p_j \in \mathbb{R}$ for $j = 1, \dots, 4$,

$$\begin{aligned} \phi_1(\alpha_1) &= \begin{cases} \bar{\alpha}_1^{p_1} \\ (\sin(\pi(n_1\bar{\alpha}_1 + \alpha_{1m})))^{p_1} \end{cases} \\ \phi_2(\alpha_2) &= \begin{cases} \bar{\alpha}_2^{p_2} \\ (\sin(\pi(n_2\bar{\alpha}_2 + \alpha_{2m})))^{p_2} \end{cases} \\ \phi_3(\alpha_1) &= \begin{cases} (1 - \bar{\alpha}_1)^{p_3} \\ (\sin(\pi(n_3(1 - \bar{\alpha}_1) + \alpha_{3m})))^{p_3} \end{cases} \\ \phi_4(\alpha_2) &= \begin{cases} (1 - \bar{\alpha}_2)^{p_4} \\ (\sin(\pi(n_4(1 - \bar{\alpha}_2) + \alpha_{4m})))^{p_4} \end{cases} \end{aligned} \quad (29.9)$$

Referring to each point (α_1, α_2) of the reference surface, the overall thickness h of the bi-dimensional model can be obtained from the superimposition of all the layers

of the stacking sequence, whose total number is denoted with l , as follows:

$$h(\alpha_1, \alpha_2) = \sum_{k=1}^l h_k(\alpha_1, \alpha_2) = \sum_{k=1}^l (\zeta_{k+1}(\alpha_1, \alpha_2) - \zeta_k(\alpha_1, \alpha_2)) \quad (29.10)$$

where $[\zeta_k, \zeta_{k+1}]$ refers to the definition interval along $\alpha_3 = \zeta$ direction of the k -th layer of the stacking sequence according to Eqn. (29.2), setting $k = 1, \dots, l$.

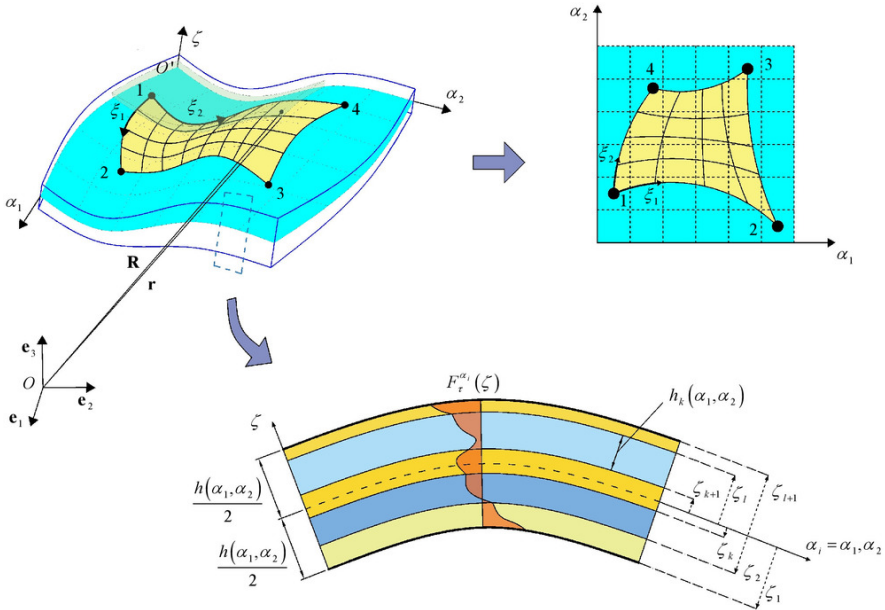


Fig. 29.1 Doubly-curved shell geometry according to the ESL approach. The shell is described starting from the reference surface position vector $\mathbf{r}(\alpha_1, \alpha_2)$ geometrical features. The distortion of the physical domain is defined in terms of NURBS curves so that arbitrary shaped surfaces can be accounted within the formulation. The kinematic field variable is described via the employment of generalized thickness functions $F_r^{\alpha_i}(\zeta)$ for $i = 1, 2, 3$ along the shell thickness.

29.3 ESL Assessment of Kinematic Quantities

In the present section the unknown field variable vector $\mathbf{U}(\alpha_1, \alpha_2, \alpha_3, t) = [U_1 \ U_2 \ U_3]^T$ referred to each point of the three-dimensional structure is analyzed. According to the ESL methodology, for each U_i with $i = 1, \dots, 3$ an axiomatic through-the-thickness distribution is taken so that a bi-dimensional model with 3D capabilities comes out. In this way, a set of displacement field variables $\mathbf{u}_i^{(\tau)}$ is

introduced for each α_i direction and for each τ -th kinematic expansion, together with a set of thickness functions $F_\tau^{\alpha_i}$. Employing a generalized expression of the field variable, one gets

$$\begin{bmatrix} U_1 \\ U_2 \\ U_3 \end{bmatrix} = \sum_{\tau=0}^{N+1} \begin{bmatrix} F_\tau^{\alpha_1} & 0 & 0 \\ 0 & F_\tau^{\alpha_2} & 0 \\ 0 & 0 & F_\tau^{\alpha_3} \end{bmatrix} \begin{bmatrix} u_1^{(\tau)} \\ u_2^{(\tau)} \\ u_3^{(\tau)} \end{bmatrix} \tag{29.11}$$

In a more compact form, Eqn. (29.11) can be written as

$$\mathbf{U}(\alpha_1, \alpha_2, \zeta, t) = \sum_{\tau=0}^{N+1} \mathbf{F}_\tau(\zeta) \mathbf{u}^{(\tau)}(\alpha_1, \alpha_2, t) \tag{29.12}$$

As can be seen, the employment of the ESL methodology allows to introduce the unknown variables \mathbf{u}^τ independently from the thickness coordinate ζ . Actually, they can be considered the DOFs of the bi-dimensional higher order differential problem. The employment of the generalized thickness functions in Eqn. (29.11) provide a generalized formulation of the structural problem, and different analytical expressions can be chosen, according to the assumption that best fits the three-dimensional solution, as shown in Fig. 29.1. In the present work, a set of power polynomial thickness functions has been selected. Moreover, a zigzag function has been adopted for each $\alpha_i = \alpha_1, \alpha_2, \alpha_3$ so that coupling effects between adjacent laminae can be simulated

$$F_{N+1}^{\alpha_i}(\zeta) = (-1)^k z_k = (-1)^k \left(\frac{2}{\zeta_{k+1} - \zeta_k} \zeta - \frac{\zeta_{k+1} + \zeta_k}{\zeta_{k+1} - \zeta_k} \right) \text{ for } i = 1, 2, 3 \tag{29.13}$$

Since different maximum power expansion orders N can be selected, a useful nomenclature is introduced in order to identify the displacement field variable selection. Accordingly, a generic bi-dimensional formulation can be named with EDZ- N , where "E" means that the ESL methodology has been followed in the formulation and "D" tells that the fundamental governing equations have been derived in terms of the unknown kinematic field. "Z" capital letter is introduced if the kinematic zig-zag thickness function of Eqn. (29.13) refers to the $N + 1$ -th order of the kinematic expansion. For instance, the EDZ4 displacement field assumption takes the following form:

$$\begin{aligned} U_1 &= u_1^{(0)} + \zeta u_1^{(1)} + \zeta^2 u_1^{(2)} + \zeta^3 u_1^{(3)} + \zeta^4 u_1^{(4)} + (-1)^k z_k u_1^{(5)} \\ U_2 &= u_2^{(0)} + \zeta u_2^{(1)} + \zeta^2 u_2^{(2)} + \zeta^3 u_2^{(3)} + \zeta^4 u_2^{(4)} + (-1)^k z_k u_2^{(5)} \\ U_3 &= u_3^{(0)} + \zeta u_3^{(1)} + \zeta^2 u_3^{(2)} + \zeta^3 u_3^{(3)} + \zeta^4 u_3^{(4)} + (-1)^k z_k u_3^{(5)} \end{aligned} \tag{29.14}$$

Starting from the ESL assumption of Eqn. (29.11), it is possible to assess the kinematic congruence relation for a three-dimensional shell. To this end, we introduce the kinematic differential operators $\mathbf{D}_\Omega^{\alpha_i}$, $i = 1, 2, 3$ to account for derivatives with

respect to in-plane coordinates α_1, α_2 . Nevertheless, \mathbf{D}_ζ accounts for the derivatives with respect to the ζ outward coordinate

$$\begin{aligned}
 \mathbf{D}_\Omega^{\alpha_1} &= \begin{bmatrix} d_{11}^{\alpha_1} & d_{21}^{\alpha_1} & d_{31}^{\alpha_1} & d_{41}^{\alpha_1} & d_{51}^{\alpha_1} & d_{61}^{\alpha_1} & d_{71}^{\alpha_1} & d_{81}^{\alpha_1} & d_{91}^{\alpha_1} \end{bmatrix}^T \\
 \mathbf{D}_\Omega^{\alpha_2} &= \begin{bmatrix} 0 & 0 & 0 & 0 & 0 & 0 & 0 & 0 & 0 \\ d_{12}^{\alpha_2} & d_{22}^{\alpha_2} & d_{32}^{\alpha_2} & d_{42}^{\alpha_2} & d_{52}^{\alpha_2} & d_{62}^{\alpha_2} & d_{72}^{\alpha_2} & d_{82}^{\alpha_2} & d_{92}^{\alpha_2} \\ 0 & 0 & 0 & 0 & 0 & 0 & 0 & 0 & 0 \end{bmatrix}^T \\
 \mathbf{D}_\Omega^{\alpha_3} &= \begin{bmatrix} 0 & 0 & 0 & 0 & 0 & 0 & 0 & 0 & 0 \\ 0 & 0 & 0 & 0 & 0 & 0 & 0 & 0 & 0 \\ d_{13}^{\alpha_3} & d_{23}^{\alpha_3} & d_{33}^{\alpha_3} & d_{43}^{\alpha_3} & d_{53}^{\alpha_3} & d_{63}^{\alpha_3} & d_{73}^{\alpha_3} & d_{83}^{\alpha_3} & d_{93}^{\alpha_3} \end{bmatrix}^T
 \end{aligned} \tag{29.15}$$

where quantities $d_{ji}^{\alpha_i}$ with $i = 1, 2, 3$ and $j = 1, \dots, 9$ read as follows:

$$\begin{aligned}
 d_{11}^{\alpha_1} &= \frac{1}{A_1} \frac{\partial}{\partial \alpha_1} & d_{12}^{\alpha_2} &= \frac{1}{A_1 A_2} \frac{\partial A_1}{\partial \alpha_2} & d_{13}^{\alpha_3} &= \frac{1}{R_1} \\
 d_{21}^{\alpha_1} &= \frac{1}{A_1 A_2} \frac{\partial A_2}{\partial \alpha_1} & d_{22}^{\alpha_2} &= \frac{1}{A_2} \frac{\partial}{\partial \alpha_2} & d_{23}^{\alpha_3} &= \frac{1}{R_2} \\
 d_{31}^{\alpha_1} &= -\frac{1}{A_1 A_2} \frac{\partial A_1}{\partial \alpha_2} & d_{32}^{\alpha_2} &= \frac{1}{A_1} \frac{\partial}{\partial \alpha_1} & d_{33}^{\alpha_3} &= 0 \\
 d_{41}^{\alpha_1} &= \frac{1}{A_2} \frac{\partial}{\partial \alpha_2} & d_{42}^{\alpha_2} &= -\frac{1}{A_1 A_2} \frac{\partial A_2}{\partial \alpha_1} & d_{43}^{\alpha_3} &= 0 \\
 d_{51}^{\alpha_1} &= -\frac{1}{R_1} & d_{52}^{\alpha_2} &= 0 & d_{53}^{\alpha_3} &= \frac{1}{A_1} \frac{\partial}{\partial \alpha_1} \\
 d_{61}^{\alpha_1} &= 0 & d_{62}^{\alpha_2} &= -\frac{1}{R_2} & d_{63}^{\alpha_3} &= \frac{1}{A_2} \frac{\partial}{\partial \alpha_2} \\
 d_{71}^{\alpha_1} &= 1 & d_{72}^{\alpha_2} &= 0 & d_{73}^{\alpha_3} &= 0 \\
 d_{81}^{\alpha_1} &= 0 & d_{82}^{\alpha_2} &= 1 & d_{83}^{\alpha_3} &= 0 \\
 d_{91}^{\alpha_1} &= 0 & d_{92}^{\alpha_2} &= 0 & d_{93}^{\alpha_3} &= 1
 \end{aligned} \tag{29.16}$$

Accordingly, \mathbf{D}_ζ matrix assumes the following extended form:

$$\mathbf{D}_\zeta = \begin{bmatrix} \frac{1}{H_1} & 0 & 0 & 0 & 0 & 0 & 0 & 0 & 0 \\ 0 & \frac{1}{H_2} & 0 & 0 & 0 & 0 & 0 & 0 & 0 \\ 0 & 0 & \frac{1}{H_1} & \frac{1}{H_2} & 0 & 0 & 0 & 0 & 0 \\ 0 & 0 & 0 & 0 & \frac{1}{H_1} & 0 & \frac{\partial}{\partial \zeta} & 0 & 0 \\ 0 & 0 & 0 & 0 & 0 & \frac{1}{H_2} & 0 & \frac{\partial}{\partial \zeta} & 0 \\ 0 & 0 & 0 & 0 & 0 & 0 & 0 & 0 & \frac{\partial}{\partial \zeta} \end{bmatrix} \quad (29.17)$$

Referring to the previously discussed principal reference system $O'\alpha_1, \alpha_2, \zeta$ (Fig. 29.1), the three-dimensional strain component vector

$$\boldsymbol{\varepsilon}(\alpha_1, \alpha_2, \zeta, t) = [\varepsilon_1 \ \varepsilon_2 \ \gamma_{12} \ \gamma_{13} \ \gamma_{23} \ \varepsilon_3]^T \quad (29.18)$$

is introduced. Thus, the kinematic relations can be derived, such that $\boldsymbol{\varepsilon}$ can be expressed in terms of the three-dimensional displacement field $\mathbf{U} = [u_1 \ u_2 \ u_3]^T$:

$$\boldsymbol{\varepsilon} = \mathbf{D}\mathbf{U} = \mathbf{D}_\zeta (\mathbf{D}_\Omega^{\alpha_1} + \mathbf{D}_\Omega^{\alpha_2} + \mathbf{D}_\Omega^{\alpha_3}) \mathbf{U} = \mathbf{D}_\zeta \left(\sum_{i=1}^3 \mathbf{D}_\Omega^{\alpha_i} \right) \mathbf{U} \quad (29.19)$$

If the generalized ESL assessment of the displacement field \mathbf{U} of Eqn. (29.11) is adopted for the computation of the three-dimensional strain component vector $\boldsymbol{\varepsilon}$ according to Eqn. (29.19), a new kinematic array

$$\boldsymbol{\varepsilon}^{(\tau)}(\alpha_1, \alpha_2, t) = [\varepsilon_1^{(\tau)} \ \varepsilon_2^{(\tau)} \ \gamma_1^{(\tau)} \ \gamma_2^{(\tau)} \ \gamma_{13}^{(\tau)} \ \gamma_{23}^{(\tau)} \ \omega_{13}^{(\tau)} \ \omega_{23}^{(\tau)} \ \varepsilon_3^{(\tau)}]^T \quad (29.20)$$

can be introduced for each $\tau = 0, \dots, N + 1$ order of the kinematic expansion, as follows:

$$\boldsymbol{\varepsilon} = \sum_{\tau=0}^{N+1} \sum_{i=1}^3 \mathbf{D}_\zeta \mathbf{D}_\Omega^{\alpha_i} \mathbf{F}_\tau \mathbf{u}^{(\tau)} = \sum_{\tau=0}^{N+1} \sum_{i=1}^3 \mathbf{Z}^{(\tau)\alpha_i} \mathbf{D}_\Omega^{\alpha_i} \mathbf{u}^{(\tau)} = \sum_{\tau=0}^{N+1} \sum_{i=1}^3 \mathbf{Z}^{(\tau)\alpha_i} \boldsymbol{\varepsilon}^{(\tau)\alpha_i} \quad (29.21)$$

In this way, a higher order expansion for the three-dimensional strain component vector $\boldsymbol{\varepsilon}(\alpha_1, \alpha_2, \zeta, t)$ is assessed. Note that the array $\mathbf{Z}^{(\tau)\alpha_i}$ with $\alpha_i = \alpha_1, \alpha_2, \alpha_3$ accounts for all the derivatives with respect to ζ coordinate. In an expanded form, it reads as follows:

$$\mathbf{Z}^{(\tau)\alpha_i} = \begin{bmatrix} \frac{F_\tau^{\alpha_i}}{H_1} & 0 & 0 & 0 & 0 & 0 & 0 & 0 & 0 \\ 0 & \frac{F_\tau^{\alpha_i}}{H_2} & 0 & 0 & 0 & 0 & 0 & 0 & 0 \\ 0 & 0 & \frac{F_\tau^{\alpha_i}}{H_1} & \frac{F_\tau^{\alpha_i}}{H_2} & 0 & 0 & 0 & 0 & 0 \\ 0 & 0 & 0 & 0 & \frac{F_\tau^{\alpha_i}}{H_1} & 0 & \frac{\partial F_\tau^{\alpha_i}}{\partial \zeta} & 0 & 0 \\ 0 & 0 & 0 & 0 & 0 & \frac{F_\tau^{\alpha_i}}{H_2} & 0 & \frac{\partial F_\tau^{\alpha_i}}{\partial \zeta} & 0 \\ 0 & 0 & 0 & 0 & 0 & 0 & 0 & 0 & \frac{\partial F_\tau^{\alpha_i}}{\partial \zeta} \end{bmatrix} \quad (29.22)$$

As can be seen from the previous equation, the generalized strain component vector lying on the reference surface $\mathbf{r}(\alpha_1, \alpha_2)$ can be computed for each τ -th order of the kinematic expansion and for each α_i principal direction according to the following relation:

$$\boldsymbol{\varepsilon}^{(\tau)\alpha_i} = \mathbf{D}_\Omega^{\alpha_i} \mathbf{u}^{(\tau)} \quad \text{for } \tau = 0, \dots, N + 1 \quad i = 1, 2, 3 \quad (29.23)$$

29.4 Generalized Constitutive Equations

Once the generalized displacement field has been assessed in Eqn. (29.11) according to the generalized ESL methodology, a description of the linear elastic constitutive behaviour of the entire lamination scheme is set, embedding the mechanical properties of each generally anisotropic layer. Moreover, a generalized relation should be derived for each τ -th kinematic expansion order. For a linear elastic anisotropic material, the stiffness matrix $\mathbf{C}^{(k)}$ should be declared for each k -th layer of the stacking sequence. Referring to the material reference system provided from the symmetry axes of the periodic unit cell, the generally anisotropic Hooke’s law can be expressed as

$$\hat{\boldsymbol{\sigma}}^{(k)} = \mathbf{C}^{(k)} \hat{\boldsymbol{\varepsilon}}^{(k)} \Leftrightarrow \begin{bmatrix} \hat{\sigma}_1^{(k)} \\ \hat{\sigma}_2^{(k)} \\ \hat{\tau}_{12}^{(k)} \\ \hat{\tau}_{13}^{(k)} \\ \hat{\tau}_{23}^{(k)} \\ \hat{\sigma}_3^{(k)} \end{bmatrix} = \begin{bmatrix} C_{11}^{(k)} & C_{12}^{(k)} & C_{16}^{(k)} & C_{14}^{(k)} & C_{15}^{(k)} & C_{13}^{(k)} \\ C_{12}^{(k)} & C_{22}^{(k)} & C_{26}^{(k)} & C_{24}^{(k)} & C_{25}^{(k)} & C_{23}^{(k)} \\ C_{16}^{(k)} & C_{26}^{(k)} & C_{66}^{(k)} & C_{46}^{(k)} & C_{56}^{(k)} & C_{36}^{(k)} \\ C_{14}^{(k)} & C_{24}^{(k)} & C_{46}^{(k)} & C_{44}^{(k)} & C_{45}^{(k)} & C_{34}^{(k)} \\ C_{15}^{(k)} & C_{25}^{(k)} & C_{56}^{(k)} & C_{45}^{(k)} & C_{55}^{(k)} & C_{35}^{(k)} \\ C_{13}^{(k)} & C_{23}^{(k)} & C_{36}^{(k)} & C_{34}^{(k)} & C_{35}^{(k)} & C_{33}^{(k)} \end{bmatrix} \begin{bmatrix} \hat{\varepsilon}_1^{(k)} \\ \hat{\varepsilon}_2^{(k)} \\ \hat{\gamma}_{12}^{(k)} \\ \hat{\gamma}_{13}^{(k)} \\ \hat{\gamma}_{23}^{(k)} \\ \hat{\varepsilon}_3^{(k)} \end{bmatrix} \quad (29.24)$$

where $\hat{\boldsymbol{\sigma}}^{(k)} = [\hat{\sigma}_1^{(k)} \hat{\sigma}_2^{(k)} \hat{\tau}_{12}^{(k)} \hat{\tau}_{13}^{(k)} \hat{\tau}_{23}^{(k)} \hat{\sigma}_3^{(k)}]^T$ and $\hat{\boldsymbol{\varepsilon}}^{(k)} = [\hat{\varepsilon}_1^{(k)} \hat{\varepsilon}_2^{(k)} \hat{\gamma}_{12}^{(k)} \hat{\gamma}_{13}^{(k)} \hat{\gamma}_{23}^{(k)} \hat{\varepsilon}_3^{(k)}]^T$ denote the three-dimensional stress and strain component vector, respectively, com-

puted with respect to the above discussed material reference system. Since Eqn. (29.23) is expressed for each k -th layer with respect to the material reference system of the actual layer, it is useful to turn it to the curvilinear principal reference system $O'\alpha_1\alpha_2\alpha_3$. In this perspective, an orthogonal transformation matrix $\mathbf{T}^{(k)}$ is introduced accounting for the three eulerian angles which completely define the material orientation. If we assume $\alpha_3^k = \zeta$ as happens in most practical applications, only a single rotation angle θ_k is required. Accordingly, the rotated stiffness matrix reads as follows:

$$\bar{\mathbf{E}}^{(k)} = \mathbf{T}^{(k)T} \mathbf{C}^{(k)} \mathbf{T}^{(k)} = \begin{bmatrix} \bar{E}_{11}^{(k)} & \bar{E}_{12}^{(k)} & \bar{E}_{16}^{(k)} & \bar{E}_{14}^{(k)} & \bar{E}_{15}^{(k)} & \bar{E}_{13}^{(k)} \\ \bar{E}_{12}^{(k)} & \bar{E}_{22}^{(k)} & \bar{E}_{26}^{(k)} & \bar{E}_{24}^{(k)} & \bar{E}_{25}^{(k)} & \bar{E}_{23}^{(k)} \\ \bar{E}_{16}^{(k)} & \bar{E}_{26}^{(k)} & \bar{E}_{66}^{(k)} & \bar{E}_{46}^{(k)} & \bar{E}_{56}^{(k)} & \bar{E}_{36}^{(k)} \\ \bar{E}_{14}^{(k)} & \bar{E}_{24}^{(k)} & \bar{E}_{46}^{(k)} & \bar{E}_{44}^{(k)} & \bar{E}_{45}^{(k)} & \bar{E}_{34}^{(k)} \\ \bar{E}_{15}^{(k)} & \bar{E}_{25}^{(k)} & \bar{E}_{56}^{(k)} & \bar{E}_{45}^{(k)} & \bar{E}_{55}^{(k)} & \bar{E}_{35}^{(k)} \\ \bar{E}_{13}^{(k)} & \bar{E}_{23}^{(k)} & \bar{E}_{36}^{(k)} & \bar{E}_{34}^{(k)} & \bar{E}_{35}^{(k)} & \bar{E}_{33}^{(k)} \end{bmatrix} \quad (29.25)$$

As can be seen, Eqn. (29.25) relates the stress and strain field in the geometric reference system, thus giving $\boldsymbol{\sigma}^{(k)} = [\sigma_1^{(k)} \sigma_2^{(k)} \tau_{12}^{(k)} \tau_{13}^{(k)} \tau_{23}^{(k)} \sigma_3^{(k)}]^T$ and $\boldsymbol{\varepsilon}^{(k)} = [\varepsilon_1^{(k)} \varepsilon_2^{(k)} \gamma_{12}^{(k)} \gamma_{13}^{(k)} \gamma_{23}^{(k)} \varepsilon_3^{(k)}]^T$, respectively. Nevertheless, the symbol $\bar{E}_{ij}^{(k)}$ for $i, j = 1, \dots, 6$ accounts for the rotated three-dimensional stiffness coefficients $\bar{C}_{ij}^{(k)}$, as well as the reduced ones $\bar{Q}_{ij}^{(k)}$ in the case of plane stress assumption. From the computation of the elastic strain energy by means of the kinematic assumption of Eqn. (29.11) it is possible to homogenize the stress-strain constitutive relationship so that a single equation is obtained for the entire lamination scheme. To this purpose, the array of generalized stress resultants $\mathbf{S}^{(\tau)\alpha_i}(\alpha_1, \alpha_2, t) = [N_1^{(\tau)\alpha_i} N_2^{(\tau)\alpha_i} N_{12}^{(\tau)\alpha_i} N_{21}^{(\tau)\alpha_i} T_1^{(\tau)\alpha_i} T_2^{(\tau)\alpha_i} P_1^{(\tau)\alpha_i} P_2^{(\tau)\alpha_i} S_3^{(\tau)\alpha_i}]^T$ is introduced. Eventually, the generalized constitutive relationship can be written in a compact matrix form for each τ -th expansion order as:

$$\mathbf{S}^{(\tau)\alpha_i} = \sum_{\eta=0}^{N+1} \sum_{j=1}^3 \mathbf{A}^{(\tau\eta)\alpha_i\alpha_j} \boldsymbol{\varepsilon}^{(\eta)\alpha_j} \quad (29.26)$$

In Eqn. (29.26) the generalized stiffness constants can be computed as follows, setting $F_\tau^{\alpha_i} = \partial^0 F_\tau^{\alpha_i} / \partial \zeta^0$ and $F_\eta^{\alpha_j} = \partial^0 F_\eta^{\alpha_j} / \partial \zeta^0$:

$$A_{nm(pq)}^{(\tau\eta)[fg]\alpha_i\alpha_j} = \sum_{k=1}^l \int_{\zeta_k}^{\zeta_{k+1}} \bar{B}_{nm}^{(k)} \frac{\partial^f F_\eta^{\alpha_j}}{\partial \zeta^f} \frac{\partial^g F_\tau^{\alpha_i}}{\partial \zeta^g} \frac{H_1 H_2}{H_1^p H_2^q} d\zeta \quad \text{for} \quad \begin{matrix} \tau, \eta = 0, \dots, N+1 \\ n, m = 1, \dots, 6 \\ p, q = 0, 1, 2 \\ \alpha_i, \alpha_j = \alpha_1, \alpha_2, \alpha_3 \\ f, g = 0, 1 \end{matrix} \quad (29.27)$$

It should be noted that the generalized relation at issue has been considered starting from the stiffness coefficients $\bar{B}_{nm}^{(k)}$, for $n, m = 1, \dots, 6$ and $k = 1, \dots, l$, being l the

total number of layers, accounting for both the three-dimensional rotated constants $\bar{C}_{nm}^{(k)}$, and the reduced elastic coefficients $\bar{E}_{nm}^{(k)} = \bar{Q}_{nm}^{(k)}$ which are successfully adopted in the case of displacement field assumptions (29.11) accounting for a plane stress state. Moreover, if the out-of-plane stretching effect is not contemplated, the so-called shear correction factor $\kappa(\zeta)$ is introduced

$$\bar{B}_{nm}^{(k)} = \begin{cases} \bar{E}_{nm}^{(k)} & \text{for } n, m = 1, 2, 3, 6 \\ \kappa(\zeta) \bar{E}_{nm}^{(k)} & \text{for } n, m = 4, 5 \end{cases} \quad (29.28)$$

In the present work, the shear correction factor is set $\kappa = 5/6$ accounting for a constant through-the-thickness distribution. Starting from the higher order constitutive relation of Eqn. (29.26) it is useful to express, in each point of the physical domain, the generalized stress resultants $\mathbf{S}^{(\tau)\alpha_i}$, defined for each $\tau = 0, \dots, N + 1$, as a combination of the displacement field vector $\mathbf{u}_\eta^{\alpha_i}$ for $i = 1, 2, 3$ and $\eta = 0, \dots, N + 1$ according to the following relation:

$$\mathbf{S}^{(\tau)\alpha_i} = \sum_{\eta=0}^{N+1} \sum_{j=1}^3 \mathbf{A}^{(\tau\eta)\alpha_i\alpha_j} \mathbf{D}_\Omega^{\alpha_j} \mathbf{u}^{(\eta)} = \sum_{\eta=0}^{N+1} \sum_{j=1}^3 \mathbf{O}^{(\tau\eta)\alpha_i\alpha_j} \mathbf{u}^{(\eta)} \quad (29.29)$$

29.5 External Loads

We discuss, now, about the distributed external loads applied on the top and the bottom surface of the structure, which are geometrically located at $\zeta = \pm h(\alpha_1, \alpha_2)/2$. From the direct application of the static equivalence principle, an equivalent set of surface loads are defined for each order of the kinematic expansion, and they are located on the middle surface of the shell. We start from the computation of the virtual work δL_{es} of the three-dimensional external loads component vector $\mathbf{q}^{(j)}(\alpha_1, \alpha_2, \alpha_3) = [q_1^{(j)} \ q_2^{(j)} \ q_3^{(j)}]^T$ in a variational form $\delta U_i^{(j)}$ for $i = 1, 2, 3$ of the three dimensional displacement field $\mathbf{U}^{(j)}$ components acting at the top ($j = 1$) and the bottom ($j = 2$) surface of the shell. Referring to the curvilinear coordinate system $(\alpha_1, \alpha_2, \zeta)$, one gets

$$\delta L_{es} = \int_{\alpha_1} \int_{\alpha_2} \left(\sum_{j=1}^2 \left(\sum_{i=1}^3 q_i^{(j)} \delta U_i^{(j)} \right) H_1^{(j)} H_2^{(j)} \right) A_1 A_2 d\alpha_1 d\alpha_2 \quad (29.30)$$

where $j = 1$ denotes the geometrical and mechanical quantities calculated at $\zeta = h/2$, whereas $j = 2$ identifies the quantities referred to the bottom surface located at $\zeta = -h/2$. For the sake of conciseness, it is useful to identify the external loads component vectors applied at the top and the bottom surface of the shell so that $\mathbf{q}^{(1)} = \mathbf{q}^{(+)} = [q_1^{(+)} \ q_2^{(+)} \ q_3^{(+)}]^T$ and, $\mathbf{q}^{(2)} = \mathbf{q}^{(-)} = [q_1^{(-)} \ q_2^{(-)} \ q_3^{(-)}]^T$ respectively. Remembering the generalized assumption of the displacement field of Eqn. (29.11), a

vector of external loads, denoted with $\mathbf{q}^{(\tau)}(\alpha_1, \alpha_2) = [q_1^{(\tau)} q_2^{(\tau)} q_3^{(\tau)}]^T$, is introduced on the reference midsurface $\mathbf{r}(\alpha_1, \alpha_2)$. The computation of the virtual work of $\mathbf{q}^{(\tau)}$ accounts, for each τ -th order of the kinematic expansion, for the generalized displacement field component vector $\mathbf{u}^{(\tau)}$ introduced in Eqn. (29.11) as follows:

$$\delta L_{is} = \int_{\alpha_1} \int_{\alpha_2} \sum_{\tau=0}^{N+1} \sum_{i=1}^3 q_i^{(\tau)} \delta u_i^{(\tau)} A_1 A_2 d\alpha_1 d\alpha_2 \quad (29.31)$$

According to the static equivalence principle, it is

$$\delta L_{es} = \delta L_{is} \quad (29.32)$$

Starting from the extended exomputation of Eqn. (29.32) by means of Eqns. (29.30)-(29.31), the following expression of $q_i^{(\tau)}$ for $i = 1, 2, 3$ can be derived

$$q_i^{(\tau)} = \sum_{j=1}^2 q_i^{(j)} F_\tau^{\alpha_i(j)} H_1^{(j)} H_2^{(j)} \quad \text{for } i = 1, 2, 3 \quad (29.33)$$

being $F_\tau^{\alpha_i(j)}$ the thickness function referred to the $\alpha_i = \alpha_1, \alpha_2, \alpha_3$ principal direction according to Eqn. (29.11), evaluated at the top ($j = 1$) and the bottom ($j = 2$) external surfaces.

29.6 Equation of Motion

In this section we focus on the determination of the fundamental relations for the statics and dynamics of a doubly-curved shell. To this end, a unified expression of the displacement field is adopted, according to Eqn. (29.12). The well-known Hamiltonian principle has been employed in its variational form, accounting for the virtual variation δ of the total elastic strain energy Φ , as well as the inertia contribution coming from the kinetic energy T of the three-dimensional structure, and the external load potential δL_e . Referring to a generic time interval $[t_1, t_2]$ of extremes t_1, t_2 , one gets

$$\delta \int_{t_1}^{t_2} (T - \Phi + L_e) dt = 0 \quad \rightarrow \quad \int_{t_1}^{t_2} (\delta T - \delta \Phi + \delta L_e) dt = 0 \quad (29.34)$$

Referring to the three-dimensional solid described by means of the principal $\alpha_1, \alpha_2, \alpha_3$ coordinates, from the application of the integration by parts rule, the kinetic energy of the structure can be expressed in terms of first order time derivative of the three-dimensional displacement field component vector $\mathbf{U} = [U_1 U_2 U_3]^T$. For a laminated structure, the following relation can be derived

$$\delta T = \sum_{k=1}^l \int_{\zeta_k}^{\zeta_{k+1}} \int_{\alpha_1} \int_{\alpha_2} \rho^{(k)} (\delta \dot{\mathbf{U}})^T \dot{\mathbf{U}} H_1 H_2 A_1 A_2 d\alpha_1 d\alpha_2 d\zeta \quad (29.35)$$

being ζ_k and ζ_{k+1} the coordinates of the external skins of the k -th lamina of the stacking sequence, characterized by a density $\rho^{(k)}$. Introducing Eqn. (29.35) into the general formulation of the Hamiltonian principle (29.34), and applying the integration by parts rule, the dependence from the three-dimensional second order time derivative array $\ddot{\mathbf{U}} = [\ddot{u}_1 \ \ddot{u}_2 \ \ddot{u}_3]^T$ can be outlined

$$\int_{t_1}^{t_2} \delta T dt = - \sum_{k=1}^l \int_{t_1}^{t_2} \int_{\zeta_k}^{\zeta_{k+1}} \int_{\alpha_1} \int_{\alpha_2} \rho^{(k)} (\delta \mathbf{U})^T \ddot{\mathbf{U}} H_1 H_2 A_1 A_2 d\alpha_1 d\alpha_2 d\zeta dt \quad (29.36)$$

It should be recalled that the previous relation is valid under a synchronous motion assumption, with zero displacements at the two instants of time t_1, t_2 . Based on the unified formulation of the displacement field assessed in Eqn. (29.11), the following expression of T is derived

$$\int_{t_1}^{t_2} \delta T dt = - \sum_{\tau=0}^{N+1} \int_{t_1}^{t_2} \int_{\alpha_1} \int_{\alpha_2} \left(\sum_{i=1}^3 \left(\sum_{\eta=0}^{N+1} I^{0(\tau\eta)\alpha_i\alpha_i} \ddot{u}_i^{(\eta)} \right) \delta u_i^{(\eta)} \right) A_1 A_2 d\alpha_1 d\alpha_2 dt \quad (29.37)$$

where the generalized inertial terms are defined for each $\alpha_i = \alpha_1, \alpha_2, \alpha_3$ with respect to the generic τ -th and η -th kinematic expansion order according to the following expression:

$$I^{0(\tau\eta)\alpha_i\alpha_i} = \sum_{k=1}^l \int_{\zeta_k}^{\zeta_{k+1}} \rho^{(k)} F_{\tau}^{\alpha_i} F_{\eta}^{\alpha_i} H_1 H_2 d\zeta \quad (29.38)$$

As far as the elastic strain energy virtual variation $\delta\Phi$ is concerned, we start from the computation in terms of three-dimensional stress and strain component vectors $\boldsymbol{\sigma}^{(k)}$ and $\boldsymbol{\varepsilon}^{(k)}$ referred to the geometric reference system $O'\alpha_1\alpha_2\zeta$. In a compact notation, it is

$$\delta\Phi = \sum_{k=1}^l \int_{\alpha_1} \int_{\alpha_2} \int_{\zeta_k}^{\zeta_{k+1}} \delta \boldsymbol{\varepsilon}^{(k)T} \boldsymbol{\sigma}^{(k)} A_1 A_2 H_1 H_2 d\alpha_1 d\alpha_2 d\zeta \quad (29.39)$$

Starting from the previous relation, the virtual variation $\delta\Phi$ of the elastic strain energy can be expressed within the ESL framework taking into account the generalized stress resultant component vector $\mathbf{S}^{(\tau)\alpha_i}(\alpha_1, \alpha_2, t)$ and the higher order strain component vector $\boldsymbol{\varepsilon}^{(\tau)\alpha_i}(\alpha_1, \alpha_2, t)$ defined for $\tau = 0, \dots, N + 1$ and $i = 1, 2, 3$ according to the following definition:

$$\delta\Phi = \sum_{\tau=0}^{N+1} \sum_{i=1}^3 \int_{\alpha_1} \int_{\alpha_2} \left(\delta\mathcal{E}^{(\tau)\alpha_i} \right)^T \mathbf{S}^{(\tau)\alpha_i} A_1 A_2 d\alpha_1 d\alpha_2 \quad (29.40)$$

Keeping in mind the virtual work $\delta L_e = \delta L_{es} = \delta L_{is}$ related to the external surface loads (29.32) in an ESL setting, it is possible to perform a time integration with respect to $[t_1, t_2]$ interval so that it can be embedded in the Hamiltonian principle of Eqn. (29.34). One gets

$$\int_{t_1}^{t_2} \delta L_e dt = \sum_{\tau=0}^{N+1} \int_{t_1}^{t_2} \int_{\alpha_1} \int_{\alpha_2} \sum_{i=1}^3 q_i^{(\tau)} \delta u_i^{(\tau)} A_1 A_2 d\alpha_1 d\alpha_2 dt \quad (29.41)$$

Introducing Eqns. (29.37),(29.40)-(29.41) into the general formulation of the Hamiltonian principle of Eqn. (29.34), the final form of the dynamic equilibrium equations is derived. In a compact notation, it is

$$\sum_{i=1}^3 \mathbf{D}_{\Omega}^{*\alpha_i} \mathbf{S}^{(\tau)\alpha_i} + \mathbf{q}^{(\tau)} = \sum_{\eta=0}^{N+1} \mathbf{M}^{(\tau\eta)} \ddot{\mathbf{u}}^{(\eta)} \quad \text{for } \tau = 0, \dots, N + 1 \quad (29.42)$$

where $\mathbf{M}^{(\tau\eta)}$ accounts for the generalized ESL inertial matrix, defined by means of the generalized inertial coefficients $I^{0(\tau\eta)\alpha_i\alpha_i}$ with $i = 1, 2, 3$ introduced in Eqn. (29.38) for each τ, η -th order of the kinematic expansion, as follows:

$$\mathbf{M}^{(\tau\eta)} = \begin{bmatrix} I^{0(\tau\eta)\alpha_1\alpha_1} & 0 & 0 \\ 0 & I^{0(\tau\eta)\alpha_2\alpha_2} & 0 \\ 0 & 0 & I^{0(\tau\eta)\alpha_3\alpha_3} \end{bmatrix} \quad \text{for } \tau, \eta = 0, \dots, N + 1 \quad (29.43)$$

The equilibrium operators $\mathbf{D}_{\Omega}^{*\alpha_1}, \mathbf{D}_{\Omega}^{*\alpha_2}, \mathbf{D}_{\Omega}^{*\alpha_3}$ are defined in an expanded form, as

$$\begin{aligned} \mathbf{D}_{\Omega}^{*\alpha_1} &= \begin{bmatrix} d_{11}^{*\alpha_1} & d_{12}^{*\alpha_1} & d_{13}^{*\alpha_1} & d_{14}^{*\alpha_1} & d_{15}^{*\alpha_1} & d_{16}^{*\alpha_1} & d_{17}^{*\alpha_1} & d_{18}^{*\alpha_1} & d_{19}^{*\alpha_1} \\ 0 & 0 & 0 & 0 & 0 & 0 & 0 & 0 & 0 \\ 0 & 0 & 0 & 0 & 0 & 0 & 0 & 0 & 0 \end{bmatrix} \\ \mathbf{D}_{\Omega}^{*\alpha_2} &= \begin{bmatrix} 0 & 0 & 0 & 0 & 0 & 0 & 0 & 0 & 0 \\ d_{21}^{*\alpha_2} & d_{22}^{*\alpha_2} & d_{23}^{*\alpha_2} & d_{24}^{*\alpha_2} & d_{25}^{*\alpha_2} & d_{26}^{*\alpha_2} & d_{27}^{*\alpha_2} & d_{28}^{*\alpha_2} & d_{29}^{*\alpha_2} \\ 0 & 0 & 0 & 0 & 0 & 0 & 0 & 0 & 0 \end{bmatrix} \\ \mathbf{D}_{\Omega}^{*\alpha_3} &= \begin{bmatrix} 0 & 0 & 0 & 0 & 0 & 0 & 0 & 0 & 0 \\ 0 & 0 & 0 & 0 & 0 & 0 & 0 & 0 & 0 \\ d_{31}^{*\alpha_3} & d_{32}^{*\alpha_3} & d_{33}^{*\alpha_3} & d_{34}^{*\alpha_3} & d_{35}^{*\alpha_3} & d_{36}^{*\alpha_3} & d_{37}^{*\alpha_3} & d_{38}^{*\alpha_3} & d_{39}^{*\alpha_3} \end{bmatrix} \end{aligned} \quad (29.44)$$

where the coefficients $d_{ij}^{*\alpha_i}$ for $i = 1, 2, 3$ and $j = 1, \dots, 9$ assume the following form:

$$\begin{aligned}
 d_{11}^{*\alpha_1} &= \frac{1}{A_1} \frac{\partial}{\partial \alpha_1} + \frac{1}{A_1 A_2} \frac{\partial A_2}{\partial \alpha_1} & d_{21}^{*\alpha_2} &= -\frac{1}{A_1 A_2} \frac{\partial A_1}{\partial \alpha_2} & d_{31}^{*\alpha_3} &= -\frac{1}{R_1} \\
 d_{12}^{*\alpha_1} &= -\frac{1}{A_1 A_2} \frac{\partial A_2}{\partial \alpha_1} & d_{22}^{*\alpha_2} &= \frac{1}{A_2} \frac{\partial}{\partial \alpha_2} + \frac{1}{A_1 A_2} \frac{\partial A_1}{\partial \alpha_2} & d_{32}^{*\alpha_3} &= -\frac{1}{R_2} \\
 d_{13}^{*\alpha_1} &= \frac{1}{A_1 A_2} \frac{\partial A_1}{\partial \alpha_2} & d_{23}^{*\alpha_2} &= \frac{1}{A_1} \frac{\partial}{\partial \alpha_1} + \frac{1}{A_1 A_2} \frac{\partial A_2}{\partial \alpha_1} & d_{33}^{*\alpha_3} &= 0 \\
 d_{14}^{*\alpha_1} &= \frac{1}{A_2} \frac{\partial}{\partial \alpha_2} + \frac{1}{A_1 A_2} \frac{\partial A_1}{\partial \alpha_2} & d_{24}^{*\alpha_2} &= \frac{1}{A_1 A_2} \frac{\partial A_2}{\partial \alpha_1} & d_{34}^{*\alpha_3} &= 0 \\
 d_{15}^{*\alpha_1} &= \frac{1}{R_1} & d_{25}^{*\alpha_2} &= 0 & d_{35}^{*\alpha_3} &= \frac{1}{A_1} \frac{\partial}{\partial \alpha_1} + \frac{1}{A_1 A_2} \frac{\partial A_2}{\partial \alpha_1} \\
 d_{16}^{*\alpha_1} &= 0 & d_{26}^{*\alpha_2} &= \frac{1}{R_2} & d_{36}^{*\alpha_3} &= \frac{1}{A_2} \frac{\partial}{\partial \alpha_2} + \frac{1}{A_1 A_2} \frac{\partial A_1}{\partial \alpha_2} \\
 d_{17}^{*\alpha_1} &= -1 & d_{27}^{*\alpha_2} &= 0 & d_{37}^{*\alpha_3} &= 0 \\
 d_{18}^{*\alpha_1} &= 0 & d_{28}^{*\alpha_2} &= -1 & d_{38}^{*\alpha_3} &= 0 \\
 d_{19}^{*\alpha_1} &= 0 & d_{29}^{*\alpha_2} &= 0 & d_{39}^{*\alpha_3} &= -1
 \end{aligned}
 \tag{29.45}$$

Taking into account the dynamic equilibrium relations (29.42) written for each $\tau = 0, \dots, N + 1$, and remembering the generalized higher order constitutive relationship (29.26) in lieu of $\mathbf{S}^{(\tau)\alpha_i}$, as well as the definition of $\boldsymbol{\varepsilon}^{(\tau)\alpha_i}$ in terms of the generalized displacement field description of Eqn. (29.11), the fundamental set of equations can be derived for each τ -th kinematic expansion order so that they are referred to the generalized displacement field component vector $\mathbf{u}^{(\eta)}$ for $\eta = 0, \dots, N + 1$,

$$\sum_{\eta=0}^{N+1} \mathbf{L}^{(\tau\eta)} \mathbf{u}^{(\eta)} + \mathbf{q}^{(\tau)} = \sum_{\eta=0}^{N+1} \mathbf{M}^{(\tau\eta)} \ddot{\mathbf{u}}^{(\eta)} \quad \text{for } \tau = 0, \dots, N + 1 \tag{29.46}$$

where $\mathbf{L}^{(\tau\eta)}$ denotes the ESL fundamental matrix, referred to each $\tau, \eta = 0, \dots, N + 1$ as follows:

$$\mathbf{L}^{(\tau\eta)} = \sum_{i=1}^3 \sum_{j=1}^3 \mathbf{D}_{\Omega}^{*\alpha_i} \mathbf{A}^{(\tau\eta)\alpha_i\alpha_j} \mathbf{D}_{\Omega}^{\alpha_j} \quad \text{for } \tau, \eta = 0, \dots, N + 1 \tag{29.47}$$

In a more expanded form, one gets

$$\mathbf{L}^{(\tau\eta)} = \begin{bmatrix} L_{11}^{(\tau\eta)\alpha_1\alpha_1} & L_{12}^{(\tau\eta)\alpha_1\alpha_2} & L_{13}^{(\tau\eta)\alpha_1\alpha_3} \\ L_{21}^{(\tau\eta)\alpha_2\alpha_1} & L_{22}^{(\tau\eta)\alpha_2\alpha_2} & L_{23}^{(\tau\eta)\alpha_2\alpha_3} \\ L_{31}^{(\tau\eta)\alpha_3\alpha_1} & L_{32}^{(\tau\eta)\alpha_3\alpha_2} & L_{33}^{(\tau\eta)\alpha_3\alpha_3} \end{bmatrix} \quad \text{for } \tau, \eta = 0, \dots, N + 1 \tag{29.48}$$

An extended expression of all the terms in the fundamental matrix $\mathbf{L}^{(\tau\eta)}$ has been provided by Tornabene and Baccocchi (2018), setting $\tau, \eta = 0, \dots, N + 1$. If all the kinematic expansion orders are taken into account, Eqn. (29.46) is assembled as follows:

$$\tilde{\mathbf{L}} \tilde{\mathbf{u}} + \tilde{\mathbf{q}} = \tilde{\mathbf{M}} \ddot{\tilde{\mathbf{u}}} \tag{29.49}$$

where $\tilde{\mathbf{L}}$ and $\tilde{\mathbf{M}}$ stand for the assembled form of the fundamental and inertial matrix introduced in Eqn. (29.48) and Eqn. (29.43) for each $\tau, \eta = 0, \dots, N + 1$. In an

expanded form, they read as follows:

$$\tilde{\mathbf{L}} = \begin{bmatrix} \mathbf{L}^{(00)} & \mathbf{L}^{(01)} & \dots & \mathbf{L}^{(0(N))} & \mathbf{L}^{(0(N+1))} \\ \mathbf{L}^{(10)} & \mathbf{L}^{(11)} & \dots & \mathbf{L}^{(1(N))} & \mathbf{L}^{(1(N+1))} \\ \vdots & \vdots & \ddots & \vdots & \vdots \\ \mathbf{L}^{((N)0)} & \mathbf{L}^{((N)1)} & \dots & \mathbf{L}^{((N)(N))} & \mathbf{L}^{((N)(N+1))} \\ \mathbf{L}^{((N+1)0)} & \mathbf{L}^{((N+1)1)} & \dots & \mathbf{L}^{((N+1)(N))} & \mathbf{L}^{((N+1)(N+1))} \end{bmatrix} \quad (29.50)$$

and

$$\tilde{\mathbf{M}} = \begin{bmatrix} \mathbf{M}^{(00)} & \mathbf{M}^{(01)} & \dots & \mathbf{M}^{(0(N))} & \mathbf{M}^{(0(N+1))} \\ \mathbf{M}^{(10)} & \mathbf{M}^{(11)} & \dots & \mathbf{M}^{(1(N))} & \mathbf{M}^{(1(N+1))} \\ \vdots & \vdots & \ddots & \vdots & \vdots \\ \mathbf{M}^{((N)0)} & \mathbf{M}^{((N)1)} & \dots & \mathbf{M}^{((N)(N))} & \mathbf{M}^{((N)(N+1))} \\ \mathbf{M}^{((N+1)0)} & \mathbf{M}^{((N+1)1)} & \dots & \mathbf{M}^{((N+1)(N))} & \mathbf{M}^{((N+1)(N+1))} \end{bmatrix} \quad (29.51)$$

On the other hand, in Eqn. (29.49) the assembled vector of the external loads $\tilde{\mathbf{q}}$ is introduced

$$\tilde{\mathbf{q}} = [\mathbf{q}^{(0)} \ \mathbf{q}^{(1)} \ \dots \ \mathbf{q}^{(N)} \ \mathbf{q}^{(N+1)}]^T \quad (29.52)$$

In the same way, the extended array of the generalized displacement field $\tilde{\mathbf{u}}$, together with his second-order time derivative $\ddot{\tilde{\mathbf{u}}}$ is defined as follows:

$$\begin{aligned} \tilde{\mathbf{u}} &= [\mathbf{u}^{(0)} \ \mathbf{u}^{(1)} \ \dots \ \mathbf{u}^{(N)} \ \mathbf{u}^{(N+1)}]^T \\ \ddot{\tilde{\mathbf{u}}} &= [\ddot{\mathbf{u}}^{(0)} \ \ddot{\mathbf{u}}^{(1)} \ \dots \ \ddot{\mathbf{u}}^{(N)} \ \ddot{\mathbf{u}}^{(N+1)}]^T \end{aligned} \quad (29.53)$$

Then, the application of the variational form of the Hamiltonian principle leads to the assessment of the external constraints enforced on the doubly-curved structure edges. In particular, the Clamped (C) boundary condition is pursued when all the components of the generalized displacement field $\mathbf{u}^{(\tau)}$ for $\tau = 0, \dots, N + 1$ are equal to zero

$$\begin{aligned} u_1^{(\tau)} = u_2^{(\tau)} = u_3^{(\tau)} = 0 \quad \text{for } \alpha_1 = \alpha_1^i \ i = 0, 1 \\ u_1^{(\tau)} = u_2^{(\tau)} = u_3^{(\tau)} = 0 \quad \text{for } \alpha_2 = \alpha_1^i \ i = 0, 1 \end{aligned} \quad (29.54)$$

A Free (F) external constraint is applied to a shell edge when

$$\begin{aligned} N_1^{(\tau)\alpha_1} = N_{12}^{(\tau)\alpha_2} = T_1^{(\tau)\alpha_3} = 0 \quad \text{for } \alpha_1 = \alpha_1^i \ i = 0, 1 \\ N_{21}^{(\tau)\alpha_1} = N_2^{(\tau)\alpha_2} = T_2^{(\tau)\alpha_3} = 0 \quad \text{for } \alpha_2 = \alpha_1^i \ i = 0, 1 \end{aligned} \quad (29.55)$$

29.7 Isogeometric Mapping of the Physical Domain

We now deal with the determination of a procedure for the mapping of the physical domain in order to account for doubly-curved shells of arbitrary shape in Eqn. (29.49). Accordingly, a description of the structural edges with respect to the principal parametric lines α_1, α_2 is provided, identified with $(\bar{\alpha}_{1(p)}, \bar{\alpha}_{2(p)})$ for $p = 1, \dots, 4$. In the same way, the four corners locations $(\alpha_{1(q)}, \alpha_{2(q)})$ are provided within the physical domain too, being $q = 1, \dots, 4$. Then, a set of generalized blending functions $\alpha_1 = \alpha_1(\xi_1, \xi_2)$ and $\alpha_2 = \alpha_2(\xi_1, \xi_2)$ is introduced (Fig. 29.1)

$$\begin{aligned} \alpha_1(\xi_1, \xi_2) &= \frac{1}{2} \left((1 - \xi_2) \bar{\alpha}_{1(1)}(\xi_1) + (1 + \xi_1) \bar{\alpha}_{1(2)}(\xi_2) + \right. \\ &\quad \left. + (1 + \xi_2) \bar{\alpha}_{1(3)}(\xi_1) + (1 - \xi_1) \bar{\alpha}_{1(4)}(\xi_2) \right) - \frac{1}{4} \left((1 - \xi_1)(1 - \xi_2) \alpha_{1(1)} + \right. \\ &\quad \left. + (1 + \xi_1)(1 - \xi_2) \alpha_{1(2)} + (1 + \xi_1)(1 + \xi_2) \alpha_{1(3)} + (1 - \xi_1)(1 + \xi_2) \alpha_{1(4)} \right) \\ \alpha_2(\xi_1, \xi_2) &= \frac{1}{2} \left((1 - \xi_2) \bar{\alpha}_{2(1)}(\xi_1) + (1 + \xi_1) \bar{\alpha}_{2(2)}(\xi_2) + (1 + \xi_2) \bar{\alpha}_{2(3)}(\xi_1) + \right. \\ &\quad \left. + (1 - \xi_1) \bar{\alpha}_{2(4)}(\xi_2) \right) - \frac{1}{4} \left((1 - \xi_1)(1 - \xi_2) \alpha_{2(1)} + (1 + \xi_1)(1 - \xi_2) \alpha_{2(2)} + \right. \\ &\quad \left. + (1 + \xi_1)(1 + \xi_2) \alpha_{2(3)} + (1 - \xi_1)(1 + \xi_2) \alpha_{2(4)} \right) \end{aligned} \quad (29.56)$$

Starting from the blending transformations, it is possible to assess the first order derivatives with respect to the in-plane coordinates α_1, α_2 in terms of the natural coordinates set ξ_1, ξ_2 , as follows:

$$\begin{bmatrix} \frac{\partial}{\partial \alpha_1} \\ \frac{\partial}{\partial \alpha_2} \end{bmatrix} = \begin{bmatrix} \frac{\partial \xi_1}{\partial \alpha_1} & \frac{\partial \xi_2}{\partial \alpha_1} \\ \frac{\partial \xi_1}{\partial \alpha_2} & \frac{\partial \xi_2}{\partial \alpha_2} \end{bmatrix} \begin{bmatrix} \frac{\partial}{\partial \xi_1} \\ \frac{\partial}{\partial \xi_2} \end{bmatrix} \quad (29.57)$$

In the same way, the derivative with respect to the natural coordinates ξ_1, ξ_2 of the parent element stems from the partial derivatives with respect to α_1, α_2 as

$$\begin{bmatrix} \frac{\partial}{\partial \xi_1} \\ \frac{\partial}{\partial \xi_2} \end{bmatrix} = \begin{bmatrix} \frac{\partial \alpha_1}{\partial \xi_1} & \frac{\partial \alpha_2}{\partial \xi_1} \\ \frac{\partial \alpha_1}{\partial \xi_2} & \frac{\partial \alpha_2}{\partial \xi_2} \end{bmatrix} \begin{bmatrix} \frac{\partial}{\partial \alpha_1} \\ \frac{\partial}{\partial \alpha_2} \end{bmatrix} = \mathbf{J} \begin{bmatrix} \frac{\partial}{\partial \alpha_1} \\ \frac{\partial}{\partial \alpha_2} \end{bmatrix} \quad (29.58)$$

where \mathbf{J} denotes the Jacobian matrix of the transformation. Accordingly, its determinant $\det(\mathbf{J})$ can be expressed as

$$\det(\mathbf{J}) = \frac{\partial \alpha_1}{\partial \xi_1} \frac{\partial \alpha_2}{\partial \xi_2} - \frac{\partial \alpha_2}{\partial \xi_1} \frac{\partial \alpha_1}{\partial \xi_2} \quad (29.59)$$

The first order derivatives of Eqn. (29.59) with respect to ξ_1, ξ_2 read as follows

$$\begin{aligned} \det(\mathbf{J}_{\xi_1}) &= \frac{\partial \alpha_1}{\partial \xi_1} \frac{\partial^2 \alpha_2}{\partial \xi_1 \partial \xi_2} - \frac{\partial \alpha_2}{\partial \xi_1} \frac{\partial^2 \alpha_1}{\partial \xi_1 \partial \xi_2} + \frac{\partial \alpha_2}{\partial \xi_2} \frac{\partial^2 \alpha_1}{\partial \xi_1^2} - \frac{\partial \alpha_1}{\partial \xi_2} \frac{\partial^2 \alpha_2}{\partial \xi_1^2} \\ \det(\mathbf{J}_{\xi_2}) &= -\frac{\partial \alpha_1}{\partial \xi_2} \frac{\partial^2 \alpha_2}{\partial \xi_1 \partial \xi_2} + \frac{\partial \alpha_2}{\partial \xi_2} \frac{\partial^2 \alpha_1}{\partial \xi_1 \partial \xi_2} - \frac{\partial \alpha_2}{\partial \xi_1} \frac{\partial^2 \alpha_1}{\partial \xi_2^2} + \frac{\partial \alpha_1}{\partial \xi_1} \frac{\partial^2 \alpha_2}{\partial \xi_2^2} \end{aligned} \quad (29.60)$$

When the transformation of Eqn. (29.56) is an invertible function, it is $\det(\mathbf{J}) \neq 0$, therefore the inverse transformation of Eqn. (29.58) can be performed, leading to the following expression:

$$\begin{bmatrix} \frac{\partial}{\partial \alpha_1} \\ \frac{\partial}{\partial \alpha_2} \end{bmatrix} = \mathbf{J}^{-1} \begin{bmatrix} \frac{\partial}{\partial \xi_1} \\ \frac{\partial}{\partial \xi_2} \end{bmatrix} = \begin{bmatrix} \frac{\partial \xi_1}{\partial \alpha_1} & \frac{\partial \xi_2}{\partial \alpha_1} \\ \frac{\partial \xi_1}{\partial \alpha_2} & \frac{\partial \xi_2}{\partial \alpha_2} \end{bmatrix} \begin{bmatrix} \frac{\partial}{\partial \xi_1} \\ \frac{\partial}{\partial \xi_2} \end{bmatrix} \quad (29.61)$$

where \mathbf{J}^{-1} can be written in an expanded form as:

$$\mathbf{J}^{-1} = \frac{1}{\det(\mathbf{J})} \begin{bmatrix} \frac{\partial \alpha_2}{\partial \xi_2} & -\frac{\partial \alpha_2}{\partial \xi_1} \\ -\frac{\partial \alpha_1}{\partial \xi_2} & \frac{\partial \alpha_1}{\partial \xi_1} \end{bmatrix} = \begin{bmatrix} \xi_{1,\alpha_1} & \xi_{2,\alpha_1} \\ \xi_{1,\alpha_2} & \xi_{2,\alpha_2} \end{bmatrix} \quad (29.62)$$

Based on Eqns. (29.61)-(29.62), the following definitions are introduced

$$\begin{aligned} \xi_{1,\alpha_1} &= \frac{\partial \xi_1}{\partial \alpha_1} = \frac{1}{\det(\mathbf{J})} \frac{\partial \alpha_2}{\partial \xi_2}, & \xi_{1,\alpha_2} &= \frac{\partial \xi_1}{\partial \alpha_2} = -\frac{1}{\det(\mathbf{J})} \frac{\partial \alpha_1}{\partial \xi_2} \\ \xi_{2,\alpha_1} &= \frac{\partial \xi_2}{\partial \alpha_1} = -\frac{1}{\det(\mathbf{J})} \frac{\partial \alpha_2}{\partial \xi_1}, & \xi_{2,\alpha_2} &= \frac{\partial \xi_2}{\partial \alpha_2} = \frac{1}{\det(\mathbf{J})} \frac{\partial \alpha_1}{\partial \xi_1} \end{aligned} \quad (29.63)$$

In this way all the transformation coefficients can be easily computed in each point of the distorted physical domain, once the external edges of the blended structure are provided with respect to the principal coordinates α_1, α_2 . Following a similar procedure, the second order derivatives can be computed within the mapped geometry in terms of ξ_1, ξ_2 natural coordinates, as follows:

$$\begin{aligned} \frac{\partial^2}{\partial \alpha_1^2} &= \xi_{1,\alpha_1}^2 \frac{\partial^2}{\partial \xi_1^2} + \xi_{2,\alpha_1}^2 \frac{\partial^2}{\partial \xi_2^2} + 2\xi_{1,\alpha_1}\xi_{2,\alpha_1} \frac{\partial^2}{\partial \xi_1 \partial \xi_2} + \xi_{1,\alpha_1\alpha_1} \frac{\partial}{\partial \xi_1} + \xi_{2,\alpha_1\alpha_1} \frac{\partial}{\partial \xi_2} \\ \frac{\partial^2}{\partial \alpha_2^2} &= \xi_{1,\alpha_2}^2 \frac{\partial^2}{\partial \xi_1^2} + \xi_{2,\alpha_2}^2 \frac{\partial^2}{\partial \xi_2^2} + 2\xi_{1,\alpha_2}\xi_{2,\alpha_2} \frac{\partial^2}{\partial \xi_1 \partial \xi_2} + \xi_{1,\alpha_2\alpha_2} \frac{\partial}{\partial \xi_1} + \xi_{2,\alpha_2\alpha_2} \frac{\partial}{\partial \xi_2} \\ \frac{\partial^2}{\partial \alpha_1 \partial \alpha_2} &= \xi_{1,\alpha_1}\xi_{1,\alpha_2} \frac{\partial^2}{\partial \xi_1^2} + \xi_{2,\alpha_1}\xi_{2,\alpha_2} \frac{\partial^2}{\partial \xi_2^2} + (\xi_{1,\alpha_1}\xi_{2,\alpha_2} + \xi_{1,\alpha_2}\xi_{2,\alpha_1}) \frac{\partial^2}{\partial \xi_1 \partial \xi_2} + \\ &+ \xi_{1,\alpha_1\alpha_2} \frac{\partial}{\partial \xi_1} + \xi_{2,\alpha_1\alpha_2} \frac{\partial}{\partial \xi_2} \end{aligned} \quad (29.64)$$

In the following, the expressions of the coefficients for second order derivatives occurring in Eqn. (29.64) are reported.

$$\begin{aligned}
 \xi_{1,\alpha_1\alpha_1} &= \frac{1}{\det(\mathbf{J})^2} \left(\frac{\partial\alpha_2}{\partial\xi_2} \frac{\partial^2\alpha_2}{\partial\xi_1\partial\xi_2} - \left(\frac{\partial\alpha_2}{\partial\xi_2} \right)^2 \frac{\det(\mathbf{J}_{\xi_1})}{\det(\mathbf{J})} - \frac{\partial\alpha_2}{\partial\xi_1} \frac{\partial^2\alpha_2}{\partial\xi_2^2} + \frac{\partial\alpha_2}{\partial\xi_1} \frac{\partial\alpha_2}{\partial\xi_2} \frac{\det(\mathbf{J}_{\xi_2})}{\det(\mathbf{J})} \right) \\
 \xi_{1,\alpha_2\alpha_2} &= \frac{1}{\det(\mathbf{J})^2} \left(\frac{\partial\alpha_1}{\partial\xi_2} \frac{\partial^2\alpha_1}{\partial\xi_1\partial\xi_2} - \left(\frac{\partial\alpha_1}{\partial\xi_2} \right)^2 \frac{\det(\mathbf{J}_{\xi_1})}{\det(\mathbf{J})} - \frac{\partial\alpha_1}{\partial\xi_1} \frac{\partial^2\alpha_1}{\partial\xi_2^2} + \frac{\partial\alpha_1}{\partial\xi_1} \frac{\partial\alpha_1}{\partial\xi_2} \frac{\det(\mathbf{J}_{\xi_2})}{\det(\mathbf{J})} \right) \\
 \xi_{1,\alpha_1\alpha_2} &= \frac{1}{\det(\mathbf{J})^2} \left(-\frac{\partial\alpha_2}{\partial\xi_2} \frac{\partial^2\alpha_1}{\partial\xi_1\partial\xi_2} + \frac{\partial\alpha_2}{\partial\xi_2} \frac{\partial\alpha_1}{\partial\xi_2} \frac{\det(\mathbf{J}_{\xi_1})}{\det(\mathbf{J})} + \frac{\partial\alpha_2}{\partial\xi_1} \frac{\partial^2\alpha_1}{\partial\xi_2^2} - \frac{\partial\alpha_2}{\partial\xi_1} \frac{\partial\alpha_1}{\partial\xi_2} \frac{\det(\mathbf{J}_{\xi_2})}{\det(\mathbf{J})} \right) \\
 \xi_{2,\alpha_1\alpha_1} &= \frac{1}{\det(\mathbf{J})^2} \left(-\frac{\partial\alpha_2}{\partial\xi_2} \frac{\partial^2\alpha_2}{\partial\xi_1^2} + \frac{\partial\alpha_2}{\partial\xi_2} \frac{\partial\alpha_2}{\partial\xi_1} \frac{\det(\mathbf{J}_{\xi_1})}{\det(\mathbf{J})} + \frac{\partial\alpha_2}{\partial\xi_1} \frac{\partial^2\alpha_2}{\partial\xi_1\partial\xi_2} - \left(\frac{\partial\alpha_2}{\partial\xi_1} \right)^2 \frac{\det(\mathbf{J}_{\xi_2})}{\det(\mathbf{J})} \right) \\
 \xi_{2,\alpha_2\alpha_2} &= \frac{1}{\det(\mathbf{J})^2} \left(-\frac{\partial\alpha_1}{\partial\xi_2} \frac{\partial^2\alpha_1}{\partial\xi_1^2} + \frac{\partial\alpha_1}{\partial\xi_2} \frac{\partial\alpha_1}{\partial\xi_1} \frac{\det(\mathbf{J}_{\xi_1})}{\det(\mathbf{J})} + \frac{\partial\alpha_1}{\partial\xi_1} \frac{\partial^2\alpha_1}{\partial\xi_1\partial\xi_2} - \left(\frac{\partial\alpha_1}{\partial\xi_1} \right)^2 \frac{\det(\mathbf{J}_{\xi_2})}{\det(\mathbf{J})} \right) \\
 \xi_{2,\alpha_1\alpha_2} &= \frac{1}{\det(\mathbf{J})^2} \left(-\frac{\partial\alpha_2}{\partial\xi_1} \frac{\partial^2\alpha_1}{\partial\xi_1\partial\xi_2} + \frac{\partial\alpha_1}{\partial\xi_2} \frac{\partial\alpha_1}{\partial\xi_1} \frac{\det(\mathbf{J}_{\xi_1})}{\det(\mathbf{J})} + \frac{\partial\alpha_2}{\partial\xi_2} \frac{\partial^2\alpha_1}{\partial\xi_1^2} - \frac{\partial\alpha_2}{\partial\xi_1} \frac{\partial\alpha_1}{\partial\xi_1} \frac{\det(\mathbf{J}_{\xi_2})}{\det(\mathbf{J})} \right)
 \end{aligned} \tag{29.65}$$

To define the external boundary conditions on a mapped shell, a local coordinate system is derived starting from the geometrical differential properties of the curves describing the shell edges. Namely, the orthogonal coordinate set of vectors $\mathbf{n}_n = [n_{n1} \ n_{n2} \ n_{n3}]^T$, $\mathbf{n}_s = [n_{s1} \ n_{s2} \ n_{s3}]^T$ and $\mathbf{n}_\zeta = [n_{\zeta1} \ n_{\zeta2} \ n_{\zeta3}]^T$ are defined in terms of their cosine directors with respect to the three-dimensional curvilinear axes $\alpha_1, \alpha_2, \alpha_3$. Accordingly, the generalized displacement field component vector $\mathbf{u}^{(\tau)}$ should be referred to the local reference system so that $\mathbf{u}^{(\tau)} = [u_n^{(\tau)} \ u_s^{(\tau)} \ u_\zeta^{(\tau)}]^T$ for each $\tau = 0, \dots, N + 1$. It should be noted that $n_{n3} = n_{s3} = n_{\zeta1} = n_{\zeta2} = 0$ and $n_{\zeta3} = 1$; whereby it is

$$\begin{bmatrix} u_n^{(\tau)} \\ u_s^{(\tau)} \\ u_\zeta^{(\tau)} \end{bmatrix} = \begin{bmatrix} n_{n1} & n_{n2} & 0 \\ n_{s1} & n_{s2} & 0 \\ 0 & 0 & 1 \end{bmatrix} \begin{bmatrix} u_1^{(\tau)} \\ u_2^{(\tau)} \\ u_3^{(\tau)} \end{bmatrix} \tag{29.66}$$

Following a similar procedure, generalized stress resultants $N_n^{(\tau)\alpha_1}$, $N_{ns}^{(\tau)\alpha_2}$ and $T_\zeta^{(\tau)\alpha_3}$ defined from the local reference system can be computed as

$$\begin{aligned}
 N_n^{(\tau)\alpha_1} &= N_1^{(\tau)\alpha_1} n_{n1}^2 + N_2^{(\tau)\alpha_1} n_{n2}^2 + N_{12}^{(\tau)\alpha_1} n_{n1} n_{n2} + N_{21}^{(\tau)\alpha_1} n_{n1} n_{n2} \\
 N_{ns}^{(\tau)\alpha_2} &= N_1^{(\tau)\alpha_2} n_{n1} n_{s1} + N_2^{(\tau)\alpha_2} n_{n2} n_{s2} + N_{12}^{(\tau)\alpha_2} n_{n1} n_{s2} + N_{21}^{(\tau)\alpha_2} n_{n2} n_{s1} \\
 T_\zeta^{(\tau)\alpha_3} &= T_1^{(\tau)\alpha_3} n_{n1} + T_2^{(\tau)\alpha_3} n_{n2}
 \end{aligned} \tag{29.67}$$

Employing the relations settled in Eqns. (29.66)-(29.67), Clamped (C) boundary condition of Eqn. (29.54) for an arbitrarily-shaped domain reads as follows:

$$\begin{aligned}
 u_n^{(\tau)} = u_s^{(\tau)} = u_\zeta^{(\tau)} &= 0 \quad \text{for } \tau = 0, \dots, N + 1, \quad \text{at } \xi_1 = \pm 1 \\
 u_n^{(\tau)} = u_s^{(\tau)} = u_\zeta^{(\tau)} &= 0 \quad \text{for } \tau = 0, \dots, N + 1, \quad \text{at } \xi_2 = \pm 1
 \end{aligned} \tag{29.68}$$

On the other hand, when the blending transformations of Eqn. (29.56) are adopted, the Free (F) edge, introduced in Eqn. (29.55), is defined in terms of $N_n^{(\tau)\alpha_1}$, $N_{ns}^{(\tau)\alpha_2}$ and $T_\zeta^{(\tau)\alpha_3}$,

$$\begin{aligned} N_n^{(\tau)} &= N_{ns}^{(\tau)} = T_\zeta^{(\tau)} = 0 \quad \text{for } \tau = 0, \dots, N + 1, \quad \text{at } \xi_1 = \pm 1 \\ N_{ns}^{(\tau)} &= N_n^{(\tau)} = T_\zeta^{(\tau)} = 0 \quad \text{for } \tau = 0, \dots, N + 1, \quad \text{at } \xi_2 = \pm 1 \end{aligned} \tag{29.69}$$

Note also that the four arbitrary-shaped sides of the distorted physical domain employed in Eqn. (29.56) are described in terms of NURBS curves. In this context, a parametrization $\mathbf{C}(u)$ of the curve is provided with $u \in [a, b]$ and $a, b \in \mathbb{R}$. A weighted interpolation is defined starting from a proper set of basis functions $N_{i,p}(u)$ with respect to n control points \mathbf{P}_i for $i = 1, \dots, n$,

$$\mathbf{C}(u) = \frac{\sum_{i=0}^n N_{i,p}(u) w_i \mathbf{P}_i}{\sum_{i=0}^n N_{i,p}(u) w_i} \tag{29.70}$$

being p the selected order of each $N_{i,p}$ and w_i the weighting coefficients. In the present Chapter it has been assumed $a = 0$ and $b = 1$. Moreover, a knot vector Ω has been introduced, setting m the number of breakpoints of the curve

$$\Omega = \left[\underbrace{a, \dots, a}_{p+1}, u_{p+1}, \dots, u_{m-p-1}, \underbrace{b, \dots, b}_{p+1} \right] \tag{29.71}$$

A recursive expression has been employed for the determination of $N_{i,p}(u)$ B-Spline basis functions

$$\begin{aligned} N_{i,0}(u) &= \begin{cases} 1 & \text{if } u_i \leq u < u_{i+1} \\ 0 & \text{otherwise} \end{cases} \\ N_{i,p}(u) &= \frac{u - u_i}{u_{i+p} - u_i} N_{i,p-1}(u) + \frac{u_{i+p+1} - u}{u_{i+p+1} - u_{i+1}} N_{i+1,p-1}(u) \end{aligned} \tag{29.72}$$

29.8 Numerical Implementation via GDQ Method

In what follows we provide the numerical assessment of the derived fundamental governing equations reported in Eqn. (29.46) for each τ, η -th kinematic expansion order. Referring to the parent element described in terms of ξ_1, ξ_2 physical coordinates, a bi-dimensional grid composed by $I_N \times I_M$ points is employed. Accordingly, if a generic bivariate function $f(\xi_1, \xi_2)$ is introduced, the derivative of the n -th and m -th order performed along natural coordinates ξ_1, ξ_2 , respectively, for $n, m = 0, 1, 2$, can be defined as follows, setting $f(\xi_{1k}, \xi_{2l})$ the values assumed by f at the arbitrary

point of the computational grid with $k = 1, \dots, I_N$ and $l = 1, \dots, I_M$,

$$\frac{\partial^{n+m} f(\xi_1, \xi_2)}{\partial \xi_1^n \partial \xi_2^m} \Big|_{\substack{\xi_1 = \xi_{1i}, \\ \xi_2 = \xi_{2j}}} \cong \sum_{k=1}^{I_N} \varsigma_{ik}^{\xi_1(n)} \left(\sum_{l=1}^{I_M} \varsigma_{jl}^{\xi_2(m)} f(\xi_{1k}, \xi_{2l}) \right) \quad \begin{matrix} i = 1, 2, \dots, I_N \\ j = 1, 2, \dots, I_M \end{matrix} \quad (29.73)$$

In other works from literature it has been demonstrated that the best performances of the GDQ Method in the previous relation are reached for non-uniform discrete grids. Referring to the bi-dimensional interval $[-1, 1] \times [-1, 1]$ described in terms of natural coordinates, the arbitrary ξ_{rp} point of the non-uniform grid employed in Eqn. (29.73) is located following the well-known Chebyshev-Gauss-Lobatto (CGL) distribution:

$$\xi_{rp} = -\cos\left(\frac{p-1}{I_P-1}\pi\right), \quad p = 1, \dots, I_P, \quad r = 1, 2, \quad I_P = I_N, I_M \quad (29.74)$$

Hereafter, the GDQ weighting coefficients for the numerical implementation of derivatives are computed employing the well-known Shu’s formula, based on the properties of the Lagrangian polynomials \mathcal{L} . If $q \geq 1$ with $q \in \mathbb{N}$ is assumed, it gives

$$\begin{aligned} \varsigma_{pv}^{\xi_r(1)} &= \frac{\mathcal{L}^{(1)}(\xi_{rp})}{(\xi_{rp} - \xi_{rv})\mathcal{L}^{(1)}(\xi_{rv})}, & \varsigma_{pv}^{\xi_r(q)} &= q \left(\varsigma_{pv}^{\xi_r(1)} \varsigma_{pp}^{\xi_r(q-1)} - \frac{\varsigma_{pv}^{\xi_r(q-1)}}{\xi_{rp} - \xi_{rv}} \right) \quad p \neq v \\ \varsigma_{pp}^{\xi_r(q)} &= - \sum_{v=1, v \neq p}^N \varsigma_{pv}^{\xi_r(q)} & & \quad p = v \end{aligned} \quad (29.75)$$

When $q = 0$, we assume that

$$\varsigma_{pv}^{\xi_r(0)} = \delta_{pv} = \begin{cases} 0 & \text{for } p \neq v \\ 1 & \text{for } p = v \end{cases} \quad (29.76)$$

As far as the numerical integration is concerned, the GDQ algorithm of Eqn. (29.73) is adopted within the fundamental theorem of integrals so that the Generalized Integral Quadrature (GIQ) is derived. Accordingly, the integral of a univariate function $f(\zeta)$ reads as

$$\int_{\zeta_k}^{\zeta_{k+1}} f(\zeta) d\zeta = \sum_{g=1}^{I_T} (w_{(k+1)g} - w_{kg}) f(\zeta_g) \quad (29.77)$$

where w_{kg} and $w_{(k+1)g}$ are the weighting coefficients that can be computed starting from Eqn. (29.75) following the procedure extensively reported in Tornabene and Baccocchi (2018). A CGL discrete grid of I_T has been introduced as well, referring to the interval $[-1, 1]$,

$$\xi_{kg} = -\cos\left(\frac{g-1}{I_T-1}\pi\right), \quad k = 1, \dots, l, \quad g = 1, \dots, I_T \quad \xi_{kg} \in [-1, 1] \quad (29.78)$$

In order to assess a discrete grid for the computation of integrals within the interval $[\zeta_k, \zeta_{k+1}]$ for $k = 1, \dots, l$ according to Eqn. (29.77), the following scaling relation is employed

$$\zeta_{kg} = \frac{\zeta_{k+1} - \zeta_k}{2} (\xi_{kg} + 1) + \zeta_k, \quad k = 1, \dots, l, \quad g = 1, \dots, I_T \quad \text{for } \xi_{kg} \in [-1, 1] \quad (29.79)$$

When the modal analysis of a generic doubly-curved shell is performed, the fundamental set of Eqn. (29.46) should be solved assuming harmonic solutions. In particular, a separation of spatial and time variables of $\mathbf{u}^{(\eta)}(\alpha_1, \alpha_2, t)$ is performed according to the following expression:

$$\mathbf{u}^{(\eta)}(\alpha_1, \alpha_2, t) = \mathbf{U}^{(\eta)}(\alpha_1, \alpha_2) e^{i\omega t} \quad (29.80)$$

where $\mathbf{U}^{(\eta)}(\alpha_1, \alpha_2)$ for each $\eta = 0, \dots, N + 1$ denotes the modal shape vector associated to the circular frequency ω . Referring to an arbitrary $\tau = 0, \dots, N + 1$ kinematic expansion order, the harmonic solution introduced in Eqn. (29.80) can be derived from Eqn. (29.46) setting $\mathbf{q}^{(\tau)} = \mathbf{0}$,

$$\sum_{\eta=0}^{N+1} \mathbf{L}^{(\tau\eta)} \mathbf{U}^{(\eta)} + \omega^2 \sum_{\eta=0}^{N+1} \mathbf{M}^{(\tau\eta)} \mathbf{U}^{(\eta)} = \mathbf{0} \quad \text{for } \tau = 0, \dots, N + 1 \quad (29.81)$$

In the same way, the fundamental set of equations of Eqn. (29.46) can be employed to define the differential relations for the statics of a doubly-curved anisotropic laminated structure under the constant assumption of the generalized displacement field, namely

$$\mathbf{u}^{(\tau)}(\alpha_1, \alpha_2, t) = \mathbf{u}^{(\tau)}(\alpha_1, \alpha_2) \quad (29.82)$$

such that $\ddot{\mathbf{u}}^{(\tau)} = \mathbf{0}$. In this way, the fundamental set of equations becomes

$$\sum_{\eta=0}^{N+1} \mathbf{L}^{(\tau\eta)} \mathbf{u}^{(\eta)} + \mathbf{q}^{(\tau)} = \mathbf{0} \quad \text{for } \tau = 0, \dots, N + 1 \quad (29.83)$$

For both the static and the dynamic problem it is possible to assess a DOFs rearrangement from the discrete form of Eqns. (29.81)-(29.83). In particular, a distinction between boundary nodes (b) and inner DOFs (d) is introduced, whose vectors are denoted as δ_b and δ_d . In the same way, the discrete assembled vector of external loads is split in \mathbf{q}_b and \mathbf{q}_d . More specifically, the static case, we will refer to the following relations:

$$\bar{\mathbf{L}} \delta = \begin{bmatrix} \bar{\mathbf{L}}_{bb} & \bar{\mathbf{L}}_{bd} \\ \bar{\mathbf{L}}_{db} & \bar{\mathbf{L}}_{dd} \end{bmatrix} \begin{bmatrix} \delta_b \\ \delta_d \end{bmatrix} = \begin{bmatrix} \mathbf{q}_b \\ \mathbf{q}_d \end{bmatrix} \quad (29.84)$$

where $\bar{\mathbf{L}}$ is the assembled discrete stiffness matrix. From the displacement field δ_b , the condensed form of the discrete system for the static analysis is introduced

$$\delta_d = (\bar{\mathbf{L}}_{dd} - \bar{\mathbf{L}}_{db} \bar{\mathbf{L}}_{bb}^{-1} \bar{\mathbf{L}}_{bd})^{-1} (\mathbf{q}_d - \bar{\mathbf{L}}_{db} \bar{\mathbf{L}}_{bb}^{-1} \mathbf{q}_b) \quad (29.85)$$

similarly, the fundamental relations (29.46) get into

$$\bar{\mathbf{L}}\boldsymbol{\delta} = \begin{bmatrix} \bar{\mathbf{L}}_{bb} & \bar{\mathbf{L}}_{bd} \\ \bar{\mathbf{L}}_{db} & \bar{\mathbf{L}}_{dd} \end{bmatrix} \begin{bmatrix} \boldsymbol{\delta}_b \\ \boldsymbol{\delta}_d \end{bmatrix} = \omega^2 \begin{bmatrix} \mathbf{0} & \mathbf{0} \\ \mathbf{0} & \bar{\mathbf{M}}_{dd} \end{bmatrix} \begin{bmatrix} \boldsymbol{\delta}_b \\ \boldsymbol{\delta}_d \end{bmatrix} \quad (29.86)$$

Employing the above-discussed DOFs condensation, it gives

$$(\bar{\mathbf{M}}_{dd}^{-1} (\bar{\mathbf{L}}_{dd} - \bar{\mathbf{L}}_{db} \bar{\mathbf{L}}_{bb}^{-1} \bar{\mathbf{L}}_{bd}) - \omega^2 \mathbf{I}) \boldsymbol{\delta}_d = 0 \quad (29.87)$$

29.9 Equilibrium-Based Recovery Procedure

Once the solution of the differential problem for the linear static analysis is found according to Eqn. (29.85), the three-dimensional distributions of kinematic and mechanical quantities can be derived starting from the ESL-based definitions of generalized strains and stresses. Accordingly, this procedure can lead to erroneous results if the constitutive relation is only used. Nevertheless, the three-dimensional governing differential equations can be used as well, since they are always valid for a doubly-curved structure. In this way, some mechanical quantities provided by the ESL procedure can be adjusted in order to provide very accurate results.

Taking into account the arbitrary k -th layer of the stacking sequence, for $k = 1, \dots, l$, for each point of the reference surface a set of I_T points is considered along the ζ thickness direction. Some discrete points $(\alpha_{1i}, \alpha_{2j}, \zeta_g^{(k)})$, are selected from the whole three-dimensional structure for $i = 1, \dots, I_N$, $j = 1, \dots, I_M$ and $g = 1, \dots, I_T$. Accordingly, the discrete form of the unknown field variable assessment of Eqn. (29.11) assumes the following form:

$$\mathbf{U}_{(ijg)}^{(k)} = \sum_{\tau=0}^{N+1} \mathbf{F}_{\tau(g)}^{(k)} \mathbf{u}_{(ij)}^{(\tau)}(\alpha_{1i}, \alpha_{2j}) \quad (29.88)$$

In expanded form, it gives:

$$\begin{bmatrix} U_{1(ijg)}^{(k)} \\ U_{2(ijg)}^{(k)} \\ U_{3(ijg)}^{(k)} \end{bmatrix} = \sum_{\tau=0}^{N+1} \begin{bmatrix} F_{\tau(g)}^{\alpha_1(k)}(\zeta_g^{(k)}) & 0 & 0 \\ 0 & F_{\tau(g)}^{\alpha_2(k)}(\zeta_g^{(k)}) & 0 \\ 0 & 0 & F_{\tau(g)}^{\alpha_3(k)}(\zeta_g^{(k)}) \end{bmatrix} \begin{bmatrix} u_{1(ij)}^{(\tau)}(\alpha_{1i}, \alpha_{2j}) \\ u_{2(ij)}^{(\tau)}(\alpha_{1i}, \alpha_{2j}) \\ u_{3(ij)}^{(\tau)}(\alpha_{1i}, \alpha_{2j}) \end{bmatrix} \quad (29.89)$$

Employing the discrete form of the higher order description of the displacement field variable, the ESL congruence relations of Eqn. (29.21) turns into

$$\boldsymbol{\varepsilon}_{(ijg)}^{(k)} = \sum_{\tau=0}^{N+1} \sum_{q=1}^3 \mathbf{Z}_{(ijg)}^{(k\tau)\alpha_q} \boldsymbol{\varepsilon}_{(ij)}^{(\tau)\alpha_q} \quad (29.90)$$

being

$$\boldsymbol{\varepsilon}_{(ijg)}^{(k)} = \left[\varepsilon_{1(ijg)}^{(k)} \ \varepsilon_{2(ijg)}^{(k)} \ \gamma_{12(ijg)}^{(k)} \ \gamma_{13(ijg)}^{(k)} \ \gamma_{23(ijg)}^{(k)} \ \varepsilon_{3(ijg)}^{(k)} \right]^T \quad (29.91)$$

In this way, the three-dimensional strain component defined in each discrete point $(\alpha_{1i}, \alpha_{2j}, \zeta_g^{(k)})$ selected from the three-dimensional solid, for $i = 1, \dots, I_N$, $j = 1, \dots, I_M$ and $g = 1, \dots, I_T$ for each k -th layer, is expressed in terms of the generalized higher order strain component $\varepsilon_{(ij)}^{(\tau)\alpha^q}$ for $q = 1, 2$ located on the corresponding point $(\alpha_{1i}, \alpha_{2j})$ belonging to the reference surface \mathbf{r} . Employing the three-dimensional constitutive relationship (29.4), the in-plane membrane stresses $\sigma_{1(ijg)}^{(k)}, \sigma_{2(ijg)}^{(k)}, \tau_{12(ijg)}^{(k)}$ can be computed in terms of $\varepsilon_{(ijg)}^{(k)}$ together with the rotated stiffness coefficients $\bar{C}_{\lambda\mu}^{(k)}$ with $\lambda, \mu = 1, \dots, 6$ of the k -th layer of the stacking sequence

$$\begin{bmatrix} \sigma_{1(ijg)}^{(k)} \\ \sigma_{2(ijg)}^{(k)} \\ \tau_{12(ijg)}^{(k)} \end{bmatrix} = \begin{bmatrix} \bar{C}_{11}^{(k)} & \bar{C}_{12}^{(k)} & \bar{C}_{16}^{(k)} & \bar{C}_{14}^{(k)} & \bar{C}_{15}^{(k)} & \bar{C}_{13}^{(k)} \\ \bar{C}_{12}^{(k)} & \bar{C}_{22}^{(k)} & \bar{C}_{26}^{(k)} & \bar{C}_{24}^{(k)} & \bar{C}_{25}^{(k)} & \bar{C}_{23}^{(k)} \\ \bar{C}_{16}^{(k)} & \bar{C}_{26}^{(k)} & \bar{C}_{66}^{(k)} & \bar{C}_{46}^{(k)} & \bar{C}_{56} & \bar{C}_{36} \end{bmatrix} \begin{bmatrix} \varepsilon_{1(ijg)}^{(k)} \\ \varepsilon_{2(ijg)}^{(k)} \\ \gamma_{12(ijg)}^{(k)} \\ \gamma_{13(ijg)}^{(k)} \\ \gamma_{23(ijg)}^{(k)} \\ \varepsilon_{3(ijg)}^{(k)} \end{bmatrix} \quad (29.92)$$

On the other hand, it is not feasible to follow a similar procedure based on the constitutive relationship (29.4) for the computation of the out-of-plane stresses $\tau_{13(ijg)}^{(k)}, \tau_{23(ijg)}^{(k)}, \sigma_{3(ijg)}^{(k)}$. Actually, the equilibrium equations for a three-dimensional doubly-curved solid described in terms of curvilinear principal coordinates $\alpha_1, \alpha_2, \zeta$ are adopted to this purpose in each k -th layer of the stacking sequence

$$\begin{bmatrix} q_{11} & 0 & 0 \\ 0 & q_{22} & 0 \\ 0 & 0 & q_{33} \end{bmatrix} \begin{bmatrix} \tau_{13}^{(k)} \\ \tau_{23}^{(k)} \\ \sigma_3^{(k)} \end{bmatrix} = \begin{bmatrix} a^{(k)} \\ b^{(k)} \\ c^{(k)} \end{bmatrix} \quad (29.93)$$

being

$$\begin{aligned} q_{11} &= \frac{\partial}{\partial \zeta} + \left(\frac{2}{R_1 + \zeta} + \frac{1}{R_2 + \zeta} \right) \\ q_{22} &= \frac{\partial}{\partial \zeta} + \left(\frac{1}{R_1 + \zeta} + \frac{2}{R_2 + \zeta} \right) \\ q_{33} &= \frac{\partial}{\partial \zeta} + \left(\frac{1}{R_1 + \zeta} + \frac{1}{R_2 + \zeta} \right) \end{aligned} \quad (29.94)$$

$$\begin{aligned}
 a^{(k)} &= -\frac{1}{A_1(1+\zeta/R_1)} \frac{\partial \sigma_1^{(k)}}{\partial \alpha_1} + \frac{\sigma_2^{(k)} - \sigma_1^{(k)}}{A_1 A_2(1+\zeta/R_2)} \frac{\partial A_2}{\partial \alpha_1} + \\
 &\quad -\frac{1}{A_2(1+\zeta/R_2)} \frac{\partial \tau_{12}^{(k)}}{\partial \alpha_2} - \frac{2\tau_{12}^{(k)}}{A_1 A_2(1+\zeta/R_1)} \frac{\partial A_1}{\partial \alpha_2} \\
 b^{(k)} &= -\frac{1}{A_2(1+\zeta/R_2)} \frac{\partial \sigma_2^{(k)}}{\partial \alpha_2} + \frac{\sigma_1^{(k)} - \sigma_2^{(k)}}{A_1 A_2(1+\zeta/R_1)} \frac{\partial A_1}{\partial \alpha_2} + \\
 &\quad -\frac{1}{A_1(1+\zeta/R_1)} \frac{\partial \tau_{12}^{(k)}}{\partial \alpha_1} - \frac{2\tau_{12}^{(k)}}{A_1 A_2(1+\zeta/R_2)} \frac{\partial A_2}{\partial \alpha_1} \\
 c^{(k)} &= -\frac{1}{A_1(1+\zeta/R_1)} \frac{\partial \tau_{13}^{(k)}}{\partial \alpha_1} - \frac{\tau_{13}^{(k)}}{A_1 A_2(1+\zeta/R_2)} \frac{\partial A_2}{\partial \alpha_1} + \\
 &\quad -\frac{1}{A_2(1+\zeta/R_2)} \frac{\partial \tau_{23}^{(k)}}{\partial \alpha_2} - \frac{\tau_{23}^{(k)}}{A_1 A_2(1+\zeta/R_1)} \frac{\partial A_1}{\partial \alpha_2} + \frac{\sigma_1^{(k)}}{R_1 + \zeta} + \frac{\sigma_2^{(k)}}{R_2 + \zeta}
 \end{aligned} \tag{29.95}$$

Starting from the membrane stresses calculated by means of the discrete constitutive relation (29.92), the out-of-plane three-dimensional stresses can be derived from Eqn. (29.93). Thus, the first order derivatives of $\sigma_1^{(k)}$, $\sigma_2^{(k)}$, $\tau_{12}^{(k)}$ with respect to α_1, α_2 are calculated in discrete form by means of Eqn. (29.73) for each $(\alpha_i, \alpha_j, \zeta_g^{(k)})$,

$$\begin{aligned}
 \sigma_{1,1(ijg)}^{(k)} &= \left. \frac{\partial \sigma_1^{(k)}}{\partial \alpha_1} \right|_{(ijg)} \cong \sum_{q=1}^{I_N} \zeta_{iq}^{\alpha_1(1)} \sigma_{1(qjg)}^{(k)} \\
 \sigma_{2,2(ijg)}^{(k)} &= \left. \frac{\partial \sigma_2^{(k)}}{\partial \alpha_2} \right|_{(ijg)} \cong \sum_{q=1}^{I_M} \zeta_{jq}^{\alpha_2(1)} \sigma_{2(qjg)}^{(k)} \\
 \tau_{12,1(ijg)}^{(k)} &= \left. \frac{\partial \tau_{12}^{(k)}}{\partial \alpha_1} \right|_{(ijg)} \cong \sum_{q=1}^{I_N} \zeta_{iq}^{\alpha_1(1)} \tau_{12(qjg)}^{(k)} \\
 \tau_{12,2(ijg)}^{(k)} &= \left. \frac{\partial \tau_{12}^{(k)}}{\partial \alpha_2} \right|_{(ijg)} \cong \sum_{q=1}^{I_M} \zeta_{jq}^{\alpha_2(1)} \tau_{12(qjg)}^{(k)}
 \end{aligned} \tag{29.96}$$

Once the discrete form of three-dimensional balance relations (29.93) is derived by means of the GDQ procedure, we can solve the problem with a proper enforcement of the natural equilibrium boundary conditions. Remembering that the relations at issue have been described within each k -th layer of the stacking sequence, the stress compatibility conditions between the discrete points $(\alpha_{1i}, \alpha_{2j}, \zeta_{I_T}^{(k)})$ and $(\alpha_{1i}, \alpha_{2j}, \zeta_1^{(k+1)})$ for each $k = 1, \dots, l - 1$ should be fulfilled

$$\begin{aligned}
 \tilde{\tau}_{13(ijI_T)}^{(k)} &= \tilde{\tau}_{13(ij1)}^{(k+1)} & i &= 1, \dots, I_N \\
 &\text{for } j &= 1, \dots, I_M \\
 \tilde{\tau}_{23(ijI_T)}^{(k)} &= \tilde{\tau}_{23(ij1)}^{(k+1)} & k &= 1, \dots, l - 1
 \end{aligned} \tag{29.97}$$

Referring to the first layer ($k = 1$), the out-of-plane shear stresses $\tau_{13(ij1)}^{(1)}, \tau_{23(ij1)}^{(1)}$ for each discrete computational point, should balance the external loads $q_{r(ij)}^{(-)} = q_{r(ij)}(-h/2)$ with $r = 1, 2$ applied to the bottom surface ($\zeta = -h/2$) of the structure along α_r principal direction

$$\begin{aligned} \tilde{\tau}_{13(ij1)}^{(1)} &= q_{1(ij)}^{(-)} \\ \tilde{\tau}_{23(ij1)}^{(1)} &= q_{2(ij)}^{(-)} \end{aligned} \tag{29.98}$$

On the other hand, the boundary conditions referred to the in-plane external surface loads $q_{1(ij)}^{(+)}, q_{2(ij)}^{(+)}$ enforced at the top surface of the shell ($\zeta = +h/2$) at each (α_i, α_j) point, are embedded in the model observing that the solution in terms of $\tilde{\tau}_{13}^{(k)}, \tilde{\tau}_{23}^{(k)}$ of the first two three-dimensional balance relations (29.93) with boundary constraints (29.97)-(29.98) is defined. Therefore, the actual value $\tau_{13}^{(k)}, \tau_{23}^{(k)}$ can be easily derived setting a new index $s = kg$. In this way, for each (α_i, α_j) discrete point of the reference surface two arrays are introduced, namely $\tilde{\tau}_{13}, \tilde{\tau}_{23}$,

$$\begin{aligned} \tilde{\tau}_{13} &= \left[\tilde{\tau}_{13(ij1)}^{(1)} \cdots \tilde{\tau}_{13(ijI_T)}^{(1)} \tilde{\tau}_{13(ij1)}^{(k)} \cdots \tilde{\tau}_{13(ijI_T)}^{(k)} \tilde{\tau}_{13(ij1)}^{(l)} \cdots \tilde{\tau}_{13(ijI_T)}^{(l)} \right]^T \\ \tilde{\tau}_{23} &= \left[\tilde{\tau}_{23(ij1)}^{(1)} \cdots \tilde{\tau}_{23(ijI_T)}^{(1)} \tilde{\tau}_{23(ij1)}^{(k)} \cdots \tilde{\tau}_{23(ijI_T)}^{(k)} \tilde{\tau}_{23(ij1)}^{(l)} \cdots \tilde{\tau}_{23(ijI_T)}^{(l)} \right]^T \end{aligned} \tag{29.99}$$

Accordingly, the adjusted out-of-plane shear stresses act as follows:

$$\begin{aligned} \tau_{13(ijs)} &= \tilde{\tau}_{13(ijs)} + \left(\zeta_s + \frac{h(ij)}{2} \right) \frac{q_{1(ij)}^{(+)} - \tilde{\tau}_{13(ijI_L)}}{h(ij)} & i = 1, \dots, I_N \\ & & \text{for } j = 1, \dots, I_M \\ \tau_{23(ijs)} &= \tilde{\tau}_{23(ijs)} + \left(\zeta_s + \frac{h(ij)}{2} \right) \frac{q_{2(ij)}^{(+)} - \tilde{\tau}_{23(ijI_L)}}{h(ij)} & s = 1, \dots, I_L \end{aligned} \tag{29.100}$$

being $h(ij) = h(\alpha_i, \alpha_j)$ and $q_{r(ij)}^{(+)} = q_{r(ij)}(\zeta = +h/2)$ for $r = 1, 2$ and $s = 1, \dots, I_L = lI_T$.

Once the adjusted shear stresses τ_{13}^k, τ_{23}^k for $k = 1, \dots, l$ have been computed throughout the entire shell thickness, they can be employed in the third equilibrium relation of Eqn. (29.93) to determine the out-of-plane normal stress σ_3^k for $k = 1, \dots, l$. As a premise, the first order derivative of τ_{13}^k, τ_{23}^k with respect to α_1, α_2 principal directions are computed by means of the GDQ Method (29.73), setting $g = 1, \dots, I_T$,

$$\begin{aligned} \left. \frac{\partial \tau_{13}^{(k)}}{\partial \alpha_1} \right|_{(ijg)} &\cong \sum_{q=1}^{I_N} \zeta_{iq}^{\alpha_1(1)} \tau_{13(qjg)}^{(k)} \\ \left. \frac{\partial \tau_{23}^{(k)}}{\partial \alpha_2} \right|_{(ijg)} &\cong \sum_{q=1}^{I_M} \zeta_{jq}^{\alpha_2(1)} \tau_{23(ijq)}^{(k)} \end{aligned} \tag{29.101}$$

Besides, normal stress compatibility conditions between two generic adjacent laminae k and $(k + 1)$, for $k = 1, \dots, l - 1$ act as follows:

$$\tilde{\sigma}_{3(ijI_T)}^{(k)} = \tilde{\sigma}_{3(ij1)}^{(k+1)} \quad (29.102)$$

Referring to each point $(\alpha_{1ij}, \alpha_{2ij}, \zeta_1^{(k)})$ of the bottom side of the shell, it is

$$\tilde{\sigma}_{3(ij1)}^{(1)} = q_{3(ij)}^{(-)} = q_{3(ij1)}(\zeta = -h/2) \quad (29.103)$$

Following a similar procedure of Eqn. (29.100), the array $\tilde{\sigma}_3$ is introduced

$$\tilde{\sigma}_3 = \left[\tilde{\sigma}_{3(ij1)}^{(1)} \cdots \tilde{\sigma}_{3(ijI_T)}^{(1)} \tilde{\sigma}_{3(ij1)}^{(k)} \cdots \tilde{\sigma}_{3(ijI_T)}^{(k)} \tilde{\sigma}_{3(ij1)}^{(l)} \cdots \tilde{\sigma}_{3(ijI_T)}^{(l)} \right]^T \quad (29.104)$$

The corrected values for the out-of-plane normal stress σ_{3ijs} are obtained for each $(\alpha_i, \alpha_j, \zeta_s)$ discrete point from a linear rotation of $\tilde{\sigma}_3$ components according to the following relation:

$$\sigma_{3(ijs)} = \tilde{\sigma}_{3(ijs)} + \left(\zeta_s + \frac{h_{(ij)}}{2} \right) \frac{q_{3(ij)}^{(+)} - \tilde{\sigma}_{3(ijI_L)}}{h_{(ij)}} \quad (29.105)$$

where $i = 1, \dots, I_N, j = 1, \dots, I_M$ and $s = 1, \dots, I_L = lI_T$.

We now focus to the adjustment of the through-the-thickness profiles of out-of-plane strains, which are conveniently arranged in the array $\mathbf{x}^{(k)} = [\gamma_{13(ijg)}^{(k)} \gamma_{23(ijg)}^{(k)} \varepsilon_{3(ijg)}^{(k)}]^T$ for $k = 1, \dots, l$. Referring to a generic k -th layer, a linear system can be determined starting from the three-dimensional generally anisotropic Hooke's law reported in Eqn. (29.4) for each $(\alpha_i, \alpha_j, \zeta_g^{(k)})$ discrete point of the k -th layer

$$\mathbf{A}^{(k)} \mathbf{x}^{(k)} = \mathbf{b}^{(k)} \quad (29.106)$$

where

$$\mathbf{A}^{(k)} = \begin{bmatrix} \bar{C}_{44(g)}^{(k)} & \bar{C}_{45(g)}^{(k)} & \bar{C}_{34(g)}^{(k)} \\ \bar{C}_{45(g)}^{(k)} & \bar{C}_{55(g)}^{(k)} & \bar{C}_{35(g)}^{(k)} \\ \bar{C}_{34(g)}^{(k)} & \bar{C}_{35(g)}^{(k)} & \bar{C}_{33(g)}^{(k)} \end{bmatrix} \quad (29.107)$$

$$\mathbf{b}^{(k)} = \begin{bmatrix} \tau_{13(ijg)}^{(k)} - \bar{C}_{14(g)}^{(k)} \varepsilon_{1(ijg)}^{(k)} - \bar{C}_{24(g)}^{(k)} \varepsilon_{2(ijg)}^{(k)} - \bar{C}_{46(g)}^{(k)} \gamma_{12(ijg)}^{(k)} \\ \tau_{23(ijg)}^{(k)} - \bar{C}_{15(g)}^{(k)} \varepsilon_{1(ijg)}^{(k)} - \bar{C}_{25(g)}^{(k)} \varepsilon_{2(ijg)}^{(k)} - \bar{C}_{56(g)}^{(k)} \gamma_{12(ijg)}^{(k)} \\ \sigma_{3(ijg)}^{(k)} - \bar{C}_{13(g)}^{(k)} \varepsilon_{1(ijg)}^{(k)} - \bar{C}_{23(g)}^{(k)} \varepsilon_{2(ijg)}^{(k)} - \bar{C}_{36(g)}^{(k)} \gamma_{12(ijg)}^{(k)} \end{bmatrix}$$

Since $\det \mathbf{A}^{(k)} \neq 0$, the linear system introduced in Eqn. (29.106) provides a unique solution that can be computed as

$$\mathbf{x}^{(k)} = \left(\mathbf{A}^{(k)} \right)^{-1} \mathbf{b}^{(k)} \quad (29.108)$$

In extended form, each component of $\mathbf{x}^{(k)}$ reads as follows:

$$\begin{aligned} \gamma_{13(ijg)}^{(k)} &= \frac{1}{\Delta^{(k)}} \left(\bar{C}_{33(g)}^{(k)} \bar{C}_{55(g)}^{(k)} - \bar{C}_{35(g)}^{(k)2} \right) \left(\tau_{13(ijg)}^{(k)} - \bar{C}_{14(g)}^{(k)} \varepsilon_{1(ijg)}^{(k)} - \bar{C}_{24(g)}^{(k)} \varepsilon_{2(ijg)}^{(k)} - \bar{C}_{46(g)}^{(k)} \gamma_{12(ijg)}^{(k)} \right) + \\ &\quad + \frac{1}{\Delta^{(k)}} \left(\bar{C}_{34(g)}^{(k)} \bar{C}_{35(g)}^{(k)} - \bar{C}_{33(g)}^{(k)} \bar{C}_{45(g)}^{(k)} \right) \left(\tau_{23(ijg)}^{(k)} - \bar{C}_{15(g)}^{(k)} \varepsilon_{1(ijg)}^{(k)} - \bar{C}_{25(g)}^{(k)} \varepsilon_{2(ijg)}^{(k)} - \bar{C}_{56(g)}^{(k)} \gamma_{12(ijg)}^{(k)} \right) + \\ &\quad + \frac{1}{\Delta^{(k)}} \left(\bar{C}_{35(g)}^{(k)} \bar{C}_{45(g)}^{(k)} - \bar{C}_{34(g)}^{(k)} \bar{C}_{55(g)}^{(k)} \right) \left(\sigma_{3(ijg)}^{(k)} - \bar{C}_{13(g)}^{(k)} \varepsilon_{1(ijg)}^{(k)} - \bar{C}_{23(g)}^{(k)} \varepsilon_{2(ijg)}^{(k)} - \bar{C}_{36(g)}^{(k)} \gamma_{12(ijg)}^{(k)} \right) \\ \gamma_{23(ijg)}^{(k)} &= \frac{1}{\Delta^{(k)}} \left(\bar{C}_{34(g)}^{(k)} \bar{C}_{35(g)}^{(k)} - \bar{C}_{33(g)}^{(k)} \bar{C}_{45(g)}^{(k)} \right) \left(\tau_{13(ijg)}^{(k)} - \bar{C}_{14(g)}^{(k)} \varepsilon_{1(ijg)}^{(k)} - \bar{C}_{24(g)}^{(k)} \varepsilon_{2(ijg)}^{(k)} - \bar{C}_{46(g)}^{(k)} \gamma_{12(ijg)}^{(k)} \right) + \\ &\quad + \frac{1}{\Delta^{(k)}} \left(\bar{C}_{33(g)}^{(k)} \bar{C}_{44(g)}^{(k)} - \bar{C}_{34(g)}^{(k)2} \right) \left(\tau_{23(ijg)}^{(k)} - \bar{C}_{15(g)}^{(k)} \varepsilon_{1(ijg)}^{(k)} - \bar{C}_{25(g)}^{(k)} \varepsilon_{2(ijg)}^{(k)} - \bar{C}_{56(g)}^{(k)} \gamma_{12(ijg)}^{(k)} \right) + \\ &\quad + \frac{1}{\Delta^{(k)}} \left(\bar{C}_{34(g)}^{(k)} \bar{C}_{45(g)}^{(k)} - \bar{C}_{35(g)}^{(k)} \bar{C}_{44(g)}^{(k)} \right) \left(\sigma_{3(ijg)}^{(k)} - \bar{C}_{13(g)}^{(k)} \varepsilon_{1(ijg)}^{(k)} - \bar{C}_{23(g)}^{(k)} \varepsilon_{2(ijg)}^{(k)} - \bar{C}_{36(g)}^{(k)} \gamma_{12(ijg)}^{(k)} \right) \\ \varepsilon_{3(ijg)}^{(k)} &= \frac{1}{\Delta^{(k)}} \left(\bar{C}_{35(g)}^{(k)} \bar{C}_{45(g)}^{(k)} - \bar{C}_{34(g)}^{(k)} \bar{C}_{55(g)}^{(k)} \right) \left(\tau_{13(ijg)}^{(k)} - \bar{C}_{14(g)}^{(k)} \varepsilon_{1(ijg)}^{(k)} - \bar{C}_{24(g)}^{(k)} \varepsilon_{2(ijg)}^{(k)} - \bar{C}_{46(g)}^{(k)} \gamma_{12(ijg)}^{(k)} \right) + \\ &\quad + \frac{1}{\Delta^{(k)}} \left(\bar{C}_{34(g)}^{(k)} \bar{C}_{45(g)}^{(k)} - \bar{C}_{35(g)}^{(k)} \bar{C}_{44(g)}^{(k)} \right) \left(\tau_{23(ijg)}^{(k)} - \bar{C}_{15(g)}^{(k)} \varepsilon_{1(ijg)}^{(k)} - \bar{C}_{25(g)}^{(k)} \varepsilon_{2(ijg)}^{(k)} - \bar{C}_{56(g)}^{(k)} \gamma_{12(ijg)}^{(k)} \right) + \\ &\quad + \frac{1}{\Delta^{(k)}} \left(\bar{C}_{44(g)}^{(k)} \bar{C}_{55(g)}^{(k)} - \bar{C}_{45(g)}^{(k)2} \right) \left(\sigma_{3(ijg)}^{(k)} - \bar{C}_{13(g)}^{(k)} \varepsilon_{1(ijg)}^{(k)} - \bar{C}_{23(g)}^{(k)} \varepsilon_{2(ijg)}^{(k)} - \bar{C}_{36(g)}^{(k)} \gamma_{12(ijg)}^{(k)} \right) \end{aligned} \quad (29.109)$$

being

$$\begin{aligned} \Delta^{(k)} = \det \mathbf{A}^{(k)} &= \bar{C}_{33(g)}^{(k)} \bar{C}_{44(g)}^{(k)} \bar{C}_{55(g)}^{(k)} + 2 \bar{C}_{34(g)}^{(k)} \bar{C}_{35(g)}^{(k)} \bar{C}_{45(g)}^{(k)} + \\ &\quad - \bar{C}_{44(g)}^{(k)} \bar{C}_{35(g)}^{(k)2} - \bar{C}_{33(g)}^{(k)} \bar{C}_{45(g)}^{(k)2} - \bar{C}_{55(g)}^{(k)} \bar{C}_{34(g)}^{(k)2} \end{aligned} \quad (29.110)$$

29.10 General Boundary Conditions

In the previous section the fundamental set of equations has been derived from the Hamiltonian principle in a variational form, together with the static and kinematic boundary conditions. Accordingly, they have been derived within the ESL approach accounting for the generalized stress resultants and displacement field variable acting on the shell reference surface $\mathbf{r}(\alpha_1, \alpha_2)$. We recall that the vector $\mathbf{S}^{(\tau)\alpha_i}$ with $\alpha_i = \alpha_1, \alpha_2, \alpha_3$ and $\tau = 0, \dots, N + 1$ has been determined in Eqn. (29.26) from a numerical through-the-thickness integration of the stresses dispersion. Referring to a generic edge of an arbitrarily-shaped domain, the three-dimensional stress component vector $\bar{\sigma}(\alpha_1, \alpha_2, \zeta) = [\bar{\sigma}_1 \ \bar{\sigma}_2 \ \bar{\tau}_{12} \ \bar{\tau}_{13} \ \bar{\tau}_{23} \ \bar{\sigma}_3]^T$ is introduced. General boundary conditions can be enforced on the doubly-curved shell structure if $\bar{\sigma}(\alpha_1, \alpha_2, \zeta)$ components are considered within the ESL approach in terms of generalized stress resultants. Referring to the points of the physical domain located at $\alpha_1 = \alpha_1^s$ with $s = 0, 1$ it gives, setting $\alpha_2 \in [\alpha_2^0, \alpha_2^1]$,

$$\begin{bmatrix} \bar{N}_1^{(\tau)\alpha_1} \\ \bar{N}_{12}^{(\tau)\alpha_2} \\ \bar{T}_1^{(\tau)\alpha_3} \end{bmatrix} = \sum_{k=1}^l \int_{\zeta_k}^{\zeta_{k+1}} \begin{bmatrix} \bar{\sigma}_1 & 0 & 0 \\ 0 & \bar{\tau}_{12} & 0 \\ 0 & 0 & \bar{\tau}_{13} \end{bmatrix} \begin{bmatrix} F_\tau^{\alpha_1} \\ F_\tau^{\alpha_2} \\ F_\tau^{\alpha_3} \end{bmatrix} \bar{\lambda} H_2 d\zeta \quad \text{for } \tau = 0, \dots, N + 1 \tag{29.111}$$

Following a similar procedure, the generalized stress resultants $\bar{N}_{21}^{(\tau)\alpha_1}, \bar{N}_2^{(\tau)\alpha_2}, \bar{T}_2^{(\tau)\alpha_3}$ acting at $\alpha_1 \in [\alpha_1^0, \alpha_1^1]$ with $\alpha_2 = \alpha_2^s$ for $s = 0, 1$ can be defined as

$$\begin{bmatrix} \bar{N}_{21}^{(\tau)\alpha_1} \\ \bar{N}_2^{(\tau)\alpha_2} \\ \bar{T}_2^{(\tau)\alpha_3} \end{bmatrix} = \sum_{k=1}^l \int_{\zeta_k}^{\zeta_{k+1}} \begin{bmatrix} \bar{\tau}_{12} & 0 & 0 \\ 0 & \bar{\sigma}_2 & 0 \\ 0 & 0 & \bar{\tau}_{23} \end{bmatrix} \begin{bmatrix} F_\tau^{\alpha_1} \\ F_\tau^{\alpha_2} \\ F_\tau^{\alpha_3} \end{bmatrix} \bar{\lambda} H_1 d\zeta \quad \text{for } \tau = 0, \dots, N + 1 \tag{29.112}$$

whose expressions account for a through-the-thickness dispersion of stresses. To this purpose, a univariate parameter $\bar{\lambda} = \bar{\lambda}(\zeta)$ has been introduced. In this way, a constant ($\bar{\lambda} = 1$), linear ($\bar{\lambda} = \frac{2\zeta}{h}$) or parabolic ($\bar{\lambda} = 1 - \left(\frac{2\zeta}{h}\right)^2$) variation along the outward normal unit direction \mathbf{n} has been implemented.

In order to provide an in-plane assessment of the external constraints along the shell edges, the dimensionless coordinates $\bar{\xi}, \tilde{\xi} \in [0, 1]$ are introduced, according to the following definitions:

$$\bar{\xi} = \frac{\alpha_r - \alpha_r^0}{\alpha_r^1 - \alpha_r^0}, \quad \tilde{\xi} = \frac{\alpha_r^1 - \alpha_r}{\alpha_r^1 - \alpha_r^0} = 1 - \bar{\xi} \quad \text{for } r = 1, 2 \tag{29.113}$$

Nevertheless, two univariate expressions in terms of $\bar{\xi}, \tilde{\xi}$ have been considered. Accordingly, a Double - Weibull (D) distribution has been implemented, letting p be a power exponent and $\bar{\xi}_m, \tilde{\xi}_m \in [0, 1]$ the position parameters

$$f(\xi) = 1 - e^{-\left(\frac{\bar{\xi}}{\bar{\xi}_m}\right)^p} + e^{-\left(\frac{\tilde{\xi}}{\tilde{\xi}_m}\right)^p} \tag{29.114}$$

Based on a Super Elliptic (S) function it is

$$f(\xi) = e^{-\left|\frac{\bar{\xi} - \bar{\xi}_m}{\tilde{\xi}_m}\right|^p} \tag{29.115}$$

where $\bar{\xi}_m \in [0, 1]$ is the position parameter, whereas $\tilde{\xi}_m \in [0, 1]$ is a shape factor. For a proper assessment of a generalized set of external constraints, it is useful to associate the boundary stress component vector to a three-dimensional dispersion of linear elastic springs acting along the three principal directions of the shell $\alpha_1, \alpha_2, \alpha_3$. Accordingly, the linear elastic springs stiffness is denoted with $k_{if}^{(k)\alpha_j^m}$, activated by the three-dimensional displacement field component U_i with $i = 1, 2, 3$. Nevertheless, the springs at issue are distributed along the edge located at α_j^m , with

$m = 0, 1$ and $j = 1, 2$. Referring to the shell sides located at $\alpha_1 = \alpha_1^m$ with $\alpha_2 \in [\alpha_2^0, \alpha_2^1]$, the following relations are valid

$$\begin{aligned} \bar{\sigma}_1^{(k)}(\alpha_1^m, \alpha_2, \zeta) &= -k_{1f}^{(k)\alpha_1^m} f(\alpha_1^m, \alpha_2) U_1(\alpha_1^m, \alpha_2, \zeta) \\ \bar{\tau}_{12}^{(k)}(\alpha_1^m, \alpha_2, \zeta) &= -k_{2f}^{(k)\alpha_1^m} f(\alpha_1^m, \alpha_2) U_2(\alpha_1^m, \alpha_2, \zeta) \quad \text{for } m = 0, 1 \\ \bar{\tau}_{13}^{(k)}(\alpha_1^m, \alpha_2, \zeta) &= -k_{3f}^{(k)\alpha_1^m} f(\alpha_1^m, \alpha_2) U_3(\alpha_1^m, \alpha_2, \zeta) \end{aligned} \quad (29.116)$$

In the same way, stresses $\bar{\tau}_{12}^{(k)}, \bar{\sigma}_2^{(k)}, \bar{\tau}_{23}^{(k)}$ act at $\alpha_1 \in [\alpha_1^0, \alpha_1^1]$, letting $\alpha_2 = \alpha_2^m$,

$$\begin{aligned} \bar{\tau}_{12}^{(k)}(\alpha_1, \alpha_2^m, \zeta) &= -k_{1f}^{(k)\alpha_2^m} f(\alpha_1, \alpha_2^m) U_1(\alpha_1, \alpha_2^m, \zeta) \\ \bar{\sigma}_2^{(k)}(\alpha_1, \alpha_2^m, \zeta) &= -k_{2f}^{(k)\alpha_2^m} f(\alpha_1, \alpha_2^m) U_2(\alpha_1, \alpha_2^m, \zeta) \quad \text{for } m = 0, 1 \\ \bar{\tau}_{23}^{(k)}(\alpha_1, \alpha_2^m, \zeta) &= -k_{3f}^{(k)\alpha_2^m} f(\alpha_1, \alpha_2^m) U_3(\alpha_1, \alpha_2^m, \zeta) \end{aligned} \quad (29.117)$$

Starting from the higher order ESL assumption for the displacement field of Eqn. (29.11), Eqn. (29.116) becomes as follows:

$$\begin{aligned} \bar{\sigma}_1^{(k)}(\alpha_1^m, \alpha_2, \zeta) &= -k_{1f}^{(k)\alpha_1^m} f(\alpha_1^m, \alpha_2) \sum_{\eta=0}^{N+1} F_{\eta}^{\alpha_1}(\zeta) u_1^{(\eta)}(\alpha_1^m, \alpha_2) \\ \bar{\tau}_{12}^{(k)}(\alpha_1^m, \alpha_2, \zeta) &= -k_{2f}^{(k)\alpha_1^m} f(\alpha_1^m, \alpha_2) \sum_{\eta=0}^{N+1} F_{\eta}^{\alpha_2}(\zeta) u_2^{(\eta)}(\alpha_1^m, \alpha_2) \quad \text{for } m = 0, 1 \\ \bar{\tau}_{13}^{(k)}(\alpha_1^m, \alpha_2, \zeta) &= -k_{3f}^{(k)\alpha_1^m} f(\alpha_1^m, \alpha_2) \sum_{\eta=0}^{N+1} F_{\eta}^{\alpha_3}(\zeta) u_3^{(\eta)}(\alpha_1^m, \alpha_2) \end{aligned} \quad (29.118)$$

On the other hand, Eqn. (29.117) applied at $\alpha_2 = \alpha_2^m$ comes into the following relations:

$$\begin{aligned} \bar{\tau}_{12}^{(k)}(\alpha_1, \alpha_2^m, \zeta) &= -k_{1f}^{(k)\alpha_2^m} f(\alpha_1, \alpha_2^m) \sum_{\eta=0}^{N+1} F_{\eta}^{\alpha_1}(\zeta) u_1^{(\eta)}(\alpha_1, \alpha_2^m) \\ \bar{\sigma}_2^{(k)}(\alpha_1, \alpha_2^m, \zeta) &= -k_{2f}^{(k)\alpha_2^m} f(\alpha_1, \alpha_2^m) \sum_{\eta=0}^{N+1} F_{\eta}^{\alpha_2}(\zeta) u_2^{(\eta)}(\alpha_1, \alpha_2^m) \quad \text{for } m = 0, 1 \\ \bar{\tau}_{23}^{(k)}(\alpha_1, \alpha_2^m, \zeta) &= -k_{3f}^{(k)\alpha_2^m} f(\alpha_1, \alpha_2^m) \sum_{\eta=0}^{N+1} F_{\eta}^{\alpha_3}(\zeta) u_3^{(\eta)}(\alpha_1, \alpha_2^m) \end{aligned} \quad (29.119)$$

Thus, the three-dimensional stresses acting at the boundaries of the structure can be expressed in terms of the generalized displacement field component vector. They can be generally distributed on both in-plane and out-of-plane directions, leading to the definition of a three-dimensional set of external constraints even though a bi-dimensional model is developed.

Rearranging Eqns. (29.118)-(29.119), it is useful to introduce a new set of fundamental coefficients $L_{i(p)\alpha_n^m}^{fb(\tau\eta)\alpha_i}$ for each $\tau, \eta = 0, \dots, N + 1$, setting $n, p = 1, 2$,

$m = 0, 1$ and $i = 1, 2, 3$,

$$L_{i(p)\alpha_n^m}^{fb(\tau\eta)\alpha_i} = \sum_{k=1}^l \int_{\zeta_k}^{\zeta_{k+1}} k_{if}^{(k)\alpha_n^m} F_{\eta}^{\alpha_i} F_{\tau}^{\alpha_i} H_p d\zeta \tag{29.120}$$

Eqn. (29.118) can be also expressed in a unified manner as follows:

$$\begin{bmatrix} \bar{N}_1^{(\tau)\alpha_1} \\ \bar{N}_{12}^{(\tau)\alpha_2} \\ \bar{T}_1^{(\tau)\alpha_3} \end{bmatrix} = - \sum_{\eta=0}^{N+1} \begin{bmatrix} L_{1(2)\alpha_1^m}^{fb(\tau\eta)\alpha_1} & 0 & 0 \\ 0 & L_{2(2)\alpha_1^m}^{fb(\tau\eta)\alpha_2} & 0 \\ 0 & 0 & L_{3(2)\alpha_1^m}^{fb(\tau\eta)\alpha_2} \end{bmatrix} \begin{bmatrix} u_1^{(\eta)} \\ u_2^{(\eta)} \\ u_3^{(\eta)} \end{bmatrix} \tag{29.121}$$

In the same way, the generalized boundary stresses defined in Eqn. (29.119) can be defined as

$$\begin{bmatrix} \bar{N}_{21}^{(\tau)\alpha_1} \\ \bar{N}_2^{(\tau)\alpha_2} \\ \bar{T}_2^{(\tau)\alpha_3} \end{bmatrix} = - \sum_{\eta=0}^{N+1} \begin{bmatrix} L_{1(1)\alpha_2^m}^{fb(\tau\eta)\alpha_1} & 0 & 0 \\ 0 & L_{2(1)\alpha_2^m}^{fb(\tau\eta)\alpha_2} & 0 \\ 0 & 0 & L_{3(1)\alpha_2^m}^{fb(\tau\eta)\alpha_3} \end{bmatrix} \begin{bmatrix} u_1^{(\eta)} \\ u_2^{(\eta)} \\ u_3^{(\eta)} \end{bmatrix} \tag{29.122}$$

29.11 Applications and Results

The proposed formulation is here applied to investigate the static and modal behaviour of different structural members. The attention is focused on different geometric properties, involving positive, zero and negative curvatures. The physical domain is described in terms of principal coordinates, and an isogeometric mapping is considered by means of the blending functions in Eqn. (29.56). Different material synergies are employed, setting different numbers of layers and material symmetry planes. Moreover, each lamina can feature a general orientation. Accordingly, different kinds of layers are modeled, namely isotropic, orthotropic and generally anisotropic materials. All the material properties are provided from the built-in database of the DiQuMASPAB software, see Tornabene et al (2018). In particular, to the first class belong Steel ($E = 2.10 \cdot 10^{11}$ Pa, $\nu = 0.3$, $\rho = 7800$ kg/m³) and the Zirconia material ($E = 1.68 \cdot 10^{11}$ Pa, $\nu = 0.3$, $\rho = 5700$ kg/m³). In addition, two different orthotropic composite materials are considered in the analyses, whose mechanical behaviour has been implemented in terms of the engineering constants. Accordingly, the graphite-epoxy ($\rho = 1450$ kg/m³) mechanical behaviour are reported below

$$\begin{aligned} E_1 &= 1.379 \cdot 10^{11} \text{ Pa}, G_{12} = 7.10 \cdot 10^9 \text{ Pa}, \nu_{12} = 0.30 \\ E_2 &= 8.960 \cdot 10^9 \text{ Pa}, G_{13} = 7.10 \cdot 10^9 \text{ Pa}, \nu_{13} = 0.30 \\ E_3 &= 8.960 \cdot 10^9 \text{ Pa}, G_{23} = 6.21 \cdot 10^9 \text{ Pa}, \nu_{23} = 0.49 \end{aligned}$$

The glass-epoxy ($\rho = 1900 \text{ kg/m}^3$) material properties are, thus, collected as

$$\begin{aligned} E_1 &= 5.38 \cdot 10^{10} \text{ Pa}, G_{12} = 8.96 \cdot 10^9 \text{ Pa}, \nu_{12} = 0.25 \\ E_2 &= 1.79 \cdot 10^{10} \text{ Pa}, G_{13} = 8.96 \cdot 10^9 \text{ Pa}, \nu_{13} = 0.25 \\ E_3 &= 1.79 \cdot 10^{10} \text{ Pa}, G_{23} = 3.45 \cdot 10^9 \text{ Pa}, \nu_{23} = 0.34 \end{aligned}$$

Moreover, two examples of generally anisotropic continuum are considered throughout the simulations, namely the trigonal material ($\rho = 2649 \text{ kg/m}^3$) and the triclinic material ($\rho = 7750 \text{ kg/m}^3$). Their stiffness matrices have been expressed with respect to the material reference system, following the notation adopted in Eqn. (29.4). The first one reads as follows:

$$\mathbf{C}^{(k)} = \begin{bmatrix} 86.74 & 6.99 & 0 & 0 & -17.91 & 11.91 \\ 6.99 & 86.74 & 0 & 0 & 17.91 & 11.91 \\ 0 & 0 & 39.88 & -17.91 & 0 & 0 \\ 0 & 0 & -17.91 & 57.94 & 0 & 0 \\ -17.91 & 17.91 & 0 & 0 & 57.94 & 0 \\ 11.91 & 11.91 & 0 & 0 & 0 & 107.20 \end{bmatrix} \text{ GPa}$$

Accordingly, the triclinic material stiffness constants are collected

$$\mathbf{C}^{(k)} = \begin{bmatrix} 98.84 & 53.92 & 0.03 & 1.05 & -0.1 & 50.78 \\ 53.92 & 99.19 & 0.03 & 0.55 & -0.18 & 50.87 \\ 0.03 & 0.03 & 22.55 & -0.04 & 0.25 & 0.02 \\ 1.05 & 0.55 & -0.04 & 21.1 & 0.07 & 1.03 \\ -0.1 & -0.18 & 0.25 & 0.07 & 21.14 & -0.18 \\ 50.78 & 50.87 & 0.02 & 1.03 & -0.18 & 87.23 \end{bmatrix} \text{ GPa} \quad (29.123)$$

The first set of analyses focuses on a rectangular plate of constant thickness under different external constrains. A central triclinic core has been considered, covered by two external sheets of orthotropic graphite-epoxy. All useful information regarding the assessment of external constraints can be found in Fig. 29.2.

A constant out-of-plane profile of linear elastic springs has been modelled in all cases, whereas the employment of the Super Elliptic distribution of Eqn. (29.115) has allowed to partially clamp a single edge of the structure. The ESL analysis has been conducted with a CGL grid characterized by $I_N = I_M = 37$. Actually, different higher order theories have been employed according to Eqn. (29.11). Moreover, the contribution of the generalized zigzag function has been checked. The reference solution for the validation of results has been obtained from a 3D FEM model composed by 242445 DOFs.

The second case study consists of a doubly-curved structure belonging to the class of shells with positive curvature. Namely, a parabolic paraboloid of arbitrary shape has been investigated (Fig. 29.3). It has been provided with a bivariate sinusoidal thickness variation so that the central part of the mapped physical domain is characterized by the maximum stiffness and width. As visible in Fig. 29.3, the mapping of the physical domain can be obtained starting from both concave and convex

NURBS curves. The central core is characterized by a non-homogeneous isotropic layer, made of zirconia and steel. Besides, two outer layers of triclinic material have been modelled. A GDQ model with $I_N = I_M = 37$ has been developed according to the present formulation employing higher order theories, here validated against a 3D FEM simulation characterized by 930810 DOFs.

A similar mapping of the physical domain has been considered for an arbitrarily-shaped hyperbolic hyperboloid, whose features are reported in Fig. 29.4. The shell at issue is obtained from a translation on a parabolic shape over another parabola of different concavity. A sinusoidal thickness variation has been considered, but a constant shift turns the central part of the structure to be the thinnest part of the entire shell. The lamination scheme is characterized by three generally-oriented layers, two trigonal external sheets and a central isotropic region made of zirconia. The ESL approach has been built with a CGL computational grid discretized by 37 points for each direction, whereas the 3D FEM simulation is developed with brick elements, leading to a refined model of 188826 DOFs.

Next example consists of a truncated cone characterized by a rhombic squared mapping, with geometric properties as reported in Fig. 29.5, together with the lamination scheme characteristics and the distorted edges dataset. The stacking sequence consists of two layers of orthotropic composite materials, namely graphite-epoxy and glass-epoxy, and a lamina of triclinic material. A sinusoidal thickness variation is considered in this case. The last case study refers to a catenoid (Fig. 29.6) of variable thickness made by two external laminae of generally anisotropic materials, and a central layer of orthotropic material singony. The main issue related to the present example is the blending assessment of the shell from the parametrization with physical coordinates. Accordingly, four circular NURBS arches with the same concavity have been considered, such that the structured CGL computational grid $I_N = I_M = 37$ developed for the GDQ model has required an extensive distortion of the physical domain.

The numerical simulations have been organized as follows: a free vibration analysis is performed, first, for each structural member under different boundary conditions. Ten mode frequencies have been calculated with the proposed formulation employing different higher order theories. Then, for the rectangular plate, the parabolic paraboloid and the catenoid a linear static analysis has been conducted. Nevertheless, the through-the-thickness displacement field assumption is identified with the notation introduced in the previous sections. In particular, in the case of unmapped rectangular plate, the parabolic paraboloid and hyperbolic paraboloid have been modelled based on a 3D finite elements whose results are here considered as reference solutions for validation purposes. The truncated cone and the arbitrary-shaped cone have been investigated via a generalized higher order ESL approach.

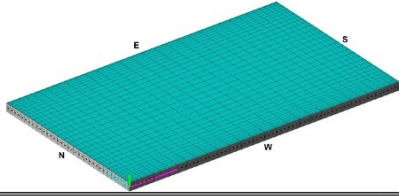
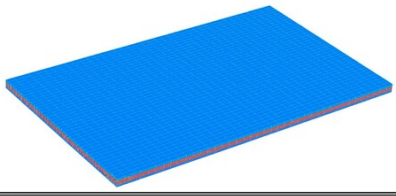
| Rectangular Plate | |
|---|---|
| Reference surface equation in principal coordinates $\alpha_1, \alpha_2 = x, y$ | |
| $\mathbf{r}(x, y) = -x \mathbf{e}_1 + y \mathbf{e}_2$ | |
| GDQ Model | 3D FEM Model – 242445 DOFs |
|  |  |
| $(\mathbf{FB}_{SSS}^K \mathbf{FC})$ | |
| Super Elliptic distribution: | $\bar{\xi}_m = 1, \tilde{\xi}_m = 0.5, p = 1000$ |
| Thickness Profile: | $\bar{\lambda} = 1$ |
| Boundary Springs: | $k_{1f}^{(k)\xi_1^1} = k_{2f}^{(k)\xi_1^1} = k_{3f}^{(k)\xi_1^1} = 1.0 \times 10^{21} \text{ Pa/m}$ |
| $(\mathbf{B}_{SSS}^K \mathbf{FB}_{SSS}^K \mathbf{B}_{SSS}^K)$ | |
| Super Elliptic distribution: | $\bar{\xi}_m = 1, \tilde{\xi}_m = 0.5, p = 1000$ |
| Thickness Profile: | $\bar{\lambda} = 1$ |
| Boundary Springs: | $k_{1f}^{(k)\xi_1^0} = k_{1f}^{(k)\xi_1^1} = k_{1f}^{(k)\xi_2^0} = 1.0 \times 10^{21} \text{ Pa/m}$ |
| | $k_{2f}^{(k)\xi_1^0} = k_{2f}^{(k)\xi_1^1} = k_{2f}^{(k)\xi_2^0} = 1.0 \times 10^{21} \text{ Pa/m}$ |
| | $k_{3f}^{(k)\xi_1^0} = k_{3f}^{(k)\xi_1^1} = k_{3f}^{(k)\xi_2^0} = 1.0 \times 10^{21} \text{ Pa/m}$ |
| $(\mathbf{B}_{SSS}^K \mathbf{FB}_{SSS}^K \mathbf{F})$ | |
| Super Elliptic distribution: | $\bar{\xi}_m = 1, \tilde{\xi}_m = 0.5, p = 1000$ |
| Thickness Profile: | $\bar{\lambda} = 1$ |
| Boundary Springs: | $k_{1f}^{(k)\xi_1^0} = k_{1f}^{(k)\xi_1^1} = 1.0 \times 10^{21} \text{ Pa/m}$ |
| | $k_{2f}^{(k)\xi_1^0} = k_{2f}^{(k)\xi_1^1} = 1.0 \times 10^{21} \text{ Pa/m}$ |
| | $k_{3f}^{(k)\xi_1^0} = k_{3f}^{(k)\xi_1^1} = 1.0 \times 10^{21} \text{ Pa/m}$ |
| Geometric Inputs: | $L_x = 2.5 \text{ m}, L_y = 1.5 \text{ m}$ |
| Stacking Sequence: | $\bar{h}_1 = \bar{h}_3 = 0.02 \text{ m}, \bar{h}_2 = 0.03 \text{ m}, (0/30/45)$ |
| | 1 st graphite-epoxy, 2 nd triclinic material, 3 rd graphite-epoxy |
| Surface Loads: | $q_3^{(+)} = -5.0 \times 10^3 \text{ Pa}$ |

Fig. 29.2 Geometric and mechanical features of a rectangular plate of constant thickness and generally anisotropic lamination scheme. Two external skins of generally oriented orthotropic graphite-epoxy are considered, with a central layer of triclinic material. The structure is studied in both its static and dynamic behaviour setting different generalized external constraints.

Parabolic Paraboloid

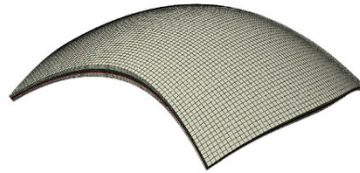
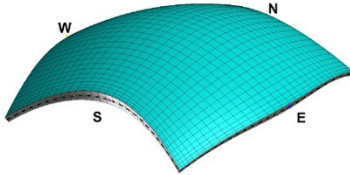
Reference surface equation in principal coordinates α_1, α_2

$$\mathbf{r}(\alpha_1, \alpha_2) = \left(\frac{k^{\alpha_1} \tan \alpha_1}{2} - \frac{k^{\alpha_2} \tan^2 \alpha_2}{4} \sin \alpha_1 \right) \mathbf{e}_1 - \left(\frac{k^{\alpha_2} \tan \alpha_2}{2} \right) \mathbf{e}_2 + \left(\frac{k^{\alpha_1} \tan^2 \alpha_1}{4} + \frac{k^{\alpha_2} \tan^2 \alpha_2}{4} \cos \alpha_1 \right) \mathbf{e}_3$$

$k^{\alpha_1} = 3, k^{\alpha_2} = 2$

GDQ Model

3D FEM Model – 930810 DOFs



Thickness Variations

$$\phi_1(\alpha_1, \alpha_2) = \left(\sin(\pi(n_1 \bar{\alpha}_1 + \alpha_{1m})) \right)^{p_1}$$

$\delta_1 = 1.2, n_1 = 1, p_1 = 2, \alpha_{1m} = 0$

$$\phi_2(\alpha_1, \alpha_2) = \left(\sin(\pi(n_2 \bar{\alpha}_2 + \alpha_{2m})) \right)^{p_2}$$

$\delta_2 = 1.2, n_2 = 1, p_2 = 2, \alpha_{2m} = 0$

Physical Domain NURBS mapping

Edge 1-2

knots → 0.0,0.0,0.0,1.0,1.0,1.0
 weights → 1.0,1.0,1.0
 c. points → (-0.50,-0.50), (0.00,-0.70), (0.50,-0.50)

Edge 2-3

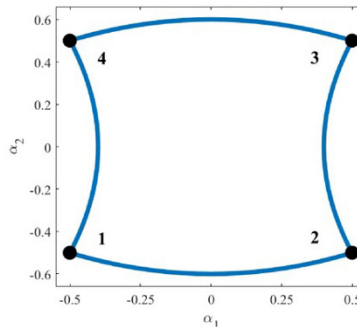
knots → 0.0,0.0,0.0,1.0,1.0,1.0
 weights → 1.0,1.0,1.0
 c. points → (0.50,-0.50), (0.30,-0.00), (0.50,0.50)

Edge 3-4

knots → 0.0,0.0,0.0,1.0,1.0,1.0
 weights → 1.0,1.0,1.0
 c. points → (0.50,0.50), (0.00,0.70), (-0.50,0.50)

Edge 4-1

knots → 0.0,0.0,0.0,1.0,1.0,1.0
 weights → 1.0,1.0,1.0
 c. points → (-0.50,0.50), (-0.30,0.00), (-0.50,-0.50)



Stacking Sequence:

(30 / 0 / 0 / 70), $\bar{h}_1 = \bar{h}_4 = 0.01$ m, $\bar{h}_2 = \bar{h}_3 = 0.005$ m

1st triclinic material, 2nd zirconia, 3rd steel, 4th triclinic material

Surface Loads: $q_3^{(t)} = -1.0 \times 10^4$ Pa

Fig. 29.3 Geometric and mechanical features of a parabolic paraboloid with a variable thickness and general lamination scheme. The structure is mapped with a generalized algorithm based on a NURBS description of the edges in the physical domain. Two external skins of generally oriented triclinic material are considered, with a central non-homogeneous core made of two isotropic materials.

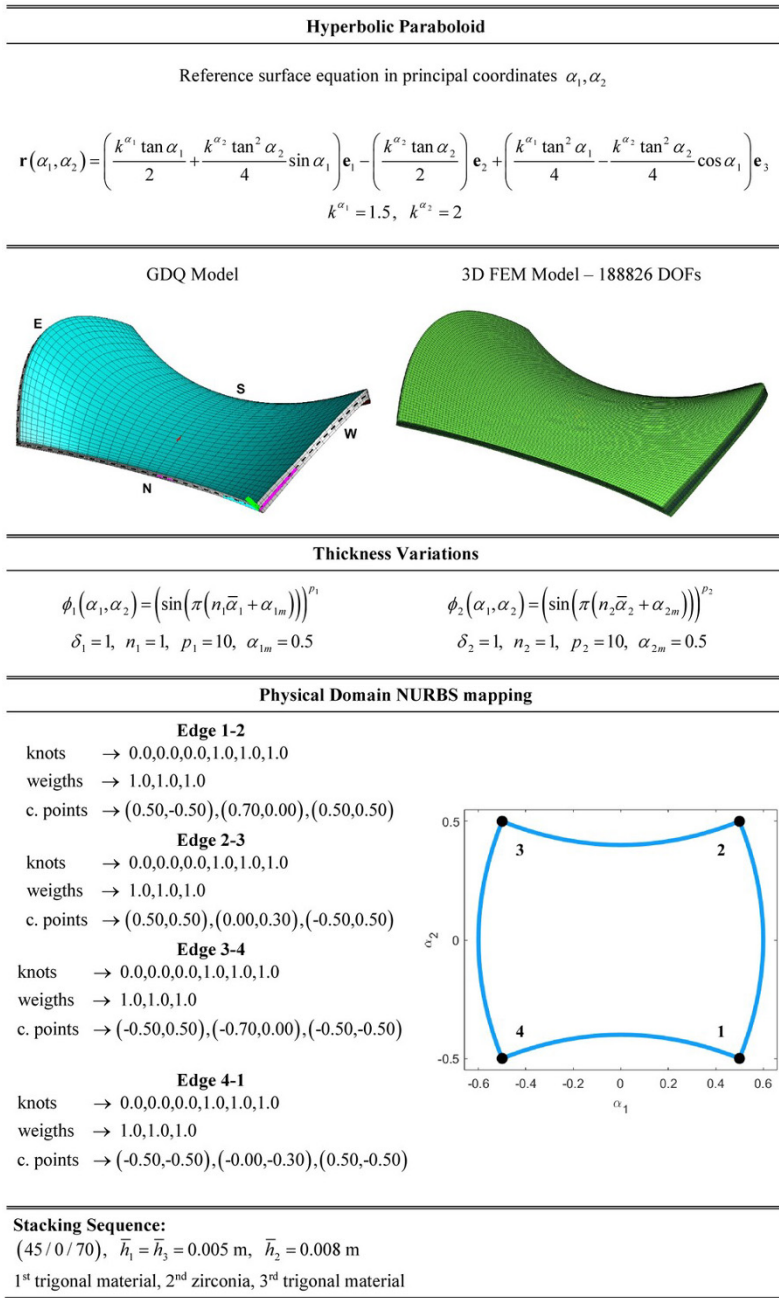


Fig. 29.4 Geometric and mechanical features of a hyperbolic paraboloid with a variable thickness and general lamination scheme. The structure is mapped with a generalized algorithm based on a NURBS description of the edges in the physical domain. Two external skins of generally oriented trigonal material are considered, with a central isotropic core made of a zirconia layer.

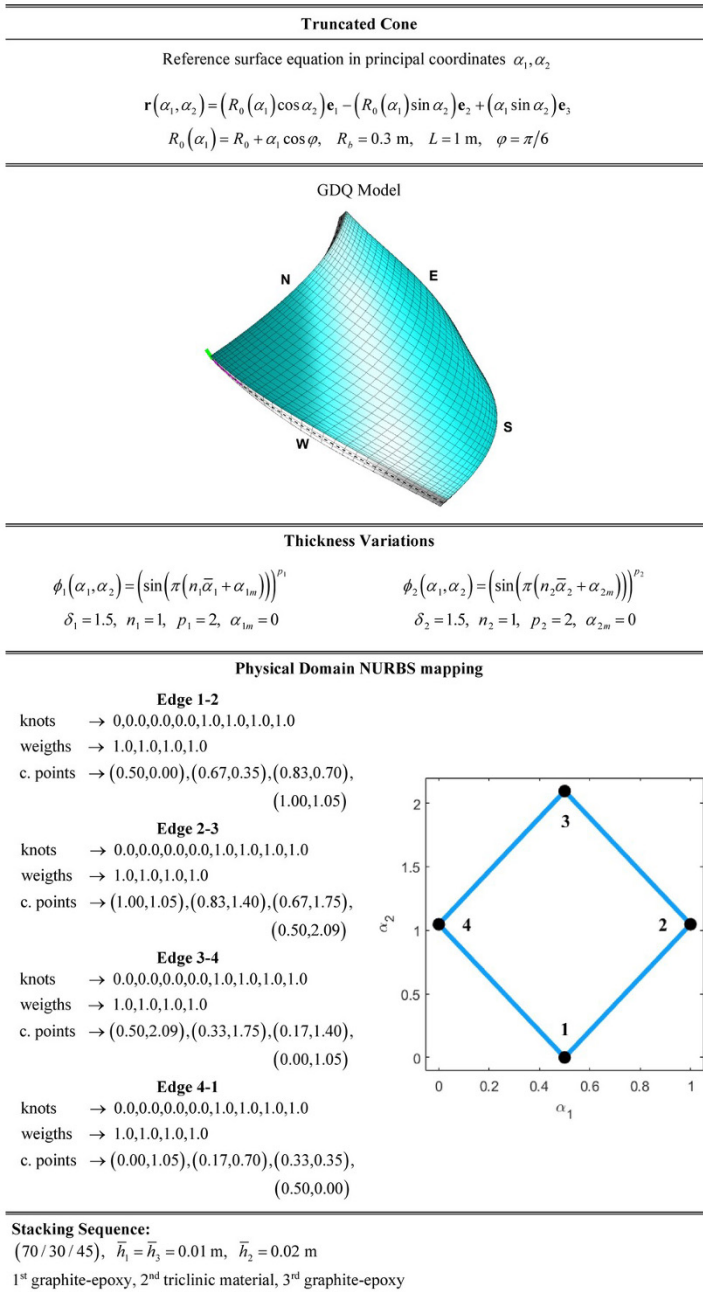


Fig. 29.5 Geometric and mechanical features of an arbitrary shaped truncated cone with a variable thickness and general lamination scheme. The structure is mapped with a generalized algorithm based on a NURBS description of the edges in the physical domain. Two external skins of generally oriented orthotropic materials are considered, with a central triclinc layer.

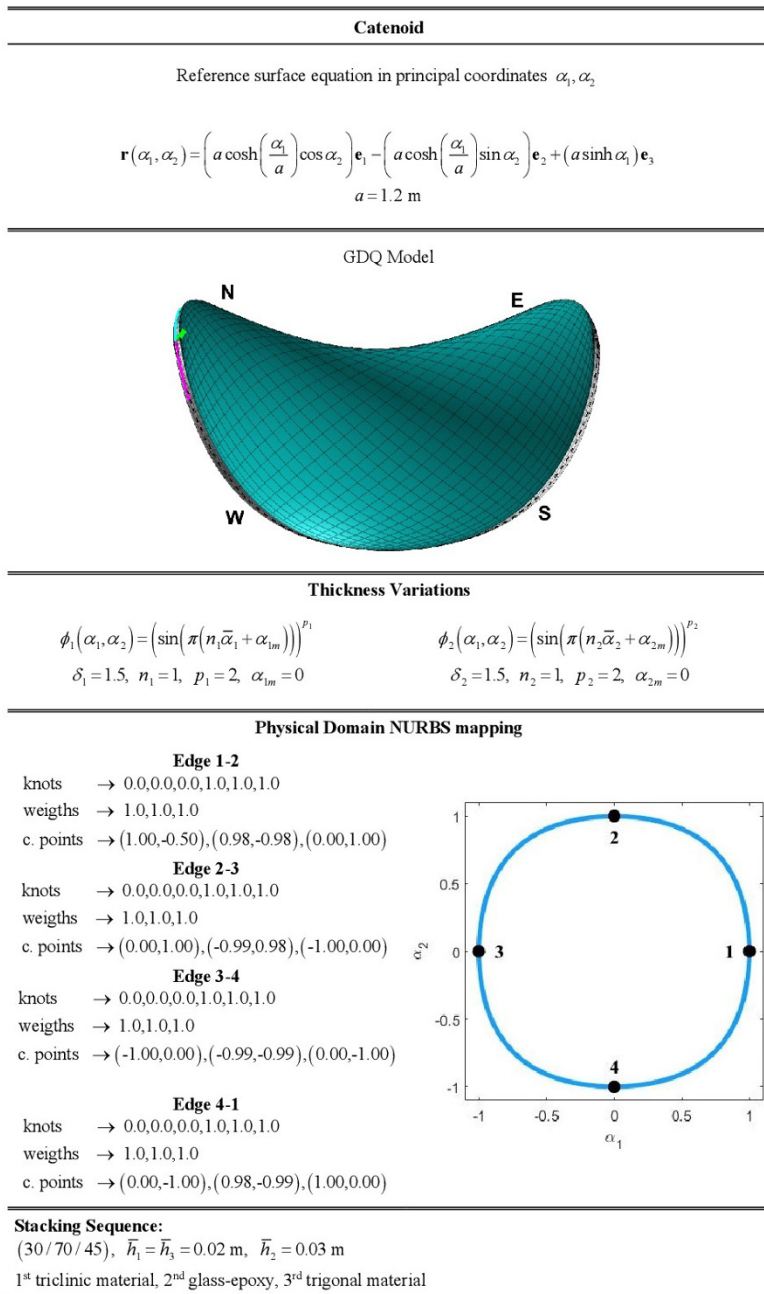


Fig. 29.6 Geometric and mechanical features of an arbitrary shaped catenoid with a variable thickness and general lamination scheme. The structure is mapped with a generalized algorithm based on a NURBS description of the edges in the physical domain. Two external skins of generally oriented triclinic and trigonal materials are considered, with a central glass epoxy core modelled as an orthotropic continuum medium.

29.11.1 Free Vibration Analysis

The mode frequencies and mode shapes are now computed for each selected structure, both based on the proposed ESL formulation and 3D FEM approach.

As far as the unmapped rectangular plate is concerned, the first ten mode frequencies are reported in Table 29.1 for all boundary conditions. In Fig. 29.7 we also report the first nine mode shapes of the rectangular plate calculated by means of the GDQ Method employing the EDZ4 displacement field assumption. Accordingly, the external constraint identified with (FB_{SSS}^KFC) has been considered. For the first mode shape a limited displacement can be observed near the partially free edge of the structure. From the second eigenvector on, the region at issue is even more interested by vibration deflections, coming into a non-conventional modal deformation. Referring to the natural frequencies reported in Table 29.1, the GDQ solution employing higher order theories best fits the 3D FEM outcomes. In particular, for the first case, the employment of a fourth order kinematic expansion ($N = 4$) yields a perfect alignment between different approaches also for higher modes. The second and the third external constraint configurations are characterized by two parallel edges (E-W) fixed at half length. On the other hand, for the second case also the North (N) edge is constrained. For both cases, the GDQ approach provide the same level of accuracy, showing a mean discrepancy from 3D FEM of about 1%.

The second set of simulations, reported in Table 29.2, is performed on a hyperbolic paraboloid under three different generalized boundary conditions. The first configuration employed the Double - Weibull distribution for the assessment of the external constraints. The dispersion parameters have been selected so that only four corners of the structure are clamped. In this case, the EDZ4 displacement field assumption is required for a proper computation of both lower and higher natural frequencies of the structure, as provided by the 3D FEM model. This means that a coupling between stretching and warping effects occurs within each lamina, together with a zigzag phenomenon between two adjacent layers. Lower order theories, as well as classical approaches (FSDT and TSDT) do not provide a perfect alignment for all the frequency ranges. In Fig. 29.8 we show the first nine mode shapes for the selected case, along with the fixed points of the structure, as well as the asymmetry of the deflection due to the anisotropy of the lamination scheme. As far as the second configuration is concerned, the employment of the Super Elliptic distribution has been adopted so that a quarter of the East (E) and West (W) edges of the mapped hyperbolic paraboloid are blocked. Since an abrupt variation of the boundary spring stiffness should be modelled, the power parameter has been chosen for $p = 1000$. Also for this case, a perfect alignment between higher order ESL theories and the 3D FEM outcomes can be noticed for both lower and higher modes.

The last simulation performed on the mapped hyperbolic paraboloid has been provided with conventional (FFCF) external constraints, so that the validity of the formulation is checked even for common configurations. Accordingly, a cantilever assessment of the structure has been considered for the present doubly-curved structure. In this case, the peculiarity of the lamination scheme required a higher order assumption of the displacement field, as the classical FSDT approach leads to rel-

Table 29.1 Mode frequencies of a rectangular plate enforced with general boundary conditions employing different higher order theories.

| Rectangular Plate | | | | | | | | | | | | | |
|---|---------|---------|---------|---------|---------|---------|---------|---------|---------|---------|---------|---------|---------|
| Mode [Hz] | 3D FEM | FSDT | FSDTZ | TSDT | TSDTZ | ED1 | EDZ1 | ED2 | EDZ2 | ED3 | EDZ3 | ED4 | EDZ4 |
| DOFs | 242445 | 7350 | 110225 | 14700 | 18375 | 7350 | 11025 | 11025 | 14700 | 14700 | 18375 | 18375 | 22050 |
| (FB ^k _{SSS} FC) | | | | | | | | | | | | | |
| 1 | 75.642 | 75.370 | 75.486 | 75.383 | 75.292 | 73.929 | 82.693 | 75.532 | 75.494 | 75.689 | 75.588 | 75.631 | 75.534 |
| 2 | 101.709 | 100.574 | 100.811 | 100.679 | 100.498 | 98.175 | 108.964 | 100.757 | 100.691 | 101.050 | 100.858 | 100.973 | 100.778 |
| 3 | 159.592 | 155.682 | 156.222 | 155.986 | 155.581 | 151.782 | 167.045 | 155.828 | 155.687 | 156.506 | 156.084 | 156.381 | 155.973 |
| 4 | 202.392 | 201.902 | 202.567 | 202.133 | 201.678 | 198.041 | 221.028 | 202.137 | 201.972 | 202.961 | 202.483 | 202.763 | 202.293 |
| 5 | 218.481 | 211.347 | 212.265 | 211.766 | 211.140 | 206.907 | 228.546 | 211.504 | 211.301 | 212.623 | 211.967 | 212.428 | 211.781 |
| 6 | 249.980 | 244.850 | 245.954 | 245.438 | 244.602 | 238.103 | 262.348 | 244.903 | 244.619 | 246.268 | 245.413 | 246.034 | 245.181 |
| 7 | 271.630 | 269.469 | 270.593 | 270.108 | 269.257 | 262.475 | 289.706 | 269.507 | 269.212 | 270.899 | 270.022 | 270.654 | 269.784 |
| 8 | 337.023 | 331.616 | 333.295 | 332.632 | 331.247 | 322.249 | 349.274 | 331.340 | 330.859 | 333.467 | 332.048 | 333.174 | 331.775 |
| 9 | 370.648 | 368.508 | 370.456 | 369.719 | 368.219 | 359.228 | 395.999 | 368.273 | 367.774 | 370.698 | 369.182 | 370.322 | 368.811 |
| 10 | 388.488 | 387.467 | 389.606 | 388.421 | 387.011 | 380.084 | 422.500 | 387.390 | 386.927 | 389.974 | 388.530 | 389.507 | 388.078 |
| Boundary Springs: | | | | | | | | | | | | | |
| Super Elliptic distribution ($\bar{\xi}_m = 1, \bar{\xi}_m = 0.5, p = 1000$) | | | | | | | | | | | | | |
| $k_{1f}^{(k)}\epsilon_1^1 = 1 \cdot 10^{21}$ Pa/m, $k_{2f}^{(k)}\epsilon_1^1 = 1 \cdot 10^{21}$ Pa/m, $k_{3f}^{(k)}\epsilon_1^1 = 1 \cdot 10^{21}$ Pa/m | | | | | | | | | | | | | |
| (B ^k _{SSS} FB ^k _{SSS} B ^k _{SSS}) | | | | | | | | | | | | | |
| 1 | 52.571 | 54.613 | 54.958 | 54.816 | 54.619 | 52.787 | 57.502 | 54.605 | 54.557 | 54.973 | 54.755 | 54.926 | 54.711 |
| 2 | 72.665 | 72.805 | 72.947 | 72.846 | 72.748 | 71.373 | 79.689 | 72.946 | 72.907 | 73.124 | 73.016 | 73.065 | 72.960 |
| 3 | 94.549 | 95.076 | 95.300 | 95.168 | 94.990 | 92.323 | 101.192 | 95.145 | 95.080 | 95.429 | 95.242 | 95.369 | 95.180 |
| 4 | 146.012 | 148.943 | 149.580 | 149.322 | 148.779 | 145.527 | 156.971 | 148.899 | 148.713 | 149.728 | 149.171 | 149.602 | 149.058 |
| 5 | 166.167 | 169.266 | 169.938 | 169.616 | 169.107 | 164.076 | 176.763 | 169.249 | 169.077 | 170.071 | 169.543 | 169.932 | 169.404 |
| 6 | 182.768 | 186.914 | 187.963 | 187.557 | 186.721 | 181.797 | 197.342 | 186.668 | 186.409 | 187.987 | 187.148 | 187.817 | 186.990 |
| 7 | 204.224 | 204.502 | 205.208 | 204.730 | 204.212 | 199.900 | 222.046 | 204.574 | 204.389 | 205.462 | 204.922 | 205.266 | 204.734 |
| 8 | 227.903 | 229.102 | 229.924 | 229.520 | 228.909 | 222.997 | 246.725 | 229.105 | 228.901 | 230.132 | 229.499 | 229.947 | 229.320 |
| 9 | 270.478 | 271.571 | 272.586 | 272.253 | 271.304 | 264.698 | 284.184 | 271.295 | 270.953 | 272.625 | 271.663 | 272.426 | 271.466 |
| 10 | 292.852 | 293.721 | 294.923 | 294.363 | 293.393 | 285.465 | 313.824 | 293.482 | 293.150 | 295.003 | 294.013 | 294.741 | 293.761 |
| Boundary Springs: | | | | | | | | | | | | | |
| Super Elliptic distribution ($\bar{\xi}_m = 1, \bar{\xi}_m = 0.5, p = 1000$) | | | | | | | | | | | | | |
| $k_{1f}^{(k)}\epsilon_1^0 = k_{1f}^{(k)}\epsilon_2^0 = k_{1f}^{(k)}\epsilon_3^0 = 1 \cdot 10^{21}$ Pa/m, $k_{2f}^{(k)}\epsilon_1^0 = k_{2f}^{(k)}\epsilon_2^0 = k_{2f}^{(k)}\epsilon_3^0 = 1 \cdot 10^{21}$ Pa/m, $k_{3f}^{(k)}\epsilon_1^0 = k_{3f}^{(k)}\epsilon_2^0 = k_{3f}^{(k)}\epsilon_3^0 = 1 \cdot 10^{21}$ Pa/m | | | | | | | | | | | | | |
| (B ^k _{SSS} FB ^k _{SSS} F) | | | | | | | | | | | | | |
| 1 | 18.458 | 19.164 | 19.240 | 19.217 | 19.170 | 18.462 | 19.625 | 19.162 | 19.154 | 19.248 | 19.197 | 19.242 | 19.192 |
| 2 | 40.695 | 41.616 | 41.827 | 41.785 | 41.661 | 40.016 | 42.952 | 41.582 | 41.555 | 41.814 | 41.684 | 41.799 | 41.672 |
| 3 | 71.219 | 71.440 | 71.563 | 71.469 | 71.385 | 70.196 | 78.378 | 71.589 | 71.553 | 71.743 | 71.652 | 71.684 | 71.593 |
| 4 | 89.348 | 89.647 | 89.806 | 89.683 | 89.554 | 87.902 | 96.428 | 89.664 | 89.623 | 89.876 | 89.734 | 89.825 | 89.688 |
| 5 | 101.102 | 102.693 | 103.021 | 102.882 | 102.653 | 99.923 | 108.448 | 102.670 | 102.597 | 103.064 | 102.826 | 103.002 | 102.769 |
| 6 | 148.433 | 150.670 | 151.096 | 150.834 | 150.429 | 146.679 | 157.876 | 150.479 | 150.333 | 151.063 | 150.650 | 150.951 | 150.545 |
| 7 | 166.148 | 169.186 | 169.824 | 169.435 | 168.880 | 164.133 | 175.213 | 168.973 | 168.784 | 169.806 | 169.236 | 169.661 | 169.101 |
| 8 | 199.764 | 200.297 | 200.835 | 200.477 | 200.099 | 196.340 | 217.774 | 200.237 | 200.099 | 200.896 | 200.509 | 200.735 | 200.356 |
| 9 | 205.929 | 206.912 | 207.555 | 207.175 | 206.694 | 202.862 | 225.110 | 206.888 | 206.725 | 207.697 | 207.196 | 207.519 | 207.030 |
| 10 | 221.906 | 222.944 | 223.624 | 223.192 | 222.648 | 215.805 | 237.908 | 222.763 | 222.577 | 223.643 | 223.074 | 223.475 | 222.918 |
| Boundary Springs: | | | | | | | | | | | | | |
| Super Elliptic distribution ($\bar{\xi}_m = 1, \bar{\xi}_m = 0.5, p = 1000$) | | | | | | | | | | | | | |
| $k_{1f}^{(k)}\epsilon_2^0 = k_{1f}^{(k)}\epsilon_3^0 = 1 \cdot 10^{21}$ Pa/m, $k_{2f}^{(k)}\epsilon_2^0 = k_{2f}^{(k)}\epsilon_3^0 = 1 \cdot 10^{21}$ Pa/m, $k_{3f}^{(k)}\epsilon_2^0 = k_{3f}^{(k)}\epsilon_3^0 = 1 \cdot 10^{21}$ Pa/m | | | | | | | | | | | | | |
| Lamination Scheme: | | | | | | | | | | | | | |
| (0/30/45), $\bar{h}_1 = \bar{h}_3 = 0.02, \bar{h}_2 = 0.03$ m | | | | | | | | | | | | | |
| Materials Sequence: 1 st layer graphite-epoxy, 2 nd layer triclinic material, 3 rd layer graphite-epoxy | | | | | | | | | | | | | |
| Computational Issues: CGL bi-dimensional computational grid with $I_N = I_M = 37$ discrete points | | | | | | | | | | | | | |

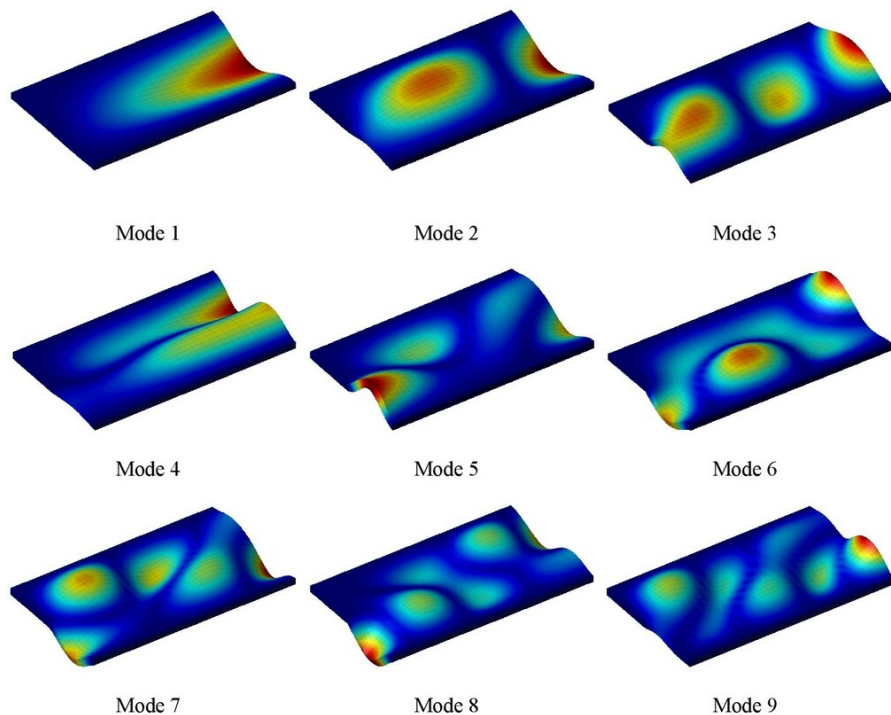


Fig. 29.7 First nine mode shapes of a rectangular plate enforced with general boundary conditions calculated by means of the ESL formulation via the GDQ Method. The employment of the higher order assumption of the displacement field allows to properly describe the deflection of the structure for each mode, accounting for the through-the-thickness warping and stretching effects coming from the lamination scheme. The areas colored with blue are characterized by minimum displacements magnitude. The maximum deflection has been highlighted with red instead.

actively erroneous natural frequencies with respect to 3D FEM. Looking at the first natural frequency, the EDZ4 approach has revealed to be capable of well predicting the 3D FEM frequency with a precision of 0.01 Hz.

We now present the results of the free vibration analysis for the generally-constrained mapped parabolic paraboloid with variable thickness. Three different arrangements of the structure have been studied, involving two non conventional boundary conditions and a (CFCF) configuration. The first ten mode frequencies are listed in Table 29.3 together with the generalized external constraints. A systematic analysis has been performed by employing various higher order theories as proposed before. The $(B_{SSS}^K B_{SSS}^K FF)$ boundary condition accounts for the clamping of two different edges of the structure, namely West (W) and South (S). The results have been compared to predictions from a 3D FEM model, with a great accuracy of results even for lower order assumptions. Besides, the first ten mode shapes are essentially characterized by a bending behaviour. On the other hand, the warping and coupling effects are

Table 29.2 Mode frequencies of an hyperbolic paraboloid enforced with general boundary conditions employing various higher order theories.

| Hyperbolic Paraboloid | | | | | | | | | | | | | |
|--|---------|---------|---------|---------|---------|---------|---------|---------|---------|---------|---------|---------|---------|
| Mode [Hz] | 3D FEM | FSDT | FSDTZ | TSDT | TSDTZ | ED1 | EDZ1 | ED2 | EDZ2 | ED3 | EDZ3 | ED4 | EDZ4 |
| DOFs | 2962260 | 7350 | 110225 | 14700 | 18375 | 7350 | 11025 | 11025 | 14700 | 14700 | 18375 | 18375 | 22050 |
| (B ^K _{DDD} B ^K _{DDD} B ^K _{DDD} B ^K _{DDD}) | | | | | | | | | | | | | |
| 1 | 106.793 | 108.824 | 108.601 | 106.705 | 106.554 | 107.505 | 108.764 | 107.116 | 105.956 | 107.122 | 106.866 | 106.846 | 106.622 |
| 2 | 301.836 | 305.973 | 305.284 | 300.830 | 300.393 | 304.208 | 309.008 | 303.188 | 300.661 | 303.114 | 302.376 | 302.122 | 301.618 |
| 3 | 348.882 | 357.390 | 356.020 | 350.518 | 349.947 | 349.002 | 356.444 | 352.763 | 348.288 | 351.828 | 350.796 | 351.151 | 350.143 |
| 4 | 359.522 | 365.396 | 364.838 | 359.855 | 359.048 | 362.862 | 368.729 | 362.382 | 359.251 | 362.137 | 361.059 | 360.942 | 360.252 |
| 5 | 418.548 | 427.332 | 426.615 | 419.755 | 418.395 | 423.896 | 429.243 | 421.832 | 417.926 | 421.454 | 419.652 | 420.295 | 419.240 |
| 6 | 449.226 | 452.598 | 450.750 | 447.083 | 446.120 | 440.862 | 453.952 | 452.885 | 447.606 | 450.974 | 448.951 | 450.438 | 448.713 |
| 7 | 486.617 | 490.384 | 488.901 | 484.378 | 483.627 | 477.201 | 491.180 | 488.586 | 483.086 | 486.982 | 485.363 | 486.167 | 484.670 |
| 8 | 489.079 | 492.745 | 490.767 | 486.944 | 485.947 | 479.504 | 493.252 | 492.282 | 486.587 | 490.418 | 488.403 | 489.841 | 488.057 |
| 9 | 581.650 | 590.076 | 588.448 | 582.028 | 580.970 | 574.587 | 589.911 | 586.920 | 579.458 | 584.894 | 582.668 | 584.014 | 582.044 |
| 10 | 614.159 | 627.665 | 625.696 | 617.119 | 616.049 | 617.466 | 630.386 | 621.959 | 615.336 | 620.443 | 618.480 | 618.980 | 617.416 |
| Boundary Springs: | | | | | | | | | | | | | |
| Double - Weibull distribution ($\bar{\xi}_m = \tilde{\xi}_m = 0.0025, p = 20$) | | | | | | | | | | | | | |
| $k_{1f}^{(k)\xi_2^0} = k_{1f}^{(k)\xi_2^1} = 1 \cdot 10^{21}$ Pa/m, $k_{2f}^{(k)\xi_2^0} = k_{2f}^{(k)\xi_2^1} = 1 \cdot 10^{21}$ Pa/m, $k_{3f}^{(k)\xi_2^0} = k_{3f}^{(k)\xi_2^1} = 1 \cdot 10^{21}$ Pa/m | | | | | | | | | | | | | |
| (B ^K _{SSS} B ^K _{SSS} B ^K _{SSS} B ^K _{SSS}) | | | | | | | | | | | | | |
| 1 | 500.369 | 511.225 | 508.840 | 502.247 | 501.304 | 505.672 | 514.413 | 506.817 | 501.596 | 505.443 | 503.998 | 503.999 | 502.860 |
| 2 | 545.860 | 559.921 | 557.334 | 551.218 | 550.029 | 551.035 | 560.692 | 555.965 | 549.479 | 554.168 | 552.373 | 553.038 | 551.209 |
| 3 | 643.635 | 656.515 | 654.213 | 647.755 | 646.520 | 638.854 | 656.545 | 653.050 | 645.427 | 650.701 | 648.224 | 649.942 | 647.556 |
| 4 | 646.508 | 660.575 | 657.251 | 651.249 | 649.436 | 642.328 | 658.500 | 657.663 | 648.479 | 653.789 | 650.861 | 652.877 | 650.529 |
| 5 | 711.494 | 726.263 | 722.724 | 715.348 | 713.707 | 713.908 | 725.706 | 721.030 | 712.217 | 718.601 | 716.090 | 717.492 | 714.983 |
| 6 | 758.888 | 773.803 | 770.217 | 762.806 | 761.205 | 756.987 | 773.463 | 768.792 | 759.736 | 766.201 | 763.580 | 764.975 | 762.606 |
| 7 | 783.808 | 800.599 | 796.965 | 789.978 | 788.481 | 781.911 | 800.639 | 797.222 | 787.201 | 793.767 | 791.016 | 792.524 | 789.794 |
| 8 | 798.964 | 822.327 | 819.546 | 808.187 | 806.640 | 814.208 | 828.601 | 815.631 | 807.264 | 813.720 | 811.516 | 811.182 | 809.532 |
| 9 | 835.187 | 849.766 | 846.475 | 837.117 | 835.830 | 829.786 | 852.050 | 845.597 | 834.864 | 841.864 | 839.137 | 840.265 | 837.604 |
| 10 | 885.723 | 909.547 | 906.768 | 894.875 | 893.082 | 895.748 | 912.807 | 901.753 | 891.612 | 899.693 | 896.971 | 897.550 | 895.268 |
| Boundary Springs: | | | | | | | | | | | | | |
| Super Elliptic distribution ($\bar{\xi}_m = 1, \tilde{\xi}_m = 0.25, p = 1000$) | | | | | | | | | | | | | |
| $k_{1f}^{(k)\xi_2^0} = k_{1f}^{(k)\xi_2^1} = 1 \cdot 10^{21}$ Pa/m, $k_{2f}^{(k)\xi_2^0} = k_{2f}^{(k)\xi_2^1} = 1 \cdot 10^{21}$ Pa/m, $k_{3f}^{(k)\xi_2^0} = k_{3f}^{(k)\xi_2^1} = 1 \cdot 10^{21}$ Pa/m | | | | | | | | | | | | | |
| (FFCF) | | | | | | | | | | | | | |
| 1 | 23.725 | 24.152 | 24.027 | 23.628 | 23.757 | 23.810 | 24.248 | 23.900 | 23.572 | 23.883 | 24.056 | 23.722 | 23.720 |
| 2 | 39.465 | 41.128 | 40.922 | 39.804 | 39.583 | 40.988 | 40.804 | 39.843 | 39.339 | 39.801 | 39.547 | 39.681 | 39.707 |
| 3 | 103.071 | 105.772 | 105.181 | 103.076 | 102.634 | 104.945 | 105.938 | 103.776 | 102.658 | 103.426 | 102.853 | 103.234 | 102.881 |
| 4 | 151.874 | 154.571 | 153.823 | 152.013 | 152.034 | 151.696 | 155.488 | 153.597 | 151.782 | 153.098 | 152.958 | 152.583 | 152.336 |
| 5 | 276.084 | 281.669 | 280.794 | 276.912 | 276.233 | 277.358 | 283.235 | 278.811 | 275.987 | 278.214 | 277.217 | 277.577 | 276.829 |
| 6 | 310.490 | 317.801 | 316.449 | 311.170 | 310.427 | 315.093 | 319.937 | 313.408 | 310.496 | 312.838 | 311.719 | 311.910 | 311.303 |
| 7 | 472.480 | 479.486 | 477.880 | 473.940 | 473.109 | 462.830 | 478.643 | 478.025 | 471.608 | 475.707 | 473.789 | 475.335 | 473.503 |
| 8 | 551.882 | 561.807 | 559.949 | 553.124 | 552.267 | 554.358 | 566.984 | 557.818 | 552.727 | 556.766 | 555.424 | 555.065 | 553.740 |
| 9 | 584.307 | 596.849 | 595.274 | 586.618 | 585.308 | 587.784 | 599.415 | 590.245 | 584.231 | 589.118 | 586.936 | 587.939 | 586.300 |
| 10 | 597.510 | 610.857 | 608.790 | 598.170 | 597.068 | 602.206 | 613.062 | 602.243 | 595.910 | 601.017 | 599.130 | 599.583 | 598.221 |
| Lamination Scheme: | | | | | | | | | | | | | |
| (45/0/70), $\bar{h}_1 = \bar{h}_3 = 0.005, \bar{h}_2 = 0.008$ m | | | | | | | | | | | | | |
| Materials Sequence: 1 st layer trigonal material, 2 nd layer zirconia, 3 rd layer trigonal material | | | | | | | | | | | | | |
| Computational Issues: CGL bi-dimensional computational grid with $I_N = I_M = 37$ discrete points | | | | | | | | | | | | | |

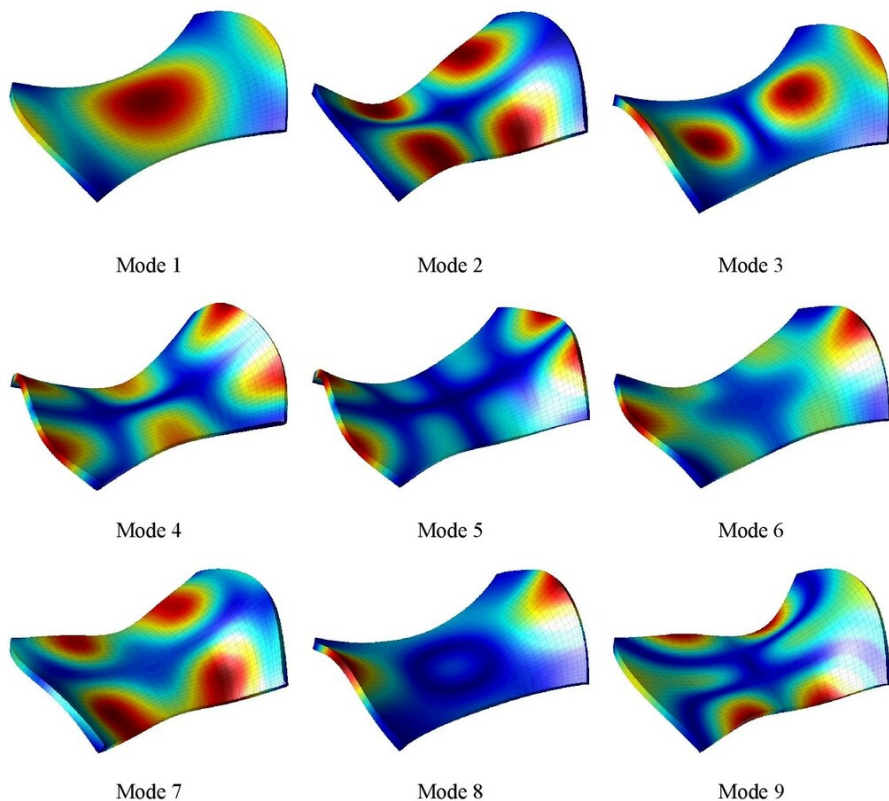


Fig. 29.8 First nine mode shapes of a mapped hyperbolic paraboloid of variable thickness enforced with general boundary conditions calculated by means of the ESL formulation via the GDQ Method. The employment of the higher order assumption of the displacement field allows to properly describe the deflection of the structure for each mode, accounting for the through-the-thickness warping and stretching effects coming from the lamination scheme. The areas colored with blue are characterized by minimum displacements magnitude. The maximum deflection has been highlighted with red instead.

limited, but always present, as clearly visible from mode shapes in Fig. 29.9. As far as the second layup is concerned, the Super Elliptic analytical expression of Eqn. (29.115) has been employed so that a quarter of the East (E) and West (W) sides of the doubly-curved shell gets fixed. Also in this case, a very good agreement between GDQ and 3D FEM approaches can be noticed. The results show a clear bending of the structure during the modal deflection, since even lower order displacement field assumptions predict quite well the free vibration response. In the last investigation, the same edges of the paraboloid (E-W) have been completely clamped. In this case, the best agreement can be found with the ED4 field variable configuration ($N = 4$). The employment of the zigzag function within Eqn. (29.11) induces a little discrepancy with respect to the reference finite element solution for both lower and higher

modes. On the other hand, lower order theories like the FSDT and the TSDT kinematic assumptions do not show the same level of accuracy of higher order theories, especially for the first four modes.

Table 29.3 Mode frequencies of a parabolic paraboloid enforced with general boundary conditions employing various higher order theories.

| Parabolic Paraboloid | | | | | | | | | | | | | |
|--|---------|----------|---------|---------|---------|---------|---------|---------|---------|---------|---------|---------|---------|
| Mode [Hz] | 3D FEM | FSDT | FSDTZ | TSDT | TSDTZ | ED1 | EDZ1 | ED2 | EDZ2 | ED3 | EDZ3 | ED4 | EDZ4 |
| DOFs | 930810 | 7350 | 110225 | 14700 | 18375 | 7350 | 11025 | 11025 | 14700 | 14700 | 18375 | 18375 | 22050 |
| (B ^K _{sss} B ^K _{sss} FF) | | | | | | | | | | | | | |
| 1 | 86.001 | 86.195 | 86.298 | 86.267 | 86.262 | 83.548 | 89.020 | 86.687 | 86.665 | 86.523 | 86.516 | 87.720 | 87.857 |
| 2 | 111.499 | 111.589 | 111.727 | 111.691 | 111.685 | 109.618 | 110.092 | 111.943 | 111.914 | 111.881 | 111.866 | 112.728 | 112.826 |
| 3 | 175.841 | 178.105 | 178.346 | 178.282 | 178.274 | 171.514 | 167.020 | 178.325 | 178.260 | 178.747 | 178.707 | 178.748 | 178.668 |
| 4 | 202.198 | 202.754 | 202.951 | 202.864 | 202.858 | 196.609 | 182.768 | 202.786 | 202.743 | 203.078 | 203.042 | 202.788 | 202.714 |
| 5 | 268.918 | 268.822 | 269.397 | 269.295 | 269.273 | 266.335 | 255.280 | 268.822 | 268.731 | 269.615 | 269.538 | 268.495 | 268.334 |
| 6 | 328.673 | 331.314 | 332.241 | 332.068 | 332.035 | 324.996 | 318.081 | 331.636 | 331.472 | 332.774 | 332.616 | 331.756 | 331.583 |
| 7 | 343.885 | 348.796 | 350.297 | 350.180 | 350.124 | 344.056 | 358.835 | 349.428 | 349.297 | 351.081 | 350.925 | 350.800 | 350.722 |
| 8 | 404.321 | 411.102 | 412.541 | 412.420 | 412.368 | 391.217 | 427.651 | 412.995 | 412.807 | 413.828 | 413.654 | 413.770 | 413.657 |
| 9 | 438.558 | 439.081 | 440.309 | 440.161 | 440.115 | 431.497 | 444.834 | 440.200 | 439.989 | 441.115 | 440.953 | 442.061 | 442.033 |
| 10 | 483.522 | 483.949 | 484.640 | 484.402 | 484.373 | 461.677 | 494.432 | 484.607 | 484.374 | 485.041 | 484.852 | 485.419 | 485.309 |
| Boundary Springs: | | | | | | | | | | | | | |
| Super Elliptic distribution ($\bar{\xi}_m = 0(W), \bar{\xi}_m = 1(S), \bar{\xi}_m = 0.53, p = 1000$) | | | | | | | | | | | | | |
| $k_{1f}^{(k)\xi_1^0} = 1 \cdot 10^{21}$ Pa/m, $k_{2f}^{(k)\xi_1^0} = 1 \cdot 10^{21}$ Pa/m, $k_{3f}^{(k)\xi_1^0} = 1 \cdot 10^{21}$ Pa/m | | | | | | | | | | | | | |
| $k_{1f}^{(k)\xi_2^0} = 1 \cdot 10^{21}$ Pa/m, $k_{2f}^{(k)\xi_2^0} = 1 \cdot 10^{21}$ Pa/m, $k_{3f}^{(k)\xi_2^0} = 1 \cdot 10^{21}$ Pa/m | | | | | | | | | | | | | |
| (B ^K _{sss} CB ^K _{sss} F) | | | | | | | | | | | | | |
| 1 | 63.543 | 64.72259 | 64.909 | 64.882 | 64.877 | 64.404 | 67.262 | 64.717 | 64.695 | 65.076 | 65.059 | 64.925 | 64.888 |
| 2 | 75.229 | 76.75496 | 76.891 | 76.876 | 76.870 | 71.877 | 78.310 | 77.004 | 76.980 | 77.118 | 77.127 | 76.863 | 76.795 |
| 3 | 159.343 | 160.5996 | 160.889 | 160.818 | 160.811 | 159.363 | 164.704 | 160.829 | 160.792 | 161.097 | 161.063 | 161.163 | 161.151 |
| 4 | 182.497 | 185.0347 | 185.687 | 185.605 | 185.580 | 183.410 | 188.946 | 185.463 | 185.397 | 185.944 | 185.895 | 185.996 | 185.968 |
| 5 | 213.368 | 214.9603 | 215.370 | 215.237 | 215.223 | 210.834 | 222.860 | 215.288 | 215.230 | 215.696 | 215.630 | 215.624 | 215.602 |
| 6 | 336.569 | 339.0331 | 339.872 | 339.727 | 339.697 | 329.727 | 353.213 | 339.595 | 339.468 | 340.350 | 340.244 | 340.052 | 339.934 |
| 7 | 361.366 | 363.064 | 363.939 | 363.678 | 363.648 | 354.827 | 386.241 | 363.328 | 363.121 | 364.517 | 364.355 | 364.541 | 364.428 |
| 8 | 385.468 | 389.2896 | 390.332 | 390.149 | 390.114 | 377.055 | 404.575 | 389.583 | 389.383 | 391.022 | 390.881 | 390.926 | 390.790 |
| 9 | 463.153 | 468.0446 | 469.216 | 469.053 | 469.014 | 451.597 | 486.304 | 469.029 | 468.873 | 470.172 | 470.052 | 470.261 | 470.175 |
| 10 | 469.721 | 472.754 | 473.837 | 473.683 | 473.649 | 452.254 | 490.034 | 473.136 | 472.987 | 474.115 | 473.964 | 474.197 | 474.131 |
| Boundary Springs: | | | | | | | | | | | | | |
| Super Elliptic distribution ($\bar{\xi}_m = 1, \bar{\xi}_m = 0.25, p = 1000$) | | | | | | | | | | | | | |
| $k_{1f}^{(k)\xi_2^0} = k_{1f}^{(k)\xi_2^1} = 1 \cdot 10^{21}$ Pa/m, $k_{2f}^{(k)\xi_2^0} = k_{2f}^{(k)\xi_2^1} = 1 \cdot 10^{21}$ Pa/m, $k_{3f}^{(k)\xi_2^0} = k_{3f}^{(k)\xi_2^1} = 1 \cdot 10^{21}$ Pa/m | | | | | | | | | | | | | |
| (CFCF) | | | | | | | | | | | | | |
| 1 | 296.274 | 294.705 | 295.377 | 295.245 | 295.219 | 289.921 | 317.904 | 295.624 | 295.451 | 296.243 | 296.079 | 296.100 | 295.992 |
| 2 | 370.090 | 368.9118 | 369.570 | 369.418 | 369.393 | 359.850 | 387.195 | 369.673 | 369.529 | 370.197 | 370.065 | 370.105 | 370.011 |
| 3 | 428.102 | 426.3081 | 427.096 | 426.960 | 426.933 | 389.099 | 442.974 | 427.548 | 427.392 | 428.051 | 427.911 | 427.947 | 427.850 |
| 4 | 448.421 | 446.6566 | 447.389 | 447.243 | 447.219 | 408.337 | 460.731 | 447.759 | 447.616 | 448.174 | 448.047 | 448.077 | 447.990 |
| 5 | 549.193 | 549.147 | 549.320 | 549.116 | 549.109 | 498.638 | 563.556 | 549.541 | 549.420 | 549.380 | 549.278 | 549.313 | 549.250 |
| 6 | 580.704 | 579.7162 | 580.827 | 580.586 | 580.543 | 546.737 | 612.570 | 580.784 | 580.502 | 581.656 | 581.405 | 581.476 | 581.314 |
| 7 | 590.313 | 587.9078 | 589.082 | 588.877 | 588.830 | 567.415 | 615.824 | 589.636 | 589.409 | 590.535 | 590.330 | 590.392 | 590.248 |
| 8 | 632.400 | 629.2459 | 630.715 | 630.453 | 630.395 | 591.277 | 668.318 | 631.882 | 631.585 | 632.861 | 632.585 | 632.664 | 632.480 |
| 9 | 658.097 | 657.6485 | 658.369 | 658.024 | 657.993 | 614.353 | 697.867 | 658.526 | 658.220 | 658.905 | 658.629 | 658.762 | 658.579 |
| 10 | 728.586 | 726.7233 | 728.735 | 728.345 | 728.264 | 691.962 | 742.991 | 728.456 | 728.001 | 730.161 | 729.757 | 729.932 | 729.661 |
| Lamination Scheme: | | | | | | | | | | | | | |
| (30/0/0/70), $\bar{h}_1 = \bar{h}_4 = 0.01, \bar{h}_2 = \bar{h}_3 = 0.005$ m | | | | | | | | | | | | | |
| Materials Sequence: 1 st layer triclinic material, 2 nd layer zirconia, 3 rd layer steel, 4 th layer triclinic material | | | | | | | | | | | | | |
| Computational Issues: CGL bi-dimensional computational grid with $I_N = I_M = 37$ discrete points | | | | | | | | | | | | | |

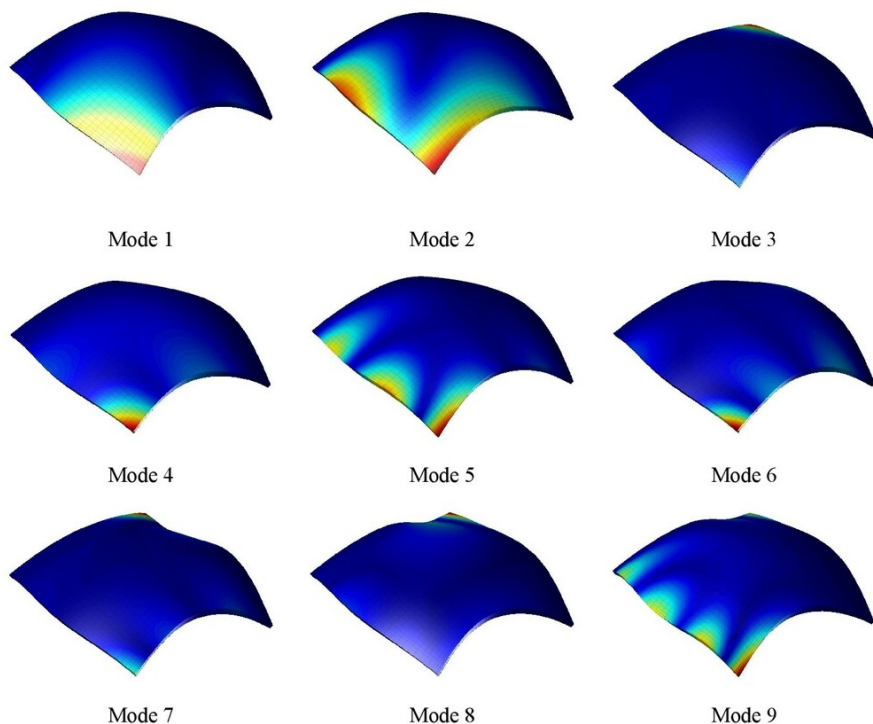


Fig. 29.9 First nine mode shapes of a mapped parabolic paraboloid of variable thickness enforced by general boundary conditions, as computed by the ESL formulation and GDQ Method. The employment of the higher order assumption of the displacement field allows to describe the deflection of the structure for each mode, accounting for the through-the-thickness warping and stretching effects coming from the lamination scheme. The areas colored with blue are characterized by minimum displacements magnitude. The maximum deflection has been highlighted with red instead.

In the next simulation, a singly-curved structure has been investigated. A free vibration analysis of a truncated cone mapped with a rhombic shape (see Fig. 29.5) has been performed via the GDQ approach, and different higher order assumptions of the displacement field. The results sensitivity has been outlined when the zigzag function is introduced. Three different configurations have been developed employing the Super Elliptic distribution. Namely, East (E) and North (N) sides of the shell have been progressively constrained by setting a proper value of $\tilde{\xi}_m$. A refined 3D FEM solution has been provided as reference value for each case. As observable in Fig. 29.10, the first layup provides mode shapes featuring different warping and coupling phenomena. This aspect is evident since the accuracy of the solution with respect to FEM increases as the order N of the kinematic expansion gets higher. Moreover, the EDZ4 provides outcomes more accurate results than an ED4, for both lower and higher modes, as visible in Table 29.4. In the second case, two adjacent shell edges are fully constrained for an half length, whereas the remaining part is

kept free. In this case the application of an EDZ4 assumption becomes decisive for seeking good accuracy, since other ESL theories are unable of well predicting the structural response. Nevertheless, higher modes are properly predicted regardless the field variable assumptions, with an acceptable accuracy in any case. For a conventional boundary condition configuration (FFCC), the performance of the proposed formulation is very high. Note that the zigzag displacement field assumption is a key for the determination of the actual modal response of the mapped shell. If $N = 3$ or $N = 4$ is assumed in Eqn. (29.11), a higher accuracy of results is obtained by an EDZ3 and the EDZ4 theory rather than an ED3 and ED4.

Up to now, all the proposed case studies provide a validation of the structural theory for the static analysis of doubly-curved structures, accounting for the presence of angle-ply lamination schemes with generally anisotropic layers. Moreover, the validity of the formulation has been checked also with respect to the presence of a single and a double curvature, as well as different kinds of physical domain distortion and thickness variation. The influence of the governing parameters has been considered for the assessment of non-conventional boundary conditions.

We now present a modal analysis of a catenoid of variable thickness and arbitrary shape. All the geometric and mechanical features of the structure at issue have been commented in the previous section, see Fig. 29.6 for the three-dimensional representation of the geometry. In this case the mapping of the physical domain gets a significative distortion on the structured CGL computational grid. Three non conventional boundary conditions have been considered. In the first two layups, the structure has been fixed in four points, namely the shell corners (in the first configuration) and the half point of each boundary edge (for the second layup). In the last case, an area surrounding one corner position has been fixed. The first ten mode frequencies have been calculated for all boundary conditions, as provided by various higher order theories, see Table 29.5, and mode shapes in Fig. 29.11.

In the first case, the structure has been constrained at its four half edges by employing the Super Elliptic distribution while properly setting the shape and position parameters. A very good agreement between GDQ simulations can be noticed regardless the displacement field assumption. Generally speaking, a slight decrease in the mode frequency can be traced if the N -th order of the kinematic expansion increases. Moreover, when N assumes an odd value, higher values are provided with respect to structural theories embedding $N = 2, 4$. The same behaviour can be noticed when the zigzag function is embedded in the model. In the second set of simulations, the doubly-curved catenoidal panel is constrained at the corners of the physical domain via the adoption of the Double - Weibull distribution. The fundamental frequency seems to decrease under higher order theoretical assumptions. The adoption of zigzag theories provides a significative relaxation of the model, leading to lower eigenvalues. In the last configuration, the shell is fixed for a quarter of two adjacent curved edges so that a cantilever configuration is reached. Accordingly, for lower modes a certain agreement between different structural theories outcomes is observed except for the EDZ1 theory. On the other hand, different values of natural frequencies are provided for higher modes.

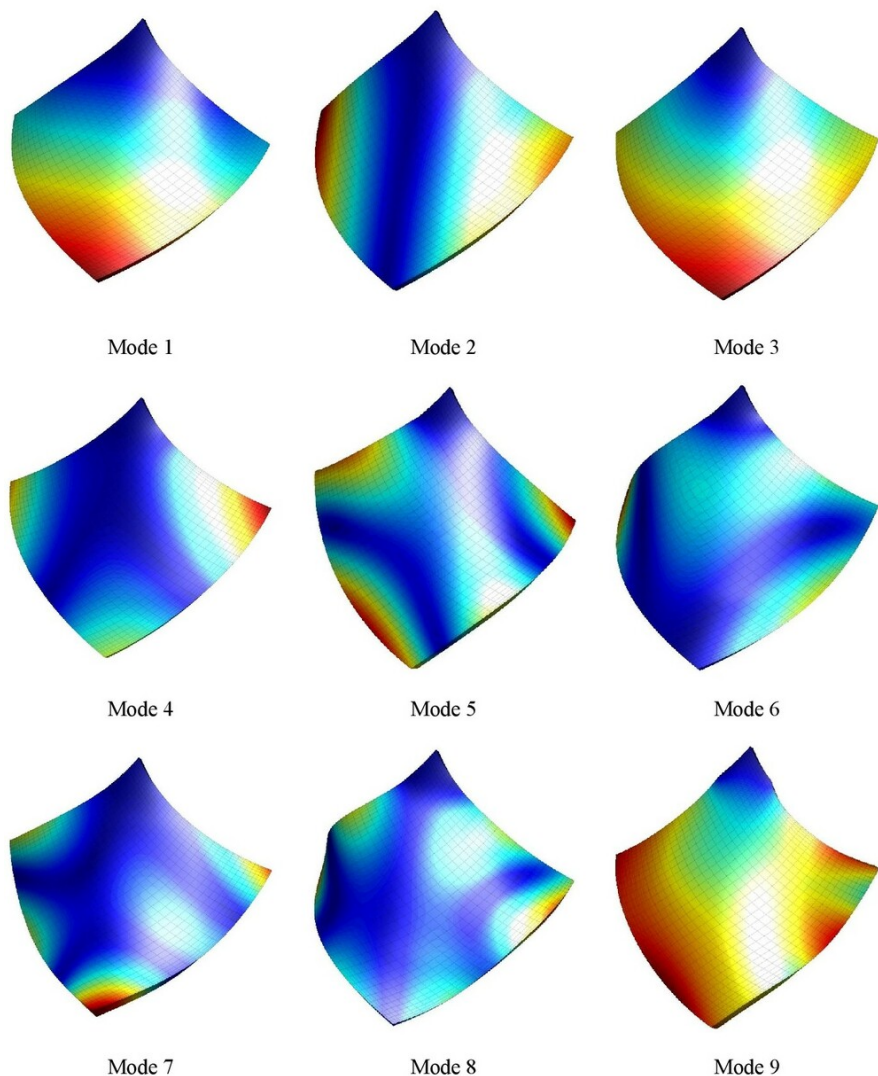


Fig. 29.10 First nine mode shapes of a mapped truncated cone of variable thickness enforced by general boundary conditions, as computed by the ESL formulation and GDQ Method. The employment of the higher order assumption of the displacement field allows to describe the deflection of the structure for each mode, accounting for the through-the-thickness warping and stretching effects coming from the lamination scheme. The areas colored with blue are characterized by minimum displacements magnitude. The maximum deflection has been highlighted with red instead.

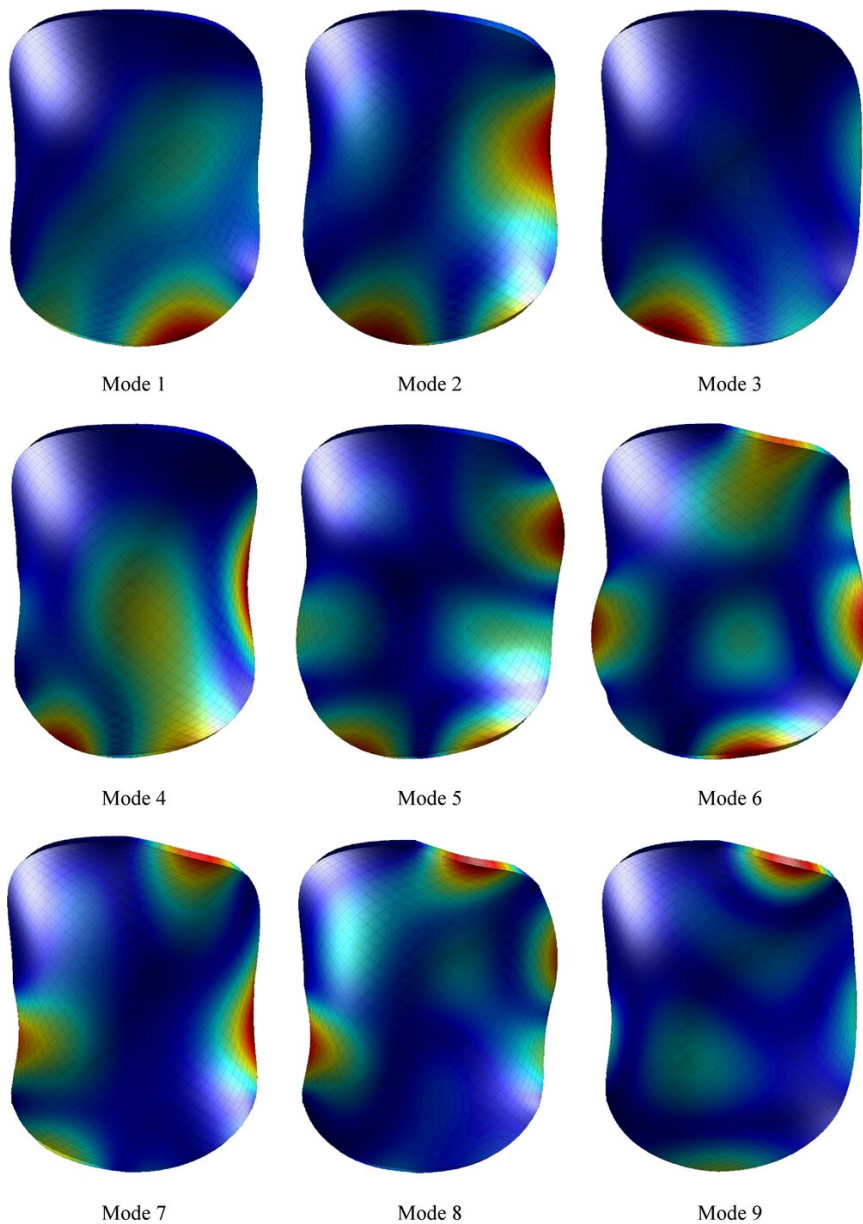


Fig. 29.11 First nine mode shapes of a mapped catenoid of variable thickness enforced by general boundary conditions, as computed by the ESL formulation and GDQ Method. The employment of the higher order assumption of the displacement field allows to describe the deflection of the structure for each mode, accounting for the through-the-thickness warping and stretching and effects coming from the lamination scheme. The areas colored with blue are characterized by minimum displacements magnitude. The maximum deflection has been highlighted with red instead.

Table 29.4 Mode frequencies of a mapped truncated cone enforced with general boundary conditions employing various higher order theories.

| Truncated Cone | | | | | | | | | | | | | |
|--|----------|----------|----------|----------|----------|----------|----------|----------|----------|----------|----------|----------|----------|
| Mode [Hz] | 3D FEM | FSDT | FSDTZ | TSDT | TSDTZ | ED1 | EDZ1 | ED2 | EDZ2 | ED3 | EDZ3 | ED4 | EDZ4 |
| DOFs | 244800 | 7350 | 110225 | 14700 | 18375 | 7350 | 11025 | 11025 | 14700 | 14700 | 18375 | 18375 | 22050 |
| (FFB _{SSS} ^k B _{SSS} ^k) | | | | | | | | | | | | | |
| 1 | 23.354 | 23.372 | 23.452 | 23.349 | 23.193 | 22.685 | 24.889 | 23.357 | 23.322 | 23.393 | 23.257 | 23.352 | 23.209 |
| 2 | 59.337 | 57.196 | 57.750 | 57.565 | 56.977 | 56.982 | 58.369 | 57.134 | 57.045 | 57.601 | 57.033 | 57.564 | 56.970 |
| 3 | 108.779 | 108.957 | 108.980 | 108.685 | 108.650 | 97.252 | 109.923 | 109.578 | 109.458 | 109.631 | 109.517 | 109.566 | 109.448 |
| 4 | 192.572 | 193.119 | 193.915 | 193.405 | 192.720 | 186.255 | 195.820 | 192.705 | 192.554 | 193.398 | 192.739 | 193.275 | 192.593 |
| 5 | 278.473 | 283.363 | 284.945 | 284.248 | 283.396 | 274.494 | 291.226 | 282.929 | 282.518 | 284.355 | 283.483 | 284.155 | 283.266 |
| 6 | 383.277 | 378.037 | 380.182 | 379.075 | 378.056 | 365.520 | 391.989 | 378.005 | 377.450 | 379.886 | 378.888 | 379.473 | 378.444 |
| 7 | 462.697 | 437.682 | 438.916 | 437.805 | 437.206 | 425.406 | 448.488 | 436.663 | 436.056 | 437.731 | 437.116 | 437.412 | 436.772 |
| 8 | 573.179 | 562.095 | 565.464 | 563.925 | 562.173 | 497.247 | 574.961 | 561.333 | 560.571 | 564.649 | 562.893 | 564.218 | 562.443 |
| 9 | 584.780 | 581.488 | 582.106 | 581.188 | 580.862 | 555.734 | 585.645 | 582.912 | 582.225 | 583.264 | 582.656 | 583.055 | 582.437 |
| 10 | 644.948 | 645.296 | 647.783 | 645.999 | 644.859 | 631.789 | 680.828 | 645.176 | 643.696 | 646.991 | 645.777 | 646.152 | 644.882 |
| Boundary Springs: | | | | | | | | | | | | | |
| Super Elliptic distribution ($\tilde{\xi}_m = 0(E)$, $\tilde{\xi}_m = 1(N)$, $\tilde{\xi}_m = 0.25$, $p = 1000$) | | | | | | | | | | | | | |
| $k_{1f}^{(k)\varepsilon_2^0} = k_{1f}^{(k)\varepsilon_2^1} = 1 \cdot 10^{21}$ Pa/m, $k_{2f}^{(k)\varepsilon_2^0} = k_{2f}^{(k)\varepsilon_2^1} = 1 \cdot 10^{21}$ Pa/m, $k_{3f}^{(k)\varepsilon_2^0} = k_{3f}^{(k)\varepsilon_2^1} = 1 \cdot 10^{21}$ Pa/m | | | | | | | | | | | | | |
| (FFB _{SSS} ^k B _{SSS} ^k) | | | | | | | | | | | | | |
| 1 | 71.568 | 73.664 | 73.844 | 73.624 | 73.443 | 68.722 | 76.389 | 73.838 | 73.777 | 74.057 | 73.848 | 74.009 | 73.802 |
| 2 | 108.471 | 110.118 | 110.774 | 110.488 | 110.200 | 108.460 | 115.367 | 110.218 | 110.117 | 110.853 | 110.555 | 110.799 | 110.506 |
| 3 | 249.584 | 253.052 | 254.111 | 253.591 | 253.053 | 245.050 | 258.461 | 252.996 | 252.728 | 254.117 | 253.561 | 254.035 | 253.471 |
| 4 | 331.115 | 339.840 | 340.116 | 339.431 | 339.216 | 307.651 | 342.822 | 341.103 | 340.927 | 341.522 | 341.163 | 341.369 | 341.013 |
| 5 | 368.493 | 374.091 | 376.361 | 375.289 | 374.234 | 362.882 | 382.012 | 372.794 | 372.369 | 375.144 | 374.086 | 375.008 | 373.953 |
| 6 | 488.993 | 492.950 | 494.995 | 492.724 | 491.991 | 486.694 | 501.853 | 490.608 | 490.103 | 492.706 | 491.937 | 492.453 | 491.681 |
| 7 | 569.718 | 578.575 | 581.933 | 580.361 | 579.037 | 555.391 | 610.621 | 576.912 | 576.389 | 580.466 | 579.146 | 580.110 | 578.766 |
| 8 | 683.228 | 690.505 | 694.310 | 692.068 | 690.450 | 672.884 | 723.656 | 688.344 | 687.729 | 692.300 | 690.673 | 691.938 | 690.299 |
| 9 | 775.175 | 786.867 | 792.914 | 790.414 | 787.748 | 749.968 | 820.686 | 784.921 | 784.059 | 791.411 | 788.680 | 790.933 | 788.176 |
| 10 | 881.111 | 892.821 | 894.406 | 893.088 | 892.258 | 791.773 | 899.722 | 892.549 | 892.035 | 894.409 | 893.324 | 894.067 | 892.990 |
| Boundary Springs: | | | | | | | | | | | | | |
| Super Elliptic distribution ($\tilde{\xi}_m = 0(E)$, $\tilde{\xi}_m = 1(N)$, $\tilde{\xi}_m = 0.5$, $p = 1000$) | | | | | | | | | | | | | |
| $k_{1f}^{(k)\varepsilon_2^0} = k_{1f}^{(k)\varepsilon_2^1} = 1 \cdot 10^{21}$ Pa/m, $k_{2f}^{(k)\varepsilon_2^0} = k_{2f}^{(k)\varepsilon_2^1} = 1 \cdot 10^{21}$ Pa/m, $k_{3f}^{(k)\varepsilon_2^0} = k_{3f}^{(k)\varepsilon_2^1} = 1 \cdot 10^{21}$ Pa/m | | | | | | | | | | | | | |
| (FFCC) | | | | | | | | | | | | | |
| 1 | 228.963 | 228.695 | 229.326 | 228.867 | 228.240 | 215.731 | 230.395 | 228.452 | 228.250 | 229.105 | 228.420 | 229.042 | 228.336 |
| 2 | 275.099 | 275.179 | 276.096 | 275.599 | 274.608 | 267.012 | 279.304 | 274.768 | 274.466 | 275.826 | 274.781 | 275.737 | 274.691 |
| 3 | 484.070 | 485.471 | 486.485 | 485.175 | 484.295 | 468.869 | 496.492 | 484.427 | 484.093 | 485.572 | 484.652 | 485.350 | 484.427 |
| 4 | 542.098 | 541.417 | 543.422 | 542.350 | 540.993 | 526.440 | 571.196 | 540.820 | 540.301 | 543.027 | 541.706 | 542.709 | 541.413 |
| 5 | 803.085 | 808.084 | 811.941 | 810.640 | 807.308 | 775.072 | 824.844 | 805.486 | 804.382 | 809.762 | 806.432 | 809.381 | 806.024 |
| 6 | 890.224 | 890.695 | 895.387 | 893.037 | 889.086 | 805.714 | 905.471 | 889.456 | 888.174 | 895.062 | 890.950 | 894.661 | 890.489 |
| 7 | 899.689 | 899.991 | 904.431 | 901.925 | 899.938 | 884.620 | 949.850 | 898.711 | 897.971 | 903.134 | 901.179 | 902.710 | 900.705 |
| 8 | 982.755 | 985.893 | 991.819 | 988.673 | 983.864 | 955.878 | 1022.577 | 982.736 | 981.427 | 989.064 | 984.323 | 988.433 | 983.665 |
| 9 | 1125.182 | 1125.538 | 1134.735 | 1133.333 | 1126.526 | 1078.476 | 1168.324 | 1122.274 | 1120.359 | 1132.481 | 1125.708 | 1131.894 | 1125.074 |
| 10 | 1295.975 | 1297.864 | 1309.458 | 1306.468 | 1298.529 | 1276.744 | 1336.798 | 1292.017 | 1289.798 | 1305.120 | 1297.293 | 1304.412 | 1296.519 |
| Lamination Scheme: | | | | | | | | | | | | | |
| (70/30/45), $\bar{h}_1 = \bar{h}_3 = 0.01$, $\bar{h}_2 = 0.02$ m | | | | | | | | | | | | | |
| Materials Sequence: 1 st layer graphite-epoxy, 2 nd layer triclinic material, 3 rd layer graphite-epoxy | | | | | | | | | | | | | |
| Computational Issues: CGL bi-dimensional computational grid with $I_N = I_M = 37$ discrete points | | | | | | | | | | | | | |

29.11.2 Static Analysis

We now deal with a static analysis of shell structures according to Eqn. (29.85). Three structures have been considered, namely an unmapped rectangular plate (Fig. 29.2), an arbitrary shaped parabolic paraboloid (Fig. 29.3) and a catenoid (Fig. 29.6). For each panel, the same general external constraints considered for the free vibration analysis simulations provided for the first case of Table 29.1, Table 29.3 and

Table 29.5 Mode frequencies of a catenoid of arbitrary shape enforced by general boundary conditions employing various higher order theories.

| Catenoid | | | | | | | | | | | | |
|--|---------|---------|---------|---------|---------|---------|---------|---------|---------|---------|---------|---------|
| Mode [Hz] | FSDT | FSDTZ | TSDT | TSDTZ | ED1 | EDZ1 | ED2 | EDZ2 | ED3 | EDZ3 | ED4 | EDZ4 |
| DOFs | 7350 | 110225 | 14700 | 18375 | 7350 | 11025 | 11025 | 14700 | 14700 | 18375 | 18375 | 22050 |
| (B ^K _{SSS} B ^K _{SSS} CB ^K _{SSS}) | | | | | | | | | | | | |
| 1 | 174.747 | 166.690 | 184.000 | 166.234 | 172.254 | 168.878 | 174.481 | 164.723 | 184.622 | 165.305 | 185.330 | 165.417 |
| 2 | 199.101 | 196.914 | 184.000 | 192.412 | 190.797 | 201.966 | 197.731 | 195.445 | 184.622 | 195.518 | 185.330 | 195.273 |
| 3 | 208.315 | 207.218 | 198.452 | 202.613 | 202.538 | 209.169 | 206.949 | 202.370 | 200.833 | 207.335 | 199.937 | 207.558 |
| 4 | 224.635 | 221.396 | 228.014 | 224.117 | 217.343 | 225.768 | 223.789 | 219.501 | 227.971 | 220.117 | 227.579 | 219.674 |
| 5 | 272.826 | 262.833 | 264.820 | 258.893 | 268.598 | 263.758 | 272.223 | 257.662 | 266.144 | 261.907 | 265.721 | 261.718 |
| 6 | 289.470 | 280.450 | 282.682 | 278.772 | 285.390 | 282.541 | 287.558 | 275.694 | 283.032 | 278.326 | 282.015 | 277.895 |
| 7 | 315.635 | 308.338 | 313.344 | 304.081 | 305.475 | 313.301 | 313.617 | 304.265 | 314.949 | 306.648 | 311.642 | 306.355 |
| 8 | 336.873 | 322.014 | 320.116 | 316.534 | 331.142 | 329.706 | 335.435 | 316.697 | 321.751 | 320.842 | 321.201 | 320.180 |
| 9 | 340.041 | 331.582 | 327.934 | 328.871 | 331.918 | 335.479 | 337.668 | 327.559 | 328.983 | 329.175 | 328.899 | 328.686 |
| 10 | 382.669 | 364.314 | 373.752 | 363.695 | 374.947 | 372.281 | 380.289 | 359.106 | 374.865 | 364.350 | 373.588 | 364.099 |
| Boundary Springs: | | | | | | | | | | | | |
| Super Elliptic distribution ($\bar{\xi}_m = 0.5, \tilde{\xi}_m = 0.01, p = 40$) | | | | | | | | | | | | |
| $k_{1f}^{(k)\xi_2^0} = k_{1f}^{(k)\xi_1^2} = 1 \cdot 10^{21}$ Pa/m, $k_{2f}^{(k)\xi_2^0} = k_{2f}^{(k)\xi_1^2} = 1 \cdot 10^{21}$ Pa/m, $k_{3f}^{(k)\xi_2^0} = k_{3f}^{(k)\xi_1^2} = 1 \cdot 10^{21}$ Pa/m | | | | | | | | | | | | |
| (B ^K _{DDD} B ^K _{DDD} B ^K _{DDD} B ^K _{DDD}) | | | | | | | | | | | | |
| 1 | 64.064 | 63.064 | 56.707 | 61.827 | 63.457 | 63.242 | 63.390 | 62.052 | 79.088 | 61.127 | 61.444 | 60.035 |
| 2 | 87.263 | 83.991 | 85.686 | 83.127 | 85.178 | 84.526 | 86.215 | 81.789 | 82.578 | 83.007 | 83.352 | 83.503 |
| 3 | 95.566 | 91.494 | 93.505 | 90.587 | 93.216 | 91.401 | 94.433 | 89.356 | 93.445 | 90.815 | 92.972 | 89.985 |
| 4 | 123.276 | 120.018 | 121.401 | 119.094 | 120.286 | 122.391 | 122.378 | 118.073 | 120.762 | 119.484 | 118.550 | 121.904 |
| 5 | 131.323 | 126.187 | 121.401 | 124.541 | 129.638 | 129.663 | 130.922 | 124.571 | 141.397 | 122.554 | 122.643 | 121.904 |
| 6 | 150.443 | 145.180 | 147.656 | 144.189 | 148.310 | 150.308 | 150.184 | 143.014 | 147.836 | 144.997 | 143.634 | 149.225 |
| 7 | 187.448 | 183.491 | 184.221 | 182.426 | 181.593 | 187.988 | 186.938 | 181.724 | 170.311 | 182.793 | 194.013 | 170.688 |
| 8 | 237.053 | 232.549 | 228.912 | 230.181 | 232.594 | 234.023 | 235.154 | 229.376 | 194.613 | 228.666 | 232.409 | 230.436 |
| 9 | 259.707 | 257.331 | 258.019 | 256.073 | 252.616 | 258.159 | 258.422 | 252.255 | 255.587 | 255.557 | 244.712 | 252.836 |
| 10 | 270.351 | 258.081 | 265.308 | 256.734 | 266.265 | 259.451 | 268.292 | 255.502 | 255.587 | 257.161 | 258.792 | 273.273 |
| Boundary Springs: | | | | | | | | | | | | |
| Double - Weibull distribution ($\bar{\xi}_m = \tilde{\xi}_m = 0.0025, p = 20$) | | | | | | | | | | | | |
| $k_{1f}^{(k)\xi_2^0} = k_{1f}^{(k)\xi_1^2} = 1 \cdot 10^{21}$ Pa/m, $k_{2f}^{(k)\xi_2^0} = k_{2f}^{(k)\xi_1^2} = 1 \cdot 10^{21}$ Pa/m, $k_{3f}^{(k)\xi_2^0} = k_{3f}^{(k)\xi_1^2} = 1 \cdot 10^{21}$ Pa/m | | | | | | | | | | | | |
| (B ^K _{SSS} FFB ^K _{SSS}) | | | | | | | | | | | | |
| 1 | 16.046 | 16.112 | 15.536 | 16.059 | 16.428 | 15.993 | 16.165 | 16.208 | 16.329 | 16.496 | 16.718 | 17.100 |
| 2 | 22.519 | 22.895 | 20.761 | 23.089 | 23.051 | 22.413 | 22.952 | 23.114 | 21.603 | 23.692 | 21.765 | 24.099 |
| 3 | 56.278 | 55.133 | 56.872 | 54.842 | 55.808 | 55.738 | 56.038 | 54.611 | 56.895 | 55.027 | 56.419 | 54.658 |
| 4 | 77.273 | 76.103 | 77.367 | 75.905 | 76.299 | 79.600 | 77.546 | 75.982 | 77.393 | 76.026 | 76.832 | 75.691 |
| 5 | 128.197 | 127.706 | 126.430 | 127.170 | 126.214 | 128.291 | 127.678 | 126.717 | 126.467 | 127.261 | 125.888 | 126.991 |
| 6 | 143.660 | 140.855 | 142.376 | 140.071 | 140.733 | 145.000 | 143.067 | 139.101 | 142.674 | 140.310 | 142.363 | 140.091 |
| 7 | 165.398 | 162.823 | 159.161 | 161.579 | 158.628 | 167.625 | 165.037 | 160.959 | 160.076 | 162.241 | 159.318 | 162.349 |
| 8 | 191.859 | 185.184 | 190.214 | 183.868 | 189.426 | 186.514 | 190.145 | 182.193 | 190.211 | 184.006 | 189.751 | 183.722 |
| 9 | 243.940 | 236.193 | 241.810 | 234.787 | 240.978 | 238.120 | 242.123 | 232.484 | 242.086 | 234.958 | 241.589 | 234.768 |
| 10 | 271.341 | 264.447 | 266.870 | 262.588 | 264.191 | 270.061 | 270.181 | 260.568 | 267.970 | 263.327 | 267.380 | 263.353 |
| Boundary Springs: | | | | | | | | | | | | |
| Super Elliptic distribution ($\bar{\xi}_m = 0, \tilde{\xi}_m = 0.25, p = 1000$) | | | | | | | | | | | | |
| $k_{1f}^{(k)\xi_1^0} = k_{1f}^{(k)\xi_2^0} = 1 \cdot 10^{21}$ Pa/m, $k_{2f}^{(k)\xi_1^0} = k_{2f}^{(k)\xi_2^0} = 1 \cdot 10^{21}$ Pa/m, $k_{3f}^{(k)\xi_1^0} = k_{3f}^{(k)\xi_2^0} = 1 \cdot 10^{21}$ Pa/m | | | | | | | | | | | | |
| Lamination Scheme: | | | | | | | | | | | | |
| (45/0/70), $\bar{h}_1 = \bar{h}_3 = 0.005, \bar{h}_2 = 0.008$ m | | | | | | | | | | | | |
| Materials Sequence: 1 st layer triclinic material, 2 nd layer glass-epoxy, 3 rd layer trigonal material | | | | | | | | | | | | |
| Computational Issues: CGL bi-dimensional computational grid with $I_N = I_M = 37$ discrete points | | | | | | | | | | | | |

Table 29.5, respectively, have been assessed according to Eqns. (29.118)-(29.119) employing different in-plane and out-of-plane linear springs distributions. In all the investigated cases, a uniform loading distribution has been applied at the top surface of the structure ($\zeta = h/2$) acting along the outward normal unit direction of the reference surface $\mathbf{r}(\alpha_1, \alpha_2)$ defined in Eqn. (29.113). The through-the-thickness dispersion of both static and kinematic quantities has been provided for each case. The influence of the kinematic order assumption of Eqn. (29.11) has been also highlighted. Once again, a 3D FEM evaluation of the structural response has been provided as reference solution for comparative purposes.

The first simulation considers an unmapped rectangular plate (see Fig. 29.2), under a surface loading equal to $q_3^{(+)} = -5.0 \times 10^3$ Pa applied on the external layer of the structure. The boundary conditions configuration is $\text{FB}_{\text{SSS}}^{\text{K}}\text{FC}$, as obtained from a Super Elliptic distribution delined in Table 29.1. The through-the-thickness plots refer to the point of the physical domain located at $(\xi_1, \xi_2) = (0.50 (\xi_1^1 - \xi_1^0), 0.50 (\xi_2^1 - \xi_2^0))$, whose results have been found via the GDQ formulation and different higher order theories. In Fig. 29.12 we depict the three-dimensional displacement field vector \mathbf{U} , whereas the kinematic primary variables are collected in Fig. 29.13, and the stress components are shown in Fig. 29.14. From a comparison with the refined FEM it is shown that for very complex lamination schemes a higher order assumption of the displacement field is mandatory in order to get accurate results. Lower order theories characterized by $N = 1$ do not provide good results in terms of in-plane displacement field, even when using the zigzag function. Moreover, the employment of a higher order assumption of the displacement field can predict well the stretching effect acting along the $\alpha_3 = \zeta$ principal direction, as visible from the dispersion of U_3 field component obtained from a 3D FEM. This means that the EDZ4 approach gives the best accuracy of results. The same considerations can be repeated for the strain distributions reported in Fig. 29.13. The employment of complicated through-the-thickness displacement field assumptions in Eqn. (29.11) is capable of well predicting both the in-plane and out-of-plane deformations for all the laminae embedded in the stacking sequence. The stress distributions reported in Fig. 29.14 provided by the 3D FEM are well predicted by the ESL approach. Unlike the former distribution, the latter one perfectly fulfills the boundary values of the applied loads on the top and bottom surfaces of the shell, since they are directly enforced during the stress recovery procedure. The finite element approach applies a local extrapolation to element nodes of the calculated stresses starting from the internal sampling points, thus showing a dispersion of values.

The second simulation for the static analysis considers a mapped parabolic paraboloid with geometric and mechanical properties as reported in Fig. 29.3, with external constraints as reported in Table 29.3, and subjected to a surface load $q_3^{(+)} = -1 \times 10^4$ Pa. The thickness plots now refer to the point located at the center of the physical domain, of coordinates $(\xi_1, \xi_2) = (0.50 (\xi_1^1 - \xi_1^0), 0.50 (\xi_2^1 - \xi_2^0))$. The three-dimensional displacement field is reported in Fig. 29.15, whereas the strain and stress field are depicted in Fig. 29.16 and Fig. 29.17, respectively. The in-plane displacement field provided by a refined 3D FEM simulation is well predicted by the

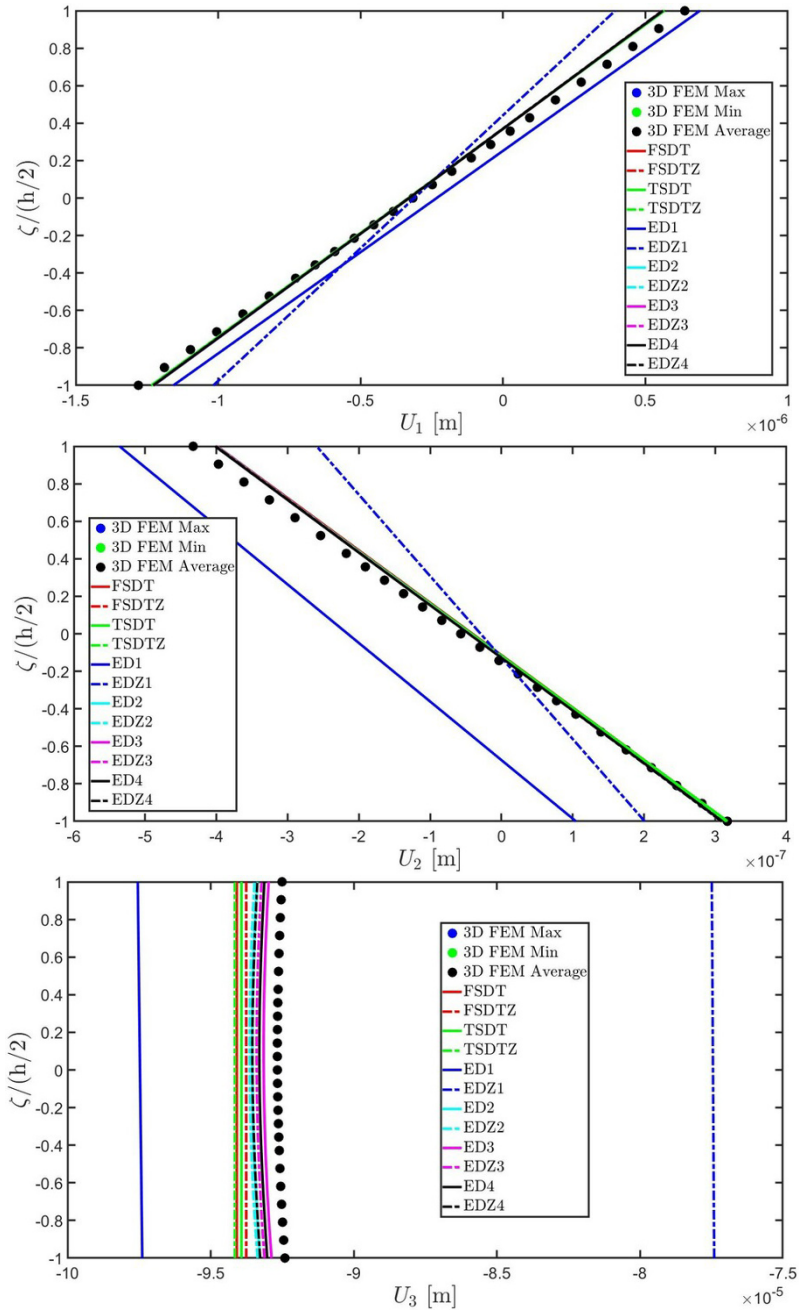


Fig. 29.12 Static analysis of a rectangular plate of constant thickness enforced by general boundary conditions (FB_{SSS}^KFC). Representation of the through-the-thickness displacement field at the point of the physical domain located at $(\xi_1, \xi_2) = (0.50 (\xi_1^1 - \xi_1^0), 0.50 (\xi_2^1 - \xi_2^0))$. The GDQ solution, calculated employing various higher order theories, is compared to predictions from a refined three-dimensional model.

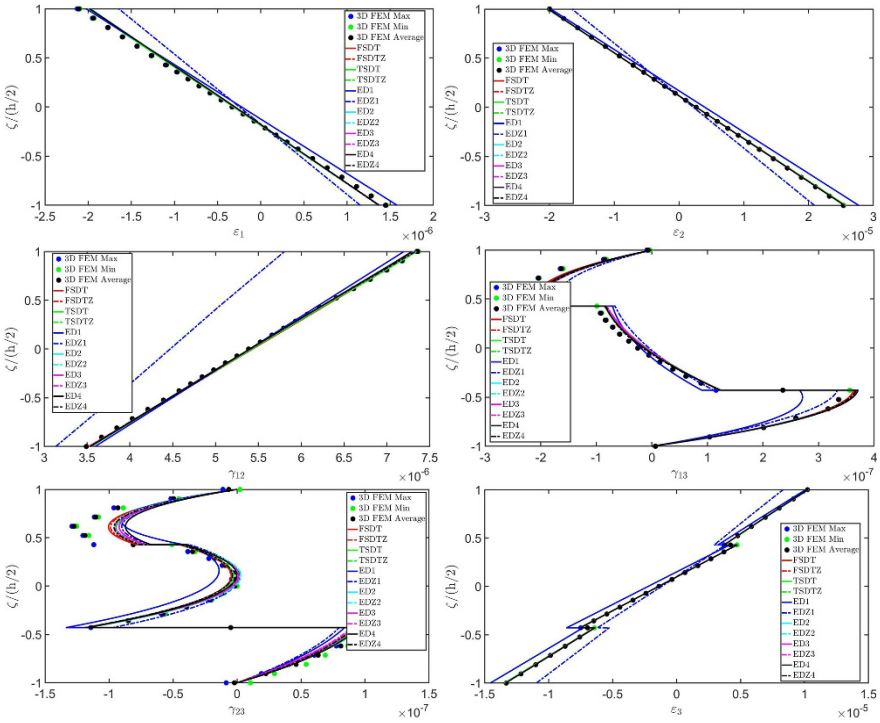


Fig. 29.13 Static analysis of a rectangular plate of constant thickness enforced by general boundary conditions (FB^K_{SSFC}). Representation of the through-the-thickness strain dispersion at the point of the physical domain located at $(\xi_1, \xi_2) = (0.50 (\xi_1^1 - \xi_1^0), 0.50 (\xi_2^1 - \xi_2^0))$. The GDQ solution, calculated employing various higher order theories, has been compared to predictions from a refined three-dimensional model.

proposed formulation. A linear dispersion of U_1 and U_2 can be outlined; on the other hand, the out-of-plane U_3 component requires at least the ED4 theory, due to the meaningful presence of through-the-thickness stretching and warping phenomena. The classical ESL approaches provide only a constant distribution of the out-of-plane displacement field. As far as the three-dimensional strain component vector is concerned (Fig. 29.16), a perfect agreement between different ESL kinematic assumptions is noticed, whereas some discrepancies emerge in the out-of-plane deformations $\gamma_{13}, \gamma_{23}, \epsilon_3$. Accordingly, the proposed formulation best predicts the 3D FEM outcomes, whereas ESL theories characterized by $N = 4$ do not provide good results, even when the zigzag function is implemented. A similar behaviour can be observed in Fig. 29.17. The in-plane stress predictions are in perfect alignment with the 3D FEM ones, whereas the out-of-plane components are well described by the EDZ3 theory. As far as the σ_3 component is concerned, the recovery procedure points out the value of the applied load at the top surface of the shell. The last numerical investigation studies the structural behaviour of an arbitrary shaped catenoid

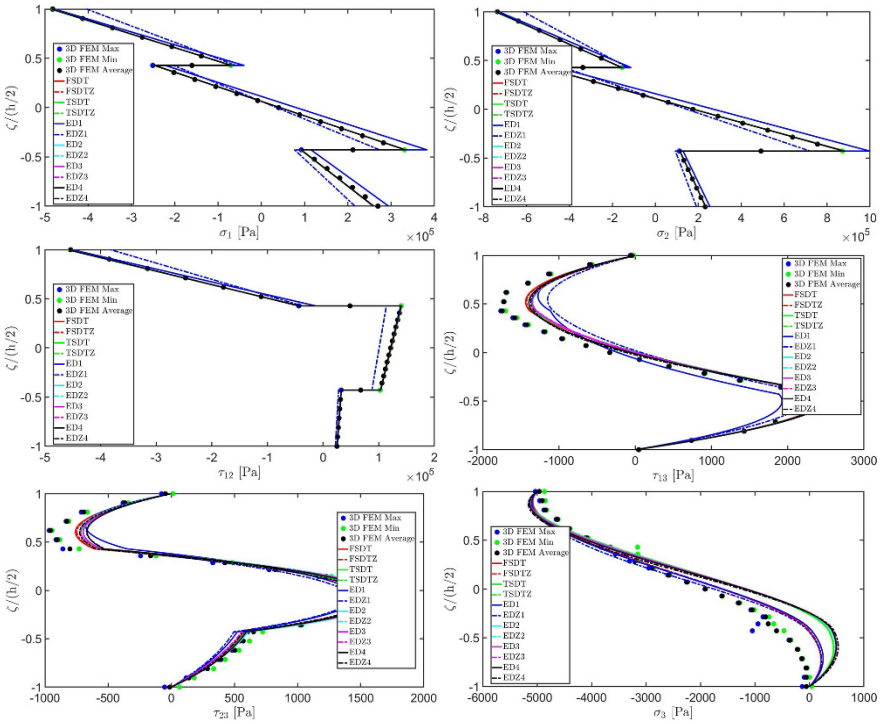


Fig. 29.14 Static analysis of a rectangular plate of constant thickness enforced by general boundary conditions (FB^K_{SSS}FC). Representation of the through-the-thickness stress dispersion at the point of the physical domain located at $(\xi_1, \xi_2) = (0.50 (\xi_1^1 - \xi_1^0), 0.50 (\xi_2^1 - \xi_2^0))$. The GDQ solution, calculated employing various higher order theories, is compared to predictions from a refined three-dimensional model.

under a static loading, see Fig. 29.6. The structure has been externally fixed at three points located in the corner of the mapped physical domain, whereas the remaining edge is fully clamped, as reported in Table 29.5. The static deflection has been checked, as well as the induced strain and stress fields, setting a uniform load equal to $q_3^{(+)} = -5 \times 10^3$ Pa. A systematic investigation has been performed employing various through-the-thickness kinematic assumptions. Referring to the point of the reference surface located at $(\xi_1, \xi_2) = (0.50 (\xi_1^1 - \xi_1^0), 0.50 (\xi_2^1 - \xi_2^0))$, the distribution of the three-dimensional displacement field component vector $\mathbf{U} = [U_1 \ U_2 \ U_3]^T$ has been outlined (see Fig. 29.18). In this case, the EDZ4-based results do not match the other ESL outcomes. On the other hand, deflections based on lower order theories with $N = 1, 2$ are in line with the ones obtained from the FSDT formulation when the zigzag through-the-thickness assumption is employed. Looking at Fig. 29.19, it can be observed that in-plane deformations are characterized by a piecewise linear distribution. Moreover, we outline the presence of differently oriented layers with various stiffnesses. Some discrepancies can be found between findings from differ-

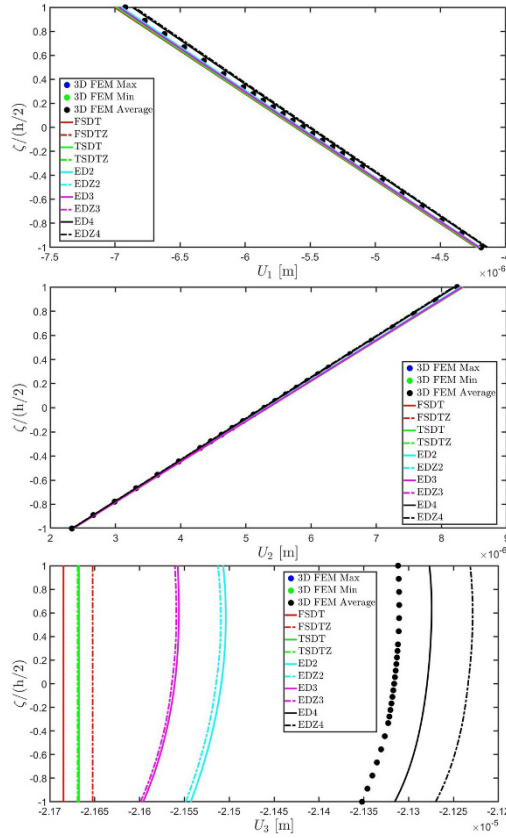


Fig. 29.15 Static analysis of an arbitrary shaped parabolic paraboloid of variable thickness enforced by general boundary conditions ($B_{SSS}^k B_{SSS}^k FF$). Representation of the through-the-thickness displacement field dispersion at the point of the physical domain located at $(\xi_1, \xi_2) = (0.50 (\xi_1^1 - \xi_1^0), 0.50 (\xi_2^1 - \xi_2^0))$. The GDQ solution, calculated employing various higher order theories, is compared to predictions from a refined three-dimensional model.

ent approaches in terms of out-of-plane deformations. The ED3 and ED4 theories, indeed, provide different results from classical FSDT theory. The same behaviour can be observed in the stress distributions from Fig. 29.20. The recovery procedure provides the exact fulfillment of the boundary conditions induced by the external loads. Moreover, the profiles obtained for $N = 4$ are almost the same regardless the employment of the zigzag function. The present example yields good results in line with the EDZ4 formulation.

To sum up, it can be said that the present formulation is an affordable numerical technique characterized by great efficiency and accuracy. It can be considered as a valid alternative to widespread commercial codes for the structural analysis of doubly-curved structures. For both the static and free vibration simulations a very

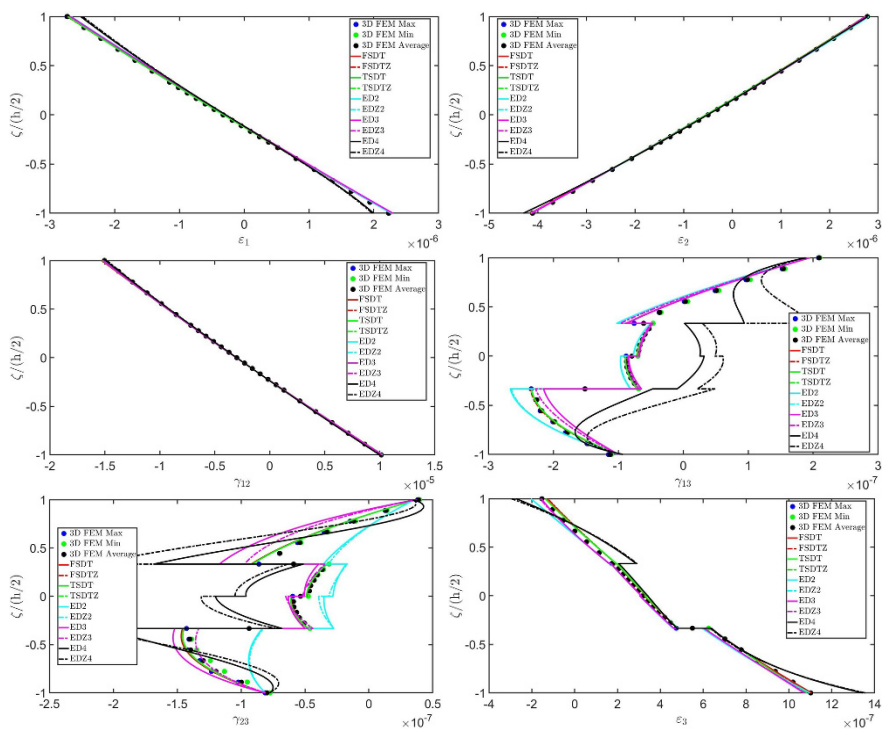


Fig. 29.16 Static analysis of an arbitrary shaped parabolic paraboloid of variable thickness enforced with general boundary conditions ($B_{sss}^k B_{sss}^k FF$). Representation of the through-the-thickness strain components dispersion at the point of the physical domain located at $(\xi_1, \xi_2) = (0.50 (\xi_1^1 - \xi_1^0), 0.50 (\xi_2^1 - \xi_2^0))$. The GDQ solution, calculated employing various higher order theories, is compared to that obtained from a refined three-dimensional model, pointing out the accuracy of the formulation.

good agreement with respect to refined predictions has been observed, providing a unified framework in which systematic investigations can be performed.

29.12 Conclusion

In the present Chapter a theoretical formulation based on the ESL approach has been proposed for the static and the dynamic analysis of doubly-curved shells under general external constraints. A geometric representation has been provided employing curvilinear principal coordinates, together with a distortion mapping based on a NURBS description of the structure alongside the physical domain. A generalized approach has been adopted for the assessment of the displacement field variable. In this way, higher order theories have been introduced, accounting for stretching, warping and coupling three-dimensional effects occurring in the structure. An effective

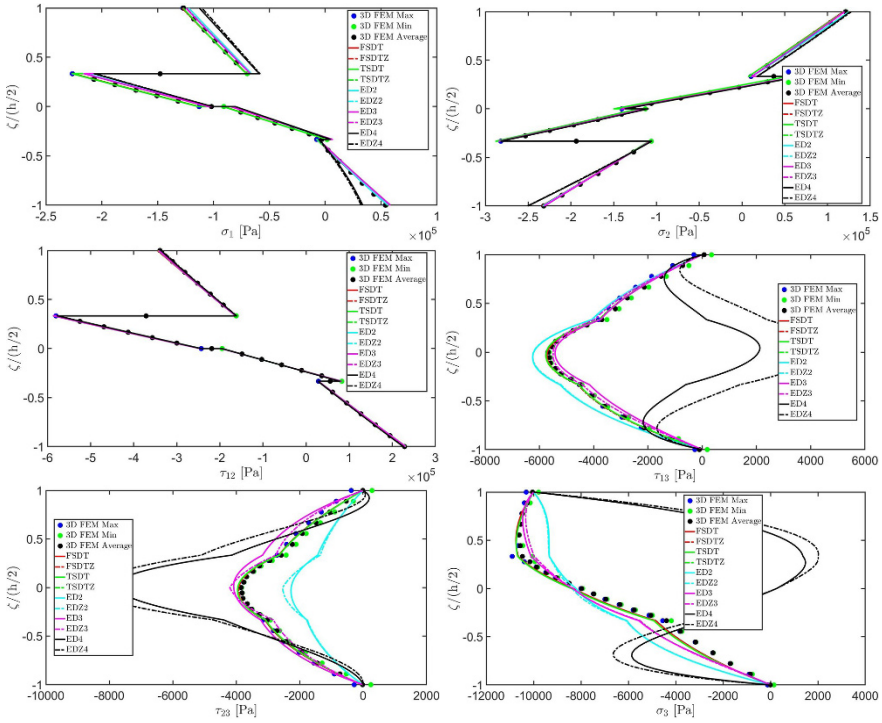


Fig. 29.17 Static analysis of an arbitrary shaped parabolic paraboloid of variable thickness enforced by general boundary conditions. Representation of the through-the-thickness stress components dispersion at the point of the physical domain located at $(\xi_1, \xi_2) = (0.50 (\xi_1^1 - \xi_1^0), 0.50 (\xi_2^1 - \xi_2^0))$. The GDQ solution, calculated employing various higher order theories, is compared to predictions from a refined three-dimensional model.

homogenization on the reference surface of the shell mechanical properties has been performed taking into account the elastic strain energy of the structure. An arbitrary orientation of each lamina has been considered, setting a generally anisotropic material in all the layers of the stacking sequence. External loads have been applied on the top and the bottom surfaces of the structure, accounting for arbitrary distributions along each parametric line. The governing equations have been derived from the Hamiltonian principle, together with the external boundary conditions. Generalized in-plane and out-of-plane distributions of linear elastic springs have been considered for each shell edge, thus setting a comprehensive set of external constraints. For static analyses, an effective through-the-thickness reconstruction of stresses and strains allowed the determination of the three-dimensional quantities starting from a bi-dimensional formulation. The theoretical assessment has been numerically tackled from a discretization of derivatives employing the GDQ technique. Some case studies have been presented and the accuracy of the proposed formulation has been checked from a benchmark with the outcomes of refined three-dimensional Finite Element simulations for both the static and the free vibration analysis. The presented

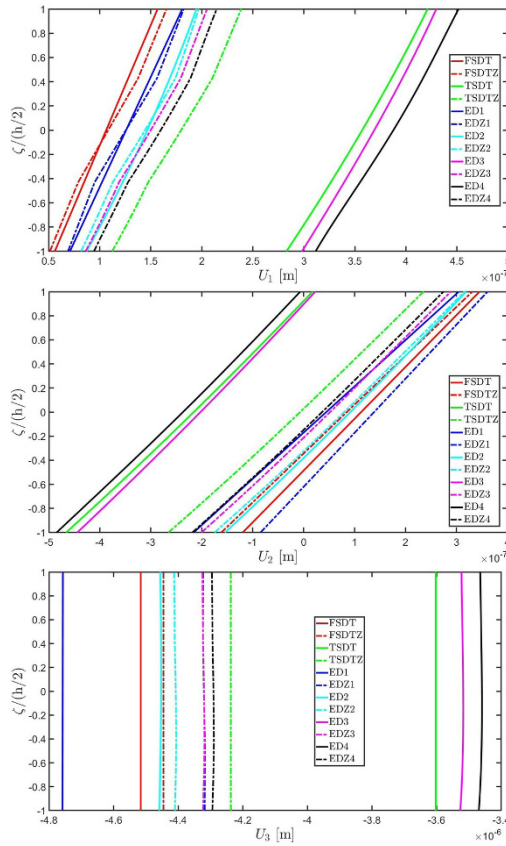


Fig. 29.18 Static analysis of an arbitrary shaped catenoid of variable thickness enforced by general boundary conditions ($B_{SSS}^K B_{SSS}^K CB_{SSS}^K$). Representation of the through-the-thickness displacement field dispersion at the point of the physical domain located at $(\xi_1, \xi_2) = (0.50 (\xi_1^1 - \xi_1^0), 0.50 (\xi_2^1 - \xi_2^0))$. The GDQ solution has been calculated employing various higher order theories.

ESL model has demonstrated to be very reliable for a proper prediction of very complex three-dimensional effects especially when higher order assumptions of the displacement field are assumed, even with a reduced computational cost with respect to more expensive reference solutions.

References

Ansari R, Darvizeh M (2008) Prediction of dynamic behaviour of FGM shells under arbitrary boundary conditions. Composite Structures 85:284–292

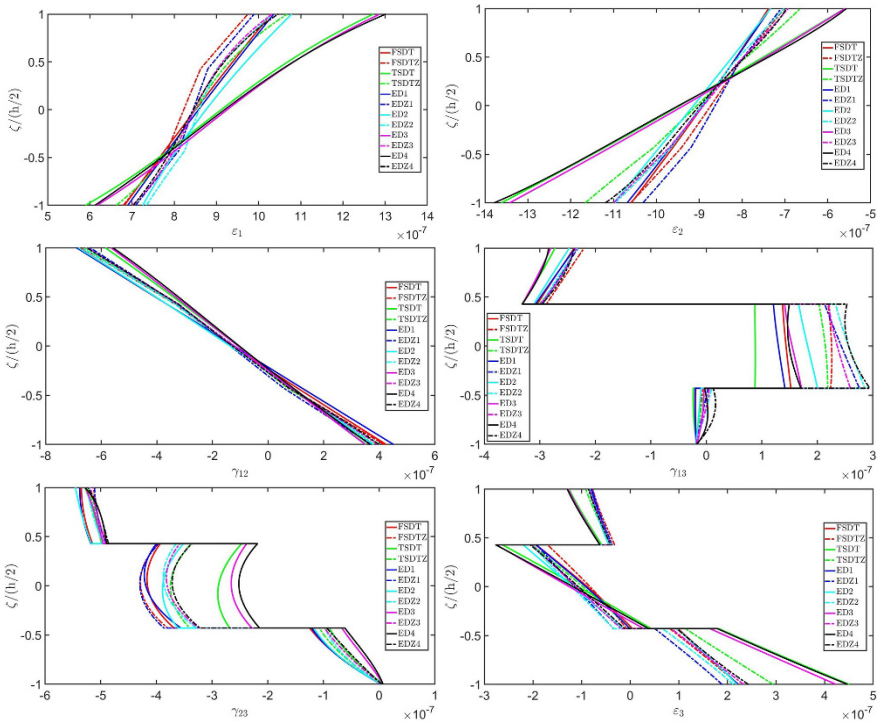


Fig. 29.19 Static analysis of an arbitrary shaped catenoid of variable thickness enforced by general boundary conditions ($B_{SSS}^K B_{SSS}^K C B_{SSS}^K$). Representation of the through-the-thickness strain components dispersion at the point of the physical domain located at $(\xi_1, \xi_2) = (0.50 (\xi_1^1 - \xi_1^0), 0.50 (\xi_2^1 - \xi_2^0))$. The GDQ solution has been calculated employing various higher order theories.

Bellman R, Casti J (1971) Differential quadrature and long-term integration. *Journal of Mathematical Analysis and Applications* 34:235–238

Brischetto S, Tornabene F, Fantuzzi N, Bacciocchi M (2017) Interpretation of boundary conditions in the analytical and numerical shell solutions for mode analysis of multilayered structures. *International Journal of Mechanical Sciences* 122:18–28

Chapelle D, Bathe KJ (1998) Fundamental considerations for the finite element analysis of shell structures. *Computers & Structures* 66:19–36

dell’Isola F, Lekszycki T, Pawlikowski M, Grygoruk R, Greco L (2015) Designing a light fabric metamaterial being highly macroscopically tough under directional extension: first experimental evidence. *Zeitschrift für angewandte Mathematik und Physik* 66:3473–3498

Demasi L, Biagini G, Vannucci F, Santarpia E, Cavallaro R (2017) Equivalent single layer, zig-zag, and layer wise theories for variable angle tow composites based on the generalized unified formulation. *Composite Structures* 177:54–79

Dimitri R, Tornabene F (2018) Numerical study of the mixed-mode delamination of composite specimens. *Journal of Composites Science* 2:30

Dimitri R, Fantuzzi N, Tornabene F, Zavarise G (2016) Innovative numerical methods based on SFEM and IGA for computing stress concentrations in isotropic plates with discontinuities. *International Journal of Mechanical Sciences* 118:166–187

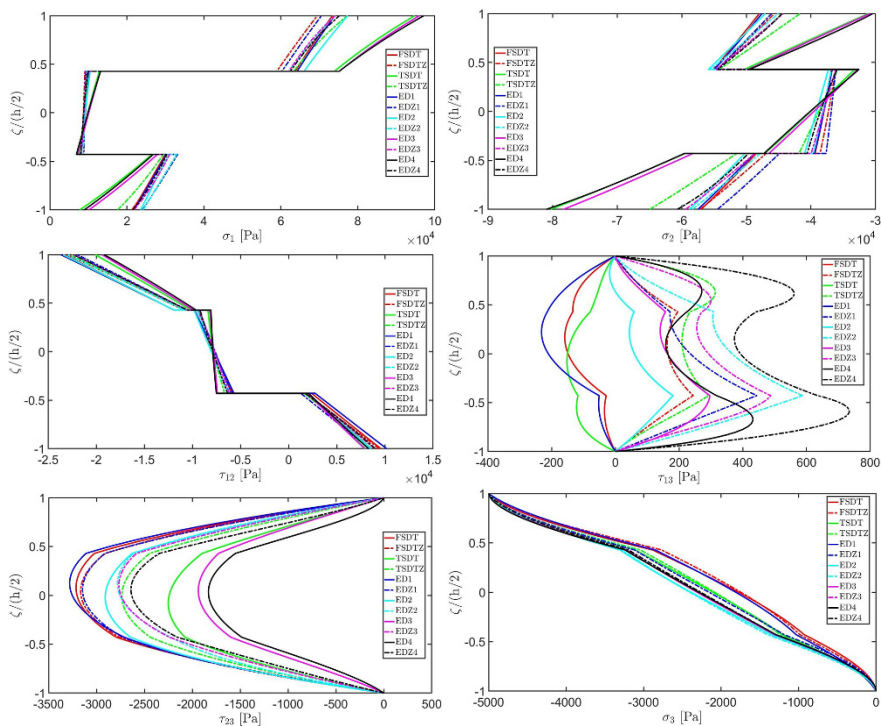


Fig. 29.20 Static analysis of an arbitrary shaped catenoid of variable thickness enforced with general boundary conditions $(B_{SSS}^K B_{SSS}^K C B_{SSS}^K)$. Representation of the through-the-thickness stress components dispersion at the point of the physical domain located at $(\xi_1, \xi_2) = (0.50 (\xi_1^1 - \xi_1^0), 0.50 (\xi_2^1 - \xi_2^0))$. The GDQ solution has been calculated employing various higher order theories.

Dimitri R, Tornabene F, Zavarise G (2018) Analytical and numerical modeling of the mixed-mode delamination process for composite moment-loaded double cantilever beams. *Composite Structures* 187:535–553

Fazzolari FA, Viscoti M, Dimitri R, Tornabene F (2021) 1D-Hierarchical Ritz and 2D-GDQ formulations for the free vibration analysis of circular/elliptical cylindrical shells and beam structures. *Composite Structures* 258:113,338

Finlayson B, Scriven L (1966) The method of weighted residuals—a review. *Applied Mechanics Reviews* 19:735–748

Ganzosch G, dell’Isola F, Turco E, Lekszycki T, Müller WH (2017) Shearing tests applied to pantographic structures. *Acta Polytechnica CTU Proceedings* 7:1–6

Giorgio I (2021) Lattice shells composed of two families of curved kirchhoff rods: an archetypal example, topology optimization of a cycloidal metamaterial. *Continuum Mechanics and Thermodynamics* 33:1063–1082

Giorgio I, Rizzi N, Turco E (2017) Continuum modelling of pantographic sheets for out-of-plane bifurcation and vibrational analysis. *Proceedings of the Royal Society A: Mathematical, Physical and Engineering Sciences* 473:20170,636

Giorgio I, Varano V, dell’Isola F, Rizzi N (2021) Two layers pantographs: a 2d continuum model accounting for the beams’ offset and relative rotations as averages in so (3) lie groups. *International*

- Journal of Solids and Structures 216:43–58
- Gürdal Z, Haftka RT, Hajela P (1999) Design and optimization of laminated composite materials. John Wiley & Sons, New York
- Katili I, Makhun IJ, Tjahjono E, Alisjahbana I (2017) Error estimation for the DKMQ24 shell element using various recovery methods. *International Journal of Technology* 6:1060–1069
- Li D (2021) Layerwise theories of laminated composite structures and their applications: A review. *Archives of Computational Methods in Engineering* 28:577–600
- Mindlin RD (1951) Influence of rotatory inertia and shear on flexural motions of isotropic, elastic plates. *Journal of Applied Mechanics* 18:31–38
- Murakami H (1986) Laminated composite plate theory with improved in-plane responses. *Journal of Applied Mechanics* 53:661–666
- Patton A, Antolin P, Dufour JE, Kiendl J, Reali A (2021) Accurate equilibrium-based interlaminar stress recovery for isogeometric laminated composite kirchhoff plates. *Composite Structures* 256:112,976
- Piegl L (1991) On NURBS: a survey. *IEEE Computer Graphics and Applications* 11:55–71
- Pilato L, Michno M (1994) Advanced composite materials. Springer Science & Business Media, Berlin
- Rah K, Van Paeppegem W, Habraken AM, Degrieck J (2012) A mixed solid-shell element for the analysis of laminated composites. *International Journal for Numerical Methods in Engineering* 89:805–828
- Reddy J (1993) An evaluation of equivalent-single-layer and layerwise theories of composite laminates. *Composite Structures* 25:21–35
- Reddy J, Wang C, Lee K (1997) Relationships between bending solutions of classical and shear deformation beam theories. *International Journal of Solids and Structures* 34:3373–3384
- Reddy JN (1984) A simple higher-order theory for laminated composite plates. *Journal of Applied Mechanics* 51:745–752
- Reissner E (1945) The effect of transverse shear deformation on the bending of elastic plates. *Journal of Applied Mechanics* 12:A69–A77
- Shu C, Du H (1997a) A generalized approach for implementing general boundary conditions in the GDQ free vibration analysis of plates. *International Journal of Solids and Structures* 34:837–846
- Shu C, Du H (1997b) Implementation of clamped and simply supported boundary conditions in the GDQ free vibration analysis of beams and plates. *International Journal of Solids and Structures* 34:819–835
- Shu C, Richards BE (1992) Application of generalized differential quadrature to solve two-dimensional incompressible Navier-Stokes equations. *International Journal for Numerical Methods in Fluids* 15:791–798
- Shu C, Chen W, Xue H, Du H (2001) Numerical study of grid distribution effect on accuracy of DQ analysis of beams and plates by error estimation of derivative approximation. *International Journal for Numerical Methods in Engineering* 51:159–179
- Sokolnikoff I, Specht, Dickerson R, et al (1956) *Mathematical theory of elasticity*, vol 83. McGraw-Hill, New York
- Tessler A, Di Sciuva M, Gherlone M (2009) A refined zigzag beam theory for composite and sandwich beams. *Journal of Composite Materials* 43:1051–1081
- Toledano A, Murakami H (1987) A high-order laminated plate theory with improved in-plane responses. *International Journal of Solids and Structures* 23:111–131
- Tornabene F, Baccocchi M (2018) Anisotropic Doubly-Curved Shells: Higher-Order Strong and Weak Formulations for Arbitrarily Shaped Shell Structures. *Società Editrice Esculapio, Bologna*
- Tornabene F, Reddy J (2013) FGM and laminated doubly-curved and degenerate shells resting on nonlinear elastic foundations: a GDQ solution for static analysis with a posteriori stress and strain recovery. *Journal of the Indian Institute of Science* 93:635–688
- Tornabene F, Liverani A, Calgiana G (2011) FGM and laminated doubly curved shells and panels of revolution with a free-form meridian: a 2-D GDQ solution for free vibrations. *International Journal of Mechanical Sciences* 53:446–470

- Tornabene F, Liverani A, Caligiana G (2012) Laminated composite rectangular and annular plates: A GDQ solution for static analysis with a posteriori shear and normal stress recovery. *Composites Part B: Engineering* 43:1847–1872
- Tornabene F, Fantuzzi N, Baccocchi M, Viola E (2015a) Accurate inter-laminar recovery for plates and doubly-curved shells with variable radii of curvature using layer-wise theories. *Composite Structures* 124:368–393
- Tornabene F, Fantuzzi N, Ubertini F, Viola E (2015b) Strong formulation finite element method based on differential quadrature: a survey. *Applied Mechanics Reviews* 67:020,801
- Tornabene F, Dimitri R, Viola E (2016a) Transient dynamic response of generally-shaped arches based on a GDQ-time-stepping method. *International Journal of Mechanical Sciences* 114:277–314
- Tornabene F, Fantuzzi N, Baccocchi M (2016b) The local GDQ method for the natural frequencies of doubly-curved shells with variable thickness: a general formulation. *Composites Part B: Engineering* 92:265–289
- Tornabene F, Fantuzzi N, Baccocchi M (2018) DiQuMASPAB: Differential Quadrature for Mechanics of Anisotropic Shells, Plates, Arches and Beams. Società Editrice Esculapio, Bologna
- Tornabene F, Baccocchi M, Fantuzzi N, Reddy J (2019) Multiscale approach for three-phase CNT/polymer/fiber laminated nanocomposite structures. *Polymer composites* 40:E102–E126
- Tornabene F, Viscoti M, Dimitri R, Aiello MA (2021a) Higher order formulations for doubly-curved shell structures with a honeycomb core. *Thin-Walled Structures* 164:107,789
- Tornabene F, Viscoti M, Dimitri R, Aiello MA (2021b) Higher-order modeling of anisogrid composite lattice structures with complex geometries. *Engineering Structures* 244:112,686
- Tornabene F, Viscoti M, Dimitri R, Reddy JN (2021c) Higher order theories for the vibration study of doubly-curved anisotropic shells with a variable thickness and isogeometric mapped geometry. *Composite Structures* 267:113,829
- Tornabene F, Viscoti M, Dimitri R (2022) Generalized higher order layerwise theory for the dynamic study of anisotropic doubly-curved shells with a mapped geometry. *Engineering Analysis with Boundary Elements* 134:147–183
- Tu LW (2017) *Differential geometry: connections, curvature, and characteristic classes*, vol 275. Springer, Cham, Switzerland
- Vasiliev VV, Morozov EV (2018) *Advanced mechanics of composite materials and structures*. Elsevier, Amsterdam
- Viola E, Tornabene F, Ferretti E, Fantuzzi N (2013) On static analysis of composite plane state structures via GDQFEM and cell method. *CMES* 94:421–458
- Wang FF, Dai HH, Giorgio I (2021) A numerical comparison of the uniformly valid asymptotic plate equations with a 3d model: Clamped rectangular incompressible elastic plates. *Mathematics and Mechanics of Solids* July:1–27
- Wang Q, Shao D, Qin B (2018) A simple first-order shear deformation shell theory for vibration analysis of composite laminated open cylindrical shells with general boundary conditions. *Composite Structures* 184:211–232
- Wang X, Redekop D (2005) Natural frequencies and mode shapes of an orthotropic thin shell of revolution. *Thin-Walled Structures* 43:735–750
- Whitney J (1969) The effect of transverse shear deformation on the bending of laminated plates. *Journal of composite materials* 3:534–547
- Whitney J, Pagano N (1970) Shear deformation in heterogeneous anisotropic plates. *Journal of Applied Mechanics* 37:1031–1036
- Zienkiewicz OC, Taylor RL, Nithiarasu P, Zhu J (1977) *The finite element method*, vol 3. McGraw-Hill, London

Part III

Experiments



Chapter 30

Characterisation of Mechanical Properties of Wood: Size Effect

Reza Afshar

Abstract In the areas such as cultural heritage, there are various non-standard sample sizes and shapes to characterise the mechanical properties of materials. In addition, there is a need for minimum intervention, which leads to minimisation of samples in sizes and numbers. The aim of this study is to investigate the size effect on material properties of hard wood, as an orthotropic material, in terms of stiffness properties. The compression tests in combination with image analysis technique were used to find the stiffness of the oak samples in the radial direction of wood. Small clear specimens made from oak (*Quercus robur* L.) were tested. The specimens were divided into two groups: A and B. The testing volumes of group A and B were $10 \times 10 \times 10 \text{ mm}^3$ and $25 \times 25 \times 25 \text{ mm}^3$ respectively. A total number of 8 samples from group A and 9 samples from group B were tested. The results show that the average difference between the two sizes of the samples in term of stiffness in radial direction is 5.5%, with slightly higher values for smaller cubic specimens. More experiments in all orthogonal directions of wood are needed to confirm the results of this study.

Keywords: Size effect · Wood material · Digital Image Correlation (DIC) · Compression test

R. Afshar

Division of Applied Mechanics, Department of Materials Science and Engineering, Uppsala University, 751 03 Uppsala, Sweden
e-mail: reza.afshar@angstrom.uu.se

30.1 Introduction

30.1.1 Wood Properties and Importance

Since prehistoric times, wood has been used as a building material due to its unrivaled properties and abundance. It is still considered an excellent building material due to its high stiffness to weight ratio, flexibility and damage tolerance. Recently, wood is seeing a renaissance as a renewable and sustainable building material.

Wood and biological tissues like bone are examples of non-homogenous and anisotropic materials. Wood is a biomaterial with a cellular structure and imperfections (defects) such as knots that are influencing its strength properties. For the case of small clear samples, the assumption of Cartesian orthotropic behaviour of wood is valid. The stiffness matrix C is the inverse of the compliance matrix D such that

$$C^{-1} = D \quad (30.1)$$

where

$$D = \begin{pmatrix} \frac{1}{E_L} & -\frac{\nu_{LT}}{E_T} & -\frac{\nu_{LR}}{E_R} & 0 & 0 & 0 \\ -\frac{\nu_{TL}}{E_L} & \frac{1}{E_T} & -\frac{\nu_{TR}}{E_R} & 0 & 0 & 0 \\ \frac{E_L}{-\nu_{RL}} & \frac{E_T}{-\nu_{RT}} & \frac{1}{E_R} & 0 & 0 & 0 \\ 0 & 0 & 0 & \frac{1}{G_{LT}} & 0 & 0 \\ 0 & 0 & 0 & 0 & \frac{1}{G_{LR}} & 0 \\ 0 & 0 & 0 & 0 & 0 & \frac{1}{G_{TR}} \end{pmatrix} \quad (30.2)$$

in the orthotropic case, where L represents longitudinal direction, T is for tangential and R is for radial direction of wood. In this study the R -direction of wood is considered.

The structural properties of both green as well as dry wood are the result of its complex structure from the macroscale annual rings down to the composite-like microstructure of its cell walls. Properties vary within a single tree, between species and due to growth conditions. Even after harvesting, the properties of wood depend on the climate (humidity and temperature) and change over time due to chemical and biological influences. Clear straight-grained wood is used for determining fundamental mechanical properties (Green et al, 1999). Mechanical properties of wooden specimens are dependent on the specimen dimensions (Showalter, 1987; Bohannon, 1966). This phenomenon is often called size effect.

30.1.2 Size Effect

In the areas such as cultural heritage, there are various non-standard sample sizes and shapes to characterise the mechanical properties of materials, which inherently are heterogeneous. In addition, there is a need for minimum intervention, which leads to minimisation of samples in sizes and numbers (Válek and Veiga, 2005). It

is well known that size effects play an important role in the mechanical behavior of heterogeneous material, like bone tissues at different scales (Giorgio et al, 2017, 2021). One should note that, it is not the absolute size of the sample that is related to the size effect; instead, it is the ratio between a characteristic size of the microstructure and the overall size of the sample that can trigger such an effect.

The first-order gradient elasticity theory is accurate for structure in the meter length-scale; however, it is inaccurate for structure in the micrometer length-scale, where the substructure of the material becomes dominant. Therefore, in Abali et al (2017); Vazic et al (2021) a second-order theory is used, which is able to model the deformation of structure even on smaller length-scales, with an adequate amount of computational cost. To incorporate the scale of the microstructure of a heterogeneous material within the continuum framework, a number of phenomenological approaches have been proposed that involve the relaxation of the local action hypothesis of classical continuum mechanics. Among others, higher-order gradient models are proposed in dell'Isola et al (2015, 2009).

In order to explain the size effect phenomenon for wood, there are different suggested approaches in the literature. The most famous approach is Weibull's weakest link theory (Weibull, 1939). Weibull states that increased stressed volume is attended by a decrease in wood strength due to stochastically appearing weak locations in the wood. Thus, there is an increased probability of encountering a strength-reducing flaw, when the volume of the material under stress is increased (Pedersen et al, 2003). Only few literature addresses the effect of specimen size on stiffness parameters of the wooden material (Schlotzhauer et al, 2017). In Madsen and Tomoi (1991), the influence of span length in bending testing on stiffness parameters are given. The effect of size and geometry on strength values and stiffness in longitudinal (L) direction of selected hardwood species were investigated in Schlotzhauer et al (2017). They found that for the case of compression and bending stiffness, in most cases, the dimensions did not influence the stiffness parameters. In tensile testing, E_L differed significantly for the different specimen sizes.

30.2 Materials and Method

Materials: Small clear specimens made from oak (*Quercus robur* L.) were tested. Before the sampling, boards were conditioned in a climate condition at 22°C and 55% relative humidity (RH). The boards were cut into the small cubic specimens, in two different sizes, with the dimensions displayed in Fig. 30.1. The specimens were divided into two groups: A and B. The testing volume of group A and B was $10 \times 10 \times 10 \text{ mm}^3$ and $25 \times 25 \times 25 \text{ mm}^3$ respectively. The total number of 8 samples from group A and 9 samples from group B were tested. The mass density of all of the samples is measured and summarised in Table 30.1. The average and standard deviation of samples in group A and B are $705 \pm 11 \text{ (kg/m}^3\text{)}$ and $686 \pm 15 \text{ (kg/m}^3\text{)}$, respectively.

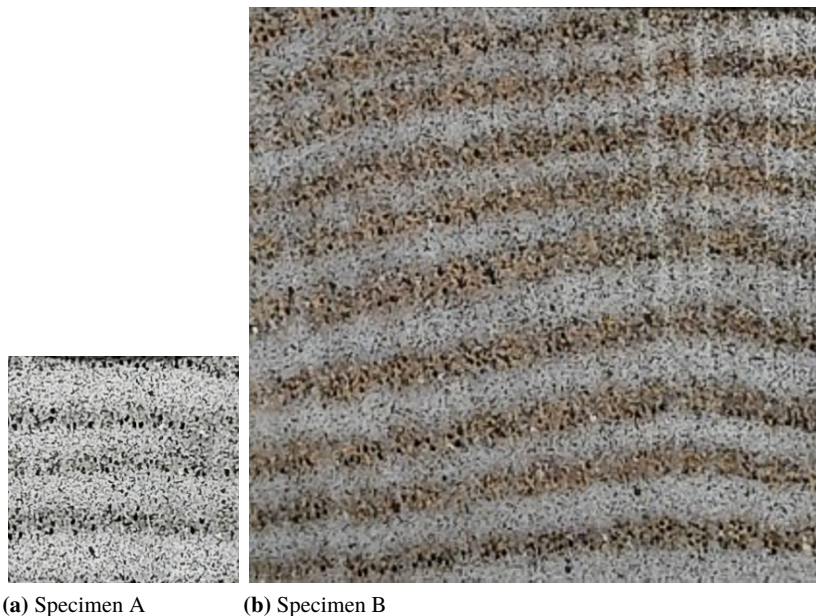


Fig. 30.1 Cross section of the two specimens

Table 30.1 The mass density values for each group of samples

| | | | | | | | | | | |
|-----------------------------------|-----|-----|-----|-----|-----|-----|-----|-----|--------------|--------------|
| Sample | 1A | 2A | 3A | 4A | 5A | 6A | 7A | 8A | Average± STD | |
| Mass density (kg/m ³) | 687 | 694 | 714 | 715 | 712 | 797 | 695 | 714 | 705±11 | |
| Sample | 1B | 2B | 3B | 4B | 5B | 6B | 7B | 8B | 9B | Average± STD |
| Mass density (kg/m ³) | 717 | 702 | 693 | 682 | 675 | 676 | 672 | 680 | 679 | 686±15 |

Method: In this study, all the tests were performed in compression by using a compression rig (Fig. 30.2), which previously was used in creep experiments in Afshar et al (2020). The area of applied load for each sample is considered for calculation of applied stress. For both samples the applied stress was in linear elastic range of material. The average applied stress for sample A and B was 4.78 MPa and 1.88 MPa respectively. The applied stresses are in elastic range of material in the R-direction, which allows us to test the same sample in other wood's orthogonal directions. The samples loaded for 100 s. For each sample a camera recorded the deformation with an interval of every 1 s until 100 s. The strain field was obtained by using digital image correlation (DIC) method (also called digital speckle photography), by considering the deformations between 4-13 s. The strains in R-direction (ϵ_R) as a function of time for some of the samples are given in Fig. 30.3, where it is evident that response of the

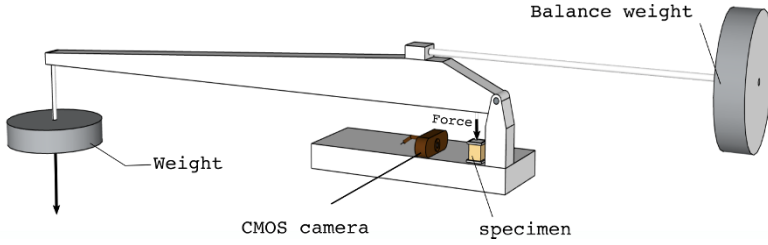


Fig. 30.2 Test rig used for compression tests.

samples within first 13 s is instantaneous response, i.e, it is strain-rate independent. This means that the E_R of the samples can be calculated within this time period.

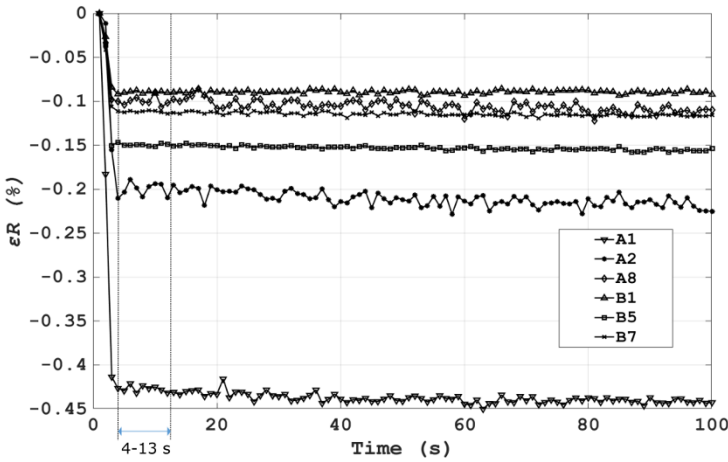


Fig. 30.3 Strain in R-direction (ϵ_R) as a function of time for some of the samples.

30.2.1 Digital Image Correlation (DIC) Method

The Digital Image Correlation (DIC) method is a robust non-contact technique for measuring material deformation (Peters and Ranson, 1982), (Chu et al, 1985), (Vendroux and Knauss, 1998). Digital speckle photography is well suited for measurements on small objects (Jernkvist and Thuvander, 2001). An open source 2D DIC Matlab code ncorr (Blaber et al, 2015) was used for image analysis in this study.

The basic principle of DIC is to record a series of images of the sample during deformation, and then to calculate the degree of displacement from the images. The strain field then can be calculated from the displacement field. Any DIC implementation consists of three main steps: sample preparation, image recording and image processing. If only one camera is used (2D DIC analysis), it is best suited for strain measurements in which there are modest deformations of planar surfaces. The sample surface needs to have a random texture that does not have a specific orientation and is non-periodic (Sutton et al, 2009). This can be achieved by spray paint, where by spraying a black colour on a white background a random black and white speckles are generated. For the recordings of the displacements, only a digital camera and natural light, or a white light source, are needed. The image processing starts by dividing the image into subsets. The displacement is then calculated separately for each subset. The basic principle of DIC is to use cross correlation to identify the same subset in the images recorded both before and after the deformation. The correlation function is a function of 2D displacement and the location of the peak of the correlation function gives the position of the deformed subset. An iterative cross-correlation algorithm is needed for more complex deformation fields. Deformation of the subset can be accounted for by introducing a shape function that translates the pixel coordinates in the reference subset into coordinates in the image after deformation. The grey values can be interpolated between the pixels in the image to achieve sub-pixel accuracy (Sutton et al, 2009).

30.2.2 Steps for Stiffness Parameter Calculation

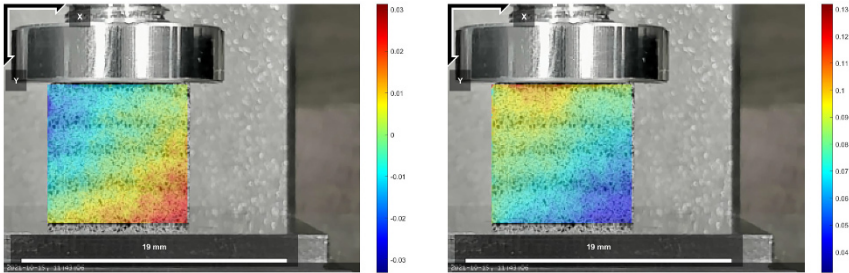
As it is mentioned in the Introduction, in this study, only radial direction is considered to calculate the stiffness parameter (E_R). The steps for the E_R calculation is as follows:

- First, the applied load on the sample, according to Fig. 30.2, was set by having the known weight at the end of the rig and the known arm distance.
- Then, the applied stress on each sample is evaluated by dividing the applied force divided to the cross-section at the top of each sample (LT-plane).
- After that, the average strain in the loading direction (ε_R) in a plane parallel to applied load (RT-plane) by using DIC method is calculated.
- Finally, E_R is obtained by simply dividing the applied stress to the computed average strain (ε_R)

30.3 Results and Discussions

By using DIC method, the 2D displacement fields, where x -axis represents tangential and y -axis denotes radial direction, as well as 2D strain fields in normal directions T and R and shear strain RT of the two groups of specimens (A and B) are measured.

The displacement fields of one of the samples from group A (1A) are given in Fig. 30.4 and the strain fields are depicted in Fig. 30.5.



(a) u_T (b) u_R

Fig. 30.4 The displacement fields of sample 1A: x -axis represents tangential and y -axis denotes radial direction.

The displacement fields of one of the samples from group B (1B) are given in Fig. 30.6 and the strain fields are depicted in Fig. 30.7.

As it is mentioned in Section 30.2, the average strain in the loading direction (ϵ_R) in a plane parallel to applied load (RT-plane) is used for calculation of stiffness parameter in R-direction. As it can be seen from Fig. 30.5 and Fig. 30.7, the strain field in loading direction (ϵ_R) is quite uniform for both samples with different sizes.

The results in terms of modulus of elasticity in R-direction of the samples for the two size of the samples are summarised in Table 30.2. Notice that, the results for one of sample from group B (3B) was excluded in Table 30.2 due to error in measurements. As it can be seen from Table 30.2, the average E_R for the small

Table 30.2 Modulus of elasticity in R-direction for the two groups of samples.

| Sample | 1A | 2A | 3A | 4A | 5A | 6A | 7A | 8A | Average±STD |
|----------------|------|------|------|------|------|------|------|------|-------------|
| E_R (GPa) | 1.25 | 5.15 | 1.32 | 1.30 | 2.77 | 1.56 | 2.27 | 5.88 | 2.70±1.83 |
| Sample | 1B | 2B | 4B | 5B | 6B | 7B | 8B | 9B | Average±STD |
| E_R (GPa) | 2.37 | 4.72 | 2.69 | 1.26 | 2.69 | 1.55 | 2.68 | 2.34 | 2.54±1.04 |
| Difference (%) | | | | | | | | | 5.53 |

samples (group A) is 2.70 ± 1.83 GPa, whereas this value is lower (5.53%) for the large samples (group B) with 2.54 ± 1.04 GPa. The standard deviation (STD) is relatively high for the both groups, which requires more number of samples to be tested in order to have a higher coefficient of confidence of the results. In addition,

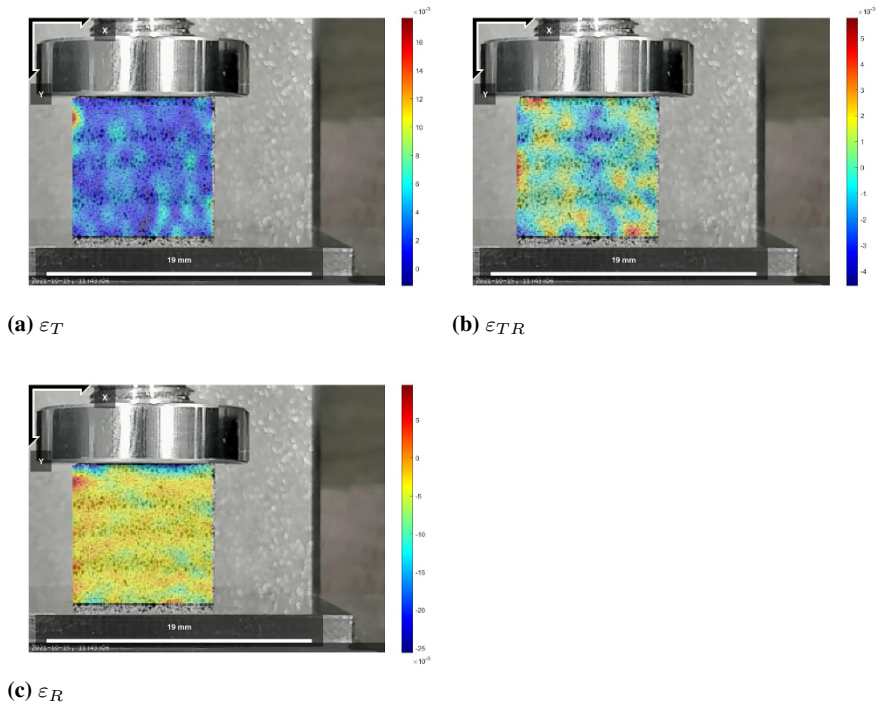


Fig. 30.5 The strain fields of sample 1A.

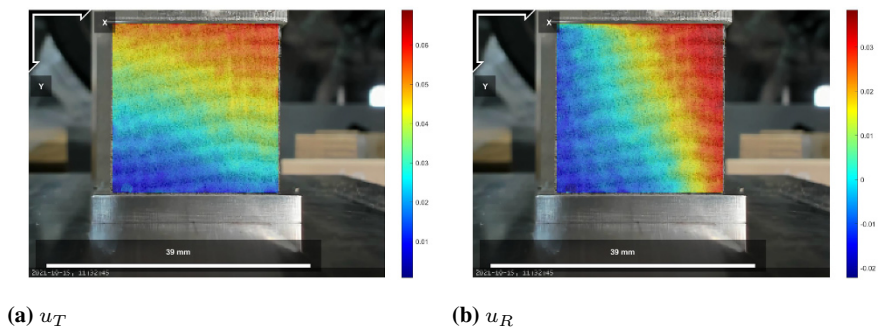


Fig. 30.6 The displacement fields of sample 1B: x-axis represents tangential and y-axis denotes radial direction.

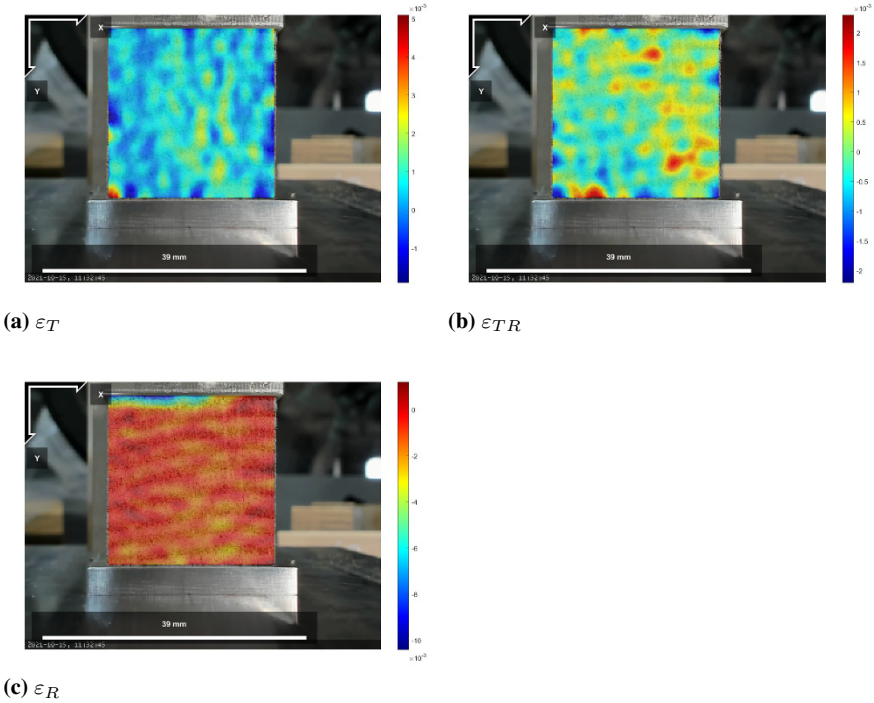


Fig. 30.7 The strain fields of sample 1B.

it indicates the higher sensitivity of the small samples (group A) in term of average strain field evaluation compared to the large samples (group B).

According to Jernkvist and Thuvander (2001), samples with larger curvature of annual rings are expected to have higher stiffness. It worth mentioning that, a similar high STD for stiffness of hard wood samples in L-direction is reported in Schlotzhauer et al (2017), where a possible reason for this phenomenon stated as the resulting stiffness would be a result of compression and buckling.

The E_R of recent oak cubic samples with the same size as group B is reported in Table 1 in Vorobyev et al (2016). The samples were tested using quasi-static method, with the value of 2.01 ± 0.15 MPa, which has a difference of about 20% with the finding of this study. The conditioning of samples in that study was similar to this work.

30.4 Conclusions and Future Work

This study was an effort to investigate the size effect on material properties of hard wood, as an orthotropic material, in term of stiffness properties. The compression tests in combination with image analysis technique were used to find the stiffness in radial direction (E_R) of the oak samples. The results show that the difference between the two sizes of the samples in term of E_R is 5.53%, with lower values for larger cubic specimen. One expects to have higher stiffness in the R-direction with larger curvature of annual rings in the smaller samples. More experiments in all orthogonal directions of wood are needed to confirm the results of this study.

The idea for future work is:

- to continue investigating the oak samples in the other two directions, i.e., tangential (T) and longitudinal (L) direction to obtain the corresponding stiffness parameters in those directions.
- After that, the samples will be loaded until failure to find the strength properties in the three normal directions.
- Regarding the shear properties of wood, another set of samples with inclined fiber directions (45°) are needed.
- The more detailed properties of sample such as moisture content, annual rings, early wood and late wood distributions and modular ray angles will be needed to understand the relationship between the stiffness parameters of each sample and its properties.
- In addition, the possibility of 3-D image analysis, i.e. using two cameras aiming a surface with a certain angle, to avoid measurement error due to out-of-plane movement of the sample will be explored.

Acknowledgements The financial support from UU-innovation through AIM-day material made this study possible. For that I would like to thank Harris Stamatopoulos, who was supportive through application process.

In addition, I would like to thank Anders Ahlgren, engineer at the Vasa Museum for scientific discussions, Rhodel Bengtsson, PhD student at the applied mechanics division, for his help in experiments and Åsa Egerquist, ship carpenter at collections Unit at the Vasa Museum, for preparing the samples.

References

- Abali BE, Müller WH, dell'Isola F (2017) Theory and computation of higher gradient elasticity theories based on action principles. *Archive of Applied Mechanics* 87(9):1495–1510
- Afshar R, Cheylan M, Almkvist G, Ahlgren A, Gamstedt EK (2020) Creep in oak material from the vasa ship: verification of linear viscoelasticity and identification of stress thresholds. *European Journal of Wood and Wood Products* 78(6):1095–1103
- Blaber J, Adair B, Antoniou A (2015) Ncorr: open-source 2d digital image correlation matlab software. *Experimental Mechanics* 55(6):1105–1122
- Bohannon B (1966) Effect of size on bending strength of wood members, vol 56. Forest Product Lab./USDA Forest Service

- Chu T, Ranson W, Sutton MA (1985) Applications of digital-image-correlation techniques to experimental mechanics. *Experimental mechanics* 25(3):232–244
- dell'Isola F, Sciarra G, Vidoli S (2009) Generalized Hooke's law for isotropic second gradient materials. *Proceedings of the Royal Society A: Mathematical, Physical and Engineering Sciences* 465(2107):2177–2196
- dell'Isola F, Seppecher P, Corte AD (2015) The postulations á la D'Alembert and á la Cauchy for higher gradient continuum theories are equivalent: a review of existing results. *Proceedings of the Royal Society A: Mathematical, Physical and Engineering Sciences* 471(2183):20150,415
- Giorgio I, Andreus U, dell'Isola F, Lekszycki T (2017) Viscous second gradient porous materials for bones reconstructed with bio-resorbable grafts. *Extreme Mechanics Letters* 13:141–147
- Giorgio I, Spagnuolo M, Andreus U, Scerrato D, Bersani AM (2021) In-depth gaze at the astonishing mechanical behavior of bone: A review for designing bio-inspired hierarchical metamaterials. *Mathematics and Mechanics of Solids* 26(7):1074–1103
- Green DW, Winandy JE, Kretschmann DE (1999) Mechanical properties of wood. *Wood handbook: wood as an engineering material* Madison, WI: USDA Forest Service, Forest Products Laboratory, 1999 General technical report FPL; GTR-113: Pages 41–445 113
- Jernkvist L, Thuvander F (2001) Experimental determination of stiffness variation across growth rings in *picea abies*. *Holzforschung* 55:309–317
- Madsen B, Tomoi M (1991) Size effects occurring in defect-free spruce–pine–fir bending specimens. *Canadian journal of civil engineering* 18(4):637–643
- Pedersen MU, Clorius CO, Damkilde L, Hoffmeyer P (2003) A simple size effect model for tension perpendicular to the grain. *Wood Science and Technology* 37(2):125–140
- Peters W, Ranson W (1982) Digital imaging techniques in experimental stress analysis. *Optical engineering* 21(3):213,427
- Schlottzhauer P, Nelis P, Bollmus S, Gellerich A, Militz H, Seim W (2017) Effect of size and geometry on strength values and moe of selected hardwood species. *Wood Material Science & Engineering* 12(3):149–157
- Showalter K (1987) Effect of length on tensile strength in structural lumber, vol 482. US Department of Agriculture, Forest Service, Forest Products Laboratory
- Sutton MA, Ortu JJ, Schreier H (2009) Image correlation for shape, motion and deformation measurements: basic concepts, theory and applications. Springer Science & Business Media
- Válek J, Veiga R (2005) Characterisation of mechanical properties of historic mortars—testing of irregular samples. *WIT Transactions on The Built Environment* 83
- Vazic B, Abali BE, Yang H, Newell P (2021) Mechanical analysis of heterogeneous materials with higher-order parameters. *Engineering with Computers* pp 1–17
- Vendroux G, Knauss W (1998) Submicron deformation field measurements: Part 2. improved digital image correlation. *Experimental Mechanics* 38(2):86–92
- Vorobyev A, Arnould O, Laux D, Longo R, van Dijk NP, Gamstedt EK (2016) Characterisation of cubic oak specimens from the vasa ship and recent wood by means of quasi-static loading and resonance ultrasound spectroscopy (rus). *Holzforschung* 70(5):457–465
- Weibull W (1939) A statistical theory of the strength of material. *Proc Roy Swedish Inst Eng Res* 151(1):1–45



Chapter 31

Covering a Surface with Pre-Stressed Ribbons: From Theory to Nano-Structures Fabrication

Alexandre Danescu, Philippe Regreny, Pierre Cremillieu,
Jean-Louis Leclercq, Ioan R. Ionescu

Abstract The paper deals with the fabrication of nano-shells from pre-stressed nano-plates release. Due to geometrical and technological restrictions we have to cover a given surface with three-dimensional thin ribbons. We discuss the key role of the geodesic curvature in the design of such shell-ribbons. We show that including small-strains but large rotations we are able to control the metric tensor of both un-deformed (or planar) and deformed (or shell) ribbons by an appropriate choice of the width and thickness of the ribbons. Moreover, the strain tensor is controlled by the difference between the curvature of the planar (un-deformed) ribbon and the geodesic curvature of the supporting curve of the shell (deformed) ribbon. Under suitable constitutive assumptions, we deduce the field equations, the boundary conditions and the design equations. The former relate the pre-stress in the planar layer to the final geometry of the desired shell-ribbon. A fine tuning of the composition, geometry and of the pre-stress of the plate-ribbon is necessary to design and fabricate the shell-ribbon. We design and fabricate a partial cover of the sphere with constant latitude ribbons starting from planar multi-layer semiconductor materials grown by molecular beam epitaxy. The details of fabrication method and its limitations are discussed in detail.

Keywords: Nonlinear elasticity · Pre-stressed structures · Shell-design · Nano-structures · Fabrication · Epitaxial thin films

A. Danescu, Ph. Regreny, P. Cremillieu and Jean-Louis Leclercq
Univ Lyon, Ecole Centrale de Lyon, CNRS, INSA Lyon, University Claude Bernard Lyon 1, CPE
Lyon, CNRS, INL, UMR5270, 69130 Ecully, France
e-mail: alexandre.danescu@ec-lyon.fr, philippe.regreny@ec-lyon.fr, pierre.cremillieu@ec-lyon.fr,
jean-louis.leclercq@ec-lyon.fr

Ioan R. Ionescu
LSPM, University Sorbonne-Paris-Nord, 93430 Villetaneuse, France and IMAR, Romanian
Academy, Bucharest, Romania
e-mail: ioan.r.ionescu@gmail.com

31.1 Introduction

Nowadays the fabrication processes in semiconductor industry use essentially the planar technology and among the various methods of crystal growth, the molecular beam epitaxy (MBE) presents the significant advantage of highly accurate control of composition (up to 1%) and thickness (up to monolayer). Composition control endow multi-layered planar structures with pre-stress which may be beneficial for the design on 3D objects by pre-stress relaxation. The prototype of this phenomena is the bi-layer material where the presence of the pre-stress in one of the layers induced the bending of the free bi-layer structure. Initiated in Prinz et al (2000) (see also Prinz et al, 2001; Prinz, 2003; Seleznev et al, 2003; Prinz and Golod, 2006; Prinz et al, 2017) for simple rolls, curls and developable ribbons the method was extended to cover more complex situations in Danescu et al (2013, 2018). Introduced by an heuristic method in Danescu et al (2013) and later reconsidered in the framework of small-strains and large-rotations in Danescu and Ionescu (2021), the geodesic curvature represents the key concept for the design of 3D structures from planar pre-stresses films. From a different point of view, the equilibrium shape of a pre-stressed material was investigated by using dimension reduction in Le Dret and Raoult (1995); Friesecke et al (2002a,b, 2006); de Benito Delgado and Schmidt (2020); Wang et al (2019); de Benito Delgado, Miguel and Schmidt, Bernd (2021) leading to a hierarchy of non-linear elastic models (Lewicka and Raoult, 2018).

These previous results concerning relaxation of pre-stressed bi-layer materials focus on straight ribbons that relax toward rolls and curls, all based on isometric transformations. However, it is well-known that the class of isometries between planar and three-dimensional surfaces, extensively studied in Fosdick and Fried (2016), is too narrow to cover simple non-developable surfaces occurring in pre-stressed relaxation design problems. To circumvent this theoretical drawback, in a recent paper (Danescu and Ionescu, 2020), we developed a shell design model built on a non-isometric perturbation assumption of Love-Kirchhoff type superposed on a plate-to-shell theory. Extending shell models in Steigmann (2013); Ciarlet and Mardare (2018); Steigmann (2007b,a); Steigmann and Ogden (2014), the geometric description involves a single small parameter $\delta \ll 1$, the product between shell's thickness and its curvature.

The main difficulty in applying the shell-design model in Danescu and Ionescu (2020) is of a geometric nature. Indeed, for several common mid-surfaces the small-strain assumption drastically reduces the surface width. However, since we are focusing on brittle-elastic materials (such as semiconductors), the small deformations assumption is merely a technological restriction and not a mathematical simplification. To encompass this limitation, in Danescu and Ionescu (2021) another type of shell, (called a strip-shell) is constructed, for which this assumption can be fulfilled by an appropriate choice of an additional geometric parameter, namely the strip width. In this restricted framework, if the product between the strip-shell width and its curvature is of order $\delta^{1/2}$ the assumptions of plate-to-shell theory (Danescu and Ionescu, 2020) are fulfilled so that, for any strip of a given shell we provide a simple model able to design the corresponding plate-strip (i.e., to compute the shape

and pre-stress momentum of the plate). The next step analyzed here is to cover the given surface (shell) with one or several strips, situation in which we can provide an explicit design of the corresponding planar (plate) strips.

The paper is organized as follows: the first two sections recall the geometric and mechanical assumptions of the plate to shell model for design proposed in Danescu and Ionescu (2020). We relate the geometric aspects to the pre-stress via constitutive relations and field equations in finite strains through the assumption of weak-transversal heterogeneity, fulfilled here by the weak variation of the composition in our crystal growth process. The third section discuss the main geometric aspects of the theory (see Danescu and Ionescu (2021) for more details), with a particular accent on the metric tensors for planar ribbons along curves and three dimensional ribbons as subsets of arbitrary surfaces in \mathbb{R}^3 . The main result shows that the distance between the curvature of the planar curve (the planar design) and the geodesic curvature of the three dimensional supporting curve of the ribbon controls the Green-Lagrange strain tensor, so that the small-strain (but large rotations) assumptions can be fulfilled by an appropriate choice of the planar geometry. The fourth section describes a specific application: fabrication of a partial cover of the sphere from a planar pre-stressed bi-layer material by using a design based on the geodesic curvature of constant-latitude circles.

31.2 Geometric and Kinematical Settings

Let us consider a plate with mid-surface $R_0 \subset \mathcal{R}^2$ and thickness $H = H(\bar{X})$ in the Lagrangian configuration (here $\bar{X} = (X_1, X_2)$) and let $S_0 \subset \mathcal{R}^3$ be the mid-surface of an Eulerian shell of thickness h , with e_3 the unit normal and \mathcal{K} the curvature tensor acting from the tangent plane into itself.

In what follows, $\delta \ll 1$ will be a small parameter characterizing the Eulerian and Lagrangian shell thickness and such that

$$h|\mathcal{K}| = \mathcal{O}(\delta), \quad H/L_c = \mathcal{O}(\delta), \quad |\nabla_2 H| = \mathcal{O}(\delta), \quad (31.1)$$

where L_c is the characteristic length of the surface and ∇_2 is the gradient with respect to $\bar{X} \in R_0$.

The main geometric assumption in Danescu and Ionescu (2020) is that there exists a transformation $\mathbf{x} : R_0 \rightarrow S_0$ of the Lagrangian mid-surface R_0 into the designed Eulerian one S_0 such that the associated deformation of the geometric transformation is small, i.e.,

$$|\mathbf{E}_2| = \frac{1}{2} |\nabla_2^T \mathbf{x} \nabla_2 \mathbf{x} - \mathbf{I}_2| = \mathcal{O}(\delta). \quad (31.2)$$

Here $\mathbf{I}_2 = \mathbf{c}_1 \otimes \mathbf{c}_1 + \mathbf{c}_2 \otimes \mathbf{c}_2$ is the identity tensor on \mathcal{R}^2 and $\{\mathbf{c}_1, \mathbf{c}_2, \mathbf{c}_3\}$ is the Cartesian basis in the Lagrangian description and hereafter we denote by $\mathbf{K} = \nabla_2^T \mathcal{K} \nabla_2 \mathbf{x}$ the Lagrangian curvature tensor acting from \mathcal{R}^2 into itself.

The kinematics of the plate deformation considered in Danescu and Ionescu (2020) involves the classical Love–Kirchhoff assumption, i.e.: *the normal to the plate mid-plane remains normal to the designed mid-surface* but in a finite deformation context and thus including large rotations. In addition, the transversal deformation is affine with respect to the plate thickness. Superposed to the kinematics associated to the exact design which reproduces the target mid-surface, we consider a small perturbation of Love-Kirchhoff type in order to compensate the small (membrane) deformation of the proposed geometric transformation. As a consequence, the mid-surface of this overall kinematics will be close to the designed mid-surface, and for this reason we called it *approximate design kinematics*.

31.3 Weak Transversal Homogeneity and the Moment Equations

Although, the general theory developed in Danescu and Ionescu (2020) can cover the general anisotropic framework, here we restrict to cubic materials since our designed experiment involve multilayered cubic III-V semiconductor alloy $\text{In}_{1-\alpha}\text{Ga}_\alpha\text{P}$ for α small. In order to account for small-strains but large rotations including inhomogeneous pre-stress we consider a linear constitutive relation between the second Piola–Kirchhoff stress \mathbf{S} tensor and the Green strain-tensor $\mathbf{E} = \frac{1}{2}(\mathbf{F}^T \mathbf{F} - \mathbf{I})$ in the form

$$\mathbf{S} = \mathbb{C}(X_3)[\mathbf{E}] + \mathbf{S}^*(X_3) + \Sigma \mathcal{O}(\delta^2), \quad (31.3)$$

where Σ is a characteristic stress and both the material parameters $\mathbb{C} = (C_{ij})$ (Voigt notation) and the pre-stress \mathbf{S}^* depends on the normal coordinate in the reference configuration. Moreover, following Danescu and Ionescu (2021) we assume that the elasticities \mathbb{C} obey the *weak transversal heterogeneity* condition, i.e.,

$$\langle C_{ij} \rangle_2 = \Sigma \mathcal{O}(\delta), \quad \langle C_{ij} \rangle_3 = \frac{1}{12} \langle C_{ij} \rangle_1 + \Sigma \mathcal{O}(\delta), \quad (31.4)$$

where the successive averages (moments) of a X_3 -dependent function $\langle f \rangle_n$ ($n = 1, 2, 3$) are defined through

$$\langle f \rangle_n = \frac{1}{H^n} \int_{-H/2}^{H/2} X_3^{n-1} f(X_3) dX_3. \quad (31.5)$$

Taking into account that during the MBE growth the upper surface of the multi-layer structure is stress-free, we assume that the pre-stress acting surfaces parallel to the mid-surface vanishes, so that $\mathbf{S}^* \mathbf{e}_3 = \mathbf{0}$. Then, following Danescu and Ionescu (2020), the moments equations are

$$\text{div} \left(\frac{H}{12} \mathbb{M}[\mathbf{K}] + \langle \mathbf{S}_2^* \rangle_2 \right) = \mathbf{0} \text{ in } R_0, \quad \left(\frac{H}{12} \mathbb{M}[\mathbf{K}] + \langle \mathbf{S}_2^* \rangle_2 \right) \nu_{ext} = \mathbf{0} \text{ on } \partial R_0, \quad (31.6)$$

$$\left(\frac{H}{12}\mathbb{M}[\mathbf{K}] + \langle \mathbf{S}_2^* \rangle_2\right) : \mathbf{K} = \mathbf{0} \quad \text{in } R_0, \tag{31.7}$$

where \mathbf{S}_2^* is the in-plane pre-stress and $\mathbb{M} = \{M_{ij}\}$ is related to the in-plane reduced elasticity, i.e.,

$$\mathbb{M}[\mathbf{A}] = \langle \mathbb{D}_2 \rangle_1[\mathbf{A}] - \frac{\langle C_{12} \rangle_1^2}{\langle C_{11} \rangle_1} (\mathbf{I} : \mathbf{A}) \mathbf{I} \tag{31.8}$$

and \mathbb{D}_2 is the in-plane part of the Voigt tensor.

Obviously, equations (31.6)-(31.7) are satisfied if the pre-stress \mathbf{S}^* is such that

$$\langle \mathbf{S}_2^* \rangle_2 = -\frac{H}{12}\mathbb{M}[\mathbf{K}]. \tag{31.9}$$

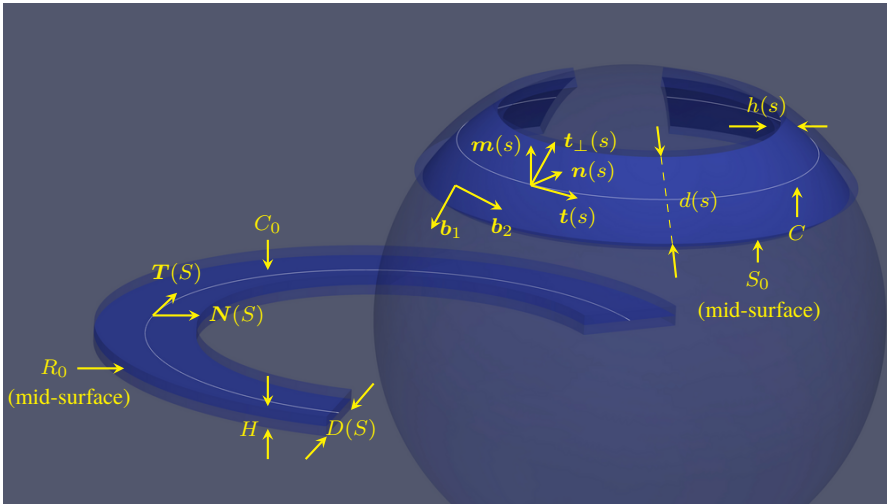


Fig. 31.1 Geometric elements of the planar ribbon: thickness $H(S)$, width $D(S)$, the tangent and normal vectors $\mathbf{T}(S)$ and $\mathbf{N}(S)$ along the curve C_0 located in the mid-surface R_0 and the geometric elements for the shell-ribbon with mid-surface S_0 along the curve C : $\{\mathbf{t}(s), \mathbf{n}(s), \mathbf{m}(s)\}$ Frenet frame along C , the vector \mathbf{t}_\perp (located in the tangent plane to S_0), thickness $h(s)$ and width $d(s)$.

31.4 Small Strain Deformation of a Ribbon

If $S \in [0, L]$ and $\kappa_0(S)$ are the arc-length and the curvature of a planar curve C_0 located at $\mathbf{R}(S) \in \mathbb{R}^2$ with tangent $\mathbf{T}(S)$ and normal $\mathbf{N}(S)$, we define (see Fig. 31.1) the planar ribbon $R_0 \subset \mathbb{R}^2$ along C_0 of width $D = D(S)$ as

$$R_0 = \{\mathbf{R}(S) + Q\mathbf{N}(S); S \in (0, L), Q \in (-D(S), D(S))\}. \tag{31.10}$$

Let S_0 denotes the mid-surface of a shell, given by its parametric description $\mathbf{u} \rightarrow \mathbf{r}_{S_0}(\mathbf{u}) \in \mathbb{R}^3$, where $\mathbf{u} = (u_1, u_2)$ are coordinates in some subset $\Omega \subset \mathbb{R}^2$. If $\delta \ll 1$ is a small parameter, our goal is to provide conditions for the existence of a map $\mathbf{x} : R_0 \rightarrow S_0$ with small strain, i.e. (31.2) holds uniformly with respect to $\mathbf{X} \in R_0$.

Let us compute the (Lagrangian) metric tensor of the planar ribbon defined in (31.10). The local basis, associated to the coordinates (S, Q) , is $\mathbf{b}_S = \mathbf{T} - Q\kappa_0\mathbf{N}$ and $\mathbf{b}_Q = \mathbf{N}$ and thus the Lamé coefficients and metric tensor are

$$L_S^2 = g_{SS} = 1 - 2Q\kappa_0 + Q^2\kappa_0^2, \quad g_{SQ} = 0, \quad L_Q^2 = g_{QQ} = 1. \tag{31.11}$$

In order to chose among the multiple ways that map a ribbon on a surface, we study the particular case in which the ribbon cover the shell mid-surface along a given curve $C \subset S_0$ (see Fig. 31.1). As a curve in \mathbb{R}^3 , C posses its intrinsic geometric features: arc-length s , Frenet frame $(\mathbf{t}(s), \mathbf{n}(s), \mathbf{m}(s))$, curvature $\kappa(s)$ and torsion $\tau(s)$ and, obviously, the tangent plane to the shell mid-surface S_0 contains the tangent vector $\mathbf{t}(s)$ to C .

Let $\mathbf{u}^0(s) = (u_1^0(s), u_2^0(s))$ be the arc-length parametrization of the curve $C \subset S_0$. Then, $\mathbf{t} = \frac{\partial \mathbf{r}}{\partial u_i^0} \frac{du_i^0}{ds} = \mathbf{b}_i \frac{du_i^0}{ds}$ is the description of the tangent vector to C in the covariant basis $\{\mathbf{b}_1, \mathbf{b}_2\}$ on S_0 . The main idea is to map the q coordinates in a neighborhood of the curve $C \subset S_0$ in the direction $\mathbf{t}_\perp(s)$, which is orthogonal to its tangent vector of the curve and belongs to the tangent plane of the surface , i.e. $\mathbf{t}_\perp(s) = \mathbf{e}_3(\mathbf{u}^0(s)) \wedge \mathbf{t}(s)$. More precisely, if we put

$$u_i(s, q) = u_i^0(s) + qv_i(s, q), \quad v_i^0(s) = v_i(s, 0), \quad i = 1, 2, \tag{31.12}$$

then the ribbon surface is given by

$$S_0 = \{\mathbf{r}_{S_0}(\mathbf{u}(s, q)); s \in (0, l), q \in (-d(s), d(s))\}, \tag{31.13}$$

where d is the ribbon width, and from $\mathbf{t}_\perp(s) = \frac{\partial \mathbf{r}}{\partial q}(s, 0) = \frac{\partial \mathbf{r}}{\partial u_i} \frac{\partial u_i}{\partial q}(s, 0) = \mathbf{b}_i v_i^0(s)$ we get

$$v_i^0(s) = \mathbf{t}_\perp(s) \cdot \mathbf{b}^i(\mathbf{u}^0(s)). \tag{31.14}$$

If the order of magnitude for the ribbons widths with respect to the curvatures of the curves C_0 and C as well as to the curvature tensor of the surface S_0 , are such that

$$D(S)\kappa_0(S) = \mathcal{O}(\delta^{1/2}), \quad d(s)|\mathcal{K}(\mathbf{u}^0(s))|, \quad d(s)\kappa(s)(\mathbf{t}_\perp \cdot \mathbf{m}) = \mathcal{O}(\delta^{1/2}), \tag{31.15}$$

then an estimation of the Lagrangian and Eulerian metric tensors at order $\mathcal{O}(\delta)$ was obtained in Danescu and Ionescu (2021). To see that, let us compute the (Eulerian) metric tensor of the surface S_0 up to first-order with respect to q . We have successively

$$\begin{aligned}
g_{qq}(s, q) &= g_{ij}(s, q) \frac{\partial u_i}{\partial q} \frac{\partial u_j}{\partial q} = \left(g_{ij}(s, 0) + q \frac{\partial g_{ij}}{\partial q}(s, 0) \right) \frac{\partial u_i}{\partial q} \frac{\partial u_j}{\partial q} + \mathcal{O}(\delta) = \\
&g_{ij}(s, 0) v_i^0 v_j^0 + q \left(4g_{ij}(s, 0) v_i^0 \frac{\partial v_j}{\partial q}(s, 0) + \frac{\partial g_{ij}}{\partial u_k}(s, 0) v_i^0 v_j^0 v_k^0 \right) + \mathcal{O}(\delta) \\
&= |\mathbf{t}_\perp(s)|^2 + q v_i^0(s) \left(4g_{ij}(s, 0) \frac{\partial v_j}{\partial q}(s, 0) + \frac{\partial g_{ij}}{\partial u_k}(s, 0) v_j^0(s) v_k^0(s) \right) + \mathcal{O}(\delta),
\end{aligned}$$

and by choosing

$$\frac{\partial v_l}{\partial q}(s, 0) = -\frac{1}{4} g^{li}(s, 0) \frac{\partial g_{ij}}{\partial u_k}(s, 0) v_j^0(s) v_k^0(s), \quad (31.16)$$

we obtain $g_{qq} = 1 + \mathcal{O}(\delta)$. Moreover,

$$\begin{aligned}
g_{sq} &= g_{ij} \frac{\partial u_i}{\partial s} \frac{\partial u_j}{\partial q} = \left(g_{ij}(s, 0) + q \frac{\partial g_{ij}}{\partial q}(s, 0) \right) \frac{\partial u_i}{\partial s} \frac{\partial u_j}{\partial q} + \mathcal{O}(\delta) = \\
&= g_{ij}(s, 0) \frac{du_i^0}{ds} v_j^0 + q \left(g_{ij}(s, 0) \frac{dv_i^0}{ds} v_j^0 + 2g_{ij}(s, 0) \frac{du_i^0}{ds} \frac{\partial v_j}{\partial q}(s, 0) + \right. \\
&\quad \left. + \frac{\partial g_{ij}}{\partial u_k}(s, 0) v_k^0 \frac{du_i^0}{ds} v_j^0 \right) + \mathcal{O}(\delta)
\end{aligned}$$

and, since $g_{ij}(s, 0) \frac{du_i^0}{ds} v_j^0 = \mathbf{t} \cdot \mathbf{t}_\perp = 0$, using (31.16) we obtain

$$\begin{aligned}
g_{sq} &= \frac{q}{2} \left(2g_{ij}(s, 0) \frac{dv_i^0}{ds} v_j^0 + \frac{\partial g_{ij}}{\partial u_k}(s, 0) \frac{du_i^0}{ds} v_k^0 v_j^0 \right) + \mathcal{O}(\delta) = \\
&= \frac{q}{2} \frac{d}{ds} (\mathbf{t}_\perp \cdot \mathbf{t}_\perp) + \mathcal{O}(\delta).
\end{aligned}$$

Finally,

$$\begin{aligned}
g_{ss}(s, q) &= \left(g_{ij}(s, 0) + q \frac{\partial g_{ij}}{\partial u_k} \frac{\partial u_k}{\partial q} \right) \frac{\partial u_i}{\partial s} \frac{\partial u_j}{\partial s} + \mathcal{O}(\delta) = g_{ij}(s, 0) \frac{du_i^0}{ds} \frac{du_j^0}{ds} + \\
&+ q \left(2g_{ij}(s, 0) \frac{du_i^0}{ds} \frac{dv_j^0}{ds} + \frac{\partial g_{ij}}{\partial u_k}(s, 0) v_k^0 \frac{du_i^0}{ds} \frac{du_j^0}{ds} \right) + \mathcal{O}(\delta) = \\
&= |\mathbf{t}(s)|^2 + 2q \left(\frac{d\mathbf{t}_\perp}{ds} \cdot \mathbf{t} \right) + \mathcal{O}(\delta) = 1 + 2q \left(\frac{d\mathbf{t}_\perp}{ds} \cdot \mathbf{t} \right) + \mathcal{O}(\delta).
\end{aligned}$$

But, since $\mathbf{t}_\perp \cdot \mathbf{t} = 0$ we have $\mathbf{t}_\perp = (\mathbf{t}_\perp \cdot \mathbf{n})\mathbf{n} + (\mathbf{t}_\perp \cdot \mathbf{m})\mathbf{m}$ so that, using the Frenet formulae, we obtain

$$\frac{d\mathbf{t}_\perp}{ds} \cdot \mathbf{t} = -\frac{d\mathbf{t}}{ds} \cdot \mathbf{t}_\perp = -\kappa(\mathbf{t}_\perp \cdot \mathbf{m}). \quad (31.17)$$

This last result emphasize the role played by the *geodesic curvature* $\kappa^{geo} = \kappa(\mathbf{t}_\perp \cdot \mathbf{m})$, which is the projection of the curvature of C into the tangent plane of the manifold

S_0 , in the estimation of the metric tensor. To summarize, we obtained

$$g_{ss} = 1 - 2q\kappa(s)\mathbf{t}_\perp \cdot \mathbf{m} + \mathcal{O}(\delta), \quad g_{sq} = \mathcal{O}(\delta), \quad g_{qq} = 1 + \mathcal{O}(\delta), \quad (31.18)$$

$$g_{SS} = 1 - 2Q\kappa^0(S) + \mathcal{O}(\delta), \quad g_{SQ} = 0, \quad g_{QQ} = 1 + \mathcal{O}(\delta). \quad (31.19)$$

By using $(s, q) = (S, Q) \in (0, L) \times (-D, D)$, we are now able to estimate the Green-Lagrange strain tensor of the map $\mathbf{x} : R_0 \rightarrow S_0$. Since the gradient tensor \mathbf{F} can be written as $\mathbf{F} = \mathbf{b}_s \otimes \mathbf{b}^S + \mathbf{b}_q \otimes \mathbf{b}^Q$, taking into account (31.19) and (31.18), we obtain

$$\mathbf{F}^T \mathbf{F} = L_s^2 \mathbf{b}_S \otimes \mathbf{b}_S + \mathbf{b}_Q \otimes \mathbf{b}_Q + \mathcal{O}(\delta) = \mathbf{I} - (1 - g_{ss}/g_{SS})\mathbf{e}_S \otimes \mathbf{e}_S + \mathcal{O}(\delta)$$

and thus

$$\begin{aligned} \mathbf{E}_2 &= \frac{1}{2} \left(\frac{g_{ss}}{g_{SS}} - 1 \right) \mathbf{e}_S \otimes \mathbf{e}_S + \mathcal{O}(\delta) = \\ &= Q[\kappa_0(S) - \kappa(S)(\mathbf{t}_\perp \cdot \mathbf{m})] \mathbf{e}_S \otimes \mathbf{e}_S + \mathcal{O}(\delta). \end{aligned} \quad (31.20)$$

We conclude that by choosing the curvature of the planar curve C_0 equal to the geodesic curvature of the supporting curve of the shell-ribbon $C \subset S_0$ the Green-Lagrange tensor is small, i.e.

$$\text{if } \kappa_0 = \kappa^{geo} = \kappa \mathbf{t}_\perp \cdot \mathbf{m}, \quad \text{then } \mathbf{E} = \mathcal{O}(\delta). \quad (31.21)$$

31.5 From Theory to Fabrication of a Nano-Sphere

Let (r, θ, ϕ) be the spherical coordinates in \mathbb{R}^3 and denote by $\mathbf{e}_r = \mathbf{e}_r(\theta, \phi)$, $\mathbf{e}_\theta = \mathbf{e}_\theta(\theta, \phi)$, $\mathbf{e}_\phi = \mathbf{e}_\phi(\phi)$ the local physical basis. Let S_0 denote the surface of the sphere of radius R_* with Lamé coefficients $L_\theta = R_*$, $L_\phi = R_* \sin(\theta)$ and the unit normal $\mathbf{e}_3(\theta, \phi) = \mathbf{e}_r(\theta, \phi)$. Then, the curvature tensor on S_0 is

$$\mathcal{K} = -\frac{1}{R_*} (\mathbf{e}_\theta \otimes \mathbf{e}_\theta + \mathbf{e}_\phi \otimes \mathbf{e}_\phi).$$

Let $C \subset S_0$ be a given curve with arc-length s , parametric description $s \rightarrow (\theta^0(s), \phi^0(s))$ and geodesic curvature $\kappa^{geo}(s)$. If C_0 is the planar curve with curvature $\kappa_0(s) = \kappa^{geo}(s)$ and R_0 is the planar ribbon along C_0 (see definition (31.10)) with the width $d(s)$ such that (31.15) holds then, from the small-strain membrane condition (31.2) we get

$$\mathbf{K} = \frac{1}{R_*} (\mathbf{I}_2 + \mathcal{O}(\delta)).$$

From the plate-to shell model we find that a shell-ribbon S_0 of a spherical shell of radius R_* along the curve C , could be designed from a planar ribbon R_0 along a curve C_0 if (31.21) holds. The pre-stress momentum have to be designed such that

$\langle \mathbf{S}_2^* \rangle_2 = -\frac{H^3}{12R_*} \mathbb{M}[\mathbf{I}_2]$ and can be obtained with an isotropic and homogeneous pre-stress, i.e., $\mathbf{S}_2^* = \sigma^* \mathbf{I}_2$, where

$$\langle \sigma^* \rangle_2 = \frac{H}{12R_*} \frac{\langle C_{11}^2 \rangle_1 + \langle C_{12} \rangle_1 \langle C_{11} \rangle_1 - 2\langle C_{12} \rangle_1^2}{\langle C_{11} \rangle_1}. \tag{31.22}$$

31.5.1 Optimal Covering with Constant Parallel Ribbons

For constant latitude curves, i.e., $\theta(s) = \theta^0$, we have $\phi^0 = s/(R_* \sin(\theta_0))$ so that $d/R_* = \mathcal{O}(\delta^{1/2})$, $d \cot(\theta^0)/R_* = \mathcal{O}(\delta^{1/2})$ and the geodesic curvature is $\kappa_0 = \kappa^{geo} = \cot(\theta^0)/R_*$. This means that the width of successive ribbons will decrease with the latitude. As a straightforward consequence, the fit of successive positions and widths of constant latitude ribbons for a complete cover of the sphere is a nontrivial problem. We recall here a result from Danescu and Ionescu (2021) concerning a semi-analytical optimal covering of the sphere.

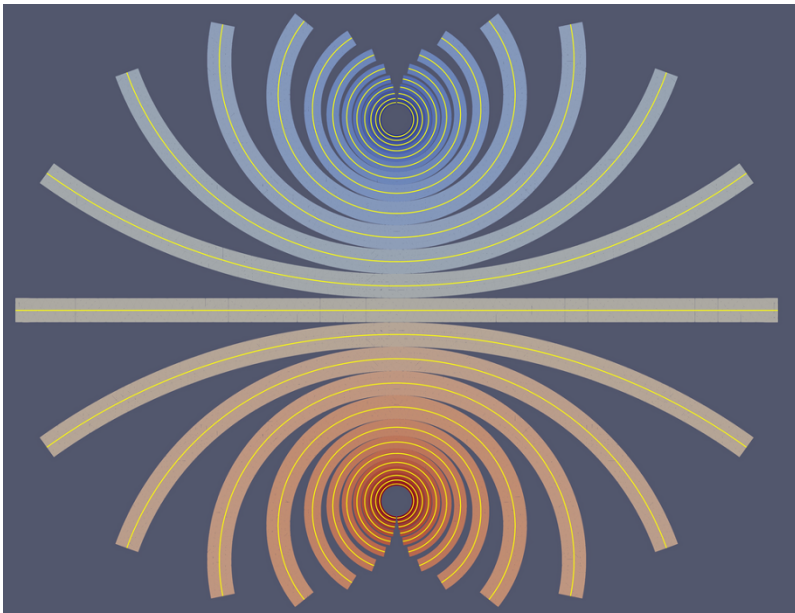


Fig. 31.2 An optimal covering of the sphere with constant latitude ribbons obtained by implementing the solutions of recursive system (31.24) for $\delta = 10^{-2}$.

If θ_k denote the latitudes of the supporting curve for successive ribbons then, for the k^{th} ribbon, the arc-length is such that $s \in (-\pi R_* \cos \theta_k, \pi R_* \cos \theta_k)$ and the angular variable $\theta(q) = \pi/2 - \theta_k - q/R_*$ for $q \in (-d_k, d_k)$. A symmetric solution

can be obtained as follows: take $\theta_0 = 0$, $\theta_k = -\theta_k$ and notice that the covering condition and (31.15) can be expressed as

$$d_k \leq \delta^{1/2} R_* \min(1, \cot \theta_k), \quad R_*(\theta_{k+1} - \theta_k) = d_k + d_{k+1}. \quad (31.23)$$

It follows that for $\theta < \pi/4$ we can consider constant width ribbons with $\theta_k = 2k\delta^{1/2}$ and thus $d_k = \delta^{1/2} R_*$ for $|k| \leq \lfloor \frac{\pi}{8\sqrt{\delta}} - \frac{1}{2} \rfloor$ (here $\lfloor x \rfloor$ is the entire part of x) while for $k > \lfloor \frac{\pi}{8\sqrt{\delta}} - \frac{1}{2} \rfloor$ we have to solve recursively the nonlinear equation

$$x - \delta^{1/2} \cot x = \theta_k + \frac{d_k}{R_*}, \quad (31.24)$$

whose solution θ_{k+1} provide

$$d_{k+1} = R_*(\theta_{k+1} - \theta_k). \quad (31.25)$$

An implementation of this procedure for $\delta = 10^{-2}$ provide the design illustrated in Fig. 31.2.

31.5.2 Elastic Layers with Pre-Stress: Material Parameters

The experimental implementation of the sphere covering with variable width ribbons, presented in the previous subsection, is difficult due to very sharp angles between successive ribbons near the vertical symmetry axis, and thus incompatible with the spatial resolution of the photo-lithography processes. However, in order to illustrate the role of the geodesic curvature in the design problem we focus here on the partial cover of the sphere with constant latitude ribbons.

Since the planar design is dependent on the target surface curvature we start by the epitaxial growth of the bi-layer semiconductor structure: a 60 nm thick $\text{In}_{0.88}\text{Ga}_{0.12}\text{P}$ layer (further denoted InGaP) grown on a 145 nm thick InP layer. The bi-layer was grown on an InP substrate previously covered by a 500 nm thick InGaAs sacrificial layer. Using data from the literature, we have

$$\begin{aligned} C_{11}^{\text{InP}} &= 101.1 \text{ GPa}, & C_{11}^{\text{InGaP}} &= 105.8 \text{ GPa}, \\ C_{12}^{\text{InP}} &= 56.1 \text{ GPa}, & C_{12}^{\text{InGaP}} &= 56.8 \text{ GPa}, \\ C_{44}^{\text{InP}} &= 45.6 \text{ GPa}, & C_{44}^{\text{InGaP}} &= 48.5 \text{ GPa}, \end{aligned} \quad (31.26)$$

so that the characteristic stress $\Sigma = 100$ GPa. For $\delta = 10^{-2}$ we verify that indeed

$$\langle C_{ij} \rangle_2 = \Sigma \mathcal{O}(\delta), \quad \langle C_{ij} \rangle_3 - \frac{1}{12} \langle C_{ij} \rangle_1 = \Sigma \mathcal{O}(\delta), \quad (31.27)$$

so that the assumption of weak transversal homogeneity is fulfilled. The lattice parameters for the InP and InGaP layers are respectively

$$a_{\text{InP}} = 5.8687 \text{ \AA}, \quad a_{\text{In}_{0.88}\text{Ga}_{0.12}\text{P}} = 5.8185 \text{ \AA}, \quad (31.28)$$

and correspond to a spherical pre-strain (extension) in the upper layer of $m = \text{diag}(0.86\%, 0.868\%)$. For practical applications, it is the fraction of Ga in the upper layer ($\text{In}_\alpha\text{Ga}_{1-\alpha}\text{As}$) which has to be fixed as a function of the radius of the target sphere, but for simplicity here we use the equation (31.9) in order to compute the radius of the object that can be obtained at $\alpha = 0.12$.

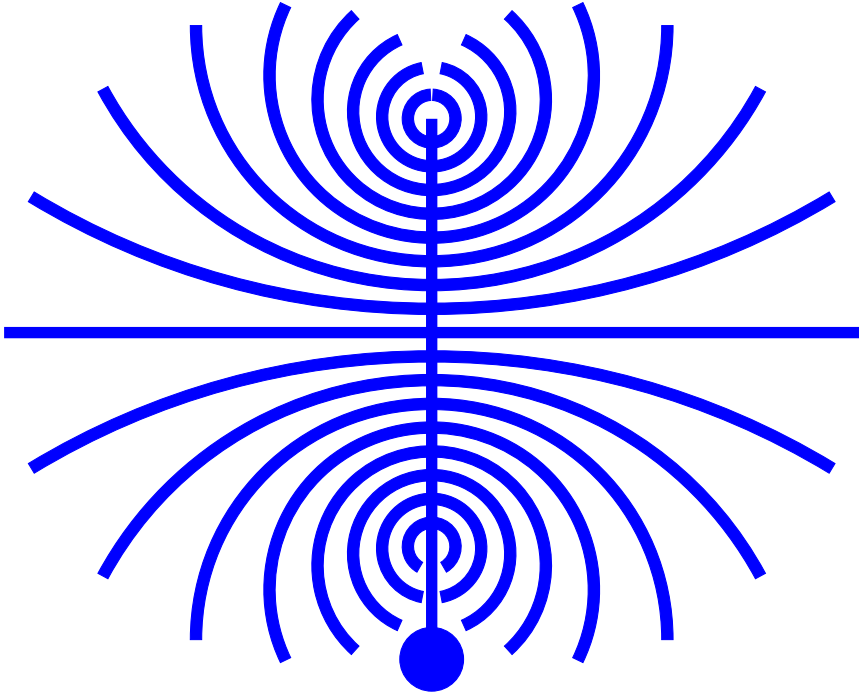


Fig. 31.3 The planar grid designed to cover the sphere. The horizontal straight line will fully cover the equator while the lower and upper parts will cover the North and South hemispheres, respectively. Notice the slight modification of the length for small arcs near the South pole needed in order to keep the relaxed structure attached through the filled round dot (with a characteristic size larger than the lateral dimensions of the curved ribbons) to the substrate during the under-etching process.

31.5.3 Design and Fabrication

In order to cover the sphere of radius R_* with constant latitude ribbons we notice that the radius of the ribbon at latitude θ is $R_* \cos \theta$ and their geodesic curvature,

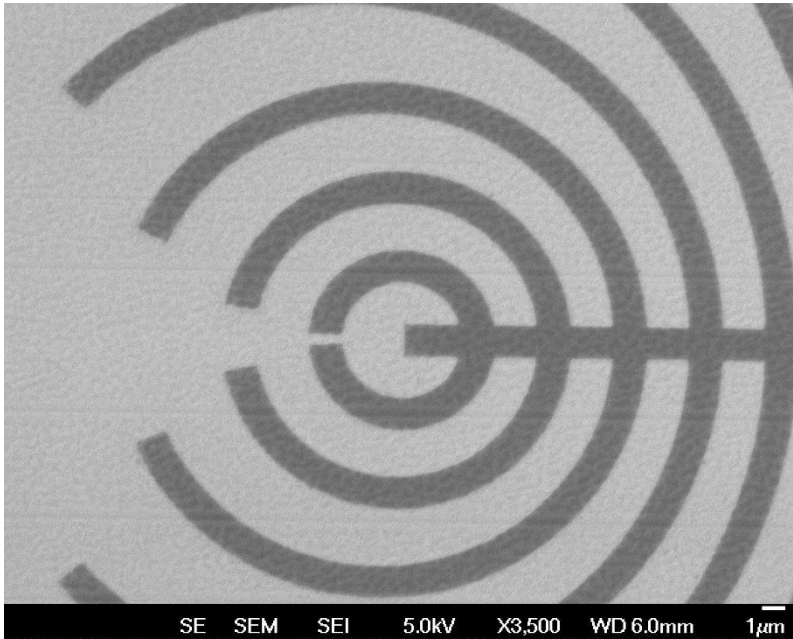


Fig. 31.4 SEM image of the sample after the development process before the reactive ion etching (RIE).

which is exactly the inverse of the planar design radius, is constant and equal to $\kappa(\theta) = \frac{1}{R_*} \tan \theta$. For simplicity, we chose the width of all ribbons equal to $1.5 \mu\text{m}$ (for visual comfort, the actual scale in Fig. 31.3 is not the same as the implemented design in 31.5) and design a geodesic half-circle to ensure connectivity between the constant latitude ribbons. Using the intersection of the two straight lines in figure 31.3 as the origin of the coordinate system in the plane, positions of the 8 pairs of symmetric arcs corresponding to constant latitude arcs located at $\pm \frac{n\pi}{18}$ ($n = 1, \dots, 8$) in the North and South hemi-sphere. Their corresponding centers radii and angular extensions are

$$C_n^\pm = \left(0, \pm R \left(\frac{n\pi}{18} + \frac{1}{\tan \theta} \right)\right), \quad R_n = R / \tan \theta, \quad \theta_n = \pi \sin \left(\frac{n\pi}{18} \right). \quad (31.29)$$

Fabrication of the design illustrated in Fig. 31.3 involves several steps: we start by the deposition of a 90 nm thick SiO_2 hard mask followed by the deposition of a 130 nm thick negative resist film (AR-N7520.07). Next step is electron beam lithography performed by using a modified SEM (FEI Inspect F) and the RAITH Elphy Quantum software. The result after the development of the lithographic process is illustrated in Fig. 31.4. The reactive ion etching (RIE) is then performed in order to transfer the pattern into the silica mask and then into the multilayer structure. The result of this process is represented in Figures 31.5 (both optical microscope and SEM images). At

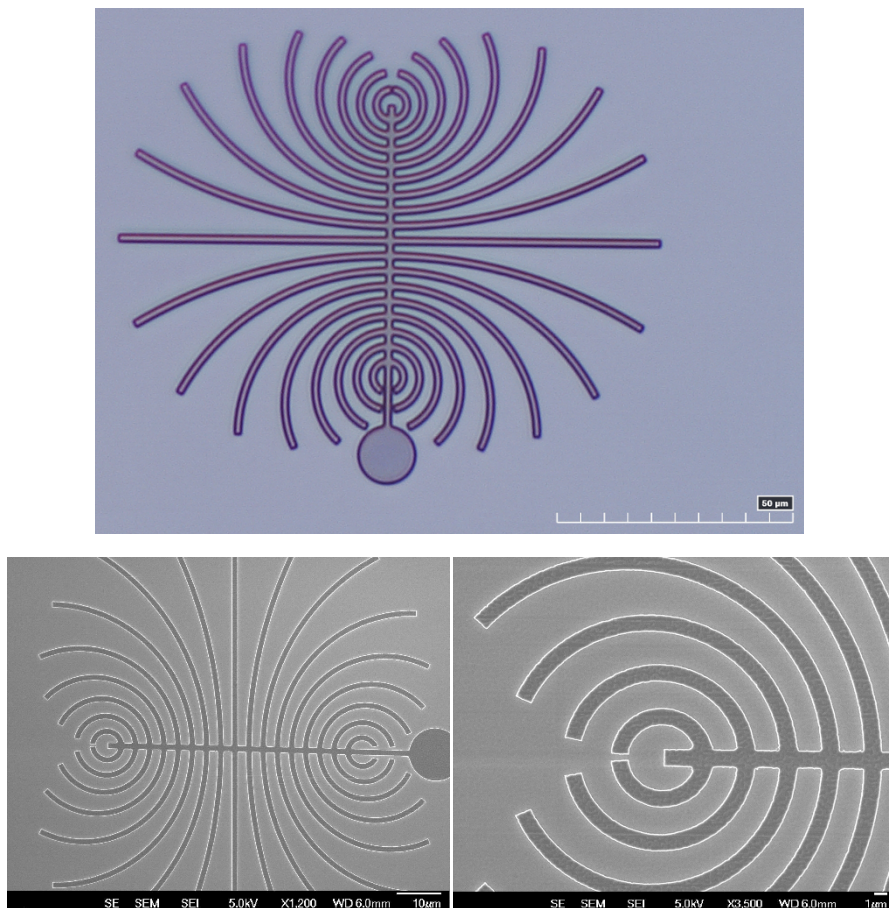


Fig. 31.5 Optical microscope view of the structure obtained after etching the multilayer material, still maintained attached to the substrate by the sacrificial layer.

this step, the structure is still attached on the sacrificial layer but the lateral relaxation of the pre-stress in the bi-layer material takes place. Despite the small width ($1.5 \mu\text{m}$) and the ultra-small thickness (205 nm) the axial pre-stress is still present in the structure and will be released only during the process of under-etching of the sacrificial layer. In order to keep the relaxed structure attached to the substrate the radius of the attachment circle (designed in the lower part of Fig. 31.3) have to be slightly larger than the width of various arcs of the design.

Next, the under-etching is performed using diluted FeCl_3 to selectively remove the InGaAs sacrificial layer so as to release the pre-stress in the multi-layer. Successive H_2O , acetone and methanol rising baths were performed before a CO_2 supercritical drying step, needed in order to circumvent the mechanical actions induced by the surface tension at liquid/solid interfaces. As expected, the fully relaxed structure

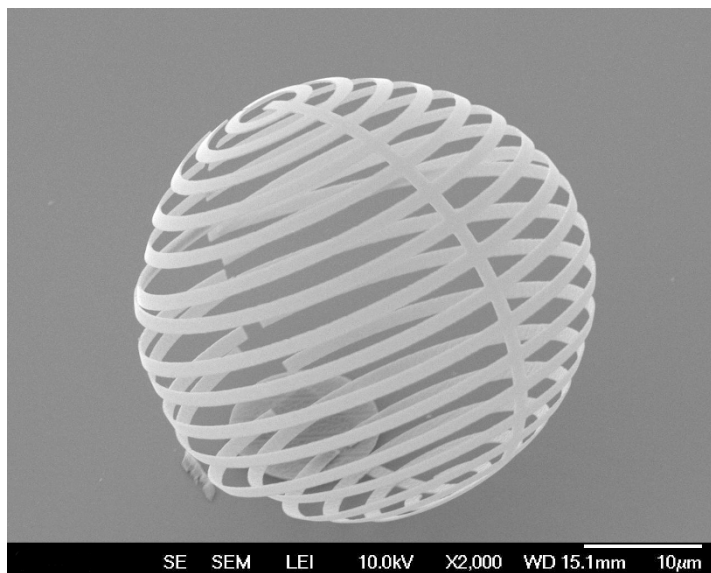


Fig. 31.6 The relaxed shape confirms that the geodesic curvature design relax as expected into constant latitude circles on the sphere.

covers the surface of the sphere with constant latitude ribbons, with only small alignment defects at the ends. Obviously, a large variety of different designs can be implemented but, as already stated, technological limitations associated with the photolithographic process (sharp angles) do not allow all of these designs to be successfully implemented.

31.6 Conclusions and Perspectives

The fabrication of nano-shells, is in itself a technological challenge as it encompasses the traditional planar technology. One way to obtain such structures is to release the pre-stressed nano-plates, fabricated by layer-by-layer deposition, to obtain a target shell geometry. The presence of several geometrical and technological restrictions can be circumvented by the use of three-dimensional thin ribbons in order to cover a desired surface. The geodesic curvature plays a fundamental role for the design of both the geometry of ribbons that cover arbitrary surfaces starting from planar structures and the pre-stress needed to obtain them. The main result shows that, for multilayered structures with weak-transversal homogeneity, if the curvature of the planar ribbon is equal to the geodesic curvature of the supporting curve then there exists a pre-stress such that a small-width and small-thickness planar ribbon relaxes toward a 3D ribbon covering the surface along the supporting curve. We illustrate our theoretical results by the design and fabrication of a partial cover of the sphere with

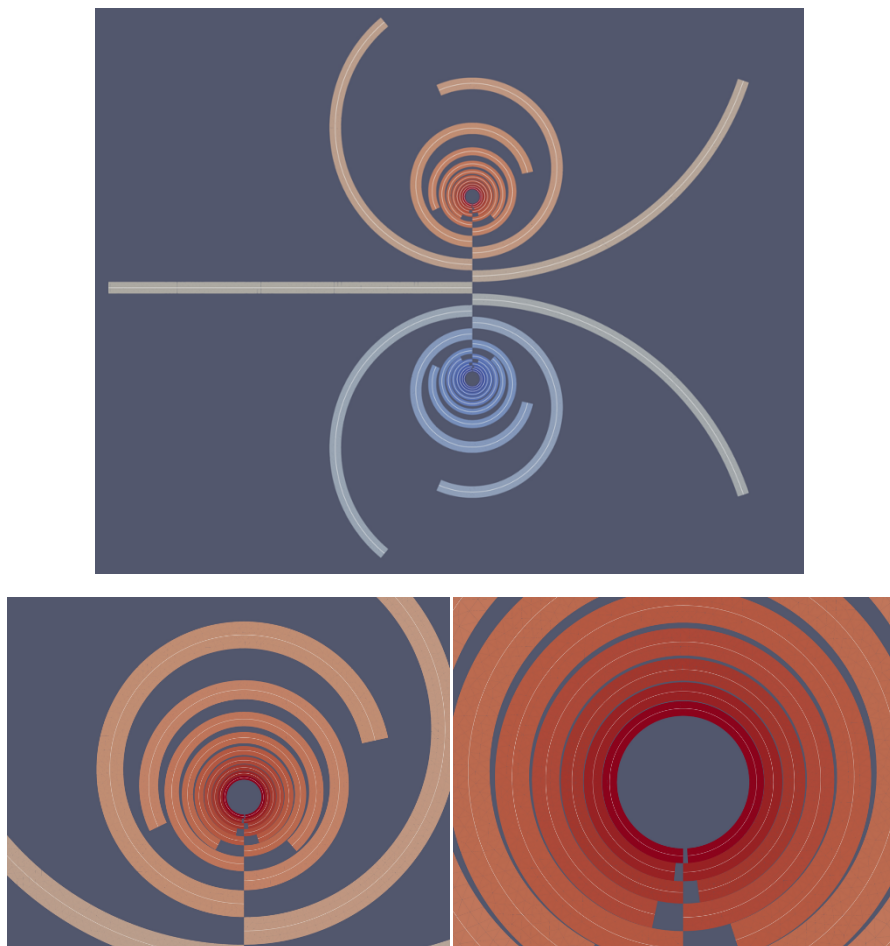


Fig. 31.7 Top: Optimal covering of the sphere for $\delta = 10^{-2}$. Alternative distribution of the constant latitude arcs on the left (respectively right) part of the initial design present in Fig. 31.2 to avoid sharp angles along the vertical symmetry axis. Bottom: zoom on the central zone.

constant-latitude ribbons starting from a planar design containing arcs with constant curvature and a bilayer semi-conductor bi-layer material with controlled composition ($\text{In}_{0.88}\text{Ga}_{0.12}\text{P}/\text{InP}$).

Extensions of these results to obtain a complete cover of the sphere are limited by the resolution of the lithographic process, difficult to implement at very sharp angles. A solution to overcome this technological drawback of the (sharp angles) lithographic process is illustrated in Fig. 31.7. Here, in order to avoid the sharp angles between successive ribbons located at constant latitude we chose to design alternative left and right constant radius arcs corresponding to successive constant latitude ribbons. The ideal picture in Fig. 31.7 does not include a small vertical segment, which is

nedded in order to attach the constant curvature arcs to the structure. In fact, the design in Fig. 31.7 contains exactly the same arcs as that of the Fig. 31.2 but their positions are such that sharp angles along the vertical symmetry line in Fig. 31.2 are avoided. However, a closer look to the design in Fig. 31.7, reveals very small distances between successive ribbons (also present in the initial design in Fig. 31.2 between large latitude ribbons).

The general results in Danescu and Ionescu (2021) provide solutions to both partial and total covers of other non-developable (orientable or not) three-dimensional surfaces as the torus and the Mobius ribbon, extending the classical setting of isometric transformations. We mention here two interesting extensions: the first one concerns the class of arbitrary transversal homogeneity (and not only weak transversal homogeneity) in which case one has to adapt the general setting in Danescu and Ionescu (2020). The second perspective concerns the fabrication of more complex geometries which require not only bending but also torsion, a problem already discussed in Danescu and Ionescu (2021) which is dependent to more complex (not only hydro-static) pre-stress. Controlled spatial modulation of the pre-stress, and in particular including controlled shear still remains a technological landmark at the nano-scale.

References

- de Benito Delgado M, Schmidt B (2020) Energy minimising configurations of pre-strained multilayers. *Journal of Elasticity* 140:1–33
- Ciarlet PG, Mardare C (2018) A nonlinear shell model of koiter's type. *Comptes Rendus Mathématique* 356(2):227–234
- Danescu A, Ionescu IR (2020) Shell design from planar pre-stressed structures. *Mathematics and Mechanics of Solids* 25(6):1247–1266
- Danescu A, Ionescu IR (2021) Non-developable shell-strips design from pre-stressed plate-strip. submitted, ArXiv preprint
- Danescu A, Chevalier C, Grenet G, Regreny P, Letartre X, Leclercq JL (2013) Spherical curves design for micro-origami using intrinsic stress relaxation. *Applied Physics Letters* 102(12):123,111
- Danescu A, Regreny P, Cremillieu P, Leclercq J (2018) Fabrication of self-rolling geodesic objects and photonic crystal tubes. *Nanotechnology* 29(28):285,301
- de Benito Delgado, Miguel, Schmidt, Bernd (2021) A hierarchy of multilayered plate models. *ESAIM: COCV* 27:S16
- Fosdick R, Fried E (2016) *The mechanics of ribbons and Möbius bands*. Springer
- Friesecke G, James RD, Müller S (2002a) A theorem on geometric rigidity and the derivation of nonlinear plate theory from three-dimensional elasticity. *Communications on Pure and Applied Mathematics: A Journal Issued by the Courant Institute of Mathematical Sciences* 55(11):1461–1506
- Friesecke G, Müller S, James RD (2002b) Rigorous derivation of nonlinear plate theory and geometric rigidity. *Comptes Rendus Mathématique* 334(2):173–178
- Friesecke G, James RD, Müller S (2006) A hierarchy of plate models derived from nonlinear elasticity by gamma-convergence. *Archive for rational mechanics and analysis* 180(2):183–236
- Le Dret H, Raoult A (1995) The nonlinear membrane model as variational limit of nonlinear three-dimensional elasticity. *Journal de mathématiques pures et appliquées* 74(6):549–578

- Lewicka M, Raoult A (2018) Thin structures with imposed metric. *ESAIM: Proceedings and Surveys* 62:79–90
- Prinz VY (2003) A new concept in fabricating building blocks for nanoelectronic and nanomechanic devices. *Microelectronic engineering* 69(2-4):466–475
- Prinz VY, Golod S (2006) Elastic silicon-film-based nanoshells: formation, properties, and applications. *Journal of Applied Mechanics and Technical Physics* 47(6):867–878
- Prinz VY, Seleznev V, Gutakovskiy A, Chehovskiy A, Preobrazhenskii V, Putyato M, Gavrilova T (2000) Free-standing and overgrown ingaas/gaas nanotubes, nanohelices and their arrays. *Physica E: Low-dimensional Systems and Nanostructures* 6(1-4):828–831
- Prinz VY, Grützmacher D, Beyer A, David C, Ketterer B, Deckardt E (2001) A new technique for fabricating three-dimensional micro-and nanostructures of various shapes. *Nanotechnology* 12(4):399
- Prinz VY, Naumova EV, Golod SV, Seleznev VA, Bocharov AA, Kubarev VV (2017) Terahertz metamaterials and systems based on rolled-up 3d elements: designs, technological approaches, and properties. *Scientific reports* 7:43,334
- Seleznev V, Yamaguchi H, Hirayama Y, Prinz V (2003) Single-turn GaAs/InAs nanotubes fabricated using the supercritical CO₂ drying technique. *Japanese journal of applied physics* 42(7A):L791
- Steigmann DJ (2007a) Asymptotic finite-strain thin-plate theory for elastic solids. *Computers & Mathematics with Applications* 53(2):287–295
- Steigmann DJ (2007b) Thin-plate theory for large elastic deformations. *International Journal of Non-Linear Mechanics* 42(2):233–240
- Steigmann DJ (2013) Koiter shell theory from the perspective of three-dimensional nonlinear elasticity. *Journal of Elasticity* 111(1):91–107
- Steigmann DJ, Ogden RW (2014) Classical plate buckling theory as the small-thickness limit of three-dimensional incremental elasticity. *ZAMM-Journal of Applied Mathematics and Mechanics/Zeitschrift für Angewandte Mathematik und Mechanik* 94(1-2):7–20
- Wang FF, Steigmann DJ, Dai HH (2019) On a uniformly-valid asymptotic plate theory. *International Journal of Non-Linear Mechanics* 112:117–125



Chapter 32

Experimental and Theoretical Investigations of Auxetic Sheet Metal

Arash Gordanshekan, Tobias Heib, Wolfgang Ripplinger,
Hans-Georg Herrmann, Stefan Diebels

Abstract This paper deals with the mechanical and thermal behavior of aluminum sheets with a rectangular perforation structure exhibiting an auxetic behaviour. The negative Poisson's ratio is basically achieved by the rigid rotation mechanism of the squares between the perforations. In this work uniaxial quasistatic tensile tests are carried out to characterize the perforation pattern. During the mechanical tests, the samples are observed simultaneously with an optical camera, used for Digital Image Correlation (DIC) to determine the local deformation fields, and passive thermography to visualize the heat evolution in the sample due to plastic deformation process. This led to the in situ thermomechanical characterization of the component and moreover to the determination of the effective material parameters such as Young's modulus, Poisson's ratio and thermoelastic constant. The results were then compared and validated by means of FEM simulations. Furthermore, the thermographic images were optimized in this work by using optical images to segment the sample from the background. These improved images were used to extract the temperature change due to plastic deformation to determine the yield stress.

Keywords: Auxetics · Continuum mechanics · Finite element method · Nondestructive testing · Perforated aluminum sheets · Thermomechanical simulation

A. Gordanshekan, W. Ripplinger, S. Diebels
Chair of Applied Mechanics, Saarland University, Campus A4 2, 66123 Saarbrücken, Germany
e-mail: arash.gordanshekan@uni-saarland.de, w.riplinger@mx.uni-saarland.de,
s.diebels@mx.uni-saarland.de

T. Heib
Chair of Lightweight Systems, Saarland University, Campus E3 1, 66123 Saarbrücken, Germany
e-mail: tobias.heib@uni-saarland.de

H.-G. Herrmann
Chair of Lightweight Systems, Saarland University, Campus E3 1, 66123 Saarbrücken, Germany
Fraunhofer IZFP Institute for Nondestructive Testing, Campus E3 1, Saarbrücken, 66123, Germany
e-mail: hans-georg.herrmann@izfp.fraunhofer.de

32.1 Introduction

Most natural materials are isotropic and characterized by a positive Poisson's ratio. Nevertheless, materials with negative Poisson's ratio can exist based on the classical theory of elasticity. Such materials are known as "auxetic" after Evans (1991), which means a lateral expansion in response to stretching, as well as a uniform and opposite densification in the compressed state (Lakes, 1987; He et al, 2005). From the requirement that the deformation energy of an isotropic elastic solid cannot become negative, it is concluded that the Poisson's ratio for a linear elastic isotropic material theoretically lies between -1 and 0.5 (Timoshenko, 1955).

Auxetic behavior can occur on different scales. On the molecular level, auxetic properties can be caused by a special microstructure, on the macro level by a suitable mechanism (Evans and Alderson, 2000; Prawoto, 2012; Stavroulakis, 2005). Pyrolytic graphite (Voigt, 1888), α -cristoblaite (Evans et al, 1991) and some biological tissues (Lees et al, 1991) are examples of such naturally occurring molecular auxetics. Artificial auxetic materials and structures are found much more frequently than natural ones, often as cellular materials such as honeycomb structures and foams, which are also called metamaterials (Lakes, 1993, 1987). The currently widespread topic of metamaterials refers not only to auxetics but also to a vast number of other materials whose mechanical properties are mainly caused by their complex geometry e.g. pantographic metamaterials (dell'Isola et al, 2015, 2019b). Design, manufacturing and modeling of the pantographic metamaterials are widely discussed especially in the works of Seppecher et al (2019); dell'Isola et al (2019a); dell'Isola and Steigmann (2020). Such man-made materials, which mostly exhibit an anisotropy in the macro-scale, can have any positive or negative values for the Poisson's ratio as long as the strain energy function is positive and it is not necessarily required for them to have a Poisson's ratio between -1 and 0.5 (Norris, 2006; Ting and Barnett, 2005).

Due to the cellular structures and the reduced density and the relatively improved mechanical properties of the auxetic structures such as higher shear modulus, enhanced load-carrying capacity, higher resistance to indentation, larger fracture toughness and enhanced vibration absorption, their applications are basically found in lightweight constructions and they are used specially as crash absorbers (Friedrich, 2017; Grima and Gatt, 2010; Lakes, 1987). Furthermore, auxetic geometries are increasingly finding their place in the development of novel products mostly in the fields of intelligent expandable actuators, shape memory structures and minimally invasive implantable devices (Scarpa et al, 2010; Bianchi et al, 2010). The fact that auxetic materials are no longer exotic but are already widely used is described, for example, in the paper of Seppecher et al (2019).

The structures that potentially exhibit auxetic behavior are divided into three main groups, namely "rotating unit structures" (Fig. 32.1a) proposed by Chetcuti et al (2014); Gatt et al (2015); Grima and Evans (2000), "chiral structures" (Fig. 32.1b) proposed by Scarpa et al (2007); Prall and Lakes (1997) and the most common and widely researched "re-entrant structures" such as auxetic honeycombs (Fig. 32.1c) proposed by Choi and Lakes (1992); Dong et al (2019), whose deformation mech-

anisms respectively are based on rotation, rolling up and unfolding of their cellular structures (Elipse and Lantada, 2012).

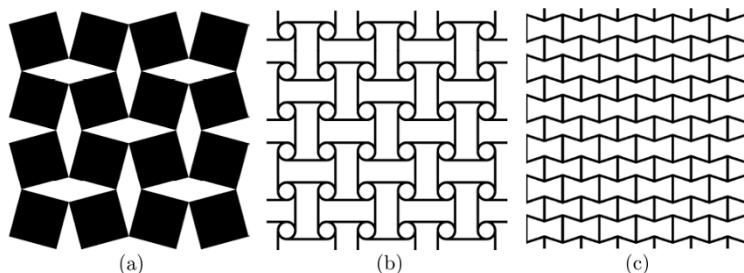


Fig. 32.1 Typical auxetic structures; a) rotating unit; b) chiral; c) re-entrant structures

Besides these relatively simple models there is a vast number of other auxetics with a more complex structure and deformation mechanism such as auxetic microporous and molecular polymers (Alderson and Evans, 1997), auxetic composites (Milton, 1992) and auxetic open-cell foam as the first auxetic material with irregular pattern (Lakes, 1987). Their deformation process is rather complex, however it can be simplified through the use of different models such as the nodule-fibre-model for auxetic molecular polymers or the rod-and-hinge model for auxetic composites.

By assuming that the macroscopic behavior of auxetic structures is essentially caused by their microstructure, the in situ-characterization of the component is of great importance. The mechanical and thermal behaviour of materials during the deformation can be coupled via thermomechanical investigations. Deformation is accompanied with heat transfer, which can vary depending on the material and strain rate. This is typical for Polymeric materials, such as elastomers, because of the high heat transfer to use such coupled thermomechanical calculation. However, based on a high thermal conductivity, metals show lower temperature changes (usually less than 1 °C). Therefore highly precise measurement techniques are required to perform coupled thermomechanical investigations (Lee and Chen, 1991). Lord Kelvin in 1851 (Swalin and Rice, 1963) has demonstrated for the first time that material becomes colder during elastic deformations, while during plastic deformations the heat dissipates and, accordingly, the material becomes warmer. This phenomenon, is also called the Joule Thomson effect, which is comparable to the ideal gas law (temperature decrease of a gas leads to increasing volume), only for solid materials. The minimum of this temperature evolution in a tensile test can be used to determine the yield point (Vitzthum et al, 2019).

In this work we investigate experimentally and numerically the in-plane thermo-mechanical characterization of deformation behavior of sheet metal with rectangular perforations, which belongs to the auxetic group “rotating unit structure” due to its deformation mechanism. The analysis is carried out by combination of digital image correlation (DIC) for measuring local strain fields and infrared thermography for measuring local temperature fields during the deformation process.

32.2 Material and Methods

32.2.1 Sample Material

In the present work, all the samples are made out of the aluminium alloy AlMg3 (EN AW-5754). Its mechanical properties as written in the technical datasheet are a Young's modulus of $E = 70$ GPa, a Poisson's ratio of $\nu = 0.34$ and a yield strength of $R_{0.2} = 80$ MPa. For the following experimental tests, these values were taken into account to set up the testing machine. Further properties are presented in the results section in Table 32.3. The AlMg3 alloy has excellent corrosion resistance also in seawater. Therefore this material is widely used in the maritime industry, constructions in railways, car body elements, pressure vessels and facade applications.

32.2.2 Perforated Aluminium Sheet

As shown in Fig. 32.2 the sheet metal of an aluminium alloy (AlMg3) has a regular pattern of rectangular perforations, which are perpendicular to each other. The perforations have been cut in the sheet by micro waterjet cutter. Waterjet cutting technology enables the production of such perforated metallic samples in small dimensions with optimal results in terms of dimensional accuracy and residual stresses. The plate consists of a cellular core area and two small solid areas at the two ends, each with five holes in it, which only contribute to clamping the specimen in the testing machine and are not taken into account in the data evaluation. To calculate the volume fraction of perforations (V_p) in the sheet, only one unit cell should be considered because of the periodicity. This can be determined as Eq.32.1:

$$V_p = 4 \frac{A_p}{A_{uc}} = \frac{4ab}{(a + b + 2c)^2} \quad (32.1)$$

where a is the length, b the width and c the distance of the perforations. A_p and A_{uc} represent area of a single perforation and area of the unit cell respectively. The auxetic sheet metal used in this study has the parameters $a = 10$ mm, $b = 2$ mm, $c = 2$ mm and thickness of 1 mm, which results an aspect ratio of $AR = \frac{a}{b} = 5$ and according to Eq.32.1 a porosity of $V_p = 31\%$. Ripplinger et al (2018) have demonstrated the significant influence of aspect ratio of rectangular perforation on the effective mechanical behavior of such auxetic structures with the same volume fraction of perforations.

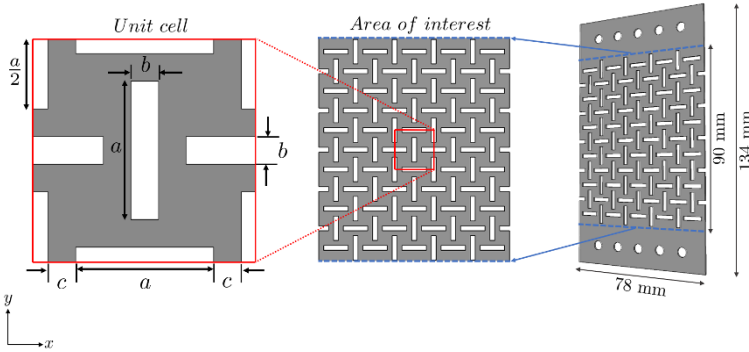


Fig. 32.2 AlMg3 Sheet sample with rectangular perforations including corresponding geometry parameters. From left to right: unit cell with rectangular perforation, measurement area of the sample, full sample including clamping area. All perforations have the same dimensions (a , b) and distance to its neighbours (c) within the entire sheet.

32.2.3 Experimental Setup

In a first step tensile tests of bulk samples are performed. A universal material testing machine ElectroPuls™ E10.000 of Ltd. Instron, Pfungstadt, Germany equipped with a ± 10 kN and ± 100 Nm Dynacell load sensor was used. The tensile specimens were prepared according to DIN 50125-E. For evaluating the local deformation of the sample and therefore the Poisson's ratio an optical camera for digital image correlation is used. For this reason one side of the specimen is first coated with a frosted white spray paint followed by a black speckle pattern.

In a second step tensile tests of the auxetic samples are performed. A biaxial testing machine with a ± 25 kN loadcell (ME measuring systems KD9363s, Hennigsdorf, Germany) was used. The machine is self developed by the Chair of Applied Mechanics at Saarland University¹. One speciality are the synchronised electrical axis, which deform the sample on both sides of the clamping simultaneously in such a way, that the middle of the sample stays stationary during the whole test. The further setup consists of an optical camera (Manta MG-235B, Allied Vision, Stadroda, Germany) used for digital image correlation and a thermography camera (Infratec Variocam HD, Dresden, Germany). The optical camera with a resolution of 1920×1200 pixels is equipped with a 12.5 mm lens (Fujifilm HF12.5SA-1, Minato, Japan). On the other hand the thermography camera has a spectral range from 7.5 to 14 μm and a resolution of 1024×768 pixels. Both cameras are aligned in one axis facing their lenses to each other. In the middle the sample is positioned. To minimize the influence of temperature from the surrounding and the optical camera in combination with the illumination, a glass pane is placed between the sample and the camera. In the spectral range of the thermographic camera nearly the whole thermal radiation is absorbed. The setup for these experiments is displayed in Fig. 32.3. The test routine

¹ <https://www.youtube.com/watch?v=C0KcvnHf6Wc>

is set up in discrete deformation steps with a constant deformation rate. For each deformation step the testing machine is sending a trigger signal to the optical and the thermal camera. Meanwhile, the current load and position are recorded.

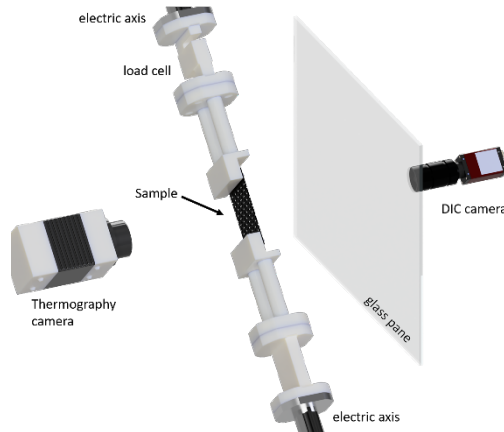


Fig. 32.3 Experimental setup for tensile tests with stationary sample, DIC camera and thermography camera.

32.2.4 Sample Preparation

Optical and thermographic camera systems have different requirements to the surface finish of the sample. For performing digital image correlation with the optical camera the sample background has to be homogeneous in a dull matt colour while the stochastic speckle pattern has a high contrast to the background. A white primer spray paint is used for the background to get a good adhesion on the rolled aluminum surface, even when the sample is highly deformed. The speckle patterns are made with a black acrylic spray paint and must be distributed stochastically and as finely as possible on the surface to achieve higher resolution. In order to have the correct gray value contrast, the ratio of 30%-black 70%-white should be kept.

On the other side, the thermographic camera has as well the requirement of a homogeneous surface. Furthermore, it is necessary to have a low reflecting surface. Therefore this side of the sample is painted with a black varnish, called Tetenal Kameralack (Tetenal, Norderstedt, Germany), with a emissivity of $\epsilon = 0.97$ (Silva et al, 2019).

32.3 Results and Discussion

32.3.1 Mechanical Properties of Bulk AlMg3

The experiments were started with a displacement controlled and quasi-static uniaxial tensile test on a bulk AlMg3-sample at room temperature. The mechanical properties of the bulk sample primarily provided the input values for FE-modeling of the associated auxetic sample. They also present basic values for later comparison with their auxetic counterparts. The resulting stress-strain curve is shown in Fig. 32.4. The Young's modulus was determined by a self-developed MATLAB[®]-Tool, which is based on an advanced tangent method and provides the value with minimal error. The first step in this method is to gather a set of measurement data points within the elastic range from the stress-strain curve, where the tangent moduli deviates the least from the mean value. These are the data points which successively show the maximum linearity. The intersection point of the line drawn through this data point set and the x-axis is used as the new origin to calculate the secant moduli. Finally, the value of Young's modulus is obtained as the average value of the secant moduli of this data set. Transverse strain to determine Poisson's ratio was calculated using DIC. The resulting material parameters are shown in Table 32.1.

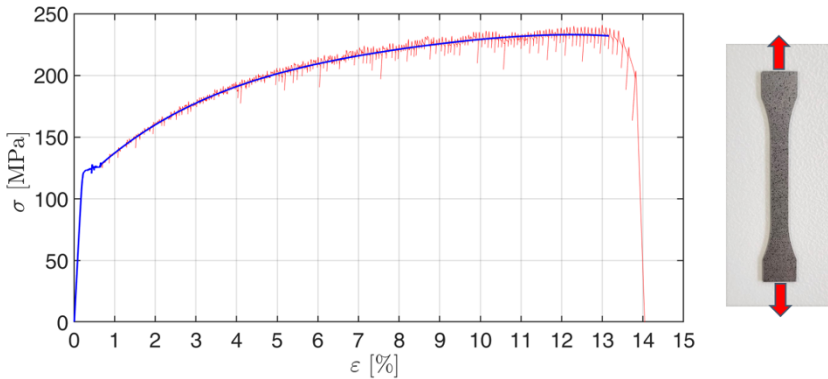


Fig. 32.4 Stress-strain curve of the bulk AlMg3-sample with noisy experimental data (red) and low-pass filtered data (blue)

Table 32.1 Material parameters of bulk AlMg3

| Young's modulus | Yield stress | Poisson's ratio | Ultimate stress | Fracture strain |
|-----------------|--------------|-----------------|-----------------|-----------------|
| 60.04 GPa | 119.6 MPa | 0.33 | 233.86 MPa | 13.87% |

32.3.2 Experiment on the Auxetic Sheet

The uniaxial strain-controlled tensile test was performed quasi-static at room temperature and a strain rate of $\dot{\epsilon} = 0.0025 \text{ s}^{-1}$. As mentioned in Section 32.1 the auxetic structure used in this study belongs to the group of “rotating unit structures”. This is due to the special nature of its deformation mechanism. As shown in Fig. 32.5, when the auxetic sheet is loaded, the squares surrounded between the perforations rotate while retaining their original shape. In order to evaluate this phenomenon more accurately, the principal strains of the unit cell at the center of the plate were calculated using DIC, as shown in Fig. 32.9. The results show that the plate does not experience any elongation within the area of the squares, which confirms that the squares do not undergo any deformations but a rigid body rotation upon loading. The direction of rotation of the squares caused by the uniaxial tension allows the sheet to expand in both directions. This leads to the auxetic behavior in the sheet metal.

The observations of deformed and non-deformed areas in the sample can be proven with electron backscatter diffraction (EBSD) as a part of a scanning electron microscope (SEM). In Fig. 32.6 two images of inverse pole figures are shown. In the left image the measured area is in the middle of the rotating square. The different grain orientations can be identified. Furthermore, in each grain the color is homogeneous, which is an indicator for a non deformed texture. In contrast to that, in the right image the probed area is between the rotating squares. Besides the grain orientations, in each grain a color gradient is visible. Due to plastic deformation the lattice parameters change slightly and differ from the reference lattice which was used to register the grain orientation.

In addition to this information the grain size can be identified in the range of $10 \mu\text{m}$ to $50 \mu\text{m}$.

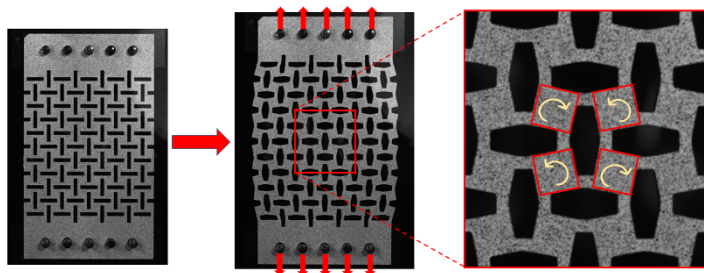
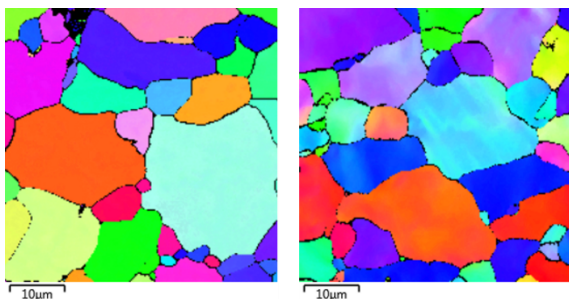


Fig. 32.5 Representation of rotating squares responsible for the auxetic behavior in deformed state.

Concerning the mechanical properties of the auxetic sheet and as shown in Fig. 32.7, the stress-strain curve in contrast to the bulk AlMg3 develops continuously from the elastic range to the plastic range without showing any Lüders strain. In this case a self-developed MATLAB[®]-Tool was used to determine the more precise yield point by analytically calculating the second derivative at each data point

Fig. 32.6 Inverse pole figure of an area in the middle of the square of the red square (left) and in the area of the small section between the rotating squares (right).



on the fitted transition curve and selecting the data point as the yield point at which the absolute value of second derivative is a maximum. For calculation of the Young’s modulus, the advanced tangent method was also used here, as for bulk AlMg3. The resulting material parameters of auxetic sheet are shown in Table 32.2

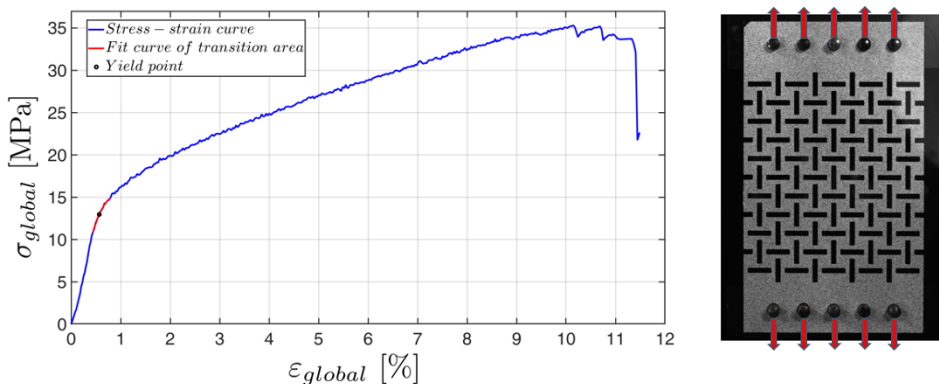


Fig. 32.7 Low-pass filtered stress-strain curve of auxetic sheet metal in blue. Fit curve for the computation of the yield point in red.

Table 32.2 Material parameters of auxetic sheet metal

| Young’s modulus | Yield stress | Ultimate stress | Fracture strain |
|-----------------|--------------|-----------------|-----------------|
| 2.63 GPa | 12.98 MPa | 35.32 MPa | 10.67% |

DIC was used to determine the local strain fields both in the axial and in the transverse direction. The commercial DIC software ISTR4D V4.4 by Dantec Dynamics (Skovlunde, Denmark) was employed for post-processing and visualization of the displacements during the deformation. The local displacements in both directions at a deformation of 10% global strain are shown in Fig. 32.8. To determine

the effective Poisson's ratio, the difference in the mean displacements of all material points in opposite edges of the specimen was calculated and then divided by their initial distance. It should be noted that the calculated Poisson's ratio by this method is basically influenced by the boundary effects in the clampings of the sample.

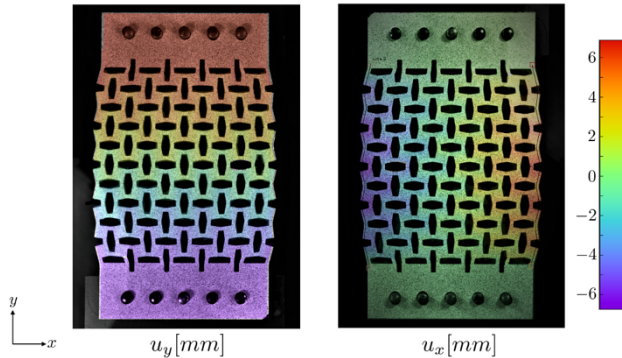


Fig. 32.8 Local displacement fields after approx. 10% of global strain. The widening of the specimen in transversal direction can clearly be seen.

In order to eliminate the boundary effects and to represent the Poisson's ratio in an infinite system, the displacements of a unit cell in the center of the sheet were then observed upon the tensile test. The course of deformation of the unit cell is shown incrementally in Fig. 32.9. The resulting Poisson's ratios in both cases of global and local evaluation during deformation are shown in Fig. 32.10 and indicate that the maximum auxetic effect occurs in the center of the sheet, where the boundary effects have the least influence. It should also be noted that the boundary effects increase with increasing deformation, so that the minimum auxetic behavior occurs by the consideration of Poisson's ratio over the edges and especially at large deformation.

Thermography was used to determine the local temperature fields and to monitor the damage evolution in the material. As a non-destructive testing method, passive thermography, can be used in situ during a mechanical loading test, as shown by (Summa et al, 2018). As the sample is made of an aluminum alloy with a high thermal conductivity and numerous perforations, it is hard to distinguish between the sample and the background in the thermograms. Therefore in this paper a method is developed to use the thermographic information in combination with the optical images to get more usefully thermograms. The single steps are shown exemplary in Fig. 32.11 and 32.12 for an image at the end of the tensile test with a global deformation of approx. 10%. All image processing steps are performed with a self-developed MATLAB[®]-Tool. As the lenses of both cameras are facing each other (see Fig. 32.3) with the sample in the middle, they record a similar region. This algorithm, developed by the author, was already used in (Klein et al, 2021). Only one image is mirrored from one to the other. It is assumed that the heat generation

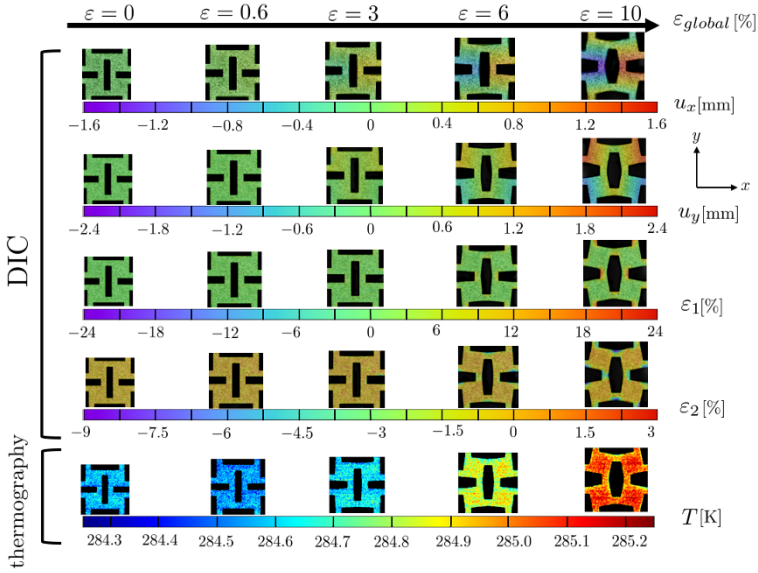


Fig. 32.9 Local displacements, principal strains and temperature changes of the unit cell at the center of the sheet during the tensile test.

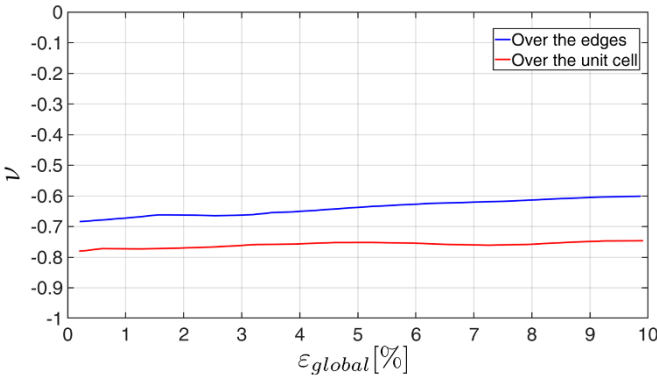


Fig. 32.10 Resulting Poisson's ratio during deformation up to 10% of global strain. The maximum auxetic effect can be observed in the center of the sample using a local evaluation of the Poisson's ratio.

and deformation of the sample is the same on both faces, due to the small sample thickness of only 1 mm.

At first, the optical images are corrected. In Fig. 32.11 (a) the original image is shown. The optical axis of the camera is not perfectly perpendicular to the sample surface, which can be recognised by the perspective distortion of the upper and lower edges. They are not parallel to each other. To correct this distortion two boundaries are set. First, it is necessary that the sample is a flat sheet and second, the real geometry of the sample is rectangular with known dimensions (length, width). All four edge points of the sample are selected and registered to a rectangular geometry with the dimensions of the real sample. Then, the projective mapping is done with the help of the “image processing toolbox” in MATLAB[®]. The result is shown in step (b). For reducing data in step (c) the image is cropped to a region of interest with the perforated area. For matching the thermographic and optical image the displayed image was flipped along the vertical axis to get the illusion that both cameras seem to be on the same side.

In the following procedure, the thermographic images are processed. The original image is shown in Fig. 32.12 (a) in false colors from blue (low temperature) to yellow (high temperature). As both cameras have a different resolution for their combination a common coordinate systems is required. In Fig. 32.12 (b) the thermography image is set to the same coordinate system as the optical image, in their resolution and position. The following step (c) is a binarization of the last image in Fig. 32.11, with the sample as a white level and the background in black. By a multiplication of the images (b) and (c) the final processing is done. Step (d) shows the sample with temperature information and the fade out of the background. These processing steps are done for each image.

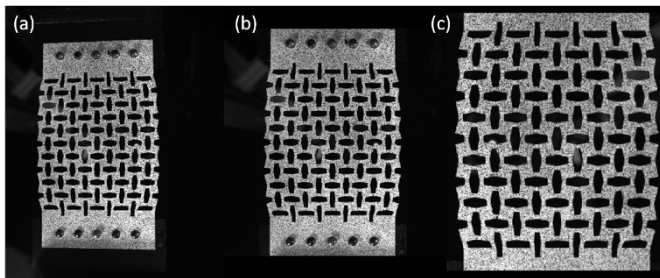


Fig. 32.11 Processing of optical camera data with MATLAB[®]. (a) original image; (b) image after perspective correction; (c) cropped and mirrored image.

With these results it is possible to determine the temperature evolution during the tensile test. The results are already shown in Fig. 32.9. In the first picture of the thermography row at $\varepsilon_{global} = 0\%$ the sample is unloaded and in an equilibrium state with the surrounding. With rising displacement, in a first step the sample gets colder. The deformation mechanism is predominated by elastic deformation, which is energy consuming from the surroundings. This is the so-called thermoelastic effect.

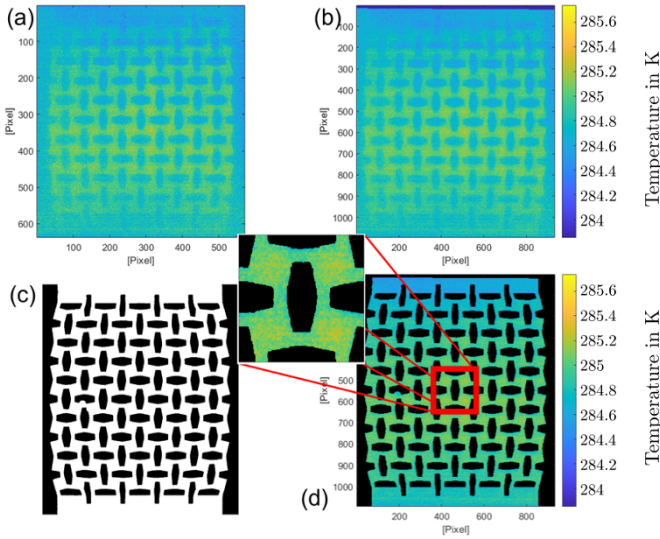


Fig. 32.12 Processing of thermography data with MATLAB[®]. All images are displayed in false colors representing the temperature. (a) original thermogram; (b) thermogram with adjusted coordinate system; (c) binarized optical image; (d) final thermogram obtained by multiplication of (b) and (c) and section of the middle unit cell.

In the further development of the test the dominating deformation mechanism is changing to plastic deformation. As can be seen the sample temperature is rising until the end of the test, at $\varepsilon_{global} = 10\%$. In contrast to the localized strains (ε_1 and ε_2), the temperature doesn't show localized higher values at the small seams. Instead the temperature seems to be lower in these areas than in the squares. A possible reason for this behaviour is the high thermal conductivity of the aluminum alloy. While heat is generated in the small cross-sections due to plastic deformation, in the larger sections no heat generation occurs. Conduction is the main mode, in which the energy is transferred from warmer to colder areas. Besides generated heat can dissipate by convection with the surrounding, which has a lower energy level.

As already mentioned, the high thermal conductivity of AlMg3 restricts a localized temperature distribution during the quasi-static tensile test. By calculating the mean temperature change in comparison to the first image of the experiment we get a strain-temperature curve that can be overlaid with the strain-stress data. Both curves are shown in Fig. 32.13. In the beginning of this section the mechanical parameters of the auxetic sheet are calculated by traditional techniques of the experimental mechanics (see Table 32.2). With the combination of thermographic and mechanical data by using the thermoelastic effect we can use a new method to determine the yield point. This point is defined by the beginning of the plastic deformation and corresponds with the minimum of the temperature deviation curve.

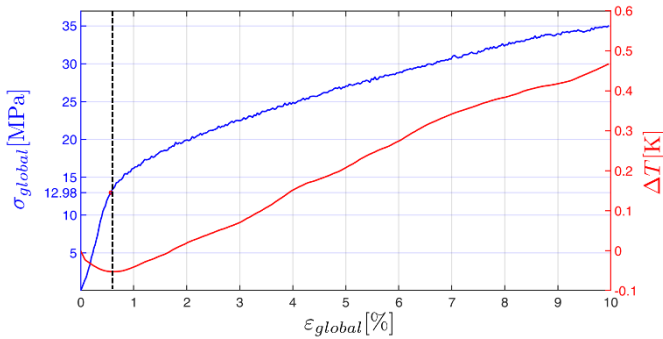


Fig. 32.13 Consideration of the thermoelastic effect to determine the yield point.

32.3.3 Simulation

The purpose of the before mentioned experiments is to generate specific parameters of an auxetic structure that can be used to develop a material model, e.g. for finite element simulations.

In order to compare the experimental results of the deformation and temperature evolution a coupled temperature-displacement FEM-simulation is generated with ABAQUS[®] (Dassault Systems, United States). As a model the whole sample is loaded into the software tool with a 3D geometry. The element type C3D8T (8-node thermally coupled brick, trilinear displacement and temperature) with a seed size of 0.5 is used. The load is applied on each side of the sample on the five holes which are in direct contact with the fixtures of the machine. To be comparable to the deformation rate of $\dot{\epsilon} = 0.0025 \text{ s}^{-1}$ a boundary condition with a displacement of 5 mm for each side and a step time of 84 s is set.

For the material model a large number of parameters are necessary. The basic parameters are listed in Tables 32.3 and 32.4. Values of the Young's modulus, Poisson's ratio and for the plastic deformation are used from the experiments in Section 32.3.1. Further properties are taken by literature (Gleich, 2020; Pottier et al, 2011). As the surface of the sample in the real experiment is painted with a black camera varnish the emissivity is considered to 0.97 corresponding to Silva et al (2019). Since this is a first coupled temperature-displacement FEM-simulation of an auxetic aluminum sheet, several assumptions are made. The convection between the surrounding air and the sample surface, as well as the heat transfer by conduction from the sample to the clamping are out of scope. Both limitations may lead to higher temperature values than in the experiment.

In Fig. 32.14 a comparison of the nodal temperature change in the FEM simulation and the thermographic image at the end of the tensile test at 10% global deformation is shown. It is interesting to note that both images look similar even under the strong assumptions made for the simulation. In both images the heat evolution has a higher level in the middle of the sample and gets lower in the directions of the clamping.

Table 32.3 Input Parameters for the thermomechanical simulation.

| Parameter | Value |
|-------------------------|--|
| Young’s modulus | 60.04 GPa |
| Mass density | $2.67 \times 10^{-9} \text{ t mm}^{-3}$ |
| Poisson’s ratio | 0.33 |
| Thermal conductivity | $145 \text{ mJ s}^{-1} \text{ mm}^{-1} \text{ K}^{-1}$ |
| Thermal expansion | $2.39 \times 10^{-5} \text{ K}^{-1}$ |
| Specific heat | $9 \times 10^9 \text{ mJ t}^{-1} \text{ K}^{-1}$ |
| Inelastic heat fraction | 0.65 |

Table 32.4 Input Parameters for the hardening simulation of the auxetic sheet obtained from the experiment results of the bulk sample instead of using a classic plasticity model.

| True stress (MPa) | True plastic strain |
|-------------------|---------------------|
| 119.64 | 0 |
| 126.24 | 0.004151 |
| 158.40 | 0.017051 |
| 195.00 | 0.041381 |
| 227.84 | 0.093941 |
| 232.7 | 0.127941 |

Higher plastic deformation leads to higher temperatures. Due to the clamping in the upper and lower areas, the auxetic behaviour and therefore the plastic deformation is restrained. By comparing the maximum temperature change of the middle unit cell, the one with the highest degree of free deformation, the simulation shows a temperature rise of 0.94 K, while the thermogram shows up 0.50 K. These differences can be explained by convection, non-exact material parameters and an uncertainty of the thermographic camera.

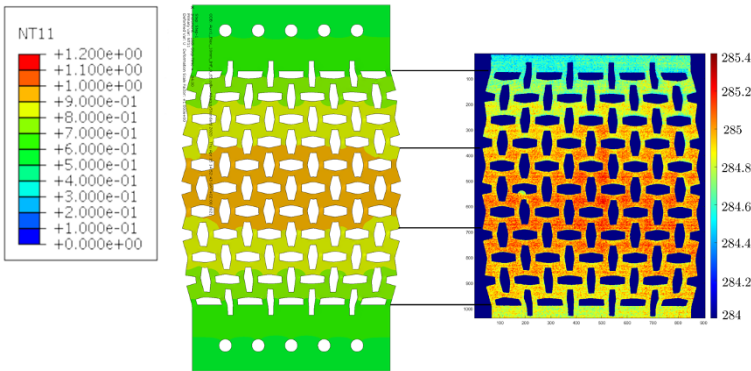


Fig. 32.14 Simulated nodal temperature change and thermogram at 10% of global strain.

The global stress-strain curve from the simulation was calculated analogously to the experiment. In this regard the simulation results are in a acceptable accordance with the experimental results according to Fig. 32.15. The small deviations between the simulation and the experiment can be justified because of the idealized situation in the simulation with respect to the edges, clamping areas as well as the homogeneity of the material in the whole sample. in addition, the local von Mises stresses in the

sheet metal at 10% of global strain is also shown in Fig. 32.15. The results indicate that the maximum stresses occur in the thin areas between the squares and the minimum stresses in the area of the squares. In the center of the squares, the stresses are even close to zero. These were to be expected based on the local strain fields calculated by DIC shown in Fig. 32.9.

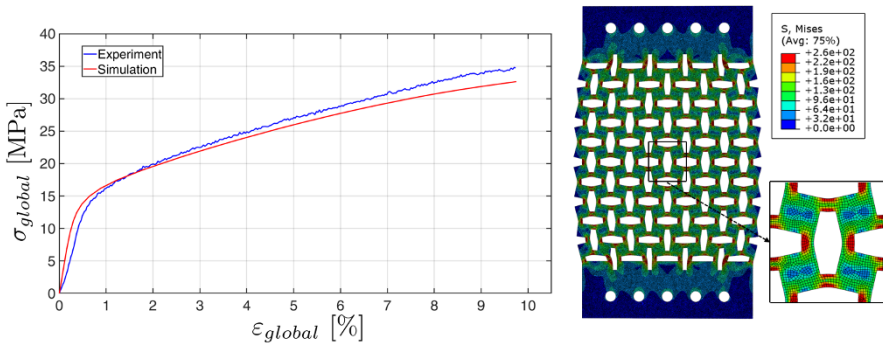


Fig. 32.15 Global stress-strain curves from simulation and experiment (left) and local von Mises stresses (in MPa) at 10% of global strain (right).

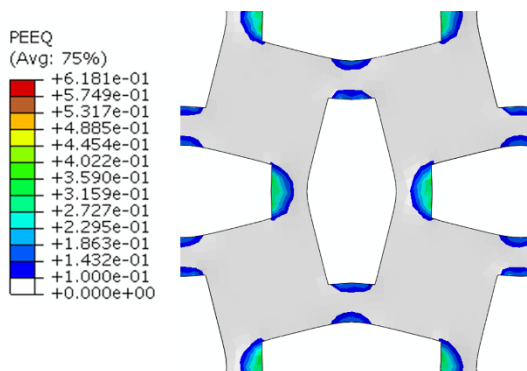
In Fig. 32.16 the equivalent plastic strain is presented, which is a scalar variable that is used to represent the material's inelastic deformation. If this value is greater than zero, the material is above its yielding point. In the figure only values greater than zero are displayed in color. In order to compare the plastic deformed areas with those of the DIC Analysis in Fig. 32.9, they are the same. When monitoring of the sample condition is the aim, the highly deformed edges may lead to cracks by further deformation.

Future work will also investigate the natural convection with the surroundings to reproduce the real experiment even more accurate.

32.4 Conclusion

The aim of this study is to extend current knowledge of the deformation behaviour of the auxetic sheets with rectangular perforations made of aluminum alloy. The combination of DIC and thermography during the tensile test expressed the correlation between deformation and heat transport in the specimen successfully. For this purpose, a method was proposed to determine the yield point by considering the thermoelastic effect in the specimen, which showed a good agreement with the analytically calculated yield point. In addition, the in situ micromechanical deformation mechanism was investigated by identifying the deformed and non-deformed areas in the sample. The effective material parameters such as Young's modulus, Poisson's

Fig. 32.16 Simulation result of the equivalent plastic strain (PEEQ) at 10% of global strain.



ratio, etc. were carefully calculated, which can be used as reference values for later comparison of the specimens with different aspect ratio, cell size and pattern orientation angle. They are also used as the specific parameters for the development of the corresponding macroscopic material model. To validate the experimental results, a coupled temperature-displacement finite element simulation was performed. The measured parameters of the bulk material were used for the material model. Temperature evolution and plastic deformation were compared with the real experiments, which were in a good agreement with each other.

The results obtained in this work serve as a basis for understanding the deformation behavior of such rotating unit structures for their extended 2.5D or 3D cases such as shell structures and tubes, respectively. Future works will concentrate on the variation of aspect ratio and the resulting anisotropy in these auxetic structures is investigated explicitly. Finally it is intended to develop an effective 2D or 3D elastoplastic material model for the considered auxetic sheet metal. Moreover, further non-destructive testing methods, like ultrasound and computer tomography, will be used to inspect the sample before and after a tensile test with respect to cracking or geometry changes.

Acknowledgements The authors gratefully acknowledge the funding by Deutsche Forschungsgemeinschaft (Grant No. HE7079/6-1, DI430/32-1).

References

- Alderson A, Evans K (1997) Modelling concurrent deformation mechanisms in auxetic microporous polymers. *Journal of materials science* 32(11):2797–2809
- Bianchi M, Scarpa F, Smith C (2010) Shape memory behaviour in auxetic foams: mechanical properties. *Acta Materialia* 58(3):858–865
- Chetcuti E, Ellul B, Manicaro E, Brincaat JP, Attard D, Gatt R, Grima JN (2014) Modeling auxetic foams through semi-rigid rotating triangles. *physica status solidi (b)* 251(2):297–306
- Choi J, Lakes R (1992) Non-linear properties of polymer cellular materials with a negative Poisson's ratio. *Journal of Materials Science* 27(17):4678–4684

- dell'Isola F, Steigmann DJ (2020) *Discrete and Continuum Models for Complex Metamaterials*. Cambridge University Press
- dell'Isola F, Giorgio I, Andreus U (2015) Elastic pantographic 2d lattices: a numerical analysis on the static response and wave propagation. *Proceedings of the Estonian Academy of Sciences* 64(3):219
- dell'Isola F, Giorgio I, Placidi L, Spagnuolo M, Peyre P, Dupuy C, Dirrenberger J, Pawlikowski M, Igumnov LA (2019a) Pantographic metamaterials: A view towards applications. *Materials Physics and Mechanics* 42:637–645
- dell'Isola F, Seppacher P, Alibert JJ, Lekszycki T, Grygoruk R, Pawlikowski M, Steigmann D, Giorgio I, Andreus U, Turco E, et al (2019b) Pantographic metamaterials: an example of mathematically-driven design and of its technological challenges. *Continuum Mechanics and Thermodynamics* 31(4):851–884
- Dong Z, Li Y, Zhao T, Wu W, Xiao D, Liang J (2019) Experimental and numerical studies on the compressive mechanical properties of the metallic auxetic reentrant honeycomb. *Materials & Design* 182:108,036
- Elipe JCÁ, Lantada AD (2012) Comparative study of auxetic geometries by means of computer-aided design and engineering. *Smart Materials and Structures* 21(10):105,004
- Evans KE (1991) Auxetic polymers: a new range of materials. *Endeavour* 15(4):170–174
- Evans KE, Alderson A (2000) Auxetic materials: functional materials and structures from lateral thinking! *Advanced materials* 12(9):617–628
- Evans KE, Nkansah M, Hutchinson I, Rogers S (1991) Molecular network design. *Nature* 353(6340):124–124
- Friedrich HE (2017) *Leichtbau in der Fahrzeugtechnik*. Springer-Verlag
- Gatt R, Mizzi L, Azzopardi JJ, Azzopardi KM, Attard D, Casha A, Briffa J, Grima JN (2015) Hierarchical auxetic mechanical metamaterials. *Scientific reports* 5(1):1–6
- Gleich (2020) Technical datasheet -EN AW 5754. Gleich Aluminiumwerk GmbH u. Co. KG
- Grima JN, Evans KE (2000) Auxetic behavior from rotating squares. *Materials Science Letters* 19:1563–1565
- Grima JN, Gatt R (2010) Perforated sheets exhibiting negative Poisson's ratios. *Advanced engineering materials* 12(6):460–464
- He C, Liu P, McMullan PJ, Griffin AC (2005) Toward molecular auxetics: Main chain liquid crystalline polymers consisting of laterally attached para-quaterphenyls. *physica status solidi (b)* 242(3):576–584
- Klein S, Heib T, Herrmann HG (2021) Estimating thermal material properties using step-heating thermography methods in a solar loading thermography setup. *Applied Sciences* 11(16)
- Lakes R (1987) Foam structures with a negative Poisson's ratio. *Science* 235:1038–1041
- Lakes R (1993) Advances in negative Poisson's ratio materials. *Advanced Materials* 5(4):293–296
- Lee HT, Chen JC (1991) Temperature effect induced by uniaxial tensile loading. *Journal of Materials Science* 26(21):5685–5692
- Lees C, Vincent JF, Hillerton JE (1991) Poisson's ratio in skin. *Bio-medical materials and engineering* 1(1):19–23
- Milton GW (1992) Composite materials with Poisson's ratios close to—1. *Journal of the Mechanics and Physics of Solids* 40(5):1105–1137
- Norris AN (2006) Poisson's ratio in cubic materials. *Proceedings of the Royal Society A: Mathematical, Physical and Engineering Sciences* 462(2075):3385–3405
- Pottier T, Toussaint F, Louche H, Vacher P (2011) Experimental estimation of the inelastic heat fraction from thermomechanical observations and inverse analysis. In: *Thermomechanics and Infra-Red Imaging*, Volume 7, Springer New York, pp 33–37
- Prall D, Lakes R (1997) Properties of a chiral honeycomb with a Poisson's ratio of—1. *International Journal of Mechanical Sciences* 39(3):305–314
- Prawoto Y (2012) Seeing auxetic materials from the mechanics point of view: a structural review on the negative Poisson's ratio. *Computational Materials Science* 58:140–153
- Ripplinger W, Schwarz M, Diebels S, Herrmann HG (2018) Auxetic aluminum sheets in lightweight structures. *Materials Testing* 60(11):1071–1076

- Scarpa F, Blain S, Lew T, Perrott D, Ruzzene M, Yates J (2007) Elastic buckling of hexagonal chiral cell honeycombs. *Composites Part A: Applied Science and Manufacturing* 38(2):280–289
- Scarpa F, Jacobs S, Coconnier C, Toso M, Di Maio D (2010) Auxetic shape memory alloy cellular structures for deployable satellite antennas: design, manufacture and testing. In: *EPJ Web of Conferences*, EDP Sciences, vol 6, p 27001
- Seppacher P, Spagnuolo M, Barchiesi E, Hild F, Lekszycki T, Giorgio I, Placidi L, Andraus U, Cuomo M, Eugster SR, et al (2019) Advances in pantographic structures: design, manufacturing, models, experiments and image analyses. *Continuum Mechanics & Thermodynamics* 31(4):1231–1282
- Silva AR, Vaz M, Leite S, Mendes J (2019) Non-destructive infrared lock-in thermal tests: Update on the current defect detectability. *Russian Journal of Nondestructive Testing* 55(10):772–784
- Stavroulakis G (2005) Auxetic behaviour: appearance and engineering applications. *physica status solidi (b)* 242(3):710–720
- Summa J, Becker M, Grossmann F, Pohl M, Stommel M, Herrmann HG (2018) Fracture analysis of a metal to cfrp hybrid with thermoplastic interlayers for interfacial stress relaxation using in situ thermography. *Composite Structures* 193:19–28
- Swalin RA, Rice SA (1963) Thermodynamics of solids. *Physics Today* 16(1):72
- Timoshenko S (1955) *Strength of Materials.-1: Elementary Theory and Problems*. Van Nostrand
- Ting T, Barnett D (2005) Negative Poisson's ratios in anisotropic linear elastic media. *Applied Mechanics* 72(6):929–931
- Vitzthum S, Hartmann C, Eder M, Volk W (2019) Temperature-based determination of the onset of yielding using a new clip-on device for tensile tests. *Procedia Manufacturing* 29:490–497
- Voigt W (1888) Bestimmung der Elasticitätsconstanten von Flussspath, Pyrit, Steinsalz, Sylvin. *Annalen der Physik* 271(12):642–661



Correction to: Theoretical Analyses, Computations, and Experiments of Multiscale Materials

Ivan Giorgio , Luca Placidi , Emilio Barchiesi ,
Bilen Emek Abali , and Holm Altenbach 

Correction to:
I. Giorgio et al. (eds.), *Theoretical Analyses, Computations, and Experiments of Multiscale Materials*, Advanced Structured Materials 175, <https://doi.org/10.1007/978-3-031-04548-6>

The book was inadvertently published with incorrect author name in XML, which has now been corrected in Chapters 4, 5, and 10. The book has been updated with the change.

The updated version of these chapters can be found at
https://doi.org/10.1007/978-3-031-04548-6_4
https://doi.org/10.1007/978-3-031-04548-6_5
https://doi.org/10.1007/978-3-031-04548-6_10

© The Author(s), under exclusive license to Springer Nature Switzerland AG 2022
I. Giorgio et al. (eds.), *Theoretical Analyses, Computations, and Experiments of Multiscale Materials*, Advanced Structured Materials 175,
https://doi.org/10.1007/978-3-031-04548-6_33